FAA CENTER OF EXCELLENCE FOR ALTERNATIVE JET FUELS & ENVIRONMENT

Annual Technical Report

2021

For the period

October 1, 2020 – September 30, 2021

Boston University
Georgia Institute of Technology
Massachusetts Institute of Technology
Missouri University of Science and Technology
Oregon State University
Pennsylvania State University
Purdue University
Stanford University
University of Dayton
University of Hawaii
University of Illinois
University of North Carolina
University of Pennsylvania
University of Tennessee
University of Washington
Washington State University

This work was funded by the US Federal Aviation Administration (FAA) Office of Environment and Energy as a part of ASCENT Project AJFE under FAA Award Number 13-C. Any opinions, findings, and conclusions or recommendations expressed in this material are those of the authors and do not necessarily reflect the views of the FAA or other ASCENT Sponsors.

Table of Contents

Overview

This report covers the period October 1, 2020, through September 30, 2021. The Center was established by the authority of FAA solicitation 13-C-AJFE-Solicitation. During that time the ASCENT team launched a new website, which can be viewed at ascent.aero. The next meeting will be held April 5-7, 2022, in Alexandria, VA.

Over the last year, the ASCENT team has made great strides in research, outreach, and education. The team's success includes the following:

- **64 active research projects.**

The projects are divided into five main categories: tools, operations, noise, emissions, and alternative fuels, with cross-cutting research in aircraft technology innovation and supersonics. See the project category descriptions for more detail on each category and a summary of the projects. Funding for these projects comes from the FAA in partnership with Transport Canada. Note that projects 001, 059 and 065 include several separately funded projects within a single project number. An individual report section is provided for each of these funded "sub-projects" and are titled Projects 001A-001E, 059A-059E, and 65A-B.

- **117 publications, reports, and presentations by the ASCENT team.**

Each project report includes a list of publications, reports, and presentations. A comprehensive list of the publications, reports, and presentations for all projects is available in the publications index.

- **202 students participated in aviation research with the ASCENT team.**

ASCENT research projects were supported by 179 graduate students and 23 undergraduate students.
Each project report includes the names and roles of the graduate and undergraduate students in the investigator's research. Students are selected by the investigators to participate in this research.

- **62 industry partners involved in ASCENT.**

ASCENT's industry partners play an important role in the Center. Five new industry partners joined the Advisory Board in 2021. Advisory Board members provide insight into the view of stakeholders, advice on the activities and priorities of the Center's co-directors, and ensure research will have practical application. The committee does not influence FAA policy. Industry partners also play a direct role in some of the research projects, providing matching funds, resources and expertise to the project investigators.

Leadership

Dr. Michael Wolcott
Center Director and Technical Lead for Alternative Jet Fuels Research
Washington State University
(509) 335-6392
wolcott@wsu.edu

Dr. R. John Hansman
Center Co-Director and Technical Lead for Environmental Research
Massachusetts Institute of Technology
(617) 253-2271
rjhans@mit.edu

Dr. Jonathan Male
Federal Research Laboratories and Agency Liaison
Jonathan.male@pnnl.gov

Dr. James Hileman
Chief Scientific and Technical Advisor for Environment and Energy
Office of Environment and Energy
Federal Aviation Administration
james.hileman@faa.gov

Research Topics

Research projects within ASCENT are divided into five categories: alternative fuels, emissions, noise, operations, tools, aircraft technology innovation and supersonics. The list below includes all ASCENT funded research projects. This report includes research on active projects only. Reports for projects marked as COMPLETE are available on the ASCENT website at: https://ascent.aero/project/.

Alternative Fuels

The development of alternative jet fuels (AJFs) -- or sustainable aviation fuels (SAF) -- is of great interest to an array of aviation stakeholders, including aircraft and engine manufacturers and airlines. Alternative fuels that are produced from bio-based materials provide sustainable jet fuel alternatives that not only help alleviate environmental impacts from aviation emissions but can also create jobs in rural areas and lessen our reliance on foreign petroleum supplies.

Effective research and development, co-funded by the federal government and industry, enables SAF development by reducing the costs of producing renewable fuel. ASCENT research provides the scientific expertise and data to evaluate the environmental benefits associated with these sustainable fuels. ASCENT's collaborative R&D activities focuses on evaluating promising sustainable aviation fuel pathways to ensure environmental and social benefits, reduce technical uncertainties, inform aviation emission policies, and promote private sector investment in production.

Projects include:

- 001A-F - Alternative Jet Fuel Supply Chain Analysis
- 025 - National Jet Fuels Combustion Program – Area #1: Chemical Kinetics Combustion Experiments
- 026 - (COMPLETE) - National Jet Fuels Combustion Program – Area #2: Chemical Kinetics Model Development and Evaluation
- 027 - (COMPLETE) National Jet Fuels Combustion Program – Area #3: Advanced Combustion Tests
- 028 - (COMPLETE) National Jet Fuels Combustion Program – Area #4: Combustion Model Development and Evaluation
- 029A - National Jet Fuels Combustion Program – Area #5: Atomization Tests and Models
- 030 - (COMPLETE) National Jet Fuels Combustion Program – Area #6: Referee Swirl-Stabilized Combustor Evaluation/Support
- 031 - Alternative Jet Fuels Test and Evaluation
- 032 – (COMPLETE) - Worldwide LCA of GHG Emissions from Petroleum Jet
- 033 - Alternative Fuels Test Database Library
- 034 - National Jet Fuels Combustion Program – Area #7: Overall Program Integration and Analysis
- 052 - Comparative Assessment of Electrification Strategies for Aviation
- 065 - Fuel Testing Approaches for Rapid Jet Fuel Prescreening
- 066 - Evaluation of High Thermal Stability Fuels
- 067 - Impact of Fuel Heating on Combustion and Emissions
- 073 - Combustor Durability with Alternative Fuel Use

Emissions

The demand for passenger and cargo air transportation has grown rapidly over the last several decades. According to the International Air Transport Association (IATA), in 2016 there were 3.8 billion air travelers, a number it predicts will rise to 7.2 billion passengers by 2035—a near doubling of current levels. This staggering growth is accompanied by airport expansions and increases in emissions from aircraft, ground services equipment, and vehicle traffic on and near airports. The increases in these activity-based emissions impact the air quality around airports, cumulatively contribute to global climate change, and can negatively affect human health.

ASCENT researchers are analyzing data and improving predictive models to understand the effects of aircraft and ground vehicle emissions, create and refine emission-based analytical techniques at both airport-specific and global scales, and assess how policy changes affect emissions and its impacts.

Projects include:

- 002 - Ambient Conditions Corrections for Non-Volatile PM Emissions Measurements
- 013 - (COMPLETE) - Micro-Physical Modeling & Analysis of ACCESS 2 Aviation Exhaust Observations
- 014 - (COMPLETE) - Analysis to Support the Development of an Aircraft CO2 Standard

- 018 - Community Measurement of Aviation Emission Contribution of Ambient Air Quality
- 019 - Development of Improved Aviation Emissions Dispersion Capabilities for AEDT
- 020 - (COMPLETE) - Development of NAS wide and Global Rapid Aviation Air Quality
- 021 - (COMPLETE) - Improving Climate Policy Analysis Tools
- 022 - Evaluation of FAA Climate Tools
- 024 - (COMPLETE) - Emissions Data Analysis for CLEEN, ACCESS, and Other Recent Tests
- 039 – (COMPLETE) - Naphthalene Removal Assessment
- 047 - Clean Sheet Supersonic Aircraft Engine Design and Performance
- 048 - Analysis to Support the Development of an Engine nvPM Emissions Standard
- 051 - Combustion Concepts for Next-Generation Aircraft Engines
- 052 - Comparative Assessment of Electrification Strategies for Aviation
- 058 - Improving Policy Analysis Tools to Evaluate Higher-Altitude Aircraft Operations
- 064 - Alternative Design Configurations to Meet Future Demand
- 067 - Impact of Fuel Heating on Combustion and Emissions
- 068 - Combustor Wall Cooling Concepts for Dirt Mitigation
- 069 - Transitioning a Research nvPM Mass Calibration Procedure to Operations
- 070 - Reduction of nvPM emissions via innovation in aero-engine fuel injector design
- 071 - Predictive Simulation of nvPM Emissions in Aircraft Combustors
- 074 - Low Emissions Pre-Mixed Combustion Technology for Supersonic Civil Transport

Noise

ASCENT researchers work to understand all aspects of the aircraft operations that contribute to aviation's noise impact. They are working on understanding how aircraft and rotorcraft performance and operation affect noise generation and how they could be modified for mitigation measures. Research is also under way to look how noise propagates from the source to the ground and how it affects human health, wellbeing, and quality of life. This research will improve the modeling tools used to estimate the noise impacts from aviation operations and provide data to inform policy development as well as public engagement and education.

Projects include:

- 003 - Cardiovascular Disease and Aircraft Noise Exposure
- 004 - (COMPLETE) - Estimate of Noise Level Reduction
- 005 - (COMPLETE) - Noise Emission and Propagation Modeling
- 007 - (COMPLETE) - Civil, Supersonic Over Flight, Sonic Boom (Noise) Standards Development
- 008 – (COMPLETE) - Noise Outreach
- 009 - Geospatially Driven Noise Estimation Module
- 017 – (COMPLETE) -Pilot Study on Aircraft Noise and Sleep Disturbance
- 038 – Rotorcraft Noise Abatement Procedures Development
- 040 – Quantifying Uncertainties in Predicting Aircraft Noise in Real-world Situations
- 041 – Identification of Noise Acceptance Onset for Noise Certification Standards of Supersonic Airplane
- 042 – (COMPLETE) Acoustical Mode of Mach Cut-off
- 043 – Noise Power Distance Re-Evaluation
- 044 - Aircraft Noise Abatement Procedure Modeling and Validation
- 049 - Urban Air Mobility Noise Reduction Modeling
- 050 - Over-Wing Engine Placement Evaluation
- 053 - Validation of Low Exposure Noise Modeling by Open Source Data Management and Visualization Systems Integrated with AEDT
- 055 - Noise Generation and Propagation from Advanced Combustors
- 057 - Support for Supersonic Aircraft En-route Noise Efforts in ICAO CAEP
- 059A-E - Modeling and Measurements of Supersonic Civil Transport Jet Noise
- 061 – Noise Certification Streamlining
- 062 - Noise Model Validation for AEDT
- 063 - Parametric Noise Modeling for Boundary Layer Ingesting Propulsors
- 072 - Aircraft noise exposure and market outcomes in the US
- 075 - Improved Engine Fan Broadband Noise Prediction Capabilities
- 076 - Improved Open Rotor Noise Prediction Capabilities

Operations

Aviation operations result in fuel burn, emissions, and noise impacts. The nature and scale of these effects depends on a number of related factors, including:

- Aircraft flight paths and profiles,
- Schedule and frequency of operations, and
- Aircraft fleet mix.

ASCENT research focuses on identifying and accelerating the implementation of operational concepts that will reduce aviation environmental impacts and/or improve energy efficiency while maintaining the efficiency of the National Airspace System. The research spans multiple phases of flights and targets all environmental impact areas.

Projects include:

- 006 - (COMPLETE) - Rotorcraft Noise Abatement Operating Conditions Modeling
- 015 - (COMPLETE) - Cruise Altitude and Speed Optimization
- 016 - (COMPLETE) - Airport Surface Movement Optimization
- 023 - Analytical Approach for Quantifying Noise from Advanced Operational Procedures
- 038 - Rotorcraft Noise Abatement Procedures Development
- 044 - Aircraft Noise Abatement Procedure Modeling and Validation
- 053 - Validation of Low Exposure Noise Modeling by Open Source Data Management and Visualization Systems Integrated with AEDT
- 077 - Measurements to Support Noise Certification for UAS/UAM Vehicles and Identify Noise Reduction Opportunities

Tools

The aviation system operation involves complex interactions between many different components when aircraft are on the ground, taking off, in the air, and when landing. Aviation system operations also require the understanding of how to optimize aviation activities, which is best done by implementing advanced modeling tools.

The Federal Aviation Administration's suite of modeling tools have been developed to characterize and quantify the interdependences of aviation-related noise and emissions, impacts on human health and welfare, and the costs and market impacts to industry and consumers under varying policies, technologies, operations and market scenarios.

The ASCENT researchers are further developing and expanding the capabilities of these modeling tools in a variety of ways, from improving the way basic physical properties are represented and effectively modeled to how new technologies will enter the aircraft fleet and identifying the benefits of such technologies.

Projects include:

- 009 - Geospatially Driven Noise Estimation Module
- 010 - Aircraft Technology Modeling and Assessment
- 011 - (COMPLETE) - Rapid Fleet-wide Environmental Assessment Capability
- 012 - (COMPLETE) - Aircraft Design and Performance Assessment Tool Enhancement
- 035 - (COMPLETE) - Airline Flight Data Examination to Improve flight Performance Modeling
- 036 - (COMPLETE) - Parametric Uncertainty Assessment for AEDT2b
- 037 – CLEEN II Technology Modeling and Assessment
- 040 - (COMPLETE) - Quantifying Uncertainties in Predicting Aircraft Noise in Real-world Situations
- 043 - Noise Power Distance Re-Evaluation (NPD+C) to Include Airframe Noise in AEDT
- 045 – (COMPLETE) Takeoff/Climb Analysis to Support AEDT APM Development
- 046 – Surface Analysis to Support AEDT APM Development
- 049 - Urban Air Mobility Noise Reduction Modeling
- 053 - Validation of Low Exposure Noise Modeling by Open Source Data Management and Visualization Systems Integrated with AEDT
- 054 - AEDT Evaluation and Development Support
- 058 - Improving Policy Analysis Tools to Evaluate Higher-Altitude Aircraft Operations
- 060 - Analytical Methods for Expanding the AEDT Aircraft Fleet Database

- 062 - Noise Model Validation for AEDT
- 064 - Alternative Design Configurations to meet Future Demand

Aircraft Technology Innovation

The evolution of airframes and engines has resulted in modern designs that significantly reduce aviation fuel use, emissions and noise on a per-flight basis. ASCENT researchers conduct the analyses, modeling and testing required to demonstrate the viability of innovative airframe, engine and flight management technologies that reduce noise, emissions, and fuel burn. Future innovations will drive further improvements and the ASCENT research helps accelerate technology development.

Projects include:

- 010- Aircraft Technology Modeling and Assessment
- 037 - CLEEN II System Level Assessment
- 047 - Clean Sheet Supersonic Aircraft Engine Design and Performance
- 050 - Over-Wing Engine Placement Evaluation
- 051 - Combustion Concepts for Next-Generation Aircraft Engines
- 052 - Comparative Assessment of Electrification Strategies for Aviation
- 055 - Noise Generation and Propagation from Advanced Combustors
- 056 - Turbine Cooling through Additive Manufacturing
- 059 - Modeling and Measurements of Supersonic Civil Transport Jet Noise
- 063 - Parametric Noise Modeling for Boundary Layer Ingesting Propulsors
- 064 - Alternative Design Configurations to Meet Future Demand
- 066 - Evaluation of High Thermal Stability Fuels
- 067 - Impact of Fuel Heating on Combustion and Emissions
- 068 - Combustor Wall Cooling with Dirt Mitigation
- 070 - Reduction of nvPM emissions via innovation in aero-engine fuel injector design
- 071 - Predictive Simulation of Soot Emission in Aircraft combustors
- 074 - Low Emissions Pre-Mixed Combustion Technology for Supersonic Civil Transport
- 075 - Improved Engine Fan Broadband Noise Prediction Capabilities
- 076 - Improved Open Rotor Noise Prediction Capabilities
- 077 - Measurements to Support Noise Certification for UAS/UAM Vehicles and Identify Noise Reduction Opportunities

Supersonics

ASCENT supersonics research supports implementation of new technologies by advancing the understanding of the perception of sonic boom noise over a range of sonic boom levels, assessing Mach cut-off levels that will allow supersonic flight over land and furthering development of supersonic aircraft noise certification standards.

Projects include:

- 007 (COMPLETE) - Civil, Supersonic Over Flight, Sonic Boom (Noise) Standards Development
- 010- Aircraft Technology Modeling and Assessment
- 022 - Evaluation of FAA Climate Tools
- 041 - Identification of Noise Acceptance Onset for Noise Certification Standards of Supersonic Airplanes
- 042 - (COMPLETE) Acoustical Model of Mach Cut-off
- 047 - Clean Sheet Supersonic Aircraft Engine Design and Performance
- 057 - Support for Supersonic Aircraft Noise Efforts in ICAO CAEP
- 058 - Improving Policy Analysis Tools to Evaluate Aircraft Operations in the Stratosphere
- 059 - Jet Noise Modeling to Support Low Noise Supersonic Aircraft Technology Development
- 074 - Low Emissions Pre-Mixed Combustion Technology for Supersonic Civil Transport

Project 050 Over-Wing Engine Placement Evaluation

Georgia Institute of Technology

Project Lead Investigator

Principal Investigator
Professor Dimitri N. Mavris
Director, Aerospace Systems Design Laboratory
School of Aerospace Engineering
Georgia Institute of Technology
Phone: (404) 894-1557
Fax: (404) 894-6596
Email: dimitri.mavris@ae.gatech.edu

Co-Principal Investigator
Dr. Chung Lee
Research Engineer
Aerospace Systems Design Laboratory
School of Aerospace Engineering
Georgia Institute of Technology
Phone: (404) 894-0197
Fax: (404) 894-6596
Email: chung.h.lee@ae.gatech.edu

University Participants

Georgia Institute of Technology

- PI: Dr. Dimitri Mavris; Co-PI: Dr. Chung Lee
- FAA Award Number: 13-C-AJFE-GIT-057
- Period of Performance: February 5, 2020 to June 4, 2022
- Tasks relevant for this period:
  1. Architecting design strategy
  2. Select aero-propulsion integration method
  3. Create aircraft mission and engine models
  4. Reduce dimensionality using active subspace methods
  5. Perform computational fluid dynamics (CFD) grid sensitivity analysis
  6. Complete first stage design study (nacelle location selection)
  7. Create Aircraft Noise Prediction Program (ANOPP) noise surrogate models

Project Funding Level

The Georgia Institute of Technology (Georgia Tech) was funded at $590,000 for a two-year project and has agreed to a total of $590,000 in matching funds. This total includes salaries for the project director, research engineers, and graduate research assistants, as well as computational, financial, and administrative support, including meeting arrangements. The institute has also agreed to provide tuition remission for the students, paid for by state funds.

Investigation Team

PI: Dimitri Mavris
Co-Investigator: Chung Lee
Aerodynamics and parametric geometry: Jai Ahuja, Srujal Patel, Kenneth Decker
Multidisciplinary Design Analysis and Optimization (MDAO) methods: Christian Perron
Mission and systems integration: Evan Harrison

Graduate students: Mengzhen Chen, Sam Crawford, Marc Koerschner, Bilal Mufti, James Van der Linden, Anish Vegesna

Project Overview

The over-wing nacelle (OWN) aircraft concept has promising environmental benefits due to shielding of engine noise by the wings and the potential to reduce landing gear height and therefore gear noise. However, if not optimized, engine placement in OWN aircraft may cause penalties in fuel burn due to aerodynamic interactions between the wing and propulsor. Our project involves developing a multidisciplinary analysis and optimization (MDAO) method for OWN aircraft. This task builds on past efforts by including noise shielding effects and analyzing multiple flight conditions to minimize fuel burn. One major challenge in this project is the computational expense of analyses such as CFD. Our approach relies on MDAO and efficient adaptive sampling techniques to use high fidelity analyses only where they are most needed for system analysis.

The optimization of an OWN aircraft configuration over a mission with noise constraints will enable accurate assessments of the tradeoffs between noise benefits and fuel burn. As a secondary benefit, the MDAO method will demonstrate efficient sampling methods for coupled, computationally intensive simulations in system analysis. These methods are useful to the FAA because many current applications require high-fidelity simulations to accurately assess physical phenomena such as noise and emissions. Both the OWN results and the MDAO techniques used here will enable more physics-informed decisions about the environment.

The 2020 work focused on preliminary tasks to prepare a software tool chain and workflow for optimization, and in 2021, it focused on executing a full-scale MDAO process using supercomputing resources. The 2021 project thus focused on a two-stage design process: nacelle location selection followed by preliminary shape optimization of the wing and nacelle. Over the first six months of 2022, we will finish the optimization analysis, integrate aero-propulsion with mission and systems, and conduct supporting studies of detailed design sensitivities and scenarios.

We emphasized two major themes in our 2021 research methodology: 1) a more controlled comparison of OWN vs. under-wing nacelle (UWN) and 2) careful accounting for numerical uncertainty.

A more controlled comparison of OWN and UWN

Uncertainty in the physics code dominated the MDAO and research strategies. There can be significant discrepancies between un-calibrated CFD predictions and the flight performance of actual vehicles. Therefore, in the absence of validation data, it would be uninformative or misleading to compare the CFD-based performance of an optimized OWN vehicle with that of actual UWN vehicles. In addition to the physics discrepancy, there is an inconsistency in that the MDAO problem for OWN has only been studied for two years, whereas the UWN configuration has been refined by the aircraft industry for around seventy years!

The present OWN study cannot practically include additional aspects of design physics such as flight mechanics, static and dynamic structural constraints, nacelle geometry constraints due to acoustical liners and de-icing components, and pylon aero-thermo-structural mechanics. However, this can result in OWN performance that is overly optimistic due to an under-constrained problem formulation. It can lead to unrealistic conclusions about OWN compared to traditional UWN.

The goal is to provide FAA stakeholders with evidence to assess the intrinsic aero-propulsive advantages and disadvantages of OWN and UWN aircraft. It is impossible to pose a perfectly controlled experiment. However, we adopted a “drag race” approach in which we optimized OWN and UWN vehicles under the same MDAO formulation. This is an important decision in study methodology: it halves the computational budget available to optimize each configuration but leads to a more controlled comparison and more credible conclusions.

Uncertainty is a key theme

During our 2021 research, we found that careful quantification of uncertainty is crucial to avoiding misleading or less credible conclusions about the benefits of OWN. There are no relevant empirical data for the direct validation or calibration of OWN or even UWN with powered turbofan engines. However, even controlling the numerical uncertainties due to CFD or MDA is important. We have incorporated such uncertainty tracking into the optimization strategy itself. For example, we avoid optimization or adaptive sampling below an “uncertainty floor” of the physics code.

We found that much of the recent published literature on OWN relied on CFD meshes on the order of 0.8 to 30 million cells or nodes. Different CFD meshes and solvers have different dependences between mesh density and solution accuracy. For

example, solvers may be either node-centered or cell-centered, and different solvers will have different orders of formal accuracy due to their different computational stencils. Variation in user skill can also lead to different accuracy given similar cell counts. Nonetheless, most previous academic and industry studies have not included mesh sensitivity studies or accounted for the numerical uncertainty due to the mesh. This of critical importance. For example, there is a risk of reporting a "-1% Δfuel burn benefit of OWN vs. UWN," even though the uncertainty is much greater than 1%.

Careful attention to valid OWN vs UWN comparison and numerical uncertainty thus informed much of the detailed work in our 2021 tasks. We believe that such a research strategy prevents us from making a simplistic performance comparison between the two configurations and will instead yield more credible and complex conclusions that can inform FAA stakeholders about the potential environmental impacts of each configuration.

Details of 2021 tasks are described in following sections.

Notation and Abbreviations

α: angle of attack
ANN: artificial neural network
C_D: drag coefficient
C_L: lift coefficient
CFD: computational fluid dynamics
CRM: NASA Common Research Model
η_{pr}: inlet pressure recovery
MDAO: multidisciplinary design analysis and optimization
OWN: over-wing nacelle
p_{s2}: static pressure at inlet
p_{t8}: total pressure at core nozzle exit
p_{t18}: total pressure at bypass nozzle exit
T_{t8}: total temperature at core nozzle exit
T_{t18}: total temperature at bypass nozzle exit
UWN: under-wing nacelle
O( ): order of magnitude

Task 1 - Architecting of Design Process

Georgia Institute of Technology

Objective(s)

The overall goal is to design a problem architecture for multidisciplinary analysis and optimization (MDAO) to assess a single-aisle OWN transport aircraft. The MDAO process will use CFD, noise analysis codes such as ANOPP, as well as weights, engine cycle, and mission analysis. The formulation was stated in the first year of the project and has evolved during the project due to physics results. However, the working MDAO problem statement was adopted:

- **Minimize** fuel burn for a baseline mission
- **Subject to** design variables including aircraft range, takeoff field length, and detailed side constraints
- **With respect to** design variables including engine nacelle position (focusing on forward placement), nacelle and wing geometry, engine cycle, and operating condition
- **Given** a baseline single-aisle aircraft model and mission profile
- **Returning** fuel burn and noise

In discussion with FAA technical advisors, it was decided to place more emphasis on aerodynamic performance optimization rather than noise reduction, which is necessarily of lower fidelity. Thus, the single objective function in our MDAO problem statement is minimizing fuel burn, but noise is still evaluated as a response with respect to design variables. It is anticipated that the MDAO problem will undergo several iterations as more information accumulates, so noise may be later treated as a constraint or secondary objective.

Research Approach

Aerodynamics is the most computationally expensive physics discipline, coupled closely with propulsion cycle analysis. Therefore, the 2021 efforts were focused on the most important aero-propulsion aspects of MDAO, which drive the overall architecture of the problem.

Preliminary aero-propulsion subset of the MDAO problem:

Minimize	fuel burn
With respect to	geometry, angle of attack α, and engine mass flow
Given	fixed engine cycle design and throttle assumptions; no pylon
Subject to	continuity (mass flow balance between inlet and outlet)
	momentum balance (e.g., lift = weight, thrust = drag in steady level flight)
	interdisciplinary consistency:
	inlet pressure recovery $p_{t2,CFD} = p_{t2,cycle\ analysis}$
	core nozzle total pressure $p_{t8,CFD} = p_{t8,cycle\ analysis}$
	core nozzle total temperature $T_{t8,CFD} = T_{t8,cycle\ analysis}$
	bypass nozzle total pressure $p_{t18,CFD} = p_{t18,cycle\ analysis}$
	bypass nozzle total temperature $T_{t18,CFD} = T_{t18,cycle\ analysis}$
Returning	fuel burn

Two-Stage Design Strategy

The geometry design variables included 45 shape parameters for the nacelle and wing, which were reduced to smaller dimensions in a task described later in this report. Due to the curse of dimensionality (or the rapid increase in computational expense with increased dimensionality), the MDAO process was staged into two distinct steps:

- Stage 1: Commit to a nacelle location based on an "open-loop" aero-propulsion parametric optimization
- Stage 2: Perform MDAO of nacelle and wing shape given the fixed nacelle location

Stage 1 Strategy

Stage 1 assumed a fixed Y (spanwise) location for the nacelle because that location is typically optimized using structural analysis. The nacelle location plays a major role in relieving both static and dynamic loads on the wing. The baseline geometry for this study is the NASA Common Research Model (CRM) scaled to a typical 150-pax size [Vassberg et al, 2008]. Because structural analysis is beyond the scope of the project, we conservatively defaulted the spanwise location to that of the scaled CRM.

Stage 1 used a parametric optimization approach. We defined f as an objective function of parameter or scenario variables and "choice" variables:

$$f = f(\underline{\mathbf{X}}_{parameter}, \underline{\mathbf{X}}_{choice})$$

In this case, $\underline{\mathbf{X}}_{parameter}$ are the nacelle locations ($x_{nacelle}$, $y_{nacelle}$) following the coordinate directions in Figure 1. $\underline{\mathbf{X}}_{choice}$ are more detailed shape variables. The goal of parametric optimization is to minimize f with respect to $\underline{\mathbf{X}}_{choice}$ for any instance of $\underline{\mathbf{X}}_{parameter}$. In other words, we aimed to provide a map of aero-propulsive performance over locations ($x_{nacelle}$, $y_{nacelle}$) while sufficiently optimizing the shape at each location. The intent was to "give a fair shake" to potential nacelle locations by conducting

balanced optimization for each. The cartoon in Figure 2 shows notionally that there is a grid or DoE of settings for $\underline{\mathbf{X}}_{parameter}$. For each instance of $\underline{\mathbf{X}}_{parameter}$, there is a search in the direction of $\underline{\mathbf{X}}_{choice}$ to find the particular optimum.

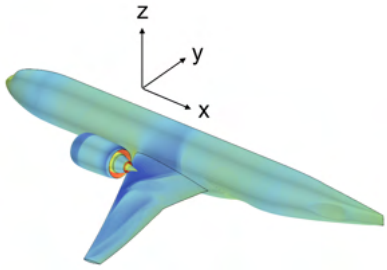

Figure 1. Coordinate system.

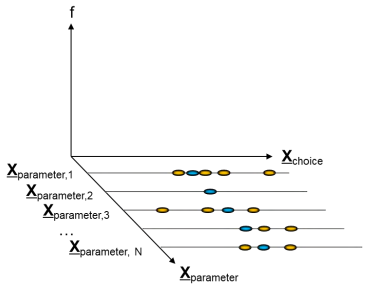

Figure 2. Cartoon representation of parametric optimization
(Adaptive sampling typically began with a "warm-start" of blue seed points).

An equally weighted sum of the lift-to-drag ratio (L/D) and the excess thrust (normalized to a reference case) was used as the objective function *f*. To limit the number of analysis iterations, this initial study used open-loop aero-propulsion MDA. Iterative looping (Gauss-Seidel) or similar procedures were not used to tightly enforce interdisciplinary consistency between a propulsion cycle analysis and CFD aerodynamics.

The Stage 1 parametric optimization was performed with a Bayesian adaptive sampling technique. This approach sequentially fit a Gaussian Process or kriging model and added new sample points according to an acquisition function or infill criterion. In our case, we used the expected improvement (EI) infill criterion. EI has been described by previous literature such as Jones, Schonlau, and Welch (1998) and is shown notionally in Figure 3 below.

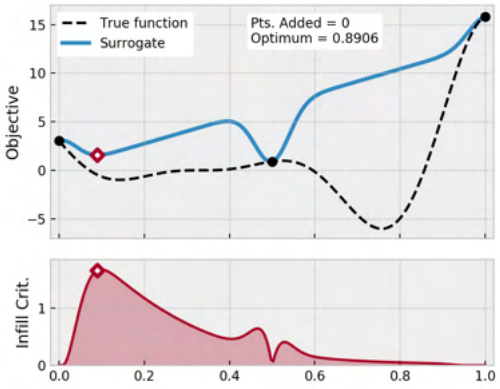

Figure 3. Snapshot of an adaptive sampling process. The infill criterion is maximized to identify the most favorable location for evaluating a sample point.

A grid of x-z nacelle locations was sampled, and propulsion/CFD analyses were sequentially run at design points that maximized the expected improvement within each particular x-z location. This procedure was carried out until the EI was of a similar order of magnitude as the numerical uncertainty due to the CFD grid (described in a later section).

Earlier in this period of performance, we were aware of a major risk of this Stage 1 parametric optimization: that it may not reveal a truly optimal location for the over-wing nacelle. We discussed with our FAA technical advisors that this outcome is both possible and likely due to an under-constrained MDAO problem. A full MDAO problem would include the physics of many other disciplines, including structural weight penalties and trim drag due to pitching moments. In our limited project scope, we focused on static aerodynamics and propulsion analyses, so we might find that L/D and excess thrust simply improve monotonically as the nacelle moves farther up and forward (i.e., farther from the influence of the wing). Indeed, this is the result discussed under a later task.

Because this ambivalent outcome for Stage 1, we discussed with FAA advisors that we would quantify a map of performance over nacelle x-z locations but may then simply select a new reference location for further optimization in Stage 2. This was indeed the outcome of Stage 1.

Stage 2 Strategy

After selecting a new reference location for the OWN, the number of design variables was expanded. Rather than repeat the parametric optimization used in Stage 1, this larger-scale MDAO uses a simple optimization formulation. As with Stage 1, this optimization will be performed for both OWN and UWN. This stage is currently in progress; it began in late 2021 and will finish in early 2022.

Milestones

The MDAO strategy is under continuous development until high-fidelity optimization is complete. However, during this project period, the following milestones were achieved:

- Planned and executed the first-stage nacelle placement selection study
- Settled the formulation for the second-stage study
- Launched initial runs of the second-stage study

Major Accomplishments

- Stage 1 and 2 strategies, and potential risks, were planned and discussed with FAA technical advisors in advance.
- Our plan was implemented with a sufficient schedule margin such that we could completely redo the Stage 1 analysis upon discovering an error in our first attempt.
- We identified potential sources of uncertainty that would influence the strategy in the final, remaining period of performance in 2022.

Publications
None

Outreach Efforts
None

Awards
None

Student Involvement
- Mengzhen and Bilal Mufti are continuing PhD students who contributed by testing different MDAO formulations using coupled propulsion cycle and CFD analyses.
- Anish Vegesna, Marc Koerschner, Sam Crawford, and Andrew Burrell contributed to system/mission analysis formulation.

Plans for Next Period
The remaining six months of performance in 2022 will focus on final execution of the MDAO process and additional supporting studies using the optimization environment. In particular, we will integrate the aero-propulsion analysis with a wider system-level mission analysis.

References
Jones, D.o R., Schonlau, M., & Welch, W. J. (1998). Efficient global optimization of expensive black-box functions. Journal of Global Optimization, *13*, 455–492. https://doi.org/10.1023/A:1008306431147

Vassberg, J., Dehaan, M., Rivers, M., & Wahls, R. (2008). Development of a common research model for applied CFD validation studies [Paper presentation]. 26th AIAA Applied Aerodynamics Conference.

Task 2 - Select Aero-Propulsion Integration Method
Georgia Institute of Technology

Objective(s)
One of the most computationally intensive aspects of the MDAO formulation is the aero-propulsion coupling analysis problem. The discipline of aerodynamics uses results from propulsion cycle analysis (the Numerical Propulsion System Simulation [NPSS] code) as boundary conditions, and vice-a-versa. A valid MDA solution can be found only when these coupling variables shared between disciplines converge. There are different MDA methods to achieve such interdisciplinary closure, and they each have different costs with respect to the number of function calls.

In our study, each CFD simulation can cost at least O(1000 core-hours), so it was important to minimize the number of iterative function calls to converge a single MDA.

Research Approach
The overall MDAO design problem discussed in the previous task has constraints related to physical equilibrium. These were restated as equality constraints for interdisciplinary consistency:

- Core flow consistency: $h_1 = \left|W_7^{NPSS} - W_7^{CFD}\right| \leq \epsilon_1$
- Bypass flow consistency: $h_2 = \left|W_{17}^{NPSS} - W_{17}^{CFD}\right| \leq \epsilon_2$
- Inlet pressure recovery consistency: $h_3 = \left|\eta_{PR}^{NPSS} - \eta_{PR}^{CFD}\right| \leq \epsilon_3$
- Streamwise force balance: $h_4 = \left|\sum F_x^{CFD} + F_x^{FLOPS}\right| \leq \epsilon_4$
- Stream-normal or lift force balance: $h_5 = \left|C_L^{CFD} - C_L^{Target}\right| \leq \epsilon_5$

In these equations, W is the weight (or mass) flow, with the subscripts 7 and 17 indicating the engine stations equivalent to the CFD boundary condition plenum for exhaust flow. F_x^{FLOPS} is the streamwise force contribution from empirical drag models for components other than the wing-body-nacelle modeled in CFD. All of these constraints h_i were set to small tolerances ϵ_i.

Several MDA methods were tested with different levels of geometric complexity before selecting a final method. Initial research focused on a relatively simple, two-dimensional axisymmetric, isolated nacelle to test MDA strategies using a subset of the above constraints h_i. For example, a simple looping method (Gauss-Seidel) was used in Figure 4.

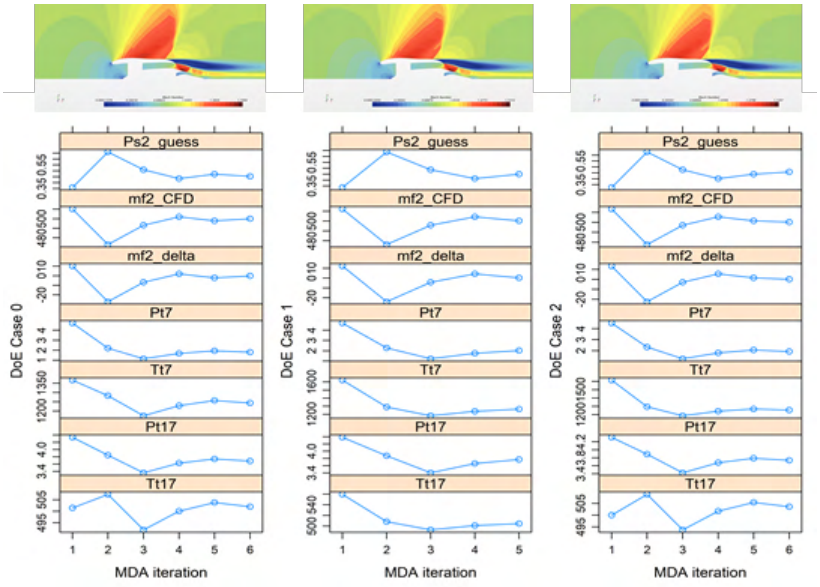

Figure 4. Example convergence history of aero-propulsion coupling variables for three design cases of a 2-D/axisymmetric nacelle.

During this research, we realized an important potential discrepancy between NPSS propulsion cycle assumptions and CFD boundary conditions. Specifically, the "0-D" NPSS code does not spatially discretize flow equations but rather connects analytically/empirically tuned flow equations for different turbomachinery elements at different stations in the engine. For example, at a nozzle station, 1D isentropic nozzle flow equations (with any tuning factors) can be used along with entry/exit areas to yield a solution coupled with all other cycle elements.

This nozzle element is of particular interest. In typical propulsion cycle analysis, it is assumed that the nozzle exhausts a flow to external boundary conditions, which are typically free-stream conditions. However, the nozzle exit flow may not actually reach free-stream conditions at the nominal outlet location and area. Figure 5 shows an example CFD case in which the bypass and core exhaust streams may not reach free-stream pressure at their respective, nominal "A_8" and "A_{18}" exit areas.

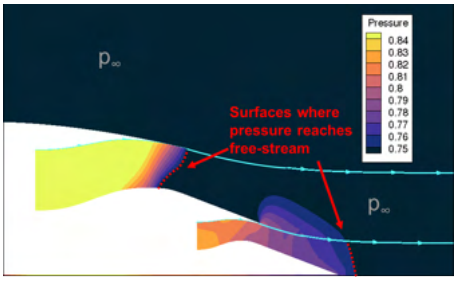

Figure 5. Areas at which exhaust streams reach free-stream pressure can be significantly different from nominal bypass and core exit areas.

This leads to a physics inconsistency between cycle analysis and CFD – which may be considered as essentially internal and external aero-thermal analyses which must pass consistent information over boundary conditions. The situation is worse in

forward-mounted OWN applications because the presence of a wing aft of the engine strongly affects exhaust flow compared to the isolated engine assumed in NPSS.

Figure 6. Mach contour plot shows the influence of the wing on exhaust streams from the engine.

One of our major developments in 2021 was adjusting the aero-propulsion MDA problem to enforce the consistency constraints. We achieved this by manipulating fictitious "exit areas" A_8 and A_{18} in the propulsion cycle analysis to help converge the MDA consistency constraints shown earlier. This is tantamount to an iterative CFD-based calibration of an NPSS model to account for complex OWN aero-propulsive interactions.

In 2021, we tested several different MDA and MDAO architectures to find a method that efficiently enforces the five MDA equality constraints listed earlier (h_1, h_2,…,h_5). For example, Figure 7 shows a snapshot of a Bayesian adaptive sampling approach based on Lee (2012) that progressively learns the settings for coupling variables that most likely satisfy the constraints.

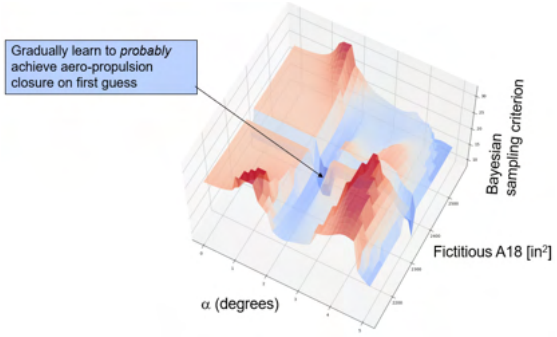

Figure 7. Bayesian method shows regions of the coupling variable domain that have a high probability of satisfying MDA closure constraints.

We ultimately selected a simple method based on the macro scripts of the commercial Star-CCM+ CFD code. This was an intrusive alteration of the CFD solution process to enforce the MDA constraints. Surrogate NPSS models were created and included inside the CFD solver script. While the CFD code iteratively solves its governing equations with respect to flow-field state variables, it also manipulates coupling variables by querying the NPSS surrogates until MDA closure is achieved.

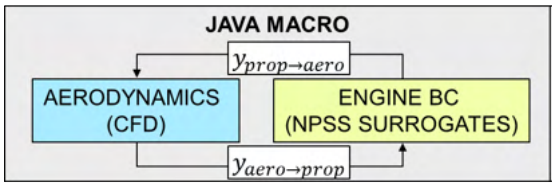

Figure 8. Final aero-propulsion coupling method relies on solver macros to intrusively enforce MDA consistency within the CFD code.

Milestone(s)

- Tested various methods for aero-propulsion coupling
- Tested direct multi-disciplinary feasible (MDF) method on 2D axisymmetric, isolated nacelles
- Tested direct multi-disciplinary feasible (MDF) method on full aircraft
- Tested rejection sampling method using 3D nacelle and wing (no fuselage)
- Tested Bayesian adaptive sampling method for 3D nacelle and wing
- Tested Fully coupled, intrusive method with full aircraft wing-body-nacelle.

Major Accomplishments

- Selected and implemented an aero-propulsion MDAO method. We specifically implemented a fully coupled method to incorporate propulsion cycle surrogate models within CFD macro solver scripts; this method is currently in use in Stage 2 optimization.

Publications

None

Outreach Efforts

None

Awards

None

Student Involvement

Bilal Mufti and Mengzhen Chen tested different MDA architectures using CFD and NPSS propulsion cycle analysis.

References

Lee, C., & Mavris, D. (2012, July). Bayesian collaborative sampling for aero-propulsion design of an engine and nacelle [Presentation]. 48th AIAA/ASME/SAE/ASEE Joint Propulsion Conference & Exhibit.

Martins, J. R. R. A., & Lambe, A. B. (2013). Multidisciplinary design optimization: A survey of architectures. AIAA Journal, *51*(9), 2049-2075.

Plans for Next Period

None

Task 3 - Create Aircraft Mission and Engine Models

Georgia Institute of Technology

Objective(s)

An aircraft-level model is necessary to compute fuel burn for a specified mission and develop a corresponding engine model for use within CFD.

Research Approach

This model wasin the Environmental Design Space (EDS) framework [1], which integrates the engine cycle analysis code NPSS, the engine weight prediction tool WATE++, and the aircraft performance and mission analysis code FLOPS. The main ingredients for an aircraft model are as follows:

1. Development of an engine architecture model in NPSS
2. Selection of engine cycle design variables
3. Development of an airframe model in FLOPS
4. Specification of requirements such as a mission profile, desired range, cruise Mach number and altitude, etc.

The baseline engine selected for this vehicle is based off a notional Pratt and Whitney geared turbofan (the PW1133GTF). A general model of the mechanical design, geometry, and thermodynamics of the engine was created in NPSS using publicly available information. This model was then 'calibrated' to International Civil Aviation Organization (ICAO) databank values of sea level static thrust and fuel flow, based on the assumption that the calibration factors applied for that flight condition are valid throughout the operating envelope. However, because the engine is rubberized, the engine can be scaled up or down in thrust for a fixed thrust to weight ratio (T/W), based on the results of the mission analysis. The baseline T/W selected for this vehicle is 0.31, based on public information for the A320neo, which is in the same passenger class considered for this study.

The airframe model in FLOPS was built around the CFD geometry of the vehicle. Key variables like fuselage length, width, depth, wing planform area, aspect ratio, taper ratio, quarter chord sweep, and dihedral were matched between the CFD geometry and the FLOPS representation of this geometry. These variables impact the weight and aerodynamic performance predictions in FLOPS. The FLOPS aircraft model is sized for 150 passengers, with an assumed weight of 225 pounds per passenger (weight of the passenger + baggage). The design range is specified to be 3415 nmi, with a cruise Mach number of 0.8 at 39,000 ft. A reserve mission for a 200 nmi trip to an alternate airport is also part of the requirements.

The mission analysis was initially conducted with FLOPS internal predictions for aerodynamics. The resulting engine dimensions and engine deck were then used to update the CFD model of the engine (both the geometry and boundary conditions). Reynolds-averaged Navier-Stokes (RANS) simulations of the airframe and engine (under-wing) were performed at cruise for an angle of attack sweep to generate a drag polar. A typical cruise part power condition is assumed to obtain the engine boundary conditions for this polar run. The resulting polar was then used to 'tune' the FLOPS internal aerodynamic predictions by adjusting FLOPS scaling factors on parasitic and induced drag (referred to as FCDO and FCDI in FLOPS terminology) such that the cruise polar predicted by FLOPS matched the polar generated by CFD. Following this tuning, EDS was re-run using the same inputs as before to determine a new engine size that meets the mission requirements. This new engine was used for all subsequent CFD analyses on both the OWN and UWN configurations.
Although EDS and CFD should theoretically be evaluated in a coupled manner until there is consistency between the engine used in the mission analysis and the engine used to generate the polars that feeds into the mission analysis, this iterative procedure is quite costly. As such, only a one-pass update was used to establish the vehicle model and the engine model in CFD. Overall, the focus of our project is to solve the aero-propulsive coupling problem within the CFD domain. Thus, for a fixed engine size, our goal was to match the engine operating conditions and inputs assumed by the NPSS model to those in the CFD domain through an iterative exchange of boundary conditions between the two disciplines, as described in the previous section. The engine size convergence between the NPSS model and that assumed in CFD is not closed. Table 1 and Figure 9 summarize some key characteristics of the airframe and engine model.

Table 1. Summary of 150-passenger aircraft model.

Name	Value
Fuselage Length (ft)	128.7
Fuselage Max Width (ft)	12.2
Fuselage Max Depth	12.2
Wing Planform Area (ft^2)	1642
Wing Aspect Ratio	8.4
Wing Quarter Chord Sweep (°)	33.76
Wing Taper Ratio	0.2
Wing Dihedral (°)	7.95
Design Payload (lb)	33,750
SLS Thrust/Engine (lb)	26,580
Thrust to Weight Ratio	0.31
Design Fan Pressure Ratio	1.525
Overall Pressure Ratio	47.91
Bypass Ratio	11.06
Design Range (nmi)	3451
Cruise Mach	0.8
Cruise Altitude (ft)	39,000

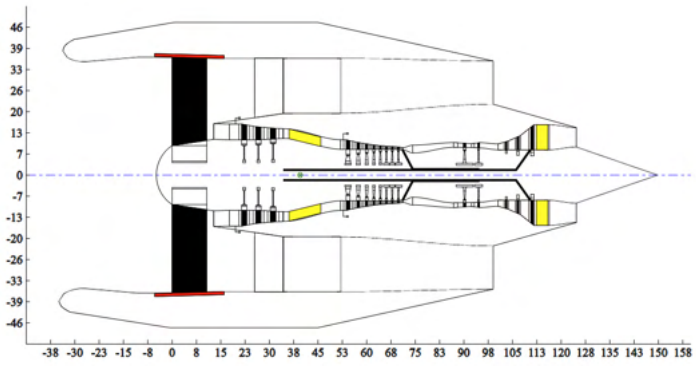

Weights		Dimensions	
Bare Engine Weight	4928.5	Engine Length	124.7
Accessories Weight	731.2	Engine Pod C.G.	39.5
Engine Weight	5659.7	Engine Max Diameter	72.6
Inlet/Nacelle Weight	89.4	Nacelle Max Diameter	0.0
Total Engine Pod Weight	5749.1	Total Engine Pod Length	124.7

Figure 9. WATE++ outputs for the final engine model used in CFD (all dimensions are in inches, and weights are in pounds).

Milestone
Completed initial system-level modeling to compute fuel burn and develop an engine model.

Major Accomplishments
Developed an engine model, in terms of geometry and boundary conditions, for use in CFD analysis of both the OWN and UWN configurations.

Publications
None

Outreach Efforts
None

Awards
None

Student Involvement
None

References
Nunez, L. S., Tai, J., & Mavris, D. N. (2021). The environmental design space: Modeling and performance updates [Presentation]. AIAA SciTech Forum. https://doi.org/10.2514/6.2021-1422.

Plans for Next Period
We will use the existing vehicle model, with our latest CFD-tuned drag polars, for mission analysis on both OWN- and UWN-optimized geometries to compare fuel burn differences.

Task 4 - Reduce Dimensionality Using Active Subspace Methods

Georgia Institute of Technology

Research Approach

The external shape of aerodynamic bodies, such as wings and nacelles, is characterized by complex and detailed surfaces. In turn, the definition of these surfaces necessitates many design parameters. The design problem in our current study contains a total of 45 variables, which are listed in Table 2. This large number of design variables hinders the exploration of the aircraft design due to a phenomenon referred to in the machine learning literature as the curse of dimensionality. To effectively tailor the airframe for a given engine location, steps must therefore be taken to reduce the dimensionality of the design space to a more reasonable value.

Table 2. List of original design variables before reduction.

Group	Variable Name	Dimension
Nacelle	Highlight lip radius	1
	Cowl maximum radius	1
	Cowl maximum radius location	1
	Cowl trailing edge angle	1
	Cowl trailing edge curvature	1
	Inlet throat location	1
	Nacelle X location	1
	Nacelle Z location	1
Wing	Wing CST coefficients (upper surface)	16
	Wing CST coefficients (lower surface)	16
	Wing twist distribution	4
Aircraft	Angle of attack	1
	Total	**45**

We reduced the dimensionality of the design space using the active subspace method described by Constantine (2015), which is a type of supervised dimensionality reduction technique. This method assumes a generic function that depends on many inputs and identifies a linear subspace of the input spaces that is responsible for most of the variability of the function. The active subspace is defined using an orthogonal basis in which the vectors represent a linear combination of the original design variables. Designs in the original space can then be projected into the active subspace, and the resulting coordinates are called the active variables. Note that the transformation, from the active variables to the original design variables, is also straightforward as it only requires the transpose of the computed orthogonal basis. Conceptually, the active subspace can alternatively be considered as a rotated set of axes in the design space that best captures the variation in the function, as shown in Figure 10.

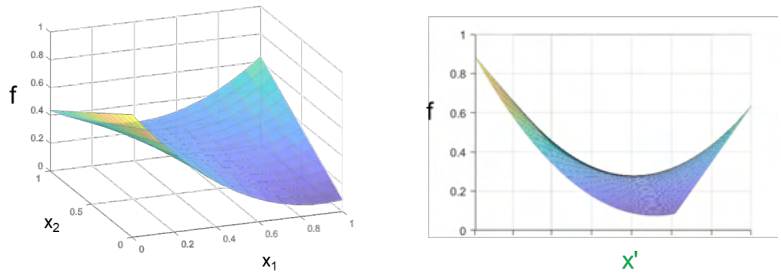

Figure 10. Notional view of the active subspace for two original design variables (left). The rotated view (right) shows that a single new variable x' captures important features of function f.

The classical active subspace method requires the computation of the gradient of the function of interest. However, in the last few years, some authors have proposed alternative methods that can extract the subspace in a gradient-free manner. One such methods is the manifold optimized active subspace (MOAS), which was initially proposed by Tripathy et al. (2016)

and improved by Rajaram et al. (2020). The MOAS method uses a Gaussian process (GP) to link the function inputs and outputs and obtains the active subspace by maximizing the likelihood of the GP via a manifold optimization algorithm. While the analysis tools used in this work can provide gradient information, the airframe uses the gradient-free MOAS approach. This decision was motivated by the additional computational cost of computing the gradient and the result of initial testing that showed noise in the gradient results, which negatively impacted the accuracy of the active subspace. The MOAS results were computed using the framework developed by Gautier et al. (2020), which is openly available[1].

Although the active subspace method can facilitate the exploration of a high-dimensional design space, it still requires generation of a substantial amount of training data. This can be quite costly when used in combination with high-fidelity RANS simulations. To further reduce the computational cost of design exploration, the active subspace in this work was computed using inviscid results obtained with Cart3D. The computed subspace was then used directly for the generation of RANS results. While the inviscid active subspace is likely different than the RANS active subspace, it is assumed that the difference between the two is relatively small because the aerodynamic performance of the aircraft is expected to depend strongly on inviscid effects such as shock waves and induced drag. The potentially lower accuracy of our approach is also compensated by the inexpensive generation of inviscid data.

Milestone(s)
Compared and selected active subspace methods for dimension reduction.

Major Accomplishments
- Active subspace variables were used successfully in the Stage 1 design study.
- Variables were selected for ongoing Stage 2 optimization.

Publications
None

Outreach Efforts
None

Awards
None

Student Involvement
Bilal Mufti and Mengzhen Chen contributed to CFD implementation and testing.

References
Constantine, P. (2015). *Active subspaces: Emerging =ildeas for dimension reduction in parameter studies.* Society for Industrial and Applied Mathematics. https://doi.org/10.1137/1.9781611973860

Gautier, R., Pandita, P., Ghosh, S., & Mavris, D. A fully bayesian gradient-free supervised dimension reduction method using gaussian processes," 2020, arXiv preprint arXiv:2008.03534

Rajaram, D., Gautier, R. H., Perron, C., Pinon-Fischer, O. J., & Mavris, D. (2020). Non-intrusive parametric reduced order models with high-dimensional inputs via gradient-free active subspace [Presntation]. AIAA AVIATION Forum. https://doi.org/10.2514/6.2020-3184

Tripathy, R., Bilionis, I., & Gonzalez, M. (2016). Gaussian processes with built-in dimensionality reduction: Applications to high-dimensional uncertainty propagation. Journal of Computational Physics, *321*, 191-223. https://doi.org/10.1016/j.jcp.2016.05.039

Plans for Next Period
The surrogate may be updated and used along with aero-propulsion optimization results for final conclusions.

[1] Source code available at https://gitlab.com/raphaelgautier/bayesian-supervised-dimension-reduction

Task 5 - CFD Grid Sensitivity Analysis

Georgia Institute of Technology

Objective(s)

The goal of this task is to generate CFD grids of different resolutions and compare the solutions for accuracy. The impact of the accuracy on the fuel burn calculations was quantified. The results were used to guide MDAO convergence criteria such that the optimization is not continued beyond the uncertainty "floor" of the physics analysis.

Research Approach

STARCCM+ Reynolds Averaged Navier Stokes CFD solver was used for this optimization study. The STARCCM+ in-built unstructured grid generator was used to generate hybrid volume mesh containing orthogonal prismatic cells (also known as prism cells) near the surface to resolve the boundary layer. and polyhedral cells were generated for the remaining volume mesh. Based on a survey of recent literature, it was found that previous OWN configuration optimization studies have used meshes ranging from 0.8M to 30M cells [1-3]. Therefore, for this study, detailed grid sensitivity analysis before finalizing the grid to establish a reference uncertainty floor. The six grids that were used (see Table 3) ranged from the coarsest size of 19.5M cells to the finest size of 475M cells, with the latter being used as the reference case for comparing the accuracy. The net L/D calculation error for all cases relative to the reference case was within 2% for the coarsest grid. Based on these findings, 76M grid was chosen for the optimization study.

Table 3. Grid convergence study results.

	CFD mesh cell count					
	19.5M	33M	76M	161M	303M	475M (Reference)
% L/D Error	1.955	1.495	0.476	-0.329	0.179	0

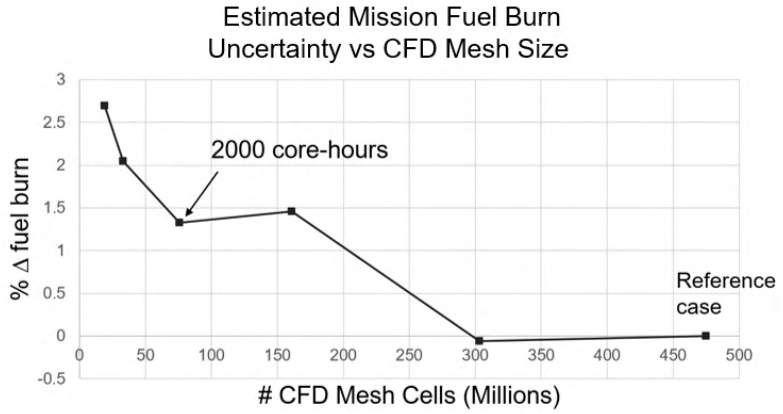

The CFD error in the drag computations associated with different grid sizes was propagated to the change in mission fuel burn via a rapid estimate. This study was performed using a modified version of FLOPS that allows user-specified data tables for the aerodynamic model of aircraft. As before, the change in the drag coefficient (ΔC_D) for only the cruise condition was obtained for all cases by keeping the drag value obtained from the 475 million cell grid as baseline. To obtain a rough estimate of the uncertainty impact of CFD mesh-related error, the ΔC_D was applied to the empirically based aerodynamics models in FLOPS. The drag polar for complete aircraft at different flight conditions was computed using empirical drag estimation techniques (EDET). This baseline drag polar was perturbed by adding ΔC_D using a blending function, such that the change in drag is maximized at the flight conditions at which ΔC_D was computed and decreases linearly as we change the Mach number.

Table 4. CFD error propagation to mission fuel burn calculations.

Grid Size (Millions)	ΔC_D	Estimated % Discrepancy in Mission Fuel Burn
19.5	6.78E-4	2.69
33	5.19E-4	2.05
76	3.37E-4	1.32
161	3.72E-4	1.46
303	-0.154E-4	-0.06
475 (Reference)	**0**	**0**

When examining the CFD solutions, there were often only subtle physical differences in flowfields. For example, there was over a 2% discrepancy in the estimated mission fuel burn between the two mesh settings shown in Figure 11. However, much of the recently published OWN literature may be qualitatively similar to the coarser of these two mesh settings.

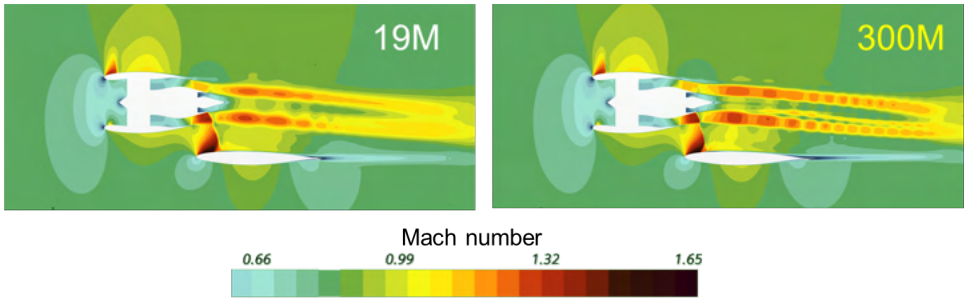

Figure 11. Subtle differences in the flowfields of different mesh cell counts result in significant discrepancies in mission fuel burn.

Milestone(s)
Completed mesh sensitivity study.

Major Accomplishments
The uncertainty impact of CFD mesh was propagated to uncertainty in the system-level metric (i.e., fuel burn).

Publications
None

Outreach Efforts
None

Awards
None

Student Involvement
PhD student Bilal Mufti propagated the CFD numerical uncertainty through the mission analysis to estimate its effect on fuel burn.

References
Berguin, A., Renganathan, S. A., Ahuja, J., Chen, M., Tai, J., & Mavris, D. N. (2018). Sensitivity analysis of aero-propulsive coupling for over-wing-nacelle concepts [Presentation]. 2018 AIAA Aerospace Sciences Meeting.

Fujino, M., & Kawamura, Y. (2003). Wave-drag characteristics of an over-the-wing nacelle business-jet configuration Journal of Aircraft, *40*(6), 1177-1184.
Hill, G. A., Kandil, O. A., & Hahn, A. S. (2009). Aerodynamic investigations of an advanced over-the-wing nacelle transport aircraft configuration. Journal of Aircraft, *46*(1), 25-35.

Task 6 - First Stage Design – Nacelle Location Selection

Georgia Institute of Technology

Objective(s)

To control the "curse of dimensionality," the MDAO process was staged into two steps. The first step focused on determining the nacelle location and was followed by more detailed shape optimization in the ongoing Stage 2 design.

Research Approach

A parametric optimization approach (formulated in Task 1) was implemented.

The efficient, integrated aero-propulsion MDA method had not yet been developed by this period of the project. Due to the expected high cost of MDA convergence for each design point, an open-loop aero-propulsion analysis was used for the first-stage study to explore nacelle locations.

Recall that a parametric optimization approach was used to minimize $f = f(\underline{\mathbf{X}}_{parameter}, \underline{\mathbf{X}}_{choice})$ with respect to shape variables $\underline{\mathbf{X}}_{choice}$ given particular settings of $\underline{\mathbf{X}}_{parameter}$. The parameter variables are the nacelle position, discretized as a 3x5 grid of engine reference location points as shown below in Figure 12.

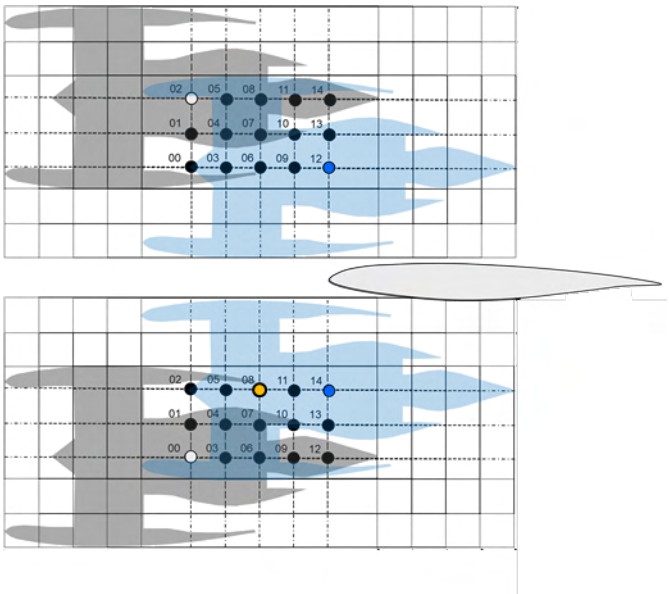

Figure 12. Grid of nacelle locations for OWN and UWN. Dots show the positions of reference locations in the engine.

The objective function is a weighted sum of L/D and excess thrust, each normalized by a reference solution in the middle of the nacelle location domain shown in Figure 12. The sign is flipped to follow the optimization convention in which lower values are better. There are two choice variables which are active subspace variables – they are hybrids or combinations of 45 wing and nacelle variables that are reduced according to the methods described in an earlier task.

A Gaussian process regression model was fit to an initial seed of warm-start design points. An expected improvement (EI) sampling criterion was calculated with respect to the current best solution for each nacelle position. The objective function is shown in Figure 13 for OWN and Figure 14 for UWN.

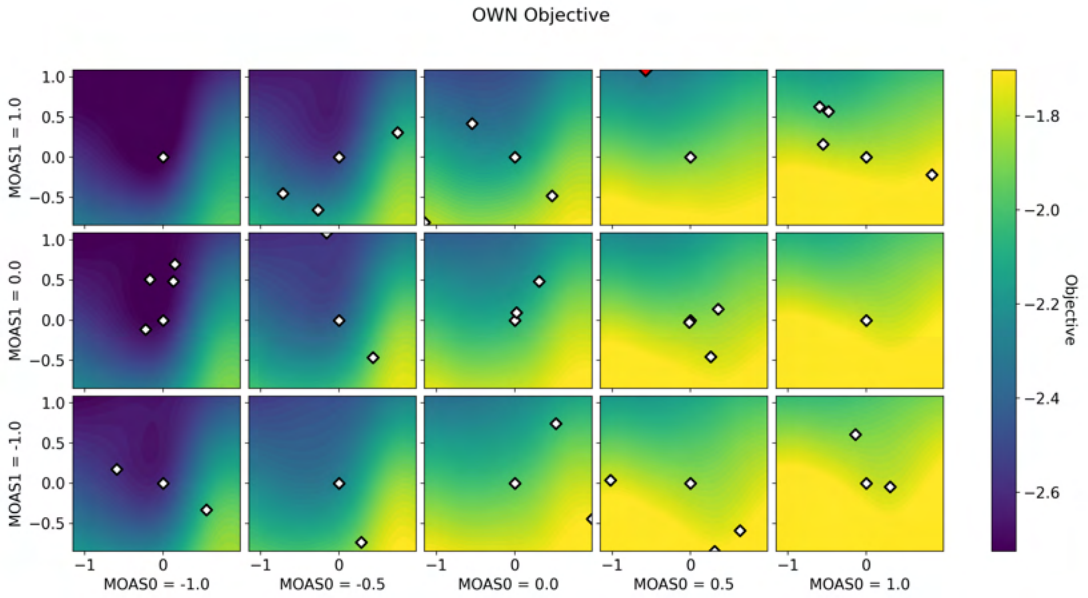

Figure 13. Parametric adaptive sample results for OWN. Lower is better. MOAS0 is nacelle x-position (streamwise) and MOAS1 is the z-position (vertical) of the nacelle. Within each box, the two axes are active subspace variables that combine nacelle and wing shape variables.

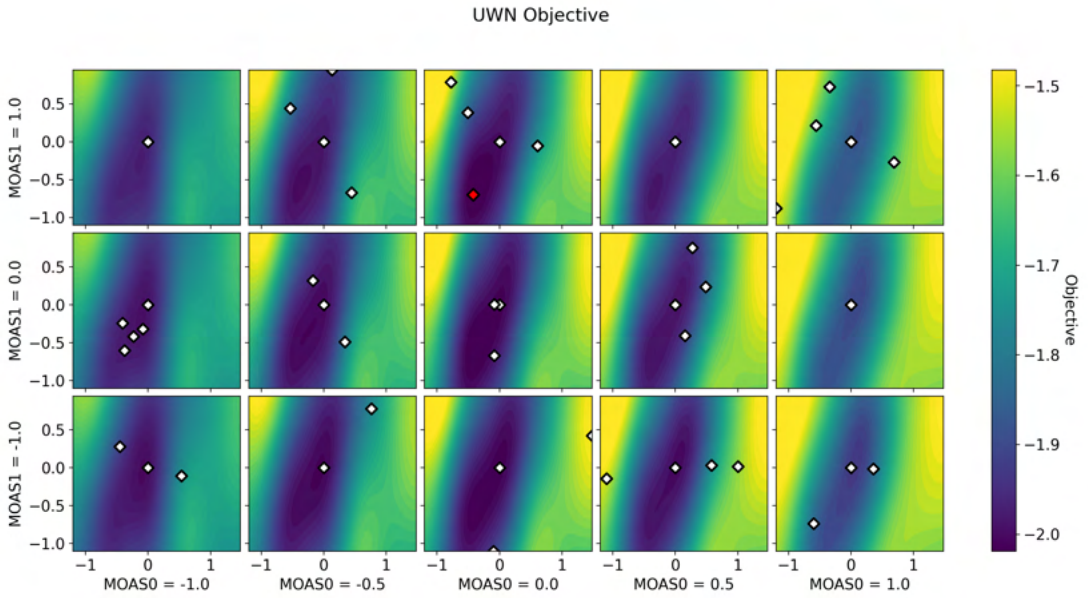

Figure 14. Parametric adaptive sample results for UWN. Axes are defined as in Figure 13.

We performed a sequential sampling process until the EI was roughly of order O(1%) of the objective function, which corresponds to the numerical uncertainty due to the CFD mesh density.

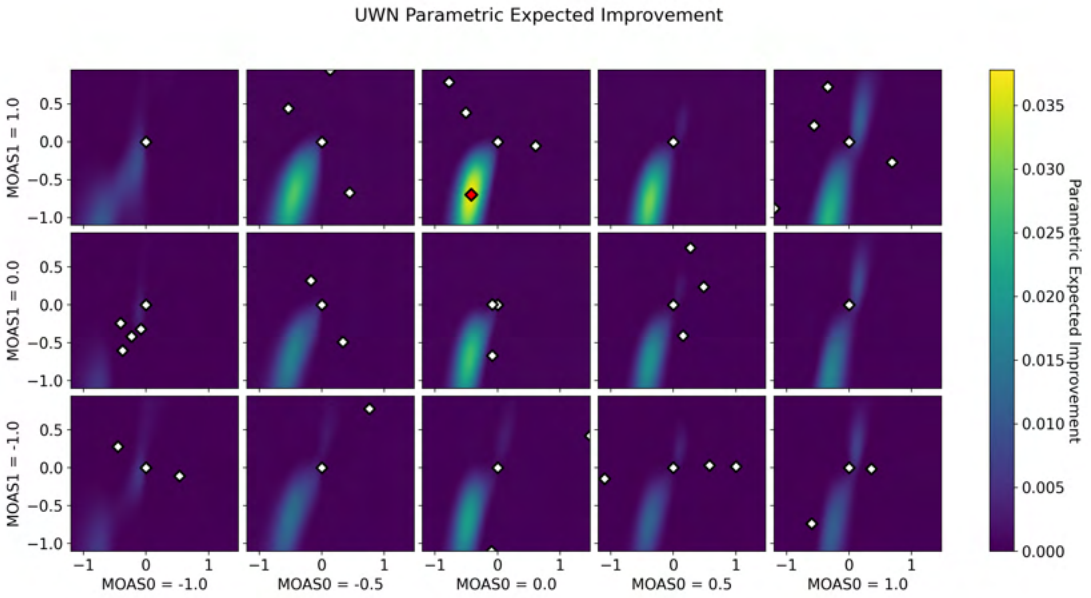

Figure 15. Example expected improvement results during the UWN adaptive sampling campaign. Note that the scale of the expected improvement is for the sum of the normalized lift-to-drag ratio and excess thrust.

The results in Figure 15 show that the problem is not sufficiently constrained, because the boxes to the top left (i.e., farther forward and higher than the wing) are clearly more favorable. There are no physics in the present MDAO scope to prevent an optimizer from continuing to move in that direction outside the specified design domain. Therefore, a subjective decision was made to a freeze single representative OWN location and pursue further wing/nacelle shape optimization. The UWN location was similarly frozen at its CRM baseline. These representative locations are shown in Figure 16.

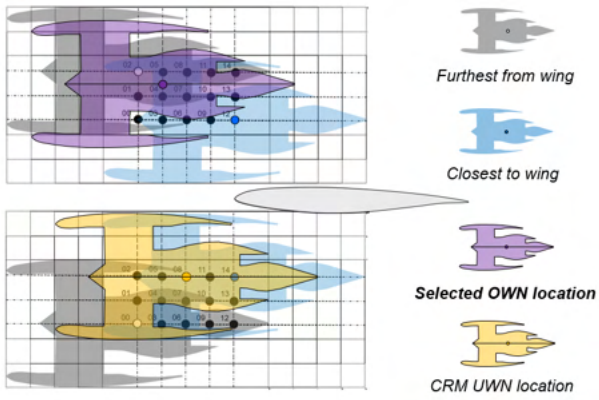

Figure 16. Subjective nacelle locations chosen for Stage 2 detailed optimization.

These decisions on nacelle locations were made in consultation with FAA advisors, with reference to our parametric optimization results. This was a human decision and therefore suffers from arbitrariness; however, this was not the result of ignorance of rigorous optimization methods, but rather an unavoidable consequence of limiting our scope to aero-propulsion physics. In future research, a detailed pylon design as well as structures and flight mechanics discipline would penalize nacelle placements that are too high or too far from the wing. For the present study, the nacelle location selections shown above will be used for deeper optimization. This will likely be followed by a sensitivity study of the Stage 2 optimum design with respect to small perturbations in nacelle x,z locations.

Milestone
Completed adaptive sampling for OWN and UWN to provide estimates of realizable optimum performance for a grid of nacelle positions.

Major Accomplishments
Selected baseline nacelle locations for OWN and UWN in discussion with FAA technical advisors

Publications
None

Outreach Efforts
None

Awards
None

Student Involvement
Bilal Mufti and Mengzhen Chen supported the CFD and study of mission fuel burn impacts

References
None

Plans for Next Period
The baseline nacelle locations selected in this task will be used in an expanded MDAO in the next stage of our analysis.

Task 7 - Create ANOPP Noise Surrogate Model
Georgia Institute of Technology

Objective(s)
The goal of this task is to use a noise analysis code, such as the ANOPP, to generate approach, cutback, sideline, and cumulative noise data via a design of experiments. This will allow surrogate models to be fit to the data set to predict changes in aircraft noise due to nacelle location.

Research Approach
ANOPP was selected as a suitable noise analysis code based on the required level of detail and the tools available. Five-level full factorial and 100-case Latin hypercube design of experiments were combined into a single experimental design to thoroughly sample the nacelle location design space within ANOPP. The ANOPP noise responses are fit to the nacelle location parameters using a single-layer artificial neural network with hyperbolic tangent nodes, resulting in a root mean square EPNdB error of less than 0.105.

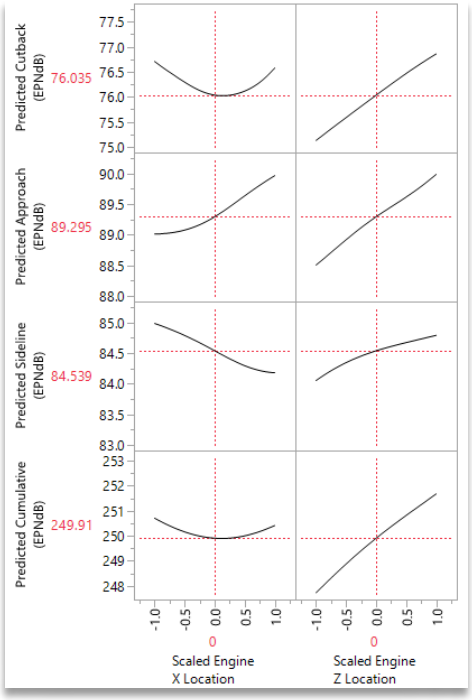

Figure 17. Example view of the Aircraft Noise Prediction Program surrogate model.

Milestone(s)
Performed initial ANOPP noise analysis.

Major Accomplishments
Artificial neural networks were fit to the approach, cutback, sideline, and cumulative forward mounted OWN and UWN noise responses as a function of the nacelle location parameters. This directly supported Task 6 (generating data to select the nacelle location).

Publications
None

Outreach Efforts
None

Awards
None

Student Involvement
Andrew Burrell ran ANOPP and fit surrogate models to the noise responses.

References
Zorumski, W. E. (1982). Aircraft noise prediction program, parts I & II (Report No. NASA TM-83199.) National Aeronautics and Space Administration.

Plans for Next Period
The surrogate may be updated and used along with aero-propulsion optimization results for final conclusions.

Project 051 Combustion Concepts for Next-Generation Aircraft Engines

Massachusetts Institute of Technology

Project Lead Investigator

Steven R. H. Barrett
Professor of Aeronautics and Astronautics
Director, Laboratory for Aviation and the Environment
Massachusetts Institute of Technology
77 Massachusetts Ave, Building 33-322, Cambridge, MA 02139
(617) 253-2727
sbarrett@mit.edu

University Participants

Massachusetts Institute of Technology (MIT)

- PI: Professor Steven R. H. Barrett
- FAA award number: 13-C-AJFE-MIT, Amendment Nos. 061, 071, and 079
- Period of Performance: February 5, 2020 to August 31, 2022 (reporting here with the exception of funding level and cost sharing only for the period October 1, 2020 to September 30, 2021)
- Task:
    1. Evaluate water injection to extend the operating envelope and reduce emissions

Project Funding Level

This project received $600,000 of FAA funding and $600,000 of matching funds (approximately $140,000 from MIT plus third-party in-kind contributions of $460,000 from NuFuels LLC).

Investigation Team

- Professor Steven Barrett (MIT) serves as PI for the A51 project as head of the Laboratory for Aviation and the Environment. Professor Barrett coordinates internal research efforts and maintains communication among investigators in the various MIT research teams.
- Dr. Raymond Speth (MIT) serves as co-PI for the A51 project. Dr. Speth directly advises students on research in the Laboratory for Aviation and the Environment focused on the assessment of fuel and propulsion system technologies targeting reduction of aviation's environmental impacts. Dr. Speth also coordinates communication with FAA counterparts.
- Dr. Jayant Sabnis (MIT) serves as co-investigator for the A51 project. Dr. Sabnis co-advises students on research in the Laboratory for Aviation and the Environment. His research interests include turbomachinery, propulsion systems, gas turbine engines, and propulsion system–airframe integration.
- Syed Shayan Zahid is a graduate student in the Laboratory for Aviation and the Environment. He is primarily responsible for evaluating the impacts of emissions reduction technologies on fuel consumption and making engine cycle models in pyCycle to evaluate the feasibility of new technologies in different engine configurations.
- Yang Chen is a graduate student in the Laboratory for Aviation and the Environment. He is primarily responsible for extending engine and emissions models to incorporate advanced combustion concepts and to expand the types of pollutants simulated in Pycaso.

Project Overview

The purpose of this project is to identify design concepts for aircraft engine combustors that could decrease the combustor emissions of future aircraft engines that incorporate higher pressures and temperatures. The need to increase the thermal

efficiency of the gas generator in aircraft engines has required designers to increase the overall pressure ratio (P_{03}/P_{02}) as well as the temperature ratio (T_{04}/T_{02}). A higher pressure ratio increases the overall temperature in the combustor, thereby accelerating NO_x production. Increased combustor exit temperatures result in higher cooling air requirements for the engine cycle, thus reducing the air available for NO_x reduction within the combustor. Hence, higher-thermal-efficiency engine cycles frequently result in higher NO_x production. The current state of the art requires a trade-off between engine fuel consumption and NO_x. In this project, we plan to develop numerical models for engine design concepts with promising new technologies. We will determine and compare the performance characteristics associated with these technologies and will leverage detailed combustion chemistry models to understand how changes in fuel composition affect engine performance and emissions characteristics.

The design of combustors for aircraft engines is governed by the simultaneous need to ensure operability at low-power conditions (i.e., preventing combustion instabilities, blowout, etc.) and enabling operation at high power without excessive NO_x or soot emissions. For aircraft engines, the flight conditions and thrust setting of the engine fully determine the inlet conditions of the combustor, i.e., the temperature, pressure, and fuel flow rates, with very little adjustments to increase stability or decrease emissions being available. However, the introduction of additives into the engine at specific locations would provide secondary inputs that could be used to extend stability limits or reduce emissions.

When the fuel flow rate is the only engine control parameter, the consequent variations in the equivalence ratio result in wide variability in the combustion characteristics, e.g., flammability limits and flame speeds, that must be accommodated across thrust settings ranging from idle to takeoff. Previous work has shown that the addition of a high-reactivity additive while holding the equivalence ratio constant can extend the lean blowout limit in a gas-turbine-like combustor (Speth and Ghoniem, 2009). By changing the fuel composition to counteract the effect of the equivalence ratio, the combustor would not need to operate over as wide a range of conditions and consequently allow for more opportunities to optimize the combustor to control emissions at its design point. Furthermore, variations in fuel composition have been shown to decrease soot emissions from aircraft engines (Moore et al., 2015; Speth et al., 2015), thus suggesting that the use of a fuel additive could be effective in reducing emissions during specific operating regimes.

Although water injection is not used in any current commercial aircraft engines, it has been used in several engines to augment thrust at takeoff, such as in the J-57 engines used on the B-52 and the JT9D engines used on the 747-200 (Daggett, 2004). The use of water injection at takeoff provides increased thrust without increasing the turbine inlet temperature. The temperature reduction, and therefore the density increase, from the evaporation of the injected water allows the engine to accommodate a larger mass flow rate of air resulting in greater thrust. In modern engines with higher compression ratios, water injection into the compressor may also alleviate limitations due to compressor exit temperature. Water injection has also been evaluated for its ability to reduce takeoff NO_x emissions (Daggett, 2004). Although older engines that used water injection were known to have higher soot production, controlling soot emissions was not a design goal of these engines; however, this aspect does not imply that a modern engine design using water injection could not meet limits for nonvolatile particulate matter emissions.

The work proposed here builds on work performed in other ASCENT projects. Work under ASCENT Project 39 has provided a combustor model that can predict soot emissions from conventional combustor designs and can use detailed chemical kinetic models to enable evaluation of the effects of different fuel compositions on emissions. Work performed under ASCENT Project 47 has extended this model to include predictions of NO_x formation, as well as coupling the model to an engine cycle model, thereby creating a consistent framework for modeling both ground and cruise emissions.

Task 1 - Evaluate Water Injection to Extend the Operating Envelope and Reduce Emissions

Massachusetts Institute of Technology

Objective(s)

Water injection can be used to control temperatures in the engine, which may expand the design space and enable decreases in mission fuel burn and emissions. For this task, we evaluated the impacts of water injection (a) at the low-pressure compressor inlet, (b) at the high-pressure compressor inlet, and (c) at the combustor inlet. For each option, the effect of water injection on the engine cycle was evaluated to determine engine designs, which are optimized for the impacts of water injection, i.e., considering allowable limits on compressor discharge temperature and turbine inlet temperature. Water

injection is expected to reduce peak temperatures and therefore NO_x formation. Tradeoffs with soot formation will also be evaluated. In the past, water injection was primarily used for thrust augmentation purposes when emissions were not thoroughly evaluated as part of the aircraft design process. For this reason, the existing literature on the effect of water injection on tailpipe emissions is sparse, thus justifying the need to conduct analyses on its feasibility.

To determine the effectiveness of water injection as a potential emission reduction technique, water injection will also be evaluated using different combustor configurations, including both rich-quench-lean (RQL) and staged lean-burn combustors. The impacts of water injection using different burner configurations will then be compared to determine whether an optimal configuration to incorporate this technology exists. Even though water injection is expected to decrease NO_x emissions, the incorporation of water injection in lean-burn staged combustors may pose challenges, because lean combustion is acoustically less stable than rich combustion. Therefore, before implementation of this technology, the benefits of water injection will eventually need to be weighed against feasibility and operability considerations.

Research Approach

This research targets three sections for analysis: a thermodynamic cycle analysis, a chemical emissions analysis, and an overall mission analysis. To evaluate the feasibility of this technology, a water evaporation model was also developed. A zero-order analysis for contrail formation was considered to evaluate potential trade-offs that need to be taken into consideration for this technology.

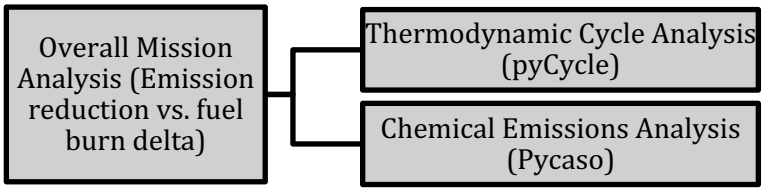

Figure 1. Evaluating the feasibility of water injection: analysis approach.

Thermodynamic Cycle Analysis

Water injection at different points in the Brayton cycle has varying effects on engine performance, depending on the state of the water being injected. A thermodynamic cycle model was developed to assess the dominant effect of water injection at different points in the cycle to determine the extent to which performance parameters—such as the thermodynamic states at various cycle locations, thrust, burner exit temperature, and overall thrust-specific fuel consumption (TSFC) are affected as a result of this approach.

PyCycle, an open-source code for thermodynamic cycle analysis, was chosen as a tool for this cycle analysis because of its flexibility in modifying the source code to simulate water injection. First, psychrometry calculations were performed to ensure that the amount of water injected into the system under the assumption of complete evaporation does not exceed the saturation limits (100% relative humidity) at the injection locations. After establishing the cutoff limits for each injection location, the pyCycle model was run to size the engine according to the amount of water injected. The thrust and combustor outlet temperatures were set to be constant across runs to evaluate the effect of water injection on fuel consumption for an engine designed to operate with water injection. The pyCycle results were then used as inputs to the combustor model as well as the overall mission analysis to determine the change in fuel consumption and the emission indices of the pollutants of interest for different missions. The approach to determine the feasibility of water injection is shown in Figure 1.

Chemical Emissions Analysis

The ASCENT 39 project developed an emissions model (Pycaso) based on Cantera to predict the NO_x and soot formation inside a CFM56-7B engine by using a reactor network to simulate the combustor. We aim to expand this model to simulate different combustor configurations and to cover various engine operating conditions. Evaluating new emission reduction technologies for a wider range of engines will help determine the overall effect on emissions. In general, the formation of pollutants, such as NO_x, CO, nvPM, and SO_2, depends on complicated reaction mechanisms. Thus, in emissions modeling, Cantera will be used with appropriate reaction mechanisms to calculate the species reaction rates in the combustor. Moreover, the emission model (Pycaso) will be utilized to calculate the total emissions level by solving a set of conservation laws that are properly simplified. Approximations such as a well-stirred reactor and plug-flow reactor sufficiently capture the

flow field structure and greatly reduce the computational cost relative to that of three-dimensional computational fluid dynamics (CFD) simulations. Shown below is the one-dimensional reactor network structure for an RQL-type combustor used in the Pycaso emissions model.

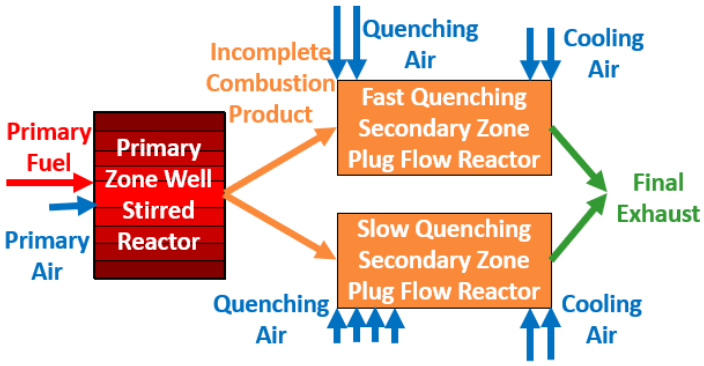

Figure 2. Pycaso combustor emissions model.

Inputs to the Pycaso emissions model are taken from the pyCycle thermodynamic cycle analysis, which includes the combustor inlet mass flow rate and thermodynamic state at the inlet. The estimated emissions help quantify the benefits and disadvantages associated with water injection as a function of design parameters such as combustor configuration and water injection location.

Overall Mission Analysis

Water injection can reduce NO_x formation inside the combustor by lowering the combustor temperature. This leads to a lower emission index for NO_x, where the emission index is the mass of NO_x emitted per mass of fuel consumed. However, this does not imply that the total amount of NO_x emitted per mission decreases, because the amount of fuel consumed could increase for a mission using water injection. The use of water injection could add significant weight to the aircraft in terms of the weight of the water and the associated system such as pumps, tanks, etc. This extra weight would require additional fuel burn (if the other aircraft parameters, such as the lift-to-drag ratio, remain unchanged). Therefore, when considering the benefit of using water injection to reduce NO_x emissions, it is important to account for the penalty due to the additional weight and the additional fuel burn associated with carrying the water injection system. A simplified overall mission analysis was performed using the Breguet range equation to assess whether this penalty would be significant and therefore limit the use of water injection. The results of the weight analysis depend on several factors, including the weight of the water to be injected, the mission range, the effect of water injection on the thrust-specific fuel consumption (TSFC), the desired NO_x reduction, and the associated water flow rate.

An exploratory contrail analysis was also conducted by considering ambient conditions as well as flight conditions to determine the extent to which water injection changes the likelihood of contrail formation, through evaluation of the Schmidt–Appleman criterion for different water injection ratios.

Milestone(s)

The existing pyCycle model was modified to include water injection capability, and the results were compared with a thermodynamic cycle model developed manually in Python to verify the accuracy of the results. After the results were obtained from the pyCycle model as well as the pyCaso model for various water injection quantities, an overall mission analysis was successfully performed to obtain the results and evaluate the feasibility of this technology. A combustor model was also developed for the twin-annular, pre-mixing swirler (TAPS) II burner used in the CFM LEAP engine. This model is currently being validated.

Major Accomplishments

The thermodynamic cycle model for water injection revealed increased cycle efficiency in the case of water injection before the compression in both pre-LPC and pre-HPC water injection cases. This is because the evaporative cooling effect of water reduces the work required to compress the same amount of air to the desired pressure after compression. The pre-LPC water injection case yielded the maximum benefit, followed by the pre-HPC water injection up to the saturation limits. When water is injected upstream of the combustor after the compression has already occurred, the evaporation no longer yields the

compression work benefit, and the cooling effect implies only an increase in the heat input required to raise the temperature to the same level. Hence, the fuel consumption increases, as shown in Figure 3. The Pycaso emission model was expanded to simulate water injection in an RQL-type combustor. The NO_x emissions index (EI) was obtained as shown in Figure 4.

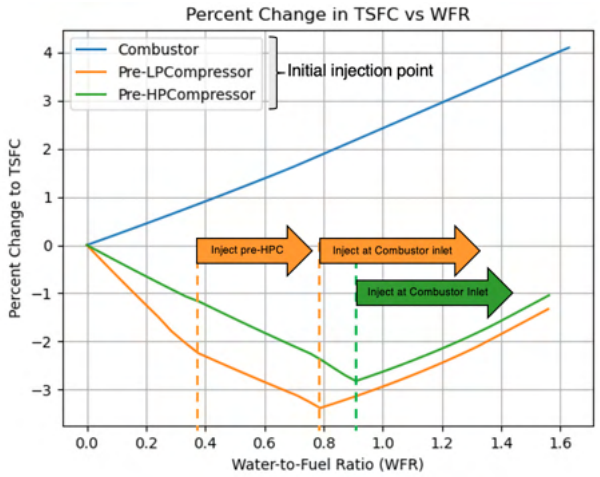

Figure 3. Thermodynamic cycle analysis: effect of water injection on fuel consumption.

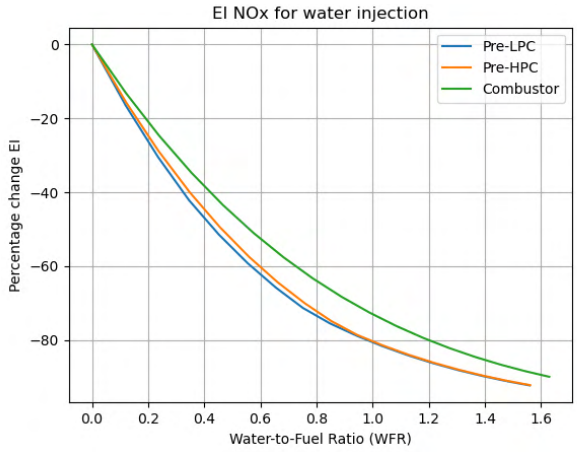

Figure 4. Combustor analysis: effect of water injection on NO_x emissions.

Finally, the results were combined for the most beneficial (pre-LPC) case to study the overall effect of water injection on fuel consumption and NO_x emissions. It was assumed that water is injected for the entire cruise duration at a cruise speed of 900 kph, and a lift-to-drag ratio of 16 was considered for all the ranges. As shown in Figure 5, water injection is more beneficial for shorter range flights because of the lower weight of water carried.

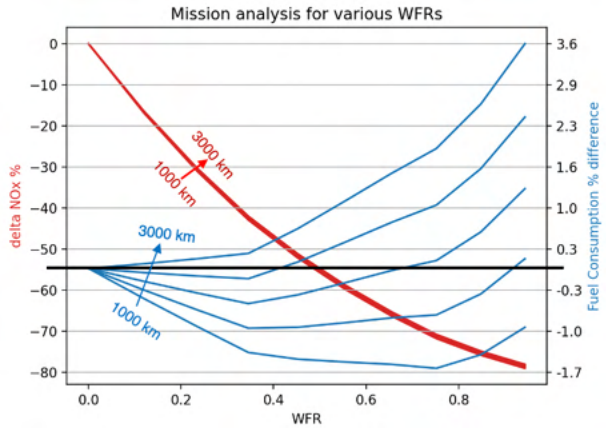

Figure 5. Overall mission analysis: effect of water injection on total fuel consumption and NO_x emissions.

The Pycaso emission model was also expanded to simulate a staged lean-burn combustor type, such as TAPS or TAPS II. Both experimental and computational fluid dynamics (CFD) data of the combustor internal flow field and reaction field were used in model construction. A simple fuel splitting technique is assumed, which dictates a fixed fuel flow rate ratio between the pilot flame and the main flame fuel injection during staging. Water injection can be performed into combustor pilot flow swirlers, the main flow premixing passage, and the final dilution region. Coupling with an engine model that resembles the CFM-LEAP-1A engine, the simulated NO_x and CO emissions at the sea level static condition have been found to be consistent with the experimental emissions measurements from the International Civil Aviation Organization Aircraft Engine Emissions Databank. The impact of water injection on emissions with the staged lean-burn combustor will be investigated in the future.

An exploratory contrail analysis was also performed for all flights flown in the year 2016. Water injection was found to yield a significant increase in persistent contrail formation, because of the higher tendency of water vapor to condense in the plume. The increase in the proportion of flight distance leading to persistent contrail formation is shown in Figure 6 for varying water-to-fuel ratios.

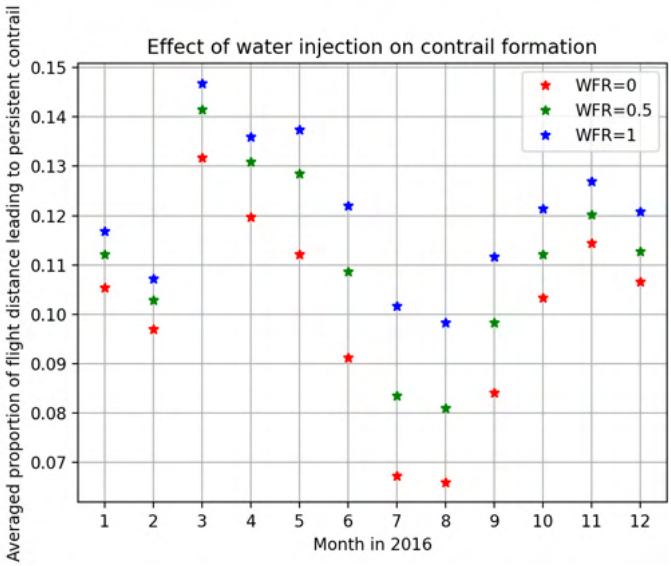

Figure 6. Effect of water injection on contrails.

Publications
None

Outreach Efforts
None

Awards
None

Student Involvement
This task was conducted primarily by Yang Chen and Syed Shayan Zahid, graduate research assistants working under the supervision of Dr. Jayant Sabnis and Dr. Raymond Speth.

Plans for Next Period
This model is based on a key assumption that considers the full evaporation of the water droplet under study. In addition to the thermodynamic analysis already conducted, it is also important to evaluate the time required for the injected water droplets to evaporate with the residence time available at the location of interest in the engine. This evaluation will be performed by modeling the energy and mass conservation equations for the injected water droplets to calculate the evaporation time. The water injection strategy will be explored for other parts of the mission, such as takeoff and climb-out, to determine the marginal benefit of this technology at different power conditions. Finally, a sensitivity analysis will be conducted for various engine parameters, such as the overall pressure ratio (OPR) and fan pressure ratio (FPR).

In terms of extending the functionality of the Pycaso emission model, the impacts of water injection on NO_x and CO emissions will be further studied for different combustor configurations, such as the TAPS combustor. Emissions of other types of pollutants, such as soot, will also be simulated by the Pycaso model.

References
Daggett, D. L. H. (2004). Water misting and injection of commercial aircraft engines to reduce airport NOx (Report No. NASA/CR—2004-212957). National Aeronautics and Space Administration.

Moore, R. H., Shook, M., Beyersdorf, A., Corr, C., Herndon, S., Knighton, W. B., Miake-Lye, R., Thornhill, K. L., Winstead, E. L., Yu, Z., Ziemba, L. D., & Anderson, B. E. (2015). Influence of jet fuel composition on aircraft engine emissions: A synthesis of aerosol emissions data from the NASA APEX, AAFEX, and ACCESS missions. Energy Fuels, *29*(4), 2591–2600.

Speth, R. L., & Ghoniem, A. F. (2009). Using a strained flame model to collapse dynamic mode data in a swirl-stabilized syngas combustor. Proceedings of the Combustion Institute, *32*, 2993–3000.

Speth, R. L., Rojo, C., Malina, R., and Barrett, S. R. H. (2015). Black carbon emissions reductions from combustion of alternative jet fuels. Atmospheric Environment, *105*, 37–42.

Project 052 Comparative Assessment of Electrification Strategies for Aviation

Massachusetts Institute of Technology

Project Lead Investigators

Steven R. H. Barrett
Professor of Aeronautics and Astronautics
Director, Laboratory for Aviation and the Environment
Massachusetts Institute of Technology
77 Massachusetts Ave, Building 33-207, Cambridge, MA 02139
(617) 452-2550
sbarrett@mit.edu

Florian Allroggen
Research Scientist
Laboratory for Aviation and the Environment
Department of Aeronautics and Astronautics
Massachusetts Institute of Technology
77 Massachusetts Ave, Building 33-115A, Cambridge, MA 02139
(617) 715-4472
fallrogg@mit.edu

Raymond Speth
Principal Research Scientist
Laboratory for Aviation and the Environment
Department of Aeronautics and Astronautics
Massachusetts Institute of Technology
77 Massachusetts Ave, Building 33-322, Cambridge, MA 02139
speth@mit.edu

University Participants

Massachusetts Institute of Technology (MIT)

- PI: Professor Steven R. H. Barrett; Co-PIs: Dr. Florian Allroggen, Dr. Raymond Speth
- FAA Award Number: 13-C-AJFE-MIT, Amendment Nos. 062, 072, and 080
- Period of Performance: October 1, 2020 to September 30, 2021
- Tasks:
    1. Develop a suite of roadmaps for aircraft electrification (covered in the previous reporting period; not reported for this period)
    2. Develop a system-level engineering model of power conversion processes and aircraft energy requirements
    3. Develop a model for analyzing the economics of electrification strategies
    4. Comparative validation runs (to be started in the following reporting period; not covered in the current reporting period)
    5. Analyze the system-level costs and benefits of the electrification strategies (to be started in following reporting periods; not covered in the current report)

Project Funding Level

This project received $600,000 of FAA funding and $600,000 of matching funds. The sources of matching funds were approximately $140,000 from MIT, plus third-party in-kind contributions of $460,000 from NuFuels LLC.

Investigation Team

PI:	Professor Steven Barrett (MIT) (all MIT tasks)
Co-PIs:	Dr. Florian Allroggen (MIT) (all MIT tasks)
	Dr. Raymond Speth (MIT) (Tasks 1, 2, and 4)
Co-investigator:	Dr. Sebastian Eastham (MIT Task 5)
Postdoctoral Associates:	Haofeng Xu (MIT, Tasks 2, 3, and 4)
	Christoph Falter (all MIT tasks)
Graduate Research Assistants:	Nicolas Gomez-Vega (MIT, Tasks 1, 2, and 4)
	James Abel (MIT Tasks 2 and 3)
	Dun Tan (MIT Task 2)

Project Overview

The long-term goal of this project is to quantify the costs, emissions, and resulting environmental impacts (i.e., climate and air-quality impacts) of different electrification approaches for commercial aviation. The electrification pathways considered range from battery-electric (or "all-electric") aircraft to electrofuel-powered and liquid hydrogen (LH_2)-powered aircraft, for which electrofuels and hydrogen are produced by using renewable electricity. The project will help identify the best approach for using one unit of electric energy to power aviation.

In the project, we analyze the costs, emissions, and atmospheric impacts associated with each electrification strategy. We develop both system-level engineering and system-level economic models, which include electricity generation, fuel production, transport and storage, aircraft energy requirements, and aircraft operations. The models analyze different electrification pathways by using what can be described as a "power station to wake" approach. The models quantify differences in costs and emissions associated with each electrification approach, as compared with a set of baseline aircraft powered by conventional petroleum-derived fuels or drop-in sustainable aviation fuels (SAF). The outputs from these models will be used in a cost–benefit model, which will provide insights into the costs associated with each technology—both investment and operating cost—and compares them with the lifecycle climate and air-quality abatement potential. When comparing electrification scenarios with the conventional petroleum-derived baseline, we take various electricity production scenarios (e.g., different fossil fuels and renewables) into account.

Task 2 - Develop a System-level Engineering Model of Power Conversion Processes and Aircraft Energy Requirements

Massachusetts Institute of Technology

Objectives

The goal of this task is to develop an aircraft technology, production, and operation model, as well as a fuel production model. Jointly, these models provide a technical representation of the power conversion processes from the initial power generation to propulsion onboard the aircraft. These models provide a technical basis for the comparative assessments in this project.

During the reporting period, our analysis focused on defining the mass and energy balances, as well as key technologies for producing electrofuels, specifically drop-in power-to-liquid (PtL) fuels and LH_2. In addition, a modeling platform for estimating the production cost of aircraft was developed.

Research Approach

Modeling of PtL production

PtL fuel is modeled to be produced from water via electrolysis and from CO_2 captured either from the atmosphere via direct air capture or from waste CO_2 streams. Electricity is a major input to these processes; we assume that this electricity comes

from renewable, low-carbon sources, such as wind and photovoltaics (PV). This assumption is based on prior analyses showing that most current grids do not allow PtL fuels to be produced with lower lifecycle greenhouse gas (GHG) emissions than petroleum-derived fuels, because of the high reliance on fossil fuels for power generation in many grids worldwide. PV and wind energy are low-emission sources of electricity that can be applied in many regions at relatively low cost. A main difference between these two renewable sources of electricity is their capacity factor, i.e., the share of full load hours per year: whereas PV is limited to capacity factors of up to about 35% (single-axis tracked modules in sunny regions), wind energy significantly surpasses this value in many regions.

For the purposes of this analysis, the fuel production processes rely on an electrolyzer to produce hydrogen. This hydrogen is used as a constituent of synthesis gas (H_2 + CO, syngas) and to reduce CO_2 to CO in the reverse water–gas shift reaction (RWGS). CO_2 for the process is assumed to be captured from the atmosphere with a temperature–pressure swing adsorption process. Direct air capture of CO_2 requires electricity and low-temperature heat. Because of the low temperatures required to regenerate the sorbent (~100 °C), the thermal energy input can be at least partly covered by waste heat from other process steps, such as Fischer–Tropsch synthesis. Syngas is converted into liquid fuels in the Fischer–Tropsch process, which produces hydrocarbons with different chain lengths, from methane to waxes. Aftertreatment increases the yield of jet fuel by adjusting the chain lengths to the desired range.

The transport of PtL fuels leverages the established infrastructure of oil pipelines, ships, and trucks.

The total energy demand of PtL production is estimated to be 2.6–3.1 MJ of electricity per MJ of fuel today and 2.2–2.6 MJ (electricity)/MJ (PtL) in the year 2050.

Modeling of LH_2 production

Similar to PtL fuel production, we model the LH_2 fuel production pathway to utilize electrolysis. Based on an extensive literature review, we assume that electrical energy is transported via high-voltage direct-current lines from the location of PV and wind power generation to the location of fuel production, which is often close to the airport. This method of energy distribution has been found to be favorable, given the difficulties in transporting hydrogen, especially in liquid form (i.e., low temperatures of LH_2 transport).

For the electrolysis, a proton-exchange membrane (PEM) electrolyzer is considered in the modeling, because of its responsiveness to changing electricity loads and its projected costs. The produced hydrogen is then liquefied via established processes (different pre-cooling steps and gas expansion).

The total energy demand for LH_2 production is estimated to be 1.8–2.2 MJ of electricity per MJ of LH_2 today and is expected to be within 1.4–1.7 MJ (electricity)/MJ (fuel) in the year 2050.

Aircraft cost model

Two models were developed to estimate the production cost of a novel aircraft design using non-drop-in fuels: one for the airframe and one for the propulsion system.

The airframe cost model is based on the Development and Procurement Costs of Aircraft (DAPCA) IV cost estimation model, as presented by Raymer. This model breaks down the cost of a new airframe into development, tooling, production, and flight-testing. The primary input to this model is a modified operating empty weight (OEW), and component weights are re-weighted according to their contribution to the overall cost of a typical airframe. Additional corrections are added to account for the higher research and development costs of aircraft using novel propulsion concepts.

The lack of established cost models for novel aircraft propulsion concepts (e.g., turboelectric systems and hydrogen-powered systems) necessitated the development of cost estimates from analogs in non-aerospace contexts. Cost models for electric motors and motor controllers in a turboelectric aircraft, for example, were scaled from estimates of the costs of these parts in industrial, automotive, and power-generating sectors. Similarly, the costs of fuel tanks for LH_2 (whose design drives many of the changes to the overall configuration of LH_2-fueled aircraft) was scaled from the costs of tanks currently used in LH_2 tanker trucks. Additional adjustment factors were added to the costs of these systems to account for the increased development costs for aerospace-compatible components.

Milestone
The modeling of fuel production pathways has been completed. The results have been presented to the International Civil Aviation Organization (ICAO) Committee on Aviation Environmental Protection (CAEP) Long-Term Aspirational Goal (LTAG) Task Group and are contributions to the final report of the LTAG fuel subgroup.

Major Accomplishments
MIT has developed models representing the physical and technical processes to produce PtL and LH_2 fuels under both current and future technologies.

The MIT team has used the methods and data developed under this effort to provide scientific input to ICAO's development of a LTAG for decarbonizing the aviation sector.

Publications
None

Outreach Efforts
- The team summarized the fuel production modeling during the Fall 2020 and Spring 2021 ASCENT meetings.
- The team gave multiple presentations to ICAO's LTAG Task Group and actively participated in numerous expert discussions.
- Presentation at the Cryogenic Engineering Conference and International Cryogenic Materials Conference (CEC-ICMC) on the use of hydrogen to reduce the carbon footprint of aviation.
- Presentation to the Aviation Emissions Characterization (AEC) Meeting, April 2021.
- Presentation to numerous stakeholders, including NASA, Advanced Research Projects Agency–Energy (ARPA-E), and industry.

Awards
None

Student Involvement
During the reporting period, the MIT graduate students involved in this task were Nicolas Gomez Vega, James Abel, and Dun Tan.

Plans for Next Period
Over the coming year, the team will expand the existing capabilities of the aircraft design tool TASOPT, which are currently limited to A320-class aircraft powered by drop-in fuels and batteries. In particular, the team will work to implement a hydrogen aircraft in TASOPT.

In addition, the current aircraft implementations in TASOPT are limited to single-aisle aircraft for medium-haul routes. The team will ramp up work on including aircraft models with longer or shorter ranges, as well as higher or lower passenger capacity.

Task 3 - Develop a Model for Analyzing the Economics and Emissions of Electrification Strategies
Massachusetts Institute of Technology

Objective(s)
The goal of this task is to develop a system-level analysis capability for assessing the possible electrification pathways (e.g., battery electric, or hydrogen fuel cell) and their deployment in various aircraft electrification scenarios (e.g., replacing regional flights below 1,000 nmi at a specific airport). The system model focuses on the processes upstream of the fueling, by using the fuel production model as outlined under Task 2, and on the operation of the aircraft itself. Outcomes of interest include the operating costs, required investments, and lifecycle GHG emissions of the system.

During the current period, the focus of the team was: (a) to quantify the energy system interactions of scaling up PtL and LH_2 production; (b) to quantify the environmental footprint and economics (cost and investment pathways) of LH_2 and PtL production; and (c) to outline and assess the LH_2 distribution infrastructure at airports.

Research Approach

Energy system implications of scaling up PtL or LH_2 production

As shown under Task 1, the production of LH_2 or PtL fuel requires substantial amounts of electricity, because of the energy intensity of electrolysis, the capture of CO_2, and the liquefaction of hydrogen. The implications of fuel replacement on the power generation sector are shown below in a case study of the Paris Charles de Gaulle airport (CDG). We note that the energy efficiency of hydrogen-powered aircraft is assumed to be identical to that of the current aircraft using Jet-A fuel.

If all fuel at CDG in 2019 were to be replaced by LH_2, and the fuel efficiency of LH_2 aircraft were the same as that of conventional aircraft, 8.4 GW of annually averaged electrical power generation would be required to produce the required LH_2 (Figure 1). Most of the energy would be used for water electrolysis. Replacing all fuel with PtL would require even more power generation – between 10 and 17 GW annually averaged, depending on the assumed technology standard. It should be noted that in the calculations, only the electricity attributable to the jet fuel fraction is counted; the power generation for the entire output slate leading to the required jet fuel production is significantly larger. The numbers reported for the jet fuel share compare to a total installed power generation capacity in the French grid of 130 GW (nameplate capacity) and of 7 GW for the largest nuclear power plant in the world (nameplate capacity). Taking the intermittency of renewable power generation into account, the required area for solar-PV-based power generation for LH_2 would be >585 km² if LH_2 is produced completely remotely (production and liquefaction) in a solar-optimal location, and >490 km² for offsite H_2 production plus >130 km² for onsite local liquefaction. If PtL were used, more than 700 km² of land would be required (offsite) to run PtL fuel production for CDG.

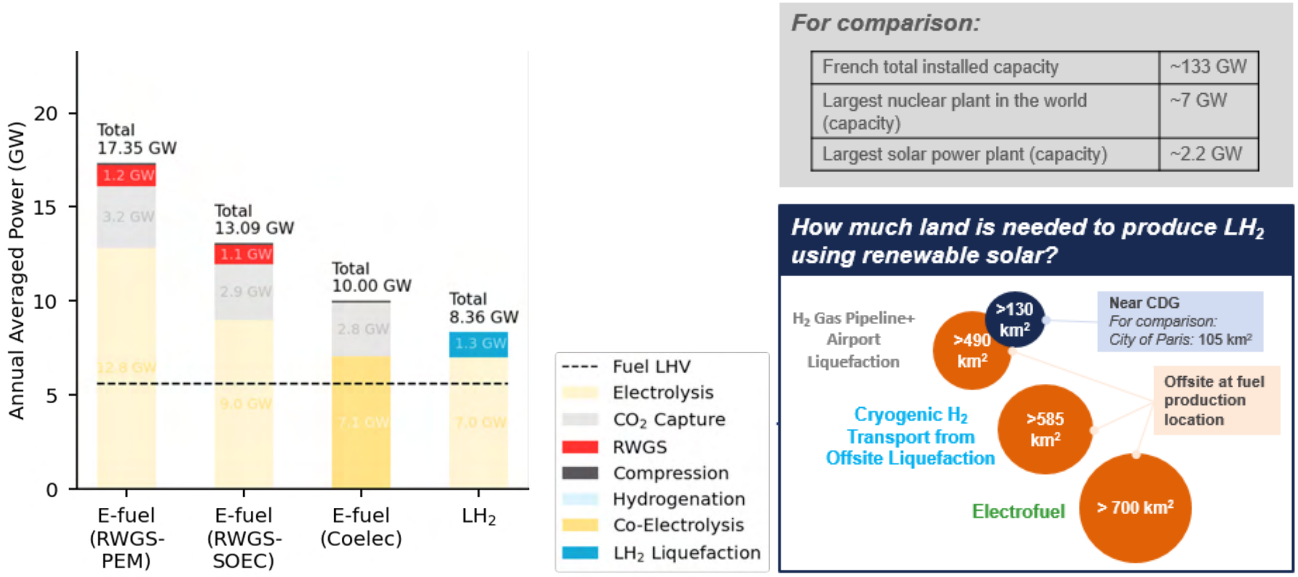

Figure 1. Energy system implications of supplying Paris Charles-de-Gaulle airport with LH_2 or PtL.

It is important to note that CDG is not an exception. Figure 2 shows the annually averaged electrical power generation requirements for full LH_2 replacement at the 20 airports with the highest energy demand, on the basis of the traffic in 2019. The largest power generation requirement is found for London Heathrow, with 12.8 GW (annually averaged). However, if hydrogen were (hypothetically) used only for flights shorter than 2,000 nmi, the power requirements would decrease to 1.5 GW. This strong sensitivity to flight length is unique to London Heathrow. For example, for the Atlanta airport, we find that replacement for flights shorter than 2,000 nmi would require electric power generation at 4.0 GW (annually averaged), whereas full replacement for all flights would require 5.6 GW (annually averaged).

If all airports were served with LH_2 at 2019 traffic levels, 536 GW of power generation (annually averaged) would be required. This requirement would increase to 640–1,113 GW in the case of PtL, depending on technological progress in the energy intensity for PtL production (Figure 3). For comparison, the estimated global PV power generation capacity (nameplate) is approximately 950 GW (end of 2021), and the total power generation capacity in the US grid is approximately 1,200 GW. However, the number should also be considered in the context of future scale-up of renewable power generation, e.g., as modeled in the International Energy Agency's Sustainable Development Scenario, which assumes a global annually averaged power generation from PV and wind of 3,000 GW by the year 2050.

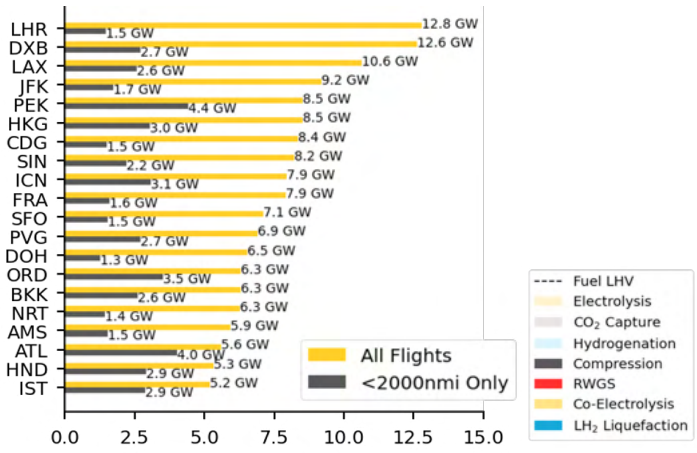

Figure 2. Energy system implications of replacing jet fuel with LH_2 at the 20 airports with the highest energy intensity (according to 2019 traffic).

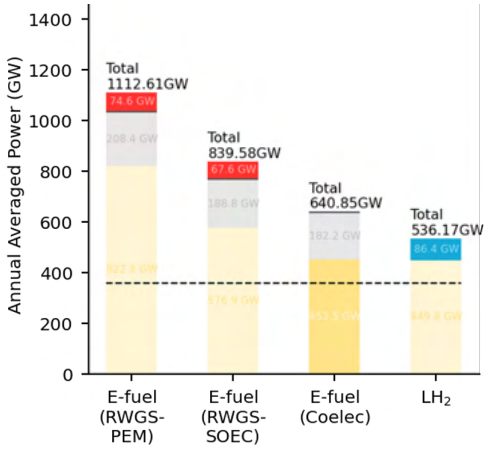

Figure 3. Energy system implications of replacing jet fuel with either LH_2 or PtL in a global replacement scenario (according to 2019 traffic).

Environmental and economic footprints of LH_2 and PtL

The production costs for PtL are estimated in three scenarios of different ambition regarding the transition speed to a renewable energy base. In Figure 4, the minimum selling price of PtL, as calculated in a joint effort with researchers from Washington State University, is shown for the three scenarios in the timeframe from 2020 to 2050. Today, the production costs for PtL fuel production using waste CO_2 are estimated to be in the range of 2.8–4.6 $/L in the most ambitious scenarios. In the least ambitious scenario, the costs are estimated to be in the range 3.4–6.2 $/L. These costs are expected to decrease to 1.3–1.7 $/L and 1.8–3.0 $/L in the most and least ambitious scenarios, respectively.

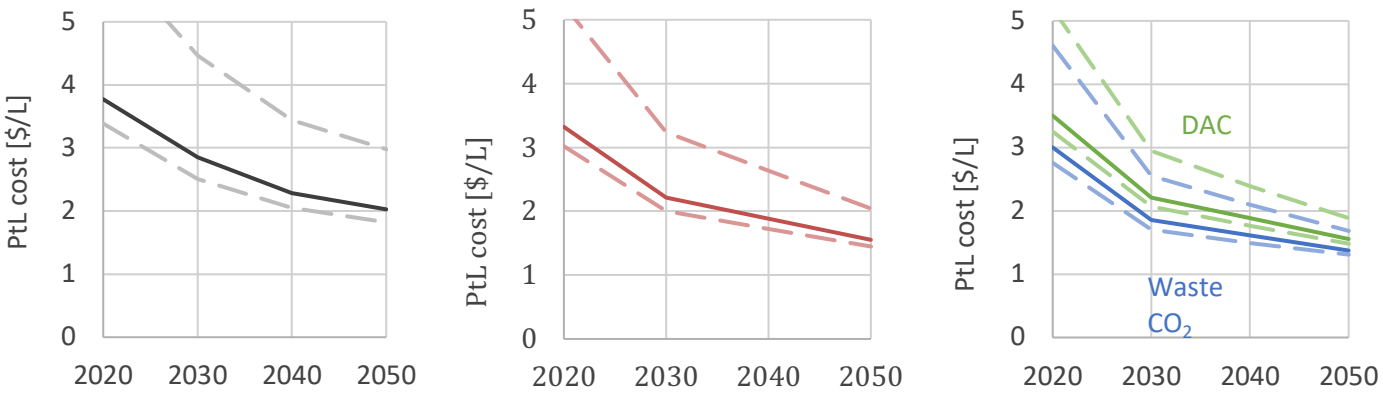

Figure 4. Minimum selling price of PtL for three integrated scenarios reflecting different levels of ambition in the transition to a renewable energy base (left: least ambitious; middle: average scenario; right: most ambitious). Solid lines show the median scenario, and dotted lines show the minimum and maximum estimates. DAC=direct air capture.

The production cost projections for LH_2 are shown in Figure 5. The expected minimum selling price today is in the range of 6–13 $/kg (or 2.0–4.8 $/L of jet fuel equivalent). These costs are expected to decrease to the range of 1.9–4.9 $/kg (or 0.5–1.4 $/kg of jet fuel equivalent) in 2050, mainly driven by cost reductions and efficiency gains in water electrolysis and hydrogen liquefaction. At the lower end, the cost estimates in 2050 approximately reach cost parity with conventional jet fuel at today's market prices.

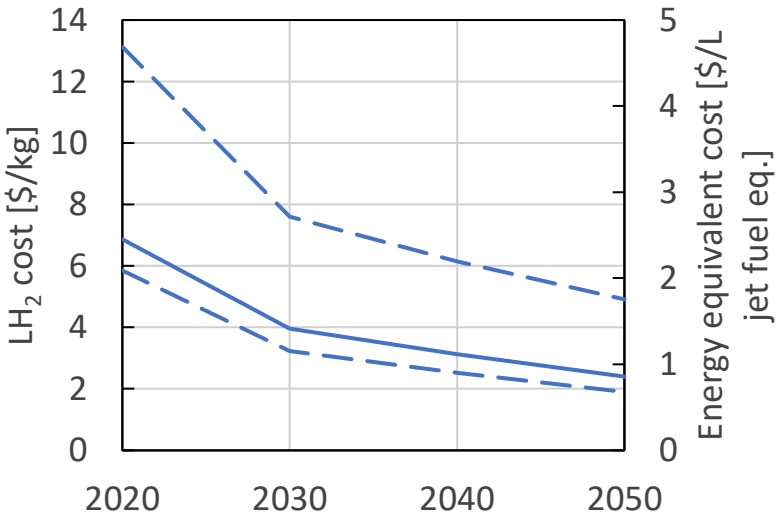

Figure 5. Minimum selling price of LH_2 fuel. Minimum, average, and maximum estimates are indicated.

The use of renewable energy for producing alternative fuels has the potential to reduce the lifecycle GHG emissions associated with LH_2 and PtL. In Figure 6, the GHG emissions of PtL fuel production are shown from 2020 to 2050 for three scenarios with different level of ambition regarding the introduction of renewable energy. Embedded emissions are taken into account, which raises the specific emissions per megajoule of fuel above zero. The resulting emissions of PtL fuel using a mix of PV and wind energy are on the order of 10–20 g/MJ, whereas wind achieves significantly lower emissions than PV. If the electricity for PtL production is assumed to come from the grid (at the global grid average), PtL fuels currently do not provide an emissions benefit over conventional jet fuel (conventional jet fuel carbon intensity at 89 gCO_2e/MJ). This finding changes only under ambitious grid decarbonization scenarios.

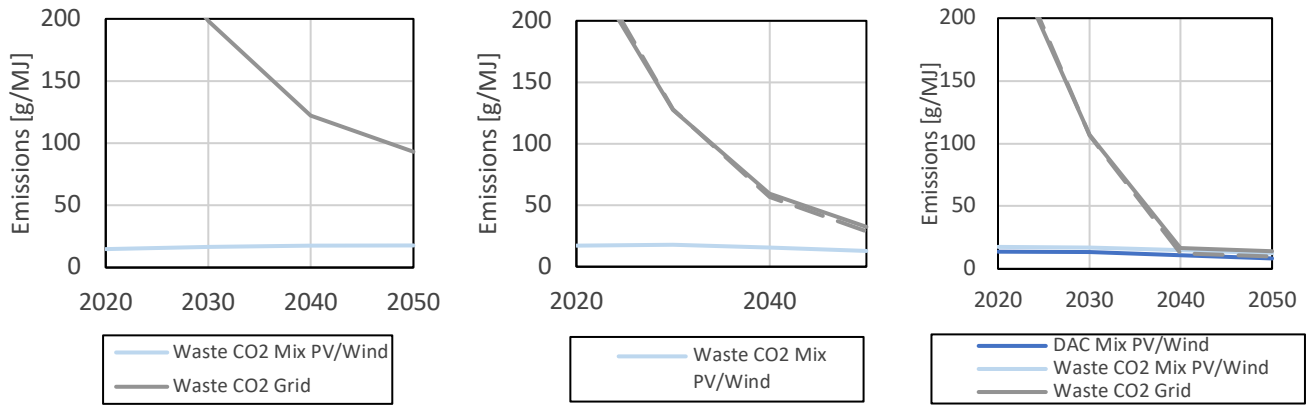

Figure 6. Emission trajectories of PtL production for three integrated scenarios reflecting different levels of ambition in the transition to a renewable energy base (left: least ambitious; middle: average scenario; right: most ambitious). Either waste CO_2 or atmospheric CO_2 is used for the production of PtL.

The GHG emissions of LH_2 production are shown in Figure 7 for both grid electricity and a mix of PV and wind energy. Similar to PtL, the use of renewable energy is required to achieve a significant reduction of GHG emissions relative to fossil fuels. If PV/wind energy is exclusively used for LH_2 production, lifecycle GHG emissions of 6–10 g CO_2e/MJ can be reached, while considering embedded emissions. Under ambitious global grid decarbonization, as modeled in the International Energy Agency Net Zero Emissions 2050 scenario, LH_2 could provide GHG emissions savings over conventional jet fuel from the late 2020s, if the global grid average is assumed.

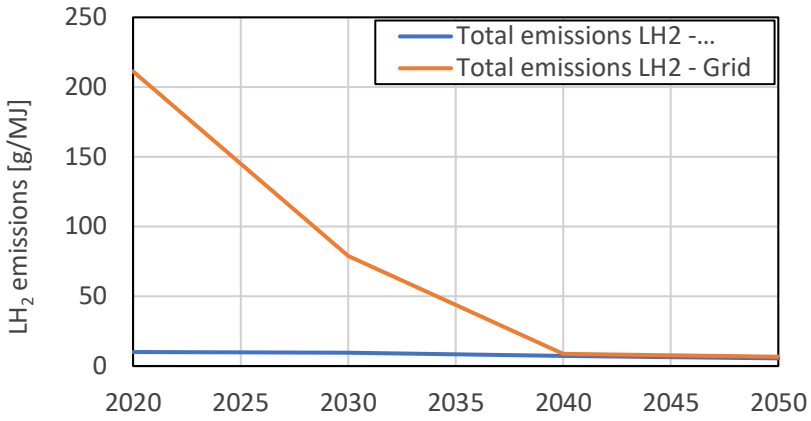

Figure 7. Lifecycle GHG emissions of LH_2 production assuming ambitious grid decarbonization.

LH_2 distribution infrastructure at airports

Because LH_2 is a non-drop-in fuel, new airport infrastructure would be required for fuel distribution. We therefore determined the scale of the required investments. To estimate this cost, three potential refueling strategies for LH_2 aircraft were analyzed: (a) using tanker trucks to deliver fuel to aircraft at the gate, (b) using an underground hydrant system to deliver fuel to the gate, and (c) moving aircraft to a remote bay closer to the fuel storage farm for refueling. The scale of each of these systems was assessed by using flight schedule data to estimate energy demand, and information regarding airport layouts (e.g., locations of gates) to estimate the physical size of the infrastructure required (e.g., the length of refueling pipelines). After the refueling system was sized, its cost was calculated with a parametric cost model. This model was used to calculate capital and operating costs of a potential LH_2 refueling system (e.g., trucks, pipelines, storage tanks, labor, etc.) for each global airport and to estimate the additional land required for this system. Cost assumptions were derived from an extensive

literature study and were largely rely on the extrapolation of values from existing hydrogen systems used in other industries (e.g., automotive and spaceflight). In addition, the model explicitly considers the unique physical properties of hydrogen infrastructure, such as the requirement to install hydrogen pipelines in open trenches for safety.

No single refueling strategy was found to be optimal. Instead, the optimal infrastructure setup varied depending on the geometric layout and demand profile of each airport. In general, airports with expansive layouts favored truck-based refueling systems, because the large distances between fuel storage infrastructure and gates would make hydrant-based systems uneconomical. In contrast, more compact airports with frequent movements favor hydrant-based systems. These trends are illustrated in the two case studies shown in Figure 8: the expansive multi-terminal layout of Kuala Lumpur Airport and the more compact layout of Helsinki Airport.

In many cases, the greatest additional cost imposed by hydrogen refueling was found to be from the lost revenue resulting from longer aircraft turnaround times. Longer fueling times are potentially caused by LH_2's lower volumetric energy density as compared to conventional jet fuel, if flow rates in hydrogen refueling hoses are comparable to those achieved by existing conventional fuel hoses. The extent to which longer fueling times affect turnaround times depends on (a) the flight distance and required fuel volume, and (b) the ground operations that can safely be carried out in parallel with refueling (e.g., boarding/de-boarding). The analysis shows that, for most short-haul flights, the additional refueling time falls within the existing turnaround-time window, even if boarding and loading cannot commence during fueling. With increasing flight distances, these restrictions become more binding and can lead to significant increases in turnaround times.

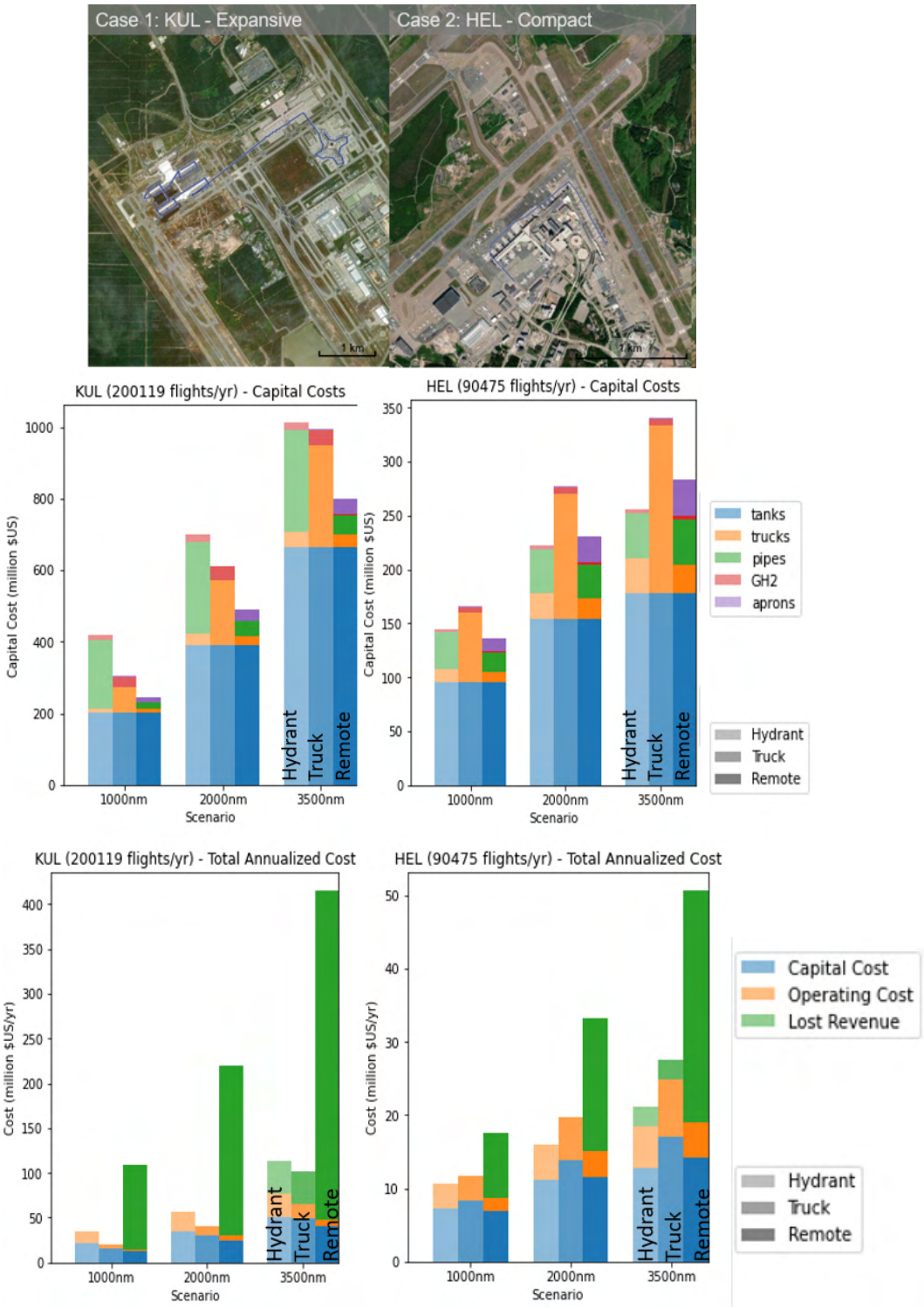

Figure 8. LH_2 airport distribution infrastructure case studies for Kuala Lumpur Airport (left) and Helsinki Airport (right), showing terminal layout (top), system CapEx (middle), and yearly annualized costs (bottom).

Milestones
The system-level modeling of fuel production and distribution has been completed for LH_2 and PtL. The results have been presented to ICAO CAEP's Long-Term Aspirational Goal (LTAG) Task Group and form the basis for the final report of LTAG's fuel subgroup.

Major Accomplishments
The team has compiled a full modeling chain for evaluating the production and distribution of PtL and LH_2 at scale.

The results from this research provide scientific input for the development of an LTAG for decarbonizing the aviation sector.

Publications
None

Outreach Efforts
- The team summarized key findings during the Fall 2020 and Spring 2021 ASCENT meetings.
- The team gave multiple presentations to ICAO's LTAG Task Group and actively participated in numerous expert discussions.
- Presentation to the CEC/ICMC Conference on the use of hydrogen to reduce the carbon footprint of aviation.
- Presentation to the Aviation Emissions Characterization (AEC) Meeting, April 2021.
- Presentation to numerous stakeholders, including NASA, ARPA-E, and industry.

Awards
None

Student Involvement
During the reporting period, the MIT graduate students involved in this task were Nicolas Gomez Vega and James Abel.

Plans for Next Period
The next step is to integrate the fuel production and distribution models with more detailed aircraft models, which are developed under Task 2. This integration will allow the team to consider additional feedbacks of energy carrier choice on the specific energy consumption of the aircraft and subsequently on the entire system.

Project 053 Validation of Low Exposure Noise Modeling by Open-source Data Management and Visualization Systems Integrated with AEDT

Stanford University

Project Lead Investigator

Juan J. Alonso
Vance D. and Arlene C. Coffman, Professor
Department of Aeronautics & Astronautics
Stanford University
Stanford, CA 94305
Phone: (650) 723-9954
E-mail: jjalonso@stanford.edu

University Participants

Stanford University

- PI(s): Prof. Juan J. Alonso
- FAA Award Number: 13-C-AJFE-SU-022
- Period of Performance: October 1, 2020 to September 30, 2021
- Task(s):
    1. Complete the Metroplex Overflight Noise Analysis (MONA) prototype, including Aviation Environmental Design Tool (AEDT) integration
    2. Validate and verify AEDT noise predictions in DNL 55–65 dB areas
    3. Develop data science formats and perform scientific computations for large-scale airspace analyses
    4. Investigate viable alternative approach routes into the San Francisco Bay Area metroplex

Project Funding Level

Year 2 of ASCENT Project 53 has been allocated FAA funds in the amount of $400,000. Cost sharing in excess of this amount has been identified from various sources. Mr. Thomas Rindfleisch is contributing all of his time, uncompensated, and Mr. Donald Jackson is also contributing part of his time, uncompensated, to the project. In addition, contractor costs for the development of the MONA project website, the cost of support for undergraduate students and summer interns, and some equipment purchases (including installation costs) are also being used to generate cost sharing for this project. During the first 18 months of this project, more than $850,000 of cost sharing had already been accounted for.

Investigation Team

The investigation team consists of the faculty, graduate and undergraduate students, and collaborators listed below with their respective areas of expertise/contribution:

1. Juan J. Alonso (PI, Stanford Aeronautics & Astronautics): Overall responsibility for the project and its technical and administrative elements
2. Nick Bowman (Graduate Student, Stanford Computer Science): MONA project cloud infrastructure, cloud-based execution of AEDT analyses, and Apache Kafka-based data collection (Jan. 1–Aug. 31, 2021)
3. Brynne Hurst (Graduate Student, Stanford Computer Science): Flight trajectory database analysis and synthesis (Jan. 1–Mar. 31, 2021)
4. Donald Jackson (Collaborator, Independent Consultant): Overall MONA project infrastructure (servers, databases, hardware/software monitoring), geographical information systems (GIS), web-based visualization deployment, and technical guidance (full period of performance)

5. Priscilla Lui (Co-term Student, Stanford Computer Science): Real-time sound-level monitor (SLM) software, metrics, and raspberry Pi connectivity (Jan. 1–Jun. 30, 2021)
6. Vikas Munukutla (Graduate Student, Stanford Computer Science): Automation of AEDT analyses via generation/query of input/output databases on the cloud (Oct. 1–Dec. 31, 2020)
7. Chetanya Rastogi (Graduate Student, Stanford Computer Science): Overall database infrastructure improvements and noise monitoring/filtering software (Oct. 1–Dec. 31, 2020)
8. Thomas Rindfleisch (Collaborator, Stanford University Emeritus): Noise monitoring and filtering, aircraft trajectory collection/processing, and visualization (full period of performance)
9. Aditeya Shukla (Undergraduate Student, Stanford Aeronautics & Astronautics): Artificial intelligence (AI)/machine learning (ML) classification of aircraft trajectories and real-time SLM software (full period of performance)

Project Overview

The Metroplex Overflight Noise Analysis project (MONA) was initiated to provide real-time and objective data, analyses, and reports to key stakeholders and policy makers to mitigate the noise impacts of the deployment of new NextGen procedures. This system (a) collects and archives air traffic data using a network of antennae and receivers, (b) analyzes noise impacts using a variety of metrics, (c) visualizes resulting large-scale datasets, and (d) uses a network of sound-level monitors to enhance the quality of noise predictions. The goal of this ASCENT project is to improve upon the noise predictions of MONA through tighter integration with AEDT. In particular, our work is focused on the following three tasks: (1) integrate and automate AEDT's noise analysis capabilities, (2) validate and verify (V&V) AEDT's noise predictions in DNL 55–65 dB areas, and (3) propose software engineering/architectural choices for future AEDT development to enhance usability in multiple workflows, including API formulation, visualization interfaces, resilient data acquisition and storage, and cloud computing.

The expected benefits of this project mirror the tasks mentioned above, including (a) the ability to automate complex noise analyses in metroplexes so that they are available in near-real time after the preceding 24-hr period, (b) a better understanding of the accuracy of AEDT's current noise models in low-noise (DNL 55–65 dB) areas and the reasons for discrepancies (if any) in existing predictions, and (c) recommendations for software developers on flexible architectures and APIs for AEDT to make the tool more versatile and generally applicable. AEDT predictions are built around the policy context of an average annual day. All of the V&V results produced and shared by the MONA team will be focused on a cumulative daily basis for which flight track data are directly collected.

Background and Previous Accomplishments

The MONA project started approximately three years ago with the main objective of providing real-time and objective data, analyses, and reports to key stakeholders and policy makers to help in mitigating noise impacts from the deployment of new NextGen procedures. Since then, we have developed and deployed a system that (a) collects, archives, and makes available air traffic data using a series of networked antennae and receivers 24/7, (b) analyzes noise impacts using a variety of metrics (based on both a MONA-developed noise prediction tool and the noise prediction tools within AEDT), (c) visualizes resulting large-scale datasets in a simple, user-friendly fashion using both a bespoke website and Uber's kepler.gl and deck.gl large-scale data visualization toolboxes, and (d) has deployed a small network of low-cost, Stanford-owned sound-level monitors scattered across the Bay Area and has included data from noise monitors deployed by San Francisco International Airport (SFO) to cross-calibrate measurements by MONA and SFO monitors, collect noise measurements over a broader geographic region, and enhance noise predictions so they describe exactly the actual noise levels experienced.

The longer-term objectives of the MONA project are to (a) ensure the validation and verification of all noise predictions provided by AEDT or other tools for areas near the airport and areas further away from the airport, (b) achieve full automation of complex noise analyses in regions around airports in the United States, including AEDT-based noise predictions, (c) make all results web-accessible for in-depth interpretations of historical and proposed changes, (d) eventually study potential alternative traffic patterns in complex airspace to mitigate aviation environmental impacts, and (e) export the proven and validated MONA technology to other airport regions via open-source software/hardware.

At the present time (December 2021), the MONA software has achieved a number of significant objectives that well position the team to achieve the work described in this grant proposal. First, MONA has deployed a small network of ADS-B/MLAT antennae, and the necessary software has been completed to merge data streams from all of these antennae including de-duplication of sightings, identification of aircraft equipment and routes flown, physical interpolation of data missing from joint observations, and archiving (in appropriate database formats) of information collected for successive analysis. Second, MONA has achieved a level of integration with FAA's AEDT software that enables fully automatic processing of noise exposure

at arbitrary receptor locations for arrival routes into the San Francisco Bay Area airports. Third, MONA has incorporated measurements from networked sound-level monitors into the system via the Apache Kafka system and has developed and validated approaches for non-aircraft-noise filtering (of raw noise data) based on digital filtering, aircraft position information, and automated identification of background noise levels that have been validated and verified.

Finally, over the past year, we have continued our efforts to interface the above-described MONA software modules with the kepler.gl open-source visualization framework, developed by Uber, to be able to visualize and animate aircraft positions and paths, noise predictions, various routes and procedures, etc., in order to better communicate the results of our work (see Figure 1). A preliminary version of the MONA website, which provides access to and visualization of the same information for a less experienced user and leverages the deck.gl library, has also been created (see Figure 2). Furthermore, our capabilities now allow us to compare traffic and noise patterns for multiple days (see Figure 3).

Figure 1. MONA visualization (using kepler.gl and deck.gl) of traffic patterns in the San Francisco Bay Area, including a 24-hr view of aircraft traffic patterns. Trajectories are colored by altitude, with purple/magenta indicating low altitudes and blue indicating high altitudes.

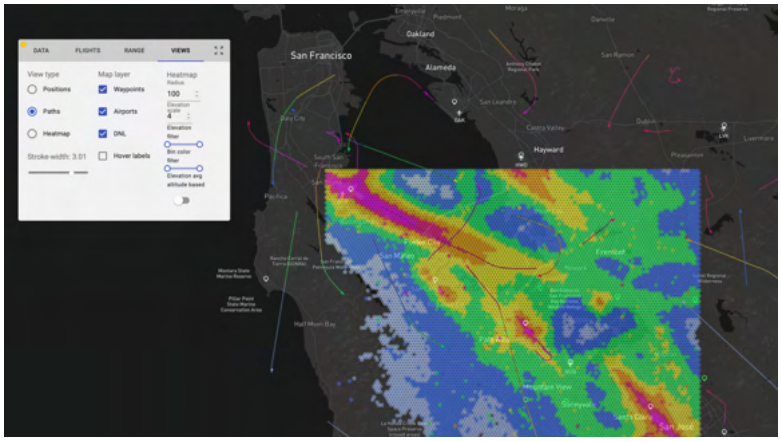

Figure 2. Current MONA web-access prototype for real-time aircraft location and 24-hr DNL contours.

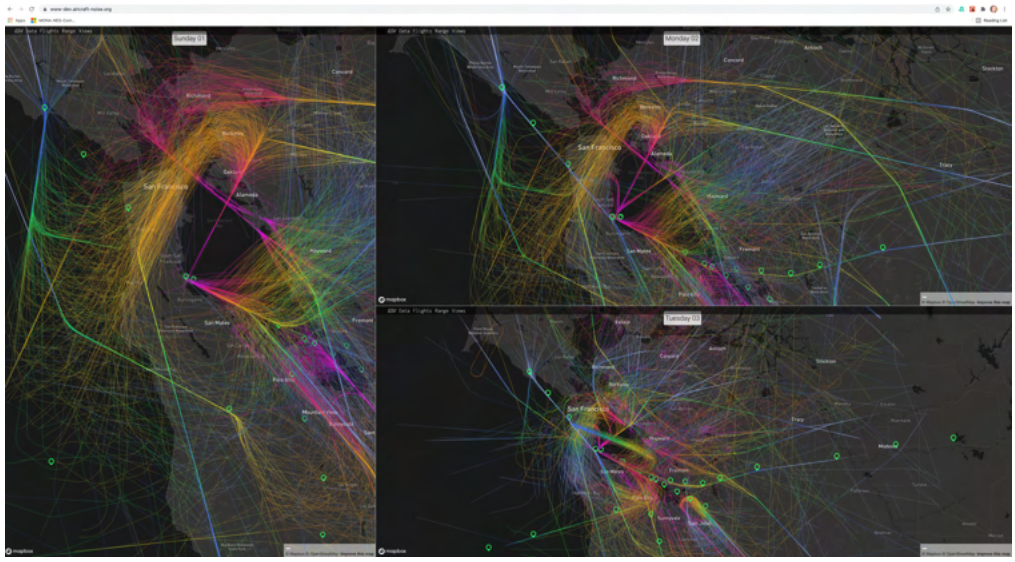

Figure 3. Comparative analysis of San Francisco Bay Area traffic patterns on different days obtained fr
visualization system.

Task 1 – Complete the MONA Prototype, Including AEDT Integration
Task 3 – Develop Data Science Formats and Perform Scientific Computing for Large-scale Airspace Analyses

Stanford University

Given that the vision of MONA is to make 24/7 aircraft noise information available through a simple visualization interface, predictions of aircraft noise are a fundamental component of the overall effort. We have begun to validate noise predictions with data collected from strategically located, Stanford-owned and SFO-owned, sound-level monitors (SLMs) whose raw sound level data has been appropriately filtered to eliminate non-aircraft noise sources. This section focuses on the development and completion of the first MONA prototype, including hardware, software, and data formats (corresponding to Tasks 1 and 3 of this Annual Report), with a description of our progress on integrating AEDT as seamlessly and tightly as possible.

The automation of the entire workflow has required the implementation and automation of a number of key steps, including:

1. Starting from a set of MONA-acquired and preprocessed flight paths and associated aircraft equipment for the previous 24-hr period, the necessary AEDT inputs are generated in an SQL study database that can be later consumed by AEDT. The input database must contain the actual location and three-dimensional geometry of the aircraft flight profile as a function of time, the specific aircraft equipment, and other auxiliary parameters needed for the analysis.
2. The setup of a noise analysis in AEDT, including all of the necessary metric descriptions, receptor locations, annualizations, and additional input data, must be automatically generated and included in the input study database as permitted by AEDT v3.
3. Automated execution of arbitrary analyses can then be pursued to allow AEDT to be run through a batch process without user intervention. For this batch process, we have developed and improved a cloud-based solution that automatically fires up a cloud instance, sets up the necessary communication structures, runs the AEDT study, and returns the study results to the computer executing the study.
4. A module for extracting the computed metrics and their spatial distributions for arbitrary metric computations has also been developed. Interactions with the output of AEDT analyses occur directly through the SQL output study database, which contains and stores all of the necessary information.

During the period covered by this report, we have continued to build upon the progress made during the first year of the grant to deploy a fully operational prototype that has been used to (see Task 2 progress) carry out preliminary comparisons between SLM experimental data and AEDT predictions for arrival routes into SFO. Our automation methodology is based on our own cloud-based AEDT execution environment (which we have named **`raedt`** for *remote* AEDT) that works on Google Cloud Project instances of arbitrary size (number of processors, memory, etc.). The reader is referred to the Project 53, 2020 Annual Report for additional details regarding **`raedt`**. The remainder of this section gives a detailed description of the current state of the MONA system and our efforts over the period of performance to complete our proposed tasks.

Overview

As a consequence of community complaints regarding changes in air-traffic patterns over the San Francisco Bay Area metroplex during the past five years, it has become increasingly clear to the PIs that there is a dearth of high-quality aircraft noise data (from measurements and/or predictions), particularly for areas away from the airport boundary that have not traditionally been the main focus of noise complaints. In addition, through a number of community interactions, we have also become aware of the difficulties involved in relating potential flight route changes to noise impacts on the ground. This lack of actionable data and methods for effectively communicating with broad and often nontechnical communities led us to develop the MONA system. The MONA project set out to achieve the following objectives:

- To measure and analyze ground noise data generated by aircraft overflights in complex metroplex situations,
- To create, curate, and archive experimental datasets that can serve as an openly available database for verifying and validating improved noise prediction methods,
- To fully automate noise analyses based on the AEDT without the need for user intervention, and
- To share key analysis results with broad communities of stakeholders through compelling and interactive visualizations.

Once ASCENT 53 started, the main goals of MONA were set up as research tasks to be accomplished, two of which are described in this section of our annual report. Our hope is that experimental and computational studies conducted using the MONA system can inform decisions involving aircraft noise, aircraft routes, and potential impacts of the FAA's NextGen procedure changes on overflown communities at varying distances from the airport. We also hope that the open-source nature of the design, software, and hardware of the MONA system can be easily replicated in many metroplexes around the world at relatively low cost, to provide a source of high-quality data to inform conversations and future steps.

A secondary goal of the MONA project is to share, through analyses and visualizations, key results with broad communities of stakeholders who generally lack access to this kind of data. In this section of the annual report, we describe the MONA system architecture, its design, and its current set of capabilities.

Data Measurement and Collection

To quantify and analyze the noise impact of aircraft overflights, we need to know both the trajectories of aircraft flights and the resulting ground noise. To that end, we collect the following types of data:

- Aircraft flight profiles (via ADS-B) and speed over ground
- Sound levels,
- Flight and aircraft metadata,
- Air traffic routes and procedures, and
- Wind and weather conditions.

To date, MONA ground stations have been deployed primarily at the houses of interested and motivated members of the public, with costs borne by those volunteers, including the PIs. In the following subsections, we describe the key elements of the MONA ground station and measurement and collection system.

Sensor Controller

Measurements of sound levels and reception of ADS-B transmissions require a distributed network of sensors mounted outdoors throughout the geographic region of interest and the means to access/retrieve these data. For the MONA project,

we have implemented a series of sensor controllers, incorporating a single-board computer (SBC) and a global positioning system (GPS) receiver (to provide highly accurate time pulses and three-dimensional (3D) location data), with both network connectivity and power via Power over Ethernet (PoE). These components are integrated within a waterproof/weatherproof enclosure to support long-term outdoor deployments. The sensor controller runs a network time protocol (NTP) daemon, configured to utilize the pulse per second (PPS) output of the integrated GPS receiver, to provide a Stratum-1 time base and to minimize time differences between our distributed sensor network. We have developed software to collect each sensor output and transmit/publish the output in real time to a centralized aggregator hosted in a data center via the internet. A single sensor controller is capable of simultaneously supporting both ADS-B reception and sound-level monitoring. Because of the long-term field deployment of the sensors, autonomous operation and secure remote access are essential. Remote access is accomplished by using reverse-SSH tunnels established by the sensor controller to another server, and whenever possible, maintenance of the sensor host is performed via Ansible configuration management scripts through these SSH tunnels.

Figure 4 shows our standard MONA ground station installation and a view of the sensor controller components inside a weatherproof enclosure.

Figure 4. Sensor controller rooftop deployment with ADS-B and a SLM (left). Sensor controller components (right).

ADS-B Receiver

The primary ADS-B receivers in the MONA network are based on the PiAware/`dump1090-fa` software from FlightAware, with a standard RTL-SDR dongle (inside the sensor controller enclosure in the right panel of Figure 4), connected to an ADS-B antenna affixed to the same enclosure. Every second, the JSON output of `dump1090-fa` is captured by a software daemon, and the ADS-B messages within are minimally processed and then transmitted/published to our centralized aggregator, implemented as an Apache Kafka cluster. The collector daemon also publishes receiver metadata (including GPS location and sensor controller status) to the same aggregator. For sites that prefer the commercial, fully integrated Radarcape ADS-B product, we developed a variant of the collector daemon to capture and transmit messages and metadata from this receiver.

Sound-Level Monitor (SLM)

We used SLMs (Convergence Instruments [CI]) connected via USB to the sensor controller to measure noise levels. Another software daemon captures the SLM outputs and transmits/publishes the outputs in real time to a centralized server, again using Apache Kafka. Recent models of the CI SLM optionally support a USB-audio feature, providing access to the sampled audio waveform, which we selectively save/transmit in order to capture both noise metrics and audio recordings of aircraft overflights. The SLM collector daemon publishes SLM metadata (including SLM configuration, GPS location, and sensor controller status) to the central server.

Flight and Aircraft Metadata
Aircraft ADS-B positions alone do not provide a complete description of the flight. Important/valuable missing metadata include:

- Airport(s) of arrival and departure,
- Assigned runways,
- Air traffic control (ATC)-assigned routes and procedures, and
- Airframe, engine, and ownership.

Arrival and departure airport information can often be obtained via external API access or can be inferred by comparing the first or last known ADS-B position with airport/runway locations. ATC-assigned procedures, routes, and runways can be inferred by comparing the aircraft's trajectory to the locations (and sequence) of waypoints and runways. An area of ongoing development is the integration/incorporation of the FAA System-Wide Information Management (SWIM) data feeds, in order to fuse this rich source of metadata with ADS-B aircraft positions. SWIM messages are ingested into Kafka topics, providing reliable reception of these real-time data feeds. Airframe, engine, and ownership information are obtained by joining the aircraft's ICAO24 unique identifier (included in the ADS-B message) with aircraft registration datasets, including the FAA Aircraft Registry (for U.S. aircraft) and OpenSky's Aircraft Metadata Database (for others).

Air Traffic Routes and Procedures
The FAA Coded Instrument Flight Procedures (CIFP) is one definitive source for air traffic route and procedure information, which we download, parse, and archive monthly. The CIFP provides airport, runway, and waypoint locations that can be used for geospatial processing and queries. Flight procedures are converted to a directed-graph representation and are then processed using both standard and custom graph algorithms.

Wind and Weather
ADS-B messages usually provide the aircraft's ground speed, but not its airspeed, which is an important factor for predicting noise. We obtain wind speed and direction measurements from the National Oceanic and Atmospheric Administration (NOAA) High-Resolution Rapid Refresh (HRRR) dataset, and in conjunction with the ADS-B-provided ground speed and heading information, we estimate the net airspeed, which is used to define the specific aircraft trajectory for noise prediction.

Data Collection, Archival Storage, Access, and Management
Real-time ADS-B messages, SLM measurements, and SWIM data feeds are received and stored by a distributed-event streaming platform implemented using Apache Kafka. These streams are processed and subsequently ingested into a Postgres database, augmented with both PostGIS (supporting geospatial queries) and TimescaleDB (supporting very large time-series tables). ADS-B messages from multiple receivers are de-duplicated and segmented into flights, and relevant metadata are added. Trajectories are included in each flight record/row, encoded as PostGIS 4D LineStrings, which enables arbitrary spatiotemporal queries supporting statistical analyses on vast numbers of flights over arbitrary time periods. In our work, we often need to know the point, distance, and/or time of closest approach (PCA, DCA, and TCA, respectively) of an aircraft trajectory with respect to a location of interest (LOI) such as the position of an SLM. PostGIS queries can dynamically compute, filter, and return these values for any stored flight trajectory and LOI combination. Visualization of a full day of flights, including each aircraft position over the entire San Francisco Bay Area, requires low-latency access to thousands of flight records, which contain millions of positions. Thus, the ability to rapidly sequence/step/animate through a range of dates is important tool to understand flight traffic changes over time. Local access to these data is key for reasonable performance, and an optimized binary representation of a trajectory is included in the database to minimize visualization processing delays. MONA applications and services can use/access real-time data streams and/or historic data in the database as needed.

Data Processing and Analysis
The raw data acquired by the MONA system must be processed before it can be used as input to our analyses and to compute statistics of the collected information. This section describes some of the data analyses we have automated in MONA. Once aircraft trajectories and measured noise have been captured, stored, and made available for future use, we process, analyze, quantify, compare, categorize, and summarize the noise impacts.

Attribution of Sound Levels to Aircraft Overflights

The sound-level measurements obtained both from MONA SLMs and other providers (such as SFO's sound monitoring stations) include sampled aggregate sound power levels generated from every source, but only the noise resulting from aircraft overflights is relevant to our research. A number of techniques for attributing sound peaks to aircraft are described in the literature. Particularly relevant examples include threshold-and-duration methods, directional and/or arrayed microphones, and spectral identification/categorization. Based on our experience, we have identified an effective methodology, which we have termed "Determined Aircraft Position/Location for Aircraft Noise Extraction." (DA-PLANE). This algorithm involves computing the time and distance of an aircraft's closest approach to the SLM location (from ADS-B trajectory data), which gives the estimated time of arrival of the aircraft sound peak maximum at the SLM. Then, we use time-series filtering and analysis to locate peaks above the time-varying background in the sound profile that may have been caused by aircraft overflights. These peaks are time-matched with the closest approach data to isolate and identify sound peaks resulting from specific aircraft. The net profile amplitudes of isolated peaks above the background are then analyzed to extract desired noise metrics for each identified overflight event. Other implementations of this technique include those of Harding and Ferrier and Giladi (see references). In the MONA system, the maximum $LAeq_{1s}$ value and SEL metric are extracted and stored in the database, with relations to both the flight (aircraft) and SLM (measurement) location.

Metric Computation

With aircraft trajectories encoded as geospatial datatypes and measured noise metrics attributed to specific aircraft flights and precise locations, we compute standard noise metrics such as the number above noise level, DNL/CNEL, time above noise level, and background level. Non-noise metrics such as overflight counts per day (within a distance or range) are also computed.

Geographic Aggregation of Metrics

It is desirable to analyze both aircraft overflight counts and noise metrics over aggregated geographic areas to estimate annoyance, health, and other impacts on affected populations. These aggregation processes can be performed for either civic regions or grids, which are described below and illustrated in Figure 5.

- Civic regions: City, county, and U.S. congressional district boundaries are published in common GIS formats, which we use in conjunction with PostGIS and client-side GIS software libraries to aggregate and report metrics by civic region.
- Grids: Aggregation over a regular grid is a powerful technique for representing metrics with uniform granularity over a geographic area. We use the H3 hexagonal hierarchical geospatial indexing system in a variety of resolutions (sizes) as a standard, regular, geometric grid defined for the entire Earth. H3 hexagon grids are fused with other geographic data sources; for example, we have computed population count estimates for H3 hexagons by apportioning U.S. Census block population data by the block boundary's percentage containment within the hexagon. The resulting population count of each hexagon enables weighting of metrics aggregated per hexagon by the number of people impacted.

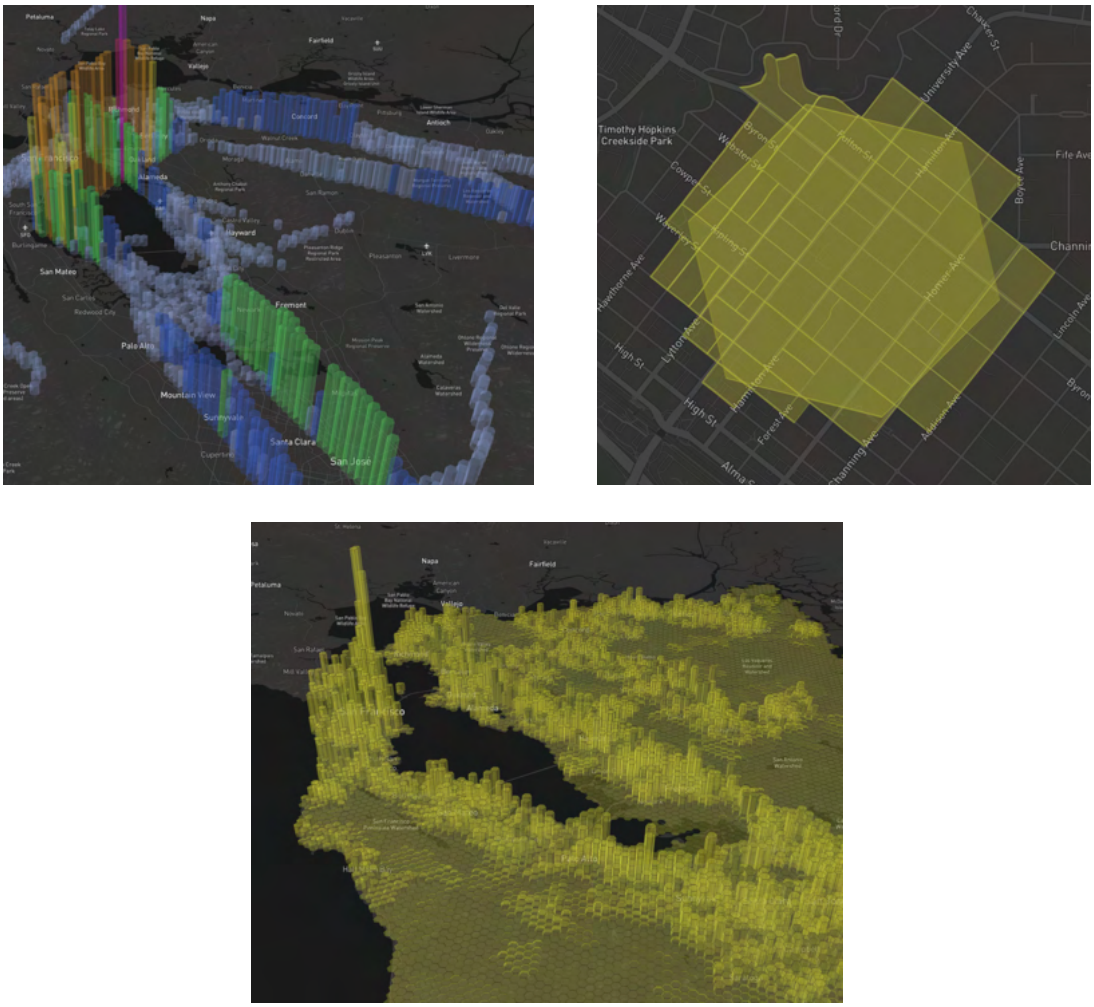

Figure 5. Full-day overflight count by hexagon (top left), apportioning the census-block population to a hexagon (top right), and population per hexagon in the San Francisco Bay Area (bottom).

Aircraft Noise Prediction It is infeasible to deploy SLMs with sufficient number and geographic density to obtain measured noise throughout an entire set of geographically connected airports (cost and logistics being two significant constraints). However, it is feasible to capture all flight traffic via ADS-B by deploying a relatively small number of receivers over the metroplex. Ideally, we could use the collected trajectory data to predict the noise generated by each and every aircraft on a fine-grained receptor grid to estimate noise metrics across the entire region of interest.

The FAA's AEDT is the required software application for assessing U.S. regulatory actions related to aircraft noise and emissions. Our (aspirational) goal is to run AEDT predictions for every aircraft flight across the San Francisco Bay Area each day and aggregate the resulting predicted noise metrics to provide quantified noise impacts across the entire metroplex as a function of location and time.

To this end, we are working to:

- Automate AEDT study creation, execution, and metric result extraction,
- Accurately model AEDT flight trajectories using ADS-B data, and
- Evaluate and compare AEDT's noise predictions to measured noise levels, in a manner similar to that of Giladi and Menachi.

More detailed descriptions of these individual tasks are provided below.

AEDT automation
Current AEDT implementation and workflows are primarily focused on desktop personal computer use via a graphical user interface. This usage model does not support the automated processing of thousands of flights per day over many years. To implement an automation capability, we leveraged AEDT's use of and reliance on a Microsoft SQL Server database. Using AEDT's database schema documentation in conjunction with a database table "diff" tool we developed, we gained an understanding of how to create and populate the tables necessary to describe a complete AEDT study. We then developed a software library to facilitate scripted study creation over a network connection to the SQL Server database used by AEDT. AEDT provides a command-line utility, `RunStudy.exe`, to initiate the execution of a specified study that we can invoke over the network. The computed metrics of an AEDT study are written into the SQL Server database, which allows us to access and extract these results over the network.

We created a virtual machine (VM) disk image including AEDT and all pre-installed supporting packages, which can be instantiated and run at any scale, on a commercial cloud provider. We then developed a study-executor application that takes a study description as input, orchestrates and connects to an AEDT VM, creates an AEDT study using the trajectory of the flight's database ID (provided in the study description) including altitude and speed controls to match the observed trajectory, executes the study, and extracts/stores the metric results in our database. Next, we developed a study-creation application that generates any number of study descriptions (based on SQL queries specifying any desired database column criteria) and submits each resulting study description onto a job queue. Finally, the study executor was enhanced to query the job queue for a study description to process. As a result, we can run any number of AEDT studies in parallel, limited only by the number of AEDT VMs and study executors we create. Both the job and extracted metric queues are implemented using the Apache Kafka cluster.

AEDT trajectory modeling from ADS-B data
AEDT is typically used to model flights from a number of specified ground track positions (without altitude). AEDT combines the specified ground track with flight performance models from the Aircraft Noise and Performance (ANP) Database and EUROCONTROL's Base of Aircraft Data (BADA) to simulate the aircraft's trajectory for its predictions. This computed, simulated trajectory may differ from the trajectory reported by ADS-B. The AEDT provides additional functionality to add altitude and airspeed control codes to the ground track (Section 3.9.1 "Track Control Flights" in the AEDT3d Technical Manual), which we utilize to more closely model the reported trajectory.

We use the following ADS-B trajectory processing steps:

- Smoothing and filtering to remove anomalies that AEDT would reject (e.g., increases in altitude during a descent),
- Line segment simplification (see Douglas, Peucker, Ramer 1973), and
- Estimation of the aircraft's airspeed, using the ADS-B-provided ground speed and heading in combination with wind speed and direction data obtained from NOAA.

Comparison of AEDT noise prediction to measured noise
Our AEDT studies specify the LAMAX and SEL noise metrics, per flight at each receptor (SLM) location. These metric values are stored in our database, with relations to the flight and location, just as we do with the measured noise peaks attributed to aircraft (described previously). With both predicted and measured noise, comparisons are made across various cohorts of flights, which can be specified by filtering, grouping, analyzing, and reporting for any available set of metadata fields (e.g., aircraft model and route). At present, we are actively using this system to predict and compare thousands of flights each day over several years (see Task 2 progress). We plan to publish the results of these comparisons once we have carefully reviewed and validated an amount of data that we deem to be statistically significant. This step is likely to take place during the summer of 2022.

Visualization
Flight traffic information and noise metric contours are visualized using a web-based application that provides 3D geospatial views, based on the `deck.gl` library (see Figure 6). Historic flight-track visualizations obtain archived flight trajectories from the database, and real-time flight visualizations obtain streaming trajectories from Kafka. Real-time access to both SLM and ADS-B data has provided unanticipated benefits: we recently developed another web application that displays SLM metrics overlaid with aircraft TCAs (see Figure 7). Viewing this real-time visualization while simultaneously hearing passing aircraft is a powerful tool to generate ideas and form hypotheses about how and when overflights may result in community concerns.

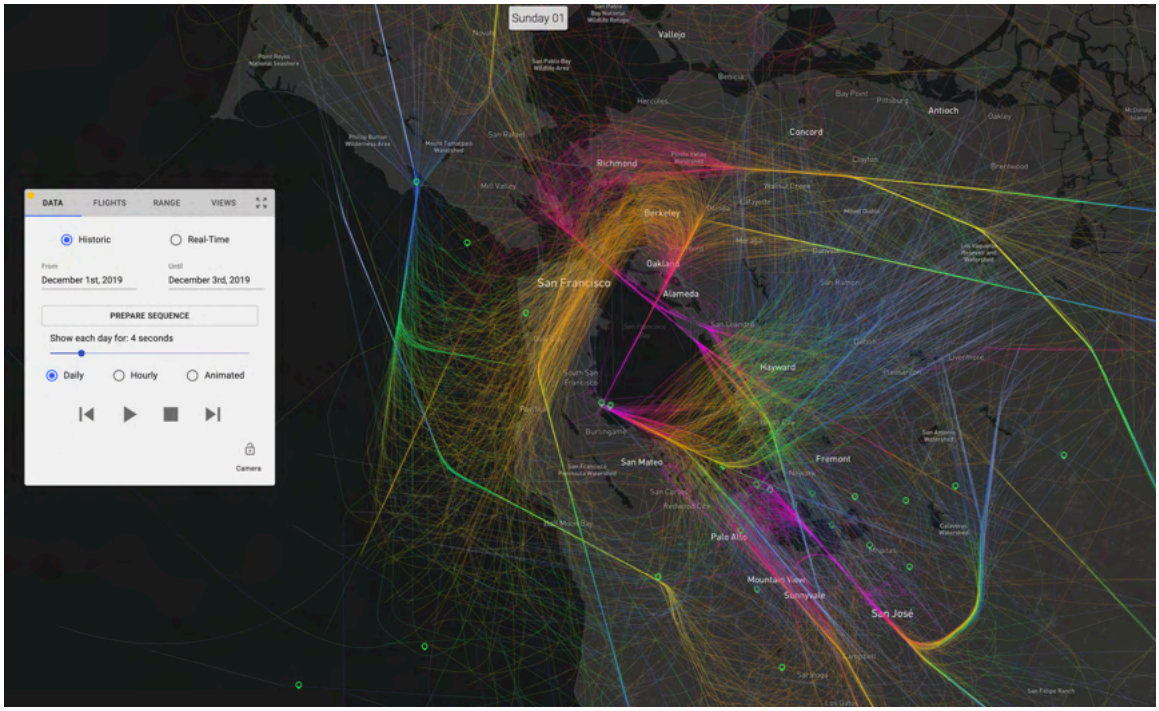

Figure 6. Visual representation of historic traffic patterns over the San Francisco Bay Area metroplex.

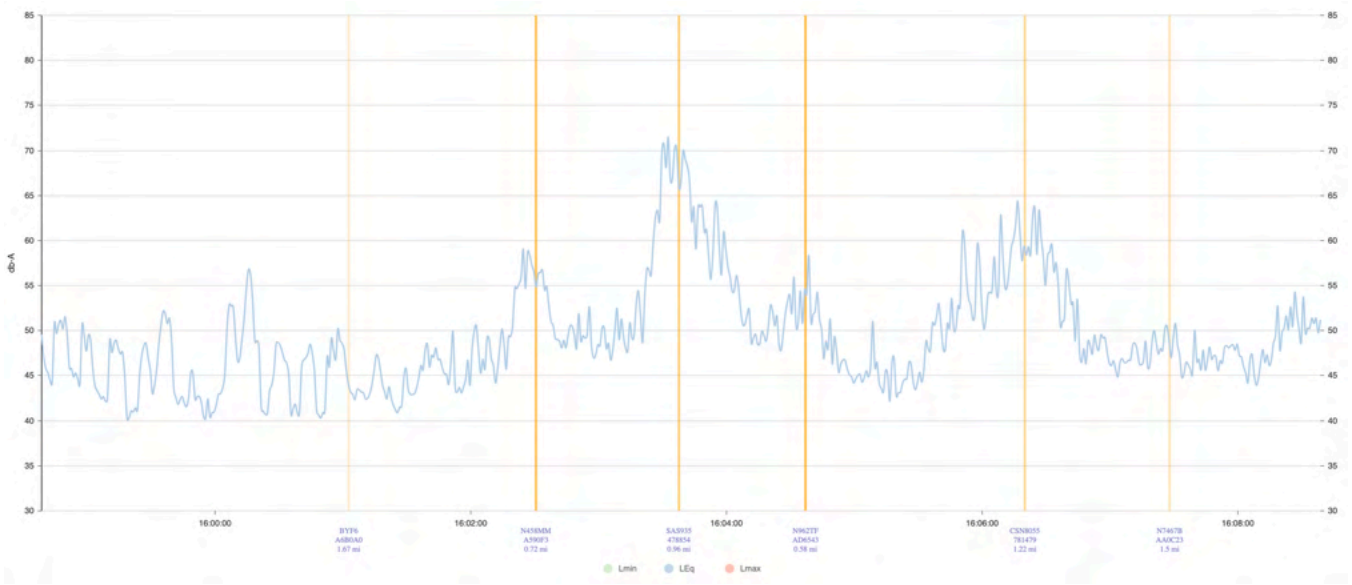

Figure 7. Real-time visualization of sound profiles with aircraft peaks and times-of-closest-approach indicated/overlaid.

Task 2. Validation and Verification of AEDT Noise Predictions in DNL 55–65 dB Areas

Stanford University

The noise prediction modules of AEDT, based on noise power distance (NPD) relationships and certification data, were primarily developed and calibrated for areas of objectionable noise close to airports (> DNL 65 dB), at a constant velocity (160 knots), and for a particular aircraft high-lift system and landing gear configuration. Despite efforts such as those in ASCENT Project 53 (which re-evaluated NPD curves using ANOPP analyses and the ability to change the aircraft configuration during arrival/departure procedures) there is evidence that the accuracy of AEDT's predictions in areas of lower noise (between DNL 55 and 65 dB) may warrant review and improvement. For these reasons, in this task, we have undertaken a preliminary evaluation of the accuracy of AEDT's predictions when measured against sound level readings from a small network of SLMs that the MONA project has acquired, tested, and cited. These efforts *must be viewed as preliminary and do not provide final conclusions*. To issue a final set of conclusions, the ASCENT 53 team is increasing the number of flights in our datasets from 4,000 to nearly 100,000. In addition, we will compare predictions for a larger set of SLM locations beyond the two presented in this annual report. Once available, our final recommendations will include our best efforts to control for individual factors (aircraft weight, weather/airspeed, performance model accuracy, aircraft state, atmospheric column variability, and accuracy of NPD curves for different aircraft models) affecting the discrepancies between measurements and predictions. This step will require significantly more data than we currently have collected and generated and a rigorous apportioning of the variability in prediction errors to the various factors identified. This work is ongoing and is expected to be completed during the summer of 2022.

Currently (December 2021), we are in the process of incorporating additional SLM sources (generously contributed by SFO) across areas with different noise levels for both arrival and departure routes, in order to lend statistical credibility to any results that are eventually published in a peer-reviewed forum.

Research Approach

To accomplish the objectives of this task, we pursued the following steps:

1. We are performing data acquisition and archiving for noise measurements at 3–4 locations under arrival routes into SFO. We have completed the acquisition of raw noise data (Leq samples at 1-second intervals) over a period of approximately three years. All of these data have been curated to provide meaningful comparisons with AEDT predictions.
2. As a pre-processing step to the verification and validation () portion of this work, we developed a series of non-aircraft noise removal algorithms (described in a previous section) that combine filtering techniques, automatic identification of multiple aircraft peaks, automatic detection of background and peak noise levels, and real-time information regarding the position, velocity, and heading of aircraft to maintain high levels of accuracy.
3. We are conducting a validation process based on experimental observations in the DNL 55–65 dB areas of the Bay Area metroplex. This step is the primary component of Task 3, for which we present preliminary results below.

All of the data used for validation purposes will be processed at both the aggregate level and the level of individual flight predictions so that data-driven methods can be pursued in the future to improve the noise and performance data used in AEDT (or data produced in ASCENT Project 43). For example, if all of the recorded overflights of a particular aircraft type, which have variability in aircraft weight, atmospheric conditions, high-lift system configuration, etc., have a corresponding time history for the recorded sound pressure level at an observer location, a learning algorithm could be devised to correct the AEDT predictions as a function of altitude, airspeed, and distance to the observer. Such a data-driven methodology may lead to improved predictions in AEDT.

Raw SLM data for multiple locations are currently being captured and stored in an Apache Kafka centralized database with associated timestamps, that can be retrieved by running respective SQL queries. These data come from calibrated networked Convergence Instruments equipment that we have installed at various locations around the San Francisco Bay Area (as described earlier in this report) and that we have tested with co-located sound measurement equipment loaned by SFO, which agree with our equipment to within 0.1–0.2 dB.

The result of our raw noise data processing algorithm is a filtered signal that is guaranteed to correspond to a conservative estimate of the actual aircraft noise, as the possibility exists that some aircraft noise events (such as sensitive flights) are recorded but not identified in our simultaneously collected flight database. This process can also be run for any subset of the day (a subset of the recorded data) to prepare actual recordings of flight events at multiple locations for comparisons with AEDT predictions. For example, flight recordings obtained during the early hours of the day (1am –4 am) tend to have very low levels of background noise and, therefore, are prime candidates for comparisons with AEDT predictions.

Using filtered noise data for two SLM locations, we have been able to arrive at a number of preliminary conclusions, which are provided at the end of this section. It is important to note that these preliminary conclusions are based on the data we have acquired thus far; however, we are in the process of conducting a significantly larger number of simulations and collecting additional sources of data that will allow us to clarify the main causes of any measurement–prediction discrepancies in the near future. Until these additional data are examined, processed, and analyzed, it would be premature to strongly state the reasons for the discrepancies observed thus far. To provide current evidence of our preliminary conclusions (restricted to arrival routes into SFO and observations at two SLM locations), we present a number of statistically significant comparisons based on approximately 3,700 flights.

The two SLM locations in our plots are: (see Figure 8):

- SIDBY: This SLM is located near the SIDBY waypoint of the SERFR route, but is also overflown by aircraft following the BDEGA and PIRAT routes. This SLM is located in an approximately DNL 55 dB area and is approximately 15 miles (along the standard flight path) from touchdown at runways 28L/R of SFO.
- SFO-12: This SLM is located directly under the final approach to runways 28 L/R of SFO and approximately 6 miles from touchdown. The SLM is located in an area of approximately DNL 62.5 dB and thus has a considerably higher noise level than the SIDBY SLM. Aircraft approaching SFO along the SERFR, PIRAT, BDEGA, and DYAMD routes either directly overfly or fly nearby (1/2 miles north, in the case of DYAMD approaches) this SLM.

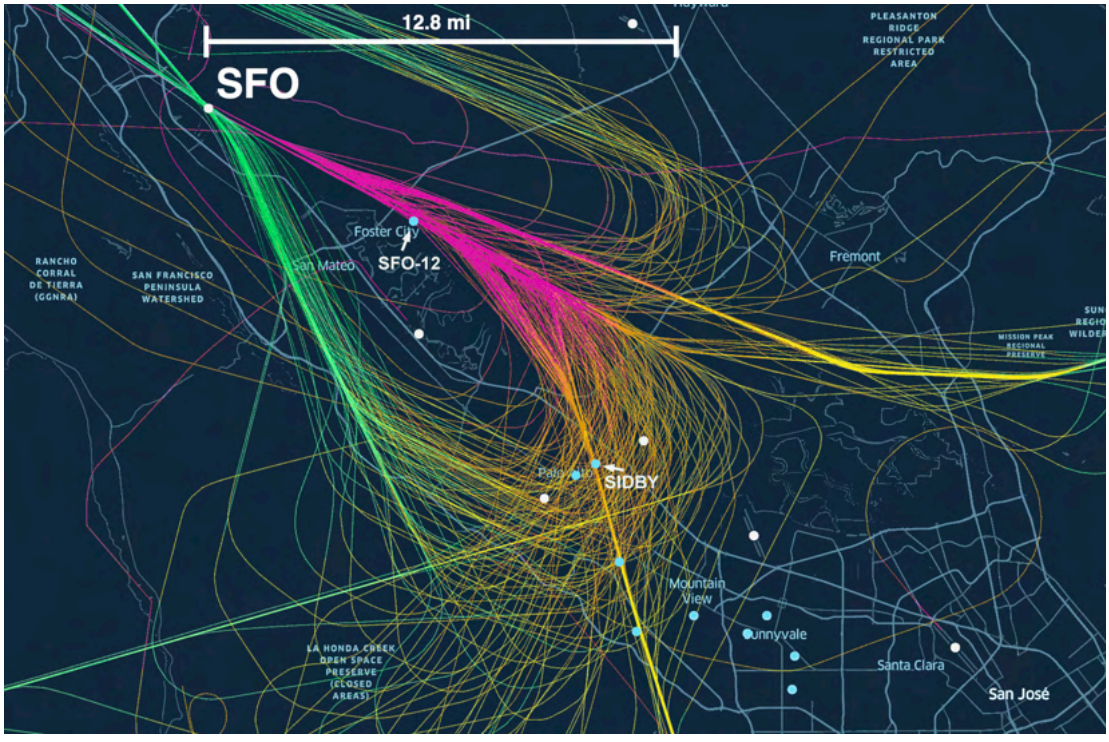

Figure 8. Locations of two SLMs (SFO-12 and SIDBY) used in this study.

Among the various SLMs for which we have data, these two are particularly interesting because, even though they are both under arrival tracks, they correspond to two very different noise-level areas. SFO-12 is, presumably, in an area for which the

noise predictions of AEDT are relatively accurate (near the airport), whereas SIDBY is significantly farther from the airport and in an area that was not specifically targeted during the development of the noise prediction algorithms in AEDT. The use of these two locations will allow us to test the hypothesis that AEDT is more accurate in its predictions for SFO-12 than for SIDBY.

The following figures are meant to provide statistically significant information. Conclusions are preliminary because as we have yet to understand the reasons for the observed discrepancies. These reasons must be understood before final conclusions are drawn from this study. For the results presented below, we believe that the dataset contains a sufficient number of flights for the variabilities to average out: the entire dataset contains approximately 3,679 flights from the 4-week period spanning July 19, 2021 to August 18, 2021. The dataset includes all types of aircraft, but predominantly E75L, B73X (B737-800, B737-900), and A320/A321. We have removed all general aviation flights from this dataset and have ensured that no flights are included whose line-of-sight elevation at the point of closest approach (PCA) to a SLM is less than 40 degrees (so that aircraft not in the proximity of the SLM are disregarded).

SIDBY SLM Results

Figure 9 presents a histogram of all 3,679 flights considered in this study. The data have been binned in 0.5-dB intervals and represent the difference (for each individual flight) between the AEDT LAmax prediction and SLM measurement (after background noise has been removed). The dataset includes aircraft/flights that can be modeled only with BADA3 and aircraft/flights that can be modeled with BADA4. In this dataset, the mean shows an underprediction of 2.2 dB by AEDT when compared with the SLM measurements. Surprisingly, the variability in the differences between measurements and predictions is rather broad: the standard deviation in the histogram is approximately 4.7 dB. This observation clearly implies that the variability in input variables not considered in AEDT (aircraft weight, headwind, aircraft state, atmospheric conditions, etc.) leads to significant variability in the observations.

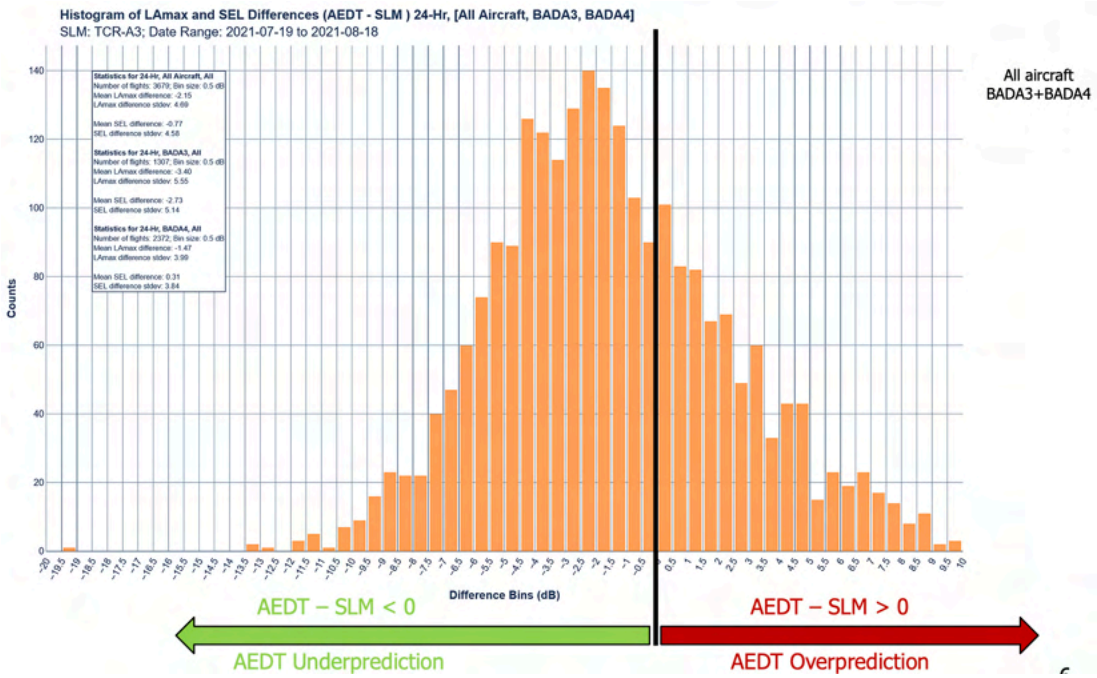

Figure 9. Histogram of the LAmax difference between AEDT predictions and SLM measurements at the SIDBY SLM. Positive values indicate overprediction by AEDT, whereas negative values indicate underprediction by AEDT.

Figure 10 shows the same dataset but includes only E75L-type aircraft, which are modeled by AEDT using BADA4, representing a total of 905 flights during the period under consideration. Similar trends in standard deviation (4.2 dB) are observed, but the mean difference between the prediction and measurement is significantly smaller, with an overprediction of only 0.3 dB, which can be considered quite accurate in comparison with results for other aircraft types that we have

observed. As shown in Figure 11, the same trend is not observed for B73X aircraft, including B737, B738, and B739, which are largely modeled using BADA4.The large value of the standard deviation is still significant, implying that the over/underprediction of AEDT for individual flights can typically be as high as +0.75 db and -6.3 db. Such differences indicate that the current prediction error variability is significantly higher than desired, and additional improvements in the modeling strategy might be required if the standard deviation of the differences needs to be reduced. Such improvements may include some or all of the following: better assessments of aircraft weight, more detailed airspeed measurements (or inferences based on flight path data), a better understanding of the aircraft state, and improved NPD curves. The relative importance of each of these factors is currently under investigation, but at this point, we do not have sufficient information to conclusively state anything beyond what has been written.

Figure 11 shows the same data as Figure 10 for B737, B738, and B739 aircraft, for which we observed 815 flights in the dataset, with the vast majority (808 flights) being simulated using BADA4. As briefly mentioned above, the predictive quality of AEDT is worse in this case than for the E75L aircraft, with a mean difference (underprediction) of 2.9 dB and a large standard deviation of 3.4 dB. The difference in the mean between the E75L and B73X aircraft types is sizable, and further investigation is warranted to determine why the mean values of the prediction errors differ by more than 3 dB. Although not presented here, a similar trend was observed for A32X-type aircraft (data are available upon request and were presented at the ASCENT Annual Meeting in October 2021).

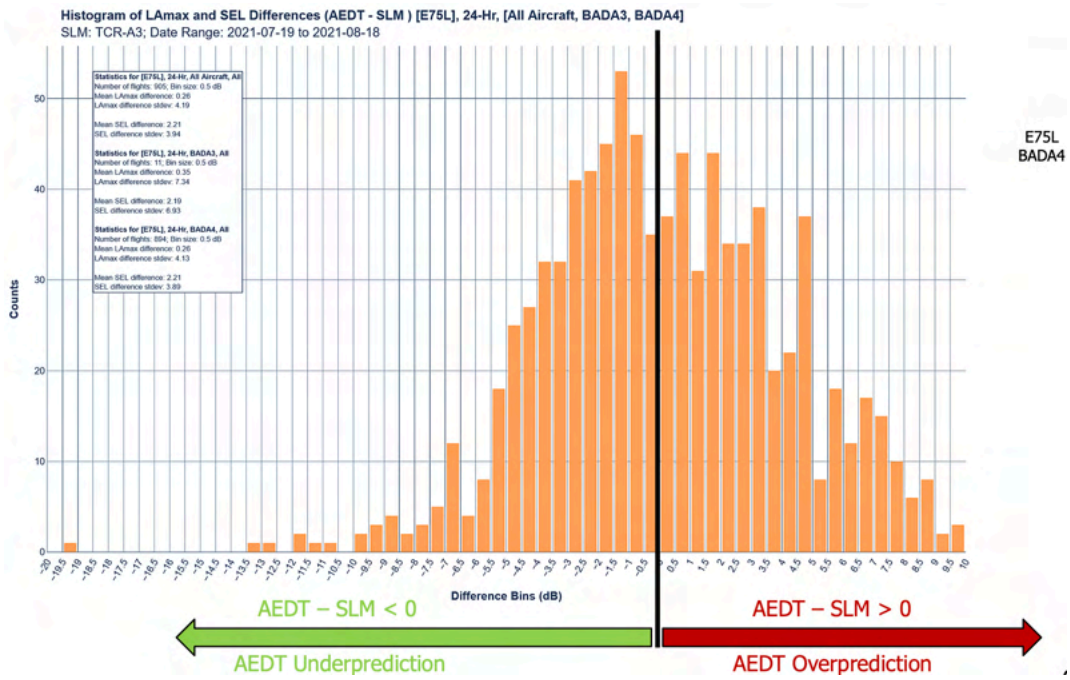

Figure 10. Histogram of the LAmax difference between AEDT predictions and SLM measurements at the SIDBY SLM for E75L aircraft. Positive values indicate overprediction by AEDT, whereas negative values indicate underprediction by AEDT.

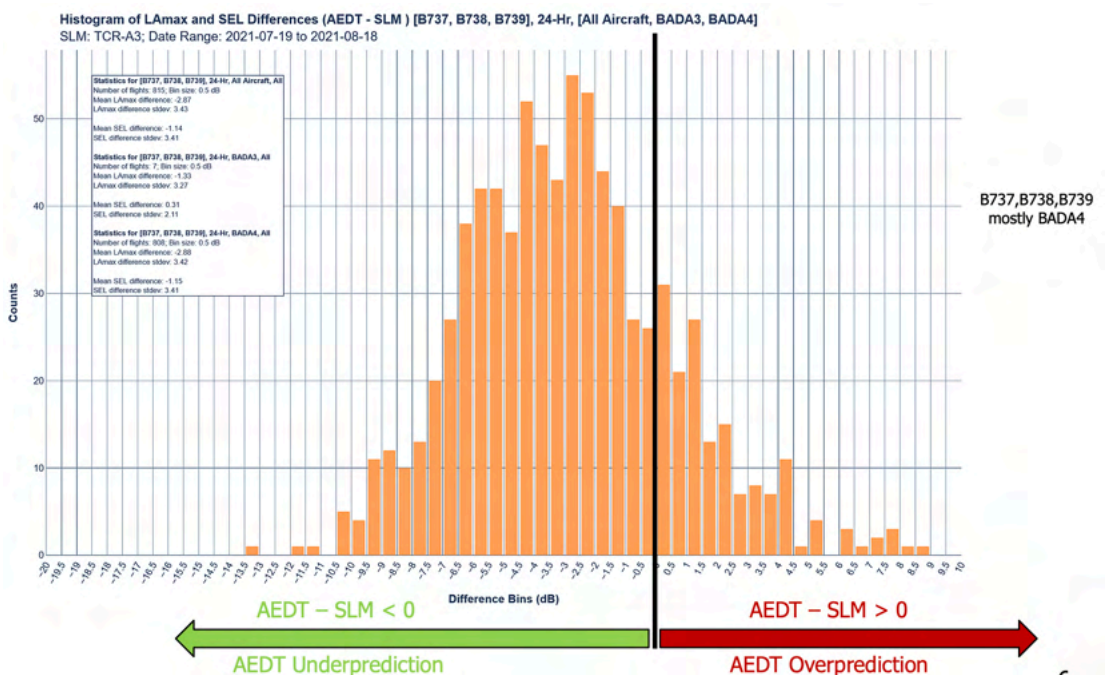

Figure 11. Histogram of the LAmax difference between AEDT predictions and SLM measurements at the SIDBY SLM for B737, B738, and B739 aircraft. Positive values indicate overprediction by AEDT, whereas negative values indicate underprediction by AEDT.

SFO-12 SLM Results

Figures 12–14 show similar results for the predictions and measurements at the SFO-12 SLM, in contrast to the results for the SIDBY SLM. It should be noted that because SFO-12 is located alongside the runways for all approaches to SFO, including DYAMD, in addition to SERFR, BDEGA, and PIRAT, there are more aircraft in the cohort (6,228 vs. 3,679 at SIDBY). Given that this SLM is in an area of higher noise (~ DNL 65 dB) and assuming that AEDT is "tuned" to be more accurate at higher noise levels, we would expect the mean error in the AEDT predictions to be smaller. However, the data we have collected thus far do not support this observation. The aggregate plot in Figure 12 shows an overall mean LAmax difference of -3.1 dB, an underprediction for nearly all flights in the neighborhood of this SLM location. However, the standard deviation of the error at this location is lower than that at SIDBY (3 dB vs. 4.7 dB). This smaller standard deviation can likely be attributed to the significantly higher concentration of flight trajectories during the final approach to SFO and the reduced level of uncertainty about the aircraft state close to the touchdown location. At this location, AEDT noise models can over/underpredict aircraft noise by up to 0.6 dB and -6.3 dB on average.

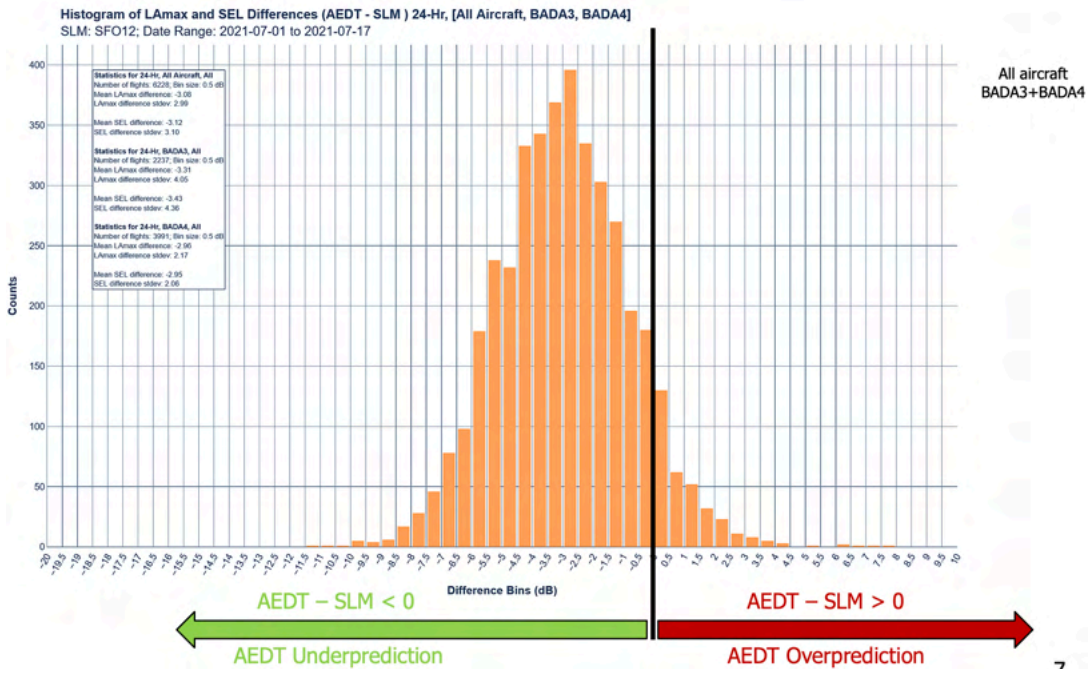

Figure 12. Histogram of the LAmax difference between AEDT predictions and SLM measurements at the SFO-12 SLM. Positive values indicate overprediction by AEDT, whereas negative values indicate underprediction by AEDT.

Figure 13 shows the same dataset errors for the E75L cohort. Just as for the SIDBY SLM, the AEDT predictions for the SFO-12 SLM improve for the E75L cohort (-2.4 dB) compared with other aircraft types. In fact, similar to Figure 11, Figure 14 shows that the predictions at SFO-12 for B73X aircraft have a mean underestimation of -3.7 dB, which was not expected, given that the mean underestimation at SIDBY was only -2.9 dB. Thus, the expected trends do not seem to be materializing. We note that the SFO-12 data include DYAMD flights, but it is not clear why this inclusion should skew the results.

At the moment, one can only argue that all of these data have been collected at only two arrival locations and for approximately 4,000–6,000 flights, and thus, the conclusions cannot yet be generalized. As our work proceeds, we expect to extend these comparisons to additional SLM locations, including some under departure flight tracks.

Finally, Figure 15 shows the estimated and measured 24-hr DNL metric for each of the 30 days in our sample dataset. As can be observed, the underestimation of AEDT predictions in the DNL metric can be as good as 1 dB and as bad as 2.6 dB with an average value of approximately 2 db.

Overall, the preliminary conclusions of our early comparisons between AEDT predictions and SLM measurements can be summarized as follows, with the caveat that these conclusions are preliminary and will be strengthened once additional predictions and measurements, which we are currently pursuing, become available:

- Preliminary investigations point to a potential underestimation of noise predictions for individual-event sound levels on arrival operations by ~2–3 dB (mean values) regardless of the DNL area. More data are needed to refine this conclusion.
- BADA4 aircraft modeling results in a significant improvement in noise predictions over BADA3 aircraft of ~0.5–2 dB depending on the DNL area. This improvement is likely related to the better aircraft performance model available in BADA4 (for some aircraft types only), leading to a better estimation of the engine noise component. Further comparisons across multiple aircraft classes (with BADA3 vs. BADA4) are planned to strengthen this observation.
- Variability in the difference between measurement and prediction is *very significant*, with a standard deviation of ~3–5 dB. We believe that this is important area that warrants further investigation to ascertain the main causes of such large variability. We intend to understand this variability by attempting to control for variables such as aircraft

weight and aircraft state, as we continue to increase the size of our datasets to hundreds of thousands of flights. The larger cohorts will allow us to subdivide the traffic along more parameter values and thus better understand the impact of input unknowns and their ranking in order of importance.

- In the dataset that we have processed, we observed significant bias for different aircraft models (especially when the performance of some aircraft models can only be represented using BADA3). The observed trends appear to be consistent regardless of the DNL area (low or high).
- The expectation of improved AEDT accuracy in noise estimates for higher DNL noise areas does not appear to be borne by the data for the two arrival locations examined. As our study progresses, we intend to examine this preliminary conclusion for a number of other locations and with significantly more data to ascertain whether our observations change.
- AEDT predictions for aggregate noise metrics (not individual flights) still show significant differences (e.g., DNL 1–2.6 dB for different 24-hr periods), which are only slightly better than the predictions for individual flights. We are continuing our work to determine whether this assertion holds for additional SLM locations under both arrival and departure routes.

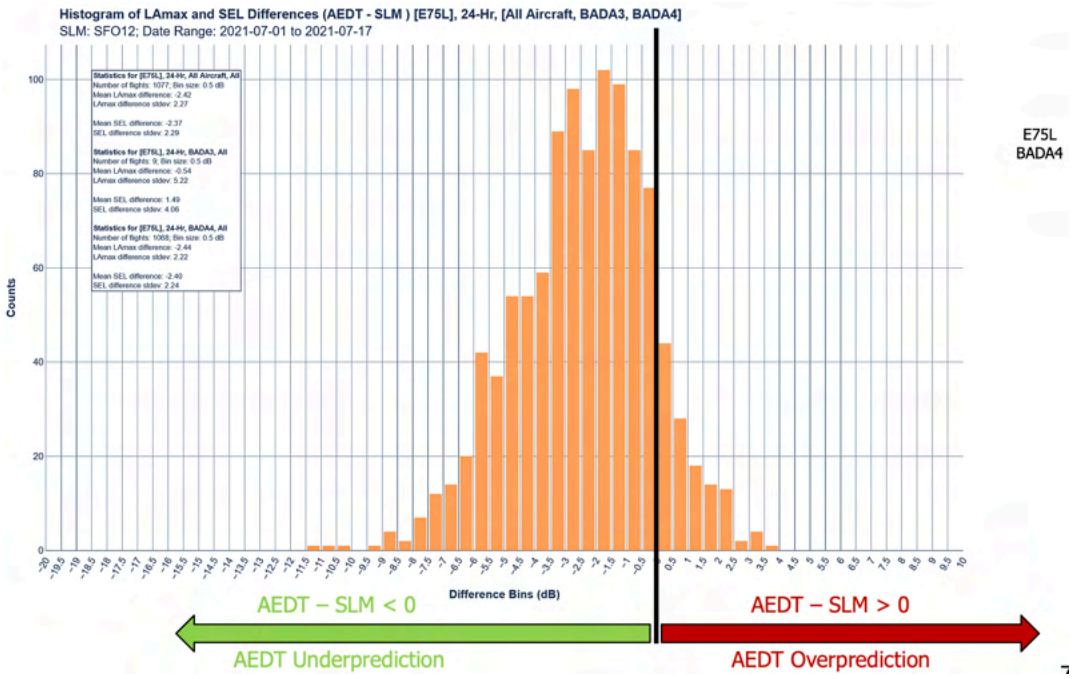

Figure 13. Histogram of the LAmax difference between AEDT predictions and SLM measurements at the SFO-12 SLM for E75L aircraft. Positive values indicate overprediction by AEDT, whereas negative values indicate underprediction by AEDT.

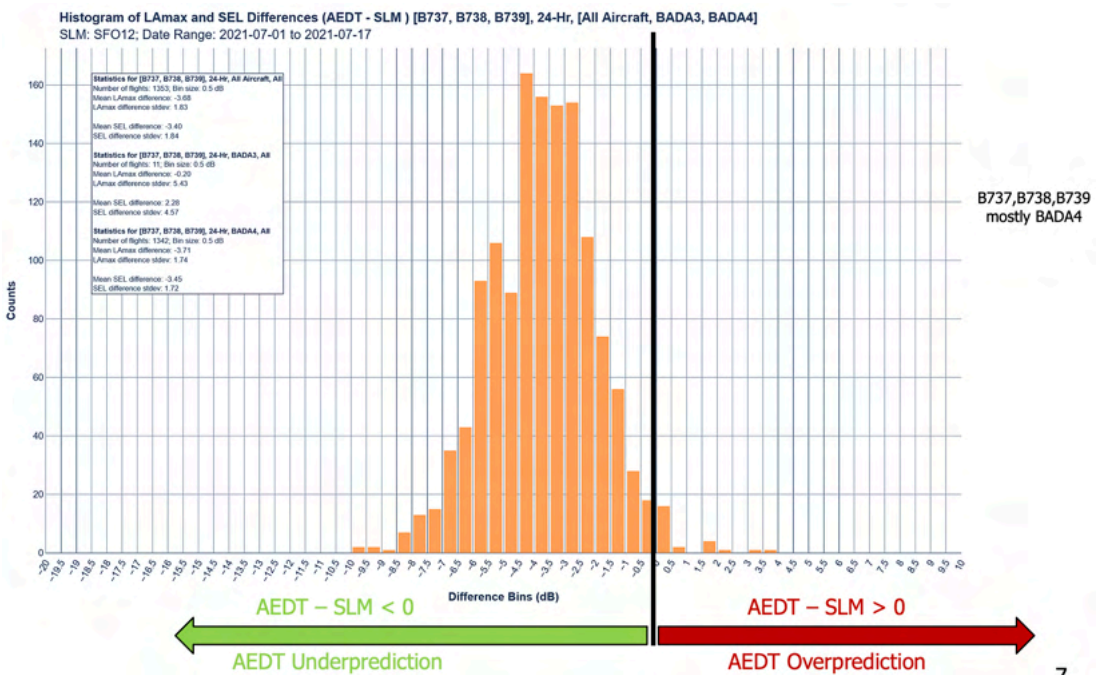

Figure 14. Histogram of the LAmax difference between AEDT predictions and SLM measurements at the SFO-12 SLM for B737, B738, and B739 aircraft. Positive values indicate overprediction by AEDT, whereas negative values indicate underprediction by AEDT.

Figure 15. AEDT predictions (red) and SFO-12 SLM measurements (blue) of 24-hr DNL levels. Minimum (1 dB) and maximum differences between measurements and predictions are highlighted for July 10 and July 13, 2021.

Task 4. Investigate Viable Alternative Approach Routes into the San Francisco Bay Area Metroplex

Stanford University

This task is still in its beginning stages and will continue to develop over the coming months. In this task, in collaboration with FAA staff and other technical experts, we plan to continue the process of proposing and analyzing alternative procedure designs for the SERFR arrival route into SFO and for approaches that currently tie into SERFR. The longer-term intent of this task is to propose procedure designs for two alternative arrival routes and to assess the potential of those routes to reduce noise, while maintaining airspace efficiency and safety. This task can be viewed as a first step toward proposing routes and flight procedures that may lead to noise benefits for a variety of stakeholders.

In particular, we have been investigating the possibility of splitting the SERFR arrival route and the approaches that merge into SERFR at significant distances away from the airport into a number of sub-routes that will then merge into the existing SERFR route in a *herringbone pattern* so that the distances flown are kept essentially constant while the number of overflights (measured with a metric similar to the number above LAmax noise level, i.e., the number of overflights above a specified maximum noise exposure level) for different portions of the existing SERFR route can be substantially decreased, by a factor of two or three, depending on the distance from the runway.

There are no additional substantial results to report at this time.

Major Accomplishments

- Created a completely new infrastructure for ASCENT 53/MONA that can scale to the types of data collection and analysis expected for a complex metroplex such as that of the Bay Area
- Developed a working version of the non-aircraft noise filtering process to compare sound recordings with AEDT predictions
- Created a cloud-based automated approach to conduct AEDT studies to enable automation in the Bay Area metroplex
- Demonstrated full automation of the AEDT analysis pipeline and of noise prediction/measurement comparisons for arbitrarily large datasets
- Demonstrated the use of modern databases, data formats, and data acquisition methodologies (based on Apache Kafka) in the context of airspace and noise analysis
- Collected necessary data to generate a database of almost 4,000–6,000 individual flights which was used in our preliminary AEDT verification and validation study
- Drew preliminary conclusions from comparisons between AEDT predictions and SLM measurements at two locations (SIDBY and SFO-12) under arrival routes to SFO

Publications

Jackson, D. C., Rindfleisch, T. C., & Alonso, J. J. (2021). A system for measurement and analysis of aircraft noise impacts. Engineering Proceedings, *13*, 6. https://doi.org/10.3390/engproc2021013006

Outreach Efforts

Over the past few months, we have developed a closer relationship with SFO and the technical leads at EnviroSuite, which deploys, monitors, and makes available noise data for approximately 40 locations around the Bay Area. These outreach efforts have resulted in the sharing of noise data at a large number of locations including historical datasets and a commitment to continue sharing datasets as they are acquired in the future.

Awards

None

Student Involvement

A number of undergraduate and graduate students have been part of our team during this past year, as described at the beginning of this document. Several of these students have graduated during the current period of performance, but we

have managed to enlist new students to continue our work. Their contributions are acknowledged here, as the project would not be as far along without them.

Plans for Next Period

We intend to complete all three tasks in our Statement of Work as planned. In addition to the completion of all milestones, we expect to release appropriate parts of the ASCENT 53/MONA project and demonstrate various capabilities through participation in aircraft noise-related meetings and conferences, as permitted by the COVID-19 situation.

References

Aircraft Noise and Performance (ANP) Database. (n.d.). EUROCONTROL. Retrieved November 7, 2021, from https://www.aircraftnoisemodel.org/

Base of Aircraft Data (BADA). (n.d.). EUROCONTROL. Retrieved November 7, 2021, from https://www.eurocontrol.int/model/bada

Benjamin, S. G., Weygandt, S. S., Brown, J. M., Hu, M., Alexander, C. R., Smirnova, T. G., Olson, J. B., James, E. P., Dowell, D. C., Grell, G. A., Lin, H., Peckham, S. E., Smith, T. L., Moninger, W. R., Kenyon, J. S., & Manikin, G. S. (2016). A North American hourly assimilation and model forecast cycle: The rapid refresh. Monthly Weather Review, *144*, 1669–1694. https://doi.org/10.1175/MWR-D-15-0242.1

Coded Instrument Flight Procedures (CIFP). (2021). FAA. Retrieved November 7, 2021, from https://www.faa.gov/air_traffic/flight_info/aeronav/digital_products/cifp/

Deck.gl. (2021). WebGL-powered visualization framework for large-scale datasets (8.4) [Computer software]. Retrieved November 7, 2021, from https://deck.gl

Douglas, D. H., & Peucker, T. K. (1973). Algorithms for the reduction of the number of points required to represent a line or its caricature. Cartographica: The International Journal for Geographic Information and Geovisualization, *10*, 112–122. https://doi.org/10.3138/FM57-6770-U75U-7727

FAA. (2021). Next Generation Air Transportation System (NextGen) [Computer software]. Retrieved November 7, 2021, from https://www.faa.gov/nextgen/

FAA. (n.d.). Aviation Environmental Design Tool (AEDT) [Computer software]. Retrieved November 7, 2021, from https://aedt.faa.gov

FAA. (n.d.). System Wide Information Management (SWIM) [Computer software]. Retrieved November 7, 2021, from https://www.faa.gov/air_traffic/technology/swim/

FlightAware. (n.d.). AeroAPI [Computer software]. Retrieved November 7, 2021, from http://flightaware.com/commercial/aeroapi/

FlightAware. (n.d.). PiAware [Computer software]. Retrieved November 7, 2021, from http://flightaware.com/adsb/piaware/

Giladi, R. (2020). Real-time identification of aircraft sound events. Transportation Research Part D: Transport and Environment, *87*, 102527. https://doi.org/10.1016/j.trd.2020.102527

Giladi, R., & Menachi, E. (2020). Validating aircraft noise models. Proceedings, *59*, 12. https://doi.org/10.3390/proceedings2020059012

Harding, M., & Ferrier, D. (2014). Using post analysis of a noise sample stream in place of noise monitor based thresholds in the detection of aircraft noise. INTER-NOISE and NOISE-CON Congress and Conference Proceedings, *249*, 5386.

Jetvision. (n.d.). Radarcape (MR2) [Computer software]. Retrieved November 7, 2021, from https://shop.jetvision.de/radarcape_en

Kafka. (2017). Apache Kafka (2) [Computer software]. Retrieved November 7, 2021, from https://kafka.apache.org/

Microsoft. (2019). Microsoft SQL server [Computer software]. Retrieved November 7, 2021, from https://www.microsoft.com/en-us/sql-server/sql-server-2019

OpenSky Aircraft Metadata Database. (2021). OpenSky. Retrieved November 7, 2021, from https://opensky-network.org/datasets/metadata/

Ramer, U. (1972). An iterative procedure for the polygonal approximation of plane curves. Computer Graphics and Image Processing, *1*, 244–256. https://doi.org/10.1016/S0146-664X(72)80017-0

The PostgreSQL Global Development Group. (2021). Postgres (14.1) [Computer software]. Retrieved November 7, 2021, from https://www.postgresql.org/

Uber Technologies, Inc. (n.d.). H3: Hexagonal Hierarchical Geospatial Indexing System (3.x) [Computer software]. Retrieved November 7, 2021, from https://h3geo.org

Wynnyk, C. (2012). Wind analysis in aviation applications [Presentation]. 31st IEEE/AIAA Digital Avionics Systems Conference (DASC). https://doi.org/10.1109/DASC.2012.6382366

Convergence Instruments. Sound Level Meters. https://dev.convergenceinstruments.com/pc/sound-level-meter-data-loggers/, accessed on November 7, 2021.
(n.d.). Aircraft Registry. (2021). FAA. Retrieved November 7, 2021, from https://www.faa.gov/licenses_certificates/aircraft_certification/aircraft_registry/
(n.d.). (2021). PostGIS [Computer software]. Retrieved November 7, 2021, from https://postgis.net/
(n.d.). (2021). TimescaleDB (2.5.1) [Computer software]. Retrieved November 7, 2021, from https://www.timescale.com/

Project 054 AEDT Evaluation and Development Support

Georgia Institute of Technology

Project Lead Investigator

Principal Investigator:
Professor Dimitri N. Mavris
Director, Aerospace Systems Design Laboratory
School of Aerospace Engineering
Georgia Institute of Technology
Phone: (404) 894-1557
Fax: (404) 894-6596
Email: dimitri.mavris@ae.gatech.edu

Co-Principal Investigator:
Dr. Michelle Kirby
Chief, Civil Aviation Division
Aerospace Systems Design Laboratory
School of Aerospace Engineering
Georgia Institute of Technology
Phone: (404) 385-2780
Fax: (404) 894-6596
Email: michelle.kirby@ae.gatech.edu

University Participants

Georgia Institute of Technology

- PIs: Dr. Dimitri Mavris, Dr. Michelle Kirby
- FAA Award Number: 13-C-AJFE-GIT-054
- Period of Performance: February 5, 2021 to February 4, 2022
- Tasks:
    1. Improved Departure Modeling through Comparison of Noise Abatement Departure Procedures (NADP) Profiles to Real-world Operations
    2. Arrival Profile Modeling
    3. Full Flight Modeling
    4. System Testing and Evaluation of AEDT

Project Funding Level

The project is funded at the following levels: Georgia Institute of Technology ($700,000). In terms of cost-share details, Georgia Tech has agreed to a total of $700,000 in matching funds. This total includes salaries for the project director, research engineers, and graduate research assistants, as well as computing, financial, and administrative support, including meeting arrangements. Georgia Tech has also agreed to provide tuition remission for the students, paid for by state funds.

Investigation Team

Prof. Dimitri Mavris, Principal Investigator, Georgia Institute of Technology
Dr. Michelle Kirby, Co-Investigator, Georgia Institute of Technology
Dr. Yongchang Li, Research Faculty, Georgia Institute of Technology
Dr. Tejas Puranik, Research Faculty, Georgia Institute of Technology
Dr. Dushhyanth Rajaram, Research Faculty, Georgia Institute of Technology
Dr. Mohammed Hassan, Research Faculty, Georgia Institute of Technology
Dr. Holger Pfaender, Research Faculty, Georgia Institute of Technology

Mr. David Anvid, Research Faculty, Georgia Institute of Technology
Ameya Behere, Graduate Student, Georgia Institute of Technology
Ayaka Miyamoto, Graduate Student, Georgia Institute of Technology
Rukmini Roy, Graduate Student, Georgia Institute of Technology
Jirat Bhanpato, Graduate Student, Georgia Institute of Technology
Hyungu Choi, Graduate Student, Georgia Institute of Technology
Howard Peng, Graduate Student, Georgia Institute of Technology
Bogdan Dorca, Graduate Student, Georgia Institute of Technology
Zhenyu Gao, Graduate Student, Georgia Institute of Technology
Santusht Sairam, Graduate Student, Georgia Institute of Technology

Project Overview

This project is providing data and methods to continue to improve the aircraft weight, takeoff thrust, and departure and arrival procedure modeling within the FAA's Aviation Environmental Design Tool (AEDT), as well as the AEDT's full-flight modeling capabilities. Some of the modeling assumptions in AEDT are considered overly conservative and could be improved using industry and airport flight operations data. Funding for this project will continue to support the implementation of these methods and data into AEDT4. To facilitate this, the Georgia Tech team will utilize real-world data flight and noise monitoring data to improve departure, full flight, and arrival modeling.

Task 1 – Improved Departure Modeling: Comparison of NADP Profiles to Real-world Operations

Georgia Institute of Technology

Objectives

Prior research in ASCENT Project 45 provided recommendations for Noise Abatement Departure Procedures (NADPs) to be modeled in future versions of AEDT. Comparisons were made between NADP profiles within the NADP library to determine the differences between each profile. As a result, two profiles were found most representative of the variability among each type of NADP. This task aims to investigate the similarities between the recommended NADPs and real-world departure operations for multiple airlines and airports.

Research Approach

Methodology

Previous studies recommended that the NADP 1-1 and NADP 2-11 profiles to be implemented in future versions of AEDT based on comparisons with real-world trajectories from a single airline. This task extends those efforts by comparing the two profiles to a larger real-world Threaded Track dataset containing multiple airlines and departure airports. Three additional NADP profiles with 1,500 ft thrust cutback altitude were for wide-body aircraft. These additional profiles were selected from the NADP library based on their similarity to NADP 1-1 and NADP 2-11. Trajectory comparisons are made between NADP profiles and Threaded Track trajectories at 12 airports for eight narrow-body and four wide-body aircraft types. Origin-destination pair information is utilized to compute stage length (SL) based on great-circle distance, thus enabling comparisons against procedural profiles with the same SL. Table 1 **Error! Reference source not found.**lists the combinations of profiles investigated in this task, and Table 2 lists the ANP ID investigated for each aircraft type. In the "Final Accel." column, the term CONT indicates that the aircraft accelerates to 250 kts after the initial acceleration and flaps transition steps without a constant speed climb between accelerations.

The initial data point available in the Threaded Track data varies greatly from flight to flight. As such, trajectories with initial data points >1,000 ft above ground level (AGL) are excluded. The modeled NADP profiles and real-world trajectories are resampled at 0.33 nmi ground track distance interval and aligned at 1,000 ft AGL. Because real-world trajectories that either (i) do not climb to 10,000 ft above mean sea level (MSL) or (ii) reach such altitude at a ground track distance greater than three standard deviations away from similar operations are considered irregular departures, we also excluded such trajectories from our analysis. Figure 1 shows an example visualization of the procedural profiles modeled overlaid on real-world trajectories.

Table 1. Combinations of profiles investigated (*wide-body only).

Profile	Cutback	Initial Accel.	Final Accel.	Thrust Level	Weight	Stage Length	Departure Airport	Aircraft Type
STANDARD	Various	Various	Various	RT0 (100% Takeoff, 100% Climb) RT15 (85% Takeoff, 90% Climb)	Alternate Weight	All SL with real flights	KLAX KORD KDFW KLAS KJFK KLGA KDCA KSNA KSFO KATL KSLC KDEN	B737 B738 B739 B752 B763 B77W B712 A319 A320 A321 A332 A333
NADP 1-1	800	1,500	3,000					
NADP 2-11	1,000	1,000	3,000					
NADP 1-7*	1,500	3,000	CONT					
NADP 2-12*	1,500	1,500	CONT					
NADP 2-13*	1,500	1,500	3,000					

Table 2. ANP ID investigated for each Threaded Track aircraft type.

Aircraft Type	ANP ID
B737	737700
B738	737800
B739	
B752	757PW
	757RR
B763	767300
B77W	7773ER
B712	717200
A319	A319-131
A320	A320-232
A321	A321-232
A332	A330-343
A333	

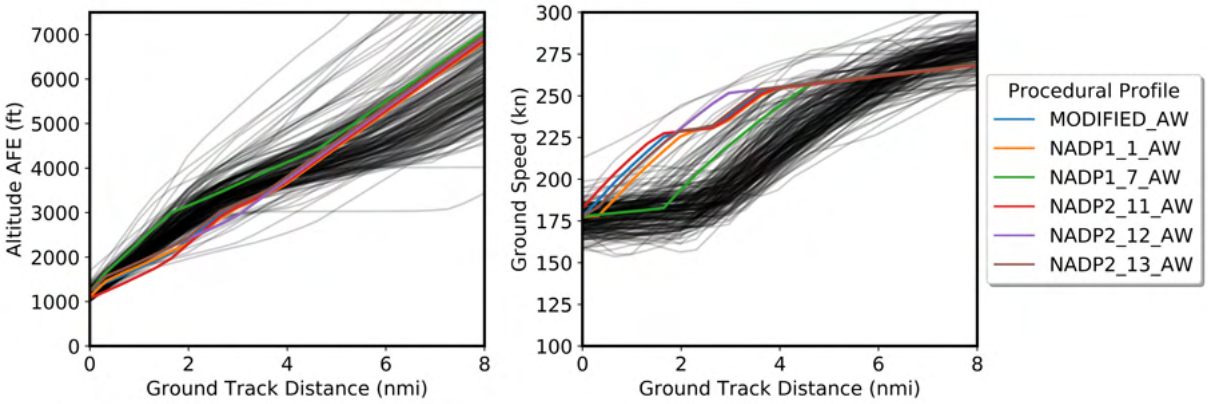

Figure 1. Sample comparison of KSFO B77W procedural profiles, with Threaded Track flights shown in black.

In this task, altitude and ground speed values are utilized are used to compute comparison metrics because these parameters are available across both the real-world and NADP data sets. Because both real-world and NADP trajectories are aligned and resampled at equal intervals, pair-wise comparisons along the profiles can be made.

Pearson correlation coefficient is used as a shape-based comparison metric to measure how two trajectories co-vary over time and identify the most representative NADP profile. The coefficient is invariant to shift between the two trajectories, thus mitigating the uncertainties due to the lack of information below 1,000 ft AGL. The equation below is used to compute Pearson Correlation, in which x is the parameter being compared and μ is the mean value of the parameter for a single profile.

$$\text{Pearson}(x_{AEDT}, x_{Real}) = \frac{\sum(x_{AEDT} - \mu_{x_{AEDT}})(x_{Real} - \mu_{x_{Real}})}{\sqrt{\sum(x_{AEDT} - \mu_{x_{AEDT}})^2 \sum(x_{Real} - \mu_{x_{Real}})^2}}$$

The values computed using the equation above vary from -1 to 1, indicating negative or positive correlations, respectively. The following three equations are then used to convert the resulting Pearson correlations for altitude and ground speed to an overall dissimilarity P'. The overall dissimilarity between each real-world trajectory and NADP profile is then scaled to a range of $[0,1]$ using the MinMax scaler, and the most representative profile can be identified by computing the minimum P^*.

$$P'_x = 1 - \text{Pearson}(x_{AEDT}, x_{Real})$$

$$P' = \frac{1}{2}(|P'_{Alt}| + |P'_{GS}|)$$

$$P^* = \frac{P' - P'_{min}}{P'_{max} - P'_{min}}$$

Distance-based comparison metric Mean Percentage Error (MPE) is to compute the degree of over- or under-prediction of the most representative NADP profile for each group of real-world trajectories. This computation enables the determination of the most representative reduced thrust (RT) level for the corresponding NADP profile used to represent a group of real-world trajectories. Note that only climb thrust may be considered due to the lack of information below 1,000 ft AGL. The equation below is used to compute MPE, where x is the parameter being compared and n is minimum number of points between the two profiles being compared.

$$\text{MPE}(x_{AEDT}, x_{Real}) = \frac{100\%}{n} \sum_{i=0}^{n} \frac{x_{AEDT,i} - x_{Real,i}}{\frac{1}{2}(x_{AEDT,i} + x_{Real,i})}$$

Results and Discussion

Narrow-body aircraft

The scaled overall Pearson dissimilarity are computed between all real-world trajectories and combinations of AEDT STANDARD (labeled as MODIFIED_AW) and NADP profiles of equal stage length departing the same airport. Figure 2 shows the distribution of real-world trajectories that are most similar to each procedural profile for narrow-body aircraft. In general, NADP 1-1 was the most similar profile to most real-world flights for all aircraft types. However, there are flights for every aircraft type that were classified as more similar to either the STANDARD or NADP 2-11 profiles due to the inherent variability in real-world operations.

Figure 3 illustrates this variability for A320 aircraft by airline and departure airport, where the color in each box indicates the NADP profile most representative of real-world operations for each airline and departure airport combination. Note that STANDARD is not the most representative profile for any airline and departure airport combination for the A320, even though there are A320 flights classified as similar to the STANDARD profile in Figure 2.

When averaging profile behavior across all airports and stage lengths, NADP 1-1 is generally the most representative profile for the targeted set of narrow-body aircraft types. Analysis at the airline and departure airport level, as shown in Figure 3, can be used to identify the most representative profile at a more detailed level.

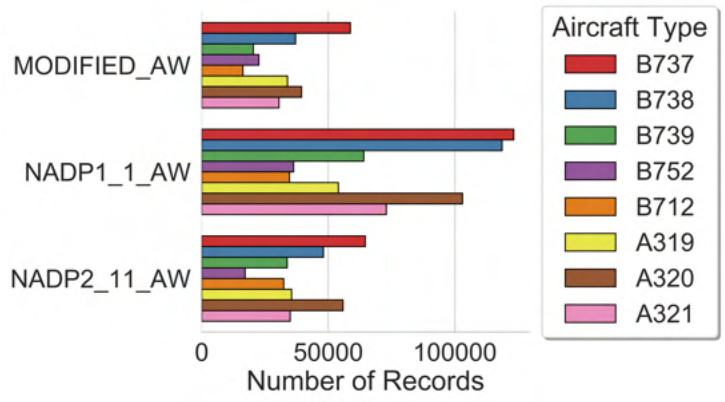

Figure 2. Narrow-body aircraft distribution of most similar procedural profiles by aircraft type.

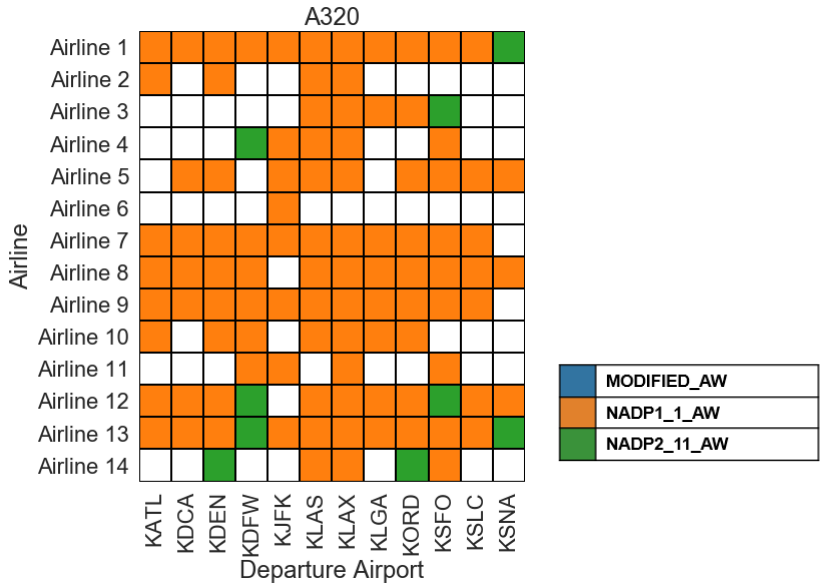

Figure 3. Sample A320 most representative procedural profile by airline and departure airport.

Figure 4 shows the differences in altitude and ground speed between real-world narrow-body aircraft trajectories and the NADP 1-1 RT0 and RT15 profiles. Positive MPE values indicate over-prediction by the NADP and that the real-world trajectories are lower in altitude or ground speed. Results show that altitude differences are much more prominent than ground speed differences. Overall, the B737, B738, and B739 aircraft are most similar to the RT15 profile, whereas the B752, A319, A320, and A321 aircraft are most similar to the RT0 profile. These aircraft types can therefore be represented using the NADP 1-1 profile with the appropriate reduced thrust amount, with errors in altitude and ground speed within $\pm 5\%$ of the averaged behavior across the 12 airports investigated and all stage lengths. Real-world trajectories for the B712, however, were substantially different from the NADP profile due to the lack of acceleration steps during flaps transition in the B712 STANDARD and NADP profile definitions. Adjustments to the B712 procedural profile definitions may be necessary to better represent B712 real-world operations.

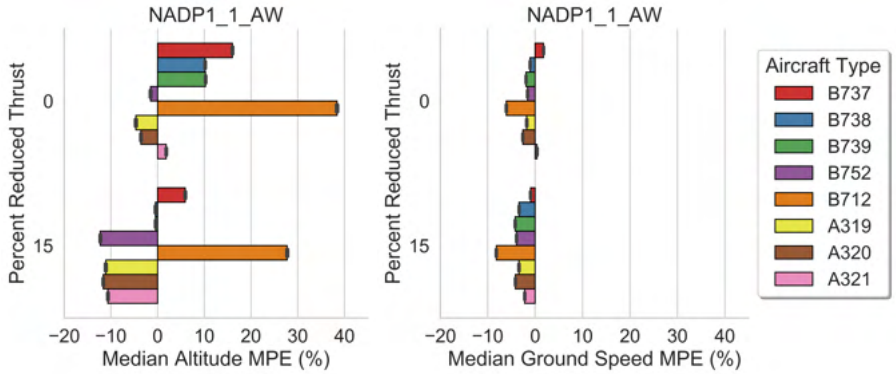

Figure 4. Narrow-body aircraft trajectory comparison to NADP 1-1 at maximum and 15% reduced thrust.

Figure 5 illustrates the variation in results for the altitude and ground speed comparisons between A319 and A320 real-world trajectories and the NADP 1-1 RT0 profile. Results are aggregated by departure airport, and the list of airports is sorted in order of decreasing airport elevation. As shown in the figure, NADP 1-1 RT0 substantially underpredicts the altitude profiles of real-world trajectories for these two aircraft types at high altitude and temperature airports (KDEN, KLSC, and KLAS). Further investigation into the thrust level utilized by AEDT for ANPs ID A319-131 and A320-232 reveals that high temperature climb thrust is used instead of the maximum climb thrust, especially at these airports. As shown in Figure 6, the high-temperature thrust coefficients for these ANP IDs produce thrust levels similar to the RT15 profile at high altitude and temperature airports. Adjustments to the high-temperature thrust coefficients for ANPs ID A319-131 and A320-232 may improve representativeness of NADP at high altitude and temperature airports.

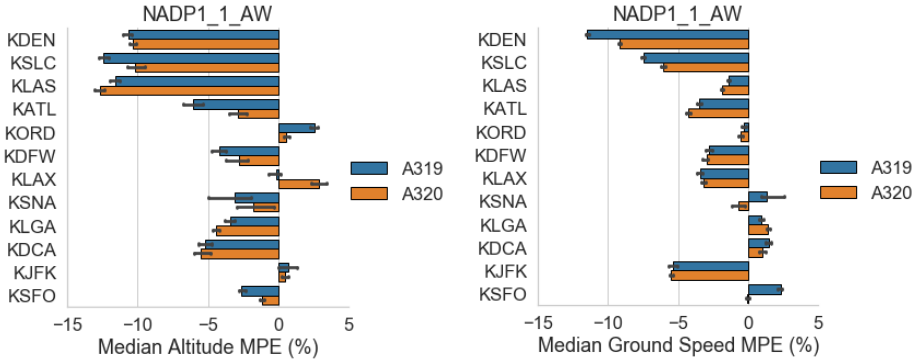

Figure 5. Sample A319/A320 trajectory comparison to NADP 1-1 at max thrust, aggregated by departure airport.

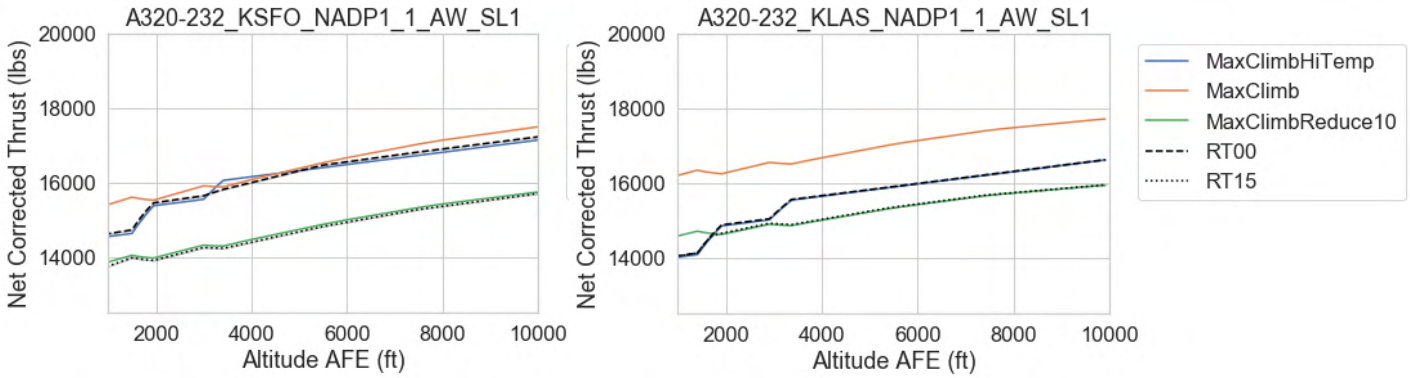

Figure 6. Sample ANP ID A320-232 thrust profile results at low- and high-altitude/temperature airports. Results for the A319-131 were similar.

Wide-body aircraft

The same analysis was also performed for wide-body aircraft. Figure 7 demonstrates the distribution of real-world trajectories that were most similar to each procedural profile for wide-body aircraft. In general, NADP 2-12 was the most similar profile to most A332 and A333 real-world trajectories while NADP 1-1 and NADP 1-7 were most representative of the B763 and B77W, respectively.

Figure 8 illustrates the variability in B763 and B77W profile use by airline and departure airport combinations. Higher variability in real-world procedures was observed for wide-body aircraft. While narrow-body aircraft may generally be represented by a single NADP profile that captures their overall behavior, grouping operations by airline and/or departure airport may be necessary for wide-body aircraft.

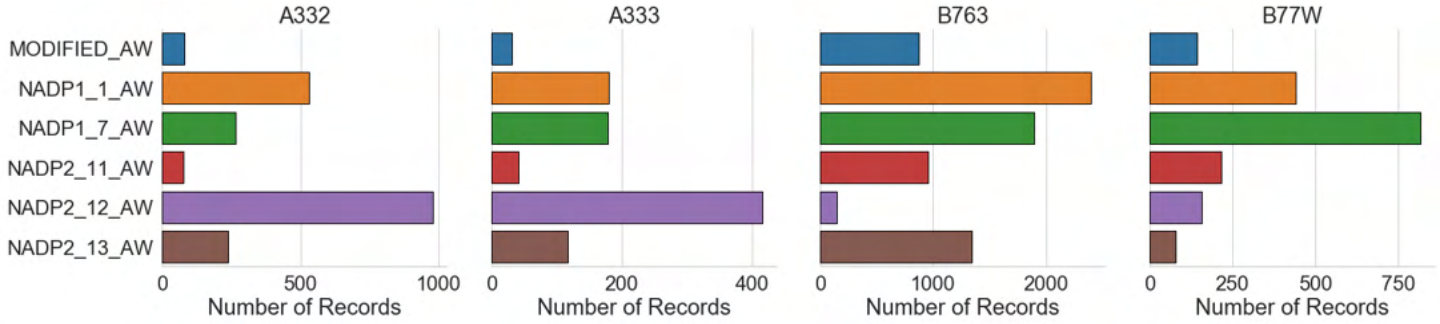

Figure 7. Distribution of the most similar procedural profiles by aircraft type for wide-body aircraft.

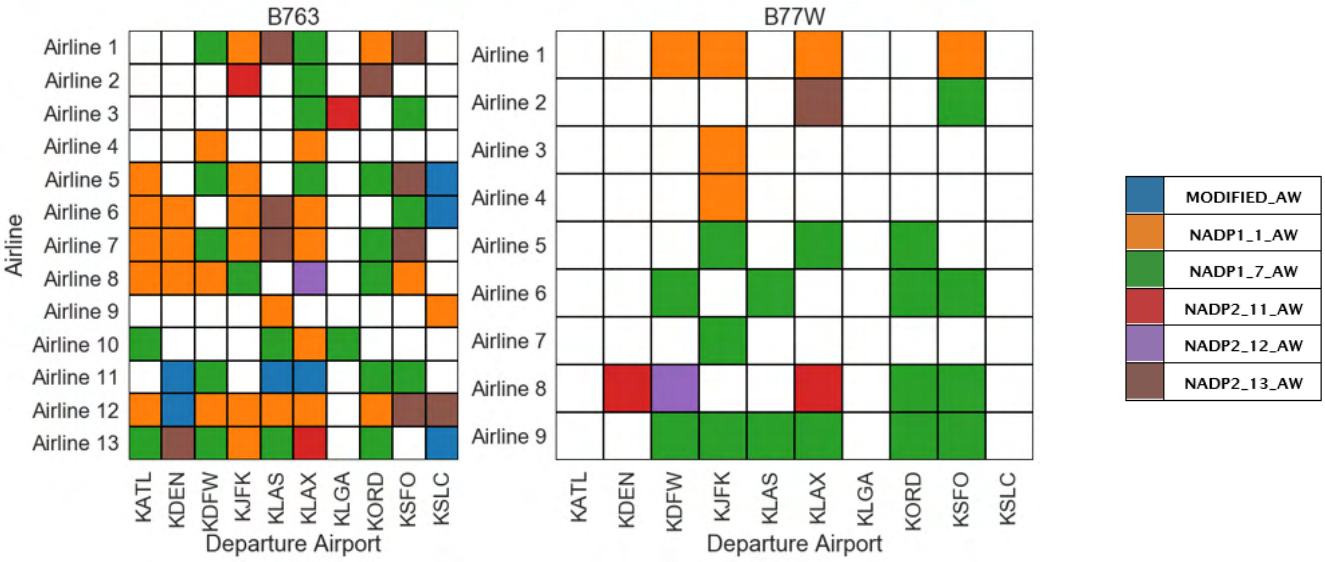

Figure 8. Most representative NADP profiles by airline and departure airport for the B763 and B77W aircraft.

Figures 9, 10, and 11 illustrate the differences in altitude and ground speed between real-world wide-body aircraft trajectories and their most representative NADP profile at RT0 and RT15. Results indicate that the A332, A333, and B77W real-world trajectories are most similar to the RT15 profile, whereas the B763 real-world trajectories are most similar to the RT0 profile. These aircraft types can therefore be represented by their most representative NADP using the appropriate RT amount, with errors in altitude and ground speed within ±5% of the averaged behavior across the 12 airports investigated and all stage lengths. However, real-world trajectories for wide-body aircraft may need to be analyzed at the airline and airport levels to determine the most representative RT amount corresponding to the most representative NADP, as shown in Figure 8.

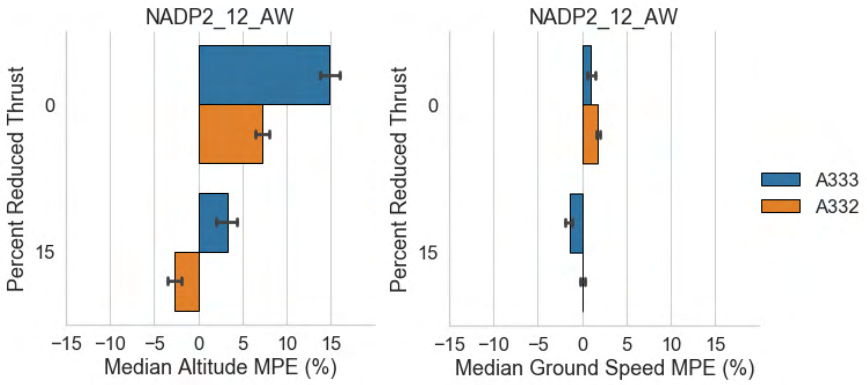

Figure 9. A332/A333 trajectories compared to NADP 2-12 at maximum and 15% reduced thrust.

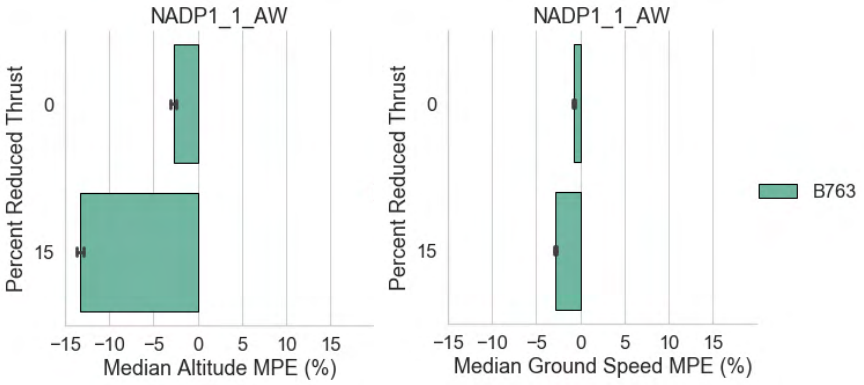

Figure 10. B763 trajectory compared to NADP 1-1 at maximum and 15% reduced thrust.

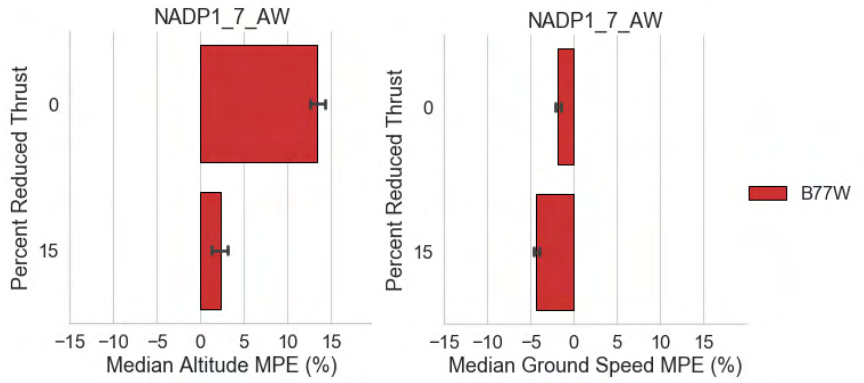

Figure 11. B77W trajectory compared to NADP 1-7 at maximum and 15% reduced thrust.

Following the methodology outlined above, this task identified the most representative NADP profile and RT level for each aircraft type. Trajectories were compared from 1,000 ft AGL to 10,000 ft MSL. Using the most representative profile and reduced thrust level, the overall differences in altitude and ground speed were quantified per aircraft type and the variability in profile usage by airline and airport were identified. However, this study only assesses the representativeness of NADP profiles in terms of trajectories. Uncertainties remain due to factors such as the lack of real-world trajectory information below 1,000 ft AGL, the lack of takeoff weight information for stage length classification, and the lack of actual thrust levels. Additionally, comparisons in the portion of the departure where climb thrust is most likely used. Further analyses to quantify errors arising from using distance-based stage length and the variability in RT usage are ongoing.

Task 2 – Arrival Profile Modeling

Georgia Institute of Technology

Objective

The objective of Task 2 is to find and develop recommendations for AEDT that will allow it to better capture aircraft behavior during arrival. The specific focus of this task is to (1) accurately capture the arrival of aircraft at airports based on real-life data and (2) enhance the ability of AEDT to identify incoming aircraft approaches and classify them as one of several arrival profiles suggested by the analysis of real-life data. The goals for 2021 were to identify the number and properties of arrival profiles that AEDT needs to accurately capture real life approaches, and, if required, apply machine learning-based methods for data reduction to consolidate the vast number of level-offs into a few significant ones. At the end of this project, a series

of recommendations will be made as to which AEDT arrival profiles should be integrated into the system and what information those profiles should include.

Introduction

AEDT currently models arrival profiles using specified fixed-point trajectories or manufacturer-provided procedures and can classify incoming aircraft into four categories during the approach. This task (Task 2: Arrival Profile Modeling) compares data from real flights to the models in AEDT to make recommendations on how to improve AEDT models to better capture real flight operations.

Research Approach

In previous stages of the project, we found that the level-offs leading to the approach, as identified from real-life operational data, contained several modes (i.e., the data were multi-modal). The data analysis provided clear evidence that the level-off definitions within AEDT needed modification. In addition, some initial recommendations for new, more accurate level-off definitions could be provided. However, when all the relevant parameters were taken together, the data did not show any discernible groupings that could be recommended for implementation within AEDT. For some airports, many of the arriving aircraft were approaching in a roughly similar manner, which provided clusters of data that could be approximated as a single or several arrival profiles. However, when taken as a whole, the data across all the airports did not have evident peaks that could be used as arrival profile approximations. This can be seen in Figures 12 and 13, which show the variation in level-off heights and level-off distance to airport.

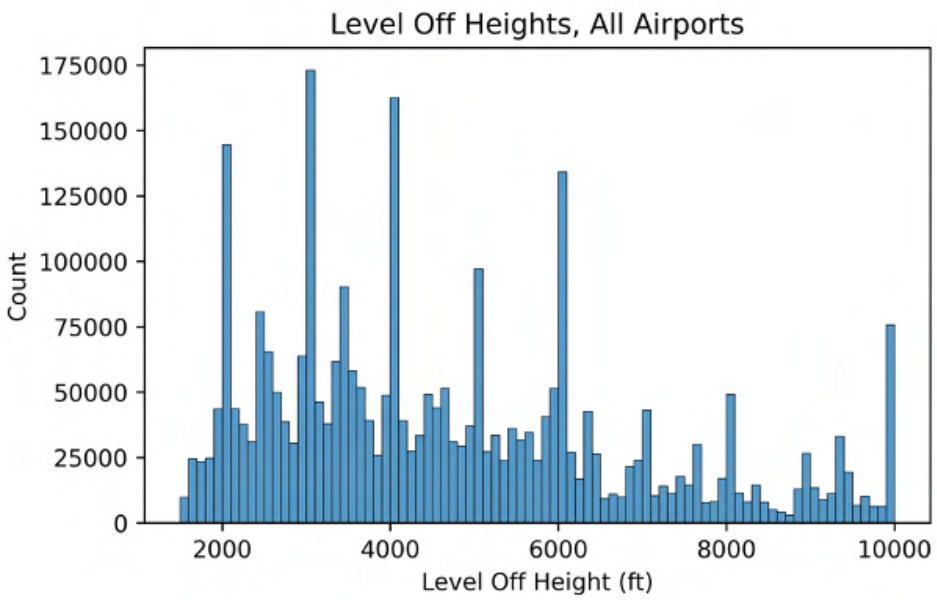

Figure 12. Level-off heights across all airports.

For example, when bin widths were varied from 100, 200 and 500 for the level off height metric, four major peaks were seen across the airports in the ranges of 2000, 3000, 4000, and 6000 ft. To analyze this further, the top five level-off heights for the ten busiest airports were rank ordered (Table 3).

Table 3. Rank-ordered level-off heights for the ten busiest airports.

Airports	Level-off heights (ft)				
	Rank 1 (Largest)	Rank 2	Rank 3	Rank 4	Rank 5 (Smallest)
ATL	6000	4000	3000	2300	2000
LAX	9900	7600	6900	3900	2300
ORD	9300	6400	5300	4300	3300
DFW	5400	4400	3500	2600	2400
DEN	7600	5600	4600	3800	3600
JFK	6300	4000	3000	2200	2000
SFO	8000	7000	6400	5000	4000
SEA	9700	7600	6800	5900	3700
LAS	8800	7900	6000	5800	3900
MCO	8900	6900	5900	3000	2400

The level-off heights for the three busiest airports are shown in Figure 13. As seen in the figure, there are 2-3 main level-off heights at each of these airports.

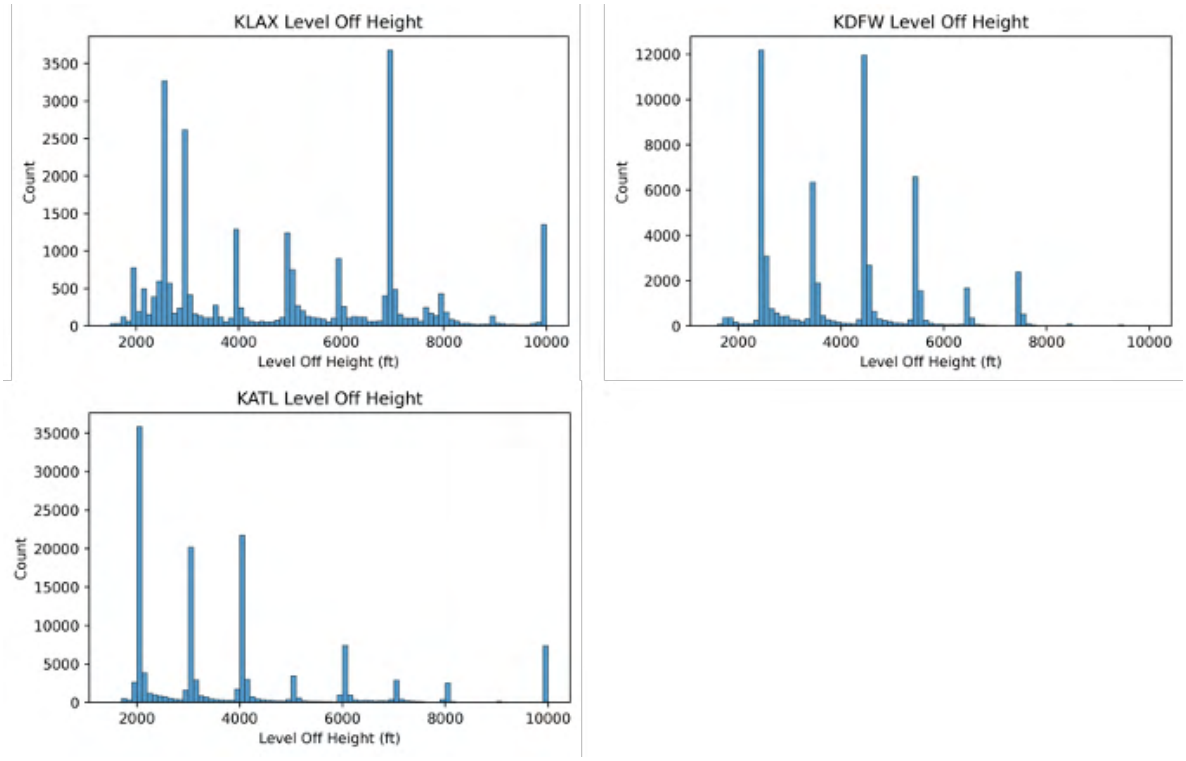

Figure 13. Level-off heights at LAX, ATL and DFW.

Figure 13 shows that level-off heights at LAX are at 7000, 3000, and 2500 ft, while at ATL they are at 4000, 3000, and 2000 ft. Because of these varying results, specific recommendations made within AEDT would need to be implemented on an airport-by-airport basis.

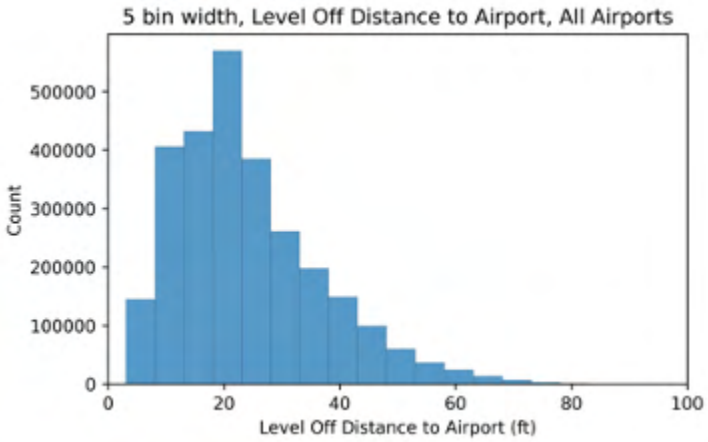

Figure 14. Level-off distance to airport across all airports.

To accomplish the objective of this project, the research team turned to machine learning and data clustering to determine if these approaches could consolidate the statistical similarity in the data into a limited number of profiles that could be provided as recommendations. Specifically, for this endeavor, it was proposed that level-off data be gathered and cleaned to remove any outliers. Airport metrics such as geographic location, runways, level-off altitudes and lengths, etc., would allow the features of analysis and comparison to be determined and then, the clustering task would be performed. The results of the clustering analysis can then be used to make recommendations for level-off definitions. Figure 15 presents a flow chart outlining this process. The team is currently at the 'perform clustering' stage.

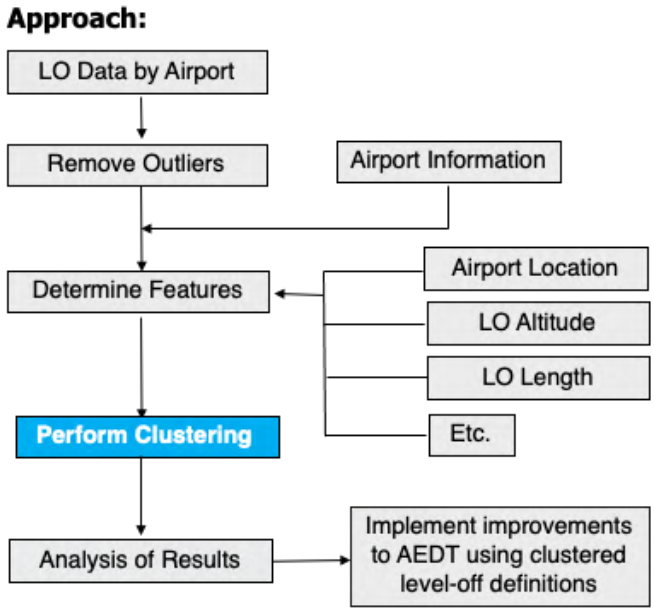

Figure 15. Task 2 Research Approach.

Methodology

Following the research approach outlined above, it was determined that clustering would be the best method for accomplishing the goals of this task. Clustering is an application of machine learning where an algorithm is used to aggregate a set of data points into some number of clusters. The primary purpose of clustering is data reduction. By aggregating points into clusters, each cluster can then be represented by a single point, or centroid. Further data processing can be done using

these centroids rather than the entire set of data points, thus reducing the amount of time and resources necessary for such processing.

There are a range of potential algorithms that could be used to perform clustering, each with a different mathematical approach. In order to test the algorithms, a small test dataset was created in order to speed up the testing process due to the sheer size of the available data. It was decided that the level off data from the three busiest airports would provide an excellent range of flight data that would be indicative of the larger dataset. The combined data from Atlanta Hartsfield-Jackson (ATL), Dallas-Fort Worth (DFW), and Los Angeles (LAX) were aggregated into a single file. However, these data points still proved to be rather inefficient, as it took long periods of time for the created scripts to perform clustering even with the reduced data. As a result, the team decided to further reduce the test dataset to include only 25,000 points, randomly selected from ATL, DFW, and LAX.

The data set that was used for this project was the aircraft approach data from the 95 airports provided as part of the Threaded Track Analysis. After obtaining all level off data from the available airports, each file was cleaned using a Python script to remove all data that did not include any level offs. This resulted in a database of level offs separated by airports. Next, the team determined the set of potential clustering algorithms that could be used to perform the clustering. These methods are given below, with a summary of the associated advantages and disadvantages of deploying them. The methods highlighted in blue indicate a need to specify the number of clusters when running the algorithm, thereby needing knowledge of the number of appropriate clusters for such a task.

Table 4. Clustering algorithms explored for Task 2.

Method	Details	Advantage	Disadvantage
K-Means	Distance-based	Fastest algorithm; tighter clusters compared to hierarchical	Requires knowledge of number of clusters
K-Medoid	Distance-based	More robust to noise compared to k-means	Assumes spherical data; requires knowledge of number of clusters
Agglomerative	Hierarchical	Orders objects	Requires knowledge of number of clusters
DBSCAN	Reachability and density-based	No need to pre-specify number of clusters	Does not handle different densities well
Mean Shift	Centroid-based	No need to pre-specify number of clusters	Cannot control number of clusters
OPTICS	Reachability and density-based	Handles different densities better then DBSCAN; no need to pre-specify number of clusters	Slower than DBSCAN
BIRCH	Hierarchical	Faster than other hierarchal algorithms	Slower than k-Means; requires knowledge of number of clusters

Capturing the distribution of data points to make recommendations for level-off definitions within AEDT requires insight into how many clusters are appropriate. This requires comparing scores across multiple runs with varying numbers of clusters. The plan was to use a small test data to quantitatively evaluate each clustering method using clustering scoring methods. Twenty clusters produced the highest scores when varied between 3-24 clusters, hence cluster numbers needed to be pre-specified the number 20 was used. As shown in Figure 16, this initial stage of testing using normalized data showed that the k-means and BIRCH algorithms produced the best results.

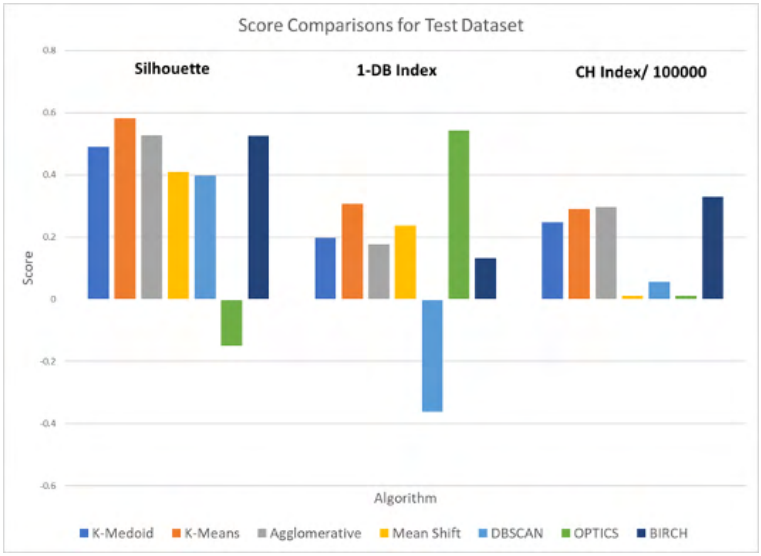

Figure 16. Clustering algorithm scores for the smaller (test) dataset.

The next step was twofold. First, the team wanted to investigate the results of the testing, to check which metrics and parameters most heavily influenced clustering. Since the distribution of cluster points can tell us how the data can be generalized for AEDT recommendations, if certain clusters had similar behavior across the metrics, and were not distinct, they could be removed, leading to reduced number of points for AEDT generalizations. Seven metrics were explored for this: airport locations, level-off height, length, distance to the airport, and delta velocity, total flight distance, and longitude and latitude. Ultimately it was found that 3 out of 7 metrics (level-off height, level-off length, level-off distance to airport) could be grouped into similar clusters. However, the 'total flight distance' and 'level-off delta v' metrics produced plots that showed more significant separations between clusters that were similar for the other metrics. This indicates that it may be possible to reduce the number of required clusters without losing much information if two of the metrics were not included as training features in the model.

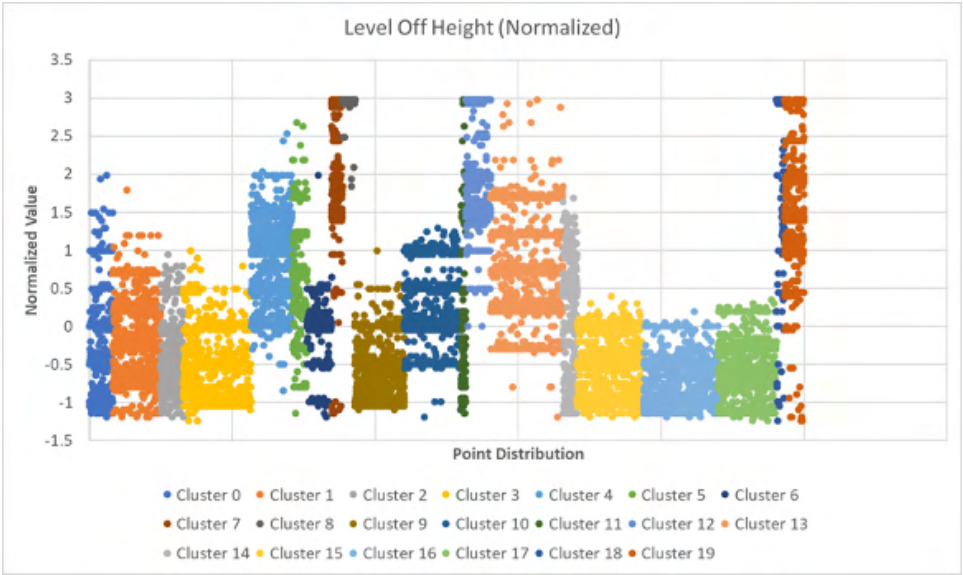

Figure 17. Level-off height plot.

With respect to airport locations, the clusters from the DFW and ATL airports were distinct (i.e., no same clusters are seen at both airports, see Figure 18). However, the LAX airport shows many overlaps between the clusters across ATL and DFW. This indicates that airport location is a very big factor in the training model, however, the overlapping clusters indicate that clustering solely based on airport would not produce good results.

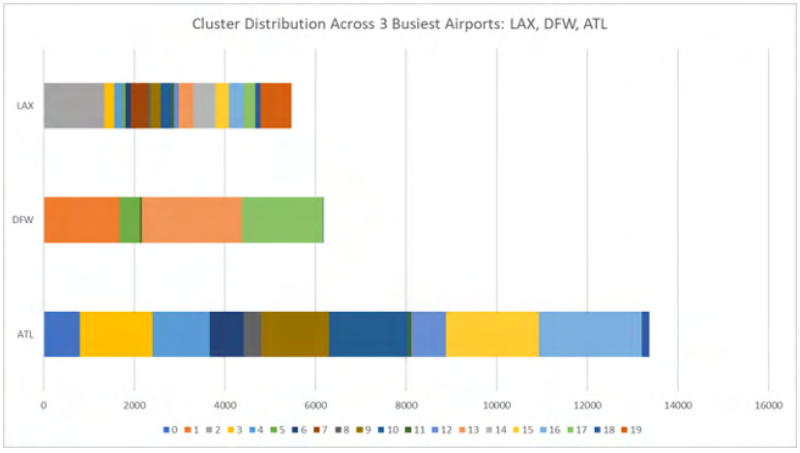

Figure 18. Airport cluster distribution.

In addition to identifying the variables with the strongest influence on the clusters, the team also wanted to expand the dataset used to generate the clusters. Because the test dataset only included 25,000 points randomly selected from the three busiest airports, we repeated our clustering analyses using all the level-off data from those three airports.

Our team is prepared to make some preliminary recommendations to the FAA regarding AEDT arrival profiles for metrics such as level-off height and distance to airport, etc. However, for specific recommendations to be made within AEDT, they would need to be implemented airport-by-airport based on the varying results among airports. We will continue working to produce recommendations for all such metrics using the k-means and BIRCH clustering algorithms.

Task 3 – Full Flight Modeling

Georgia Institute of Technology

Objectives

The objective of this task is to improve the usability of the full flight modeling within AEDT without employing the often complicated and time-consuming process of using the sensor path functionality that is the current standard for AEDT. To conduct a full flight study in AEDT, a sensor path based on radar track data must currently be defined for each aircraft type and origin-destination city pair. The goal of Task 3 is to develop an alternative method where a statistically representative trajectory and lateral routing can simulate the path of each origin-destination city pair for all commercial aircraft types operating within a centrally controlled airspace environment. The focus of this task is to demonstrate the reasonableness of this statistical approach by leveraging "real world" Flight Operations Quality Assurance (FOQA) data provided by a major U.S. air carrier.

Investigative Iterations

Over the past 12 months, the methods and modeling investigated have taken several directions. Although each investigative branch has provided additional information relevant to this task, some provided more clarity on what methods were not appropriate or productive for obtaining a satisfactory solution for plotting a straight-line path to an answer. As a result, the work supporting Task 3 has been somewhat iterative, with several loops back to the original source material and re-examination of the original remit. The following summary reflects the most recent approach that has been developed for a solution proposal.

Research Approach

Methodology

This section describes the methods used to determine the average behavior of city pair-specific routing data down-selected from the original FOQA dataset. The original FOQA data included approximately 21,000 flights representing 14 different aircraft types. The key elements for the city pair down-selection process were frequency of flights, representative stage lengths, and variety of aircraft. Our earlier work included many more city pair combinations; however, we found that more city pairs (as opposed to higher flight frequency for a given city pair) were not adding value to the analysis. The final down-selection criteria were based on subject-matter expertise from team members with extensive knowledge of airline operations, fleeting practices, and flight planning methods.

As shown in Table 5, six-city pairs were identified to investigate the average behavior of FOQA flights. Among these city pairs, the highest number of flight operations is from ATL to LAS (238 flights), while the lowest number is from LAS to ATL (15 flights). The city pair from LAS to SLC has the shortest stage length.

Table 5. City pairs down-selected from FOQA data.

City pair	No. of flights	City pair	No. of flights	*Great-Circle Distance (nm)*	*Stage Length*
ATL – LAS	238	LAS – ATL	15	1518	4
ATL – MSP	22	MSP – ATL	21	788	2
ATL – SEA	31	SEA – ATL	28	1896	4
ATL – SLC	188	SLC – ATL	21	1382	3
ATL – NY (EWR, JFK, LGA)	134	NY(EWR, JFK, LGA) – ATL	86	648 / 660 / 662	2
LAS – SLC	77	SLC – LAS	190	320	1

Note 1: The FOQA data set that the Aerospace Systems Design Laboratory received from its partner airline does not include all flights for a given city pair over the selected time. The data provided is heavily weighted toward flights that experienced some type of performance deviations that are desirable for tracking by the airlines flight safety department. Thus, for city pairs like ATL-LAS-ATL, the number of flight records for ATL-LAS is much higher than for LAS-ATL. This is because high descent rates into LAS are common and tracked by flight safety. Similar events are less common for arrivals into ATL. This results in the large numerical directional difference in the number of flights available for analysis for each city pair.

FOQA flights corresponding to the relevant city pair were extracted from the raw FOQA file using an automated Python script. Then, 100 trajectory data points, for each extracted flight of the corresponding city pairs based on Great-Circle Distance (nm), were selected and grouped. The density-based spatial clustering of applications with noise (DBSCAN) algorithm was used to analyze average patterns, if any, for each city pair. DBSCAN is a popular data-clustering algorithm in machine learning; it groups points that are close to each other based on distance measurement. We calculated the distance between trajectories within each city pair using Dynamic Time Warping (DTW) distance. The DTW distance measures the comparative separation between two trajectories that have the same origin/destination but may vary in time or speed.

Two parameters of the DBSCAN algorithm are required to adjust the optimal clustering results. The first parameter, eps, is the maximum distance between two samples for one sample to be considered in the other's neighborhood. The second parameter, min_samples, is the number of points in a neighborhood that are considered a core point. We took an iterative approach to fine-tuning our DBSCAN model. We iterated through a range of values for eps and min_samples. Specifically, we iterated through eps values ranging from 0.1 to 200 (at intervals of 0.1) and min_samples values ranging from 2 to 20. The “for” loop that performed this iteration ran the DBSCAN algorithm using each pair of values and generated a Silhouette score. After finding the best pair of eps and min_samples values with the highest Silhouette score. We produce a core path using the clustering algorithm. The Silhouette score is a metric used to calculate the goodness of a clustering technique. The detailed procedure is shown in Figure 19.

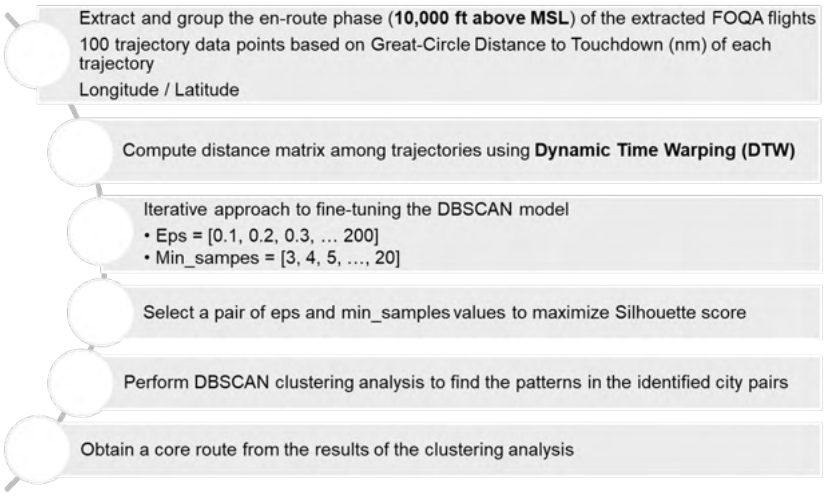

Error! No text of specified style in document.Figure 19. Flowchart of the DBSCAN clustering analysis.

Results and Discussion

Average behavior within the FOQA data

Table 6 summarizes the results of DBSCAN clustering analysis to determine the average behavior of selected city pairs. We found the most median path in the cluster after choosing the optimal pair of eps and min_samples values with the highest silhouette score. The Silhouette score of 1 means that clusters are well apart from each other and clearly separated. On the other hand, the score of -1 indicates clusters are assigned in the wrong way. The number of clusters generated due to applying the DBSCAN clustering algorithm is one for the city pairs except for the city pair from ATL to NY and the city pair from SLC to LAS.

Table 6. Results of the DBSCAN clustering analysis for six city pairs.

City pair	No. of flights	Eps	Min_ samples	# clusters	Outliers (%)	Silhouette score	City pair	No. of flights	Eps	Min_ samples	# clusters	Outliers (%)	Silhouette score
ATL - LAS	**238**	56.3	8	**1**	5	**0.599**	LAS - ATL	**15**	59.5	3	**1**	20	**0.704**
ATL - MSP	**22**	173	3	**1**	9.1	**0.857**	MSP - ATL	**21**	39.7	3	**1**	14.3	**0.764**
ATL - SEA	**31**	86.9	11	**1**	38.7	**0.673**	SEA - ATL	**28**	74.8	13	**1**	42.9	**0.575**
ATL - SLC	**188**	56.2	10	**1**	5.3	**0.610**	SLC - ATL	**21**	36.5	5	**1**	19	**0.655**
ATL - NY	**134**	27.5	19	**2**	5.2	**0.735**	NY - ATL	**86**	10.3	3	**1**	5.8	**0.848**
LAS - SLC	**77**	5.6	10	**1**	31.2	**0.605**	SLC - LAS	**190**	6.6	12	**2**	5.3	**0.687**

Figure 20 shows the results for city pairs from ATL to NY among the results of applying the DBSCAN clustering algorithm. Most of the full flight trajectory from ATL to NY is represented by two different patterns. The first cluster represents 78.4% of the total flights, and the second cluster represents 16.4%. Outliers account for 5.2% of total flights.

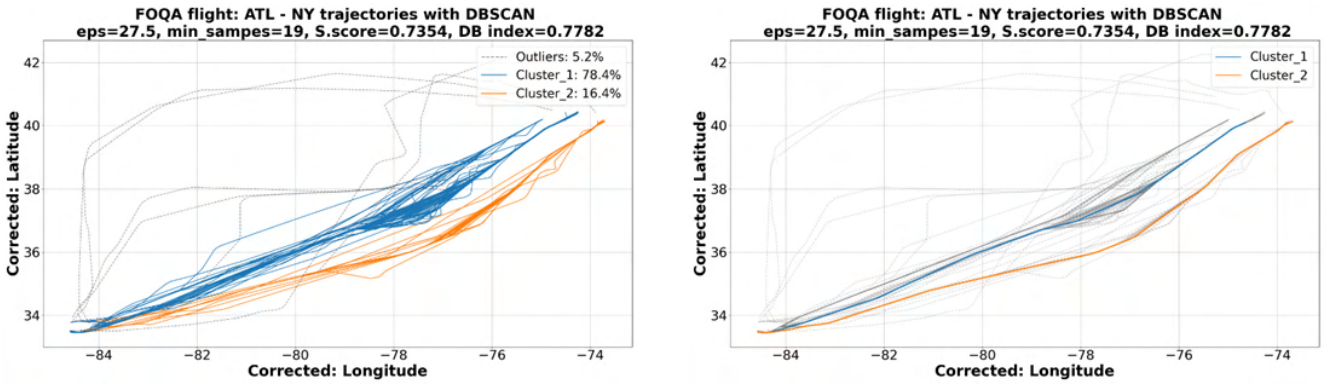

Figure 20. Clustering result and core paths extracted for the ATL-NY city pair.

Clustering exercises using the FOQA data have provided results consistent with expectations for the most common/frequent routing between city pairs and outliers due to weather or ATC disruptions.

Table 7. Comparison of the core path obtained through the DBSCAN clustering analysis with Great-Circle Distance.

City pair	*Great-Circle Distance (nm)*	*Ground Track Distance (nm) via DBSCAN*	*% Difference*	City pair	*Great-Circle Distance (nm)*	*Ground Track Distance (nm) via DBSCAN*	*% Difference*
ATL – LAS	1518	1534.8	1.1%	LAS – ATL	1518	1560.6	2.8%
ATL – MSP	788	836	6.1%	MSP – ATL	788	844.7	7.2%
ATL – SEA	1896	1972.5	4.0%	SEA – ATL	1896	1936.4	2.1%
ATL – SLC	1382	1462.1	5.8%	SLC – ATL	1382	1444.4	4.5%
ATL – NY (EWR, JFK, LGA)**	662 (LGA)	740	11.8 %	NY(EWR, JFK, LGA) – ATL	662 (LGA)	691.6	4.5%
	660 (JFK)	811.8	23.0%				
LAS – SLC	320	349.8	9.3%	SLC – LAS	320	351.1	9.7%
					320	349.2	9.1%

Table 7 compares the core path distances obtained through the DBSCAN clustering analysis to the great-circle distance between city pairs. As shown in the table, the great-circle distance and core path from ATL to NY differ significantly compared to other city pairs. The differences between the great-circle distance and the two core paths to NY are 11.8% and 23%, respectively. ATL and NY have some of the most congested terminal areas, and the airport arrival procedures can significantly impact travel distance.

In that the goal of the analysis is to demonstrate the statistical analysis of actual flight operations, a reasonable route model (simpler than using the SPI function) can be developed to reduce the time burden associated with large airspace and fuel burn studies. For example, Table 7 shows the validity of using a great-circle distance + percent difference model. It also helps identify specific conditions that must be accounted for in the next level of analysis. Two examples would be 1) accounting for the added distance/flight time associated with congested airspace such as the NYC area 2) Adjusting geographical constraints which may also add distance to a route (e.g., the mountains surrounding the SLC airport.) Terminal area procedures can add significant distance to ideal point to point routing but can be addressed in a statistically consistent manner.

Cumulative fuel burn between FOQA flights and AEDT modeling processes

After obtaining the core path between each city pair using the clustering analysis, we compared the cumulative fuel burn between the FOQA core path and AEDT modeling processes. The SPI tool reads aircraft flight trajectory data and then adjusts the speed, altitude, latitude, and longitude along the trajectory using a smoothing and filtering algorithm. Two input files

are needed to import flight trajectory data into the AEDT study database using the SPI tool. We therefore generated the necessary files (an input trajectory file and an input operation file) from our core trajectory data using Python scripts. The input trajectory file contains trajectory data for the core path, and the input operation file contains data for a single operation per flight in the trajectory file. Using MERRA-2 weather data, we ran a fuel consumption study in AEDT based on the trajectory data in the AEDT study database. We then compared the cumulative fuel burn between the FOQA data and the AEDT modeling process.

Table 8. Comparison of cumulative fuel burn between the FOQA core path and AEDT's performance models.

City pair	Airframe	Cum. Fuel Burn (lbs)			Fuel Diff. (%)		Avg. Headwind (knots)		
		FOQA	BADA3	BADA4	BADA3	BADA4	FOQA	BADA3	BADA4
ATL - LAS	B753	37538	-	50747	-	35.2	66.8	-	80.7
LAS - ATL	B753	27802	-	29358	-	5.6	-40	-	-74.1
ATL - MSP	B753	18402	-	13068	-	-29.0	29.3	-	25.6
MSP - ATL	MD90	15088	15672	-	3.9	-	11.5	7.5	
ATL - SEA	B739	30614	28853	26892	-5.8	-12.2	16.8	-4.9	-3.8
SEA - ATL	B752	30507	31333	31669	2.7	3.8	-41.1	-53.6	-43.5
ATL - SLC	A333	47771	45101	43864	-5.6	-8.2	41.3	44.6	50.7
SLC - ATL	B739	20247	19635	18870	-3.0	-6.8	3.2	-15	-19.4
ATL - NY	B739	12057	11610	11620	-3.7	-3.6	0	-30.7	-33.5
	A320	12887	13309	12401	3.3	-3.8	-27.6	-41.2	-30.6
NY - ATL	B739	12912	12963	12966	0.4	0.4	62.7	53.6	54.3
LAS - SLC	B739	6080	6696	6414	10.1	5.5	-11.7	-17.3	-17.1
SLC - LAS	B712	5213	4838	4614	-7.2	-11.5	19.3	-2.6	-21.6
	B739	6775	6845	6547	1.0	-3.4	35.4	15	20.8

Table 8 shows the cumulative fuel burn comparison for the core path and the AEDT performance model. The results include 12 city pairs and seven aircraft types. In the total fuel comparison between the core path and the BADA3 model, seven core paths out of 11 have less than 5% error. The city pair of LAS-SLC showed the most significant percentage error at 10.1%. And in the total fuel comparison between the core path and the BADA4 model, there are four cases where the percentage error is 10% or more. However, in the case of a city pair of ATL-LAS and ATL-MSP, discontinuities occurred in calculating total fuel burn using the BADA4 model. Therefore, only city pairs of ATL-SEA and SLC-LAS show a high percentage error in comparing cumulative total fuel burn.

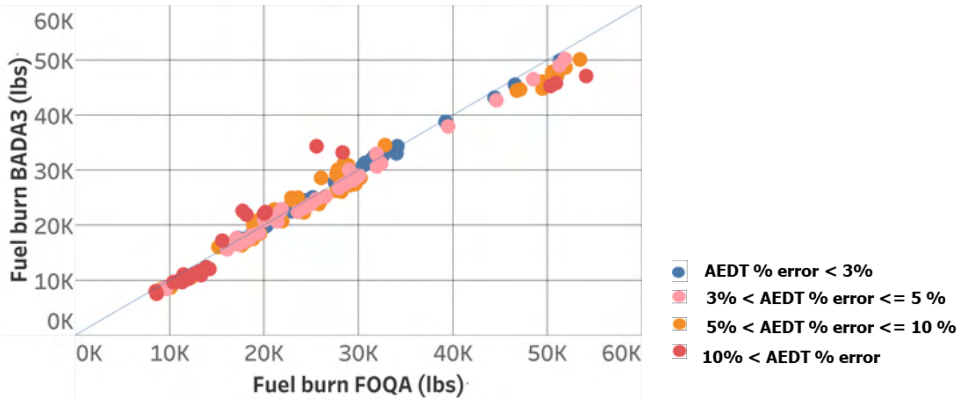

Figure 21. Total fuel burn comparison between FOQA data and BADA3 modeling in AEDT.

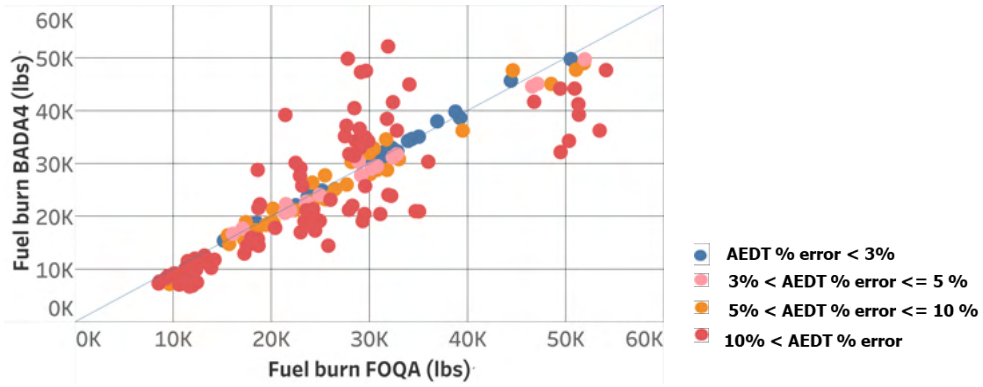

Figure 22. Total fuel burn comparison between FOQA data and BADA4 modeling in AEDT.

Each point in Figures 21 and 22 represents the cumulative fuel burn for one flight. The location of each point along the x- and y-axes represents the cumulative fuel burn for the flight in FOQA data and the AEDT model, respectively. The figures also show the line where the values along the horizontal and vertical axes are equal, such that if a data point falls on this line, the total fuel burn predicted by AEDT matches the total fuel burn reported by FOQA data. Values above and below the line represent over- and under-prediction of the total fuel burn by AEDT, respectively.

For the BADA3 model (Figure 21), most points are at the bottom of the line and have a percent error of less than 10 percent in the total fuel burn comparison compared to FOQA data. and the BADA3 model. In contrast, the total fuel burn comparison for the BADA4 model and FOQA data (Figure 22) shows a more significant scatter pattern. Figure 23 shows exceptional cases where discontinuities appeared in the total fuel burn calculation using the BADA4 model. This increased error level is primarily driven by the use of the 757-200 and 757-300 BADA4 datasets.

Numerous cases/conditions produced fuel flow discontinuities (high FF over a short time period) in the AEDT output. This resulted in a step function additive to the integrated fuel burn when using the BADA4 model. This behavior was not repeated when using the BADA3 datasets. It is recommended that Volpe conduct further investigation into the quality of BADA4 datasets or the applicable AEDT logic to determine the source of these discontinuities. Lastly, it should be noted that the amount of total fuel obtained from FOQA data may vary measurably from the AEDT calculations depending on factors such as engine degradation and the status of engine maintenance. AEDT does not have a function to factor in this "by tail number" variance.

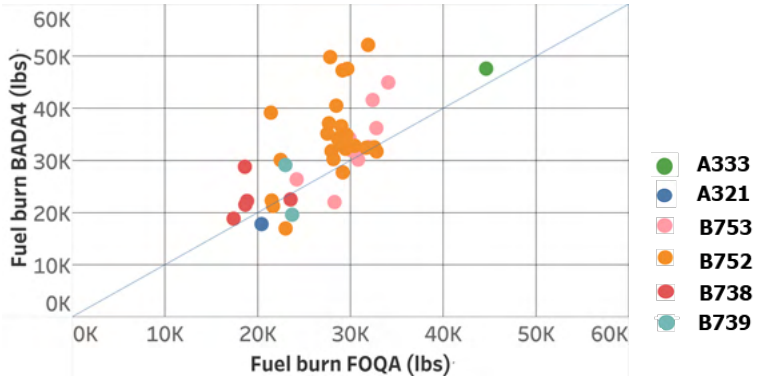

Figure 23. Exceptional cases in total fuel burn calculated using BADA4 modeling in AEDT.

The findings from the cumulative fuel combustion rate comparison are summarized below.

- FOQA data contain potentially thousands of individual fuel, time, distance, and speed measurements. The results of the down-sampling exercise demonstrate that a much simpler trajectory model will provide reasonable predictions of fuel consumption.
- The amount of fuel required from FOQA data may vary substantially depending on factors such as engine degradation and the status of engine maintenance
- The BADA3 model has been validated to be reasonable for the aircraft that can compare the total fuel burn using FOQA data
- Using the MERRA-2 weather data significantly reduced the differences in cumulative fuel burn between the FOQA data and AEDT models.
- Exceptional cases are identified when calculating the instantaneous fuel burn using BADA4 and high-resolution data input
- BADA4 modeling for individual aircraft (e.g., 757-200) may need review and re-validation.

Task 4 – System Testing and Evaluation of AEDT

Georgia Institute of Technology

Objective

To provide the best possible environmental impacts modeling capabilities in AEDT, the FAA AEE continues to develop AEDT by improving existing modeling methods and data and adding new functionalities. The AEDT development team has been exercising an agile development process, where minor updates are released in new Sprint versions every three weeks, and major updates and/or new functionalities are incorporated as new versions of AEDT. The FAA AEE seeks an independent effort in system testing to evaluate the accuracy, functionality, and capabilities of AEDT and support the future model development process. The objective of this task is to provide the FAA with high-quality systematic testing and evaluation of the capabilities of AEDT 3 and its future releases and to identify gaps in the tools' functionality and areas for further development.

Research Approach

Within this task area, the Georgia Tech research team has been coordinating with the FAA and Volpe National Transportation Systems Center on the upcoming AEDT features and testing and evaluating newly incorporated capabilities. For each AEDT release, depending on the type of updates, key features and functionalities are identified for capability demonstration to ensure the implemented features are working properly. We are then either provided with, or define for ourselves, the scope and test cases for the system testing and evaluation effort. These are typically defined based on the key changes to the AEDT version from the previous releases. Due to the dynamic nature of the AEDT development process, we remain flexible in the choice of the testing and evaluation approach and the scope of our work. The best available methods and data are used to ensure accuracy in the functionalities of newly released AEDT versions. When required, uncertainty quantification analysis is conducted to understand the sensitivities of output responses to variation in input variables and to quantify the major contributors to output uncertainties.

In the following subsections, the various features and functionalities that were tested from October 2020 to September 2021.

TGO/CIR Profile Development

This task focused on the development of Touch-and-Go (TGO) and Circuit (CIR) profiles, using the existing approach and departure procedures as the baseline. This development was performed for all 146 ANP fixed-wing civil aircraft with defined procedural profiles, and the developed profiles were provided to the AEDT Development team for integration into the FLEET Database.

Profiles were created using programming scripts to copy appropriate steps from the relevant departure or arrival profile. All created profiles were tested for correctness by modeling noise metric results over a noise grid.

AEDT Weather Updates
This represented a significant update in the way the weather database worked when compared to INM, EDMS, or previous versions of AEDT. The airport weather database now stores the most recent 10-year averaged definitions as single-year averages along with a rolling 10-year average. AEDT users have the option to select either a 10-year or single-year weather definition for their metric results. Figure 24 shows a screenshot from the AEDT GUI with a single-year averaged weather definition.

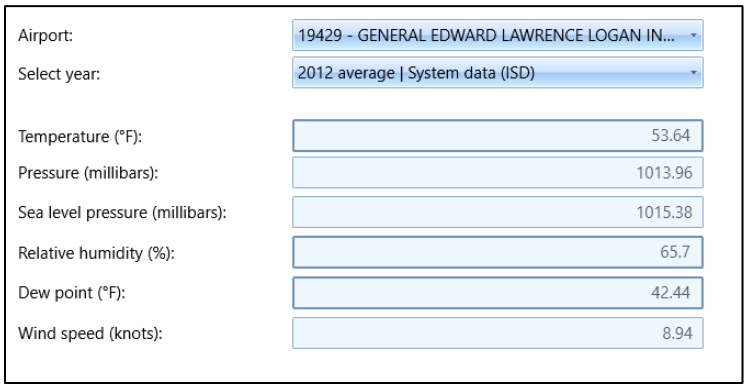

Figure 24. Newly-added single-year weather definition in AEDT.

For this feature, we assessed the implementation in the GUI, determined the effect of weather settings on aircraft performance, and determined AEDT's response in the absence of weather data. The implementation in the GUI was tested with various checks in the SQL database and in the GUI. For example, the calculation of dew point temperature from ambient temperature and relative humidity was verified. The effect of weather settings on aircraft performance was checked for various aircraft. As expected, minor differences in aircraft performance were observed due to slightly differing weather definitions. Finally, it was verified that in the absence of a weather definition for a particular year, AEDT will default to using ISA weather definitions.

ASOS Wind Speed Adjustment
From AEDT 3d onwards, the user was given an option to turn on or off the ASOS wind speed adjustment when preparing emissions dispersion weather data.

Re-Implementation of the Calculation of Speciated Organic Gases
In previous AEDT versions, viewing results for speciated organic gases (SOGs) would significantly increase AEDT run-time and memory usage, and would likely cause AEDT to fail when running a full-year emissions dispersion job. The SOG calculation was therefore redesigned as a post-processing step and implemented as a replacement to the current process.

To test this implementation, two aircraft operations and a non-aircraft operation were created in AEDT. All sources were then assigned an appropriate location, and a receptor set consisting of a single receptor was defined. A single day of surface and upper air data was then selected and processed using the "Generate emissions dispersion weather" dialog box in AEDT. Finally, an annualization was created and a metric result was defined. Overall, it was confirmed that the new implementation of the SOG calculation accurately predicted metric results.

Fixed-Point Trajectory Processing in the BADA4 Workflow
Fixed-point trajectories provide users with a way to model aircraft trajectories from available trajectory data without running an AEDT performance model. Such fixed-point trajectories are modeled in AEDT using the ANP-dominant performance workflows. However, because such a workflow did not exist in BADA4, fixed-point profiles could not be modeled with BADA4. This feature was added to enable such modeling.

Testing was performed by comparing the input trajectories with the resultant output performance reports and ensuring a close match between the two.

ASIF Import of Spectral Data
The existing ASIF import mechanism supported user-defined aircraft but not user-defined spectra. Aircraft manufacturers and the research community expressed desire for the ability to load aircraft-specific spectra into AEDT via ASIF to support internal testing prior to the data being officially transmitted to the FAA.

Different helicopters and military jets were used to test this feature with different user-defined spectral datasets. Noise metric results were modeled and compared. It was observed that there were slight differences in noise contours between aircraft with existing and user-defined spectral definitions, thus confirming that AEDT was able to use user-defined spectral data for noise modeling.

Running Multiple Pollutants Simultaneously in Emissions Dispersion
This feature was introduced as an interim solution to speed up Emissions Dispersion computations. In this feature, the functionality to combine certain steps from two or more Emissions Dispersion jobs was introduced to reduce overall runtime. This enhancement is only possible for Emissions Dispersion jobs that share identical options/settings for flight performance and emissions inventory and for which the annualizations and modeled receptor set(s) are identical.

To test this functionality, an emissions dispersion study was modeled in two ways: (i) the traditional AEDT implementation and (ii) with the enhanced functionality. An example study containing an average day with 24 hours of operations was used and ground-level concentrations were modeled at 10 different receptors. Nine metric results were created corresponding to emissions dispersion of CO, NMHC, NO_2, NO_x, SO_2, SO_x, THC, TOG, and VOC. Figure 25 shows the benefits obtained by this feature, where the modeling time was reduced from 20 minutes to 8 minutes.

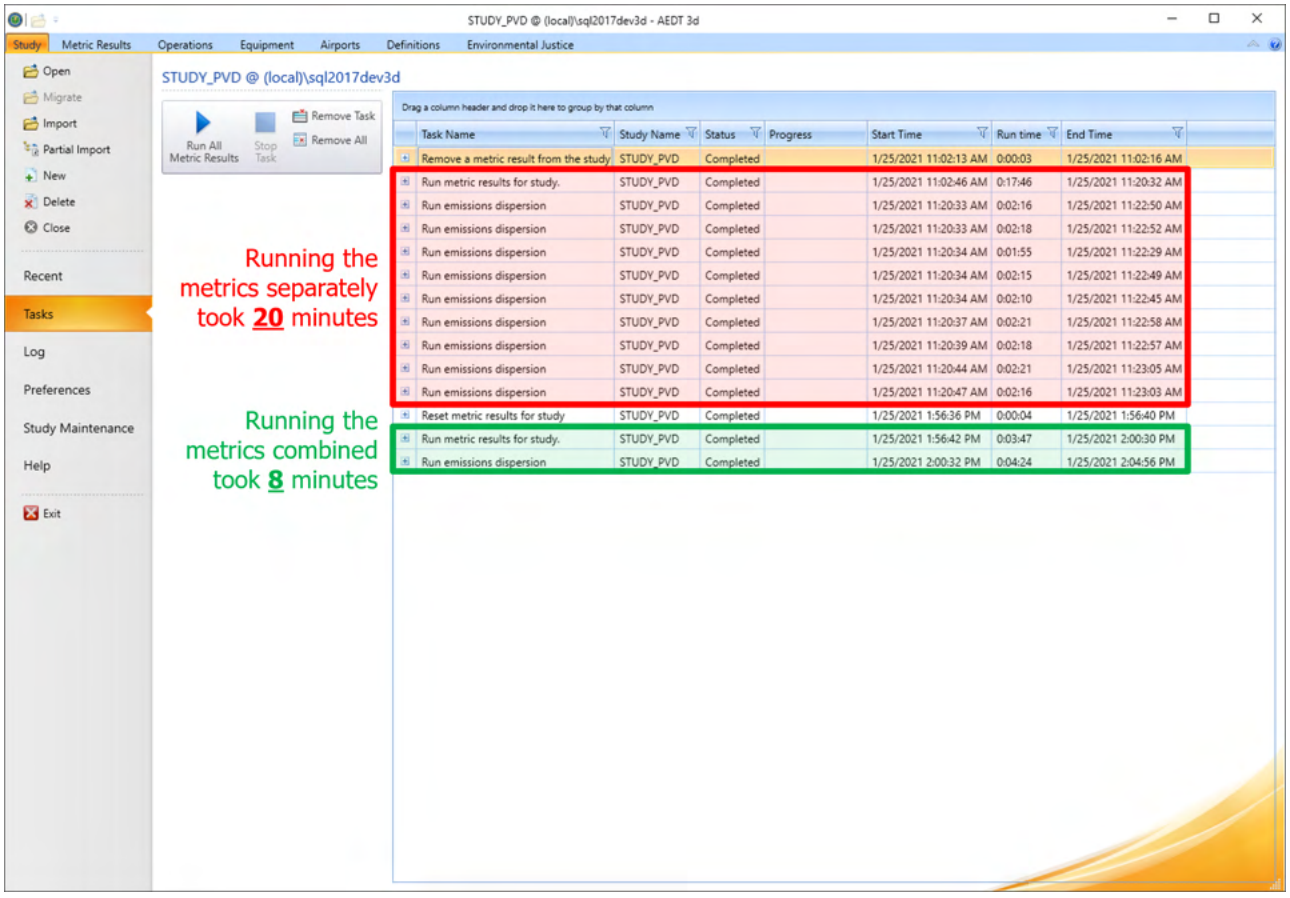

Figure 25. Benefits introduced by running emissions dispersion calculations simultaneously.

Emissions Report Improvement
In newer versions of AEDT, the emissions report has been updated to include additional information. The following improvements have been made:

1. Altitude MSL is now output in addition to Altitude AFE.
2. Unit X, Y, and Z columns are now populated for Taxi segments.
3. The duration of each segment is reported.
4. When the nvPM number cannot be calculated, N/A is reported.

Testing for this task was conducted to confirm that the desired changes had been made correctly, and that the output emissions report was correct.

Revised Stationary Source Modeling
AEDT was still making use of AP-42 methods and data from 1992 and/or 1997 editions, even though the Environmental Protection Agency's (EPA) updated method was published in 2020. The modeling method was updated to reflect the EPA updates. System testing was performed to ensure that the changes were implemented correctly.

Creation of Flight.txt file for Helicopters
In older versions, AEDT had been updated to export the INM Legacy flight.txt file for use by the ProfDev program. This feature extends that functionality to include helicopter operations and noise data. Testing was performed to ensure the flight.txt file was being generated correctly and that it could be used by the ProfDev program.

Viewing of selected tracks only
This feature was added in response to user support requests and a URG request. In older AEDT versions, all airport features would be displayed simultaneously when viewing an airport layout. For studies with a large number of user tracks, this would cause a delay due to the time required to render. This feature was introduced to change the behavior of the "View Layout" button and context menu so that, by default, only the airport's physical layout and features (i.e., runways, taxiways, gates, buildings, etc.), but not the tracks, are displayed. Testing was conducted to ensure this feature was implemented correctly.

Implementation of SAE-AIR-6297 Start-of-Takeoff Roll Directivity Adjustment
Start-of-Takeoff-Roll (SOTR) Noise Directivity in AEDT was updated to reflect the methodology in ICAO Doc 9911 update based on SAE-AIR-6297. The new directivities include separate directivities for jet aircraft and turboprop aircraft. The 6297 jet SOTR is applied for all jets (commercial and military), and the 6297 turboprop SOTR is applied for all props (commercial and military for both turboprop and piston prop). No SOTR directivity is applied to helicopters.

Testing for this feature consisted of noise contour comparisons between SEL metric results for the departure operations of several aircraft. By comparing noise contours, it was confirmed that the implementation of the new directivity adjustment was affecting noise results.

Milestones

- Not applicable

Major Accomplishments

Comparison of NADP Profiles to Real-world Operations

- Developed a process for identifying the most representative NADP profile and reduced thrust amount for large-scale aircraft trajectory data
- Identified the most representative NADP trajectories, variations in NADP usage by airline and airport, and the corresponding reduced thrust amount for eight narrow-body and four wide-body aircraft types at 12 airports for various airlines.
- Quantified altitude and ground speed differences between real-world trajectories and the most representative NADP by aircraft type, airline, and airport.

Arrival Profile Modeling

- Provided recommendations for initial level-off height, delta velocity, distance to airport, and number of level-offs based on real-life operational data
- Identified the two best algorithms for clustering analysis by testing and scoring several potential algorithms

Full Flight Modeling

- Identified the most representative city pairs from FOQA data based on frequency of flights, representative stage lengths, and variety of aircraft
- Modified a Python script to apply the DBSCAN clustering algorithm to find specific trajectory patterns after obtaining the pair of the two parameters of the algorithm, eps and min_samples,
- Implemented comparison of the core path obtained through the DBSCAN clustering analysis with the great-circle distance (GCD)
- Conducted cumulative fuel burn comparison between the core path and AEDT's performance models

System Testing and Evaluation of AEDT

- Conducted several in-depth investigations with system testing for new AEDT features
- Communicated bugs in feature implementation to the AEDT development team and coordinated their resolution

Publications

Bhanpato, J., Puranik, T. G., Mavris D. N. (2021). Data-driven analysis of departure procedures for aviation noise mitigation [Presentation]. OpenSky Symposium (Virtual).

Outreach Efforts

Bi-weekly calls with the FAA, Volpe, and ATAC. Bi-annual ASCENT meetings. Attendance at the AIAA Aviation Conference and OpenSky Symposium to present a conference paper.

Awards

None

Student Involvement

Ameya Behere, Ayaka Miyamoto, Rukmini Roy, Jirat Bhanpato, Hyungu Choi, Bogdan Dorca, Zhenyu Gao, Santusht Sairam (Graduate Research Assistants, Georgia Institute of Technology)

Plans for Next Period

The primary focus for the next period will be:

Task 1:

- Quantify errors in comparison results arising from the use of distance-based stage length in the absence of takeoff weight data.
- Continue investigating variability in reduced thrust usage and level.
- Improve the comparison procedure and automate it for large-scale analysis.

Task 2:

- Run clustering for larger test datasets.
- Make recommendations for all metrics identified.

Task 3:

- Continue the sensitivity analysis between the FOQA flights and a range of great-circle distance additives.
- Rerun the study using the Threaded Track data after validating the preliminary results obtained with FOQA data.

Task 4:

- Continue system testing to support new AEDT features.
- Create a comprehensive UQ Report to inform AEDT users of new features and their effect on environmental impacts.

Project 055 Noise Generation and Propagation from Advanced Combustors

Georgia Institute of Technology (GT)
Raytheon Technologies Research Center (RTRC)

Project Lead Investigator

Timothy Lieuwen
Professor
Aerospace Engineering
Georgia Institute of Technology
270 Ferst Drive, G3363 (M/C 0150)
Atlanta, GA 30332-0150
Phone: 404-894-3041
E-mail: tim.lieuwen@aerospace.gatech.edu

University Participants

Georgia Institute of Technology

- PI(s):
  - Timothy Lieuwen, Professor
  - Suresh Menon, Professor
  - Adam Steinberg, Professor
  - Vishal Acharya, Senior Research Engineer
  - Benjamin Emerson, Senior Research Engineer
  - David Wu, Research Engineer
- FAA Award Number: 13-C-AJFE-GIT-058
- Period of Performance: February 5, 2020 to February 4, 2022
- Tasks:
  1. **Facility Development at Georgia Institute of Technology (GT):** This task addresses the design of experiments that will be performed at GT. The task involves coordination between the teams to develop and define the aerodynamic design of a rich-quench-lean, quick quench, lean burn (RQL) combustor for this study. The task is led by Tim Lieuwen and Adam Steinberg, with support from Ben Emerson and David Wu.
  2. **Simulations of the GT Experiment:** This task includes simulating the GT experiment, with a focus on the pre-combustion flow dynamics, flame dynamics, and post-combustion dynamics of pressure and entropy disturbances. This task is led by Suresh Menon.
  3. **Reduced-order Modeling:** This task consists of creating a reduced-order modeling (ROM) framework for the unsteady response of the flame as well as the generation of entropy disturbances due to unsteady heat release. This task is led by Vishal Acharya.

Raytheon Technologies Research Corporation

- PIs:
  - Jeffrey Mendoza, Technical Fellow Acoustics
  - Duane McCormick, Principal Research Engineer
  - Julian Winkler, Staff Research Engineer
  - Peter Cocks, Project Leader, Pratt & Whitney (P&W) Program Office
  - Lance Smith, Principal Research Engineer
- FAA Award Number: 13-C-AJFE-GIT-058 (subaward through GT)
- Period of Performance: February 5, 2020 to February 4, 2022

- Tasks:
  4. **Facility Development at Raytheon Technologies Research Corporation (RTRC):** This task addresses the design of experiments that will be performed at RTRC. The task involves coordination between the teams to develop and define the aerodynamic design of an RQL combustor for this study. This task is led by Jeffrey Mendoza, Lance Smith, and Duane McCormick.
  5. **Post-combustion Modeling:** This task consists of both postprocessing and simulation efforts. First, the post-combustion simulation data from the simulation of the GT experiment are mined to understand the dynamics of entropy fluctuations and their transport. Next, simulations are used to model noise propagation in the post-combustion architecture of the engine. The simulations are split across the different sections: nozzle, turbine, and far-field. This task is led by Jeffrey Mendoza and Julian Winkler.

Project Funding Level

FAA funding: $3,000,000 split equally between GT and sub-awardee RTRC
Cost-share: $3,000,000 total, split equally between GT and RTRC
Total funding: $6,000,000

Investigation Team

Tim Lieuwen (GT): Principal Investigator. Professor Lieuwen is the lead PI overseeing all tasks. Specifically, he leads the GT experiments and design in Tasks 1 and 2 along with Professor Steinberg. In addition, he co-leads the modeling tasks in Task 1 for pre-combustion, flame response, and post-combustion along with Dr. Acharya.
Adam Steinberg (GT): Co-Principal Investigator. Professor Steinberg manages the design of experiment diagnostics and measurements.
Suresh Menon (GT): Co-Principal Investigator. Professor Menon manages the tasks for simulations of the GT experiment.
Vishal Acharya (GT): Co-Principal Investigator. Dr. Acharya co-manages all modeling tasks for the pre-combustion, combustion, and post-combustion physics along with Professor Lieuwen. In addition, as administrative coordinator, he is responsible for general project management, such as project deliverables, group meetings, and interfacing with the FAA project manager.
Benjamin Emerson (GT): Co-Principal Investigator. Dr. Emerson is responsible for designing and maintaining experimental facilities, as well as experimental operations and management and the safety of graduate students.
David Wu (GT): Co-Principal Investigator. Mr. Wu is responsible for designing and maintaining experimental facilities, as well as experimental operations and management and the safety of graduate students.
Vedanth Nair (GT): Research Engineer. Dr. Nair is a research faculty member reporting to Professor Steinberg. He is responsible for designing the post-combustion diagnostic capabilities for the GT experiment.
Orlando Ugarte-Almeyda (GT): Postdoctoral Researcher. Dr. Ugarte-Almeyda reports to Professor Menon and works on simulations of the GT experiment.
Sangjae Kim (GT): Graduate Student. Mr. Kim is working on large-eddy simulation (LES) studies for the GT rig.
Amalique Acuna (GT): Graduate Student. Mr. Acuna works on and operates the experiment at GT.
Shivam Patel (GT): Graduate Student. Mr. Patel works on and operates the experiment at GT.
Parth Patki (GT): Graduate Student. Mr. Patki works on the hydrodynamics modeling subtask (pre-combustion disturbances).
Tony John (GT): Graduate Student. Mr. John works on the entropy modeling subtask (post-combustion disturbances).
Jeffrey Mendoza (RTRC): Co-Principal Investigator. Dr. Mendoza is the leader of the RTRC team and oversees their contributions to the project. He leads the subtasks related to modeling, measurements, and simulation for post-combustion disturbances, nozzle interactions, turbine interactions, and far-field sound propagation.
Lance Smith (RTRC): Co-Principal Investigator responsible for the design and measurements of the RTRC experiment. He works closely with the GT team to ensure similarities between both experiment setups.
Duane McCormick (RTRC): Co-Principal Investigator responsible for the design and measurements of the RTRC experiment as well as finite element calculations in the design process.
Jordan Snyder (RTRC): -responsible for the design, measurements, and data processing using tunable diode laser absorption spectroscopy (TDLAS) and chemiluminescence in the RTRC combustor rig.
Julian Winkler (RTRC): Co-Principal Investigator responsible for the simulation tasks at RTRC and focuses on the post-combustion disturbances, nozzle interactions, turbine interactions, and far-field sound propagation.
Kenji Homma (RTRC) is responsible for the far-field sound propagation simulations.
Aaron Reimann (RTRC) is responsible for ROM and high-fidelity modeling of the propagation of direct and indirect noise sources through the turbine nozzle and supports the far-field sound propagation simulations.

Sudarshan Koushik (RTRC) is responsible for post-processing the GT LES simulation data to model post-combustion disturbances.

Project Overview

The objective of this project is to develop and validate physics-based design tools that can predict noise production mechanisms and their relative significance and ultimately reduce the noise output from future engines. The motivation for this project stems from recent and future advances in aircraft engine technology. High-bypass engine technology has significantly reduced the traditionally dominant engine noise sources: namely, fan and jet exhaust noise. Noise generated in the combustor has become a dominant source of engine noise for future advanced aircraft designs. In addition, as combustors evolve to increase efficiency and reduce pollutant emissions, methods for predicting and mitigating combustion noise have severely lagged, with legacy methods being insufficient to predict noise from next-generation combustors. This drawback has motivated the objective of this project, which addresses the critical need for physics-based design tools. The resultant understanding of noise generation and propagation, along with validated noise prediction tools, will enable more rapid and cost-effective designs of low-noise engines for future aircraft.

The project objectives will be achieved through a program of cooperative experiments, high-fidelity simulations, and physics-based reduced order modeling (ROM). The physical processes involved are tightly coupled and directly determine the project tasks, as shown in Figure 1.

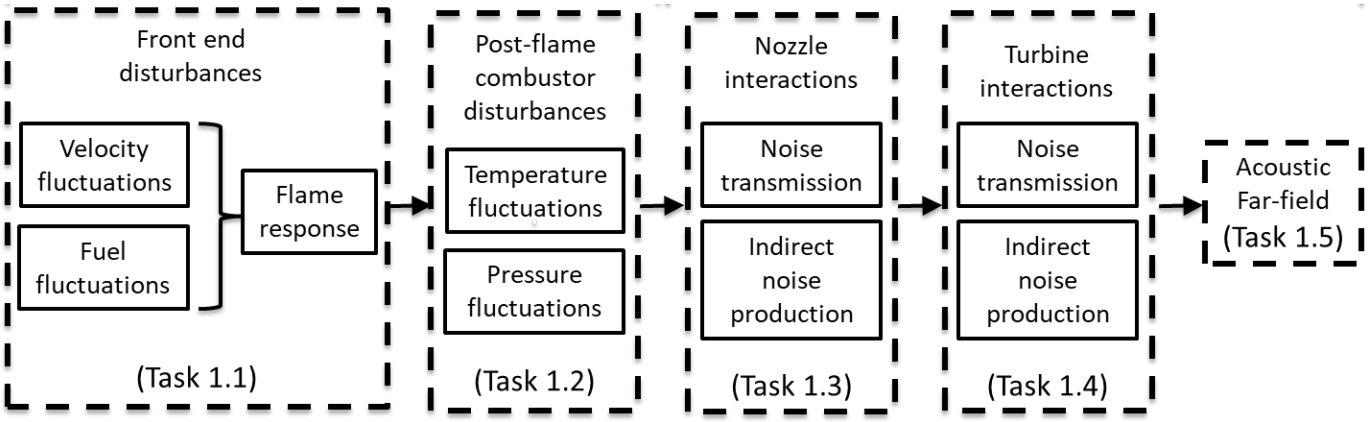

Figure 1. Physical processes and project tasks for noise generation.

The physics of noise generation begins with source disturbances upstream of the combustion zone, which involve unsteady dynamics in the flow and incoming fuel (spray), followed by the response of the combustion zone (flame) to these upstream disturbances. The fluctuations in the unsteady heat release lead to the generation of pressure fluctuations and entropy fluctuations. These fluctuations propagate further downstream in the combustor and interact with the nozzle and turbine and eventually lead to far-field sound generation. With the complex interplay of unsteady physics in the different parts of the engine, it is challenging to develop a ROMs.

An important goal of this project is to generate high-quality reference data from both measurements and validated high-fidelity simulations, including measurements of the flow, spray, and flame unsteadiness in the head end of the combustor. Subsequently, the secondary combustion zone is characterized. The generation of entropy and pressure disturbances is then characterized through measurements of temperature and pressure fluctuations, followed by measurements of noise reflection and transmission through the turbine and nozzle section and sound measurements in the far-field. The measurements are accompanied by large eddy simulations (LES) and finite element simulations that are validated against the measurements. Collectively, these data are generated across a range of operating parameters and provide a source database for the modeling task.

The main goal of this project is to develop a robust design tool that can predict noise at operating points for which prior measurements/data are unavailable. To achieve this goal, two major tasks are needed. First, ROM and frameworks must be developed for different aspects of the engine architecture: flow/spray models, flame response models, entropy generation

models, entropy propagation models, nozzle interaction models, turbine interaction models, and far-field noise generation models. The ROM for each of these aspects involves simplifications and assumptions that are validated against the source database. The validation study and iterative improvement of model predictions serve as the second task to achieve this goal.

In this report, we summarize the efforts of both teams from October 2020 to September 2021. The efforts primarily include development, fabrication, and measurement campaigns conducted at the GT and RTRC facilities. In addition, frameworks for ROM and simulations have been advanced based on earlier learnings in the beginning of the project. A workflow has been established to transfer simulation data to ROM tasks, and different subtask benchmarking targets have been identified.

Task 1 – Facility Development at GT

Georgia Institute of Technology

Objective(s)

The objective of this task was to shakedown and take initial measurements with the RQL combustor designed in the previous year. The first portion of this year was dedicated to the manufacturing and assembly of new components. Once installed in the GT facility, diagnostic tools were installed to measure the flow, flame, and pressure dynamics in the RQL combustor. A test-matrix was developed and used to allow for comparison and validation of the GT and RTRC data, as well as for GT to investigate operating regimes by varying combustion parameters to study the dynamics of noise production across a range of aircraft-relevant conditions.

Research Approach

The goal of this task at GT was to leverage an existing combustor test rig facility developed in partnership with Pratt & Whitney (P&W). In this task, the facility was modified to utilize the existing plumbing, instrumentation, data acquisition systems, pressure vessel, and structural steel. With these modifications, the new experiment setup resulted in (a) a generalized hardware whose measurements can be shared in the public domain, (b) optical access and instrumentation access to measure flow, spray, flame, pressure, and temperature dynamics, and (c) a replication of the general physics and operational characteristics of a modern RQL combustor. These modifications resulted in a new liner, fuel/air injection system, and exhaust system.

These new components were manufactured and assembled during this period to allow for initial shakedown tests of the new systems and of the diagnostic components. Non-scientific images from the first fire are shown in Figure 2. These tests help the GT experiment team to baseline the rig and determine the possible operation and data collection regimes.

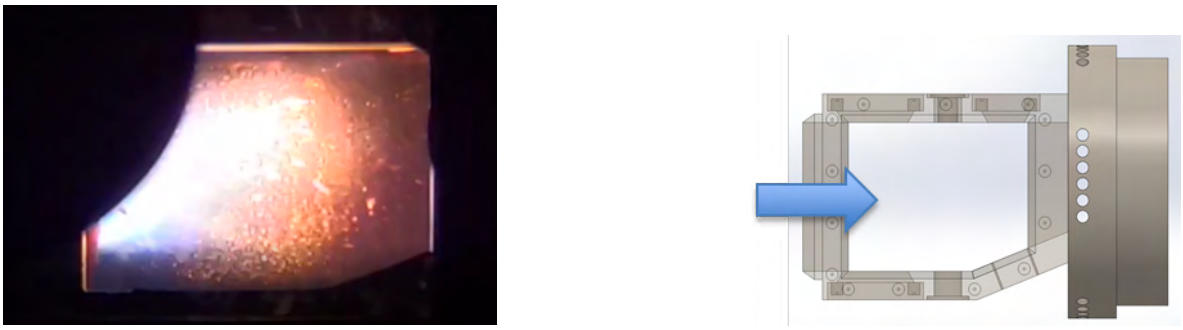

Figure 2. Images from the first fire of the GT experiment.

A test matrix was created to span various operating regimes and to allow for a detailed investigation of how various engine parameters affect flow and flame dynamics and ultimately noise production. The portions of the test matrix that were completed during the initial shakedown testing are listed in Table 1. The “Z0” and RX-X” test points allowed for direct comparison with one of the RTRC test points. Other sets of studies, such as the “BX” and “EX” series, aimed to determine how the combustion noise changed when the engine operated under low- or high-power conditions, namely via changes in the combustion air and fuel flow rates from a lean-burn configuration to an RQL regime. The remaining points in the test matrix will be captured during the next period of experimentation.

Table 1. Completed test matrix.

Date	Test	P4 [psia]	T3 [K]	Swirler ER	Global ER	Quench/Main Air Split
8/10/21	B2	68	479	1.18	0.52	1.33
8/10/21	E2	63	504	0.71	0.3	1.42
8/10/21	B1	78	524	0.91	0.39	1.37
8/10/21	E1	77	534	0.83	0.35	1.39
8/11/21	R3-3	54	648	0.91	0.41	1.24
8/11/21	R3-2	73	663	0.93	0.41	1.33
8/11/21	R3-1	89	668	0.85	0.37	1.33
8/11/21	R2-3	103	673	0.77	0.35	1.23
8/27/21	Z0	105	677	0.86	0.37	1.36

Under these conditions, high-speed chemiluminescence and pressure data were recorded to capture flame dynamics and combustor noise. For these shakedown data, we attempted to acquire PIV measurements of the flow field; however, due to facility and design constraints, the collection of high-quality PIV data was postponed to the next round of experimentation. This next attempt will also capture high-speed temperature measurements of the post-flame region to provide more information for the model validation tasks. Some of the chemiluminescence and acoustic data are shown below. Figure 3a presents a frame of chemiluminescence data showing the flame position, with blue arrows indicating areas in which air is injected. Figures 3b and 3c show normalized mean and root-mean-square heat release fields computed from 1200 frames of chemiluminescence data from the E2 condition in the test matrix.

Figure 3. Chemiluminescence images: a) an instantaneous image, b) mean chemiluminescence, and c) root-mean-square chemiluminescence.

In the combustion chamber, acoustic data are collected in three locations, with two redundant acoustic ports at the ramp upstream and downstream locations, as shown in Figure 4. These data are acquired to capture the acoustic instability of interest in this study. These locations also match the RTRC positions and are useful as a comparison point between the two rigs. All acoustics sensors were calibrated using the same ITP correction approach employed at RTRC (shown in Figure 5) to ensure that calibration errors do not affect the results.

RTRC and GT were able to obtain good agreement for the Z0 test conditions at the ramp upstream location (Figure 6, middle). The GT rig is inherently less tonal than the RTRC rig. The other two locations did not match well in amplitude, and recent investigation indicates that sensor degradation is likely an issue. Subsequent tests will have new and/or recalibrated acoustic sensors.

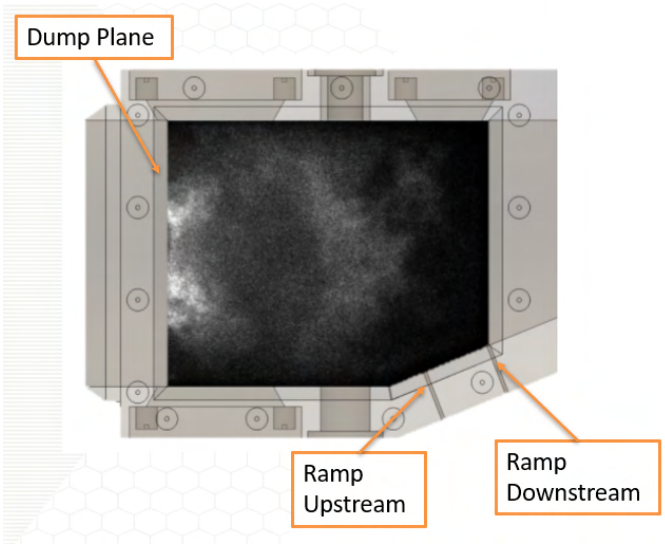

Figure 4. Acoustic sensor locations.

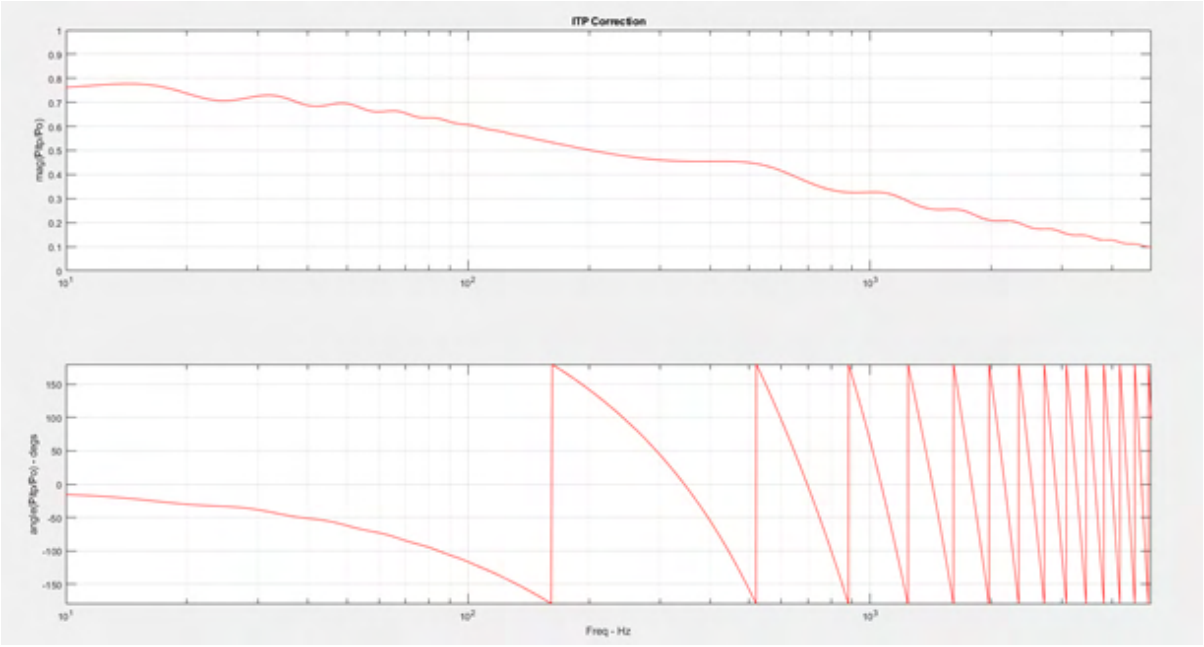

Figure 5. Example ITP calibration for acoustic sensors.

The finalized liner design is shown in Figure 7a. The liner consists of four windows: one on the top, one on the bottom, and two on the top on either side of the quench hole section. Collectively, these optical access windows allow for highly detailed measurements of the flow, spray, and flame heat release. There are also three quench holes in the top and two quench holes in the bottom. The quench holes have a “stepped” design, as shown in Figure 7b. The flow into the quench hole comes in the transverse direction, as shown in Figure 8a. The stepped design takes advantage of the recirculation flow, as shown in Figure 8b. This design creates a “turbulator” effect that induces components to the flow other than just the transverse component. This design also closely represents the engine design and the rig designed and used by RTRC.

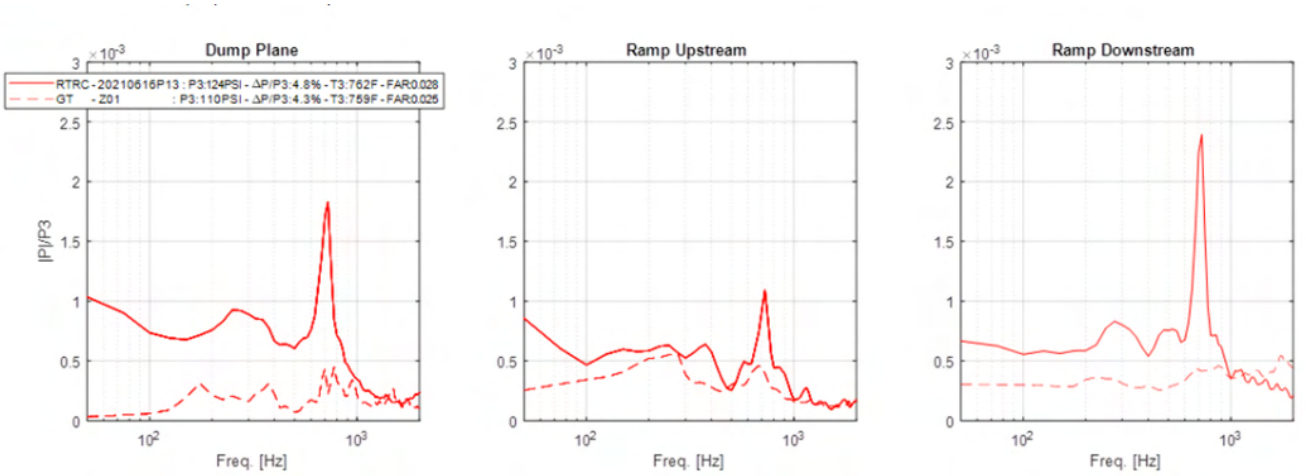

Figure 6. Comparison of GT and RTRC acoustic data.

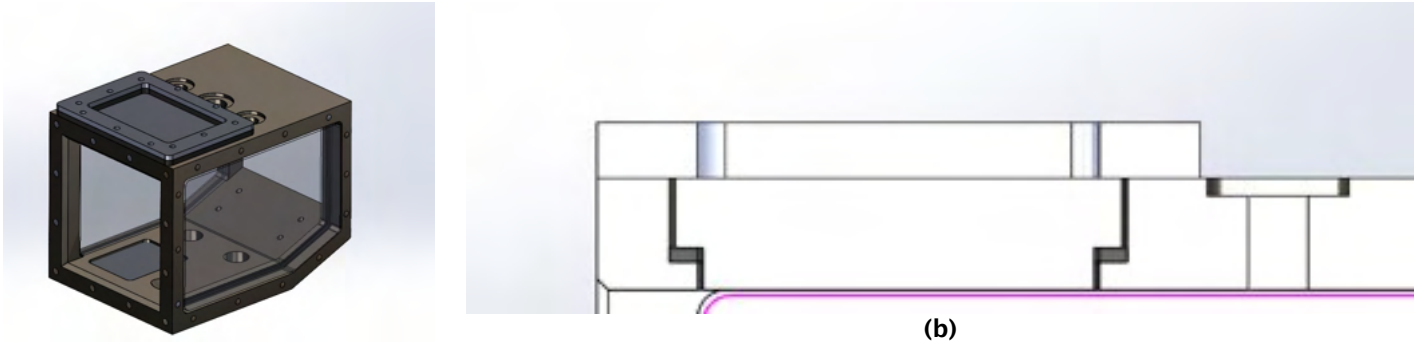

(a) (b)

Figure 7. Combustor section: (a) liner with windows and frames and (b) "stepped" quench hole design.

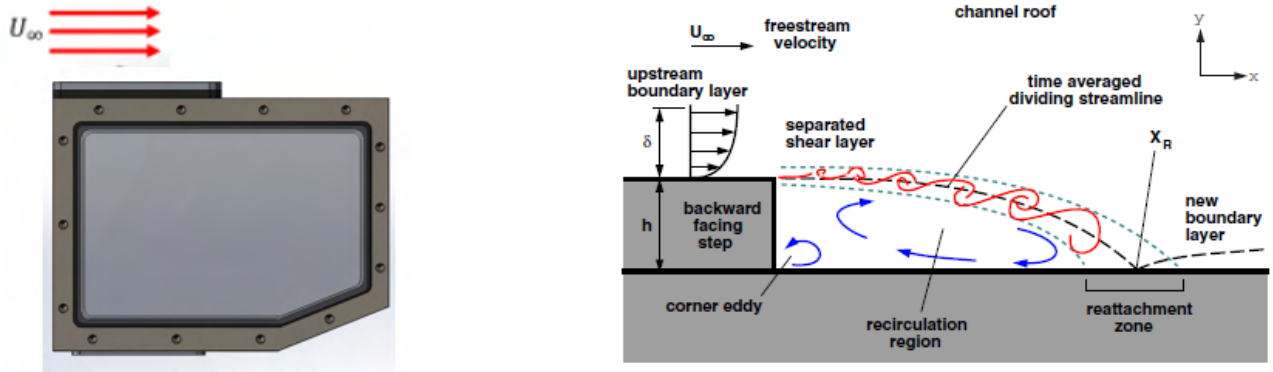

(a) (b)

Figure 8. Physics of the "stepped" quench hole design: (a) transverse flow over the liner coming to the quench and (b) flow physics at a backward-facing step.

The post-combustion zone architecture of the combustor is designed to closely resemble that of a real engine. As shown in Figure 9a, the real engine architecture involves a post-combustion converging section that leads to a blade/vane array in the

turbine section. This aspect is replicated in the GT design. The repeating array of turbine blades is replicated through a jail-bar-type design. These designs for the GT rig are shown in Figures 9b and 9c.

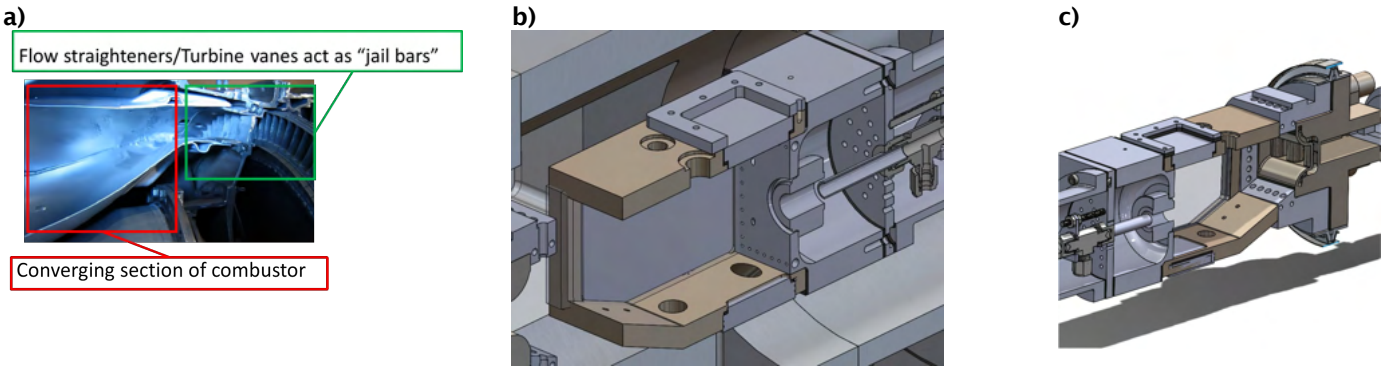

Figure 9. (a) Cross-section from a real engine showing the converging section and array of turbine vanes, (b) cross-section from the GT design showing the converging section followed by (c) "jail bars" to mimic turbine vanes.

Finally, an important diagnostic feature of this rig is the measurement of post-combustion disturbances such as temperature and pressure fluctuations. Multiple pressure taps have been installed, and the available pressure probes can be mounted at any of the taps and varied across different experiment runs. For temperature fluctuations, the Tunable Diode Laser Adsorption Spectroscopy (TDLAS) method is used. For this purpose, a TDLAS ring geometry is installed in the convergent section between the combustion zone and the jail-bar exhaust, as shown in Figure 10a. In this ring, multiple lasers and absorption probes will be installed (see Figure 10b). Collectively, these measurement probes and lasers will allow for a detailed measurement of the temperature field, which can then be used to understand the entropy fluctuations that are a source of indirect noise.

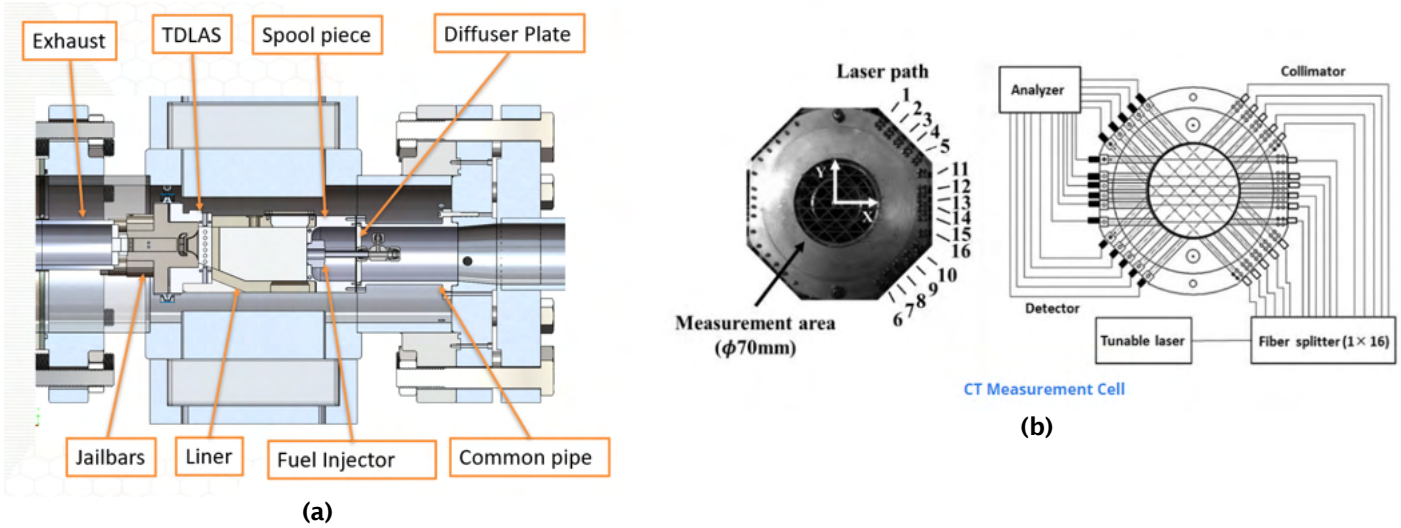

Figure 10. (a) Magnified view showing the combustion liner, TDLAS, and jail-bar exhaust system in the GT rig and (b) TDLAS probe array in the ring.

Milestone(s)

- The GT experiment shakedown has been completed.
- Preliminary data analysis has started, and workflows developed for future detailed data campaigns.
- GT has started facility improvements based on lessons learned from the shakedown.

Major Accomplishments

The designed RQL combustor was manufactured and installed at the GT facility. Preliminary data were collected to allow for comparison to and validation against the RTRC experiment. Given the initial data and lessons learned from the initial shakedown, facility and experimental improvements have been designed, and manufacturing has begun to allow for more detailed measurements of flame, flow, pressure, and temperature dynamics. These efforts will allow GT to obtain detailed and reliable measurements across a range of operating regimes and will provide a trove of validation data for the reduced order models that are being developed in other tasks.

Publications

None

Outreach Efforts

None

Awards

None

Student Involvement

- Amalique Acuna, a graduate student, has taken the lead in the design of the GT experiment.
- Shivam Patel, a graduate student, has taken the lead in the operation and data collection for the GT experiment.

Plans for Next Period

In the second year of this project, the improved GT rig design will be machined and installed in the pressure vessel, as shown in Figure 11. The first step is to shakedown the experiment, followed by initial measurements which include flow, spray, flame, pressure, and temperature dynamics. The initial array of operating conditions and corresponding measurements will serve as validation data for high-fidelity simulations. In addition, measurements from the GT experiment campaign will be compared against those from the RTRC experiment campaign under similar operating conditions. The outcome of future experiments will focus on laser diagnostics and TDLAS measurements.

GT will also upgrade its rig stand and plumbing supporting the FAA campaign. The upgraded stand and lines are optimized for minimum line lengths and footprints to minimize maintenance and preheat times. Overall, this step will improve the quality of life of the experiment, enabling troubleshooting and experiment campaigns to operate more quickly and allowing more time for data collection.

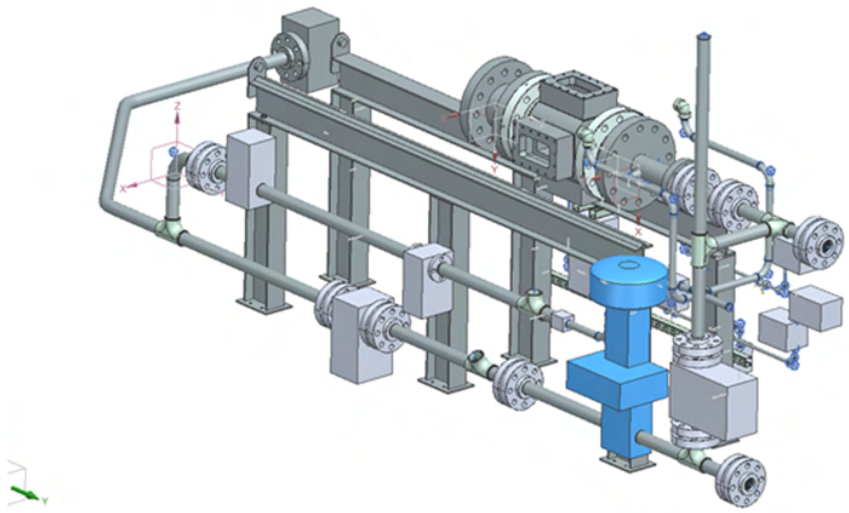

Figure 11. Experiment assembly at the GT combustion lab.

Task 2 – Simulations of the GT Experiment

Georgia Institute of Technology

Objective

The objective for the second year of this task is to update the geometry and flow conditions for the continued LES studies, including adding the swirler to the computational domain and revising the boundary conditions with respect to the experimental conditions. In addition, a key objective is to simulate both cold and reacting flow conditions using LES capabilities in the GT compressible solver (LESLIE) and to transfer the output data to RTRC.

Research Approach

Our previous effort focused on the LES of cold flow, using a reduced geometry without a swirler. To capture the physics of the shear flow and a swirl-stabilized spray flame, a swirler is included in the CAD geometry, as shown in Figure 12. The multi-block structured grid has 6.8 million cells and 4571 blocks, and grid clustering is applied to the near region of the shear flow from the swirler and the jail bars. All inlet boundary conditions are now updated to the constant mass flow inlets based on experimental data inputs, and the mass flow rate for the main inflow is set as 0.093 kg/s (based on GT rig inputs). The total mass flow rates at the top or bottom dilution holes are both 0.117 kg/s. The incoming air is at 8 atm and 673.3 K. The flow through the jail bar chokes and pressurizes the combustor to the nominal target. With choking, the outflow is supersonic at the domain outlet. As a key difference between the current LES and the GT experiment, in the latter setup, additional air flow to cool the windows is included, but the exact amount is unclear at present and is, therefore, ignored.

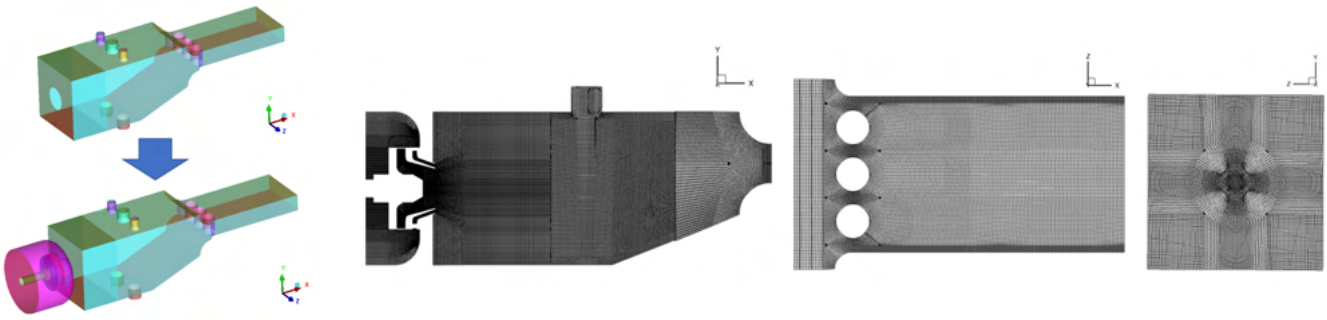

Figure 12. Revised computational domain with a swirler for LES. Left: Addition of a swirler to the CAD model. Right: Schematics for the new multi-block structured grid (main combustor at the centered xy plane, region behind the jail bars at the centered xz plane, and shear layer region at the yz plane located at one third of the axial length of the main combustor).

The reacting flow uses kerosene fuel and two-step finite-rate reactions with six species (based on past LDI studies; Patel and Menon, Combustion and Flame, 2008). LES closure is accomplished with the well-established partially stirred reactor (PaSR) subgrid combustion model (also used in earlier studies; Panchal and Menon, Combustion and Flame, 2021- submitted). The fuel mass flow rate is 0.0048 kg/s, and the equivalence ratio is 0.622. The initial droplet distribution is log normal, the SMD is 36 μm, and no droplet breakup is considered. The constant coefficient one-equation KSGS model is used for subgrid stress modeling, closure in the PaSR, and for the stochastic dispersion in the particle phase.

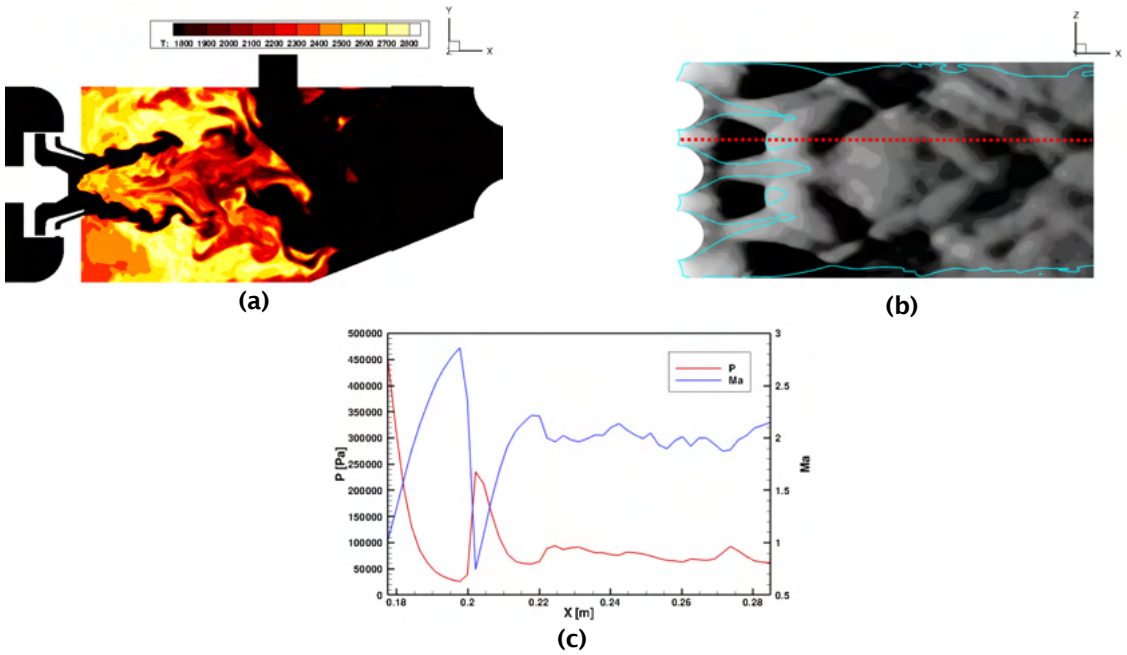

Figure 13. (a) Snapshot of the temperature in the centered xy plane, (b) pressure in the central xy plane beyond the jail bars, and (c) a one-dimensional profile of pressure and Mach number along the dotted red line behind the jail bars.

Figure 13a shows the instantaneous contour of temperature at the central (z=0) xy plane in the main combustor. A statistically stationary swirl spray flame is anchored downstream of the swirler exit, and turbulent mixing and combustion occur very close to the dump plane and is mostly completed by the dilution jet. The flow is choked at the jail bars and becomes supersonic past the bars, as shown in Figure 13b. The cyan lines in Figure 13b indicate a Mach number isoline equal to unity. Beyond the bars, oblique shocks and rarefaction waves are observed. The one-dimensional (1D) profile of pressure and Mach number along the red dotted line in Figure 13c shows the existence of a shock at approximately x=0.2m, which is the end of the Mach cone. Beyond the bars, the pressure is below 5 atm, and the exit pressure is less than 1 atm. However, the pressure in the combustor is nominally maintained at the target pressure of approximately 8 atm.

Milestone

LESs of reacting flow with a new grid that includes the GT rig swirler were completed under target conditions, and analyses of combustion noise are underway.

Major Accomplishments

The new grid has been established, the reacting spray flame has been stabilized at the proper location, and a statistical steady state at high pressure has been established. Data from LES showing the temporal evolution have been provided to the RTRC and GT modeling groups.

Publications

None

Outreach Efforts

None

Awards

None

Student Involvement

Sangjae Kim, a PhD student, is now working full-time on this project.

Plans for Next Period

In the next period, further simulations and comparisons with data from the GT rig will be conducted. Additionally, postprocessing tools, which are currently being tested, will be used to study both direct and indirect noise sources. Most of the data acquisition and analysis process conducted in the GT experiments will be reproduced in the LES, and direct comparisons will be performed. Additionally, the data will be provided to RTRC and GT to allow those teams to process and evaluate the assumptions used in their ROM approach. The correlations of direct and indirect noises with respect to the heat release rate and other contributing factors will also be analyzed to elucidate the physics of the combustion noise and to provide inputs to and assessment of the ROM.

Task 3 – Reduced-order Modeling

Georgia Institute of Technology

Objectives

The overarching objective of this task is to create quick-action, reduced order models to accurately predict different aspects of noise generation mechanisms that then collectively feed into a design tool for noise prediction. The specific objective of the GT reduced order modeling task focuses on the head-end physics in the architecture, namely the flow and spray dynamics, flame dynamics, and generation of entropy disturbances by the flame. The spray/flow dynamics feed into the flame dynamics, which cause direct combustion noise. The flame dynamics also result in entropy disturbances, which then lead to indirect combustion noise at the nozzle. The flame response modeling and the model for the generation of entropy disturbances are provided as inputs to the post-combustion models that will be developed by RTRC. Depending on the prediction results obtained from the RTRC models, these "head-end" models will be iteratively refined.

Research Approach

In this reporting period, we focused on reduced order modeling tasks that applied the flame response framework to an example configuration. In addition, we further studied the contributions of different chemical source terms to entropy generation at the flame and studied the generation of entropy disturbances at the flame using heat release models.

Flame Response Modeling

In the prior reporting period, we presented the new flame response framework for a spray flame that connects the spray phase to the gaseous phase and identified the different model input parameters for the spray combustion problem. In this reporting period, we applied perturbation expansion theory to this framework to understand the effect of input disturbances on disturbances in the flame response. The configuration used for this framework is shown in Figure 14, with fuel droplets injected in a center duct and air injected in the outer ducts. The fuel flows in the inner duct with $0 < r < R_F$, and the air/oxidizer flows in the outer ducts with $R_F < r < R$. The fuel exits the duct and enters the combustion zone as a mix of fuel gas and a spray of liquid fuel droplets, which, after evaporation and diffusive mixing, result in the spray diffusion flame being modeled.

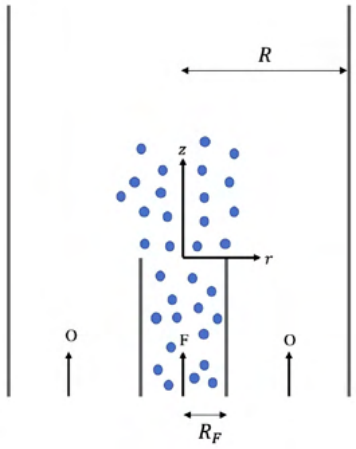

Figure 14. Schematic of the ducted spray flame configuration. Fuel droplets are injected in the center duct (shown in blue), and oxidizer gas is injected in the outer ducts.

The gaseous (Z) and droplet mixture (Z_d) fractions are one-way coupled through vaporization of the droplet, which generates fuel gas. In non-dimensional form, the governing equations become:

$$\frac{\partial Z_d}{\partial t}+u_z\frac{\partial Z_d}{\partial z}+u_r\frac{\partial Z_d}{\partial r}=\frac{1}{Pe_d}\left(\frac{\partial^2 Z_d}{\partial z^2}+\frac{\partial^2 Z_d}{\partial r^2}\right)-\Gamma_V Z_d \tag{1}$$

$$\frac{\partial Z}{\partial t}+u_z\frac{\partial Z}{\partial z}+u_r\frac{\partial Z}{\partial r}=\frac{1}{Pe_g}\left(\frac{\partial^2 Z}{\partial z^2}+\frac{\partial^2 Z}{\partial r^2}\right)+\Gamma_V Z_d \tag{2}$$

Here,

$$\begin{aligned} Pe_d &= u_0 R/\mathscr{D}_d \\ Pe_g &= u_0 R/\mathscr{D}_g \\ \Gamma_V &= \mathscr{C}_V R/u_0 \end{aligned} \tag{3}$$

The Peclet numbers for the gas (Pe_g) and droplet phase (Pe_d) denote competing effects between the diffusive time-scales and convective time-scales, and Γ_V denotes competing effects between the convective and vaporization time-scales. The boundary conditions at the inlet are given by:

$$\begin{aligned} 0\le r\le\zeta &\rightarrow \begin{cases} Z_d(r,z=0,t)=\sigma_d \\ Z(r,z=0,t)=1-\sigma_d \end{cases} \\ \zeta<r\le 1 &\rightarrow \begin{cases} Z_d(r,z=0,t)=0 \\ Z(r,z=0,t)=-\sigma_O \end{cases} \end{aligned} \tag{4}$$

Here, $\zeta=R_F/R$, and σ_d is the droplet loading, indicating that fuel droplets are injected only in the center port along with fuel gas. When $\sigma_d=0$, the fuel is injected only as a gas, and when $\sigma_d=1$, the fuel is injected only as droplets, which need to evaporate to fuel gas before combustion. The outer port consists of pure oxidizer, and thus, σ_O indicates the oxidizer mixture fraction (oxidizer mass fraction normalized by the total mass fraction of the fuel). The boundary conditions at the wall (no diffusion, penetration) imply:

$$\begin{aligned} \frac{\partial Z_d}{\partial r}(r=1,z,t)&=0 \\ \frac{\partial Z}{\partial r}(r=1,z,t)&=0 \end{aligned} \tag{5}$$

Next, consider the first order decomposition of the velocity/mixture fractions around the non-dimensional velocity amplitude parameter (ε):

$$f(r,z,t) = f_0(r,z) + \varepsilon f_1(r,z,t) \qquad f \in \left(u_r, u_z, Z, Z_d\right) \tag{6}$$

By substituting in the earlier governing equations, we obtain steady-state mixture fractions governed by:

$$u_{z,0}\frac{\partial Z_{d,0}}{\partial z} + u_{r,0}\frac{\partial Z_{d,0}}{\partial r} - \frac{1}{Pe_d}\left(\frac{\partial^2 Z_{d,0}}{\partial z^2} + \frac{\partial^2 Z_{d,0}}{\partial r^2}\right) + \Gamma_V Z_{d,0} = 0 \tag{7}$$

$$u_{z,0}\frac{\partial Z_0}{\partial z} + u_{r,0}\frac{\partial Z_0}{\partial r} - \frac{1}{Pe_g}\left(\frac{\partial^2 Z_0}{\partial z^2} + \frac{\partial^2 Z_0}{\partial r^2}\right) - \Gamma_V Z_{d,0} = 0 \tag{8}$$

The fluctuations in the mixture fractions are then governed by:

$$\frac{\partial Z_{d,1}}{\partial t} + u_{z,0}\frac{\partial Z_{d,1}}{\partial z} + u_{r,0}\frac{\partial Z_{d,1}}{\partial r} - \frac{1}{Pe_d}\left(\frac{\partial^2 Z_{d,1}}{\partial z^2} + \frac{\partial^2 Z_{d,1}}{\partial r^2}\right) + \Gamma_V Z_{d,1} = -\left(u_{z,1}\frac{\partial Z_{d,0}}{\partial z} + u_{r,1}\frac{\partial Z_{d,0}}{\partial r}\right) \tag{9}$$

$$\frac{\partial Z_1}{\partial t} + u_{z,0}\frac{\partial Z_1}{\partial z} + u_{r,0}\frac{\partial Z_1}{\partial r} - \frac{1}{Pe_g}\left(\frac{\partial^2 Z_1}{\partial z^2} + \frac{\partial^2 Z_1}{\partial r^2}\right) - \Gamma_V Z_{d,1} = -\left(u_{z,1}\frac{\partial Z_0}{\partial z} + u_{r,1}\frac{\partial Z_0}{\partial r}\right) \tag{10}$$

The boundary conditions can also be decomposed, resulting in:

$$\begin{aligned} 0 \le r \le \zeta \rightarrow & \begin{cases} Z_{d,0}(r, z=0, t) = \sigma_d & Z_{d,1}(r, z=0, t) = 0 \\ Z_0(r, z=0, t) = 1 - \sigma_d & Z_1(r, z=0, t) = 0 \end{cases} \\ \zeta < r \le 1 \rightarrow & \begin{cases} Z_d(r, z=0, t) = 0 & Z_{d,1}(r, z=0, t) = 0 \\ Z(r, z=0, t) = -\sigma_O & Z_1(r, z=0, t) = 0 \end{cases} \end{aligned} \tag{11}$$

$$\begin{aligned} \frac{\partial Z_{d,0}}{\partial r}(r=1, z, t) = 0 \qquad & \frac{\partial Z_{d,1}}{\partial r}(r=1, z, t) = 0 \\ \frac{\partial Z_0}{\partial r}(r=1, z, t) = 0 \qquad & \frac{\partial Z_1}{\partial r}(r=1, z, t) = 0 \end{aligned} \tag{12}$$

The above system is solved for both the droplet and gaseous mixture fractions. For the purpose of illustration, we consider an axial-only mean flow field as follows:

$$\begin{aligned} u_{z,0} &= 1 \\ u_{r,0} &= 0 \end{aligned} \tag{13}$$

Assuming that transverse diffusion dominates axial diffusion and that the main axial transport mechanism is the mean flow convection, we have $Pe_g, Pe_d \gg 1$. The analytical solutions for the mean mixture fractions are:

$$Z_{d,0}(r,z) = 2\sigma_d e^{-\Gamma_V z}\zeta\left(\frac{1}{2} + \sum_{n=1}^{\infty}\frac{\sin(n\pi\zeta)}{n\pi\zeta}\cos(n\pi r)e^{-\alpha_{n,d}z}\right) \tag{14}$$

$$Z_0(r,z) = -\sigma_O(1-\zeta) + \zeta\left(1 - \sigma_d e^{-\Gamma_V z}\right) + \sum_{n=1}^{\infty} 2\zeta\frac{\sin(n\pi\zeta)}{n\pi\zeta}\left[(1 - \sigma_d + \sigma_O) + \frac{\sigma_d\Gamma_V}{\beta_n}\left(e^{\beta_n z} - 1\right)\right]\cos(n\pi r)e^{-\alpha_{n,g}z} \tag{15}$$

Here, $\alpha_{n,g}Pe_g = \alpha_{n,d}Pe_d = n^2\pi^2$ and $\beta_n = \alpha_{n,g} - \alpha_{n,d} - \Gamma_V$.

To understand the effect of the spray on the mean mixture fraction field, we focus on two main parameters for the spray: the droplet loading σ_d and vaporization Damkohler number Γ_V. Figure 15 shows the effect of the droplet loading (left) and the vaporization Damkohler number (right) on the location of the stoichiometric mixture fraction. First, consider the effect of the droplet loading, as shown on the left. For the case of $\sigma_d = 0$, we have no spray, and this corresponds to the pure gaseous diffusion flame, denoted by the black curve. Note that as the droplet loading is increased, the contour locations move to locations in which the flame becomes taller. This increase in flame height can be attributed to the delay in formation of gaseous fuel due to vaporization of the droplets. In addition, note the unique flame shapes that occur at $\sigma_d = 0.8, 1.0$, where the flame near the inlet curves inward toward the centerline. This can be attributed to the diffusion of the oxidizer into the radial locations above the fuel inlet region due to the delayed generation of the fuel gases resulting from vaporization. Next, consider the effect of vaporization Damkohler number Γ_V, as shown on the right. As $\Gamma_V \rightarrow \infty$, the solution tends to the pure gaseous diffusion flame case, as shown by the dashed black curve (denoted as NP) coinciding with the

largest Γ_V case shown. For $\Gamma_V > 10$, the solution is insensitive to this parameter; however, the mean flame height varies greatly in the $\Gamma_V < 10$ region.

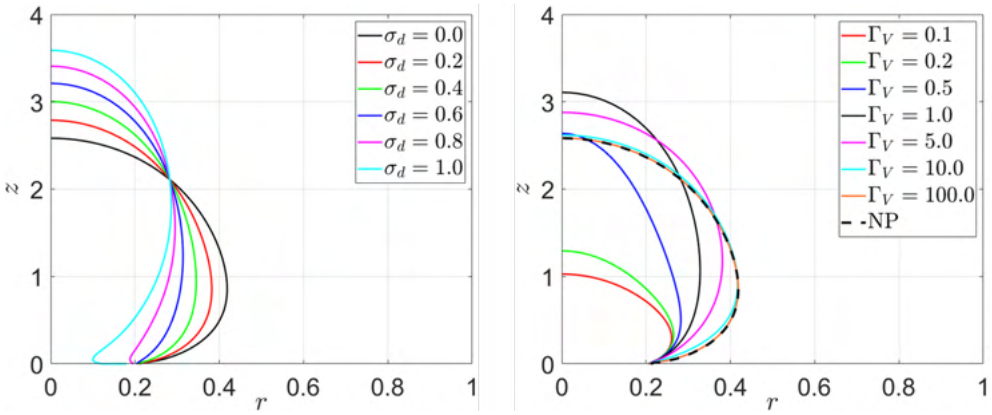

Figure 15. Variation in stoichiometric mixture fraction location due to changes in (left) droplet loading σ_d for fixed $\Gamma_V = 10$ and (right) vaporization Damkohler number Γ_V for fixed $\sigma_d = 0.5$. NP: pure gaseous non-premixed diffusion flame. Geometry fixed at $\zeta = 0.2$. Peclet numbers set to $Pe_g = 10, Pe_d = 100$.

Next, we consider the unsteady dynamics that occur when the system is subjected to spatially uniform harmonic velocity disturbances of the following form:

$$\begin{aligned} u_{z,1}(r,z,t) &= \cos(2\pi St t) \\ u_{r,1}(r,z,t) &= 0 \\ St &= \frac{f_0 R}{u_0} \end{aligned} \tag{16}$$

The unsteady mixture fraction solutions are then given by:

$$\hat{Z}_{d,1}(r,z) = \frac{i2\sigma_d\zeta}{2\pi St}\left(1-e^{i2\pi Stz}\right)\sum_{n=1}^{\infty}\left[\frac{\sin(n\pi\zeta)}{n\pi\zeta}\left(\Gamma_V+\alpha_{n,d}\right)e^{-(\Gamma_V+\alpha_{n,d})z}\cos(n\pi r)\right] \tag{17}$$

$$\hat{Z}_1(r,z) = \sum_{n=1}^{\infty}\left[\left(\frac{\kappa_a-\kappa_c}{\beta_n-i2\pi St}\right)\left(e^{\beta_n z}-e^{i2\pi Stz}\right)-\frac{\kappa_a}{\beta_n}\left(e^{\beta_n z}-1\right)e^{i2\pi Stz}-i\left(\frac{\kappa_b-\kappa_d}{2\pi St}\right)\left(1-e^{i2\pi Stz}\right)\right]\cos(n\pi r)e^{-\alpha_{n,g}z} \tag{18}$$

Here,

$$\begin{aligned} \kappa_a &= \frac{i2\Gamma_V\sigma_d\zeta\left(\Gamma_V+\alpha_{n,d}\right)}{2\pi St}\frac{\sin(n\pi\zeta)}{n\pi\zeta} \\ \kappa_b &= 2\zeta\alpha_{n,g}\left(1+\sigma_O-\sigma_d\right)\frac{\sin(n\pi\zeta)}{n\pi\zeta} \\ \kappa_c &= \frac{2\Gamma_V\sigma_d\zeta\left(\beta_n-\alpha_{n,g}\right)}{\beta_n}\frac{\sin(n\pi\zeta)}{n\pi\zeta} \\ \kappa_d &= \frac{2\Gamma_V\sigma_d\zeta\alpha_{n,g}}{\beta_n}\frac{\sin(n\pi\zeta)}{n\pi\zeta} \end{aligned} \tag{19}$$

The $\exp(i2\pi Stz)$ terms indicate that disturbances propagate axially at the mean flow velocity, similar to purely gaseous flames.

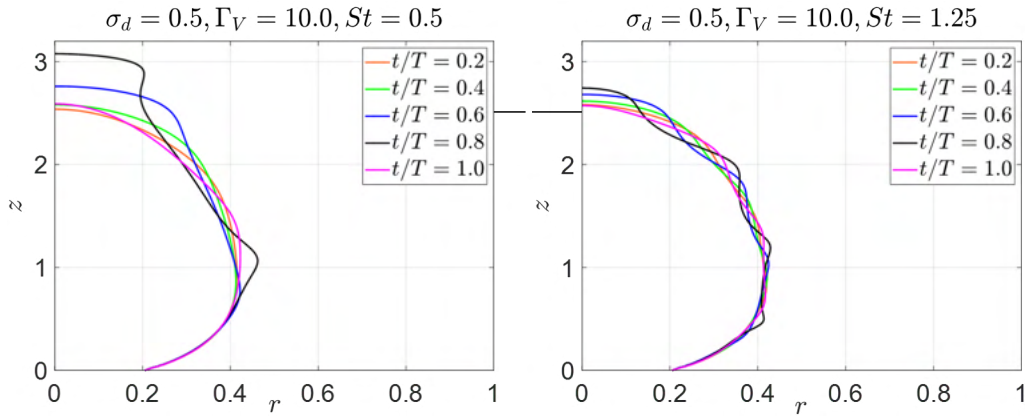

Figure 16. Spatial-temporal changes in flame shape due to bulk forcing for $\sigma_d = 0.5, \Gamma_V = 10.0$. Left: *St* = 0.5, Right: *St* = 1.25. NP: pure gaseous non-premixed diffusion flame. Geometry and Peclet numbers fixed as before.

Next, we consider the dynamics of the stoichiometric flame location due to the dynamics in the mixture fraction field. Figure 16 shows the temporal changes in the flame shape due to forcing at two different frequencies. For the lower *St* value, the flame shows a bulk-like axial pulsing with some spatial wrinkling, while the larger-*St* case shows a predominant spatial wrinkling nature. This is expected because the wavelength of wrinkling is inversely proportional to the *St* value. Additionally, the flame height oscillates with a larger amplitude for the lower-*St* case than for the higher-*St* case. This result can be better understood by considering the dynamics of the flame at the tip. By assuming that the flame length $L_f(t)$ can be decomposed into its mean and perturbation and by further decomposing the mixture fraction at the dynamic flame tip, we can express the perturbation in flame height as:

$$L_{f,1}(t) = -\frac{Z_1(r=0, z=L_{f,0}, t)}{\left.\frac{\partial Z_0}{\partial z}\right|_{(r=0, z=L_{f,0})}} \tag{20}$$

The fluctuations in flame height are directly proportional to fluctuations in the gaseous mixture fraction, which in turn vary as 1/*St*. Thus, as *St* increases, the fluctuations in flame height decrease. The instantaneous mixture fraction and instantaneous local flame position fluctuations will be used later in expressions for spatially integrated unsteady heat release rate fluctuations.

Generation of Entropy Disturbances

At the flame, where molecular transport processes are negligible compared with chemical reaction processes, the governing equation for the entropy dynamics is given by:

$$\rho T \frac{Ds}{Dt} = -\sum_{i=1}^{N} \tilde{\mu}_i \dot{w}_i \tag{21}$$

By expanding this chemical potential term further, we obtain:

$$S_e = -\sum_{i=1}^{N} \tilde{\mu}_i \dot{w}_i = \underbrace{-\sum_{i=1}^{N} h_{f,i}^0 \dot{w}_i}_{S_{e,1}} \underbrace{-\sum_{i=1}^{N} \dot{w}_i \int_{T_0}^{T} c_{p,i} dT}_{S_{e,2}} + \underbrace{\sum_{i=1}^{N} T s_i \dot{w}_i}_{S_{e,3}} \tag{22}$$

Here, $S_{e,1}$ or $\dot{q}$ is the chemical heat release term. Several prior research efforts on entropy dynamics during combustion have assumed, without evidence, that only the heat release term contributes to the generation of entropy disturbances at the flame and that the other terms are negligible. The first focus of this task was to investigate the relative contributions of the heat release term compared with the entire chemical source term, S_e. $S_{e,2}$ and $S_{e,3}$ can be expanded by assuming a constant specific heat and ideal gas relations to gain more insight:

$$S_{e,2} = p\left(\frac{\dot{n}}{n}\right)\left[\left(\frac{\gamma}{\gamma - 1}\right)\frac{T_0 - T}{T}\right] \tag{23}$$

$$S_{e,3} = S_{e,3a} + S_{e,3b} + S_{e,3c} = p \ln n \left(\frac{\dot{n}}{n} \right) + T \sum_{i=1}^{N} s_i^0 \dot{w}_i - R_u T \sum_{i=1}^{N} \frac{\dot{w}_i}{MW_i} \ln n_i \tag{24}$$

To test the dominance of the heat release rate over the remaining terms, a 1D Cantera simulation was conducted for various hydrocarbon fuel combustion scenarios. The following ratios can be computed to reflect the behavior of the terms:

$$\alpha = \frac{\int S_{e,1} dx}{\int S_e dx}, \beta = \frac{\int S_{e,2} dx}{\int S_e dx}, \kappa = \frac{\int S_{e,3} dx}{\int S_e dx} \tag{25}$$

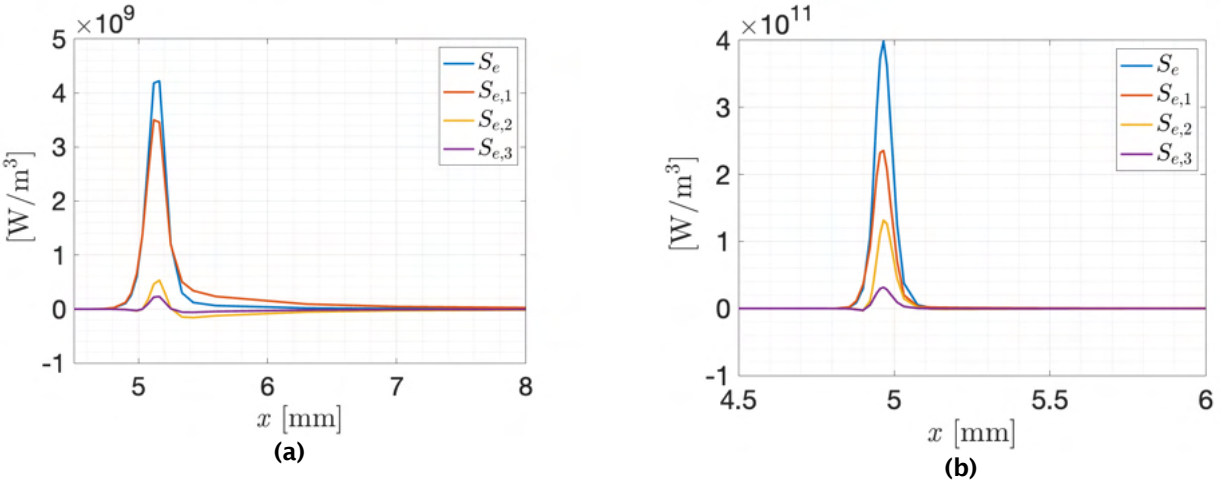

Figure 17. $S_{e,1}$, $S_{e,2}$, and $S_{e,3}$ for (a) methane–air and (b) methane–oxygen combustion at $T_u = 500$ K, $\phi = 0.75$, and $p = 1$ atm.

Figure 17 shows flame profiles of the three terms for premixed methane–air and methane–oxygen flames at $T_u = 500$ K, $\phi = 0.75$, and $p = 1$ atm. Figure 17a clearly shows that $S_{e,1}$ is dominant for methane–air combustion, in which case the entropy production terms can be equated with the heat release rate. Figure 17b displays results for oxygen, showing that although $S_{e,2}$ and $S_{e,3}$ are smaller than $S_{e,1}$, they are not negligible. Figure 18 displays the results for the same conditions used in Figure 17, but with a spatial integration. This figure shows that $S_{e,1}$ is the largest contributor and is dominant for air-fueled systems, whereas for oxygen–fuel combustion, $S_{e,2}$ and $S_{e,3}$ provide a contribution of approximately 35%.

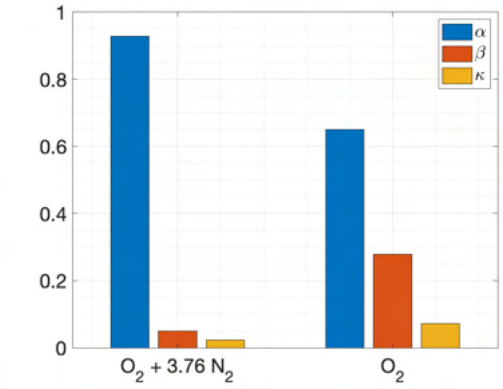

Figure 18. α, β, and κ for methane–air and methane–oxygen combustion at $T_u = 500$ K, $\phi = 0.75$, and $p = 1$ atm.

Similar analyses were conducted for a variety of hydrocarbon n-alkane fuels and jet fuels. Ratios are displayed in Figure 19 for four hydrocarbon fuels. It must be noted that dissociation has a significant influence on $S_{e,3}$ and $S_{e,2}$ due to molar

production. The bar $\kappa - \kappa_{\text{major}}$ measures the effect of dissociation. In a similar analysis for common jet fuel, the results were comparable to those of n-dodecane for combustion in air, as shown in Figure 20.

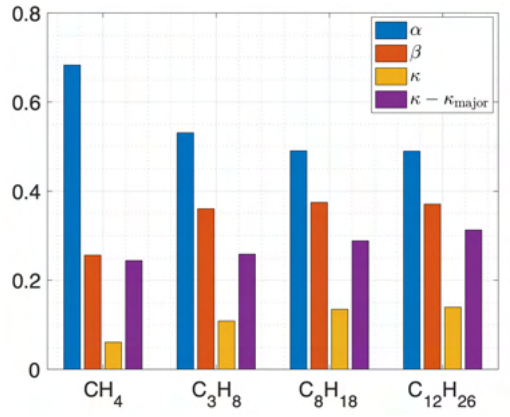

Figure 19. Flame-integrated ratios α, β, κ, and κ_{major} for four oxygen–fuel cases at $T_u = 500$ K, $\phi = 0.75$, and $p = 1$ atm.

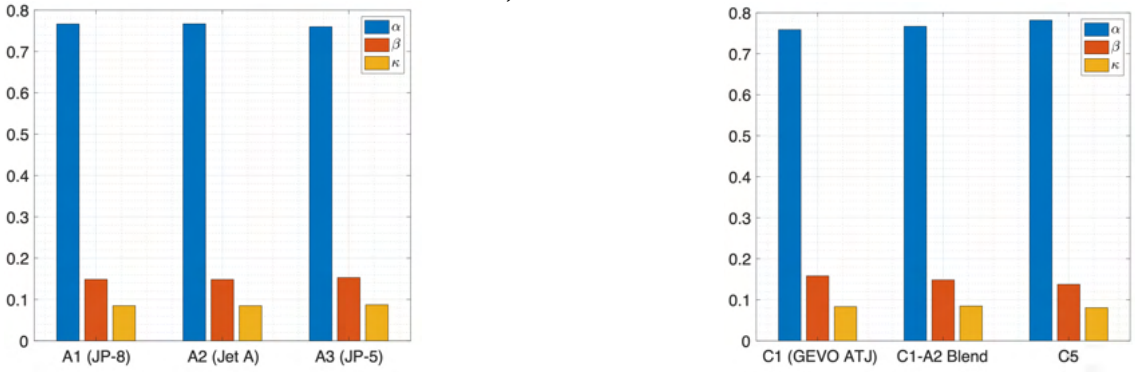

Figure 20. Flame-integrated ratios $\alpha, \beta,$ and κ for jet fuel combustion at at $T_u = 500$ K, $\phi = 0.75$, and $p = 1$ atm.

Based on the figures and analysis provided above, it can be seen that the exothermic heat release, $S_{e,1}$, is by far the dominant term in air-breathing systems. However, the combined influence of the terms $S_{e,2}$ and $S_{e,3}$ can sometimes exceed that of $S_{e,1}$ in pure oxygen systems. In turn, $S_{e,2}$ and $S_{e,3}$ are heavily influenced by dissociation. In other words, any effect that incites dissociation will tend to influence the contributions from $S_{e,2}$ and $S_{e,3}$ and, as a result, will reduce the relative contribution from $S_{e,1}$.

Estimation of Flame-generated Entropy

We have now established that for air-breathing systems, under relevant operating conditions, the heat release is the major source term at the flame for entropy generation. Hence, the entropy dynamics at the flame can more or less be determined by the following equation:

$$\rho T \frac{Ds}{Dt} = \dot{q} + \nabla \cdot \left(k \nabla T \right) \tag{26}$$

By decomposing the entropy into its base state (subscript 0) and fluctuating component (subscript 1) and assuming that the base state is spatially uniform, we can obtain the governing equation for the dynamics of the entropy fluctuations:

$$\rho_0 T_0 \frac{Ds_1}{Dt} = \dot{q}_1 + \nabla \cdot \left(k \nabla T_1 \right) \tag{27}$$

The algebraic relation $s_1 = c_p T_1/T_0$ is used to rewrite the last term on the RHS of above equation. Thus, the governing equation for entropy disturbances can be obtained in the isothermal limit (note that the base state is assumed to be uniform) as follows:

$$\frac{Ds_1}{Dt} = \dot{q}_1 + \frac{k}{\rho_0 c_p}\nabla^2 s_1 \tag{28}$$

The unsteady heat release rate disturbance term is the source of the entropy disturbance generation at the flame. Depending on the heat release model, expressions for the entropy transfer function, which is a normalized measure of entropy fluctuations generated by the flame, can be derived. Two velocity-coupled heat release response models corresponding to premixed and non-premixed flames were analyzed. The entropy transfer function obtained through this approach was compared to the entropy decay due to turbulent mixing over a flame length (see Figure 21). The results show that the decay of entropy disturbances through laminar processes for premixed and non-premixed flames is comparable in magnitude to the results for the turbulent mixing effect; neither effect is dominant for physically interesting values of β (ratio of flame length to a relevant geometry length) for a premixed flame.

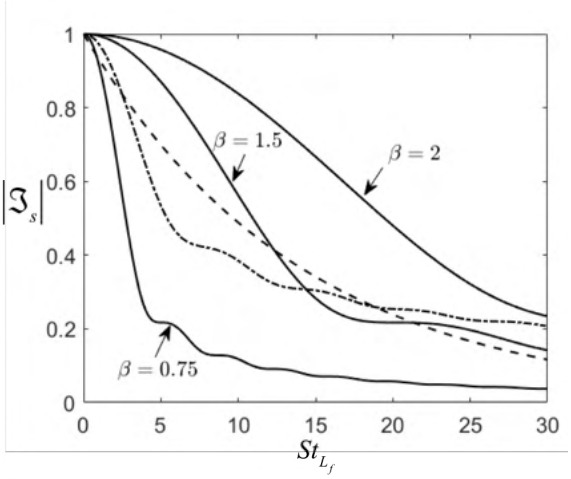

Figure 21. Comparison of the dependence of magnitude of the laminar entropy transfer function on Strouhal number (St_{L_f}) for an axisymmetric premixed wedge flame (solid lines) and a Burke–Schumann non-premixed flame (dot-dashed line) with the turbulent transfer function (dashed line).

The above calculation was performed in the isothermal limit. Because non-isothermal effects may be significant for entropy generation, a control volume analysis can be adopted to estimate the entropy generated by a flame element. A schematic of the control volume drawn around the flame element is shown in Figure 22(a). The following integral form of the entropy transport equation can be applied to this flame element:

$$\frac{d}{dt}\int \rho s dV + \int \rho s\left(\vec{u} - \vec{u}_s\right)\cdot \vec{n} dA = \int \frac{\dot{q}}{T} dV \tag{29}$$

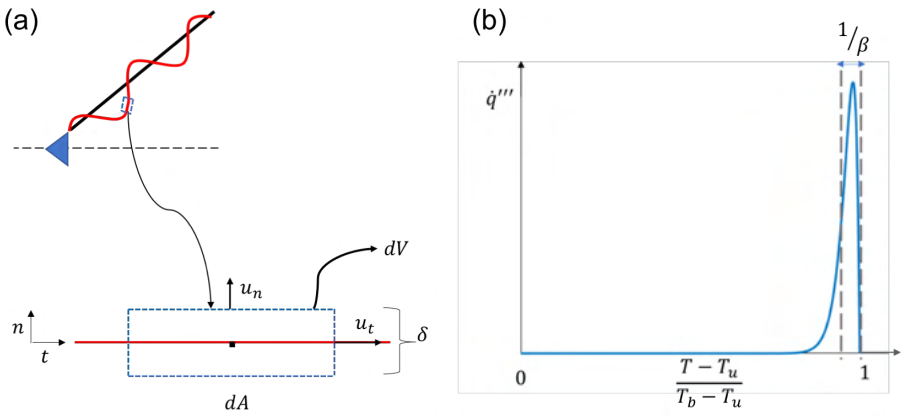

Figure 22. (a) Schematic showing control volume around a flame element and (b) heat release rate profile through the flame as a function of normalized temperature.

Note that the integral appearing on the RHS is an integral of heat release rate per volume weighted by $1/T$. This means that the functional form of the heat release profile through the flame is important when estimating the entropy generated by a flame. For single-step chemistry, the heat release rate profile through the flame as a function of temperature can be written as:

$$\dot{q} = \rho c_p (T_b - T) e^{-\frac{E_a}{RT}} \tag{30}$$

For the above profile, in the high-activation-energy limit, the following relationship holds:

$$\int_{T_u}^{T_b} \frac{\dot{q}}{T} dT = \frac{1}{T_b} \int_{T_u}^{T_b} \dot{q} dT \tag{31}$$

Here, the entire heat release will be concentrated around a small region near the burned side in the high-activation-energy limit (Figure 22b), which leads to a simplification. This simplification means that in the high-activation-energy limit, the generated entropy is a function of the integrated heat release rather than the heat release profile through the flame. For a premixed flame, this simplification implies the following:

$$s_{gen} = \frac{h_R}{T_b} \tag{32}$$

Here, h_R is the heat release per mass of the reactant consumed. For a non-premixed flamelet, the generated entropy is given by:

$$s_{gen} = \frac{h_R}{T_b u_b} \frac{(1+\varphi_{ox})}{\varphi_{ox}} D \frac{\partial Z}{\partial n} \tag{33}$$

Here, φ_{ox} is the stoichiometric mass ratio of oxidizer to fuel, u_b is the velocity at the flame, D is the diffusion coefficient, and Z is the mixture fraction. By comparing expressions for premixed and non-premixed flames, we see that the generated entropies have significant differences. For a premixed flame, the entropy production is independent of the mass burning rate; in contrast, for the non-premixed flame, the entropy generation is proportional to the mass burning rate, as evidenced by the mixture fraction gradient. The flame response modeling work feeds the heat release model to this framework. The resultant entropy fluctuations generated by the above model are then provided as inputs to the RTRC entropy wave modeling subtask.

Milestones

- Illustrated how spray parameters affect local flame responses
- Deduced that for air-breathing systems under elevated operating conditions, heat release is the dominant contributor to entropy generation
- Extended our framework for non-isothermal effects on the generation of entropy disturbances due to an unsteady heat release

Major Accomplishments

The spray flame response framework was used to derive a perturbation framework in which input disturbances can be connected to output flame response disturbances. The effects of spray parameters on flame response were illustrated using an example configuration. This work provides the beginning framework to model both the local and global unsteady heat release from a spray flame, a key input to the direct noise model as well as the source term for entropy disturbances that eventually model indirect noise.

Prior research on entropy dynamics has assumed that the heat release is the only dominant source for the generation of entropy disturbances at the flame. However, this assumption was never validated. Our chemical kinetics analysis showed that the heat release term accounts for 80%–100% of the source term, thus validating the assumption that the heat release is the sole contributor to the generation of entropy disturbances at the flame. This analysis was extended to consider a wide variety of aviation fuels to deduce that air-breathing systems at elevated conditions satisfy this assumption but any system where dissociation effects dominate cannot be modeled using just the heat release. Thus, this work validated the assumption of the entropy generation model used in a non-isothermal framework to model the generation of entropy disturbances by a premixed and non-premixed flame. As a key deduction, we found that the mass burning rate dynamics did not affect premixed flames, implying that velocity disturbances cannot generate entropy disturbances but that equivalence ratio fluctuations are required to generate entropy disturbances. In contrast, non-premixed flames respond to mass burning rate dynamics.

Publications

Acharya, V. (2021, January). Modeling the response of spray flames to velocity disturbances [Presentation]. AIAA SciTech 2021 Virtual Meeting.

Patki, P., Acharya, V., & Lieuwen, T. (2021, May). Entropy source terms from exothermic chemical reactions: Implications for indirect, premixed combustion noise [Presentation]. 12th US National Technical Meeting of the Combustion Institute Virtual Meeting.

John, T., Acharya, V., & Lieuwen, T. (2021, May). Entropy wave generation by harmonically forced, convectively non-compact flames [Presentation]. 12th US National Technical Meeting of the Combustion Institute Virtual Meeting.

Vishal Acharya's accepted submission to AIAA SciTech 2022 on Spray flame response heat release modeling.

Tony John, Vishal Acharya, and Tim Lieuwen's accepted abstract submission to ASME Turbo Expo 2022 on entropy generation modeling.

Parth Patki, Vishal Acharya, and Tim Lieuwen's manuscript preparation for submission to International Symposium on Combustion 2022.

Outreach Efforts

None

Awards

None

Student Involvement

- Graduate student Parth Patki has been involved in investigating the entropy budget of the entropy dynamics equation to determine the dominant source terms for entropy disturbances.
- Graduate student Tony John has been involved in modeling the generation of entropy disturbances due to a heat release source term.

Plans for Next Period

In the next year, the reduced order modeling task will expand to include hydrodynamics stability analysis to model the pre-combustion flow disturbances. The velocity model generated from this analysis feeds directly into the flame response model. In addition to this, the spray measurements and spray DNS will be used to generate model parameters for the spray droplets used in the flame response model. The flame response model will be further improved to relax assumptions made in the current model. Furthermore, the results from the models will be validated against the new measurement and simulation data and iteratively improved.

The model for entropy generation at the flame will be used with the validated flame response model to generate source entropy disturbances, which are then input into the entropy wave transport subtask by RTRC. The predictions from RTRC's

model at the nozzle will be validated against measured temperature fluctuations. This work will then iteratively feedback to improvements in both the GT entropy source model and the RTRC entropy wave transport model.

Task 4 – Facility Development at RTRC

Raytheon Technologies Research Center

Objective

The objective of this task is to design an RQL combustor that closely mirrors the GT design, with the specific goal being to focus on the higher-pressure operating points not possible for the GT rig. Collectively, the GT and RTRC rig capabilities will encompass a broad range of operating conditions, resulting in a robust dataset for training the design tools.

Research Approach

Fabrication of the RTRC rig was completed in early 2021, with installation and shakedown at the RTRC facility occurring in Q2 to confirm full operational capability of the rig with all instrumentation and optical equipment in place. Operation of the combustion rig was confirmed at pressures up to 250 psia, with the choked exit ("jail bars") providing backpressure to the rig at the full operating flow rate and firing temperatures and providing a combustor exit-plane acoustic boundary condition representative of a turbine inlet.

Following shakedown, a one-month test program was executed in which extensive diagnostic measurements were obtained for four operating conditions of interest: idle acceleration, approach, cutback, and sideline. The latter three represent conditions that are part of engine noise certification. For each operating condition, combustion parameter variations of FAR, inlet pressure (P_3), inlet temperature (T_3), and mass flow (i.e., flow parameter, FP_b), were evaluated, giving a total of 13 separate operating points for characterizing the effect of these parameters on combustion noise. Diagnostic data consisted of dynamic pressures at eight locations, chemiluminescence (as a surrogate for the unsteady heat release field), and TDLAS (unsteady combustor exit temperature).

Using the dynamic pressure data, the combustor noise characteristics were compared to the legacy scaling laws of NASA (Aircraft Noise Prediction Program [ANOPP]) and Pratt & Whitney (Matthews-Rekos [MR]). Figure 23 shows this comparison, which suggests that the current noise data follow the scaling laws equally well, with similar R-squared correlation and standard deviation values (the dashed lines correspond to ±2 standard deviations).

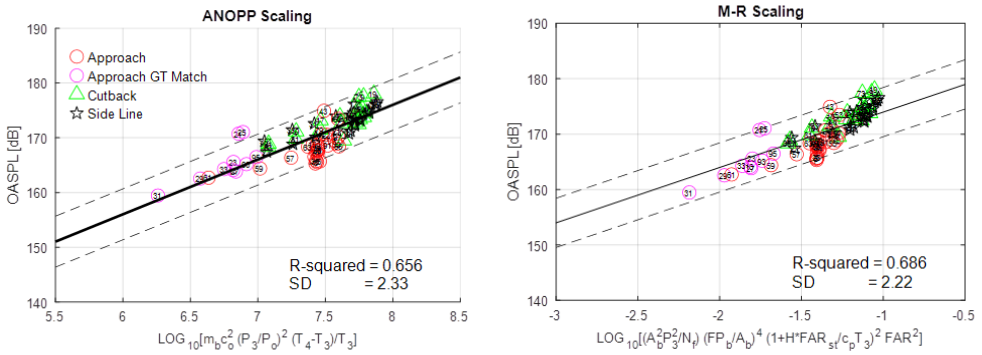

Figure 23. Legacy scaling laws (ANOPP and MR) for current dynamic pressure data.

Two approaches for separating direct and indirect combustion noise have been investigated. The first approach involves a dynamic pressure array upstream of the choke, which was used to separate downstream propagating noise from upstream propagating noise (see Figure 24). For a passive choke (i.e., no noise created by the choke), the area change of the choke reflects approximately the same amount of sound power as is incident on the choke (for a hard wall, the ratio of downstream to upstream propagating noise is unity, or ΔdB=0). Some noise would transmit through the choke, particularly at higher frequencies. The black line in Figure 24 shows this ratio for the passive choke condition (computed from an FEA pressure-acoustics model). The red line shows the measured values, which indicate the indirect noise. These results are preliminary and will be refined in the second rig test entry and through high-fidelity modeling of the rig.

The second method is to compare the measured dynamic pressure at, for example, the bulkhead with the direct noise computed from the chemiluminescence/Green's function analysis. This analysis indicates a similar result to the wave decomposition described above (increasing indirect noise level with increasing frequency). The absolute level of the direct noise is still being checked.

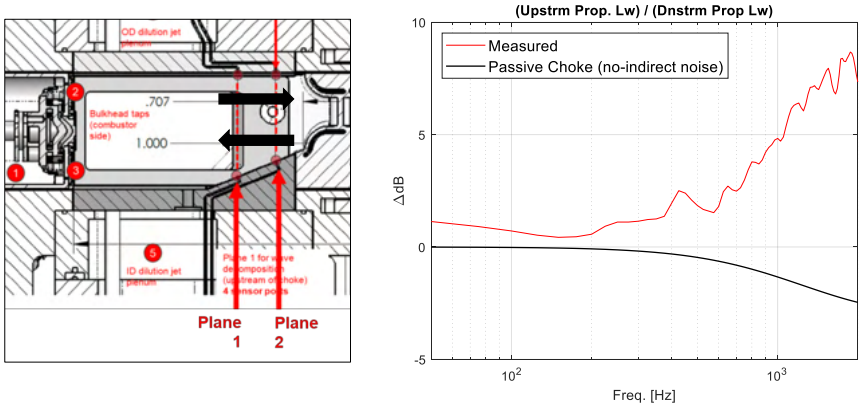

Figure 24. Wave decomposition to characterize indirect noise levels.

In addition, unsteady temperature measurements immediately upstream of the choke and downstream of the reacting region will be used to compute indirect noise using compact nozzle and/or actuator disk theory. During RTRC's first test entry, the TDLAS probe system was utilized to acquire data upstream of the choked exit. The TDLAS system was configured for near-IR operation, and data was acquired over the range of operating conditions. This effort successfully demonstrated the performance of the integrated optical probes in the harsh combustion environment (i.e., survivability, alignment, and signal quality), and data processing is currently in progress. These measurements will be refined for the next entry based on lessons learned and/or an alternative dual-TC approach will be utilized to capture unsteady temperature data and to enable indirect noise computations.

Milestones

- RTRC rig fabrication, installation, and operational shakedown completed
- First RTRC experiment entry successfully completed
- Assessment of legacy scaling laws performed, wave decomposition methodology applied to characterize indirect noise, chemiluminescence/Green's function analysis applied to compute direct noise

Major Accomplishments

Successful execution of the test program over a wide range of combustor parameter space provided quality data for quantifying indirect noise and validating noise prediction tools.

Publications

None

Outreach Efforts

None

Awards

None

Student Involvement

None

Plans for Next Period

With the first RTRC test entry now successfully completed, the next experimental step will be to return for a second test entry, focusing on improved unsteady temperature measurements and further evaluations of the effects of parameter and/or geometry variation on combustion noise.

Task 5 – Post-combustion Modeling

Raytheon Technologies Research Center

Objectives

The goal of this task is to develop transfer functions from the combustion zone to the nozzle, nozzle to turbine, and turbine to far-field. This task involves modeling the physics for:

a) Entropy wave transport post-combustion, as unsteady heat release rate disturbances at the flame generate entropy disturbances that are then transported through the post-combustion zone,
b) Direct noise modeling using a numerical Green's function approach with the heat release model,
c) Nozzle interactions for the dynamics of pressure disturbances through the nozzle, specifically the effect of the jail bar configuration used in both the GT and RTRC rigs,
d) Turbine interactions for the dynamics of pressure disturbances through the turbine, and
e) Far-field sound propagation.

Research Approach

The post-combustion-zone physics involves the effects of the combustion unsteady heat release rate disturbances and the post-combustion geometry on the eventual noise generation outside the engine. This modeling involves:

a) The direct generation of combustion noise due to heat release and the interaction of these pressure disturbances with the remainder of the engine geometry, which lead to far-field noise, and
b) The entropy disturbances generated by the flame interacting with geometric changes at the nozzle and causing pressure disturbances that then interact with the remainder of the engine geometry and lead to far-field noise.

Entropy Wave Transport Modeling

Initial simulations were performed using Fluent LES for an N+3 combustor design. The results were then used to interrogate the different terms of the entropy transport equation. This exercise (shown in Figure 25) confirmed that the primary contributors to the entropy transport are the heat release rate ($\dot{Q}_s$) and advection terms (A_s). The dissipation term (D_s) and production term (P_s) are small compared with the other two terms downstream of the flame and can be neglected. These findings imply that the entropy transport downstream of the flame can be considered as a scalar transport phenomenon within the combustor.

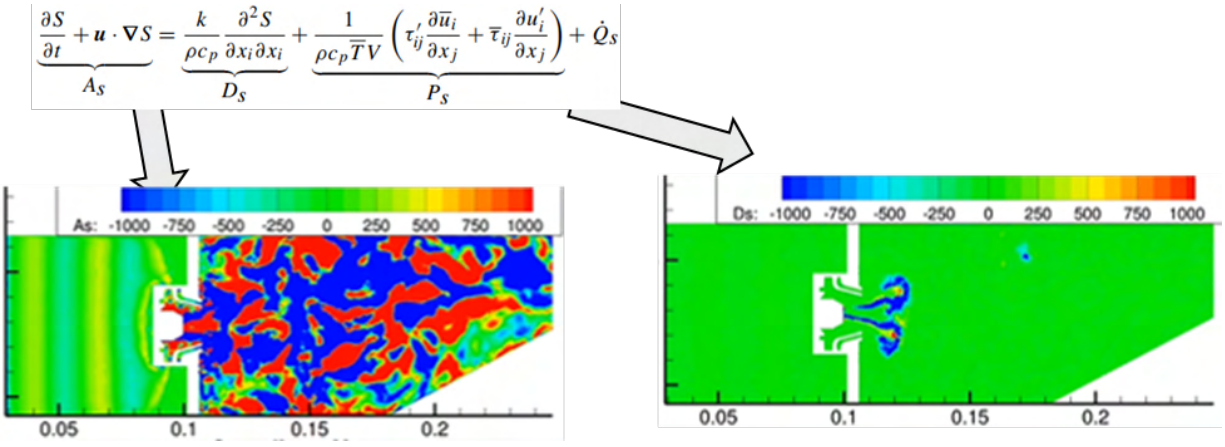

Figure 25: Relative magnitudes of the entropy transport equation terms.

The mean advection time of a scalar can be estimated using streamlines, and the entropy transport can be represented as a transfer function. The estimate of the transfer function computed for these simulations is shown in Figure 26 for both flames. When the GT LES results become available, a similar approach will be used to estimate the entropy transfer function for the current combustor. Furthermore, the LES results will be used to estimate the acoustic pressures propagating through the jail bars and to model the direct and indirect noise.

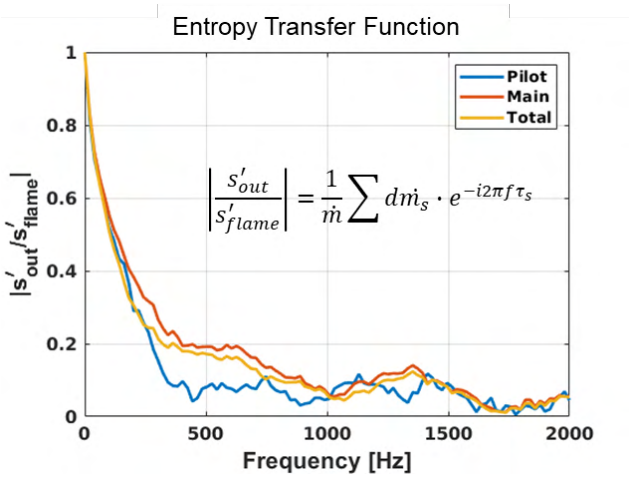

Figure 26. Flame-to-exit entropy transfer function estimate.

Direct Noise Modeling

Direct noise modeling is performed using a numerical Green's function approach, that uses an appropriate Green's function in conjunction with either a measured or simulated/modeled unsteady heat release rate disturbance field, in order to calculate the pressure disturbance at a particular location in the combustor. While this modeling was not performed during the current reporting period, a prior workflow established by RTRC under a NASA program has been reviewed and will be leveraged for this work. This work was summarized earlier in Task 4.

Nozzle Interaction Modeling

The goal of this task is to establish and improve a reduced order model (ROM) for the transmission and/or generation of direct and indirect combustion noise through a nozzle or geometrical representative of the first set of turbine vanes. The first iteration of the nozzle ROM is based on the compact nozzle theory (CNT) and the work of Marble and Candel. The ROM was validated through comparisons with existing data from a DLR entropy wave generator(EWG) experiment. A set of test cases was available from the experiment, and the test case that had undergone the most examination in the literature by other researchers was chosen for the validation case. For validation, the temperature profile was used to set an entropy profile of the test case as input to the ROM along with flow profile information at select locations within the nozzle. As shown in Figure 27, the temperature profile matches the experimental data. In addition, the good agreement with the test data for the downstream pressure spectra confirms the implementation of the CNT in the ROM.

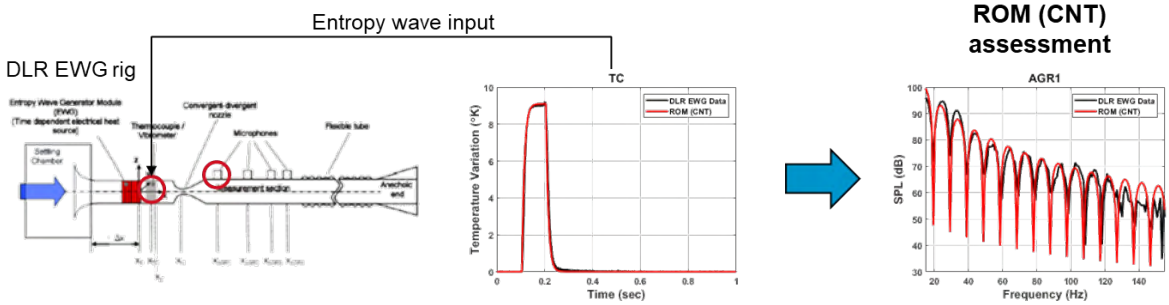

Figure 27. Snapshot of the temperature field for two different frequencies. Left: Lower frequency. Right: Higher frequency.

In addition to the simple nozzle geometry mentioned above, work continued on the more complex RTRC combustor jail bar rig, as shown for the computational model in Figure 28. The new high-fidelity LBM simulations were performed for two purposes. The first purpose was to obtain flow field data that were not captured during the testing to support the application of the nozzle ROM. As a caveat, the model does not include any reacting flow; hence, the model is focused on matching the flow conditions of the as-tested points without combustion processes. This approach is sufficient for the input required for the ROM. The second purpose was to support further investigations into the test data, as the simulations provide a means for extracting and viewing full fluid fields as compared to what is possible in certain locations for the test. To better represent the test rig setup, the high-fidelity LBM model was extended to incorporate more of the features of the test rig, compared with what was described in the last annual report. In particular, a dump plenum downstream of the jail bars was included, which represents the area change in the test rig. The piping downstream was approximated in length, and a numerical sponge zone was set to start where the test rig water mist was sprayed into the duct to damp out the acoustic waves before reaching the backpressure valve. The static outlet pressure in the simulations is defined at the approximate distance where it was measured in the experiments (location P5). This new setup is more representative of the actual flow field in the rig, and it presents more accurate acoustic boundary conditions downstream of the jail bars.

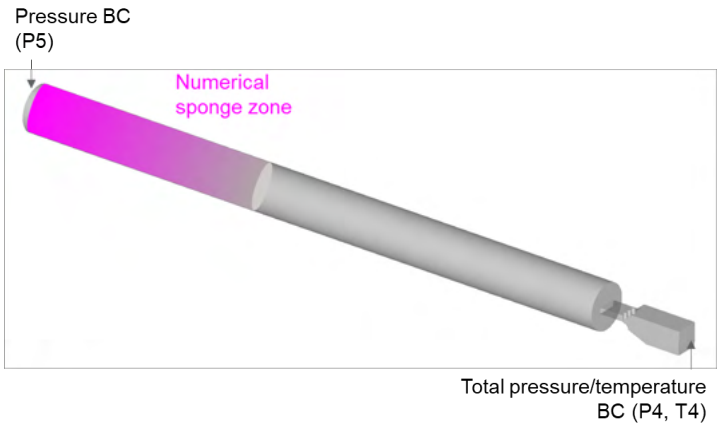

Figure 28. Extended computational domain for the RTRC jail bar rig.

Similar to what was previously reported, the new simulations were performed for different back pressure ratios ($p_{s,outlet}/p_{s,inlet}$) in order to assess the reflection and transmission of sound through the jail bars. A snapshot of the results from one of the back pressure cases is shown in Figure 29. The area change downstream of the jail bars corresponds to the transition from a rectangular to a circular duct, with the area change shown in Figure 28. In the absence of any acoustic forcing (i.e., in the absence of combustion noise in the simulations), it was found that a large amount of rig self-noise is produced downstream of the jail bars, as indicated by the time derivative of the pressure contours in Figure 29. For the operating conditions studied here, the jail bars were always found to be choked, and no rig self-noise traveled upstream, indicating there is no anticipated impact of rig self-noise on the combustion process or combustion noise sources. Therefore, the Kulite data upstream of the jail bars in the experiments should only include combustion-noise-related pressure signals. In contrast, the Kulite sensors downstream of the jail bars are expected to measure a significant amount of rig self-noise.

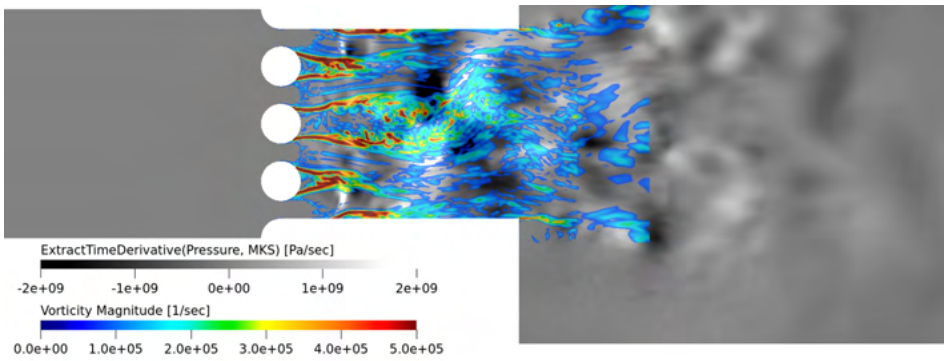

Figure 29. Snapshot of pressure field (grayscale) and vorticity (colors) for a high-power condition.

Some preliminary comparisons between the LBM results and the rig data were completed, as shown in Figure 30. The main focus of this initial comparison was to determine what level of background noise (rig flow noise) is expected to be present in the rig. As described above, the simulations were performed without acoustic forcing; hence, they include only rig self-noise, with no combustion noise. In contrast, the test data include both rig self-noise (inherently included) and direct and indirect combustion noise downstream of the jail bars. The overall agreement between the simulation and test data is good for the operating condition, as shown in Figure 30, indicating that a large amount of rig self-noise is present downstream of the jail bars. In turn, this result means that it is more difficult to separate the rig self-noise from combustion noise in the measured pressure signals downstream of the jail bars. Additional simulations with acoustic forcing are planned for further assessment.

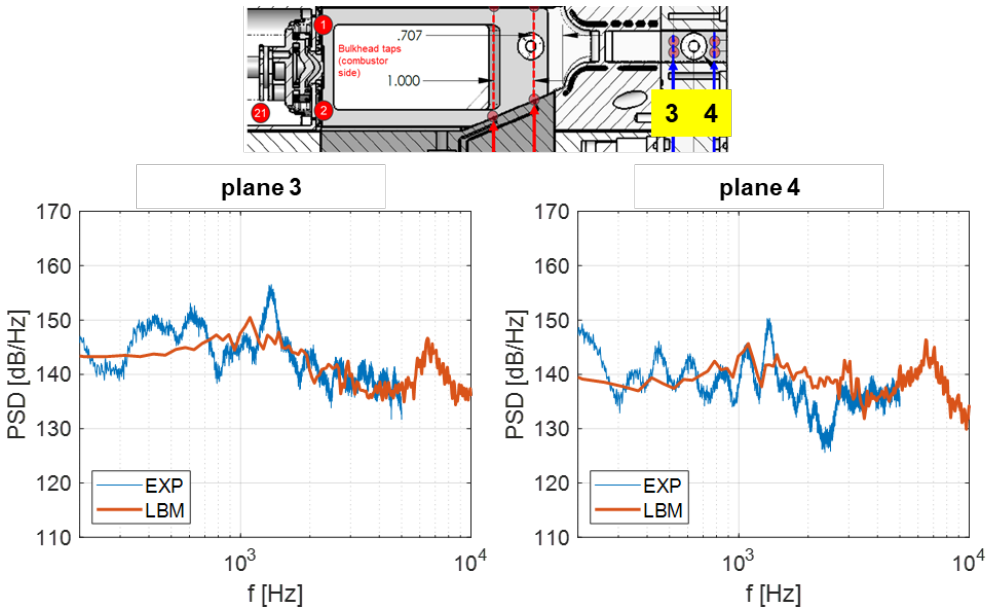

Figure 30. Comparisons of pressure power spectral density for the experimental data (blue) and LBM simulation (orange).

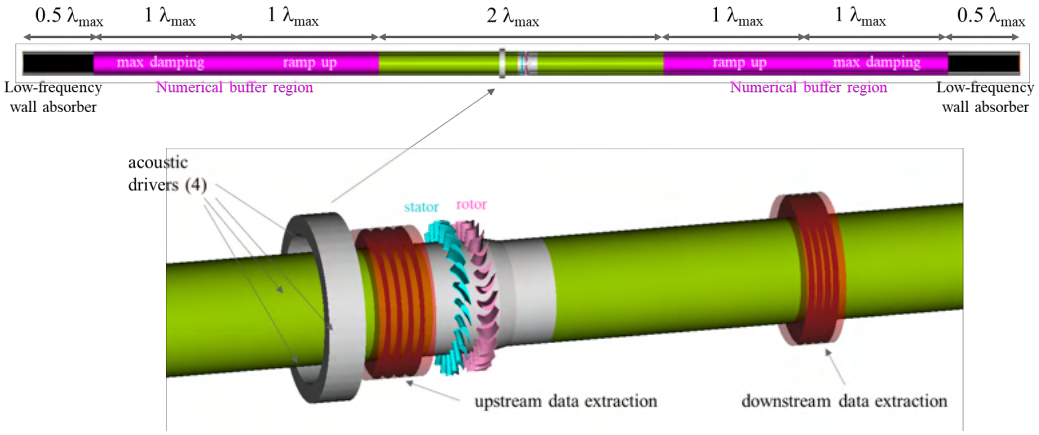

Figure 31. Simulation domain with virtual acoustic drivers for studying direct noise propagation through the turbine stage.

Turbine Interaction Modeling

This task focuses on simulations of a high-pressure public domain turbine rig from the Polytechnic University of Milan (PoliMi) and the German Aerospace Center (DLR) to understand the direct and indirect noise propagation through a representative high-pressure turbine stage. A comprehensive set of high-fidelity LBM simulations were performed for high-subsonic and transonic turbine flow conditions. The simulation results were validated using experimental data from DLR. As shown in Figure 31, the simulation setup includes a full-wheel simulation of the turbine stator and rotor rows, situated in a long annular duct with sponge zone buffer regions upstream and downstream to damp out waves. The numerical buffer zones are sized to absorb the lowest expected frequency (largest expected wavelength). Direct noise studies were performed for frequencies between 200 Hz and 1200 Hz. To be able to absorb very low frequency startup transients in the ducted simulation domain, with wavelengths well below those used to size the numerical buffer zones, additional wall absorbing boundary conditions are used on casing walls at the ends of the duct. The flow is driven via total pressure and static temperature boundary conditions at the inlet and a static pressure boundary condition at the outlet. For the direct noise study, the experimental setup is mimicked by placing four virtual speakers circumferentially on the outer duct wall. The speaker membranes are flush with the duct wall, and the speakers are excited in phase at a single frequency. These speakers are realized by vibrating wall boundary conditions.

The reflected and transmitted noise was extracted from the simulations using a mode-matching approach to determine the sound power coefficients. Figure 32 shows a comparison of the LBM simulation and experimental results for direct noise propagation through the turbine under high-subsonic flow conditions. The sound power reflection coefficient and transmission coefficient agree well between simulation and experiment. The remaining portion of the sound power (1-R-T), which is neither reflected nor transmitted, is not accounted for. This part corresponds to 60% of the total sound power, and it is hypothesized that this part is related to sound dissipation caused by the conversion of acoustic energy into shed vorticity from the blade and vane trailing edges and other sharp geometry features. Further analysis is underway to substantiate this hypothesis and will be reported in the future. Less than 10% of the sound power is transmitted through the turbine stage. These observations are consistent between simulation and experiment, indicating that the simulations are capable of predicting the correct physical processes involved in the turbine–wave interaction.

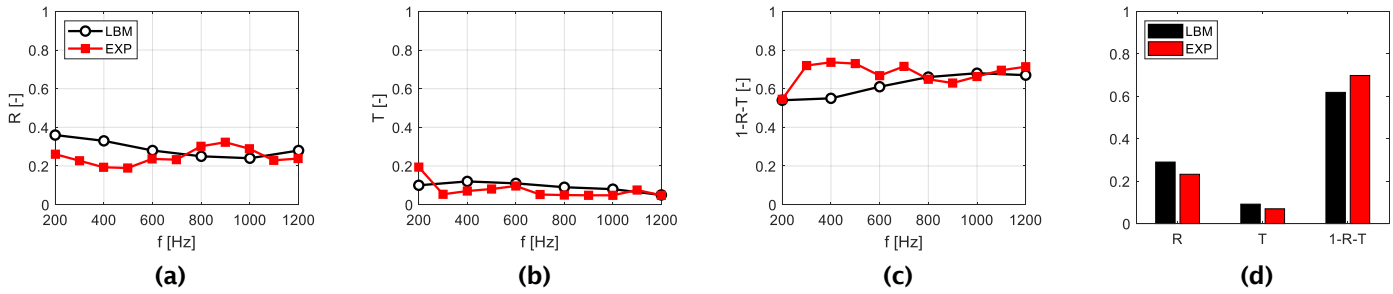

Figure 32. Sound power coefficients from LBM simulations and experiments for the high-subsonic flow condition. (a) Reflection (R), (b) transmission (T), (c) unaccounted portion (1-R-T), and (d) frequency-averaged values.

The results for the transonic flow condition are shown in Figure 33. The level of agreement between simulation and experiment as well as the overall trends are similar to those for the high-subsonic flow results. The transmitted noise tends to be lower than that for high-subsonic conditions, with only approximately 5% of the overall sound power being transmitted through the turbine. It should be noted that the transonic operating condition is more realistic for an actual high-pressure turbine stage in an engine.

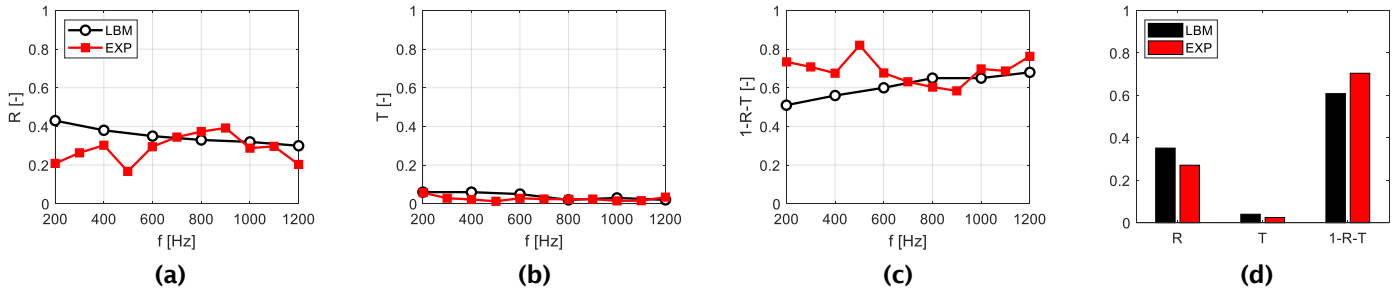

Figure 33. Sound power coefficients from LBM and experimental results for the transonic flow condition. (a) Reflection (R), (b) transmission (T), (c) unaccounted portion (1-R-T), and (d) frequency-averaged values.

Additional simulations were performed to determine the influence of the rotor row on wave interactions, meaning that direct noise studies were repeated as stator-only simulations in which the rotor was removed from the simulation, but the mass flow rate was kept the same. Figure 34 summarizes the results for the transonic flow condition. It is found that the wave reflection behavior is comparable between both configurations, while the sound transmission is higher in the stator-only case, consistent with the expectation that acoustic dissipation is reduced when one blade row is removed. Indeed, the unaccounted portion, 1-R-T, decreases by an average of 6% from approximately 62% to 56% of the total sound power when the rotor is removed. The observations for the high-subsonic flow conditions were found to be similar and are not shown here for brevity.

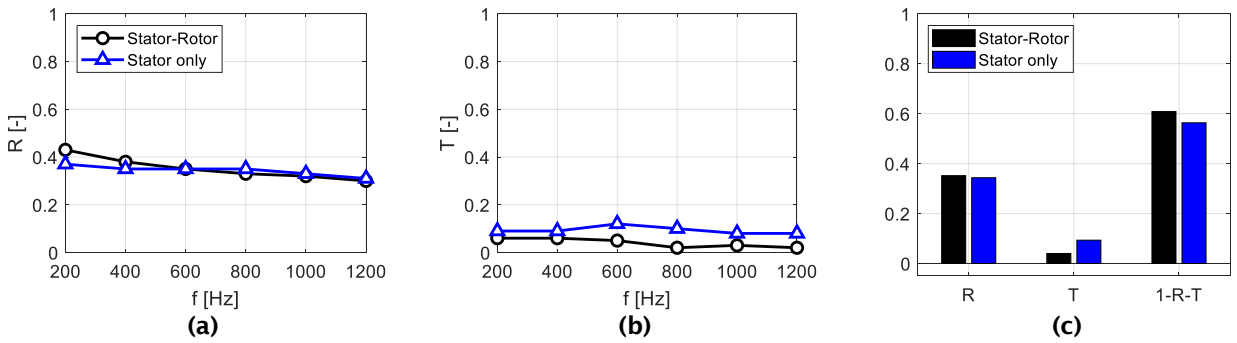

Figure 34. Sound power prediction comparisons between the turbine stage (stator-rotor) and an isolated nozzle guide vane (stator only) for the transonic operating condition. (a) Reflection coefficient, (b) transmission coefficient, and (c) frequency-averaged coefficients.

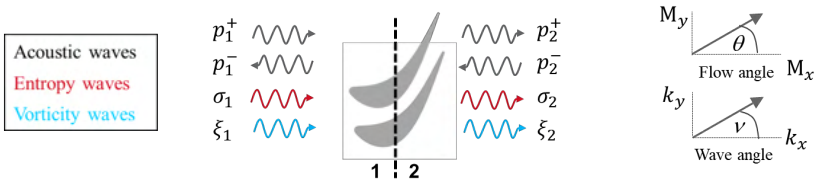

Figure 35. Wave interaction considerations with a vane row in ADT.

To further investigate the wave propagation behavior, the stator-only simulation results were compared with the Actuator Disk Theory (ADT) of Cumpsty and Marble, which is a quasi-1D reduced-order model for turbine–wave interactions. The theory considers wave interactions with a blade row, where the blade row is simplified to provide simple jump conditions for flow quantities across it. This theory is expected to be valid in the low-frequency range, where the wavelength of the impinging wave type is much larger than the chord length of the blade row. Different wave types (acoustic, entropy, and vorticity) are included in the theory (see Figure 35). Thus far, we have focused on acoustic wave interactions.

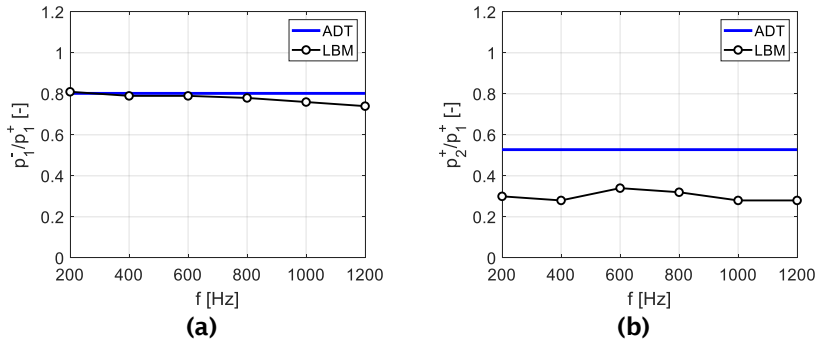

Figure 36. Comparison of ADT and LBM simulations for transonic flow conditions. (a) Reflected and (b) transmitted pressure.

The validity of the ADT was verified by applying the validated LBM simulation approach and by comparing the ADT results to the stator-alone LBM simulation results. As shown in Figure 36, the ADT results agree well with the simulation results for the pressure amplitude of the reflected wave. However, the transmitted wave amplitude is overpredicted compared with the LBM. This difference was anticipated, considering our previous discussion where a significant portion of the sound power was found to get lost in the turbine–wave interaction. The leading hypothesis is that this difference is due to acoustic

dissipation. This aspect is currently under investigation to determine if and how the ADT model can be improved as an ROM tool for turbine–wave interaction predictions.

The work described thus far has focused on direct noise (acoustic wave) interactions with a turbine stage. Additional simulation work was performed to investigate indirect noise generation and transmission through the turbine stage, in the form of injected unsteady temperature perturbations upstream of the turbine. High-fidelity simulations were performed, similar to the direct noise studies, in which the acoustic driver upstream of the turbine was replaced with circumferentially positioned injection ports. As shown in Figure 37, this setup closely mimics the experimental setup of the PoliMi/DLR rig. In the simulations, a constant elevated injection temperature was initially applied to create hot streaks, and then, the temperature was adjusted to provide a sinusoidal time variation with a frequency of 90 Hz. In this way, a maximum temperature ratio of 1.08 was generated in an effort to create entropy waves that are consistent with the DLR validation test data. The unsteady temperature field interacts with the turbine and creates acoustic waves as the temperature hot spots convect through the accelerated non-uniform turbine flow field. Figure 38 shows the total temperature field for one 90-Hz injection cycle.

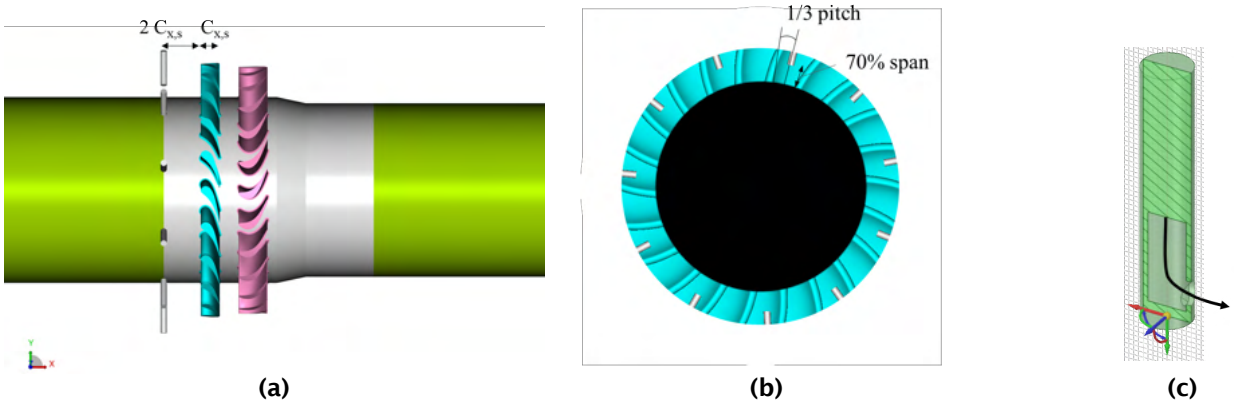

Figure 37. Magnified view of the simulation domain for indirect noise studies, with 11 circumferentially arranged injectors for entropy wave generation. (a) Side view, (b) front view, and (c) cut-away view of a single injector.

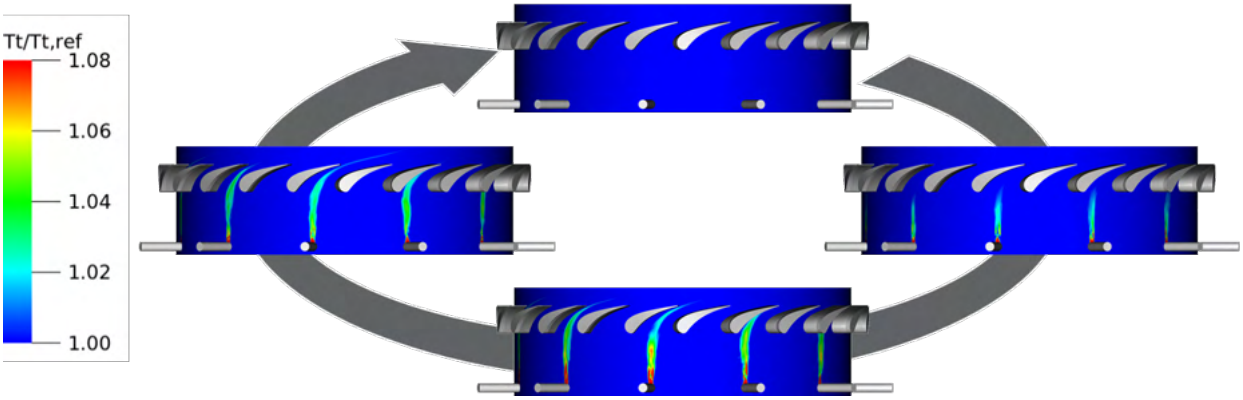

Figure 38. Entropy wave injection cycle (rotor blades not shown) for a high-subsonic turbine flow.

Following the DLR data processing steps, the increase in entropy wave noise was calculated between the case with injection and a reference solution with the injectors turned off. The results are shown in Figure 39. The LBM-predicted generation of upstream propagating noise is on the order of 18 dB higher, while the downstream propagating generated noise increase is on the order of 17 dB, compared with the reference case with the injectors turned off. The DLR test data show a much higher noise increase both downstream and upstream (~37 dB and ~26 dB, respectively) while similar trends are observed, with the

upstream propagating noise being higher than the downstream propagating noise. It must be pointed out that due to the nature of the entropy wave generation caused by flow injectors, a certain amount of vorticity wave generation is inherently included. While the injection temperature was carefully controlled in the present simulations, the amount of vorticity wave generation has not been examined separately. Therefore, it is possible that some of the observed discrepancies between simulation and experiment are due to a lack of properly accounting for the vorticity waves. In fact, DLR researchers have shown that when injectors operate without a temperature increase, called "cold entropy wave generation" the upstream propagating noise is even higher than that with temperature injection, while the downstream generated noise is a few dB lower than that with temperature injection. These results indicate that a strong component of vorticity waves is present in the test data. The direct noise validation cases were well-defined, and the agreement between experimental results and LBM simulations was very good. Due to the nature of the entropy wave generation in the experiments, there is no comparable well-defined dataset available for validation. The indirect noise trends are predicted reasonably well, but more analysis is needed to explain the observed differences in amplitude between experiment and simulation.

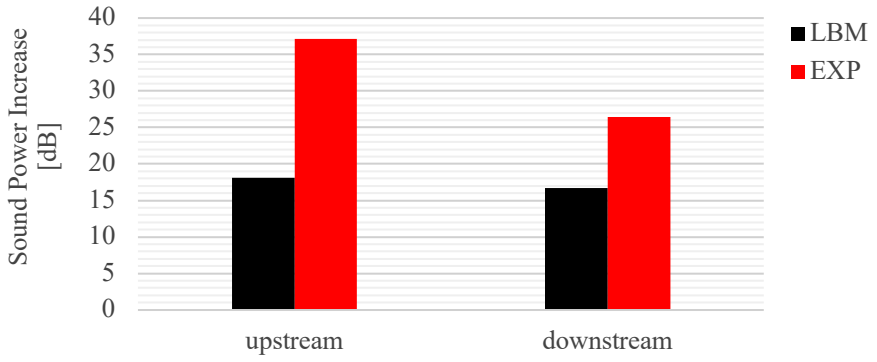

Figure 39. Comparison between simulation and experimental results of acoustic power generation by entropy wave injection for 90-Hz excitation with a peak-to-peak temperature amplitude of 25 K for a high-subsonic flow turbine operating condition.

Far-field Noise Modeling

In this task, the acoustic mode identified at the turbine exit is used as an input, and the different physics involved in far-field noise propagation are simulated. This task includes refraction due to sheared flow and temperature gradients before sound is perceived in the far-field.

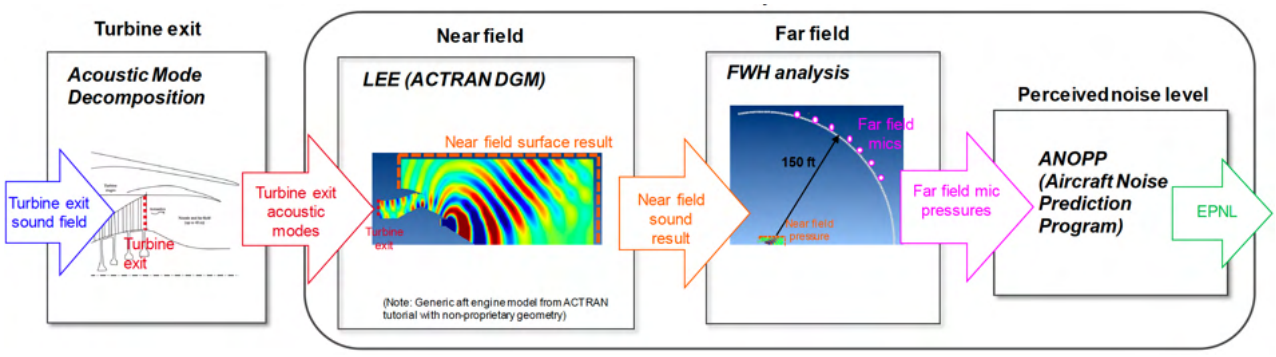

Figure 40. Simulation approach for the turbine exit for far-field pressure and perceived noise levels.

The simulation approach is shown in Figure 40. First, the acoustic modes from the turbine exit are injected into the near-field simulation, which uses a linearized Euler equation approach in Actran DGM. From the near-field simulation output, the input to the far-field analysis is provided and calculated using the Ffowcs-Williams-Hawking equations. The far-field is set at 150 ft, and from the far-field mics, the pressure is used to measure the effective perceived noise level using ANOPP.

The workflow for the developed far-field simulation tool was first exercised to calculate far-field pressures based on a generic-geometry engine model. Calculations were performed for three flight conditions (sideline, cutback, and approach) and were recorded in the form of far-field transfer functions relating turbine exit duct modes to far-field pressures as a function of frequency. Combustion noise directivity results were calculated using the far-field transfer functions, with some simplifying assumptions pertaining to the duct source mode and frequency distribution. As shown in Figure 41, reasonable agreement was achieved between the computed directivity results and reference combustion noise directivity curves from the literature. Figure 41 shows that the computed directivity results have some sensitivity depending on the particular source mode distribution, which was an unknown and is typically not measured or computed at the engine level. It has been observed that the main directivity peak angle is relatively insensitive and in good agreement with the reference models. In addition to simulating a generic engine geometry, far-field directivities were also calculated for an actual engine from the previous FAA CLEEN I program and showed reasonable agreement with the measured data, although this work is still in progress.

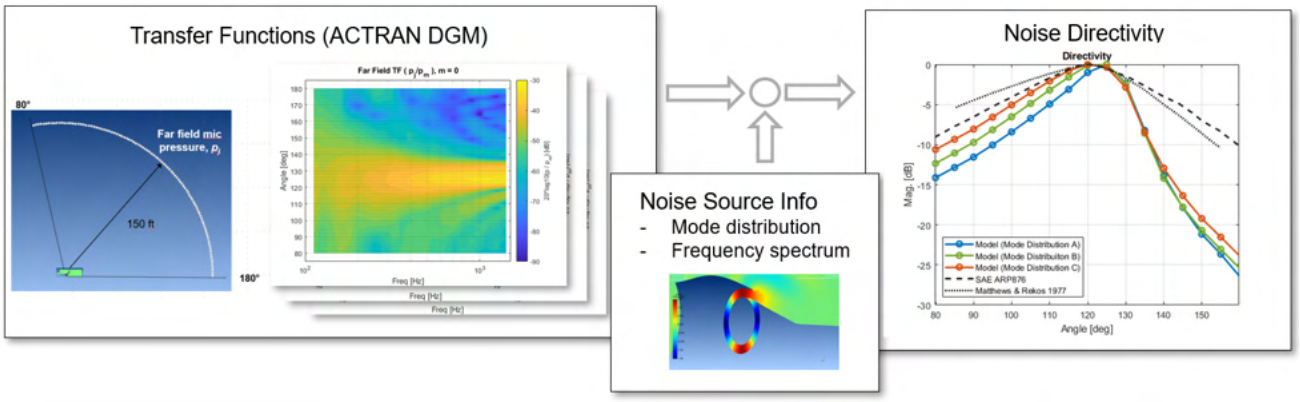

Figure 41. Computing the overall combustion noise directivity based on simulated far-field transfer functions and assumed noise source frequency spectra and model distributions. The results are for a generic-geometry engine model.

Milestones

- Entropy wave transport: Established a workflow from simulation to data processing to transfer function calculation
- Nozzle interactions: Established a validated nozzle ROM for a simple nozzle geometry based on the DLR entropy wave generator (EWG) experiment and applied an expanded LBM simulation framework to the RTRC jail bar rig to simulate as-tested conditions
- Turbine interactions: Validated the high-fidelity LBM simulation approach with DLR test data; implemented the ADT and compared simulation data to ROM results
- Far-field sound generation: Applied the multi-framework simulation workflow/ROM to a generic engine configuration and to a P&W-relevant GTF engine geometry from the FAA CLEEN I program.

Major Accomplishments

For the entropy wave transport modeling effort, a robust workflow has been established to perform simulations in Fluent, post-process the data in Tecplot, and calculate the final transfer functions in MATLAB. The simulations confirmed that the entropy transport can be considered as a scalar phenomenon downstream of the flame for the simulated combustor, and a transfer function approach has been developed. A technique for decomposing the downstream and upstream convective acoustics and entropy disturbances has been identified and will be applied to the GT LESLIE simulation results when available.

For the nozzle interaction task, a MATLAB-based ROM was established and validated for a simple nozzle based on DLR EWG test data. The LBM simulation framework was expanded to include more physical features of the RTRC jail bar rig to better represent the downstream boundary conditions, and simulations were performed for select as-tested conditions.

For the turbine interaction task, high-fidelity LBM simulations were successfully validated with experimental data from the PoliMi/DLR turbine rig. The actuator disk theory of Cumpsty and Marble was implemented as a reduced order model and the results were compared with high-fidelity LBM simulation results. It was verified that the turbine reflection behavior is accurately predicted by the ADT ROM, but a significant amount of sound power is lost during the turbine–wave interaction, which is not predicted by the ADT ROM. This discrepancy presents an opportunity to refine the model going forward.

For the far-field modeling task, the developed simulation tool workflow was exercised to calculate far-field pressures based on a generic-geometry engine model first. The predicted directivity results show reasonable agreement with generic combustion noise directivity curves found in the literature. The process was then repeated with the model of an actual engine from the previous FAA CLEEN I program. The directivity calculations showed reasonable agreement with the test data and were within the range of angles around the directivity peak angle.

Publications

Winkler, J., & Mendoza, J. (2021). Lattice Boltzmann simulations of wave propagation through a high-pressure turbine stage [Presentation]. AIAA Aviation Forum Virtual Meeting.

Outreach Efforts

None

Awards

None

Student Involvement

None

Plans for Next Period

For the entropy wave modeling task, the GT LES data will be processed using the workflow described above and estimates made of direct and indirect noise.

For the nozzle interaction task, the team will focus on applying the ROM to the RTRC jail bar rig and on performing comparisons with test data for the transmission and reflection of pressure waves. This effort will include extracting parameter values from the recently performed LBM simulations to obtain any necessary inputs for the ROM that are not directly available from the test. Additional simulations are also planned to assess the signal-to-noise ratio (combustion noise vs. rig self-noise) downstream of the jail bars.

For the turbine interaction task, the team will investigate the nature and physical cause of the unaccounted or lost sound power that was observed in the turbine–wave interaction study. The leading hypothesis that a significant amount of sound power is dissipated by the conversion of acoustic energy into shed vorticity will be assessed with additional high-fidelity simulations and comparisons to available low-order models for sound dissipation mechanisms. Additional simulations and analysis will also be performed to further refine the entropy wave interaction study with the turbine described above. Insight from all these investigations will help improve the existing ADT reduced order model that is needed for the low-order computational tool chain for combustion noise prediction.

For the far-field noise propagation task, the focus will be on completing additional comparisons of the transfer function-based far-field ROM to the FAA CLEEN I far-field engine data. In addition, the team will continue working on the ROM as part of the integration effort for the overall combustion noise model framework that can be used to compute the propagation of the combustion noise from combustor to far-field.

Project 056 Turbine Cooling through Additive Manufacturing

The Pennsylvania State University

Project Lead Investigator

Karen A. Thole
Distinguished Professor
Department of Mechanical Engineering
The Pennsylvania State University
136 Reber Building
University Park, PA 16802-4400
(814) 865-2519
kat18@psu.edu

University Participants

The Pennsylvania State University (Penn State)

- PIs: Dr. Karen Thole, Distinguished Professor; Dr. Stephen Lynch, Associate Professor
- FAA Award Number: 13-C-AJFE-PSU-054
- Period of Performance: February 5, 2021 to February 4, 2022
- Tasks:
    1. Manufacture and test existing FAA Continuous Lower Energy, Emissions, and Noise (CLEEN) II blade designs
    2. Design new double-wall cooling technologies
    3. Manufacture and test new double-wall cooling designs for linear cascade
    4. Manufacture and test optimal double-wall cooling designs for the Steady Thermal Aero Research Turbine (START) Lab turbine

Project Funding Level

The FAA has provided $800,000 of funding to date. In-kind cost sharing of $1,500,000 has been provided to Penn State from Pratt & Whitney to cover the entire program.

Investigation Team

Name	Affiliation	Role	Tasks
Distinguished Professor Karen A. Thole	Penn State	PI	Management, reporting, and oversight of all technical tasks
Associate Professor Stephen Lynch	Penn State	Co-PI	Management, reporting, and oversight of Tasks 2 and 3
Assistant Research Professor Reid Berdanier	Penn State	Staff Scientist	Task 1 and 4
Associate Research Professor Michael Barringer	Penn State	Staff Scientist	Tasks 1 and 4
Scott Fishbone	Penn State	Project Manager	Tasks 1 and 4
Jeremiah Bunch	Penn State	Laboratory Technician	Tasks 1 and 4
Justin Wolff	Penn State	Graduate Student	Tasks 1–4

Project Overview

Gains in the cooling performance of cooled turbine airfoils directly impact the efficiency and durability (lifetime) of turbine engines, and therefore have undergone substantial development. Currently, many cooling designs for turbine airfoils use complex microchannels placed within the wall of the airfoil to extract heat, in a design known as double-wall cooling. However, the geometric complexities (and thus the effectiveness) of the microchannels are limited by the current design space available using conventional investment casting and core tooling methods to manufacture relatively small intricate internal cooling features. This project will investigate potential thermal performance and aerodynamic efficiency improvements made possible through exploring the expanded cooling design space opportunities provided by direct fabrication of complex cooling geometries using three-dimensional laser powder bed fusion (L-PBF), a common metal-based additive manufacturing (AM) method. L-PBF AM has begun to see many uses in the gas turbine industry, particularly because of the new design space enabled by this new fabrication method. However, the ability to manufacture high-efficiency, intricate, complex double-wall cooling airfoils design concepts is unknown. This research would generate some of the first thermal performance data at engine-relevant conditions, comparing traditional cast airfoils to advanced airfoils manufactured through L-PBF AM. Understanding the potential of new innovative geometric heat-transfer cooling design features coupled with unique airfoil cooling configurations should serve as an important guide for future investments in advanced manufacturing and cooling design technologies.

Task 1 - Manufacture and Test Existing FAA CLEEN II Blade Designs

The Pennsylvania State University

Objective

The objective of this task is to measure the as-manufactured shape of FAA CLEEN II turbine blade airfoils using X-ray computed tomography and to use that information to fabricate additively manufactured (AM) copies for direct comparison in the rotating turbine facility at Penn State. The outcomes of this effort will be to: (1) provide a direct back-to-back comparison of cast versus additively manufactured airfoils; (2) learn the unknown challenges in creating double-wall designs via AM and how to translate them to cast parts for commercialization; and (3) work through the design, fabrication, and testing of additive blades that will spin at engine-relevant conditions.

Research Approach

CT Measurement of FAA CLEEN II Blades

At the end of the prior annual reporting period, an extensive analysis of two types of CT scans had been conducted on six cast FAA CLEEN II blades to down-select one blade to replicate through AM. One set of CT scans was from a Pratt & Whitney vendor, and another set was conducted using on-campus facilities in the Penn State Center for Quantitative Imaging (CQI). From the CT analysis, surface deviations were compared between individual blades and between the as-manufactured blades, relative to the design intent. The analysis also considered the cooling performance of the cast airfoils, as measured through infrared imaging results from a prior test campaign, and coolant flow capacity testing results. At the start of this annual reporting period, the package was reviewed with Pratt & Whitney, and one blade was selected for replication in AM.

Mechanical Analysis, AM Design, and Manufacturing

Pratt & Whitney was engaged as a subcontractor in the Task 1 effort, to provide mechanical analysis, generation of manufacturing drawings for the additively manufactured airfoils, and assistance with securing an additive manufacturing vendor. Pratt & Whitney engineers performed structural analyses of the existing FAA CLEEN II airfoil under the conditions of the START turbine rig and determined that there were no operational concerns, even after accounting for the material properties of additively manufactured airfoils.

Pratt & Whitney engineers used the CT scan data to understand the as-manufactured dimensions of the internal features of the FAA CLEEN II airfoil relative to the design intent, then updated the blade model accordingly. The final design was reviewed by the team for suitability for additive manufacturing, and Pratt & Whitney developed drawings and material specifications.

Pratt & Whitney also assisted the team in engaging additive manufacturing vendors, and two of those vendors (Keselowski Advanced Manufacturing and Vertex Manufacturing) were initially selected for demonstration trials after non-disclosure agreements were established with Penn State and Pratt & Whitney. The trials included evaluation of the overall external shape, the dimensional accuracy of internal features, and the potential to directly print small-scale cooling holes. In general, external and internal features could be reasonably replicated by the current state of the art in AM, although the cooling hole features

did not print as expected. According to the demonstration trials, Vertex Manufacturing was selected for fabrication of the AM airfoils. The manufacturing (including machining) is expected to be completed in early Q1 2022, at which point testing in the rotating turbine facility (START turbine) will commence.

Task 2 - Design New Double-Wall Cooling Technologies

The Pennsylvania State University

Objective

The objective of this task is to develop novel double-wall cooling designs that feature microchannel concepts that are being explored in the literature and could potentially be achieved via AM. The designs will be generated according to advice from Pratt & Whitney, so that the concepts can be translated to the FAA CLEEN II airfoil later in this project and leveraged for commercialization. The designs will be packaged into cascade test articles that will be measured in the high-speed linear cascade at Penn State by using infrared thermography in Year 2 of the project. The best designs will be identified for reintegration into the FAA CLEEN II airfoil shape and run in the START turbine to confirm operational benefit.

Research Approach

Design of Linear Cascade Test Articles and Infrastructure

For common testing of novel internal microchannel cooling features, the 75% span cross-section of the FAA CLEEN II airfoil was implemented into the cascade hardware design to produce a linear pattern of seven two-dimensional (2D) airfoils similar to the example shown in Figure 1. Static pressure taps were incorporated into the cascade hardware to enable validation of the flowfield before testing of new cooling technologies. The pressure taps were strategically placed within the cascade hardware design by using computational fluid dynamics (CFD) to locate the taps at important points on the airfoil. Figure 2 shows an example of a typical airfoil static pressure plot used to select static pressure tap locations with respect to the axial chord.

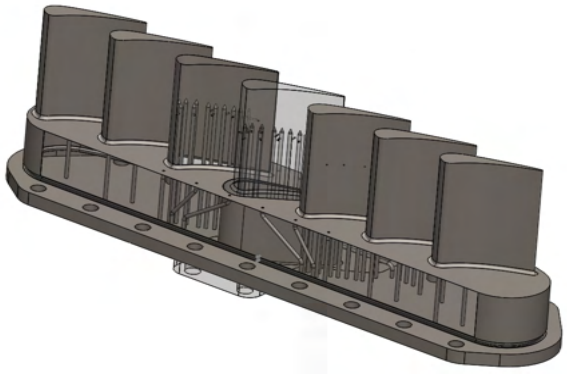

Figure 1. Example vane linear cascade with pressure tap design (the actual airfoils for this project are proprietary and therefore not shown).

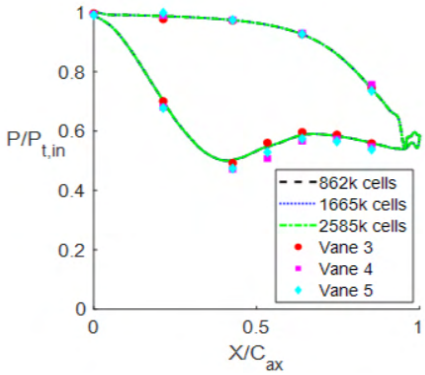

Figure 2. Example vane pressure loading plot, with points representing locations where pressures are measured.

Three removable center test airfoils were incorporated into the cascade hardware design to enable rapid changeout of novel cooling designs. In addition, the data reduction technique of the cascade requires an infrared camera calibration airfoil set, which has both spatial calibration markers that can be used to transform the IR image, as well as variable internal temperature that can be used to develop a camera-observed temperature-to-true temperature mapping. This calibration airfoil, as well as a generic microchannel cooling airfoil with appropriate coolant feeds, were designed with instrumentation enabled by AM fabrication. Figure 3 shows a schematic of the coolant routing from the base of the test airfoil insert, with flowpaths leading to the microchannels in the airfoil body and instrumentation locations at the inlets and outlets of the microchannels.

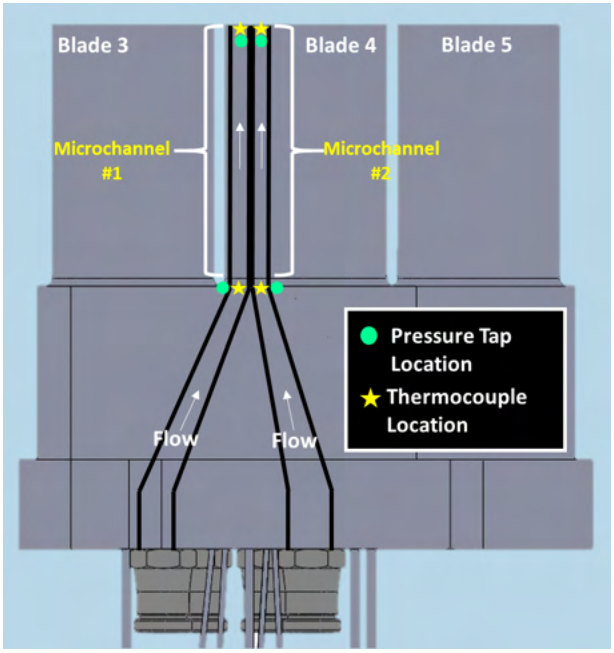

Figure 3. Design of cooling flowpath and instrumentation for microchannels in linear cascade hardware.

Several novel microchannel cooling geometries were developed for study according to concepts reported in the literature, some of which have previously been demonstrated by using AM. Figure 4 shows some of the designs, grouped by type. Pin fin designs include a standard circular pin (manufactured in AM by Kirsch & Thole [2017]), as well as a triangular pin design tested by Ferster et al. (2018). These designs are expected to have high pressure loss but also high cooling effectiveness. The second grouping is for ribs (turbulators), which do not span the entire channel but act to locally trip the flow. The discrete W shape by Wright et al. (2004) is a conventional design, but the wavy S-shaped ribs by King & Pietraszkiewicz (2018) are based on a patent and may have a similar effect to that of the wavy channels studied by Kirsch & Thole (2017).

The channel-only configurations include the baseline empty microchannel, which replicates the existing FAA CLEEN II design, as well as a wavy microchannel based on the findings of Kirsch & Thole (2017). All these designs have been packaged into the cooled airfoil shape and sent to vendors for build evaluation and quoting. We expect that the hardware will be fabricated by the end of Q4 2021 or early in Q1 2022.

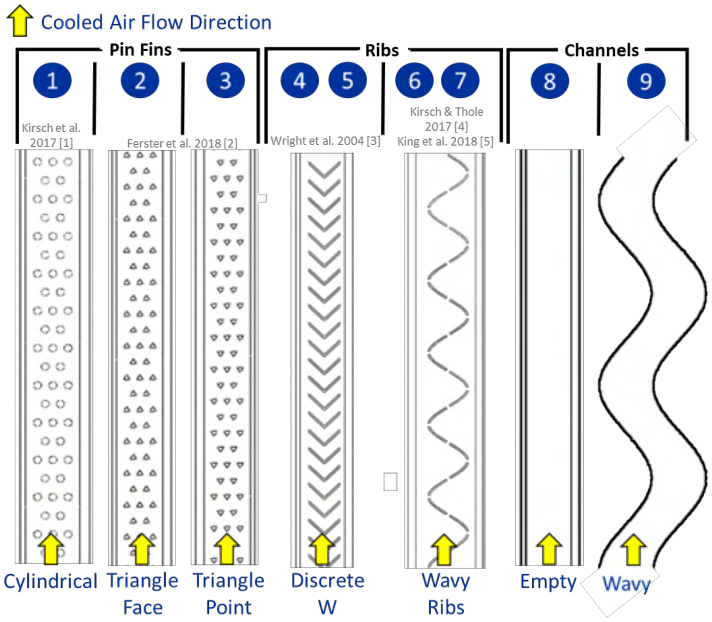

Figure 4. Examples of novel cooling concepts packaged into a microchannel.

In addition to the cooled airfoil designs, the linear cascade cooling facilities have been upgraded to account for an increased number of cooling circuits and the necessary flow control. Figure 5 shows a schematic of the cooling circuits being constructed to allow for independent control of the coolant flow to four microchannels in the test airfoils. Of note, because the cascade inlet air temperature is only 100 °C, the cooling air is cooled with liquid nitrogen to temperatures below freezing, to maintain the coolant-to-mainstream temperature ratios relevant to engine conditions.

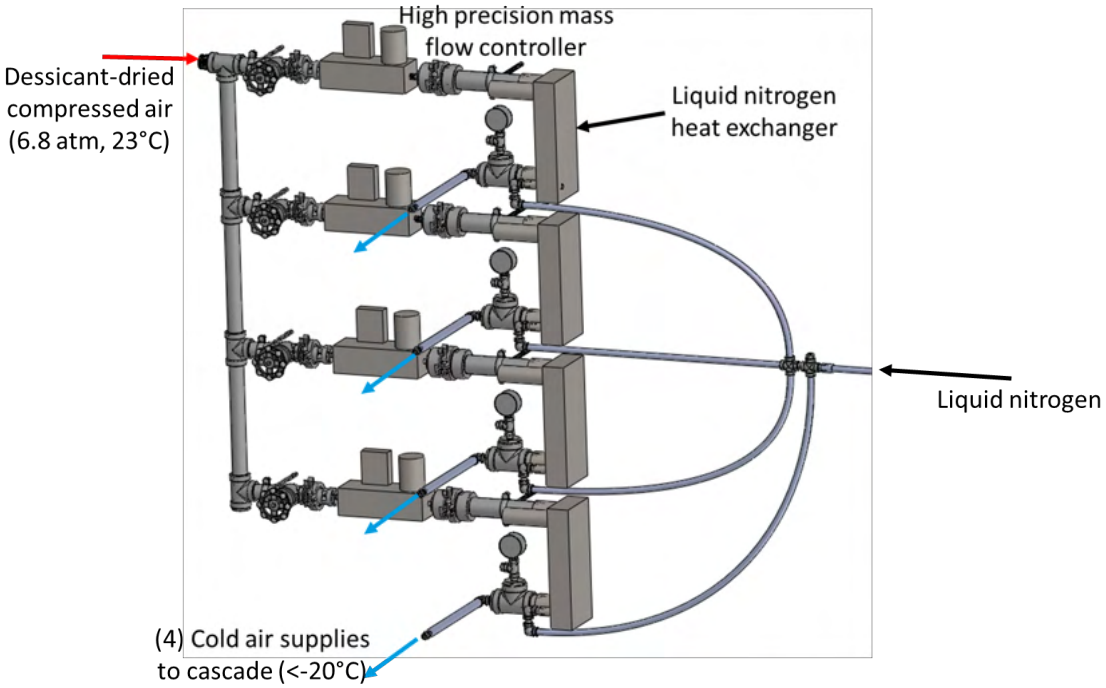

Figure 5. Upgraded cooling supply system for cascade including high-precision mass flow controllers and liquid-nitrogen-cooled cooling air.

Fabrication of Linear Cascade Hardware and Validation of the Flowfield

The FAA CLEEN II 2D airfoil pressure tap design was fabricated by Keselowski Advanced Manufacturing with L-PBF. The vendor also applied a heat treatment for stress relief and a bead-blast finish. After its receipt, the hardware was generally evaluated. The pressure tap holes were produced to satisfaction, and the required dimensions for installation into the linear cascade were met. However, some post-processing on the pressure tap holes was necessary to properly fit the pressure taps; the pressure tap holes were slightly undersized because of printing tolerance.

The flowfield of the FAA CLEEN II 2D airfoil for the linear cascade studies has also been validated. The validation was performed by comparing the pressures from computational fluid dynamics (CFD) predictions of the airfoil and the measured surface pressures from the linear cascade hardware. Figures 7–9 show the percentage difference, as in Equation (1), between the CFD and cascade pressure data at selected locations around the three center airfoils (airfoils 3, 4, and 5 of seven in total). Figure 6 provides a generic example of airfoil geometry with corresponding pressure tap locations, such as pressure side 1 (PS1) and suction side 4 (SS4). The airfoil's static pressure data were collected at three exit Mach number conditions corresponding to low, normal, and high operating conditions for turbines; Figures 7–9 correspond to an exit Mach number under normal operating conditions. Each Mach number condition was tested at two separate Reynolds numbers. The figures indicate that the percentage difference between the expected pressure and measured pressure was within approximately 3%, well within the expected variation.

$$\%\, difference = \left|\frac{P_{Cascade} - P_{CFD}}{P_{CFD}}\right| \times 100\% \quad (1)$$

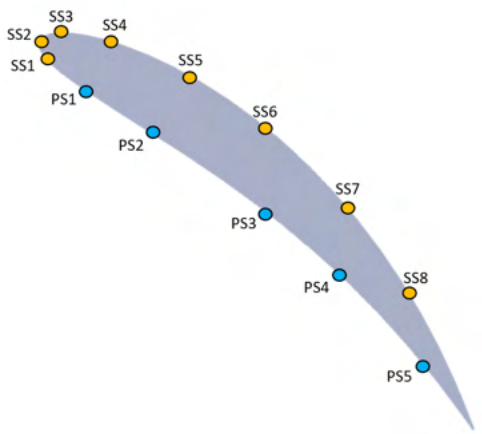

Figure 6. Generic airfoil geometry with example static tap locations.

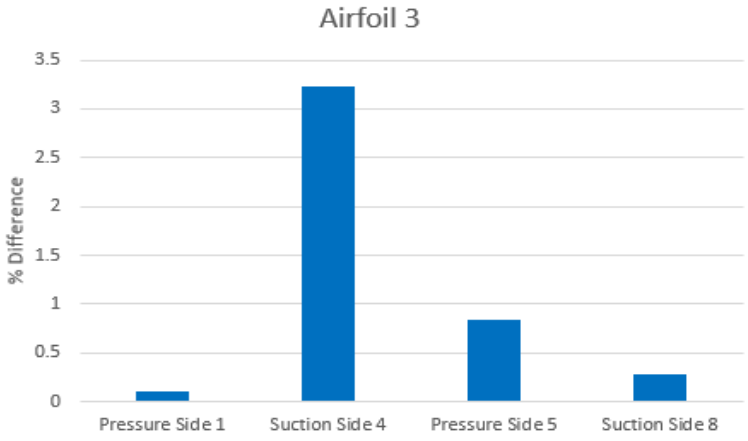

Figure 7. Percentage difference between airfoil 3 CFD and linear cascade pressure data.

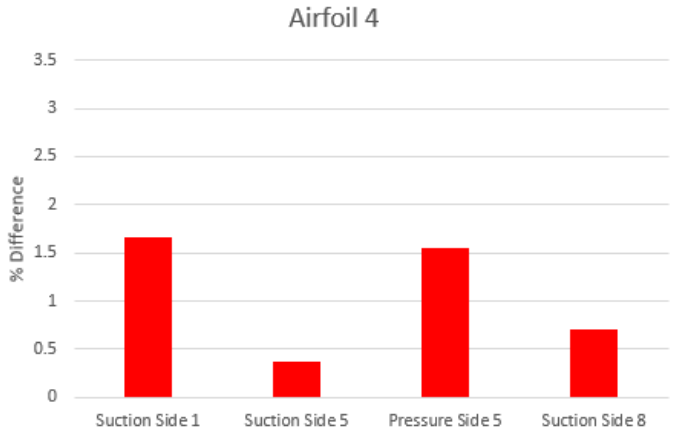

Figure 8. Percentage difference between airfoil 4 CFD and linear cascade pressure data.

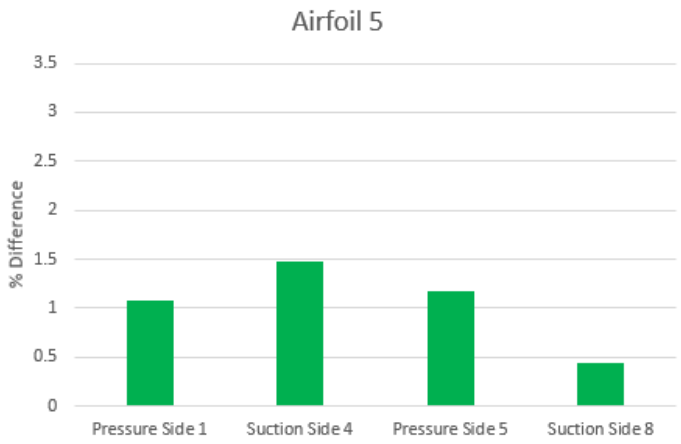

Figure 9. Percentage difference between airfoil 5 CFD and linear cascade pressure data.

With the flowfield benchmarked, we expect to begin testing cooled designs in Q1 2022 immediately after fabrication by the vendors is completed. In addition, we will use the same CT technology as that in Task 1 to evaluate the manufacturing accuracy of the microchannel features.

References

Ferster, K. K., Kirsch, K. L., & Thole, K. A. (2018). Effects of geometry, spacing, and number of pin fins in additively manufactured microchannel pin fin arrays. Journal of Turbomachinery, *140*(1). https://doi.org/10.1115/1.4038179

King, C., & Pietraszkiewicz, E. F. (2018). S-shaped trip strips in internally cooled components.

Kirsch, K. L., & Thole, K. A. (2017). Pressure loss and heat transfer performance for additively and conventionally manufactured pin fin arrays. International Journal of Heat Mass Transfer, *108*, 2502–2513.

Kirsch, K. L., & Thole, K. A. (2017). Heat transfer and pressure loss measurements in additively manufactured wavy microchannels. Journal of Turbomachinery, *139*(1). https://doi.org/10.1115/1.4034342

Wright, L. M., Fu, W. L., & Han, J. C. (2004). Thermal performance of angled, v-shaped, and w-shaped rib turbulators in rotating rectangular cooling channels (AR=4:1). Journal of Turbomachinery, *126*(4), 604–614.

Milestones

Milestone	Due Date	Estimated Date of Completion	Actual Completion Date	Status
Workplan	3/4/20	3/4/20	3/5/20	Completed
COE Meeting 1	4/1/20	4/1/20		Cancelled
COE Meeting 2	10/1/20	10/1/20	10/28-10/29/20	Completed
COE Meeting 3	10/26/21	10/26/21	10/26-10/28/21	Completed
Annual Report	12/17/21	11/22/21	11/22/21	Completed
Project Closeout	2/4/22	2/4/22		

Major Accomplishments

The major activities are as follows: (1) completion of the design of an AM version of an FAA CLEEN II airfoil; (2) fabrication of trial airfoils from two AM vendors, and down-selecting of the final vendor; (3) design, fabrication, and initial testing of linear cascade hardware. Activities 1and 2 lead directly to the completion of Task 1 in Q1 2022, and Activity 3 positions us to be able to select the top performing microchannel cooling designs in Q1-Q2 2022 for incorporation into the CLEEN II airfoil by the end of the project.

Publications
None

Outreach Efforts
Research findings were presented to Pratt & Whitney (cost-sharing partner) at bi-annual Center of Excellence review meetings on November 30, 2020 and August 19, 2021.

Awards
None

Student Involvement
Justin Wolff (currently nearing the end of his 2-year master's degree) has been responsible for analyzing CT scan data of the FAA CLEEN II blades; compiling a review package, which he presented to Pratt & Whitney; researching and designing novel cooling strategies into the linear cascade hardware; and testing linear cascade hardware to confirm the expected flowfield. Justin's role has covered all aspects of reverse engineering, AM design, fabrication, and testing.

Plans for Next Period
Fabrication of the AM version of the FAA CLEEN II airfoil will be completed in Q1 2022 and will subsequently be tested in the START turbine by using the recently developed IR thermography capability. The results will be compared with the original FAA CLEEN II cast airfoils to provide the first back-to-back comparison of cast versus AM.

The novel microchannel designs have been completed and will be fabricated in Q4 2021 through Q1 2022. They will be tested in the linear cascade in Q1 2022, and the best designs will be evaluated for incorporation into the next version of the AM FAA CLEEN II airfoil for testing in the final year of the project.

Project 057 Support for Supersonic Aircraft En-route Noise Efforts in ICAO CAEP

The Pennsylvania State University

Project Lead Investigator

Victor W. Sparrow
United Technologies Corporation Professor of Acoustics
Graduate Program in Acoustics
The Pennsylvania State University
201 Applied Science Bldg.
University Park, PA 16802
+1 (814) 865-6364
vws1@psu.edu

University Participants

The Pennsylvania State University

- PI: Vic Sparrow, United Technologies Corporation Professor, Graduate Program in Acoustics
- FAA Award Number: 13-C-AJFE-PSU Amendments 55 and 77
- Period of Performance: February 5, 2020 to February 4, 2023
- Tasks:
    1. Obtaining confidence in signatures, assessing metrics sensitivity, and adjusting for reference day conditions
    2. Assessing secondary sonic boom propagation

Project Funding Level

This project focuses on multiple tasks at The Pennsylvania State University (Penn State) and its subcontractor Queensborough Community College. The FAA funding to Penn State in 2020–2021 is $200,000. Matching funds are expected to meet cost share on both tasks. Boom Supersonic has pledged $100,000 and Gulfstream has pledged $100,000.

Investigation Team

- Victor W. Sparrow, PI (Task 1 and 2), The Pennsylvania State University
- Joshua Kapcsos, graduate research assistant (Task 1), The Pennsylvania State University
- Kimberly A. Riegel, co-investigator (Task 2), subrecipient to Penn State, Queensborough Community College, City University of New York
- Michael Rybalko, Joe Salamone, et al., Boom Supersonic [industrial partner]
- Brian Cook, Charles Etter, Gulfstream [industrial partner]

Project Overview

We are on the verge of a true revolution in passenger aircraft development. Companies such as Boom Supersonic, Gulfstream Aerospace Corporation, Lockheed Martin, Exosonic, and others are reaching the point where they can build, and deliver to users, aircraft capable of flying supersonically in an environmentally responsible way. This will allow for decreased air transportation travel times, to the great benefit of everyone.

Before introducing new supersonic aircraft, these vehicles must be certified as being quiet enough to not highly annoy the public. Preparing for such a certification process has been ongoing for several years in the FAA Office of Environment and Energy (AEE). Working with its international partners in the Committee for Aviation Environmental Protection (CAEP) of the

International Civil Aviation Organization (ICAO), FAA has been laying the groundwork for certification standards. The FAA efforts have been supported by both universities and other government agencies. Specifically, Penn State has supported FAA/AEE through Projects 8 and 24 in the PARTNER Center of Excellence (http://partner.mit.edu/) and, more recently, in Projects 7, 41, and 42 in the ASCENT Center of Excellence (https://ascent.aero/). Summaries of these research efforts can be found on the websites provided. Thus far, a group of six candidate metrics for sonic boom certification have been agreed upon in CAEP's Working Group 1 (WG1) (Noise) Supersonic Task Group (SSTG). Several schemes for certification have been generated. A few schemes have been eliminated from further consideration, and others are currently being evaluated for possible implementation. Procedures have been proposed for acquiring and processing ground measurement of the sonic boom signatures, but these remain under discussion. The extent to which atmospheric conditions will affect the measurements and the requirements and role of numerical simulations of sonic booms propagating from the aircraft to the ground are being considered. One particularly complicated part is the influence of the atmosphere creating distortions in the sonic boom signatures, due to atmospheric turbulence, and the subsequent effects on the metric values. These are just a few of the gaps that need to be filled.

All of these topics are being worked on, step by step, in FAA and in the WG1 SSTG. Recent efforts in ASCENT Project 041 support FAA with technical expertise in the development of the certification procedures and an initial understanding of secondary sonic booms. Secondary sonic booms, also known as over-the-top sonic booms, result from sound energy that travels upward at heights above the aircraft cruise altitude and land at distant locations. Secondary sonic booms are why Concorde was requested to transition from supersonic to subsonic speeds at substantial distances before entering the continental United States. ASCENT Project 041 ended in early 2021 and ASCENT Project 57 is now into its second year, but much remains to be done, as an effort lasting several more years will be required to move forward on certification standards for supersonic aircraft.

In 2022 and beyond, continued support for supersonic aircraft noise efforts will be necessary for FAA and its international partners to fill technical solution gaps and continue making progress toward certification procedures. Although other universities and industry partners continue their focus on aircraft design and landing and takeoff (LTO) studies, it is essential to continue working on the sonic boom issues as these remain the greatest barrier for environmentally responsible supersonic aircraft. ASCENT Project 57 will support the ongoing activities in ICAO CAEP and WG1 (Noise), with a focus on establishing supersonic aircraft en-route procedures and metrics for noise certification standards and will support the interface with the ICAO Air Navigation Commission to address related noise issues.

In the 2020–2023 project period, the emphasis will be on continuing support for supersonic aircraft en-route procedures. This includes the utilization of an agreed-upon reference day atmosphere, the establishment of techniques for incorporating measurement data and simulations into a draft certification procedure, and the consideration of off-design flight speed sonic booms, such as focus booms and acceleration booms. Support will also be provided for a more complete analysis of NASA's SonicBAT dataset and efforts on a methodology to remove the effects of atmospheric turbulence on measured sonic boom waveforms to support certification. The 2020–2023 research will also need to consolidate and process the results of research conducted in 2019–2020 on secondary sonic booms that is a potential noise issue for the initial supersonic airplanes. This material will be of particular interest to ICAO's Air Navigation Commission, because it could affect the operation of supersonic aircraft in the near term. The project investigator, Dr. V. Sparrow, will also be available to assist the FAA in providing expert knowledge and scientific understanding of sonic booms, as requested, and to support other CAEP committees, such as the Impacts and Science Group on their aircraft noise impacts activities.

Task 1 - Obtaining Confidence in Signatures, Assessing Metrics Sensitivity, and Adjusting for Reference Day Conditions

The Pennsylvania State University

Objective

ASCENT Project 57 is a transition from ASCENT Project 41: *Identification of Noise Acceptance Onset for Noise Certification Standards of Supersonic Airplanes*. As national aviation authorities move forward to develop noise certification standards for low-boom supersonic airplanes, several research gaps exist in the areas of signature fidelity, metrics, metrics sensitivity to real-world atmospheric effects, adjustments for reference conditions, etc. The objective of this Task is to support the FAA in the development of technical standards for civil supersonic aircraft under ICAO CAEP. This effort provides FAA with

technical noise expertise regarding the development of noise certification standards for future civil supersonic passenger aircraft, primarily in the area of en -route noise (sonic boom) minimization and/or abatement.

Task 1 in ASCENT Project 57 focuses on research initiatives needed to move toward the development of a low-boom supersonic en-route noise certification standard. An objective was to simulate the effects of turbulence within various planetary boundary layer heights above the ground and address artifacts that were found in resulting ground waveforms.

Research Approach

Background

Propagation code KZKFourier is an augmentation of the Burgers equation into a KZKFourier propagation equation to include nonlinearity, diffraction, and absorption in directional sound beams, to simulate wind and temperature fluctuation effects of the atmospheric boundary layer based on the Ostashev and Wilson (2015) model. During the 2019–2020 academic year, PCBoom 6.7.1.1 and KZKFourier were used above and within the atmospheric boundary layer, respectively, to simulate turbulence effects of atmospheric boundary layer heights of 268.2, 411.4, and 1026.7 m, corresponding to SonicBAT flight conditions. Information regarding this endeavor appears in the 2020 report for ASCENT Project 057. After propagating shaped boom signatures through 10 randomly generated atmospheres, the data were shared with WG1/SSTG/PrSG, in which zero-padding and spiking artifacts were discovered near the beginning and ends of certain ground signatures; the plots shown in the 2020 report did not span the entire retarded time domain of the ground waveform data. These artifacts may erroneously interfere with the calculation of sound-level metrics, so a focus of Task 1 was to address these artifacts.

Artifacts of KZKFourier Run

The methodology used to simulate turbulence effects of sonic boom propagation includes the use of a no-turbulence tool to propagate the sonic boom from cruise altitude to the top of the atmospheric boundary layer, followed by a turbulence tool from the top of the ABL to ground altitude, as turbulence effects are only significant within the atmospheric boundary layer. For this procedure, PCBoom 6.7.1.1 was used as the no-turbulence tool and KZKFourier was used as the turbulence tool, so the PCBoom output must be converted into KZKFourier input. Dr. Trevor Stout provided a supplemental MATLAB code in the KZKFourier code package that reads PCBoom output and converts the waveform to a file type compatible with KZKFourier input, which zero-pads the waveforms to meet a specified time interval. We discovered that, because the PCBoom output was not centered at zero pressure, it was discovered that a discontinuity occurred where it meets the zero padding, an example of which is shown below in Figure 1. The artifact propagates throughout the turbulent atmospheric boundary layer, and the resulting artifacts interfere with sound metric calculation. Zero-padding discontinuities were present both in the front and rear portions of the KZKFourier input waveform, before the first shock and after the second shock, as the supplemental code centers the PCBoom waveform within the time window. However, only the front portion zero-padding artifact was seen in the KZKFourier output (with the exception of the no-turbulence condition), because the rear portion artifact was dominated by the post-shock results of the turbulence effects as the waveforms return to zero acoustic pressure.

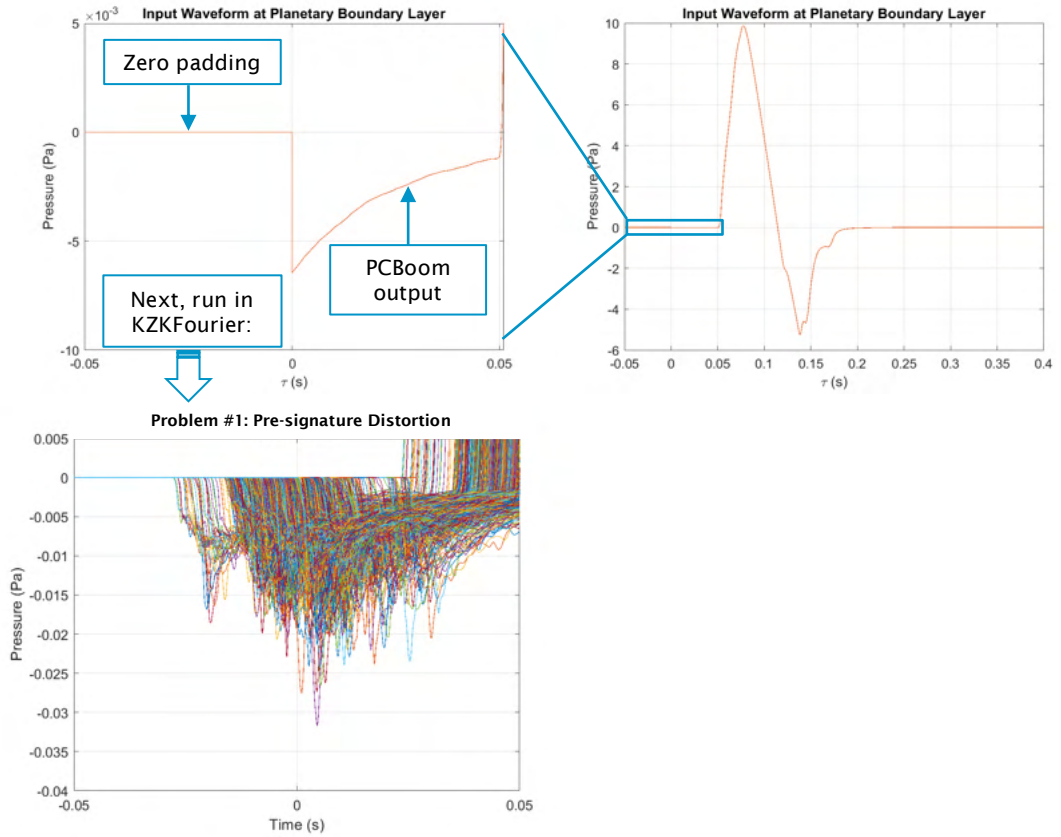

Figure 1. Plots of pre-signature distortion both before and after KZKFourier propagation through the 1026.7 m atmospheric boundary layer.

In addition to zero-padding artifacts, spiking artifacts occurred at the ends of select signatures of certain turbulence random seeds. For the ground waveforms that were propagated through a 411.38 m atmospheric boundary layer, microphones 28 through 40 (of 100) presented right-side spiking anomalies for turbulence condition 5. For waveforms that were propagated through the 1026.7 m ABL, right-side spiking anomalies were present for microphones 45 through 58 (of 100) of turbulence condition 2, as shown below in Figure 2. The spiking anomalies therefore occurred in groups of consecutive microphones and were not scattered throughout the results. None of the other turbulence conditions and respective microphones resulted in spiking anomalies. Due to improved viewing capabilities, it is known that the spiking begins near the onset of propagation at the top of the atmospheric boundary layer and distorts throughout the simulation to ground altitude, contributing to erroneous sound metrics. The cause of this spiking artifact is being further investigated.

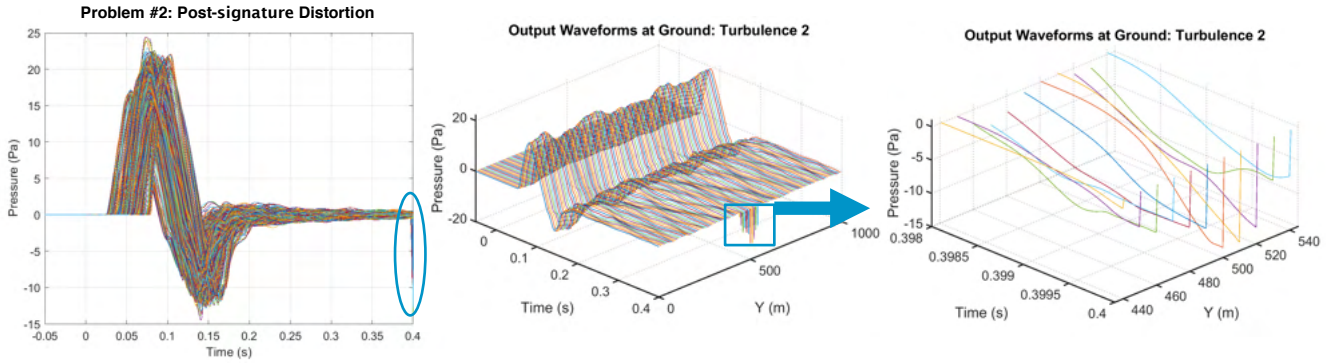

Figure 2. Plots displaying 100 different ground pressure waveforms (in pascals) for turbulence condition 2 after propagation through an atmospheric boundary layer height of 1026.7 m. Spiking artifacts are emphasized.

To circumvent the discussed artifacts, an extended cylinder file for the C609 shaped boom signature was provided by NASA and propagated through PCBoom to the top of the atmospheric boundary layer, followed by the application of a 10% taper to the ends of the KZKFourier input waveform at the top of the atmospheric boundary layer. The taper was implemented within the supplemental MATLAB code that formats the PCBoom output into a KZKFourier input. The combined use of the extended cylinder file and application of the 10% taper corrected the zero-padding artifacts just before the front shocks, which could not have been fixed by windowing alone. Additionally, the KZKFourier random seeds corresponding to turbulence conditions 2 and 5 were replaced with seeds 11 and 12 to circumvent spiking artifacts at the right ends of the waveforms. Additional time is needed to investigate the unexpected spiking at the ends of the signatures of turbulence conditions 2 and 5, corresponding to the random seeds of 2 and 5. Last, a 25% taper was implemented within the supplemental MATLAB code that reads and plots the output ground waveforms; its application to both ends of the KZKFourier output waveforms during post-processing ensured that all waveforms begin and end smoothly at zero pascals of acoustic pressure. The aggregate use of the cylinder file and both pre- and post-processing tapers is shown below in Figure 3, which resulted in more realistic sound metric calculations for use in sonic boom certification. After repeating the simulations of the original waveform database with the above changes, the resulting waveform database was made available to WG1/SSTG/PrSG.

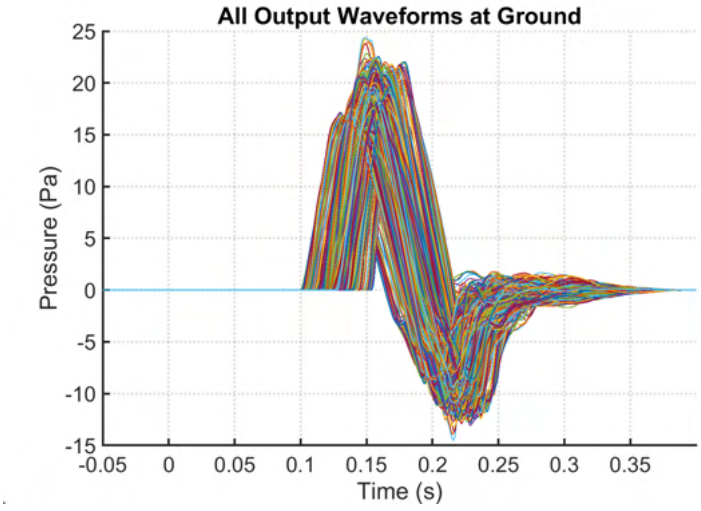

Figure 3. Plots of 1000 ground pressure waveforms (in pascals) after propagation through an atmospheric boundary layer height of 1026.7 m with extended cylinder file and pre- and post-processing tapers.

Internal Solution
The KZKFourier code includes a function called "ApplyWindow" that applies a temporal window to waveforms at each time step, ensuring that the final point of each waveform is zero. Efforts are ongoing to convert MATLAB post-processing taper to C++ for insertion within the function to prevent spiking artifacts from forming regardless of random seed.

Improved Viewing Capabilities
In order to visualize the evolution of the spiking artifact, the waveform data were converted from retarded time to real time and saved to video. A contour plot was used to display turbulence effects, as shown below in Figure 4. Within the plot, the shaped sonic boom propagates from the top of the atmospheric boundary layer to ground altitude, from left to right. The improved viewing capability of the video format helped diagnose that the spiking artifact, seen below as a dark line at the left side of the turbulence effects, does not solely appear at ground altitude but propagates throughout the simulation. This improved viewing capability will be useful in future sonic boom certification endeavors.

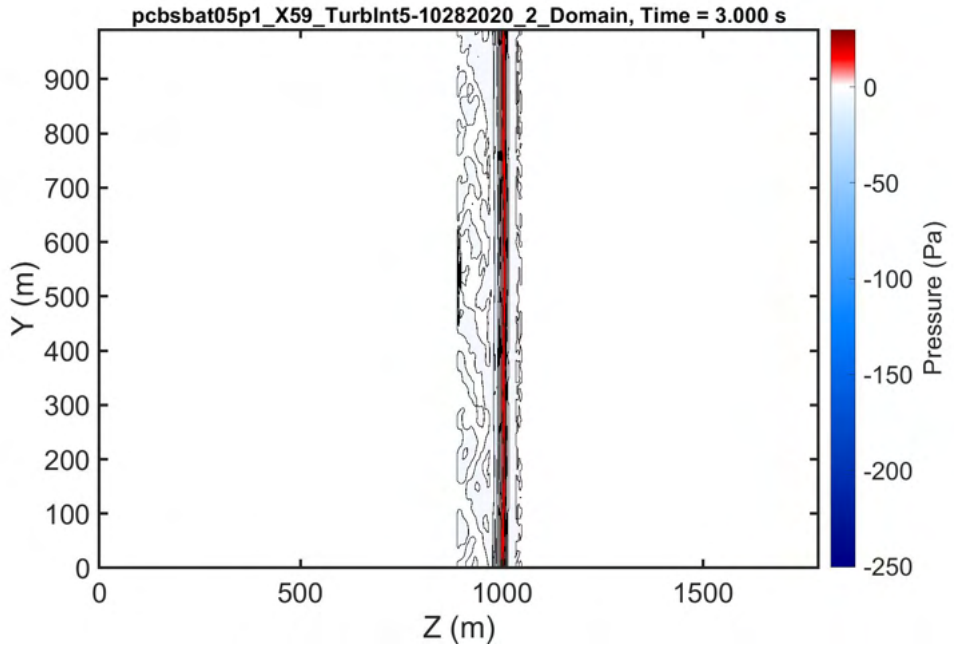

Figure 4. Still image from video of shaped sonic boom waveform progression in turbulence condition 2 from top of 1026.7 m ABL to ground.

Milestone
Pre- and post-signature distortions have been addressed and eliminated from KZKFourier output, and the resulting waveform database was made available to WG1/SSTG/PrSG.

Major Accomplishments
ASCENT Project 057 Task 1 extended the KZKFourier software methodology to eliminate artifacts from turbulized signatures, and improved visualization was used to diagnose the artifacts. The latter could be useful in viewing future simulations for use in sonic boom certification of supersonic aircraft.

Publications
Loubeau, A., Doebler, W., Wilson, S. R., Ballard, K., Coen, P. G., Naka, Y., Sparrow, V. W., Kapcsos, J., Page, J. A., Downs, R. S., Lemaire, S., & Liu, S. R. (2021). Developing certification procedures for quiet supersonic aircraft using shaped sonic boom predictions through atmospheric turbulence. The Journal of the Acoustical Society of America, 149(4), A102–A102. https://doi.org/10.1121/10.0004646

Outreach Efforts
A summary of the procedure and findings of ASCENT Project 057 were presented virtually during Acoustics in Focus, the 180th Meeting of the Acoustical Society of America. Additionally, a poster focused on Task 1 was presented during the 2021 Fall Workshop of the Penn State Center for Acoustics and Vibration.

Awards
None.

Student Involvement
Joshua Kapcsos was the Penn State graduate research assistant who worked on ASCENT Project 57 during the 2020–2021 academic year.

Plans for Next Period
Feedback is being requested from WG1/SSTG/PrSG participants on new signatures that can be produced to extend the waveform database. Additional simulations and corresponding recommendations regarding the potential sonic boom metrics for inclusion in a certification procedure will be conducted. Effort is ongoing regarding the implementation of an artifact solution within turbulence software so that all random atmospheres can be generated and used without issue.

References
Stout, T. (2018). Simulation of n-wave and shaped supersonic signature turbulent variations [Ph.D. dissertation, Pennsylvania State University].

Ostashev, V., & Wilson, D. (2015). *Acoustics in moving inhomogeneous media* (2nd ed.). CRC Press, Boca Raton, FL.

Bradley, K. A., Hobbs, C. M., Wilmer, C. B., Sparrow, V. W., Stout, T. A., Morgenstern, J. M., Underwood, K. H., Maglieri, D. J., Cowart, R. A., Collmar, M. T., Shen, H., & Blanc-Benon, P. (2020). Sonic booms in atmospheric turbulence (SonicBAT): The influence of turbulence on shaped sonic booms (Report No. NASA/CR-2020-220509). National Aeronautics and Space Administration, Armstrong Flight Research Center, Edwards, CA.

Loubeau, A., Doebler, W., Wilson, S. R., Ballard, K., Coen, P. G., Naka, Y., Sparrow, V. W., Kapcsos, J., Page, J. A., Downs, R. S., Lemaire, S., & Liu, S. R. (2021). Developing certification procedures for quiet supersonic aircraft using shaped sonic boom predictions through atmospheric turbulence. The Journal of the Acoustical Society of America, 149(4), A102–A102. https://doi.org/10.1121/10.0004646

Task 2 - Assessing Secondary Sonic Boom Propagation
The Pennsylvania State University
Queensborough Community College, City University of New York

Research Approach
PCBoom Comparison
NASA recently released a new version of PCBoom, 7.1.0; the previous version was 6.7.1.2. To ensure that there were no substantial changes between code versions, a comparison run was completed. No substantial differences were observed. In addition, runs were made to determine the correct runtime earth mode that should be used between the options of Flat, Ellipse and Spherical Comparison. No substantial differences were observed between the different modes, so all simulations were made using the Flat earth approximation.

Seattle Concorde Results
To better understand how secondary booms behave for the U.S. Pacific Northwest, arrival locations were modeled covering the years 2016 and 2018 for all 12 months of the year, with an average weather profile for each month. We looked for similarities in impact behavior compared with the impact for the southwestern coast of the United States. This simulation used a trajectory simulating a typical flight path for a commercial aircraft arriving at Seattle from Tokyo. The aircraft is slowing from Mach 2.0 to Mach 1.18, similar to the speeds modeled for an LAX approach. The Concorde pressure information built into PCBoom was used as if Concorde were flying today. Meteorological data for 2016 and 2018 were obtained using the CFS v2 database. The profiles for January, a typical winter month, are shown for both years in Figure 5, and profiles for July, a typical summer month, are shown for both years in Figure 6. The profiles show that differences between the summer and winter months are largely in the upper atmospheric winds. These wind directions were consistent between 2016 and 2018. The ray arrival locations for the arriving Seattle flight for a typical winter month in 2016 and 2018 are shown in Figure

7 and those for a typical summer month are shown in Figure 8. It is clear from Figures 7 and 8 that there are no secondary sonic boom arrivals in the summer months, but there are secondary arrivals of both Type 1 and Type 2 secondary sonic booms in the winter months. These only impact the coastline for some of the winter months. Figure 9 shows the ray arrivals for December 2016 as an example. Due to the atmospheric conditions in the Pacific Northwest, the secondary sonic booms are present for the winter months and absent in the summer months. The direct impact on the coastline is highly dependent on the weather profile and the heading angle of the trajectory. In general, this is opposite from what we saw for East Coast simulations, where the secondary sonic booms were predominantly present during the summer months. Hence, we can conclude that these secondary sonic booms would be expected to occur every winter on an annual basis if Concorde were still flying.

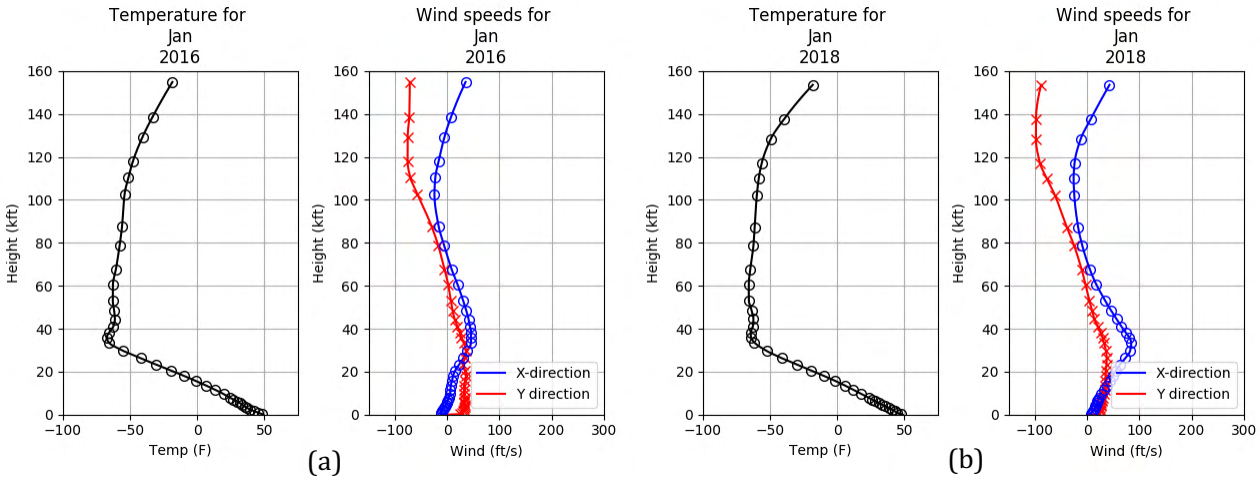

Figure 5. The monthly average temperature and wind speed profiles for January in Seattle for (a) 2016, and (b) 2018.

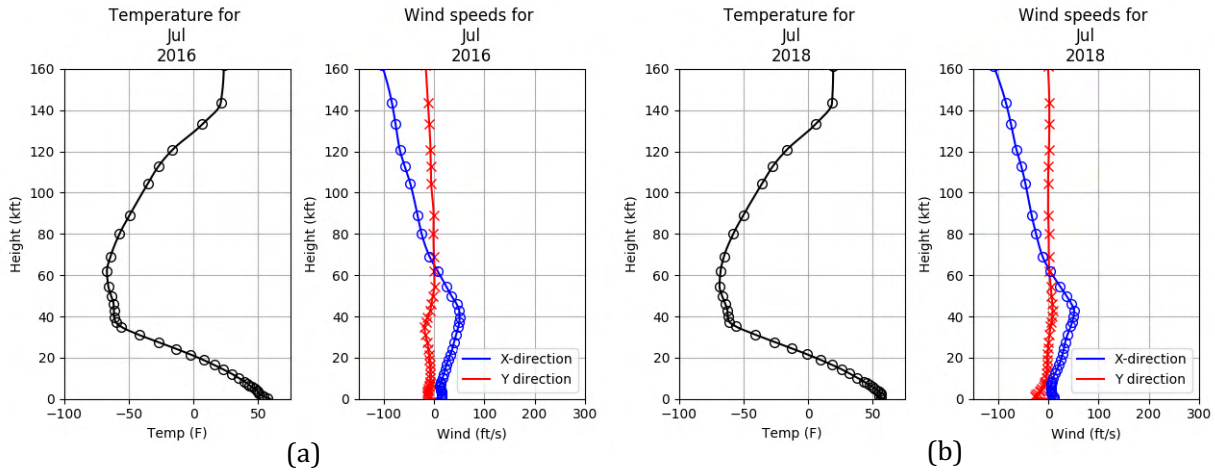

Figure 6. The monthly average temperature and wind speed profiles for July in Seattle for (a) 2016, and (b) 2018.

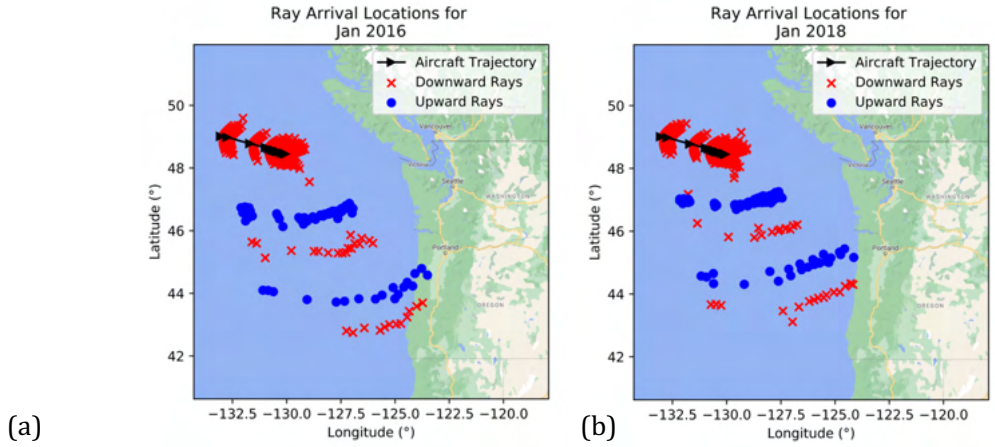

(a) (b)

Figure 7. Ray arrival locations for a hypothetical Concorde aircraft approaching Seattle in January in (a) 2016, and (b) 2018.

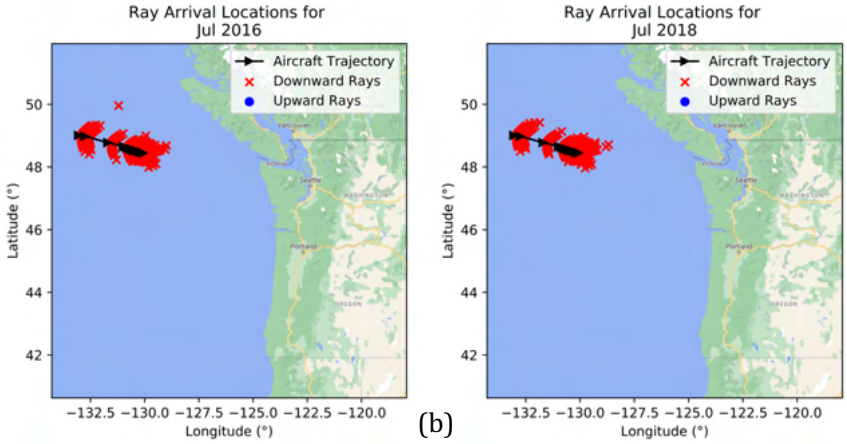

(a) (b)

Figure 8. Ray arrival locations for a hypothetical Concorde aircraft approaching Seattle in July in (a) 2016, and (b) 2018.

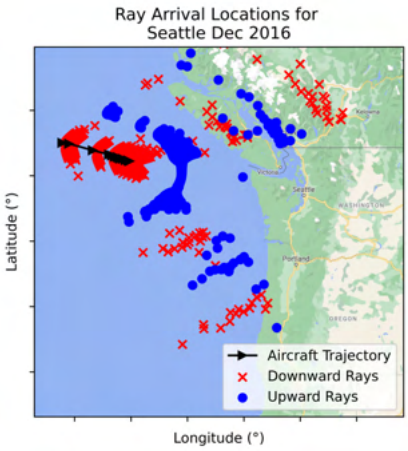

Figure 9. Ray arrival locations for a hypothetical Concorde aircraft approaching Seattle in December 2016.

Trajectory Dependence

To better understand the impact of the trajectory on the resulting secondary sonic boom arrivals on the coastline, the speed and heading of the trajectory were varied. The weather conditions used for all the trajectory simulations were the average monthly weather profiles for the year 2018, and the Concorde was used as the example aircraft. The first variable examined was trajectory speed, simulating three steady flight conditions. Then the dependence on trajectory heading was examined to determine the effect.

Trajectory Speed

Previously, all simulations were conducted with the trajectory speed profile of a decelerating aircraft. The case of steady flight was examined for Mach 2.0, Mach 1.5, and Mach 1.18. Figure 10 shows arrivals for each of the three steady flight conditions during January, a typical winter month. In this figure, it should be noted that there are no secondary boom arrivals for any of the steady-state flights and that the primary carpet is not observed for the Mach 1.18 condition, which indicates that it is flying in a Mach cutoff condition. Figure 11 shows arrivals for the steady flight conditions for a typical summer month. It should be noted that the Mach 1.18 flight is still flying at Mach cutoff but secondary arrivals are present in all three trajectories.

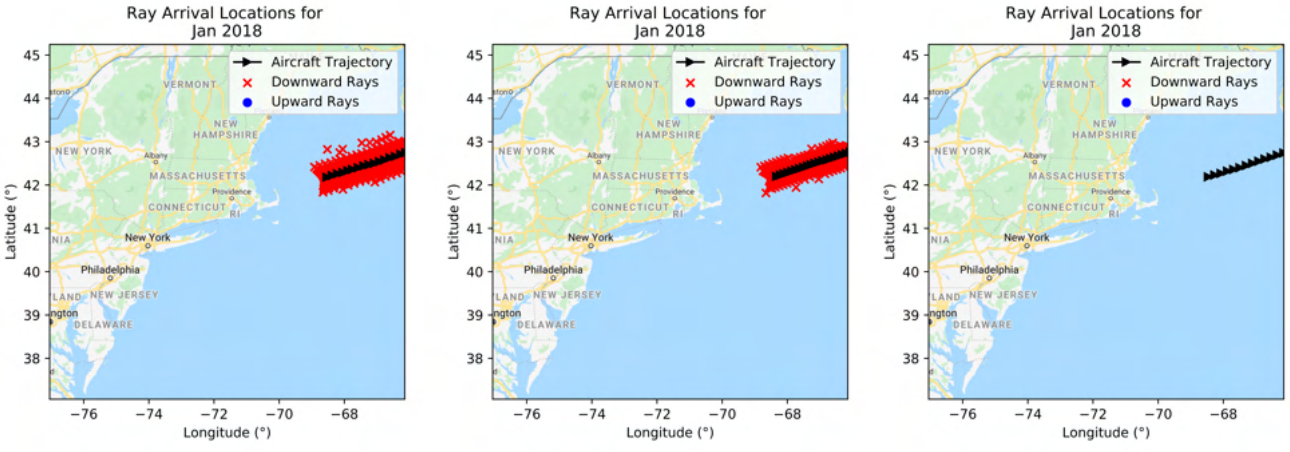

Figure 10. Secondary sonic boom arrival locations for three steady flight conditions: (a) Mach 2.0, (b) Mach 1.5, and (c) Mach 1.18 during a typical winter month.

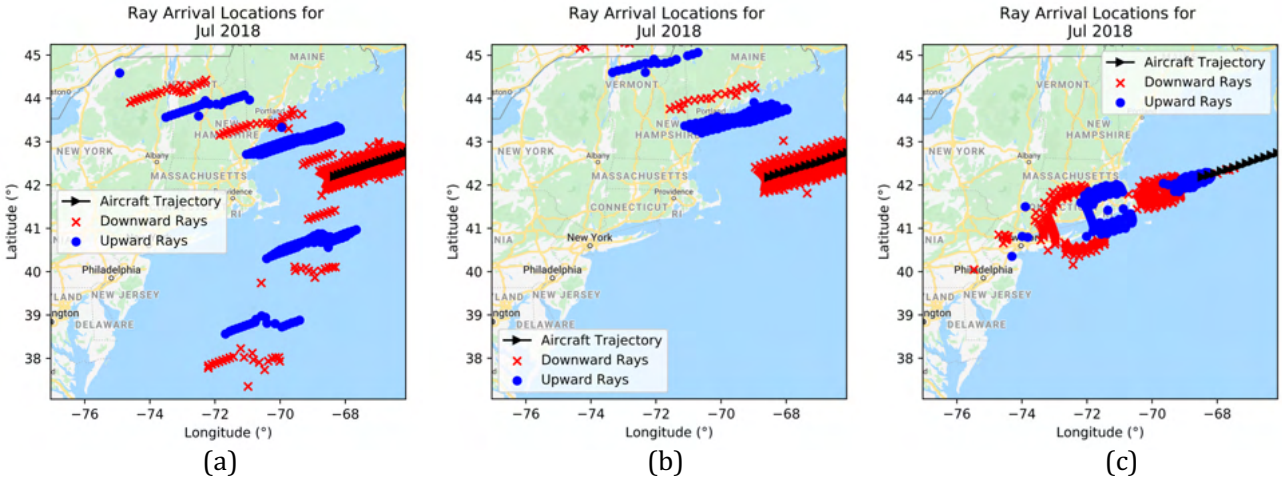

Figure 11. Secondary sonic boom arrival locations for three steady flight conditions: (a) Mach 2.0, (b) Mach 1.5, and (c) Mach 1.18 for a typical summer month.

Heading Angle

Six heading angles were considered to understand the effect of heading on resulting secondary sonic boom arrivals. A hypothetical Concorde flying a steady speed of Mach 2.0 was considered for headings 0°, 70°, 135°, 180°, 250°, and 315°, where 0° is due north. Weather data for 2018 obtained using the CFS v2 database was used for the atmospheric data. Figure 12 shows the results for January, a typical winter month. Although there are secondary sonic boom arrivals during the winter months for headings away from the coastline, they are mostly located over the ocean and are not expected to impact the coastline. Figure 13 shows the arrival locations for July, a typical summer month. The headings traveling toward the coastline create secondary sonic booms that impact the coastline, including the headings due north and south.

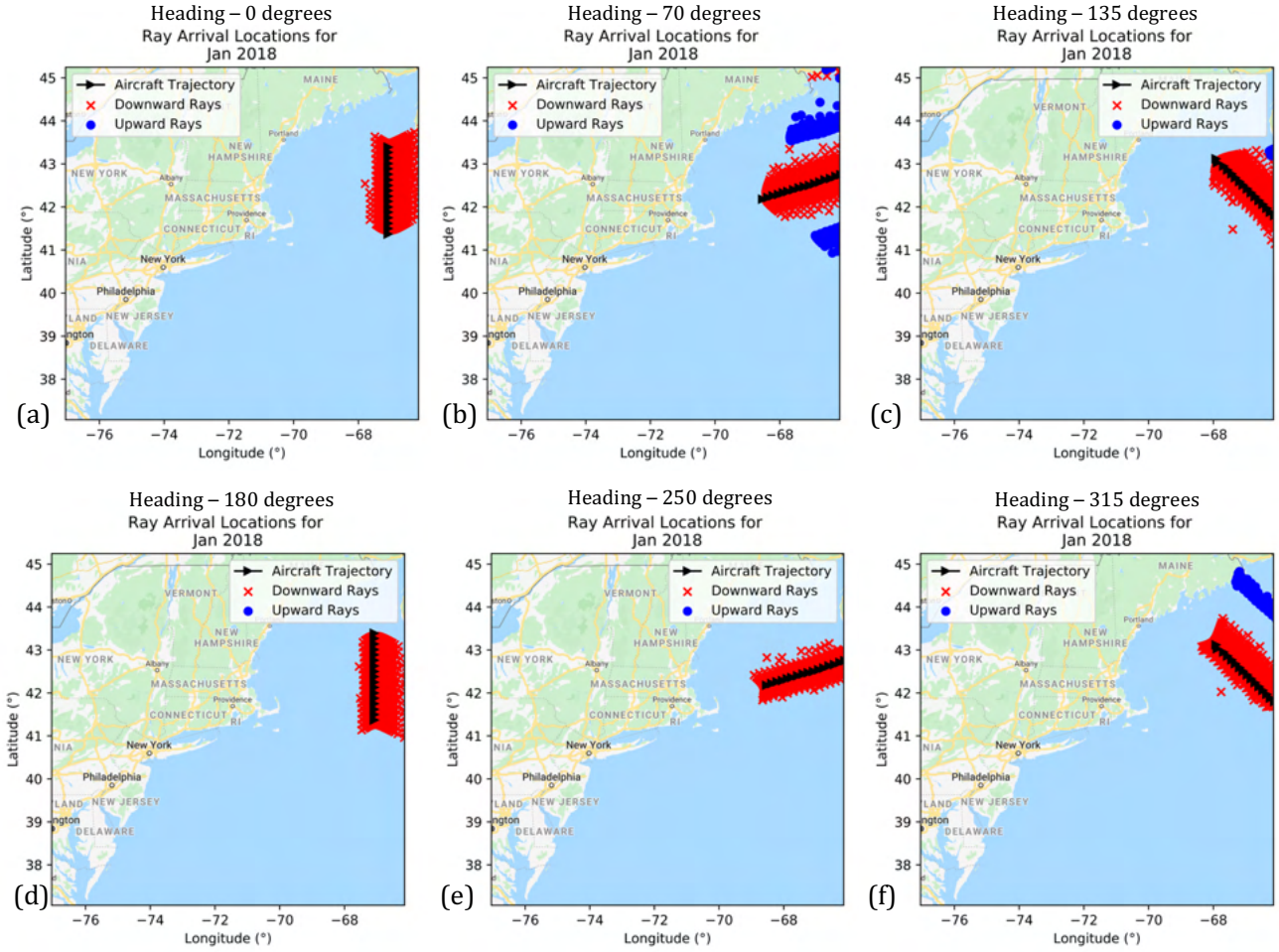

Figure 12. Ray arrival locations for a hypothetical Concorde aircraft approaching New York City at a steady speed at headings of (a) 0˚, (b) 70˚, (c) 135˚, (d) 180˚, (e) 250˚, and (f) 315˚ in January 2018.

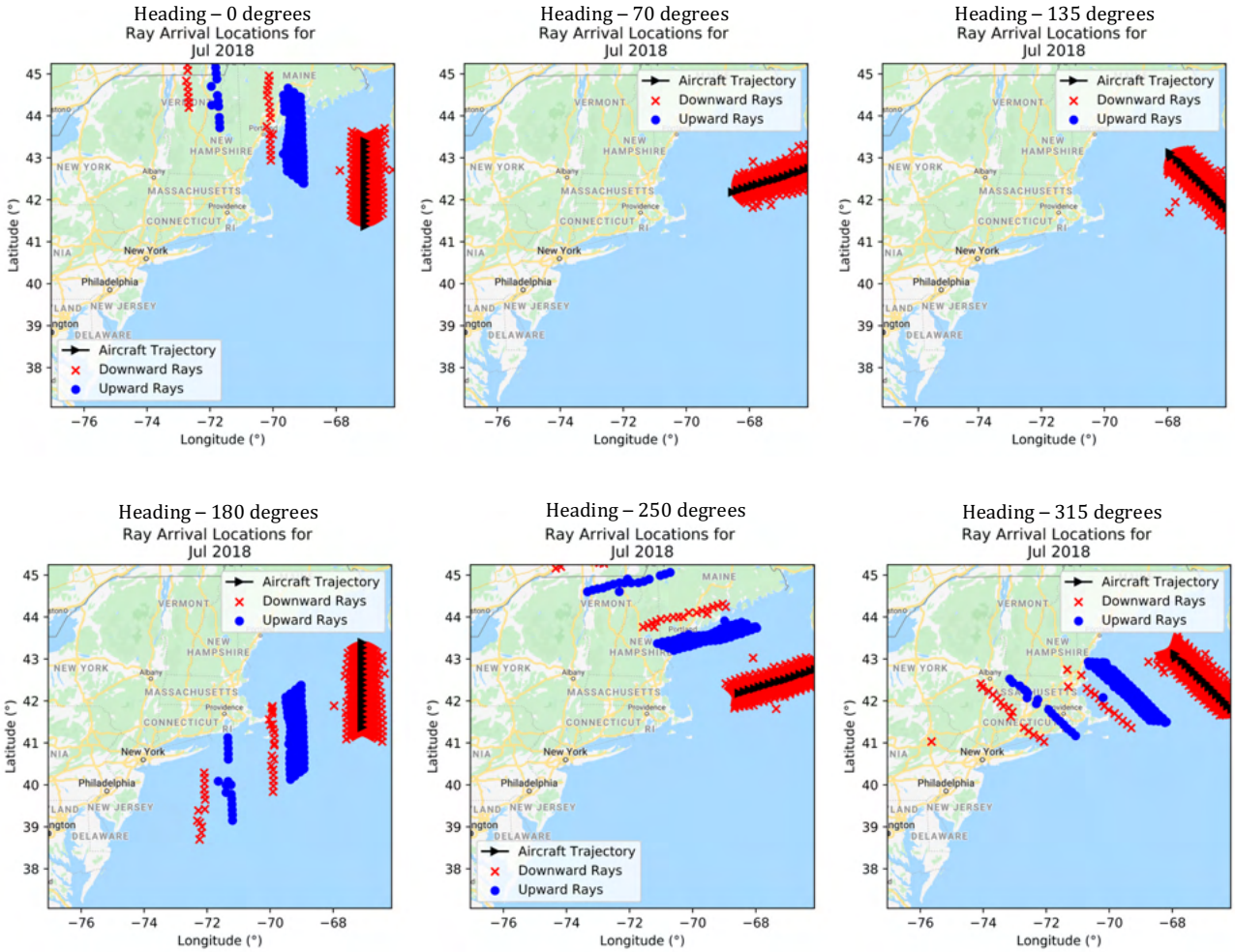

Figure 13. Ray arrival locations for a hypothetical Concorde aircraft approaching New York City at a steady speed of (a) 0˚, (b) 70˚, (c) 135˚, (d) 180˚, (e) 250˚, and (f) 315˚ in July 2018.

Trajectory and Caustic Checks

The acoustic pressure signatures from the secondary sonic booms are still not well characterized. To understand the nature of pressure calculations, the first step is to better understand the caustic predictions. A caustic occurs when the ray tube area goes to zero or when the rays cross. To better understand the nature of the trajectories, simulations for the Rickley and Pierce conditions were made with PCBoom. The trajectories were then plotted, and the ray crossing locations were identified. These ray crossing locations were then compared with the PCBoom-predicted caustic locations. There were some discrepancies in the locations of the ray crossings between the plotted trajectories and the PCBoom-predicted locations. This task is still in progress and determining the cause of the discrepancies requires further investigation.

Milestone

Secondary sonic boom results are now available for the U.S. Pacific Northwest coast for the first time.

Major Accomplishments

ASCENT Project 057 Task 2 extended our knowledge of secondary booms impacting coastlines; now the project can make secondary boom predictions for different arrival angles and speeds. The study of caustics and their effects on the acoustic pressure signatures was initiated.

Publications
A manuscript providing an overview of secondary sonic boom studies for U.S. coastlines was approved by FAA and is now under review for *The Journal of the Acoustical Society of America*.

Outreach Efforts
None.

Awards
None.

Student Involvement
None.

Plans for Next Period
In Task 2, we will continue to work toward accurate acoustic signatures for secondary sonic booms, which is essential in order to assess community impact.

References
Plotkin, K., Page, J., & Haering, E. (2007). Extension of PCBoom to over-the-top booms, ellipsoidal earth, and full 3-D ray tracing [Presentation]. 13th AIAA/CEAS Aeroacoustics Conference.

Rickley, E. & Pierce, A. (1980). Detection and assessment of secondary sonic booms in New England (Report No. FAA-AEE-80-22). Defense Technical Aviation Center, Fort Belvoir, VA.

Saha, S., Moorthi, S., Wu, X., Wang, J., Nadiga, S., Tripp, P., Behringer, D., Hou, Y.-T., Chuang, H., Iredell, M., Ek, M., Meng, J., Yang, R., Mendez, M. P., van den Dool, H., Zhang, Q., Wang, W., Chen, M., & Becker, E. (2014). The NCEP Climate Forecast System Version 2. Journal of Climate, *27*, 2185-2208. https://doi.org/10.1175/JCLI-D-12-00823.1

Project 058 Improving Policy Analysis Tools to Evaluate Higher-Altitude Aircraft Operations

Massachusetts Institute of Technology

Project Lead Investigator

PI: Steven R. H. Barrett
Professor of Aeronautics and Astronautics
Director, Laboratory for Aviation and the Environment
Massachusetts Institute of Technology
77 Massachusetts Ave, Building 33-322, Cambridge, MA 02139
(617) 452-2550
sbarrett@mit.edu

Co-PI: Dr. Sebastian D. Eastham
Research Scientist
Laboratory for Aviation and the Environment
Massachusetts Institute of Technology
77 Massachusetts Ave, Building 33-322, Cambridge, MA 02139
seastham@mit.edu

University Participants

Massachusetts Institute of Technology

- P.I.: Prof. Steven R.H. Barrett
- FAA Award Number: 13-C-AJFE-MIT, Amendment Nos. 064 and 089
- Period of Performance: Feb. 5, 2020 to Aug. 31, 2022
- Reporting Period: Oct. 1, 2020 to Sep. 30, 2021
- Tasks (Note: Tasks not covered during this reporting period are listed as "*pending*" and are discussed further only in the context of tasks for the coming period of performance):
    1. Develop a set of emissions scenarios for high-altitude aviation.
    2. Extend and validate the Massachusetts Institute of Technology's (MIT) existing atmospheric simulation capabilities.
    3. Simulate atmospheric impacts of high-altitude emissions using updated capabilities.
    4. Convert estimated impacts into sensitivities.
    5. Develop and update operational tools capable of quantifying environmental impacts of aviation.
    6. Develop parameterization of contrails.
    7. Evaluate the evolution of aviation nitrogen oxides (NO_x) impacts on climate and air quality [*pending*].

Project Funding Level

$650,000 in FAA funding and $650,000 in matching funds. Sources of matching funds are approximately $132,000 from MIT, plus third-party in-kind contributions of $391,000 from NuFuels LLC, and $127,000 from Savion Aerospace Corp.

Investigation Team

Principal Investigator:	Prof. Steven Barrett (MIT) (all tasks)
Co-Principal Investigator:	Dr. Sebastian Eastham (MIT) (all tasks)
Postdoctoral Researcher:	Dr. Sadia Afrin (MIT) (all tasks)
Graduate Research Assistants:	Inés Sanz-Morère (MIT) (Tasks 1–4)
	Jeong Suk Oh (MIT) (Tasks 3-4)
	Joonhee Kim (MIT) (Tasks 5–6)

Project Overview

Companies are proposing, developing, and testing aircraft operating at higher altitudes, such as commercial supersonic aircraft and high-altitude, long-endurance (HALE) unmanned aerial vehicles. These aircraft offer the potential to enable new use cases and business models in the aviation sector. However, the combustion emissions of these vehicles will have atmospheric impacts that differ from those of conventional subsonic aviation due to the higher altitudes of emission. Emissions at higher altitudes are associated with a different chemical environment, longer emission lifetimes, and greater distances over which the emissions will be transported. Furthermore, new developments in emissions impact estimation have enabled a more nuanced view of the environmental consequences of conventional aircraft activity. This includes recognition that both their climate and air quality impacts vary depending on the prevailing conditions of the emission and the time horizon of the assessment.

In this project, we propose to quantify the environmental consequences of such high-altitude aviation emissions. For this purpose, we will perform high-fidelity atmospheric simulations by further developing and applying the GEOS-Chem UCX tropospheric-stratospheric chemistry-transport model and its adjoint. The results will be leveraged to (1) evaluate the climate (radiative forcing) effects of high-altitude aircraft emissions; and (2) estimate the sensitivity of the global ozone column and surface air quality to these emissions. As a result, the climate, air quality, and ozone impacts for a small number of different proposed supersonic aircraft designs and performance characteristics will be quantified. We will also perform a historical assessment of the impacts of aviation emissions, quantifying how factors such as changing emissions indices and an evolving chemical background have affected—and will affect—the total impacts. Using data from these simulations, a flexible, rapid approach for assessing the impacts of sub- and supersonic aircraft will be presented.

Task 1 - Develop a Set of Emissions Scenarios for High-Altitude Aviation

Massachusetts Institute of Technology

Objective

The objective of this task is to develop emissions inputs that cover scenarios relevant to near-future aviation, extending impact estimation to cover a range of altitudes exceeding those of current commercial airline activities. The specific focus of the work during this period was to develop global supersonic emissions inventories including variations in cruise altitude, Mach number, engine NO_x emissions index, and fuel sulfur content.

Research Approach

To achieve the goals outlined above, a mathematical model is needed that can produce an estimate of emissions of key chemical species (NO_x, sulfur oxides [SO_x], water vapor, soot, etc.) resulting from a single flight. The team incorporated work from the ASCENT Project 47 engine model into a simplified supersonic civil aircraft performance model to estimate the distribution of emissions along a supersonic aircraft flight path. This was combined with a market model to produce a set of reasonable global emissions inventories for supersonic aircraft, including different assumptions regarding cruise altitude and engine NO_x emissions index. This inventory will be used as a central case for evaluation of supersonic aircraft emissions environmental impacts using the updated APMT model. An ongoing, second objective is to generate a second inventory using the ASCENT Project 10 aircraft design data, enabling comparison of impacts resulting from different assumptions (and therefore different inventories).

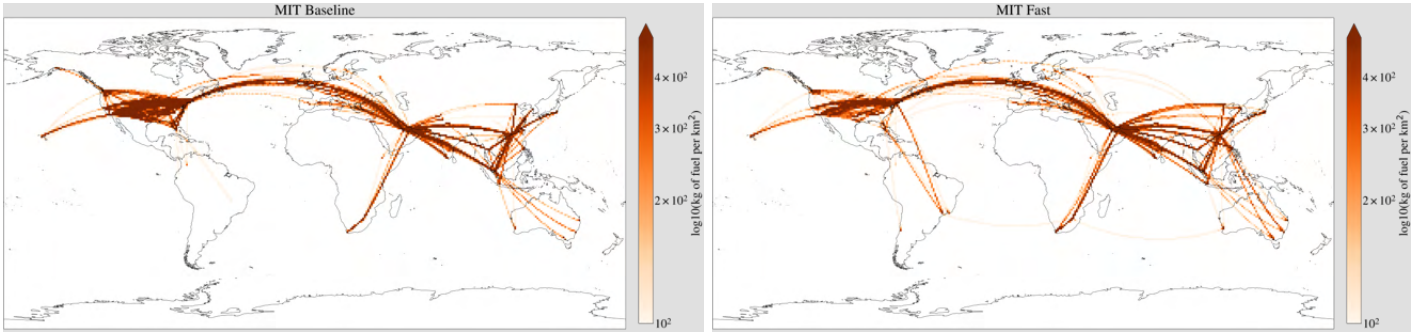

Figure 1. Emissions maps for representative supersonic aircraft developed at Massachusetts Institute of Technology for a baseline (left) and "fast" (right) case.

Milestones

- Multiple emissions datasets were generated from the supersonic aircraft engine design developed by ASCENT Project 47, as well as the emissions inventory developed by the ASCENT Project 10 supersonic fleet results.
- Emissions maps for representative supersonic aircraft were generated (Figure 1).

Major Accomplishments

- A supersonic aircraft performance and design model capable of producing global emissions inventories was finalized.
- Emissions inventories for several different representative supersonic aircraft have been estimated.
- Emissions inventories were provided to ASCENT Project 22 to enable comparison of estimated impacts using multiple different models.

Publications

None.

Outreach Efforts

Progress on all tasks was communicated during biweekly briefing calls with the FAA and reported in quarterly progress reports.

Awards

None.

Student Involvement

During the reporting period of academic year (AY) 2020/21, the MIT graduate student involved in this task was Inés Sanz-Morère.

Plans for Next Period

Task 1 was largely completed in AY 2020/21. The team will continue testing, refining, and comparing the global emissions datasets in AY 2021/22.

References

Not applicable.

Task 2 - Extend and Validate MIT's Existing Atmospheric Simulation Capabilities

Massachusetts Institute of Technology

Objective

The objective of Task 2 is to extend and validate MIT's existing atmospheric simulation capabilities, with the specific goal of ensuring that impacts on critical metrics of air quality and climate can be accurately represented. During AY 2020/21, the team developed and tested a higher-resolution version of the GEOS-Chem UCX tropospheric-stratospheric global chemistry-transport model to capture localized effects.

Research Approach

The team is using the GEOS-Chem UCX tropospheric-stratospheric global chemistry-transport model as the central tool to quantify climate, air quality, and ozone impacts resulting from high-altitude aviation (Eastham et al., 2014). It is therefore necessary to evaluate the capabilities of this model for these purposes and to extend those capabilities where necessary. Two major subtasks have been identified: Task 2a, increasing the resolution of the model to capture localized impacts at a global resolution of 2˚×2.5˚ or equivalent; and Task 2b, implementing a technique to estimate stratospherically adjusted radiative forcing (RF), rather than instantaneous RF. Task 2b was largely completed in AY 2019/20, whereas Task 2a work was completed in AY 2020/21.

The team modified GEOS-Chem v11 (UCX) to ensure that simulations could be successfully completed at the increased resolution. Although GEOS-Chem has previously been used at these resolutions, the focus has been on surface quantities (e.g., air quality); it was for this reason that the increased horizontal resolution was desired. Model viability and capability with regards to stratospheric chemistry had not been evaluated at the higher resolution. Figure 2 compares performance of the GEOS-Chem model at the increased resolution in terms of comparison to satellite observations of total ozone column, a diagnostic of the model's ability to simulate stratospheric composition. Compared to the results at the coarser 4˚×5˚ resolution (Figure 3), the 2˚×2.5˚ simulation is again able to simulate the key features of the stratospheric ozone cycle. Although a general positive bias remains, we find that the higher-resolution simulations also produce a more accurate (deeper) ozone hole in the Antarctic spring.

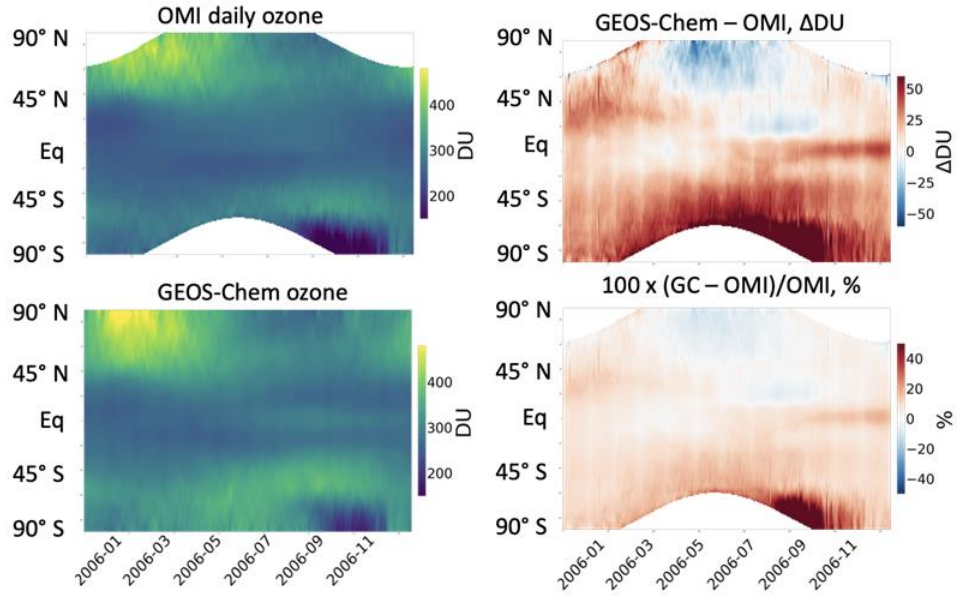

Figure 2. Global total ozone column for each day in 2006 and at each latitude. Top left: observations from the Ozone Mapping Instrument (OMI). Bottom left: simulated totals from a simulation performed at a resolution of 2˚×2.5˚ using GEOS-Chem. Top right: absolute differences between simulations and observations. Bottom right: relative differences between simulations and observations. DU = Dobson units.

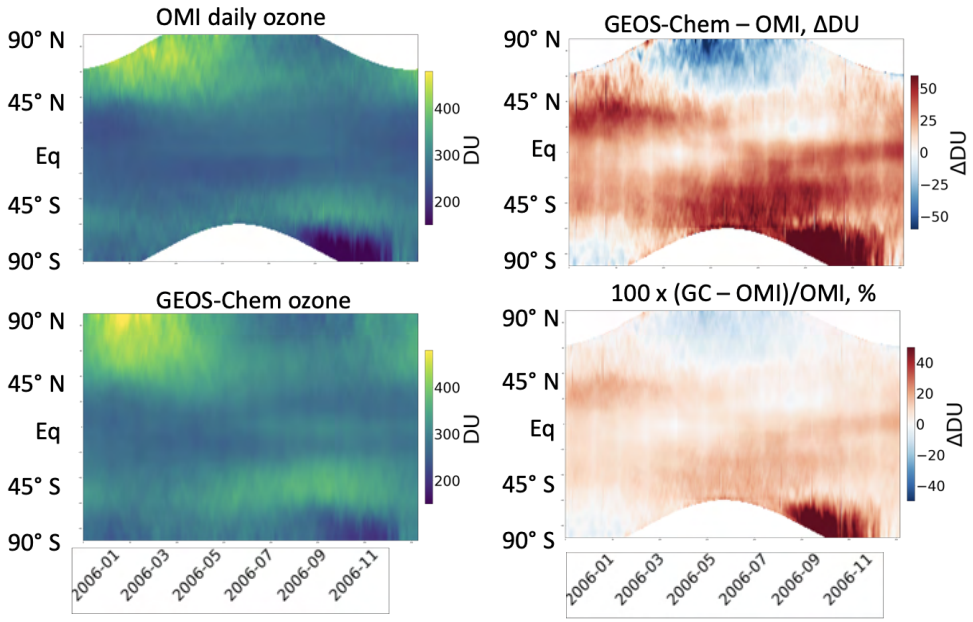

Figure 3. Global total ozone column for each day in 2006 and at each latitude. Top left: observations from the Ozone Mapping Instrument (OMI). Bottom left: simulated totals from a simulation performed at a horizontal resolution of 4˚×5˚ using GEOS-Chem. Top right: absolute differences between simulations and observations. Bottom right: relative differences between simulations and observations. DU = Dobson units.

Milestones

- GEOS-Chem simulation resolution was increased from 4˚×5˚ to 2˚×2.5˚ globally (Task 2a).
- GEOS-Chem simulation results at both resolutions were compared with observational data (Task 2a).

Major Accomplishments

A manuscript was submitted for review that used the new stratospherically adjusted radiative forcing calculations to evaluate the impacts of supersonic civil aviation on the environment.

Publications

Eastham, S. D., Fritz, T., Sanz-Morère, I., Prashanth, P., Allroggen, F., Prinn, R. G., Speth, R. L., & Barrett, S. R. H. (2021). *Atmospheric impacts of a near-future supersonic aircraft fleet: An evaluation of climate forcing resulting from a near-future supersonic aircraft fleet* [Manuscript submitted for publication].

Outreach Efforts

Progress on all tasks was communicated during biweekly briefing calls with the FAA and reported in quarterly progress reports.

Awards

None.

Student Involvement

During the reporting period of AY 2020/21, the MIT graduate students involved in this task were Inés Sanz-Morère and Jeong Suk Oh.

Plans for Next Period

Task 2 was completed in AY 2020/21.

References

Eastham, S. D., Weisenstein, D. K., & Barrett, S. R. H. (2014). Development and evaluation of the unified tropospheric–stratospheric chemistry extension (UCX) for the global chemistry-transport model GEOS-Chem. Atmospheric Environment, *89*, 52–63.

Task 3 - Simulate Atmospheric Impacts of High-Altitude Emissions Using Updated Capabilities

Massachusetts Institute of Technology

Objective

The objective of this task is to estimate the atmospheric response to the representative near-future aviation scenarios described in Task 1, and to convert the raw model outputs to impacts. These simulations will calibrate the simulated impacts and performance of the new version of the Aviation environmental Portfolio Management Tool – Impacts (APMT-I).

Research Approach

Specific outcomes to be investigated for each scenario are changes to the global ozone column; changes to the global average and Northern Hemispheric ozone layer; effects on polar ozone depletion; changes in surface air quality, including ozone and fine particulate matter ($PM_{2.5}$); changes in UV-B radiation reaching the surface; and total induced radiative forcing. This will extend to limited-scale health impact evaluation, quantifying the human and economic impact of changes in radiative forcing and surface air quality. These outcomes will be estimated by performing simulations with the GEOS-Chem UCX model at the enhanced global resolution of 2˚×2.5˚. Comparing the simulated impacts of different supersonic emissions scenarios will enable us to deduce the sensitivity of environmental impacts to changes in supersonic fleet parameters.

Milestone

With the inputs and modeling capabilities now ready, simulations for evaluating the atmospheric response from supersonic emissions scenarios have begun.

Major Accomplishments

GEOS-Chem simulations using the supersonic emissions inventory developed by MIT and informed by the ASCENT Project 47 engine design have started. The emissions inventory developed by the ASCENT 10 supersonic aircraft design team have also begun processing for simulation with GEOS-Chem.

Publications

None.

Outreach Efforts

Progress on all tasks was communicated during biweekly briefing calls with the FAA and reported in quarterly progress reports.

Awards

None.

Student Involvement

During the reporting period of AY 2020/21, the MIT graduate students involved in this task were Inés Sanz-Morère and Jeong Suk Oh.

Plans for Next Period

During the next project period, the project team will generate and refine the outputs of atmospheric responses to representative supersonic aircraft emissions and use the results to test APMT-IC. These estimates will also calibrate the climate, air quality, and ozone impacts sensitivities developed in Task 4 using GEOS-Chem simulations.

References

Not applicable.

Task 4 - Convert Estimated Impacts into Sensitivities

Massachusetts Institute of Technology

Objective

The objective of this task is to convert the impacts calculated under Task 3 for each scenario into sensitivities of environmental impacts with regards to key parameters. This will then support the operationalization of emissions impacts estimation in Task 5.

Research Approach

Two approaches are being taken in this task. First, a number of different supersonic aircraft emissions scenarios are to be simulated using the updated GEOS-Chem model, covering different assumptions regarding the aircraft fleet (e.g., NO_x emissions index, cruise Mach number). Differences in outcomes from these simulations will provide an estimate of the sensitivity of environmental impacts with respect to variations in these parameters.

Second, we will investigate the use of a gridded sensitivity approach consistent with that used in prior iterations of APMT. This will require a set of GEOS-Chem simulations in which representative perturbations of a species are included over a predefined region, with these regions defined based on a literature review. Changes in model output (i.e., air quality, ozone column, radiative forcing etc.) will be taken as the sensitivity of that output to an emission anywhere within the source region. By covering the full range of target altitudes, a gridded sensitivity map can be reconstructed where changes in gridded outputs can be evaluated through element-wise multiplication of the sensitivities with a gridded aircraft emissions distribution.

Consistency between the two approaches will be evaluated by calculating impacts for each of the MIT inventories using both methods and quantifying differences. Where necessary, additional simulations will be performed to refine the regions for which sensitivities are calculated.

Milestones

- A preliminary set of target regions for perturbations was identified.
- Simulations in GEOS-Chem to evaluate the atmospheric responses to representative perturbations in each region for each key species have begun.

Major Accomplishments

- Emissions files required to generate sensitivity matrices from GEOS-Chem simulations were generated.
- Perturbation emissions files have been prepared and initialized. This will generate the preliminary climate and air quality sensitivity arrays which will quickly evaluate impacts from emissions in varying altitudes and regions.

Publications

None.

Outreach Efforts

Progress on all tasks was communicated during biweekly briefing calls with the FAA and reported in quarterly progress reports.

Awards

None.

Student Involvement

For the AY 2020/21reporting period, graduate students Inés Sanz-Morère and Jeong Suk Oh were involved with this task.

Plans for Next Period

During the next project period, the project team will generate both scenario-specific and gridded sensitivity data to account for variations in altitude, latitude, and season. The team will also estimate uncertainty bounds for these sensitivities.

References

Not applicable.

Task 5 - Develop and Update Operational Tools Capable of Quantifying Environmental Impacts of Aviation

Massachusetts Institute of Technology

Objective

The objective of this task is to operationalize the results of Tasks 1 to 4. The eventual outcome will be a re-engineered version of APMT for climate and air quality impacts, calibrated based on updated sensitivity data and upgraded to provide monetized impacts that consider the possibility of different cruise altitudes (among other characteristics).

Research Approach

This task aims to produce a more broadly capable operational tool. During AY 2020/21, the existing version of APMT-IC in MATLAB was updated to incorporate new information on the impacts of aviation from the Lee et al. (2020) assessment as APMT-IC v24c. This included estimating the effective radiative forcing (ERF) for contrail-cirrus with updated uncertainty distributions.

The team also began re-engineering APMT-IC in the programming language Julia. The new version of the model will evaluate climate, air quality, and ozone impacts from gridded emissions using the sensitivity-based approach described in Task 4. Air quality impacts will be regionalized to show impacts by country.

Figure 4 describes, at a high level, how the updated APMT will function. The main inputs will include parameters such as the number of Monte Carlo (MC) simulations, time horizon, lens or RCP scenario, and emissions. Based on the chosen RCP lens, the model will determine which distributions of predefined parameters to sample from for the MC runs. Emissions inputs will be specified either as (1) gridded emissions, gridded flight distances, and years or (2) default settings from predefined emissions inventories. The model will use the emissions inputs and sensitivity matrices embedded in APMT to obtain the global radiative forcing, change in surface ozone and $PM_{2.5}$ concentrations, and Dobson units for each key emissions species.

After the model parameters are defined and emissions are specified, the model will loop over the same set of calculations for every MC run (e.g., emissions to RF to temperature change to damages, or emissions to change in air quality to health impacts). This is shown in the central black box of Figure 4. All the inputs fed into this section are deterministic, as the model provides one set of parameters *N* times (where *N* is the specified number of MC simulations). Similarly, the model obtains one set of results for every MC run so that it can calculate a distribution of results for the variables of interest.

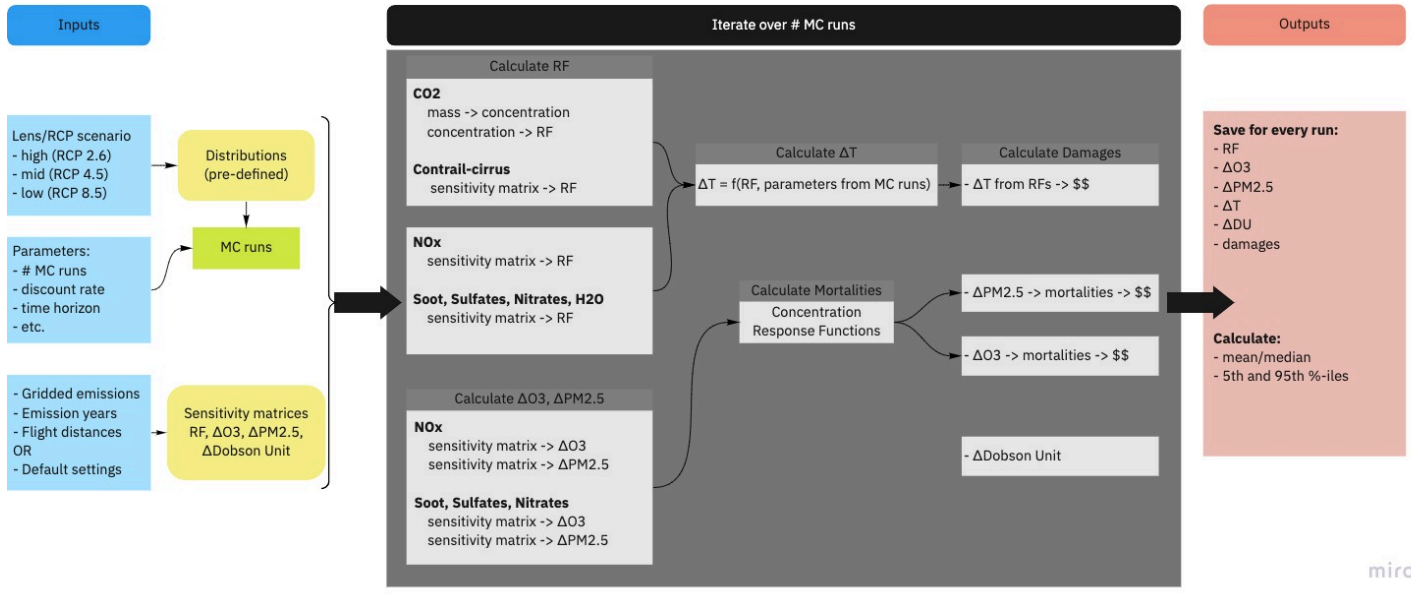

Figure 4. Flowchart of the new internal structure of Aviation Environmental Portfolio Management Tool (APMT).

Milestones
The current version of APMT-IC was updated to match Lee et al. (2020)'s estimates for stratospherically adjusted radiative forcing and the impact metrics listed in Grobler et al. (2019) accordingly. The team briefed FAA on the architectural changes required to restructure APMT and incorporate sub- and supersonic aviation in a single evaluation tool.

Major Accomplishments
The current version of APMT-IC (v24c) now includes the latest estimates of the impacts of current-day aviation NO_x, in addition to the effects of contrails on a per unit of fuel burn basis. Updates to the existing version of APMT were documented in an updated APMT-IC Design Document (v24c). A demonstration of the in-development APMT in Julia showed the new structure of gridded inputs and outputs of climate, air quality, and ozone impacts from both subsonic and supersonic emissions.

Publications
None.

Outreach Efforts
Progress on all tasks was communicated during biweekly briefing calls with the FAA and reported in quarterly progress reports.

Awards
None.

Student Involvement
During the reporting period of AY 2020/21, the MIT graduate student involved in this task was Joonhee Kim.

Plans for Next Period
The project team will integrate the Task 4 sensitivities from GEOS-Chem into the new version of APMT and calibrate the results using the outputs of atmospheric impacts from Task 3. After integration and calibration, the team aims to provide another demonstration of the re-engineered APMT and updated outputs. The tool will also include an option to run APMT using the original, subsonic-only data (v24c) as described in the design document. The team also plans to generate a development plan of changes required in APMT to update the CO_2 background concentration from RCP to SSP scenarios based on the latest IPCC Working Group I Sixth Assessment Report.

References
Grobler, C, Wolfe, PJ, Dasadhikari, K, Dedoussi, IC, Allroggen, F, Speth, RL, Eastham, SD, Agarwal, A, Staples, MD, Sabnis, JS, Barrett, SRH: Marginal climate and air quality costs of aviation emissions, Environ. Res. Let. 14 114031, 2019.

Lee, DS, Fahey, DW, Skowron, A, Allen, MR, Burkhardt, U, Chen, Q, Doherty, SJ, Freeman, S, Forster, PM, Fuglestvedt, J, Gettelman, A, De León, RR, Lim, LL, Lund, MT, Millar, RJ, Owen, B, Penner, JE, Pitari, G, Prather, MJ, Sausen, R and Wilcox, LJ: The contribution of global aviation to anthropogenic climate forcing for 2000 to 2018, Atmos. Environ., 117834, 2020.

Task 6 – Develop Parameterization of Contrails
Massachusetts Institute of Technology

Objective
This task aims to parameterize contrails, linking distance flown in a given region to the expected radiative forcing. In the existing version of APMT-IC (v24c), the total impacts of emissions are quantified per unit of additional fuel burned for the current subsonic fleet. Lee et al. (2020)'s review of aviation's impacts from 2000 to 2018 highlighted the need for a more sophisticated representation of the relationship between the number and distribution of flights and their contrail impacts.

Research Approach
Parameterization of contrail production which are based only on quantity of fuel burned, or even total global cruise flight distance, do not consider the localized nature of the likelihood of contrail formation as a function of region or the climate impact resulting from a persistent contrail. Recent work from Agarwal et al. (in preparation) demonstrates the spatial and temporal variations of contrail impacts for current cruise altitudes between 9 km and 12 km (Figure 5). The climate impacts

of contrails will be incorporated into the in-development version of AMPT-IC as an "RF by location," with a similar sensitivities-based approach as described in Task 5.

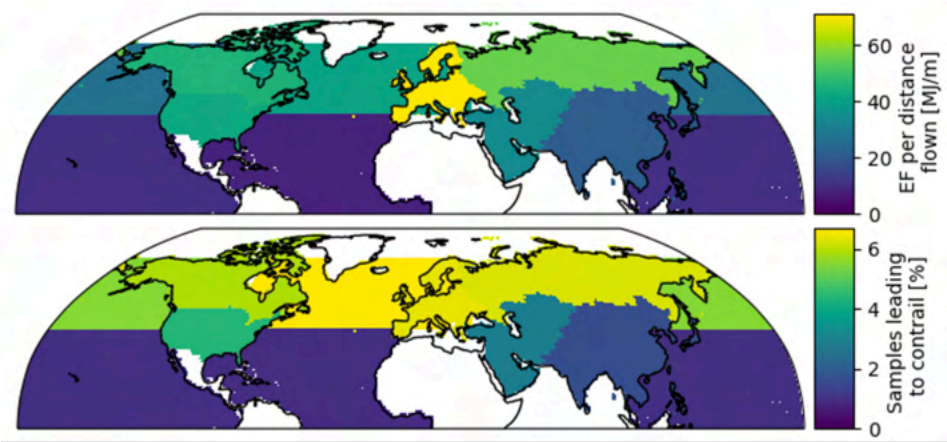

Figure 5. Spatial distribution of mean contrail energy forcing (EF) per distance flown (upper panel) and proportion of samples leading to a contrail (lower panel) in the Northern Hemisphere (Agarwal et al. [in preparation]).

Milestones

The in-development APMT-IC in Julia has been updated to accept gridded flight distances. Coarsely defined regions and the expected, average contrail forcing resulting from 1 km of flight in those regions have been estimated based on Agarwal et al (in preparation).

Major Accomplishments

Inputs of gridded flight distance to calculate the impacts of contrails per distance flown have been successfully implemented in APMT-IC.

Publications

None.

Outreach Efforts

Progress on all tasks was communicated during biweekly briefing calls with the FAA and reported in quarterly progress reports.

Awards

None.

Student Involvement

During the reporting period of AY 2020/21, the MIT graduate student involved in this task was Joonhee Kim.

Plans for Next Period

The project team will integrate "RF by location" sensitivities in APMT in the next reporting period by extending the embedded dataset to include alternative estimates of contrail impact per unit distance and validating and calibrating the results with a comparison to literature estimates. This will result in the first reduced-order, flexible tool for rapid evaluation of aviation's contrail-related climate impacts.

References

Agarwal, A., Fritz, T. M., Sabnis, J. S., Eastham, D. S., Speth, R. L., & Barrett, S. R. H. (2021). *Global contrail radiative forcing inferred using an intermediate fidelity contrail model* [Manuscript in preparation].

Lee, D. S., Fahey, D. W., Skowron, A., Allen, M. R., Burkhardt, U., Chen, Q., Doherty, S. J., Freeman, S., Forster, P. M., Fuglestvedt, J., Gettelman, A., De León, R. R., Lim, L. L., Lund, M. T., Millar, R. J., Owen, B., Penner, J. E., Pitari, G., Prather, M. J., Sausen, R., & Wilcox, L. J. (2020). The contribution of global aviation to anthropogenic climate forcing for 2000 to 2018. Atmospheric Environment, 117834.

Task 7 - Evaluate the Evolution of Aviation NO_X Impacts on Climate and Air Quality

Massachusetts Institute of Technology

Objective

This task aims to quantify how climate and air quality impacts of aviation emissions have changed over time, and the degree to which these changes are due to the evolution of background—rather than aviation—emissions. Continuous growth in aviation emissions has resulted in near-term impacts having greater significance relative to the expected impacts based on a "steady-state emissions" model. This has been partially explored in recent work in the context of aviation NO_x and its climate impacts only (Lee et al., 2020), suggesting that its impacts are small and uncertain relative to those of aviation CO_2 (Skowron et al., 2021). However, these analyses have neglected the air quality impacts of aviation NO_x, which previous studies have found to be substantial (Barrett et al., 2010; Cameron et al., 2017; Eastham & Barrett, 2016; Yim et al., 2015), and for which monetized damages may be of a similar order of magnitude to aviation's net climate impacts (Grobler et al., 2019). The objective of this task is to estimate quantitatively the impacts of aviation NO_x on both climate and air quality in the context of a changing atmosphere, including the latest scientific understanding of the mechanisms underlying these impacts. This is a future task of the project and will begin in the coming project year.

Research Approach

The project team will process schedule data from OAG covering the period from 1980 onward, and identify which aircraft and engine types are needed from the Base of Aircraft Data (BADA) and ICAO Aircraft Engine Emissions Databank (EEDB). Flights for each schedule year will be simulated to produce gridded estimates of fuel burn, distance flown, and aircraft emissions. Estimated fuel burn totals will be validated, and emissions for years in which schedule data are not available will be estimated by linear interpolation. Pending future funding, the team will perform a retrospective analysis to quantify how the climate and air quality impacts of aviation NO_x have evolved over time, and the degree to which this has been due to factors within, or outside of, the aviation industry's control.

Milestone

This task is planned to begin in 2022.

Major Accomplishments

None.

Publications

None.

Outreach Efforts

None.

Awards

None.

Student Involvement

None.

Plans for Next Period

During the next project period, the project team will acquire the OAG schedule data and identify surrogates for aircraft and engine types where information is not available. The feasibility of using the Aviation Environmental Design Tool (AEDT) to

generate aviation emissions for each year will be evaluated. The team will also generate initial estimates for daily, gridded aircraft emissions based on schedule years.

References

Barrett, S. R. H., Britter, R. E., & Waitz, I. A. (2010). Global mortality attributable to aircraft cruise emissions. Environmental Science & Technology, *44*(19), 7736–7742. https://doi.org/10.1021/es101325r

Cameron, M. A., Jacobson, M. Z., Barrett, S. R. H., Bian, H., Chen, C. C., Eastham, S. D., Gettelman, A., Khodayari, A., Liang, Q., Selkirk, H. B., Unger, N., Wuebbles, D. J., & Yue, X. (2017). An intercomparative study of the effects of aircraft emissions on surface air quality. Journal of Geophysical Research: Atmospheres, *122*(15), 8325–8344. https://doi.org/10.1002/2016jd025594

Eastham, S. D., & Barrett, S. R. H. (2016). Aviation-attributable ozone as a driver for changes in mortality related to air quality and skin cancer. Atmospheric Environment, *144*, 17–23. https://doi.org/10.1016/j.atmosenv.2016.08.040

Grobler, C., Wolfe, P. J., Dasadhikari, K., Dedoussi, I. C., Allroggen, F., Speth, R. L., Eastham, S. D., Agarwal, A., Staples, M. D., Sabnis, J., & Barrett, S. R. H. (2019). Marginal climate and air quality costs of aviation emissions. Environmental Research Letters, *14*(11), 114031. https://doi.org/10.1088/1748-9326/ab4942

Lee, D. S., Fahey, D. W., Skowron, A., Allen, M. R., Burkhardt, U., Chen, Q., Doherty, S. J., Freeman, S., Forster, P. M., Fuglestvedt, J., Gettelman, A., De León, R. R., Lim, L. L., Lund, M. T., Millar, R. J., Owen, B., Penner, J. E., Pitari, G., Prather, M. J., Sausen, R., & Wilcox, L. J. (2020). The contribution of global aviation to anthropogenic climate forcing for 2000 to 2018. Atmospheric Environment, 117834.

Skowron, A., Lee, D. S., De León, R. R., Lim, L. L., & Owen, B. (2021). Greater fuel efficiency is potentially preferable to reducing NOx emissions for aviation's climate impacts. Nature Communications, *12*(1). https://doi.org/10.1038/s41467-020-20771-3

Yim, S. H. L., Lee, G. L., Lee, I. W., Allroggen, F., Ashok, A., Caiazzo, F., Eastham, S. D., Malina, R., & Barrett, S. R. H. (2015). Global, regional and local health impacts of civil aviation emissions. Environmental Research Letters, *10*(3), 034001. https://doi.org/10.1088/1748-9326/10/3/034001

Project 059(A) Jet Noise Modeling to Support Low-Noise Supersonic Aircraft Technology Development

Georgia Institute of Technology and Pennsylvania State University

Project Lead Investigators

Dimitri Mavris (PI)
Regents Professor
School of Aerospace Engineering
Georgia Institute of Technology
Mail Stop 0150
Atlanta, GA 30332-0150
404-894-1557
dimitri.mavris@ae.gatech.edu

Jimmy Tai (Co-PI)
Senior Research Engineer
School of Aerospace Engineering
Georgia Institute of Technology
Mail Stop 0150
Atlanta, GA 30332-0150
404-894-0197
jimmy.tai@ae.gatech.edu

University Participants

Georgia Institute of Technology

- PI(s): Dr. Dimitri Mavris (PI), Dr. Jimmy Tai (Co-PI)
- FAA Award Number: 13-C-AJFE-GIT-070
- Period of Performance: October 1, 2020 to September 30, 2021

Project Funding Level

The project is funded at the following levels. Georgia Institute of Technology: $100,000. Cost-sharing details are below.

The Georgia Institute of Technology has agreed to a total of $100,000 in matching funds. This total includes salaries for the project director, research engineers, and graduate research assistants, as well as funds for computing, financial, and administrative support, including meeting arrangements. The institute has also agreed to provide tuition remission for the students, paid from state funds. During the period of performance, in-kind cost-sharing is also obtained.

Investigation Team

- PI: Dimitri Mavris (Georgia Institute of Technology)
- Co-Investigator: Jimmy Tai (Georgia Institute of Technology)
- Program Manager: Joshua Brooks (Georgia Institute of Technology)
- Students: Edan Baltman, James Kenny, Noah Chartier, Jeremy Decroix, Andrew Tai, and Madeline Bowne (Georgia Institute of Technology)

Project Overview

The original purpose of this project was to develop and assess computational tools to simulate the flow and noise of civil supersonic aircraft engines and to identify novel methods for noise reduction. In addition to noise predictions, the impact of the noise reduction methods on overall engine performance was planned to be assessed. The predictions were planned to include consideration of the engine inlet, the engine cycle, mixers and ejectors, and the unsteady jet exhaust. Accurate prediction of the engine exhaust flow would enable the generated noise to be computed. Predictions were planned to be assessed through comparison with available experimental measurements.

In discussion with FAA, the overall direction of the project has been changed. Instead of developing and simulating jet noise reduction technologies, Project 59A will be supported by experimental data provided by Project 59 (led by Dr. Krishnan Ahuja) at Georgia Institute of Technology (Georgia Tech). The operating conditions for the initial experimental geometry will be the result of discussions with other Project 59 performers.

This year's work will focus on moving toward the new end of the project. The work includes the assembly of zeroth-order methods for predicting supersonic inlet performance, as well as the deployment of these methods for the identification of competitive supersonic inlet designs for overcoming the performance impacts accompanying noise-reducing nozzle technologies across the flight envelope.

If successful, the ASCENT Project 59 research will develop methods to predict the noise generated and radiated by civil supersonic aircraft engines. The developed tools will enable airframe and engine manufacturers to assess the noise impacts of engine design changes and to determine whether particular designs will meet current or anticipated noise certification requirements. In future years, the assessment of jet noise reduction technologies as originally proposed will be reconsidered.

Project Introduction

The primary objective of this research project is to develop and assess computational tools to simulate the flow and noise of civil supersonic aircraft engines. In Task 1, Georgia Tech and Pennsylvania State University (Penn State) collaborated to select an initial jet nozzle geometry. In Task 2, Georgia Tech analyzed the engine cycle developed by ASCENT Project 10 to estimate the best operating conditions for takeoff and landing for minimizing certification noise levels (Mavris et al., 2015; Welge et al., 2010). The resulting mixer and nozzle conditions are being used to advise the researchers of ASCENT Project 59 on relevant test conditions. These test conditions for the initial geometry will also provide boundary conditions for Task 3. In Task 3, an internal and external flow simulation aimed at uncovering noise source information will be performed. In Task 4, a process for converting high-fidelity simulation results into jet noise sources will be developed, and Task 5 will yield a final report detailing this research effort.

In line with the updated project trajectory, the original leading Tasks 1 and 2.1 have been replaced with the coordination task with Project 59 performers and stakeholders.

Milestone(s)

The major milestones and planned due dates are as follows:

Task No.	Milestone	University	Planned Due Date
Task 1	Selection of initial geometry in coordination with other Project 59 investigators	Penn State and Georgia Tech	12/15/2020
Task 2.1	Assembly of zero-order methods to predict inlet performance	Georgia Tech	11/30/2021
Task 2.2	Determination of boundary conditions from "Vision SST Engine Cycle"	Georgia Tech	2/5/2021
Task 4	Script construction for generation of Aircraft Noise Prediction Program (ANOPP) custom jet noise source	Penn State and Georgia Tech	9/1/2022
Task 5	Submission of interim project report	Penn State and Georgia Tech	11/1/2022

Major Accomplishments

- To capture thrust recovery due to improved inlet performance, the Georgia Tech team must complete the supersonic inlet performance analysis.
    - Validation for zeroth-order supersonic inlet performance analysis for two-dimensional (2D) inlets against IPAC (Barnart, 1997).
    - A sensitivity study was performed to evaluate the thrust recovery potential of inlet variable geometric settings at takeoff and landing.

Task 1 - Select Jet Nozzle Geometry

Georgia Institute of Technology and Pennsylvania State University

Objective(s)

To unify and maximize the impact of work across relevant ASCENT projects, Georgia Tech and Penn State will coordinate efforts to select an initial jet nozzle geometry. Through collaboration with Dr. Krishnan Ahuja, the experimental data from this standard geometry (gathered in ASCENT project 59) will be used to inform the work of ASCENT project 59A.

Research Approach

The combined Penn State and Georgia Tech research team will work together to identify promising geometries for use across the ASCENT projects. The selected geometry must be relevant to the project goals while also being achievable in terms of experimental measurements, computational analysis, and other supporting tasks. Specific evaluation criteria may include jet velocity reduction and thrust loss.

Task 2 - Translate Installed Cycle Performance Requirements into Boundary Conditions

Georgia Institute of Technology

Objective(s)

Task 2 aims to leverage engine cycle modeling capabilities to determine the installed thrust for an engine of interest that is appropriate for commercial supersonic transport. The thermodynamic properties across this mixed flow turbofan engine, alongside the installed thrust value, are used to characterize the mixer exit, nozzle entrance, and nozzle exit operating conditions during takeoff. Because the initial testing and high-fidelity simulations are not yet representative of a mixed flow turbofan, these operating conditions (e.g., total pressure, total temperature, mass flow, and geometry) will inform the testing team regarding relevant testing conditions.

Research Approach (Georgia Tech)

Task 2.1 - Determine Installed Thrust

To ensure that minimum thrust is lost due to the implementation of potential jet noise reduction technology, the installed thrust requirement must be determined, because it is directly proportional to jet velocity. A major contributor to installed thrust is inlet performance, which is highly dependent on how the engine is integrated with the vehicle. Therefore, another element of this task is the investigation of zero-order methods to predict inlet performance for different inlet configurations.

Task 2.2 - Generate Boundary Conditions

Georgia Tech will analyze the engine cycle developed by ASCENT Project 10 to estimate the best operating conditions for takeoff and landing to minimize certification noise levels. The resulting mixer and nozzle conditions (i.e., total temperature, total pressure, and mass flow rate) will inform the researchers of ASCENT Project 59 regarding the relevant test conditions. These test conditions for the initial geometry will also provide boundary conditions for the high-fidelity simulations to be performed in Task 3. The inlet investigation will insure against any thrust loss due to any mixer or nozzle design to minimize noise.

Task 2.1 - Zero-order Methods to Predict Inlet Performance

Inlet performance, a major contributor to the installed thrust, is highly dependent on how the engine is integrated with the vehicle. To capture thrust recovery due to improved inlet performance, the Georgia Tech team must complete the supersonic inlet performance analysis.

In the past year, the Georgia Tech team has completed the model development for the 2D inlet case in Python. In addition, the team has completed an initial validation of a 2D inlet case with satisfactory preliminary results. Table 1 compares the developed tool's predicted total pressure recovery to that produced by IPAC across the mission-relevant range of freestream Mach number (Barnart, 1997). Here, the supersonic inlet was designed for a freesteam Mach number of 5 and has been evaluated across a range of lower "off-design" operating freestream Mach settings. The maximum and average error values were found to be 3.69% and 0.82%, respectively, across this range.

Table 2 compares the total drag coefficient predicted by the developed tool and that produced by IPAC across the mission-relevant range of freestream Mach number (Barnart, 1997). This drag term includes the contributions of spillage, bleed, and bypass drag upon the engine inlet. Again, the supersonic inlet was designed for a freesteam Mach number of 5 and was evaluated across a range of lower "off-design" operating freestream Mach settings. The maximum and average error values were found to be 9.88% and 1.19%, respectively, across this range.

Table 1. Validation case: total pressure recovery.

Freestream Mach Number	Modeled	Reference	Error (%)
0.01	0.9586	0.9608	−0.23
0.2	0.9586	0.9608	−0.23
0.4	0.9586	0.9608	−0.23
0.6	0.9586	0.9608	−0.23
0.8	0.9586	0.9608	−0.23
1.0	0.9586	0.9608	−0.23
1.2	0.9517	0.9539	−0.23
1.4	0.9404	0.9456	−0.55
1.6	0.9233	0.9285	−0.56
1.8	0.8767	0.8816	−0.55
2.0	0.8107	0.8153	−0.57
2.5	0.8591	0.8760	−1.97
3.0	0.7873	0.7875	−0.03
4.0	0.6618	0.6427	2.88
5.0	0.5349	0.5152	3.67

Table 2 Validation case: total drag coefficient.

Freestream Mach Number	Modeled	Reference	Error (%)
0.01	0.0000	0.0000	0.00
0.2	0.0000	0.0000	0.00
0.4	0.1976	0.1799	9.88
0.6	0.3086	0.3024	2.05
0.8	0.3831	0.3811	0.53
1.0	0.4809	0.4797	0.25
1.2	0.6537	0.6617	−1.21
1.4	0.3953	0.3855	2.53
1.6	0.3264	0.3265	−0.01
1.8	0.3245	0.3250	−0.15
2.0	0.3426	0.3411	0.45
2.5	0.3007	0.3000	0.23
3.0	0.2994	0.2987	0.23
4.0	0.2315	0.2307	0.35
5.0	0.0175	0.0175	0.00

The developed inlet performance analysis tool is intended to help identify competitive supersonic inlet designs for overcoming negative performance impacts accompanying the use of noise reduction nozzle technologies across the flight envelope. To this end, a sensitivity study was performed to evaluate inlet variable geometry settings that may be capable of recovering thrust across off-design flight segments (takeoff and landing).

The inlet performance tool will be extended to include the axisymmetric configuration, which will then be integrated into an inlet design tool capable of identifying competitive inlet designs for overcoming thrust losses due to adjustment to the nozzle.

Task 4 - Source Integration and Propagation

Georgia Institute of Technology and Pennsylvania State University

Objective(s)

The knowledge acquired through the simulations performed within Task 3 must be translated into functional noise sources for use in onboard aircraft analyses. These noise sources will allow for the assessment of observer-perceived noise and therefore the ability to assess the specific impacts of each of the promising noise technologies. The aim is to perform these analyses in terms of both certification noise levels and noise contours.

Research Approach

The combined research team will develop a process for converting high-fidelity simulations (i.e., computational aeroacoustics [CAA]) results into jet noise sources by using ANOPP2's custom noise source feature. After the process is developed and verified, the research team will be able to input CAA-simulated jet noise sources and propagate the noise to the observer by using ANOPP2's propagation module to assess the perceived noise levels. The latter step will require the research team to also establish a baseline case with no active technology to assess the level of jet noise reduction. Furthermore, the combined research team will also coordinate with ASCENT Project 10 to integrate the jet noise source results from the proposed research with other noise sources captured by the ASCENT Project 10 team, to examine the impact of the jet noise reduction technology in terms of both certification noise levels and noise contours.

Publications

None

Outreach Efforts

ASCENT Advisory Board Meeting

Awards
None

Student Involvement
The Georgia Tech student team consists of five graduate research assistants (GRAs). Over the past performance period, all five GRAs engaged in formulating the approach being pursued for the inlet modeling activity. The team is divided into supersonic inlet aerodynamic and thermodynamic performance, and mechanical and structural analysis. Each student is involved with multiple topics, and GRA leads are identified for each topic. Mr. James Kenny is the student lead for aerodynamic and thermodynamic performance, and Mr. Noah Chartier is the student lead for mechanical and structural analysis.

Plans for Next Period
Georgia Tech

The Georgia Tech team plans to complete the indicated tasks listed in Table 3. Work will continue toward completion of the assembly of a zero-order inlet design and analysis environment, including the following:

- Completion of validation of the first iteration of a zeroth-order inlet performance analysis environment
- Conversion of the developed inlet analysis tool into a supersonic inlet design tool
- Implementation of on-design single-ramp compressible flow analysis capability for axisymmetric inlets
- Implementation of on-design multi-ramp compressible flow analysis capability for axisymmetric inlets
- Implementation of off-design multi-ramp compressible flow analysis capability for axisymmetric inlets

Table 3. Anticipated milestones for the next research period.

Milestone	University	Planned Due Date
Zero-order methods to predict inlet performance	Georgia Tech	11/30/2021
Script for generation of ANOPP custom jet noise source	Penn State and Georgia Tech	9/1/2022
Annual report submission	Penn State and Georgia Tech	11/1/2022

References
Barnhart, P. J. (1997). *IPAC--Inlet Performance Analysis Code*. National Aeronautics and Space Administration.

Mavris, D., Tai, J., Kirby, M., & Roth, B. (2015). Systems analyses of pneumatic technology for high speed civil transport aircraft (Report No. 19990105723). National Aeronatuics and Space Administration.

Welge, H., Bonet, J., Nelson, C., & Tai, J. (2010). N+2 supersonic concept development and systems integration (Report No. NASA/CR-2010-216842). National Aeronautics and Space Administration.

Project 059(B) Jet Noise Modeling and Measurements to Support Reduced LTO Noise of Supersonic Aircraft Technology Development

Georgia Institute of Technology/Gulfstream

Project Lead Investigator

Krishan K. Ahuja
Regents Professor
School of Aerospace Engineering
Georgia Institute of Technology
Atlanta, GA 30342
404-290-9873
Krish.Ahuja@ae.gatech.edu

University Participants

Georgia Institute of Technology (Georgia Tech)

- PI: Krishan K. Ahuja, Regents Professor
- FAA Award Number: 13-C-AJFE-GIT-060
- Period of Performance: June 5, 2020 to December 31, 2021
- Tasks:
  1. Form an advisory panel
  2. Identify baseline nozzle requirements and design tests
  3. Design and fabricate a baseline nozzle
  4. Test setup and experimental data acquisition
  5. Data dissemination
  6. Assess readiness of design tools for a simple baseline nozzle configuration
  7. Proposal for a follow-on effort for years 2 and 3
  8. Reporting and data dissemination

Project Funding Level

This project received $250,000 from FAA and $250,000 of cost-sharing from Gulfstream.

Investigation Team

- Dr. Krishan Ahuja, PI, Georgia Tech
- Dr. Dimitri Mavris (Co-PI) and Dr. Jimmy Tai (Co-PI), Georgia Tech
- Dr. Aharon Karon, Co-Investigator and Lead Experimentalist, Georgia Tech Research Institute (GTRI)
- Dr. Robert Funk, Experimentalist, GTRI
- David N. Ramsey, Graduate Research Assistant and Experimentalist, Georgia Tech

Project Overview

The overall goal of this project is to perform cost-effective supersonic transport (SST) jet noise research/technology experiments to enable low-, medium-, and high-fidelity jet noise prediction methods. The specific objective is to design the experiments in collaboration with industry, NASA, the Department of Defense (DOD), FAA, and modelers funded by FAA to help develop improved jet noise prediction methods with reduced uncertainty and enable industry to design quieter supersonic jet engines with higher confidence regarding the noise that will be generated. In collaboration with Gulfstream, Georgia Tech's industry partner on this project, a representative baseline nozzle design will be selected for experiments at

Georgia Tech. The data acquired will consist of far-field noise, high-speed flow visualization, source location, and detailed mean and unsteady flow measurements.

The experimental data acquired by Georgia Tech will be provided to key stakeholders and other computational teams funded by FAA to validate their computational simulations to confirm that jet noise predictions using semi-empirical and computational modeling approaches can be reliably used for jet noise evaluation.

Task Objectives, Research Approach, and Accomplishments

This project has eight tasks, as listed below. The task titles are self-descriptive and reflect the task objectives. A short objective statement, research approach, and summary of the accomplishments to date for each task is provided after each task description.

Task 1 - Form an Advisory Panel

Georgia Institute of Technology

Objective

The objective of this task is to receive regular feedback from industry and NASA subject-matter experts (SMEs) in supersonic jet noise.

Research Approach

Dr. Liu, the FAA Project Manager for ASCENT 59, has already formed an advisory panel consisting of representatives of FAA, DOD, NASA, Aerion, GE, and Gulfstream. A kick-off meeting has already been held, and feedback from the meeting was used in the design of the test nozzle and determination of the test conditions, as described below.

Task 2 - Identify Baseline Nozzle Requirements and Design Tests

Georgia Institute of Technology

Objective

The objective of this task is to define the nozzle requirements and design the experiments.

Research Approach

The baseline nozzle and tests were based on a paper engine design created by the Georgia Tech Aerospace Systems Design Laboratory (ASDL), guided by ASCENT Project 10, on engine cycle selection for the GT Medium SST (55-passenger class). For simplicity, it was decided that the GT nozzle model tested under this project would not have a plug. For calculation of the area of the outer (secondary flow) duct, the annular areas of the paper engine were used to calculate the area of the secondary flow duct in the model nozzle facility. The GTRI model is at a scale of 0.045 with respect to the paper engine. The mixing length/exhaust nozzle exit diameter (L_e/D_e) ratios will be: 0.7, 1, 2, and 3. The contributions of the ASDL are summarized in Appendix A.

As described below, tests have been designed with variations in nozzle design and/or operating parameters to explore the accuracy of semi-empirical and computational tools for predicting jet noise. The test conditions are summarized in Figure 1, which reflects the planned test conditions for each L_e/D_e and each core temperature (unheated and 500 °F). Additionally, PIV, source location, and flow visualization are restricted to unheated set points. Of note, the small extraction ratio (ER) acoustic measurements were acquired with a primary pressure ratio (PR) of 1.69 for all configurations except the L_e/D_e = 1.0 configuration, and the condition with primary pressure of 1.69 and ER of 1.04 was not tested for the shortest mixing duct, L_e/D_e = 0.7. These two caveats arose as a result of the late addition of these conditions with a higher primary pressure ratio, and thus a small ER, to the measurement program.

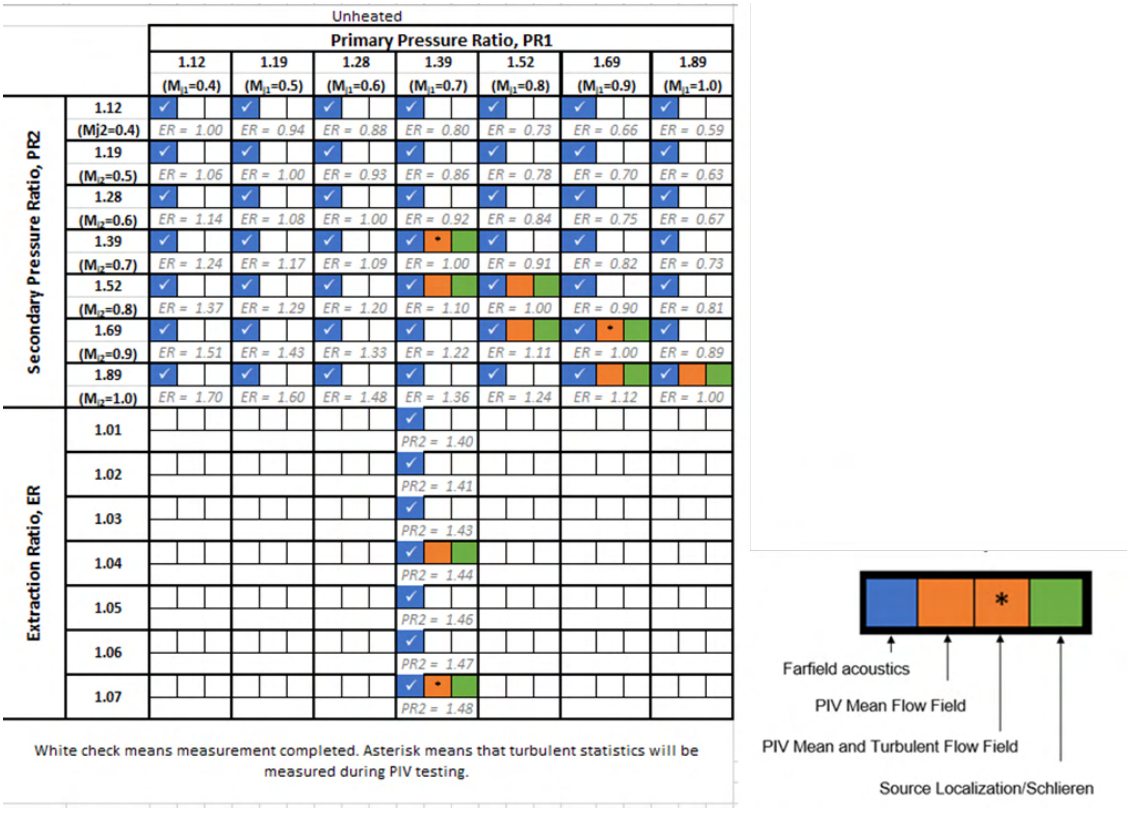

Figure 1. Test condition matrix.

Task 3 - Design and Fabricate a Baseline Nozzle

Georgia Institute of Technology

Objective

The objective of this task is to design and fabricate a baseline nozzle that meets the requirements defined in Task 2 and is also suitable for the tests required to meet the objectives of the overall program.

Research Approach

The test nozzle design is shown in Figure 2. A photographic view is shown in Figure 3. The model consists of the following parts: primary nozzle with a collar to avoid any anomalous flow effects due to any geometrical protrusions/recesses, secondary nozzle, mixer ducts, and exhaust nozzle. Three mixer ducts were fabricated to allow for different *mixing length-to-nozzle-exit diameter ratios* (L_e/D_e ratios. The test model utilizes the co-annular flow capabilities of the GTRI jet facilities. The primary and secondary flow streams merge into the mixer-duct and exhaust nozzle combination. The mixer-duct and exhaust nozzle combinations allow for L_e/D_e values of 0.7 (with the exhaust nozzle mounted directly to the secondary nozzle), 1, 2, and 3. The jet stream is ultimately formed by the exhaust nozzle, which is a converging nozzle with geometry based on the converging section of the converging–diverging nozzle from the ASDL engine design.

All components of the test model were fabricated by our Gulfstream cost-sharing partner.

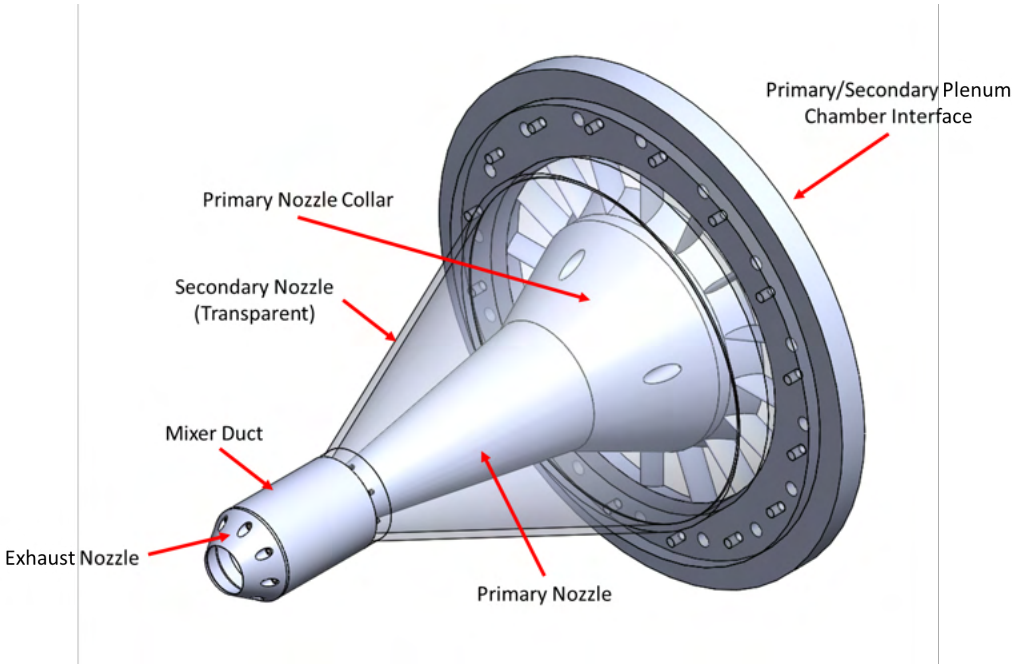

Figure 2. Experimental model design.

Task 4 - Test Setup and Experimental Data Acquisition

Georgia Institute of Technology

Objective

The objective of this task was to prepare to conduct the tests and acquire and analyze the data. All the acoustic data have been acquired. Because of a major failure in the test facility, as reported in the quarterly progress reports, PIV data could not be obtained earlier. Limited mean flow data were acquired, and the detailed PIV data acquisition is in progress.

Research Approach

Acoustic Measurements

Facility Setup and Testing Description

The test model was mounted in the GTRI Anechoic Jet-Facility for acoustic data acquisition, as shown in Figure 3. This facility has been described in detail in Burrin, Dean, & Tanna (1974), Burrin & Tanna (2005), and Ahuja (2003). Far-field microphones were mounted on a polar arc at angles between 30° and 120° with respect to the jet axis in 10° increments. The jet upstream conditions were set by controlling the ratio of the total pressure to the ambient pressure (PR = p_t/p_a) for both the primary and secondary streams. Both the primary and secondary streams were varied between pressure ratios of 1.12 and 1.89. The extraction ratio (ER=p_{t2}/p_{t1}) was also used as another approach to define the secondary pressure ratio for a given primary stream pressure, because this parameter was brought to our attention by the program partners and has practical importance. According to insights provided by Gulfstream and FAA, ERs between 1.00 and 1.07 are the most realistic conditions for a given PR_1. Additionally, the primary total temperature was set. In the unheated tests, this temperature varied between 60 °F and 70 °F and, during heated tests, it was set nominally to 500 °F. Of note, for the remainder of this program, the PR will refer to the ratio between upstream total and ambient pressures. In addition to the acoustic measurements, the primary and secondary total pressure and temperature, primary and secondary mass flow rates (measured at the control valve), and the ambient pressure, temperature, and relative humidity were measured.

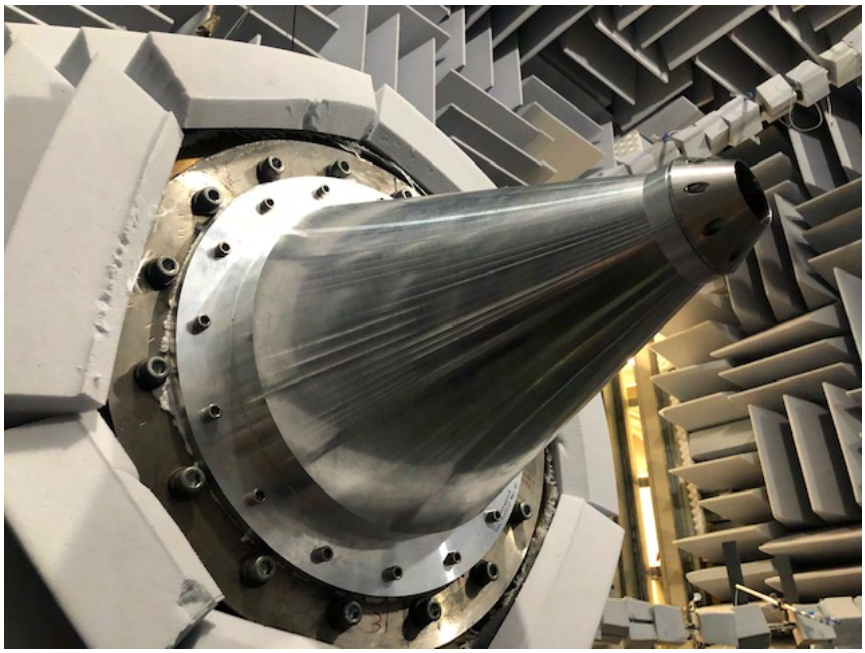

Figure 3. Project model setup in the GTRI Anechoic Jet Facility.

The microphones used for these measurements are Bruel and Kjaer (B&K) 4939 ¼-in free-field microphones and are attached to B&K 2669 preamplifiers. The microphone–preamplifier combinations are connected to B&K 2960-A-0S4 Nexus conditioning amplifiers that, in addition to amplifying the signal, act as the microphones' 200-mV power supply. The microphone signals are sampled at 204.8 kHz by using NI PXIe-4499 modules. The acoustic pressure time histories are then processed into averaged sound pressure level (SPL) spectra with a window size of 6,400 samples, 50% overlap, and a Hanning window. To render the data in lossless form for use by the modelers, the following corrections are applied to these SPL spectra: free-field response correction, windsock correction (if necessary), atmospheric attenuation, and distance. These corrections have been described in detail by Karon and Ahuja (2016).

Acoustic Analysis

In the following, only the salient observations are initially provided. Detailed discussion of the results is provided later.

Effect of changing the Extraction Ratio: Figure 4 shows the jet noise measurements for jet conditions of ER = 1.1, 1.0, and 0.92 for the $L_e/D_e = 0.7$ configuration. Of note, ER = 1.1 and 0.92 are outside the ER range that the program partners indicated are of greater practical interest; however, the data are shown here because they were acquired as part of this program, and validating the predictions made by the modelers for these conditions would provide added confidence in model fidelity. As shown in Figure 4, the noise increases with increasing secondary pressure ratio. At lower frequencies (below ~3 kHz), the noise increases by ~1 dB as the secondary pressure ratio increases from 1.28 to 1.39 and from 1.39 to 1.52. At higher frequencies, the noise increase is larger. As the secondary pressure ratio is increased from 1.28 to 1.39, the noise increases by as much as 3 dB, and when the secondary pressure ratio is increased from 1.39 to 1.52, the noise increases by as much as 5 dB. Later, we show that if the extraction ratios are maintained close to unity, e.g., up to 1.07, there is no noticeable change in SPLs at low frequencies, and there is very little change at high frequencies.

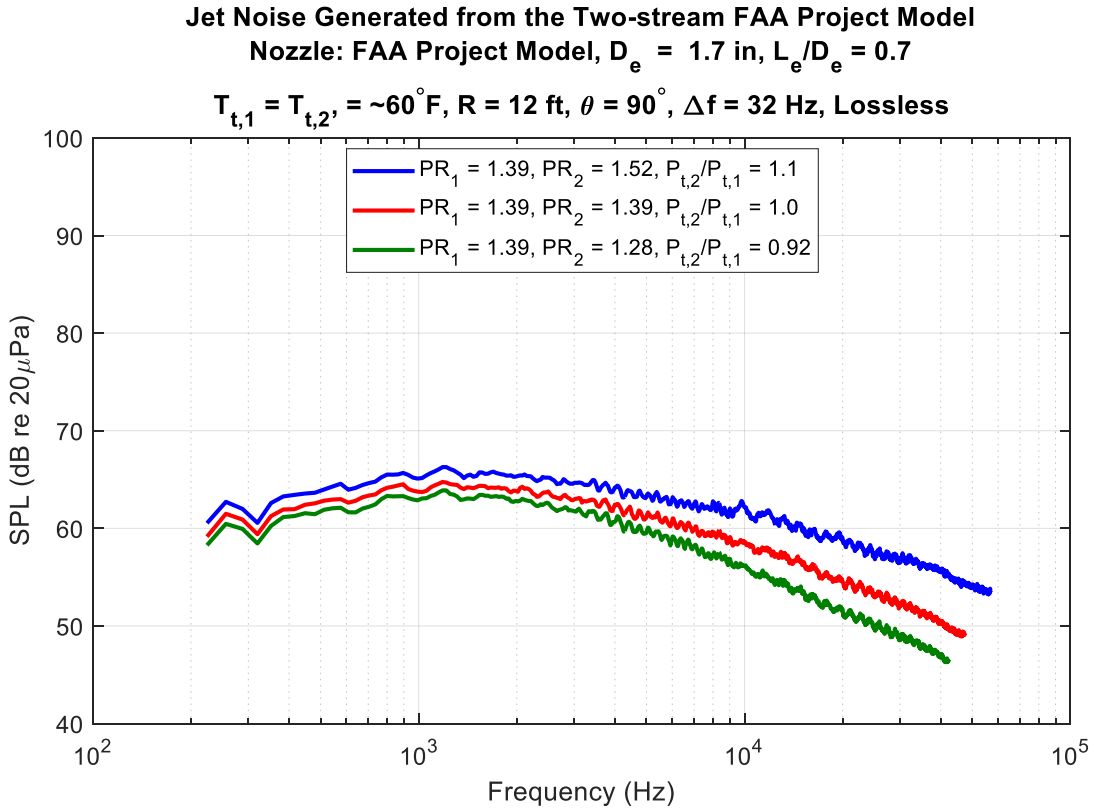

Figure 4. Typical jet noise spectra at an extraction ratios of 1 and above and below 1, for the L_e/D_e = 0.7 configuration.

Effect of increasing the mixing length: Figure 5 shows the jet noise generated from the test model with primary and secondary pressure ratios both equal to 1.39 (ER = 1.0) and L_e/D_e varied between 0.7 and 3.0. As shown in Figure 5, at frequencies below 7 kHz, the noise from the three conditions is the same. Above 7 kHz, there is a minor reduction in jet noise of 1 dB at most. This result indicates that an increase in mixing length does increase the mixing to a small degree, thus leading to reduced noise at high frequencies.

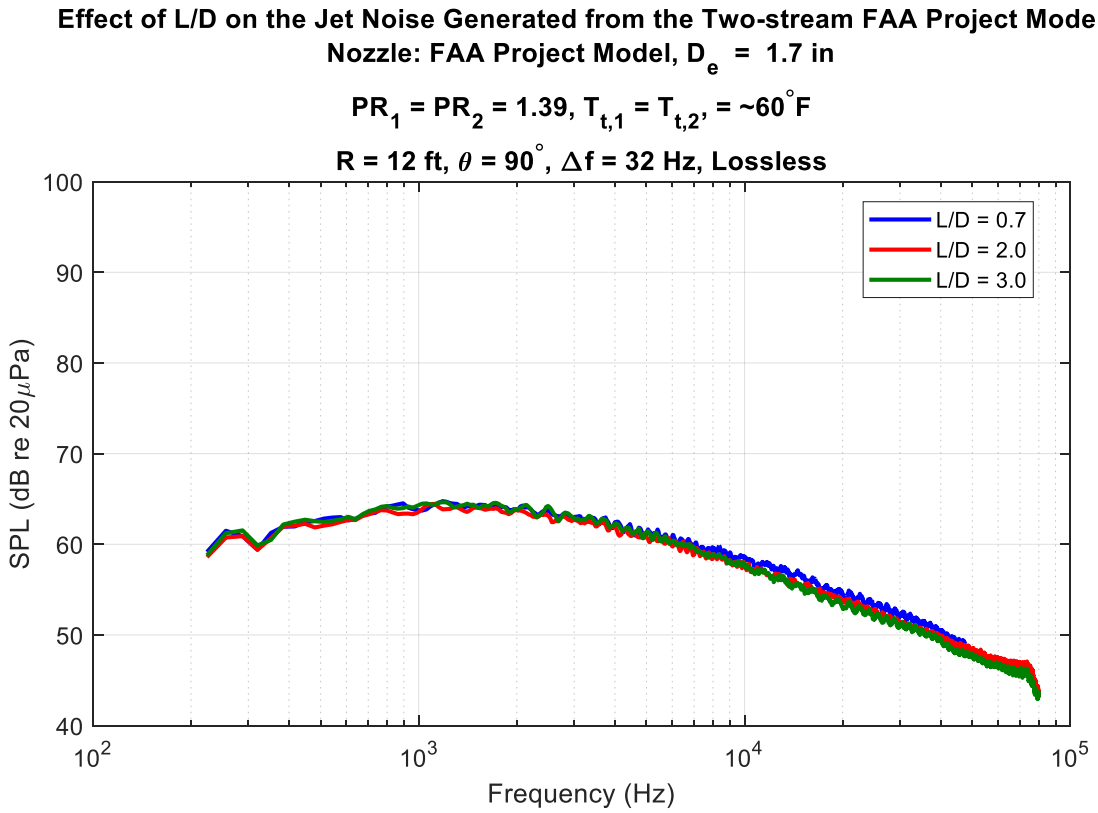

Figure 5. Effect of mixing length on the jet noise produced by the test model.

Effect of increasing the primary jet temperature: Figure 6 shows the effect of increasing the primary nozzle total temperature for an L_e/D_e of 0.7. The corresponding data for an L_e/D_e of 3 is shown in Figure 7. The unheated spectra in both cases appear to be unaltered, but the spectrum for the larger L_e/D_e with the heated primary stream has somewhat lower SPLs at higher frequencies. For example, at a frequency of 50000 Hz, the SPL for L_e/D_e = 0.7 is 51 dB, and that for L_e/D_e = 3 is 47.4 dB. This finding may be an effect of reduced speed of the heated stream via mixing with the unheated secondary jet in the longer duct.

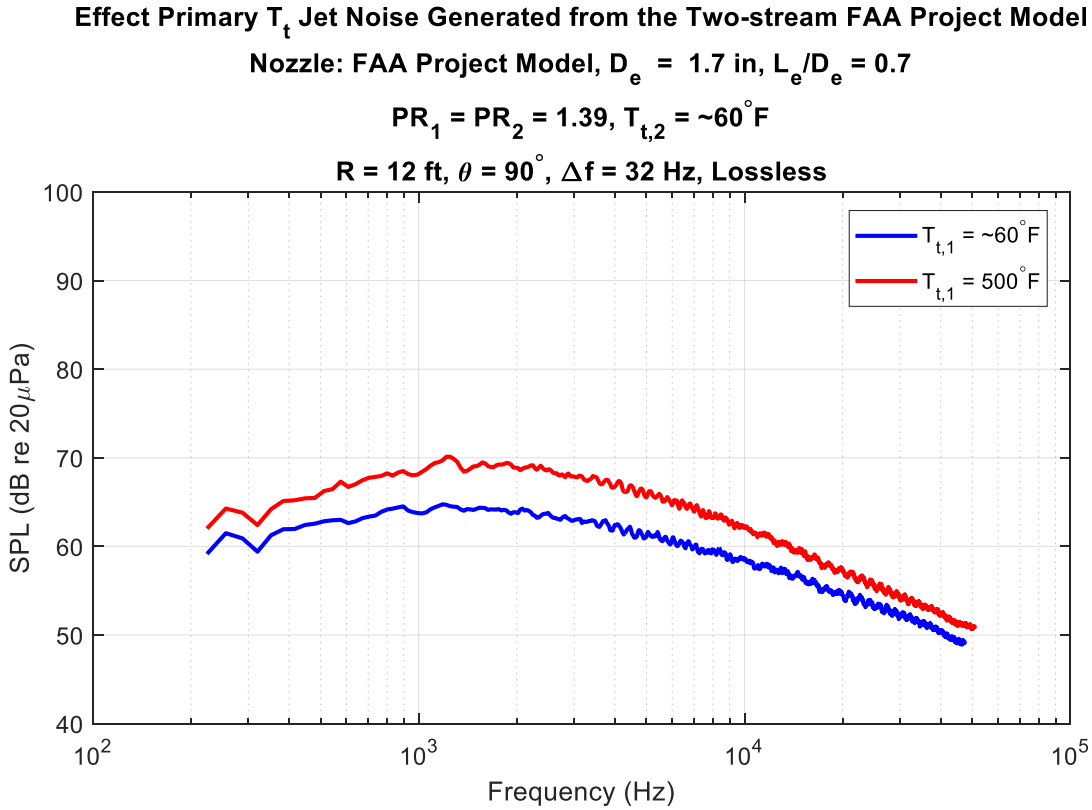

Figure 6. Effect of primary total temperature with the L_e/D_e = 0.7 configuration.

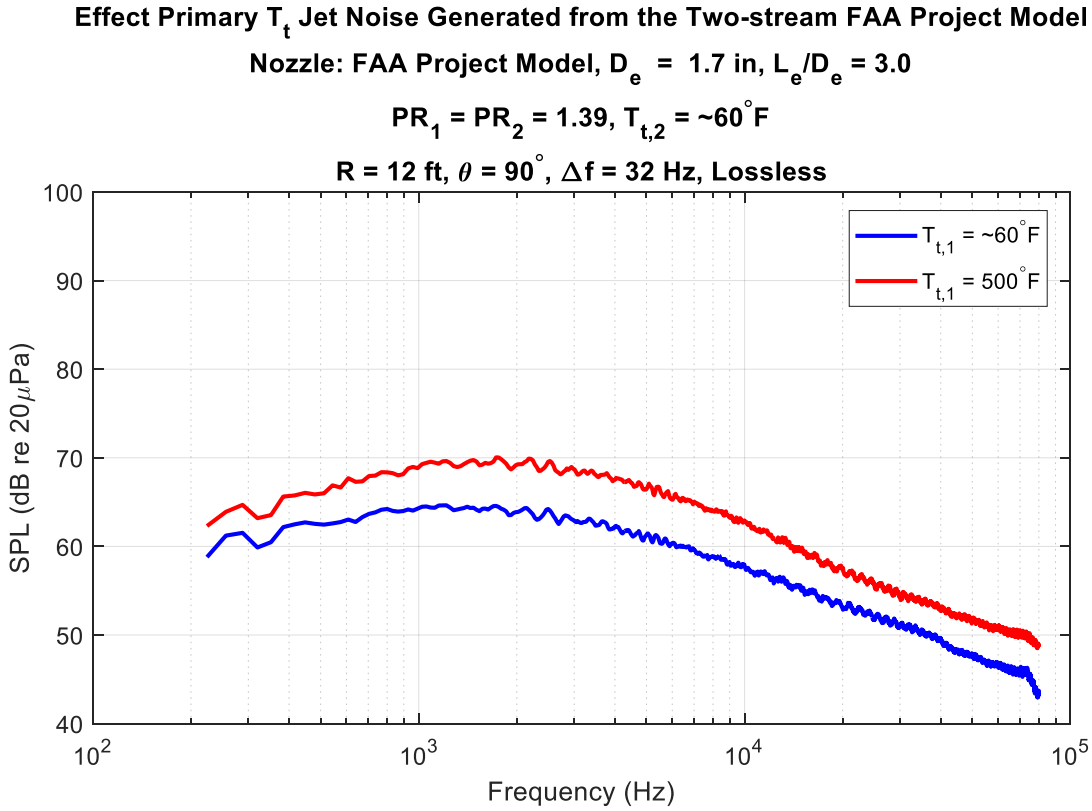

Figure 7. Effect of primary total temperature with the L_e/D_e = 3.0 configuration.

Observation of high-intensity tones at certain operating conditions: Figures 8 and 9 compare the jet noise measurements for the L_e/D_e = 0.7 and 3.0 configurations for ER = 1.0, and ERs much higher (1.22) and much lower (0.81) than unity. High-amplitude tones are generated for both these cases. An initial analysis and literature review performed by the ASCENT 59B team has led to the hypothesis that these tones may be due to a family of flow-acoustic interactions rather than to a single underlying physical mechanism. The suspected types of flow-acoustic interactions include: (1) the excitation of acoustic resonances inside the model by ducted vortex shedding, which may exist in the wake of the primary nozzle lip inside the mixing duct (2) aeroacoustic feedback, which occurs between the primary nozzle and exhaust nozzle lips, and (3) coupling between the feedback and duct resonances associated with various passages and impedance boundaries within the supply duct. The experimental evidence supporting this hypothesis includes a drop in the fundamental tone frequency that occurs when the internal mixing length exceeds a certain value for a given test point. However, without dedicated experimental evidence, this possibility remains purely a hypothesis. One challenge that arises in distinguishing the two physical mechanisms from far-field acoustic measurements alone is the tendency for both the feedback frequency and acoustic duct modes to decrease in frequency with an increase in mixing duct length (under the assumption that the acoustic mode is not purely transverse and involves the region inside the mixing duct). Although no concrete conclusions can currently be reached, a brief discussion of potential flow-acoustic interactions and how they are believed to relate to the year 1 model is provided below.

Generally, flow over a plate in a duct may excite the duct's acoustic resonances as the plate's trailing edge vortex shedding feeds energy into the acoustic field (Parker & Stoneman, 1989; Cumptsy & Whitehead, 1971). The influence of the excited duct resonance on the vortex street, which excited it, must also be considered. For instance, the most preferred frequency of vortex shedding from a plate inside a duct has been shown to "lock in" on the frequency of an acoustic mode that it has excited (Parker & Stoneman, 1989). This effect is significant when the pressure node of an acoustic resonance coincides with the vortex street's location (Parker & Stoneman, 1989). This phenomenon is not simply due to unsteady flow features exciting duct resonances, and the influence of the acoustic field on the unsteady flow field must also be considered. In the test model

used during year 1, if the frequency of the vortex shedding from the primary nozzle lip matches any of the duct resonance frequencies within the model, high-amplitude tones can result.

Regarding the feedback phenomenon, the low-bypass internally-mixed model used has a primary nozzle diameter comparable to that of the exhaust nozzle, thus forming a geometry that enables the onset of an aeroacoustic feedback phenomenon internal to the model. The feedback phenomenon initiates in the model when a core-bypass shear layer instability wave impinges on the exhaust nozzle lip and produces sound. As the sound propagates upstream to the primary nozzle lip with proper phase, it excites the core-bypass shear layer instability, and the feedback loop is set up. The excited instability wave impinges on the exhaust nozzle lip with greater intensity, higher amplitude sound is produced, and the instability is further reinforced. As this repeats, large oscillations ensue at the feedback frequency and high-intensity tones are produced. It can be shown that an increase in distance between the primary and exhaust nozzle lips tends to reduce the feedback frequency. If the feedback tones match any of the duct resonance frequencies within the test model, tones with even higher amplitude can result. The worst-case scenario occurs when the frequencies associated with vortex shedding, feedback, and duct resonance all match. This scenario could produce structural failures due to sonic fatigue.

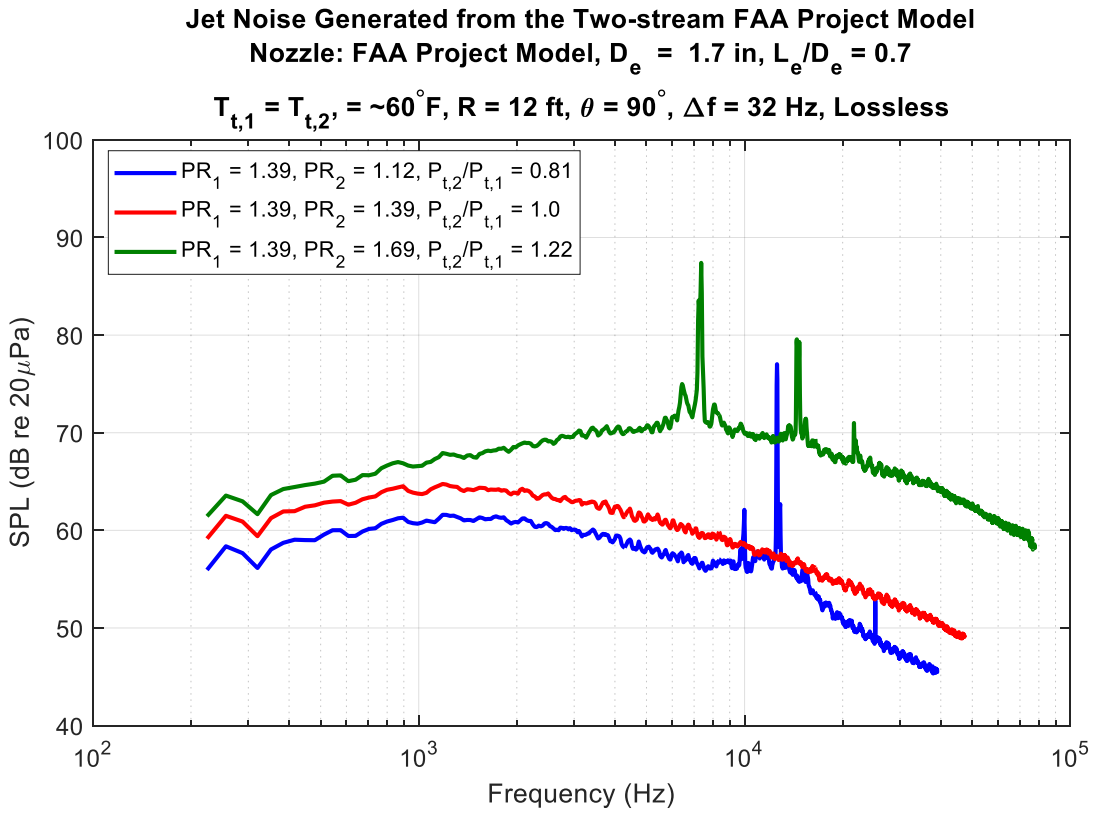

Figure 8. Jet noise measurements with pressure splits far from unity for the L_e/D_e = 0.7 configuration.

The large shift in the tone's fundamental frequency from ER = 1.22 to ER = 0.81 (Figure 8) is believed to represent a change in the underlying physical mechanism responsible for the tones, perhaps because of a change from the resonances excited by the ducted core-bypass vortex to the feedback phenomenon. Using bracketing assumptions that the convection speed of an instability wave inside the model is similar to that of a free jet, and that the two streams have approximately reached their full flow velocities before reaching the mixing duct inlet, the predicted feedback frequencies are much less than 6 kHz. This finding suggests that the tones in Figure 8 and in the upper spectrum shown in Figure 9 are unlikely to be due to feedback occurring between the primary and exhaust nozzle lips. The predictions are not sufficiently sensitive to the assumed instability wave convection speed for invalidity of the assumed value to provide a possible explanation for the differences between the measured high-frequency tones and the expected relatively low-frequency feedback tone. Furthermore, for a

given test point (PR_1 = 1.39, ER = 0.88), switching between the shortest and longest mixing duct configurations causes the tone's fundamental to jump to a much lower frequency. This is consistent with expectations for the emergence of a feedback phenomenon; namely, that there is a minimum mixing duct length for which the core-bypass shear layer instability has adequate time to grow during its convection inside the mixing duct before impingement on the exhaust nozzle lip. If the tones are due to a feedback phenomenon, when the sound wave travels from the exhaust nozzle toward the primary nozzle lip, it will take longer for the extraction ratio of 1.22 than for 0.81, because the higher-speed flow of the outer steam will slow the sound travel time to the primary nozzle to a greater extent. This will reduce the feedback frequency. Likewise, the instability wave will travel downstream slowly, because the relative velocity of the primary jet will be lower. This aspect will also contribute to the reduction of the final feedback frequency for the higher extraction ratio as seen here.

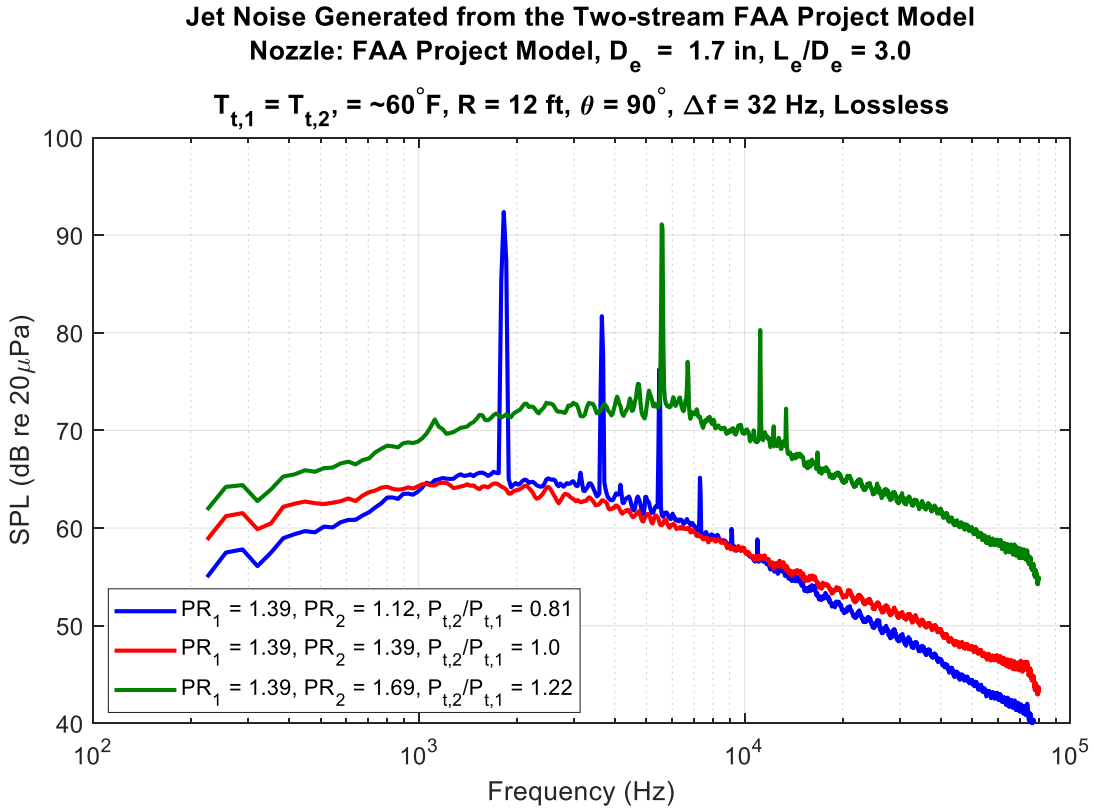

Figure 9. Jet noise measurements with pressure splits far from unity for the L_e/D_e = 3.0 configuration.

Figure 10 shows a comparison of the noise produced with the L_e/D_e = 3.0 configuration when PR_1 = PR_2 = 1.39 vs. that produced when only the primary stream is set to PR_1 = 1.39 and the secondary stream is closed off. Figure 11 shows the corresponding centerline velocity profiles. Ideally, an effect of a small change in diameter should be observed. That is, we assume that the case in which the primary nozzle is operating at PR_1 = 1.39 and the secondary stream is closed off is associated with a primary nozzle diameter of 1.6 in, and that the case of the primary and secondary stream operating at PR_1 = PR_2 = 1.39 is associated with the exhaust nozzle diameter of 1.7 in. This increase in diameter should cause an increase in low-frequency noise and a decrease in high-frequency noise when SPL is plotted as a function of frequency. When SPL is plotted as a function of Strouhal number, a constant noise increase should be observed across the entire spectrum. In this case, the nozzle diameters are nearly identical (1.6 in for the primary vs. 1.7 in for the exhaust nozzle). This would result in a theoretical 0.53 dB increase and a negligible frequency shift, if a plug flow profile is assumed at the exit of the exhaust nozzle. The above argument is presented to understand what factors would increase the low frequency and to emphasize the finding of only minor changes in peak frequency shift and changes in SPLs due to the geometry used. We are unable to determine what the internal mixing will do, except that the high-frequency noise produced near the primary nozzle exit will be partly shielded by the ducting.

However, as shown in Figure 10, when only the primary stream is active, tones are produced by the model, and the two cases exhibit large noise level differences, because operating the primary nozzle alone with the secondary ducting in place creates an acoustically excited jet. This excitation causes broadband noise amplification, as discussed by Ahuja and Blakney (1985) and Lepicovsky et al. (1985). Figure 11 shows a significant shortening of the potential core in the case of the primary nozzle operating with the secondary stream closed off, which is a characteristic of a tone-excited jet. Of note, these tones are produced inside the nozzle ducting and therefore will be much louder than measurements in the far field. As shown in Figure 10, these tones are absent in the case of the primary and secondary streams operating at the same pressure ratio. As shown below, this effect reappears at higher pressure ratios (possibly because of a mismatch in feedback frequencies and duct resonance frequencies). The feedback frequency will change as the speed of sound for the return path of the feedback is reduced by the secondary stream, as shown by Lepicovsky and Ahuja (1985). In the future, a more exact explanation is anticipated, but the modeling teams should be able to predict this effect.

This measurement also confirms a correlation between the tones and a large change in the flow field. To be certain that the change in potential core length is a tone-induced effect, as assumed in the explanation above, the potential core length for a given primary pressure ratio and a wide range of different secondary pressure ratios must be measured. The primary pressure ratio should be selected such that no tones are produced when the primary and secondary pressure ratios are matched. If, at some change in secondary pressure ratio, tones emerge, and a simultaneous decrease in the potential core length is observed, the potential core shortening can be assumed with greater confidence to be due to the tone and to be part of a flow-acoustic interaction. The detailed PIV flow-field measurements to be conducted by the end of year 1 will provide greater insight into the link between the tones and changes in the flow field.

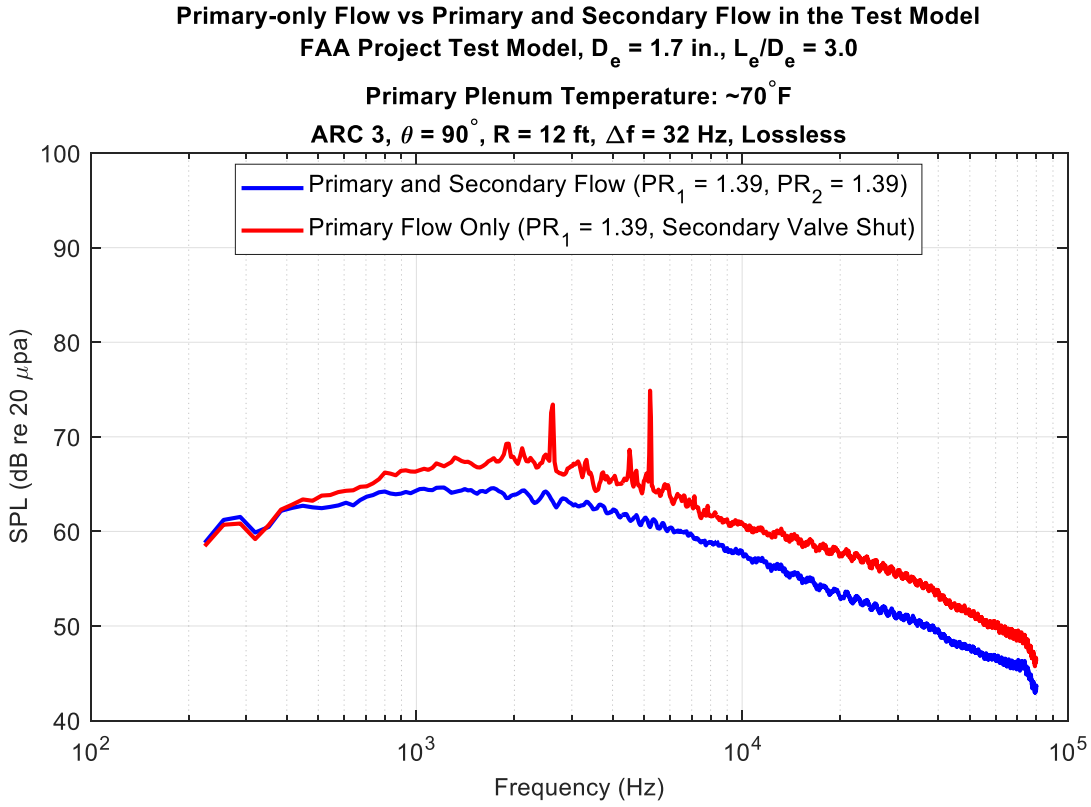

Figure 10. Comparison of the noise produced by the test model with L_e/D_e = 3.0, when $PR_1 = PR_2$ = 1.39 vs. only an active primary stream with PR_1 = 1.39.

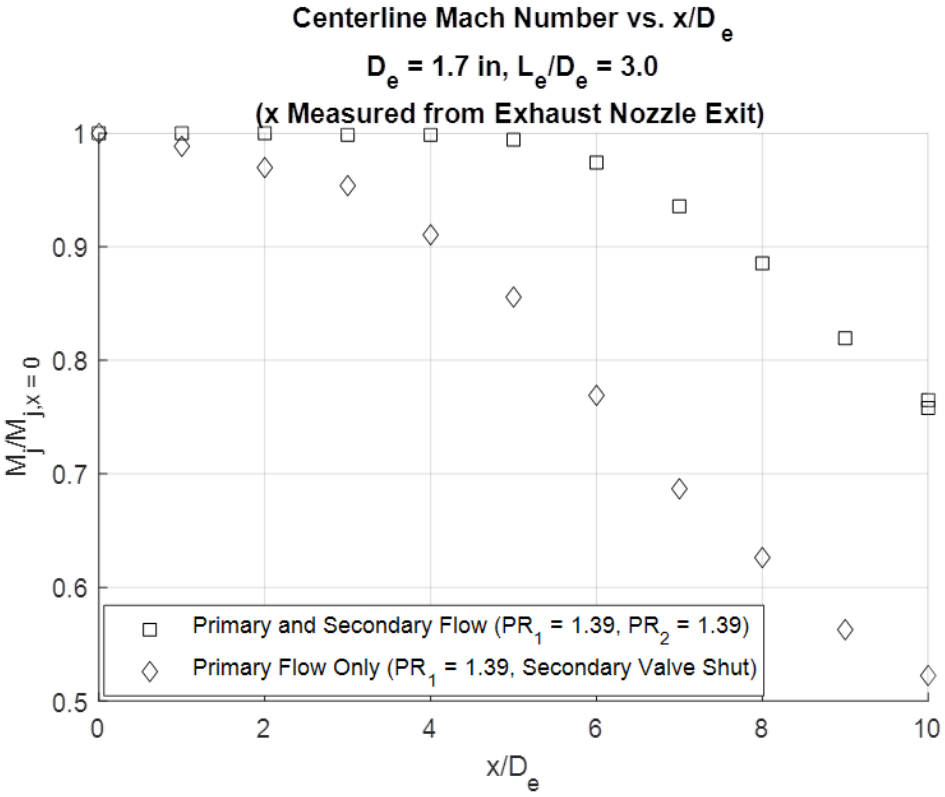

Figure 11. Centerline Mach number profile comparison of the jet produced by the test model with L_e/D_e = 3.0 and PR_1 = PR_2 = 1.39 vs. only an active primary stream with PR_1 = 1.39.

Refined Analysis of Data at Extraction Ratios between 1 and 1.07

As mentioned above, FAA and Gulfstream indicated that for mixed flow engines the extraction ratio values between 1.00 and 1.07 are the most realistic. Acoustic measurements focusing on this extraction ratio range are presented here. Figure 12 shows the results of the small variations of extraction ratio for a PR_1 = 1.39. Figure 12 shows the results as the extraction ratio is varied in steps of 0.01 from 1.00 to 1.07 at a polar angle of 90°. Figure 12 also shows cases of L_e/D_e of 0.7 and 0.3, as well as cases of unheated core flow and core flow heated to 500 °F. Comparisons of Figures 12a and 12b, as well as Figures 12c and 11d, provide some insight into the effect of heating the core flow. There are two main effects from heating the core flow: (1) the overall noise levels increases, as a result of higher jet velocities in the case of heated core flow, and (2) the jet noise spectra show greater collapse. To illustrate the first effect, for both the L_e/D_e = 0.7 and 3.0 cases, the peak noise increases by 5 as the core flow is heated to 500° F. To illustrate the second effect, for both L_e/D_e = 0.7 and L_e/D_e = 3.0, for the unheated case there is a 1-dB difference in the spectra at low frequencies, but this spread increases to 5 dB at high frequencies. For the heated core case, the spectra collapse below 8 kHz, and above 8 kHz all SPLs are within 2 dB. Of note, for the L_e/D_e = 3.0 case, the heated core flow shows very minimal variation in spectral levels. Regarding the effect of mixing length, for the unheated case, the spread in spectral levels is reduced by a maximum of 5 dB to 3 dB. In the heated core flow case, spectral differences above 8 kHz nearly disappear in the L_e/D_e = 3.0 case.

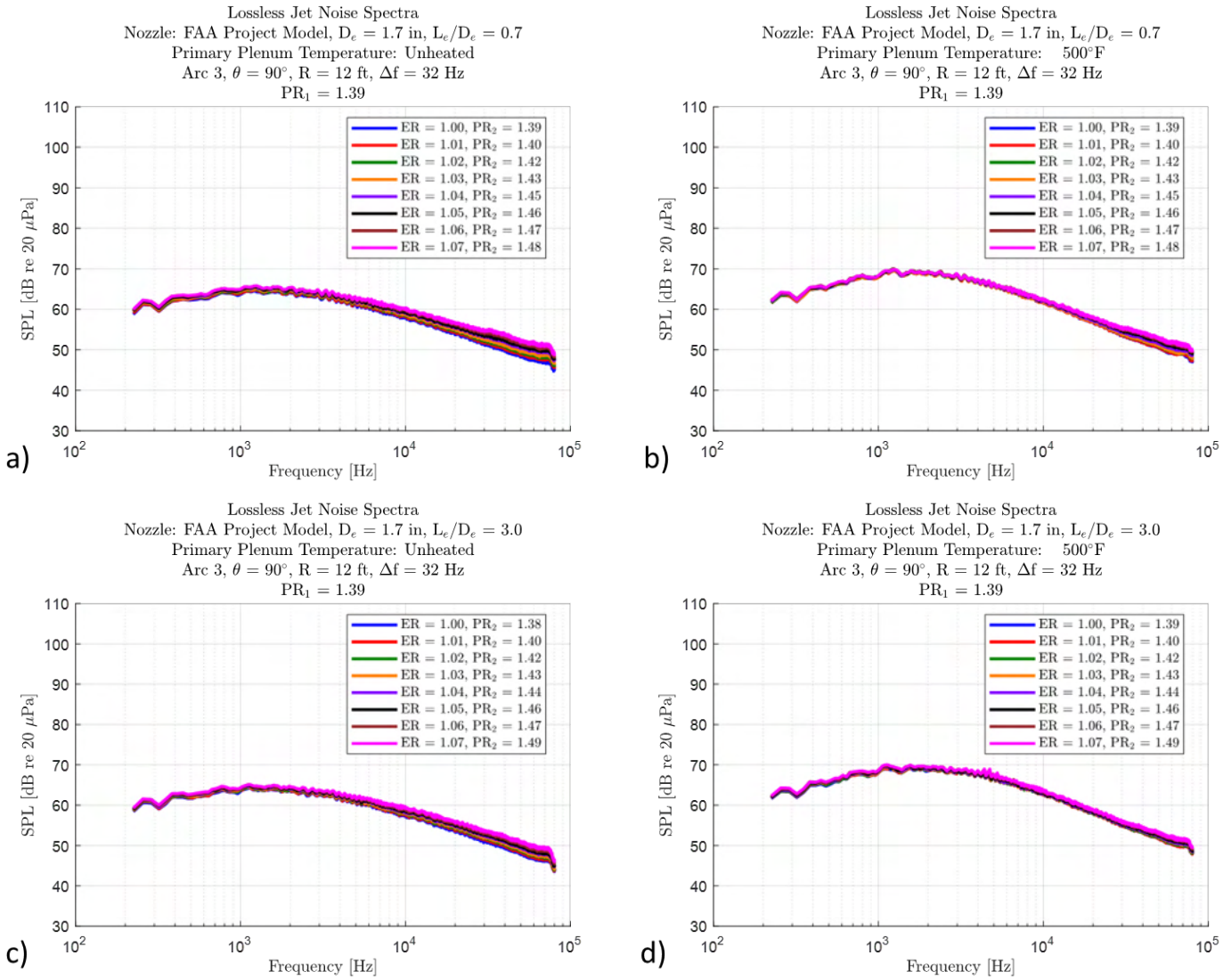

Figure 12. Example acoustic measurements for small extraction ratioER changes for PR1 = 1.39 at θ = 90°. (a) L_e/D_e = 0.7 and core flow unheated, (b) L_e/D_e = 0.7 and core flow heated to 500 °F, (c) L_e/D_e = 3.0 and core flow unheated, and (d) L_e/D_e = 3.0 and core flow heated to 500 °F.

Figure 13 shows the same type of acoustic measurements as Figure 12, but for PR_1 = 1.69. The above comments regarding the effects of heating the core flow and the change in mixing length again apply. The main difference in the data between Figures 12 and 13 is the presence of tones in the spectra with the PR_1 = 1.69. For this primary pressure ratio, tones exist even at an ER = 1.00. As can be seen in Figure 13, with the exception of Figure 13d, the tone level and frequency increase with increasing extraction ratio. Observing the effect of heating the core flow, the tone levels decrease by as much as 10–15 dB in some cases with heating of the core flow. In the unheated condition, increasing the mixing length can increase the tone levels by as much as 10 dB. For the heated condition, as shown in Figure 13d, the increased mixing length actually minimizes the tonal levels.

Importantly, for the cases discussed above, if the tones could be eliminated, there is little difference in the spectral levels primarily to the left of the spectral peak and immediately to the right of the peak, as long as the extraction ratios are maintained close to unity, on the order of 1.07. This result implies that for a fixed primary operating pressure ratio,

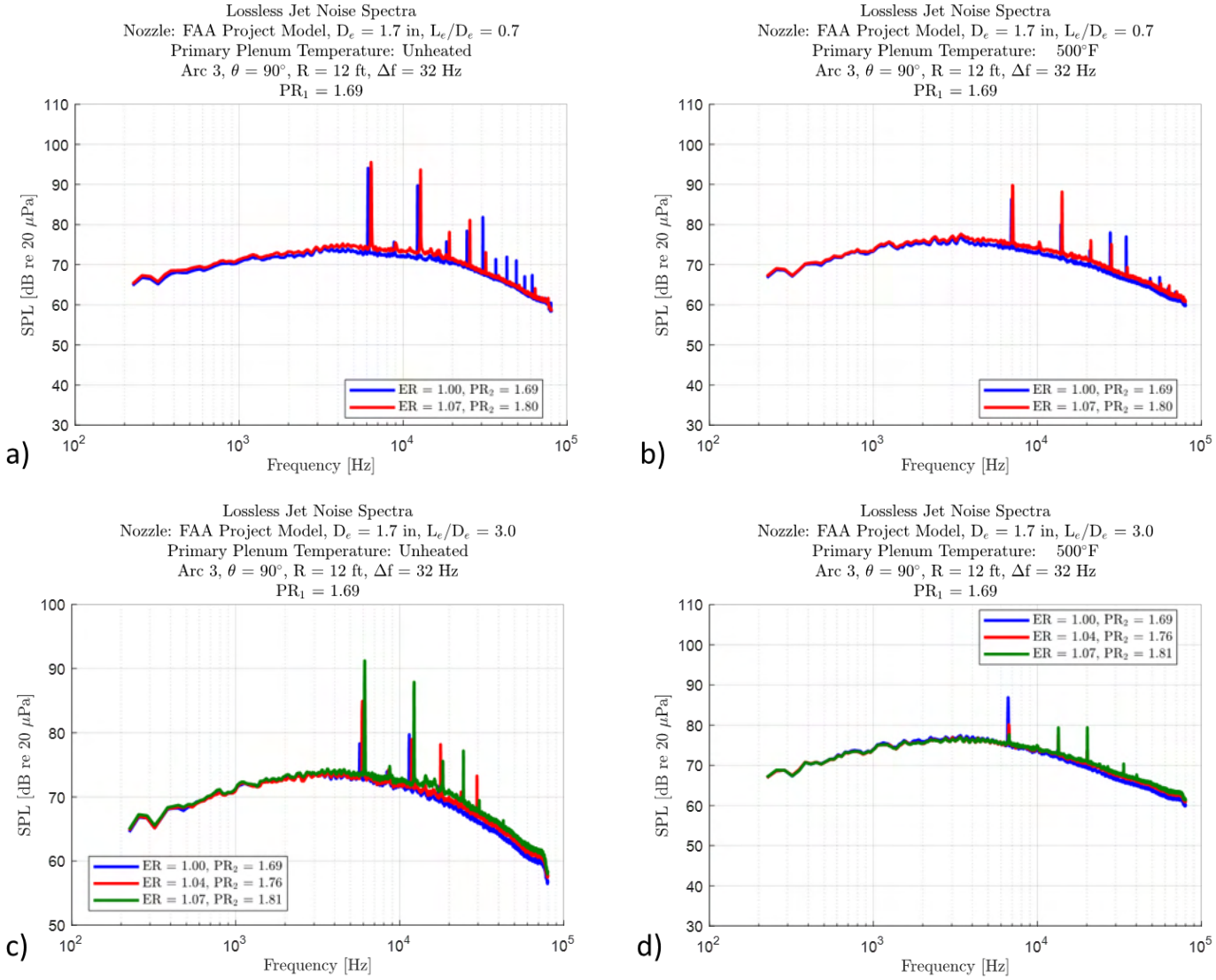

Figure 13. Example acoustic measurements for the small extraction ratio changes for PR1 = 1.69 at θ = 90°. (a) L_e/D_e = 0.7 and core flow unheated, (b) L_e/D_e = 0.7 and core flow heated to 500 °F, (c) L_e/D_e = 3.0 and core flow unheated, and (d) L_e/D_e = 3.0 and core flow heated to 500 °F.

PIV Flow-Field Measurements

Methodology: The jet flow field issued from the model-scale nozzle is characterized by using a double-pulsed PIV system in GTRI's Flow Diagnostics Facility. Details of this facility have been presented by Burrin and Tanna (2005). The instrumentation and hardware in the Flow Diagnostics Facility are shown schematically in Figure 14. The PIV measurements are used to produce mean and unsteady velocity vector fields. These two vector fields are produced for two different physical regions in the jet flow field: (1) a high-spatial-resolution, zoomed-in view of the exhaust nozzle shear layer very close to its exit and (2)

a multi-station traverse, which captures ($0 < x < 20D_e$) by positioning the camera at several stations along the jet axis and stitching the fields measured at each station together. Neighboring stations along the traverse have some viewing-window overlap. In this overlapping region, the vector fields calculated from the station furthest from the nozzle are reported.

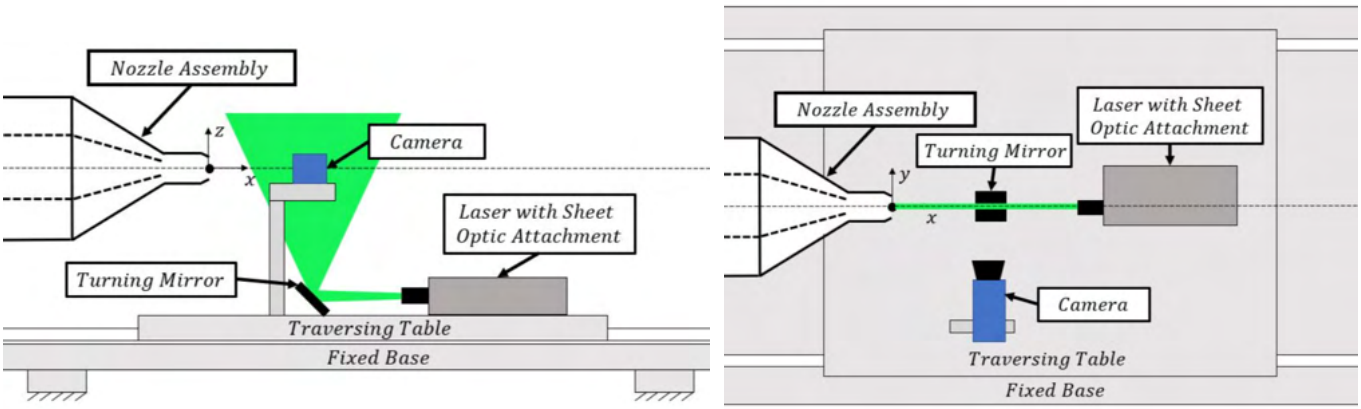

Figure 14. GTRI's Flow Diagnostics Facility: (left) side view and (right) top view.

Validation: A major focus of the experimental work has been to ensure that the measurements, particularly turbulence statistics, produced by the PIV system are accurate, in accordance with the program's objective to provide valuable, detailed turbulence measurements to modelers. To validate the PIV system setup and data-processing settings, the 1.6-inch conical primary nozzle was installed in isolation in the Flow Diagnostics Facility, as shown in Figure 15. PIV data were acquired for a jet Mach number of 0.58. This approach enabled comparison to the historical data published by Ahuja et al. (1982), which were acquired in the same facility with the same size nozzle. The historical data include mean velocity and turbulence intensity profiles along the jet's centerline and lipline. For this validation run, 750 image pairs were acquired at a nominal rate of 5 Hz and processed. This number of image pairs has been shown to provide acceptable convergence of turbulence intensity measurements during validation work. The two-dimensional mean velocity and turbulence intensity fields measured with the present setup are shown in Figure 16. In this work, the turbulence intensity is given as

$$\mathrm{TI} = \sigma_u / \bar{u}$$

where σ_u is the local standard deviation of the x-component of velocity. At all points, the turbulence intensity is calculated by normalizing the local σ_u by the mean velocity along the jet's centerline at $x/D_e = 0.5$. For mean velocity fields, the local mean velocity is normalized by the mean velocity at the jet's centerline at $x/D_e = 0.5$ as well. The locations in the two-dimensional fields at which to extract lipline and centerline profiles are shown by the black dashed lines in Figure16. Figures 17–19 show the profiles of these fields along the jet's centerline and lipline. In these plots, the solid black curves are 100-point median-filtered curves, whereas the light-gray curves are the true PIV processing outputs. The plot axis limits for velocity profile plots are those used by Ahuja et al. (1982), for ease of visual comparison. The centerline and lipline profiles show excellent agreement with the historical data and provide confidence in both the physical system and the PIV processing settings.

Figure 15. The 1.6-in primary nozzle installed in isolation for PIV measurement validation.

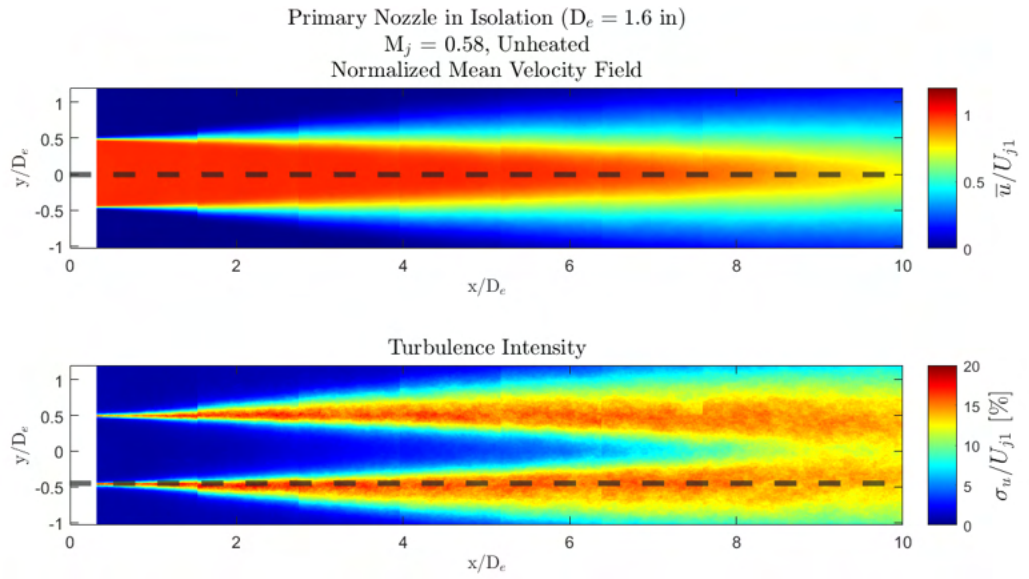

Figure 16. Validation dataset's mean velocity (top) and turbulence intensity (bottom) fields.

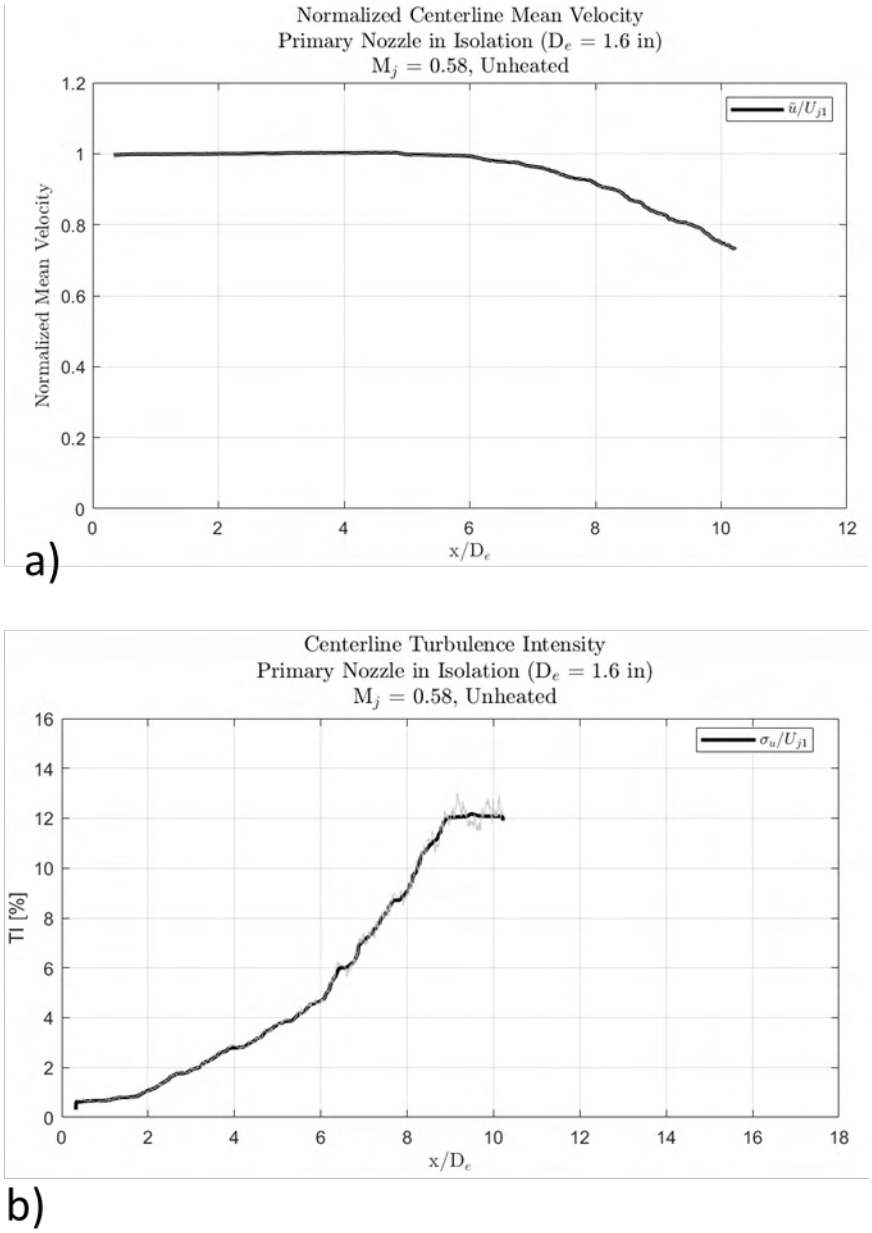

Figure 17. Validation of the dataset's (a) centerline mean velocity distribution and (b) centerline turbulence intensity distribution.

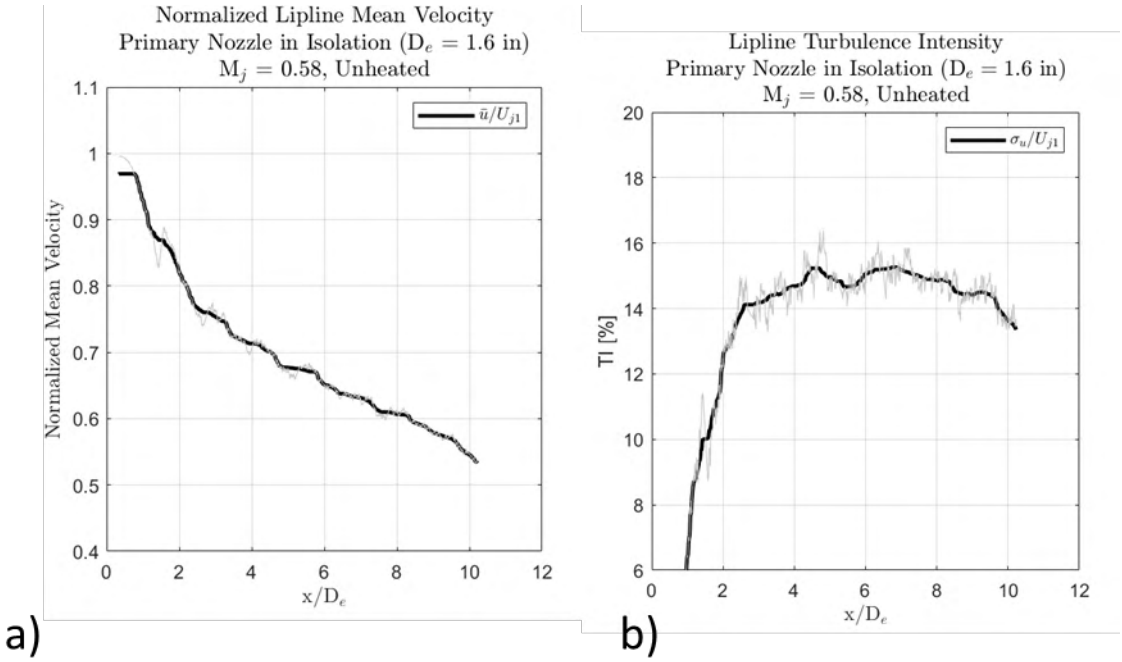

Figure 18. Validation of the dataset's (a) lipline mean velocity distribution and (b) lipline turbulence intensity distribution.

Task 5 - Data Dissemination

Georgia Institute of Technology

Objective

The objective of this task is to maintain contact with the modelers being funded by FAA under Project 59 and provide them with the nozzle design, and both the acoustic and flow data from the current project.

Research Approach

The modelers were all informed of our preliminary design during the first Advisory Panel discussion. We have now provided the finalized design to the modelers.

The modelers were provided with boundary-layer and acoustic measurements generated with the primary nozzle acquired for A. Karon's PhD thesis (2016)

At the end of this year, the FAA gave permission to begin the data dissemination. This process had begun with a few conditions, but more should be available in the near future.

Task 6 - Assess Readiness of Design Tools for a Simple Baseline Nozzle Configuration

Georgia Institute of Technology

Objective

Whereas Task 5 involves only providing the data to the modelers, the objective of this task is to interact with the modelers in terms of verification of their codes with the measurements made under this project at Georgia Tech. Our partners Gulfstream and ASDL will also be comparing their low-fidelity codes with our data. Georgia Tech is still waiting for the modelers to be ready for acoustic data comparisons.

Task 7 - Proposal for a Follow-on Effort for Years 2 and 3

Georgia Institute of Technology

The year 2 proposal was submitted at the end of March.

Task 8 - Reporting and Data Dissemination

Georgia Institute of Technology

All quarterly reports and the 2020 annual report were submitted. Progress was presented at both the Spring and Fall FAA ASCENT Advisory Committee meetings.

Milestones

The experimental model was designed and fabricated.

All acoustic measurements have been acquired.

Major Accomplishments

The experimental model was designed and fabricated. All acoustic measurements have been acquired.

Publications

None

Outreach Efforts

None

Awards

None

Student Involvement

David Ramsey assisted with the design of the experimental model and prepared the documents that were sent to the machine shop. He will continue to be the graduate research assistant on this project.

Plans for Next Period

- Complete flow measurements
- Prepare for year 2 efforts

References

Ahuja, K. K. (2003). Designing clean jet-noise facilities and making accurate jet-noise measurements. International Journal of Aeroacoustics, *2*(3), 371-412.

Ahuja, K. K., Lepicovsky, J., Tam, C. K. W., Morris, P. J., & Burrin, R. H. (1982). Tone-excited jet: Theory and experiments (Report No. 3538). National Aeronautics and Space Administration.

Ahuja, K. K., & Blakney, D. F. (1985). Tone excited jets - part IV: Acoustic measurements. Journal of Sound and Vibration, *102*(1), 93-117.

Burrin, R. H., Dean, P. D., & Tanna, H. K. (1974). A new anechoic facility for supersonic hot jet noise research at Lockheed-Georgia. The Journal of the Acoustical Society of America, *55*(2), 400.

Burrin, R., & Tanna, H. (2005). The Lockheed-Georgia coannular jet research facility. The Journal of the Acoustical Society of America, *65*(S1), S44.

Cumpsty, N. A., & Whitehead, D. S. (1971). The excitation of acoustic resonances by vortex shedding. Journal of Sound and Vibration, *18*(3), 353–369. https://doi.org/10.1016/0022-460x(71)90707-3Karon, A. Z. (2016). Potential factors responsible for discrepancies in jet noise measurements of different studies [Ph.D. thesis, Daniel Guggenheim School of Aerospace Engineering, Georgia Institute of Technology].

Lepicovsky, J., & Ahuja, K. K. (1985). Experimental results on edge-tone oscillations in high-speed subsonic jets. AIAA Journal, *23*(10), 1463-1468.

Lepicovsky, J., Ahuja, K. K., & Burrin, R. H. (1985). Tone excited jets - part III: Flow measurements. Journal of Sound and Vibration, *102*(1), 71-91.

Parker, R. & Stoneman, S. A. T. (1989). The excitation and consequences of acoustic resonances in enclosed fluid flow around solid bodies. Proceedings of the Institution of Mechanical Engineers, Part C: Mechanical Engineering Science, *203*(1), 9–19.

Appendix A – Support from ASDL

During the period of performance, the engine cycle team has been working with the ASCENT Project 10 (A10) team's matched cycle and flowpath for the nine supersonic transports shown in
Figure. The A10 researchers developed/converged on a cycle for all nine SST vehicles, and a notional flowpath is shown in
Figure. The engine cycle team is interested in the mixer exit and nozzle configuration shown in the red dotted square in
Figure and blown up with dimensional references in
Figure. To provide engine operating conditions during takeoff to the rest of the ASCENT 59 team, an optimization of the takeoff trajectory must be performed. This optimization is performed with the NASA Flight Optimization System's (FLOPS) takeoff and landing module. Based on the engine cycle thermodynamic performance, the flowpath information, detailed takeoff and landing aerodynamics for each SST, a set of variables controlling the takeoff trajectory, including the percentage program lapse rate (PLR), is perturbed within a given range. The resulting trajectories and associated certification noise levels are recorded. This dataset is examined to choose a trajectory with the lowest certification noise level subject to safety constraints. The resulting cycle conditions, mixer, and nozzle operating conditions for all nine configurations are shown in Tables A-1 to A-3. The variation (i.e., ranges) in these parameters for each class of SSTs is shown in cycle and dimensions in Tables A-4 to A-6. The variation in these parameters across all nine SSTs is shown in

Table.

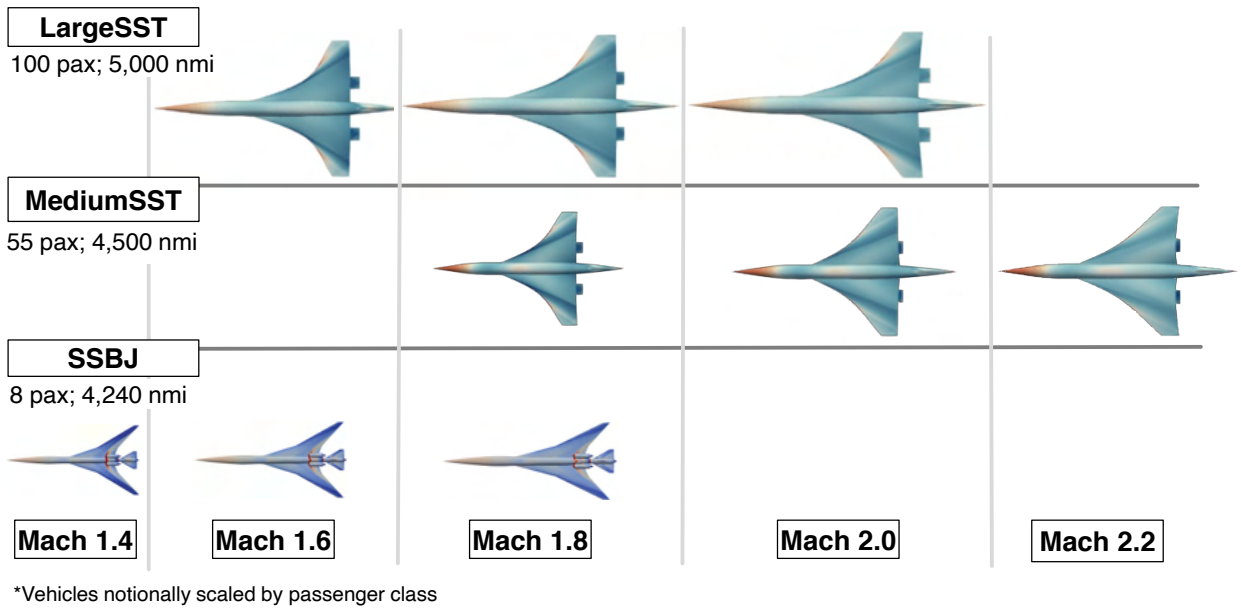

Figure A-1. Nine SST Configurations from ASCENT Project 10.

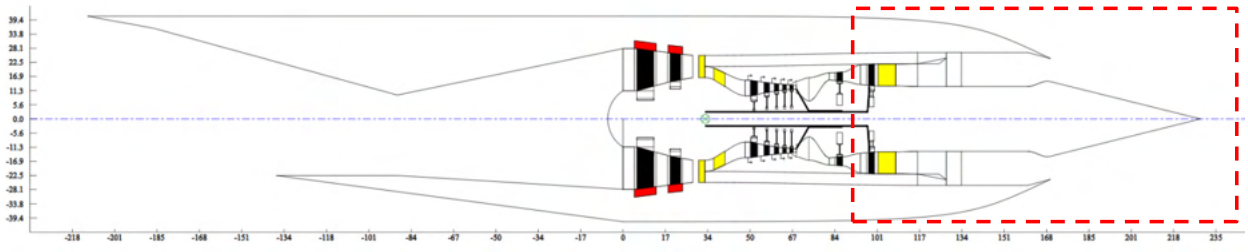

Figure A-2. Notional SST Flowpath.

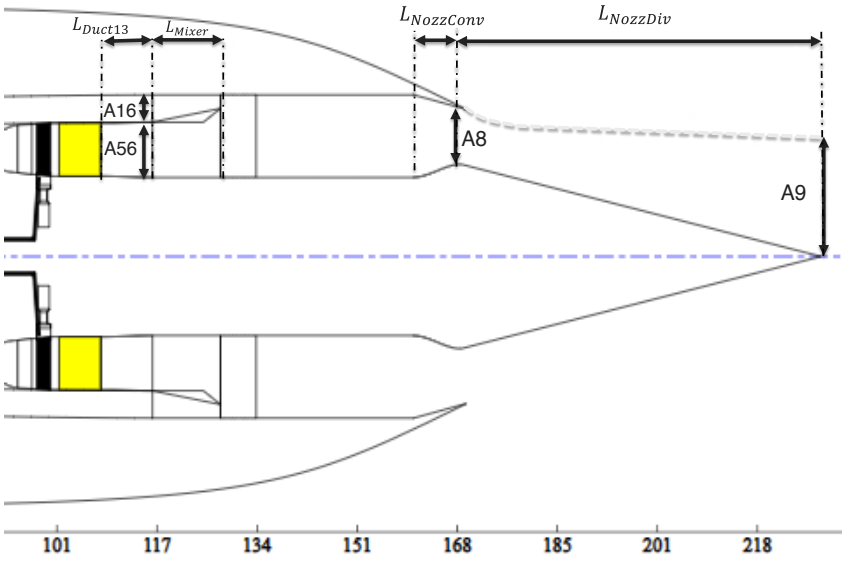

Figure A-3. Mixer and nozzle dimensional reference.

Table A-1. Cycle, mixer, and nozzle operating conditions during takeoff for three SSBJs.

Cycle Parameter @ TO, ISA+18F	**SSBJ M1.4 (v1.5)**			**SSBJ M1.6 (v1.5)**			**SSBJ M1.8 (v1.5)**		
BPR	3.68			3.45			3.66		
FPR	2.03			2.02			2.03		
NPR	1.86			1.85			1.90		
Extraction Ratio	1.11			1.10			1.05		
Duct 13 Length (in)	5.00			5.00			5.00		
Mixer Length (in)	10.19			10.74			11.34		
Nozzle Converg. Length (in)	9.76			11.22			12.77		
Nozzle Diverg. Length (in)	53.54			58.82			63.72		
Station	Area [sq. in]	Mach	Tt [deg R]	Area [sq. in]	Mach	Tt [deg R]	Area [sq. in]	Mach	Tt [deg R]
16 (Mixer secondary in)	812.2	0.560	680.7	889.4	0.548	679.7	1055.7	0.476	680.6
5.6 (Mixer primary in)	519.1	0.407	1773.1	590.5	0.406	1749.8	592.6	0.405	1861.6
6 (Mixer out)	1331.3	0.527	934.9	1479.9	0.518	940.9	1648.3	0.479	959.2
7 (Nozzle in)	1331.3	0.543	934.9	1479.9	0.534	940.9	1648.3	0.492	959.2
8 (Nozzle throat)	1082.8	0.987	934.9	1189.2	0.985	940.9	1254.9	1.000	959.2
9 (Nozzle out)	1051.0	0.987	934.9	1154.6	0.985	940.9	1214.8	1.004	959.2

Table A-2. Cycle, mixer, and nozzle operating conditions during takeoff for three medium SSTs.

Cycle Parameter @ TO, ISA+18F	**Medium SST M1.8 (v12.2)**			**Medium SST M2.0 (v12.2)**			**Medium SST M2.2 (v12.2)**		
BPR	3.38			2.93			2.58		
FPR	2.02			2.10			2.20		
NPR	1.89			1.98			2.09		
Extraction Ratio	1.06			1.04			1.02		
Duct 13 Length (in)	5.00			5.00			5.00		
Mixer Length (in)	12.50			13.30			13.59		
Nozzle Converg. Length (in)	13.47			16.16			18.50		
Nozzle Diverg. Length (in)	68.74			77.43			83.87		
Station	Area [sq. in]	Mach	Tt [deg R]	Area [sq. in]	Mach	Tt [deg R]	Area [sq. in]	Mach	Tt [deg R]
16 (Mixer secondary in)	1237.3	0.487	680.0	1363.0	0.457	688.4	1389.6	0.430	698.9
5.6 (Mixer primary in)	767.1	0.405	1824.6	904.1	0.404	1813.1	980.1	0.405	1833.0
6 (Mixer out)	2004.4	0.483	967.3	2267.1	0.462	1001.6	2369.8	0.445	1044.3
7 (Nozzle in)	2004.4	0.497	967.3	2267.1	0.475	1001.6	2369.8	0.457	1044.3
8 (Nozzle throat)	1535.2	1.000	967.3	1688.0	1.000	1001.6	1716.5	1.000	1044.3
9 (Nozzle out)	1486.4	1.003	967.3	1627.0	1.043	1001.6	1659.4	1.086	1044.3

Table A-3. Cycle, mixer, and nozzle operating conditions during takeoff for three large SSTs.

Cycle Parameter @ TO, ISA+18F	**Large SST M1.6 (v1.2)**			**Large SST M1.8 (v1.2)**			**Large SST M2.0 (v1.2)**		
BPR	3.73			3.37			2.87		
FPR	2.07			2.08			2.20		
NPR	1.92			1.94			2.06		
Extraction Ratio	1.07			1.05			1.03		
Duct 13 Length (in)	5.00			5.00			5.00		
Mixer Length (in)	14.07			14.89			15.00		
Nozzle Converg. Length (in)	13.63			16.04			18.71		
Nozzle Diverg. Length (in)	73.55			81.68			88.44		
Station	Area [sq. in]	Mach	Tt [deg R]	Area [sq. in]	Mach	Tt [deg R]	Area [sq. in]	Mach	Tt [deg R]
16 (Mixer secondary in)	1596.8	0.503	685.2	1759.7	0.476	686.3	1725.9	0.446	698.8
5.6 (Mixer primary in)	941.3	0.405	1888.2	1083.0	0.405	1886.3	1157.4	0.405	1890.7
6 (Mixer out)	2538.1	0.496	966.7	2842.7	0.478	989.4	2883.3	0.457	1037.7
7 (Nozzle in)	2538.1	0.511	966.7	2842.7	0.491	989.4	2883.3	0.469	1037.7
8 (Nozzle throat)	1986.3	1.000	966.7	2165.0	1.000	989.4	2131.6	1.000	1037.7
9 (Nozzle out)	1920.5	1.014	966.7	2090.9	1.024	989.4	2058.1	1.076	1037.7

Table A-4. Variations in cycle, mixer, and nozzle operating conditions for SSBJs (v1.5).

Cycle Parameter	**SSBJ (v1.5) Ranges**					
@ TO, ISA+18F	Low	High				
BPR	3.45	3.68				
FPR	2.02	2.03				
NPR	1.85	1.90				
Extraction Ratio	1.05	1.11				
Duct 13 Length (in)	5.00	5.00				
Mixer Length (in)	10.19	11.34				
Nozzle Converg. Length (in)	9.76	12.77				
Nozzle Diverg. Length (in)	53.54	63.72				
Station	Area (sq. in) [Low - High]		Mach [Low - High]		Tt (deg R) [Low - High	
16 (Mixer secondary in)	812.2	1055.7	0.476	0.560	679.730	680.7
5.6 (Mixer primary in)	519.1	592.6	0.405	0.407	1749.750	1861.6
6 (Mixer out)	1331.3	1648.3	0.479	0.527	934.890	959.2
7 (Nozzle in)	1331.3	1648.3	0.492	0.543	934.890	959.2
8 (Nozzle throat)	1082.8	1254.9	0.985	1.000	934.890	959.2
9 (Nozzle out)	1051.0	1214.8	0.985	1.004	934.890	959.2

Table A-5. Variations in cycle, mixer, and nozzle operating conditions for medium SSTs (v12.2).

Cycle Parameter	**Medium SST (v12.2) Ranges**					
@ TO, ISA+18F	Low	High				
BPR	2.58	3.38				
FPR	2.02	2.20				
NPR	1.89	2.09				
Extraction Ratio	1.02	1.06				
Duct 13 Length (in)	5.00	5.00				
Mixer Length (in)	12.50	13.59				
Nozzle Converg. Length (in)	13.47	18.50				
Nozzle Diverg. Length (in)	68.74	83.87				
Station	Area (sq. in) [Low - High]		Mach [Low - High]		Tt (deg R) [Low - High	
16 (Mixer secondary in)	1237.3	1389.6	0.430	0.487	679.980	698.9
5.6 (Mixer primary in)	767.1	980.1	0.404	0.405	1813.120	1833.0
6 (Mixer out)	2004.4	2369.8	0.445	0.483	967.270	1044.3
7 (Nozzle in)	2004.4	2369.8	0.457	0.497	967.270	1044.3
8 (Nozzle throat)	1535.2	1716.5	1.000	1.000	967.270	1044.3
9 (Nozzle out)	1486.4	1659.4	1.003	1.086	967.270	1044.3

Table A-6. Variations in cycle, mixer, and nozzle operating conditions for large SSTs (v1.2).

Cycle Parameter	**Large SST (v1.2) Ranges**					
@ TO, ISA+18F	Low	High				
BPR	2.87	3.73				
FPR	2.07	2.20				
NPR	1.92	2.06				
Extraction Ratio	1.03	1.07				
Duct 13 Length (in)	5.00	5.00				
Mixer Length (in)	14.07	15.00				
Nozzle Converg. Length (in)	13.63	18.71				
Nozzle Diverg. Length (in)	73.55	88.44				
Station	Area (sq. in) [Low - High]		Mach [Low - High]		Tt (deg R) [Low - High	
16 (Mixer secondary in)	1596.8	1759.7	0.4	0.5	685.2	698.8
5.6 (Mixer primary in)	941.3	1157.4	0.405	0.405	1886.320	1890.7
6 (Mixer out)	2538.1	2883.3	0.457	0.496	966.740	1037.7
7 (Nozzle in)	2538.1	2883.3	0.469	0.511	966.740	1037.7
8 (Nozzle throat)	1986.3	2165.0	1.000	1.000	966.740	1037.7
9 (Nozzle out)	1920.5	2090.9	1.014	1.076	966.740	1037.7

Table A-7. Variations in cycle, mixer, and nozzle operating conditions across all nine SSTs.

Cycle Parameter	**Ranges over all 9 configurations**					
@ TO, ISA+18F	Low	High				
BPR	2.58	3.73				
FPR	2.02	2.20				
NPR	1.85	2.09				
Extraction Ratio	1.02	1.11				
Duct 13 Length (in)	5.00	5.00				
Mixer Length (in)	10.19	15.00				
Nozzle Converg. Length (in)	9.76	18.71				
Nozzle Diverg. Length (in)	53.54	88.44				
Station	Area (sq. in) [Low - High]		Mach [Low - High]		Tt (deg R) [Low - High	
16 (Mixer secondary in)	812.2	1759.7	0.4	0.6	679.7	698.9
5.6 (Mixer primary in)	519.1	1157.4	0.404	0.407	1749.750	1890.7
6 (Mixer out)	1331.3	2883.3	0.445	0.527	934.890	1044.3
7 (Nozzle in)	1331.3	2883.3	0.457	0.543	934.890	1044.3
8 (Nozzle throat)	1082.8	2165.0	0.985	1.000	934.890	1044.3
9 (Nozzle out)	1051.0	2090.9	0.985	1.086	934.890	1044.3

Project 059(C) Modeling Supersonic Jet Noise Reduction with Global Resolvent Modes

University of Illinois Urbana-Champaign

Project Lead Investigator

Daniel J. Bodony
Blue Waters Professor
Department of Aerospace Engineering
University of Illinois Urbana-Champaign
306 C Talbot Labs
104 S. Wright
Urbana, IL 61801
(217) 244-3844
bodony@illinois.edu

University Participants

University of Illinois Urbana-Champaign (UIUC)

- PI(s): Dr. Daniel J. Bodony, Dr. Tim Colonius
- FAA Award Number: 13-C-AJFE-UI-031
- Period of Performance: June 5, 2020 to September 30, 2022
- Tasks:
    1. Establish industry-relevant low bypass ratio (BPR) engine parameters and acoustic assessment workflow with cost-sharing partner
    2. Automated Reynolds-averaged Navier–Stokes equations (RANS) predictions of jet exhaust
    3. Resolvent mode computation—primary and sensitivity
    4. Python resolvent mode interpolation tool
    5. Python optimization tool for jet noise reduction (JNR) (version 1)
    6. Application of version 1 optimization tool on Georgia Tech Research Institute (GTRI) dual-stream nozzle
    7. Self-calibrating resolvent formulation and implementation
    8. Python optimization tool update using self-calibrating resolvent formulation (version 2)
    9. Application of version 2 optimization tool on GTRI dual-stream nozzle
    10. Application of version 2 optimization tool on Boom-relevant geometry (if cost-sharing agreement is in place)

Project Funding Level

FAA provided $399,955 in funding. Proposed cost-matching with GE Aviation (contact person: Dr. Robert Babbitt) is no longer active. Negotiations with Boom (contact person: Dr. Joe Salamone) are in progress.

Investigation Team

- Dr. Daniel Bodony, UIUC, PI
- Mr. Jay Woo, UIUC, MS student (Previous student Mr. Omar Gutierrez was released from ASCENT Project 059C responsibilities in Q2 of 2021, and Jay Woo was brought on in Q3 of 2021.)
- Dr. Tim Colonius, California Institute of Technology (Caltech), Co-PI
- Mr. Liam Heidt, Caltech, PhD student (Previous student Mr. Ethan Pickering defended his PhD thesis and left Caltech.)

Project Overview

This ASCENT project will leverage recent research in global resolvent-mode-based descriptions of jet turbulence and associated noise to develop an efficient physics-based tool for estimating the impact of jet noise reduction (JNR) strategies on the takeoff noise of civil supersonic transports. The software tool will quickly identify promising JNR technologies and will more precisely evaluate the noise impact of parametric variation of a specific JNR approach. The tool will be compatible with the fleet-scale evaluation codes Global and Regional Environmental Analysis Tool (GREAT; Georgia Institute of Technology) and Fleet Level Environmental Evaluation Tool (FLEET; Purdue University) developed in ASCENT Project 10 and integrated into the ASCENT Project 47 "clean sheet" evaluation tool targeting civil supersonic transport.

The proposed research will create a multi-fidelity JNR tool that can operate in two modes: one mode for specific engine estimates and one mode for fleet-scale estimates:

1. *JNR evaluation for an engine* mode: Using the RANS-provided mean flow for a specific engine, the global resolvent description of wavepackets and their sensitivity to mean flow variations will be computed. The solutions will provide estimates of the low-frequency radiated noise, and the sensitivity derivatives will estimate how the noise changes due to changes in the engine design, thus enabling JNR optimization.
2. *Fleet-level estimation* mode: The resolvent modes and their sensitivity derivatives for existing JNR strategies (e.g., chevrons or internal mixers) will be pre-computed for canonical jet exhaust profiles and flow conditions, compressed, and stored within an efficient data layout that can be quickly evaluated within FLEET, GREAT, and/or NASA's Aircraft Noise Prediction Program (ANOPP).

The original proposal outlined six tasks to be conducted. The project tasks have since been modified in response to changes in the ASCENT Project 59 objectives as well as changes regarding our cost-sharing partner. In particular, ASCENT Project 59 now includes a Georgia Tech Research Institute- (GTRI-) provided extensible dual-stream, internally mixed nozzle that is to be studied computationally and whose noise is to be measured for validation. Furthermore, our GE Aviation cost-sharing partner has been removed because of personnel changes at GE Aviation coupled with the financial impact of the COVID-19 pandemic.

The year 2 proposal was approved for funding with a period of performance of October 1, 2021 through September 30, 2022 and a budget of $199,999. The year 2 statement of work included five tasks, listed as Tasks 6–10 above. The ordering of Tasks 6–10 above differs from the proposal to reflect available GTRI data and cost-sharing developments with Boom.

Task 1 - Establish Industry-relevant Low-BPR Engine Parameters and Acoustic Assessment Workflow with Cost-sharing Partner

University of Illinois at Urbana-Champaign

Objective

The objective of this task is to work with our cost-sharing partner to identify the anticipated range of characteristics of the low-BPR engines being considered for business-class civil supersonic transport. These parameters include, but are not limited to, diameter, BPR, mass flow rate, core and fan stream pressure ratios, core stream temperature ratio, thrust, nozzle configuration, plug designs, chevron designs, internal mixer designs, and afterburner design.

Research Approach

The research approach involves conducting face-to-face meetings and document exchanges to obtain industry-relevant low-BPR engine parameters and acoustic assessment workflows.

Milestone(s)

1. Find new cost-sharing partner candidate
2. Establish a nondisclosure agreement (NDA) to initiate discussions
3. Exchange low-BPR engine parameters and acoustic assessment workflow

Major Accomplishments
Milestone 1 has been completed with the help of Donald Scata (FAA). An initial discussion was held on October 28, 2020, between UIUC (Daniel Bodony) and Boom Supersonics (Rachel Devine, Joe Salamone, and Lourdes Maurice) to connect and establish the overall goals of the ASCENT 59 Project. Milestone 2 has been completed, and an NDA between Boom and UIUC has been established. Milestone 3 has been completed through Zoom-based conversations with Joe Salamone and Daniel Bodony.

Publications
None

Outreach Efforts
None

Awards
None

Student Involvement
None

Plans for Next Period
In the next period, a cost-sharing agreement with Boom will be finalized. In Q1 of 2021, Boom requested an extension of time to accommodate Boom's internal demands on staff and resources. PI Daniel Bodony will reconnect with Boom in Q1 of 2022.

Task 2 - Automated RANS Predictions of Jet Exhaust
University of Illinois at Urbana-Champaign

Objective
The objective of this task is to develop and verify an automated toolchain for using RANS methods to predict the jet exhaust plume from candidate near-sonic multi-stream jet nozzles.

Research Approach
Achieving JNR will require changes to the engine cycle and nozzle geometries. A Python-based software infrastructure is to be developed that takes parametrically defined computer-aided design (CAD)-based descriptions of nozzle geometries, automatically generates meshes and boundary conditions for the nozzle internal flow path and the external nozzle plume, initiates an open-source RANS solver, and curates the data.

Milestones
1. Additional developments to computational fluid dynamics flow path
2. Verification of RANS simulation results
3. Automation of Python infrastructure

Major Accomplishments
Milestone 1 progress included adjusting the boundary conditions and increasing the computational domain of the mesh grid for each nozzle model. Post-processing calculations have also been developed to monitor properties of the nozzle exhaust and thereby characterize steady flow behavior. For Milestone 2, results obtained from post-processing have been verified through comparison to a numerical solution based on quasi-1D flow theory for mixed exhaust jet nozzles. Milestone 3 is in progress; almost-complete automation of individual computational fluid dynamics processes has been achieved, with the necessary user interaction required to execute the processes in sequential order.

Publications
None

Outreach Efforts
None

Awards
None

Student Involvement
Jay Woo is responsible for developing the Python toolchain.

Plans for Next Period
- Complete Milestone 3
- Compare simulation results with experimental data to validate and revise models as necessary

Task 3 - Resolvent Mode Computation—Primary and Sensitivity
Caltech (lead) and University of Illinois at Urbana-Champaign

Objective
The objective of this task is to develop and verify a resolvent mode computation tool suitable for evaluating the JNR potential of candidate near-sonic multi-stream jet nozzles.

Research Approach
Achieving JNR will require changes to the engine cycle and nozzle geometries. Estimation of the JNR potential of candidate cycles and geometries will use resolvent mode descriptions of the coherent wavepacket-associated jet noise of the loudest sound sources. We denote the resolvent calculations that provide the input–gain–output modes of the resolvent operator $(i\omega - A)^{-1}$ as "primary," and we denote the changes in those modes due to changes in the jet nozzle geometry and engine cycle as "sensitivity." The resolvent operator requires knowledge of the linearized Navier–Stokes operator A generated for each nozzle and its exhaust plume, and a global mode computational infrastructure. The sensitivity of the resolvent input–gain–output modes requires knowledge of the change in A, e.g., δA, resulting from changes in the nozzle design and/or engine cycle.

Milestones
1. Primary resolvent mode computation capability
2. Resolvent mode training data and fitting
3. Resolvent mode sensitivity computation capability

Major Accomplishments
Milestone 1 has been completed and tested on single-stream subsonic and supersonic jets. Milestone 2 continues to be in progress for the low-BPR, near-sonic jets anticipated for the supersonic aircraft of interest to ASCENT Project 59. Milestone 3 has been completed but not validated.

Publications
Resolvent modeling of turbulent jets, Ethan Pickering PhD thesis, Caltech, 2021.

Outreach Efforts
None

Awards
None

Student Involvement
Ethan Pickering was responsible for the primary resolvent mode computation and the preliminary training data and fitting tasks; he has graduated and left Caltech. Liam Heidt is a new student who learned from Ethan and now leads the global mode computation and its data-driven alignment. Jay Woo is responsible for running and applying the resolvent calculation and its sensitivity.

Plans for Next Period
- Complete Milestone 2 by using acquired but not yet available GTRI flow acoustic data and high-fidelity LES data from the Stanford University ASCENT Project 59 team
- Complete Milestone 3 by validating the sensitivities with GTRI data

Task 4 - Python Resolvent Mode Interpolation Tool
University of Illinois at Urbana-Champaign (lead) and Caltech

Objective
The objective of this task is to develop and verify a Python-based interpolation tool for computing resolvent input–gain–output modes at nozzle geometry and/or engine cycles for which RANS data are unavailable but are near to previously known input–gain–output modes from nearby nozzle geometries and/or engine cycles.

Research Approach
By using Kriging interpolation methods, develop a response surface-based interpolation approach for estimating resolvent input-gain-output modes for estimating the radiated noise from an engine geometry/engine cycle for which previously computed RANS data, linearized operators, and resolvent data are unavailable.

Milestones
1. Identify candidate interpolation methods and down-select
2. Develop a Python tool to implement the interpolation method
3. Verify the Python tool

Major Accomplishments
Milestone 1 has been completed: a Kriging method has been chosen. Milestones 2 and 3 have not yet started.

Publications
None

Outreach Efforts
None

Awards
None

Student Involvement
Jay Woo is responsible for developing the Python toolchain.

Plans for Next Period
We will begin Milestone 2.

Conclusion - ASCENT 59 Year 1 Summary
The following key tasks and activities have been completed under the ASCENT 59 year 1 performance period:
- Signed NDA between UIUC and targeted cost-sharing partner Boom
- Developed, implemented, verified, and validated a RANS-based dual-stream jet exhaust simulation tool
- Developed, implemented, and verified an automated jet nozzle CAD → RANS simulation workflow

- Developed, implemented, and verified a resolvent analysis tool
- Developed, implemented, and verified a resolvent sensitivity analysis tool
- Applied automated CAD → RANS simulation workflow to a GTRI dual-stream nozzle with variable mixer duct lengths
- Demonstrated resolvent gain sensitivity to the GTRI dual-stream nozzle with variable mixer duct lengths

Task 5 - Python Optimization Tool for JNR

University of Illinois at Urbana-Champaign (lead) and Caltech

Objective

The objective of this task is to develop and verify a Python-based optimization tool that searches the optimization space of the engine geometry/cycle, to identify design choices that improve JNR.

Research Approach

Using gradient-informed optimization methods, develop an optimization approach for estimating JNR potential from a class of candidate engine geometries/cycles by using resolvent mode predictions of jet noise based on linearized operators described by RANS predictions of the jet exhaust plume.

Milestone(s)

1. Identify candidate optimization methods and down-select
2. Develop a Python tool to implement the optimization method
3. Verify the Python tool

Major Accomplishments

Work on this task has not yet begun.

Publications

None

Outreach Efforts

None

Awards

None

Student Involvement

Jay Woo will be responsible for implementing the optimization tool.

Plans for Next Period

We will begin Task 5.

Task 6 - Application of Version 1 Optimization Tool on GTRI Dual-stream Nozzle

University of Illinois at Urbana-Champaign (lead) with Caltech.

Objective

The objective of this task is to apply the Python-based tool developed from Tasks 2–5 to the GTRI dual-stream nozzle with extensible mixer duct lengths, to predict the quietest configuration.

Research Approach

The automated Python toolchain, starting with the moderate mixer duct length, is applied to predict the mixer duct length that yields the quietest configuration. The predictions will be compared with the GTRI-measured acoustic field.

Milestones

1. Select the GTRI operating condition of interest
2. Apply the optimization tool
3. Compare the predicted quiet configuration to the measured quiet configuration

Major Accomplishments

This task has not been started.

Publications

None

Outreach Efforts

None

Awards

None

Student Involvement

Jay Woo will be responsible for applying version 1 of the optimization tool to the GTRI nozzle.

Plans for Next Period

We will start Task 6.

Task 7 - Self-Calibrating Resolvent Formulation and Implementation

Caltech

Objective

The objective of this task is to develop a means for the resolvent gain predictions to be internally calibrated by using information from the RANS-predicted flow-fields.

Research Approach

A calibrated reconstruction of the input–output modes from the resolvent formulation is used to estimate the jet's turbulent kinetic energy, as predicted by the RANS model.

Milestone(s)

1. Finalize the calibration formulation
2. Implement the calibration procedure
3. Verify the calibration procedure

Major Accomplishments
Task 7 has not yet been started.

Publications
None

Outreach Efforts
None

Awards
None

Student Involvement
Mr. Liam Heidt will be responsible.

Plans for Next Period
We will begin Task 7.

Task 8 - Python Optimization Tool Update Using Self-calibrating Resolvent Formulation (Version 2)
University of Illinois at Urbana-Champaign (lead) with Caltech

Objective
The objective of this task is to develop and verify an updated Python-based optimization tool based on version 1 and the self-calibration procedure developed in Task 7 that searches the optimization space of the engine geometry/cycle, to identify design choices that improve JNR.

Research Approach
Using gradient-informed optimization methods, develop an optimization approach for estimating JNR potential from a class of candidate engine geometries/cycles using self-calibrated resolvent mode predictions of jet noise, based on linearized operators described by RANS predictions of the jet exhaust plume.

Milestones
1. Incorporate self-calibrated resolved mode implementation into the Python toolchain
2. Incorporate lessons-learned updates from version 1 of the Python toolchain into version 2
3. Verify implementation

Major Accomplishments
Task 8 has not yet started.

Publications
None

Outreach Efforts
None

Awards
None

Student Involvement
Mr. Jay Woo and Mr. Liam Heidt will be jointly responsible.

Plans for Next Period
We will start Task 8.

Task 9 - Application of Version 2 Optimization Tool on GTRI Dual-stream Nozzle
University of Illinois at Urbana-Champaign (lead) with Caltech

Objective
The objective of this task is to apply version 2 of the Python-based tool developed in Tasks 2–5, by using self-calibration from Task 7 and implementation in Task 8, to the GTRI dual-stream nozzle with extensible mixer duct lengths and predict the quietest configuration.

Research Approach
Apply the automated Python toolchain, starting with the moderate mixer duct length, to predict the mixer duct length that yields the quietest configuration. Predictions are compared with the GTRI-measured acoustic field.

Milestones
1. Apply the optimization tool
2. Compare the predicted quiet configuration to the measured quiet configuration

Major Accomplishments
Task 8 has not been started.

Publications
None

Outreach Efforts
None

Awards
None

Student Involvement
Jay Woo will be responsible for applying version 2 of the optimization tool to the GTRI nozzle.

Plans for Next Period
We will begin Task 9

Task 10 - Application of Version 2 Optimization Tool on Boom-relevant Geometry (if cost-sharing agreement is in place)
University of Illinois at Urbana-Champaign

Objective
The objective of this task is to work with Boom to apply version 2 of our optimization tool to a supersonic nozzle design of relevance to Boom. Performance, successes, and failures will be documented.

Research Approach
Transition version 2 of Python optimization tool to Boom (if an agreement is in place) for Boom-internal application of the tool.

Milestones

1. Develop and implement a cost-sharing agreement with appropriate intellectual-property safeguards
2. Transition code to Boom
3. Work with Boom engineers to identify cases of interest
4. Apply optimization code to Boom cases of interest

Major Accomplishments

This task has not been started.

Publications

None

Outreach Efforts

None

Awards

None

Student Involvement

Jay Woo and PI Daniel Bodony will be jointly responsible.

Plans for Next Period

We will begin Task 10.

Project 059(D) Physics-based Analyses and Modeling for Supersonic Aircraft Exhaust Noise

Stanford University

Project Lead Investigator

Sanjiva K. Lele
Professor
Department of Aeronautics & Astronautics
Stanford University
Stanford, CA 94305
Phone: (650) 723-7721
E-mail: lele@stanford.edu

University Participants

Stanford University

- PI(s): Dr. Sanjiva K. Lele, Dr. Juan J. Alonso
- FAA Award Number: 13-C-AJFE-SU-024
- Period of Performance: October 1, 2021 to December 10, 2021
- Tasks: (for a 3-year effort)
    1. Develop and refine research plans in coordination with ASCENT Project 59 partners
    2. Conduct large eddy simulation (LES)-based simulation, modeling, and validation of jet noise predictions
    3. Perform Reynolds-averaged Navier–Stokes (RANS)-based simulation, modeling, and validation of jet noise predictions

Project Funding Level

$200,000 per year from FAA, with in-kind matching from Stanford. Matching from industry is being arranged.

Investigation Team

Dr. Sanjiva K. Lele (PI), Department of Aeronautics and Astronautics, Stanford University
Dr. Juan J. Alonso (PI), Department of Aeronautics and Astronautics, Stanford University
Gao Jun Wu, Ph.D. Student, Department of Aeronautics and Astronautics, Stanford University
Tejal Shanbhag, Ph.D. Student, Department of Aeronautics and Astronautics, Stanford University
Kristen Matsuno, Ph.D. Student, Department of Mechanical Engineering, Stanford University

Project Overview

Improved methods for predicting and reducing noise from civil supersonic aircraft would be highly valuable for the research and technology development community engaged in civil supersonic aircraft development. In addition to aircraft and engine companies, organizations such as NASA, FAA, and the DoD research and technology community would also benefit from improved methods and tools. Ultimately, supersonic jet noise tools with predictive capabilities can be used to design better noise mitigation systems and to provide estimates of noise for certification studies.

This project involves a coordinated development of both low- and high-fidelity approaches for jet noise predictions for civil supersonic aircraft being considered in ASCENT and includes the tasks listed above. High-fidelity simulations of jet exhaust flow and noise will be developed for a carefully selected subset of configurations and operating points being tested by the Georgia Institute of Technology (Georgia Tech) team. In parallel, Reynolds-averaged Navier-Stokes (RANS) computations of a broader range of configurations and operating conditions relevant for civil supersonic aircraft will be performed and used to develop improved jet noise source models and more accurate far-field noise propagation kernels. This noise source and

noise propagation modeling will leverage high-fidelity simulation data and ongoing Georgia Tech experiments, as well as other noise and flow measurements available in the archival literature. Our goal is to understand the predictive quality of RANS-based noise prediction approaches with improved source and/or propagation models to enable designers to better capture tradeoffs typical in the development of full civil supersonic aircraft configurations.

Task 1 – Develop and Refine Research Plans in Coordination with ASCENT Project 59 Partners

Stanford University

Objectives

We aim to design a simulation study that covers the range of operating conditions and possible nozzle configurations relevant for civil supersonic jet exhaust. This plan must include the current test plan from our experimental partners at Georgia Tech.

Research Approach

The planning involved discussions with Project 59 partners and communications with external advisors at NASA and elsewhere in academia and industry. Based on these efforts, it was determined that the project should focus on axisymmetric dual-stream nozzles with an internal mixer and with the possibility of an internal and/or external nozzle plug. We have also searched for nozzle configurations and flow and noise measurement data in the archival literature that would be relevant for civil supersonic aircraft and could be used in the development of noise prediction methods. Comprehensive exploration indicated that the bulk of jet noise data, including studies of noise reduction concepts, falls within the regime of a moderate to high bypass ratio (BPR) and is thus not particularly relevant for civil supersonic aircraft. While this finding affirmed the need for the planned laboratory measurement campaign by Project 59 partners at Georgia Tech, it also highlighted the need to use the most relevant data from the published literature to kickstart the modeling and simulation effort. Thus, two specific datasets associated with jet noise tests at NASA Glenn were identified.

Georgia Tech Dual-stream Nozzle

A co-annular nozzle geometry with a variable-length mixing duct was designed and is being extensively tested by the Georgia Tech team. Following discussions among project collaborators and key stakeholders, a test matrix has been determined for experimental efforts in years 1–2. Each jet Mach number for the two streams varies between $M_j = 0.4$ and $M_j = 1.0$, and the length of the nozzle mixing duct can be adjusted to be 0.7, 1.0, 2.0, or 3.0 times the length of the nozzle diameter, $D_e = 1.7''$.

Bridges and Wernet Internal Mixer

In 2004, Bridges and Wernet (NASA Glenn) reported flow and noise measurements for internally mixed two-stream nozzles with variations in the mixer duct length and mixer geometry. The operating conditions involve transonic and low supersonic jet exhaust velocity and moderate BPR. This configuration has also been used in previous RANS-based noise prediction studies by Rolls Royce and Purdue University, along with a more recent large eddy simulation (LES) study. We have been in touch with Rolls Royce and NASA regarding the nozzle geometry and measurement data. It is hoped that the geometry and data will become available in the future. This configuration is of interest to us, as it is unique in providing both jet flow measurements and far-field noise for conditions relevant to civil supersonic flights.

Recent Jet Noise Measurements at NASA Glenn

As part of NASA's Commercial Supersonic Technology (CST) Project, under the Advanced Aero Vehicle Program (AAVP), Dr. James Bridges at NASA Glenn (personal communication, 2020) recently completed jet noise measurements on specially designed modular nozzle configurations at operating points selected to be relevant for commercial supersonic aircraft. He plans to make the nozzle geometry and measurement data available in the future. NASA's plans include noise predictions using a variety of computational tools. We are interested in exploring a select subset of NASA's test matrix in our Project 59 studies. We have obtained the CAD geometry for the nozzle and have initiated early efforts in geometry cleaning and mesh generation. The mesh generation for this case is fairly challenging due to the steep curvature and sharp edges in the mixer lobes.

Milestone(s)
The simulation plan for years 1–2 has been determined and followed. Our plan for year 3, which focuses on nozzles with noise mitigation concepts, is yet to be finalized, pending discussions with our partners from Project 59.

Major Accomplishments
A research plan regarding the nozzle geometry and flow conditions to be studied has been developed. The plan includes both the experimental study by our partners at Georgia Tech and other relevant works from NASA Glenn.

Publications
None

Outreach Efforts
Communication with researchers at NASA Glenn has been established, and ideas for possible collaboration have been exchanged.

Awards
None

Student Involvement
Three graduate students are involved in this part of the project. G. Wu and K. Matsuno have conducted literature research on relevant jet experiments and simulations that involve similar flow conditions and nozzle mixing devices. T. Shanbhag has performed literature reviews on acoustic modeling of jet noise.

Plans for Next Period
We will continue to refine our research plan according to ongoing discussions among the teams of Project 59. In particular, we will select nozzle geometries with noise mitigation concepts that are of interest to industrial partners for the development of next-generation supersonic civil transport aircraft.

Task 2 – Conduct LES-based Simulation, Modeling, and Validation of Jet Noise Predictions
Stanford University

Objectives
In collaboration with ASCENT partners in Project 59, we plan to develop physics-based analyses for supersonic aircraft exhaust noise. The main goals of these analyses are to develop improved jet noise prediction methods using a multi-fidelity approach. As part of the high-fidelity approach, LES will be conducted for a carefully selected set of configurations and operating points corresponding to tests conducted by the experimental team at Georgia Tech. The LES data will provide turbulence flow statistics and will be leveraged for acoustic source modeling.

Research Approach
Over the past project year, we have focused on numerical investigations of the co-annular nozzle geometry designed and tested by Georgia Tech. The operating conditions include subsonic and sonic jet exhaust velocity and low to moderate bypass ratio (BPR). A co-annular nozzle geometry with a variable-length mixing duct has been designed and is being extensively tested by the Georgia Tech team. Following discussions among project collaborators and key stakeholders, a test matrix has been determined for the experimental efforts of years 1–2. Each jet Mach number for the two streams varies between $M_j = 0.4$ and $M_j = 1.0$, and the length of the nozzle mixing duct can be adjusted to 0.7, 1.0, 2.0, or 3.0 times the length of the nozzle diameter, $D_e = 1.7''$. Our numerical study has focused on simulations of this co-annular nozzle at select test points.

Progress in Jet Noise Modeling and Simulations
LES and far-field acoustic calculations with the FW-H method have been conducted for the co-annular nozzle configuration with the shortest mixing duct using a compressible solver, CharLES, developed by Cascade Technologies. This work has been published in detail in a recent conference paper (Wu et al., 2022). Below is a summary of the key results.

The nozzle geometry (shown in Figure 1) was designed and tested by Project 59 partners at Georgia Tech. The area ratio of the secondary to primary nozzle is 2.25. An exhaust mixing duct is attached to the end of the co-annular nozzle, and the length of the mixing duct is 0.7 times the exit diameter. LESs of the jet exhaust flow and noise were conducted at $M_j = 0.8$ and 9 for both the primary conical nozzle alone and the co-annular nozzle. For the simulation of turbulent boundary layers on the nozzle interior walls, the strategy of numerical tripping via artificial geometric features in the CAD model was explored. The modification is a fixed-depth groove shortly upstream of the nozzle exit, as shown in Figure 2. Figure 3 shows the Voronoi mesh for the cases. The flow conditions and mesh size of each test case are summarized in Table 1.

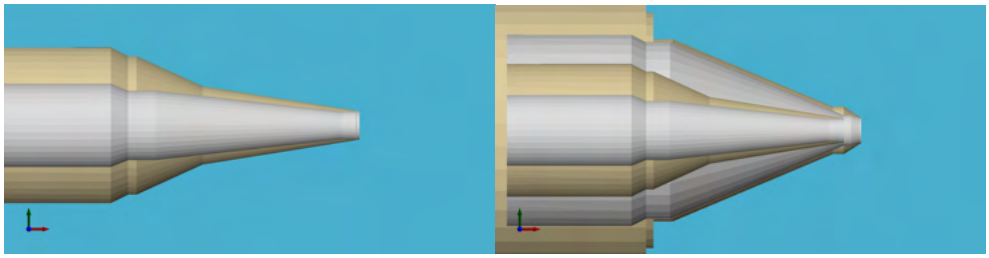

Figure 1. (Left) Primary nozzle. (Right) Co-annular nozzle designed by Georgia Tech.

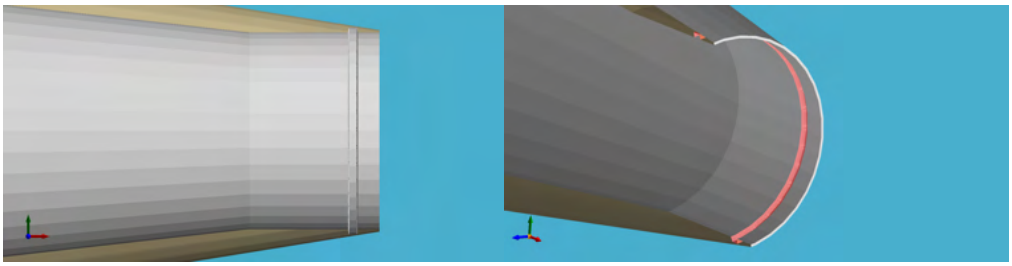

Figure 2. (Left) Cross-sectional view of the tripped primary nozzle. (Right) Isometric view of the tripping location highlighted in pink.

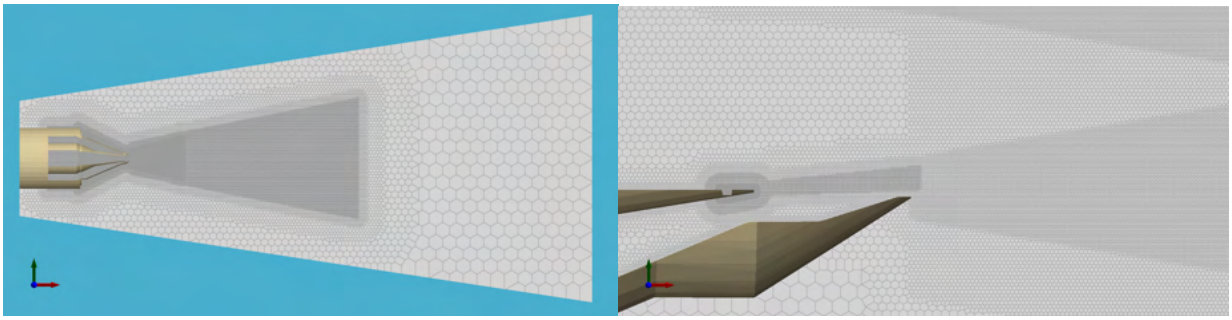

Figure 3. (Left) Overview of the Voronoi unstructured mesh. (Right) Magnified view of the Voronoi mesh near the co-annular nozzle exit.

Table 1. Summary of the test cases. All flow conditions are non-heated.

M_{j1}	M_{j1}	Mesh Size (million cells)	LES Simulation Time $t_{sim}\, c_\infty/D_{e1}$	Note
0.5	N/A	25	700	RANS and LES
0.8	N/A	18	900	LES
0.9	N/A	14, 18, 27	700-900	RANS and LES
0.8	0.8	15, 28	690 - 720	LES
0.9	0.9	28	720	LES

This tripping approach produces noticeable differences in the jet boundary layer near the nozzle exit, but no significant variability is found in the overall jet spreading or far-field jet acoustics. Simulations were conducted using an identical mesh resolution for the same duration, $t_{sim}\, c_\infty/D_{e1}$ = 900. Figures 4 and 5 show the mean streamwise velocity and Reynolds shear stress near the nozzle interior wall. Compared with the clean geometry, the tripped geometry causes the boundary to detach and reattach to the nozzle surface. Through this unsteady motion, the turbulence level of the exit boundary layer is increased. Figure 6 compares the velocity statistics just before the nozzle exit, at x/De_1=-0.02. The figure shows that the tripped geometry significantly increases the Reynolds normal and shear stress in the boundary layer. Profiles from the tripped case exhibit features similar to those of a turbulent boundary layer. The effects of turbulence tripping were further investigated by taking mean velocity and mean turbulent kinetic energy profiles at various streamwise locations in the jet plume. No significant differences were observed in the mean velocity or turbulent kinetic energy profiles between the tripped and non-tripped case.

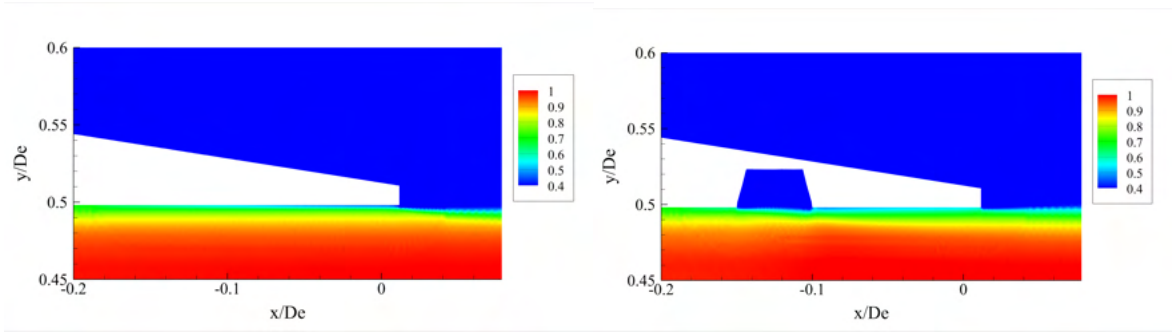

Figure 4. Mean streamwise velocity U/U_j contours for the non-tripped primary nozzle (left) and the tripped nozzle (right), M_j=0.8.

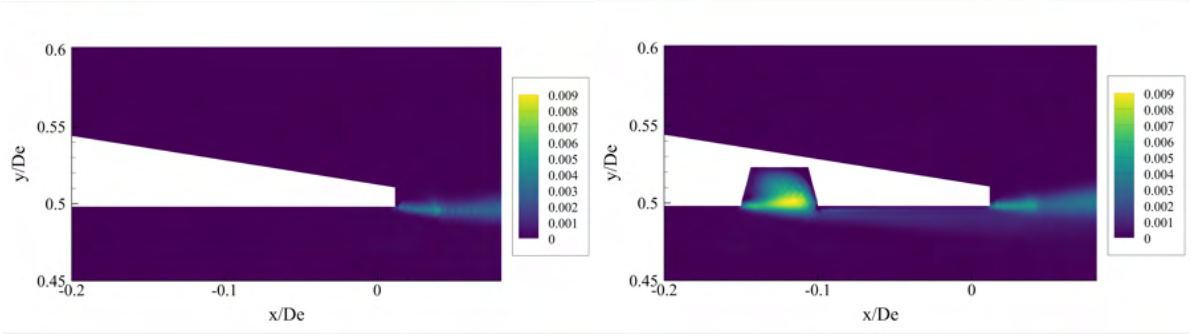

Figure 5. Reynolds shear stress $\underline{u'v'}/c_\infty{}^2$ contours for the non-tripped primary nozzle (left) and the tripped nozzle (right), M_j=0.8.

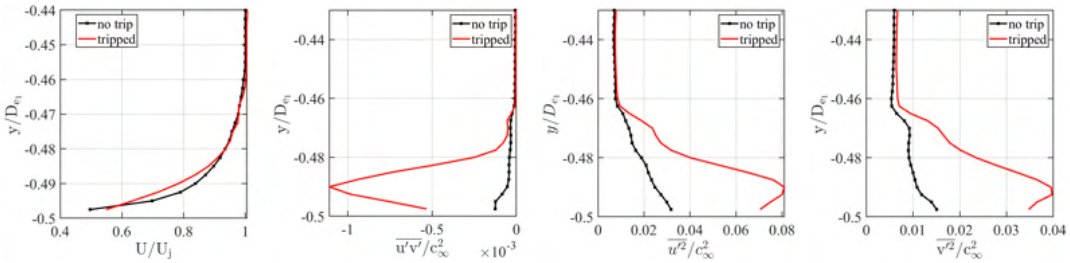

Figure 6. Velocity statistics of the exit boundary layer, M_j=0.8.

Figures 7 and 8 show the mean jet velocity and Reynolds shear stress for a co-annular case at M_j =0.8. The initial shear layer from the primary nozzle is contained inside the mixing duct and is deflected toward the centerline of the jet due to the secondary stream, as shown in Figure 8. The presence of the convergent mixing duct and the shear layer entrainment from the primary nozzle cause the secondary stream to be accelerated slightly beyond the core stream between $x/De = 0$ and $x/De = 0.7$. This trend is akin to the behavior observed in a jet ejector and generates an additional peak in the mean velocity profile near the nozzle exit. Figure 9 shows that the peaks increase the velocity gradient across the initial jet shear layer, which leads to an increase in the jet spreading rate between $\tilde{d} = 2$ and $\tilde{d} = 10$, where $\tilde{d}$ is the normalized streamwise distance over which each jet has expanded beyond the nozzle exit. Beyond $\tilde{d}$ =10, the enhanced mixing effect diminishes and the velocity profiles between the primary and co-annular cases are quite similar.

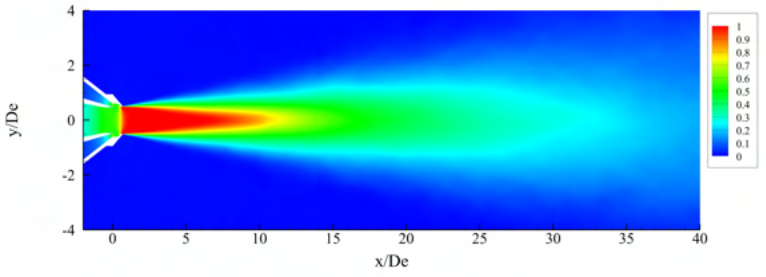

Figure 7. Mean streamwise velocity contours for the co-annular nozzle with $L/D_e = 0.7$ at $M_j = 0.8$.

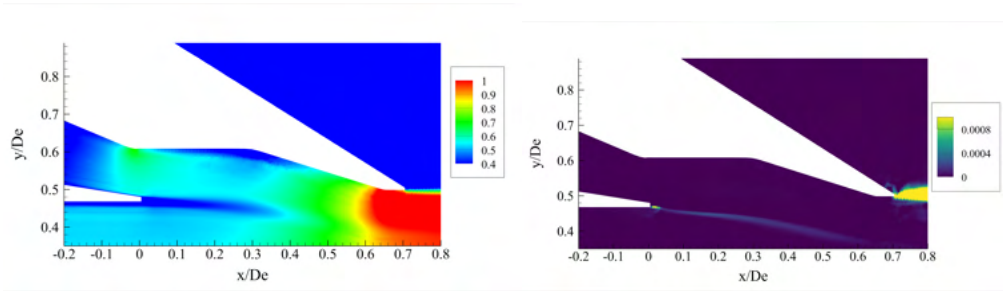

Figure 8. Magnified view of the mean streamwise velocity contours (left) and Reynolds shear stress (right) for a co-annular nozzle with $L/D_e = 0.7$ at $M_j = 0.8$.

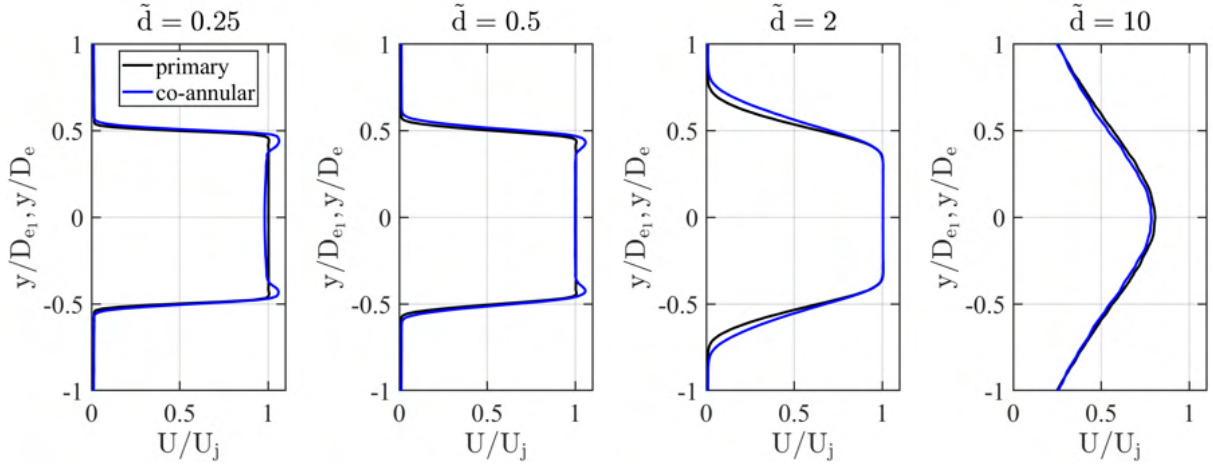

Figure 9. Comparison of mean streamwise velocity profiles between the primary nozzle and the co-annular nozzle test cases, $M_j = 0.8$.

Sound pressure level (SPL) spectra for the primary nozzle alone and the co-annular nozzle are shown in Figure 10. The radial distance of the observer location is about 12 feet away from the nozzle exit, and the jet polar angle ϕ is defined with respect to the jet upstream direction. Experimental data were obtained via private communications with Georgia Tech. Over the range of $0.02 \leq St \leq 1$, the LES results agree reasonably well with the experimental data. However, for $St > 1$, a spurious hump is present in the LES SPL spectra. The cause for such discrepancy in the noise spectra is unknown at the moment. One possible cause is the difference in the exterior nozzle surfaces. These surfaces are treated with noise absorption materials to avoid acoustic reflections in the experiments, but these noise reduction features are not included in the CAD geometry of the LES. Another possibility is that the spurious hump is generated by insufficient grid resolution in the aft portion of the jet plume. Recall that the present results were obtained using modest resolution grids. We expect to improve these results in the future. For both the tripped and non-tripped cases, the noise spectra show little difference in Figure 10, except near the spurious hump.

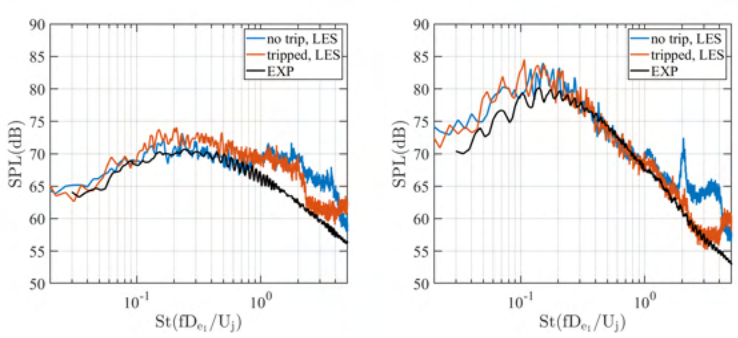

(a) Primary nozzle only, $M_j = 0.8$, $\phi = 120^\circ$(left) and $\phi = 150^\circ$(right).

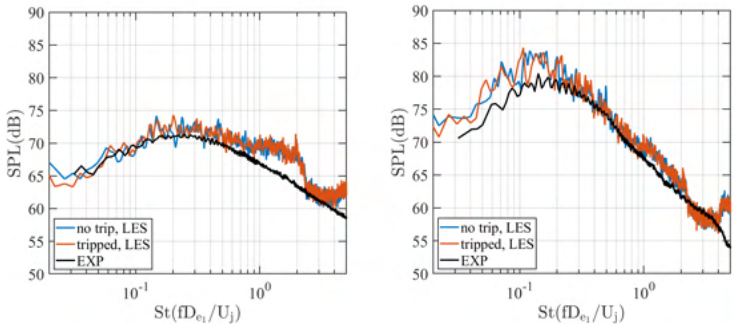

(b) Co-annular nozzle, $M_{j1} = M_{j2} = 0.8$, $\phi = 120^\circ$(left) and $\phi = 150^\circ$(right).

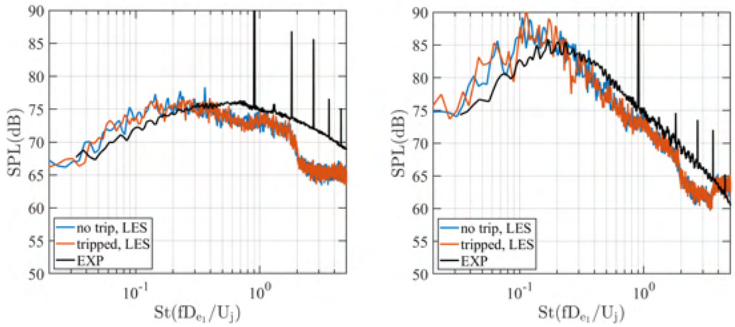

(c) Co-annular nozzle, $M_{j1} = M_{j2} = 0.9$, $\phi = 120^\circ$(left) and $\phi = 150^\circ$(right).

Figure 10. Comparison of far-field SPL spectra between LES and experiments. Experimental data were shared by Georgia Tech via private communication.

Analyses of the most energetic coherent structures in the jet plume were conducted with spectral proper orthogonal decomposition (SPOD). Figure 11 shows the first two leading SPOD modes of p' for the primary nozzle test case at $M_j = 0.9$ for the zeroth azimuthal wavenumber. Kelvin–Helmholtz and Orr-type instability waves are observed. We plan to study, in detail, the changes in growth of these coherent structures introduced by numerical tripping and the co-annular mixing device. These results will be used for acoustic source modeling in our future work.

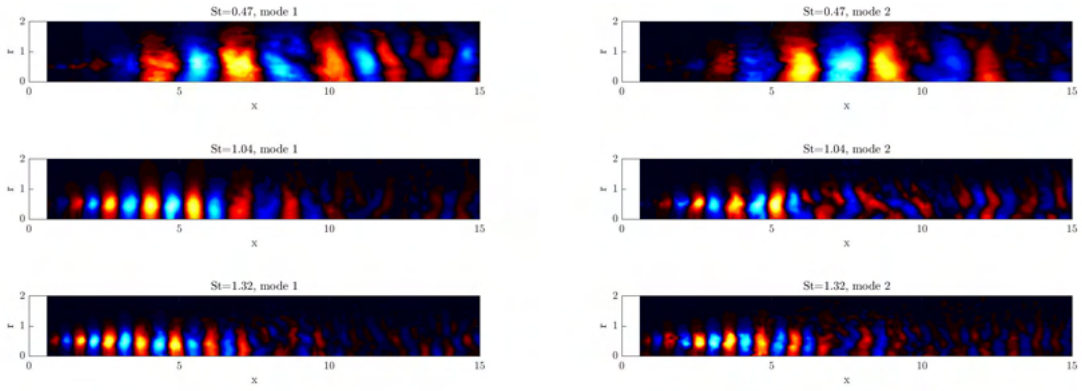

Figure 11. First two leading SPOD modes of p' at select St values for the zeroth-order azimuthal wavenumber in the primary nozzle, $M_j = 0.9$.

Milestones

LESs corresponding to the year 1 test matrix have been conducted at select test points. The numerical results are being validated with experimental data, and further numerical improvements are required.

Major Accomplishments

Over the past project year, we have made steady progress in the high-fidelity simulations of jet noise, in accordance with the test plan established by our Project 59 partners. LESs have been conducted for the Georgia Tech co-annular nozzle using the compressible solver CharLES, developed by Cascade Technologies. The nozzle configuration with the shortest mixing duct, $L/D_e = 0.7$, was considered for two Mach numbers, $M_j = 0.8$ and $M_j = 0.9$. For the simulation of turbulent boundary layers on the nozzle interior walls, the strategy of numerical tripping via artificial geometric features in the CAD model was explored. This tripping approach produces noticeable differences in the jet boundary layer near the nozzle exit, but no significant variability is found in the overall jet spreading or far-field jet acoustics. Compared with simulations involving only the primary nozzle geometry, LES data indicate that the secondary stream and mixing duct introduce faster-moving flow on the inner periphery of the jet initial shear layer, leading to faster jet spreading rate further downstream. The agreement between numerical results and experimental data is satisfactory, but discrepancies are observed in the far-field acoustics at high frequencies. Further investigation of the causes for such discrepancies is needed. Analyses of the most energetic coherent structures in the jet plume have been conducted via SPOD, and a more in-depth analysis of the SPOD modes is underway.

Publications

Conference Proceedings

Wu, G. J., Shanbhag, T. K., Matsuno, K., Lele, S. K. & Alonso, J. J. (2022). *Numerical simulations and acoustic modeling of a co-annular nozzle with an internal mixing duct*. Conference paper accepted for presentation.

Outreach Efforts

Communication with Project 59 partners in ASCENT and with NASA scientists has been established. Deeper collaboration with the Georgia Tech experiments and with NASA scientists is expected as the project progresses.

Awards

None

Student Involvement

Two graduate students are involved in this project task. G. Wu has taken the lead on single-nozzle LES computations and turbulence-tripping efforts to better match experimental acoustic data. K. Matsuno has compared co-annular nozzle LES calculations with available experimental data.

Plans for Next Period

We plan to further refine the current LES results and achieve better agreement with experimental data. SPOD analyses with LES data will be conducted to analyze the large-scale coherent structures associated with low-frequency acoustics. LES under additional flow conditions and geometries corresponding to the latest experimental study at Georgia Tech and NASA Glenn will be performed.

Task 3 – Perform RANS-based Simulation, Modeling, and Validation of Jet Noise Predictions

Stanford University

Objectives

This project involves the coordinated development of both low- and high-fidelity approaches for jet noise predictions. For the low-fidelity approach, RANS computations of a broader range of configurations and operating conditions relevant for civil supersonic aircraft will be performed and used to develop improved jet noise source models and more accurate far-field noise propagation kernels.

Research Approach

Using the open-source RANS solver SU2, simulations for the primary conical nozzle designed and tested by Georgia Tech have been performed at two jet Mach numbers, $M_j = 0.5$ and $M_j = 0.9$. The results have been compared with LES results. For acoustic modeling, models based on Goldstein's generalized acoustic analogy that are available in the literature have been tested on a benchmark problem.

The mesh resolutions are similar to the resolution used in the LES cases. Figure 12 compares the mean velocity and Reynolds stress between the LES and RANS results. The agreement is fairly good, demonstrating the validity of using low-cost RANS simulations for obtaining the mean states of a turbulent jet under a wide range of engine operating conditions for acoustic modeling.

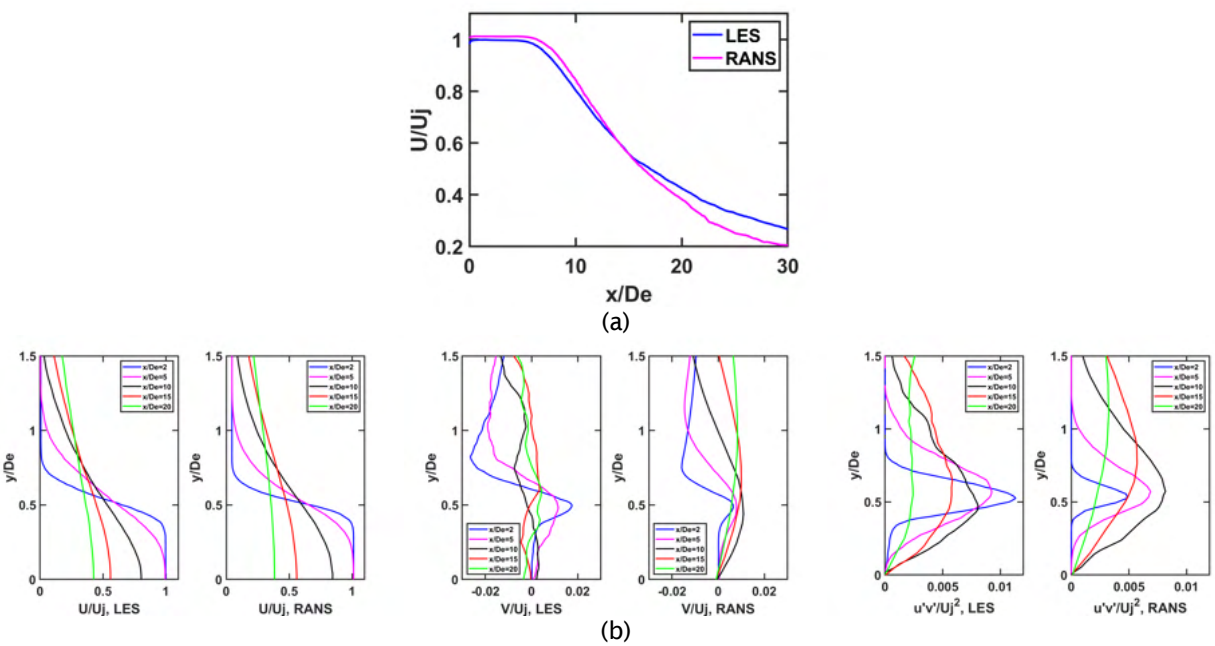

Figure 12. Comparison of the mean velocity and Reynolds shear stress between RANS and LES results. Profiles are shown along (a) the jet centerline and (b) various streamwise stations for the primary nozzle test case at $M_j = 0.9$

A number of methods have been applied to predict jet noise from RANS (mean flow) calculations alone. Several of these methods build upon Lighthill's original acoustic analogy (Lighthill, 1952), where the Navier–Stokes equations are rearranged into the form of an acoustic wave equation with a distribution of quadrupole source terms arising from local Reynolds stresses. Goldstein's generalized acoustic analogy (Goldstein, 2003) similarly rearranges the full flow equations into a linear left-hand side representing the spatially developing mean flow and a nonlinear right-hand side representing the acoustic sources. This framework allows for the effects of convection and refraction to be accounted for correctly and has been shown to be more robust to numerical errors in the jet mean flow than other commonly used acoustic analogy formulations (Samanta et al., 2006).

Many previous works have developed methods based on GAA, wherein a statistically stationary RANS realization of the flow field based on a k-epsilon turbulence model forms the basis for characterizing the acoustic sources. In these frameworks, a form is proposed for the two-point space–time correlation function of the sources, in which the amplitude and integral length and time scales are deduced from the turbulent kinetic energy and dissipation fields via empirically determined relationships. Tam and Auriault (1999) proposed one such framework based on kinetic theory, arguing an analogy between molecular pressure and turbulent pressure. Morris and Farassat (2002) later showed an equivalence between this model and the standard acoustic analogy, provided that a consistent representation is used for the source term and Green's function. Models of this type largely rely upon the assumption of isotropic turbulent Reynolds stresses. While this approach is expected to result in good sound predictions at high frequencies, where the dominant noise generation mechanisms arise from fine-scale turbulence, it is also expected that the low-frequency part of the spectrum, where the larger-scale coherent structures recovered in SPOD are of much greater importance, will be largely inaccurate. Previous authors have attempted to resolve this issue by applying a more sophisticated representation of the acoustic sources that account for anisotropy. For example, Karabasov et al. (2010) proposed a Gaussian form for the two-point correlation, in which the different components of the fourth-order correlation tensor take different relative magnitudes based on parameter fitting to an LES.

We have applied three different acoustic modeling methods based on the generalized acoustic analogy to the time average of an unsteady jet realization taken from a DDES simulation of a subsonic jet. The spectra obtained from the three methods were compared, and the limitations of this analysis approach studied in the context of SPOD results from the same jet simulation.

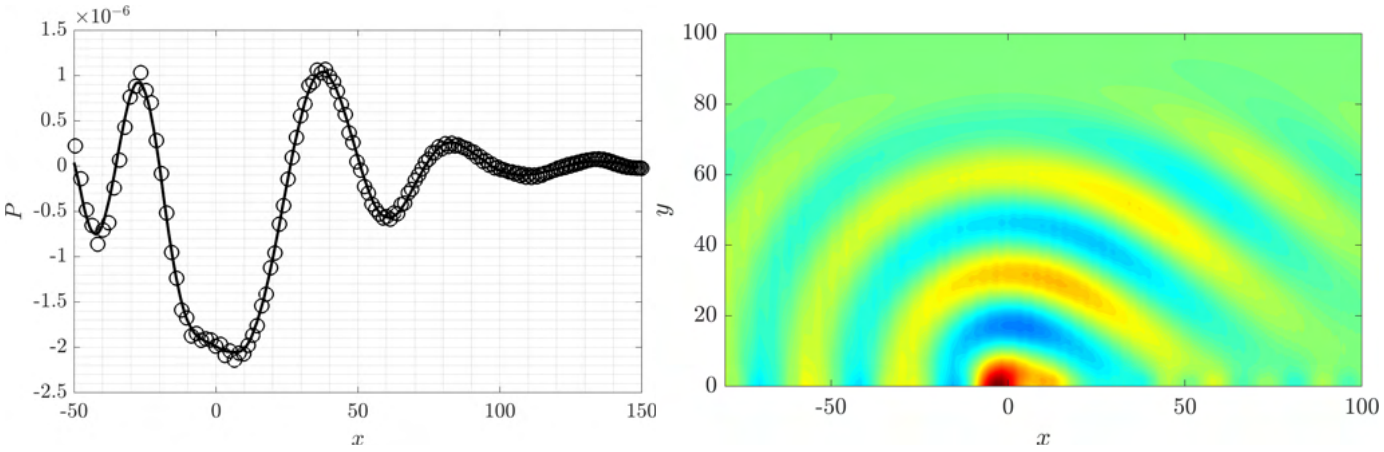

Figure 13. Numerical LEE solution to the benchmark problem (Agarwal et al.) of sound propagation from a point source through a 2D shear-layer, pressure fluctuation amplitude: (Left) Comparison of the numerical field (markers) with the analytic solution (solid line). (Right) Contours of the converged LEE solution.

In these methods, flow variables are decomposed into steady and fluctuating components using a Favre decomposition, resulting in a linearized form of the compressible flow governing equations with nonlinear source terms arising from Reynolds and shear stresses. Separate perturbation variables are defined for the momentum and stagnation enthalpy. The wave propagation problem is then efficiently solved in the frequency domain using an adjoint Green's function method (Karabasov et al., 2010). The Fourier transform of the adjoint Green's function solution satisfies the adjoint PDE system for the linearized equations already obtained. Each adjoint variable corresponds to one of the base flow state variables (density,

momentum, and temperature) and represents the sensitivity of this system to a point source placed at a given location in the domain. The adjoint equations are solved iteratively in a pseudo-time-stepping scheme. Given that this linearized Euler system governs shear layer instabilities in addition to acoustic propagation, it is important to adjust the numerical scheme accordingly, such that the Green's function solution obtained is not contaminated by the instability solution. To verify this, the adjoint LEE frequency domain solver was tested against a benchmark problem presented by Agarwal et al. at the fourth Computational Aeroacoustics Workshop, in which a two-dimensional parallel shear flow immerses a monopole Gaussian source placed at the origin. The aim of this benchmark problem is to extract only the acoustic solution, which is known analytically for this setup, from the full LEE solution, which contains both the acoustic wave and a Kelvin–Helmholtz instability. Figure 13 shows the numerical solution of the LEE system along the line y=15, together with the analytic solution and the spatial distribution of the solution containing only the acoustic component. The adjoint solver converges to the required bounded solution component with reasonably good accuracy, as shown.

Having obtained the adjoint Green's function solution, the expressions for the far-field pressure and subsequently the power spectral density are computed by taking the convolution of the second-rank wave propagation tensor (calculated from the Green's function) at each frequency with the modeled spatiotemporal cross-correlation of the turbulent source terms. The model is assumed to take the form of a multivariate Gaussian, with the imposed length and time scales being assumed to scale with standard turbulent length and time scales according to universal nondimensional constants. We have implemented three variants in the model based on assumptions suggested by Karabasov (2010), Tam and Auriault (1999), and Morris and Farassat (2002). The latter two models reduce the convolution to a single volume integral by invoking the compact eddy approximation. Our implementation has been tested on the time-averaged output of an SU2 (Molina) delayed detached-eddy simulation (DDES) calculation of a subsonic jet. This test case was previously studied in the framework of a European Union project, Go4Hybrid (G4H) (Fuchs et al., 2018), and the simulation results for this grid resolution have been validated against experimental data from Bridges and Wernet (Bridges & Wernet, 2010).

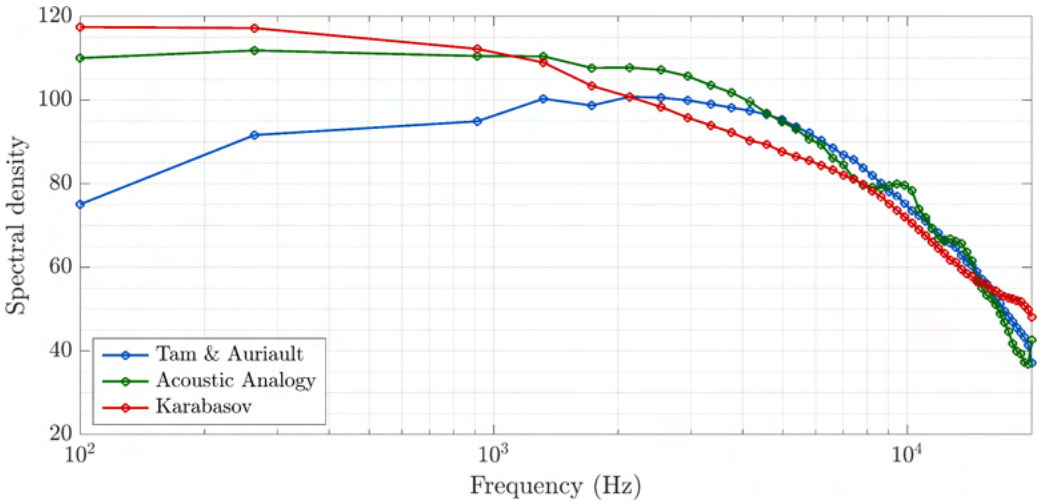

Figure 14. Spectral comparison between acoustic source models

Figure 14 shows the power spectral density calculated using each of the three RANS-based acoustic analogy methods at a 30° polar angle to the jet and a distance of r/D = 10000 from the jet origin. The spectra obtained by each of the three models capture the overall expected variation with frequency; in particular, the fall-offreduction at high frequencies is well captured in all cases. There are no significant disparities between the Tam and Auriault (1999) and acoustic analogy models, which both rely on the compact turbulent eddy approximation to simplify the convolution integral, and the Karabasov model, which does not rely on this assumption. This result suggests that the compact turbulent eddy approximation is appropriate for this type of source model. The expected fall-off at low frequencies is only observed for the Tam and Auriault model (Tam & Auriault 1999), with the other two models flattening out or rising in this frequency range. However, it is important to note that we expect this type of RANS-based modeling to be limited in this part of the spectrum. While the overall jet turbulent statistics captured in time-averaged flow modeling are sufficient to describe the sources of fine-scale noise, this type of modeling does not capture the large-scale wave-packet-type structures that dominate the more deterministic noise generation mechanisms at lower frequencies and smaller jet observation angles.

Having studied the strengths and limitations of a few GAA-based methods, we have begun to develop two additional method classes for RANS-based acoustic predictions, which we hope will enable accurate and computationally efficient calculations in both the low- and high-frequency portions of the spectrum. To improve accuracy at lower frequencies, we intend to extend the Karabasov source model (Karabasoy et al., 2010) with the present GAA implementation, incorporating a frequency dependency for the RANS-derived turbulent length and time scales. These functional dependencies have been previously studied in the context of LESs by Self and Azarpeyvand among others, and we intend to follow a similar approach by assessing these dependencies from LESs and determining the robustness with which they can be applied across different geometries and operating conditions. In addition, we are developing an alternative high-frequency acoustic code that relies on the methodology of ray tracing rather than solving for the adjoint Green's function in order to handle far-field propagation. This class of methods has been successfully applied by Ilario et al. to acoustic calculations for this type of jet flow, and we hope that by replacing the need to solve an additional coupled PDE system with a high-order ODE system, this propagation method will provide a significant reduction in computational cost while maintaining accuracy. Work on each of these methods is ongoing.

Milestone(s)

Early benchmark tests have been carried out for Task 3.

Major Accomplishments

For low-fidelity simulations, test cases with the primary nozzle at $M_j = 0.5$ and $M_j = 0.9$ have been conducted. A comparison between the RANS and LES results of mean velocity and Reynolds stress for various locations shows good agreement. Additional RANS test cases with the co-annular nozzle geometry are planned. Thus far, the agreement between RANS and LES has given us confidence in using RANS to obtain the mean states of the jet under a wide range of engine operating conditions for acoustic modeling. For acoustic modeling, models based on Goldstein's generalized acoustic analogy that are available from the literature have been tested on a benchmark problem (Goldstein, 2003).

Publications

Conference Proceedings

Shanbhag, T. K., Zhou B. Y., Eduardo, M., & Alonso, J. J. (2021, August). A comparison of jet acoustic analysis methods [Presentation]. AIAA Aviation 2021 Forum.

Outreach Efforts

None

Awards

None

Student Involvement

T. Shanbhag has led the modeling effort with the adjoint Green's function methods described in the previous sections and is developing RANS-based jet noise predictions.

Plans for Next Period

Additional RANS calculations involving co-annular nozzle geometries will be conducted and compared with LES and experimental data. RANS-based acoustic modeling with improved low-frequency predictions will be performed using the LES data.

References

Brès, G. A., Jordan, P., Jaunet, V., Le Rallic, M., Cavalieri, A. V. G., Towne, A., Lele, S. K., Colonius, T., & Schmidt, O. T. (2018). Importance of the nozzle-exit boundary-layer state in subsonic turbulent jets. Journal of Fluid Mechanics, *851*, 83–124. https://doi.org/10.1017/jfm.2018.476

Brès, G. A., Bose, S. T., Emory, M., Ham, F. E., Schmidt, O. T., Rigas, G., & Colonius, T. (2018). Large-eddy simulations of co-annular turbulent jet using a Voronoi-based mesh generation framework [Presentation]. AIAA/CEAS Aeroacoustics Conference, Atlanta, GA.

Bridges, J., & Wernet, M. (2010). Establishing consensus turbulence statistics for hot subsonic jets [Presentation]. AIAA/CEAS Aeroacoustics Conference, Stockholm, Sweden.

Fuchs, M., Mockett, C., Shur, M., Strelets, M., & Kok J. C. (2018). Single-stream round jet at M = 0.9. In: C. Mockett, W. Haase, & D. Schwamborn (Eds). *Go4Hybrid: Grey area mitigation for hybrid RANS-LES methods. Notes on numerical fluid mechanics and multidisciplinary design, vol. 134* (125-137). Springer.

Goldstein, M. E. (2003). A generalized acoustic analogy. Journal of Fluid Mechanics, *488*, 315-333.

Karabasov, S. A., Afsar, M. Z., Hynes, T. P., Dowling, A. P., McMullan, W. A., Pokora, C. D., Page, G. J., & McGuirk, J. J. (2010). Jet Noise: Acoustic Analogy informed by Large Eddy Simulation. AIAA Journal, *48*(7), 1312–1325. https://doi.org/10.2514/1.44689

Lighthill, M. J. (1952). On sound generated aerodynamically. I. General theory. Proceedings of the Royal Society of London. Series A. Mathematical and Physical Sciences, *211*(1107), 564-587.

Molina, E. "Detached Eddy Simulation in SU2 (PhD Thesis)."

Morris, P. J., & Farassat, F. (2002). Acoustic analogy and alternative theories for jet noise prediction. AIAA Journal, *40*(4), 671-680.

Samanta, A., Freund, J. B., Wei, M., & Lele, S. K. (2006). Robustness of Acoustic Analogies for Predicting Mixing-Layer Noise. AIAA Journal, *44*(11), 2780–2786. https://doi.org/10.2514/1.22186

Schmidt, O. T., Towne, A., Rigas, G., Colonius, T., & Brès, G. A. (2018). Spectral analysis of jet turbulence. Journal of Fluid Mechanics, *855*, 953–982. https://doi.org/10.1017/jfm.2018.675

Tam, C. K., &Auriault, L. (1999). Jet mixing noise from fine scale turbulence. AIAA Journal, *37*(2), 145-153.

Wu, G. J., et al. (2022). *Numerical simulations and acoustic modeling of a co-annular nozzle with an internal mixing duct*. Conference paper accepted for presentation.

Project 059(E) Moderate-Fidelity Simulations for Efficient Modeling of Supersonic Aircraft Noise

The Pennsylvania State University

Project Lead Investigator

Philip Morris (PI)
Professor
Department of Aerospace Engineering
Pennsylvania State University
233C Hammond Building
University Park, PA 16802
814-863-0157
pjm@psu.edu

University Participants

Pennsylvania State University

- PI(s): Dr. Philip Morris (PI), Dr. Daning Huang (co-PI)
- FAA Award Number: 13-C-AJFE-GIT-070
- Period of Performance: January 1, 2021 to December 31, 2021

Project Funding Level

The project is funded at the following level: FAA: $100,000. Cost-sharing of $100,000 is provided by the Pennsylvania State University through salary support of the faculty PI.

Investigation Team

Pennsylvania State University

- Principal Investigator: Dr. Philip Morris
- Co-Investigator: Dr. Daning Huang
- Graduate Students: Dana Mikkelsen and Stephen Willoughby

Project Overview

The purpose of this project is to develop and assess computational tools to simulate the flow and noise of civil supersonic aircraft engines. The simulations will focus on the models and conditions being used in validation experiments conducted at Georgia Institute of Technology (Georgia Tech) under Project 59B.

The prediction of noise from supersonic jets, particularly when noise reduction devices are present, is a challenging computational task. Methods based on Reynolds-averaged Navier–Stokes (RANS) solutions are relatively inexpensive to perform and provide satisfactory predictions of the average flow field, even for quite complicated geometries. The subsequent prediction of noise based on acoustic analogies is highly efficient but faces difficulties when the geometry of the nozzle is not a simple axisymmetric one. Methods based on large eddy simulations (LES) provide considerably more information about the unsteady flow and the noise generated. However, LES are computationally expensive, especially when the engine geometry is complex. This situation is encountered in the case of nozzles with noise reduction devices, such as internal mixers. Noise predictions based on the LES can be made quite efficiently by using the Ffowcs Williams and Hawkings (FWH) acoustic analogy (Farassat and Succi, 1983; Ffowcs Williams and Hawkings, 1969), but long time records are required to predict the noise radiated to far-field observers, thus adding additional expense to LES.

The approach in Project 59E is a compromise between the accuracy and high computational cost of LES and the noise-prediction inaccuracy of RANS-based simulations. The initial simulations being conducted in the initial stage of the project

use RANS, and these calculations serve as a starting point for the LES. In anticipation of the addition of internal mixers to the nozzle geometries, only RANS simulations are planned to be conducted for the internal flow; then LES, coupled with the Ffowcs Williams and Hawkings acoustic analogy, will be used to predict the external flow and the noise generated. The RANS solution at the jet exit will be used as an initial condition for the external LES. This will require the addition of some unsteady information, which will be guided by a very limited number of LES. This approach will reduce the total computational cost because it removes much of the geometric complexity and the associated grid requirements for LES of the internal flow.

The usefulness of this approach is that it will make LES for nozzles with noise reduction devices more accessible to more users, particularly industry engineers with very limited computational resources and time available for multiple simulations in the design process.

If successful, the ASCENT Project 59E research will develop methods to predict the noise generated and radiated by civil supersonic aircraft engines. The developed tools should enable airframe and engine manufacturers to assess the noise impacts of engine design changes and to determine whether particular designs will meet current or anticipated noise certification requirements.

Project Introduction

During the first project year, because of a change in direction from the originally proposed research, the original project 59A was split into two parts. The new project 59A, being conducted at Georgia Tech, will examine the effects of different inlets and the introduction of noise reduction devices on the performance of selected engine cycles and geometries. The new project 59E focuses on the prediction of the flow and noise from different nozzle configurations. The latter project is the work described in the present report.

Major Accomplishments

The tasks for the first project year centered on RANS simulations for the internal and external flow from a single convergent nozzle. The details of the model geometry were provided by Georgia Tech from the model used in ongoing experiments for Project 59B. The subtasks included grid development for the RANS simulations, RANS simulations, and comparisons with available experimental data. In addition, grid development for the LES has been initiated, and preliminary LES have been conducted.

Task 1 - Grid Generation for RANS Simulations

Pennsylvania State University

The primary nozzle of the co-annular nozzle geometry provided by Georgia Tech was modeled by using STARCCM+. An initial mesh was created with a base mesh size of 7.87 in, with a target surface mesh size of 10% of the base size and a minimum surface mesh size of 5% of the base size. This initial mesh contained eight prism layers near boundary walls, with a prism-layer total thickness of 5% of the base size as well as two volumetric controls in which the smallest maximum cell size was 3% of the base size. In total, this mesh had approximately 5.9 million cells. Figure 1 shows the initial surface mesh.

This initial model underwent several iterative changes to achieve the current model. An interface between the rear spoke volume and the main nozzle volume was eliminated by combining the two to create one part. The mesh was refined to a smaller base size, and additional volumetric refinements were added in the core region. To compensate for the increased mesh density, the size of the outer domain was reduced. The thickness of the nozzle wall was included, and an interface between the nozzle exit and the domain was removed.

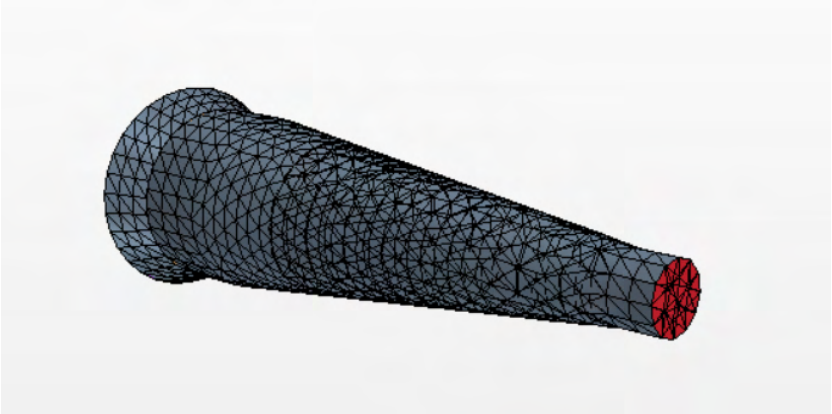

Figure 1. Initial nozzle surface mesh.

The current mesh has a base mesh size of 1.6 in, with the target and minimum surface mesh sizes held the same as before (10% and 5% of base mesh size, respectively). It contains 10 prism layers near boundary walls, with the prism-layer total thickness remaining at 5% of the base size. There are four volumetric controls. The innermost maximum cell size is 2.5% of the base size, with subsequent maximum cell sizes of 5%, 10%, and 20% of the base size. The total domain is 70 in long, with a start radius of 34 in and an end radius of 50 in for a domain size of 392,615 in^2. This mesh has approximately 13.8 million cells.

The revised surface mesh is shown in Figure 2. Figures 3a and 3b show cross-sections of the volume mesh, including the near nozzle region and the different refinement regions. The full computational domain is not shown.

Figure 2. Current refined nozzle surface mesh.

Task 2 – RANS Simulations

Pennsylvania State University

A steady RANS calculation was then performed by using STARCCM+. An implicit MUSCL third-order central-differencing scheme with an upwind blending factor of 0.1 was used. Sutherland's law was implemented for dynamic viscosity and thermal conductivity. A MinMod limiter was applied as well as a *k*-omega turbulence model.

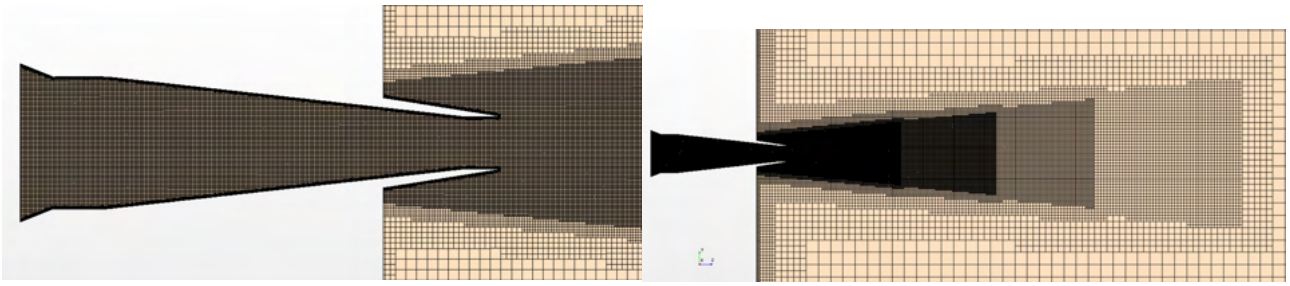

A) B)

Figure 3. RANS grid. A) Near nozzle region. B) Grid showing different resolution levels.

The run conditions for this simulation were taken from experimental data provided by Georgia Tech. The ambient pressure and temperature were set to 14.051 psi and 530.2 R, respectively. The NPR and TTR were 1.53 and 0.98, respectively, for an expected nozzle Mach number of 0.8. Figure 4 shows the calculated Mach number contours for the inner nozzle.

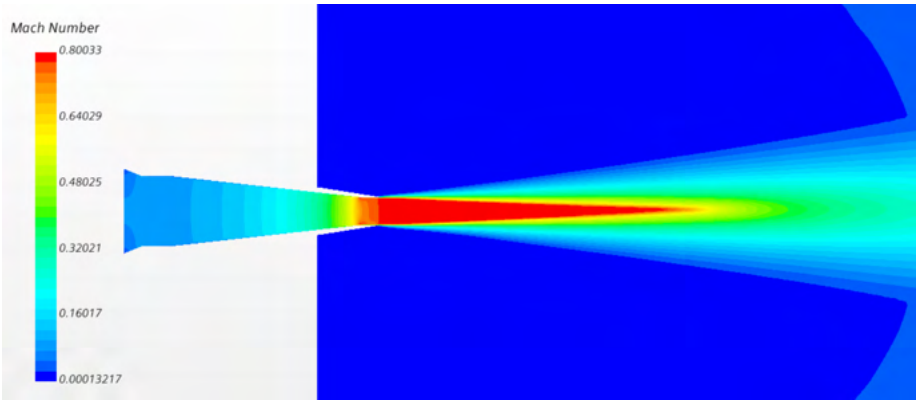

Figure 4. Mach number contours for primary nozzle RANS calculation.

The RANS calculation yielded an exit Mach number of 0.8 and an exit velocity of 256.77 m/s. This result is in good agreement with the experimental exit velocity measurement of 257.53 m/s.

The next steps concerning the RANS calculation are to complete a validation study of the primary nozzle against experimental data and to generate a grid to obtain a RANS solution of the full dual-stream nozzle.

Task 2 – Large Eddy Simulations

Pennsylvania State University

Although this task was not an original task for the first year of the project, some preliminary LES were conducted.

As with the RANS model, the grid underwent several iterative changes to achieve the current configuration. An additional complication in the LES grid is the need to include an Ffowcs Williams and Hawkings acoustic data surface. A surface control has been added to the FWH surface to improve interface conformity. Instead of modeling the two domains (inside and outside the acoustic data surface) as separate regions, they were added to the same region.

The current mesh has a base size of 1.6 in with a target surface mesh size of 10% of the base mesh size and a minimum surface mesh size of 5% of the base mesh size. It contains five prism layers near boundary walls, including the FWH surface, with a prism-layer total thickness of 5% of the base size. The four volumetric controls follow those of the RANS model: the

innermost maximum cell size is 2.5% of the base size, with subsequent maximum cell sizes of 5%, 10%, and 20% of the base size. The target surface mesh size and the minimum surface mesh size of the surface control on the FWH surface are both 4% of the base size.

The outer domain of this model is identical to that of the RANS model. It is 70 in long, with an initial radius of 34 in and an outflow radius of 50 in. The domain contained by the FWH surface is 48 in long, with an initial radius of 1.5 in and an outflow radius of 6 in. The mesh has approximately 16.6 million cells. Figure 5 shows a close-up view of the FWH surface embedded in the LES mesh.

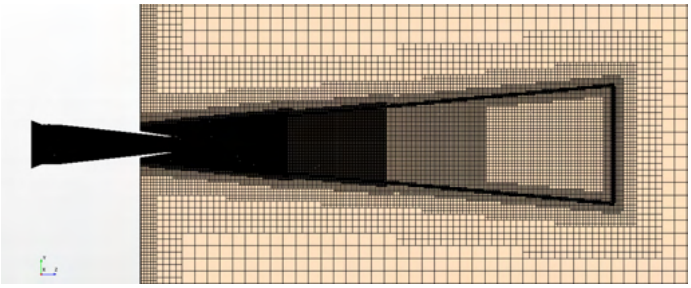

Figure 5. Close-up view of the FWH acoustic data surface embedded in the LES mesh.

An unsteady LES calculation for the primary nozzle was then performed. An implicit MUSCL third-order central-differencing scheme with an upwind blending factor of 0.25 was used. Sutherland's law was implemented for dynamic viscosity and thermal conductivity. A dynamic Smagorinsky subgrid scale was used, and a MinMod limiter was applied. A second-order temporal discretization was used with a timestep of 0.5 μs. Figure 6 shows instantaneous Mach-number contours from the preliminary LES simulations. The operating conditions are the same as those for the RANS case in Figure 4. The LES calculation yielded an exit Mach number of 0.798 and an exit velocity of 256.88 m/s. This result is in good agreement with both the RANS exit velocity of 256.77 m/s and the experimental exit velocity measurement of 257.53 m/s.

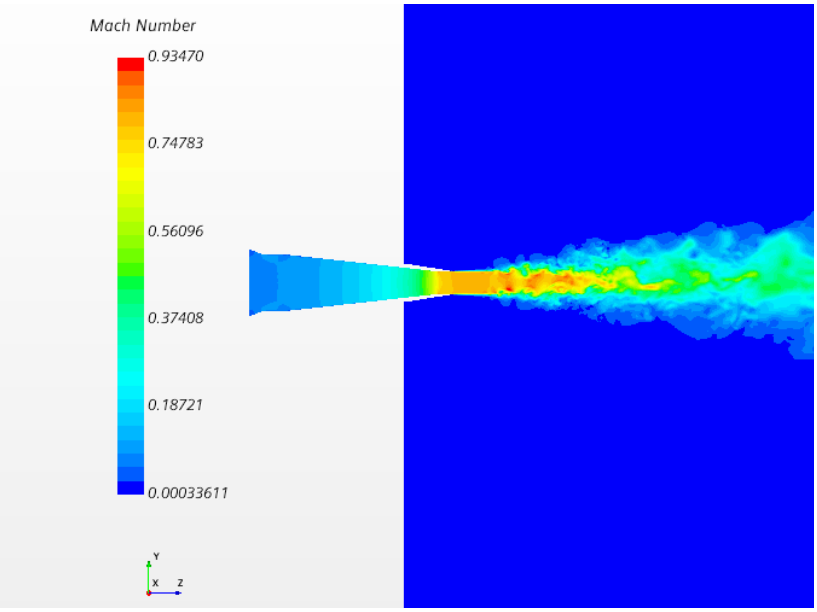

Figure 6. Mach number contours for primary nozzle LES calculation.

Publications
None

Outreach Efforts
ASCENT Advisory Board Meeting

Awards
None

Student Involvement
For the first year, the Penn State team consisted of two graduate research assistants. Ms. Dana Mikkelsen has been the lead on the computational fluid dynamics simulations and will continue in this role for the remainder of the project. Mr. Stephen Willoughby assisted with the project for 6 months and has now been assigned to a different research topic.

Plans for Next Period
During the next research period, the LES for the single nozzle will be completed. Data will be extracted from the FWH data surface, and noise predictions will be made. These predictions will be compared with experimental measurements, and modifications to the simulations will be performed. An LES using the RANS solution at the jet exit as an initial condition will be performed. RANS simulation will then be performed for the dual-stream nozzle, followed by an LES for that configuration. Finally, noise predictions will be made for the dual-stream nozzle and compared with measurements.

Table 1 shows the anticipated list of milestones for the next research period.

Table 1. List of anticipated milestones for the next research period.

Task	Milestone	Planned Due Date
1	External LES for inner nozzle completed	1/31/2022
2	FWH surface data extracted	2/28/2022
3	Inner nozzle noise predictions and comparisons with measurements completed	4/15/2022
4	LES simulations using RANS initial conditions at the jet exit	5/31/2022
5	RANS solution for dual-stream nozzle completed	5/31/2022
6	Dual-stream nozzle LES completed	6/30/2022
7	Dual-stream nozzle noise predictions and comparisons with measurements completed	7/31/2022
8	Annual report submitted	11/30/2022

References
Farassat, F., & Succi, G. P. (1983). The prediction of helicopter rotor discrete frequency noise. Vertica, *7*(4), 497–507.

Ffowcs Williams, J., & Hawkings, D. L. (1969). Sound generation by turbulence and surfaces in arbitrary motion. Philosophical Transactions of the Royal Society of London. Series A, Mathematical and Physical Sciences, *264*(1151), 321–342.

Project 060 Analytical Methods for Expanding the AEDT Aircraft FLEET Database

Georgia Institute of Technology

Project Lead Investigator

Principal Investigator: Professor Dimitri N. Mavris
Director, Aerospace Systems Design Laboratory
School of Aerospace Engineering
Georgia Institute of Technology
Phone: (404) 894-1557
Fax: (404) 894-6596
Email: dimitri.mavris@ae.gatech.edu

University Participants

Georgia Institute of Technology

- PIs: Dr. Dimitri Mavris
- FAA Award Number: 13-C-AJFE-GIT-065
- Period of Performance: June 5, 2020 to September 30, 2022
- Tasks:
    1. Identification and review of aircraft not in the AEDT
    2. Analytical method development

Project Funding Level

The current FAA funding for this project is $300,001 from June 5, 2020 to September 30, 2022. The Georgia Institute of Technology has agreed to a total of $300,001 in matching funds.

Investigation Team

- Dr. Dimitri Mavris (PI), Georgia Institute of Technology
- Dr. Yongchang Li, Georgia Institute of Technology
- Dr. Michelle R. Kirby, Georgia Institute of Technology
- David Anvid, Georgia Institute of Technology
- Dr. Dushhyanth Rajaram, Georgia Institute of Technology
- Ameya Behere, Georgia Institute of Technology
- Zhenyu Gao (graduate student), Georgia Institute of Technology
- Styliani I. Kampezidou (graduate student), Georgia Institute of Technology
- Cristian Puebla-Menne (graduate student), Georgia Institute of Technology
- Chrysoula Lydia Pastra (graduate student), Georgia Institute of Technology

Project Overview

The Aviation Environmental Design Tool (AEDT) relies on aircraft noise and performance (ANP) data provided by aircraft manufacturers to support the calculation of aircraft trajectories and noise at receptors using aircraft performance information and noise-power-distance (NPD) relationships for specific aircraft/engine combinations. In the ANP/Base of Aircraft Data (BADA) workflow, ANP performance data are also used in the calculation of emissions inventories and air quality dispersion. However, not all aircraft in the fleet are represented in the ANP database. When ANP data are not available for a specific target engine/airframe combination, AEDT uses a substitute aircraft from the ANP database to model the target aircraft by closely matching certification noise characteristics and other performance parameters. A problematic issue, however, is that the best substitute based on noise criteria does not always match the best substitute for emissions criteria. In addition,

substitute aircraft do not capture the environmental benefits of newer aircraft with noise and emissions reduction technologies, resulting in overly conservative noise and emissions estimates.

The goal of this research is to improve the accuracy of AEDT noise and emissions modeling of aircraft not currently in the ANP database. Georgia Tech will identify and review aircraft not currently modeled in the AEDT and will collect information and necessary data to better understand the characteristics of these aircraft. Various statistical analysis methods will be utilized to classify the aircraft as different types in terms of size, age, technologies, and other engine/airframe parameters. Quantitative and qualitative analytical methods will be identified and evaluated for each aircraft type to develop ANP and noise data for the aircraft. Validation data from real-world flight and physics-based modeling will be gathered to validate the methods. After validation, the models will be applied to develop ANP and noise data for the aircraft. Finally, recommendations and guidelines will be developed for implementing the developed data in the AEDT to expand the AEDT FLEET database to include noise and performance data for aircraft currently not in the ANP database.

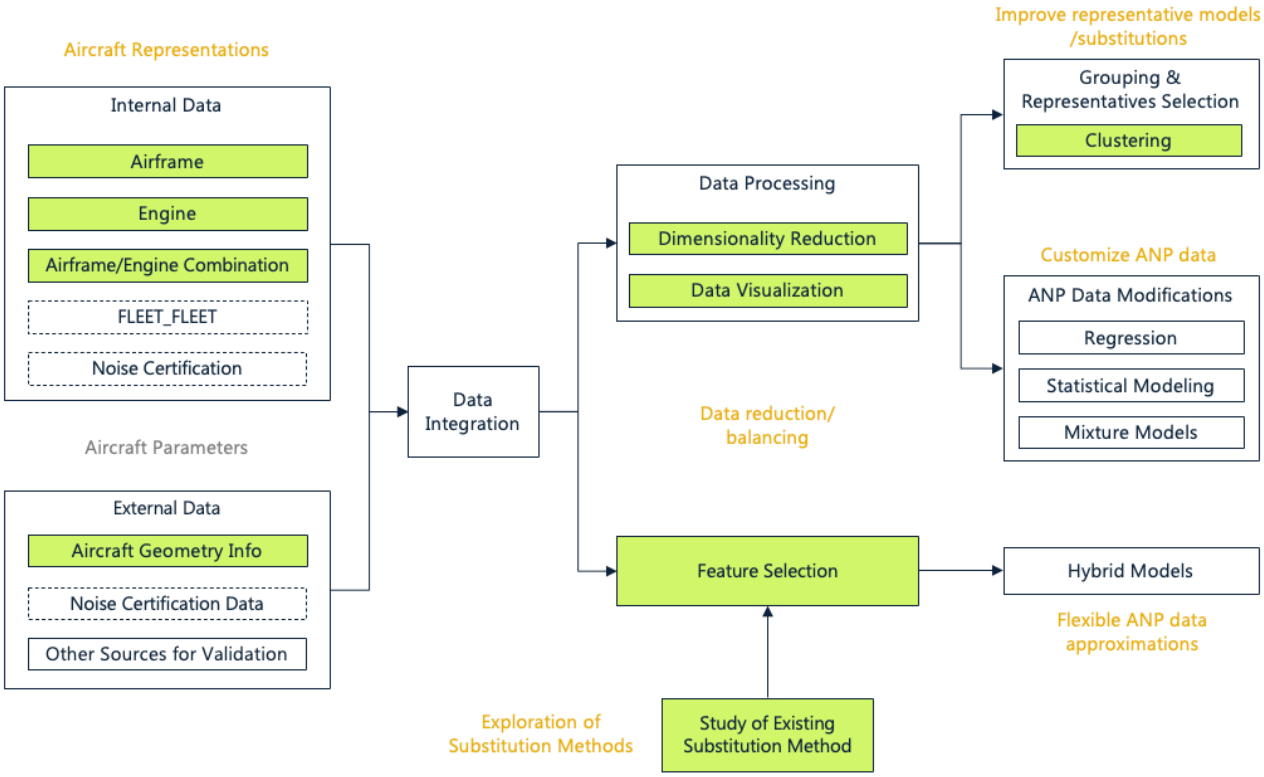

Figure 1. Overview of A60 project tasks and workflow.

The flowchart in Figure 1 presents an overview of the project approach. The first step is to identify the necessary aircraft parameters that will be used to better estimate the substitution aircraft. These parameters are already included in the internal data (FLEET database) or will be collected from external resources.

Task 1 – Identification and Review of Aircraft not in the AEDT

Georgia Institute of Technology

Objectives

The objective of Task 1 is to identify aircraft that are not currently modeled with ANP data in AEDT for noise and emissions modeling. In the FLEET database (DB), specific aircraft engine/airframe combinations are defined by a series of ANP and noise coefficients that are used with the BADA and SAE-AIR-1845 algorithms to conduct performance, emissions, and noise

modeling. The FLEET DB contains representative aircraft for the entire fleet, with some aircraft being modeled by ANP data and others represented by a substitution aircraft. This task involves the identification of aircraft that do not have ANP data and are represented by a substitution aircraft.

Research Approach

The aircraft not currently modeled with ANP data are identified by reviewing the AEDT FLEET DB and conducting a literature survey. The identified aircraft of interest are further investigated to identify gaps between them and the substitution aircraft in terms of performance, noise, and emissions. This step involves reviewing the existing literature on these aircraft and acquiring the information and data necessary to better determine the engine/airframe characteristics of these aircraft. In addition, the ANP data in the FLEET DB are studied to summarize key parameters for which the analytical methods will develop ANP data. The existing ANP aircraft substitution methods and the current substitution methods implemented in AEDT are also investigated to support the development of analytical methods. As summarized in Figure 2, the FLEET database (FAA) contains approximately 3,626 aircraft/engine combinations, of which only 288 have available ANP data. The databases below were used to introduce new parameters not already included in the FLEET database. The external data added from these databases are sparse, presenting another challenge for this project.

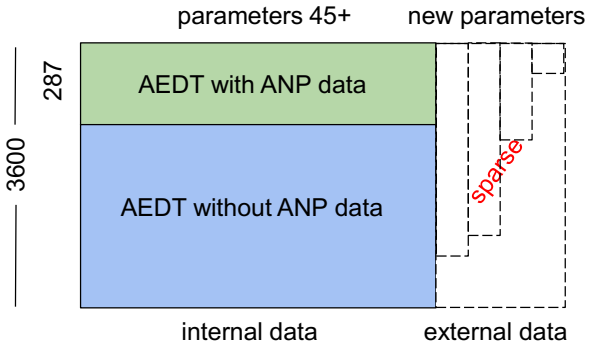

Figure 2. FLEET Database breakdown with respect to ANP data availability.

Aircraft Database Literature Study

The main objective of this task is to collect data from various databases for a wide range of aircraft. This information is helpful when determining which performance, emissions, and noise parameters will be used for the substitution algorithm. In particular, we are interested in the following categories of data:

- **Airframe**: General aircraft information and classifications (example: maximum range)
- **Engine**: Important engine specifications (example: bypass ratio)
- **Aircraft**: Information about an airframe + engine combination (example: maximum takeoff weight [MTOW])
- **Aircraft Geometry**: (example: wing area)
- **Emissions**: Main emission indices (example: unadjusted fuel flow during takeoff)
- **Noise Certification**: (example: flyover noise level)

Overview of Tables Available in the FLEET database (Internal Data) and Associated IDs:

Some of the internal data collected from the FLEET database correspond to:

- FLT_EQUIPMENT (provides the AIRFRAME_ID and ENGINE_ID for each equipment EQUIP_ID)
- FLT_AIRFRAMES (contains airframe information that one can access using the AIRFRAME_ID from the corresponding EQUIP_ID in the FLT_EQUIPMENT table)
- FLT_ANP_AIRPLANES
- FLT_FLEET
- FLT_ENGINES (contains information on engines and emissions that can be retrieved using the ENGINE_ID from the corresponding EQUIP_ID in the FLT_EQUIPMENT table)
- FLT_ENGINES.MODEL
- FLT_CAT_DESIGNATIONS

- FLT_CAT_ICAO_TYPES,
- FLT_BADA_ACFT,
- FLT_ANP_AIRPLANE_NOISE_GROUPS, and
- FLT_NOISE_CERTIFICATION.

The FLEET database contains 3,626 EQUIP_IDs, 848 unique AIRFRAME_IDs, and 686 unique ENGINE_IDs. The FLT_NOISE_CERTIFICATION table has a total of 8,288 records (rows). Amongst the 3,626 equipment types, only 535 (15%) have noise certification records. All of these records have a one-to-many match, i.e., for a certain equipment type, there exist multiple matches in the FLT_NOISE_CERTIFICATION table. The number of matches ranges from 2 to over 100. There is an ongoing effort by FAA to identify a unique path from EQUIPMENT_IDs to unique NOISEDB_IDs; hence, our team will focus on collecting noise parameter values from up-to-date reliable external data sources. In regards to noise parameter values from the FLEET database, two potential routes for retrieving NOISEDB_IDs are proposed in Figure 3.

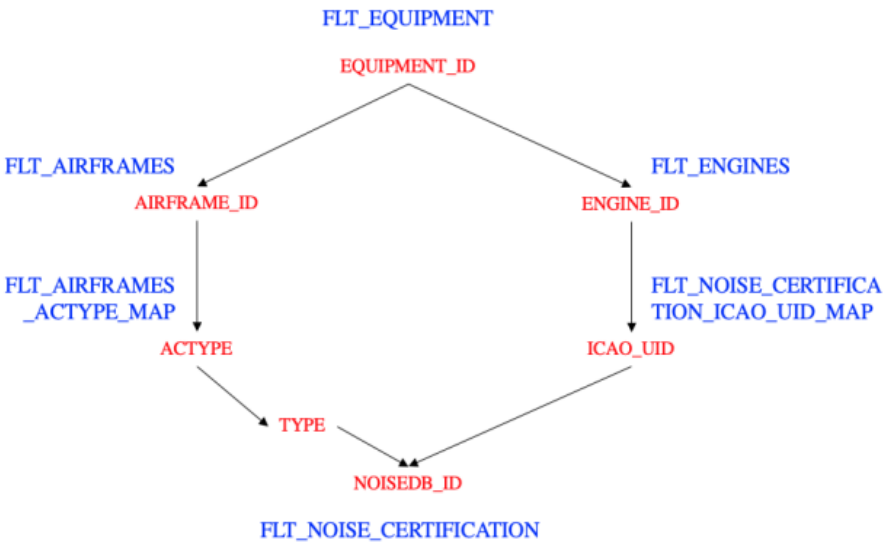

Figure 3. Two alternative FLEET DB routes for identifying the one-to-many choices from EQUIPMENT_ID to NOISEDB_ID.

To create an initial database to utilize for the analytical methods in Task 2, filtering was applied to the original number of unique equipment IDs to establish a subset of engine/airframe combinations for which external data would be gathered. The first filter eliminated the military and cargo designation codes and the small SIZE_CODE aircraft. The next filter eliminated military and general aviation based on the AIRCRAFT_TYPE designation. This filtering reduced the unique equipment IDs to 2,443. For the remaining EQUIP_IDs, the AIRFRAME_MODEL names were grouped to determine the number of unique airframes. With an initial focus on U.S. applications of AEDT, airframe models not operated in the U.S. and the production status of the airframe models were eliminated. For future spirals of this research, a broader set of aircraft types can be included to extend beyond U.S. operations. These filters reduced the total airframes for which external data are required to 138, which is manageable. It should be noted that each airframe could have multiple engine types.

Overview of Internal and External Data Resources Collected Thus Far

To augment the existing ANP database for the unique engine/airframe combinations that do not have ANP data, external data sources were identified. The databases considered to populate the extended FLEET DB table (Figure 2) are provided below. First, information from the internal FLEET DB is used, and then, various other databases are retrieved to populate the external parameters:

- **AEDT ANP** (FLEET + FLEET-FULL databases): The most complete performance database available, the FLEET database contains multiple performance parameters for a wide variety of airframe/engine combinations. Although it is not publicly available, the FLEET-FULL database contains information for all registered aircraft throughout the world. Minimum and maximum values for the same airframe/engine combinations are available for certain aircraft parameters (e.g., MTOW), depending on what aircraft equipment the airline is using onboard.

- **Cirium DB:** No access has been granted to this database yet [1].
- **Janes:** Contains aircraft information such as certification date, weight, range, production date, and status as well as corresponding engine information, i.e., thrust, number of engines, power, and speed. This database also contains wing and fuselage dimensions, maximum payload, and number of passengers [2].
- **EDBv28** [International Civil Aviation Organization (ICAO), 2020]: This Excel-based database covers turbojet and turbofan engines for which emissions are regulated (27 kN or higher static thrust). It contains engine emissions for CO, NO_x, and UHC as well as a few engine performance parameters, including bypass ratio and thrust rated output [3].
- **Jet Engines:** Contains engine information only, such as thrust type, SFC type, airflow, OPR, FPR, BPR, speed, and engine dimensions [4].
- **Piano v2.2:** Aircraft and engine combination data, including wing and fuselage dimension information, weight, payload, and SAR evaluations [5].
- **TCDC**
- **Bluebook:** Contains aircraft/engine combination information such as thrust, maximum speed, recommended speed, stall speed dirty, fuel, gross weight, empty weight, range, length, height, and wing span [6].
- **Elsevier:** Aircraft and engine information, including thrust, number of passengers, weight, payload, fuselage dimensions, and wing dimensions [7, 8].
- **EASA** certification noise databases [EASA, 2020]: A very large Excel database consisting of aircraft/engine types, effective perceived noise in decibels (EPNdB), and noise levels for lateral, flyover, and approach. EASA is a collection of four noise databases that address heavy propeller-driven airplanes, jet airplanes, light propeller-driven airplanes, and rotorcraft [9].
- **DGACv2.30:** This noise certification database offered by French authorities will be utilized along with EASA noise certification values to collect up-to-date noise certification levels [10].
- **Online photographic material:** For the purposes of identifying wingtip presence, wing location, and engine location, pictures available online have been taken into consideration.

Utilizing engineering judgement and prior research on key drivers of noise, emissions, and fuel burn, a set of parameters to define a unique engine/airframe combination were established, which include internal AEDT data and external data. The purpose of the additional parameters is to enhance the information for a particular combination so that a better substitute aircraft can be identified to represent the environmental impact of that combination (performance, noise, and emissions). In Table 1, the first column indicates whether the data have already been collected to populate the extended FLEET table (Figure 2), the second column provides the parameter name, which could be an existing FLEET DB parameter or a newly added one, the third column shows details for each parameter, and the last column lists the exact FLEET DB table where the parameter can be found or other details if the parameter does not originate from the FLEET DB. This ANP extension database will serve as the basis for the analytical methods approach in Task 2.

Table 1. Parameter summary and corresponding database

Status	Parameter Name	Details	DB/Table
Y	EQUIP_ID	Unique identifier for each entry in the Fleet DB	FLEET/FLT_EQUIPMENT
Y	DEFAULT_EQUIP_ID	The equipment ID to use if there are no ANP data	FLEET/FLT_REF_ANP_EQUIPMENT_DEFAULT
Y	Native (1) or Proxy (0)	Add the following equation: if EQUIP_ID and DEFAULT_ID are equal, then give a value of 1, else 0	
Y	AIRFRAME_MODEL	Key name of the aircraft; obtain from the FLEET DB; requires mapping from other DBs	FLEET/FLT_AIRFRAMES called MODEL
N	Airframe Status	InP, OoP, OoS (obtain from the Cirium DB); changed column name from Aircraft Production and merge with the current aircraft use column	Cirium
Y	DESIGNATION_CODE	C, M, or G (sort by this, then eliminate the "M")	FLEET/FLT_CAT_DESIGNATIONS
Y	AIRCRAFT_TYPE	C, G, or M (then sort by this and eliminate the "M")	FLEET/FLT_CAT_ICAO_TYPES
Y	SIZE_CODE	H, L, or S; use to group similar a/c classes	FLEET/FLT_AIRFRAMES
Y	USAGE_CODE	P, B, C, O, A; use to group similar a/c classes	FLEET/FLT_AIRFRAMES
Y	ACFT_DESCR	This is the group of aircraft to which the AIRFRAME_MODEL is mapped if no ANP data exist	FLEET/FLT_ANP_AIRPLANES
Y	Use Aircraft for Clustering?	Y or N (will be used for supervised learning)	
Y	MANUF_DESC		FLEET/FLT_BADA_ACFT
N	Common Aircraft Name	e.g., CNA208 is known as Cessna 208 Caravan	to be entered manually
N	Aircraft Certification Date	Use current data and augment from Cirium and Janes; this gives an indication of the technology level	FLEET, Cirium, Janes
Y	Engine Manufacturer	Obtain from FLT_ENGINES.MANUFACTURER, or for jets, obtain from EDB v28	FLEET/FLT_ENGINES
Y	ENGINE_TYPE	J, P, or T	FLEET/FLT_ENGINES
Y	ENGINE_MODEL	FLEET DB	FLEET/FLT_ENGINES.MODEL
Y	Number of Engines	FLEET DB	FLEET/FLT_AIRFRAMES.ENGINE_COUNT
Y	ENGINE_ID	FLEET DB	FLEET/FLT_ENGINES
Y	ENGINE_CODE	FLEET DB	FLEET/FLT_ENGINES
Y	ENGINE_MOD_ID	FLEET DB	FLEET/FLT_EQUIPMENT
Y	ENG_MOD_DES	FLEET DB	FLEET/FLT_ENGINE_MODS
Y	THR_STATIC	Compare information in FLEET DB with the two items below for consistency	FLEET/FLT_ANP_AIRPLANES
Y	in FLT_ENGINE called RATED_OUT	FLEET DB	FLEET/FLT_ENGINES, compare with EEDBv28
N	Max Rated Thrust (kN) or Power for TP	External sources for jets to compare with the EDBv28; for turboprops and pistons, we don't have thrust in EDB, get from "Jet-engines_data_09-13-21" file	FLEET/FLT_FLEET
Y	FENV_MMO	Cruise speed obtain from Fleet DB and cross check with Janes	FLEET/FLT_BADA_ACFT

Status	Parameter Name	Details	DB/Table
N	Max Cruise Speed (knots or Mach)	Piano first, then Janes, TCDS, Bluebook, or Elsevier; for jets, use Mach number	Wikipedia
Y	CR_CAS_1	FLEET DB	FLEET/FLT_BADA_APF
Y	CR_CAS_2	FLEET DB	FLEET/FLT_BADA_APF
Y	CR_MACH	FLEET DB	FLEET/FLT_BADA_APF
Y	MX_GW_TKO	Check with external DBs later	FLEET/FLT_ANP_AIRPLANES
Y	MX_GW_LND	Check with external DBs later	FLEET/FLT_ANP_AIRPLANES
Y	MAX_PAYLOAD	Obtain from PIANO then, augment with the FLEET DB and compare with Cirium	FLEET/FLT_FLEET
Y	Maximum Range (nmi)	Obtain from PIANO DB	FLEET/FLT_AIRFRAMES called MAX_RANGE
Y	FENV_ALT	FLEET DB	FLEET/FLT_BADA_ACFT and other
N	Typical Number of Passengers		Wikipedia, then PIANO
Y	Wingtip	Y or N	Online photos
Y	Wingspan (ft)		PIANO
Y	Wing Area (ft^2) from Fleet DB		FLEET/FLT_BADA_ACFT and check with PIANO, Janes, Bluebook, and Elsevier
Y	Wing Area (ft^2) from PIANO		PIANO
Y	Wing Aspect Ratio	Calculate	
Y	Fuselage Length (ft)		PIANO
N	Fuselage Height (ft)		Wikipedia
Y	Fuselage Width (ft)		PIANO
Y	Wing Location	High, mid, or low	Online photos
N	Number of Main Landing Gear Wheels	Affects approach noise	Janes or Wikipedia
N	Thrust Reverser	Y or N	
Y	Engine Location	Nose, under wing, mid-wing, above wing, or tail	Online photos
N	Engine Diameter		Jane's first, then TCDS/other
N	Propeller Diameter		Jane's first, then TCDS/other
N	Number of Propellor Blades	Big driver for noise	Manual
N	Combustor Type	To be determined	FLEET/FLT_ENGINES called COMBUSTOR
Y	NOISE_ID		FLEET/FLT_ANP_AIRPLANE_NOISE_GROUPS
Y	SPECT_APP		FLEET/FLT_ANP_AIRPLANE_NOISE_GROUPS

Status	Parameter Name	Details	DB/Table
Y	SPECT_DEP		FLEET/FLT_ANP_AIRPLANE_NOISE_GROUPS
N	NOISE_CAT		FLEET/FLT_ANP_AIRPLANES
N	AC_CODE		FLEET/FLT_REF_ACCODES
Y	ACFT_ID		FLEET/multiple
Y	AIRFRAME_ID		FLEET/multiple
Y	ANP_AIRPLANE_ID		FLEET/multiple
Y	BADA_ID		FLEET/multiple
Y	BADA4_ID		FLEET/multiple
Y	ICAO_UID	TF and MFTF only	FLEET/FLT_ENGINES
Y	Eng Type	For TF and MFTF, obtain from EDB; look to Turboprop_engine_data_compiled_09-13-21 for TPs	EEDB v28c
Y	Engine Identification (i.e., engine name)	TF and MTF	EEDB v28c
Y	Bypass Ratio	For TF and MFTF, obtain from EDB; look to Turboprop_engine_data_compiled_09-13-21 for TPs	EEDB v28c
Y	Pressure Ratio	Obtain from EDB based on the ICAO_UID	
Y	Rated Thrust (kN)	TF and MTF	EEDB v28c
Y	MK Added Prod Status	TF and MTF	EEDB v28c
Y	Superseded UID	MK added to see the link to new UID	
Y	HC EI T/O (g/kg)	TF and MTF	FLEET or EEDB v28c (they have the same values)
Y	HC EI C/O (g/kg)	TF and MTF	FLEET or EEDB v28c (same)
Y	HC EI App (g/kg)	TF and MTF	FLEET or EEDB v28c (same)
Y	HC EI Idle (g/kg)	TF and MTF	FLEET or EEDB v28c (same)
Y	HC Dp/Foo Avg (g/kN)	TF and MTF	EEDB v28c
Y	CO EI T/O (g/kg)	TF and MTF	FLEET or EEDB v28c (same)
Y	CO EI C/O (g/kg)	TF and MTF	FLEET or EEDB v28c (same)
Y	CO EI App (g/kg)	TF and MTF	FLEET or EEDB v28c (same)
Y	CO EI Idle (g/kg)	TF and MTF	FLEET or EEDB v28c (same)
Y	CO Dp/Foo Avg (g/kN)	TF and MTF	EEDB v28c
Y	NOx EI T/O (g/kg)	TF and MTF	FLEET or EEDB v28c (same)
Y	NOx EI C/O (g/kg)	TF and MTF	FLEET or EEDB v28c (same)
Y	NOx EI App (g/kg)	TF and MTF	FLEET or EEDB v28c (same)
Y	NOx EI Idle (g/kg)	TF and MTF	FLEET or EEDB v28c (same)
Y	NOx Dp/Foo Avg (g/kN)	TF and MTF	EEDB v28c
Y	Fuel Flow T/O (kg/sec)	TF and MTF	FLEET or EEDB v28c (same)

Status	Parameter Name	Details	DB/Table
Y	Fuel Flow C/O (kg/sec)	TF and MTF	FLEET or EEDB v28c (same)
Y	Fuel Flow App (kg/sec)	TF and MTF	FLEET or EEDB v28c (same)
Y	Fuel Flow Idle (kg/sec)	TF and MTF	FLEET or EEDB v28c (same)
Y	Fuel LTO Cycle (kg)	TF and MTF	EEDB v28c
Y	Final Test Date	TF and MTF	EEDB v28c
N	Noise Regulation Chapter	Stage 0, 2, 3, 4, or 14	EASA and DGAC (French Civil Aviation Authority)
N	Flyover Noise Level (EPNdB)		EASA and DGAC (French Civil Aviation Authority)
N	Lateral Noise Level (EPNdB)		EASA and DGAC (French Civil Aviation Authority)
N	Approach Noise Level (EPNdB)		EASA and DGAC (French Civil Aviation Authority)
N	Cumulative Noise Level (EPNdb)		EASA and DGAC (French Civil Aviation Authority)
N	OVERFLIGHT (CHAPTER 6)	Turboprops	EASA or FAA
N	TAKEOFF (CHAPTER 10)	Turboprops	EASA or FAA
N	OVERFLIGHT (CHAPTER 6) margin	Turboprops	EASA or FAA
N	TAKEOFF (CHAPTER 10) margin	Turboprops	EASA or FAA

Task 2 – Analytical Methodology Development

Georgia Institute of Technology

Objective

The objective of Task 2 is to develop analytical methodologies and solutions that can improve the modeling of aircraft types (airframe/engine combinations) that are not included in the ANP database. In this process, machine learning (ML) and data mining (DM) approaches are employed to analyze aircraft features (both internally and externally collected), ANP data, and environmental output data and to gain insights and evidence for better model substitution and approximation. The following research questions can be answered while developing these more advanced analytical methods:

- How to better assign substitutions for aircraft types that are not included in the ANP database?
- How to better choose representative aircraft models to develop more ANP data with the aim of more sufficiently covering the entire population?
- What aircraft features should be used in the identification of aircraft substitution?
- How can we make better use of the current ANP data to approximate the remaining aircraft with more flexibility?

Research Approach

The data-driven analytical methodologies used in this task are primarily based on techniques from machine learning (ML) and data mining (DM). The solution for each research question consists of multiple ML/DM algorithms. In general, the analytical techniques that are useful in this project can be classified into five categories: clustering, dimensionality reduction, regression, feature selection, and data visualization. Table 2 presents examples and objectives for all five categories.

In this project, the data collection and integration (Task 1) and analytical method development (Task 2) have been conducted in parallel. In Tasks 2.1–2.4, the proposed analytical approaches are applied to selected problems. However, it should be noted that because the master dataset has not yet been finalized, as described in previous sections, the analytical method concepts are mainly demonstrated through notional or incomplete datasets.

Task 2.1: Data Visualization of Aircraft Representations

Because the data integration process combines data from different sources, such as airframe, engine, and airframe/engine combination data, to represent an aircraft, an immediate data visualization step can help in interpreting the aircraft representation. The objective of such data visualization tasks is to visualize each aircraft in the population while unveiling the main characteristics of the population. For example, Figure 4 presents a t-distributed stochastic neighbor embedding (t-SNE) visualization of some typical aircraft types. The t-SNE visualization can also serve as a nonlinear dimensionality reduction method, which aims to retain the local structure of data while preserving some of the global structure of the data. Under the t-SNE, similar aircraft types are supposed to remain close to each other in a two-dimensional plot.

Table 2. Analytical approach components of the project.

Method Classification	Algorithm Examples	Objectives
Clustering	k-means clustering k-medoids clustering Hierarchical clustering (multiple linkages) Density-based clustering (e.g., DBSCAN) Biclustering Subspace clustering	Clustering groups aircraft types such that aircraft with similar noise and performance features belong to the same cluster. The clustering can be performed at multiple levels of granularity, after which each cluster can be represented by a single aircraft type.
Dimensionality Reduction	Principal component analysis (PCA) ISOMAP Autoencoder Uniform manifold approximation and projection (UMAP)	Dimensionality reduction maps data from a high-dimensional space to a low-dimensional space while maintaining the intrinsic features of the data. It mitigates the drawbacks of dimensionality that arise in the analysis of high-dimensional data, such as an aircraft representation.
Regression	General linear models Nonlinear regression	Regression techniques can potentially be used to estimate certain parts of ANP data for a target aircraft not included in the ANP database or to make adjustments in the current ANP data.
Feature Selection	Shrinkage methods (e.g., LASSO) Tree-based methods Information theory-based methods Correlation feature selection Feature selection for supervised learning	In general, feature selection selects a subset of original features with high relevance and low redundancy. Depending on the availability of the outputs (labels), this approach can be classified into unsupervised or supervised feature selection. It can help in improving the solution of each research question discussed above.
Data Visualization	t-distributed stochastic neighbor embedding (t-SNE) Statistical graphs Interactive data visualization	In this project, data visualization can be used as an ancillary tool to improve data interpretation. It is useful for making sense of high-dimensional data with complex structures.

The aircraft range in Figure 4 includes a total of 41 ANP aircraft and all aircraft types mapped to them in the current substitution mechanism. Each ANP aircraft and the aircraft types under it are in the same color, and the ANP aircraft are marked with their names. It can be observed that in general, similar aircraft stay close to each other. For example, the large twin-aisle aircraft are located at the central and bottom parts of the plot. However, the current substitutions may be further

improved because aircraft represented by different colors are still mixed in some regions. The results in Figure 4 indicate that the notional aircraft representation in this example is generally reasonable while also revealing some potential research opportunities to improve the current practice.

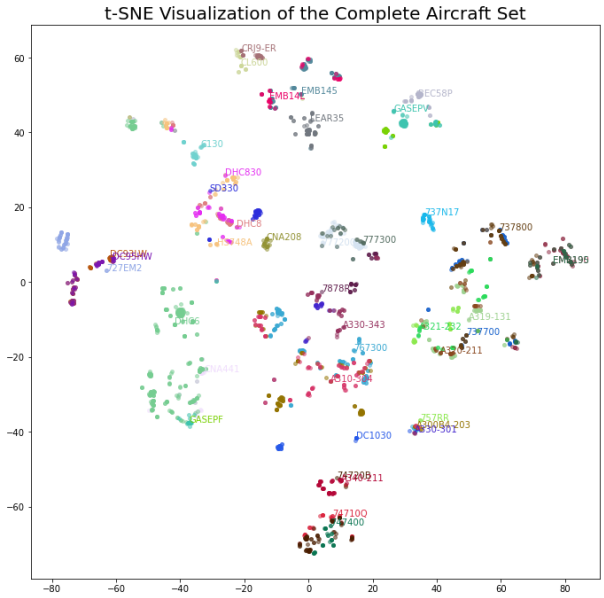

Figure 4. t-SNE visualization of groups of aircraft models.

Task 2.2: Using Clustering to Identify Representative Aircraft Model Portfolios

Clustering groups similar aircraft into the same cluster and dissimilar aircraft into different clusters. Clustering is a typical task in unsupervised machine learning, with extensive methods reported in the literature. The choice of a specific clustering algorithm depends on the objectives of the problem. In this project, clustering can be used to achieve at least two aims. The first is to group similar aircraft together and compare the results with the current ANP aircraft substitutions in order to improve the current substitution mapping and to identify gaps. Many algorithms in the literature, such as k-means, hierarchical clustering, and DBSCAN, can all achieve this objective. The second is to select representative aircraft types from the population through clustering. In a basic process, all *n* aircraft are first partitioned into *k* clusters, and then, from each cluster, one aircraft is selected to represent all aircraft in the same cluster. There are also methods for conducting clustering and representative aircraft selection simultaneously. In this example, we apply hierarchical clustering on a notional dataset to demonstrate our method.

Hierarchical clustering creates a hierarchy, represented by a tree (often referred to as a dendrogram), of partitions that may reveal interesting structure/patterns in the data at various levels of granularity. Hierarchical clustering starts from an individual cluster for each aircraft type (at the leaves) and then progressively merges the two closest clusters until all aircraft types are in a single cluster (at the root). Between the leaves and the root, this method can output intermediate clustering results with any specified number of clusters. The result of hierarchical clustering is deterministic, easy to understand and allows flexibility in choosing the number of clusters/representative aircraft. Moreover, hierarchical clustering can accommodate different objectives. A crucial choice in the process is the selection of linkages, which measure inter-cluster distances when clusters are merged. In the literature, there are four common linkages: single, complete, average, and centroid, which result in different natures of clustering. Another linkage, the minimax linkage, naturally associates one aircraft with each cluster in the clustering process. Figure 5 presents an example of hierarchical clustering with the minimax linkage applied to 24 aircraft types, with each type having only two features. Cutting the dendrogram at a height *h* creates a clustering such that no aircraft in the population is at a distance greater than *h* from its nearest selected representative aircraft.

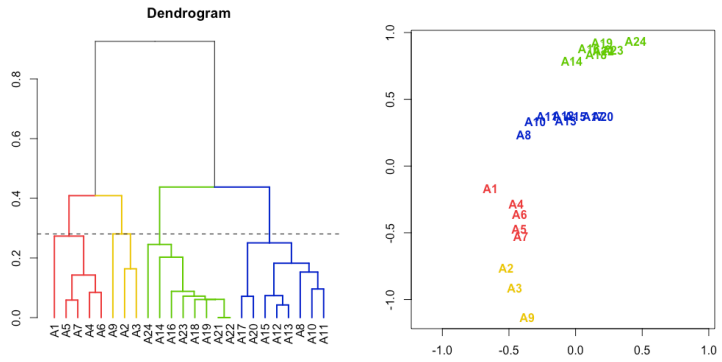

Figure 5. Simple example of hierarchical clustering with the minimax linkage.

Figure 6 displays a dendrogram obtained by applying hierarchical clustering with the minimax linkage on a larger group of aircraft. The representative aircraft associated with each cluster are also shown in the dendrogram. For example, when only two aircraft are used to represent the population, the aircraft are DHC830 and 737N17. One can observe that different classes of aircraft (general aviation, single-aisle, twin-aisle, etc.) can be effectively differentiated from a top-down view of the dendrogram. Hierarchical clustering with other linkages can also generate similar dendrograms, yet the processes of clustering and representative aircraft are separate. Other than partitioning and identifying similar aircraft groups, clustering also has natural solutions for finding substitution aircraft for those without ANP data. Such substitution mappings can then be compared with current ANP aircraft substitutions to identify anomalous substitutions, gaps, etc.

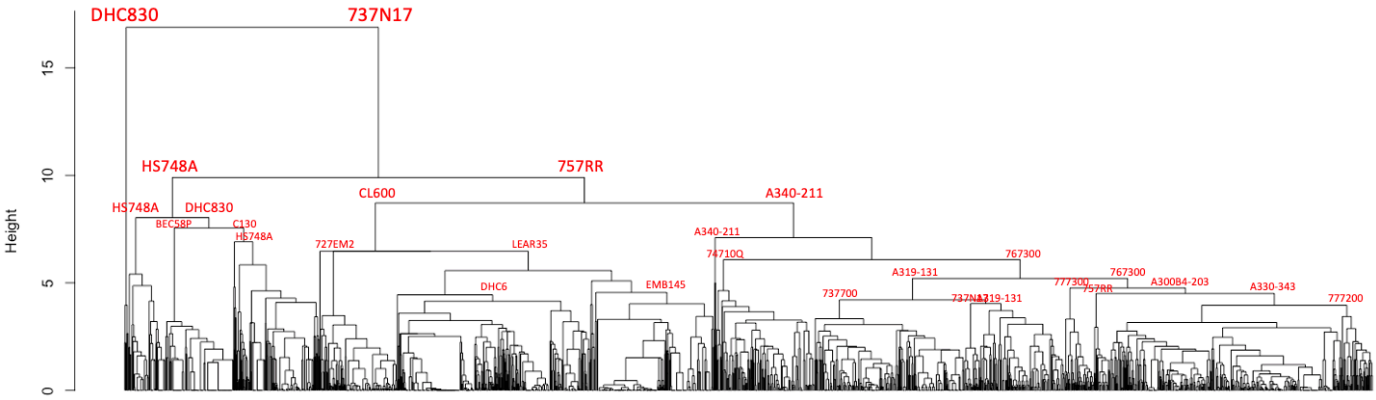

Figure 6. Example of hierarchical clustering with the minimax linkage for a large aircraft population.

Task 2.3: Initial Aircraft Feature Selection

The motivation behind a feature selection task is that, in any analytical analysis task, the collected aircraft features are not equally important for ANP model substitution/estimation or environmental impact modeling. Then, a feature selection step can improve the other analytical analysis tasks and advance our understanding of aviation environmental impacts by (1) selecting a subset of parameters that best represent an aircraft's characteristics in environmental impact modeling and (2) determining the relevant importance and ranking among the selected features. Because this feature selection step involves connections to ANP data and/or environmental impact outputs, it belongs to the category of supervised feature selection. Figure 7 shows the basic process of such a supervised feature selection task, which mainly includes three components:

1. **Large-scale experiment**: To identify important aircraft features with the best predictive power for key environmental impact outputs, such as fuel burn, emissions, and noise, a large-scale experiment is needed to obtain the values of outputs through computer simulations. The experiment will be run through AEDT to obtain performance and noise reports for each case. The details of the cases are set up by a "test matrix," which contains information such as

aircraft type, operation type, stage length, and profile for each case. Both the experimental set-up and result extraction are enabled by some existing automated tools.

2. **Postprocessing and result analysis**: After the experiment is finished, another step is needed to extract and calculate key information from the reports. Specifically, 28 metrics of interest that cover fuel burn, emissions, and noise are identified. A complete list of the outputs of interest is shown in Table 3. An automated postprocessing tool was developed in a previous project by Georgia Tech, in which noise calculations were validated against the noise contours generated by AEDT. At the end of this step, a "result matrix" is generated, where each row is a specific aircraft type. The columns of the result matrix contain both aircraft features (part I) and outputs of interest (part 2). The complete result matrix table is then ready for the subsequent supervised feature selection task.
3. **Statistical modeling and learning**: With information from both the input (aircraft features) and output (key environmental impacts) sides, any supervised statistical learning technique can be utilized to learn a group of features that are influential in the outputs. For example, the flowchart in Figure 7 applies shrinkage methods, which represent a type of feature selection method based on regression. Other methods, such as tree-based methods, can also be considered and have their respective advantages.

Table 3. Outputs of interest for feature selection.

Number	Category	Output Name	Unit
1	Noise	Departure SEL Contour Area at 80 dB	sq. n.mi.
2		Departure SEL Contour Length at 80 dB	n.mi.
3		Departure SEL Contour Width at 80 dB	n.mi.
4		Departure SEL Contour Area at 90 dB	sq. n.mi.
5		Departure SEL Contour Length at 90 dB	n.mi.
6		Departure SEL Contour Width at 90 dB	n.mi.
7		Arrival SEL Contour Area at 70 dB	sq. n.mi.
8		Arrival SEL Contour Length at 70 dB	n.mi.
9		Arrival SEL Contour Width at 70 dB	n.mi.
10		Arrival SEL Contour Area at 80 dB	sq. n.mi.
11		Arrival SEL Contour Length at 80 dB	n.mi.
12		Arrival SEL Contour Width at 80 dB	n.mi.
13	Fuel Burn	Departure Fuel Burn	g
14		Arrival Fuel Burn	g
15		Departure Fuel Burn below 3,000 ft	g
16		Arrival Fuel Burn below 3,000 ft	g
17	Emissions	Departure NO_x Emissions	G
18		Arrival NO_x Emissions	G
19		Departure CO Emissions	G
20		Arrival CO Emissions	G
21		Departure nvPM Emissions	G
22		Arrival nvPM Emissions	G
23		Departure NO_x Emissions below 3,000 ft	G
24		Arrival NO_x Emissions below 3,000 ft	G
25		Departure CO Emissions below 3,000 ft	G
26		Arrival CO Emissions below 3,000 ft	G
27		Departure nvPM Emissions below 3,000 ft	G
28		Arrival nvPM Emissions below 3,000 ft	g

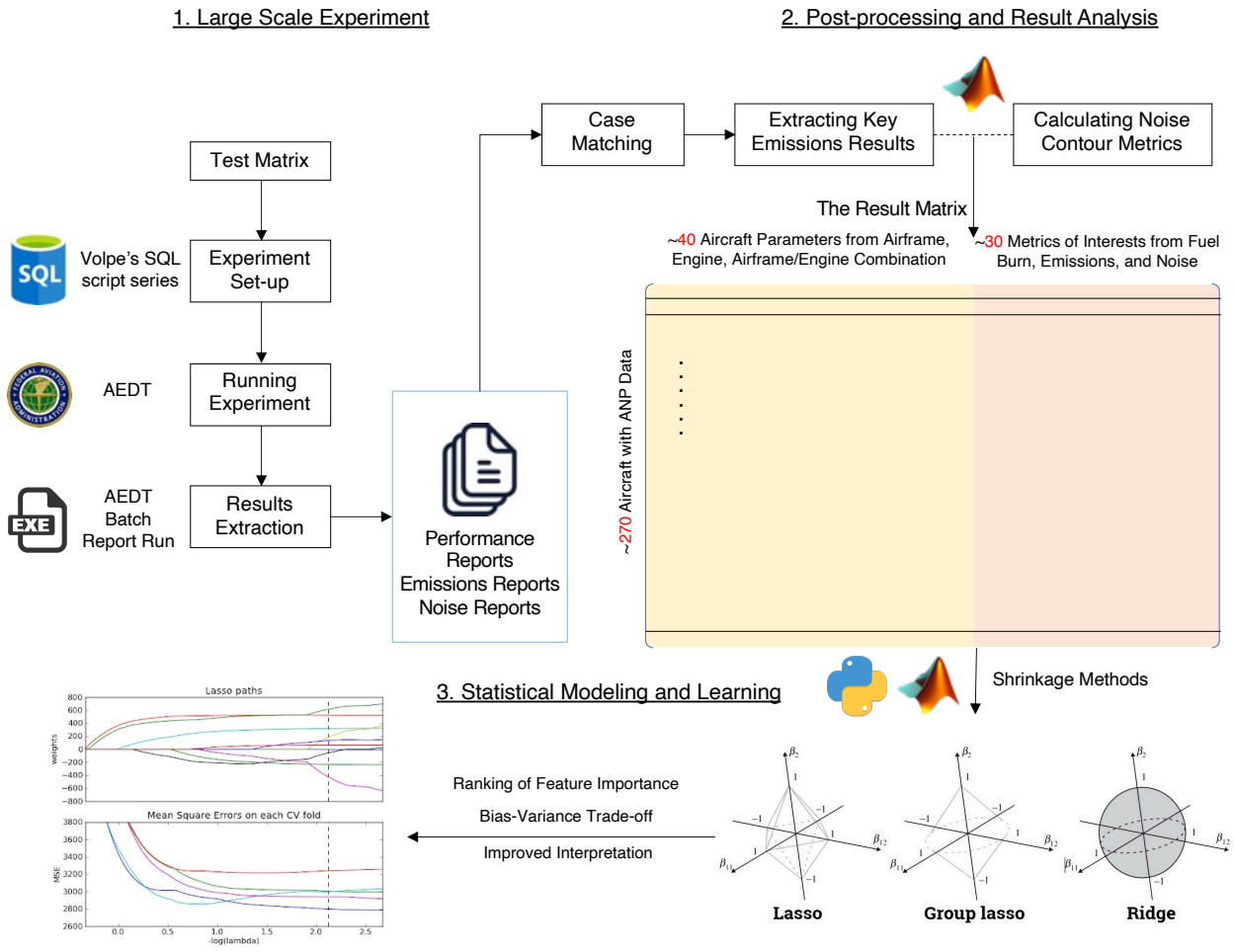

Figure 7. A supervised aircraft feature selection process.

Next, we discuss example results for applying a shrinkage method, least absolute shrinkage and selection operator (LASSO), to select important aircraft features for two key environmental impact outputs: departure 80-dB contour area and departure total fuel burn. Figure 8 displays results for the departure 80-dB contour area. The LASSO method adds a penalty term to the regression coefficients and forces certain coefficients to zero. As the regularization parameter lambda increases from zero, the regression coefficients associated with the less significant features are forced to zero, as indicated by the left plot of Figure 8. Therefore, for a sufficiently large value of lambda, only a subset of the original features has nonzero regression coefficients and are selected. The "optimal" value of lambda can be selected through a cross-validation process, as shown in the right plot of Figure 8.

The cross validation based on the mean squared error (MSE) is essentially a tradeoff between bias, which occurs in simple models with very few features, and variance, which occurs in complex models with too many features. In this case, the optimal value of lambda and the corresponding subset of features can be selected at the minimum MSE. The notional example in Figure 8 uses features from airframe, engine, and airframe/engine combination to represent aircraft and analyzes simulation results from 174 aircraft with ANP data. Both discrete and continuous features are included for selection. The significant parameters selected for the departure 80-dB contour area include (in the order of the ranking) aircraft type and usage classifications, aircraft size code, engine rated out thrust, engine bypass ratio, engine type, number of engines, and engine pressure ratio.

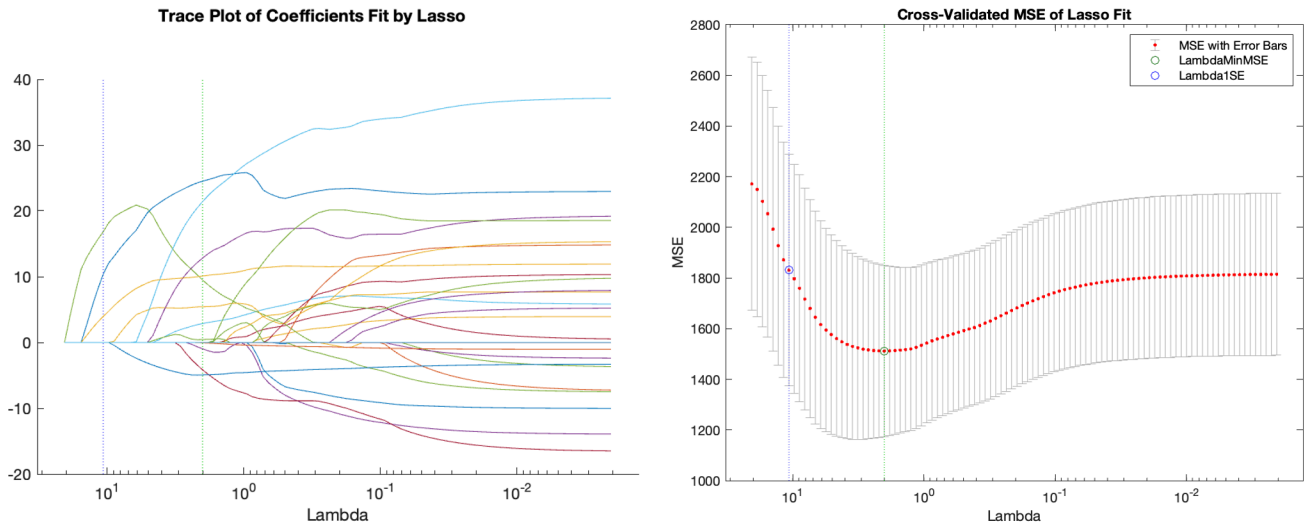

Figure 8. LASSO feature selection result for the departure 80-dB contour area.

Figure 9 displays feature selection results for another key environmental impact output: departure total fuel burn. The same LASSO feature selection process is applied to the same set of parameters as the process for Figure 8. The significant parameters selected for departure total fuel burn include (in the order of the ranking) maximum takeoff gross weight (MTGW), aircraft size code, unadjusted fuel flow (idle), number of engines, aircraft type classification, unadjusted fuel flow (takeoff), engine location, aircraft usage classification, engine bypass ratio, and engine rated out thrust. These two examples represent feature selection for individual outputs. It is also possible to conduct feature selection on multiple outputs simultaneously.

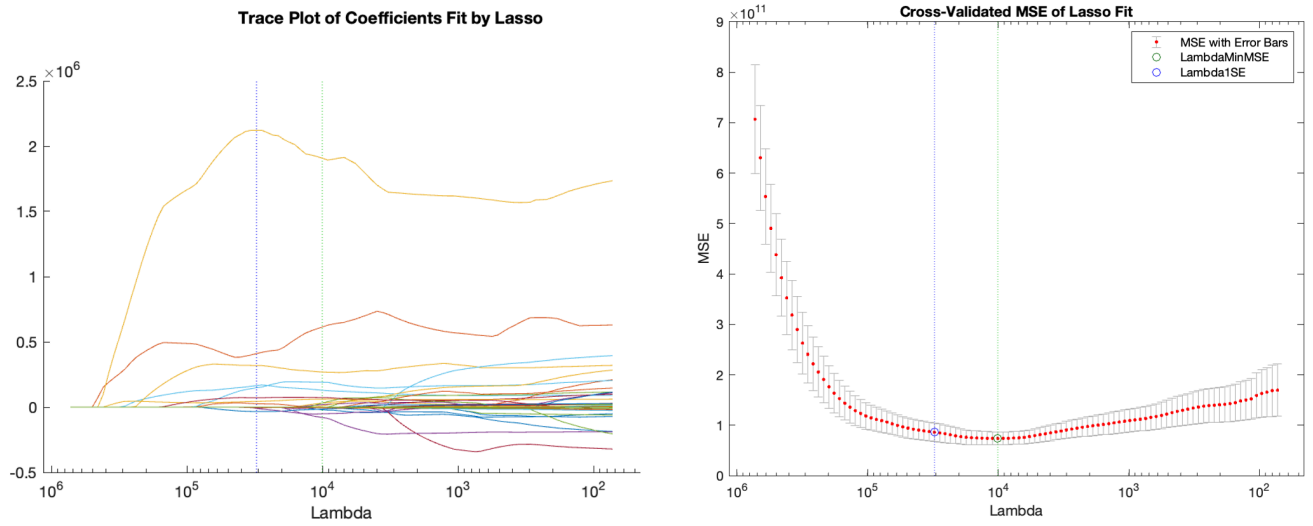

Figure 9. LASSO feature selection result for the departure total fuel burn.

Task 2.4: Hybrid Model Representations

The aircraft substitutions thus far are one-to-one substitutions, i.e., for an aircraft without ANP data, classified as a "missing aircraft," certain aircraft features are used to identify a "proxy aircraft" among the ANP aircraft that is then directly used to represent the missing aircraft. In a one-to-one substitution, all components of the proxy aircraft's ANP data are applied for the missing aircraft. A hybrid model representation aims to find more flexible ways to represent a missing aircraft than one-to-one substitution. The ANP data of an aircraft type consist of many components, such as jet engine coefficients,

aerodynamic coefficients, thrust-specific fuel consumption (TSFC) coefficients, departure/approach profiles, and NPD curves. Instead of identifying proxy aircraft, a more flexible solution could be to identify proxy components. As a result, for a missing aircraft, different ANP data components can be taken from different ANP aircraft. A hybrid model methodology could start with the feature selection results from the last section. For instance, to identify the closest NPD component, one must first identify the aircraft features that are most influential in noise-related metrics. Then, a proxy aircraft can be selected by using that specific subset of aircraft features. In the end, the NPD component of that proxy aircraft is used to fill in the NPD component of the missing aircraft. This procedure of feature selection plus proxy aircraft identification is repeated for each ANP data component, resulting in a hybrid format of ANP data for the missing aircraft. An illustration of this concept is shown in Figure 10.

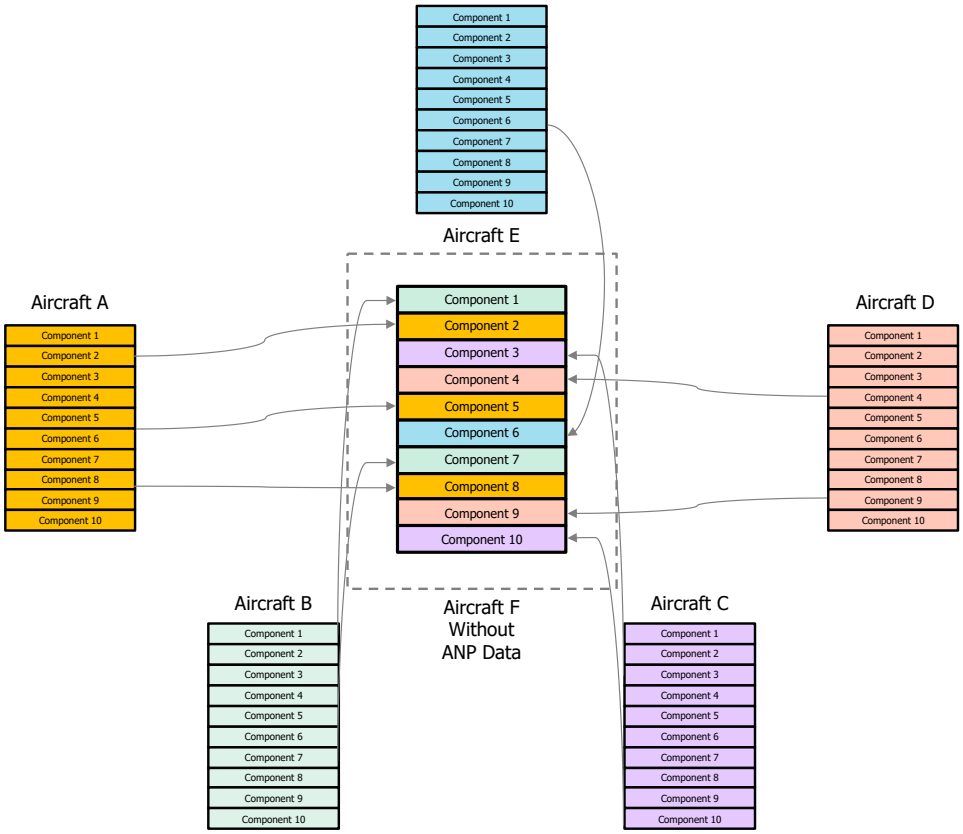

Figure 10. Concept of hybrid ANP model representation.

Major Accomplishments

The major accomplishments for this period performance include the following:

- A literature study was conducted on databases to collect performance, emission, and noise data for target aircraft.
- A new template was created for the ANP extension database and external data were gathered.
- External databases were gathered to augment the extension DB, and the population of these data was initiated.
- A literature survey was conducted on analytical methods in clustering, dimensionality reduction, feature selection, and data visualization.
- Suitable analytical approaches/workflows were identified and designed for multiple tasks of the project.
- Proposed analytical methods were applied to notional data sets, and their effectiveness was demonstrated.

Publications

None

Outreach Efforts
None

Awards
None

References
[1] https://www.cirium.com/
[2] https://customer.janes.com/janes/home
[3] https://www.easa.europa.eu/domains/environment/icao-aircraft-engine-emissions-databank
[4] http://www.jet-engine.net/
[5] https://www.lissys.uk/dbase.html
[6] https://aircraftbluebook.com/Tools/ABB/ShowSpecifications.do
[7] https://booksite.elsevier.com/9780340741528/appendices/data-a/default.htm
[8] https://booksite.elsevier.com/9780340741528/appendices/data-b/default.htm
[9] https://www.easa.europa.eu/domains/environment/easa-certification-noise-levels
[10] http://noisedb.stac.aviation-civile.gouv.fr/bdd

Plans for Next Period
- Develop an approach to identify noise certification data
- Gather engine-related parameters
- Finalize the ANP extension database to serve as the basis for Task 2
- Implement analytical methods on the new database, identify gaps in the approach, and refine as needed for extension to the remaining engine/airframe combinations within the Fleet DB
- Continue to gather additional data sources

Project 061 Noise Certification Streamlining

Georgia Institute of Technology

Project Lead Investigator

Professor Dimitri N. Mavris (PI)
Director, Aerospace Systems Design Laboratory
School of Aerospace Engineering
Georgia Institute of Technology
(404) 894-1557
dimitri.mavris@ae.gatech.edu

Dr. Jimmy Tai (co-PI)
Division Chief, Advanced Configuration Division
Aerospace Systems Design Laboratory
School of Aerospace Engineering
Georgia Institute of Technology
(404) 894-0197
jimmy.tai@ae.gatech.edu

University Participants

Georgia Institute of Technology

- PI(s): Dr. Dimitri Mavris, Dr. Jimmy Tai
- FAA Award Number: 13-C-AJFE-GIT-066
- Period of Performance: June 5, 2020 to June 4, 2021
- Tasks (for year 1):
    1. Task 1: Interview industrial partners on current noise certification process
        - Task 1.1: FAA noise certification regulation review
        - Task 1.2: Industrial partner interviews via workshops
    2. Task 2: Develop and recommend a streamlined noise certification procedure for existing aircraft
        - Task 2.1: Current process assessment
        - Task 2.2: Streamlined process definition
    3. Task 3: Develop a flexible noise certification procedure for new aircraft
        - Task 3.1: Flexibility assessment of streamlined process
    4. Task 4: Simulate streamlined and flexible noise certification procedure
        - Task 4.1: Identify modeling approach
        - Task 4.2: Noise certification process metric definition

Project Funding Level

The total amount of current funding from the FAA for ASCENT Project 61 is $250,000 for a 12-month period of performance.

Investigation Team

The ASCENT Project 61 Georgia Institute of Technology (Georgia Tech) Aerospace Systems Design Laboratory (ASDL) investigation team is shown in the organization chart below. Professor Dimitri Mavris is the PI of this project, together with co-PIs Dr. Jimmy Tai, Senior Research Engineer, and Dr. Evan Harrison, Research Engineer II. In support of the co-PIs, a team of two research faculty is leading efforts in both planning and technical development for the planned tasks. They are being joined by four graduate student assistants, who are supporting Project 61 as they work toward their M.Sc and PhD degrees. All team members are affiliated with the ASDL at the School of Aerospace Engineering, Georgia Tech.

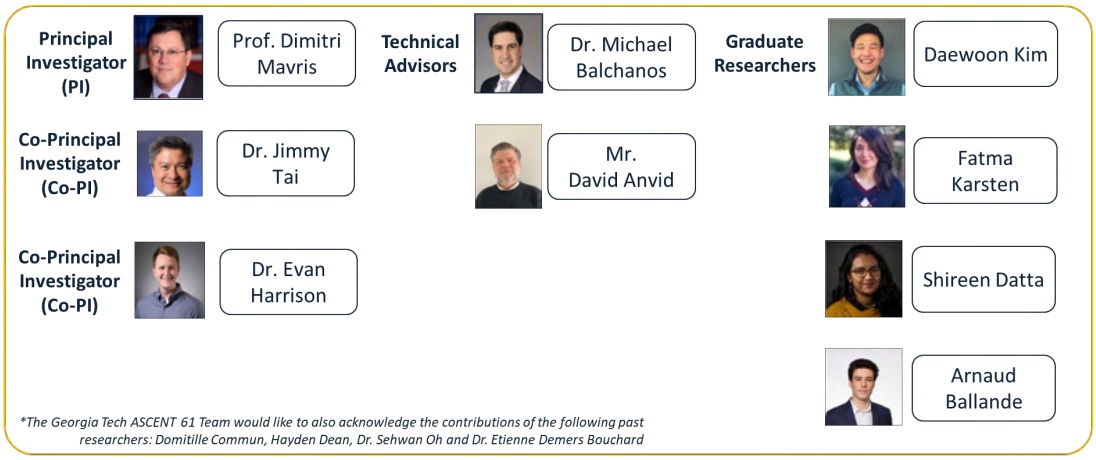

ASCENT Project 061 Georgia Tech ASDL team.

From the team of technical advisors, the following roles and responsibilities have been defined:

- **Dr. Michael Balchanos**, Research Engineer II, is serving as the technical lead for Project 61. Aside from day-to-day coordination roles, he is responsible for planning a series of workshops with the industry partners and subject-matter experts (SMEs) on benchmarking efforts under Task 1 for current noise certification procedures. Moreover, he is investigating techniques for process simulation, under the process improvement modeling task (Task 4).
- **Mr. David Anvid**, Senior Research Engineer, is supporting Task 1 efforts in understanding Parts 21 (on certification procedures) and 36 (on noise regulations) of Title 14 Part C. He joined ASDL on October 1, 2020, and his multi-year industry experience in noise certification has been invaluable in the team's efforts to benchmark current certification procedures.

The following past technical advisors contributed to the tasks:

- **Dr. Sehwan Oh**, Postdoctoral Researcher, focused on exploring current certification regulations and understanding their structure (e.g., hierarchy and associations) linked to Task 1, and provided input regarding the application of discrete event and agent-based methods as part of the efforts planned for Task 4.
- **Dr. Etienne Demers Bouchard**, Postdoctoral Researcher, explored process modeling methods from the literature, as well as formulating a canonical problem to assess the feasibility and applicability of methods.

In the team of graduate student researchers, the following roles and responsibilities have been defined:

- **Mr. Daewoon Kim**, first-year M.Sc. student, is leading the team's model-based systems engineering (MBSE) efforts in representing the baseline certification process in Systems Modeling Language (SysML).
- **Ms. Shireen Datta**, second-year M.Sc. student, has been supporting the efforts in documenting current procedures and exploring regulation-driven requirements, which are now included in the verification model.
- **Ms. Fatma Karsten**, PhD student, worked on flight testing plan implementation and the effective perceived noise level (EPNL) calculation module within the MBSE verification model.
- **Mr. Arnaud Ballande**, first year M.Sc. student, has been working on a process simulation capability as part of evaluating equivalent procedures under the process improvement modeling task (Task 4).

The following former students contributed to the tasks:

- **Ms. Hayden Dean**, first year M.Sc. student, was instrumental in capturing and understanding current regulations and certification procedures, as dictated by the Title 14 Subchapter C, Parts 21 and 36, as well as the Part 36 Advisory Circular (AC), with particular focus on AC 36-4D, and emphasis on the guidance instructions regarding flight testing for noise certification.
- **Ms. Domitille Commun**, PhD student, worked on implementing a DES model-based process simulation capability for the certification baseline.

Project Overview

Noise certification procedures (with the inclusion of equivalent procedures) have served aviation stakeholders (including original equipment manufacturers [OEMs], regulators, operators, and airports) well since the 1960s [1–3]. However, with new vehicle types and new technologies (including new entrants, digital technologies for airframes, propulsion, and measurements), the existing certification processes must be critically examined. A key aspect of current certification practices is the equivalent procedures and supporting technology, which many OEMs utilize [4]. Equivalent procedures are anticipated both for existing and new standards to further accommodate future innovation.

The project objective is to examine current noise certification procedures and identify opportunities to streamline the noise certification process, while recommending process updates for building the needed flexibility to accommodate all air vehicle types. Project 61 seeks to propose quantifiable process improvements and facilitate the application of traditional systems engineering (SE) for complex systems with, model-based systems engineering (MBSE), while leveraging these methods for the management of regulatory requirements. To perform the proposed research under this 3-year effort, Georgia Tech has teamed with several industrial partners with extensive experience in noise certification. Each industrial partner represents different types of vehicles, such as large subsonic transports, propeller-driven small aircraft, and rotorcraft.

The ASCENT Project 61 team seeks to accomplish the following goals:

- Identify opportunities for increased efficiency (through expediting steps and simplification of the process) and flexibility in the current noise certification process, to accommodate multiple vehicle categories
- Formulate and evaluate revised noise certification processes for current vehicle types and offer recommendations to the FAA (Part 36, AC 36-4D, etc.)
- Develop process modeling methods to enable quantitative assessment of noise certification
- Facilitate the application of traditional SE processes for complex systems and MBSE, leveraging these methods for the management of regulatory requirements

An overview of the ASCENT 61 roadmap toward goals and milestones is shown in Figure 1.

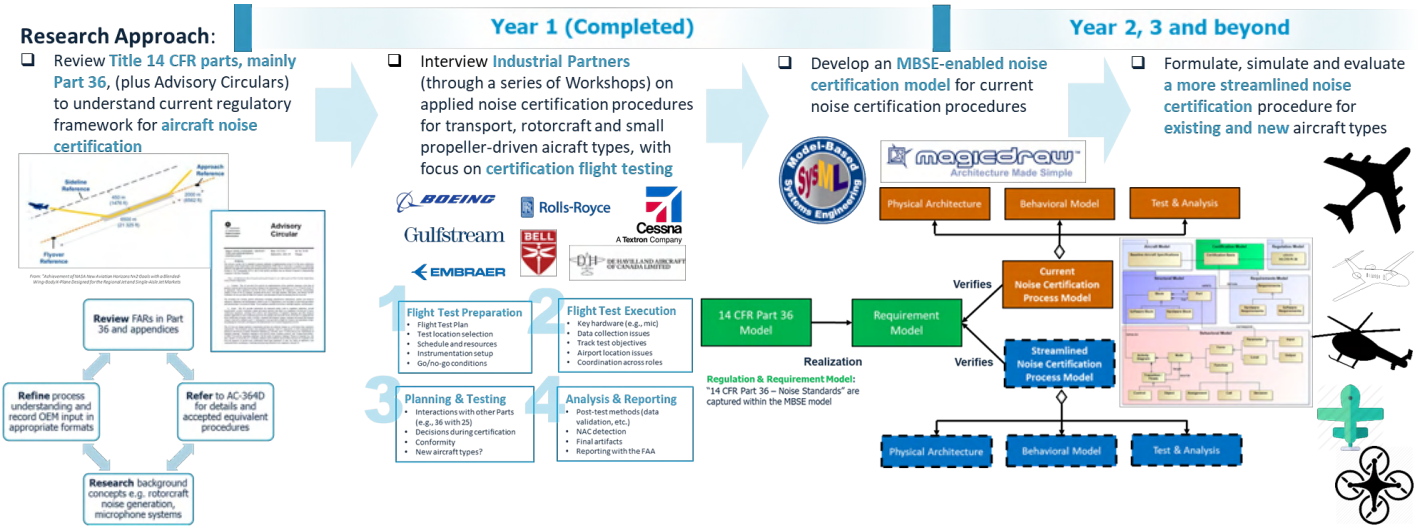

Figure 1. Roadmap toward a model-based framework for exploring current and streamlined noise certification.

The main goal is to provide recommendations to the FAA, in the form of feasible equivalent procedures, supported by the latest technologies/hardware, as well as analytic techniques to support the certification of future air vehicle types. These recommendations should be accompanied by evidence that the suggested equivalent procedures are fully compliant with Part 36, and should use case examples for future air vehicles, e.g., small propeller-driven aircraft and unmanned aircraft systems (UAS).

To implement this roadmap and achieve the targeted outcomes, four main tasks have been delineated, which are shown in Figure 2, along with the subtasks that have been prioritized for year 1 of ASCENT 61. In that figure, a status indication is shown, with completed subtasks highlighted in green, and subtasks that are currently undergoing through iterations and refinements indicated in gold.

Figure 2. Year 1 project task breakdown.

For the full 3-year period of performance, the complete timeline for finalizing all Project 61 tasks is shown in Table 1.

Table 1. ASCENT Project 61 task planning timeline.

	Task	Year 1												Year 2												Year 3											
		M1	M2	M3	M4	M5	M6	M7	M8	M9	M10	M11	M12	M13	M14	M15	M16	M17	M18	M19	M20	M21	M22	M23	M24	M25	M26	M27	M28	M29	M30	M31	M32	M33	M34	M35	M36
1	Interview Industrial Partners on Current Noise Certification Process																																				
	1.1 FAA Noise Certification Regulation Review																																				
	1.2 Industry Partner Interviews via Workshops																																				
2	Develop a Streamlined Noise Cert. Procedure for Existing Aircraft																																				
	2.1 Current Process Assessment																																				
	2.2 Streamlined Process Definition																																				
	2.3 Streamlined Process Assessment and Revision																																				
3	Develop a Flexible Noise Certification Procedure for New Aircraft																																				
	3.1 Flexibility Assessment of Streamlined Process																																				
	3.2 Flexible Process Definition																																				
	3.3 Flexible Process Assessment and Revision																																				
4	Simulation Streamlined and Flexible Noise Certification Procedure																																				
	4.1 Identify Modeling Approach																																				
	4.2 Noise Certification Process Metric Definition																																				
	4.3 Model Calibration																																				
	4.4 Certification Process Simulation																																				

On the basis of the actual and recorded Year 1 activities and efforts, these tasks have been focused around communication with our partners, and have resulted in gathering of information and knowledge that have been key for the team's clear understanding of current certification procedures (Task 1, Subtasks 1.1 and 1.2) and the formulation of the respective certification model in SysML (Task 2, Subtasks 2.1. and 2.2; Task 4, Subtasks 4.1 and 4.2). A chronological overview of key activities and milestones during Year 1 is shown in Figure 3.

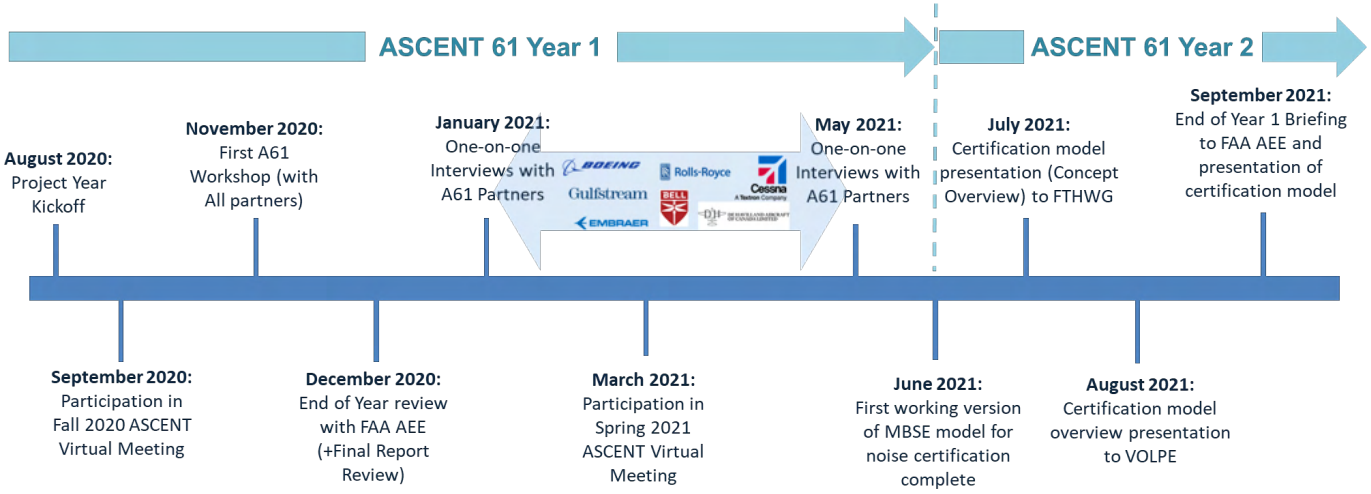

Figure 3. Chronology of A61 team activities and milestones.

The following sections provide detailed descriptions of technical progress, the research approach, key milestones, and accomplishments under each task, for all tasks and subtasks listed in Figure 2.

Task 1 - Interview Industrial Partners on Current Noise Certification Process

Georgia Institute of Technology

Objectives

In support of the main research objective of Project 61, Task 1 is examining current noise certification procedures (Task 1.1) and benchmarking against current industry practices regarding how these procedures are adopted and implemented (Task 1.2). The subtasks are organized as follows:

Task 1.1: FAA Noise Certification Regulation Review

- Perform a thorough review of FAA noise certification regulations for large subsonic jet and transport category airplanes as well as rotorcraft types of vehicles (14 CFR, Chapter 1, Subchapter C, Part 36, Subparts B and H); with input from the FAA, further explore an additional type: propeller-driven small airplanes and propeller-driven commuter category airplanes
- Include recent certification regulations for new types of aircraft (e.g., advanced air mobility), in addition to conventional configurations
- Document existing regulatory framework for aircraft noise certification, including both specified regulatory standards and accepted means of compliance

Task 1.2: Industrial Partner Interviews via Workshops

- Gather information through interviews and workshops on industry applied noise certification procedures, including equivalent procedures
- Propose workshops and invite industry partners with subject-matter expertise on airframe noise certification (large transport, small propeller aircraft, and rotorcraft)

- Facilitate a dedicated workshop for each vehicle type and plan follow-up events to iterate on the feedback obtained, and to share lessons learned and the derived recommendations
- Hold a focus workshop on identifying areas of opportunity to streamline the certification process for each type of vehicle and allow for Subject Matter Experts (SMEs) to suggest potential solutions.

Research Approach

Task 1.1

Starting with Task 1.1, the team's main activity was to review and document current noise certification procedures. The task objective is to gain an understanding of the current regulatory framework for aircraft noise certification, as required by FAA regulations and followed by OEMs to demonstrate compliance. In particular, the team conducted a thorough literature review of relevant parts of 14 CFR (mainly Part 36) and associated relevant documents (e.g., ACs, for instance AC 36-4D). With recommendations from the team's OEM partners, additional documentation from the European Union Aviation Safety Agency (EASA), the International Civil Aviation Organization (ICAO) Environmental Technical Manual, and the Volpe Center website was considered.

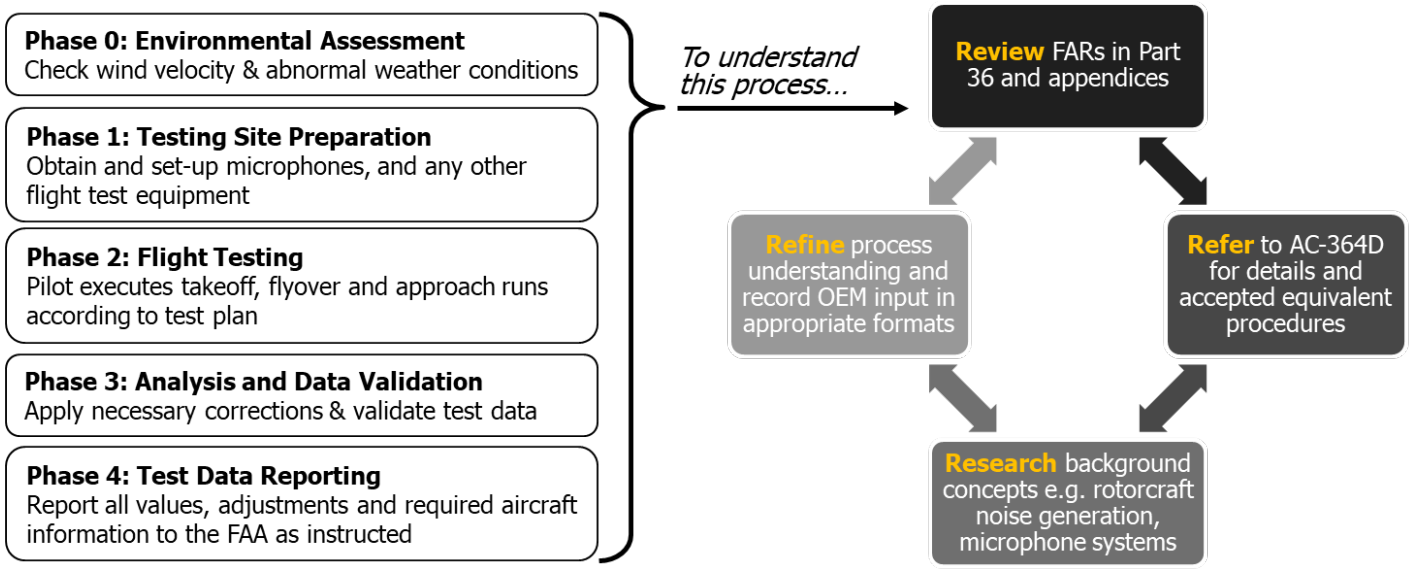

Figure 4. Noise certification regulation review (Task 1.1).

Because the full certification process is comprised of multiple processes and standard procedures, which are highly coupled, with recommendations by the FAA and the OEM partners, the team focused this exercise on the certification flight testing phases. Specific to flight testing phases, federal aviation regulations (FARs) in Part 36 and Appendix A and B have been reviewed and documented. This review included AC 36-4D for providing details on currently accepted equivalent procedures for the large transport aircraft category.

Along with the extensive review of FARs and literature regarding the regulatory framework, the team produced a series of views to demonstrate the flow of procedures, associations, and dependencies across regulatory items. Finally, the team obtained background information on noise generation for various aircraft categories, as well as the technologies used during testing, to better understand current recommended practices and the potential for alternative equivalent procedures with the use of modern technologies and equipment. Benefits of this task's outcome is that team members quickly became more knowledgeable in the certification basics in preparation for Task 1.2 (industry interviews) and able to build a comprehensive MBSE representation (in SysML) of the current framework from zero (Task 2.1). An overview of the methodology for the review of FARs and literature is provided in Figure 4. Appendix A of this document provides a full overview and documentation produced under this exercise.

Task 1.2

Task 1.2 aims to enhance the team's understanding of the current noise certification process through interaction with subject matter experts from various OEMs, with the objective of leveraging industry insight in practical aspects of noise certification requirements. This interaction occurred via virtual workshops, guided using questionnaires compiled by the team based on the reviews completed under Task 1.1. Through insights and findings from the work documented under Task 1.1, the team has identified topics in which more context and additional insight into ancillary/non-regulatory processes is needed regarding how the certification procedure is facilitated by each OEM partner. These topics are shown in Figure 5.

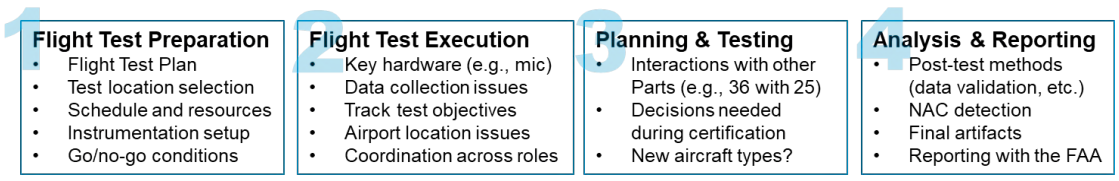

Figure 5. Workshop interview topics for transport category aircraft.

The overarching goal of these workshops was to identify common practices, checkpoints, and milestones across industry partners, while soliciting feedback on key challenges identified by the partners, as well as what recommendations each partner would provide and why. Such suggestions could provide opportunities for potential process streamlining, such as recommended practices that might be out of sync with current technology. The limitation in this exercise is that no recommendations should suggest or presume any change in the regulatory side, and hence they should be focused on equivalent procedures with simplified processes, or tied to modern technologies, which are still expected to meet the same regulations.

The first workshop was planned by the Georgia Tech team and held virtually on November 5, 2020. The discussion centered on certification practices for large transport and business jet categories for aircraft, as applied by the team's industry partners (representing airframers such as Boeing, Gulfstream, and Rolls-Royce). With the forum in place and the key connection established, a series of follow-up workshops and interviews was planned, which extended from January to May of 2021 (detailed timeline in Figure 3). In this expanded outreach, most interviews were planned with one OEM partner at a time, to ensure that the participants would be comfortable sharing their thoughts and expertise, without the time constraints of a high-participation event and with more flexibility in scheduling and necessary follow-up. The list of participating partners was expanded to include more OEMs (Embraer, Cessna, and De Havilland Canada) than those supporting the original workshop in November 2020. The Volpe Center has also participated in shaping the team's knowledge and understanding of the recommended procedures through providing technical feedback, especially regarding the flight testing portion of the process. The final set of participating OEMs who have contributed to the completion of this task is shown in Figure 6.

Figure 6. Participating partners (airframe OEMs and the Volpe Center) in workshops/interviews under Task 1.2.

To facilitate directed discussion in the workshops/interviews, the Georgia Tech team formulated questions on the discussion topics listed in Figure 5 and produced questionnaires that were distributed to the participants prior to the respective meetings. A high-level summary of the questions is as follows:

- What is the current guidance provided by the FAA for noise certification?
- How does a company interact with the FAA to ensure that requirements and constraints related to noise regulations are satisfied, and that the vehicle is compliant?
- How does the company perform the testing, internal processes, etc.?
- Can you identify procedures within flight testing that should be revised or updated to reflect the capabilities of modern configurations? Are there any opportunities for improvement?
- Are existing certification procedures and methods sufficient to meet future configurations?
- Certification amendments due to type design changes: if a vehicle needs to be recertified after making design changes, does your organization's approach change from the first round of certification?

The actual questionnaires in the format in which they were distributed to the workshop participants are included in Appendix B.

Questionnaire Discussion Topics

- Testing locations, duration and number of tests
- Usage of equivalent procedures
- Certification cost – breakdown, fluctuations, etc.
- Certification time – delays and their impact on various metrics, end to end time taken, etc.
- Certification equipment – weather, microphone, calibration, recording and other systems
- Internal/external communication & collaboration
- Ancillary practices, procedures, contingencies

Categories of Responses	Responses in various levels of detail organized by industry partner: **Boeing, Cessna/Textron, Embraer, Gulfstream, De Havilland**
Cert Plan Coordination w/ NAA	
Flight Test location	
Duration of Flight Test	
Ground Instrumentation/ Provider	
Aircraft Instrumentation /Provider	
Go/No-go conditions (Test limits)	
Go/No-go Conditions (Safety)	
General testing challenges	
Method for QA of test points	
Post test data anlaysis	
Method to Cert Incremental Acoustical Change: ACs or NACs	

Figure 7. Post-processing of collected information and categorization.

The initial workshop, along with the follow-on interviews, generated a wealth of information. Planning and following a methodological approach are necessary to post-process and direct this information to gain usable conclusions and insightful findings. One idea was to generate categories for sorting and organizing the material collected from the questionnaire responses. As part of the categorization of the responses to the questions, several categories have been defined, as shown in Figure 7.

Although there was substantial variability in the level of detail provided in the answers and feedback obtained from participants, the team was able to summarize the gist of the feedback provided under the defined categories, as illustrated in Table 2. To summarize those findings, the main takeaway messages from all OEM feedback are as follows:

- Acoustical changes (AC's/NAC's) are challenging to navigate without standardized approval procedures. More detailed feedback would be useful for OEMs to propose suitable solutions.
- Test-site selection is normally restricted by sound measurement technology and requirements (e.g., the lateral microphone component) and by weather-window options.
- Delays in flight testing are primarily weather induced and are occasionally due to communication disruptions.
- Conformity discussions can be consume substantial time and effort, especially in cases that must justify changes that are unrelated to acoustics.
- Interactions between Part 36 and Part 25/23 are of concern, because a discontinuity appears to exist between environmental and design standards, thus often leaving little space to apply acoustic improvements.
- For calculating EPNL values from noise data collected during flight testing, there is no single standardized software: each OEM's methodology and code is different.

The lack of standardization appears to be a common area of opportunity for improvements across current noise certification procedures. Within the same context, participant-recommended value-added outcomes that could be explored and evaluated

through use of the MBSE-enabled platform for streamlined certification are: (note that all need not be examined within the current Project 61 statement of work, but some could serve as appropriate use-case opportunities for years 2 and 3, or beyond):

- Along with exploring improvements in time and cost, the Project 61 team could explore options to simplify testing and instrumentation setup requirements to facilitate more test locations/weather-window options (i.e., which could allow removal of 4-ft microphones for ground planes and removal of lateral location altogether).
- Testing uncertainty could be managed through evaluation of no-acoustical-change limits.
- Conformity issues could be addressed through the formulation of a concept that could be tested and demonstrated within the MBSE-based verification framework.
- Criteria for approval for acoustical analyses could define new certification noise levels (acoustical change by analysis)
- As a longer-term goal, a framework could be defined for oversight that gives FAA confidence in manufacturers' tools/methods used in noise certification (e.g., with predefined audit guidelines/procedures).

Table 2. Summary of findings from transport category workshop/interview feedback.

Subject	Boeing	Cessna/Textron	Embraer	Gulfstream
Test deliverable setting	Not much deliberation	Some deliberation, approved easily	Follow exact regulation protocol	Early FAA involvement for flight planning
Test location	Airport for safety, restricted by lateral mic requirement	Low traffic, stable weather (current site in CA)	Remote location, restricted by season/weather and traffic	Based on acoustic & atmospheric environment (current sites in CA, GA)
Time spent on site	Final checks 1 month out (if new site, 2-year prep)	5-6 hours/day if stable weather	2-hour set up, 5/7-hour testing (10-day window)	1 series in 2 days, 1-hour sunrise setup, 6-day approach
Instrumentation	Highly optimized lab procedures	Consultant: 6 mics (1 central, 2 lateral + backups)	Consultant: approved Volpe list equipment (old	Pole & ground plane mics, daily setup/take-down
Go/ no-go conditions	Borderline test points discussed with Eng. Unit	Mainly weather related	Mainly weather related, occasional aircraft issue	Upper atmosphere weather/ wind issues
General testing challenges	Mainly weather, rarely from equipment or communications	Mainly weather, equipment old but reliable, crucial to maintain comms	Cell phone reliance, can lose comms airport-test site (must stop testing)	Mainly weather
Confirmation of meeting test objectives	Parameters printed to support decision, borderline points	Check raw noise level (test engineer/mic teams), verify GPS, monitor NPD trends	Consultant responsible: get approx. 60-80 test points	Get approx 40 points, sound pressure/exposure for NPD, monitor tolerances on PFD
Post test data anlaysis	3-4 months, flight & engine test combined in NPD to find uncertainties	Data check after test, 1-2 months for report & revisions before FAA (2-3 mth total)	Time consuming in-house analysis, matching results to predictions	
Acoustical Change - ACs or NACs	Game-changer = AC by analysis ; difficult to get FAA approved tools ; high scrutiny on small ACs ; have killed modifications that cause AC>0.3 dB	Game-changer = AC by analysis ; can be 3-6 month response time from FAA with no constructive feedback even with past accepted methods ; Textron proposed FAA procedure library to reduce guesswork	Nightmare to submit AC ; approval discussed with ANEC especially for newer ACs ; lack of common ground & standardisation between NAC reviewers	Tedious ; if performance changes, rely on NPD equivalence to provide basis for compliance plan/report ; if no performance change, do method analysis of noise increment

Finally, this exercise under Task 1.2, with the identified findings and participant-provided recommendations, has successfully established the need for a solution that enables exploration and formulation of a standardized, simplified certification procedure that can be flexible to accommodate different types of air vehicles and new technologies. The use of a comprehensive systems engineering process would enable connectivity throughout the certification steps and traceability of regulatory compliance. Because model reusability and scalability across different categories are very important, the team has been utilizing MBSE methods to effectively "re-architect" the certification procedures to achieve the goals and desired outcomes identified through the feedback obtained by Task 1.2 activities.

Milestones

Since October 2020, the following milestones have been achieved (also shown in Table 2):

- Participation in the Fall 2020 ASCENT Advisory Committee Meeting (September 30, 2020)
- Workshop 1 on transport category aircraft (November 5, 2020)
- End-of-Year review with the FAA Office of Environment and Energy plus annual report review (December 2020)
- One-on-one Interviews with A61 partners (January 2021)
- Participation in the Spring 2021 ASCENT Virtual Meeting (March 2021)
- Final round of planned one-on-one Interviews with A61 partners (May 2021)
- Participation in the Fall 2021 ASCENT Virtual Meeting (October 2021)
- Completion of Tasks 1.1 and 1.2. for the transport category (June 2021)

Table 3 ASCENT Project 61 year 1 milestone status.

Milestone	Due Date	Estimated Date of Completion	Actual Completion Date	Status
Workplan	7/5/20	7/5/20	7/5/20	Completed
Kick-off Meeting	8/30/20	8/30/20	8/24/20	Completed
Center of Excellence Meeting 1 (Fall 2020 ASCENT Meeting)	10/1/20	10/1/20	9/29/20 to 9/30/20	Completed
Center of Excellence Meeting 2 (Spring 2021 ASCENT Meeting)	4/1/21	4/1/21	4/27/21 to 4/29/21	Completed
Annual Report	6/5/21	6/5/21	9/30/21	Completed
Project Closeout	6/5/21	6/5/21	Continue for year 2	Completed

Major Accomplishments

The primary focus of the team's effort for Project 61 year 1 was the completion of Task 1.1 and planning a series of workshops with industry partners to support efforts under Task 1.2 for the identification of currently applied noise certification practices and opportunities for streamlining the certification process.

Task 1.1 is now complete. The following accomplishments are reported:

- The literature review was completed on current noise certification practices, as dictated by Title 14 Part C, Part 21 regarding certification procedures and Part 36 regarding noise regulations. The review of AC Part 36 was incorporated, with a particular focus on AC 36-4D. Emphasis was placed on the instruction regarding the flight testing for certification.
- A summary and visual representation of the regulations and their respective relationships/associations, in both flowchart and SySML views, has been provided.
- Certain gaps in understanding of the certification process have been identified and documented. These findings have enabled the production of a topic questionnaire to further support the facilitation of workshops with industry partners, as planned for Task 1.2.

For Task 1.2, the following accomplishments are reported:

- Workshop 1 for the large transport category was held virtually and completed on November 5
- Feedback and input were collected from industry partners during the workshop.
- Key takeaways became available, which are shaping the project's direction and aiding in the understanding of priorities within the problem. For instance, certification procedures must be not only more efficient in terms of time and cost, but also less complex and better aligned with use of current technology (which is an enabler of process simplification).
- The questionnaire for the workshop has been compiled with input from Task 1.1's literature review and benchmarking activities. Consideration of additional responses from our industry partners is underway and will inform our modeling efforts under Tasks 2, 3, and 4.

Task 1.2 is now complete for the transport category aircraft, and tasks will be repeated for rotorcraft and small propeller-driven air vehicles.

Publications

Peer-reviewed journal publications

None

Published conference proceedings

Mavris, D. N., Tai, J., Harrison, E., & Balchanos, M. (2020, September 29-30). ASCENT Project 61 – Noise certification streamlining [Presentation]. Fall 2020 ASCENT Advisory Committee Meeting.

Mavris, D. N., Tai, J., Harrison, E., & Balchanos, M. (2021, March 27-29). ASCENT Project 61 – Noise certification streamlining [Presentation]. Spring 2021 ASCENT Advisory Committee Meeting.

Mavris, D. N., Tai, J., Harrison, E., and Balchanos, M. (2021). ASCENT Project 61 – Noise certification streamlining [Presentation]. Fall 2021 ASCENT Advisory Committee Meeting.

Written reports

December 2020 ASCENT Quarterly Report, ASCENT Project 61, "Noise Certification Streamlining," Award number 13-C-AJFE-GIT-066, submitted January 30th, 2021.

2020 ASCENT Annual Report (period ending September 2020), ASCENT Project 61, "Noise Certification Streamlining," Award number 13-C-AJFE-GIT-066, submitted December 12th, 2020.

March 2021 ASCENT Quarterly Report, ASCENT Project 61, "Noise Certification Streamlining," Award number 13-C-AJFE-GIT-066, submitted April 30th, 2021.

June 2020 ASCENT Quarterly Report, ASCENT Project 61, "Noise Certification Streamlining," Award number 13-C-AJFE-GIT-066, submitted July 30th, 2021.

September 2020 ASCENT Quarterly Report, ASCENT Project 61, "Noise Certification Streamlining," Award number 13-C-AJFE-GIT-066, submitted October 30th, 2020.

Outreach Efforts

- Planned and held Workshop 1 with industry partners (Boeing, Gulfstream, Rolls-Royce, and the FAA) on transport category aircraft
- Completed follow-up meetings with OEM partners in Workshop 1 and through the spring of 2021
- Performed capability demonstration to the Flight Test Harmonization Working Group (FTHWG)
- Project overview and request for information and technical feedback to be provided by the Volpe Center (Department of Transportation)

Awards

None

Student Involvement

- All three participating graduate students have supported Task 1 activities by performing the literature and background search and reviewing current regulations and FAA-instructed certification procedures (Parts 21 and 36, and AC 36-4D).
- All students contributed to producing the certification process views and compiling the questionnaire for supporting discussions and feedback solicitation as part of hosting Workshop 1 and follow-on interviews.

Plans for Next Period

- Coordinate a follow-up meeting for Workshop 1 on large transport category aircraft with industry partners, to showcase our verification model capabilities and present a number of relevant use cases
- Complete planned workshops on rotorcraft category aircraft and small propeller-driven air vehicles
- Plan for submission of two articles to ICAS 2022, for further dissemination of the A61 team's developed capabilities, demonstrating the requirement generation techniques, the MBSE certification model, and the certification process evaluation and assessment model using discrete event techniques
- Publish articles with *AIAA Journal* and *AIAA SciTech*

Task 2 - Develop a Streamlined Noise Certification Procedure for Existing Aircraft

Georgia Institute of Technology

Objectives

Task 2 is focusing on the development of a more streamlined noise certification procedure, leveraging MBSE for the formulation and implementation of a certification process model. For Task 2.1, the goal is to fine-tune and adjust the MBSE certification model to represent current certification steps (ranging from regulatory-derived requirements to certification flight testing) for transport category aircraft, as identified and benchmarked in Task 1.

Task 2.1: Current Process Assessment

- Identify which aspects of the present process, would benefit from the proposed concept. As current procedures are captured and mapped against the regulatory requirements, this task seeks to enable an assessment capability for testing equivalent procedures within the overall certification model.

Task 2.2: Streamlined Process Definition

- Incorporate feedback from industry partners with identified areas of improvement over the present process to formulate a new certification process.
- Of primary interest should be the use of technology that seek to simplify the certification process while demonstrating that regulatory requirements are being met. Process modeling within Task 4 should also yield improvements in the cost and efficiency of the noise certification process.

Task 2.3: Streamlined Process Assessment and Revision

- Solicit technical feedback on the proposed process alternatives from the FAA, Volpe Center, and industry partners.
- Perform revision of suggested process, which incorporating key aspects of the collected feedback to build a consensus among the research partners.

Research Approach

Task 2.1

A key takeaway message from Task 1.2 is the need for formulating a flexible noise certification process. The process should allow for process reusability for the certification of various air vehicles and should be usable as a tool to assess current procedures and identify improvements that increase efficiency and decrease complexity. To assess current noise certification practices, a MBSE approach has been proposed. Work completed under Task 1—both benchmarking of current practices and input from the workshops—will be compiled and used to inform a certification process model formulated in SysML language (implemented in MagicDraw and Cameo Toolkit software tools).

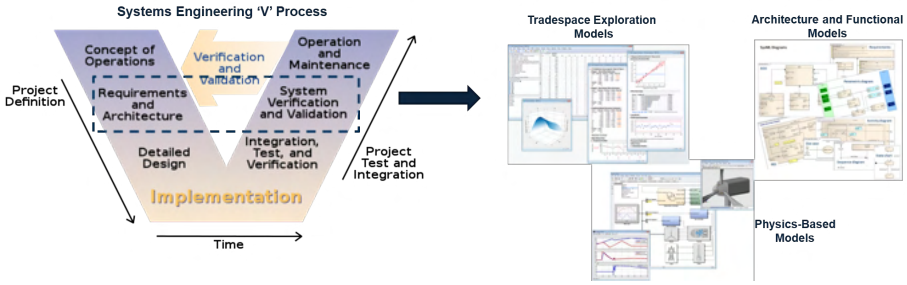

Figure 8. Systems engineering "V" and MBSE-enabled systems architecting.

MBSE is the formalized application of modeling to support system requirements, design, analysis, verification, and validation activities beginning in the conceptual design phase and continuing throughout development and later lifecycle phases. [INCOSE SE Vision 2020, Sept 2007]. MBSE supports traditional Systems Engineering (SE) activities by applying modeling

techniques to create a modular structure of system representation, as shown in Figure 8. With this approach, the models are more rigorous because of their mathematical or logical formulation, with minimum reliance on static documents and sources.

To enable reusability and effectively expedite steps through digital modeling and process execution, MBSE shifts the representation of systems from documents to explicit representation of systems via models; hence, it merges product information and engineering models. In addition, MBSE provides a consistent system model that everyone can "view"; maintaining a shared system model as the authoritative source of information a feature that is helpful in preserving common understanding for people with different roles and responsibilities. MBSE allows for linking of regulations and requirements to certification steps, and representing links and associations between regulations. It improves communication among stakeholders, management of complexity, and precision of operational use cases; as a result, it addresses common issues that arise during certification audits, e.g., requirement traceability, configuration management, document control, and change impact analysis.

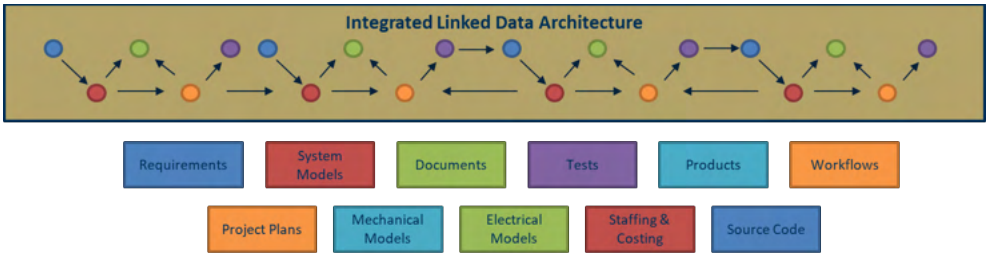

Figure 9**.** Integrating data and models through a digital thread.

Because MBSE provides a platform for knowledge transfer between projects, system models can evolve across the lifecycle, while preventing loss of knowledge and investment despite any project discontinuities. This capability can enable a digital thread, which is a framework that connects information, information flows, and relationships through the lifecycle of the system, as shown in Figure 9. Thus, information previously captured in individual silos is integrated to enable greater transparency (including technical baseline, resources, and workflow). An example is shown in Figure 10.

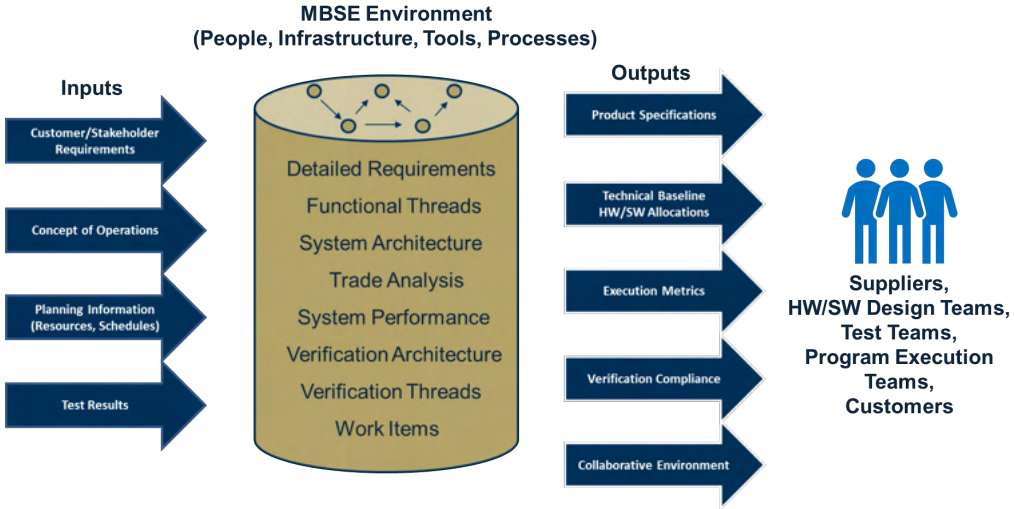

Figure 10**.** Digital thread for certification: inputs and outputs.

Under Task 2, particularly Subtask 2.1, the goal is the assessment of current noise certification procedures with an MBSE-enabled model. Typically, MBSE methods are used to represent a vehicle's lifecycle and enable the use of data and information as an integrated systems engineering approach. Because the product is usually an executable vehicle architecture, in the case of Project 61, the product is a process architecture within which current procedures will be assessed; equivalent

procedures will also be proposed, defined, implemented, and tested within this environment. The overall progression from the building blocks and subject matter expert input, made possible through Task 1, to the full MBSE model formulation for certification and implementation is shown in Figure 11.

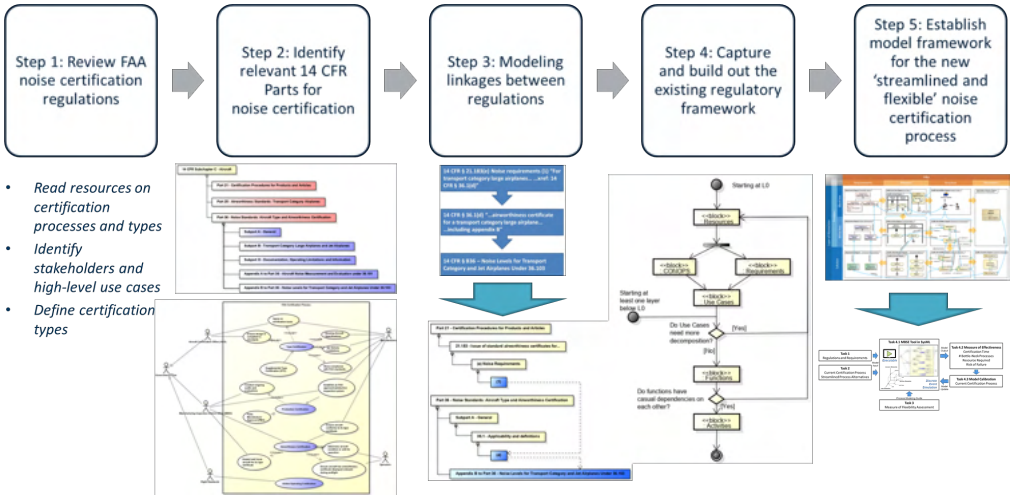

Figure 11. General roadmap toward a model-based framework for exploring current and streamlined noise certification.

The roadmap for creating an MBSE system architecture is not unique; several approaches have been introduced in the literature, but a commonly preferred option is the requirements–functional–logical–parametric (RFLP) approach, which maps to the traditional systems engineering "V" approach (Figure 8). A custom model development process was created to capture the functional architecture of the noise certification process, as shown in Figure 12. Inputs to the process that are provided by activities outside of the MBSE environment are marked in blue. This would include an operation concept of the certification (as documented in Tasks 1.1 and 1.2) as well as requirements that represent Part 36, Appendix A and Appendix B regulations for noise. Moreover, this is the placeholder for importing the validation protocol for instruments used in aircraft noise certification testing, as well as a representation for the flight test plans, as adopted by the airframe OEMs.

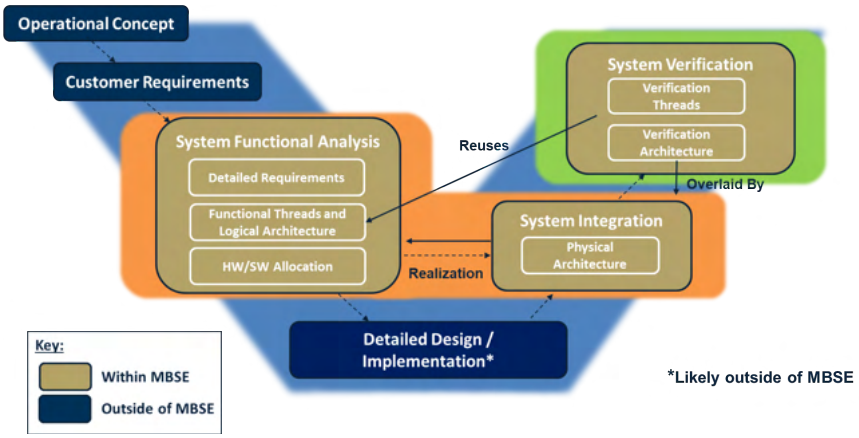

Figure 12. MBSE architecture and functional model development workflow, leveraging the RFLP approach.

The activities within the process indicated in gold are the aspects of the system modeling captured within the MBSE environment. As shown in the development flow, regulations and information about the certification process are captured as requirements and functional blocks within the model. A digital thread is created between the regulation, requirement, and function to build a verification thread. The form in the certification process that displays a function is also threaded by an <<allocation>> relationship to build a full digital thread from certification standard to the form that verifies the standard.

Following the RFLP approach, as explained in Figure 12, a more detailed workflow is formulated for the verification model implementation. This version is shown in Figure 13, in which the steps for the conversion of the input information (the artifacts in blue) into a completed model, applied in SySML is further explained. In the middle part of the figure, artifacts and templates provided by the OEMs used during the certification are converted into model representations in SySML. For instance, a requirement model in SySML is populated by requirements extracted from Title 14 CFR Part 36, Appendices A and B, through a process developed in-house (and explained later in this document).

The validation process essentially contains the steps needed to demonstrate that the vehicle noise levels calculated from flight testing results meet the requirements. Part of meeting the requirements also involves the right instrumentation setup, which is implemented as a logical architecture within the model. A library of instrument model representations is constructed, from which alternative instrumentation lineups can be modeled. This latter feature is key, because this framework should be able to allow for the evaluation of equivalent procedures, such as lateral microphone placement. Other components of the verification model include the test procedures and the test report checklist, which are prototyped as activity diagrams in SySML, as well as the vehicle configurations represented as a state machine. Completing the verification model is any applicable regulation text in the form of an applied SySML verification thread.

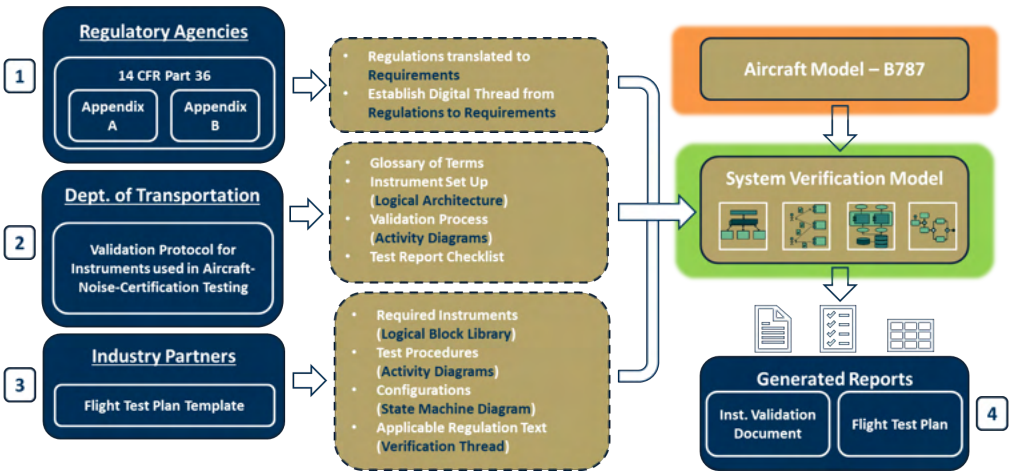

Figure 13**.** Detailed workflow for verification model development toward a digital thread.

With the verification model in place, users will then be able to import any aircraft model, perform the certification equivalent process through execution of the verification model, and generate a final report containing the instrument validation document and flight test plan. It is crucial that the overall framework is implemented in a highly modular fashion to obtain the flexibility necessary for testing equivalent procedure alternatives as well as a broader range of air vehicle designs and configurations. The complete applied SySML implementation of the verification thread in SySML is shown in Figure 14. Following the structure of the verification model as explained in Figure 13, the applied SySML implementation is currently comprised of the following modules:

1. Requirements translation & constraints
2. Noise testing instrument architecture
    a. EPNL conversion
3. Procedures, protocols, and behaviors
4. System under test (SUT)
5. System verification model overview
6. Auto-report generation
    a. Output to process evaluation model

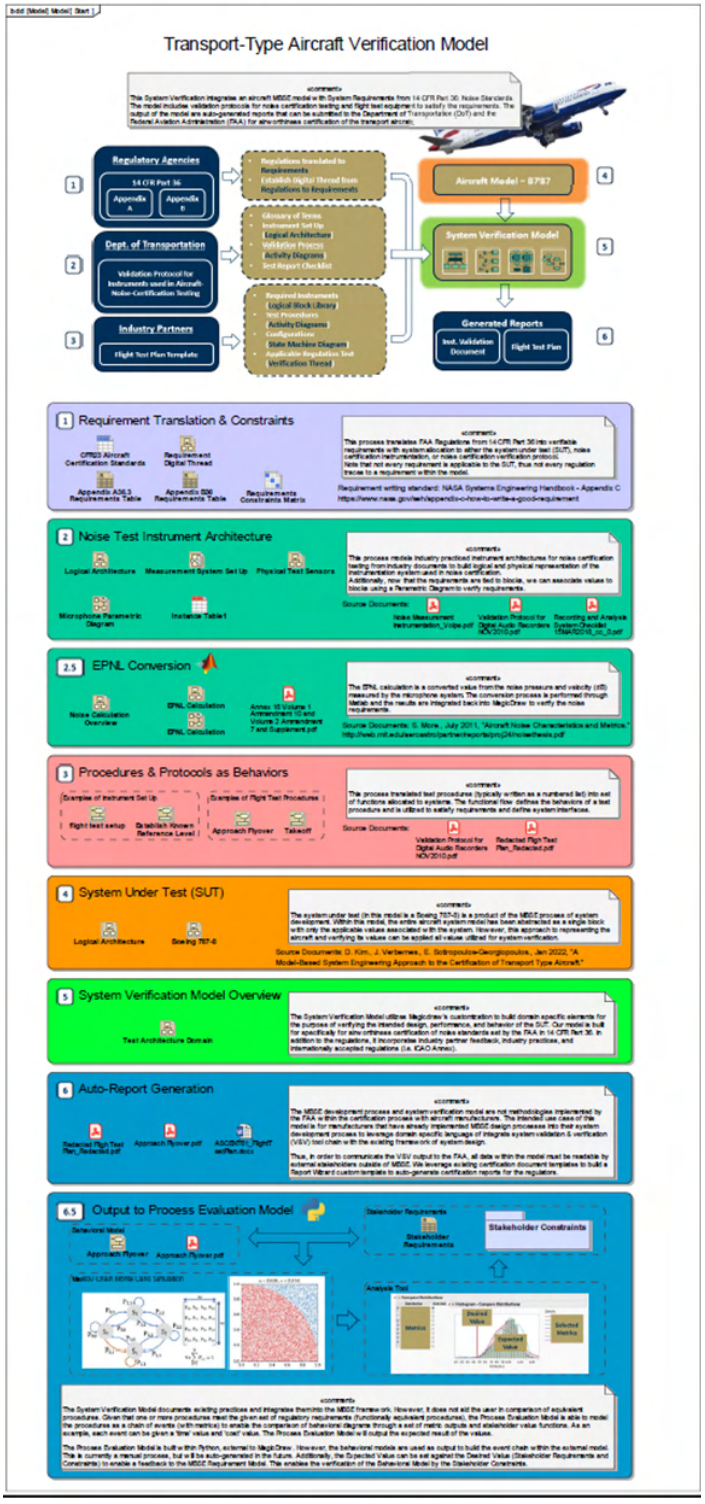

Figure 14**.** Complete aircraft type verification model for noise certification.

The following provides a brief overview of how each module has been implemented and how the integration development spiral was pursued. The integration process followed the steps shown in Figure 15.

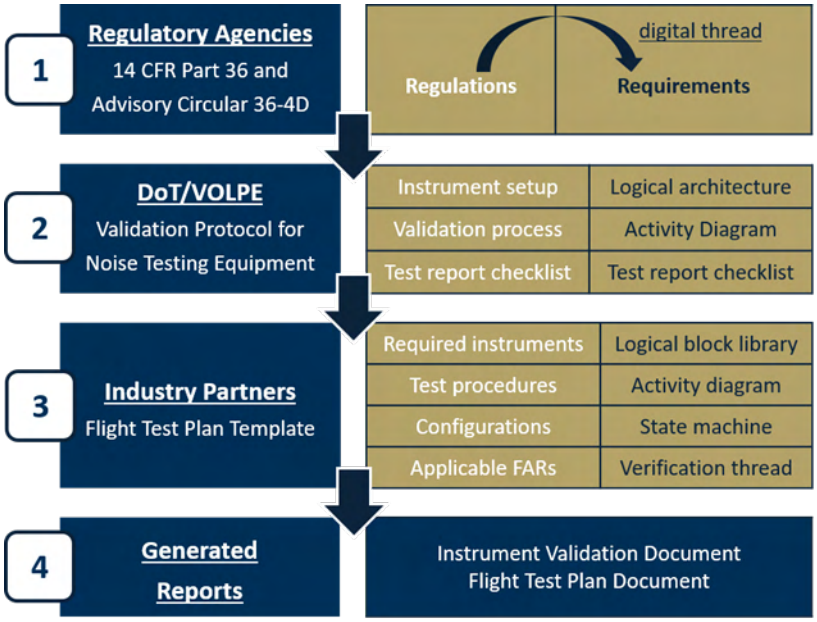

Figure 15. Verification model integration steps.

Step 1 includes the conversion of regulations to requirements. In this context, a requirement normally represents a single design constraint extracted from one or more regulations. A method of verification is required for this design constraint to be satisfied by the system under test. To provide this verification step, a constraint block is introduced as a verification mechanism by integrating engineering analysis into the model. In particular, with the use of a constraint block, the textual requirement can be quantified by using only mathematical and logical expressions. Verification simulations, which can determine whether a certain metric passes or fails a requirement, can be enabled. Overall, the constraint block acts as the interface linking a requirement model and the logical/physical model of a System under Test. An example of how a regulatory article can be imported as a requirement, linked to the verification model, and tested is shown in Figure 16.

A36.3.7.4 When slow time averaging is performed in the analyzer, the response of the one-third octave band analysis system to a sudden onset or interruption of a constant sinusoidal signal at the respective one-third octave nominal mid-band frequency, must be measured at sampling instants 0.5, 1, 1.5 and 2 seconds(s) after the onset and 0.5 and 1s after interruption. The rising response must be −4 ±1 dB at 0.5s, −1.75 ±0.75 dB at 1s, −1 ±0.5 dB at 1.5s and −0.5 ±0.5 dB at 2s relative to the steady-state level. The falling response must be such that the sum of the output signal levels, relative to the initial steady-state level, and the corresponding rising response reading is −6.5 ±1 dB, at both 0.5 and 1s. At subsequent times the sum of the rising and falling responses must be −7.5 dB or less. This equates to an exponential averaging process (slow time-weighting) with a nominal 1s time constant (*i.e.*, 2s averaging time).

ID: Name	Requirement Text	Owned By	Traced To	Satisfied By
40: Sudden Onset Response Sampling Instants	The analysis system shall have a response (to the sudden onset of a constant sinusoidal signal) that is measured at sampling instants 0.5, 1, 1.5 and 2 seconds after the onset.	Measurement System Requirements	A36.3.3.1, 1D A36.3.7.1 A36.3.7.4	Sound pressure level response (Analysis System: Value Property)
41: Interruption Response Sampling Instants	The analysis system shall have a response (to the sudden interruption of a constant sinusoidal signal) that is measured at sampling instants 0.5 and 1 second after the onset	Same as ID 40	Same as ID 40	Same as ID 40
42: Rising Response Limits	The analysis system shall have a rising response that conforms to these dB values at each sampling instant (relative to the steady-state level): −4 ±1 dB at 0.5s, −1.75 ±0.75 dB at 1s, −1 ±0.5 dB at 1.5s and −0.5 ±0.5 dB at 2s.	Same as ID 40	Same as ID 40	Same as ID 40
43: Falling Response Limits	The analysis system shall have a falling response such that the sum of the output signal levels is −6.5 ±1 dB, at both 0.5 and 1s (relative to the initial steady-state level, and to the corresponding rising response)	Same as ID 40	Same as ID 40	Same as ID 40
44: Sum of Rising and Falling Response	The analysis system shall have a sum of rising and falling responses less than or equal to -7.5dB (at subsequent times).	Same as ID 40	Same as ID 40	Same as ID 40

Figure 16. Regulation to requirement: example of design constraint formulation.

Step 2 seeks to implement the validation protocol for noise testing (as dictated by the Volpe Center's guidance) in a logical model. This step returns the representation of the physical noise instrument architecture as an applied SysML logical model. The architecture description is achieved by using "blocks," which essentially describe a system with reusable, modular units. These blocks contain structural and behavioral features that define relationships between parts via connectors. An example of a block representing the microphone type used during flight testing is shown in Figure 17. Each block is functionally verified by constraints (highlighted in blue), contains a hierarchy to define parts (highlighted in orange) and holds defined values as value properties (highlighted in green).

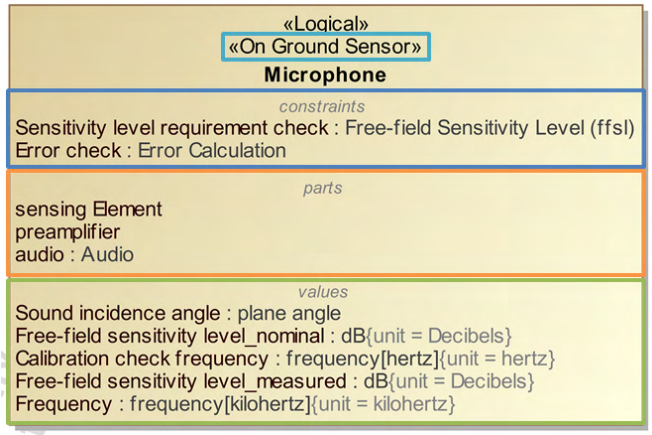

Figure 17**.** Example of a logical block representing physical microphone technology.

The instrumentation architecture is further characterized by the types of sensors used, e.g., the two types of sensors: <<on ground sensor>> (namely the microphone, as represented by the logical block in Figure 17), and <<on A/C sensor>>. An example of an applied SysML logical representation of a microphone and hardware setup as part of the Volpe Center's validation protocol is shown in Figure 18.

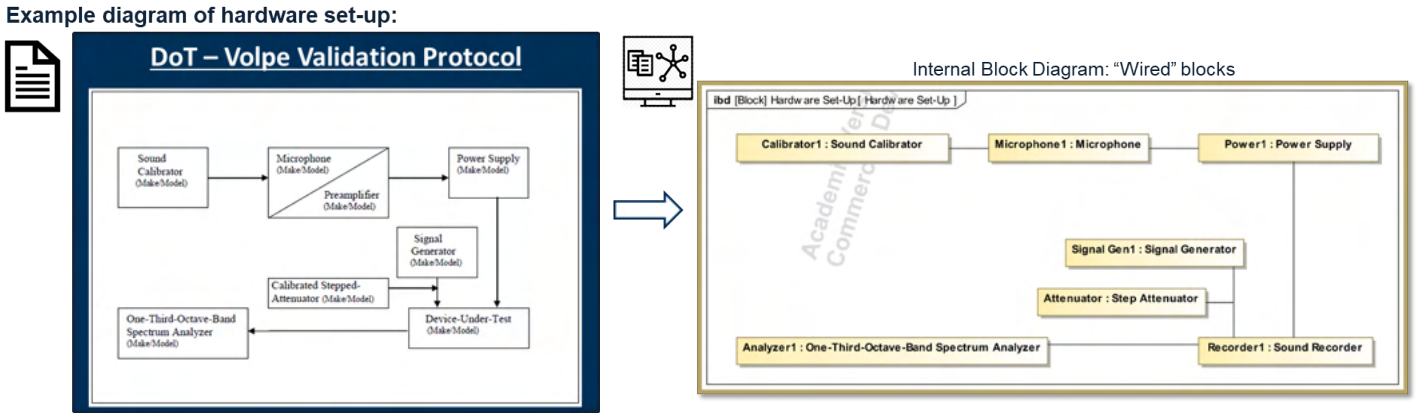

Figure 18**.** Example diagram of hardware setup.

The complete logical architecture representation in an applied SysML environment provides a unified model for all system elements (single source of truth), full transparency, and shared understanding of the system. It is an extensible representation of system, and its components and their properties, with clear definitions of interfaces between architectural elements. This architecture is described hierarchically, with the systems decomposition level being dictated by the requirements. As more architectural elements are progressively accounted for, the model can be easily updated accordingly. An example of a complete logical, hierarchical architecture is shown in Figure 19.

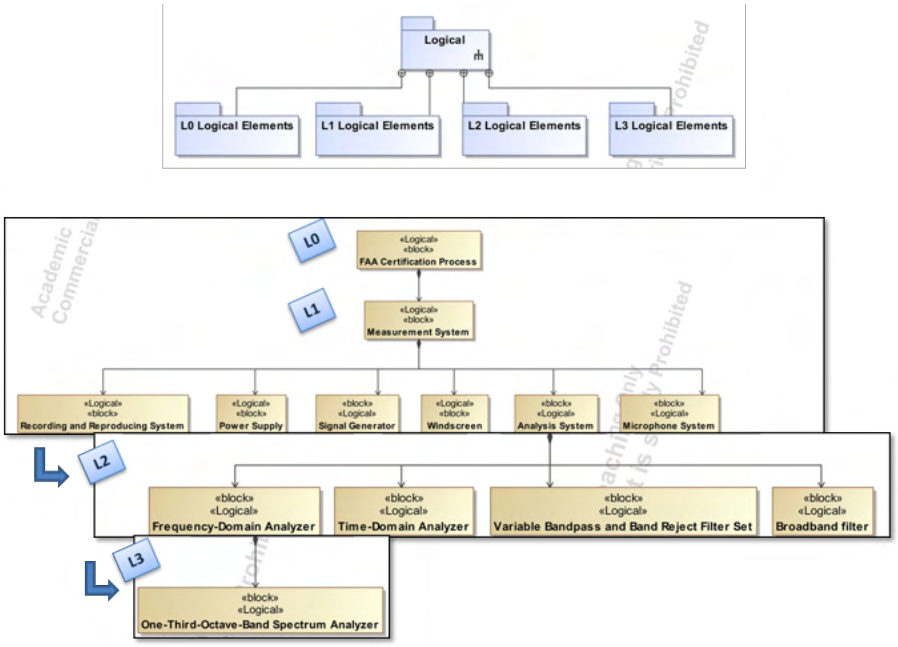

Figure 19**.** Logical architecture for the verification model.

In addition, the parametric construct allows for the logical architecture to be executable through simulations, a key aspect for performing requirement verification. This includes improved traceability between requirements, architecture, and verification information. The stored information in relevant blocks is used for requirements verification, with the quantitative characteristics defined as value properties for each block. This step does require obtaining validation/measurement data for a system under test, to create instances within the model for data representation. The requirement verification is performed by executing the logical architecture with Cameo Simulation Toolkit. An example of requirement verification for the microphone setup within the logical architecture in SysML is shown in Figure 20.

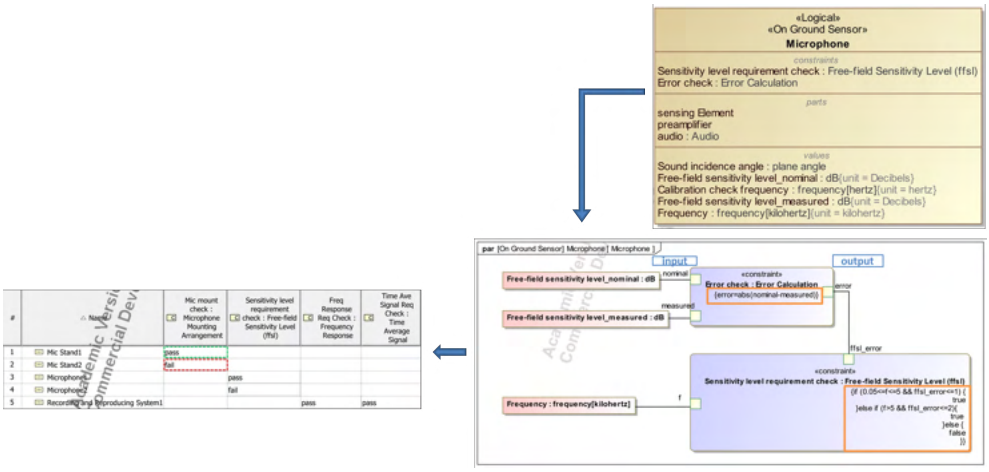

Figure 20**.** Example requirement verification of the logical architecture.

In the current state, the logical architecture model can accommodate the full aircraft noise certification test system; an example physical view is shown in Figure 23, and the corresponding logical architecture implementation is shown in Figure

21. The system under test used for the verification model development was based on a Boeing 787-8 configuration, and its logical representation applied in SySML is shown in Figure 22.

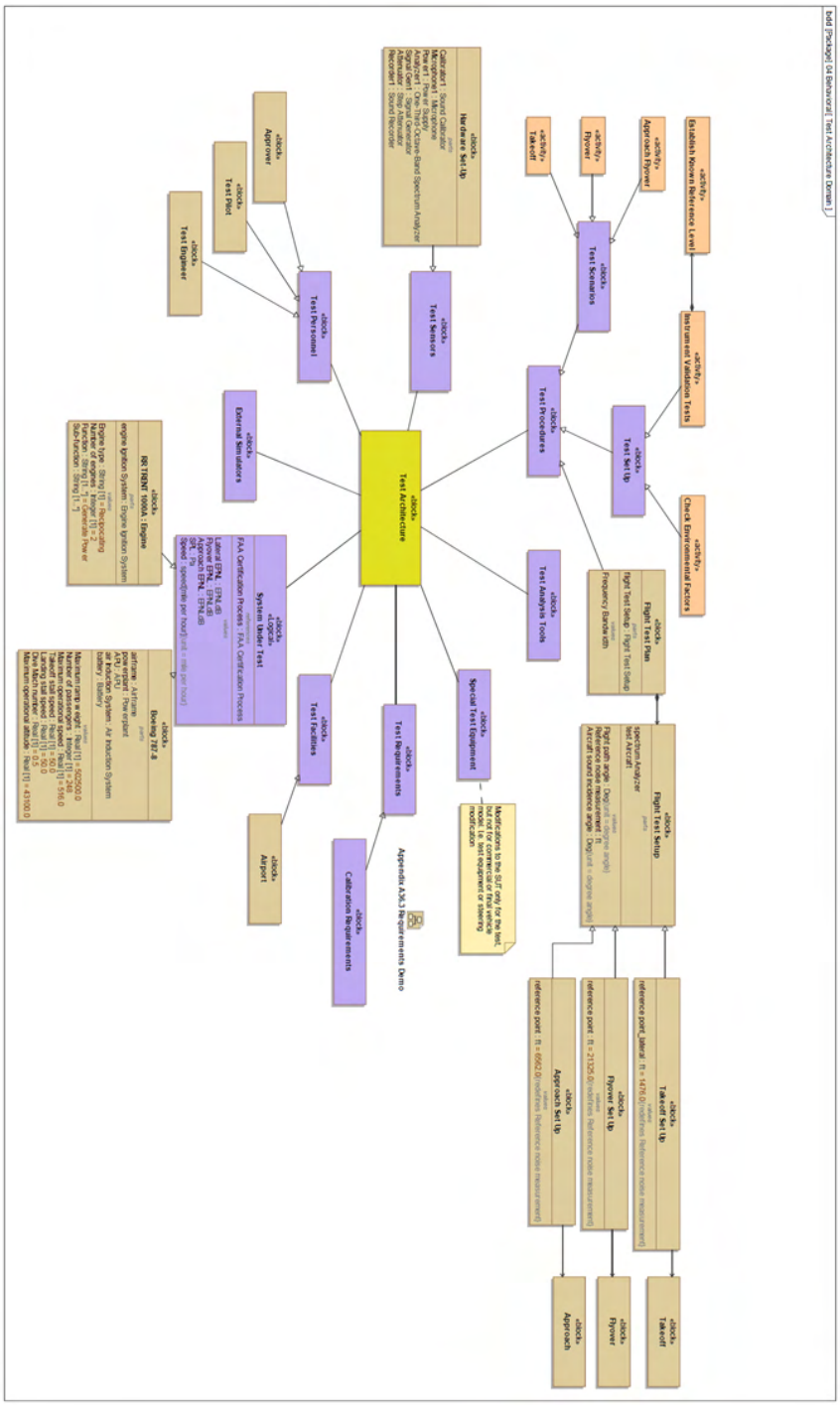

Figure 21**.** Flight testing architecture domain.

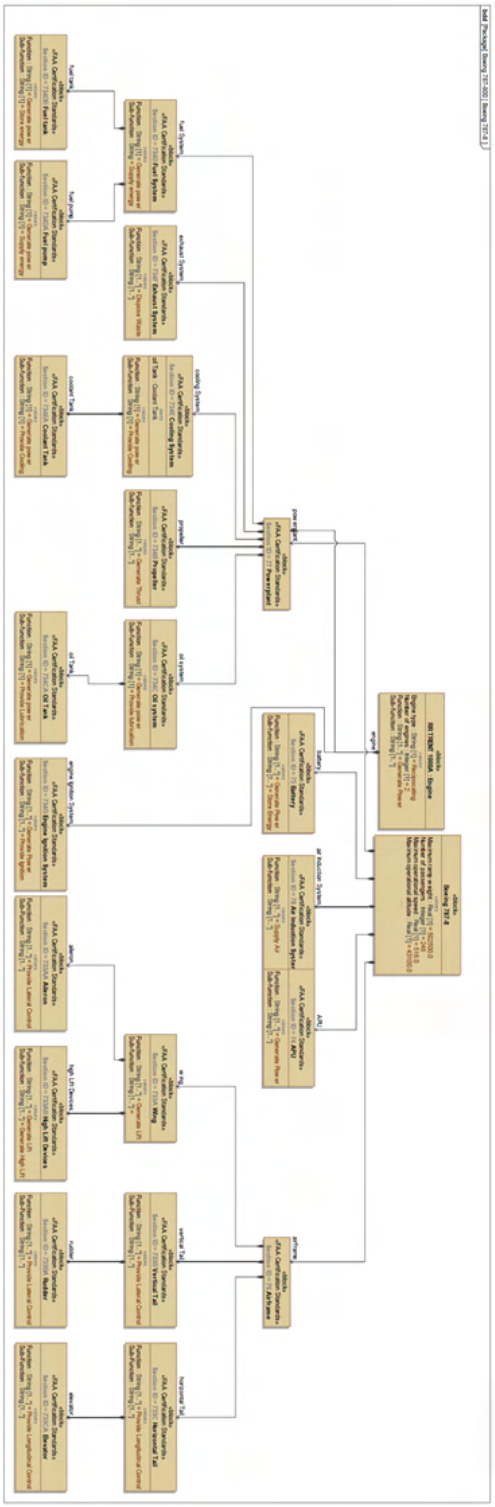

Figure 22. Aircraft model (Boeing 787-8) used as the System under Test (SUT).

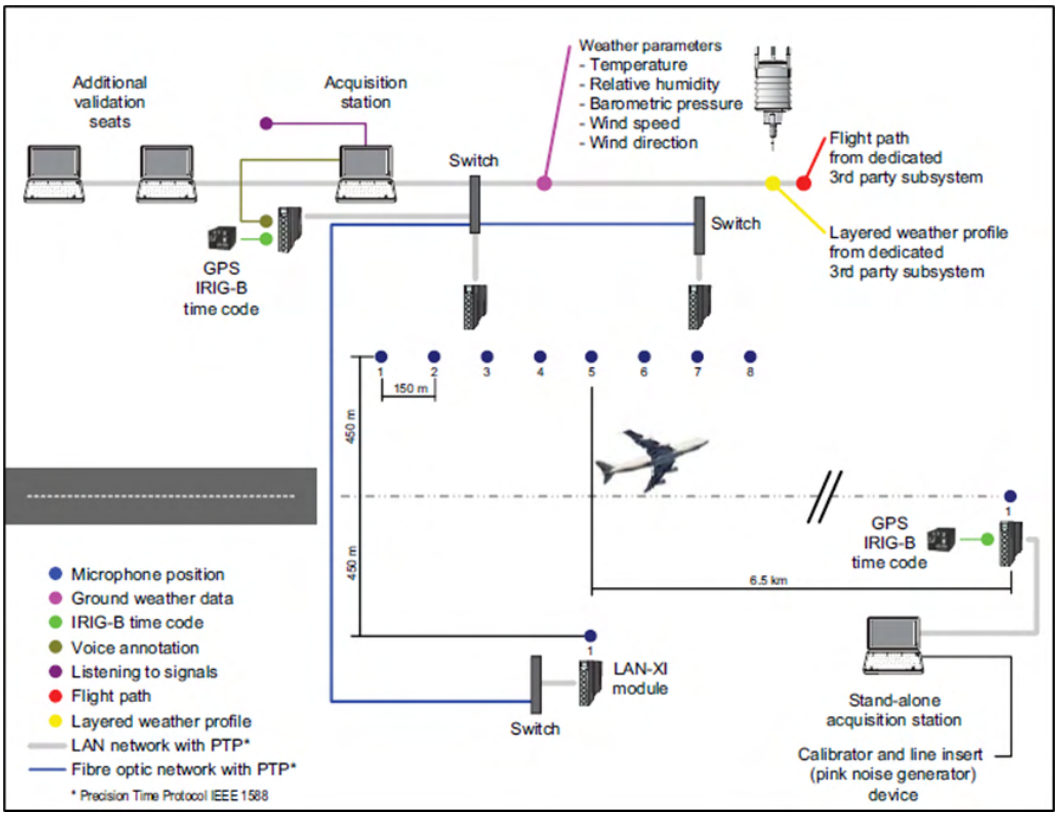

Figure 23. Schematic overview of aircraft noise certification test system by Brüel & Kjær.

Step 3 of the verification model implementation process involves the representation of the flight test procedures to behavioral models. Because test procedures are written in text (bullet points, numbered lists, etc.), the functions performed by the system are not clearly defined, nor are the external system interfaces. To model the process as behavioral diagrams, functions allocated to systems must be defined, and functional flows with defined interfaces must be established, as explained in Figure 24.

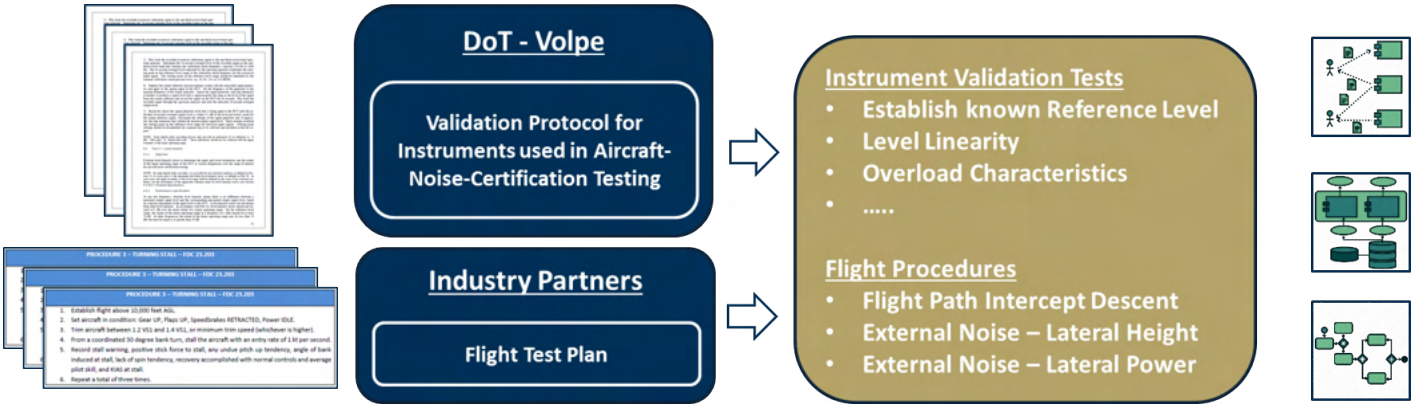

Figure 24. Process for representation of flight test procedures to behavioral models.

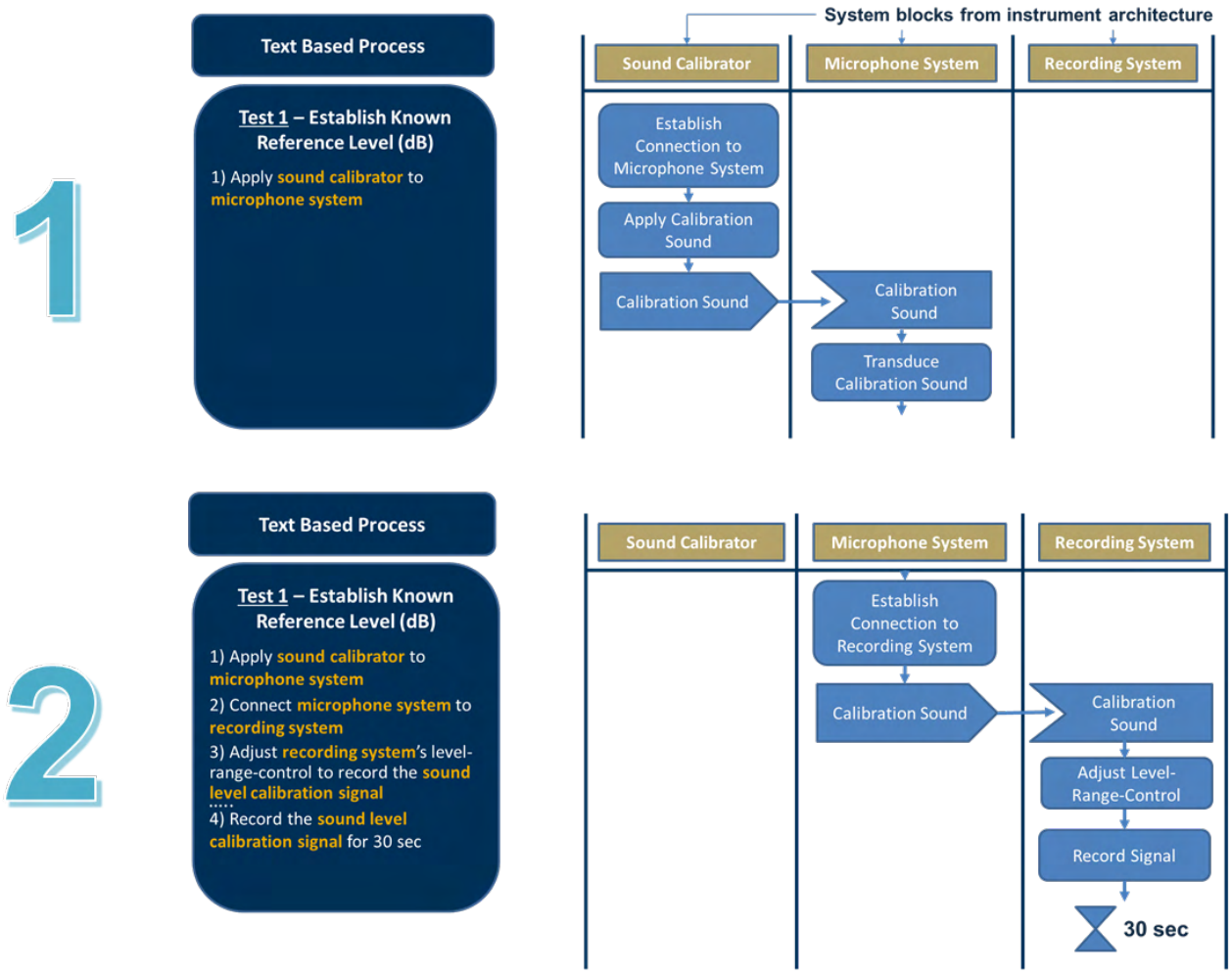

Figure 25**.** Text-based method for behavioral process model implementation.

To better understand and demonstrate how this process functions in practice, an example is provided in Figure 25. The purpose of the example test function is to establish a known reference noise level (in dB), with steps of the process listed in text format (indicated to the left side of the figure). Starting from phase 1 of the implementation (at the top of the figure), the first process step indicates that a sound calibrator is applied to the microphone system. In the behavioral process model, this means that three system blocks from the instrument architecture library are used: the sound calibrator, the microphone system, and the recording system. In terms of process steps, connection of the sound calibrator to the microphone system must be established, and the calibrator then applies the calibration sound to the microphone. In the next phase of steps (phase 2 at the bottom of the figure), the instructions are to connect the microphone system to the recording system, adjust the recording system's level-range-control to record the sound level calibration signal, and record the sound level calibration signal for 30 sec. All these process steps are then populated in the process model on the right side of the figure and mapped accordingly to the system blocks.

Continuing along that same implementation path, the completed process mode for establishing a known reference noise level is shown in Figure 26. Following similar steps, behavioral process models applied in SysML were formulated for the flight testing phases of interest, which are the approach flyover (Figure 27) and takeoff (Figure 28).

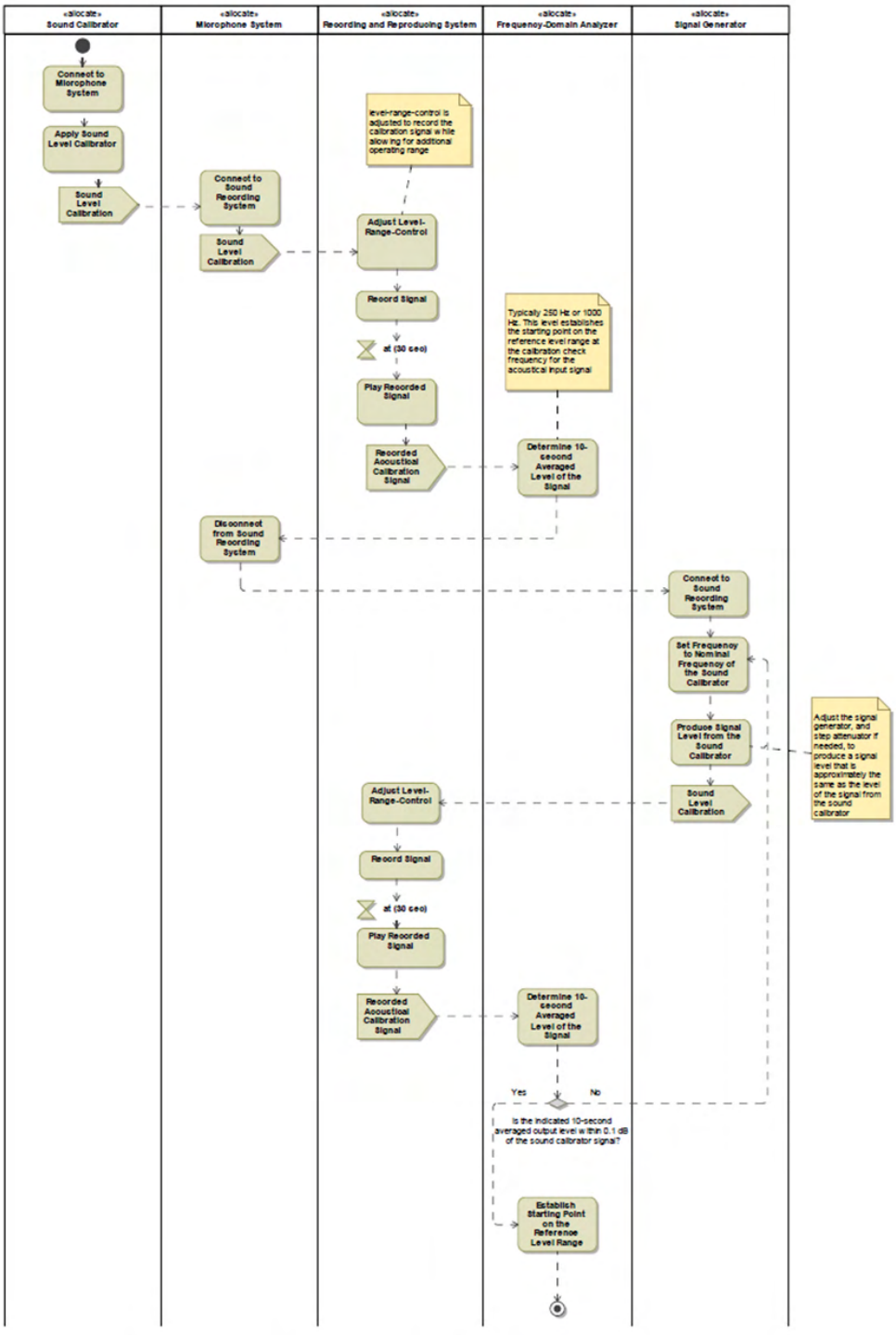

Figure 26. Process model for establishing a known reference noise level (baseline noise definition process).

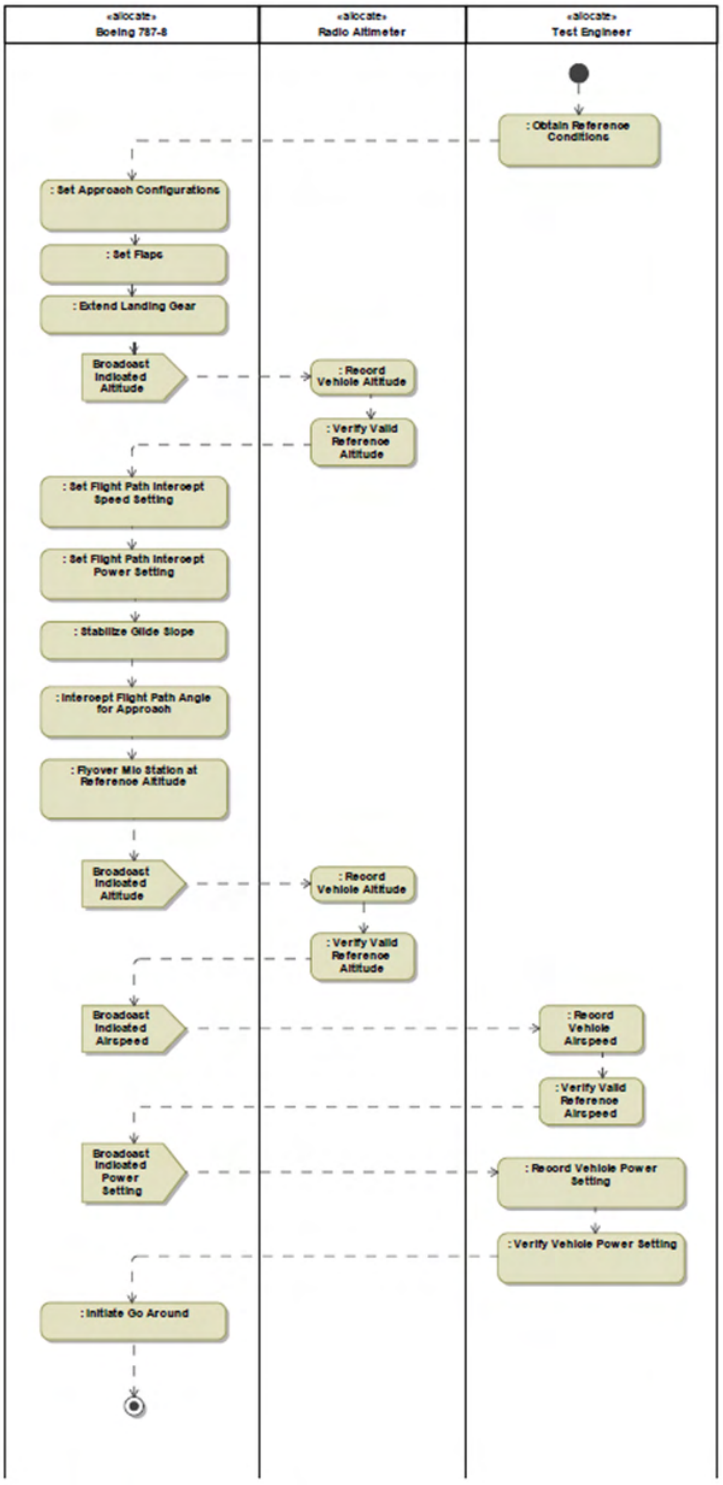

Figure 27. Behavioral process model for approach flyover.

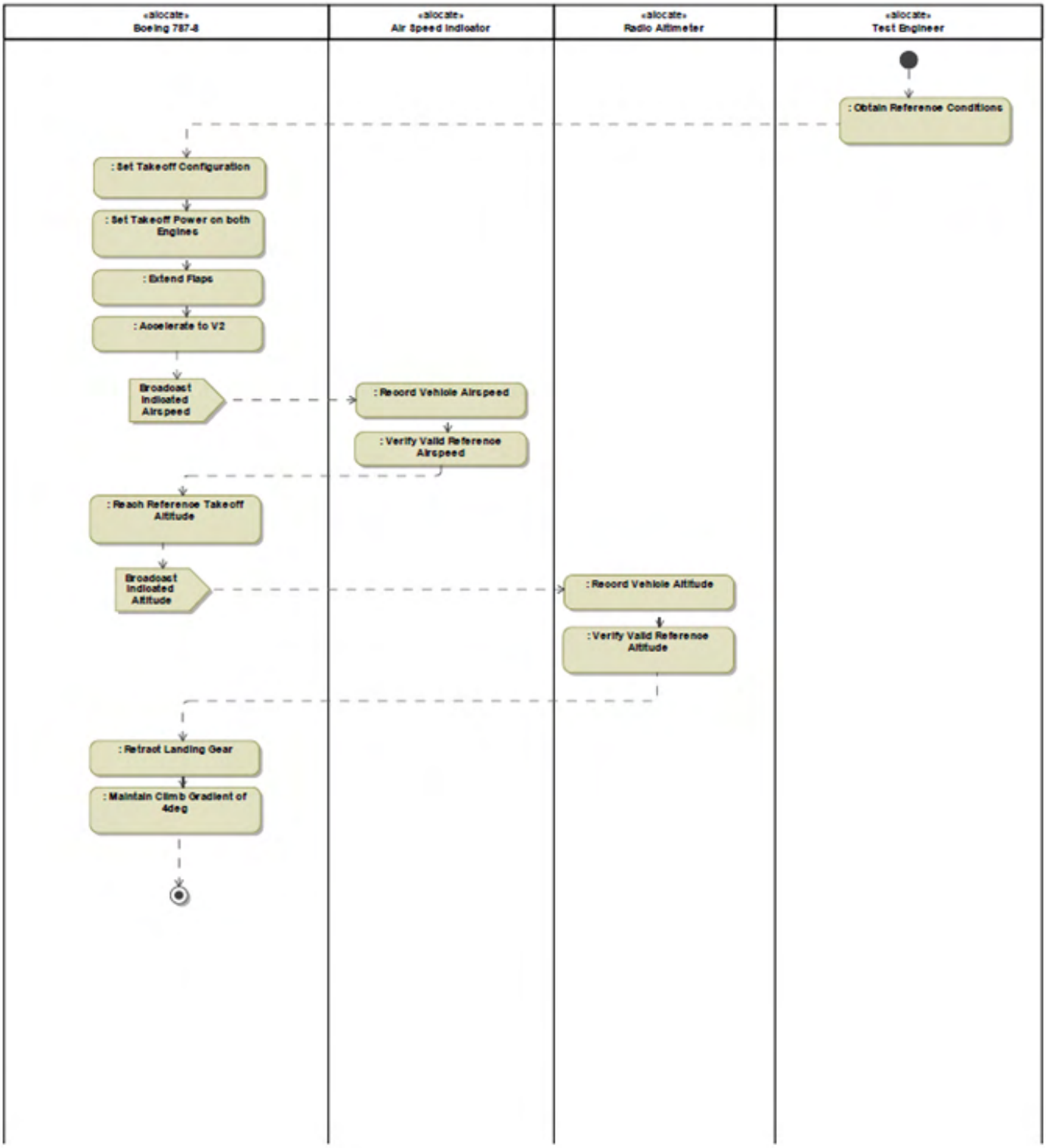

Figure 28. Behavioral process model for takeoff.

Step 4 and the final integration step for the verification model is the automated document generation. A suite of reports are generated through this function, including the following documents:

1. Product specifications
2. Technical baseline
3. Metrics
4. Verification compliance

The produced reports also include documents for certification, which include:

- Instrumentation validation document
- Flight test plan

Noise calculation is a key enabler under the noise testing instrument architecture module of the verification model. The goal of this module's function is to represent and capture the noise calculation process on the basis of flight test data within the model-based framework. The metrics of interest are as follows:

- Annoyance-based measure, or EPNL, as the effective perceived noise level (in units of EPNdB): This metric accounts for subjective effects of aircraft noise on humans over the duration of the perceived noise level (PNL). Because certification quality EPNdB cannot be directly measured, it is calculated in a standard manner, as described in Annex 16.
- Loudness-based measure: The maximum sound exposure level is calculated in dBA units.

Before calculation of EPNL, corrections must be applied to measured data, which account for uncertainties related to the measurement system, the microphone and recording system used, background noise, the actual flight path, and the meteorological conditions when the measurements were taken.

The steps for EPNL calculation, per ICAO recommended practice, are as follows:

1. Perform conversion of sound pressure level to PNL (instantaneous perceived noise level) for each 0.5-s sample, by means of a Noy table (Figure 29)

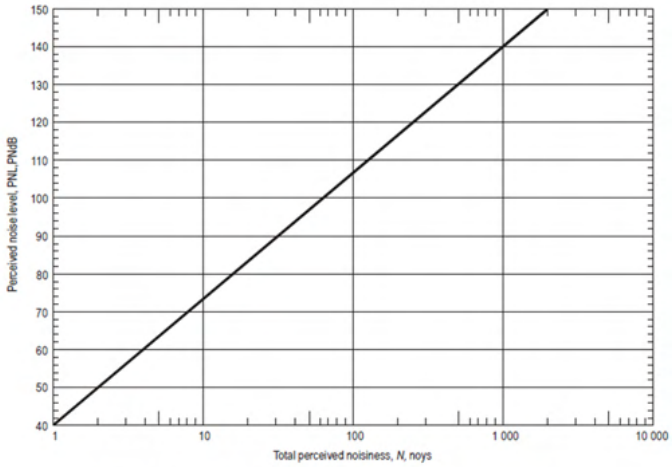

Figure 29**.** Perceived noise level as a function of total perceived noisiness.

2. Calculate tone-correction factor *C* to account for the subjective response to the presence of spectral irregularities
3. Calculate tone-corrected perceived noise level (PNLT) = PNL + *C*, at each 0.5-s increment of time
4. Calculate the duration correction *D* for the entire flight (where $T = 10$ s, and $\Delta t = 0.5$ s)

$$D = 10 \log \left[\left(\frac{1}{T} \right) \sum_{k=0}^{d/\Delta t} \Delta t \cdot \text{antilog} \ \frac{\text{PNLT}(k)}{10} \right] - \text{PNLTM}$$

5. Calculate EPNL = PNLTM + *D*, where PNLTM = max(PNLT)

For the calculation of EPNL from measured noise data, three basic properties of sound pressure must be measured: sound pressure level, frequency distribution, and time variation. The PNL(*k*) measurement requires Noy table values (perceived noisiness as a function of sound pressure level) and a mathematical formulation, which requires constants for mathematically formulated Noy values (Figure 30).

BAND (*i*)	*f* HZ	SPL (*a*)	SPL (*b*)	SPL (*c*)	SPL (*d*)	SPL (*e*)	*M*(*b*)	*M*(*c*)	*M*(*d*)	*M*(*e*)
1	50	91.0	64	52	49	55	0.043478	0.030103	0.079520	0.058098
2	63	85.9	60	51	44	51	0.040570		0.068160	"
3	80	87.3	56	49	39	46	0.036831		"	0.052288
4	100	79.9	53	47	34	42	"		0.059640	0.047534
5	125	79.8	51	46	30	39	0.035336		0.053013	0.043573
6	160	76.0	48	45	27	36	0.033333			"
7	200	74.0	46	43	24	33	"			0.040221
8	250	74.9	44	42	21	30	0.032051			0.037349
9	315	94.6	42	41	18	27	0.030675	0.030103		0.034859
10	400	∞	40	40	16	25	0.030103			
11	500		40	40	16	25				
12	630		40	40	16	25				
13	800		40	40	16	25				
14	1 000		40	40	16	25			0.053013	
15	1 250		38	38	15	23	0.030103		0.059640	0.034859
16	1 600		34	34	12	21	0.029960		0.053013	0.040221
17	2 000		32	32	9	18			"	0.037349
18	2 500		30	30	5	15			0.047712	0.034859
19	3 150		29	29	4	14			"	
20	4 000		29	29	5	14			0.053013	
21	5 000		30	30	6	15			"	0.034859
22	6 300	∞	31	31	10	17	0.029960		0.068160	0.037349
23	8 000	44.3	37	34	17	23	0.042285	0.029960	0.079520	"
24	10 000	50.7	41	37	21	29	"	"	0.059640	0.043573

NOT APPLICABLE

Figure 30**.** Constants for mathematically formulated Noy values.

No option for directly performing noise metric calculations within SysML is available. A possible solution is to create a function in MATLAB and then incorporate the analysis in the verification thread. For this purpose, a version of a software tool written in MATLAB for calculation of the effective perceived noise level, based on 14 CFR Parts 36 and 91 (More, 2011) was discovered in the literature. Expanding on the logical architecture library, the EPNL calculation has been implemented through block representation in the MBSE framework, which is shown in Figure 31. The integration was completed by effectively linking it to the MATLAB source code of this analysis through use of the Cameo Simulation Toolkit.

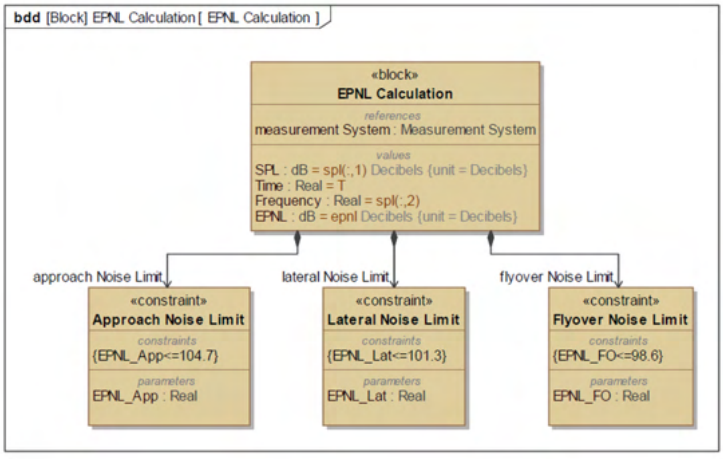

Figure 31**.** EPNL calculation model as a logical block in SysML.

After the progress made under Task 2.1, the current state of the verification model allows basic certification assessment for transport category configurations to be performed. However, the following improvements and additions will be required before the fully planned capability is in place:

- Build test constraints to the System Under Test (SUT) transport aircraft
  - Import Appendix B and translate to verifiable requirements
  - Define constraints with numerical/logical limits and apply to systems
- Document the EPNL calculation process to verify noise constraints on the SUT
  - Document the calculation process from raw noise data to EPNL
  - Import raw data into MBSE (if data become available)
  - Verify noise requirements by using EPNL converted noise data

Task 2.2

The objective for this task is to explore options for formulating and evaluating a streamlined certification process alternative. Feedback from the planned workshops and guidance by the OEM partners is used to inform the development of process alternatives in which streamlining is the main improvement criterion. Beyond the recommendations offered by the partners, the team has also been exploring what "streamlining" would mean in this context, to ensure that the chosen direction will provide added value across all partners and stakeholders. The target objectives for streamlining the certification process currently being considered are the following:

- More efficient process steps, with anticipated savings in time and cost: This direction could involve investigating time efficiencies, with the use of digital tools to expedite information exchange and reduce intermediate steps and proxies. Associated cost benefits may also be possible.
- Affordable solutions in the form of cost-effective use of technology: This direction could be operated with reduced maintenance costs and supporting resources (e.g., a technology allowing for omission of lateral microphones).
- Technology use that will facilitate data collection and predictive analysis: This direction could eventually improve planning and facilitation of flight testing campaigns.

Table 4 Summary of options for equivalent procedures, as provided by the workshop/interview feedback

Title/summary of EP or a grouping of EP's	Time savings	Cost savings	Providing compliance flexibility to the applicant
Flight path intercept in lieu of full takeoff/ landing profiles	Yes (by factors of 5-10)	Yes (less wear, less maintenance)	
Lateral mic placement (single or multi pair)	Possibly (multiple = better data)	Yes (single pair)	
Derivation of NPD data (data reduction/expansion by analysis, based on few points)	Yes (several weeks)	Yes	
Approved measurements at non-reference points (adjusted data)		Possibly	Yes (in test conditions/ site selection)
Exceeding sound attenuation limits allowed in some cases			Yes (in test conditions)
Static-to-flight projections (not making a new NPD database)	Yes (no flight test for derivations)	Yes (no flight test for derivations)	Possibly (gives a noise change range for derived versions)
Inflow Control Device & calibration options (for change of engine)			? (more of providing an option to certify engine change)
Cert by analysis (NPD extrapolation for design changes with predictable noise effects)	Yes (no flight test for derivations)	Yes (no flight test for derivations)	

(Note: This table provides an inclusive list of information collected through the partners' responses but does not indicate the final or any chosen direction; the direction remains under discussion between the team and the project partners.)

An earlier version of options for equivalent procedures (Eps) is presented in Table 4. However, in follow-up discussions with OEM partners, a consensus was reached that the use of MBSE tools provides a unique opportunity to address the technical challenges in noise certification at a level beyond only time and cost savings. Possible outcomes and use cases that would provide higher added value to streamlining noise certification (with input kindly provided by Boeing) are as follows:

- Explore options and possible recommendations for the simplification of setup requirements, to facilitate more test locations/weather windows (i.e., remove 4-ft microphones for ground plane, and remove lateral location altogether)
- Evaluate no-acoustical-change limits in the context of testing uncertainty
- Address conformity issues by formulating an acoustical conformity concept, which could be included in the MBSE-enabled framework

Another category of recommended use cases is associated with the expanded use of certification by analysis and exploration of the possibility of helping expedite the approval procedures within the FAA, as follows:

- Define criteria for approval for acoustical analyses that define new certification noise levels (acoustical change by analysis)
- Define a framework for oversight that gives the FAA confidence in manufacturers' tools/methods used in noise certification (defined audit guidelines/procedures)
- Update instrumentation/measurement recommended procedures to better align with currently available equipment/processes

Of primary interest should be the use of technology that seeks to simplify the certification process, thereby eliminating the added uncertainties and instances in which stakeholders (e.g., OEMs) have minimal or no control over process bottlenecks and unexpected emerging factors (e.g., the impacts of a pandemic, weather, or supply-chain or personnel issues). In addition, the simplification of the noise certification is directly linked to anticipated cost savings, because the same outcome could be achieved with fewer resources and reduced budget levels.

Along with the selection of the equivalent procedures of interest, based on the above feedback, the outcome of Task 2.2 is to present certain use cases in which the MBSE framework can demonstrate, through the verification model, that a streamlined noise certification procedure is possible. That is, the streamlined alternative can result in quantifiable improvements with respect to the criteria listed above while meeting the same regulatory constraints and requirements that the current benchmarked certification procedure can meet.

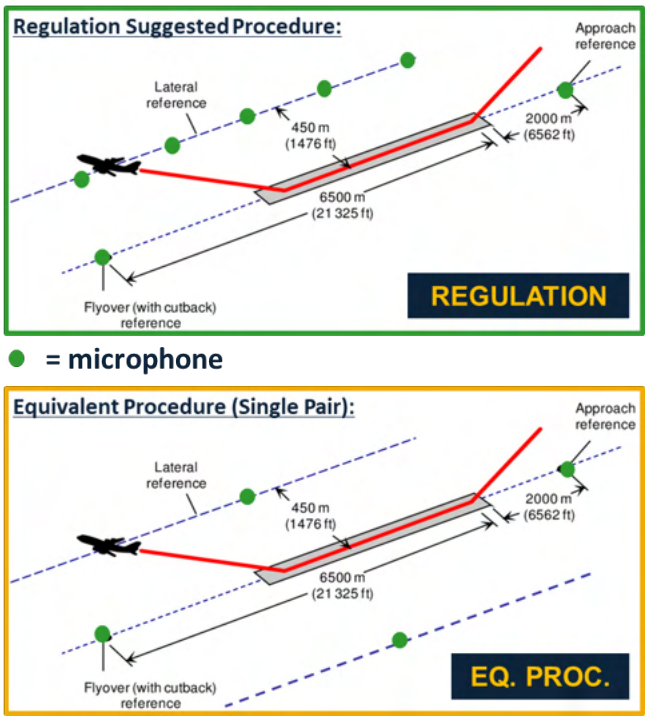

Figure 32**.** Equivalent procedure example: lateral microphone setup.

A potential use case currently under strong consideration and development by the team is the alternative setup and placement of the lateral microphone. Microphone setup must abide by regulatory requirements (B36.3, B36.4) regarding "measurement point(s) defined as point(s) on the line parallel to and 1476 ft (450 m) from the runway centerline, where noise level is a maximum during takeoff." The hypothesis on this solution being effective in terms of time and cost savings, stems from the observation that complexity difficulties encountered when using multiple microphone arrays along the lateral line (multiple interference points, need statistical independence) are avoided. However, this solution covers a smaller sound field than multiple arrays and may require more test points to obtain sufficient data for compliance (accuracy and data quality). The top portion of Figure 35 shows how the microphone setup and their locations are currently chosen.

For the proposed equivalent procedure, a single pair of symmetric microphone stations is considered, with placement as shown in Figure 35. With the use of the verification thread, for a given aircraft model as the system under testing (SUT), the following constraints and requirements must be met:

- Full takeoff power, configuration, airspeed as in Regulation B36.7(b)(3-4).
- At several specified heights above a track (covers range 200-2000 ft).
- At right angles to and midway along the line joining the 2 mic stations.
- Matching data from both lateral mics for each fly-past should be used for the lateral noise determination.
- Adjusted noise levels: symmetric or asymmetric (one or two regression curves)
    - Usually second order; exceptional use of third order needs justification.
- Confidence interval of reported EPNL within ±1.5 dB (Regulation A36.5.4)
- Minimum of six runs necessary to obtain sufficient data for compliance

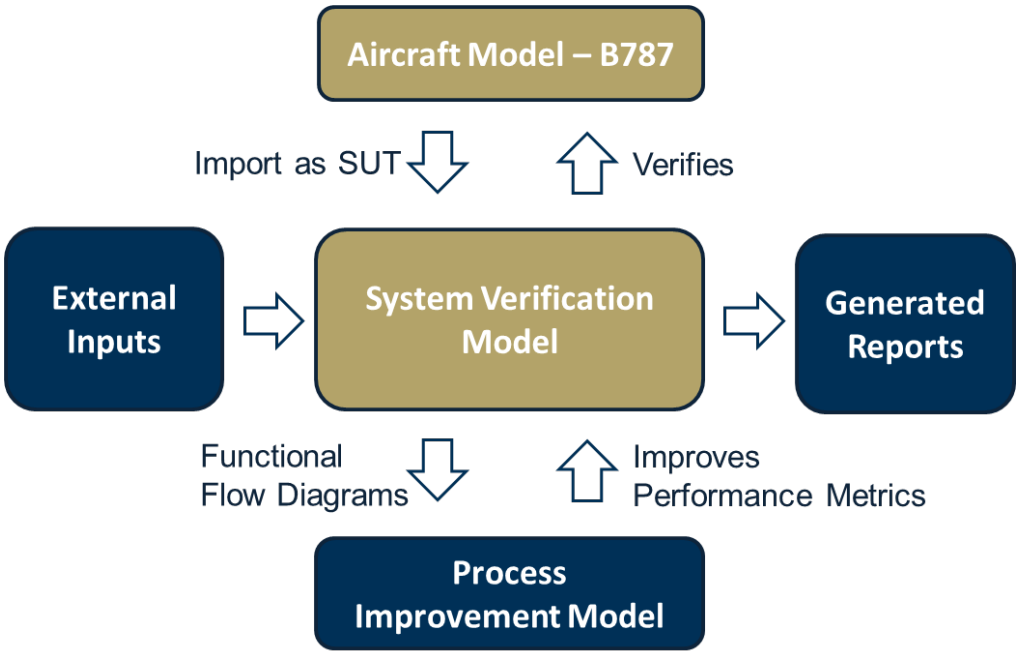

Figure 33**.** Complete MBSE framework for the evaluation of equivalent procedures, as part of exploring streamlined process alternatives for noise certification.

Because the steps of this task up to this point cover only the portion of demonstrating compliance through use of the MBSE framework, this use case will not be complete until a case is made that process improvements can be quantified regarding the use of fewer microphones. For this purpose, a process improvement model (PIM) is being developed under Task 4 and will be interfacing with the verification model, as shown in Figure 33. More information about the PIM development can be found under the section for Task 4.

Task 2.3
For this task, the objective is to further assess the viability of the proposed streamlined process and apply any revisions, according to feedback from the FAA, Volpe Center, and industry partners. The end goal is to complete a number of revisions to ensure that the streamlined process will meet expectations and provide added value across all project stakeholders. With the efforts toward completing Task 2.2 and a demonstration of a streamlined process, this task is currently underway and is pending additional workshops planned in the future, along with the team's further definition of metrics and evaluation criteria for the streamlined process assessment.

Milestones

- The first complete version of the MBSE noise certification process model has been implemented in SySML and is being updated based on feedback from workshops and interviews with the OEM partners.
- Through the verification model, the applicability of MBSE methods for this problem has been demonstrated.

Major Accomplishments

- A noise certification process model represented in SySML was completed, in which equivalent procedures can be tested through a requirement verification model.
    - Importing of FAA noise certification regulations (Task 1), an aircraft model as the SUT, industry partner interview outputs (Task 1.2), and flight testing instrumentation procedures (e.g., the Volpe Center's recommended instrument validation) (Task 2.1) was completed.
    - The current certification process was modeled into the MBSE framework (Task 2.2), including definitions for requirements, validation architecture, and creation of a digital thread for requirement verification from data input.
    - Model data were output into auto-generated reports.
- Continual community outreach and interaction with OEM partners yielded technical feedback to improve model accuracy and capability (OEMs, Volpe, and FTHWG).
- Options for formulating streamlined process alternatives were narrowed through down-selection of equivalent procedures (e.g., exploration of lateral microphone setup and placement).
- The team became familiar with MBSE methods (e.g., SySML software tutorials, the RFLP approach, etc.).

Publications

Peer-reviewed journal publications
Listed under Task 1

Published conference proceedings
Listed under Task 1

Written reports
Listed under Task 1

Outreach Efforts

- Facilitated follow-up meetings with OEM partners
- Presented a demonstration of the MBSE-enabled certification concept to the Flight Test Harmonization Working Group (FTHWG).
- Presented the project's Year 1 performance review to the FAA Office of Environment and Energy, and Volpe Center
- Planned upcoming calls and expanded communication with the Volpe Center

Awards

None

Student Involvement

- The implementation of the verification model required substantial skillset development in SySML and use of software, which all students were successfully able to acquire.

- Three major roles have been maintained within the student team for implementation of the verification thread: (a) verification model development, (b) instrumentation for flight testing and noise analysis, and (c) requirements and constraint formulation based on Part 38, Appendix A and B.
- All students participated in the integration of all main enablers into the first complete version of the verification model.

Plans for Next Period

- Finalize the baseline model for current certification practices, incorporating feedback obtained through the workshops
  - This model will consist primarily of documented regulations and certification procedures (both regulatory and equivalent procedures), all compiled in SysML views.
- Next steps for MBSE framework development:
  - Perform model fine-tuning, ensuring a consistent format, reusability, and easy navigation setup
  - Obtain data for a specific application of a known test article for verifying a set of requirements for more relatable and realistic results
  - Define interfaces between instruments
  - Update current hardware diagrams with interface definitions
- Identify use-case examples to plan for demonstration, according to selected areas of improvement: The priority is to identify solutions seeking to simplify the certification process, either through use of technology and/or different technology setup configurations, or through use of data and analytics to automate steps and/or address uncertainties.
- Implement an interactive decision support tool, to aid in further showcasing the capabilities of the MBSE framework through the selected use-case examples

Task 3 - Develop a Flexible Noise Certification Procedure for New Aircraft

Georgia Institute of Technology

Objectives

The focus of Task 3 is to define what a more flexible certification process would look like and the evaluation criteria for determining that the procedure is more streamlined than the baseline. Task 3 will build upon the capabilities of the integrated MBSE platform and leverage contributions from all other tasks. The breakdown of tasks is as follows:

Task 3.1: Flexibility Assessment of Streamlined Process

- Evaluate the flexibility of the streamlined noise certification process for new-category air vehicles

Task 3.2: Flexible Process Definition

- Define and recommend improvements to the streamlined noise certification process to accommodate for a flexible noise certification process, with respect to vehicle type

Task 3.3: Flexible Process Assessment and Revision

- Solicit feedback on the new process from the FAA and industry partners
- Perform revision of the suggested process, incorporating key aspects of the collected feedback to build consensus the research partners

Research Approach

The main objective for Task 3 is to ensure that the certification process model in MBSE is sufficiently flexible to apply to other air vehicle categories. If this is true, the framework will be capable of testing and evaluating alternative certification process options and identifying those that can successfully accommodate the vehicle types of interest. One premise underlying the use of SysML in implementing an MBSE framework for certification is the feature of modularity, which should allow for rapid formulation of multiple streamlined process alternatives and rapid identification of the preferred option, according to the characteristics of a flexible process.

Task 3.1

For Task 3.1 (flexibility assessment of streamlined process), defining what is meant by a "flexible" process is important. One strategy is to assess whether the introduction of a different vehicle configuration would introduce a large number of incompatibilities with the streamlined process under evaluation. For instance, how does the rotorcraft configuration affect the type of microphone technology, the quantity needed, and the placement in the testing facility? Although switching the noise regulations and the noise instrument validation protocols to the new configuration might be straightforward and faster, if done within the MBSE framework, the compatibility of equivalent procedures might not remain the same as it was when the streamlined process was applicable to a transport category vehicle. The flexibility criteria for a streamlined process could comprise the following:

- Compatibility and applicability of equivalent procedures
- Complexity, e.g., if a switch to another configuration requires more steps to setup, and additional instrumentation if, the vehicle is more sensitive to the variation of certain factors during testing.
- Sensitivity to non-acoustical change, different than other categories.
- Sensitivity to weather, etc.

In short, one way to evaluate the flexibility for a streamlined process alternative is to focus on the equivalent procedures that make the process more streamlined than the baseline, and to understand the factors that eliminate their benefits, if a configuration is chosen, other than the one for which it was streamlined.

Task 3.2

The definition of what constitutes a "streamlined" process may depend on the vehicle configuration. Hence, to evaluate the flexibility of a streamlined process, the vehicle type(s) for which the process is streamlined would need to be accounted for, and the assessment comparison would need to be performed on that basis. Therefore, investigation of process efficiency metrics to support characterization and comparative assessment of the current certification process and alternatives is underway, with the requirement that the metrics be agnostic to the vehicle configuration type.

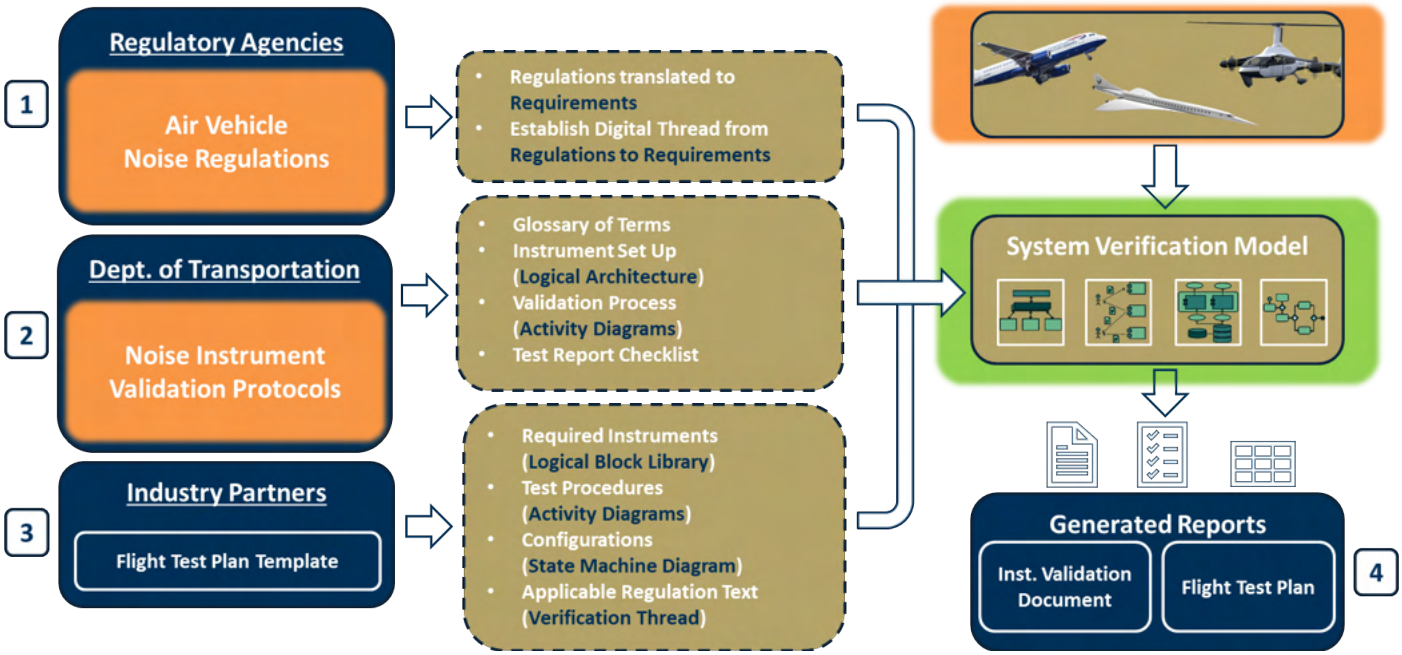

Figure 34. Verification model for multiple vehicle configurations

With the verification model now available for transport category, the first spiral iteration of the proposed concept for evaluating a flexible certification process has been formulated and is presented in Figure 34. The original model is flexible to accommodate a different set of regulations as one of the inputs which, like in the transport category example, will undergo the conversion to requirements by establishing a digital thread and a requirements model applied in SysML. While the

function is currently not "plug and play," algorithm modifications for the logical conversion are in progress. Similarly, the noise instrument validation protocol conversion to SysML views is underway. However, the vehicle representation model is more straightforward, because it is not process dependent, and the interface definitions might possibly require modifications for this module to seamlessly integrate with the verification model.

According to the workflow proposed in Figure 34, the integrated framework for flexibility assessment of the certification process is shown in Figure 35. The key difference between this view and that used under Task 2 development for the transport category vehicle is the addition of a PIM. Although this module is currently developed under Task 4 activities, it will be integrated in the flexible MBSE framework, in which process alternatives will eventually be formulated, and evaluated through the PIM.

Task 3.3
For this purpose, metrics are developed under Tasks 3 and 4, which will allow for measuring process flexibility and other relevant figures of merit as part of comparing alternatives to the baseline. The first version of the discrete event simulation model has been completed for evaluating process efficiencies. After calibration of the model with inputs and parameter definitions that will be obtained by OEM partner input, the model will return time durations between key events, and allow for statistical analysis and identification of process bottlenecks and show-stoppers. Another set of metrics for characterizing complexities are under development, which will target the need to further simplify the process through the use of technologies allowing process steps to be reduced or eliminated. More information on PIM development is provided under Task 4 reporting, and Task 3 activities will seek to provide several use cases of interest according to the input and technical feedback provided by OEM partners, FAA, and the Volpe Center.

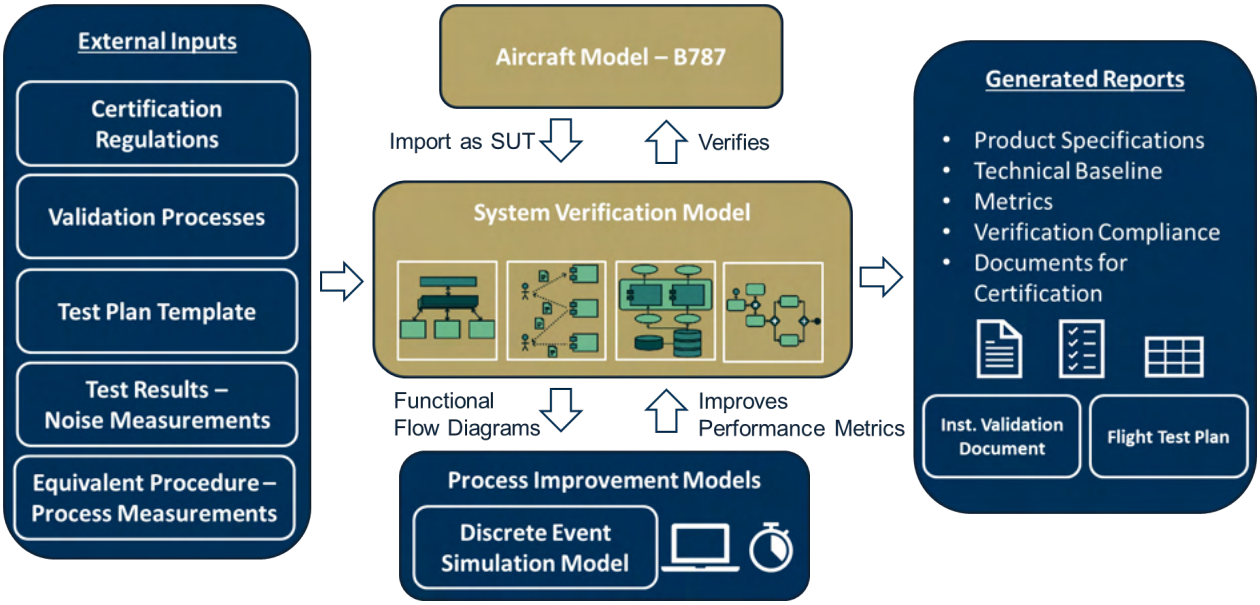

Figure 35**.** Integrated modeling and assessment framework for flexibility evaluation of certification procedures.

Milestones
Listed under Task 1

Major Accomplishments
- The initial concept for the MBSE framework has been formulated to accommodate multiple vehicle types and allow for process effectiveness and flexibility evaluation.
- Metrics development is underway, with demonstration examples planned to solicit input from OEM partners and stakeholders.

Publications

Peer-reviewed journal publications
Listed under Task 1

Published conference proceedings
Listed under Task 1

Written reports
Listed under Task 1

Outreach Efforts

Listed under Task 1

Awards

None

Student Involvement

The full student team has participated in brainstorming sessions for formulating the integrated certification process assessment framework shown in Figure 35.

Plans for Next Period

- Implement concept and demonstration of a simple use case (with input for streamlined process definition, as decided by Task 2 activities)
- Finalize metrics for assessment of process flexibility
- Formulate a decision support concept for selection of technology or equivalent procedure options, which will leverage the MBSE framework analysis and evaluation features, toward an end goal of an interactive capability allowing planners to evaluate alternatives in equivalent procedure selection and identify simplified, more flexible certification process alternatives

Task 4 - Simulate Streamlined and Flexible Noise Certification Procedure

Georgia Institute of Technology

Objectives

The aim of Task 4 is to explore options for evaluating noise certification within the MBSE framework. The purpose for this module is allow for establishment of a performance baseline for current certification procedures, and allow for evaluation and comparison of more flexible process alternatives, as they are defined and formulated in Tasks 2 and 3. The breakdown of tasks under Task 4 is as follows:

Task 4.1: Identify Modeling Approach

- Explore options for modeling approaches to simulate and evaluate the certification process within the MBSE framework

Task 4.2: Noise Certification Process Metric Definition

- Identify a set of metrics to allow for quantitative comparison of the current and proposed noise certification processes

Task 4.3: Model Calibration

- Identify a benchmark for noise certification procedure simulation
- Calibrate the noise certification procedure simulation

Task 4.4: Certification Process Simulation

- Execute simulations of current and proposed noise certification procedures

Task 4 focuses on exploring and identifying suitable process modeling approaches for the simulating the noise certification procedure. On the basis of this objective, this task aims to deliver a solution broadly referred to as a Process Improvement Model (PIM). Tasks 4.1 to 4.3. seek to explore suitable enablers of the PIM implementation, and Task 4.4 aims to integrate the PIM into the current MBSE framework. The chosen modeling approach should accommodate process performance evaluation and provide responses back to the verification model for completing steps regarding meeting requirements and compliance. In addition, the PIM must be flexible and reusable according to the definitions of the certification process, equivalent procedures, etc., as they are formulated within the verification thread. Overall, a closed loop is defined between the verification thread and the PIM(s), which are implemented under Task 4.4. An overview of the integrated verification thread and the PIM(s) is shown in Figure 36.

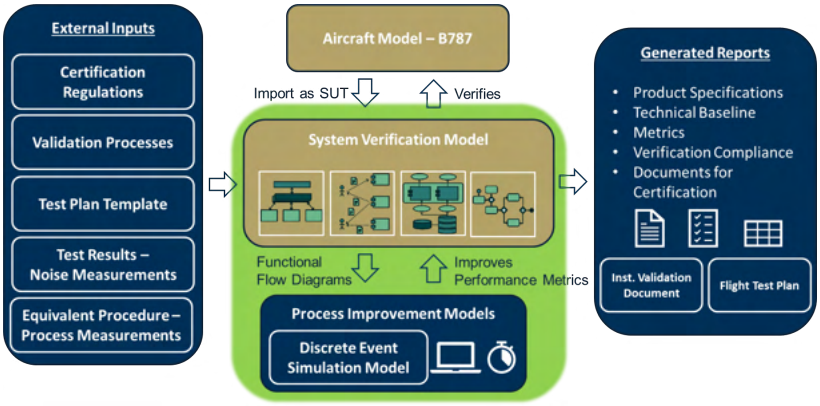

Figure 36. Process Improvement Model (PIM) integration into the verification thread within the MBSE framework for certification.

Task 4.1

The team has completed a literature review on the following process modeling methods to enable process simulation:

- Discrete Event Simulations (DES), wherein a clock tracks the duration of the transition between model states
- Agent-based simulation (ABM) methods.
- System dynamics
- Markov chain–Monte Carlo (MCMC) simulation

These techniques are evaluated according to how well they could capture and simulate actual industry-applied procedures and their ability to interface with the verification thread.

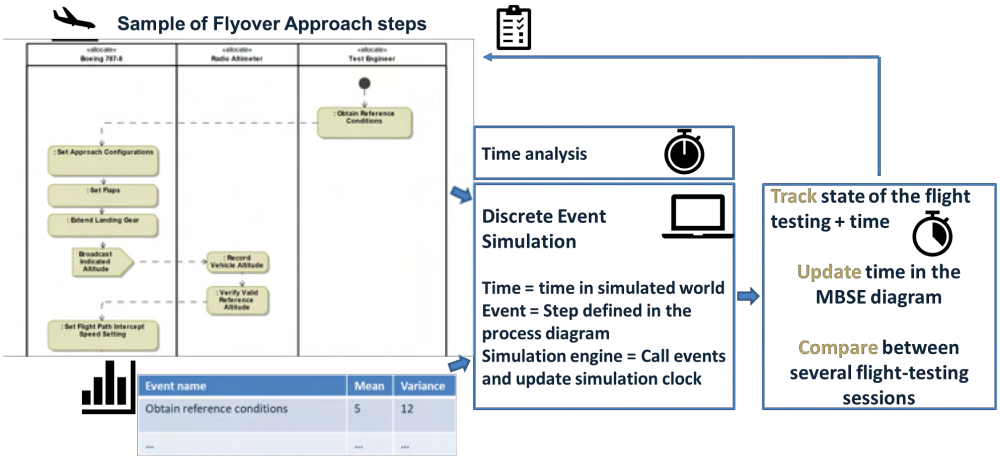

Figure 37. Discrete event simulation for flyover approach.

The first option for the DES model was the approach originally chosen. The first demonstration version of a certification process model, using DES methods in a Python-based environment, is now completed. An example for a flyover approach has been implemented and is shown in Figure 37. In this example, a proof of concept was put in place to show how the process model, as defined in the MBSE framework, can be simulated by using DES. With the model states imported, DES can track the clock and return the time points at which each event is concluded. The DES results are then fed back as an input, and the process diagram is updated in the verification model, which then performs checks against requirements and compliance.

However, because flight testing procedures carry uncertainties that must be considered as equivalent procedures are formulated, a more comprehensive modeling approach is needed. To account for the uncertainties surrounding process performance, development of a probabilistic model using Markov chains is underway to improve the process assessment capability. This approach is better suited to support use cases, where the objective is to further simplify the FAA's recommended procedures by eliminating steps, replacing, reducing, or even eliminating the presence of certain technologies. Other recommendations, such as a conformity model, could be better tested with a probabilistic approach, in which a broader range of scenarios could be tested.

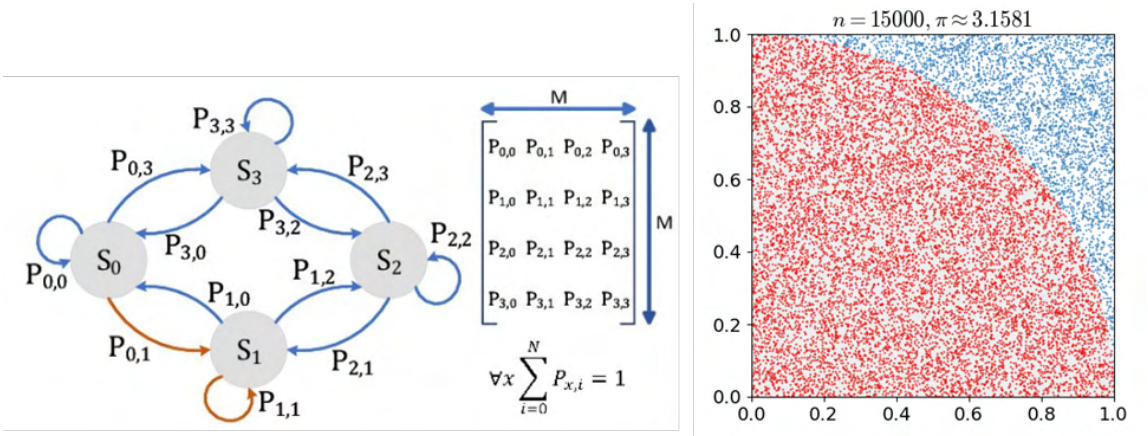

Figure 38. MCMC: Markov Chain Monte Carlo.

An example of such an approach is the MCMC approach, wherein a discrete event simulation model is used to run a Monte Carlo study to collect sample runs, given an input probability matrix and stakeholder value function. Each run will be associated with incurred time, cost, and an accuracy penalty; the output will be provided in the form of activity diagrams and responses, which are fed back to the verification model within the MBSE framework. An example view of the MCMC is shown in Figure 38.

Table 5 Step-by-step sequence MCMC data format for acceptance-rejection sampling.

Step #	1	2	3	4	...
Event	A	A	B	C	...
Time	+5	+5	+2	+2	...
Cost	+10	+8	+5	+7	...
Accuracy	1.0	1.0	0.99	0.98	...

Within the MBSE framework, the MCMC simulation data are then imported for performing acceptance-rejection sampling, wherein each run (with its associated metric) will be accepted or rejected by requirement constraints within the verification model. The format of the MCMC simulation data follows a step-by-step sequence (similar to a discrete event simulation), as shown in Table 5.

A simple example of the implementation path summarizing the development of the PIM is shown in Figure 39, in which the interfacing with the verification model is further explained. In the example of a flyover approach plan similar to that in Figure 37, the process model informs the PIM, which converts the flyover approach test into an executable simulation model. Given the type of requirement tests in which a user is interested, the appropriate response values are chosen, and parametric settings for the baseline values (e.g., time, cost, resources, disruption risks, and accuracy penalty), as well as MC distributions are chosen. The simulation then generates the PIM metrics and prepares the dataset for the verification.

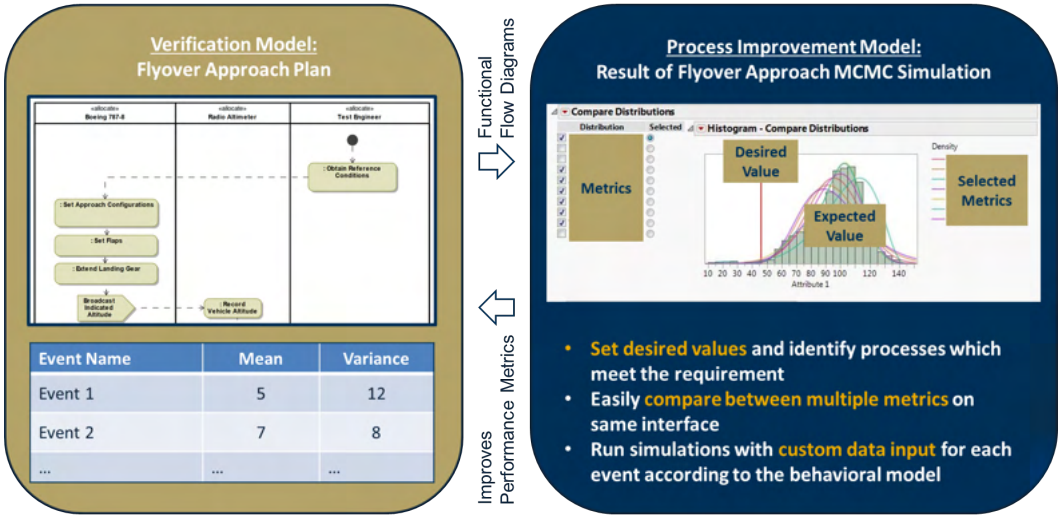

Figure 39**.** Example of DES – time analysis for a flyover approach planning scenario.

Depending on the requirement acceptance-rejection distributions, changes to the process model (e.g., by incorporating equivalent procedures, modifying recording lineups, considering conformity models, etc.) will be proposed, and then another iteration cycle will be ready to be executed. The long-term benefit is that the process will evolve as a key function for testing the feasibility of equivalent procedures, then scaling up to characterize the flexibility of the streamlined noise certification process that users actively formulate within the MBSE framework.

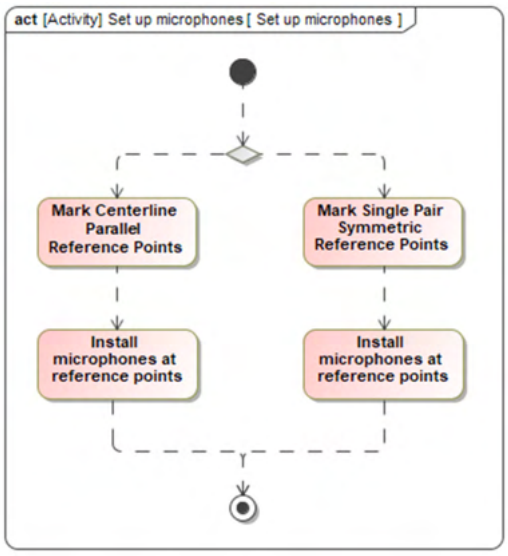

Figure 40**.** Example activity diagram for microphone setup.

Task 4.2
Within this subtask, the team has been exploring options for sets of metrics that will allow for quantitative comparison of current and proposed streamlined noise certification process options. The current list of identified metrics is the following:

- Time: schedule cost incurred to complete event
- Cost: budget cost incurred to complete event
- *P*(failure): probability of repeating the event (does incur time and cost [full or partial] for each occurrence)
- *P*(success): probability of moving out of the current event
- Accuracy penalty: impact on overall accuracy value for executing the event (does not incur additional cost for each occurrence)

A stakeholder value function is formulated to represent an overall evaluation of the process, and to help characterize flexibility and the resulting added value for a particular stakeholder. One main observation from the responses recorded in Task 1.2 was that not all OEMs and stakeholders maintain the same needs and improvement recommendations, and the priority varies. A stakeholder value metric would allow the process evaluation method to be tailored to stakeholder preferences.

$$\llbracket Value \rrbracket\ \_Process = F(Cost\_Schedule,\ Cost\_Budget,\ Risk,\ Stakeholder\ Importance\_(Schedule,\ Budget,\ Risk))$$

As mentioned previously, the team is expanding on this task to identify metrics that go beyond the efficiency-oriented focus of the original process streamlining concept. Another objective involves identifying ways to accomplish process simplification, which could be reflected in reducing or combining steps, eliminating feedbacks and redundant actions, and possibly removing tasks, if a technology in which data and information are automatically circulated could provide the same expected outcomes. Hence, new sets of metrics will be needed to characterize such alternatives and incorporate them in the MCMC analysis before the verification step.

Task 4.3
This task requires a completed process simulation capability implementation to allow the team to Identify a benchmark for noise certification, against which the PIM model can be calibrated. The current PIM development plan is shown in Figure 41. The team has identified all necessary enablers and is finalizing a demonstration version of the implementation approach. Given that scalability issues are bound to appear as this model is expanded to reflect the full verification thread, the next step is to discuss options for data that ASCENT 61 partners could provide for further calibrating the model, according to the preferred use cases.

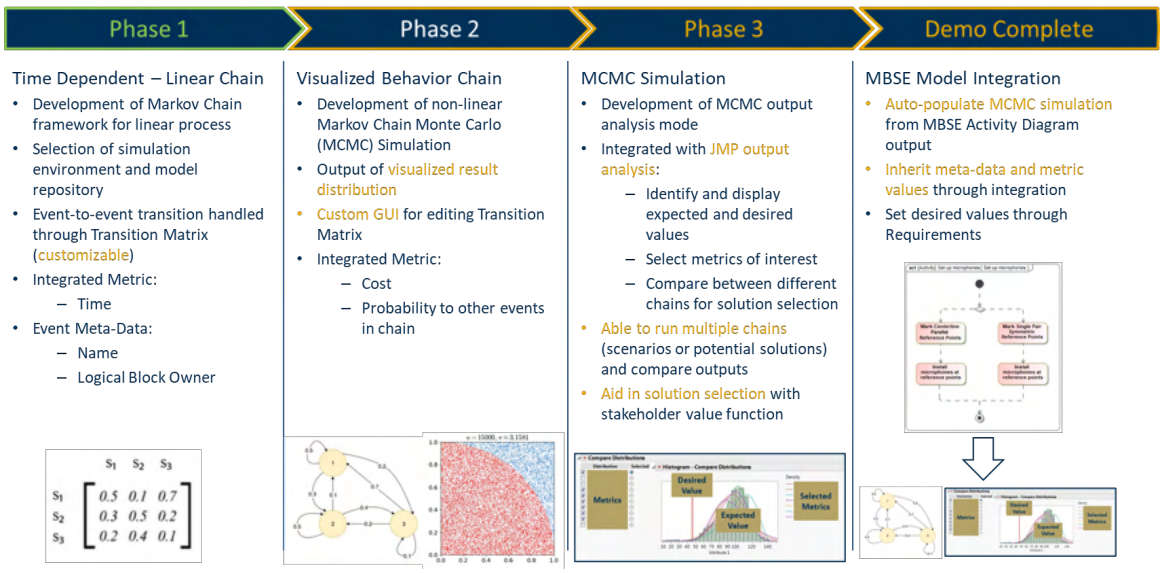

Figure 41**.** PIM functional development plan.

Task 4.4
Because this task will be performed further in the future, the team has been formulating use-case examples based on scenarios provided by the OEM partners. Under these examples, simulations of current and proposed noise certification procedures will be planned for.

Milestones
Listed under Task 1

Major Accomplishments
- Literature review on process modeling methods (DES, ABM, and SD, and stochastic [MCMC] methods) for enabling simulation and assessment of the noise certification process
- Development of a small-scale PIM by using DES
- Development of a more comprehensive stochastic model by using stochastic MCMC methods, formulated to seamlessly integrate to the verification thread within the MBSE framework
- Definition of a starting set of metrics as a working solution, with a focus on process efficiency improvements
    - Because the process improvement direction could become more diverse and consider goals for further process simplification and integration with other concepts, additional metrics have been added and mapped to use-case scenarios that the team will be using for a full-capability demonstration in the future (year 2 activities).
- Approach for Integrating the PIM model into the verification model within MBSE

Publications
Peer-reviewed journal publications
Listed under Task 1

Published conference proceedings
Listed under Task 1

Written reports
Listed under Task 1

Outreach Efforts
- Presentation of concepts to the Volpe Center, and collection of their technical feedback on the tools and analytic methods
- Discussions with experts in fields with similar problem applications, e.g., process simulations for industrial systems, manufacturing, supply chains, etc.

Awards
None

Student Involvement
Although a small portion of the team has been leading the technical approach to PIM development, involving the full team in the tasks, e.g., PIM integration with the MBSE model, will be a key enabler to be addressed earlier in the process.

Plans for Next Period
- Complete the PIM implementation steps as described in Figure 41, in which the outcome should be at the full verification model scale
    - Finalize interface with the MBSE verification model
    - Determine equivalent procedures to showcase
    - Fabricate data to show functionality
    - Select metrics for test scenarios
    - Develop value function for multi-factor optimization between equivalent processes
    - Calibrate model according to technical input from industry OEMs and the Volpe Center

- Expand on metrics definition beyond process inefficiencies (e.g., directly addressing time and costs), and consider complexities that could affect the process with bottlenecks and the unnecessary use of resources (e.g., duplicate testing, time-intensive procedures, etc.), with a primary focus on the flight-testing part of the process
- Formulate a simple certification problem per vehicle type and use it in pilot tests for comparing and selecting the appropriate method

Conclusion – ASCENT 61 Year 1 Summary

The following key tasks and activities have been completed under the ASCENT 61, year 1 performance period:

- Completed documentation of current noise certification regulatory framework (14 CFR Part 36, AC 36-4D) with input from the literature and partner interviews/workshops
- Hosted workshops/interviews with industry partners for transport category aircraft (jet and turboprop)
- Benchmarked current practices in certification flight testing, and identified key technical challenges and improvement opportunities
- Developed a working version of the process model on current noise certification procedures in SysML, made possible by input and guidance from OEM participation in interviews
- Established connection with the Volpe Center, and plans for model review and technical feedback
- Performed broader outreach of A61 to the aviation community on noise certification
    - ASCENT Fall/Spring meetings
    - Presentation to Flight Test Harmonization Working Group (FTHWG).
- Annual and quarterly reports made available to the ASCENT KSN database
- Plan for publication of OEM contributions and applied SysML technical capabilities in conferences and peer-reviewed journal articles

References

[1] Metzger, F., & Foley, W. (1970). STOL Aircraft Noise Certification: A Rational Approach. SAE Transactions, 79, 1021-1031.
[2] Federal Aviation Regulation, Part 21, Certification Procedures for Products and Ports; Part 36, Noise Standards: Aircraft Type Certification. December 1969.
[3] J. B. Ollerhead, "Subjective Evaluation of General Aviation Aircraft Noise." FAA Technical Report NO-68-35, April 1968.
[4] Senzig, D.A. and Marsan, M., 2018. UAS Noise Certification.
[5] FAA 14 CFR Part 36 - NOISE STANDARDS: AIRCRAFT TYPE AND AIRWORTHINESS CERTIFICATION.
[6] FAA Advisory Circular 36-4D - Noise Standards: Aircraft Type and Airworthiness CertificationAdvisory Circular 36-4D - , date Issued October 12, 2017.
[7] FAA, *Details on FAA Noise Levels, Stages, and Phaseouts* Available: https://www.faa.gov/about/office_org/headquarters_offices/apl/noise_emissions/airport_aircraft_noise_issues/levels/.
[8] Aleksandraviciene, A. “MagicGrid Book of Knowledge. Kansas, 2018. NoMagic.
[9] More, “Aircraft Noise Characteristics and Metrics”, Ph.D thesis Dissertation, Purdue University, 2011.

Appendix A - Survey of Title 14, Part 21, and Part 36

Federal Aviation Administration rules are in the U.S. Code of Federal Regulations, Title 14 (14 CFR), Chapter 1. Aircraft certification procedures and noise standards are found in Subchapter C, Parts 21 and 36, respectively. Additional relevant sections of Subchapter C include the following:

- **Part 21: Certification Procedures**
- Parts 23–31: Airworthiness standards for aircraft
- Parts 33–35: Airworthiness standards for aircraft engines
- **Part 36: Noise standards**
- Part 39: Airworthiness directives
- Part 43: Maintenance
- Part 45: ID and registration marking
- Part 47: Aircraft registration
- Part 48: Registration and marking for small unmanned aircraft
- Part 49: Recording of aircraft titles and security documents

Benchmarking of current certification practices will be driven by Part 21, Part 36, and Advisory Circular 36-4D (procedures and steps for noise certification) [6]. Please note that this list of requirements is derived from the FAA standards, guidance, and practices alone. The FAA works closely with the international community to ensure their standards align with International Civil Aviation Organization (ICAO) noise regulations and adapt to changing noise mitigation technologies [7]. ICAO noise regulations (Chapter 3) used the FAA's FAR36 Stage 3 as a starting point. Other national aviation authorities, such as the European Union Aviation Safety Agency (EASA), have practices that may differ from FAA requirements.

The intent is to identify any potential gaps in the team's understanding of the noise certification procedures, or detect any equivalent procedures and accepted means of compliance that should be noted. In Figure A1, an overview of the process is summarized and divided into five phases. This review covered the mapping of all detailed procedures contained in AC 36-4D on the testing practices (the "how"), whereas Part 36 focuses on the regulatory side (the "what") for compliance.

In the following subsections, the team's findings and high-level process views are included.

Figure A1. Overview of the noise certification process, as described in Parts 21 and 36, and AC 36-4D.

Phase 0: Checking Environmental Factors
The goal of this phase is to measure and verify that the weather and testing conditions are appropriate. The process includes checking the wind velocity and abnormal meteorological conditions. In addition, the terrain must be verified to meet the appropriate FAA specifications. If a non-airport test site is sought, the test-site criteria must be followed. Figure A2 provides a visual summary of the checks that must be put in place before field setup.

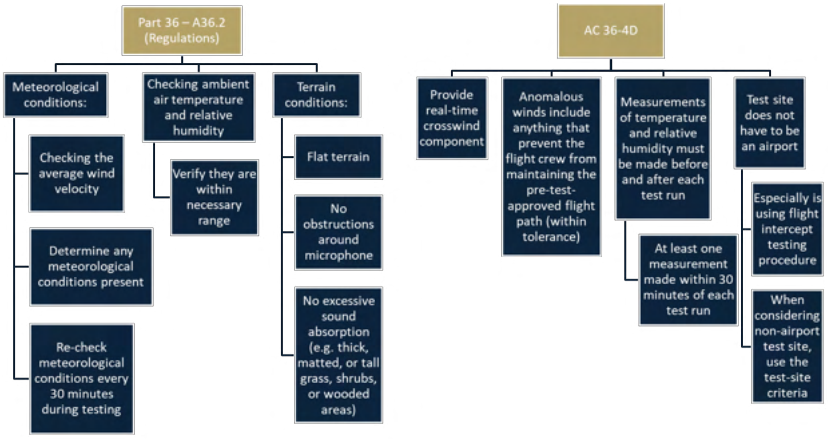

Figure A2. Phase 0: Checking environmental factors.

Based on Phase 0 benchmarking, the team prioritized the following inquiries to the industry partners in support of Task 1.2:

- Is an airport used for testing, or is there another location that is typically used? If elsewhere, where are the certification procedures completed?
- How difficult is obtaining FAA approval to conduct the test at another location besides an airport?
- If an organization has multiple certification sites, how does testing differ among them (e.g., in the number of trials needed for successful certification)?

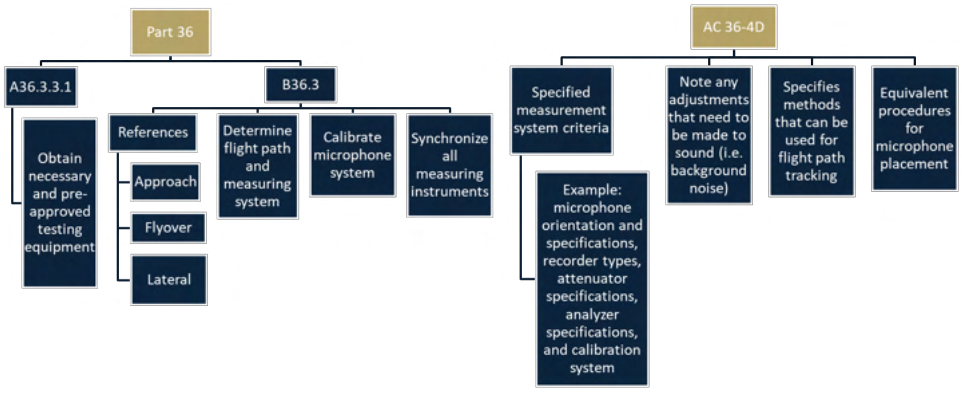

Figure A3. Phase 1: Field Setup.

Phase 1: Field Setup

For Phase 1, the field setup procedures prioritize the selection and setup of equipment, calibration, and ensuring that equivalent procedures are fully defined. Figure A3 shows the complete steps of the setup procedure. Testing equipment must be preapproved. Much of the hardware setup involves setting up the approach, takeoff, and lateral microphones, which must be calibrated. Two equivalent procedures can be used for lateral microphone placement. Flyover and approach reference points remain the same. A flight tracking system must be determined, and all measuring instruments must be synchronized.

According to Phase 1 benchmarking, the team has identified the following inquiries addressed to industry partners:

- What equipment is used for certification?
- What equipment (if any) could be seen as an opportunity for upgrading, or is potentially replaceable by a newer technology but is required to be used by the FAA?

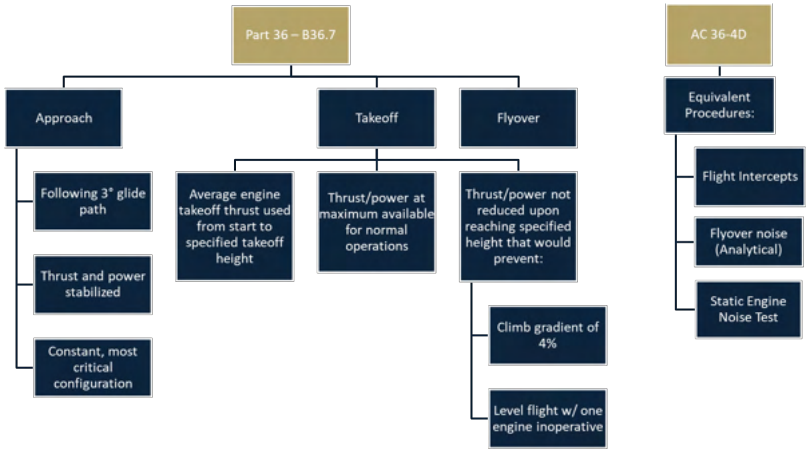

Figure A4. Phase 2: Testing.

Phase 2: Testing
Testing procedures, as listed in Part 36 and AC 36-4D, are outlined in Figure A4. The benchmarking exercise has also identified three equivalent testing procedures: flight intercepts, flyover noise, and static engine noise testing.

In lieu of the full takeoff and/or landing profiles described in A36.9.2.1 and A36.9.2.2 of Part 36, flight path intercepts can be used. This procedure eliminates the need for actual takeoffs and landings. Moreover, it leads to significant operational and cost advantages at high gross weight, while substantially decreasing the test time required and site selection issues. The shorter test time additionally provides a high probability of stable meteorological conditions, reduced wear, and reduced fuel consumption, while increasing the consistency of the data generated.

Flyover noise levels with thrust (power) reduction may also be established without making measurements during takeoff with full thrust (power) followed by thrust (power) reduction, by merging measurements of PNLT versus time measurements obtained during constant power operations.

Finally, static engine noise tests and projections to flight noise levels (403.a.3) are performed when changes are made to powerplants or similar powerplants are installed. This process is also preferred after initial noise certification of a "datum" airplane. This procedure provides sufficient additional data or source noise characteristics to enable predictions regarding the effects of changes on the airplane certification noise levels.

In summary, phase 2 requires takeoff, flyover, and approach flight tests for noise certification to be completed. Three types of equivalent procedures are recommended. When applicable, static engine noise tests are used, and flyover noise certification can be completed analytically.

As part of the team's assessment for this phase, the following inquiries were addressed to our industry partners:
- How often are equivalent procedures used instead of procedures specified in Appendix A/B?
- How many test(s) (e.g., approach, takeoff, and flyover) are usually conducted for noise certification?

Phase 3: Analysis
Phase 3 involves the analysis for determining the EPNL. This phase involves the following steps, as also outlined in detail in Figure A5:
- Find perceived noise level PNL(*k*)
- Correct for spectral irregularities
- Determine duration correction
- Determine EPNL

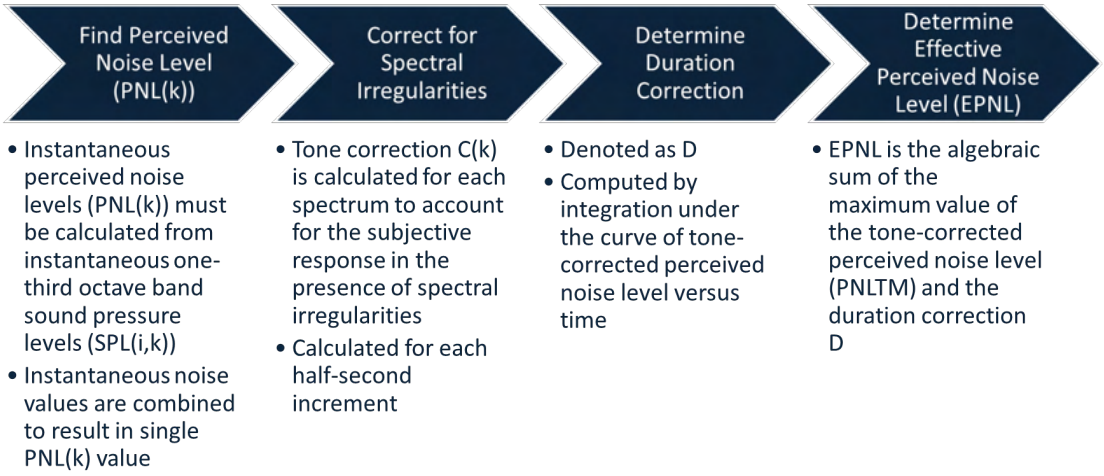

Figure A5. Phase 3: analysis steps for calculating EPNL.

EPNdb is a measure of human annoyance in response to aircraft noise, which has special spectral characteristics and persistence of sounds. The EPNL (measured in EPNdB) consists of instantaneous PNL corrected for spectral irregularities (tone-correction factor) and for duration.

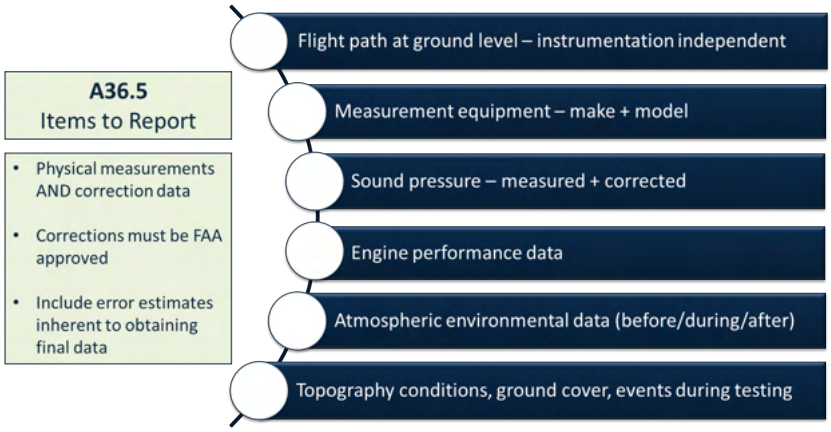

Figure A6. Phase 4: reporting.

Phase 4: Reporting

In this phase, the goal is to ensure that the correct types of data that must be recorded during analysis are selected and meet the given FAA requirements, e.g., inclusion of error estimates. This phase also determines what material must be reported for FAA inspection and approval, ranging from test data and adjustments to noise recordings and instrument calibrations. The reporting requirements based on current regulations are summarized in Figure A6.

Appendix B – Workshop Interview Questionnaires

Comprehensive Questionnaire (original version for November 2020 workshop)

SUBJECT MATTER EXPERT FEEDBACK REQUEST SHEET
Project 61: Noise Certification Streamlining – FAA ASCENT
Workshop 1 – Transport Category Aircraft
Conducted by the Georgia Institute of Technology

What is the purpose of this study and workshop?
"Noise Certification Streamlining" is Project 61 within the Center of Excellence for Alternative Jet Fuels and Environment (ASCENT), the Federal Aviation Administration Aviation Sustainability Center. The purpose of the project is to examine, and document current noise certification processes as applied by the industry and develop a more streamlined and flexible noise certification process for all applicable air vehicles. As part of this approach, the Project 61 team will seek to identify opportunities for increased efficiency and flexibility in the existing noise certification process, develop revised noise certification processes, and perform quantitative assessments. Lastly, the team will extensively apply Systems Engineering (SE) processes for complex systems, enabled by Model-Based Systems Engineering (MBSE) techniques, to facilitate certification process benchmarking and management of regulatory requirements.

The purpose of this questionnaire is to acquire Subject Matter Experts' (SME) opinions about the future of noise certification and the related research areas that should be addressed. The Project 61 team is expected to have 5-8 participants.

Who can I contact if I have questions about the study?
If you have questions, comments, or concerns about this study, you can talk to one of the researchers. Please contact Dr. Jimmy Tai (Email: jimmy.tai@ae.gatech.edu, Phone: (404) 894-0197), Dr. Evan Harrison (Email: evan.harrison@asdl.gatech.edu, Phone: (706) 401-0976), or Dr. Michael Balchanos (Email: michael.balchanos@asdl.gatech.edu, Phone: (404) 894-9799).

Research Area: Noise Certification Process

Goal: *Examine and understand current noise certification procedures and recommend guidelines to the FAA for a more streamlined and flexible noise certification process for all applicable air vehicles*

Overview
Noise certification procedures were developed in the 1960s and many parts of the regulations may reference processes and equipment that are obsolete. Consequently, many Original Equipment Manufacturers (OEMs) utilize equivalent procedures and technology not explicitly addressed in the regulations. The objective of this research is to properly document the current noise certification procedures, examine the current process and identify areas of improvement, and develop a streamlined noise certification process for all applicable air vehicles. To perform the proposed research,

Georgia Tech has teamed with several industrial partners with extensive experience in noise certification, across different classes of vehicles, ranging from large subsonic transports to business jets to rotorcraft.

The main focus for Workshop 1 will be transport category aircraft.

At present, the research team at Georgia Tech are members of two FAA Centers of Excellence: The Partnership to Enhance General Aviation Safety, Accessibility and Sustainability (PEGASAS) and the Aviation Sustainability Center (ASCENT). Through its participation in these centers, Georgia Tech has demonstrated its ability to collaborate with industry and the FAA to study various safety and certification problems and provide key understanding and insight.

Disruptors

Disruptors are defined as novel technologies or concepts of operation that are likely to disrupt the current paradigm. Based on previous benchmarking exercises and SME feedback, we have identified the following potential disruptors relevant to the current research area:

- Application of traditional Systems Engineering (SE) processes for complex systems, Model-based Systems Engineering (MBSE), and utilization these methods for the management of regulatory requirements
- Digital documentation of the noise certification process
- Modeling methods for simulating current certification process and simulation-based experimentation for testing improved and streamlined process alternatives

Are there any other disruptors or scenarios that you would include in this list?

Description of current certification practices

Noise Certification regulations contained in *Title 14* of the Code of Federal Regulations *Part 36* (14 CFR Part 36). Title 14 includes most of the regulations specifying the FAA's charter and regulations. *Part C* of Title 14 contains aircraft regulations, divided into Parts numbered 21-49 (Parts 50-59 reserved). These are the following:

- ***Part 21 – Certification Procedures***
- Part 23-31 – Airworthiness standards for aircraft
- Part 33-35 – Airworthiness standards for aircraft engines
- ***Part 36 - Noise Standards***
- Part 39 – Airworthiness Directives
- Part 43 – Maintenance
- Part 45 – ID and Registration Marking
- Part 47 – Aircraft Registration
- Part 48 – Registration and Marking for Small Unmanned Aircraft
- Part 49 – Recording of Aircraft Titles and Security Documents

Benchmarking of current certification practices will be driven by ***Part 21*** (Certification Procedures) and ***Part 36*** (Noise Standards). Please note that this list of regulatory practices is derived from the FAA methods and standards alone. They are a sub-set of the original ICAO standards. It is acknowledged that other NAAs such as EASA may have practices that may vary from FAA requirements.

What questions must be answered to describe the overall process for current noise certification practices adopted by the industry?

Q1. What is the current guidance provided by the FAA for noise certification?

a. Who is currently responsible for overseeing existing noise certification procedures?

Q2. How does a company interact with the FAA to ensure that requirements for noise are satisfied and that the vehicle is compliant?

a. How will these requirements change for different vehicles?
b. What does a nominal testing timeline look like?
c. What type of certification phases are taking place?
d. What kinds of delay factors exist? How do they affect the timeline?
e. What happens if you fail a noise certification demonstration?
f. Does your company factor in potential noise certification failures?

Q3. How does the company perform the testing, internal processes, etc.?

a. What technologies and methods are standard in support of the certification process?
b. How is data being collected, managed, and facilitated?
c. How is storage of the data handled?
d. How are the instruments calibrated? Under what schedule?
e. What is the process for acquiring and operating the right hardware?
f. How do companies decide upon the testing conditions (e.g., weather, seasonality effects, location, etc.)?

Q4. Can you identify regulations that are obsolete and should be eliminated, as well as any opportunities for improvement?

a. Can you provide an example?

Q5. Are existing certification procedures and methods sufficient to meet future configurations?

a. Can you provide an example as it relates to transport category aircraft?
b. If not, what improvements must be made and how soon should these changes be implemented?
c. Has your organization already faced any challenges to certify newer designs with the existing certification framework? If so, what aspect of the regulations were the challenges faced in?

Q6. Certification Amendments Due to Type Design Changes – If a vehicle needs to be recertified after making design changes, does your organization's approach change from the 1st round of certification?

a. Does it take almost as much time/effort as the first time, or significantly less? If the former, why do you think there is no gain in time efficiency?
b. If your organization created any models/interpretations of the original regulations (to understand them better), are these used for certification amendments due to type design changes or do you return to the full collection of original documents?
c. Are there any instances where a type design change may require a full noise certification test?

Topic 1: Benchmarking of current practices: *Transport Category Aircraft*

*Goal: Benchmark, evaluate and identify inefficiencies in current noise certification procedures for **Transport Category Aircraft** noise and provide recommendations to the FAA on streamlining certification practices.*

General

Q1.1 How many tests (e.g. Approach, Takeoff, and Flyover) do you usually conduct for noise certification?

- **a.** Are tests completed in a single day or must they be completed over multiple days?

Q1.2 Do you use an airport for testing or elsewhere?

- **a.** If elsewhere, where do you complete the certification procedures?
- **b.** How hard is it to get FAA approval to conduct the test at another location besides an airport?
- **c.** If your organization has multiple certification sites, do you see a difference between them (e.g. in number of trials needed to successfully certify)?

Q1.3 How often are equivalent procedures used instead of the procedures specified in appendix A/B?

- **a.** If you used an equivalent procedure, which procedure are you using?
- **b.** What is the main reason for using the specified equivalent procedure?
- **c.** Do you see a need to use more equivalent procedures for newly developed vehicles rather than the established versions that may need re-certification?
- **d.** Are there particular sections where equivalent procedures make more sense to use rather than the originally specified procedures?

Impact Area 1: Certification Cost

Q1.4 What is the relative breakdown of cost associated with noise certification of an aircraft?

- **a.** What percentage of the certification budget is devoted to the relative phases outlined in question 2 in the previous section?

Q1.5 What are areas in noise certification that have fluctuating costs (e.g. fuel)?

- **a.** How often do these cost fluctuations affect noise certification?
- **b.** Can you provide an example where fluctuating costs prevented the noise certification of an aircraft?
- **c.** Is there a specific configuration of aircraft that are more impacted by fluctuating costs? Why is this type of aircraft more impacted?

Impact Area 2: Certification Time

Q1.6 What sort of delays frequently occur in the certification process?

- **a.** What metrics do these delays eventually affect (e.g. revenue loss from delivery delays, unsatisfactory reports from inspectors, post-delivery issues or need to recall)?
- **b.** What role does weather/location of your facilities play in delays (if any)?

Q1.7 How much time is spent completing the certification procedure for large transport category aircraft? (e.g. hours, days, weeks, etc.)

- **a.** Are there particular sections of certification that take longer than others?

Q1.8 Where do you see an area to minimize the time taken to complete the certification process?

Q1.9 How many times a year are you conducting noise certifications?

Impact Area 3: Certification Equipment

Q1.10 What equipment does your team use for certification?

- **a.** What meteorological system is used?
- **b.** What microphones are used?
- **c.** What recording and reproducing equipment is used?
- **d.** What calibration systems are used?

Q1.11 What equipment (if any) do you see as "out of date" but are required to use by the FAA?

Q1.12 Is there a piece of equipment that you prefer to use over the specified equipment in appendix A/B?

- **a.** How long does it take for an equipment approval by the FAA?

Critical Milestones & Task Outputs

Q1.13 What process (if any) do you use to "translate" the appendix materials into requirements that are easy to check off?

Q1.14 How often is there confusion between various departments conducting noise certification?

- **a.** Do you get reports of confusion/misunderstanding from technicians or engineers who are responsible for reading the requirements from the FAA?
- **b.** Is there any confusion with the pilots who are responsible for flying the aircraft during testing?

Summary & Outcomes

Q1.15 Is there anything that is not directly specified in advisory circulations or in the FAA regulations, that is important to know when conducting transport category certification?

Topic 2: Ancillary Practices, Procedures, and Contingencies

Goal: *Please describe ancillary practice or procedures that may be required to support the certification effort but do not directly demonstrate compliance to the regulations. Do these practices shorten, lengthen, or provide economic benefit to the applicant? Also, do these practices support contingency efforts if initial efforts to demonstrate compliance are not achieved?*

Description

Q2.1 Has there ever been a project that was canceled because there was not a way to noise certify it with the FAA?

- **a.** If so, why couldn't it be noise certified?

b. Did you seek FAA approval to certify the aircraft?

Q2.2 Are there any non-regulatory procedures (e.g. anything recorded and procedural that is not required by the FAA regulations) that your team uses to certify your aircraft?

a. If so, please explain the procedure(s) in as much detail as possible.

b. Do you believe your procedures are more efficient?

i. If so, please explain why.

ii. If not, please explain the motivation for using the prescribed procedures.

Deviations from Certification Requirements of Part 36:

Q2.3 What, if any, are common alternative procedures for Part 36 noise certification? For each alternative procedure, please answer each of the parts separately.

a. What is the reason for the change?

b. What are the potential benefits of this change from the as written standard?

c. What is the process of documentation for the change?

Summary & Outcomes

Q2.4 Summary of the required outcomes for this topic area. How do the tasks from the research fill the gap described before?

Simplified Questionnaire (Used on January 2021 and after)

Topics of discussion:

- **Flight Test Preparation**
  - Negotiation process of Flight Test objectives (with FAA)
  - Is access to a Flight Test Plan document and/or Sample Test Card for a noise measurement test possible?
  - Selection of testing location (e.g., airport, and why?)
  - Up-front preparation steps
  - Detail of typical schedule (typical number of allotted days/hours & FTEs)
  - Set up of DAS/DAU and key instruments.
  - Go/No-go conditions
- **Test Execution**
  - Details of key hardware set up.
    - Microphone type selection, location.
    - Specifically, about how information is relayed.
  - General challenges during data collection
    - Physical barrier (weather, environment, etc.)
    - Common instrument issues
    - Key points of difficulty (specific data type, communication amongst teams, etc.)
  - How do the test engineers confirm test objectives were met during test?
  - Challenges of airport testing
  - Sensitivities of airport/testing site location? (e.g., data quality issues… trees, snow, freezing temperatures, moisture from humidity/rain/etc.?)

- Coordination between roles (test pilot, ATC, ground crew, test engineers, etc.)

- **Miscellaneous in planning and testing**
  - [Comment from Workshop 1]: "The 'decision process for Part 36 is not as 'easy to set up' as some of the other parts. Also, Part 36 does not 'interact very well' with the other parts, e.g., 25."
    - What decisions need to be made at different points in the certification process?
    - What does your decision process look like, is it more difficult for new aircraft?
- **Analysis & Reporting**
  - Discuss general post-test analysis method(s).
    - How to match predicted versus actual for verification.
    - Effort length and duration
  - Discussion of final artifact from flight test
  - How is the data stored with the FAA (report/database/etc.)?
  - Analysis Methods for small items: Determination of NAC
    - Is AC 36-4D the sole source of guidance and methods for small changes?
    - What tools / methods might make NAC determinations simpler?
    - Would analysis methods that allowed cumulative changes greater than 0.30 db be beneficial? (i.e., reduced flight demonstrations)

Project 062 Noise Model Validation for AEDT

Georgia Institute of Technology
The Pennsylvania State University

Project Lead Investigator

Principal Investigator
Professor Dimitri N. Mavris
Director, Aerospace Systems Design Laboratory
School of Aerospace Engineering
Georgia Institute of Technology
Mail Stop 0150
Atlanta, GA 30332-0150
Phone: (404) 894-1557
Fax: (404) 894-6596
dimitri.mavris@ae.gatech.edu

Principal Investigator
Dr. Victor W. Sparrow
Director and United Technologies Corporation Professor of Acoustics
Graduate Program in Acoustics
The Pennsylvania State University
201 Applied Science Bldg., University Park, PA 16802
Phone: (814) 865-6364
vws1@psu.edu

University Participants

Georgia Institute of Technology

- PIs: Dr. Dimitri Mavris, Dr. Michelle Kirby
- FAA Award Number: 13-C-AJFE-GIT-061
- Period of Performance: June 5, 2021, to June 4, 2022

The Pennsylvania State University

- PI: Dr. Victor Sparrow
- FAA Award Number: 13-C-AJFE-PSU-059
- Period of Performance: June 5, 2021, to June 4, 2022

Project Funding Level

The project is funded by the FAA at the following levels: Georgia Institute of Technology (Georgia Tech) $235,000, and The Pennsylvania State University (PSU) $115,000. Cost-share details are below:

Georgia Tech has agreed to a total of $235,000 in matching funds. This total includes salaries for the project director, research engineers, and graduate research assistants; and computing, financial, and administrative support, including meeting arrangements. Georgia Tech has also agreed to provide tuition remission for the students, paid for by state funds.

PSU's industrial partner, Spire Global (spire.com), is providing cost-share funds at a level of $115,000 in the form of meteorological data and research support. The point of contact for this cost-share is Mr. Cromarty [+1 (650) 300-9997, william.cromarty@spire.com].

Investigation Team

Prof. Dimitri Mavris, PI, Georgia Institute of Technology
Dr. Michelle Kirby, Co-investigator, Georgia Institute of Technology
Dr. Tejas Puranik, research faculty, Georgia Institute of Technology
Dr. Mayank Bendarkar, research faculty, Georgia Institute of Technology
Ana Gabrielian, graduate student, Georgia Institute of Technology
Emily Lembcke, graduate student, Georgia Institute of Technology
Vinh Bui, graduate student, Georgia Institute of Technology
Sabastian Abelezele, graduate student, Georgia Institute of Technology
Amber Willitt, graduate student, Georgia Institute of Technology
Jennifer Nolan, undergraduate student, Georgia Institute of Technology

Prof. Victor Sparrow, PI, The Pennsylvania State University
Harshal Patankar, graduate student, The Pennsylvania State University
Emma Shaw, graduate student, The Pennsylvania State University

Project Overview

The focus of this project is to assess the accuracy of the Aviation Environmental Design Tool (AEDT) in estimating noise both in the vicinity of airports as well as further afield. The foundation of AEDT noise modeling is based on the Integrated Noise Modeling (INM) tool, which has undergone a number of validation and verification efforts in the past, specifically at the Denver International Airport (DIA), and it has shown continually improving agreement of modeling with measurement data. During the development of AEDT, multiple algorithm updates have occurred, and this project seeks to quantify the new noise modeling capabilities based on comparison to field measurement data from DIA and other airport monitoring systems. The research team will develop a detailed model validation plan, review the plan with the FAA for concurrence, execute the plan, and make recommendations for future AEDT development. The research, once completed, is expected to provide a noise model validation benchmark that can be used not only to respond to questions on AEDT noise prediction accuracy, but also to allow the tool development team to prioritize further development of modeling features and enhancements. The research team will also collaborate with The Pennsylvania State University (PSU) on the assessment of the noise propagation assumptions and the use of higher-fidelity weather data.

Introduction and Background

Georgia Institute of Technology

The last decade has witnessed demand for air passenger services grow with a long-term average of over 5% in terms of revenue passenger miles (RPK) [1]. To mitigate the impact of this growth in aviation on the environment and to maximize the economic benefit that can be achieved from added efficiency and performance, NASA's Environmentally Responsible Aviation (ERA) project has suggested aggressive goals [2]. Within these set of goals is a target to reduce the noise emissions created by aviation over the 2015, 2020, and 2025 timeframes. The first step in mitigating noise emissions is having the capability to model them with a high level of accuracy. The FAA's AEDT (https://aedt.faa.gov/) is one of the most advanced capabilities for both modeling aircraft operations and computing the associated environmental metrics. AEDT is a software system that models aircraft performance in space and time to estimate fuel consumption, emissions, noise, and air quality consequences. AEDT's primary objective is to facilitate the environmental review of federal actions associated with changes to airport, airspace, and other applicable aviation activity.

Several past efforts have studied the improvement of modeled procedures in AEDT or the comparison between AEDT capabilities and real-world operational data. Noise abatement departure procedures (NADPs) are commonly used for mitigation of community noise either closer to the airport or further afield. Lim et al [3] provided a set of 20 different NADP profiles suitable for modeling a large variety of operations that are typically observed in the real world. Behere et al. [4-5] focused on quantifying impacts of such NADP profiles on noise modeling and identified the most representative NADP profiles. AEDT has also been used in creation of alternative rapid noise modeling tools [6-7], comparing aviation environmental impact mitigation strategies [9], and various other community noise quantification studies [9-11]. Other efforts have focused on using large amounts of real-world data to produce reduced order models for rapid computation of noise impacts [12] or for estimating the impact of average types of operations at different airports [13].

Prior studies related to noise model validation date back to AEDT's predecessor, the Integrated Noise Model (INM). Several prior efforts have focused on validation of AEDT or INM to quantify the level of agreement between model prediction and data recorded from actual operations. Page et al. [14] investigated a 1997 dataset from Denver International Airport (KDEN) to determine how INM's prediction accuracy changed with different thrust prediction methods. They found that manufacturers' look-up values of normalized thrust were the most accurate. They then used this information to improve the noise-power-distance (NPD) curves in INM from historical manufacturer data. In 2006, Forsyth and Follet [15] used the same 1997 KDEN data with an interest in updating INM's database with an emphasis on higher altitudes. Spectral classes were created as a result to correct the NPD information with respect to SAE AIR-1845 atmospheric absorption. In another study performed with the 1997 KDEN data, Plotkin et al. [16] studied options to further enhance the modeling capability by accounting for effects of weather and terrain.

Since its introduction by the FAA in 2015, numerous studies have been performed on AEDT. Hobbs et al. [17] proposed an easily implementable method for including ground cover effects on noise propagation calculations by using algorithms originally implemented in the Advanced Acoustic Model (AAM) [14]. These algorithms use optical straight-ray theory as adapted for acoustics to model noise propagation in addition to the Fresnel ellipse method. This was shown to improve noise propagation calculations compared with empirical data after using data from Portland International Airport (PDX), San Francisco International Airport (SFO), and Oakland International Airport (OAK). Downing et al. (2019) investigated a method for including terrain and manufactured structural effects in AEDT's noise propagation calculations in 2019. Three separate models were evaluated with respect to their ability to accurately predict how buildings and barriers affect aircraft noise: Traffic Noise Model (TNM) [19], SoundPLAN 7.4 (which uses ISO 9613-2), and the National Cooperative Highway Research Program's Reflection Screening Tool. After validation using data from Los Angeles International Airport (LAX) and Long Beach Airport (LGB), the TNM method was recommended as the best option because its noise calculations have similar variability and consistency as AEDT's baseline calculations. In previous research by Gabrielian et al. [20], an automated framework was demonstrated for validation of noise modeling capabilities within AEDT using real-world flight and noise monitor data. In another work, the authors studied AEDT's noise prediction capability while using high-fidelity weather data [21].

The rest of this report provides information on noise modeling data sources, AEDT assumptions, and automation capabilities developed for the current work. It also discusses the results generated for the bulk flight operations modeled along with any particular or aggregate insights.

Noise Modeling in AEDT

Georgia Institute of Technology

System-level noise modeling in this report follows the procedure detailed in previous work by the authors [20]. Two important elements to this modeling are summarized here for completeness: (A) the data sources utilized during modeling, and (B) the modeling assumptions and alternatives available for each assumption.

Data Sources Utilized

Several data sources of different fidelity can be utilized for noise modeling, ranging from simple ground-based radar observations to data fusion from multiple sensors on an aircraft itself. The two main datasets that are relevant for this paper are described below.

1. **Flight Operational Quality Assurance (FOQA)** data consists of data recorded by the airline operating the flight. The basis for the FOQA program is laid out by FAA Advisory Circular 120-82, which states "The value of FOQA programs is the early identification of adverse safety trends that, if uncorrected, could lead to accidents" [22]. To this effect, FOQA systems record large amounts of data at one recording per second (i.e., 1 Hz), with these data having been used for a number of safety-related applications in prior work [23-24]. The important elements of the FOQA data for this paper relate to the detailed time history of parameters such as altitude, speed, thrust, weight, configuration (flaps, gear), and so on, for each flight that is modeled in AEDT.
2. **Noise Monitoring Data** contains five key parameters: A unique flight ID, noise monitor locations, class of noise reading, sound exposure level (SEL), and L_max metrics of associated noise events. The flight ID in the noise monitor data allows flights to be matched to the appropriate flight from FOQA data, thereby matching the aircraft configuration and the time of the noise event with the noise metric value. The class of the noise reading identifies the confidence with which the noise reading has been matched with the corresponding flight ID. The highest confidence is marked as a class 1 reading. These locations (except for their altitude) are used in flight modeling

discussed in subsequent sections. The noise monitor data are used as a benchmark comparison for noise results calculated by AEDT.

The framework for modeling and automation developed in this paper is independent of the data source used and will only need to be modified to account for the availability of parameters in case other data sources are used. In this work, the data used is obtained from flight operations at San Francisco International Airport (KSFO) and noise monitoring readings obtained from the SFO airport noise program (https://webtrak.emsbk.com/sfo13).

Modeling Assumptions and AEDT Capabilities

Modeling in AEDT offers users multiple settings for critical assumptions related to the modeling of performance and noise. A matrix of alternatives for these options is shown in Tables 1 and 2. While the possible options and their combinations may be large, not all listed options are compatible or included in the present work. These limitations are noted while discussing the modeling assumptions individually.

Table 1. Modeling options for departure operations.

Assumption	AEDT Default	Option 2	Option 3	Option 4	Option 5
Thrust	Full	FOQA	RT05	RT10	RT15
Weight	AEDT	FOQA	Alternate Weight		
Ground Track	Standard	FOQA			
Procedure	Standard	FOQA	NADP1_1	NADP2_11	
Weather	Standard	FOQA	ASOS	High Fidelity	
Surface	Soft	Hard			
Terrain	None	Actual			
Flaps	AEDT	FOQA			
Gear	AEDT	FOQA			
NPDs	AEDT	NPD+C			

Table 2. Modeling options for arrival operations.

Assumption	AEDT Default	Option 2	Option 3	Option 4	Option 5
Thrust	Full	FOQA			
Weight	AEDT	FOQA			
Ground Track	Standard	FOQA			
Procedure	Standard	FOQA			
Weather	Standard	FOQA	ASOS	High Fidelity	
Surface	Soft	Hard			
Terrain	None	Actual			
Flaps	AEDT	FOQA			
Gear	AEDT	FOQA			
NPDs	AEDT	NPD+C			

The SFO airport is selected for the present work because the research team has access to real-world noise monitoring data from SFO. For the purpose of this study, 52 Boeing 737-800s departing and arriving SFO have been down selected.

A number of settings are available under every assumption (row) of Tables 1 and 2, which can affect the performance and noise for each flight operation. This section aims to provide a summary of each option and an idea of how it might affect the calculations. For further details, readers are referred to the AEDT technical manual [25].

1. **Thrust Settings:** The options for thrust in AEDT can be seen through some of the procedures in the FLEET database. Apart from a full thrust assumption, the true thrust value at different points along the departure or arrival is available from the FOQA data and can be used. RT15 corresponds to a 15% reduced thrust during the takeoff procedure. Investigating thrust settings upon takeoff and cutback in ASCENT Project 45 identified 15% reduced thrust as being regularly used by operators in real-world operations. This decrease in takeoff and cutback thrust results in a 30%

decrease in area of the 80 dB SEL contour for a single-aisle aircraft [26]. Other options available within AEDT include 5% and 10% reduced thrust; however, these are not studied in the present work. The final thrust option available is the actual thrust from the flight given in the FOQA data.

2. **Procedure:** The FLEET database has two types of profiles that can be used: procedural profiles and fixed-point profiles (FPPs). Procedural profiles define an aircraft's thrust, speed, and trajectory in a series of steps. These include the standard, noise abatement departure procedure (NADP)1, and NADP2. FPPs fully define the location and state of the aircraft in the sky as well as its state: thrust and speed. FPPs are used to model FOQA data within AEDT because they can include the speed and thrust from flight data.

3. **Weight:** Modified alternate weight procedures are available within AEDT that can be combined with the standard or reduced thrust procedures. FOQA weight can also be used within AEDT while using FPPs. This way, the information regarding weight, thrust, and speed can be used in one FPP for each flight modeled.

4. **Ground Track:** The ground track is the latitude and longitude points on the ground of the aircraft during its flight. The default AEDT modeling for ground tracks are straight into the airport, parallel with whichever runway the aircraft is using upon arrival, or straight out of the airport upon departure. These default settings are likely to result in incorrect predictions when compared with real-world noise observations and are therefore not included in the current analysis. The FOQA ground track data are used in the present work, which reflects the true flight paths into or leaving airports.

5. **Weather:** The default weather settings that are used in AEDT studies are located in the AIRPORT database. These settings include temperature, relative humidity, wind speed, sea-level pressure, and dew point, which affect performance and acoustic calculations. The wind direction is always assumed to be a headwind direction. Although AEDT has the capability to utilize high-fidelity weather data in multiple formats [21], the present work is limited to the default setting.

6. **Surface and Terrain:** The surface options within AEDT are available for propeller aircraft, including hard and soft surface options that affect the ground reflection and other properties in noise calculations. For the present work, the AEDT default value is assumed for these settings.

7. **Flaps and Landing Gear:** The flap and gear schedule for modeling in AEDT are provided with each of the procedures, or the flap schedule defined in the FOQA data.

8. **Noise Power Distance (NPD) Curves:** Noise calculations in AEDT rely on NPD curves derived in a process similar to that used in aircraft noise certification. Noise levels are obtained as a function of observer distance via spherical spreading through a standard atmosphere. In a noise analysis, AEDT applies other correction factors to obtain the desired sound field metrics at the location of the receiver. NPD + configuration (NPD+C) curves that may enable more accurate noise prediction due to aircraft configuration and speed changes are under study [27] and not included in the present work.

Compatibility of Settings

Of the settings discussed previously, those that are varied in this study include the procedures and profiles, thrust, and weight. It is important to note that not all of these variations are compatible with each other. For example, the FOQA FPP are incompatible with reduced thrust or alternate weight settings because the prior specify the thrust at every step and the weight at the start of the takeoff or landing segments, while the latter two settings calculate it with respect to the standard profile. Likewise, the FOQA thrust values cannot be used in a procedural profile because they are numerical (in pounds), whereas the procedural profiles require thrust type and step type definitions that subsequently produce their own thrust values. This leads to the creation of a compatibility matrix yielding the actual number of combinations for flights to be modeled. Arrivals have fewer combinations of modeling settings. The only profiles available are standard and FPP from the FOQA data, and one thrust setting is available.

In the present study, the combination of settings yields seven different jobs per noise metric for departures. For arrival modeling, it yields two different jobs for each noise metric. Running these cases on 27 departures and 25 arrivals requires some form of automation capability discussed in detail in Reference. [20] and summarized below.

Automation Capability

An automation capability was developed to handle these combinations in a more time-efficient manner. Automation is required not only in setting up the large combinations of settings within AEDT (also called pre-AEDT automation), but also for post-processing of the results generated (post-AEDT automation). The pre-AEDT automation consists of 9 SQL automation scripts as shown in Figure 1. The user specifies the profiles to be modeled (either procedural or FPP), the ground tracks, and a combination matrix. This matrix maps Profile IDs and Ground Track IDs together with runway specifications to model the correct combinations from the matrix options in Tables 1 and 2. These scripts work on multiple AEDT and user-created databases to set up the studies. Once scripts 0a through 4b have been executed, script 5 can be executed, which gathers all of the information from the previous scripts and sets up the metric results within a new AEDT study. Once the user runs all studies within the AEDT graphical user interface, the results, including performance, emissions, and noise, are exported into csv files using a batch report run tool. Each case in the combination test matrix results in four reports, which are then processed using MATLAB and Python post-processing scripts (post-AEDT automation).

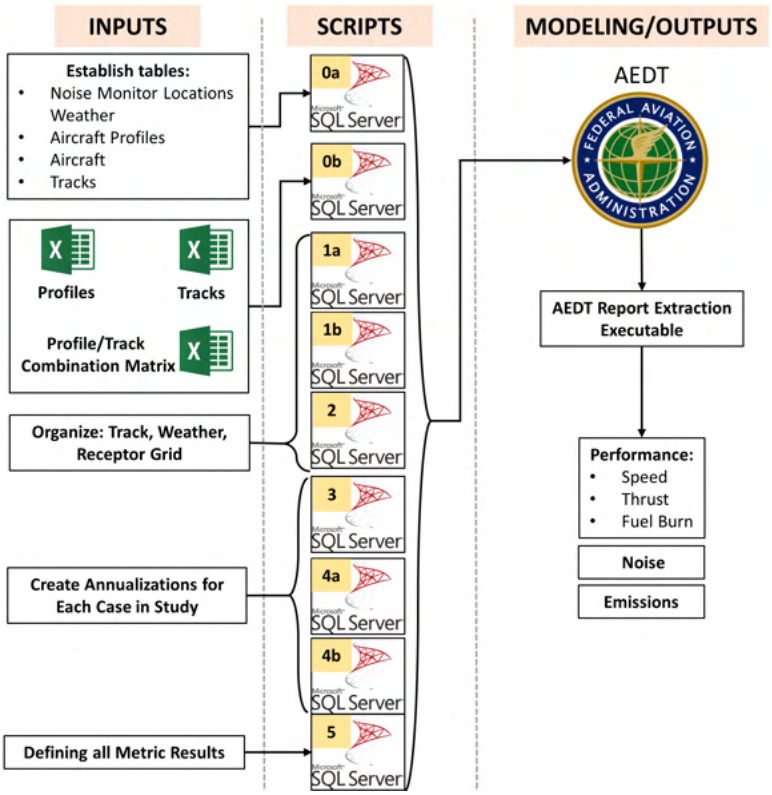

Figure 1. Noise modeling process automation steps.

Implementation of Noise Modeling Automation Framework

Georgia Institute of Technology

The modeling framework was implemented on 27 departing and 25 arriving flights at San Francisco International Airport (KSFO) using AEDT version 3c. These flights have been given arbitrary flight IDs (GT-xxx) to anonymize the real-world flight details. Figure 2 shows a map of the noise monitor locations in the SFO airport area along with their assigned IDs. All noise monitors triggered with the highest confidence (class 1) and mapped to the corresponding flight are used as truth values for comparing AEDT predictions. In this section, detailed results are provided for one departure and one arriving flight at KSFO, followed by results on AEDT prediction accuracy on a per-noise-monitor basis.

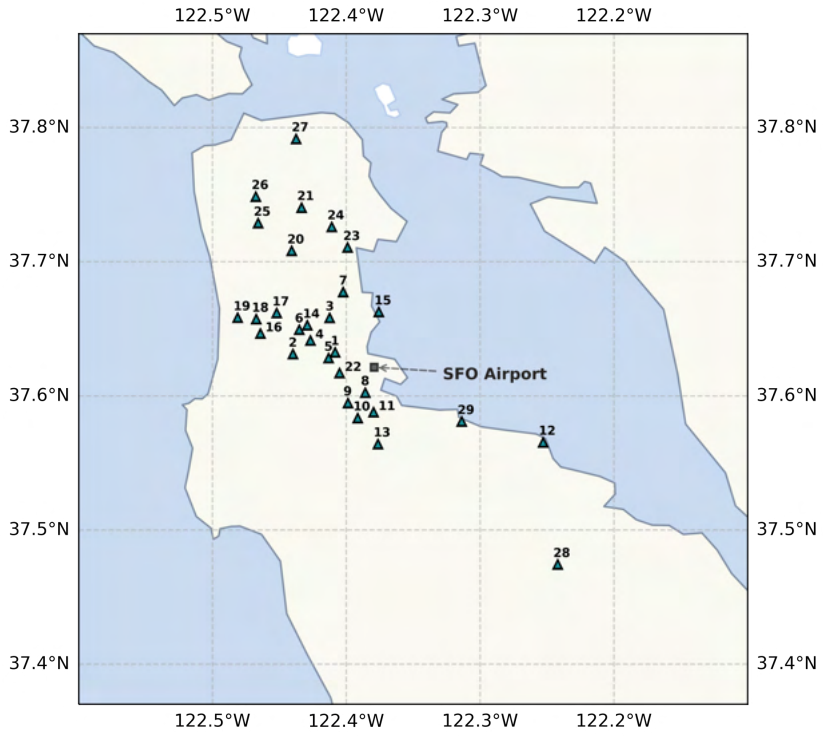

Figure 2. Location of noise monitors around San Francisco International Airport (SFO).

Although using the FOQA flight track and trajectory are expected to result in aircraft performance and noise predictions that are closest to actual, they are not necessarily always available to AEDT users. Therefore, investigating AEDT noise prediction accuracy under various modeling options is important from a usability perspective. The individual flight modeling results are elaborated in the following subsection.

Individual Flight Results

Detailed performance and noise results are available for all 52 flights, but one departure flight has been reported below as an example. Table 3 provides the AEDT airport weather parameters for the two flights of interest in the present work. AEDT airport weather uses the average annual weather and therefore is the same for both flights modeled because they operated in the same year.

Table 3. Airport weather conditions for the flights.

Weather	Temp [F]	Sea-Level Pressure [mb]	Dew Point P [F]	Relative Humidity [%]	Wind Speed [kts]	Wind Dir [°]
AEDT Default	61	1018.3	53.1	75.2	9	N/A

Flight Number: GT1015

Flight GT1015 was a Boeing 737-800 with an origin-destination pair (OD Pair) of SFO-LAX, making this a stage length 1 departure. The real-world flight data give the gross weight at takeoff as 145,591 lbs.

Figure 3 shows the performance plots for flight GT1015. This is part of the data that is extracted from AEDT using the AEDT report extraction executable. The aircraft performance using procedural profiles shows that the alternate weight reduced thrust for 15 profiles are shallower than the others, while the FOQA FPP (actual flight) is shallowest. The monitors triggered by this flight as well as the ground track can be seen in Figure 4. The noise comparison for flight GT1015 given in Figure 5 shows both underpredictions and overpredictions of the noise created at the noise monitor locations. An interesting trend is observed when the noise monitor predictions are compared to the aircraft ground track and monitor locations from Figure

3. Noise values at monitors 1, 4, 6, 18, and 19 tend to be underpredicted. They also seem to be below the aircraft flight paths. Monitors 5, 14, 16, and 17 are all further away from the flight's ground track and tend to be overpredicted. While these comparisons may not provide conclusive insights alone, they can prove valuable when aggregated across different flights and modeling assumptions.

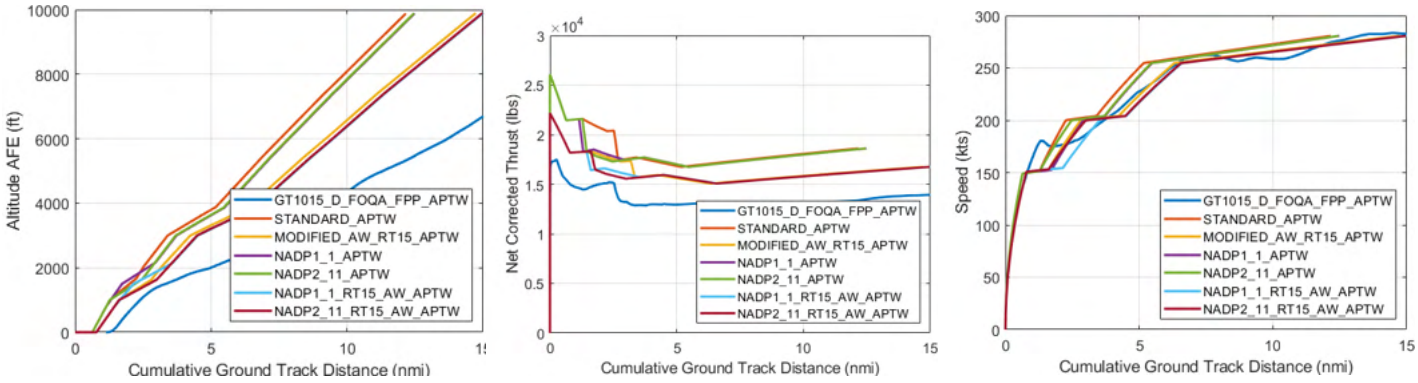

Figure 3. Altitude, thrust, and ground speed performance for flight GT1015.

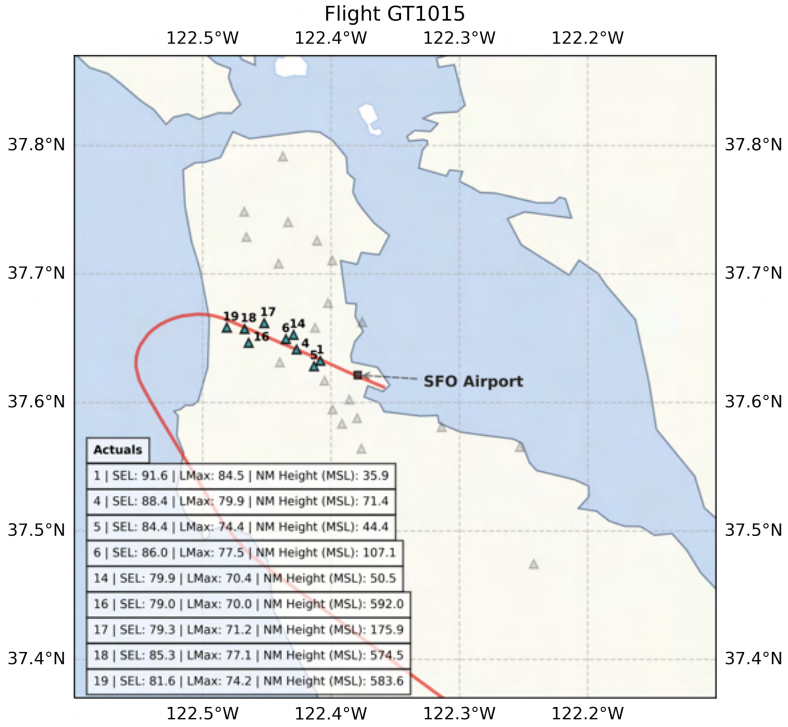

Figure 4. Trajectory and monitors triggered for flight GT1015.

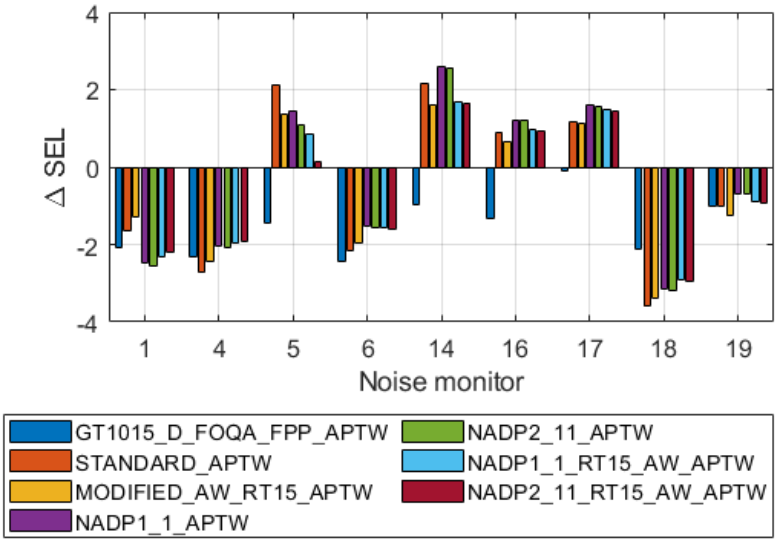

Figure 5. AEDT predicted – actual noise (dB) results for flight GT1015. SEL = sound exposure level.

Aggregate Flight Modeling Results

Individual flights can be analyzed to compare the performance and noise prediction accuracy of the different modeling options within AEDT as shown previously. To obtain more meaningful inferences, a statistical analysis of all 52 modeled flights is carried out in this section. To this end, a per-noise-monitor prediction capability was calculated using the results generated. In these, instead of viewing one flight at a time, all flights that triggered a particular noise monitor are considered. The difference between the AEDT predictions and actual noise observations for these monitors is computed and analyzed using box plots shown in Figures 6 and 7. Ideally, these box plots would show a median of zero and a small spread to show small error in predicting multiple operations compared to real-world data.

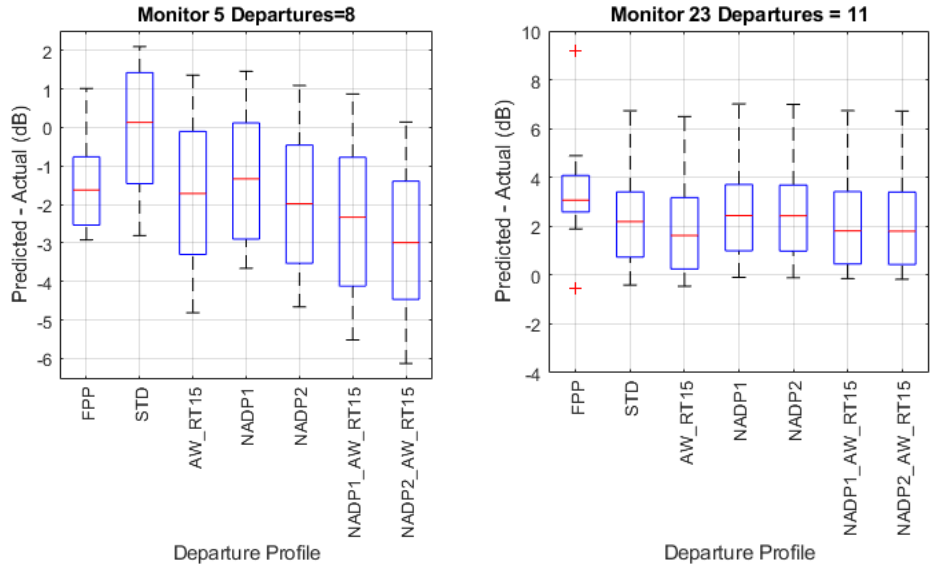

Figure 6. Predicted – actual sound exposure level (dB) noise boxplot for noise monitors 5 and 23 triggered by departing flights. FPP = fixed-point profile; STD = standard profile.

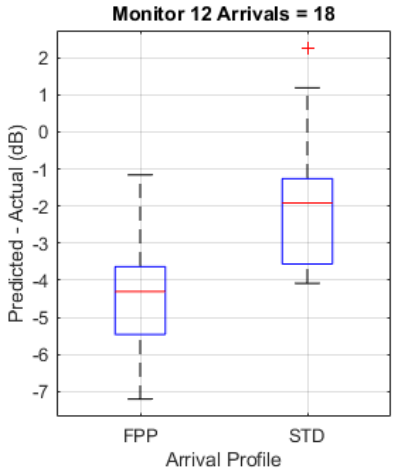

Figure 7. Predicted – actual sound exposure level (dB) noise boxplot for noise monitor 12 triggered by arriving flights. FPP = fixed-point profile; STD = standard profile.

The box plots shown in Figure 6 are generated by subtracting real-world observed SEL values from the AEDT-predicted SEL results for the 27 departures modeled. Not all flights trigger a particular monitor with class I confidence. For instance, only eight flights triggered monitor 5, whereas 11 flights triggered monitor 23. From the initial set of results of the 27 departures, it seems like the standard profile provides the best prediction accuracy for monitor 5 based on the median error being closer to 0 dB. The FOQA FPP profile provides the lowest spread between the 25% and 75% quantiles. In general, there is a trend of slight underprediction at monitor 5. For monitor 23, the overall trend seems to be slight overprediction by AEDT, with the alternate weight profiles providing results closest to actual. The FPP once again provides the lowest spread with a couple of outlier flights.

Arrivals in AEDT are modeled using just the FOQA FPPs and the standard profile. Figure 7 shows the noise results for 18 arriving flights (out of 25 modeled) that triggered monitor 12. Many of these flights flew directly over monitor 12 before touching down at SFO. Overall, AEDT modeling underpredicted the actual measurements at monitor 12, with the standard profile performing slightly better than the FOQA FPP.

The results in Figures 6 and 7 are initial and tentative results that will be updated once bulk studies of hundreds of flights have been performed within AEDT for the different modeling assumptions. They are provided here to provide a glimpse of the statistical analysis capability currently under development at Georgia Tech.

Using High-Fidelity Meteorological Data in AEDT

The Pennsylvania State University

Objective

One of the challenges in validating aircraft noise models is knowing the state of the atmosphere during field tests. In collaboration with industrial partner Spire Global (www.spire.com), the PSU team is providing relevant high-fidelity meteorological data to support the AEDT noise model validation work being conducted by Georgia Tech.

Research Approach

Spire Global has launched a fleet of low Earth orbit satellites that will provide virtual soundings of the atmosphere worldwide. Additional satellites are being launched presently, and the new meteorological data eventually will have a spatial resolution of 1 km × 1 km parallel to the ground and a vertical resolution of 500 m for every hour of the day. In contrast, the best alternative available with the same time resolution is NOAA's High Resolution Rapid Refresh (HRRR) reanalysis dataset with a 3 km × 3 km resolution, which is only available over North America [28]. In short, the GPS signals sent out by other satellites are refracted (bent) by the atmosphere, and the Spire satellites analyze the data to provide virtual soundings. This could provide a very useful resource yielding high-quality meteorological data for aviation studies.

Choice of meteorological data bundle from Spire Global

For the noise model validation work, the project team is looking at flight data and noise monitor data for KSFO. As mentioned in the 2020 annual report, the PSU team worked with Spire Global to ascertain the availability of meteorological data for the period and location of interest of the project team. The next step was to identify a meteorological data bundle from Spire Global that could be used as an input for the noise validation efforts in AEDT. At present, the publicly available version of AEDT can ingest 4-dimensional (4D; space and time) meteorological data but requires the data in a very specific structure and format. Specifically, AEDT uses geopotential heights to specify the vertical coordinate when using meteorological data. This matches the structure of the vertical grid of the data provided by the "upper-air" bundle from Spire Global; hence, this bundle was chosen for the validation work. Although the upper-air bundle contains most of the meteorological variables needed by AEDT, sea-level pressure is not included. Hence, the PSU team requested and obtained this information from Spire Global in the basic bundle, which does include the sea-level pressure data.

Preprocessing the Spire Global data before feeding it into AEDT

Although AEDT can ingest 4D meteorological data, the data first need to be converted into a structure and format that can be efficiently handled by AEDT. To achieve this, AEDT provides "weather editors" for preprocessing the meteorological data from publicly available sources. For example, AEDT can ingest data from Modern-Era Retrospective analysis for Research and Applications version 2 (MERRA-2), but the data must be preprocessed through an editor (NC4WXEditor) provided by AEDT (this is shown in the top part of Figure 8).

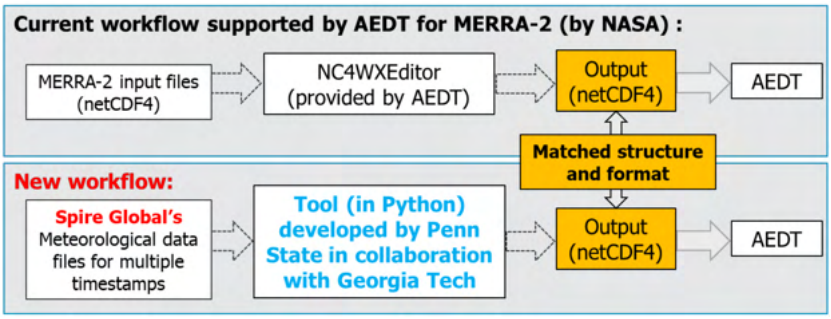

Figure 8. Using high-fidelity meteorological data in AEDT: Current and newly developed workflows. MERRA-2 = Modern-Era Retrospective analysis for Research and Applications version 2.

The Georgia Tech team previously used MERRA-2 data with AEDT and did have preprocessed versions of the MERRA-2 files (i.e., the netCDF4 output files from the weather editor). The PSU team carefully investigated these files to gain a deeper understanding of the exact format and structure of the data required by AEDT. To preprocess the meteorological files from Spire Global, PSU developed a tool written in Python (as explained in the bottom part of Figure 8). This tool combines information for multiple timestamps from the upper-air and basic bundles provided by Spire Global and converts it into a structure and format required by AEDT. The tool was tested in collaboration with Georgia Tech. The Georgia Tech team successfully ran multiple test cases in AEDT using the Spire Global meteorological data preprocessed using PSU's in-house Python code.

Working with meteorological data for a smaller geographical area and padding the data to match AEDT requirements

While attempting to match the structure and format of meteorological data as required by AEDT, the PSU team noticed that the data boundary required by AEDT spanned (at least) the whole continental US (the purple region shown in Figure 9). Spire Global noted that requesting data for the whole continental U.S. would result in a higher cost. To work around this issue, the PSU team proposed an approach of only requesting the data in the vicinity of the KSFO airport (the 100 km × 100 km area shown in red in Figure 9) and filling the rest of the grid with dummy data. The resulting meteorological data files were supplied to the Georgia Tech team. By running the same AEDT study with and without the dummy data, the Georgia Tech team confirmed that the use of dummy data did not affect the AEDT study results obtained in the vicinity of the KSFO airport.

Finally, using the data provided by Spire Global (the basic and upper-air bundles) for the area around KSFO, PSU generated meteorological files for use in AEDT (for three arrival events and three departure events). These were shared with the Georgia Tech team.

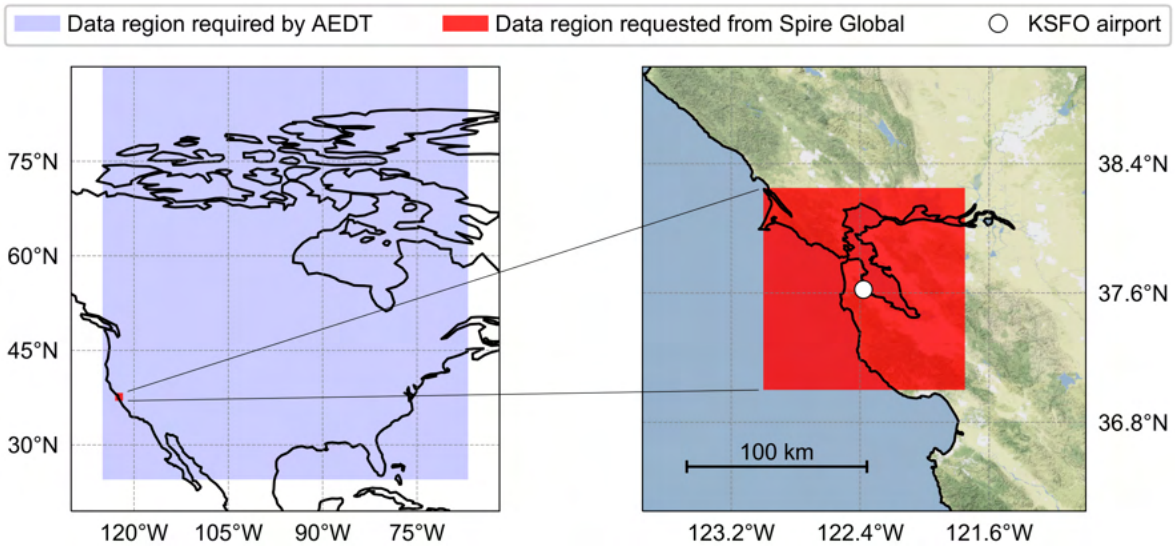

Figure 9. Maps showing (1) the region over which meteorological data is required by AEDT (shown in purple), and (2) the data region around San Francisco International Airport (KSFO) requested from Spire Global (shown in red).

Ensuring the correctness of the meteorological data and exploring alternative sources of data

To gain more confidence in the data supplied to Georgia Tech, the Penn State team compared the Spire Global data with data obtained from ERA5 (obtained from the European Centre for Medium-Range Weather Forecasts [29]). The Spire Global data and the meteorological data from ERA5 do not have the same spatial resolution; hence, a comparison was made at grid points common to both datasets. As an example, a spatial grid point closest to KSFO was chosen (latitude 37.5˚ N, longitude 122.5˚ W). The meteorological data were obtained for August 14, 2019, at 00:00 UTC. A comparison between the two datasets is shown in Figure 10. The strong agreement in temperature and humidity profiles is reassuring. The wind profiles seem to be more sensitive to the source of the meteorological data and the forecasting model used. Nevertheless, the good comparison between the data from ERA5 and Spire Global indicates that the PSU team is reading both datasets correctly and we have confidence in the meteorological data provided to Georgia Tech. This exercise also demonstrates that if Spire Global data are not available for any reason, the ERA5 data could be used as a substitute. The PSU team is also aware and capable of reading meteorological data from other publicly available sources such as HRRR [28].

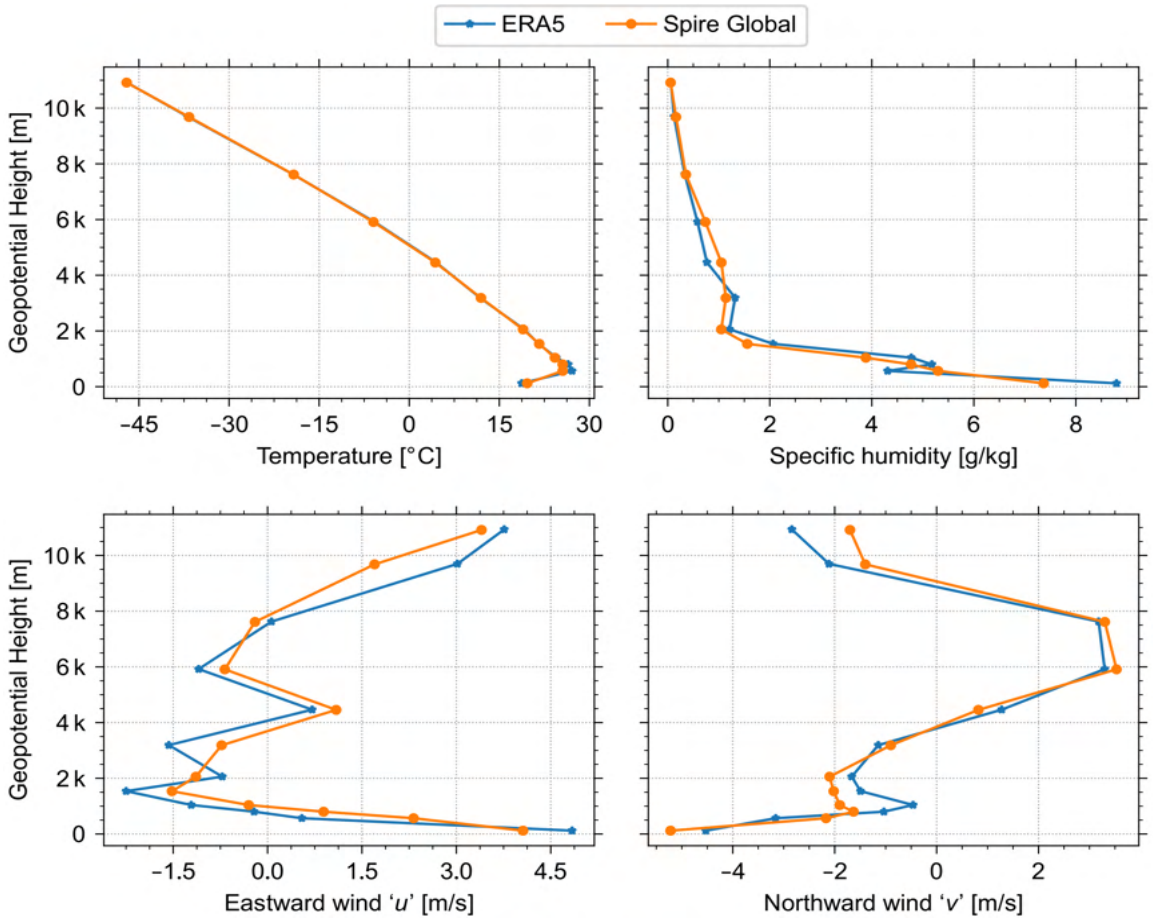

Figure 10. Comparing meteorological data from Spire Global's upper-air bundle and ERA5 (vertical grids of both data sources are not the same; hence, the figures show only the grid points common to both).

Beginning a new effort regarding AEDT's atmospheric absorption and acoustic impedance adjustments

Starting in the summer of 2021, PSU team began looking at methods to incorporate high-fidelity meteorological data into the atmospheric absorption and acoustic impedance adjustments that are used to make noise level predictions in AEDT. The PSU team has developed in-house ray tracing codes that might help improve the accuracy of AEDT noise predictions, but it is likely that incorporating those methods might slow down AEDT's noise calculation runtimes. Alternatively, using the high-fidelity meteorological data to modify the existing acoustic impedance and atmospheric absorption adjustments already utilized in AEDT might yield more accurate noise calculations while adding few additional calculations, preserving AEDT's current calculation speed.

High-fidelity meteorological data from Spire Global were accessed using Python scripts, giving the research team the ability to view data collected for multiple variables over the area surrounding the SFO airport. The data that have been collected and opened can be used to calculate multiple acoustic properties of the air, most notably the acoustic impedance and atmospheric absorption adjustments used within AEDT. Both of these properties are used in calculating noise levels. Thus far, the research team has developed maps of acoustic impedance adjustment over and around the SFO airport and are assessing the correctness and usability of those maps for possible incorporation into AEDT noise predictions.

Milestones
None.

Major Accomplishments
(Note that the project started in July 2020)
Georgia Tech accomplishments
- Completed the successful implementation of AEDT automation pipeline for (1) modeling real-world flights at various settings, and (2) extracting and visualizing results from noise modeling efforts
- Successfully ran 52 flights at all identified settings from the test matrix and ran over 300 flights with the reduced set of modeling settings
- Coordinated with PSU team to provide flight data required for tasks relevant to PSU tasks

PSU accomplishments
- Successfully wrote a tool in Python to convert Spire Global data into a structure and format usable by AEDT
- Obtained high-fidelity meteorological data from Spire Global, processed the data, and provided it to Georgia Tech for three departure and three arrival events
- Demonstrated the ability to obtain meteorological data from alternative sources
- Initiated a study on high-fidelity meteorological data affecting AEDT's atmospheric absorption and acoustic impedance adjustments

Publications
None

Outreach Efforts
Held biweekly calls with the FAA, Volpe, and ATAC, and participated in biennial ASCENT meetings.

Awards
None

Student Involvement
Georgia Institute of Technology
Graduate research assistants: Ana Gabrielian, Emily Lembcke, Vinh Bui, Sabastian Abelezele, Amber Willitt.
Undergraduate student: Jennifer Nolan

The Pennsylvania State University
Graduate research assistants: Harshal Patankar, Emma Shaw.

Plans for Next Period
The primary focus for the next period will be on the following:
- GT will continue to model the remaining flights that have been matched with corresponding noise monitor data at all the identified settings in AEDT.
- GT will provide insights into statistical significance of results at various noise monitoring stations.
- GT will build an interactive dashboard that contains the modeling results with all different settings combined for performing trade-off studies.
- PSU plans to continue supporting the Georgia Tech team, considering the differences in AEDT noise predictions with and without high-fidelity weather and assessing whether updating the atmospheric absorption and acoustic impedance adjustments with high-fidelity weather has a noticeable effect on AEDT noise predictions.

References
[1] Juniac, A. d., "IATA Annual Review 2018," retrieved July 4, 2019, [Online]. Available: https://www.iata.org/publications/Documents/iata-annual-review-2018.pdf, 2018.Suder, K., "Overview of the NASA Environmentally Responsible Aviation Project's propulsion technology portfolio,"48thAIAA/ASME/SAE/ASEE Joint Propulsion Conference & Exhibit, 2012, p. 4038.

[3] Lim, D., Behere, A., Jin, Y.-C., Li, Y., Kirby, M., Gao, Z., and Mavris, D. N., "Improved Noise Abatement Departure Procedure Modeling for Aviation Environmental Impact Assessment," AIAA Scitech 2020 Forum, 2020. doi:10.2514/6.2020-1730.
[4] Behere, A., Lim, D., Li, Y., Jin, Y.-C., Gao, Z., Kirby, M., and Mavris, D. N., "Sensitivity Analysis of Airport level Environmental Impacts to Aircraft thrust, weight, and departure procedures," AIAA Scitech 2020 Forum, 2020. doi:10.2514/6.2020-1731.
[5] Behere, A., Isakson, L., Puranik, T., Li, Y., Kirby, M., and Mavris, D. N., "Aircraft Landing and Takeoff Operations Clustering for Efficient Environmental Impact Assessment," AIAA Aviation 2020 Forum, 2020. doi:10.2514/6.2020-2583.
[6] LeVine, M. J., Lim, D., Li, Y., Kirby, M., and Mavris, D. N., "Quantification of Error for Rapid Fleet-Level Noise Computation Model Assumptions," Journal of Aircraft, Vol. 56, No. 4, 2019, pp. 1689–1696. doi:10.2514/1.C035169.
[7] Monteiro, D. J., Prem, S., Kirby, M., and Mavris, D. N., "React: A Rapid Environmental Impact on Airport Community Tradeoff Environment,"2018 AIAA Aerospace Sciences Meeting, 2018. doi:10.2514/6.2018-0263.
[8] LeVine, M. J., Bernardo, J. E., Pfaender, H., Kirby, M., and Mavris, D. N., "Demonstration of a Framework for Comparing Aviation Environmental Impact Mitigation Strategies," Journal of Aircraft, Vol. 56, No. 3, 2019, pp. 1116–1125. doi:10.2514/1.C035170.
[9] Yu, A., and Hansman, R., "Approach for Representing the Aircraft Noise Impacts of Concentrated Flight Tracks," AIAA Aviation2019 Forum, 2019. doi:10.2514/6.2019-3186.
[10] Salgueiro, S., Thomas, J., Li, C., and Hansman, R. J., "Operational Noise Abatement through Control of Climb Profile on Departure," AIAA Scitech 2021 Forum, 2021. doi:10.2514/6.2021-0007.
[11] Thomas, J. L., and Hansman, R. J., "Framework for Analyzing Aircraft Community Noise Impacts of Advanced Operational Flight Procedures," Journal of Aircraft, Vol. 56, No. 4, 2019, pp. 1407–1417.
[12] Behere, A., Rajaram, D., Puranik, T. G., Kirby, M., and Mavris, D. N., "Reduced Order Modeling Methods for Aviation Noise Estimation," Sustainability, Vol. 13, No. 3, 2021. doi:10.3390/su13031120.
[13] Behere, A., Bhanpato, J., Puranik, T. G., Kirby, M., and Mavris, D. N., "Data-driven Approach to Environmental Impact Assessment of Real-World Operations," AIAA Scitech 2021 Forum, 2021. doi:10.2514/6.2021-0008.
[14] Page, J. A., Hobbs, C. M., Plotkin, K. J., and Stusnick, E., "Validation of aircraft noise prediction models at low levels of exposure," Report NASA/CR-2000-210112, NASA, April 2000. Retrieved 27 Oct 2021, [Online]. Available: https://ntrs.nasa.gov/api/citations/20000068518/downloads/20000068518.pdf
[15] Forsyth, D. W., and Follet, J. I., "Improved Airport Noise Modeling for High Altitudes and Flexible Flight Operations," 2006.
[16] Plotkin, K. J., Page, J. A., Gurovich, Y., Hobbs, C. M., et al., "Detailed weather and terrain analysis for aircraft noise modeling," Tech. rep., John A. Volpe National Transportation Systems Center (US), 2013
[17] Hobbs, C. M., Gurovich, Y. A., Boeker, E., Hasting, A., Rapoza, A., Page, J., and Senzig, D., "Improving AEDT Noise Modeling of Mixed Ground Surfaces," Tech. rep., 2017
[18] Downing, J. M., Calton, M. F., Page, J. A., and Rochat, J. L., "Improving AEDT Modeling for Aircraft Noise Reflection and Diffraction from Terrain and Manmade Structures," Tech. Rep. ACRP 02-79, TRB, 2019.
[19] Hastings, A. L., "Traffic Noise Model 3.0 - Technical Manual," Tech. Rep. FHWA-HEP-20-012, U.S. Department of Transportation, Volpe National Transportation Systems Center, Cambridge, MA, December 2019
[20] Gabrielian, A. B., Puranik, T. G., Bendarkar, M. V., Kirby, M., Mavris, D., and Monteiro, D., "Noise Model Validation using Real World Operations Data,"AIAA AVIATION Forum, 2021. doi:10.2514/6.2021-2136.
[21] Gabrielian, A., Puranik, T., Bendarkar, M., Kirby, M., and Mavris, D., "Validation of the aviation environmental design tool's noise model using high fidelity weather," 2021, pp. 4810–4822. doi:10.3397/IN-2021-2846.
[22] "Advisory Circular, 120-82 - Flight Operational Quality Assurance," , April 2004. Url: https://www.faa.gov/regulations_policies/advisory_circulars/index.cfm/go/document.information/documentID/23227
[23] Puranik, T. G., and Mavris, D. N., "Anomaly Detection in General-Aviation Operations Using Energy Metrics and Flight-Data Records," Journal of Aerospace Information Systems, Vol. 15, No. 1, 2018, pp. 22–35. doi:10.2514/1.I010582.
[24] Lee, H., Madar, S., Sairam, S., Puranik, T. G., Payan, A. P., Kirby, M., Pinon, O. J., and Mavris, D. N., "Critical Parameter Identification for Safety Events in Commercial Aviation Using Machine Learning," Aerospace, Vol. 7(6), 2020, p. 73.doi:10.3390/aerospace7060073.
[25] Ahearn, M., Boeker, E., Gorshkov, S., Hansen, A., Hwang, S., Koopmann, J., Malwitz, A., Noel, G., Reherman, C. N., Senzig,D. A., et al., Aviation Environmental Design Tool (AEDT) Technical Manual Version 2c, FAA, 2016.
[26] Mavris, D., Kirby, M., Lim, D., Li, Y., Pfaender, H., Levine, M., Brooks, J., Behere, A., Gao, Z., Chan Jin, Y., and Kim, J. "Project 045 Takeoff/Climb Analysis to Support AEDT APM Development," Tech. Rep. ACRP 02-79, ASCENT, 2018.

[27] Mavris, D., “Project 043 Noise Power Distance Re-Evaluation,” 2019. URL: https://s3.wp.wsu.edu/uploads/sites/2479/2020/05/ASCENT-Project-043-2019-Annual-Report.pdf, last accessed 14 June 2020.
[28] Horel, J., and B. Blaylock. "Archive of the High-Resolution Rapid Refresh model." *University of Utah: Salt Lake City, UT, USA* (2015).
[29] Copernicus Climate Change Service (C3S) (2017): ERA5: Fifth generation of ECMWF atmospheric reanalyses of the global climate. Copernicus Climate Change Service Climate Data Store (CDS), *Accessed in February/March 2020*. https://cds.climate.copernicus.eu/cdsapp#!/home

Project 063 Parametric Noise Modeling for Boundary Layer Ingesting Propulsors

Georgia Institute of Technology

Project Lead Investigator

Principal Investigator:
Professor Dimitri N. Mavris
Director, Aerospace Systems Design Laboratory
School of Aerospace Engineering
Georgia Institute of Technology
Phone: (404) 894-1557
Fax: (404) 894-6596
Email: dimitri.mavris@ae.gatech.edu

Co-Principal Investigator:
Dr. Jonathan Gladin
Chief, Propulsion and Energy Division
Aerospace Systems Design Laboratory
School of Aerospace Engineering
Georgia Institute of Technology
Phone: (404) 894-5788
Fax: (404) 894-6596
Email: jgladin3@gatech.edu

University Participants

Georgia Institute of Technology

- P.I.(s): Dr. Dimitri N. Mavris, Dr. Jonathan Gladin
- FAA Award Number: 13-C-AJFE-GIT-064
- Period of Performance: October 1, 2020 to September 30, 2021
- Task(s):
    1. Literature review and problem parameterization
    2. Development of a parametric noise model
    3. Model validation exercises
    4. Tool documentation

Project Funding Level

The project funding amount is $300k from the FAA with a cost-share match of $300k from Georgia Tech.

Investigation Team

Dr. Jonathan Gladin, Research Engineer II: Co-PI, overall task lead (Tasks 1 and 4)
Dr. Miguel Walter, Research Engineer II: Technical aeroacoustics lead, Task 2 and Task 3 lead
Dr. Jai Ahuja, Research Engineer II: RANS computational fluid dynamics (CFD) design lead
Mr. Ross Weidman, Graduate Research Assistant: CAD and geometry
Mr. José Zavala, Graduate Research Assistant: CFD analysis
Mr. Grant Stevenson, Graduate Research Assistant: Aeroacoustics

Project Overview

A previous work by Clark et al. (https://doi.org/10.2514/6.2018-3124) presents a first-cut approach for quantifying the impact of boundary layer ingestion (BLI) due to distortions based on experiments; however, several factors may call such approaches into question. The first factor is the validity of an open rotor experiment for predicting the sound pressure level (SPL) impact to represent the tonal noise impact on an embedded turbofan engine. The second factor is the fact that there are many ways to achieve BLI, and interactions may vary significantly depending on the type and quantity of the distortion ingested and varying fan applications, such as applications for ducted electric fans, propellers, or turbofan engines. Therefore, Georgia Tech proposes to close this gap in the literature by developing a parametric fan noise module for a generic BLI propulsor based on the specifics of the BLI configuration and propulsor design. Parameters influencing the model will include distortion intensity, character (i.e., radial vs. circumferential), frequency, multiple-per-rev, fan design parameters, location on the airplane, embedded vs. flush mounted, and potentially other relevant physical parameters. The module will attempt to quantify the impact of BLI on turbulent ingestion and mean flow distortion noise based on lower-order methods but will seek to validate such methods against higher-fidelity approaches and publicly available experimental datasets, such as those used in the above paper or others. The module will also seek to model the effects of ducted vs. unducted shielding of BLI noise sources to quantify the validity of using “equivalent” experimental data sources for BLI approximations. A validation exercise will be conducted whereby the lower-order methods are tested against higher-fidelity analyses for a D8/HWB-type ingestion configuration and compared against empirical approaches.

Task 1 – Literature Review and Problem Parameterization

Georgia Institute of Technology

Objective

The objective of this task is to research existing approaches for quantifying noise sources related to BLI fans and to determine an appropriate modeling approach for the parametric modules. The approach should fit within the statement of work and numerical computational budget afforded to this project.

Research Approach

The approach for this task is to scan the literature associated with BLI and distortion-related noise generation for ducted fans. Each reference will be ranked by relevance and appropriateness and will be assessed to determine whether it is directly applicable or usable.

Literature Review Results

A literature review on BLI, noise generation and prediction, model validation, and other related topics was conducted. The topics and research goals covered within a subset of the review are shown in Table 1. Most of the researched literature involved BLI, noise prediction, experimental validation, and numerical modeling. One limitation was the difficulty in finding literature that treated turbofans instead of open rotor engines. For the numerical models found, the reports emphasized that having well-understood correlations between the upwash of different rotor blades and the turbulence space–time correlations is critical for accurate noise estimation. These correlations are critical in part because the widely used rapid distortion theory (RDT) is not as useful in cases of inhomogeneous flow distortion; in such cases, sampling the correlation function is essential as a substitute to RDT. There also may be situations in which using this correlation function as a sampling distribution considerably accelerates the computational time.

Table 1. Literature review topics.

Study Title	Topic Covered: BLI	Topic Covered: Inlet Distortions	Research Goal: Noise Prediction	Research Goal: Performance Prediction	Validation Method: Experimental Validation	Validation Method: CFD Validation	Results: Numerical Model Created	Topic Covered: Turbofans	Topic Covered: Open Rotor
- Modelling of A Boundary Layer Ingesting Propulsor	X			X			X	X	
- Predicting the Inflow Distortion Tone Noise of the NASA Glenn Advanced Noise Control Fan With a Combined Quadrupole-Dipole Model		X	X		X		X	X	
- Discretized Miller approach to assess effects on boundary layer ingestion induced distortion	X			X	X	X	X	X	
- An Analytical Model for Predicting Rotor Broadband Noise Due to Turbulent Boundary Layer Ingestion	X		X		X		X		X
- Noise Produced by Turbulent Flow into a Rotor		X	X				X		X
- Noise from a rotor ingesting a thick boundary layer and relation to measurements of ingested turbulence	X		X		X				X
- Noise from a Rotor Ingesting a Planar Turbulent Boundary Layer	X		X		X				X
- Rotor Inflow Noise Caused by a Boundary Layer: Inflow Measurements and Noise Predictions	X		X		X				X
- Enhanced Fan Noise Modeling for Turbofan Engines			X		X		X	X	

Problem Parameterization and Approach

Based on the literature review results, an approach to parameterize the problem was developed. To develop a noise module that parametrically accounts for the impact of BLI across a range of different applications, this module was developed using a "delta" approach. This approach will utilize a baseline non-BLI fan noise prediction from NASA's Aircraft Noise Prediction Program (ANOPP) tool and will attempt to correct noise based on a semi-empirical model that accounts for the impact of BLI on fan noise. To achieve this goal, the Georgia Tech team proposes to use computational aeroacoustics to capture the acoustic impact of BLI parametrically, starting with one BLI configuration/architecture: a BLI tail cone thruster similar to NASA's STARC-ABL concept. This aim will be accomplished by parametrizing the modeling approach according to Figure 1.

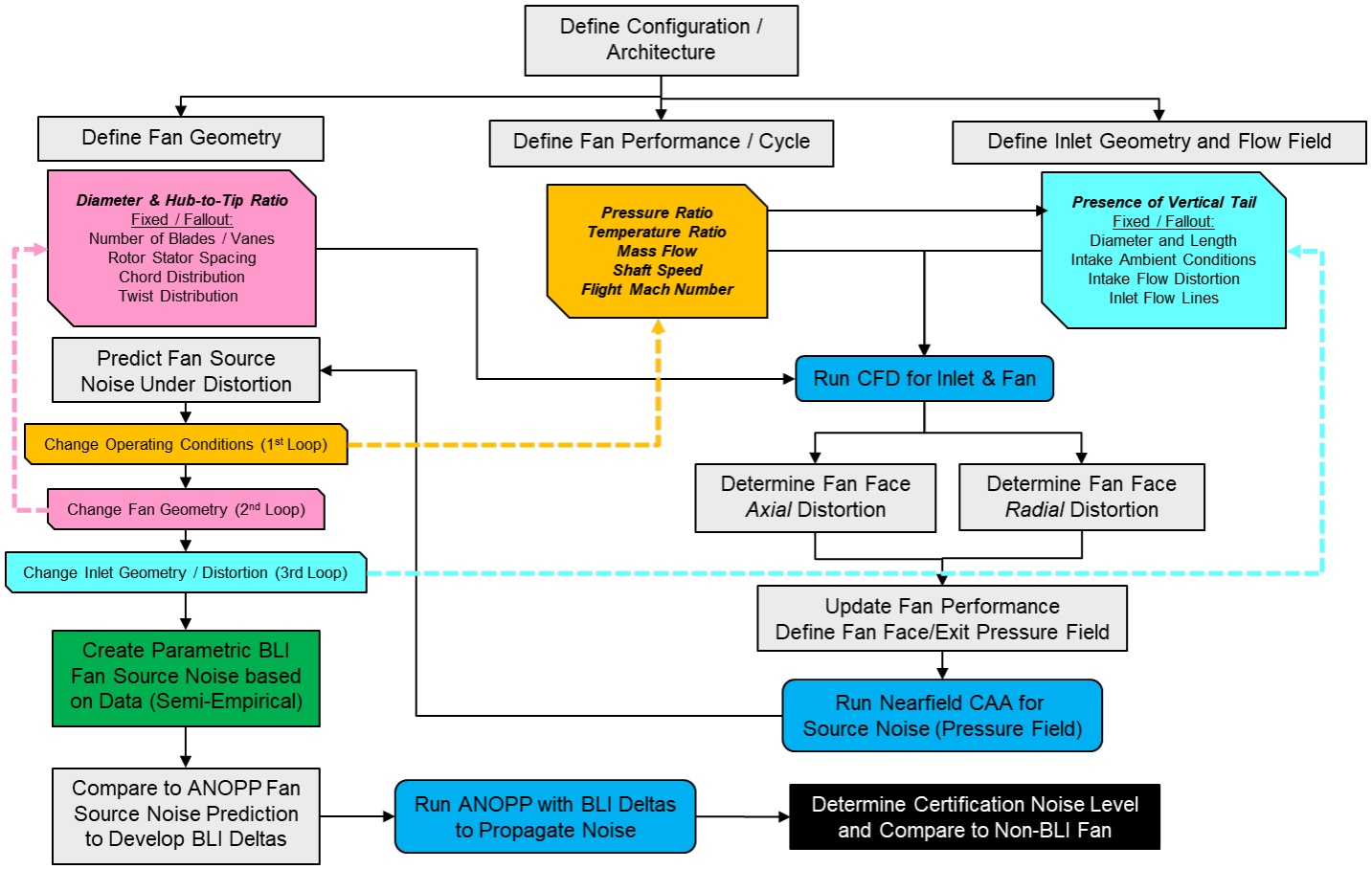

Figure 1. Proposed modeling approach to create a parametric BLI noise module.

To capture the sensitivity of the noise impact to a wide range of BLI conditions, we will attempt to capture the acoustic impact of BLI for various fan geometries, operating conditions, and flow fields. To achieve the required number of runs needed to develop such a noise model, the scope of the varying parameters under each category was limited.

Milestone(s)

Task 1 has been completed.

Major Accomplishments

Task 1 was completed, and an approach for defining the methodology was established and finalized with FAA sponsor approval.

Publications

None

Outreach Efforts

The Source Diagnostic Test (SDT) geometry was retrieved from NASA. An approach for modeling noise was presented to NASA acoustic engineers, and feedback was received for this approach.

Awards
None

Student Involvement
Two graduate students are involved with this work: Ross Weidman and José Zavala. These students are graduate research assistants in their first year at Georgia Tech.

Plans for Next Period
No steps are planned for the next reporting period because the task has been completed.

Task 2 – Development of a Parametric Noise Model
Georgia Institute of Technology

Objective
The objective of this task is to develop a parametric noise model, which will be the primary deliverable for this project. This module should be compatible with ANOPP.

Research Approach
Baseline Clean Fan Geometry with the SDT Fan and Modifications
The baseline configuration chosen for the current project is based on the STARC-ABL geometry and the NASA SDT fan. The former was chosen because of its BLI effect on the rear electric propulsor, while the latter was chosen because it is a benchmark geometry for acoustic fan studies. These two geometries are integrated, with the SDT fan geometry replacing the original STARC-ABL propulsor geometry. A few modifications are needed to accomplish this integration.

The first modification concerns the NASA SDT fan. The SDT is a 1/5-scale model of a representative high-bypass turbofan, with three different vane variants. The first variant has 54 vanes, focusing on cutting-off the blade passing frequency (BPF) rotor–stator interaction tone, the second has 26 vanes cut-on for reduced broadband noise, and the third has 26 swept vanes for reduced BHP noise. The SDT, provided by NASA, for the current project is the first variant, and it is termed SDT-A hereafter. The SDT-A has a flat surface at the rear because it was developed to address fan noise only, and thus, there was not a focus on noise that would otherwise be generated from the rear part of the core. In the current project, the chosen STARC-ABL utilizes an electric propulsor at the rear of the fuselage. Because the original STARC-ABL fan geometry is replaced with that of the SDT-A, while maintaining the concept of an electric propulsor, there is no core flow. Consequently, the SDT-A geometry is modified to have a plug shape at the rear such that it resembles the original STARC-ABL propulsor. The SDT-A geometry was modified in CAD with a conical shape starting at the axial location of the trailing edge of the nacelle. The half-angle of the cone is 20°, and the cone vertex is smoothed with a small spherical cap. The resulting geometry is shown in Figure 2.

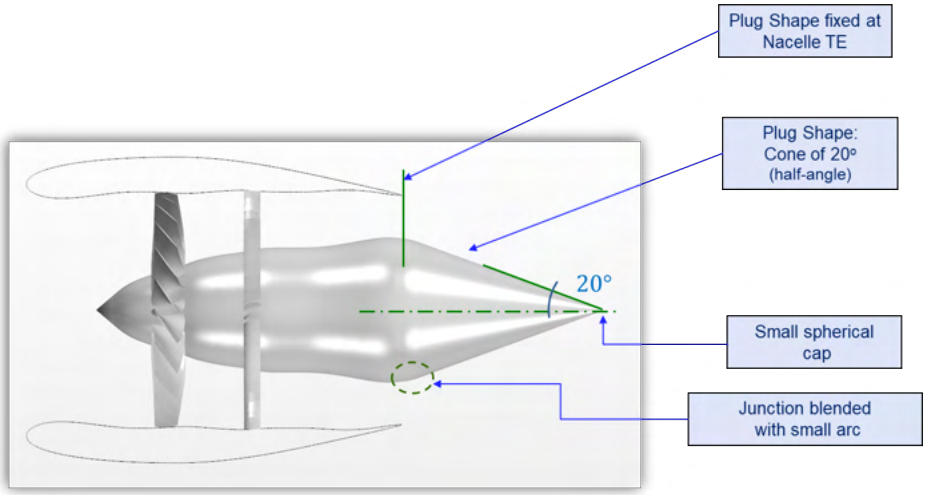

Figure 2. Modification to the SDT-A geometry.

The second modification concerns changes in the STARC-ABL fuselage so that it can be integrated with the modified SDT-A geometry. This integration uses two geometrical references to replace the original electric propulsor with that of the modified SDT-A. The first reference is the distance between the nose of the fuselage and the leading edge of the nacelle, which is held constant. The second reference is the axis of the original propulsor, which is also maintained. These geometrical references are shown in Figure 3. Next, the modified SDT-A fan geometry is scaled up by a factor of 2.7272 so that it approximately meets the dimensions at the hub of the STARC-ABL propulsor. Then, the rear part of the fuselage is modified to allow a smooth transition with the scaled and modified SDT-A geometry. These modifications are shown in Figure 4.

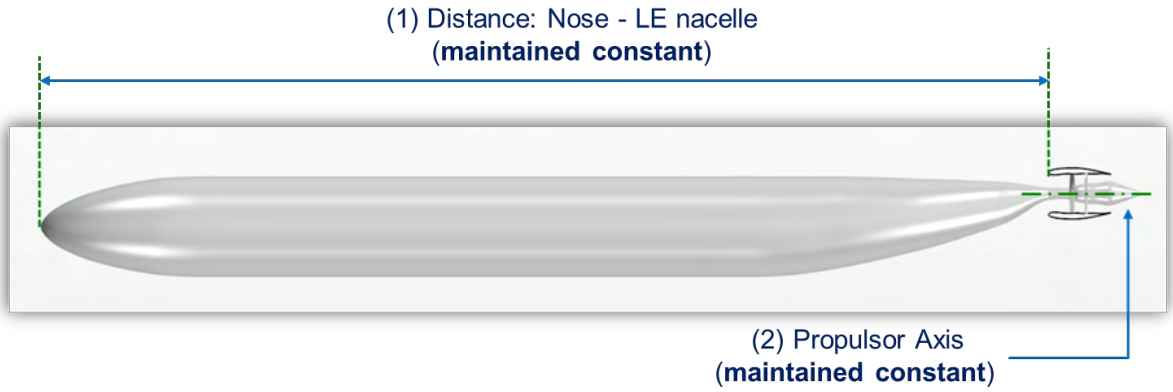

Figure 3. Geometry references for integration between the STARC-ABL and modified SDT-A.

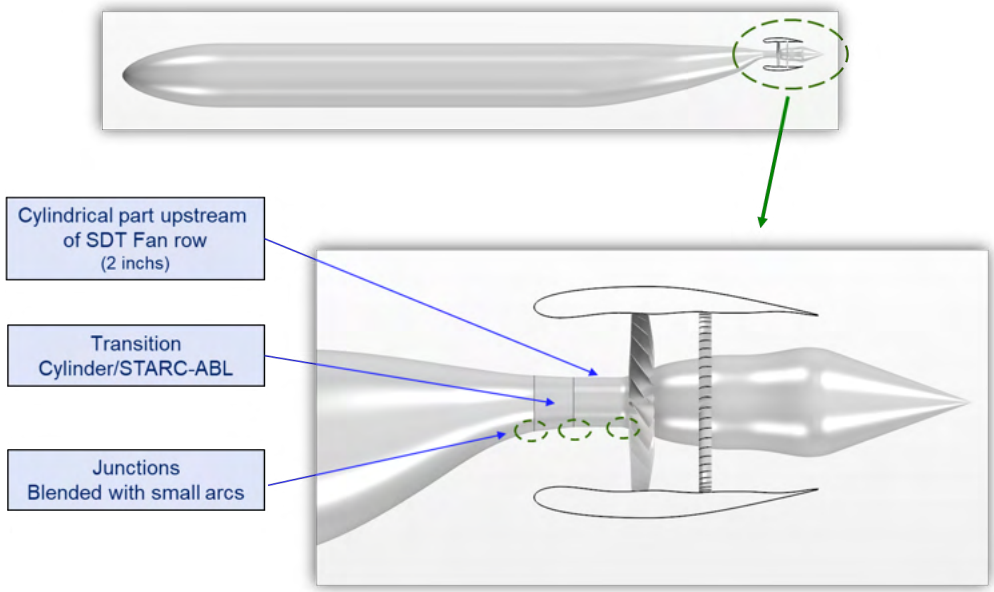

Figure 4. Modification at the fuselage for integration.

Baseline Fan Performance Model for ANOPP

To create a baseline ANOPP noise model for a ducted SDT fan, it is necessary to model the performance of the fan over a range of flight conditions. For this purpose, a fan map was digitized from the reference material for the SDT fan, as shown in Figure 5. The data points in the plots represent data digitized from the SDT results, and the lines are the output of a computer code called "CMPGEN," a NASA code that was used to approximately match the SDT fan map. This map is used to model the fan performance under off-design conditions.

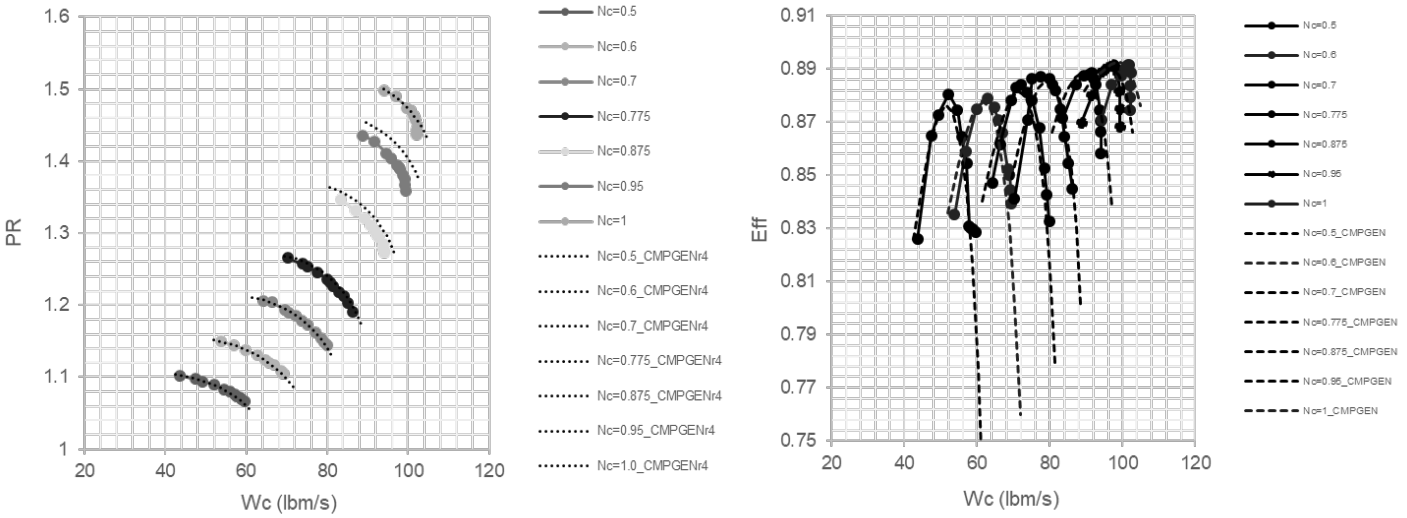

Figure 5. SDT fan map digitized from the SDT test data references. The lines represent the CMPGEN fan map performance matched to the SDT dataset.

Next, the SDT fan needed to be scaled up to the size of the STARC-ABL geometry. To perform this step, the fan shaft power was held constant at 3,500 hp, a value taken from the STARC-ABL aircraft design. The criteria for scaling was to create a geometrically similar fan with a size corresponding to 3,500 hp. The scaling exercise results are shown in Table 2. The scale factors for each of the main fan parameters are shown in the right column. The power of 3,500 hp was used to determine the fan weight flow scale factor of 5.378. Therefore, the square root of this number (2.31905) is the geometric scale factor because the corrected flow is proportional to the area, which is proportional to the radius of the fan squared. Therefore, the scale factor on the radii is 2.31905. The RPM of the machine is also adjusted to hold the tip speed of the fan constant in order to maintain a roughly constant aerodynamic performance. In this process, the stage pressure ratio and corrected specific flow are held constant. An NPSS model of the ducted fan with these specifications and the fan map above was created and then used to produce state tables to feed into the fan noise model.

Table 2. Parameters for the SDT and geometrically scaled SDT and scale factors derived to scale the fan.

Parameter	SDT	Scaled SDT	Scale Factor
Tip Diameter	22 in	51.0191 in	2.31905
Hub Diameter	6.6 in (assuming 0.3 h/t ratio)	15.30573 in	2.31905
Corrected Rotational Speed	12657 rpm	5457.83 rpm	1/2.31905
Corrected Tip Speed	1,215 ft/s	1,215 ft/s	1.0
Corrected Fan Weight Flow	100.5 lbm/sec	540.49	5.378 (2.31905^2)
Corrected Specific Flow	41.8 lbm/sec-ft^2	41.8 lbm/sec-ft^2	1.0
Stage Pressure Ratio	1.47	1.47	1.0

Baseline Fan Noise Model

Before developing the parametric noise model, a baseline ANOPP noise model was created using only the fan's performance and geometry. This ANOPP model was used to predict the hard-wall forward and aft fan noise, using the Heidmann fan noise module within ANOPP. The baseline noise model will be used alongside a computational aeroacoustics model, with the results for an identical non-BLI baseline case used to create a set of "baseline deltas" between ANOPP and computational aeroacoustics (CAA) results. These deltas will serve as a calibration tool for developing the BLI integrated model. This step is applied to ensure that the application of the module within ANOPP is accurately captured, only the magnitude of the BLI impact on noise is represented, and the variance due to the different modeling methods is limited. An outline of this process is shown in Figure 6.

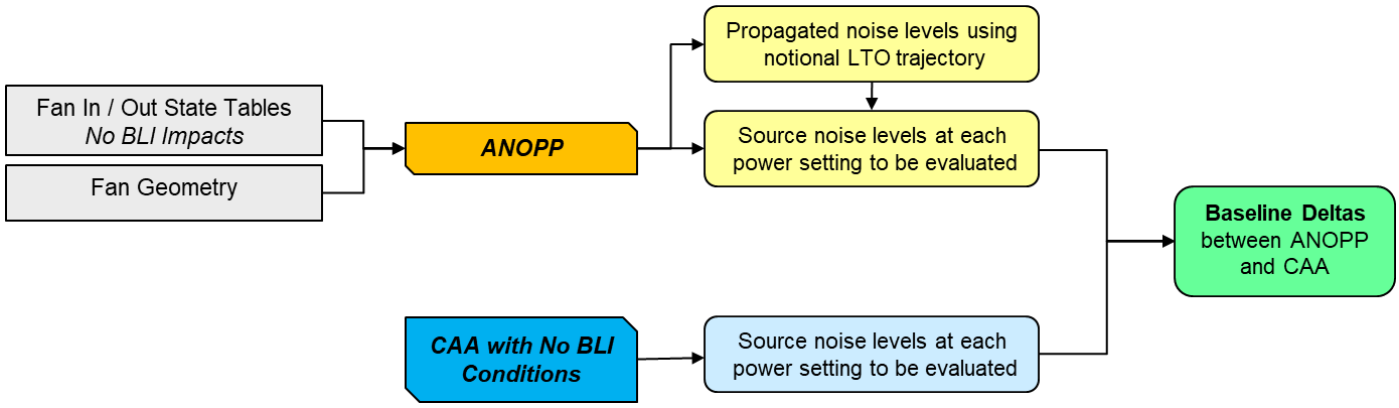

Figure 6. Modeling process to capture differences between ANOPP and CAA.

The baseline noise model was designed around three representative flight conditions for noise certification: sideline, flyover, and approach. Each condition used the engine parameters given in Table 1 for fan noise estimations using the General Electric-revised Heidmann method, an updated formulation for improved large fan predictions. The resulting forward-radiated and aft-radiated noise was calculated using the NASA hard-wall engine noise estimations. For the baseline case, no additional noise sources or reflections were included. Additionally, we decided to forego modeling acoustic liners in developing the BLI noise module, with the intent of capturing the impact of BLI and removing acoustic liner assumptions.

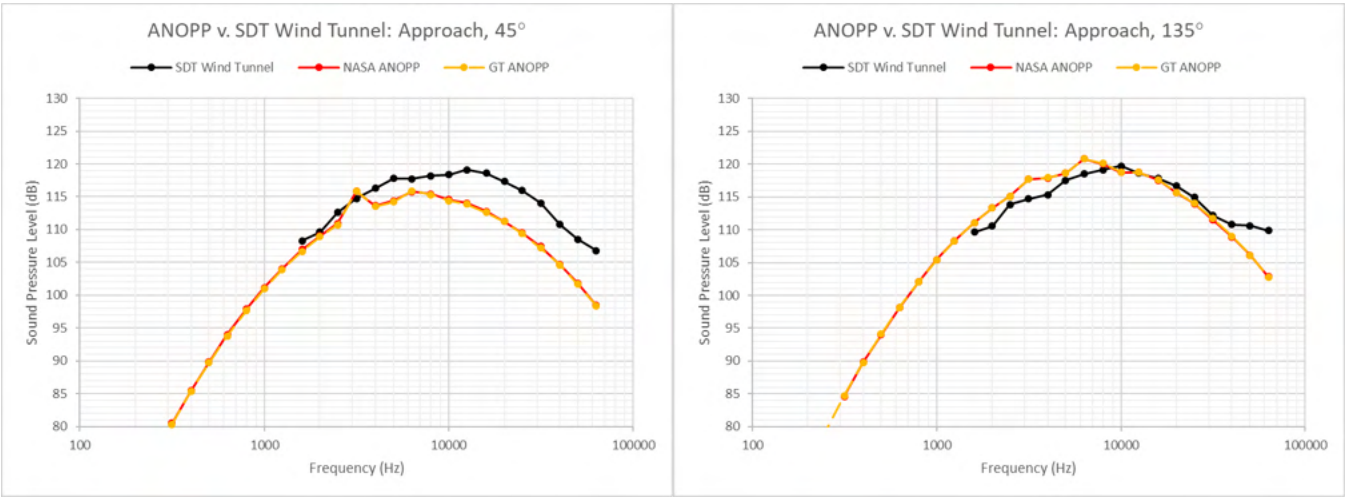

Figure 7. GT ANOPP baseline SDT model approach comparison.

Table 3. ANOPP baseline model approach error.

Comparison	GT ANOPP – EXP SDT		NASA ANOPP – EXP SDT		NASA ANOPP – GT ANOPP	
Directivity Angle	45°	135°	45°	135°	45°	135°
RMS Error (dB)	4.8579	2.5529	4.7523	2.549	0.15597	0.074428

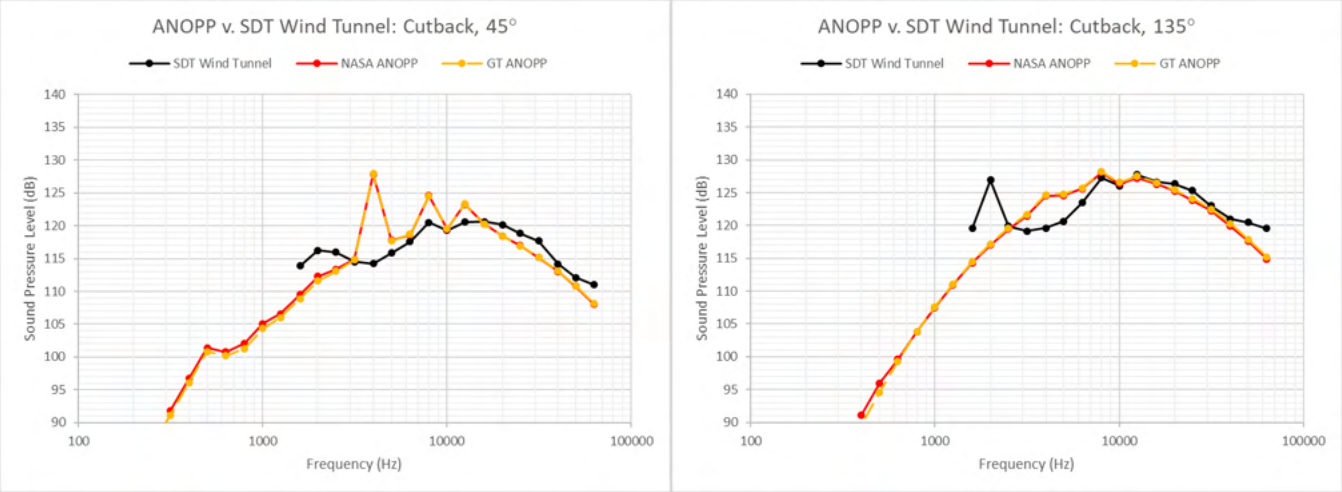

Figure 8. GT ANOPP baseline SDT model cutback comparison.

Table 4. ANOPP baseline model cutback error.

Comparison	GT ANOPP – EXP SDT		NASA ANOPP – EXP SDT		NASA ANOPP – GT ANOPP	
Directivity Angle	45°	135°	45°	135°	45°	135°
RMS Error (dB)	4.1761	3.4692	4.0591	3.5218	0.41517	0.47159

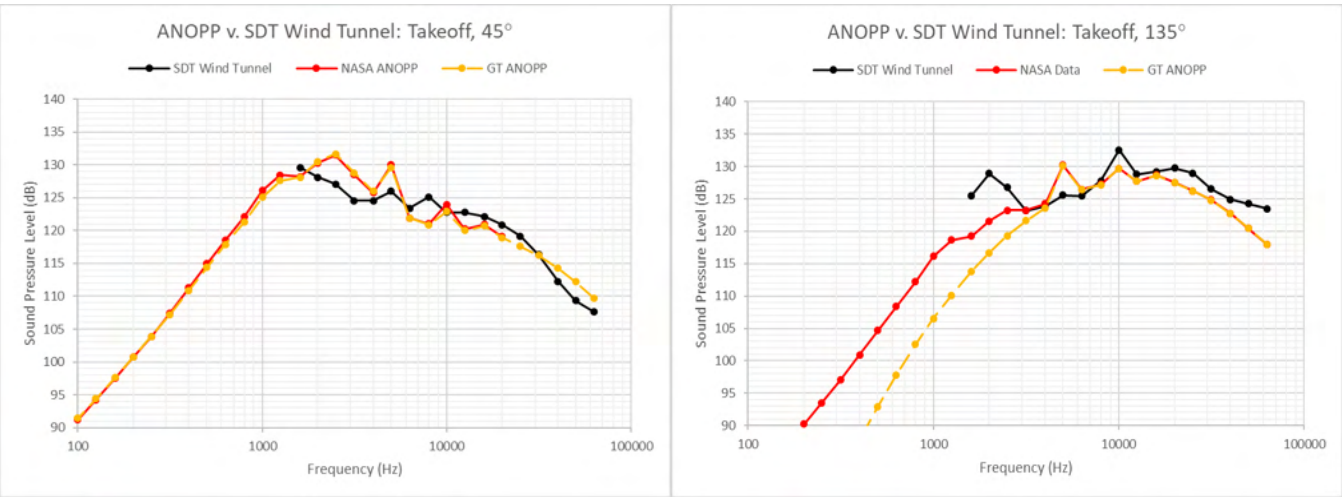

Figure 9. GT ANOPP baseline SDT model takeoff comparison.

Table 5. ANOPP baseline model takeoff error.

Comparison	GT ANOPP – EXP SDT		NASA ANOPP – EXP SDT		NASA ANOPP – GT ANOPP	
Directivity Angle	45°	135°	45°	135°	45°	135°
RMS Error (dB)	2.6080	5.0944	2.5755	3.4633	0.42983	8.1166

Integrated Geometry Design [COMPLETE]

The aircraft geometry considered for CFD analysis is shown in Figure 7. The vehicle is similar in size to the 737-8. Based on findings in the literature [1,2], the vertical tail and wing wakes are expected to have non-negligible contributions to the ingested distortion and are thus included in the model.

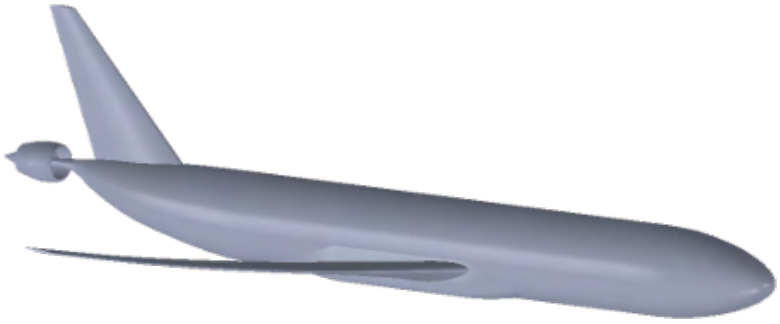

Figure 10. BLI aircraft geometry model.

The nacelle is a scaled version of the SDT geometry. The highlight and throat areas were increased further (for a fixed fan area), based on preliminary RANS CFD findings that showed a strong shock at the throat for typical cruise conditions, as displayed in Figure 8. As a result of these modifications, the peak upper throat Mach number decreased from 1.27 to 1.14, and the peak lower throat Mach number decreased from 1.18 to 0.9.

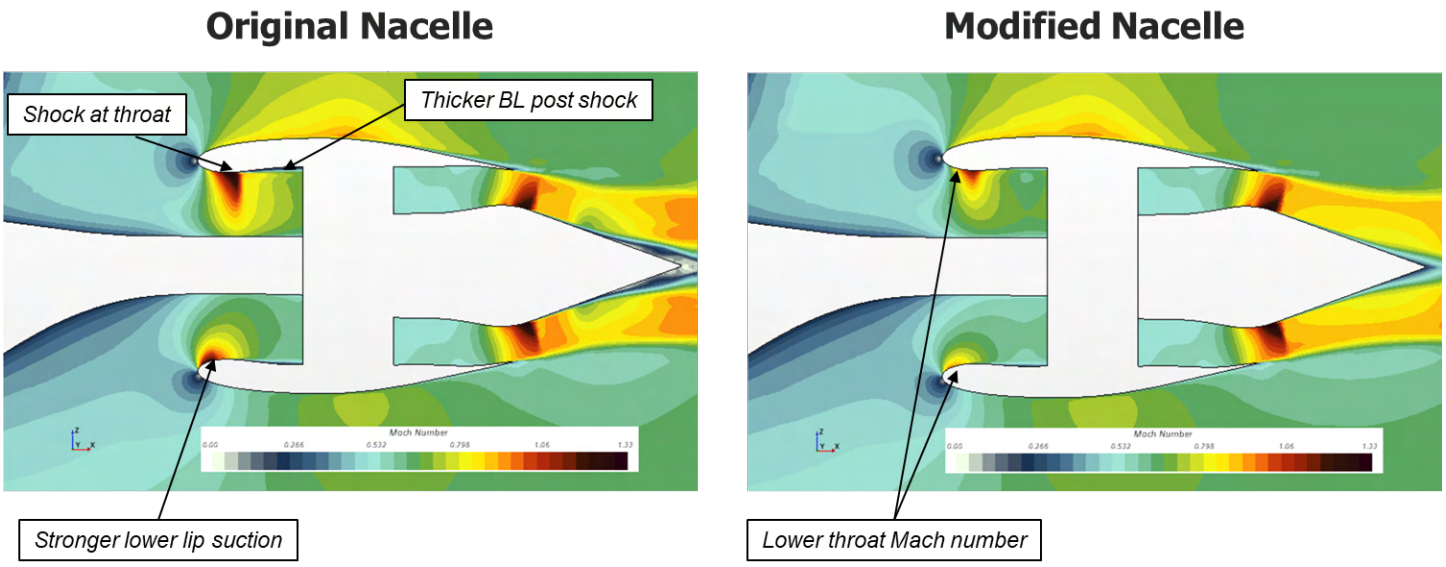

Figure 11. Comparison of performance for the original scaled SDT inlet and modified SDT inlet under cruise conditions.

RANS CFD Methodology [COMPLETE]

To determine which variables have significant impacts on inlet distortion, it was prudent to conduct preliminary CFD studies under steady-state conditions with a simplified propulsor model. For this purpose, a one-dimensional powered boundary condition (BC) representation of the engine is considered, where the fan face is treated as a pressure outlet and the fan exit is modeled as a stagnation inlet. A target mass flow rate is specified at the fan face, with the static pressure and temperature being iteratively updated by the CFD solver to meet this requirement. At the fan exit, total pressure and temperature BCs obtained from one-dimensional engine cycle analysis are imposed in the CFD model. While this level of fidelity for CFD

analysis and propulsor modeling is not adequate for CAA, it is sufficient to gain some preliminary insight into how the ingested boundary layer is affected by certain operation and geometry parameters. In addition, the significantly lower cost of steady-state RANS makes it easier to conduct several studies, which can then be used to prioritize certain variables over others when conducting the final CAA runs with a higher-fidelity model.

For the steady-state RANS cases, an unstructured Cartesian grid is developed using STAR-CCM+'s grid generation tools. Prism layers are used for near-wall refinement to capture the boundary layer. The near-wall spacing is calculated such that the wall y-plus of less than one is achieved. Volumetric refinement zones are defined over critical regions of the geometry, such as around the tail cone and engine. Standard atmosphere properties and fully turbulent conditions are assumed for this study, using the SST k-ω turbulence model. The geometric and flow symmetry around the X-Z plane (for all cases considered) allows for half of the domain to be modeled.

Variable Sensitivity Study and Down-Selection [COMPLETE]
The primary objective of this sub-study was to determine which parameters can be varied to produce significant and meaningful changes in fan noise. In this case, the term "significant" implies that the sensitivity of noise to a parameter change must be high, whereas the term "meaningful" implies that the change in parameter value cannot be arbitrary and should be relevant in conceptual design. At this early stage, without CAA, there is no way to directly link variable changes to fan noise. However, because there is a correlation between noise and the level of inlet distortion, it is logical to assume that significant changes in the fan face distortion profile will correlate with significant changes in fan noise. As such, the current goal is to assess the sensitivity of the ingested boundary layer and the corresponding distortion profile to certain variables. This study is conducted under takeoff conditions, defined by the flight Mach number, altitude, angle of attack (AoA), and fan RPM. RPM in this lower fidelity CFD study is modeled by a change in target mass flow rate. From studies in [1,3] some variables typically considered in conceptual design can be investigated:

- Angle of attack (AoA)
- Fan diameter
- Fuselage length

All of these variables have been shown to influence the characteristics of the ingested boundary layer. The AoA captures the impacts of the control surface, wing, and airframe design on distortion and noise through the weight-required lift-AoA relation and exhibits a strong impact on distortion. Additionally, changing the AoA is easy in a CFD simulation, as it does not involve any geometry changes or re-meshing. Fan diameter is another key variable that impacts the magnitude of the ingested boundary layer and thus fan face distortion. However, changing the fan diameter involves changing both the hub and tip diameters (to maintain the same hub-to-tip ratio), which in turn requires changing the tail cone design for this particular geometry. Not only is this variable change more difficult than a simple AoA perturbation, owing to the geometry changes involved, but a one-to-one mapping between the fan diameter alone and distortion changes is not possible because of the required changes in tail cone design. However, the fan diameter is a major parameter that varies in conceptual design and, as such, cannot be ignored for this study despite these challenges. Fuselage length is a relatively easier geometry parameter to investigate and also impacts the ingested distortion through Reynolds number effects on the developing boundary layer. The following cases were considered in this study:

- Angle of Attack: Baseline (8.5˚) +25%, +50%
- Fan Diameter: Baseline (51 in), +10%
- Fuselage Length: Baseline (131 ft), +25%

The baseline case was run to obtain reference values for distortion, fan face pressure recovery, and qualitative assessments of the flow field through various scalar views. Each perturbation was then considered individually. To calculate the distortion at the fan face, the ARP 1420 standard was used to define the probe locations, as shown in Figure 12.

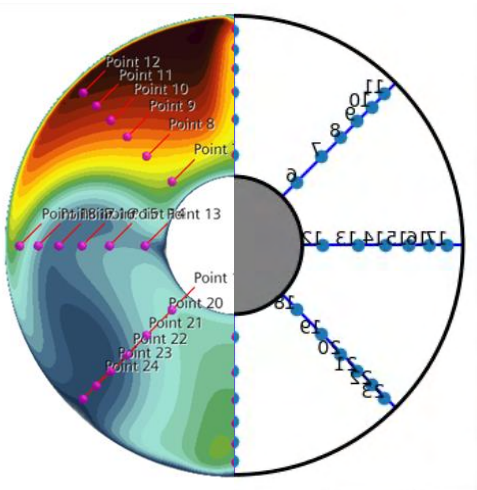

Figure 12. ARP 1420 distortion rake at the fan face.

Figure 13 shows the circumferential distortion intensity while Figure 14 shows the radial distortion intensity. The baseline case is shown in dark blue. Figure 13 shows that the AoA and fuselage length perturbations produce the largest change in circumferential distortion relative to the baseline case. However, there is no clear candidate for radial distortion, as shown in Figure 14, where the peak changes in radial distortion caused by the three parameter perturbations occur at different locations.

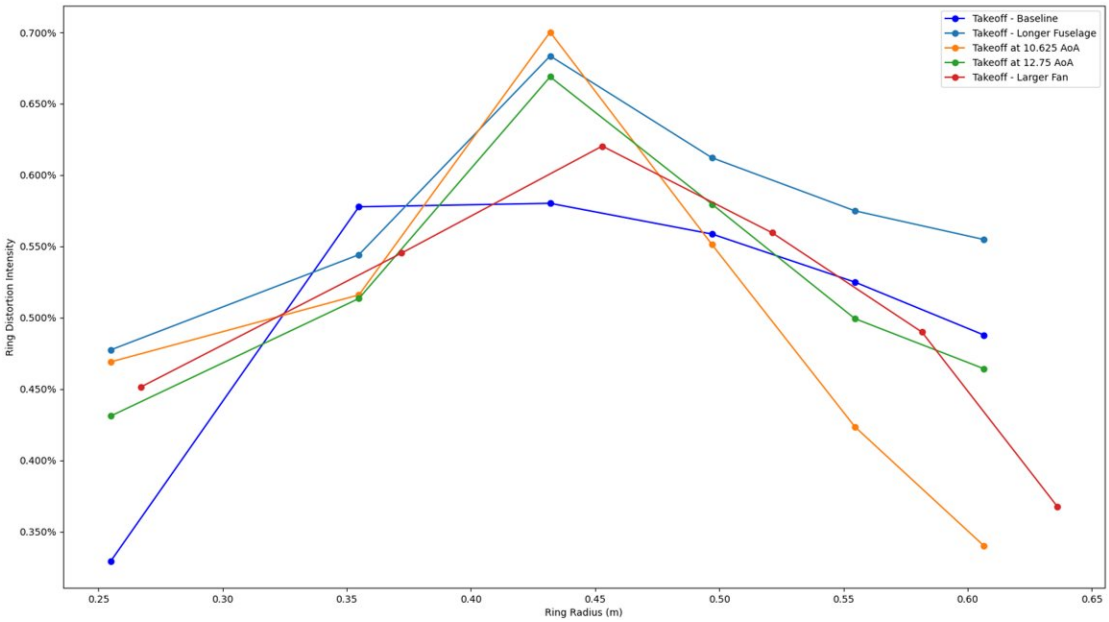

Figure 13. Circumferential distortion at takeoff for all cases.

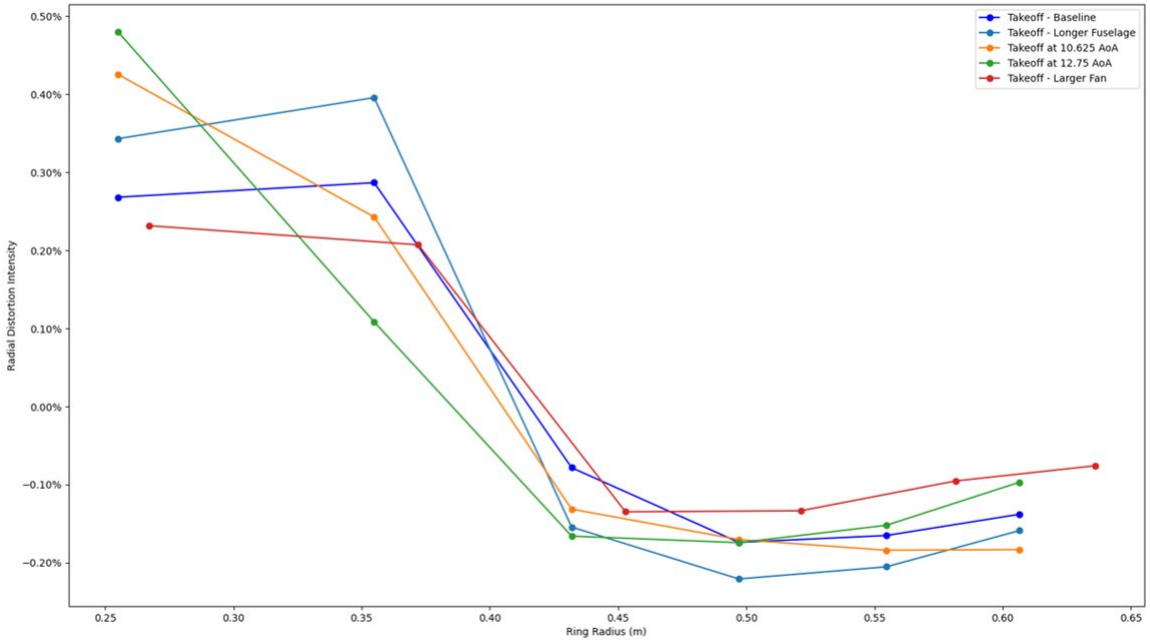

Figure 14. Radial distortion at takeoff for all cases.

Based on these results, we proceeded with only the AoA as an input to the noise model, in addition to the rotational speed RPM. As such, the noise model is now parametric with respect to operating conditions only, and not geometry. While the diameter and fuselage length also have a relatively equal claim for consideration, the increased dimensionality of the input space for the noise model would have required substantially more CAA runs, which would have exceeded the computational time and budget constraints for this project. The final sampling space for constructing the noise surrogate model is shown in Figure 15. The ranges of AoA and RPM are sufficiently large to consider takeoff, approach, and flyover, the three main noise measurement conditions. Training points are circled in red, with the blue 'V's' showing additional cases that could be run for model validation, depending on time and budget availability.

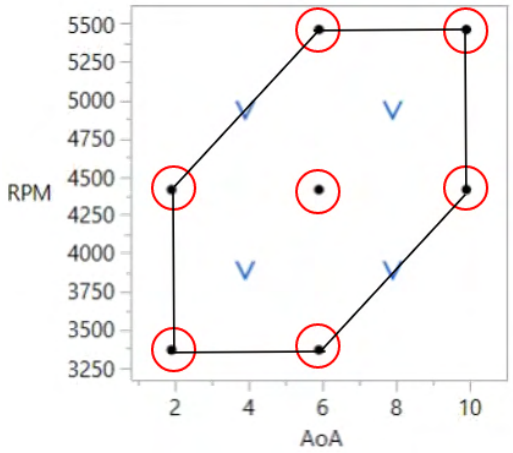

Figure 15. RPM and AoA sampling space for parametric noise model generation.

CFD/CAA Setup

Approach for Creating an ANOPP Module

Continued development from the ANOPP baseline will focus on the implementation of aircraft geometry and parametric ability. To pursue this aim, the baseline model will be updated from ANOPP standards to ANOPP2, which provides decreased run times and enables integration into Python. Python will provide flexibility for testing multiple cases, which is crucial for developing the response equations used to parametrically model the input variables.

After integrating the basic aircraft geometry, ANOPP will calculate reflection effects due to the airframe and other aircraft components, adding a layer of complexity and detail to the baseline model. The integrated model will then be used in junction with a hemispherical surface below the aircraft to generate a mapping of noise levels about the aircraft (see Figure 16). The same surface will then be generated and filled with CAA data, providing a direct comparison with the noise estimates from ANOPP.

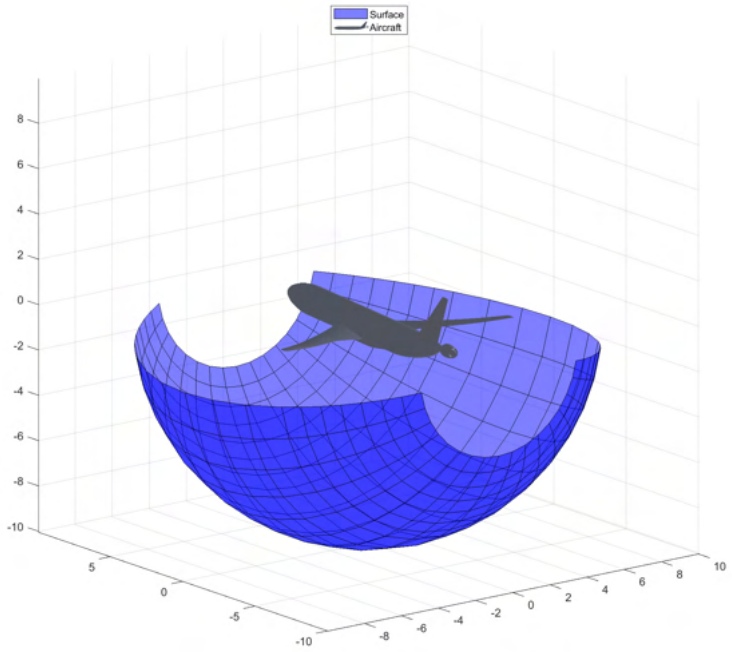

Figure 16. Example of a noise surface.

Because ANOPP lacks accuracy and detail compared with CAA methods for unsteady flow simulations, the integrated ANOPP model will not take distorted flow effects into consideration, leaving these effects to be calculated solely by CAA.

The resulting noise level surfaces will be compared to calculate the overall impact of distorted flow due to the fuselage elements. This process will be repeated for each experiment detailed in Figure 15.

References

1. Ahuja, J., and Mavris, D. N., "Sensitivity of Boundary Layer Ingestion Effects to Tube and Wing Airframe Design Features," *AIAA SciTech Forum*, AIAA, 2020. https://doi.org/10.2514/6.2020-1523.
2. Kenway, G. K., and Kiris, C., "Aerodynamic Shape Optimization of the STARC-ABL Concept for Minimal Inlet Distortion,"*AIAA SciTech Forum*, AIAA, 2018. doi:10.2514/6.2018-1912.
3. Ahuja, J., and Mavris, D. N., "Assessment of Propulsor On-Design and Off-Design Impacts on BLI Effects," *AIAA SciTech Forum*, AIAA, 2021. https://doi.org/10.2514/6.2021-0605.

Milestones

- A baseline SDT fan performance model has been created.
- A baseline ANOPP model has been created, and validation exercises were conducted.

Major Accomplishments

- A baseline SDT fan performance model has been created.
- An integrated BLI scaled fan performance model has been established.
- A baseline ANOPP model has been developed.
- A baseline CFD/CAA geometry and mesh have been created.
- An integrated, scaled CFD/CAA geometry and mesh have been created.
- Sets of cases to be performed in CAA have been defined by conducting lower-fidelity RANS CFD cases to identify key sensitivities.

Publications

None

Outreach Efforts

None

Awards

None

Student Involvement

Two graduate students are involved with this work: Ross Weidman and José Zavala. These students are graduate research assistants in their first year at Georgia Tech.

Plans for Next Period

The plan for the next reporting period is to complete all of the tasks specified in the research approach under Task 3 and to fully finish the first phase of the task before the end of the current period of performance.

Task 3 – Model Validation Exercises

Georgia Institute of Technology

Objective

The purpose of this task is to validate the parametric noise models created with existing data or high-fidelity simulations.

Research Approach

Baseline Validation Approach

To validate the baseline fan noise, the fan noise predicted by the ANOPP model will be compared with published acoustic results for the SDT fan, and the difference will be documented. If there is a significant difference between the ANOPP predictions and published data, a correction function in the ANOPP model can be introduced to minimize these differences. To account for differences between the CAA results generated for the study and ANOPP results, we will apply the proposed method described in Section 1.2 and Figure 6. Further validation exercises may be needed depending on the results of the parametric model. The module will be used to generate both BLI and non-BLI noise results for various flight/operating conditions, which will be compared with CAA results obtained for corresponding conditions.

High-fidelity Computational Aero-Acoustics Modeling (CAA)

Because the objective is to understand the effect of BLI on noise, the effect of distortion on noise must be addressed. BLI, as well as other flow perturbations upstream of the fan, leads to nonuniformity in the axial flow ingested by the fan, which in turn causes variations in blade loading in the azimuthal direction. Consequently, the aeroacoustics performance is degraded.

To capture the effects of nonuniformity in the ingested flow, the aerodynamics analysis must be unsteady. In this study, the adopted analysis for performing computational aeroacoustics (CAA) is a hybrid approach, consisting of an unsteady CFD approach and an integral method based on the Ffowcs Williams and Hawkings (FW-H) equations. The unsteady CFD simulates the aerodynamic flow field, which in turn provides noise sources. The FW-H approach is then used to propagate the noise sources to the far-field.

To assess the ability of our chosen numerical approach, validation was conducted with experimental acoustic data from a turbofan. Details and results from the validation are described below.

Validation Case and Experimental Data

Validation was based on SDT experiments performed by NASA [1,2]. The SDT is a GE-designed turbofan wind tunnel model (1/5 scale) with a rotor diameter of 22 in. The rotor is composed of 22 blades, whereas the stator is composed of 54 vanes. In this validation, we focus on the approach condition, as shown in Table 6.

Table 6. Validation case details.

	Value	Unit
Mach number	0.10	
Pressure	101,325	Pa
Temperature	288.15	K
Angle of attack	0	degree
Rotor speed	7809	RPM

Acoustic measurements were acquired at 48 sideline microphones at a distance of 89.3 in. For our validation purposes, a subset of these receivers is considered. Therefore, a total of 21 sideline receivers are considered and arranged as shown in Figure 17.

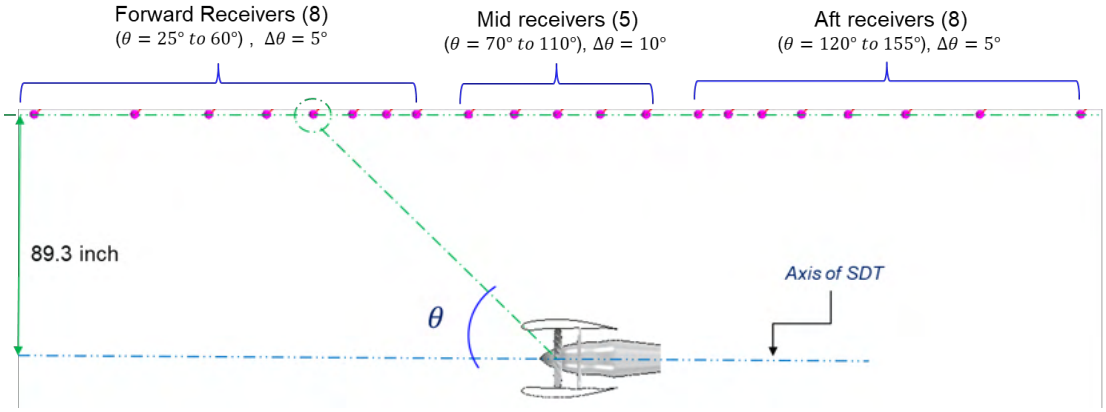

Figure 17. Arrangement of sideline receivers.

Numerical Approach

The unsteady aerodynamics are obtained by utilizing a commercial lattice Boltzmann method (LBM) solver, PowerFLOW. Unlike the traditional CFD method, which solves for macroscopic fluid quantities via Navier–Stokes (N-S) equations, the LBM solves for microscopic particle distributions. Thus, modeling occurs at a level where the physics are more fundamental. Such solvers exhibit low dissipation properties, rendering them appropriate for aeroacoustics applications.

The boundary conditions (BC) are as follows: for the outer boundaries, pressure/velocity BC types are prescribed, whereas non-slip wall BCs are used in surfaces of the rotor, vanes, center body, and nacelle. However, in the extension of the center body, slip walls are used in order to avoid the influence of boundary layers. Spatial discretization is accomplished by means of variable refinement (VR) regions. Note that the discretization sizes decrease by half with each variable refinement level. The smallest discretization sizes are located in regions between the tip of the blades and nacelle, the second smallest sizes are located in regions in the leading and trailing edges of the blades and vanes, and the third smallest in the boundary layers of the blades and vanes. Some details regarding the simulation setup are given in Table 7.

Table 7. LBM simulation setup.

LBM Simulation	***Value***	***Remark***
Smallest spatial discretization	0.125 mm	Gaps between blade tips & nacelle
	0.250 mm	LE & TE blades & vanes
Time step	0.1626×10^{-6} s	
Mesh size	~ 400 million	

The aeroacoustics are predicted using a FW-H solver. This solver uses flow data recorded from the unsteady simulation at a chosen surface. The surface is permeable and surrounds the SDT turbofan. Moreover, the FW-H surface is an open shell with an opening in the downstream end in order to avoid contamination from wakes. The far-field acoustic receivers set to the FW-H solver are located as shown in Figure 17. Some details regarding the FW-H simulation are given in Table 8.

Table 82. FW-H simulation setup.

FW-H Simulation	***Value***	***Remark***
FW-H spatial discretization	4.00 mm	Permeable surface
FWH Time step	5.2×10^{-6} s	
Maximum frequency resolved	6.4 kHz	
Time for collecting flow data	10 rev	Time for one revolution

Results

Numerical predictions of the sideline directivity overall sound pressure level (OASPL) along with experimental values are shown in Figure 17. Moreover, for reference, results from previous LBM simulations [3] are also plotted. Excellent agreement is found for upstream emission angles lower than 70°. However, the OASPL values exhibit some overprediction for emission angles between 70° and 100° with a maximum discrepancy of approximately 2 dB near 80°. The downstream OASPL directivity, i.e., for emission angles larger than 100°, is progressively underpredicted. Despite these discrepancies, the predicted OASPL directivity exhibits correct trends.

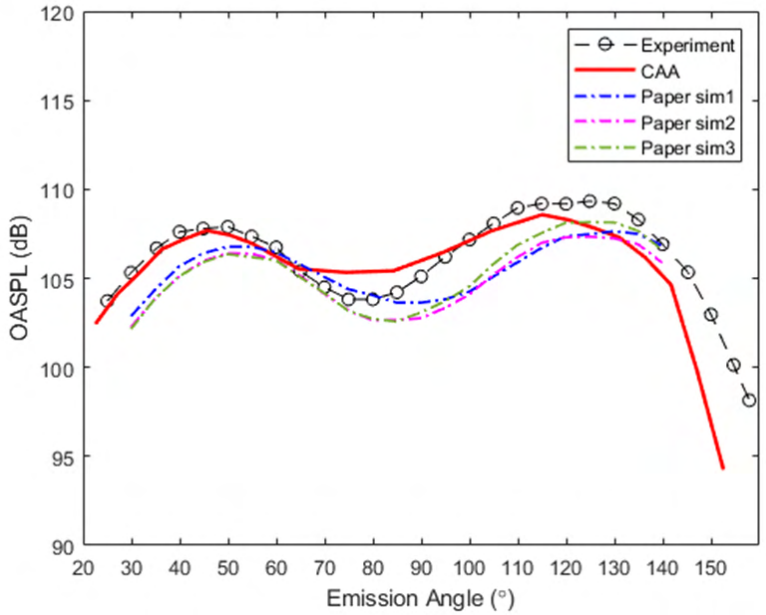

Figure 18. Comparison between numerical prediction and experiments, along with previous numerical simulations.

The predicted OASPL directivity compares well with those of previous simulations [1,2,3]. Note that these simulations span a smaller range of angles, between 30 and 140, and are apparently not converted from geometric angles to emission angles and are thus shifted to the right. Quantification of the discrepancy – root mean squared error (RMSE) - between simulations and experiments is shown in Table 9. It is noted that the discrepancy level in our simulation is in agreement with those of previous simulations.

Table 9.3. Comparison of average discrepancies for simulations.

	Discrepancy (RMSE)
CAA	1.70 dB
Sim 1 [*]	1.78 dB
Sim 2 [*]	2.04 dB
Sim 3 [*]	1.77 dB

Milestones
Our CFD/CAA approach was validated for the baseline SDT geometry.

Major Accomplishments
The high-fidelity numerical CAA approach was validated for the SDT turbofan under approach conditions.

Publications
None

Outreach Efforts
None

Awards
None

Student Involvement
Three graduate students are involved with this work: Grant Stevenson, Ross Weidman, and José Zavala. These students are graduate research assistants in their second year at Georgia Tech.

Plans for Next Period
During the next period, we will implement the simulation campaign for the integrated geometry.

Task 4 – Tool Documentation
Georgia Institute of Technology

Objective
The purpose of this task is to create documentation of the parametric noise tool created.

Research Approach
Georgia Tech will thoroughly document the tool and each of its modules, including the parameters involved, theoretical approach, algorithms utilized, output structure, and example use cases. This theoretical manual will be developed in addition to the validation results, which will be documented as a separate report.

Milestone(s)
None; this task has not yet begun.

Major Accomplishments
None; this task has not yet begun.

Publications
None

Outreach Efforts
None

Awards
None

Student Involvement
Three graduate students are involved with this work: Grant Stevenson, Ross Weidman, and José Zavala. These students are graduate research assistants in their first and second years at Georgia Tech.

Plans for Next Period
The documentation for the modules will be completed during the next annual period of performance.

References
[1] Woodward, R. P., Hughes, C., Jeracki, R., & Miller, C. (2002, June 17-19). Fan noise source diagnostic test – far-field acoustic results [Presentation]. 8th AIAA/CEAS Aeroacoustics Conference & Exhibit, Breckenridge, CO.
[2] Heidelberg, L. J. (2002, June 17-19). Fan noise source diagnostic test – tone modal structure results [Presentation]. 8th AIAA/CEAS Aeroacoustics Conference & Exhibit, Breckenridge, CO.
[3] Casalino, D., Hazir, A., & Mann, A. (2018). Turbofan broadband noise prediction using the Lattice Boltzmann Method. AIAA Journal, 56(2), 609–628. https://doi.org/10.2514/1.j055674
[4] Casalino, D., Hazir, A., & Mann, A. (2018). Turbofan broadband noise prediction using the Lattice Boltzmann Method. AIAA Journal, 56(2), 609–628. https://doi.org/10.2514/1.j055674

Project 064 Alternative Design Configurations to Meet Future Demand

Georgia Institute of Technology

Project Lead Investigator

Professor Dimitri N. Mavris (PI)
Director, Aerospace Systems Design Laboratory
School of Aerospace Engineering
Georgia Institute of Technology
Mail Stop 0150
Atlanta, GA 30332-0150
Phone: (404) 894-1557
Fax: (404) 894-6596
Email: dimitri.mavris@ae.gatech.edu

Dr. Michelle Kirby (Co-PI)
Chief, Civil Aviation Division
Aerospace Systems Design Laboratory
School of Aerospace Engineering
Georgia Institute of Technology
Mail Stop 0150
Atlanta, GA 30332-0150
Phone: (404) 385-2780
Fax: (404) 894-6596
Email: michelle.kirby@ae.gatech.edu

University Participants

Georgia Institute of Technology

- PIs: Dr. Dimitri N. Mavris (PI), Dr. Michelle Kirby (Co-PI)
- FAA Award Number: 13-C-AJFE-GIT-062
- Period of Performance: June 5, 2020 to September 30, 2022
- Tasks:
    1. Support of Long-Term Aspirational Goal Task Group (LTAG-TG) meetings and technical ad hoc group (Tadg) meetings
    2. Assessment of 2030, 2040, and 2050 projections of advanced tube and wing (ATW) aircraft
    3. Assessment of 2030, 2040, and 2050 projections of advanced concept aircraft (ACA)
    4. Collection of LTAG-TG inputs to the Committee on Aviation Environmental Protection Modeling and Databases Group (MDG)

Project Funding Level

The FAA provided $250,000 in funding, and the Georgia Institute of Technology (Georgia Tech) has agreed to a total of $250,000 in matching funds. This total includes salaries for the project director, research engineers, and graduate research assistants, as well as funds for computing, financial, and administrative support, including meeting arrangements. The institute has also agreed to provide tuition remission for the students, paid from state funds.

The project will continue in FY22 with an additional $1,199,999 in FAA funding and matching funds from Georgia Tech.

Investigation Team

Faculty and Research Staff
Dr. Dimitri Mavris, Georgia Institute of Technology
Dr. Michelle Kirby, Georgia Institute of Technology
Mr. Greg Busch, Georgia Institute of Technology
Dr. Jon Gladin, Georgia Institute of Technology
Dr. Gokcin Cinar, Georgia Institute of Technology
Dr. Burak Bagdatli, Georgia Institute of Technology
Dr. Mingxuan Shi, Georgia Institute of Technology

Graduate Researchers
Melek Ozcan, Georgia Institute of Technology, Tasks 2-4
Luis Salas Nunez. Georgia Institute of Technology, Tasks 2-4

Project Overview

To understand the environmental aspects of the projected growth in international aviation, this project will investigate how trends in innovative aircraft technology and design will impact fuel burn and CO_2 emissions. Mature, in-development, and foreseen technologies and aircraft design concepts will be considered, and technology readiness, feasibility, effects on aircraft configurations, designs, and performance will be assessed. The goal is to forecast the impacts of new technologies on fuel burn and CO_2 emissions from international aviation through and beyond the year 2050, under a variety of scenarios related to technology, market factors, and constraints.

The focus of this ASCENT project is to support the Committee on Aviation Environmental Projection (CAEP) task group for a Long-Term Aspirational Goal (LTAG-TG), focusing on aircraft technology modeling, and analysis of fuel burn and CO_2 emissions. The LTAG-TG is working under the 12th CAEP cycle to develop scenarios that combine technology, fuels, and operations, that represent a range of readiness and attainability regarding future air transportation. The work will be framed in the context of an analysis aimed at achieving the current International Civil Aviation Organization (ICAO) aspirational goals. The future scenarios will be analyzed to understand the impacts on CO_2 emissions and their relationship with current CO_2 levels. The costs associated with the scenarios and the economic impacts on aviation growth, noise, and air quality will be considered, and the results will be placed in the context of the latest consensus scientific knowledge. Georgia Tech is supporting the modeling and simulation aspects of these analyses, with a focus on aircraft technology, by leveraging the FAA's investment in Georgia Tech's Environmental Design Space (EDS) tool set, existing technology models, and previous work performed in support of other CAEP efforts. The goals of Project 064, described at a high level, are as follows:

- Supporting LTAG-TG and technical ad hoc group (Tahg) meetings
- Execution and assessment of 2030, 2040, and 2050 projections for all advanced tube and wing aircraft (ATW), including all five classes of vehicles (turboprop, business jet, regional jet, narrow body, and wide body)
- Execution and assessment of 2030, 2040, and 2050 projection of advanced configuration aircraft, including all five classes of vehicles (turboprop, business jet, regional jet, narrow body, and wide body)
- Collection of LTAG-TG inputs to MDG

The completion of these tasks will inform the LTAG-TG regarding the potential of aircraft technology to reduce fuel burn and CO_2 emissions under a variety of future scenarios.

Task 1 - Support of LTAG-TG Meetings and Technical Ad Hoc Group Meetings

Georgia Institute of Technology

Objective

The objective of Task 1 is to support LTAG-TG meetings and technical ad hoc group (TAHG meetings within the LTAG technology subgroup (LTAG tech SG). The CAEP/12 LTAG-TG currently has four primary subgroups: operations, fuels, technology, and scenario development. The key interactions in the overall modeling process for the LTAG-TG are shown in Figure 1.

Georgia Tech is primarily supporting the technology subgroup but also is actively participating in the other subgroups to facilitate coordination across the entire LTAG task group. The LTAG tech SG is divided into three Tahgs: airframe, propulsion, vehicle impact assessment (VIA), and advanced concepts and energy sources (ACES). The VIA Tahg also contains an ad hoc subgroup dedicated to modeling and simulation (M&S group). Dr. Dimitri Mavris is a co-chair of the technology subgroup, Dr. Michelle Kirby is a lead focal for the airframe Tahg, and Dr. Dimitri Mavris is the focal for the M&S group of the VIA Tahg. A breakdown of the LTAG technology subgroup is shown in Figure 2.

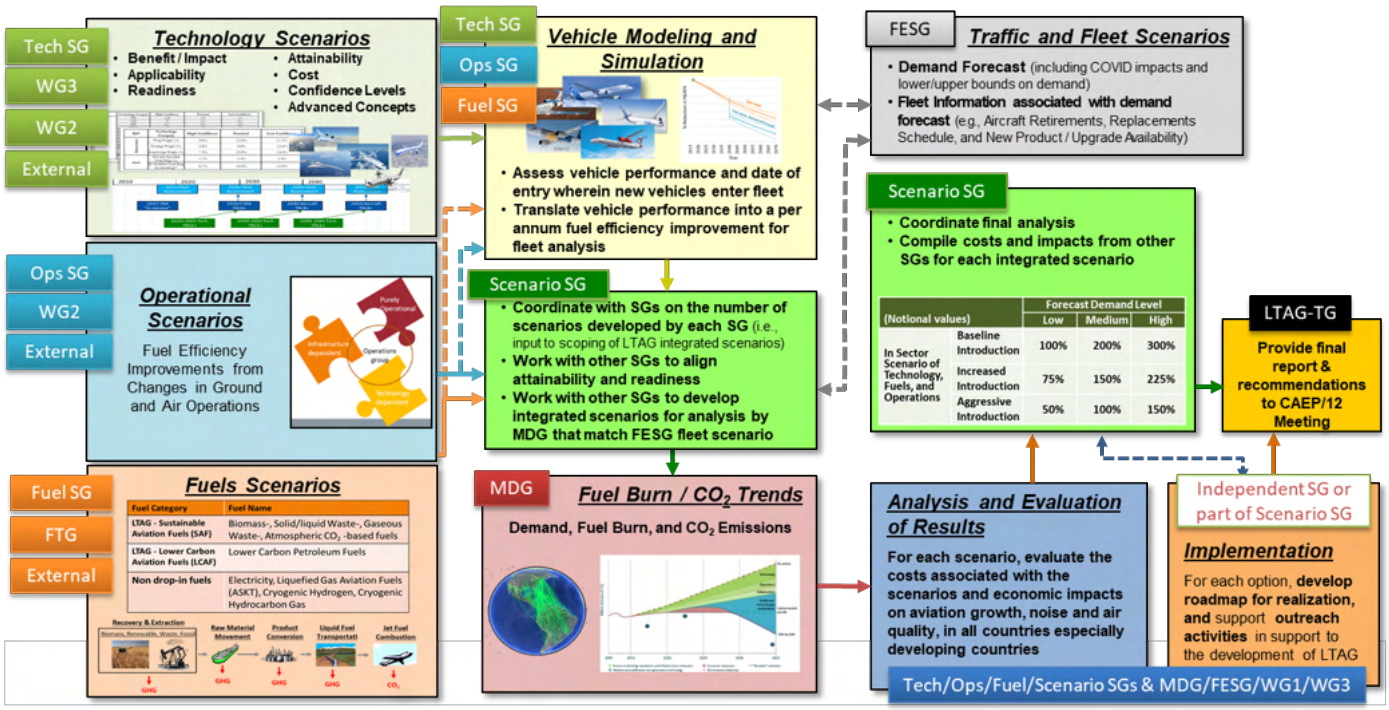

Figure 1. Key interactions in the LTAG-TG modeling process.

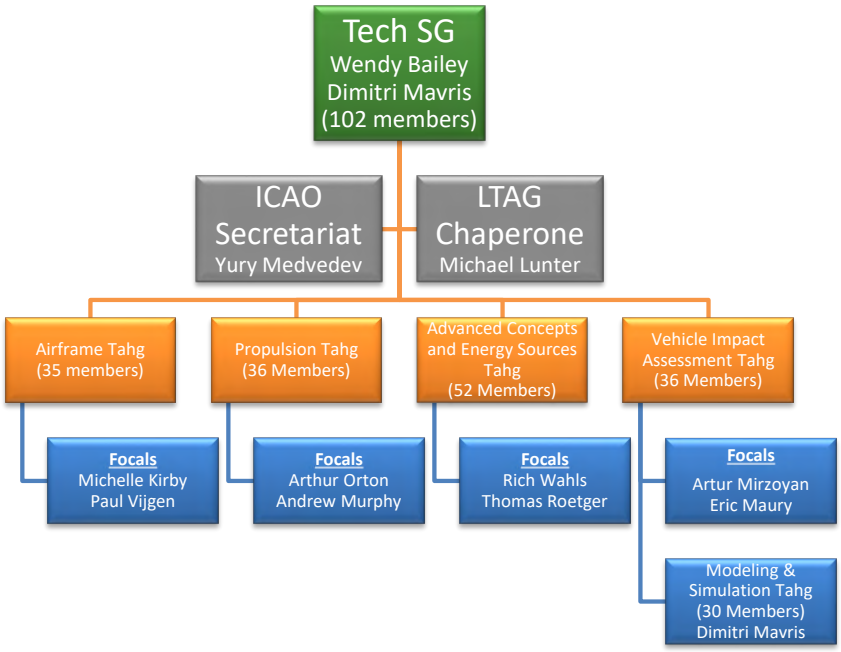

Figure 2. LTAG technology subgroup structure.

Research Approach

Georgia Tech is supporting the task through hosting and attending various LTAG tech SG calls, coordinating discussions among its members, and developing workplan proposals for the group. Georgia Tech has also taken on the responsibility of preparing presentations for these meetings, particularly the LTAG tech SG and M&S meetings. Many LTAG-related calls/meetings and many hours have been dedicated to supporting this task. Other activities related to supporting this task are preparing presentations for plenary calls, writing status papers, information papers (IPs) and working papers (WPs), and presenting work summaries at CAEP/12 Steering Group meetings.

Milestones

- Developed work plan for ASCENT Project 064.
- Supported LTAG-TG at CAEP/12 steering group 2 (SG/2).

Major Accomplishments

- Co-chairing the LTAG tech SG and focals for the Airframe Tahg and M&S ad hoc group
- Participating in all LTAG-related meetings and calls
- Participating in weekly LTAG tech SG calls and ad hoc group meetings to develop technology impacts across five vehicle classes and preparing material for those calls
- Refining the methodology, metrics, and processes to assess the feasibility of a long-term aspirational goal
- Participating in recurring calls with MDG on fleet-level modeling and assumptions
- Attending both ICAO CAEP stocktaking events
- Reviewing further submitted questionnaire responses on aircraft technology that could reduce CO_2 emissions
- Writing status papers for CAEP/12 steering groups 2 and 3
- Writing LTAG-TG SG report

Publications

None

Outreach Efforts
None

Awards
None

Student Involvement
None

Plans for Next Period
None

Task 2 - Assessment of 2030, 2040, and 2050 Projections of Advanced Tube and Wing (ATW) Aircraft
Georgia Institute of Technology

Objectives
Similar to the CAEP Independent Expert Integrated Review (IEIR), the LTAG M&S group selected technology reference aircraft (TRA) as representative vehicle models for each vehicle category. In this study, in addition to the vehicle classes considered in IEIR, i.e., business jet, regional jet, narrow body (single aisle) and wide body (twin aisle), the LTAG requested development of an additional TRA for the turboprop vehicle class, because electrification is likely to occur earlier for this class of aircraft than the other vehicle classes. Georgia Tech led the effort to develop the TRA models to be used in this project.

The technology impacts for the timeframes 2030, 2040, and 2050 and for each vehicle class were provided by the propulsion and airframe Tahgs within the LTAG technology subgroup and implemented in the TRA models by Georgia Tech.

The objective of Task 2 is to perform assessments of ATWs. This task includes taking technology impacts for three different timeframes (2030, 2040, and 2050) and applying them to the following five technology reference aircraft classes:
- Turboprop
- Business Jet
- Regional Jet
- Narrow body
- Wide body

Research Approach
The LTAG-TG developed a methodology to assess the ATWs, as shown in Figure 3, which was used to accomplish the objectives of Task 2.

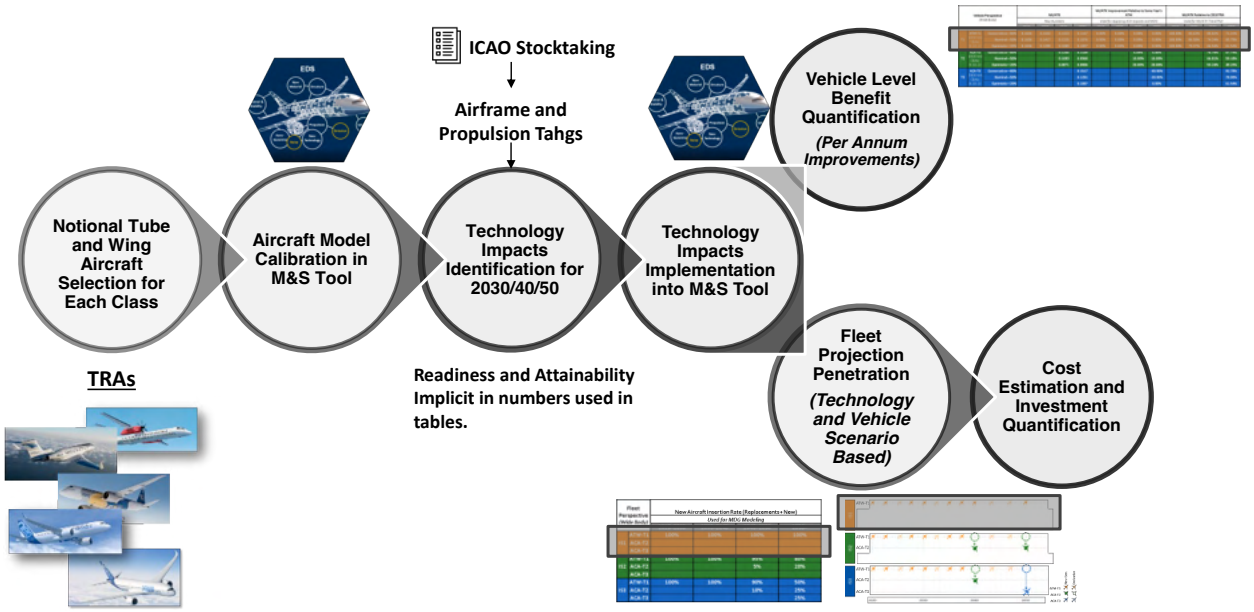

Figure 3. ATW assessment process overview.

The assessment process started with the selection of notional tube and wing aircraft for each vehicle category. These notional aircraft were then simulated in EDS based on public-domain data. The model calibration process involved two phases: engine model calibration and airframe model calibration. These aircraft models were verified in an iterative manner between the M&S team and LTAG-TG members until they were deemed "fit for purpose." This process yielded five TRA on which the 2030, 2040, and 2050 technology impacts were implemented.

Airframe and Propulsion Tahgs provided the technology impacts in four categories: propulsion technology impacts, system technology impacts, structures/materials technology impacts, and aerodynamic technology impacts. The Airframe and Propulsion Tahgs' input consisted of technology impacts at three levels of progress (higher/medium/lower) for each vehicle category for each timeframe. Surrogate models were created to allow for rapid design space exploration. The final selected ATWs for each timeframe had the minimum fuel burn at the range at maximum takeoff mass and payload. The focus was on fuel burn, because the LTAG study is aimed at carbon emissions. The optimized vehicle results were used to quantify the vehicle-level benefits with respect to optimized 2018 TRA. The metric of interest was energy intensity per available tonne-kilometer (MJ/ATK) in each timeframe at different technology progress levels. Fleet penetration and cost/investment predictions were also determined in coordination with the Cost Estimation ad hoc group.

Milestones

- Established ATW assessment process for the LTAG tech SG
- Performed the assessment process for each vehicle category in each timeframe

Major Accomplishments

- Verified the performance of 2018 TRA models for business jet, turboprop, regional jet, narrow body, and wide body classes
- Established the technology impacts for all vehicle classes in each timeframe
- Developed the "fit for purpose" ATW models for 2030, 2040, and 2050
- Documented the ATW assessment process in the LTAG-TG report in detail

Publications

None

Outreach Efforts
None

Awards
None

Student Involvement
Melek Ozcan, graduate research assistant, supported modeling and simulation with EDS.
Luis Salas Nunez, graduate research assistant, supported modeling and simulation with EDS.

Plans for Next Period
- Refine input to LTAG as needed according to feedback from CAEP
- Coordinate with MDG to determine how to best improve the fleet modeling approach

Task 3 - Assessment of 2030, 2040, and 2050 Projections of Advanced Concept Aircraft (ACA)
Georgia Institute of Technology

Objective
The objective of Task 3 is to perform assessments of future advanced aircraft variants of the technology reference aircraft models. Because of time and resource constraints, LTAG-TG needed to develop an assessment method different from that in Task 2.

These advanced configurations can include advanced airframe architectures, propulsion architectures, and unconventional fuel systems. The ACES Tahg grouped the potential ACA under three technology scenarios:

- T1: Advanced tube and wing
- T2: Advanced concept aircraft, drop-in fuels, and limited infrastructure change
- T3: Advanced concept aircraft, non-drop-in fuels and energies, and major infrastructure change

Georgia Tech worked with the focals of the ACES Tahg to determine the advanced concepts to be used and to estimate the energy intensity improvements with respect to ATWs for each progress level in each timeframe.

Research Approach
The methodology developed for the assessment of ACA is shown in Figure 4. Because of the uncertainties regarding ACA models as well as time and resource constraints, this methodology was developed to leverage existing authoritative studies.

The assessment process starts with broad scanning of potential advanced aircraft concepts for each vehicle category from ICAO Stocktaking events, LTAG-TG members, and literature searches using published reports from/for research organizations. This literature review resulted in the earliest possible entry into service (EIS) years for ACAs in each vehicle size class. Figure 5 shows the earliest EIS years identified for the narrow body aircraft class and is included in this report as an example. These concepts are then grouped under each technology scenario. The next step is identifying the technical and non-technical barriers to each advanced concept. These barriers can affect a wide variety of stakeholder groups inside and partly outside of aviation, including governments, original equipment manufacturers (OEMs), airlines, airports, passengers, and energy suppliers. The importance of non-technological feasibility ("attainability") due to political, regulatory, economic, societal, infrastructural, and operational challenges will be magnified for advanced alternative concepts, because they generally represent a substantial departure from currently accepted approaches, and their achievement requires major efforts from multiple stakeholders.

In the following step of the process, scorecards are used to assess a range of ACAs side by side. The scorecard allows for collection of subject matter experts' (SMEs) perspectives regarding the readiness, attainability, and potential benefits of each aircraft concept for each technology scenario. Each group of aircraft is characterized as a whole, and that characterization is

carried through the remaining steps of this methodology. In this manner, the potential benefits representative of a group of relevant concepts have been characterized without identifying or implying any single concept as a "winner."

The vehicle-level benefits of the groups of relevant concepts are quantified with reference to authoritative studies previously performed by/for reliable research and development organizations. Because the advanced concepts are usually compared with conventional tube and wing configurations, the assumptions regarding the configurations are extracted from each study, and the impacts of advanced concepts are isolated with the support of propulsion and airframe Tahgs. The step changes in energy intensity (MJ/ATK) introduced with the application of advanced concepts are estimated for each group of ACAs, i.e., ACA-T2 and ACA-T3, at each technology progress level (higher/medium/lower) and for each timeframe. Of note, direct comparisons across reports and concepts are quite challenging, because the baselines, technology assumptions, and timelines differ. Therefore, some level of expert qualitative assessment was used to normalize the differences. The restrictions on the mission performance of the ACAs are also noted for the fleet-level analysis.

Aircraft market-share projections of ACAs and cost assessments were also performed for each vehicle class, with the help of the cost estimation ad hoc group.

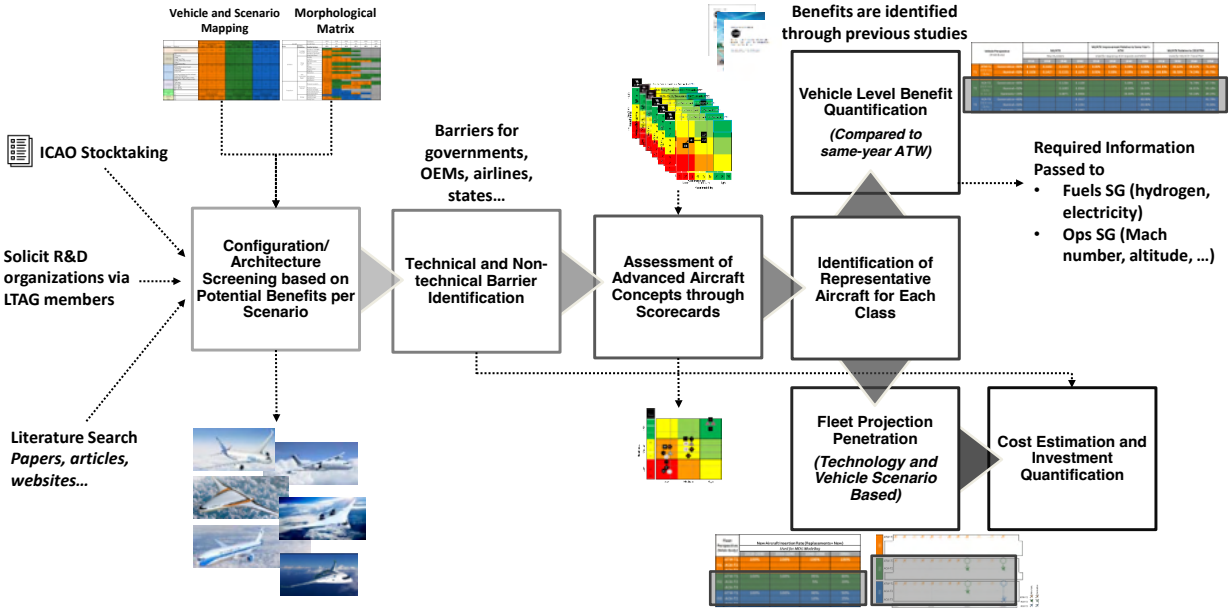

Figure 4. ACA assessment process overview.

Figure 5. Narrow body ACA identification of earliest EIS.

Milestones
None

Major Accomplishments
- Established an assessment methodology for the ACAs
- Performed extensive literature research on ACAs
- Performed the ACA assessment process for all vehicle classes, covering a range of timeframes
- Documented the details of the ACA assessment process in the LTAG-TG report

Publications
None

Outreach Efforts
None

Awards
None

Student Involvement
Melek Ozcan, graduate research assistant, supported modeling and simulation with EDS.
Luis Salas Nunez, graduate research assistant, supported modeling and simulation with EDS.

Plans for Next Period
- Refine input to LTAG as needed according to feedback from CAEP
- Coordinate with MDG to determine how to best improve the fleet modeling approach for ACA

Task 4 - Collection of LTAG-TG Inputs to MDG

Georgia Institute of Technology

Objective

The objective of Task 4 was to gather the LTAG-TG inputs to MDG for the system-wide assessment in a format useful for MDG. The process essentially consists of summarizing the outputs of vehicle performance assessments for the ATW and ACA aircraft in a format that the LTAG-TG process can use for fleet-level analysis. The key inputs for MDG are the trends in energy intensity per available tonne-kilometers (MJ/ATK), and the mix of ATW-T1 vs. ACA-T2 vs. ACA-T3 entering the fleet in a given year, i.e., the market share, of all vehicle classes.

Research Approach

First, the fuel burn/ATK values of 2018 TRA are taken from the EDS models. Multiplying the fuel burn/ATK value by the energy density of Jet-A fuel, which is 42.8 MJ/kg, gives the energy intensity in MJ/ATK. Differences in energy intensity with respect to the reference of 2018 TRA for the narrow body class are shown in Table 1. Similar tables are created for other vehicle classes.

Table 1. Narrow body ATW-T1 energy intensity at each waypoint, normalized to 2018 TRA.

Energy Intensity Relative to 2018 TRA			Narrow Body			
			2018	2030	2040	2050–2070
T1	ATW-T1	Lower Progress	100.00%	96.01%	86.90%	81.32%
		Medium Progress		89.22%	81.13%	75.80%
		Higher Progress		82.74%	75.79%	72.03%

The differences in energy intensity deltas for the ACA-T2 and ACA-T3 concepts with respect to same year's ATW are shown in Table 2. As mentioned before, the introduction of ACAs results in a step change from ATWs. In the table, negative numbers represent reduction in energy intensity (more efficient energy use) relative to ATW-T1, whereas positive numbers represent an increase in energy intensity (less efficient energy use). In this example, ACA-T2 is expected to be between 5% and 15% more energy efficient in 2035 than the ATW in the same year, thus reflecting the application of advanced concepts that use drop-in fuels and have limited infrastructure changes. The increase in energy intensity for ACA-T3, in the lower- and medium progress scenarios, relates to this aircraft being the first possible application of non-drop-in hydrogen as an energy source, and reflects the challenges with the volume that fuel occupies and the implications of that volume on vehicle design.

Table 2. Narrow body ACA energy intensity deltas from the respective ATW-T1 of the same year.

ACA Energy Intensity Change Relative to Same Year's ATW			Narrow Body			
			2018	2030	2035	2050–2070
T2	ACA-T2	Lower Progress	—	—	-5.00%	-5.00%
		Medium Progress	—	—	-10.00%	-10.00%
		Higher Progress	—	—	-15.00%	-20.00%
T3	ACA-T3	Lower Progress	—	—	20.00%	20.00%
		Medium Progress	—	—	15.00%	15.00%
		Higher Progress	—	—	-5.00%	-5.00%

Figures 6 and 7 show the alternative representations of the tabular data, including uncertain progress bands. The former combines the EIS and technology impact of new advanced concepts, whereas the latter demonstrates the relative scale of the uncertainties in future years, as compared with the medium expected progress. As shown in Figure 7, remarkable uncertainty exists in the efficiency of the ACA-T3 concept, which is the first-generation hydrogen-powered narrow body. The colors in

these figures are consistent with those used in Tables 1 and 2: orange represents ATW-T1 aircraft, green represents ACA-T2 aircraft, and blue represents ACA-T3 aircraft.

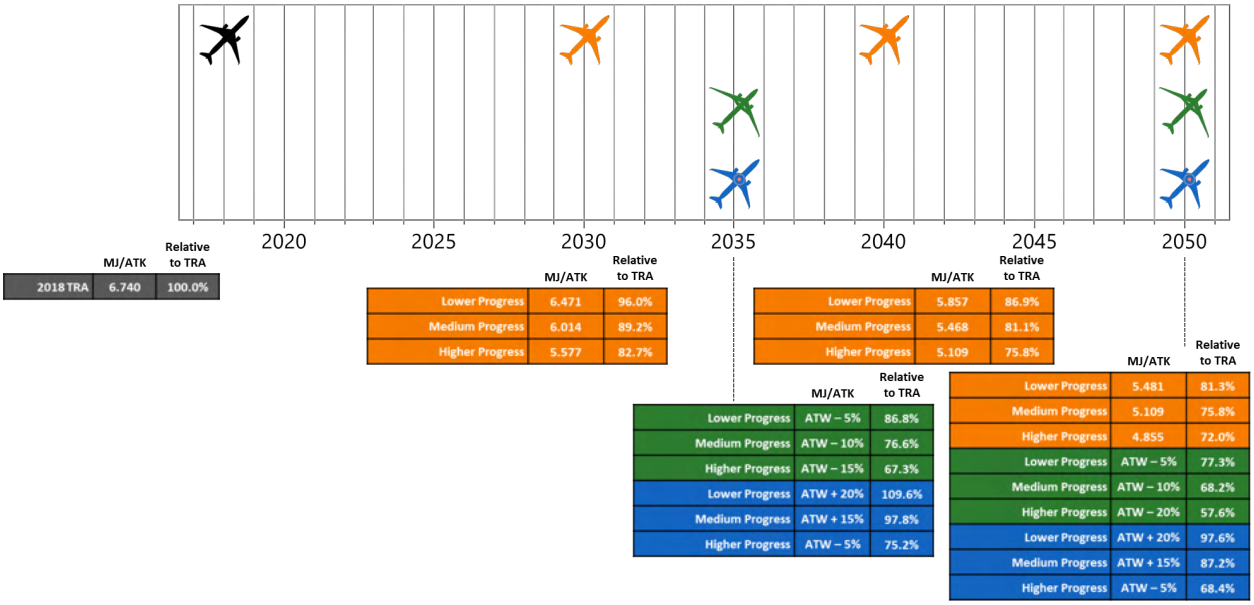

Figure 6. Narrow body ATW waypoints, ACA Entry into Service and energy intensity values.

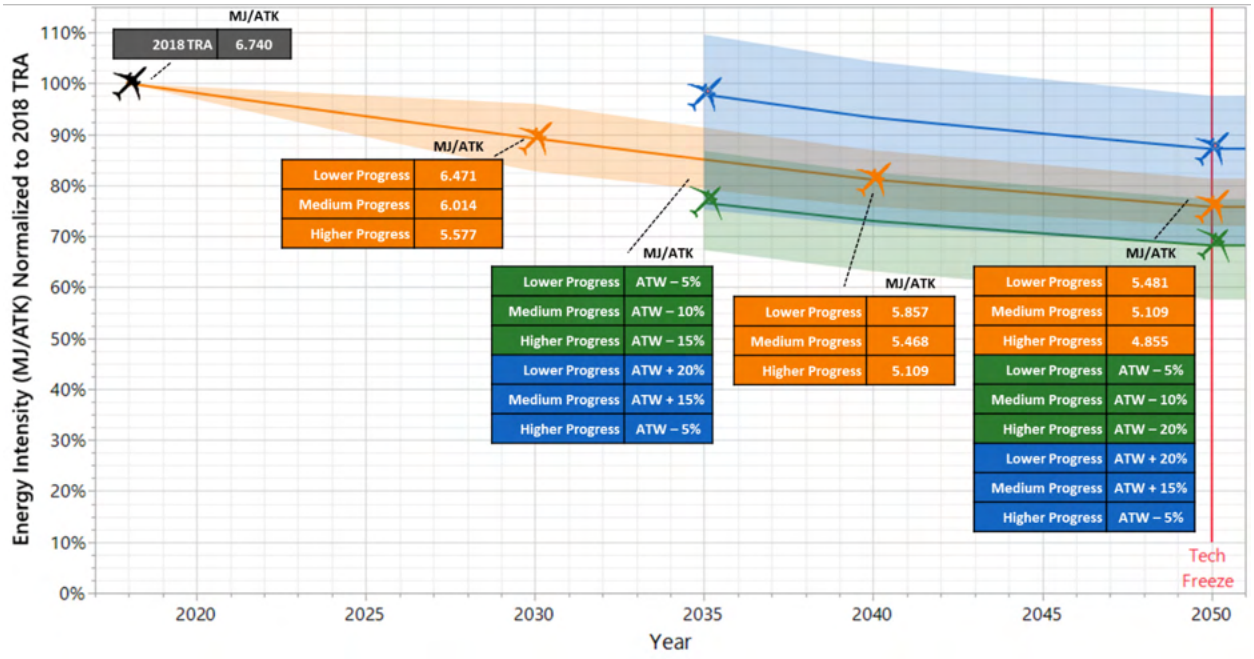

Figure 7. Narrow body technology and concept energy intensity trend, normalized to the 2018 TRA.

The last part of the input to MDG is the market-share information, as given in Table 3 and Figure 8. This provides the LTAG-TG process with inputs regarding the aircraft fleet mixture expected under different scenarios (integrated scenarios 1, 2,

and 3), to aid in conducting a full system-level analysis including the impacts of sustainable aviation fuels and operational measures.

Table 3. Narrow body market shares for new entry and replacements

Market Share for New Deliveries		Narrow Body					
		2018	2030	2040	2050	2060	2070
IS1	ATW-T1	100%	100%	100%	100%	100%	100%
IS2	ATW-T1	100%	100%	70%	40%	10%	0%
	ACA-T2			30%	60%	90%	100%
IS3	ATW-T1	100%	100%	50%	20%	10%	0%
	ACA-T2			25%	40%	45%	50%
	ACA-T3			25%	40%	45%	50%

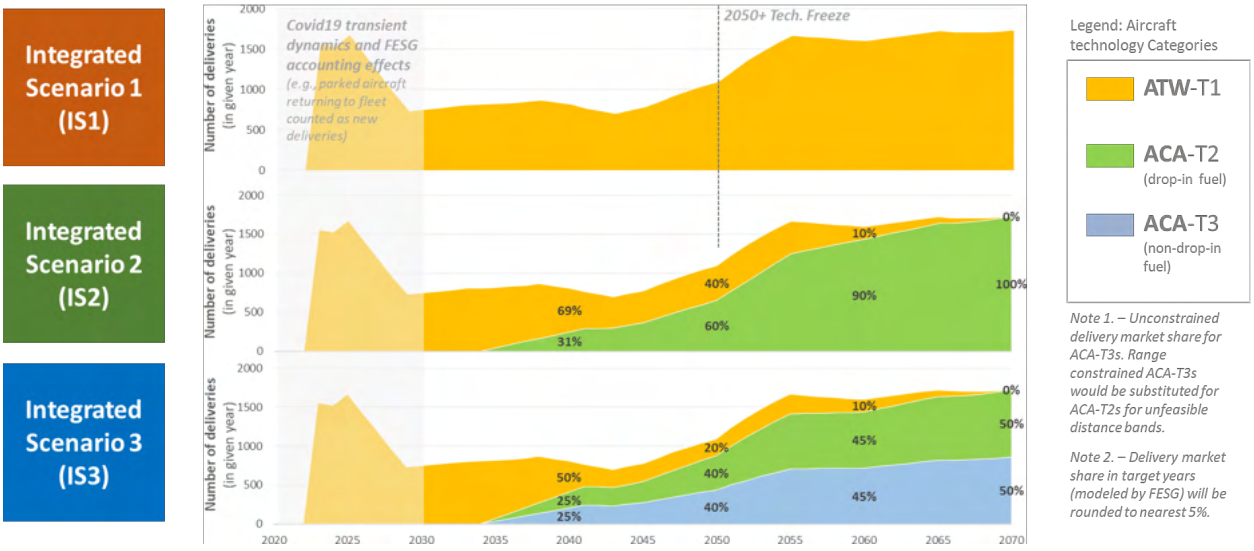

Figure 8. Market-share timeline for the narrow body class of vehicles.

Milestones

None

Major Accomplishments

- Submitted the LTAG-TG inputs to MDG on time to support fleet-level/system-level analysis
- Documented the details of calculations in the LTAG-TG report

Publications

None

Outreach Efforts

None

Awards
None

Student Involvement
Melek Ozcan, graduate research assistant, supported modeling and simulation with EDS.
Luis Salas Nunez, graduate research assistant, supported modeling and simulation with EDS.

Plans for Next Period
- Refine input to LTAG as needed according to feedback from CAEP
- Coordinate with MDG to determine how to best improve the fleet modeling approach

Project 065(A) Fuel Testing Approaches for Rapid Jet Fuel Prescreening

University of Dayton

Project Lead Investigator

Joshua Heyne
Associate Professor
Mechanical Engineering
University of Dayton
300 College Park
Dayton, OH 45458
937 229-5319
Jheyne1@udayton.edu

University Participants

University of Dayton

- PI: Joshua Heyne
- FAA Award Number: 13-C-AJFE-UD, Amendments 26, 31 and 34
- Period of Performance: June 5, 2020 to September 30, 2021
- Task:
    1. Prescreening of sustainable aviation fuels (SAF).
    2. Develop novel testing methods for the evaluation of SAF candidates.

Project Funding Level

Amendment No. 026: $159,998 (June 5, 2020, to June 4, 2021)
Amendment No. 031: $250,000 (Aug 11, 2020, to Aug 10, 2021)
Amendment No. 034: No Cost Extension (August 10, 2021, to February 10, 2022)
Cost share is from the University of Dayton, VUV Analytics, Greenfield Global, and DLR Germany.

Investigation Team

- Joshua Heyne (University of Dayton) is the Project Lead Investigator for coordinating all team members (both ASCENT and non-ASCENT efforts) and communicating prescreening results with SAF producers.
- Linda Shafer (University of Dayton Research Institute) is a senior research engineer responsible for GCxGC measurement of SAFs.
- David Bell (University of Dayton) is a Ph.D. student developing two-dimensional gas chromatography (GCxGC)-vacuum ultraviolet (VUV) detection methods and software.
- John Feldhausen (University of Dayton) is an M.S. student developing GCxGC-VUV methods and software.
- Zhibin (Harrison) Yang (University of Dayton) is a Ph.D. student conducting Tier Alpha prediction and Tier Beta measurement.

Project Overview

This project focuses on further developing the Tier Alpha and Beta test methods, which can help minimize the fuel volume needed for testing and improve a fuel's potential for meeting ASTM approval criteria. Tier Alpha refers to low-volume analytical testing approaches (i.e., GCxGC, nuclear magnetic resonance [NMR], and infrared [IR] analytical testing). Tier Beta tests focus on directly testing the physical and chemical properties of a fuel rather than predicting them from GCxGC methods.

Task 1 – Prescreening of Sustainable Aviation Fuels

University of Dayton

Objectives

The objective of this task is to develop a tiered prescreening process for new alternative jet fuels that uses low fuel volumes and will improve a fuel's potential to meet ASTM approval criteria. This work facilitates the flow of meaningful information to fuel producers while their production processes are at a low technology readiness level (TRL) while simultaneously strengthening a producer's readiness for the approval process.

Research Approach

Paper 1: Lower Heating Value of Jet Fuel from Hydrocarbon Class Concentration Data and Thermo-Chemical Reference Data: An Uncertainty Quantification

Introduction

The net heat of combustion, often called the lower heating value (LHV), is important to both fuel consumers and suppliers because it is the source of the energy that is ultimately converted to usable power. Engine manufacturers and their customers rely on LHVs to gage engine performance and thermal efficiency, which are two quality assurance measurements taken at the product level before shipping a new engine for installation in an aircraft or power generation platform. During his 20-year tenure working in combustor design for industry, the corresponding author has observed that terms or requirements around the performance margins measured by these tests may be written into sales contracts. An accurate LHV is necessary for establishing the performance margins for an engine model during the product development phase of a gas turbine engine. An accurate LHV is also needed to optimally interpret and assess test data pertaining to other engine-level requirements. However, once in a fuel is in service, the LHV of a fuel that is consumed by an engine used for air transportation (unlike fuel used for power generation platforms) is generally known only to be within the range specified by ASTM D1655 (for example), which is "greater than or equal to 42.8 MJ/kg." Accurate and precise predictive determinations are therefore critical to the decarbonization of aviation

The LHV of sustainable aviation fuel (SAF) blend components can be higher or lower than conventional fuels. All current SAF blend components covered by ASTM D7566 specifications have LHVs greater than 42.8 MJ/kg and 1-2% higher than conventional fuels, largely because they are composed almost entirely of saturated hydrocarbons. In contrast, conventional fuels may contain up to 25% aromatics by volume. Higher LHVs offer the potential for lower fuel consumption rates and the ability to potentially impact other emissions and environmental outcomes of aviation kerosene combustion. Inconsistencies that arose during investigations with these alternative aviation fuel blend components, particularly with the ASTM D3338 estimation method, motivated an alternative LHV determination approach. SAF prescreening currently aims to predict key fuel properties using minimal fuel volumes.

For ground-based applications of gas turbine engines, the LHV of a fuel destined for consumption is frequently measured by the consumer, as the LHV is a required input to the engine control software that has been advanced in part by the corresponding author. In some cases, LHV is determined using a continuous recording calorimeter (e.g., ASTM D1826 – 94), and in other cases, LHV is determined periodically using species concentration measurements via gas chromatography [1,2]. The total number of chemical species in a gaseous fuel, including N2 and CO2, is typically ~10. It is a straightforward application of Hess's Law to construct LHV of the fuel from its components' concentrations and a small library of thermo-chemical data. However, heavier fuels such as propane, butane, gasoline, kerosene, and diesel have more molecular components. The number of molecular components increases factorially with the average carbon number, making it progressively more difficult to derive LHV from composition data and a reference library containing thermo-chemical data for pure molecules.

For fuels within the jet fuel volatility range, the range and concentration of molecules in the fuel is bounded by a flash point (38 ˚C) and T10 (205 ˚C) on the light end. The freeze point (-40 or -47 ˚C) and the endpoint of distillation (300 ˚C) limit the heavy species. There are thousands of molecules between the light and heavy ends of the range, and accurate measurement of every molecular concentration is not practical. However, a fundamental approach for LHV determination is still possible. Multidimensional gas chromatography with flame ionization detection (GCxGC-FID) has been used in the past [3,4]; however, previous approaches using GCxGC-FID have relied on correlative methods, whereas the fundamental approach described in this work is based on Hess's Law.

A physics-based modeling approach using GCxGC-FID data is attractive because such a method requires minimal sample volume and labor but still yields a diverse array of additional property determinations or predictions [3–5]. For example, GCxGC-FID requires <1 ml of sample, whereas ASTM methods D4809 (higher heating value [HHV]), D2622 (sulfur), and D5291 (hydrogen) collectively require 1-2 ml of sample. Comparatively, a total volume of 50 ml was requested for just the calorimetry measurement in our recent experience with a commercial lab; so, 50 mL may be closer to the industry standard. Until now, one concern with a physics-based modeling approach that leverages GCxGC-FID experimentation has been the absence of any thorough assessment of the accuracy and precision of its property determinations. For reference, the stated reproducibility (i.e., 95% confidence interval) for LHV measurements determined using the ASTM D4809 protocol is 0.324 MJ/kg, which is less than 0.1% of the LHV.

ASTM D4809 clearly defines the conversion from gross heat of combustion at constant volume (Q_{bomb}, measured in ASTM D4809) to the net heat of combustion at constant pressure (Equation 1).

$$\begin{aligned} HHV &= Q_{bomb} + 0.006145 * H_{\%m} \quad \& \\ \text{LHV} &= Q_{bomb} - 0.2122 * H_{\%m} \quad \therefore \\ HHV - LHV &= 0.218345 * H_{\%m} \end{aligned} \tag{1}$$

However, the reference enthalpy ($H_{\%m}$) for the H_2O and CO_2 products is not entirely clear, which could lead to differences between research labs or industries who may not all be referring to ASTM D4809. For hydrocarbons, it turns out that (HHV-LHV) = 2.444 MJ/(kg-of-water), which is water's heat of vaporization at 25 °C. In this work, HHV is calculated from the heats of formation of the products and reactants in their respective ground states at 25 °C and 1 atm, and the mass percent hydrogen is determined from GCxGC-FID measurements to determine LHV. A comparison between the different methods to determine hydrogen content is out of the scope of this work.

Our current methodology differs in several ways relative to our previously reported approach [5]. For example, we now use liquid at 25 °C as the reference state for water and all reactant molecules. As a result of our work, the reference database has also grown to include 1077 molecules within the jet fuel range and another 2047 molecules that are unlikely to be present in jet fuel but may be present in samples that have yet to be tailored into a potential alternative jet fuel. We also now propagate the uncertainties in concentration measurements and database heats of formation through our calculations so that they contribute to the reported uncertainty of the determined LHV.

Vozka and Kilaz [6] and Gautam et al. [7] (provide thorough literature reviews of other fuel characterization techniques. In contrast to the fundamental approach described in this work, all the methods they describe use correlation to train a statistical model. The model can then, in theory, be used to predict the LHV of fuel samples that are not part of the training dataset. Such correlation methods are good for interpolations, as similar methods are used in many ASTM methods (e.g., ASTM D3338 and D2887). For example, Caswell et al. [8] used proton NMR to derive the average structures of the fractions eluted via liquid chromatography, which then serve as the basis functions for correlation to middle distillate fuel properties. Johnson et al. [9] performed partial least squares regression with 45 fuel samples to evaluate the correlations between fuel specification properties and near-infrared, Raman, and GC-MS data. Fodor et al. [10] and Wang et al. [11] correlated fuel specification properties and Fourier transform infrared spectra. Striebich et al. [12] correlated fast (five minutes) GC data with fuel volatility and freeze point properties. Although these correlation approaches generally show good agreement with measured fuel properties, the accuracy of predictions for fuel compositions that are outside the range of the training data is unknown.

Perhaps more importantly, the physical uncertainty of correlation methods remains unclear. Confidence intervals and R^2 values are only one type of uncertainty output from the predictions of a regression model. Statistical and correlative methods that train data directly to observations need many more observations than physics-based models. For example, one correlative method described later in this paper requires a minimum of 100 observations to determine coefficients for each independent variable, as well as many additional observations for testing. Two to three times that number of observations (i.e., 200-300 total observations) would be needed to bound upper and lower limits for each of the coefficients. In contrast, physics-based models require no training data, and all results can be viewed as untrained test data. The typical '80-20' rule for training and testing data (i.e., 80% of data is used for training, and the remaining 20% is used for evaluation of the method) data does not hold for physics-based models.

Here, we apply a physics-based LHV calculation method, GCxGC-FID data, and reference thermo-chemical data to a diverse array of aviation turbine fuels and blend components leveraging a large heat of formation database and includes

comprehensive uncertainty quantification.

Materials

A total of 17 samples were used for the evaluation of LHV determinations. The samples included four petroleum-derived jet fuels, six neat SAFs, and six hydrocarbon mixtures that were defined under the National Jet Fuels Combustion Program [13] to have some properties outside of jet fuel specification (ASTM D1655). Table 1 provides more information about these 17 fuels. These samples were chosen due to the availability of existing multidimensional gas chromatography (Striebich et al., 2005) and ASTM D4809 (Edwards, 2017) data and because they span a wide range of physical and chemical properties. For example, the LHV range of these samples is 42.9 - 44.1 MJ/kg, which is somewhat broader than the LHV range of conventional jet fuels (42.9-43.3 MJ/kg; [13]) and is significantly broader than the range covered by at least one prior correlation-based study [15]. Several of the samples reported here have been studied extensively, and those results are reported in other publications [11,14].

Data

Two types of data are required to determine LHV using the fundamental approach: species concentrations and reference heats of formation. Species concentration data was provided by L. Shafer and has been desctibed previously [5]. We mined reference heats of formation (including uncertainties) for 1,077 molecules within the jet fuel volatility range from the NIST Standard Reference 203: TRC Web Thermo Tables [16]. As with any data-gathering endeavor, this process included evaluation of the reported NIST data. Working together with NIST, we resolved any inconsistencies before incorporating the data into our internal database. The NIST database is built from a variety of measurements and analysis methods, resulting in a precision that, in many cases, is an order of magnitude smaller than ASTM D4809.

The LHV data was provided by T. Edwards and is also available through the Federal Aviation Administration National Alternative Jet Fuels Test Database [17]. That same database was also mined for the input data required by ASTM D3338. None of this data is required to make an LHV determination via the fundamental approach; in our work, this data was used strictly for model validation.

Table 1. Fuel sample composition. Sample numbers are identical to those assigned by the Air Force Research Laboratory upon receipt, and many of the names match those designated by the National Jet Fuel Combustion Program [13]. Sample names starting with 'A-' indicate the conventional fuels selected to represent the range of operational experience. The names starting with 'C-' indicate solvent blends created to evaluate the impact of specific fuel properties on combustion figures of merit.

Sample name	POSF	Molecular weight, kg/kmol	H/C	Composition, mass% (n/iso/cyclo/aro/alkene)	LHV, MJ/kg (ASTM D4809)
Syntroleum FT-SPK (S-8)	5018	167.52	2.17	24.2 / 75.2 /0.6 /0. /0.0	44.10
C-4	12344	162.17	2.17	0.2 /98.9 /0.4 /0.4 /0.0	43.81
Sasol FT-SPK (SPK)	7629	153.15	2.17	0.3 /91.3 /5.2 /0.6 /2.7	43.80
UOP HEFA-SPK (UOP)	10301	170.18	2.16	10.1 /86.1 /3.7 /0.1 /0.0	43.90
Dynamic HEFA-SPK (HEFA)	7272	175.89	2.16	9.5 /88.4 /2.0 /0.0 /0.0	43.90
Lanzatech ETJ (L.T.)	12756	166.00	2.16	0.8 /96.3 /2.8 /0.0 /0.0	43.90
Gevo	11498	178.45	2.16	0.0 /99.6 /0.1 /0.0 /0.3	43.93
A-1	10264	151.79	2.01	26.1 /37.5 /22.9 /13.6 /0.0	43.24
C-2	12223	173.00	2.00	5.2 /77.5 /0.1 /17.1 /0.2	43.39
C-6	10279	166.84	1.99	7.5 /8.9 /83.1 /0.5 /0.0	43.30
C-3	12341	179.55	1.97	9.2 /45.2 /31.7 /13.6 /0.0	43.30
C-7	12925	169.77	1.97	3.3 /29.5 /62.3 /4.9 /0.0	43.30
A-2	10325	158.96	1.94	20.0 /29.7 /31.8 /18.5 /0.0	43.06
C-5	12345	135.41	1.92	17.7 /51.6 /0.1 /30.7 /0.0	43.01
A-3	10289	166.29	1.89	13.4 /18.9 /47.4 /20.4 /0.0	42.88
JP-5	10376	169.00	1.89	13.7 /18.6 /47.3 /20.4 /0.0	43.00
C-8	12923	160.39	1.86	13.7 /21.0 /38.0 /27.3 /0.0	42.90

Methodology

The concentration of 73 different classes of hydrocarbons, ranging from 7 to 20 (n) carbon atoms and (2n+2) to (2n-12) hydrogen atoms, are determined by integrating the signal from an FID detector which is positioned at the back end of the second column in a GCxGC configuration, the details of which are described by Striebich et al. [18], over a stenciled boundary of elution times corresponding to the time spent in the first and second columns, respectively. The integrated FID signal was converted to concentration units with the help of calibration mixtures of molecules that cover the range of the 73 classes of hydrocarbons being quantified. Figure 1 shows an example stencil in time/time-space marking the boundaries of each hydrocarbon class. Table 2 presents the total number of isomers of the ten most common hydrocarbon classes within the jet fuel range, along with the total number of isomers in each class for which liquid-phase heat of formation values are available in the database.

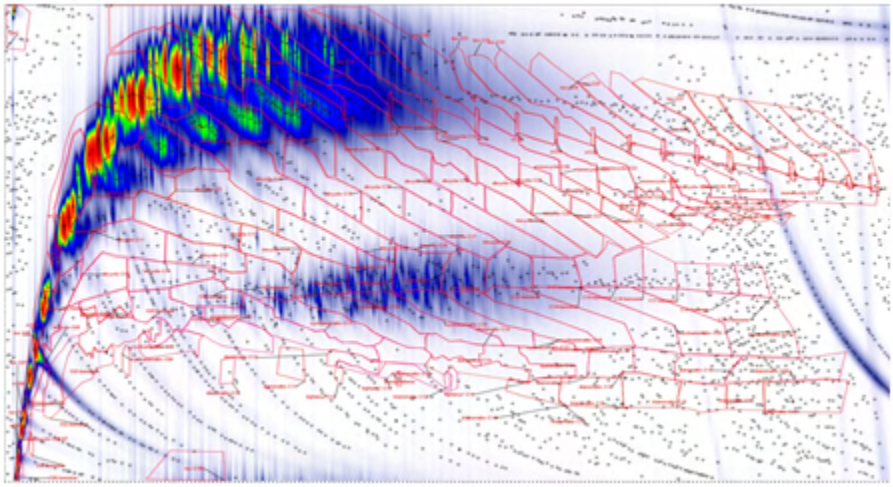

Figure 1. Definition of hydrocarbon classes. Species classes with relatively high concentrations show up as orange spots, and the corresponding bins that subtend each are of particular interest. Figure provided by L. Shafer [5].

The class concentration data can then be used to calculate or estimate other properties of interest via physical models, such as the fundamental approach taken in this work, or regression models, such as the approach taken by Shi et al. (2017) and by Berrier et al. [4]. Properties that are physically dictated by molecular bonds and atomic characteristics can be accurately determined by physical models, whereas properties that are more heavily influenced by inter-molecular interactions in the condensed phase are typically harder to determine accurately from first principles. Examples of the former properties include molecular weight, H/C ratio, and heat of combustion, and examples of the latter properties include viscosity and surface tension. Although the utility of regression models linking molecular weight, H/C ratio, or LHV to other data is unclear, recent innovations in regression software have made it easy to select any property as a dependent variable.

To rigorously apply the physical model for LHV [2] it is necessary to know the concentration and standard heat of formation of each constituent in the fuel and to have some quantification of the error associated with any assumptions or approximations related to inter-molecular interactions. For the LHV of liquid fuels, the contribution from inter-molecular interactions is called the heat of mixing or heat of solution in most physical chemistry textbooks. Based on measurements of 27 different binary solutions of hydrocarbons in the jet fuel distillation range by Lundberg (1964), the heat of mixing is 0.15 ± 0.15 kJ/kg, which is orders of magnitude less than the heat of combustion.

Table 2. Representative sample coverage of isomer populations. The table covers 60% of the average fuel composition.

Class	Isomer Population (N)	Samples in Database (n)	n/N
iso-C9	34	34	1.00
iso-C10	74	71	0.86
iso-C11	158	42	0.27
iso-C12	354	48	0.14
iso-C13	801	38	0.05
iso-C14	1857	30	0.02
iso-C15	4346	30	0.01
cyc-C11	1231	36	0.03
cyc-C12	3232	38	0.01
C9 aromatics	8	6	0.75

The lack of detailed knowledge of every species' concentration and their corresponding heats of formation prevents the direct application of a physical model for liquid fuels the same way such models are routinely applied to gaseous fuels [1]. However, the same model structure can be used with species class concentration measurements supplemented by some informed guess at the heat of formation corresponding to each class. In this study, we advance this fundamental approach and describe how to make these informed heat of formation approximations. The heat of formation of each class of hydrocarbons is determined by performing a Monte Carlo analysis in which the mole fraction of a random member of the database class is set to one and the mole fraction of all other species in that class is set to zero. This process is repeated for each of the hydrocarbon classes, resulting in 73 sets of isomeric mass fractions that each sum to one. Figure 2 provides a graphic representation of the relationship between real fuel and the database, where P is a uniform distribution of all possible isomers, M is the uniform distribution of the isomers in the database, and F is the real distribution of the fuel and could have any shape. Although the total isomer population (P) could be statistically represented by either the model population or the fuel population, Figure 2 indicates that the model and fuel population are related to each other by their respective relationships to the total population.

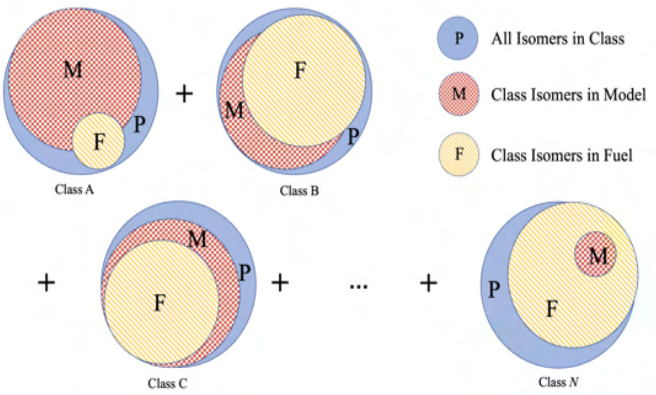

Figure 2. Graphic representation of the relationship between fuels and the database.

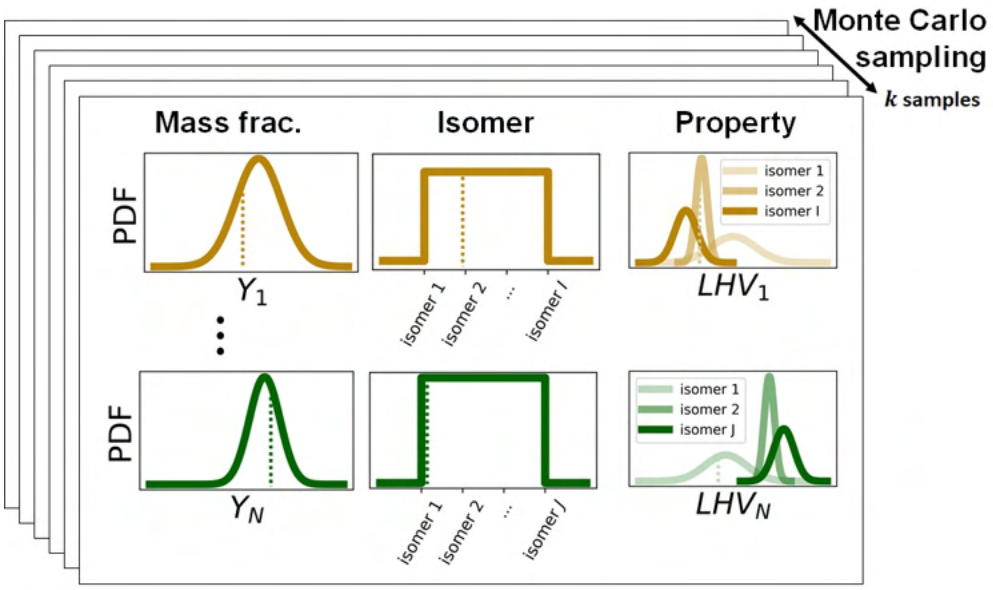

Figure 3. Graphic representation of the simulation sampling methodology.

Figure 3 shows a graphic representation of the simulation methodology. For each element of the simulation and each hydrocarbon class within that element, a random isomer is selected from the database and decorated with its associated property, which is sampled from a normal distribution centered on its mean reported value. This property is then weighted by the mass fraction of the whole hydrocarbon class, where the mass fraction is sampled from a normal distribution about the GCxGC-FID measurement [20]. Upon summing over all hydrocarbon classes, one element of the Monte Carlo simulation is completed. In total, these Monte Carlo simulations were comprised of 10,000 such elements, which has been shown previously [5] to be sufficiently large to achieve sampling convergence.

The HHV of a fuel with the chemical formula C_xH_y can be calculated using Equation 2, where $\Delta H_{f,m}$ is the standard heat of formation of material *m*.

$$HHV_{fuel} = X * \Delta H_{f,CO2(g)} + \frac{Y}{2} * \Delta H_{f,H2O(l)} - \Delta H_{f,fuel(l)} \quad (2)$$

$$\Delta H_{f,fuel(l)} = \sum_j c_j * \sum_i c_{i,j} * \Delta H_{f,i,j(l)} = \sum_j c_j * \Delta \overline{H}_{f,j(l)} \quad (3)$$

Equation 3 is the cornerstone of the fundamental approach; this equation is rigorously correct as written save for the absence of ΔH_{mix}, which is negligibly small. The summation over isomers (i) in this expression distinguishes this approach for liquid fuels from its conventional usage for gaseous fuels, for which no such term is required. The first coefficient c_j is the measured concentration of hydrocarbon class *j*. The second coefficient $c_{i,j}$ represents the unknown population distribution of all molecules that belong to class *j*. The average heat of formation ($\Delta \overline{H}_{f,j(l)}$) for class *j* is determined by using that population distribution to calculate a weighted sum of the heats of formation of each molecule in class *j*.

The values of X and Y in the empirical formula of the fuel are determined by the measured concentrations of each hydrocarbon class, as shown in Equation 4, where X_j and Y_j are the number of carbon and hydrogen atoms in class *j*, respectively:

$$X = \sum_j c_j * X_j \quad \text{and} \quad Y = \sum_j c_j * Y_j \quad (4)$$

The total differential of HHV_{fuel}, as expressed through Equations 2-4, produces seven terms (not nine, because X_j and Y_j are constant). The differential elements, including d HHV_{fuel} and d c_j, can be replaced with any (consistent) metric of change or uncertainty (e.g., 95% confidence intervals were used for this work) to derive an expression for the uncertainty in the HHV by quadrature addition. The two terms for the uncertainty in the heats of formation of gaseous carbon dioxide and liquid water have been neglected in this work because those quantities are well-known compared to the heats of formation of most hydrocarbons. That leaves five terms.

Three of these terms relate to the uncertainty in the hydrocarbon class concentration measurements; the sum of these terms is designated as $UQ1$ and shown in Equation 5. Because the sum over all mole fractions must always be exactly one, one is placed as a constraint. In principle, $UQ1$ could be evaluated by quadrature addition of each component uncertainty, but we chose to use Monte Carlo analyses for convenience. Term $UQ2$, defined in Equation 6, accounts for the uncertainties associated with the data pulled from the NIST database. This term could also be evaluated analytically. Because the population distribution of isomers in class *j* (designated by $c_{i,j}$ in Equation 3) is unknown, we have approximated it with a uniform distribution designated by $\overline{c_{i,j}}$ in Equation 6. Term $UQ3$, defined in Equation 7, accounts for the uncertainties arising from the unknown population distribution of isomers within each hydrocarbon class. This term must be evaluated via Monte Carlo analyses. The σ in Equation 7 notionally represents the 95% confidence interval of the modeled isomer population distribution for each hydrocarbon class. These three terms ($UQ1, UQ2, UQ3$) are captured for each simulation, and their resulting values are shown in the lower right of Figure 4.

$$UQ1 = \sum_j \sigma c_j * X_j * \Delta H_{f,CO2(g)} + 0.5 * \sum_j \sigma c_j * Y_j * \Delta H_{f,H2O(l)} + \sum_j \sigma c_j * \Delta \overline{H}_{f,j(l)} \mid 1 = \sum_j c_j \quad (5)$$

$$UQ2 = \sum_j c_j * \sum_i \overline{c_{i,j}} * \sigma \Delta H_{f,i,j(l)} \quad (6)$$

$$UQ3 = \sum_j c_j * \sum_i \sigma c_{i,j} * \Delta H_{f,i,j(l)} \mid 1 = \sum_i c_{i,j} \quad (7)$$

Results and Discussion

The uncertainty of determinations made using the fundamental approach involves three principal components: "$UQ1$," the measurement error associated with the concentration of each class of hydrocarbon; $UQ2$, the error associated with the heats of formation of individual molecules as determined by NIST, and $UQ3$, the uncertainty of the population distribution of isomers that belong to the same class of hydrocarbon. The uncertainty resulting from the unknown isomer population distribution ($UQ3$) has two sub-components: a) the confidence interval associated with the potential difference between the population mean and the fuel sample and b) the confidence interval associated with the potential difference between the population mean and the modeled mean. However, the second sub-component is much smaller than the first because the number of components in each modeled class is high (or a high fraction of the total population), whereas the number of components within a given class in the real fuel could be as few as one.

Naturally occurring isomer population distributions, developed over geological timescales of exposure to high temperature and pressure, may be determined by minimizing the Gibbs free energy of the system, or at least be influenced by free energy more than chemicals manufactured by any of several potential synthetic pathways. Although the population distribution of

synthesized isomers remains unknown for most samples, farnesane by Amyris (ASTM D7566.A3) is primarily a single isomer synthesized through a biological mechanism, and alcohol-to-jet fuel by GEVO (ASTM C7566.A5) is primarily two isomers made from isobutanol. We expect that the database used to simulate the full population is also biased toward isomers that are more readily produced and purified because, until recently, heats of formation needed to be determined experimentally. However, by incorporating *ab initio* calculations (e.g., Paulechka & Kazakov [21], Paulechka & Kazakov [22]), any isomer can be included in the model's database regardless of whether it is produced naturally (in an appreciable fraction) or by any known synthetic pathway. Unbiased sampling from the database produces an unweighted mean of the database, which is greater than the mean obtained by sampling from a Boltzmann population distribution. Strategies to correct for this bias are not well-defined and are therefore left for future work.

By quantifying the sources of uncertainty in the fundamental approach used here, we found that the largest contribution to uncertainty is the range of heats of formation within each hydrocarbon class (i.e., term $UQ1$). The left half of Figure 4 compares our results to those from two other methods, the ASTM D4809 calorimetry-based method and the ASTM D3338 correlation-based estimation referenced in the ASTM D7566 fuel specification. Statistics comparing the fundamental approach with the ASTM D3338 estimation are provided in Table 3. Relative to the ASTM D3338 method, the fundamental approach has a lower mean absolute error (0.18 compared to 0.29) and a tighter correlation with calorimetry measurements (R^2=0.77 compared to R^2=0.39), arguing for its eventual inclusion as an acceptable method for LHV determination in the ASTM D7566 (and D1655) fuel specifications.

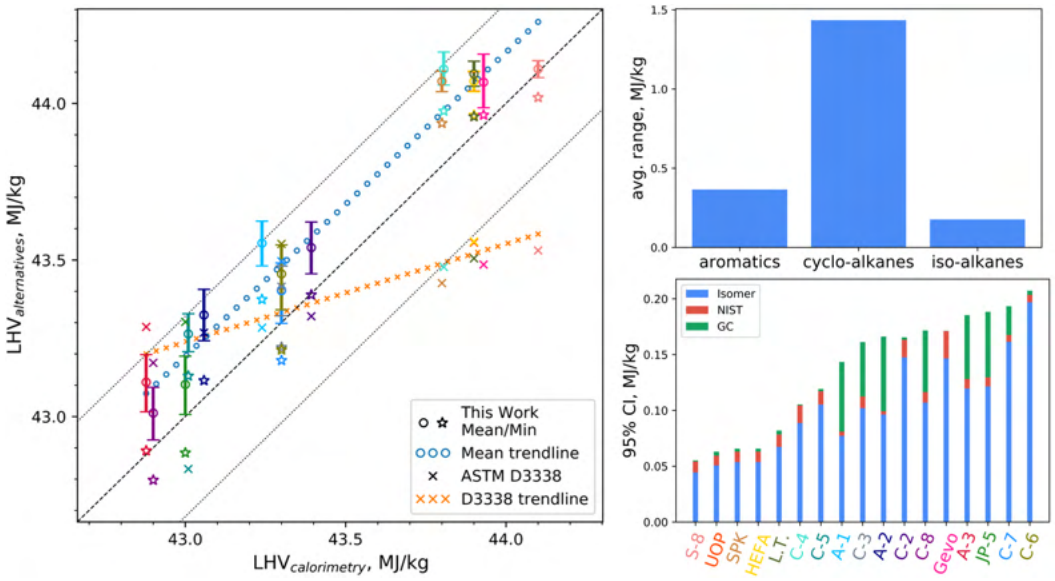

Figure 4. (Left) Unity plot comparing three methods of LHV determination. The black dotted lines correspond to the reproducibility (95% confidence intervals) of the ASTM D4809 test method. The colored circles represent the mean value from the fundamental approach, and the colored stars represent the minimum LHV based on the measured fuel composition and the NIST database value for the most stable isomer in each class. The colored x's represent estimations made via the ASTM D3338 method. The vertical lines through each circle represent 95% confidence intervals. Each color represents a different fuel sample, which are named along the x-axis of the lower right panel.
(Upper right) Range of LHV values, averaged across carbon number for each category of compound.
(Lower right) Components of uncertainty in this work. Blue bars represent the contribution originating from the unknown population distribution of isomers within each class ($UQ1$), red bars represent the contribution arising from the reported uncertainties of the thermo-chemical reference data ($UQ2$), and green bars represent the contribution arising from the GCxGC-FID concentration measurement ($UQ3$).

Table 3. Uncertainty statistics comparing this work to ASTM D3338.

	This '	ASTM I
Mean Error (ME)	0.1	-0.(
Mean Absolute Error (M	0.1	0.2
Mean Square Error (MS	0.0	0.0
Coefficient of Determinati	0.7	0.3
Slope	0.9	0.3

The mean of all seventeen LHV values determined using the fundamental approach is within the 95% confidence band around the ASTM D4809 measurements. On average, the values determined in this work are 0.18 MJ/kg higher than those measured by ASTM D4809. Some of this offset is caused by our use of unbiased (i.e., uniform) sampling instead of sampling to represent a population in thermodynamic equilibrium (i.e., biasing the distribution sampling with Gibbs energy). To provide a lower bound on the LHV determinations, we performed an additional calculation in which the lowest-energy isomer in each class was used to represent the whole class. These results are shown using the star symbols on the left side of Figure 4. Even this bounding extreme produces a mean offset of 0.06 MJ/kg relative to ASTM D4809, but this offset is within the reported "net bias (0.089 MJ/kg) of ASTM D4809 as determined by the statistical examination of interlaboratory test results." Trace impurities, including oxygenated species in the conventional fuels (A-1, A-2, A-3 and JP-5) were not considered in this fundamental approach, which may also lead to some overestimation of LHV. However, A-1 is a carefully selected, best-case petroleum fuel (Colket & Heyne [13]) with low sulfur content, low total acid number, and low existent gum, and it should therefore have the lowest hetero-atom content of any of the petroleum-derived samples considered in this study. Our decision to not correct for trace impurities does not explain the relatively high difference between ASTM D4809 and the fundamental approach for this sample.

The 95% confidence intervals shown on the left side of Figure 4 are sorted from lowest to highest and are re-displayed in the bar chart in the lower right of the figure. As this bar chart demonstrates, most of the uncertainty in the LHV determinations made here originates with the unknown isomer population distributions; the uncertainties in molecular heats of formation add only 0.01 MJ/kg to the uncertainty in our determination. The uncertainty arising from the reproducibility of measured class concentration (labeled "GC" in the bottom right of Figure 4) varies significantly from sample to sample for two reasons. First, the percent uncertainty of the concentration measurement for a given class scales inversely with concentration, such that samples comprised of many classes will not be characterized as well as samples comprised of few classes. Second, samples with constituents from across the range of possible LHVs (i.e., with a range of hydrocarbon types) will not be characterized as well as those that are comprised almost entirely of constituents with nearly the same LHV (e.g., C-4 is 99% iso-alkanes). The main reason for the observed differences in the uncertainty arising from the unknown isomeric population distribution is that some hydrocarbon classes have a greater range of heats of formation (and therefore a greater range of HHV and LHV) across their population than others. This can be seen in the bar chart in the upper right of Figure 4, which shows the average range of heats of formation for three common categories of species in jet fuel. The LHV of samples with a relatively high concentration of cyclo-alkanes will be determined less precisely than others, while those with a relatively high concentration of normal alkanes (range=0) will be determined more precisely than others.

Figure 5 provides a more detailed representation of class-wise variation in LHVs. On the left side, LHV is plotted as a function of H/C ratio to show that LHV trends higher as proportionately more water is produced by the reaction. This figure also provides general observations about the LHV of different categories of hydrocarbons: neither alkynes or dienes are normally present in jet fuels, but their inclusion in this figure demonstrates the importance of hydrocarbon type on both LHV and the range of LHV by carbon number. Generally, small normal- or iso-alkanes have the highest LHV while aromatic compounds have the lowest LHV due to their low H/C and unique stability (i.e., aromaticity). On the right side of Figure 5, LHV is plotted as a function of molecular weight to highlight the variation in LHV both from category to category and within each category as the carbon number varies.

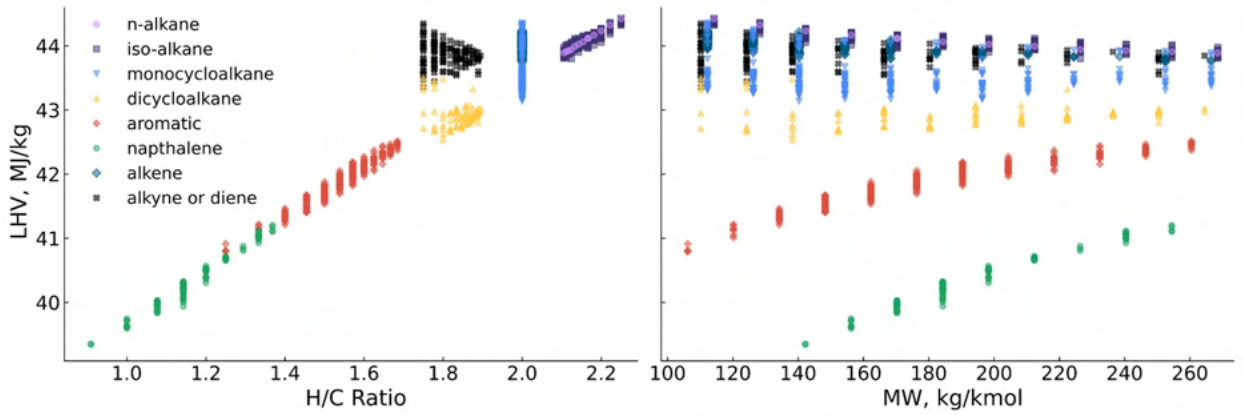

Figure 5. Variation in the heat of combustion within and among hydrocarbon classes.

Near-misses between this work and ASTM D4809

The LHV values that we calculated for two fuels, A-1 and C-4, were in the tails of the probability distributions expected from ASTM D4809. The case of C-4 illustrates how and why a fuel with a relatively simple composition can produce disagreements between the method used in this work and ASTM D4809. C-4 is composed of almost 99% by mass (%m) iso-alkanes, with only six iso-alkane classes represented by >97%m. Figure 6 shows the LHV data, calculated as described above, along with cumulative distribution functions for the ASTM D4809 measurements (imagined) and the Monte Carlo simulations of this work. Histograms for the LHV of molecules in these six hydrocarbon classes are shown in the background. The histograms reported here are the conglomeration of all molecules in the database that meet the criteria in the figure legend (i.e., C9 to C16 iso-alkanes). The vast majority (>97%m) of the C-4 sample is composed of the reported hydrocarbon groups in Figure 6, with 42%m alone composed of C12 iso-alkanes. Unsurprisingly, the C12 iso-alkane LHV grouping is near the expected value for the bulk mixture. The tails of the ASTM D4809 confidence intervals marginally overlap the 95% confidence interval of this work and the C12 iso-alkane distribution. In other words, it is highly unlikely that the actual LHV for this fuel is below the confidence interval reported for this work because this could only occur if the NIST database was incorrect or missing the most stable isomers of each class, which is itself highly unlikely.

To evaluate the other near miss, two samples of A-1 from the same container were given different labels and sent to a commercial laboratory for ASTM D4809 testing. Figure 7 compares these new D4809 results for A-1 (42.1 and 43.5 MJ/kg) to the initial ASTM D4809 results (reported earlier) and the results from this study. Notably, the newly measured D4809 data points are not within the reported reproducibility of measurement. Although neither of the recent LHV measurements should be trusted because they do not agree with each other, we report them here to illustrate another source of uncertainty with all fuel property data from a customer's perspective—namely, that not all technicians follow procedures or maintain equipment as expected, but the customer usually has no way of knowing when this has happened.

These two near misses are consistent with previous experience in the National Jet Fuels Combustion Program (Colket & Heyne, 2021). In that program, several conventional fuels were tested multiple times with inconsistent results, while another fuel composed of very few hydrocarbon classes was reported with a non-physical LHV. Overall, these near-miss observations reinforce the need to have more properties determined by diverse experimental and numerical methods (such as GCxGC-FID chromatograms, IR absorption spectra, or NMR spectra), regardless of approach, because the stakeholders-in-aggregate benefit from the additional validation.

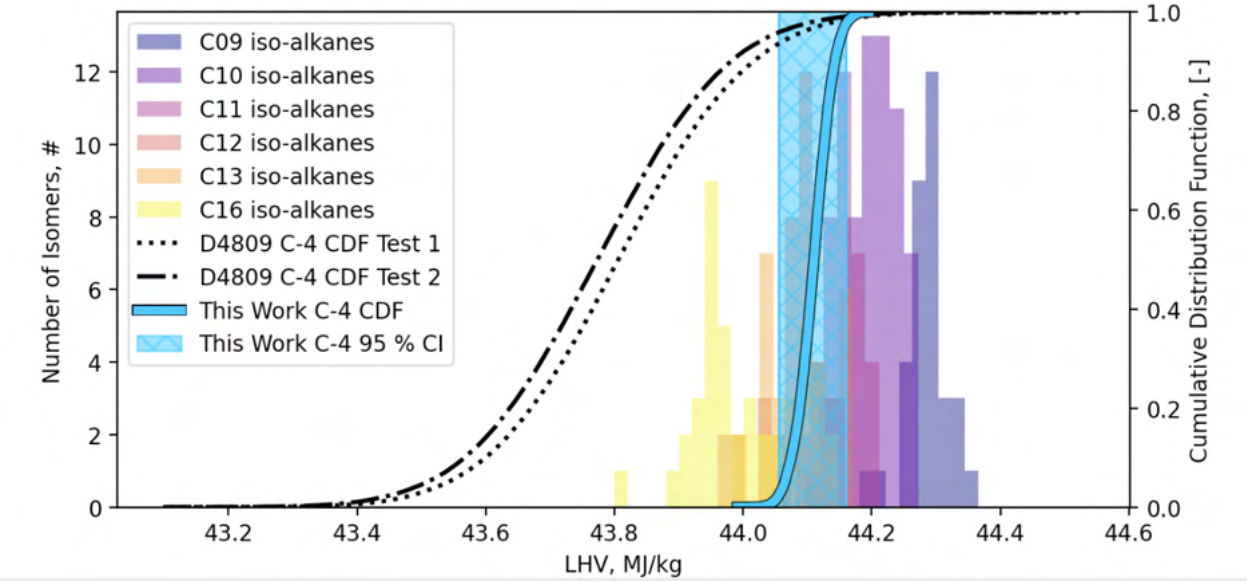

Figure 6. Histograms for LHV values from the six major hydrocarbon classes are plotted along the left vertical axis, and the (imagined) cumulative distribution function for two ASTM D4809 measurements (dotted and dashed-dotted line) and this work's Monte Carlo simulation (black outlined teal line) are compared along the right vertical axis. The 95% confidence interval for the simulations conduced in this work are bounded by the teal hashed and filled region.

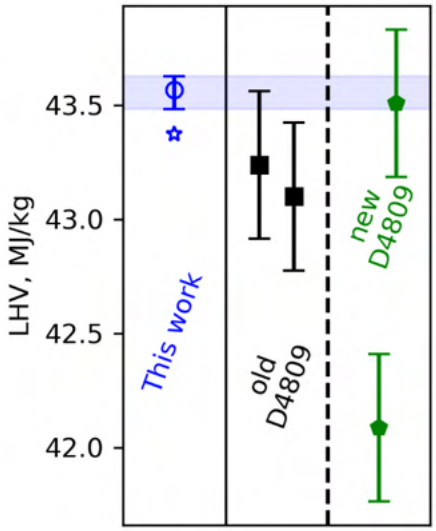

Figure 7. Comparison of LHVs from initial ('old') ASTM D4809 testing (black squares), recent ('new') ASTM D4809 testing (green pentagons), and this work (open blue circle). Error bars represent the 95% confidence interval for each method.

Conclusion

We have demonstrated that the LHV of jet fuel and sustainable alternative fuel candidates can be determined from hydrocarbon class concentration data and thermo-chemical reference data with high precision and accuracy. Although we tested fewer samples (n=17) than previous studies, all determinations reported here were made in the absence of any training data. A correlation method based on the standard 80/20 rule for training and test data would require at least 85 samples

overall to support seventeen predictions. The 95% confidence interval of the LHV of fuel candidates that are comprised entirely of normal and iso-alkanes was less than 0.1 MJ/kg while higher cyclo-alkane content led to 95% confidence bands that approached 0.2 MJ/kg. However, the accuracy of LHV determinations made by the fundamental approach depends on how well the population distribution of isomers in each hydrocarbon class is represented. In this work, we assumed that the distributions are uniform (i.e., no Boltzmann-type weighting), which is likely to bias the result toward a higher LHV. To evaluate the possible magnitude of this bias, we ran a set of simulations using the lowest LHV isomer in each class to represent the whole class. The average difference between these two bounding assumptions was 0.13 MJ/kg.

References

[1] Zhang, J. (n.d.). Application note energy & chemicals author calculation of natural gas calorific value with the Agilent 990 PRO Micro GC System 2. Retrieved April 23, 2021, from https://www.agilent.com/cs/library/applications/application-natural-gas-calorific-value-990-pro-micro-gc-5994-1374en-agilent.pdf

[2] Stufkens, J. S., & Bogaard, H. J. (1975). Rapid method for the determination of the composition of natural gas by gas chromatography. Analytical Chemistry, *47*(3), 383–386. https://doi.org/10.1021/ac60353a060

[3] Shi, X., Li, H., Song, Z., Zhang, X., & Liu, G. (2017). Quantitative composition-property relationship of aviation hydrocarbon fuel based on comprehensive two-dimensional gas chromatography with mass spectrometry and flame ionization detector. Fuel, *200*, 395–406. https://doi.org/10.1016/j.fuel.2017.03.073

[4] Berrier, K. L., Freye, C. E., Billingsley, M. C., & Synovec, R. E. (2020). Predictive modeling of aerospace fuel properties using comprehensive two-dimensional gas chromatography with time-of-flight mass spectrometry and partial least squares analysis. Energy & Fuels, *34*(4), 4084–4094. https://doi.org/10.1021/acs.energyfuels.9b04108

[5] Yang, Z., Kosir, S., Stachler, R., Shafer, L., Anderson, C., & Heyne, J. S. (2021). A GC × GC Tier α combustor operability prescreening method for sustainable aviation fuel candidates. Fuel, *292*, 120345. https://doi.org/10.1016/j.fuel.2021.120345

[6] Vozka, P., & Kilaz, G. (2020). A review of aviation turbine fuel chemical composition-property relations. Fuel, *268*, 117391. https://doi.org/10.1016/j.fuel.2020.117391

[7] Gautam, K., Jin, X., & Hansen, M. (1998). Review of spectrometric techniques for the characterization of crude oil and petroleum products. Applied Spectroscopy Reviews, *33*(4), 427–443. https://doi.org/10.1080/05704929808002061

[8] Caswell, K. Allen., Glass, T. E., Swann, Madeline., & Dorn, H. C. (1989). Rapid prediction of various physical properties for middle distillate fuels utilizing directly coupled liquid chromatography/proton nuclear magnetic resonance. Analytical Chemistry, *61*(3), 206–211. https://doi.org/10.1021/ac00178a004

[9] Johnson, K. J., Morris, R. E., & Rose-Pehrsson, S. L. (2006). Evaluating the predictive powers of spectroscopy and chromatography for fuel quality assessment. Energy & Fuels, *20*(2), 727–733. https://doi.org/10.1021/ef050347t

[10] Fodor, G. E., Mason, R. A., & Hutzler, S. A. (1999). Estimation of middle distillate fuel properties by FT-IR. Applied Spectroscopy, *53*(10), 1292–1298. https://doi.org/10.1366/0003702991945542

[11] Wang, Y., Ding, Y., Wei, W., Cao, Y., Davidson, D. F., & Hanson, R. K. (2019). On estimating physical and chemical properties of hydrocarbon fuels using mid-infrared FTIR spectra and regularized linear models. Fuel, *255*, 115715. https://doi.org/10.1016/j.fuel.2019.115715

[12] Striebich, R. C., Motsinger, M. A., Rauch, M. E., Zabarnick, S., & Dewitt, M. (2005). Estimation of select specification tests for aviation turbine fuels using fast gas chromatography (GC). Energy & Fuels, *19*(6), 2445–2454. https://doi.org/10.1021/ef050136o

[13] Colket, M., & Heyne, J. (2021). *Fuel effects on operability of aircraft gas turbine combustors.* American Institute of Aeronautics and Astronautics.

[14] Edwards, T. (2017). Reference jet fuels for combustion testing [Presentation]. 55th AIAA Aerospace Science Meeting. https://doi.org/10.2514/6.2017-0146

[15] Kehimkar, B., Hoggard, J. C., Marney, L. C., Billingsley, M. C., Fraga, C. G., Bruno, T. J., & Synovec, R. E. (2014). Correlation of rocket propulsion fuel properties with chemical composition using comprehensive two-dimensional gas chromatography with time-of-flight mass spectrometry followed by partial least squares regression analysis. Journal of Chromatography A, *1327*, 132–140. https://doi.org/10.1016/j.chroma.2013.12.060

[16] Kroenlein, K., Muzny, C., Kazakov, A., Diky, V., Chirico, R., & Magee, J. (2012). NIST Standard Reference 203: TRC Web Thermo Tables (WTT). National Institute of Standards and Technology.

[17] AJF:TD. (n.d.). University of Illinois. Accessed June 5, 2021, from https://altjetfuels.illinois.edu/

[18] Striebich, R. C., Shafer, L. M., Adams, R. K., West, Z. J., DeWitt, M. J., & Zabarnick, S. (2014). Hydrocarbon group-type analysis of petroleum-derived and synthetic fuels using two-dimensional gas chromatography. Energy & Fuels, *28*(9), 5696–5706. https://doi.org/10.1021/ef500813x

[19] Data, *9*(2), 193–198. https://doi.org/10.1021/je60021a013

[20] Flora, G., Kosir, S., Heyne, J., Zabarnik, S., & Gupta, M. (2019). Properties calculator and optimization for drop-in alternative jet fuel blends [Presentation]. AIAA SciTech Forum.
[21] Paulechka, E., & Kazakov, A. (2017). Efficient DLPNO–CCSD(T)-based estimation of formation enthalpies for C-, H-, O- and N-containing closed-shell compounds validated against critically evaluated experimental data. The Journal of Physical Chemistry A, *121*(22), 4379–4387. https://doi.org/10.1021/acs.jpca.7b03195
[22] Paulechka, E., & Kazakov, A. (2018). Efficient estimation of formation enthalpies for closed-shell organic compounds with local coupled-cluster methods. Journal of Chemical Theory and Computation, *14*(11), 5920–5932. https://doi.org/10.1021/acs.jctc.8b00593.

Paper 2: Towards fuel composition and properties from two-dimensional gas chromatography with flame ionization and vacuum ultraviolet spectroscopy

1. Introduction

Advances in analytical chemistry and computational capabilities have facilitated the development of sustainable, clean, and efficient transportation technologies. These methods have enabled feedstock conversion ideas to become real processes that produce requisite testing volumes in less than a year (Huq, et al. [1]). Several groups in the field of turbine aviation fuels have recently published studies describing predictions of fit-for-purpose properties (Heyne et al., Yang et al., Hall et al., Wang, Ding, et al., Vozka et al., [2– 6]) Such predictions are intended to help evaluate the potential of sustainable aviation fuel (SAF) candidates and de-risk low-carbon technologies by eclipsing the standard fuel evaluation process (ASTM D4054) at low technology readiness levels). ASTM standards and research tools have been developed In parallel to support computational fluid dynamics and chemical kinetic model development (Yang et al. [3]; D02 Committee, [7]; Ahmed et al, 2015; Govindaraju et al.[9]).

Two predictive methodologies have been the focus of recent advancements: (1) ground-up approaches leveraging fuel composition data derived from multidimensional gas chromatography with fundamental (Boehm, Yang, et al. [10]) or semi-empirical models (Yang et al. [3]) and (2) top-down interpolative models leveraging the relationships between chemical structure, spectroscopic data, two-dimensional gas chromatography hydrocarbon type determinations, and other material properties (Hall et al., Wang, Ding, et al., Vozka et al., Dussan et al., Wang, Wei, et al., Wang, Cao, et al., Vozka & Kilaz, Shi et al., Abdul Jameel et al., Pinkowski et al., [4-6,11-15]). These two methodologies are being advanced to maximize the impact of measurements taken from minimal fuel volumes. However, both approaches have practical implications for the quantification of uncertainty. Ground-up models can define ‘known-unknowns’ as a function of the potential of isomeric structures and other physical parameters, but these models are limited in accuracy by root data and by the models used to make predictions. In other words, the quantification of uncertainty is straightforward but tedious in ground-up approaches, but the predictive fidelity is not derived from the measurement it is aiming to predict.

Previous work has shown that the LHV of a fuel can be determined accurately if (a) the root data is accurately defined; (b) a significant amount of data is available on the influence of isomers, and (c) the model for determining the LHV of a mixture is fundamentally defined (Boehm, Yang, et al. [10]. However, issues within this approach arise in the case of viscosity: (a) the root data is less accurately defined; (b) less data exists on the influence of isomers; and (c) a semi-empirical model has historically been used because a fundamental model is computationally expensive.

Top-down approaches suffer from the inverse problems of bottom-up approaches: quantifying uncertainty is experimentally tedious, and the accuracy of the predictions is rooted in the data on which the models are trained. Because ground-up approaches are not tuned to target data, they do not need training data, and modeling uncertainties are sourced elsewhere. Top-down approaches need training data, and, depending on the complexity of the model, many times more data are needed for uncertainty quantification.

For top-down methods, thermochemical properties and chemical kinetic models have been developed from infrared measurements of quiescent and reacting systems and from nuclear magnetic resonance (Dussan et al., Wang, Wei, et al., Wang, Cao, et al., Shi et al., Abdul Jameel et al., Pinkowski et al. [11–13,15–17]). These models are then coupled to statistical packages that approximate kinetics or predict relevant physical properties. To date, one such model (Wang, Wei, et al. [12]) using a training data set with 15-32 samples has demonstrated a strong correlation (adjusted R^2 greater than 0.9) between FTIR data and several fit-for-purpose properties, including surface tension, LHV, derived cetane number (DCN), bubble point, and final boiling point. These predictive methods are still relatively new relative to other engineering methods, and the boundaries of their applicability have yet to be defined. One apparent limitation of these methods is the lack of compositional

and other variances across the distillation range. For example, gradients that are important across the distillation curve cannot yet be captured with mid-infrared or nuclear magnetic resonance without either coupling to a gas chromatogram or performing fractional distillation with multiple samples. Specifically, events like preferential vaporization (Bell et al. [18]) are likely unpredictable with mid-infrared spectroscopy and nuclear magnetic resonance unless they are coupled with a separation method. Additionally, specific chemical compositions cannot be fractionated or identified by hydrocarbon type and carbon number, but this data is important for informing fuel producers about how feedstocks and processing methods impact fuel composition.

Two-dimensional gas chromatography has been shown to consistently separate hydrocarbons into bins (Yang et al. [3], Striebich et al. [19]), with three-dimensional chromatography showing even more promise for distinguishing analytes based on their separation in non-polar, moderately polar, and highly polar columns (Trinklein et al. [20]. In these methods, analytes are separated to the first order by their volatility and polarity. Analytes are modulated between columns to maintain separations from the previous column, with each modulation potentially consisting of several species, ideally, separated on subsequent columns. After all separations are complete, analytes are sent to a detector, such as a flame ionization detector (FID), mass spectrometer (MS), or optical spectral analyzer. FIDs, known for their consistency and broad detection ranges, are typically used for quantification but provide no information about the specific isomers that may coelute through each column of the gas chromatography machine. As a result, there is significant uncertainty associated with fuel properties determined from GCxGC-FID data and a large (1,226 molecule) reference database (Yang et al. [3]). At the root of this variance is the wide range of properties among molecules in the same hydrocarbon class. For example, the variance for freeze point across 17 iso-alkanes with eight carbons is more than 200°C, indicating that freeze points determined without specific isomeric information will retain significant uncertainty. Overall, multidimensional gas chromatography with FID quantification is excellent for precise (better than 0.1%m) and accurate (~0.2%m) quantification and characterization of fuel compositions by hydrocarbon type and carbon number (Johnson et al. [21]).

Mass spectrometers (MS) or optical spectral analyzers are used in tandem with FID to identify analytes. A complete review of all the strengths and weaknesses of MS detectors is beyond the scope of this report; however, we note that MS detectors are excellent for delineating major hydrocarbon structure classifications (i.e., aromatics from saturates) but are not known for providing data sufficient to reliably identify specific isomers (e.g., o-, m-, or p-xylene or the stereoisomers of 1,2,4-trimethylcyclohexane). Gas chromatography can alternatively be coupled with absorption spectroscopy to speciate analytes. For example, Wang [22]recently applied GCxGC-VUV to analyze diesel fuel, and Anthony et al. [23] demonstrated that GC-VUV-MS has enhanced isomer selectivity relative to GC-MS. Lelevic et al., [24] published a review on VUV, and another study showed that VUV can quantitatively deconvolute co-eluting peaks Lelevic et al. [25]. These studies have thus demonstrated the ability to distinguish between structural and stereo-isomers. Figure 1 illustrates some examples of VUV spectra that distinguish between trimethyl benzenes (TMB) and decalins. Coupling multidimensional gas chromatograms to spectroscopy thus offers the potential to identify stereo and structural isomers, which contribute significantly to the variance in aviation fuel properties.

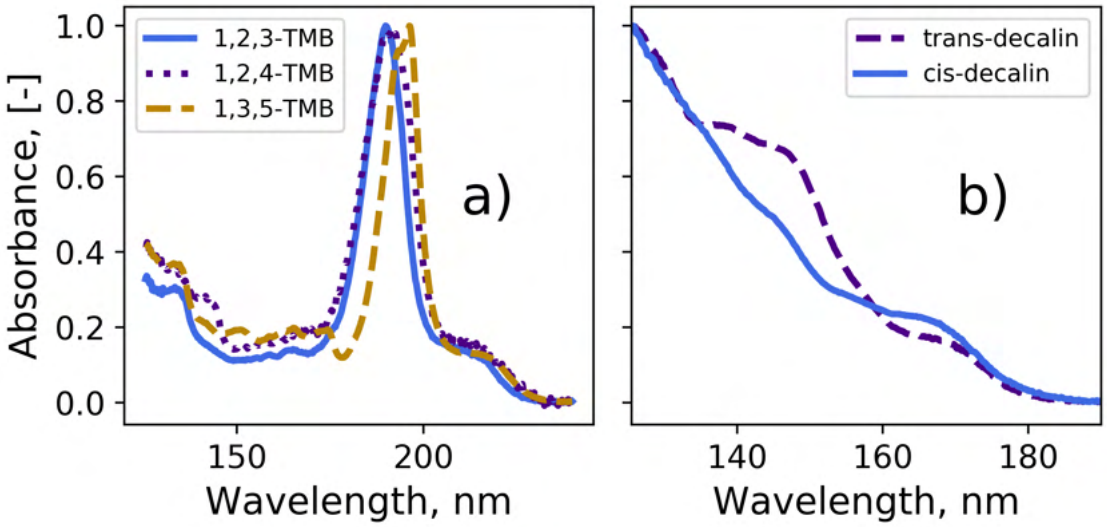

Figure 1. Normalized sample reference spectra for (a) trimethyl benzene (TMB) structural isomers and (b) decalin stereoisomers. The variance between TMBs and decalins are easily distinguished and repeatable with a VUV detector.

Analyte identification and quantification using multidimensional gas chromatography, in conjunction with a library of constituent properties and fundamental or semi-empirical blending rules for each property of interest, enables accurate downstream predictions of many fuel properties. Moreover, uncertainty quantification is well-defined for this approach; for examples, see Yang et al. [3] and Boehm et al. [10]. Conversely, approaches that train diagnostic data directly to known properties (regardless of the statistical method) are inherently top-down and it is difficult to comprehensively quantify the uncertainty that arises from the uncertainties in all the independent data and models. Predictive error is not comprehensive uncertainty; for more on this, see the discussion by Heyne et al. [2]. The quantification of uncertainty is beyond the statistical variance of a numerical method. Species size (i.e., molecular weight), structural features, and chemical bonds (~polarity) are all critical parameters for prescreening alternative fuels. Assumptions cannot be made about the population distribution of molecular sizes or types without also conveying the uncertainty introduced by these assumptions. For example, two sustainable aviation fuel blend components defined by ASTM D7566 specifications are composed of very selective and specific isomers (Annexes A3 and A5 [iso-butanol] (D02 Committee, 2020 [26])). If a predictive method for these fuels is not tempered with comprehensive uncertainty quantification, recommendations could be unfounded, and resources could be squandered, at a critical moment in transportation decarbonization. There is a growing list of ASTM methods that are useful for conventional fuels but ill-suited for alternative fuels, including ASTM D3338 (for LHV) (Boehm, Yang, et al. [10]) and ASTM D4737 (for the cetane index).

Robust separations with calibrated multidimensional gas chromatograms, absorption spectroscopy, and large hydrocarbon databases offer the potential to directly quantify and identify analytes and predict many nuanced properties of hydrocarbon fuels. Here, we provide the first case study that uses two-dimensional gas chromatography for mixture separation, VUV spectroscopy for analyte identification, and flame ionization detection for analyte quantification along with mined single-component properties and blending rules to predict the fuel properties important for early modeling and prescreening of SAFs. Analytes were identified in the absence of any retention time information from the GCxGC, and identification was not calibrated to the chromatogram because separation here was only meant to separate analytes for VUV spectra matching. For one aviation turbine surrogate composition, we compare our predictions and confidence intervals for 10 properties to those obtained using the method of Yang et al. (2021). Several of these comparisons also include a nominal reference value corresponding to a direct measurement derived from an applicable ASTM standard experimental method.

1 Experimental and computational methods

We used two deterministic approaches to derive fit-for-purpose fuel properties that either impact combustor/engine operability in jet engines (Heyne et al. [2]) or that are useful for chemical process modeling. The materials and methods

used to gather the data needed for property predictions are detailed in Sections 2.1 and 2.2, respectively, and the mathematical approach is described in Section 2.3.

1.1 Hydrocarbon reference materials

Sixteen hydrocarbon materials were sourced from three vendors and two fuel producers. These materials and their compositions were selected based on the ability to formulate a surrogate that would mimic many of the properties of Jet A. The final formulation of the mixture largely followed previous work on the formulation of surrogate compositions targeting aviation fuels (Dooley et al. [27] [28], 2012; Yang et al. [29], Kosir et al. [31] [32]) Material purity, cost, and availability also played a role in these decisions. We note that this blend was intended to represent the first-order properties of an aviation turbine fuel, not necessarily to mimic all relevant properties or exhibit all specification requirements of a Jet A/A-1. The details of the materials that we sourced are included in Table 1.

Table 1. Blended volumes, materials, purities, reference numbers, and suppliers for the surrogate fuel tested here.

Material name	Purity or POSF No.	Supplier	Blended vol. (23 ˚C), mL
Methylcyclohexane	99%	Sigma-Aldrich	2.2
cis-1,2-dimethylcyclohexane	98%	TCI	7.5
2,2,4-trimethylpentane	>99%	Sigma-Aldrich	7.5
1,2,4-trimethylcyclohexane	98%	Sigma-Aldrich	21.3
n-butylcyclohexane	99%	Alfa Aesar	10.5
iso-butylcyclohexane	>97%	TCI	10.5
trans-decahydronaphthalene	96.5%	MilliporeSigma	10.5
cis-decahydronaphthalene	98%	TCI	10.5
1-methylnaphthalene	96%	Alfa Aesar	26.8
n-undecane	>99%	Sigma-Aldrich	28.8
n-hexylbenzene	98%	Alfa Aesar	15.5
1,4-diisopropylcyclohexane	98%	Alfa Aesar	15.5
n-tridecane	>99%	Sigma-Aldrich	19
2,2,4,4,6,8,8-heptamethylnonane	98%	Sigma-Aldrich	5.05
ATJ (ASTM D7566 A5 [iso-butanol])	13718	Gevo	46.5
Farnesane	11832	Amyris	14.0

1.2 Gas chromatography and analyte detection

Data from two GCxGC units were used for this initial study, a GCxGC-MS/FID and a GCxGC-VUV/FID. Both units used an FID for analyte quantification and split samples to another detector. Hydrocarbon type and carbon number distribution were determined on a Zoex thermal modulation system (GCxGC-MS/FID) following a previously reported method (Yang et al. [3]). The MS for this system was not used, but the system was chosen because it has a calibrated hydrocarbon type template. The

other GCxGC system (a GCxGC-VUV/FID), built upon an Agilent 8890, employed a flow modulation system with sample splitting to FID and a VGA-101 VUV. This detector and the associated analysis are described in Section 2.2.1. Flow modulation was maintained with a SepSolve INSIGHT modulator. Figure 2 provides a schematic of the GCxGC-VUV/FID system.

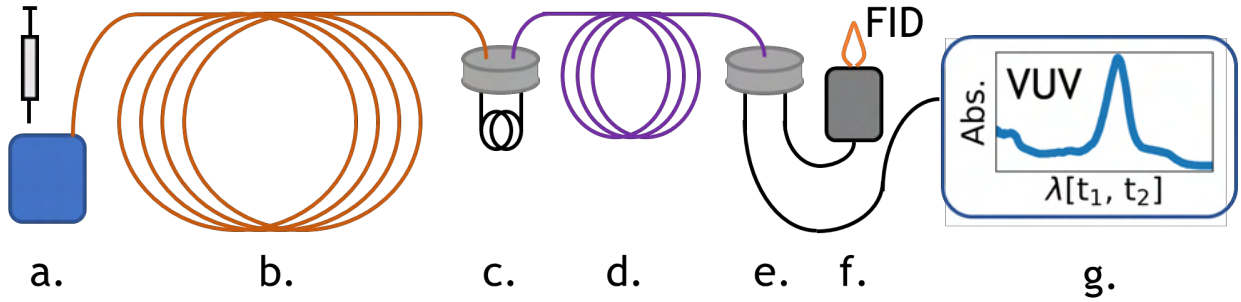

Figure 2. Illustration of the GCxGC-FID/VUV system. Samples are injected (a) and then travel through a primary column (b), flow modulation system (c), and secondary column (d). The sample is then split (e), with one fraction going to a flame ionization detector (f) and the other fraction to a vacuum ultraviolet light absorption system (g). Additional valves and gas lines are not pictured here.

1.2.0 GCxGC-VUV/FID Method

The GC temperature profile was initiated at 40 °C, held for 6 seconds at 40 °C, increased at a rate of 2 °C per minute to a temperature of 280 °C, and then terminated. FID quantification for this GCxGC system used the INSIGHT ChromSpace software (Version 1.5.1). One μL of the undiluted sample was injected with a Hamilton 10 μL syringe and a Merlin MicroShot manual injector at a split ratio of 300:1 and inlet temperature of 250°C (Figure 2a). In our two-column setup, the first column was an SGE BPx5 with a stationary phase composed of 5% phenyl and 95% dimethyl polysiloxane (Figure 2.b), and the second column was an SGE BPx50 with a stationary phase made of 50% phenyl polysilpenylene-siloxane (Figure 2.d). The primary column had a length of 20 m, ID of 0.18 mm, and film thickness of 0.18 μm. The secondary column had a length of 5 m, ID of 0.25 mm, and film thickness of 0.10 μm. The connector lines from the split plate to the FID and to the VUV were both 1 meter long with an ID of 0.25 mm. We used a modulation time of 4 seconds, fill time of 3700 ms, and flush time of 300 ms for the modulator. The primary column had a carrier gas flow rate of 0.75 mL/min of grade 5.0 helium sent through a Restek Triple Filter. The secondary column used a flow rate of 24 mL/min. The FID was set to 300 °C. The air (ultra-zero grade), H_2 (grade 6.0), and N_2 (grade 5.0) flows to the FID were set to 400, 40, and 25 mL/min, respectively.

1.2.1 GCxGC-VUV/FID mass concentration determinations

We used FID response data and a set of blended calibration samples to determine the mass concentrations of each species. Calibration samples were measured via the relative response factors for each isomer individually. To accomplish this, each species was tested in four blends at four different concentrations. Each individual blend included four species, for a total of 16 calibration samples. Each species was blended by volume, though we recorded the concentration of each species by mass. Species were mixed at ratios of 20 μL/1080 μL, 50 μL/1200 μL, 50 μL/700 μL, and 100 μL/900 μL using dichloromethane as the solvent. We observed linear relationships between the calculated masses of these test species and the total ion current response (TIC), which were then applied to each individual peak to convert from the FID response to mass fractions. Peaks that were not within the calibration matrix were assumed to be the average of the measured relationships. Peak areas were calculated using a pseudo-Gaussian curve-fitting algorithm implemented in Chromspace, with Top-hat noise cancellation. The calibration curves for the analytes had R^2 values exceeding 0.998.

1.2.2 Vacuum ultraviolet analyte identification

We used a VGA-101 (VUV Analytics) to obtain vacuum ultraviolet absorption spectra and match them to known spectra. Analytes were identified solely with the VUV/VGA-101, meaning that the two-dimensional separations were only used to isolate spectra; no retention time information was used for matching. The detector we used measures the transmission of

light between 125 nm and 430 nm and records at 76.92 Hz. Signal averaging is accomplished during post-processing. At the interface between the VGA-101 and the gas chromatograph, the sample transfer line is maintained at a temperature of 250 °C. Reference materials described in Section 2.1 were used to augment the licensed reference library, and the spectra from these materials were gathered from a series of measured points in the absence of overlapping spectra. The matching algorithms we used leveraged in-house code that compares measured spectra to the reference library spectra. Our code filters the data to focus on regions of the spectrograph with significant absorptions while ignoring regions with a low signal-to-noise ratio, which can vary with the analyte type and concentration. Reference spectra were correlated with measured spectra at an R-squared value >0.99.

Using internally constructed codes, we also synchronized time measurements between the methods to associate the VUV absorption spectra with FID signals. This software averaged VUV light absorption spectra in two dimensions (i.e., across multiple modulations), identified as t_1 and t_2. Averaging over multiple modulations improves the identifications, as the consequent reduction in the signal-to-noise ratio increases confidence in the matching spectra. The software we used allowed for the selection of data points away from coeluting analytes, thus negating the need for any signal deconvolution.

Figure 3. continues from Figure 2 and shows the process of data acquisition and analyte quantification, classification, and identification. The signal from the FID (Figure 3.i) is processed to two dimensions (Figure 3ii), where peaks are placed in the class bins with their associated carbon numbers (Figure 3iii). Data from the VGA-101 (Figure 3iv) was similarly processed into two dimensions, and the signal for a given peak was then averaged (Figure 3v). These averaged data were matched to reference data to identify the analyte. In cases where the analytes are not matched with reference spectra, the specific isomer is unknown.

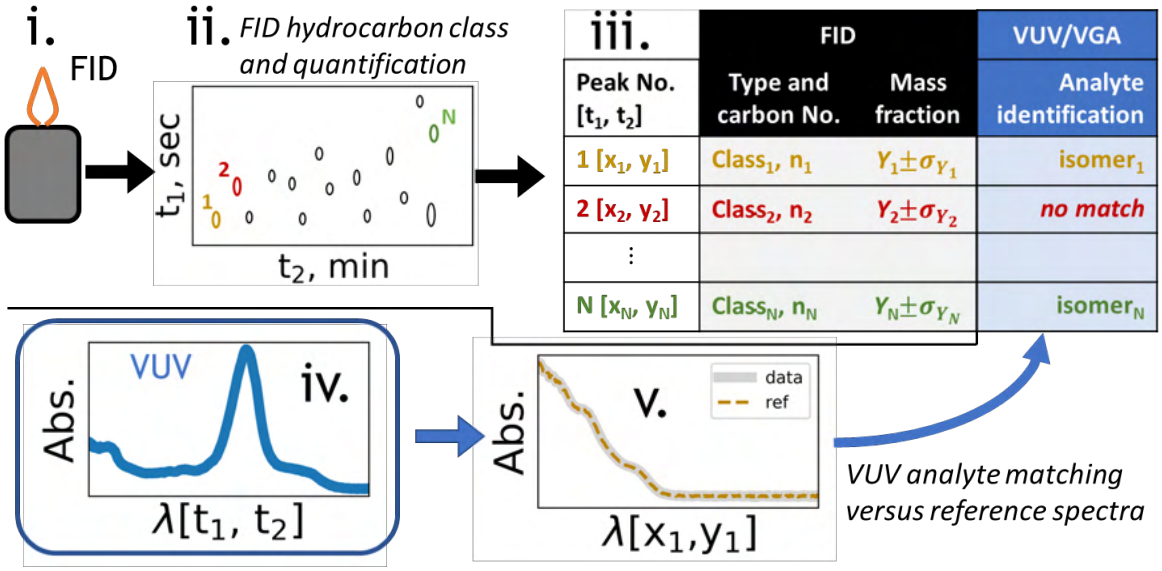

Figure 3. Illustration of the path from data acquisition to quantification with FID (i) and identification with VGA-101 (iv). The two-dimensional FID peaks (ii) are used to distinguish hydrocarbon types (i.e., empirical formulas) for given peaks as well as their associated mass fractions (iii). The VGA-101 absorption signal is matched to corresponding FID time stamps to identify specific species from reference data (v).

1.3 Mathematical Approach

1.3.0 Database of hydrocarbon properties

The properties predicted in this study follow the work of Yang et al. (2021), although some individual components properties were measured directly in our lab instead of relying solely on data mined from the open literature.

1.3.1 Blending rules

The blending rules for density, viscosity, surface tension, DCN, distillation curve calculations, freeze point, flash point, heat capacity, and thermal conductivity used here follow previous work (Yang et al. [3] Kosir, Stachler, et al. [30], Bell et al. [32], Flora et al. [33], Boehm, Scholla, et al. [34]).

1.3.2 Uncertainty quantification

1.3.2.1 Sources of uncertainty considered

Following the approach used here, uncertainties in property determinations come from three principal sources: UQ1) the measured concentration data (σ_{Y_i}); UQ2) the source property data from the NIST library and laboratory measurements (σ_{Z_i}); and UQ3) known-unknowns from analytes that are identified by class but not a specific isomer (σ_{isomer}) (i.e., the unidentified peaks in the FID-measured mass concentrations, such as analyte 2 in Figure 3, for which there is no VUV match). These uncertainties were quantified as follows.

- UQ1 Analyte quantification (σ_{Y_i}): The uncertainty of the concentration measurements was determined by considering the uncertainty arising from the calibration curves. Although the calibration curves achieved R^2 values >0.998, some level of uncertainty still exists with respect to the actual concentration of the analyte. We assumed a normal distribution centered on the calibration coefficient and randomly selected values from this distribution.
- UQ2 Root property data (σ_{Z_i}): Sourced property data uncertainties were used from the NIST database, and the measurement uncertainties for individual compounds were measured in the lab. As above, we assumed a normal distribution of these properties. Individual properties for each analyte were randomly sampled before the individual properties were blended/modeled together, as described for UQ3 below.
- UQ3 Isomeric uncertainty (σ_{isomer}): In the event that an analyte was below the limit of detection for the VUV or not currently identifiable when reference spectra were not available, the analyte was 'blinded,' meaning that we made no assumptions about its identification aside from its determined hydrocarbon class and associated carbon number. For these analytes, we considered all molecules in the database that fit the class and carbon number for that analyte peak. Mathematically, σ_{isomer} for a given property is the uniform weighted distribution for all the isomers with the defined hydrocarbon class and carbon number (such that $\sigma_{isomer} = f(Z_i \pm \sigma_{Z_i}\ \forall\ i \in [\text{Class}_j, \text{n}_j])$, where j is determined from the FID data). The uncertainty is therefore calculated by randomly sampling all isomers in the database that belong to each class and carbon number. A specific example of this calculation is given later in the text. This uncertainty term is typically the largest of the three uncertainty terms (Boehm et al. [10]), and it has the most dramatic impact on properties that vary significantly among species within the same class and carbon number, e.g., viscosity; (Yang et al.) see Figure 2b.

The uncertainty of the concentration measurements (UQ1) and the individual constituent property data (UQ2) is represented in these predictions by an assumed normal distribution. In contrast, the uncertainty arising from the unidentified analytes (UQ3) is captured by random sampling of all species within the library that are eluted into the same GCxGC bin and not further parsed via VUV spectral data. These three uncertainty components are determined individually, in parallel, and collectively in separated Monte Carlo simulations to parse out the contribution from each source.

The three types of uncertainty and the general approach for calculating them are described below and illustrated in Figure . First, mass fraction data and analyte identification information (Figure A) are linked to the property database (Figure B). Analytes that were not identified are simulated by random sampling from the database as shown for analyte/peak number 2. For example, analyte 2 is not assumed to be any specific isomer, and instead, all isomer candidates that meet the limiting class and carbon number for that peak are considered. For example, if analyte 2 was a ten-carbon iso-alkane, all 73 ten-carbon iso-alkane isomers would be used for the prediction sequence. In that sequence, a specific mass fraction (UQ1) (Figure A), isomer (UQ3) (Figure A), and associated property (UQ2) (Figure B) are selected. The mass fraction and property are selected using uncertainties and assumed normal distributions, whereas the specific isomer for unidentified analytes is randomly selected from a uniform distribution as illustrated in Figure 4. If a property value for an identified analyte is not known, its value is estimated from all other isomers in that class and carbon number, analogous to the procedure used for undetermined analytes. This is illustrated in Figure 4B for the *N*th analyte, for which the LHV is unknown. In this case, all the isomers in that hydrocarbon class are sampled randomly.

The associated properties from any random sampling procedure are then combined via a blending rule. First, the sequence of mass fraction, property, and isomer sampling is repeated at least 10,000 times until the predictions converge (Figure C) at an apparent asymptote. These statistics are then communicated in the aggregate (Figure D). For example, Figure D shows 10,000 predictions ("Ind. Predictions") for the LHV of the *N*th analyte, with all three uncertainties included. The aggregate in Figure D communicates the mean value for all 10,000 predictions (open circle), the 68% confidence interval (CI) (solid blue line), and the 95% CI (capped dashed line). This process is repeated for each isomer and property that we randomly sample.

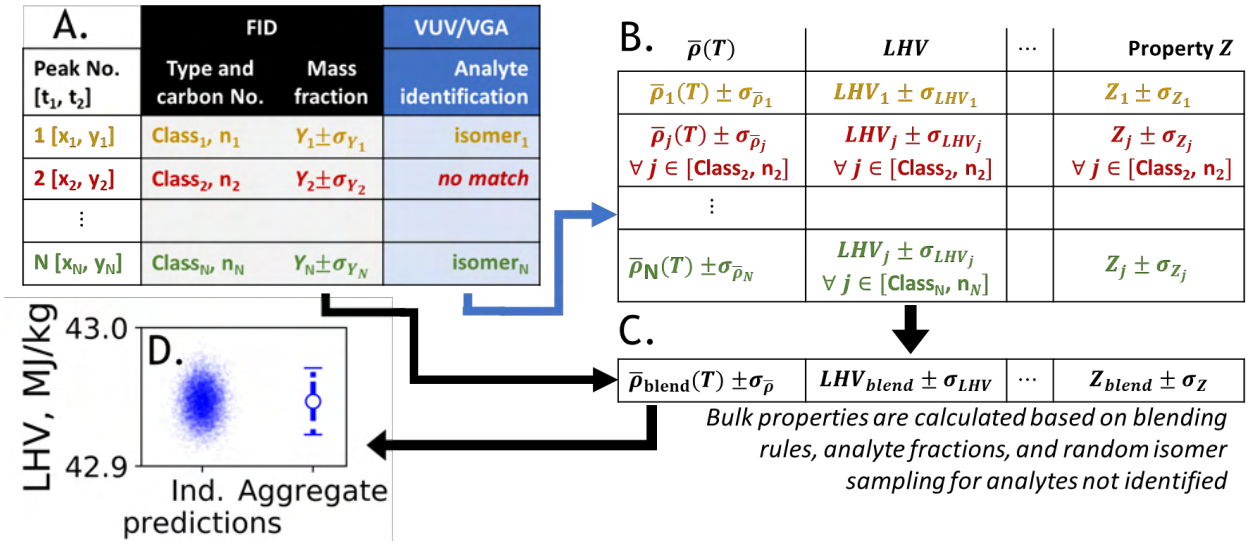

Figure 4. Illustration of our computational approach, showing the data generated, properties from the database, and the process of incorporating various types of uncertainty. The data from the FID and VUV/VGA-101 (A) are first coupled to a database (B). The blend properties (C) are then calculated from individual properties while accounting for all three sources of uncertainty (property uncertainty, σ_Z; measurement uncertainty, σ_{Y_i}; and isomeric uncertainty, σ_{isomer}). Properties are calculated thousands of times while sampling from uncertainty distributions, and the resulting aggregate (D) is reported.

1.3.2.2 Monte Carlo sampling

We evaluated 10,000 or more predictions for every property and, where reported, each temperature condition. Predictions were repeated until a corresponding histogram of outcomes had a smooth profile when the histogram bin size was ≤10% of the precision of the corresponding measurement method. For example, the repeatability of the DCN was 0.81 for a DCN of 43 (the value of the surrogate here), and the histogram bin size for this property was 0.08.

Our calculated uncertainties for the variance resulting from the inability to identify a given species (UQ3, σ_{isomer}) follow the method reported by Yang et al. [3], with a key distinction being the addition of VUV identification. Yang et al. randomly assigned all the carbon detected via FID to a specific isomer in the hydrocarbon database that had similar volatility and polarity to the detected carbon or class/carbon number combination. Here, we were able to assign most of that carbon to specific isomers based on VUV results. The remaining unidentified carbon was assigned to random isomers following the previous method. We assumed that all assignments were correct, but we acknowledge that some analyte spectra in future work may not be uniquely matched by spectra in the reference library. Although this was not the case for any of the principal components in the surrogate fuel created for this work, future generalization of this approach to more complicated mixtures of hydrocarbons will need to include each of the probable (or unverifiable) matches in the Monte Carlo simulation of the mixture. Relative to FID alone, for which a detected peak could be any of hundreds of possible isomers, the VUV-based identification here reduces the uncertainty substantially.

We determined species concentration uncertainties (UQ1) from multiple experiments using a more complex hydrocarbon mixture (JP-8, POSF 4751). For this analysis, we calculated repeatability using the hydrocarbon type/carbon number bins, measurements from experimental data, and the associated calibration curves. The reproducibility (σ) of hydrocarbon

type/carbon number bins used here ranged from 0.03 to 0.07%m. This reproducibility was subsequently sampled when developing the blended property predictions, and the repeatability of the measurements for reference samples were incorporated into the property prediction variance. Measurement repeatability variance (UQ2) from viscosities, densities, surface tensions, flash points, and freeze points for the reference materials reported in Section 2.1 were incorporated into the property predictions in the Results and Discussion section of this paper.

Figure 5 illustrates the process of uncertainty quantification described here. For each Monte Carlo sample, we sampled a random value from the mass fraction and property distributions for all analytes and all properties (vertical dotted lines). In this example, the first and *N*th peaks were identified by their VUV spectra but the second peak was not, as illustrated in the absorbance versus wavelength plots on the left of Figure 5. The isomeric uncertainty for the first and *N*th analyte is therefore zero for all Monte Carlo samples. For each Monte Carlo simulation for the second (unidentified) analyte, we sampled a random isomer that belongs to the corresponding class and carbon number. A specific property value (vertical dotted line) is then sampled from each property distribution. The plot in the center of Figure 5 illustrates several property distributions for the unidentified analyte. In this example, the second isomer in the bin is randomly selected, and a random property on the distribution for property Z is assigned. The bulk property (*Z*) is then predicted for each simulation, *k* times. The *k* property predictions are subsequently aggregated into confidence intervals, as shown in Figure D.

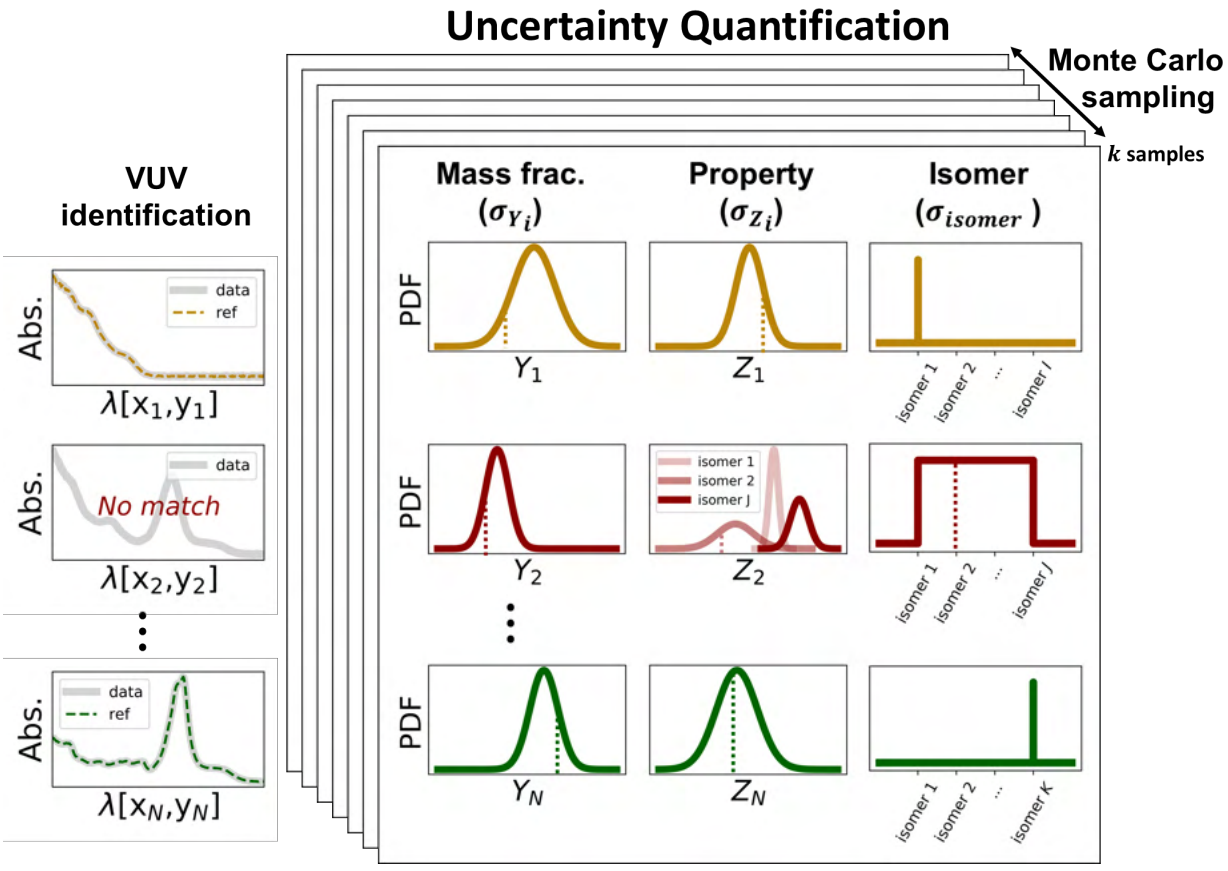

Figure 4. Illustration of one Monte Carlo sampling sequence and the types of uncertainty considered here.

2 Results and Discussion

2.1 Identification and quantification

We found that 98.7%m of the bulk composition of the surrogate hydrocarbon analyzed here could be classified into nine major bins (>1.0%m) with carbon numbers from seven (C7) to sixteen (C16), as reported in Table 2. The remaining 1.3%m of the fuel is composed of small amounts of alkenes from Amyris (0.3%m), C20 iso-alkanes from Gevo (0.3%m), and other small (<0.05%m) concentrations of contaminants in procured solvents used for blending. Figure 6 shows a chromatogram of the GCxGC-VUV/FID spectra, and Table 3 shows the hydrocarbon composition of the significant fractions. Figure 6 illustrates the method for identifying analytes using data from the VUV detector. For example, Figure 6a shows the measured absorbance of a peak (black circles) and the reference spectra matched to that peak (solid line). In this case, the measured spectra is best matched to 2,2,4-trimethylpentane (i.e., iso-octane). The spectrum for 2,2,3-trimethylpentane (dashed line) is also plotted in Figure 7a for reference, showing the clear identification of the measured peak as 2,2,4-trimethylpentane instead of the structural isomer. The remaining spectra in Figure 7 (b, c, and d) illustrate molecules with one additional methyl group (b), the stereoisomers trans- and cis-decalin (c), and the clear differences between aromatics and aliphatic molecules (d).

We found that the species concentrations of the sample material were near the typical range for conventional fuels (Edwards, [35]), with the exception of diaromatics. C11 diaromatics had the highest concentration of any diaromatic compounds, at 13.7%m of the fuel sample. Figure 8 compares the carbon distribution of the surrogate studied here (thin, multi-colored bars) to that of an average Jet A/A-1 (thicker, green bars) reported by Edwards [35]. The bulk surrogate had a molecular weight of 152 g/mol, a hydrogen content of 13.5%m, and an average empirical formula of $C_{10.9}H_{20.3}$. In contrast, the 'average' Jet A had a molecular weight of 159 gm/mol and a hydrogen content of 14.0%m (Edwards, [35]). Despite these differences, we note that our motivation in the selection and composition of this surrogate was not to mimic combustion property targets or develop a fully drop-in conventional fuel. Instead, we aimed to illustrate a method to dramatically reduce the uncertainty in predictions of key operability properties for sustainable aviation fuel candidates, develop ground-up property models for computational fluid dynamics, and other novel applications.

Table 2 Carbon number, hydrocarbon class, number of isomers in the corresponding class, names of specific molecules identified from that class, and measured concentrations for bins and individual peaks that exceeded 1%m.

Hydrocarbon Class, GCxGC-FID/MS	Isomers in Class, (-)†	Hydrocarbon Molecules, GCxGC-VUV/FID (Fig. 6 ref.)	MS/FID | VUV/FID, %m ††
C7 cyclo-alkanes	4	Methyl cyclohexane (ii.)	1.15 | 1.08
C8 iso-alkanes	17	2,2,4 Trimethyl pentane (i.)	2.81 | 2.72
C8 cyclo-alkanes	≥ 37	cis 1,2 Dimethyl cyclohexane (iii.)	3.15 | 2.77
C9 cyclo-alkanes	≥ 53	1,2,4-trimethylcyclohexane stereoisomers (iv. and v.)	8.67 | 8.14
C10 cyclo-alkanes	≥ 70	n-butylcyclohexane (viii.)	8.32 | 3.90
		iso-butylcyclohexane (vii.)	4.94
C10 dicyclo-alkanes	≥ 7	cis-decalin (xi.)	9.32 | 4.70
		trans-decalin (ix.)	4.25
C11 di-aromatic	2	1-methylnaphthalene (xvii.)	13.70 | 12.86
C11 n-alkane	1	n-undecane (x.)	9.89 | 10.98

C12 alkyl benzenes	≥ 58	n-hexylbenzene (xiv.)	6.30 | 6.82
C12 iso-alkanes	354	2,2,4,6,6-pentamethylheptane (vi.)	12.54 | 9.61
C12 cyclo-alkanes	≥ 38	1,4-diisopropylcyclohexane stereoisomers (xii. and xiii.)	6.04 | 5.91
C13 iso-alkanes	801	Not resolved	1.04 | -----
C13 n-alkane	1	n-tridecane (xv.)	6.57 | 6.87
C15 iso-alkanes	4,346	Farnesane (xviii.)	4.79 | 5.43
C16 iso-alkanes	10,359	2,2,4,4,6,8,8-heptamethylnonane (xvi.)	4.40 | 2.99
Total			98.69 | 93.96

† The number following the ≥ symbol corresponds to the number of isomers in the NIST database that are part of the stated hydrocarbon class and therefore used in this study. The total number of possible isomers is greater than or equal to this value.
†† The number preceding the vertical divide | is the species class concentration data provided by GCxGC-FID/MS. The second number is the concentration of that species as determined by GCxGC-VUV/FID.

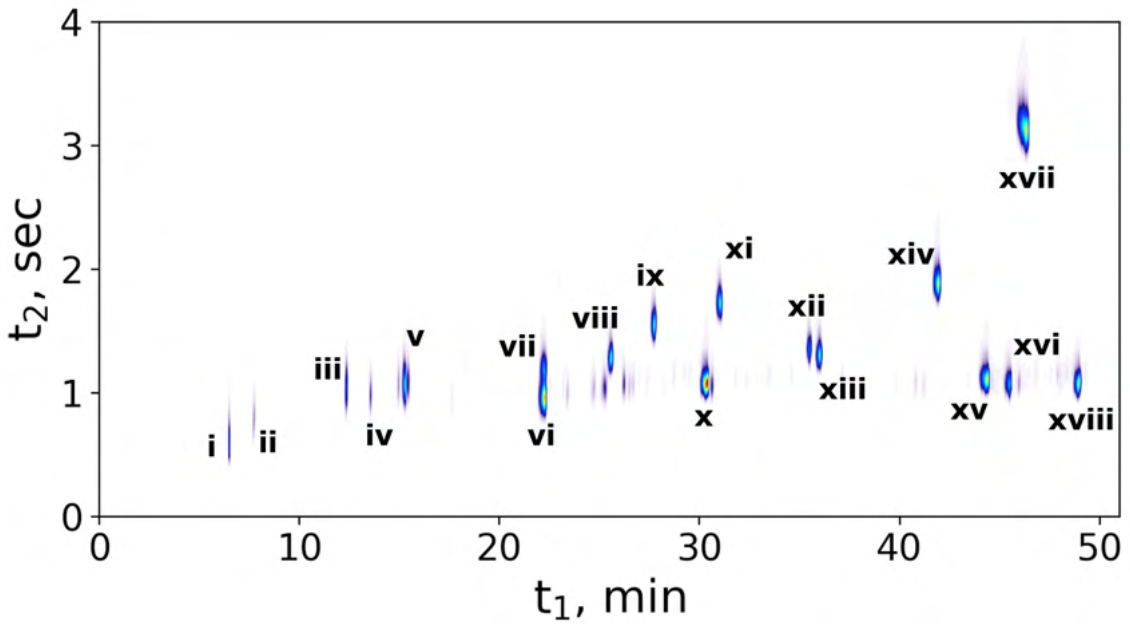

Figure 5 GCxGC-VUV/FID chromatogram of the surrogate fuel.

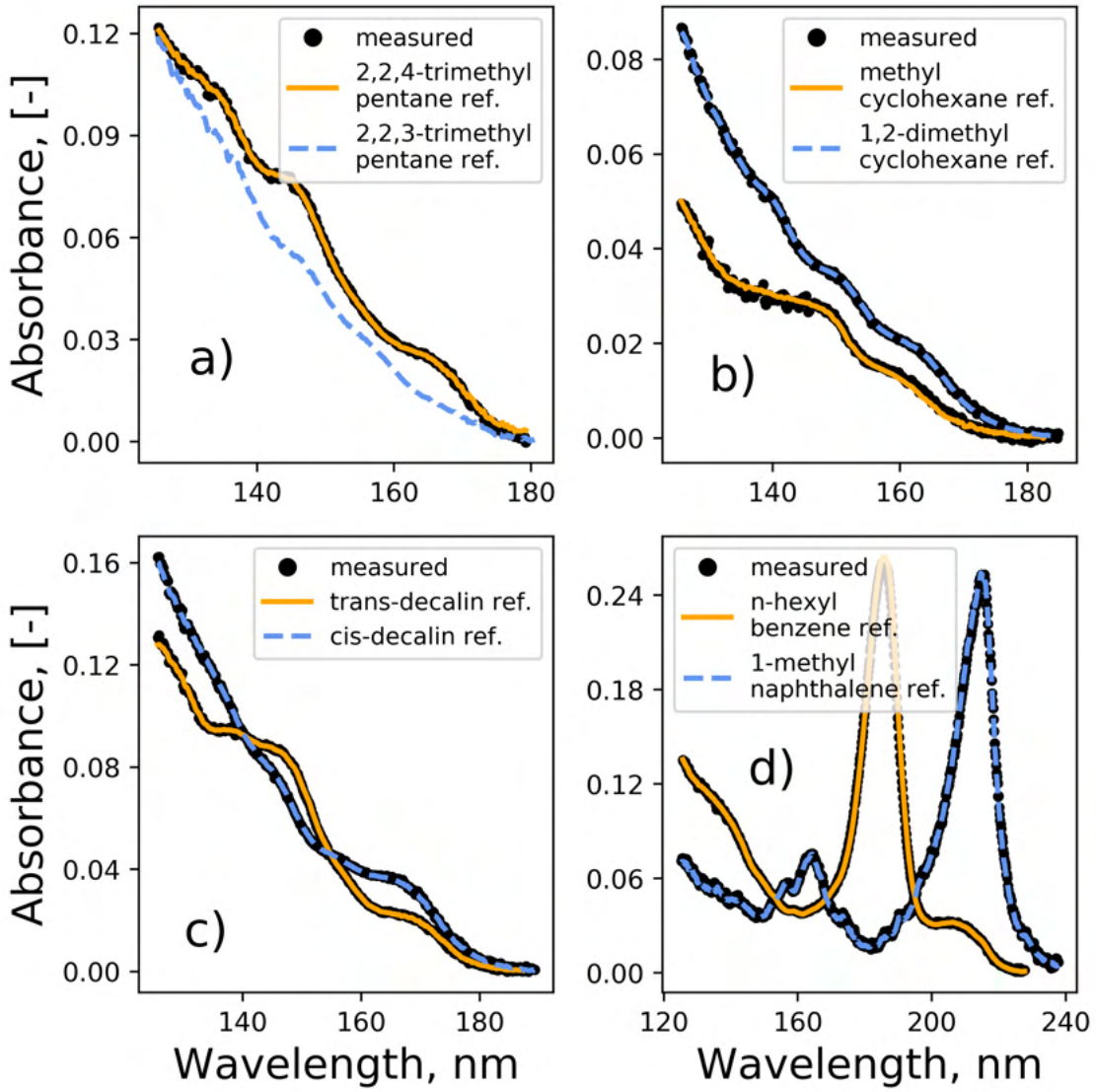

Figure 6 VUV absorbance of sample analytes (symbols) compared to reference spectra (dashed and solid lines). The use of VUV absorption spectroscopy distinguishes the analytes in this study from other similar structures.

Table 3. Hydrocarbon concentrations of the surrogate fuel in this study compared to a representative Jet A (POSF 10325).

Hydrocarbon class	This study, %m	Ref. Jet A/A-1, %m
alkylaromatics	6.4	12.9
diaromatics	13.7	2.3
iso-alkanes	26.2	29.7
n-alkanes	16.5	20.0
monocycloalkanes	27.5	25.1
dicycloalkanes	9.4	6.6

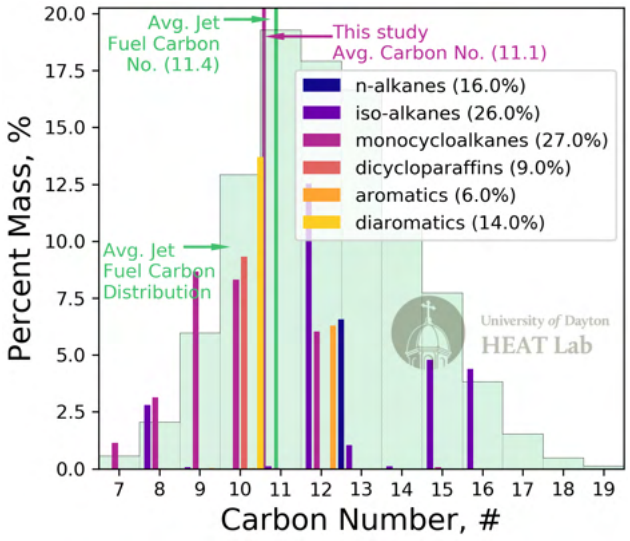

Figure 7. Comparison of carbon number distribution and the average carbon number for an average Jet A/A-1 and the surrogate fuel studied here.

Overall, VUV absorption spectra identified 16 analytes with a carbon balance of 93.96%m (Table 2). However, a prominent C13 iso-alkane peak (1.03%m by GCxGC-FID/MS) could not be identified by VUV. Other minor unidentified peaks include heavy (>C16) n- and iso-alkanes, as well as several alkenes observed in low concentrations. The class and carbon number concentrations determined by GCxGC-FID/MS (Yang et al. [3]) should be greater than or equal to those determined by GCxGC-FID/VUV in Table 3, because the former method integrates carbon over a region that includes all isomers in the bin whereas the latter currently integrates only the carbon within visible peaks. We observed two notable inconsistencies in measured mass concentrations between the two GCxGC systems: namely, the VUV system measured a greater mass fraction for the n-undecane and farnesane peaks than FID/MS. Because these two molecules are directly calibrated in the VUV system, the system is unlikely to have any issues with molecule identification at the time of this study.

2.2 Property predictions

We predicted several properties of the surrogate fuel for comparison with measured values, as well as several additional properties for which no experimental data are available. The set of properties we chose to evaluate is not intended to be illustrative of restrictions to future work. However, we purposefully predicted a diverse set of properties to illustrate the reach and future potential of the analytical, diagnostic, and numerical approach employed here. These properties follow the NJFCP results for prescreening sustainable aviation fuel candidates (Heyne et al. [2], Colket & Heyne, [36], Peiffer et al. [37],

Boehm, Colborn, et al. [38]), and our associated predictions for these properties are reported in Figures 9, 10, and 11. These properties were identified by the NJFCP to constrain the operability variance of sustainable aviation fuels to within the experience range of conventional fuels.

Figure 8Figure 8 compares an experience range of conventional fuels (green shaded region) and their specification limits (red lines and regions) to our measurements and predictions. (Note that the DCN is not a specification property for aviation fuel, but the DCN has been identified as necessary for combustor operability compliance (Colket & Heyne, [36], Stachler et al. [39]). The measurements shown in Figure 9 (black circles) are reported with their corresponding ASTM reproducibility or effective 95% confidence intervals (black lines). Overall, measurements of these properties are within the range of conventional fuel requirements, with the exception of the flash point, which is below the required 38°C (ASTM D1655). The predictions in Figure 9 with (red left triangle) and without (blue open circles) leveraged VUV identification are reported with their corresponding 68% and 95% confidence intervals (solid and capped-dashed lines, respectively). The LHV predictions show the lowest possible LHV value for the given hydrocarbon classes and carbon number distribution (star) alongside a range of probabilistic values (i.e., capped dashes for the 95% confidence interval, solid lines for the 68% confidence interval, and symbols for the most probable values). Further discussion on LHV determinations and measurements can be found in Boehm, Yang, et al. (2021).

Overall, all predictions in Figure 8 agree with the measured values. However, leveraging the VUV identification decreased the average absolute error between measurements by more than two-fold, from 4.99 to 2.24%. Most notably, the uncertainty associated with the two approaches dropped significantly when the VUV/VGA system was employed; for example, the 68% and 95% confidence intervals for surface tension predictions were reduced up to 21- and 18-fold, respectively, with the VUV system. However, the confidence intervals for freeze point and DCN were only modestly reduced. This is likely because the uncertainty due to specific molecular properties (UQ2) is considerable for freeze point and DCN, and their variance for a given class and carbon number (UQ3, σ_{isomer}) is similarly significant. For example, consider the DCN variance between n-octane (-10 octane rating) and iso-octane (100 octane rating), or the fact that one iC8 isomer (2,2,3,3-tetramethyl butane) is a solid at room temperature while others freeze below -90 °C. Furthermore, our LHV predictions illustrate that the specific isomers selected in this study have a significantly lower LHV than the average molecule in their classes.

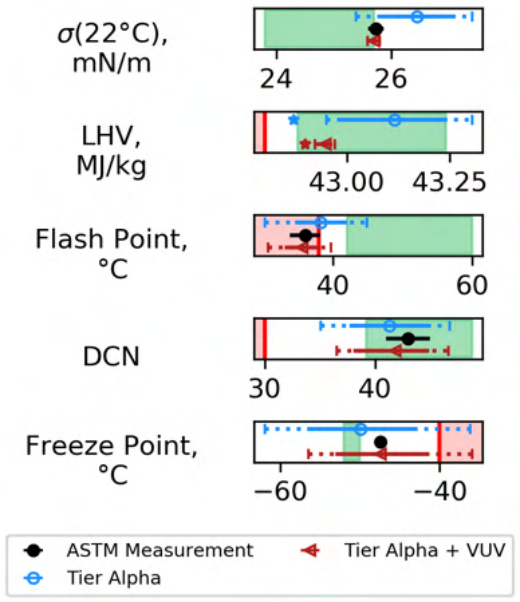

Figure 8. Comparison of the current, VUV-based prediction method (red symbols and lines) with the previous method (blue symbols and lines). Nominal values determined by an ASTM standard method for direct property measurement are shown for reference (black symbols). Fuel specification limits are denoted by a vertical red bar. The green shaded region shows the range of known values for petroleum-derived fuels, and the red shaded region corresponds to 'out-of-specification.'

The distillation simulation via ASTM D2887 (black circles and line) are compared in Figure 10 with the current determination method (solid red line), including the 95% confidence interval (shaded region). The two numerical methods are in fair agreement with each other, although the light fraction deviates the most substantially. As in Figure 8, values for a range of conventional Jet A/A-1 fuels (green shaded region) and the ASTM D1655 specification limits (red line and shaded region) are provided for reference.

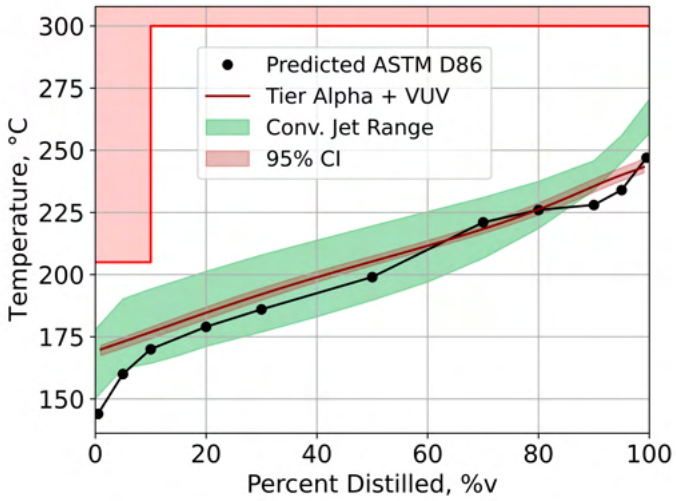

Figure 9. Simulation of an ASTM D86 distillation via the method described in ASTM D2887 (Predicted ASTM D86) compared with a simulated distillation using the current method, informed by VUV identification of specific isomers (Tier Alpha + VUV)

Densities and viscosities for the surrogate fuel are reported in Figure 10. Measured values (black circles), blind predicted values (blue line), and VUV-informed predicted values (red line) are compared over a range of relevant operability temperatures for jet fuels (Colket et al. [42]), and the corresponding uncertainties are reported for the blind (blue shaded regions) and VUV-informed (red shaded regions) predictions. Both prediction methods show excellent agreement with the density measurements, with only a modest difference among the three slopes (i.e., $\Delta\rho/\Delta T$). The measured density gradient differs from the blind prediction by +3.0% and from the VUV-informed prediction by +0.8%. These modest but distinguishable differences in slopes make the blind density predictions higher/lower than the measured values at the lowest/highest temperatures.

The most noticeable difference between the blind and VUV-informed predictions for density is the dramatic reduction of prediction uncertainty. This reduction is due to the decrease in isomers considered for UQ3 when quantifying uncertainty for the VUV-informed predictions. Numerically, the use of VUV identification reduced the 95% confidence interval range from an average of 24.8 kg/m³ to 1.70 kg/m³. In comparison, the experimental reproducibility for density measurements is 2.7 kg/m³ at -20°C (ASTM D4052), while the experiment's reproducibility is 0.5 kg/m³ (Anton Paar, SVM 3001). Because most of the individual molecules in this study were measured directly, $2\sigma_{\rho_i} = 0.5$ kg/m³ for those compounds. For reference, the uncertainty reported by NIST for a representative molecule (2-methyl decane) at -20 °C is 2.92 kg/m³.

Viscosity predictions (Figure 11, bottom) also agree well with measured values. The most probable blind and VUV-informed predictions vary between 1.6 to 70% and -1.0 to 6.8% error, respectively, relative to the measured values, and the experimental repeatability for the measurements is 0.35%. The 95% confidence interval for the blind viscosity prediction overlaps with the measured values for the entirety of the temperature range. However, the nominal VUV-informed predictions agree with measurements (within the uncertainty of the measurements) at temperatures above -21°C. At lower temperatures, non-linear interactions between the surrogate components may be responsible for the growing difference between measurements and model predictions. The variance between the measurements and predictions is the motivation for developing higher-fidelity models and quantifying predictive error (i.e., adding a fourth uncertainty quantification term UQ4 [σ_{model}]). As evidenced in Figure 11, the model uncertainties are substantially reduced by including VUV identification.

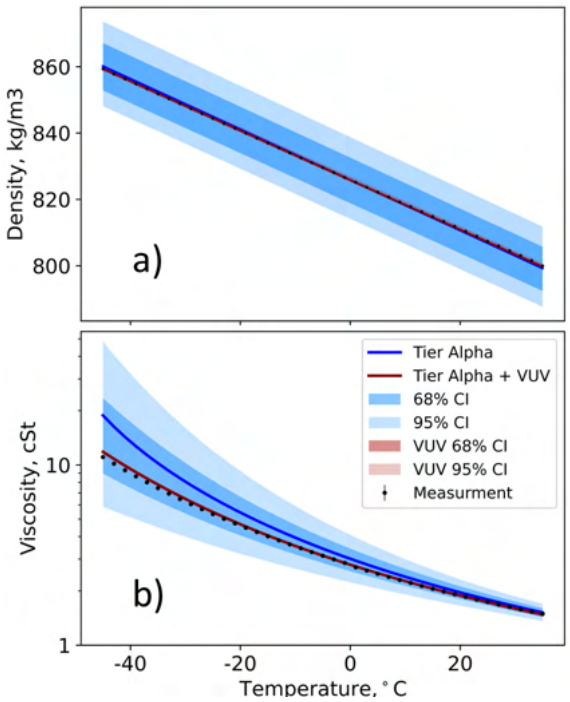

Figure 10. Predicted and measured densities (a) and viscosities (b) for a range of relevant jet fuel conditions. Measurements and their uncertainties are shown with black-filled circles. The Tier α predictions (based on FID only) are shown as solid blue lines, with the corresponding shaded regions illustrating the 68% (dark blue) and 95% (light blue) confidence intervals. The predictions leveraging the VUV data are illustrated by a solid red line and corresponding red-filled areas.

Figure 12 shows data for two additional properties, thermal conductivity and heat capacity, to illustrate the current and ongoing ability to leverage VUV-based isomer identification for bottom-up predictions of mixture properties. Blind predictions (blue line and shaded regions) and VUV-informed predictions (red line shaded areas) are each shown over a range of temperatures. The thermal conductivity predictions agree almost completely with each other, though the VUV-informed prediction uncertainties are lower, as observed for other properties. Interestingly, the uncertainty reduction for thermal conductivity is only modest, suggesting that isomer uncertainty (UQ3) is not the dominant source of uncertainty in this property. The heat capacity predictions for the two methods are likewise in good agreement. As with thermal conductivity, the uncertainty is not substantially reduced by the addition of VUV identification, again suggesting that the predominant source of uncertainty is not isomer uncertainty but rather the root property data.

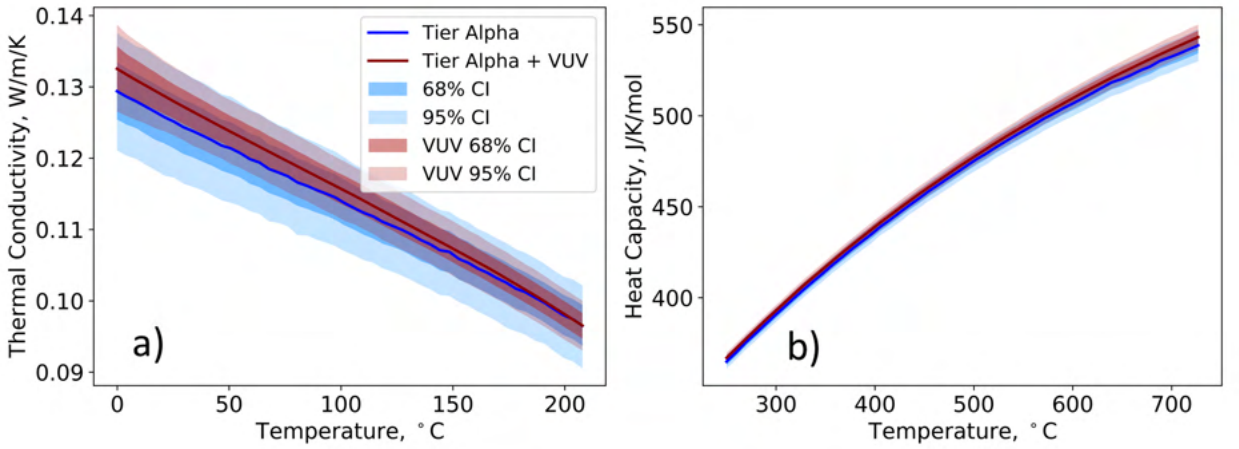

Figure 11. Predictions of thermal conductivity and heat capacity across a range of temperatures. Tier Alpha (blue line and shaded regions) and Tier Alpha + VUV predictions (red line and shaded regions) are shown.

As mentioned previously, gradients of key properties for evolved material from solution can impact operability. This has been observed with preferential vaporization (Bell et al. [18]). Figure 12a predicts the DCN of the evaporated fraction based on the percentage of material that has been distilled. As the distillation fraction increases, the nominal DCN value is predicted to rise from ~36 to a maximum of ~44 before falling to approximately ~43. The initially low DCN is due to the preferential evaporation of methylcyclohexane and iso-octane, as the calculated DCN represents the evaporated fraction. The subsequent rise in DCN occurs as species with higher DCN start to evaporate, and the final drop in DCN at high distillation fractions is from the evaporation of heavy aromatics (i.e., 1-methylnapthalene). The uncertainty for these predictions, also illustrated in Figure 12a, represents the uncertainty of the vapor pressure calculations (UQ4), reproducibility in root DCN measurements (UQ2), and mass fraction uncertainties (UQ1). It does not include isomeric uncertainty (UQ3), which was shown in Figure 8. Absent any isomeric uncertainty, the uncertainty of the predictions is near the uncertainty of the measurements because the vapor pressure and mass fraction uncertainties are minimal compared to the reproducibility of ASTM D6890.

Figure 12b shows the predicted concentrations of the various chemical species in the liquid fuel as the percent distilled increases.

Table 3 can be used as a reference for identifying the various molecules referred to in Figure 12b; note that the concentrations listed in Table 3 are the y-intercepts for each compound in Figure 13b.

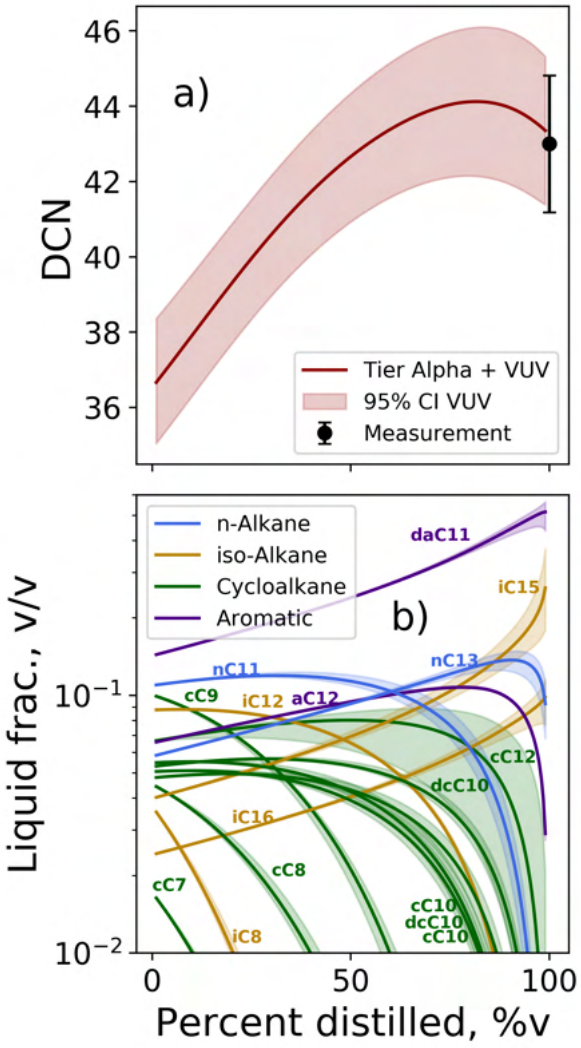

Figure 12 (a) Predicted DCN for the surrogate used in this study as a function of the distillation fraction; (b) the volume fraction of the remaining sample as a function of the distillation fraction. Hydrocarbon types in (b) are denoted with 'i,' 'a,' 'n,' or 'c' for iso-alkanes, aromatics, n-alkanes, and cycloalkanes, respectively. The number after the 'C' denotes the carbon number of the species. Diaromatics and dicycloalkanes are denoted with a 'd.'

3 Conclusions

Advances in analytical chemistry experimentation and computation can advance the characterization of aviation fuels, the fidelity of computational fluid dynamic models, and the ability of fuel producers to model reactor behavior at low volumes. In this report, we presented a novel approach for predicting key aviation fuel properties and uncertainties with GCxGC-VUV identification. We used our method (i.e., VUV-informed) along with the method previously reported by Yang et al. (blind) to predict various properties for a surrogate fuel with a reduced number of chemical constituents. When possible, we also compared our predictions to empirical measurements. Nominal property predictions improved with VUV identification. However, the most substantial improvements were in the reduction of uncertainty. Using the VUV data substantially reduced the uncertainty associated with isomeric variance, as more than 94%m was identified in the surrogate.

In addition to predicting measured properties, we expanded our experimental and computational method to include heat capacity and thermal conductivity. Once again, the uncertainty of those predictions was reduced by using the VUV data. We also used our new method to predict the DCN of the surrogate with respect to the distillation fraction of the fuel. We predicted that the DCN of the surrogate could increase and decrease over the distillation curve. This behavior is important near lean blowout in gas turbine combustors.

Applying GCxGC-VUV to more complex mixtures (i.e., conventional fuels) will be more difficult than for the mixture reported here. However, most carbon (~80%m) in conventional Jet A (POSF 10325) is found in 186 peaks, while >1123 other molecules compose the remaining fraction. In other words, 80% of the fuel's mass is contained in 21% of the analytes. The VUV database used for this study currently contains 242 spectra for molecules in the jet range, with additional spectra available. Remaining questions include whether carbon balances nearing 80% are sufficient for constraining the properties reported here and additional properties of interest, as well as whether GCxGC-VUV can positively identify all or most of the 186 major peaks in POSF 10325.

The previous numerical method has been used to evaluate more complex mixtures for a wide range of aviation fuels and blend components (Yang et al.. [3]). However, the predictive fidelity and uncertainty of the numerical method, as illustrated here and in Boehm, Yang, et al. [10], depends on the accuracy of the mass determinations, the accuracy of the database properties, the accuracy of the models that convert molecular properties to bulk mixture properties, and the identification of isomers or the reduction of UQ3. Because the strength of the method described here is its ability to reduce the isomeric uncertainty of the analytes, future work to predict properties from GCxGC-VUV measurements will need more spectra, specific columns and GC test methods tailored for the VUV, and possibly the calibration of the unit to subtle changes in isomer retention times.

Milestone(s)

- Tier Alpha performed a total of 81 times.
- Tier Beta performed a total of 60 times.
- Maximum blending ratio determined for a total of 16 SAF.

Major Accomplishments

Predicted key combustor operability properties for 81 SAFs, measured key combustor operability properties for 60 SAFs, and determined the maximum blending ratio for 16 SAFs.

Publications

Peer-reviewed Publications

Boehm, R. C., Yang, Z., Bell, D. C., Feldhausen, J., & Heyne, J. S. (2022). Lower heating value of jet fuel from hydrocarbon class concentration data and thermo-chemical reference data: An uncertainty quantification. Fuel, *311*, 122542. https://doi.org/10.1016/j.fuel.2021.122542

Heyne, J., Bell, D., Feldhausen, J., Yang, Z., & Boehm, R. (2022). Towards fuel composition and properties from Two-dimensional gas chromatography with flame ionization and vacuum ultraviolet spectroscopy. Fuel, 312, 122709. https://doi.org/10.1016/j.fuel.2021.122709

Huq, N. A., Hafenstine, G. R., Huo, X., Nguyen, H., Tifft, S. M., Conklin, D. R., Stück, D., Stunkel, J., Yang, Z., Heyne, J. S., Wiatrowski, M. R., Zhang, Y., Tao, L., Zhu, J., McEnally, C. S., Christensen, E. D., Hays, C., Allsburg, K. M. V., Unocic, K. A., & Meyer, H. M. (2021). Toward net-zero sustainable aviation fuel with wet waste-derived volatile fatty acids. Proceedings of the National Academy of Sciences, *118*(13). https://doi.org/10.1073/pnas.2023008118

Yang, Z., Kosir, S., Stachler, R., Shafer, L., Anderson, C., & Heyne, J. S. (2021). A GC × GC Tier α combustor operability prescreening method for sustainable aviation fuel candidates. Fuel, *292*, 120345. https://doi.org/10.1016/j.fuel.2021.120345

Outreach Efforts

Conference presentation

ACS Fall 2021 National Meeting & Exposition in San Diego, CA

Awards

Shane Kosir,

- WSU/PNNL Distinguished Graduate Research Program Recipient.

Joshua Heyne,
- 2021 Net Good Summit on sustainable travel, honored guest
- 2021 US Frontiers of Engineering Symposium, National Academies of Engineering, selected participant
- 2021 Vision Award for Excellence in Scholarship, School of Eng., University of Dayton

Student Involvement

David Bell, Ph.D. student, leads this effort.
John Feldhausen, M.S. student, participates in this effort.
Zhibin (Harrison) Yang, Ph.D. student, participates in this effort.
Steven Ivec, M.S. student, participates in this effort.
Aaron Spelies, undergraduate student, participates in this effort.
Allison Coburn, undergraduate student, participates in this effort.

Plans for Next Period

Finalize the publication in progress, improve Tier Alpha prediction accuracy, and reduce the volume required for Tier Beta measurement.

References

[1] Huq, N. A., Hafenstine, G. R., Huo, X., Nguyen, H., Tifft, S. M., Conklin, D. R., Stück, D., Stunkel, J., Yang, Z., Heyne, J. S., Wiatrowski, M. R., Zhang, Y., Tao, L., Zhu, J., McEnally, C. S., Christensen, E. D., Hays, C., Allsburg, K. M. V., Unocic, K. A., & Meyer, H. M. (2021). Toward net-zero sustainable aviation fuel with wet waste-derived volatile fatty acids. Proceedings of the National Academy of Sciences, *118*(13). https://doi.org/10.1073/pnas.2023008118

[2] Heyne, J., Rauch, B., Le Clercq, P., & Colket, M. (2021). Sustainable aviation fuel prescreening tools and procedures. Fuel, *290*, 120004. https://doi.org/10.1016/j.fuel.2020.120004

[3] Yang, Z., Kosir, S., Stachler, R., Shafer, L., Anderson, C., & Heyne, J. S. (2021). A GC × GC Tier α combustor operability prescreening method for sustainable aviation fuel candidates. Fuel, *292*, 120345. https://doi.org/10.1016/j.fuel.2021.120345

[4] Hall, C., Rauch, B., Bauder, U., Le Clercq, P., & Aigner, M. (2021). Predictive capability assessment of probabilistic machine learning models for density prediction of conventional and synthetic jet fuels. Energy & Fuels, *35*(3), 2520–2530. https://doi.org/10.1021/acs.energyfuels.0c03779

[5] Wang, Y., Cao, Y., Wei, W., Davidson, D. F., & Hanson, R. K. (2019). A new method of estimating derived cetane number for hydrocarbon fuels. Fuel, *241*, 319–326. https://doi.org/10.1016/j.fuel.2018.12.027

[6] Vozka, P., Modereger, B. A., Park, A. C., Zhang, W. T. J., Trice, R. W., Kenttämaa, H. I., & Kilaz, G. (2019). Jet fuel density via GC × GC-FID. Fuel, 235, 1052–1060. https://doi.org/10.1016/j.fuel.2018.08.110

[7] D02 Committee. (2021). ASTM D2887 - Standard test method for boiling range distribution of petroleum fractions by gas (Report No. ASTM D2887-19ae2) ASTM International. https://doi.org/10.1520/D2887-19AE02.2

[8] Ahmed, A., Goteng, G., Shankar, V. S. B., Al-Qurashi, K., Roberts, W. L., & Sarathy, S. M. (2015). A computational methodology for formulating gasoline surrogate fuels with accurate physical and chemical kinetic properties. Fuel, *143*, 290–300. https://doi.org/10.1016/j.fuel.2014.11.022

[9] Govindaraju, P. B., & Ihme, M. (2018). Formulation of optimal surrogate descriptions of fuels considering sensitivities to experimental uncertainties. Combustion and Flame, *188*, 337–356. https://doi.org/10.1016/j.combustflame.2017.09.044

[10] Boehm, R. C., Yang, Z., Bell, D. C., Feldhausen, J., & Heyne, J. S. (2022). Lower heating value of jet fuel from hydrocarbon class concentration data and thermo-chemical reference data: An uncertainty quantification. Fuel, *311*, 122542. https://doi.org/10.1016/j.fuel.2021.122542.

[11] Dussan, K., Won, S. H., Ure, A. D., Dryer, F. L., & Dooley, S. (2019). Chemical functional group descriptor for ignition propensity of large hydrocarbon liquid fuels. Proceedings of the Combustion Institute, *37*(4), 5083–5093. https://doi.org/10.1016/j.proci.2018.05.079

[12] Wang, Y., Wei, W., Zhang, Y., & Hanson, R. K. (2021). A new strategy of characterizing hydrocarbon fuels using FTIR spectra and generalized linear model with grouped-Lasso regularization. Fuel, *287*, 119419. https://doi.org/10.1016/j.fuel.2020.119419

[13] Wang, Y., Ding, Y., Wei, W., Cao, Y., Davidson, D. F., & Hanson, R. K. (2019). On estimating physical and chemical properties of hydrocarbon fuels using mid-infrared FTIR spectra and regularized linear models. Fuel, *255*, 115715.

https://doi.org/10.1016/j.fuel.2019.115715
[14] Vozka, P., & Kilaz, G. (2020). A review of aviation turbine fuel chemical composition-property relations. Fuel, *268*, 117391. https://doi.org/10.1016/j.fuel.2020.117391
[15] Shi, X., Li, H., Song, Z., Zhang, X., & Liu, G. (2017). Quantitative composition-property relationship of aviation hydrocarbon fuel based on comprehensive two-dimensional gas chromatography with mass spectrometry and flame ionization detector. Fuel, *200*, 395–406. https://doi.org/10.1016/j.fuel.2017.03.073
[16] Abdul Jameel, A. G., Naser, N., Issayev, G., Touitou, J., Ghosh, M. K., Emwas, A.-H., Farooq, A., Dooley, S., & Sarathy, S. M. (2018). A minimalist functional group (MFG) approach for surrogate fuel formulation. Combustion and Flame, *192*, 250–271. https://doi.org/10.1016/j.combustflame.2018.01.036
[17] Pinkowski, N. H., Ding, Y., Johnson, S. E., Wang, Y., Parise, T. C., Davidson, D. F., & Hanson, R. K. (2019). A multi-wavelength speciation framework for high-temperature hydrocarbon pyrolysis. Journal of Quantitative Spectroscopy and Radiative Transfer, *225*, 180–205. https://doi.org/10.1016/j.jqsrt.2018.12.038
[18] Bell DC, Heyne JS, Won SH, Dryer FL. The Impact of Preferential Vaporization on Lean Blowout in a Referee Combustor at Figure of Merit Conditions. ASME Proc | Fuels, Combust Mater Handl 2018. doi:https://doi.org/10.1115/POWER2018-7432.
[19] Striebich, R. C., Motsinger, M. A., Rauch, M. E., Zabarnick, S., & Dewitt, M. (2005). Estimation of select specification tests for aviation turbine fuels using fast gas chromatography (GC). Energy & Fuels, *19*(6), 2445–2454. https://doi.org/10.1021/ef050136o
[20] Trinklein, T. J., Prebihalo, S. E., Warren, C. G., Ochoa, G. S., & Synovec, R. E. (2020). Discovery-based analysis and quantification for comprehensive three-dimensional gas chromatography flame ionization detection data. Journal of Chromatography A, 1623, 461190. https://doi.org/10.1016/j.chroma.2020.461190
[21] Johnson KJ, Loegel TN, Metz AE, Wrzesinski PJ, Shafer LM, Striebich R, et al. Method for Detailed Hydrocarbon Analysis of Middle Distillate Fuels by Two- Dimensional Gas Chromatography. 2020.
[22] Wang, F. C.-Y. (2020). Comprehensive two-dimensional gas chromatography hyphenated with a vacuum ultraviolet spectrometer to analyze diesel—a three-dimensional separation (GC × GC × VUV) approach. Energy & Fuels, *34*(7), 8012–8017. https://doi.org/10.1021/acs.energyfuels.0c00688
[23] Anthony, I. G. M., Brantley, M. R., Gaw, C. A., Floyd, A. R., & Solouki, T. (2018). Vacuum ultraviolet spectroscopy and mass spectrometry: A tandem detection approach for improved identification of gas chromatography-eluting compounds. Analytical Chemistry, *90*(7), 4878–4885. https://doi.org/10.1021/acs.analchem.8b00531
[24] Lelevic, A., Souchon, V., Moreaud, M., Lorentz, C., & Geantet, C. (2020). Gas chromatography vacuum ultraviolet spectroscopy: A review. Journal of separation science, 43(1), 150–173. https://doi.org/10.1002/jssc.201900770
[25] Lelevic, A., Geantet, C., Moreaud, M., Lorentz, C., & Souchon, V. (2021). Quantitative analysis of hydrocarbons in gas oils by two-dimensional comprehensive gas chromatography with vacuum ultraviolet detection. Energy & Fuels, 35(17), 13766–13775. https://doi.org/10.1021/acs.energyfuels.1c01910
[26] D02 Committee. (2020). ASTM D7566: Specification for aviation turbine fuel containing synthesized hydrocarbons [Presentation]. ASTM International Meeting, Conshokocken, PA. https://doi.org/10.1520/D7566-20
[27] Dooley, S., Won, S. H., Chaos, M., Heyne, J., Ju, Y., Dryer, F. L., Kumar, K., Sung, C.-J., Wang, H., Oehlschlaeger, M. A., Santoro, R. J., & Litzinger, T. A. (2010). A jet fuel surrogate formulated by real fuel properties. Combustion and Flame, *157*(12), 2333–2339. https://doi.org/10.1016/j.combustflame.2010.07.001
[28] Dooley S, Won SH, Heyne JS, Farouk TI, Ju Y, Dryer FL, et al. The experimental evaluation of a methodology for surrogate fuel formulation to emulate gas phase combustion kinetic phenomena. Combust Flame 2012;159:1444–66. doi:http://dx.doi.org/10.1016/j.combustflame.2011.11.002.
[29] Yang, Z., Stachler, R., & Heyne, J. S. (2020). Orthogonal Reference Surrogate Fuels for Operability Testing. Energies, *13*(8), 1948. https://doi.org/10.3390/en13081948
[30] Kosir, S., Stachler, R., Heyne, J., & Hauck, F. (2020). High-performance jet fuel optimization and uncertainty analysis. Fuel, *281,* 118718. https://doi.org/10.1016/j.fuel.2020.118718
[31] Kosir, S., Heyne, J., & Graham, J. (2020). A machine learning framework for drop-in volume swell characteristics of sustainable aviation fuel. Fuel, 274, 117832. https://doi.org/10.1016/j.fuel.2020.117832
[32] Bell, D., Heyne, J. S., August, E., Won, S. H., Dryer, F. L., Haas, F. M., & Dooley, S. (2017). On the development of general surrogate composition calculations for chemical and physical properties [Presentation]. AIAA SciTech Forum - 55th AIAA Aerospace Science Meeting. https://doi.org/10.2514/6.2017-0609
[33] Flora, G., Kosir, S., Heyne, J., Zabarnik, S., & Gupta, M. (2019). Properties calculator and optimization for drop-in alternative jet fuel blends [Presentation]. AIAA SciTech Forum.
[34] Boehm RC, Scholla LC, Heyne JS. Sustainable alternative fuel effects on energy consumption of jet engines. Fuel 2021;304:121378. doi:https://doi.org/10.1016/j.fuel.2021.121378.
[35] Edwards, T. (2017). Reference jet fuels for combustion testing [Presentation]. 55th AIAA Aerospace Science Meeting.

https://doi.org/10.2514/6.2017-0146
[36] Colket, M., & Heyne, J. (2021). *Fuel effects on operability of aircraft gas turbine combustors*. American Institute Of Aeronautics and Astronautics.
[37] Peiffer, E. E., Heyne, J. S., & Colket, M. (2019). Sustainable Aviation Fuels Approval Streamlining: Auxiliary Power Unit Lean Blowout Testing. AIAA Journal, *57*(11), 4854–4862. https://doi.org/10.2514/1.j058348
[38] Boehm, R. C., Colborn, J. G., & Heyne, J. S. (2021). Comparing alternative jet fuel dependencies between combustors of different size and mixing approaches. Frontiers in Energy Research, 9. https://doi.org/10.3389/fenrg.2021.701901
[39] Stachler, R., Heyne, J., Stouffer, S., & Miller, J. (2020). Lean blowoff in a toroidal jet-stirred reactor: Implications for alternative fuel approval and potential mechanisms for autoignition and extinction. Energy & Fuels, *34*(5), 6306–6316. https://doi.org/10.1021/acs.energyfuels.9b01644
[40] ASTM. (2017). Standard specification for aviation turbine fuel containing synthesized hydrocarbons (Report No. ASTM D7566-11). ASTM International. https://doi.org/10.1520/D1655-10.2
[41] Hoffman, E. J. (1969). Relations between true boiling point and ASTM distillation curves. Chemical Engineering Science, *24*(1), 113–117. https://doi.org/10.1016/0009-2509(69)80013-8
[42] Colket, M., Heyne, J., Rumizen, M., Gupta, M., Edwards, T., Roquemore, W. M., Andac, G., Boehm, R., Lovett, J., Williams, R., Condevaux, J., Turner, D., Rizk, N., Tishkoff, J., Li, C., Moder, J., Friend, D., & Sankaran, V. (2017). Overview of the National Jet Fuels Combustion Program. AIAA Journal, *55*(4), 1087–1104. https://doi.org/10.2514/1.j055361

Project 065(B) Fuel Testing Approaches for Rapid Jet Fuel Prescreening

University of Illinois Urbana-Champaign

Project Lead Investigator

Tonghun Lee
Professor
Mechanical Science & Engineering
University of Illinois at Urbana-Champaign
1206 W. Green St.
Urbana, IL 61801
517-290-8005
tonghun@illinois.edu

University Participants

University of Illinois at Urbana-Champaign

- PI: Tonghun Lee, Professor
- FAA Award Number: 13-C-AJFE-UI, Amendments 30, 35
- Period of Performance: October 1, 2020 to September 30, 2021
- Tasks:
    1. Baseline ignition behavior of the M1 combustor (high-altitude testing)
    2. Fuel injection optimization

Project Funding Level

FAA funding level: $150,000
Cost share: 100% match provided by software license support from Converge, Inc.

Investigation Team

- Tonghun Lee, Professor, University of Illinois at Urbana-Champaign (UIUC): Overall research supervision
- Eric Wood (Graduate Student, UIUC), Caleb Trotter (Undergraduate Student, UIUC): Experimental efforts characterizing the M1 combustor, including laser and optical diagnostics

Project Overview

This study (Prescreening 65b) aims to introduce a new compact test rig (M1 combustor), developed with OEM support within the National Jet Fuel Combustion Program (NJFCP), that can screen fundamental combustor behavior for a much lower fuel volume (~gallons) prior to Tier 3 and 4 tests in the ASTM D4054 evaluation. In the NJFCP, the referee rig at the Air Force Research Laboratory (AFRL) was utilized as a foundational test rig for this goal. The M1 may have the potential to carry out these tasks at reduced fuel volumes (~gallons versus ~hundreds of gallons) in a simplified and open architecture that can be readily shared and operated at different locations at a fraction of the cost. Both the Army Research Laboratory (ARL) and Argonne National Laboratory (ANL) will be partners in the effort to fully characterize the M1 facility. If successful, these efforts will allow fuel providers and OEMs to conduct basic combustor tests using an identical testing architecture and identical test conditions at multiple test locations, in contrast to the referee rig, which is housed in a secure government facility (AFRL). Tests in smaller test rigs can provide a platform for each supplier or researcher to independently test their new fuels and to make predictions without requiring the use of one single facility. Over time, as test data are accumulated, the potential for test rigs, such as the M1 to predict actual Tier 3 and 4 performance, will increase and may reduce the burden of relying on capital-intensive ASTM rig and engine tests.

Background of the M1 Combustor

Under the FAA-funded NJFCP, the referee rig combustor at AFRL was used to determine the sensitivity of combustor performance parameters, such as lean blowout (LBO) and ignition parameters, to the chemical composition of novel fuels. The results from this investigation were instrumental in establishing a relationship between fuel chemistry and its impact on combustor performance. Professor Tonghun Lee's research group conducted a significant portion of the laser and optical diagnostic work for the referee rig as part of the NJFCP, including quantitative phase Doppler particle analysis, which provided key quantitative data for the simulation efforts.

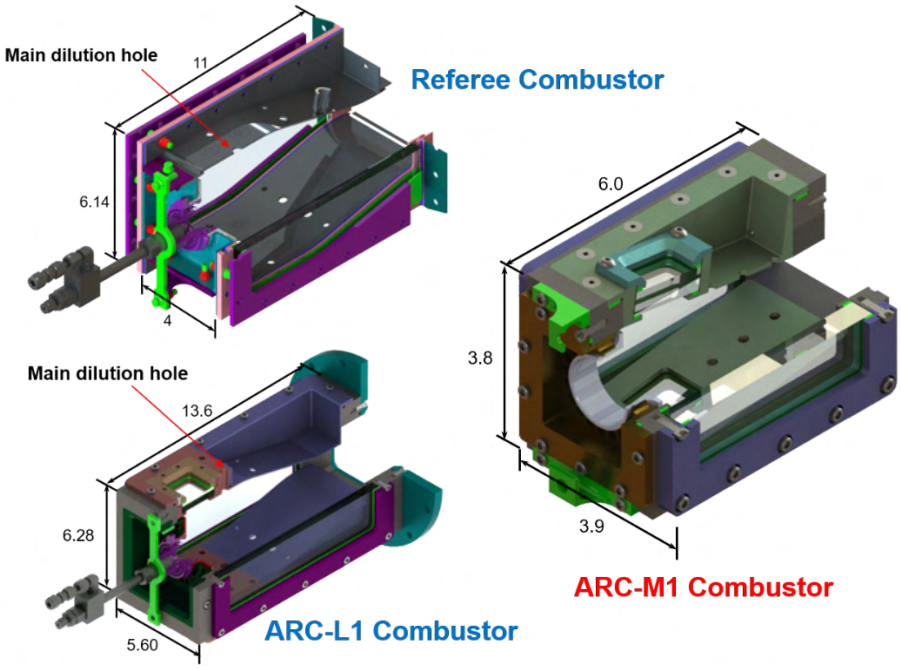

Figure 1. The referee combustor at AFRL, the ARC-L1 combustor, and the ARC-M1 combustor.

Simultaneously, the ARL team worked with NJFCP researchers to complement the referee combustor efforts by performing high-altitude relight tests at the ARL Aberdeen Proving Grounds, where a new altitude test chamber had just been commissioned. During the planning phase, ARL decided to build two new combustors to address some shortcomings of the referee combustor, namely, shortcomings related to optical access and flow split uncertainty. The first combustor would have the exact same dimensions as the referee combustor but with enhanced optical access and a less-complicated liner for air cooling. A lack of vertical optical access had made velocity field measurements in the referee combustor virtually impossible, and the complicated liner had caused difficulties in accurately predicting air flux into the combustor. This new combustor would be termed ARC-L1 (Army Research Combustor-L1). Additionally, an effort was made to build a smaller combustor for more flexible testing with less fuel and air requirements. This smaller version would be termed the ARC-M1, and the main architecture proposed in this study is based on this design. Both combustors were designed by a subcommittee composed of NJFCP researchers and OEM representatives. The construction of both combustors was originally conducted by the research group of the PI (Tonghun Lee) at UIUC.

The referee combustor, L1, and M1 are shown in Figure 1. Continuing this heritage, ARL will be a key partner in the analysis of this combustor in terms of both numerical simulation efforts as well as X-ray imaging of spray break-up, which will be performed at the Advanced Photon Source of ANL. In addition to the laser and optical measurements available at UIUC, the goal is to characterize the operating characteristics of the M1 combustor in an unprecedented way so that it can be widely adopted in the academic/industrial community as a test platform for new fuel blends. Once this characterization is complete, the basic physics, dimensions, and operational envelope of the combustor will be openly shared with the academic and commercial sectors. This work is expected to provide a common platform not only for prescreening sustainable aviation fuels (SAFs) but also for performing other sustainability-related experiments involving novel fuels in a laboratory setting.

Task 1 – Baseline Ignition Behavior of the M1 Combustor

University of Illinois at Urbana-Champaign

Objectives

The objective of this task is to establish baseline combustor ignition performance for the ARC-M1 combustor when operating under cold-start and altitude relight scenarios. Combustor ignition performance under suboptimal inlet conditions is a key performance metric that must be met to integrate SAF into any gas turbine system. These experiments represent an important first step toward establishing baseline ignition performance in the M1 combustor under these conditions using conventional jet fuel.

Research Approach

Overview of Experimental Altitude Relight Testing

To collect baseline ignition performance metrics on the ARC-M1 combustor, the ARL's altitude chamber at Aberdeen Proving Ground, MD was utilized to perform ignition testing under both ground cold-start and altitude relight conditions. The Small Engine Altitude Research Facility (SmEARF) can simulate altitudes of up to 30,000 ft, corresponding to chamber pressures between 0.30 and 1.00 atm and chamber temperatures from 229 K to 327 K. The air supply system can deliver up to 1.361 kg/s of dry air into the chamber for testing a wide array of engine types, including small piston and gas turbine engines.

The ARC-M1 combustor is operated inside the altitude chamber for this testing, with the chamber air inlet being connected to the combustor inlet by a large duct. A portion of the incoming chamber air is diverted to a bypass air stream, which does not pass through the combustor and is instead used to help maintain the desired ambient temperature inside the chamber. The combustor dilution jets are supplied from manifolds that divert a supply stream from the main combustion air. While this experimental setup does not allow direct mass flow control of the air flowrate through the combustor during testing, the pressure drop across the combustor correlates with measurements made through the system ahead of time using a laminar flow element condition where testing is conducted. Figure 2 shows a picture of the SmEARF altitude chamber and the combustor installed within the test chamber. During testing, the fuel is chilled to testing temperatures by using an air-driven pump that drives the fuel through a cooling loop, where a Thermonics -60˚C two-stage chiller and brazed plate heat exchanger cool the fuel to the desired temperature. The fuel flowrate through the cooling loop is controlled by a Bronkhorst M15 0-300 g/min flow controller. Fuel from the chilling loop can be directed into the combustor by actuation of a three-way solenoid valve. The fuel pressure in the cooling loop is maintained by a proportional solenoid valve to ensure that the system is at the correct pressure when fuel injection begins.

To understand combustor ignition behavior in the ARC-M1 combustor, testing is conducted under several operating conditions to simulate relevant cold-start and altitude relight conditions. Table 1 lists the different operating conditions that are tested. Three temperature conditions are tested at near-ambient pressure conditions, simulating ground cold-start scenarios. Additionally, one condition is tested to simulate a low-altitude relight scenario.

Figure 2. The SmEARF high-altitude chamber at the Army Research Laboratory at Aberdeen Proving Ground, MD (left). The M1 combustor installed in the altitude chamber, ready for cold-start and altitude relight testing (right).

Table 1. Combustor operating conditions for baseline ignition testing.

	Cold-Start	Altitude Relight
Fuel	F-24	F-24
Air Temperature	25˚C, -10˚C, -35˚C	-5˚C
Fuel Temperature	25˚C, -10˚C, -35˚C	-5˚C
Total Air Flowrate	30 g/s, 31 g/s, 32 g/s	23 g/s
Combustor Absolute Pressure	92.5 kPa	69.4 kPa
Target Combustor Pressure Drop	3%	3%

Ignition Testing Procedure

To collect ignition probability measurements for each case, the following procedure was followed. An ignition attempt is started by directing chilled fuel into the combustor without sparks for 3 seconds to allow the fuel flowrate to stabilize at the desired value. After this period, DC power is supplied to the exciter, and the igniter is allowed to spark at a frequency of ~3.7 Hz for up to 10 seconds, at which point the sparks and fuel flow are stopped. Upon successful ignition of the combustor, the test is considered complete, and the fuel and sparks may be stopped early. An analysis script uses the recorded photodiode signal to measure the emission from the sparks and the flame to determine which spark resulted in successful ignition. Based on this process, a maximum of one successful spark can be found in each ignition attempt. Figure 3 shows an example photodiode signal collected during an ignition attempt. After each ignition attempt, air is allowed to flow through the combustor for at least 2 minutes to clear out any remaining liquid fuel inside the combustor before the next test begins. This procedure is repeated many times at fuel flowrates across the ignition probability curve to ascertain the overall ignition behavior, ranging from no-ignition cases to the maximum reasonable fuel flowrate for the testing conditions.

Ignition probability curves are determined from the recorded datasets by first analyzing all tests runs and determining the number of successful and unsuccessful sparks in each test. The actual air and fuel flowrates from each test are also calculated from the recorded data to obtain the exact equivalence ratio for each test run. The data are then split into equally sized bins based on the equivalence ratio, and the total number of unsuccessful and successful sparks is used to calculate the overall ignition probability for each bin. It is important to note that in this test procedure, it is assumed that each spark event is independent of all other events, which may not always be the case. While this assumption may not hold due to fuel accumulation in the combustor or slight variations in flowrates throughout the test runs, every effort is made to maintain these parameters to ensure that all test points can be considered independent.

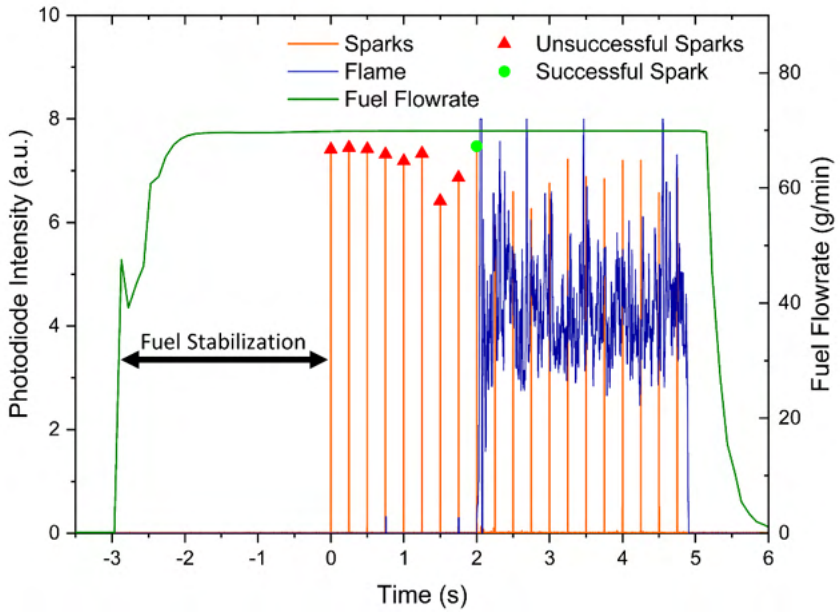

Figure 3. Example of the ignition testing procedure, demonstrating the fuel stabilization time and analyzed photodiode signals.

Ignition Performance Results

To collect baseline ignition performance data for the ARC-M1 combustor, the ignition measurement procedure described above was performed many times across a wide range of equivalence ratios for the three cold-start scenarios listed in Table 1. Figure 4 shows results from these measurements and binomial fits of ignition probability (fitted using data up to the maximum ignition probability). These results demonstrate the impact of reducing the combustor inlet temperature on combustor ignition performance. The highest temperature conditions demonstrate a very rapid transition from a zero ignition probability (no ignitions) to a very high ignition probability (consistent ignition on an early spark). For the middle temperature condition (-10˚C), a much slower rise to high ignition probabilities is observed, likely due to the more difficult process of vaporizing and starting combustion in a lower-temperature environment. It is likely that combustion is still possible under these conditions, but the correct balance between liquid spray behavior, turbulent fluctuations in the combustor, and spark propagation is required for successful ignition. Additionally, in this middle temperature case, for higher equivalence ratio conditions, beyond the maximum ignition probability, a decrease in the ignition probability is observed. It is hypothesized that this result is caused by the increased amount of cold fuel in the combustor, which can quench any high-temperature region created by the spark in a very short amount of time. This greater quantity of cold fuel reduces the likelihood that the flame will reach the point at which it releases more chemical power than it is losing to the surrounding gases and increases the likelihood that the flame will blow out. For the lowest-temperature case, only a very narrow range of equivalence ratios allows ignition, and the ignition probabilities never rise to high levels (maximum of ~10%). The effects seen for the middle temperature condition are even more extreme here, with the -35˚C air and fuel requiring significantly more energy to heat up to reaction temperatures, making it much less likely that a spark will make it all the way to a sustained flame without blowout occurring. These results provide a good baseline for ignition performance under cold-start conditions in the ARC-M1 combustor and illustrate how varying inlet temperature conditions impacts global ignition performance.

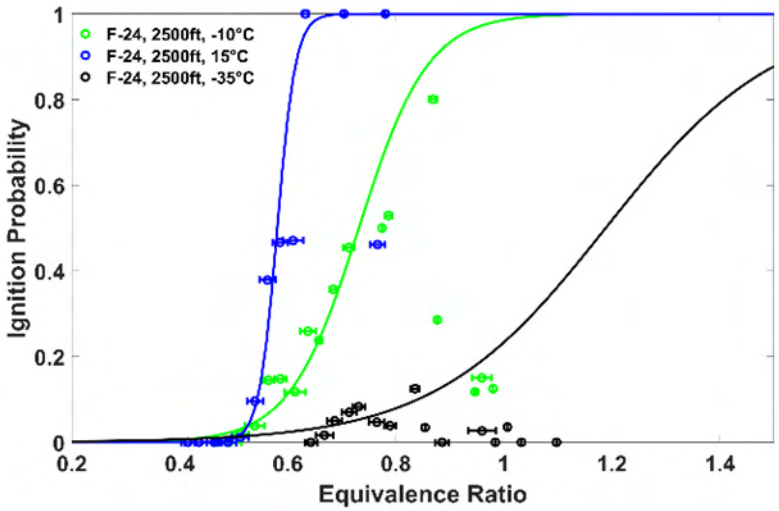

Figure 4. Baseline ARC-M1 ignition performance data collected under near-ambient pressure conditions in the SmEARF altitude chamber.

Figure 5 shows results of ignition testing on the ARC-M1 combustor performed under altitude relight conditions. Although the temperature conditions are much more favorable than the -35˚C testing conditions shown in Figure 4, the results appear very similar. The lower ambient pressure conditions of this testing appear to inhibit successful ignition in a manner similar to that observed for the -35˚C testing above, with no equivalence ratio yielding ignition probabilities greater than 10%. However, the range of equivalence ratios for which ignition does occur is significantly higher than that in the above testing. It is hypothesized that ignition does not occur until this point due to the inherent balance between fuel flowrate, fuel pressure, and droplet size. The fuel nozzle needs a sufficiently high inlet pressure to allow for favorable atomization performance; however, this results in a relatively high fuel flowrate, especially for these low-pressure (low air density) conditions. As such, ignition probabilities over a relatively wide range of equivalence ratios show similar, extremely low ignition probabilities under altitude relight conditions.

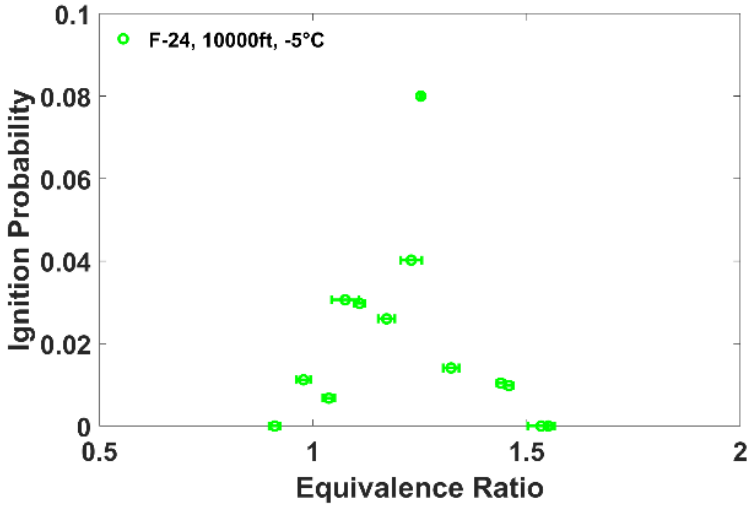

Figure 5. Altitude relight testing results (10,000-ft-equivalent conditions) for the M1 combustor in the SmEARF altitude chamber.

During the cold-start and altitude relight testing described above, high-speed broadband imaging was simultaneously collected to visualize the spark and the flame luminosity after the spark. The goal of this imaging was to investigate the link

between flame trajectories in the time period immediately after the spark and successful ignition performance. Images were collected using a Photron SA-Z operating at 20,000 fps. Figure 6 shows images collected at several different time steps after the spark event for three unsuccessful sparks and one successful spark. This type of diagnostics provides an extremely powerful tool for identifying the high-speed dynamics governing these important phenomena. Future analysis of these images and the collection of additional diagnostics data will provide an even deeper understanding of the factors influencing successful ignition in gas turbine environments.

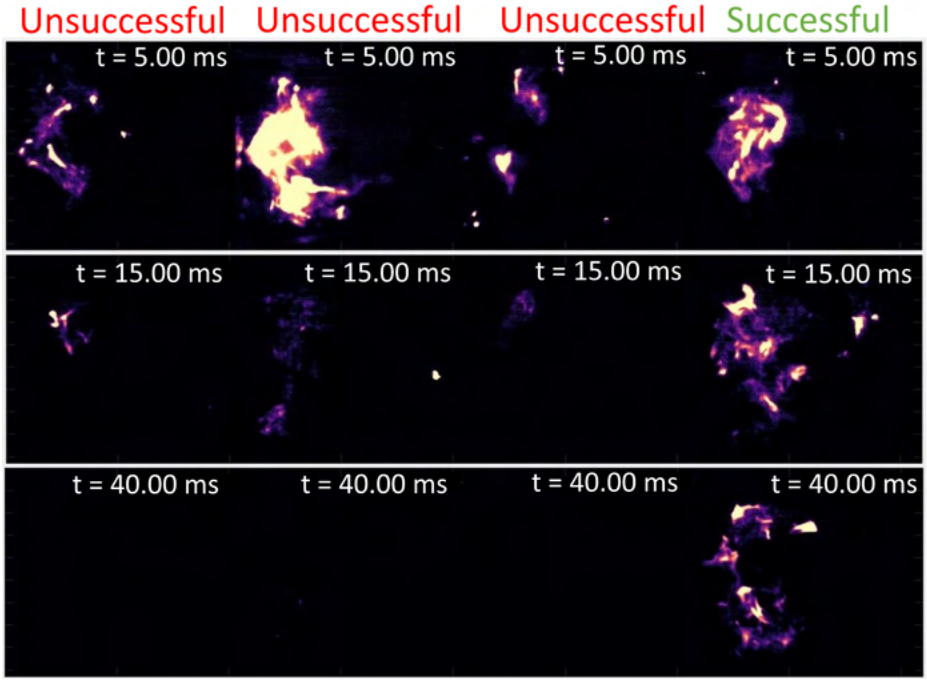

Figure 6. High-speed broadband image data from the M1 combustor during cold-start ignition testing.

These measurements represent initial baseline ignition testing in the M1 combustor and provide an important first step toward understanding the general combustor performance in the ignition regime in the M1 combustor. Further optimization of injection nozzles and test conditions will be needed. Combustor performance under ignition scenarios is a key performance metric to enable the introduction of SAF to the jet fuel supply pipeline. The M1 combustor is designed to enable a wide array of diagnostic techniques to study this phenomenon in more detail, including high-speed laser diagnostics such as PLIF and PIV, in addition to high-speed X-ray phase contrast imaging at ANL. Future efforts will apply these diagnostics of the M1 combustor to develop a deeper understanding of the physics leading to successful combustor ignition, in addition to providing an invaluable set of boundary conditions for combustor ignition simulation efforts. This work will provide the information necessary to determine whether small-scale combustors like the M1 can provide the data needed to inform large-scale programs aiming to integrate SAF on a wider level throughout the aviation industry.

Milestones

3 months: M1 combustor and control system setup and testing at UIUC.
6 months: High-altitude relight experiments at ARL (first attempt) – failed due to a fire in the facilities.
9 months: High-altitude relight experiments at ARL (second attempt) – successful.
12 months: Data analysis and identification.

Major Accomplishments

We have successfully collected baseline ignition performance data for the ARC-M1 combustor under cold-start and altitude relight operating conditions. We observed interesting phenomena for high-flowrate and low-temperature conditions, which we believe warrant further investigation using more advanced diagnostic techniques, such as X-ray phase contrast imaging. Additionally, the results from this testing suggest that it may be interesting to perform ignition testing on multiple nozzles

to determine how nozzles with different droplet breakup behavior affect global ignition performance. These measurements will provide key information for identifying directions for future study to enable small-scale combustors to be used more widely as test platforms for SAF.

Publications
Wood, E., Motily, A., Trotter, C., Lee, T., Mayhew, E., Coburn, V., Temme, J., & Kweon, C. (2022). *Fuel spray and operating condition impact on ignition performance in the ARC-M1 combustor.* Conference paper in preparation.

Outreach Efforts
All test data will be made accessible through https://altjetfuels.illinois.edu/.

Awards
None

Student Involvement
This project was primarily conducted by one graduate student, Eric Wood (Ph.D.), and one undergraduate student, Caleb Trotter.

Plans for Next Period
A deeper investigation into the effects observed in our baseline testing will be conducted by using high-speed X-ray phase contrast imaging.

Task 2 – LBO Measurements for the M1 Combustor
Objective
The objective of this task is to conduct baseline lean blowout measurements for the M1 combustor, similar to those carried out in the referee combustor as part of the NJFCP. These measurements will indicate how this smaller standard combustor compares with the referee rig under similar test conditions.

Research Approach
Throughout the NJFCP, the referee combustor and several other combustors were carefully characterized under a variety of relevant operating regimes, including blowout and ignition. These studies were conducted under a range of standard operating conditions relevant to gas turbine operational regimes that are likely to expose differences between fuels with varying properties. While experiments in the referee combustor have provided valuable data regarding fuel effects near LBO, operating the referee rig comes with some disadvantages. The scale of the referee combustor brings large air and fuel flowrate requirements, which can make setup and operation expensive, especially for studies of new alternatively derived fuels, which may be difficult to manufacture. As such, it would be beneficial if similar results could be obtained from a smaller combustor with reduced fuel and air requirements. The M1 combustor uses significantly less air and fuel, reducing the overall instrumentation expense and complexity and reducing the volume of fuel needed to conduct tests over a range of conditions. With these advantages, the M1 combustor could be used to evaluate the performance of new fuels with much less fuel, reducing the supply requirements for a potential new fuel supplier. To achieve this goal, we must ensure that the trends observed in a smaller combustor can convey the physics observed in other test combustors, such as the referee combustor.

Lean Blowout Testing Procedures
Performing lean blowoff measurements on a combustor in a reliable and repeatable manner involves careful control of all combustor operating parameters, including the fuel flowrate, air flowrate, air temperature, and combustor pressure. To ensure that combustor conditions are stable before the lean blowoff test is conducted, the combustor is ignited at a fuel flowrate above the lean blowoff point, and combustion is sustained at that flowrate until the combustor wall temperature and air outlet temperature reach steady-state conditions. After steady-state temperatures are reached, the fuel flowrate is slowly reduced until blowout occurs. For these experiments, the fuel flowrate is reduced by approximately 0.025 g/min each second. This low ramp rate helps to ensure that the combustor wall temperature does not bias the lean blowoff point. This fuel ramp rate was chosen as a balance between ensuring a steady, repeatable approach to LBO and minimizing the total amount of fuel needed for the experiments. As the fuel flowrate is stepped down, all other combustor operating parameters

are closely monitored to ensure that they stay within the specified parameter range. The specific lean blowoff point is monitored by recording a photodiode signal simultaneously with all other combustor parameters at 10 Hz. The lean blowoff point is determined for each test by finding the equivalence ratio at the point where the photodiode signal indicates that blowoff has occurred. To reduce random variations in LBO from affecting the reported results, each test is conducted at least 20 times at each combustor condition. Operating conditions for these experiments have been chosen to facilitate comparison with previous experiments conducted in the NJFCP referee combustor. Table 2 includes the conditions tested for an initial comparison between four fuels under a single set of combustor conditions.

Table 2. Operating conditions for fuel comparison in the ARC-M1.

Fuels	F-24, C-1, C-3, C-5
Combustor Absolute Pressure (atm)	2.0
Main Air Flowrate (g/s)	55.3
Air Preheat Temperature (K)	394
Pressure Drop – ΔP/P (%)	3

Lean Blowout Results

Figure 7 shows LBO results from the M1 combustor for the selected reference conditions listed in Table 2 to compare the blowout behavior of fuels with varying properties in the relatively small M1 combustion environment. The results are normalized by the equivalence ratio for the reference jet fuel, F-24, and are presented against four fuel properties: the 20% distillation temperature (T20), 90% distillation temperature (T90), DCN, and kinematic viscosity. The error bars represent two standard deviations of the LBO equivalence ratio. These results show a strong correlation between LBO performance and T20 as well as the kinematic viscosity, while a weaker correlation is shown for T90. Meanwhile, there is no apparent dependence on the DCN, which is related to the fuel's chemical characteristics. While this finding does not match some of the DCN results shown in previous works on the larger referee combustor (not all referee combustor results had a DCN correlation), previous work on the M1 combustor has shown significant differences in near-nozzle droplet sizes between these fuels while operating under similar combustor conditions. Meanwhile, droplet sizes, measured inside the referee combustor for several tested fuels, were relatively similar between the fuels. As such, the LBO performance in the M1 combustor appears to be dominated by fuel atomization behavior (linked to kinematic viscosity) and initial vaporization of the fuel. The relatively lower dependence on T50 (not pictured) and T90 demonstrates that the ability to vaporize the initial 20% of the fuel determines the overall LBO performance of the combustor under these conditions. This observation of LBO performance also suggests that preferential vaporization effects are important to LBO behavior in small-scale combustors such as the ARC-M1, an aspect that warrants further investigation. Additionally, it is acknowledged that there is often a correlation between fuel distillation temperatures and kinematic viscosity; thus, one of these factors may be far more dominant than the other, presenting another consideration that must be investigated further in future work.

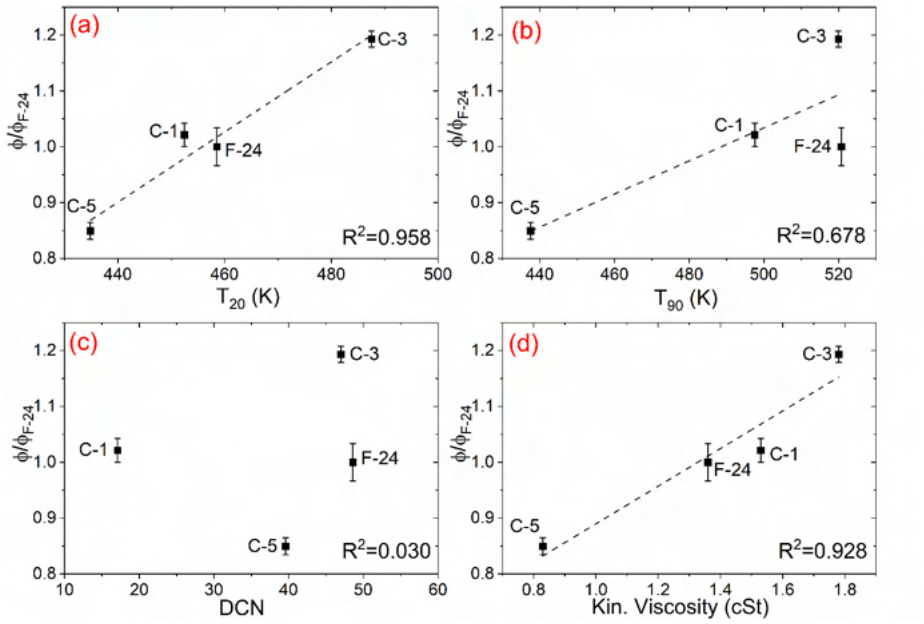

Figure 7. LBO results for the ARC-M1: T20 (a), T90 (b), DCN (c), and kinematic viscosity (d). Combustor conditions for this data are included in Table 2. Error bars represent two standard deviations.

These results demonstrate a strong dependence on fuel properties governing atomization and vaporization, in contrast to many of the results shown for the referee combustor in the NJFCP, which raises the important question of whether the fuel nozzle used for all of these baseline measurements is appropriately sized for the smaller combustor size of the M1 combustor, as compared with the much larger referee combustor. The clear dependence of lean blowoff performance on parameters governing fuel atomization and vaporization suggests that the existing nozzle may produce droplets that are far too large to be vaporized and combusted within the length scales of the smaller M1 combustor and that a new, smaller nozzle may be necessary to capture the physics that are dominant in larger combustors, which are more representative of those used in currently operating aircraft. As such, in the upcoming months, testing will be conducted on a range of new fuel nozzles, which should offer significantly improved fuel atomization performance compared with the existing nozzle, which may shift the operating regime of the M1 combustor to the chemically dominated regime as compared to the physically dominated regime in which it is currently operating. Figure 8 presents a photograph of some of the new fuel nozzles (with smaller fuel droplet sizes) that will be tested in the near future.

Figure 8. New nozzles being tested in the ARC-M1 combustor to evaluate ignition performance.

Milestone(s)

6 months: M1 combustor setup, shake-down, and selection of LBO test conditions.
9 months: Preliminary data collection for LBO in the M1 combustor for select fuels.

12 months: Comparison of lean blowout measurements for select NJFCP fuels in the M1 combustor with referee combustor data.

Major Accomplishments

We have conducted a baseline LBO measurement in the M1 combustor for comparison with the referee combustor using key NJFCP fuels. The results show an overwhelming dependence on the physical properties of the fuels, and new efforts to optimize a nozzle with lower flowrates (and a higher degree of atomization) will be implemented in the near future.

Publications

Wood, E., Motily, A., Trotter, C., Lee, T., Mayhew, E., Coburn, V., Temme, J., & Kweon, C. (2022). *Fuel spray and operating condition impact on ignition performance in the ARC-M1 combustor.* Conference paper in preparation.

Outreach Efforts

All test data will be made accessible through https://altjetfuels.illinois.edu/.

Awards

None

Student Involvement

This project will be primarily conducted by two students: Eric Wood (Ph.D.) and Caleb Trotter (undergraduate).

Plans for Next Period

New injectors with smaller atomization droplet sizes will be optimized for the M1 combustor to ensure that the chemistry aspect of the fuel is properly reflected in the overall combustor performance. This effort will require new imaging of the droplet sizes at the ANL's Advanced Photon Source to acquire initial conditions for numerical simulations, as the droplet sizes will change.

Project 066 Evaluation of High Thermal Stability Fuels

University of Dayton and University of Dayton Research Institute

Project Lead Investigator

Joshua Heyne
Associate Professor
Mechanical Engineering
University of Dayton
300 College Park
Dayton, OH 45458
937 229-5319
Jheyne1@udayton.edu

University Participants

University of Dayton

- P.I.(s):
  1. Joshua Heyne, Associate Professor
  2. Randall Boehm, Research Engineer
- FAA Award Number: 13-C-AJFE-UD, Amendments 27 and 30
- Period of Performance: June 5, 2020 to August 26, 2022
- Tasks:
  1. Identify/create a jet engine model including all components necessary to evaluate the impact of fuel properties
  2. Build and apply a heat transfer model for the fuel system
  3. Identify engine cooling tradeoffs that can be leveraged to optimize engine/aircraft system efficiency
  4. Estimate gains in fuel efficiency
  5. Identify critical blend components and solvents to study
  6. Create and test blends for thermal stability in JFTOT and QCM

Project Funding Level

FAA provided $284,997 in funding which is allocated between amendments 27 and 30 as indicated below:

- 13-C-AJFE-UD-027: $184,997
- 13-C-AJFE-UD-030: $100,000

Cost sharing is provided by DLR Germany.

Investigation Team

- Joshua Heyne (University of Dayton) is the project lead investigator, responsible for building the team and coordinating team activities, driving toward the completion of major milestones.
- Randall Boehm (University of Dayton) is a research engineer with 20 years of relevant industry experience and is responsible for leading the technical efforts on this project.
- Lily Behnke (University of Dayton) is a graduate student research assistant who is responsible for integration of the engine performance models (EPMs) and the fuel properties models with JudO, a tool developed internally to help optimize fuel composition against user-defined objectives.
- Jack Hoog (University of Dayton) is an undergraduate student research assistant who is assisting with the implementation of a Python program option to mix aircraft operating conditions used as the basis of fuel impact comparisons.

- Jeffrey Spruill (General Electric [GE]-Aviation) is a product performance engineer who is responsible for applying audited EPMs as necessary to judge potential drop-in fuel effects on a variety of engines for various mission points, environmental conditions, and engine deterioration levels. Additionally, Jeff is responsible for estimating non-drop-in fuel effects that arise from conceptual design changes to engine thermal management systems that lead to increased reliance on fuel as a coolant instead of compressed air.
- Gurhan Andac (GE-Aviation) is a combustion engineer who is responsible for coordinating the efforts at GE in support of this project.

Project Overview

It has long been understood that increasing the reliance on jet fuel as a primary coolant for both the engine and the aircraft has significant performance and efficiency benefits relative to the use of air as a coolant [1], but fuel degradation and coking at high temperatures restrict how much heat can be put into the fuel. In some military applications, the performance benefits are sufficiently large to justify the creation of specialty fuels such as JP7 and JPTS, which can tolerate much higher temperatures than petroleum-derived Jet A or Jet A1 (JP8) [2]. In land-based applications of gas turbines, weight is of little consequence; thus, the operations of waste heat recovery (WHR) for plant efficiency or the cooling of combustor inlet temperature for emission reductions can be accomplished in a wide variety of ways, all of which are impractical for flight because of their impact on the mass of the power plant. Nonetheless, these applications provide some common examples of how controlling the air temperature along its flow path through the engine can have a large impact on performance, durability, and energy efficiency [3]. The flurry of works relating to fuel deoxygenation [4] and other ways to decrease coking propensity and its impacts [5] is largely motived at the sponsorship level by these benefits.

More recently, sustainable alternative fuels (SAF) have received much attention because they can contribute to high-priority geopolitical goals to diversify energy supply chains and reduce greenhouse gas emissions. Most of these efforts have focused on streamlining the evaluation and approval processes to use synthetic fuels at some blend ratio with petroleum-derived jet fuel to create a so-called drop-in fuel that can be used within existing infrastructure without objection from any stakeholders [6],. Additionally, there have been discussions regarding characteristics of synthetic blend components (such as low aromatics, high specific energy, and high thermal stability) that would make these components attractive to consider as potential specialty fuels (such as JPTS) or high-performance fuels. Kosir et al. [7] recently published work highlighting the efficiency gain that can be expected from the use of fuels with high specific energy, which relates to a lower aircraft weight at take-off, corresponding to a lower mass that must be moved and held against the force of gravity.

The weight of fuel uplifted to an aircraft, as necessary to complete its mission, is certainly an important component to consider in assessing the integrated engine/aircraft energy demand and efficiency. The energy efficiency of the engine is also expected to be influenced by other fuel properties, including the following:

1. **Hydrogen/carbon (H/C) ratio**. Through its impact on combustor exhaust gas composition, this ratio has a small impact on the ratio of heat capacities (gamma), combustor exit temperature, and work extracted during expansion through the turbine, even when the total enthalpy created at the combustor is unchanged.
2. **Viscosity**. Viscosity impacts the heat transfer coefficients, which ultimately determine how much waste heat is recovered by the fuel (coolant) and delivered back to the engine via the combustor.
3. **Energy density**. Energy density, measured in joules per liter (J/L), impacts volumetric flow rates, which also impact heat transfer coefficients.
4. **Specific heat**. The specific heat influences heat transfer coefficients but, perhaps more importantly, also has a direct impact on the temperature rise in the fuel per unit of heat energy absorbed, which in turn may impact the coking rate.
5. **Coking rate**. The coking rate drives several high-level design decisions relating to the thermal management of an engine. Coking rate is also known as fuel thermal stability,

Task 1 – Identify/Create Model of Jet Engine Including All Components Necessary to Accomplish Evaluation of the Impact of Fuel Properties

University of Dayton

Objectives

This work has three primary objectives. The potential impact of fully synthetic SAFs on the specific fuel consumption (SFC) of a jet engine with no associated change in engine design or logic will be assessed in Phase 1. In Phase 2 the impact of leveraging the high thermal stability of SAF candidates by increasing WHR up to a limit driven by the requirement that the fuel vapor pressure must remain below the normal working fuel pressure for all operating conditions will be evaluated. To achieve an increased WHR for this phase of the assessment, only straightforward, evolutionary design changes will be considered. In Phase 3, the aim is to identify and examine the coupled influence of increased WHR with optimized cooling flow schedules [8] will be identified and discussed.

Research Approach

At some level, one might argue that the maximum additional WHR is determined by the proposed shift in the maximum fuel temperature requirement, for instance, (160-127)*Cp, where 160 °C is the proposed temperature for high-thermal-stability fuels, 127 °C is the requirement corresponding to petroleum-derived Jet A, and Cp is the heat capacity of the proposed fuel. While this is true at some level, it provides only part of the story. For this study, a fuel system thermal model (FSTM, Figure 1) was created to simulate the heat pickup of fuel in real engines. This model allows us to quantify the influence of fuel property variations on the temperature rise and WHR within existing architectures. This model also enables evaluations of conceptual-level design changes that are intended to drive more heat into the fuel. A high-level EPM (Figure 2) was created to enable evaluations and comparisons of different conceptual designs that drive the same amount of total heat into the fuel (approximately 33*Cp more than baseline) but take heat from difference sources. The EPM also enables evaluations of the H/C impact on combustor exit temperature and turbine work extraction, which is usually neglected in performance models because it is thought to be a small impact and the H/C ratio of fuel onboard an aircraft is generally not known. The final component in the overall impact on system efficiency is the weight, including the difference (decrease) in fuel weight necessary to complete the same representative mission, as well as the difference (increase) in weight created by the conceptual-level design changes being considered.

A distribution of properties for potential SAFs is created by virtually blending individual molecules by a random association of mole fractions, whose values are also randomly determined, with specific molecules possessing known physical and chemical properties [9,10]. The fuel properties of the mixtures are derived from the mixture definition and constituent properties according to ideal mixture blending rules, which have been documented elsewhere [11]. This trial guess at a SAF candidate is then passed through a filter to determine whether it is expected to pass ASTM D1655 and ASTM D7566 fuel specifications. If the candidate passes this filter, it is included within the distribution that is input to the FSTM and EPM as part of a simulation. See Figure 3 for a graphical representation of the fuel selection methodology. The motivation behind this approach was to maintain a physical link between different properties, as the full set of properties is derived from each fuel and the property variation is driven by fuel composition variation rather than arbitrary simulation. All liquid fuel properties include first-order temperature dependence, whereas none of the properties include pressure dependence.

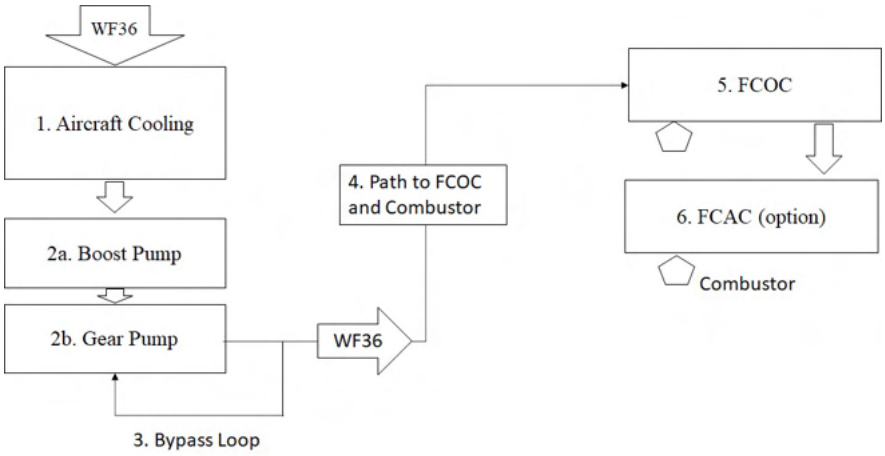

Figure 1. Block diagram of Fuel System Thermal Model for the pilot study [12] and fuel optimization. The optional sixth element is a fuel-cooled air cooler.

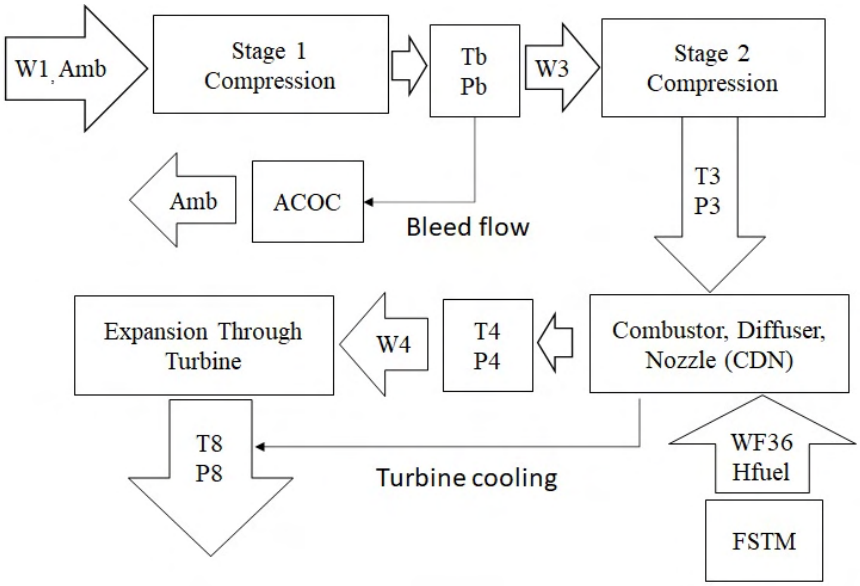

Figure 2. Block diagram of Engine Performance Model for the pilot study [12] and fuel optimization.

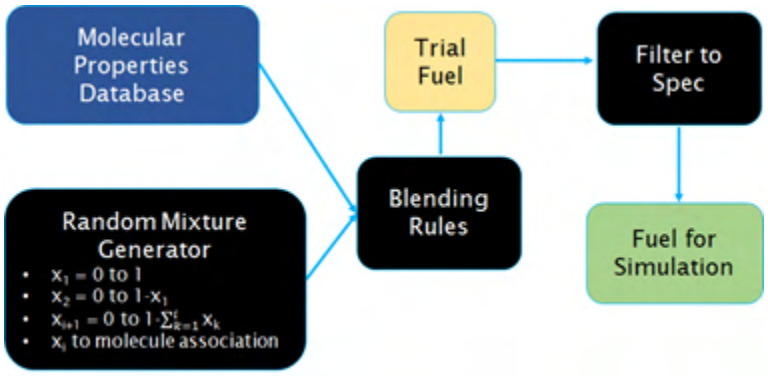

Figure 3. Fuel creation flow chart.

For bookkeeping convenience, the total enthalpy supplied to the engine per unit time, (W_f * LHV), is to be conserved for all initial simulations. The net work per unit time (P_{net}) from the engine (expansion plus compression) varies in these simulations depending on fuel composition and conceptual design, in contrast to real applications, where thrust * air speed (~P_{net}) would be conserved and the fuel flow (W_f) would be changed to meet that demand. Once the initial calculation is made, the fuel flow is varied in the simulation, as it would be in a real engine, until P_{net} is equal to its value for the baseline engine model and reference fuel. The relative difference in fuel flow between the initial and final calculation is the energy savings.

A graphical summary of the methodology is provided in Figure 4. Major inputs include the diameters and lengths of each element in the FSTM, engine operating conditions such as the pressure ratio and air flow splits at each station in the EPM, the baseline fuel-to-air ratio, and temperature boundary conditions for the FSTM. Several fuel properties are provided to the FSTM, while the EPM receives the H/C ratio and lower heating value (LHV) as input.

A validation of this model, relative to fuel property influences and cooling strategy, will be accomplished by comparison to audited performance models of jet engines produced by GE-Aviation.

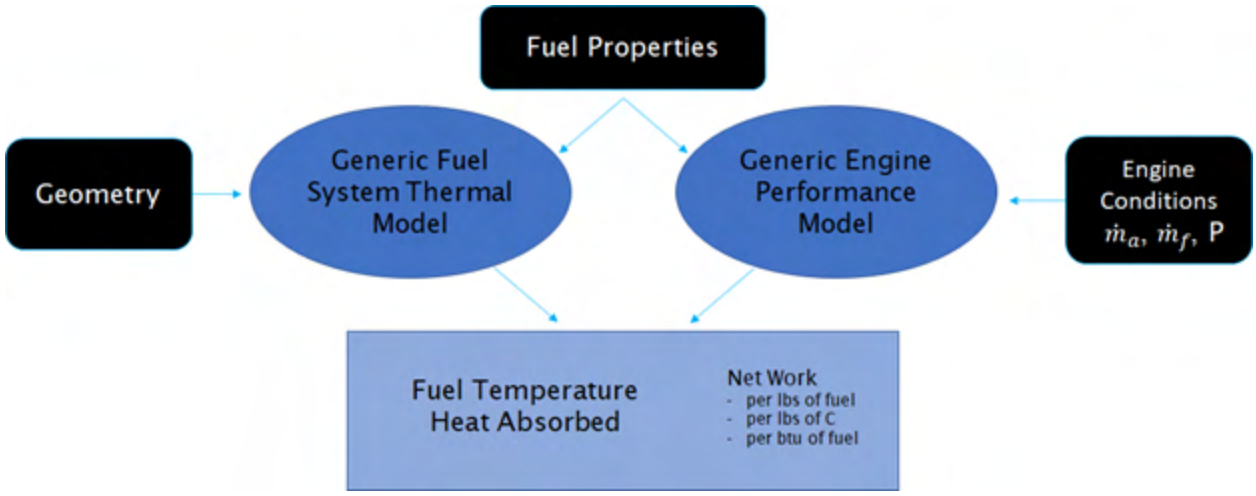

Figure 4. Flow chart of fuel effects and conceptual design evaluation.

Task 2 – Build and Apply a Heat Transfer Model for the Fuel System

University of Dayton

Objective

The goal of this task was to create a model that would output heat absorption, representative of real jet engine fuel systems, based on applied boundary conditions such as fuel properties, fuel velocity and momentum, and hot-side temperatures.

Research Approach

The fuel system was broken down into elements for which the author had experience-based guidance relating to fuel inlet and outlet temperatures. In concert with experience-based guidance relating to fuel momentum and system pressure losses, the fuel system geometry, including the flow diameter and length, and hot-side boundary conditions were established for a baseline fuel flow through the modeled fuel system. This model then became the basis for assessing the impact of varying fuel properties.

In the pilot study [12], Monte Carlo simulations resulted in population distributions plotted against the normalized waste heat recovery (WHR), as shown in Figure 5. In this context, the recovered waste heat is defined as the total heat absorbed by the fuel in route from the fuel tank to the combustor, which is then divided by the reference enthalpy of the fuel ($LHV*W_f$) supplied to the combustor for the initial calculation of P_{net}. At high power, the fuel flow rate is approximately ten times higher than it is at low power, and the flow within the fuel system is turbulent regardless of the fuel properties. Under these circumstances, heat transfer coefficients are not very sensitive to fuel property variations, and thus, the two curves representing high-power operation are nearly vertical. At low-power operation, the flow within the fuel system starts out as laminar and transitions to turbulent as the viscosity drops with increasing fuel temperature. Under these circumstances, heat transfer coefficients are quite sensitive to fuel property variations, and thus, the two curves representing low-power operation show 0.2% variation in the normalized WHR.

This term is not expected to have a large impact on the overall system efficiency because relatively little fuel is used at low power (top of descent) relative to take-off, climb, or long-haul cruise and because WHR is small compared with $LHV*W_f$. Nonetheless, this savings is worth optimizing because it can be potentially realized without sacrificing any other measure of fuel performance and without any change to the engine. We have already begun to optimize the fuel composition to maximize the LHV and total savings resulting from WHR, which will be discussed further under Task 4. In support of this goal, we have collected the necessary property data for thousands of molecules, which have been pruned to 1,124 molecules based on volatility, expected thermal stability, data completeness, and data consistency relative to similar molecules. We have also added the capability to predict the smoke point for each random composition.

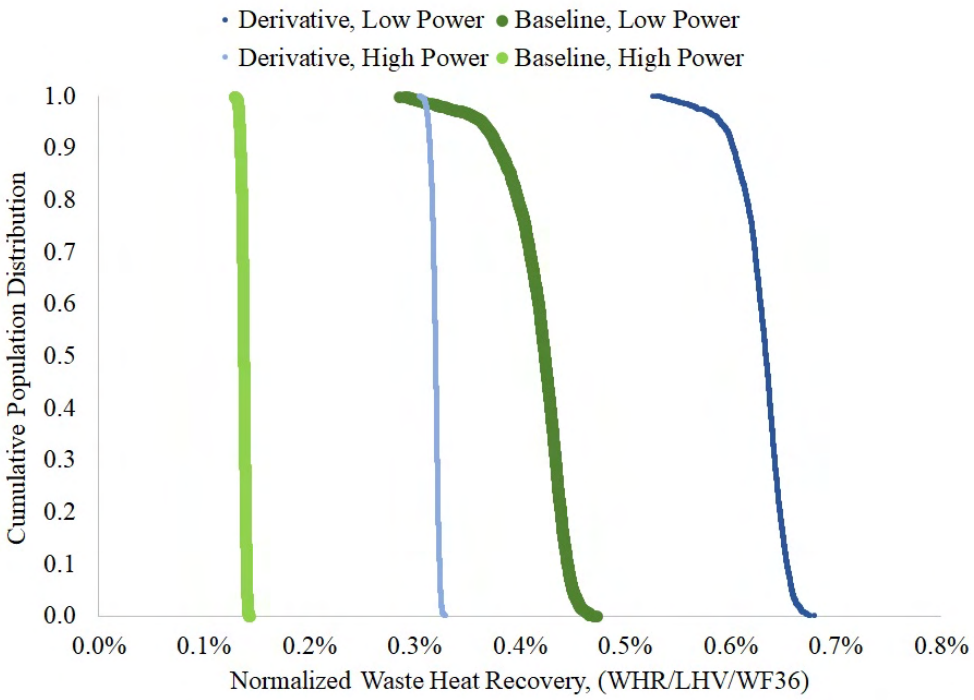

Figure 5. Impact of fuel properties on heat recovered from the engine by the fuel.

Task 3 – Identify Engine Cooling Trades That Can Be Leveraged to Optimize Engine/Aircraft System Efficiency

University of Dayton and GE-Aviation

Objective

The goal of this task was to document ideas relating to how OEMs might design an engine thermal management system to minimize air pressure losses due to cooling or to reduce the overall system weight by capitalizing on the improved thermal stability of fully synthetic SAFs. This task also focused on estimating the savings afforded by each design change concept.

Research Approach

One advantage of simplified EPMs is that they facilitate conceptual design trades. For this project, we have considered four conceptional design variations to the thermal management system that increase the reliance on fuel as a coolant. The simplest concept is to add a heat exchanger anywhere in the system, sized such that the fuel temperature at the limiting design point is increased from its current limit, taken as 127 °C, up to a new higher limit, taken as 160 °C. The current limit is driven by fuel thermal stability. Once this limit is elevated via high-quality synthetic fuel, the next temperature limit is driven by elastomeric material specifications or platform/fuel volatility requirements, which coincidentally are both near 160 °C for existing elastomeric seals and conventional jet fuels. Provided that the heat recovered by this new heat exchanger is truly waste heat and neglecting the impact of the exchanger's weight on aircraft fuel efficiency, the afforded energy savings of this configuration can be determined without an EPM or FSTM under the design-limiting operating condition, although the FSTM is necessary for other operating conditions. This simple configuration is labeled as "D" in Figure 6. In the next simplest concept, the fuel-cooled oil cooler is enlarged just enough to enable elimination of the air-cooled oil cooler. Such a configuration would be lighter than the baseline engine, which would provide some fuel efficiency benefit at the system level, but this aspect is neglected in the calculations summarized in Figure 6. This configuration is labeled as "C" in Figure 6. The large difference between the savings at high power and the savings at low power for this configuration arises because the sink pressure (altitude-dependent ambient pressure) is unrelated to the pressure ratio achieved by the first stage of compression. The savings at the design point are driven by an input to the model, namely, the fraction of heat taken out of

the lube oil by air, with the remaining heat taken out by fuel. Presently, there is significant uncertainty in the aero-savings estimate for this configuration; thus, work is underway at GE-Aviation to make a much better estimate by using a derivative of an audited performance model of a GE engine for a narrow-body airframe. This estimate will also include the influence of the weight savings. However, based on an NPSS map function representation of the heat exchanger performance, GE has

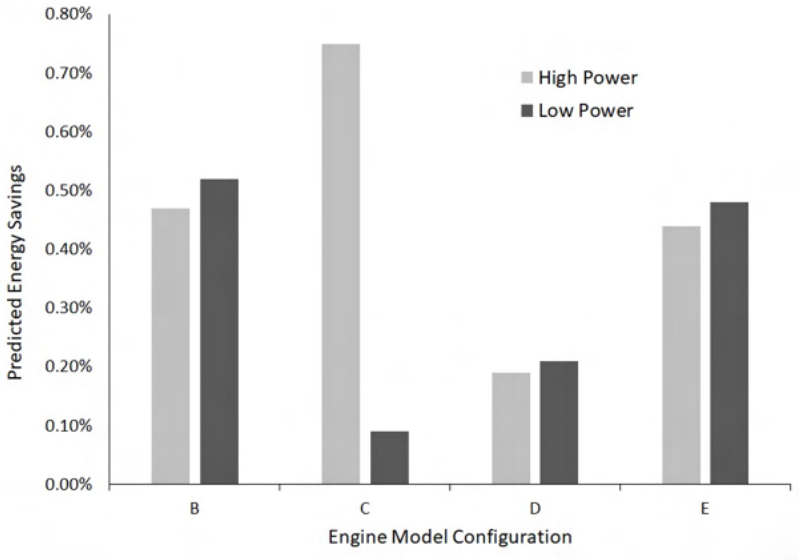

Figure 6. Summary of predicted energy savings for a variety of engine model configurations. B. Cooled cooling air with a reduced cooling flow. C. Enlarged fuel-cooled oil cooler in place of an air-cooled oil cooler. D. Cooled cooling air alone. E. Cooled cooling air and improved turbine efficiency (0.700 to 0.701)

determined that complete elimination of the ACOC in this application would not be possible unless the maximum fuel temperature limit were raised by 107 °C instead of the 33 °C increase presumed for this analysis based on the fuel system material limits (e.g., elastomers) and fuel volatility. In the most involved concept, the cooled cooling air is coupled with active clearance control of the turbine airfoils. The configuration representing this concept is labeled as "E" in Figure 6. The turbine efficiency is an input to the EPM, and the difference between the savings of configuration E and the savings of configuration D is primarily driven by this input. The fuel savings is approximately double the increase in turbine efficiency because the Brayton cycle efficiency (i.e., overall engine efficiency) is approximately 50%. While this term is represented by the arbitrary choice of a 0.1% improvement in turbine efficiency for all operating conditions, a detailed design of an active clearance control concept is needed to estimate how airfoil clearances change with cooling airflow split variation. The airflow supplied to the regions that most need cooling (usually the mid span of the blades and vanes) can be reduced when the cooling air is cooled. This frees up air flow that can be used to cool the case (outer diameter) under operating conditions (usually high power) in which the clearance between the case and the blades is highest. To determine the impact on gap height, a detailed heat transfer analysis is required, and to gauge the impact of a gap height change on the aerodynamic efficiency of the engine, a detailed fluid dynamics calculation is needed. These analyses require a full definition of product geometry, which is obviously OEM-proprietary. Although we have requested that GE-Aviation include representative results of such a concept as part of their contribution to this project, they have not agreed to this request. Because turbine inefficiency is generally the largest source of engine inefficiency after accounting for the unavoidable heat engine (Brayton cycle) inefficiency, there is a strong possibility that cooled cooling air can be utilized most effectively by coupling it with active clearance control.

The configuration labeled as "B" in Figure 6 is the same configuration labeled as "derivative" in Figures 5 and 7. For this configuration, the total turbine cooling air flow budget is reduced such that the change in enthalpy of the cooling air is matched to that of the baseline configuration at high power. In this study, the cooling flow was reduced to 29.75% of W3, compared with 30.00% of W3 for the baseline configuration, where 30% was an input to the model. By comparing the results for configuration B with those for configuration D, we can see that the savings achieved by reducing parasitic air flows can exceed the savings obtained from improvements in WHR.

By definition, none of the thermal management system design changes considered here correspond to drop-in fuel benefits. To take advantage of the higher thermal stability of SAFs relative to conventional jet fuel and to improve specific fuel consumption, some design changes are necessary. Such changes should be expected to afford an improvement of 0.5%, which compares favorably with the savings that could potentially be realized on a drop-in basis, as discussed in the next section.

Task 4 – Estimate Gains in Fuel Efficiency

University of Dayton and GE-Aviation

Objectives

The first goal of this task is to estimate the impact of fuel property variation on engine-level fuel consumption (specific fuel consumption (SFC). The second goal is to optimize fuel composition in order to minimize the SFC while maximizing the specific energy (LHV), which could minimize aircraft fuel consumption where fuel LHV is factored into the mass of fuel uplifted into the aircraft.

Research Approach

To accomplish the first goal, the tools developed in Tasks 1 and 3 were used in conjunction with a Monte Carlo simulation of fuel composition derived from a database of 94 molecules, where a filter was used to eliminate random compositions that led to certain properties outside of fuel specifications or fit-for-purpose properties, as predicted via algebraic blending rules. For the second goal, we improved our approach regarding the SAF volatility requirements, added a requirement for the smoke point, and placed a limit on the number of ingredients allowed in the fuel. In addition, the database was expanded to 1,124 molecules. A small (un-converged) Monte Carlo simulation serves as the starting point for optimizing the randomly chosen mole fractions of each molecule from the master database. The engine-level fuel economy and LVH are maximized via mixed-integer distributed ant colony optimization (MIDACO). To arrive at a global solution set, this process is repeated multiple times until all molecules in the database have been chosen at least once by the initializing small Monte Carlo simulation.

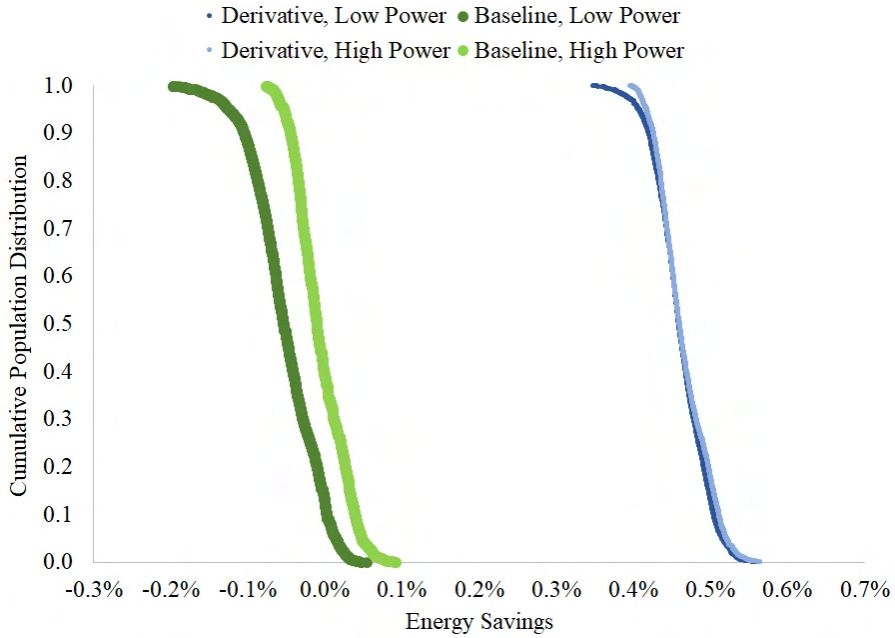

Figure 7. Impact of design and fuel property on fuel energy savings.

A summary of the predicted energy savings relative to the baseline EPM model and the reference petroleum fuel labeled as "A-2" by the National Jet Fuel Combustion Program is provided in Figure 7, which shows the following key trends. First, by leveraging the improved thermal stability, the design change has a significantly larger impact on savings (i.e., fuel efficiency) than fuel property variation. Second, the impact of fuel property variation, including the width of each curve (shown) and the rank order of SAF candidates (not shown), is nearly the same for each EPM configuration, hinting at insensitivity to engine-to-engine variation. Third, the impact of fuel property variation changes for various engine operating conditions (note the differences in curve width and how much of each baseline (green) curve is above 0%). While not evident from this plot, the primary driver of this sensitivity is the fuel-to-air ratio. For a high fuel-to-air ratio and high fuel flow rate, the composition of the combustor exhaust air (driven by the fuel H/C ratio) has the greatest effect. In contrast, for a low fuel-to-air ratio and low fuel flow rate, the WHR is just as important as the vitiated air composition. This sensitivity has directed us to generate a realistic mission mix of operating conditions as a basis for assessing drop-in fuel effects on engine efficiency.

Our pilot study showed that ~20% of the 2,000 randomly chosen SAF candidates afford some savings relative to the reference fuel (A-2) at low power, while 50% afford some benefit at high power. The status of our SAF composition has identified two SAF candidates with an engine SCF benefit as well as a weight savings relative to A2 and hundreds of solutions that offer one or the other, as shown in Figure 8. The candidates on the lower end of this range have higher LHVs than those on the higher end of this range.

While the SAF composition optimization is in progress, GE-Aviation is also working to provide an estimate of savings that could result from configurations B and C (see Figure 6). If they determine that the savings from configuration C exceed our estimate for both B and C, it may be unnecessary to make an estimate for B because C is viewed as a configuration that is relatively easy to implement, while configuration B would be met with skepticism and resistance from the turbine design team.

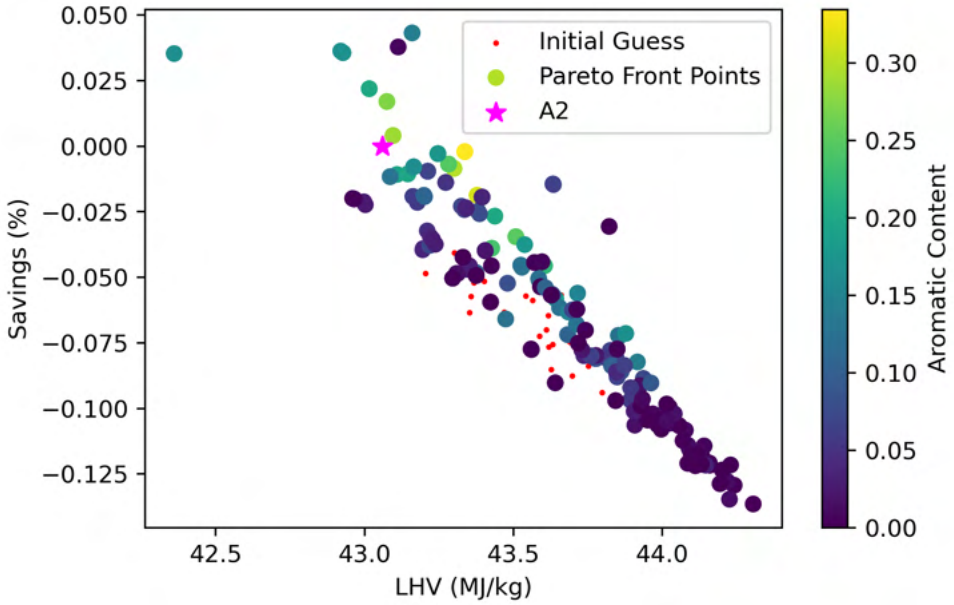

Figure 8. Current status of SAF composition optimization.

Tasks 5 & 6 – Identify, Create, and Test Blends for Thermal Stability in JFTOT and QCM

Objective

The goal of these tasks is to evaluate the solutions identified by Task 4, goal 2 for thermal stability.

Research Approach

The solutions identified in Task 4.2 will be analyzed to find common threads in terms of fuel properties and compositions. It is expected that a relatively small number of molecules will show up with high concentration in several solutions, and we will discuss these molecules with experts regarding their potential impact on thermal stability. Any such molecule, judged by subject-matter experts to present an elevated risk of coking relative to isoparaffins, will be targeted for experimental evaluation of thermal stability at varying concentrations. Other factors to consider in these selections include availability of the molecule and its potential impact on seal swelling and freeze points.

These tasks cannot be initiated until more progress is made on the fuel optimization. Meanwhile, significant progress (under FAA project 65) toward a simple and reliable blending rule for the freeze point may facilitate automated evaluation of freeze points of solutions along the pareto front, which could significantly narrow the scope of the thermal stability evaluations.

Milestones

1) The conceptual design of a model jet engine to serve as a tool for evaluating the impact of fuel property variation on jet engine fuel efficiency was completed (Aug. 2020).
2) Preliminary construction of this model, including integration with Monte Carlo methods and verification of heat transfer coefficient correlations, was completed (Oct. 2020).
3) Three potential cooling trades have been identified, and the sub-models needed to execute these trade studies were built (Nov. 2020).
4) A database of 2,000 fully synthetic SAF candidates and a variety of reference fuels was created (Nov. 2020).
5) The simulations necessary to support the proof of concept were completed (Nov. 2020).
6) A scientific paper summarizing this progress was accepted for publication (Jul. 2021).
7) The number of entries in the molecular properties database was increased from 94 to over 2,000 (Jul. 2021).
8) Data consistency and completeness were verified (Oct. 2021).
9) A model was built and validated to generate smoking propensity data for all molecules in the database (Oct. 2021).
10) A scientific paper covering smoking propensity models was submitted for publication (Nov. 2021).
11) All models used in proof-of-concept work were integrated into JudO, which has been previously used [7] to optimize fuel composition against defined objectives (Sep. 2021).
12) A smoke point filter was added to JudO, and volatility-related predictions and filters were streamlined (Aug. 2021).
13) The first successful evolution toward optimized SAF composition was achieved (Nov. 2021).

Major Accomplishments

- As a major accomplishment, we constructed and verified the FSTM and EPM and their integration with Monte Carlo methods, which was necessary to complete most of the remainder of this project.
- A proof-of-concept paper was published in the journal *Fuel*.
- All tools needed to assess fuel effects on SFC were integrated into our internal code for SAF optimization (JudO).
- The molecular properties database was expanded 10-fold.
- A model was created to estimate the smoking propensity of potential SAF constituents.

Publications

Boehm, R. C., Scholla, L. C., & Heyne, J. S. (2021). Sustainable alternative fuel effects on energy consumption of jet engines. Fuel *304*, 121378. https://doi.org/10.1016/j.fuel.2021.121378

Boehm, R. C., Yang, Z., & Heyne, J. S. (2021). *Threshold sooting index of sustainable aviation fuel candidates from composition input alone: Progress toward uncertainty quantification. energy and fuels.* Manuscript submitted for publication.

Outreach Efforts
None

Awards
None

Student Involvement
- Logan Scholla (University of Dayton) is a graduate student research assistant who was responsible for the properties databases used in the proof-of-concept work during his tenure of involvement with this project.
- Lily Behnke (University of Dayton) is a graduate student research assistant who integrated the fuel efficiency models in JudO and is responsible for the ongoing fuel optimization. She will also be primarily responsible for Tasks 5 and 6 going forward.
- Jack Hoog (University of Dayton) is an undergraduate student research assistant who is assisting with the implementation of a mission mix of engine operating conditions for assessing the fuel effects on SFC determinations. Hoog is also helping with the evaluation of SAF definitions produced by JudO / MIDACO.

Plans for Next Period
- Complete integration of the mission mix into the energy savings objective function
- Complete engine cooling and weight trade studies
- Complete a sketch/map of fuel effects on engine performance
- Complete SAF composition optimization
- Identify a set of molecules that strongly contribute to optimized SAF compositions (golden molecules)
- Evaluate the seal swell, freeze point, T90–T10, and producibility options for a random selection of pareto-front SAF candidates
- Evaluate system energy savings by integrating fuel weight effects on aircraft energy consumption with engine energy savings
- Submit a scientific paper on high-performance SAF candidates
- Qualitatively evaluate the coking risk of golden molecules and hand-picked pareto-front SAF candidates
- Execute thermal stability tests of promising SAF candidates

References
[1] Bruening GB, Chang WS. Cooled cooling air systems for Turbine thermal management. Proc ASME Turbo Expo 1999;3. https://doi.org/10.1115/99-GT-014.
[2] Edwards T. Advancements in gas turbine fuels from 1943 to 2005. J Eng Gas Turbines Power 2007;129:13–20. https://doi.org/10.1115/1.2364007.
[3] Wilfert G, Sieber J, Rolt A, Baker N, Touyeras A, Colantuoni S. New Environmental Friendly Aero Engine Core Concepts. ISABE-2007-1120. 18th Int Symp Air Breath Engines 2007:1–11.
[4] Zabarnick S, West ZJ, Arts A, Griesenbrock M, Wrzesinski P. Studies of the impact of fuel deoxygenation on the formation of autoxidative deposits. Energy Fuels 2020;34:13814–21. https://doi.org/10.1021/acs.energyfuels.0c02603.
[5] Mancini AA, Ackerman JF, Richard LK, Stowell WR. Method and Coating System for Reducing Carbonaceous Deposits on Surfaces Exposed to Hydrocarbon Fuels at Elevated Temperatures. 6808816 B2, 2004.
[6] Colket M, Heyne J. Fuel Effects on Operability of Aircraft Gas Turbine Combustors. August. AIAA, Progress in Astronautics and Aeronautics; 2021. https://doi.org/10.2514/4.106040.
[7] Kosir S, Stachler R, Heyne J, Hauck F. High-performance jet fuel optimization and uncertainty analysis. Fuel 2020;281:118718. https://doi.org/10.1016/j.fuel.2020.118718.
[8] Deveau PJ, Greenberg PB, Paolillo RE. Gasturbine Engine Active Clearance Control. 4513567, 1985.
[9] Lemmon, E.W., Bell, I.H., Huber, M.L., McLinden MO. NIST Standard Reference Database 23: Reference Fluid

Project 067 Impact of Fuel Heating on Combustion and Emissions

Purdue University

Project Lead Investigator

Robert P. Lucht
Ralph and Bettye Bailey Distinguished Professor of Combustion
School of Mechanical Engineering
Purdue University
West Lafayette, IN 47907-2088
765-714-6020
Lucht@purdue.edu

University Participants

Purdue University

- P.I.s: Dr. Robert P. Lucht and Dr. Carson D. Slabaugh
- FAA Award Number: 13-C-AJFE-PU-038
- Period of Performance: October 1, 2020 to September 30, 2021
- Task:
    1. Investigate the effects of fuel heating on combustion and emissions for aviation gas turbines

Project Funding Level

Project 67 is funded by the FAA at the level of $250,000 for the project period June 5, 2020 to June 4, 2021, and an additional $250,000 for the time period from June 5, 2021 to September 30, 2022. The required cost sharing 1:1 match of $500,000 is provided by Purdue University.

Investigation Team

- PI for the project is Professor Robert P. Lucht. Professor Lucht is the major advisor for Colin McDonald.
- Co-PI is Professor Carson D. Slabaugh. Professor Slabaugh is the major advisor for John Philo and Tristan Shahin.
- PhD graduate students are Colin McDonald, John Philo and Tristan Shahin. The graduate students are responsible for the design of system components, such as the fuel heating system, and will be responsible for executing test operations. Research Engineer Dr. Rohan Gejji is also working on the project, is helping the graduate students with their design projects, and will be supervising the test operations.

Project Overview

The goal of this project is to evaluate the effects of heating jet fuel before injection in an aviation gas turbine combustor on the combustion efficiency, pollutant emissions, and dynamics. In an aircraft engine, heat that would otherwise be wasted can be directed into the fuel to increase its sensible enthalpy before injection. Thermochemistry dictates that this increase in sensible enthalpy must lead to lower fuel consumption for a given combustor exit temperature. However, the effects of elevated fuel temperature on combustion performance characteristics (such as the fuel spray pattern, spatial distribution of reaction zones, pollutant emissions, and combustion dynamics) are not yet well understood. We will perform experiments with heated fuels by using a piloted, partially premixed fuel injector located in an optically accessible combustor. This process will allow us to apply advanced laser diagnostic techniques to compare the behavior of the combustor at different fuel temperatures over a wide range of operating conditions.

The platform for the planned experiments is the Combustion Rig for Advanced Diagnostics (COMRAD). The test rig, shown in Figure 1, is designed to operate at steady-state conditions with thermal powers as high as 8 MW, inlet air pressures (P_3)

as high as 4.0 MPa, and inlet air temperatures (T_3) as high as 1000 K. To facilitate operation at these conditions, the test article is made out of aviation-grade alloys and thoroughly water-cooled, and the inner windows are film-cooled with heated nitrogen. Before this project, extensive testing with ambient-temperature fuels was performed in this rig, with a focus on 5- and 10-kHz particle image velocimetry (PIV) measurements in the downstream boundary condition window section, and 50- and 100-kHz PIV measurements in the flame zone.

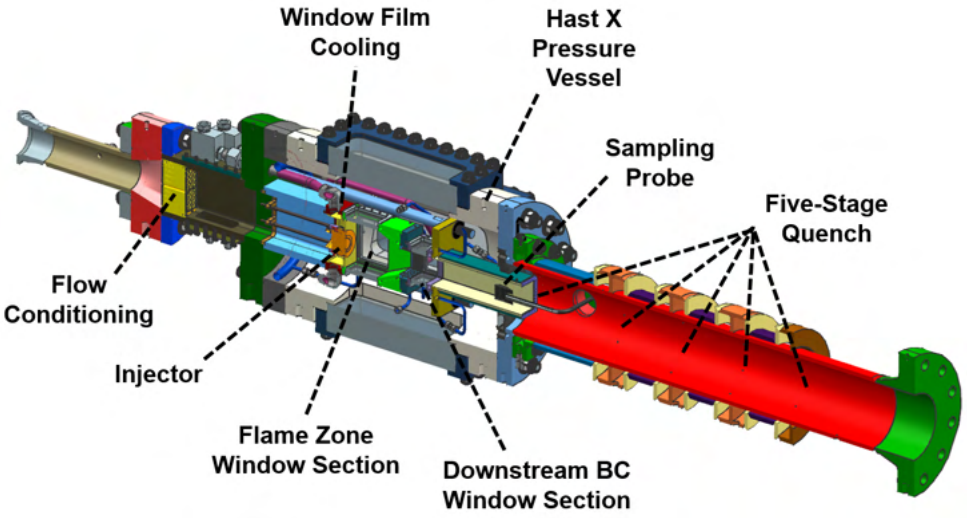

Figure 1. Schematic diagram of the Combustion Rig for Advanced Diagnostics (COMRAD).

Task 1 - Investigate the Effects of Fuel Heating on Combustion and Emissions for Aviation Gas Turbines

Purdue University

Objective

The goal of this project is to determine the effects of fuel heating on the performance of aviation gas turbines. Fuel heating can potentially lead to higher efficiency, but can also lead to changes in the fuel distribution pattern and in the location of reaction zones in the combustor. These changes may also impact pollutant emissions and combustion dynamics during engine operation. We will perform experiments using heated fuels and will measure the fuel distributions, reaction zone distributions, pollutant emissions, and combustion dynamics at a range of fuel temperatures from near room temperature to above the supercritical temperatures for hydrocarbon fuels.

Research Approach

We will perform experiments with heated fuels by using a piloted, partially premixed fuel injector located in an optically accessible combustor. This setup will allow us to apply advanced laser diagnostic techniques to compare the behavior of the combustor at different fuel temperatures over a wide range of operating conditions. These advanced diagnostic techniques include fuel planar laser-induced fluorescence (PLIF) imaging to monitor fuel distribution patterns, hydroxyl (*OH*) radical PLIF (*OH* PLIF) imaging to monitor reaction zones, and PIV to measure the flow-fields. We will also measure emissions with probe sampling and will use pressure transducers to measure combustion dynamics.

Milestones

The milestones for the work performed in fiscal year 2021 are listed below:

1. A fuel heater capable of heating three independent circuits of jet fuel to 700 K at 4.0 MPa was developed and successfully deployed in the test cell.
2. The operational sensitivity of the experiment to fuel temperature on the emissions and flame structure was evaluated for a range of operating conditions through emissions sampling with a Fourier-transform infrared

spectroscopy (FTIR) gas analyzer and 50-kHz *OH** chemiluminescence imaging. Measurements were performed at 1.0-MPa and 2.0-MPa inlet air pressures at a range of equivalence ratios and fuel temperatures.

3. Detailed measurements of the flow-field in the combustion zone were conducted through the application of 10-kHz stereoscopic PIV (SPIV) measurements at a down-selected range of operating conditions from the parametric survey with emissions measurements.
4. *OH* PLIF measurements were successfully demonstrated at 10 Hz to characterize the reaction zone location as a function of fuel temperature.

Major Accomplishments

In the current reporting period, we successfully characterized the effects of injection of heated jet fuel on the combustion efficiency and emissions in a model aviation gas turbine combustor. Toward this goal, we designed and demonstrated the operation of a fuel heating system capable of heating three independent fuel circuits to temperatures and pressures exceeding the critical point of the fuel. Combustion experiments with heated fuel were performed at a range of equivalence ratios at pressures of 1.0 and 2.0 MPa. The initial tests focused on emission sampling and high-speed flame imaging to characterize the effects of fuel heating on the combustion process. After a survey of emissions was completed, down-selected cases were characterized in detail with SPIV and *OH* PLIF measurements.

A. Fuel Heater Development

The fuel heater is designed to heat a continuous flow of 50 g/s of jet fuel up to 700 K at pressures up to 4 MPa. For heating, the fuel flows through stainless steel tubing that is wrapped between pairs of copper blocks heated with cartridge heaters. In total, five pairs of copper blocks and 100 cartridge heaters are used, resulting in a combined heating power of 81 kW. The cartridge heaters are split into 20 independently controlled zones of five cartridges, enabling flexibility and control of the fuel temperature of both the pilot and main fuel circuits exiting the heater. An image of the assembled fuel heater is shown in Figure 2.

Figure 2. Photograph of the assembled fuel heating system.

The fuel in three independent circuits is carried from the heater to the experiment in stainless steel tubing that is trace heated and insulated to minimize heat loss. The fuel flow to the heater and the experiment is controlled with metering valves and measured with Coriolis flow meters. The temperature of the fuel is monitored in the fuel heater (to ensure that no phase change is encountered) and immediately upstream of the injector. An inert gas purge circuit is used to avoid collection of

stagnant fuel in the heater and the tubing to the experiment when fuel is not flowing to the experiment. This purge displaces the fuel to a collection tank through a bypass circuit and counter-flow heat exchanger that cools the fuel temperature to ambient temperature with water as the heat transfer medium. The plumbing and instrumentation diagram shown in Figure 3 details the fuel supply layout.

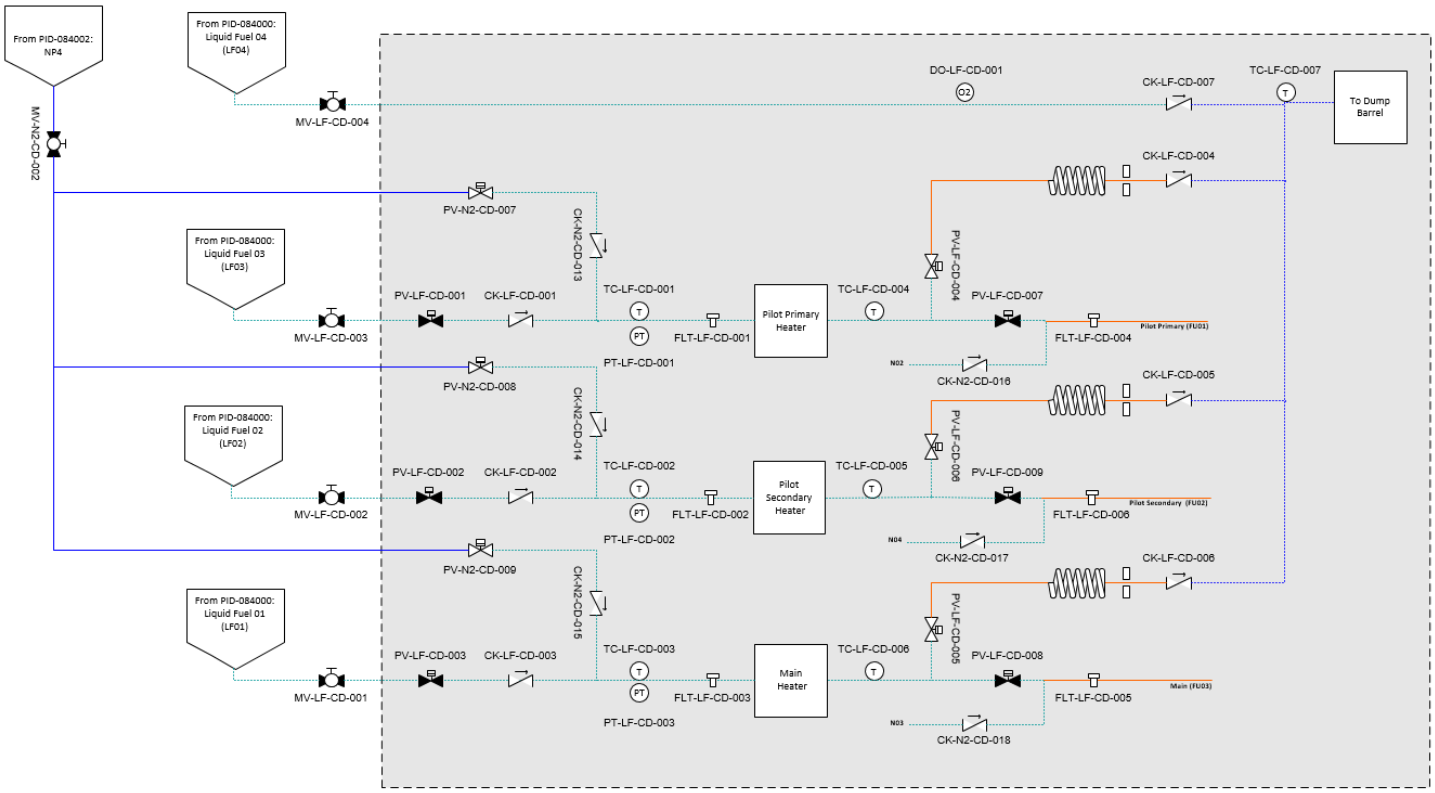

Figure 3. Plumbing and instrumentation diagram for the heated fuel supply to the experiment.

Fuel heater operation was successfully demonstrated after completion of the assembly process, first by heating fuel independently of the combustor and finally in combustion experiments. Sufficient control to enable repeated measurements in the combustor with fuel temperatures of 370 K, 470 K, and 570 K was demonstrated for a range of fuel flow rates to enable understanding of trends in combustion efficiency in the experiment.

B. Emissions Sampling and *OH** Imaging

Emissions sampling began with unheated, ambient-temperature fuel to test the emissions sampling system. For these measurements, a sampling probe was placed in the center of the exhaust channel as shown in the "old" configuration in Figure 4. The initial results did not yield the expected trends because the measurement was missing the near-wall region. Other experiments have shown that gradients in product gas species concentrations exist in the radial direction in similar burner configurations; therefore, the near-wall region was expected to have a different gas composition from that of the bulk flow in the combustor. For the measurements with heated fuel, the probe was reconfigured and placed offset to one side of the exhaust channel, as shown in the "new" configuration in Figure 4. This updated sampling configuration provided a more representative sample of the exhaust. While the emissions samples were being acquired, *OH** chemiluminescence images were acquired at 50 kHz. A high-speed camera (Phantom v2512) was coupled to an ultraviolet (UV)-sensitive intensifier (Lambert HiCATT) to image flame emission optically filtered to 320 ± 20 nm. These images captured a line-of-sight integrated representation of the heat release in the experiment.

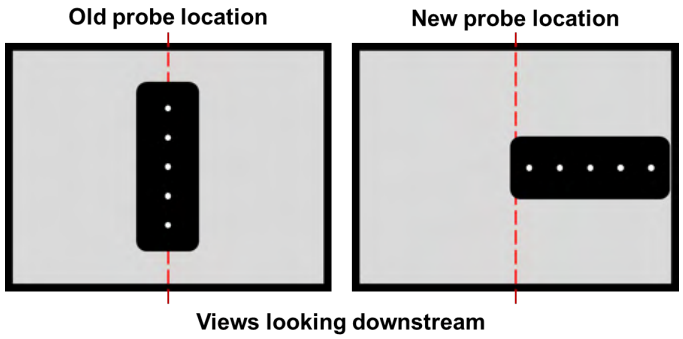

Figure 4. Emissions probe installation locations. The new probe location was used for all measurements reported herein.

Experiments with heated fuel began in March of 2021 after the fuel heater fabrication was completed. The emissions sampling and *OH** chemiluminescence imaging were performed at the conditions listed in Table 1. A range of fuel–air equivalence ratios were tested for three fuel temperatures at an inlet air pressure of 1.0 MPa. Additional measurements were taken at an inlet air pressure of 2.0 MPa at the highest fuel temperature to determine the effect of increased pressure on emissions. Because the fuel heater heats the pilot and main fuel circuits independently, the fuel temperature reported herein is a mass-flow-weighted average of the fuel temperature of each circuit. The inlet air temperature and the pressure drop across the injector were held constant for all conditions. Measured quantities of key species are shown in Figures 6–9. Combustion efficiency is defined according to Eq. 1, in which the emissions index (*EI*) is the quantity of a species in grams of the species per kilogram of fuel consumed, and H_c is the heating value of the fuel.

Table 1. Test conditions. The equivalence ratio was varied within the specified range for each set of conditions.

P_3 (MPa)	T_3 (K)	Overall φ	$T_{fuel,av}$ (K)	Pilot/Total (%)	$\dot{m}_{air}$ (kg/s)
1.00 ± 0.12	755 ± 17	0.37 – 0.50	373 ± 6	30.0 ± 1.0	0.585 ± 0.005
		0.37 – 0.47	473 ± 7		
		0.36 – 0.51	568 ± 3		
2.00 ± 0.06		0.33 – 0.47	584 ± 2		1.170 ± 0.012

$$\eta_b = \left[1.00 - 10.109\frac{EI_{CO}}{H_C} - \frac{EI_{UHC}}{1000}\right] \quad (1)$$

From the emissions results, several observations were made regarding pollutant formation in the combustor. As shown in Figure **5**(a), the combustion efficiency increased with an increase in fuel temperature, particularly at the lower equivalence ratios studied herein. Combustion efficiency was also higher at increased inlet air pressures, as shown in Figure **5**(b). Concomitant decreases in CO and unburnt hydrocarbons (UHC) with increasing fuel temperatures and pressures are shown in Figures 6 and 7, respectively. Another important result from the emissions testing is shown in Figure 8: nitrogen oxide (NO_x) production increased by 20%–30% with an increase in $T_{fuel,av}$ from 373 K to 473 K, and an additional increase of 10%–15% was observed for lower equivalence ratios when $T_{fuel,av}$ was increased again to 568 K. At equivalence ratios of approximately 0.43 and above, no conclusive change in NO_x was observed between $T_{fuel,av}$ = 473 K and $T_{fuel,av}$ = 568 K. The results in Figure 9 show that, for an increase in pressure at constant fuel temperature, the measured NO_x emissions index indicates a pressure dependence with an exponent between approximately 0.4 and 0.8. For all fuel temperatures at an inlet air pressure of 1.0 MPa, the ratio of NO to NO_x was nearly constant between fuel temperatures but varied strongly with the

equivalence ratio. Likewise, this ratio did not vary substantially with the increase in pressure but again varied strongly with the equivalence ratio. Detailed laser-based diagnostics are in progress to study the flow and flame features that led to these measured changes in pollutant emissions.

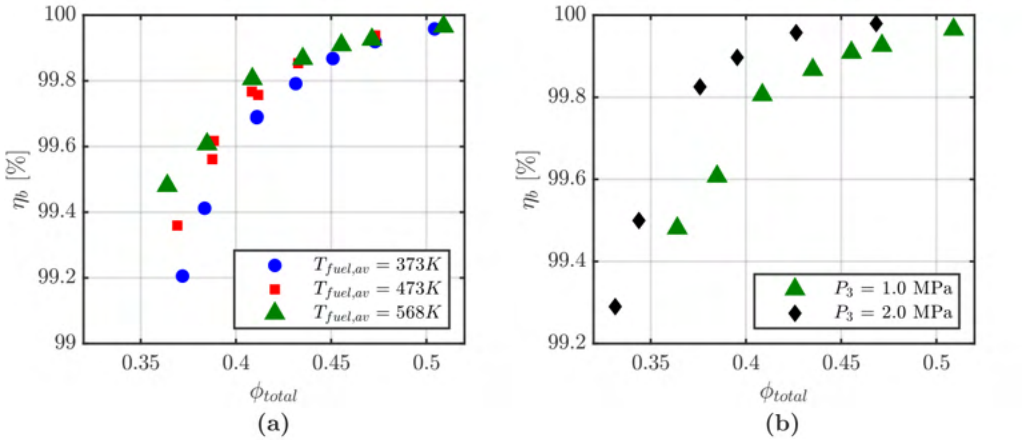

Figure 5. Combustion efficiency, measured at a range of equivalence ratios at (a) three different fuel temperatures with P_3 = 1.0 MPa and (b) two different inlet air pressures with $T_{fuel,av}$ = 573 K.

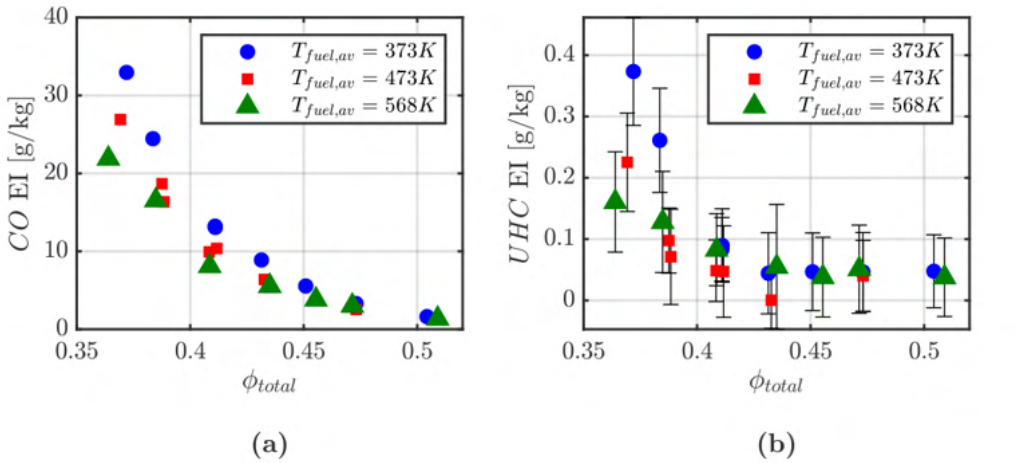

Figure 6. Carbon monoxide and unburnt hydrocarbon emissions, measured at a constant inlet air pressure of 1.0 MPa.

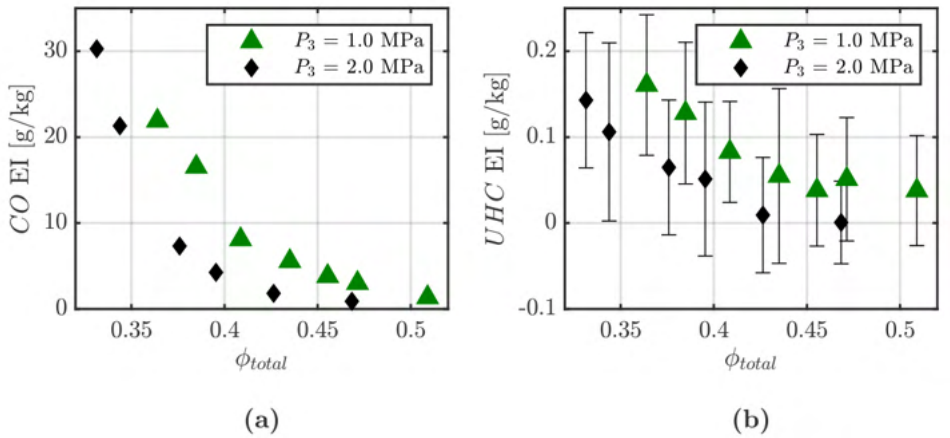

Figure 7. Carbon monoxide and unburnt hydrocarbon emissions, measured at a constant $T_{fuel,av}$ of 573 K.

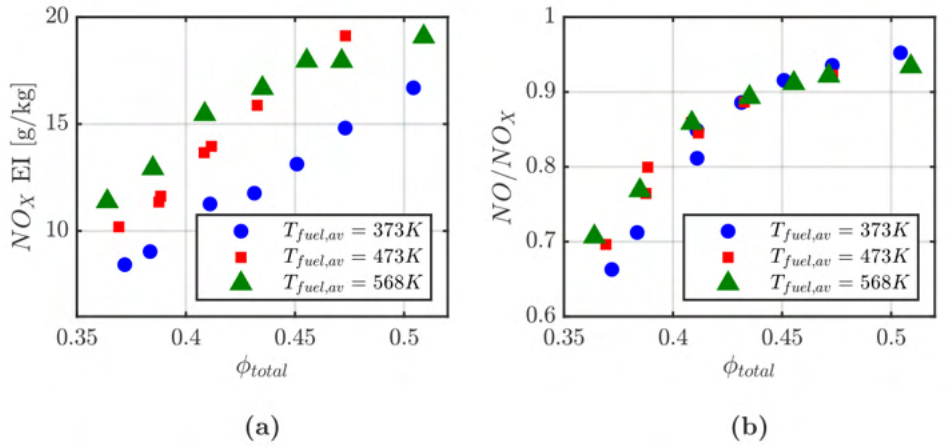

Figure 8. NO_x emissions, measured at a constant inlet air pressure of 1.0 MPa.

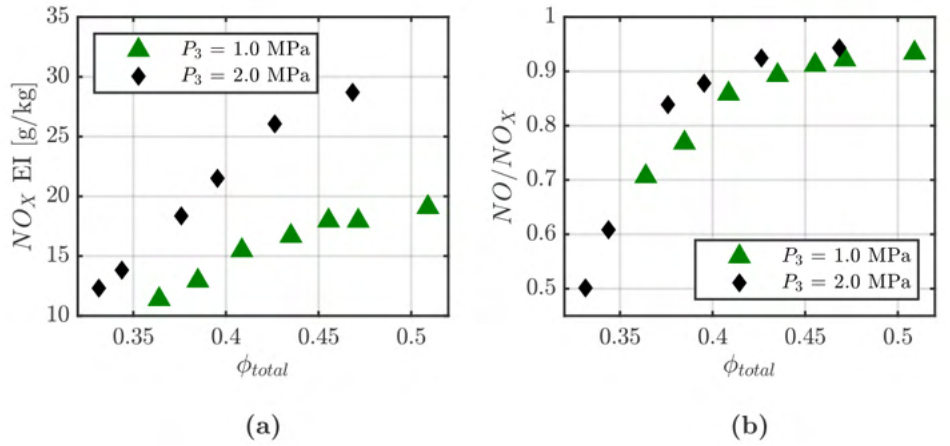

Figure 9. NO_x emissions, measured at a constant $T_{fuel,av}$ of 573 K.

The *OH** chemiluminescence images showed significant changes in the spatial distribution of flame luminosity when the fuel temperature and inlet air pressure were varied. Figures 10 and 11 illustrate the observed changes. When the fuel temperature was increased at a constant inlet air pressure of 1.0 MPa, the time-averaged flame grew appreciably longer, especially for the increase in $T_{fuel,av}$ from 373 K to 473 K. This finding is further clarified by the line plot in Figure 10, which shows the vertically summed intensity along each average flame. Analogous images showing the increase in pressure with constant fuel temperature of 573 K are presented in Figure 11, which show that the increased pressure led to a subtle increase in the presence of *OH** in the downstream portion of the flame. Using the region denoted by the white rectangle in Figure 11, the intensity was summed in the vertical direction to show how the flame changes in the region where the main reactants interact with the pilot flame. The results shown in Figure 12 indicate a small shift in the main flame toward the face of the injector in the region near x/D_j = 0.3 for cases with P_3 = 1.0 MPa as well as the lengthening effect seen in other figures. For the increase in inlet air pressure, no discernible change was observed in the near-injector portion of the flame in the selected area.

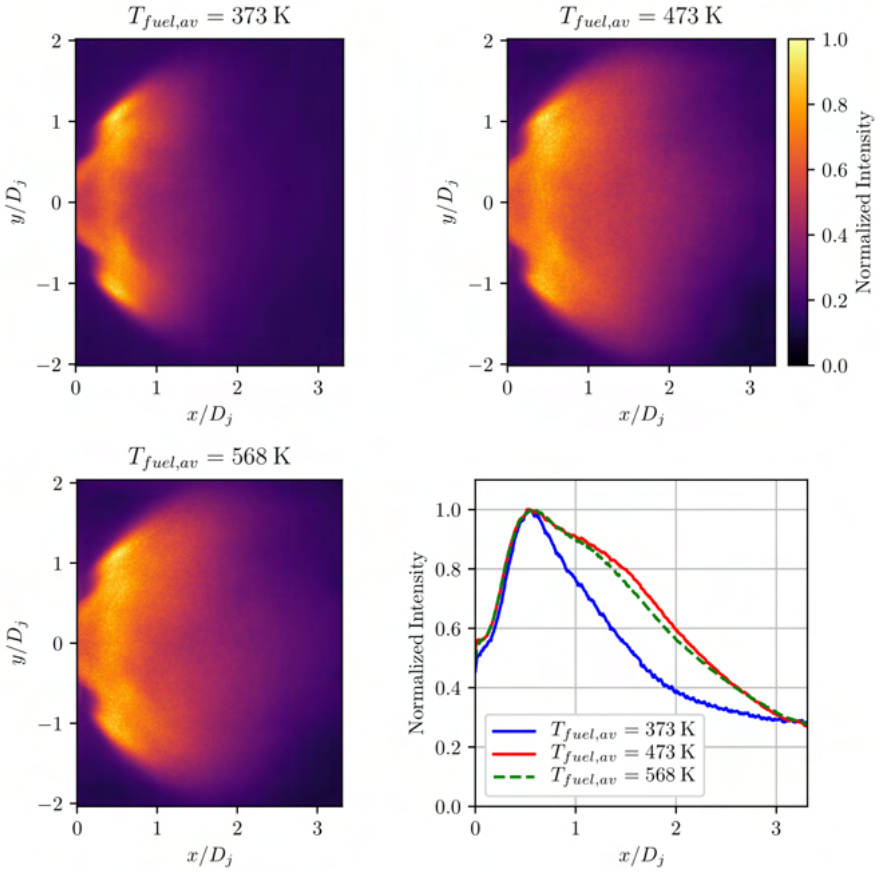

Figure 10. Variation in average flame luminosity with changes in $T_{fuel,av}$. The plot at the lower right shows the luminosity summed in the *y* direction as a function of x/D_j.

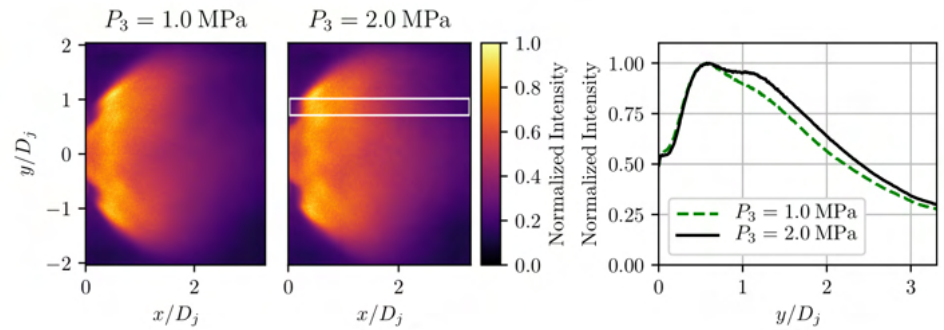

Figure 11. Variation in average flame luminosity with changes in P_3. The plot in the lower right shows the luminosity summed in the y direction as a function of x/D_j. The white rectangle on the right flame image corresponds to the area used for the plot in Figure 12.

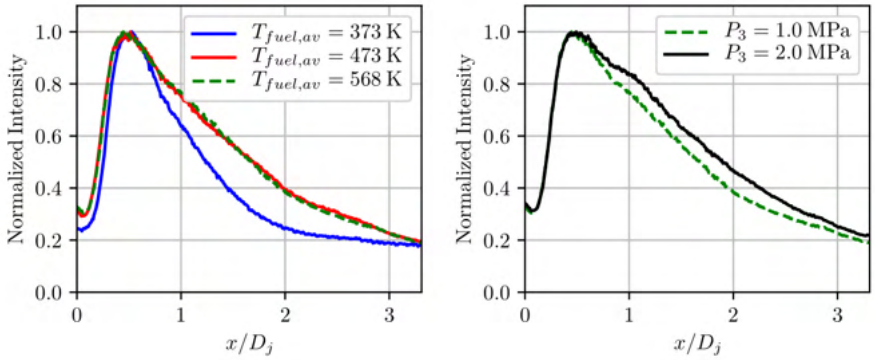

Figure 12. Variation in horizontally summed average flame luminosity in the region between $y/D_j = 0.7$ and $y/D_j = 1.0$, indicated with a white rectangle in Figure 11.

C. Stereoscopic PIV Measurements

After completing the parametric survey of operating conditions with emissions sampling in May of 2021, we transitioned to applying laser diagnostics to better understand how the flow and flame change relative to the observed emissions trends. We began with 10-kHz stereoscopic PIV (SPIV) with simultaneous 10-kHz *OH** chemiluminescence. SPIV enables all three components of velocity to be measured in a plane coincident with the vertical centerline of the combustor. The diagnostic configuration for this measurement is depicted in Figure 13. A dual-cavity, diode-pumped solid-state (DPSS) Nd:YAG-based laser provides pulse doublets of 532-nm light at 10 kHz with a pulse separation of 3.0 µs. The laser pulse separation was selected to optimize the particle displacement between slow-moving regions in the recirculation zones and high velocities in the reactant jets. Four cylindrical lenses form and collimate the laser sheet, which is then directed along the centerline of the combustor using a series of mirrors. The beam is focused such that the beam waist is located just below the measurement domain, and the resulting sheet thickness is less than 1 mm. The air is seeded with 200-nm zirconia (ZiO_2) particles with an independently controlled and metered air circuit. Two high-speed CMOS cameras (Phantom V2512) are used to capture the scattered light signal with a spatial resolution of 63 µm/pixel for the measurement field of view. The cameras are located on opposite sides of the rig, angled approximately 30° relative to the laser sheet. A 200-mm focal-length, $f/4.0$ lens is mounted to each camera with a Scheimpflug adapter, which ensures that the entire measurement domain is in focus. An ultra-steep bandpass filter centered at 532 nm with 3-nm full width at half maximum is used to isolate the signal from background flame luminosity, and an additional wide-band bandpass filter is used to block the remaining wavelengths of light within the CMOS sensor sensitivity range. The camera setup for the *OH** chemiluminescence measurement is the same as that for the above emissions results, but with a different CMOS camera that limits the repetition rate to 10 kHz for the given image resolution.

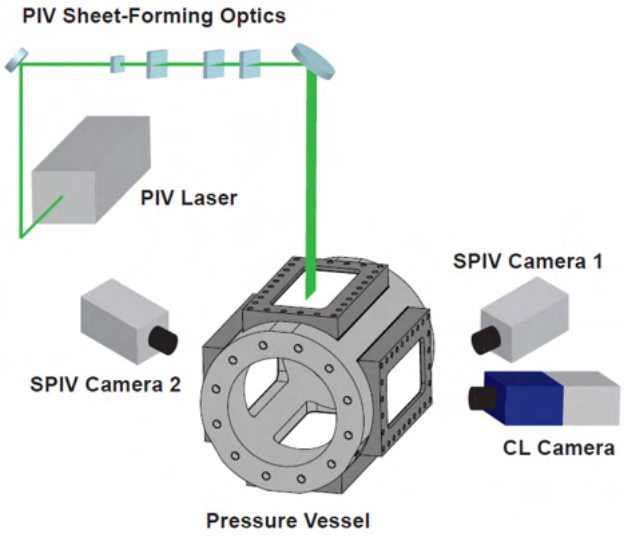

Figure 13. Schematic diagram of the stereo PIV measurement system.

Multiple difficulties arise in performing PIV measurements in high-pressure reacting flow-fields, especially those using liquid fuels. Mie scattering off unevaporated fuel droplets can saturate local regions of the acquired images, thus hiding any seed particles that are present. Large density gradients in the flow-field can lead to difficulties in supplying a uniform seed density throughout the measurement domain, and the wide range of velocities present requires a measurement with high dynamic range. Glare from the scattered laser light off surfaces in the combustor can also reduce the signal-to-noise ratio, particularly as seed particles are deposited on the combustor windows. In the present experiment, PIV data were acquired during 5- to 10-second seed flows, which could occur approximately 10 times on a given test day before window fouling from seed particles began to affect the measurement quality. For all fuel temperatures tested, most of the liquid fuel was evaporated before entering the measurement domain, and primarily small droplets remained that could not be distinguished from the seed particles.

Many of the above issues can be addressed either in the experimental configuration or during data processing. The SPIV image processing and vector calculation were performed using LaVision DaVis 8.4. Background intensity was removed by subtraction of the minimum intensity using a seven-image sliding window, then subtracting a sliding average over a window of 9 × 9 pixels. Intensities were then normalized using the minimum and maximum intensity in a window of 7 × 7 pixels. Before performing the vector calculation, all images were spatially calibrated with the DaVis self-calibration feature. The vector calculation was performed using multiple passes with decreasing interrogation window size, with a final interrogation window of 32 × 32 pixels and 75% overlap. Spurious vectors were removed after the vector calculation using a universal outlier detection median filter. The resulting vector fields yielded a high percentage of valid vectors, as shown in Figure 14. For most locations in the measurement domain, a valid vector was present for more than 90% of the time series. Issues with glare on the burner face and the large out-of-plane velocity component in the main reactant flow in the top-left and bottom-left corners reduce the vector yield in those locations.

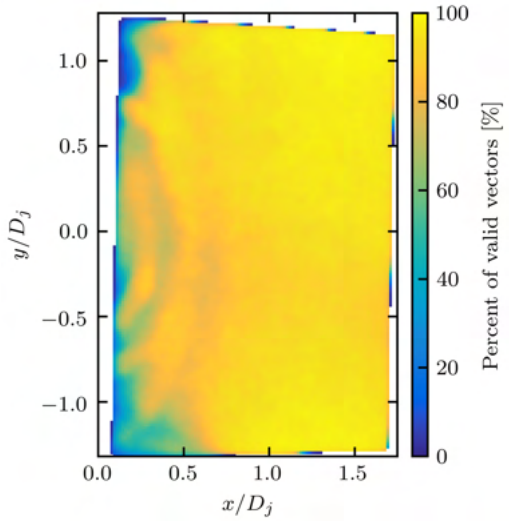

Figure 14. Percentage of valid vectors at each location in the measurement domain for a typical test.

Multiple techniques exist to fill in missing data in PIV measurements. One option involves spatial interpolation of an instantaneous vector field to replace gaps in the data based on the velocity at surrounding points. This procedure can be performed simply by iteratively taking the average of surrounding points with empty spaces until all gaps are removed. More advanced spatial interpolation techniques, such as Kriging interpolation, can yield better results but have the drawback of increased computational cost. For this work, we used gappy proper orthogonal decomposition (GPOD) to fill in the gaps in the data with both spatial and temporal information from the measured vector fields. This method performed POD iteratively, using an increasing number of modes to reconstruct the velocity fields, until the error calculated based on artificial gaps in the data reached a minimum. A median filter was applied to the reconstruction at the end of each iteration to determine whether to use the newly predicted value of velocity as the initial guess for the next iteration. This technique has been shown to yield reconstruction errors as good as or better than those with Kriging interpolation, with a much lower computational cost. For each condition tested, 2,000 vector fields were generated using DaVis and filled with GPOD. GPOD was performed on each component of velocity independently, and each component generally required between 800 and 1,000 modes to reconstruct the velocity field before the minimum error was achieved. The results from this process are illustrated in Figure 15 with a sample velocity field. The original axial velocity field with gaps in the data is shown in Figure 15(a), and a smaller region of the velocity field is highlighted in Figure 15(b). Figure 15(c) shows the resulting velocity field after the missing data were filled with GPOD, thus yielding reasonable results for the missing velocity at all points.

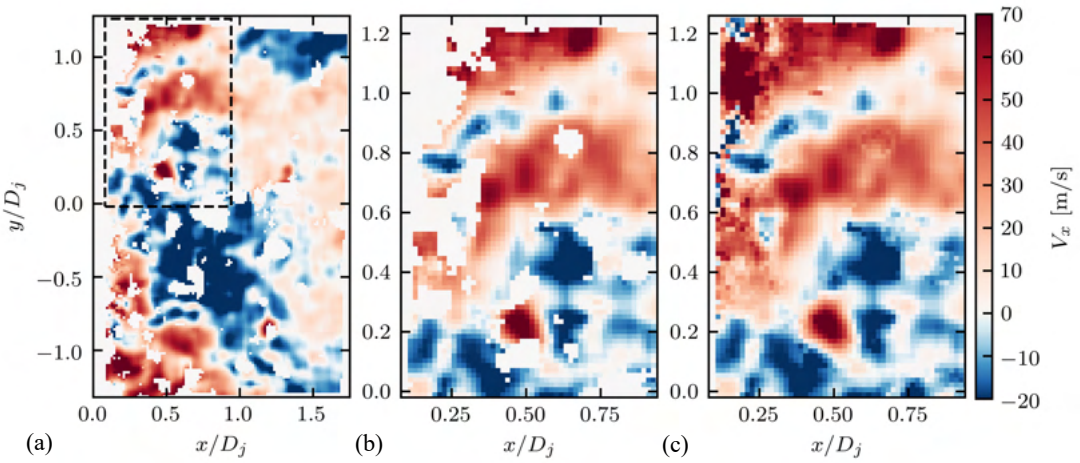

Figure 15. (a) Sample original axial velocity field. (b) Original axial velocity field in the region denoted by the dashed box in (a). (c) Original velocity field from (b), with missing data filled in with MF-GPOD.

To date, high-quality SPIV data have been recorded at 12 conditions at an inlet air pressure of 1.0 MPa and at four conditions at an inlet air pressure of 2.0 MPa. A total of 2,000 vector fields have been calculated at each condition, and the missing vectors have been filled in with GPOD. Detailed analysis of this data is ongoing and should be completed early in the upcoming year of the project. Figures 16–18 display some initial results from this work. The average magnitude of the velocity over 2,000 vector fields is depicted in Figure 16, with the important flow features labeled. Annotation 1 is the high-velocity region corresponding to the main reactant flow, and annotation 2 is the high-velocity region corresponding to the pilot reactant flow. Because these features are axisymmetric, they are also present in the bottom half of the mean velocity field. Annotation 3 corresponds to the inner recirculation zone (IRZ) that forms downstream of a bluff-body feature on the injector, between the two high-velocity regions. Annotation 4 is the central recirculation zone (CRZ), a low-velocity region that provides high-temperature product gases to the flame root, thereby sustaining stable combustion. Unlike the pilot and main reactant jets, this recirculation zone is not symmetric across the horizontal centerline, probably because of the rectangular shape of the combustor cross-section.

To compare the mean velocity fields over the range of conditions tested, iso-contours defining the border between different features in the flow-field were determined. The mean axial velocity field is shown in Figure 17(a) for the same case shown in Figure 16. The black lines correspond to iso-contours where the axial velocity is equal to 5 m/s, as determined using a marching squares algorithm. The iso-contours were set to 5 m/s, because this value allowed the lines to follow the shear layer between the pilot reactant jet and CRZ for both the top and bottom halves of the flow-field, and biased the lines toward regions of higher shear. An iso-contour also surrounds the region of positive axial velocity along the centerline of the combustor that occurs inside the CRZ. These iso-contours of V_x = 5 m/s were determined in a similar manner for the mean flow-fields for all conditions tested. Figure 17(b) shows three iso-contours on the same plot corresponding to conditions at three different fuel temperatures with approximately the same equivalence ratio and inlet air pressure. At the upstream portion of the flow-field, near the injector, no clear difference is present between the iso-contour locations, but the lines begin to diverge further downstream. The circled region highlights the area where the differences are most evident over all conditions tested. This region coincides with the interaction between the pilot and main reactant jets. As the fuel temperature rises, the iso-contours move downstream.

The iso-contours generated from all 16 cases of PIV data are compared in Figure 18. A single value that defines the location of each iso-contour was determined by taking the average axial location of the part of the iso-contours within the circled region in Figure 17(b). The minimum value of the average iso-contour axial location in each plot in Figure 18 was subtracted from each point to give the relative positions of the iso-contours. As shown in Figure 18(a) the iso-contours move downstream both as the fuel temperature rises and as the equivalence ratio is increased. Additionally, similar to the changes in measured NO_x during the emissions sampling, the change in position from $T_{fuel,av}$ of 367 K to 486 K is greater than the change from 486 K to 577 K. This downstream shift in the location of the iso-contours may correspond to the increased *OH** chemiluminescence intensity present in the downstream region as the fuel temperature is increased, and the planned *OH* PLIF measurements will help clarify the observed changes. As the inlet air pressure is increased from 1.0 MPa to 2.0 MPa, no

clear shift occurs in the iso-contour location for a given equivalence ratio and fuel temperature, as shown in Figure 18(b). This result is expected, because the injector pressure drop is maintained as the pressure rises.

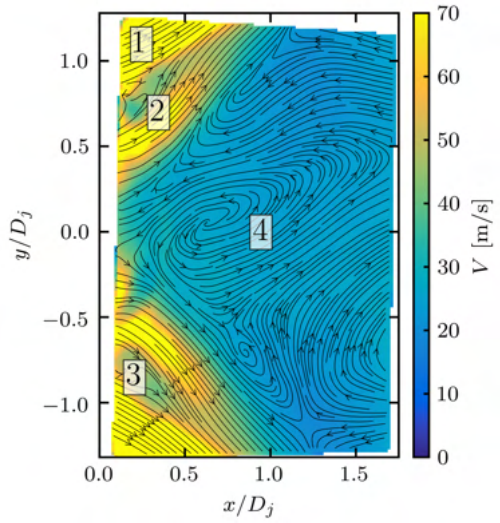

Figure 16. Mean velocity field with streamlines overlaid for P_3 = 1.0 MPa, $T_{fuel,av}$ = 367 K, and ϕ = 0.36.

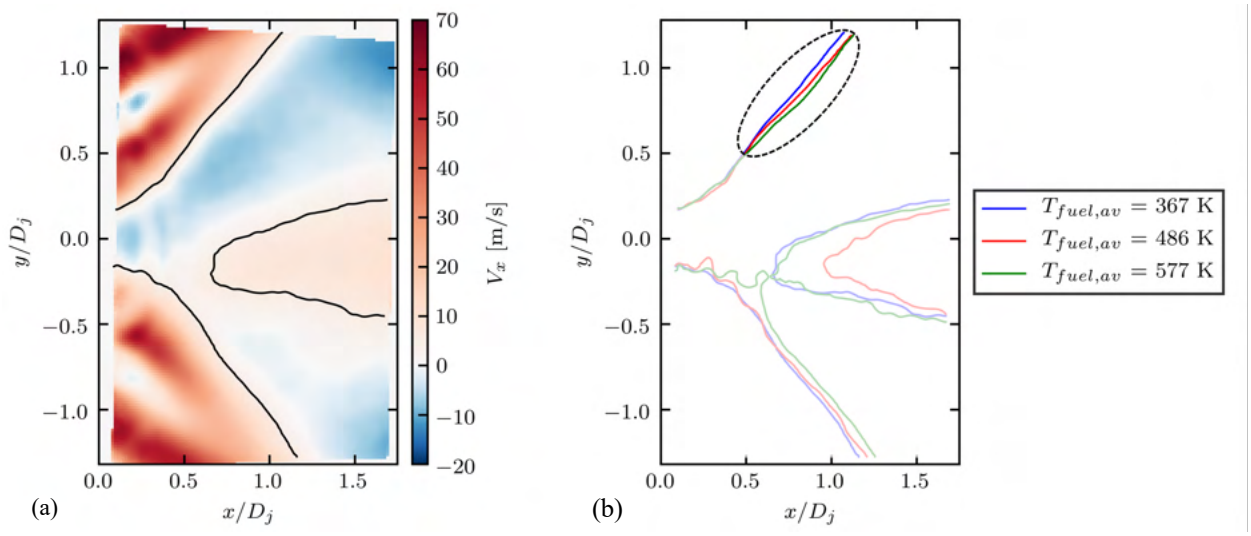

Figure 17. (a) Mean axial velocity field for P_3 = 1.0 MPa, $T_{fuel,av}$ = 367 K, and ϕ = 0.36 with iso-contours of mean V_x = 5 m/s denoted by black lines. (b) Iso-contours of mean of V_x = 5 m/s for three fuel temperature conditions with P_3 = 1.0 MPa and ϕ = 0.36. The circle highlights the region where the largest changes between conditions occur.

Further analysis of the acquired PIV data is ongoing, and includes extending the analysis using iso-contours to instantaneous flow-fields in addition to the mean flow-fields. The time series of iso-contours can be used to condition various turbulent flow parameters, such as shear and vorticity. Averaging the data only at locations and times when an iso-contour is present can help elucidate some of the differences between the average flow-fields.

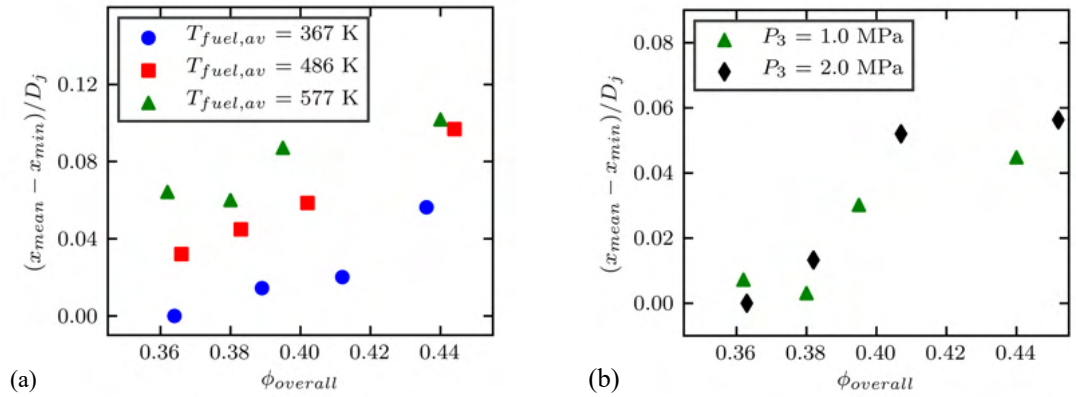

Figure 18. Mean axial location of the portion of the stagnation line in the circled region in Figure 17(b) for all conditions tested. Values are plotted relative to the minimum value of the mean axial stagnation line location for (a) constant inlet air pressure of 1.0 MPa and (b) constant $T_{fuel,av}$ = 577 K.

D. *OH* PLIF Imaging

OH PLIF imaging was successfully demonstrated in August 2021 at 10 Hz, allowing a region approximately 40 mm in width to be captured in each frame. For this experiment, a 532-nm pump laser beam was directed into a dye laser filled with rhodamine 590 dye. The output of the dye laser was tuned to an electronic transition in the Q branch of the *OH* molecule near 283 nm, thus resulting in the short-lived fluorescence (for several nanoseconds) of a fraction of these molecules as they relaxed back to their ground electronic state. With each laser shot, this fluorescence was captured by a CMOS camera (Phantom v2512) with an -sensitive intensifier (Lambert HiCATT). Locations with high gradients in *OH* (particularly in the upstream part of an image), are indicative of the reaction front (or "flame surface"), where the highest levels of heat release occur.

Because of variations in intensity along the laser sheet and absorption effects, *OH* PLIF images cannot be treated as quantitative maps of *OH* concentration. Instead, these images must be processed to generate useful statistics. By converting the images into binarized maps showing which regions contain *OH*, quantitative information about the flame can be obtained. To do so, a robust edge detection method is required. For this project, a method known as semantic segmentation is used to separate each *OH* PLIF image into regions of signal and background. Semantic segmentation involves training a convolutional neural network to recognize these regions by learning from human-labeled images. To date, 176 images have been manually labeled, of which 156 were used as training images, and 20 were used as validation images. From this dataset, the semantic segmentation model has exceeded, in accuracy, most of the thresholding methods typically used by our group and others. Two representative images and their detected edges are shown in Figure 19. Further refinement of the edge detection model is in progress, and the model will be applied to future *OH* PLIF images taken for this project. At present, too few *OH* PLIF experiments have been performed to draw meaningful conclusions regarding differences in the flame between conditions, but sufficient results are expected early in the next year of the project.

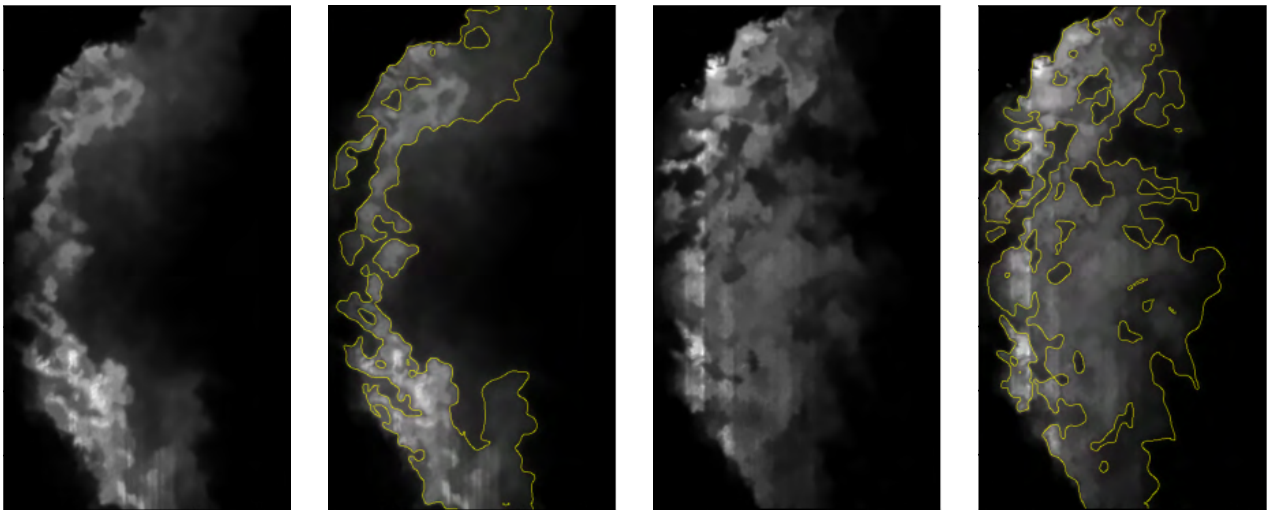

Figure 19. Two representative *OH* PLIF images with detected edges from the semantic segmentation model shown in yellow on duplicate images.

Publications

Published conference proceedings

McDonald, C. T., Philo, J. J., Shahin, T. T., Gejji, R. M., Slabaugh, C. D., & Lucht, R. P. (2021). Effect of fuel temperature on emissions and structure of a swirl-stabilized flame [Presentation]. AIAA Propulsion and Energy 2021 Forum, Virtual Meeting. Paper Number AIAA 2021-3480.

Outreach Efforts

None

Awards

None

Student Involvement

Three PhD graduate students are working on the project. The project provides outstanding research experiences for the graduate students, including the design of system components for, and the operation of, a sophisticated aviation gas turbine combustion test rig, as well as application of advanced laser diagnostic methods for measurements in this test rig. As noted above, the graduate students have been responsible for the design of system components, such as the fuel heating system, and for executing test operations.

Plans for Next Period

During the next year of the project, we plan to perform more experiments with heated fuel with various diagnostic techniques. Multi-scale PIV, *OH* PLIF, fuel PLIF, and coherent anti-Stokes Raman scattering (CARS) measurements will be performed to further characterize the flow-fields at the range of operating conditions considered for the emissions measurements.

A. Multi-scale PIV Measurements

We will perform multi-scale PIV to simultaneously measure the in-plane components of velocity over the majority of the flame at 10 kHz and in a more localized area at 100 kHz. Figure 20 shows the expected field of view (FOV) for each of these measurement regions. The 10 kHz 2D2C PIV will have the same spatial resolution as the previous 10-kHz stereo PIV measurements, but the 100-kHz 2D2C PIV will be configured to have a spatial resolution with twice as many pixels per millimeter. The improved spatial and temporal resolution of the 100-kHz PIV will enable measurements of small-scale flow dynamics, such as vortex shedding in the shear layer between the pilot and CRZ, that are missed by the 10-kHz PIV. The 10-

kHz measurement will be performed with the same laser as that in the 10-kHz stereo PIV, which provides pulse doublets of 532-nm laser radiation. For the 100-kHz measurements, an Nd:YAG based pulse-burst laser (PBL) along with an optical parametric oscillator (OPO) will be used to provide laser emission tuned to 566 nm for burst durations of 10 ms. Since PIV is an elastic scattering process, the use of two different laser wavelengths is necessary to distinguish the scattering signals from the different laser pulses. Separate high-speed, CMOS cameras with the appropriate optical filters will be used for the two measurements. Extending the standard PIV measurement to this multi-scale configuration will make it possible to resolve how the increase in fuel temperature affects the interactions between flow dynamics over a wide range of scales.

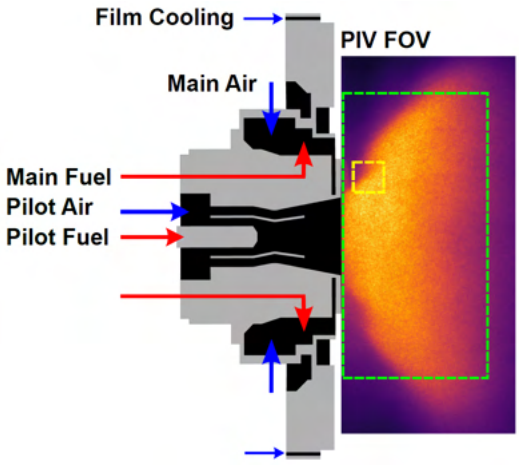

Figure 20. Schematic of multi-scale PIV showing expected fields-of-view for the 10-kHz measurement (green box) and the 100-kHz measurement (yellow box) overlaid on a mean *OH** CL emission field at P_3 = 1.0 MPa and ϕ = 0.36.

B. *OH* PLIF Imaging and Emissions Measurements

We will continue taking *OH* PLIF images while repeating some points from our emissions dataset with a new emissions sampling probe. Because of concerns regarding the potential of unchoked holes to create nonuniform sampling between holes in the current probe, a new emissions probe was designed and is currently being procured. The new design, shown in Figure 21, features a Hastelloy X body with a yttrium-stabilized zirconia thermal barrier coating and internal water cooling passages to ensure survivability. The probe's discrete sample passages enable sampling of species profiles across the exhaust channel, which will not be performed as part of this experiment but may be used for future work.

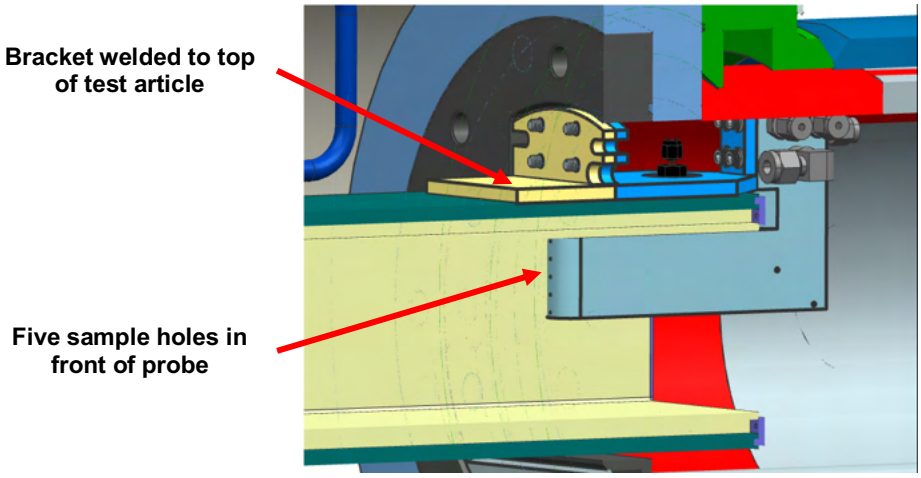

Figure 21. CAD rendering of the new emissions probe design.

Additional *OH* PLIF images will be recorded at a down-selected range of equivalence ratios and fuel temperatures similar to those chosen for the stereoscopic PIV measurements, and emissions measurements will be recorded simultaneously. This experiment will create a dataset showing the locations of reaction zones for each condition with the associated changes in emissions. Image analysis will be performed to draw conclusions regarding how the changing reaction zones may affect pollutant production by the flame.

C. Fuel PLIF Imaging

By adding a small percentage of Jet A fuel to our current Fischer–Tropsch fuel, we will raise the aromatic content of the fuel mixture to a level that enables PLIF imaging of the fuel spray from the injector. The 10-Hz pump laser used for *OH* PLIF imaging will also be used for fuel PLIF. By capturing fuel fluorescence in the near-injector region, we will be able to detect changes in the fuel spray pattern that occur with changes in operating conditions, including changes in the fuel temperature. These images will be used in concert with the *OH* PLIF images to provide a more comprehensive understanding of the effects of fuel temperature on the combustion process at the range of equivalence ratios and inlet air pressures considered.

D. Coherent Anti-Stokes Raman Scattering (CARS) Measurements

CARS, a laser-based technique for measuring temperature and species concentration in gases, will be used to measure the temperature in the flame zone of the COMRAD test rig by targeting N_2 molecules. Because fuel heating is expected to change the temperature field within the flame zone, CARS measurements are an important means of characterizing the effect of heated fuel on the flame. The local temperature throughout the flame strongly affects the rates of many combustion reactions, including the formation of nitric oxide. Thus, the CARS measurements will help us understand how fuel heating leads to the measured changes in emissions.

Project 068 Combustor Wall Cooling with Dirt Mitigation

The Pennsylvania State University

Project Lead Investigator

Karen A. Thole
Distinguished Professor
Department of Mechanical Engineering
The Pennsylvania State University
136 Reber Building
University Park, PA 16802-4400
(814) 865-2519
kat18@psu.edu

University Participants

The Pennsylvania State University

- PI(s): Dr. Karen Thole and Dr. Stephen Lynch
- FAA Award Number: 13-C-AJFE-PSU-057
- Period of Performance: October 1, 2020 to September 31, 2021
- Tasks:
  1. Manufacturing and testing of combustor liner cooling concepts with small coupons
  2. Testing of scaled models of optimal cooling concepts
  3. Facility planning for 1× scale combustor simulator

Project Funding Level

FAA funding to-date totals $150,000. Matching funds of $150,000 were provided by Pratt & Whitney.

Investigation Team

Name	Affiliation	Role	Tasks
Distinguished Professor Karen A. Thole	The Pennsylvania State University	PI	Management, reporting, and oversight of all technical tasks
Associate Professor Stephen Lynch	The Pennsylvania State University	Co-PI	Management, reporting, and oversight of Tasks 1–3
Scott Fishbone	The Pennsylvania State University	Project Manager	Tasks 1–3
Brandon Fallon	The Pennsylvania State University	Graduate Student	Task 1
Cynthia Letting	The Pennsylvania State University	Graduate Student	Tasks 1 and 2
Sarah Fox	The Pennsylvania State University	Undergraduate Student	Task 1

Project Overview

A critical issue related to the operation of a gas turbine in today's world is the ingestion of dirt and other fine particles, that can block the cooling holes and passages required for effectively cooling the walls of the combustion chamber. Because of the growing need to fly in dirty environments, the criticality of operations in dirty environments is increasing. Modern gas turbine engines typically use a double-walled combustor liner with impingement and effusion cooling plates, whereby impingement cooling enhances the backside internal cooling, and effusion cooling creates a protective film of coolant along the external liner walls. Dirt accumulation on the internal and external surfaces severely diminishes the heat-transfer capability of these cooling designs. This study aims to initially investigate practical designs for reduced dirt accumulation at representative temperature conditions, then explore how the designs are insensitive through detailed flow and heat-transfer measurements on a scaled geometry.

Task 1 - Manufacturing and Testing of Liner Cooling Concepts

The Pennsylvania State University

Objective

The goal of this research is to produce an effective cooling design for combustor walls that is insensitive to dirt accumulation at existing or lower coolant flow rates. Various parameters, such as dirt deposition, flow behavior, and heat-transfer effectiveness, will be investigated and quantified to compare the efficiency of candidate designs and improve understanding of the reasons underlying dirt sensitivity and deposition behavior.

Research Approach

Background

The focus of the project is on the impacts of the ingestion of dirt and other fine particulate matter in gas turbine engines. These particles are known to block the cooling holes and passages needed to effectively cool the combustion chamber walls. Gas turbine engines often use double-walled combustor liners comprised of impingement and effusion cooling plates, as shown in Figure 1A. The impingement plate enhances backside internal cooling, and the effusion plate creates a protective film of coolant along the external liner walls. As particulate matter accumulates on these plates, the heat-transfer performance severely decreases and ultimately leads to component failure.

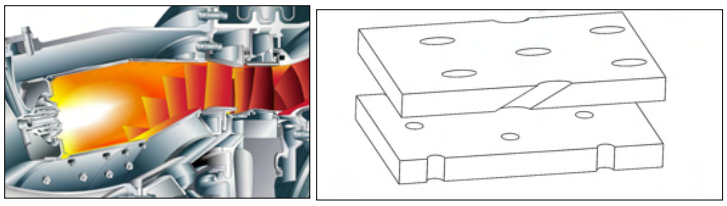

Figure 1A. Schematic of double-walled combustor liner geometry.

Dirt Simulation Test Facility

In the past year, a test facility was developed and refined to incorporate both slug and continuous feeds for the introduction of dirt, to account for different ingestion possibilities. In addition, a vertical test facility (Figure 1B) was developed to replace a horizontal facility. In a vertical setup, gravity acts in parallel to the flow direction, thus promoting dirt movement toward the coupon and avoiding dirt sticking to the pipe walls.

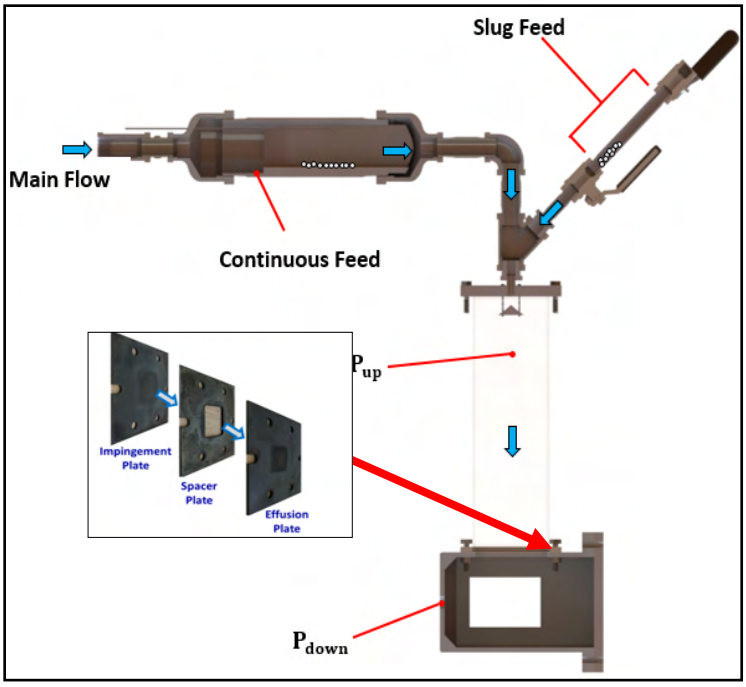

Figure 1B. Dirt testing facility and an illustration of the testing coupon (inset).

For the slug feed method shown in Figure 1B, dirt is introduced to the test facility in intervals. The dirt is sequentially placed inside a separate chamber attached to the main flow and pressurized slightly above the mainstream pressure. When opened, the slug is injected into the freestream. In continuous feed tests, also shown in Figure 1B, dirt is introduced through a constant stream by injecting air through a capillary tube directed at a plate containing a line of dirt. A stepper motor is attached to the capillary tube, thus allowing it to traverse the length of the plate and effectively blowing the dirt into the mainstream. A plenum is attached just below the slug feed entrance. To disperse the inlet air, a splash plate is placed just downstream of the pipe at the plenum entrance. The coupons, shown in the inset of Figure 1A, consist of an effusion plate, spacer plate, and impingement plate stacked together. The impingement plate is placed at the plenum outlet and is followed by the spacer and effusion plates.

The dirt particles used in these studies are AFRL-05 with a size distribution as shown in Figure 2. The mean diameter of the particles is 1.2 μm. During the testing, two requirements are key to accurately quantify the necessary metrics to compare the test coupons: (i) testing repeatability and (ii) tracking of the dirt to accurately account for the amount of dirt reaching the coupon. The second requirement for tracking is important because much of the dirt that enters the testing facility can adhere to the walls, given the nature of the particles. However, this dirt must then be removed from the mass considered to pass through the coupons. Figures 3a and 3b show the experimental repeatability as well our ability to track the dirt. The repeatability indicates that performing three tests and then averaging the results leads to a repeatability of the capture efficiency (η_c) of 5.6% for slug flow and 8.1% for continuous flow. The tracking results indicate that we are able to account for between 80% and 90% of the dirt, and therefore we can confidently use our capture efficiency value as a representative metric, as further described in the next section.

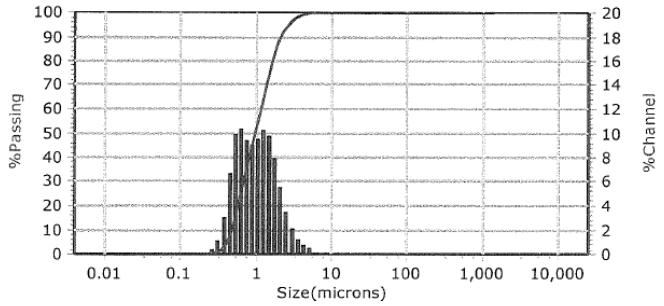

Figure 2. Particle size distribution of the AFRL-05 dirt used in testing.

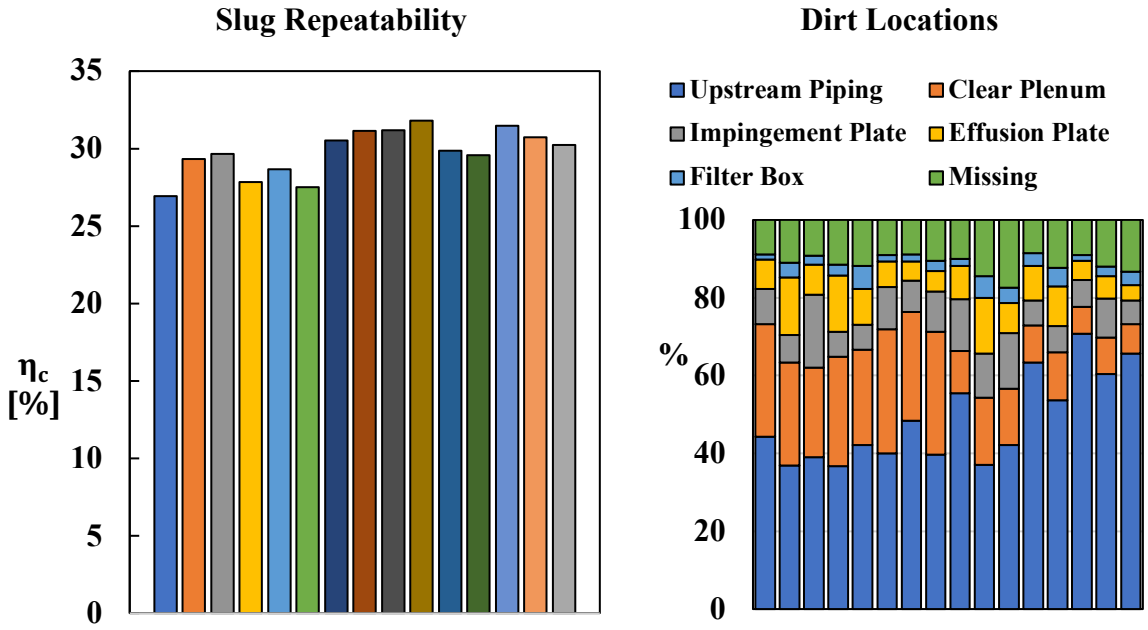

Figure 3. Repeatability (left) and dirt tracking (right) for a single coupon.

Double-Wall Test Coupon Descriptions

During the past year, many coupons were evaluated, as discussed in the next section of this report. The specific geometric details for each of the coupons are shown in Table 1, and further illustrations of the geometries are shown in Figure 4. Excluding pin-cone aligned (PCA)-613S, all plates contained 55 holes in a 5 × 11 array representing a portion of an actual combustor liner. The impingement plate paired with PCA-613S used 24 holes to match the total flow area to the 0.0405-inch jet diameter impingement plates. Of note, the total flow area, A_f, remained constant for all effusion plates. All impingement and effusion plates were printed on a FormLabs Form 3 SLA 3D printer with high-temperature resin.

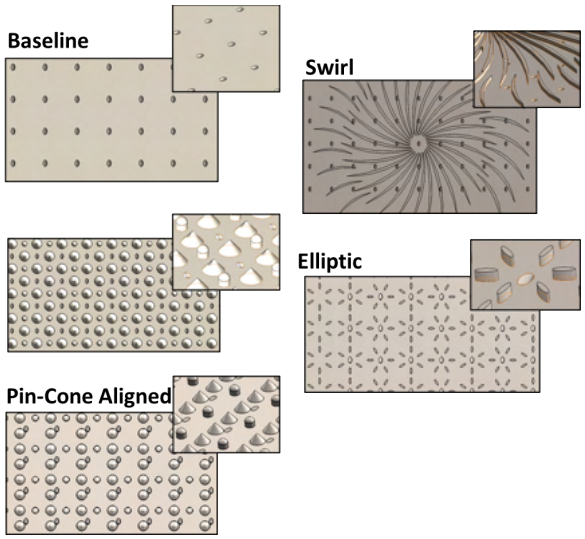

Figure 4. Illustrations of the double-wall combustor liner concepts, as described in Table 1.

Table 1. Test geometry dimensions.

Name	Impingement Plate				Effusion Plate				
	D (in)	x/D	S/D	A_f (in²)	Dh (in)	x/Dh	S/Dh	A_f (in²)	Layout
Baseline-405	0.0405	6.17	6.17	0.0709	0.00309	5	5	0.259	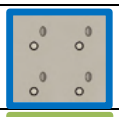
Swirl-405	0.0405	6.17	6.17	0.0709	0.00309	5	5	0.259	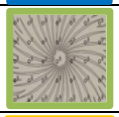
Ellipse-405	0.0405	6.17	6.17	0.0709	0.00309	5	5	0.259	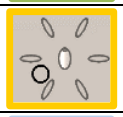
Pin-Cone-405	0.0405	6.17	6.17	0.0709	0.00309	5	5	0.259	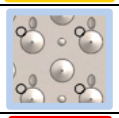
Pin-Cone Aligned-405	0.0405	6.17	6.17	0.0709	0.00309	5	5	0.259	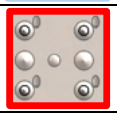
Pin-Cone Aligned-613S	0.0613	4.07	4.07	0.0709	0.00309	5	5	0.259	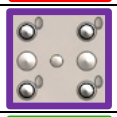
Pin-Cone-625	0.0625	4	4	0.169	0.00309	5	5	0.259	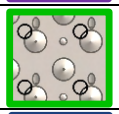
Pin-Cone Aligned-625	0.0625	4	4	0.169	0.00309	5	5	0.259	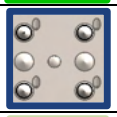
Pin-Cone Aligned-845	0.0845	2.96	2.96	0.308	0.00309	5	5	0.259	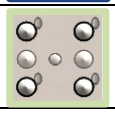

Coupon Metrics and Analyses

For comparison of each of the coupons in a similar manner, a fixed pressure ratio (PR) of 1.045 was used with 2 grams of dirt. For each test, the flow rate, PR, and dirt captured were measured. These measurements were then used to calculate the capture efficiency (η_c), flow parameter (FP), and jet Reynolds number (Re) for the impingement and effusion plates. Definitions for FP, η_c, and jet Re are shown below. The η_c is determined by subtraction of the dirt mass on the effusion plate surface from the total mass of dirt successfully passing through the coupon. Upstream dirt located on the first impingement plate, piping, and plenum is not included in the η_c, as previously described.

$$\mathrm{FP} = \frac{4\dot{m}\sqrt{T_{oc}R}}{\pi P_{up} N D^2} \tag{1}$$

$$\eta_c = \frac{M_{eff} - M_{cl}}{D_{int}} \times 100 \tag{2}$$

$$\mathrm{Re} = \frac{4\dot{m}}{N\pi D\mu} \tag{3}$$

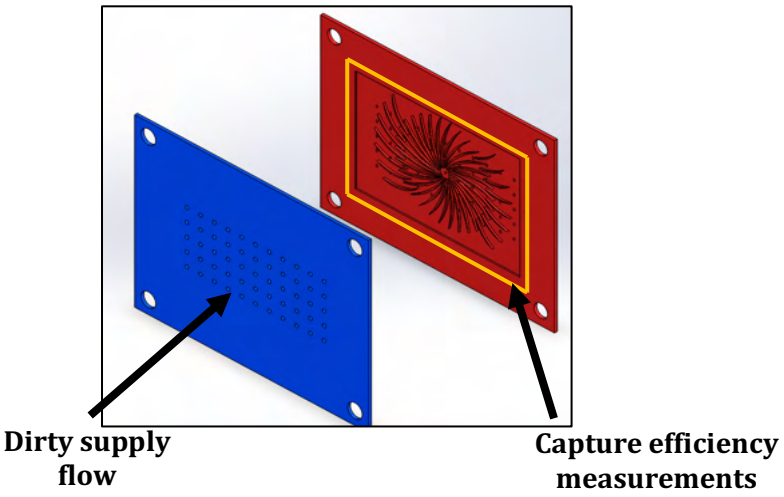

Figure 5. Dirt deposition location (orange) relative to the coupon assembly.

Figure 5 demonstrates locations where dirt was evaluated relative to the coupon assembly. The dirt passes through the impingement plate (blue) and impinges on the cold side of the effusion plate (red) not in contact with the hot combustion gases.

Computational Simulations of Dirt Trajectories

With a commercially available computational fluid dynamics (CFD) code Star CCM+, pre-test prediction methods were used to evaluate flow patterns and particle deposition behavior within the double-walled combustor liner. Simulations were performed on previously tested coupons to benchmark flow and deposition behavior. Development of the simulations required contriving a mesh to accurately define the coupon geometry while maintaining grid independence and determining the boundary conditions and physics models required to model previous experimental conditions. For achieving the mesh shown in Figure 6, an iterative approach was used. The parameters investigated were the cell count, base size, and cell shape. Among the shapes, the polyhedral mesh was found to be approximately 0.4% more accurate than trimmer cells, as compared with experimentally determined Re values through the impingement jets. However, the computational time and storage space was markedly increased. The polyhedral mesh used a base cell size of 1.5×10^{-4} m, whereas the trimmer successfully reached a base size of 8.0×10^{-5} m, thereby increasing the cell count from 7.9 million to 11.9 million. The trimmer-based mesh was selected for the CFD predictions because it was less computationally expensive, required less storage space, and had less than a 0.5% difference with respect to the polyhedral mesh.

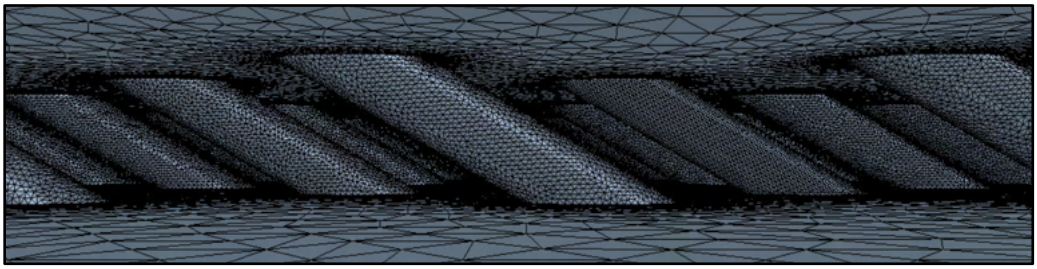

Figure 6. Illustration of a CFD mesh for the effusion holes.

After the geometry had a viable mesh, boundary conditions were required to perform simulations. In previous experiments, the upstream and downstream pressure were controlled and held at a constant back flow margin (BFM). To model flow through the coupon, the simulation was set up such that the coupon was placed inside a wind tunnel matching the coupon dimensions. A stagnation inlet boundary condition was applied 10 hole diameters upstream of the coupon, and a pressure outlet boundary condition was applied 10 hole diameters downstream of the coupon.

Double-Wall Test Results

Figure 7 displays post-test images of the effusion plates, comparing dirt deposition on the baseline and pin-cone aligned (PCA) geometries for a slug feed test with 2 grams of dirt at a PR of 1.045. Each configuration qualitatively shows how surface obstructions on the effusion plate and impingement jet diameters can change the resulting dirt deposition behavior. The baseline effusion plate showed dirt deposits where the impingement jet impinged on the effusion plates surface, creating a dirt "peak" that quickly tapered off in the radial direction. For PCA coupons, the dirt peak height increased as the jet diameter increased. Of note, PCA-613S (Figure 7E) used 24 holes concentrated at the center of the coupon, thus resulting in higher concentrations of dirt than observed for the other coupons.

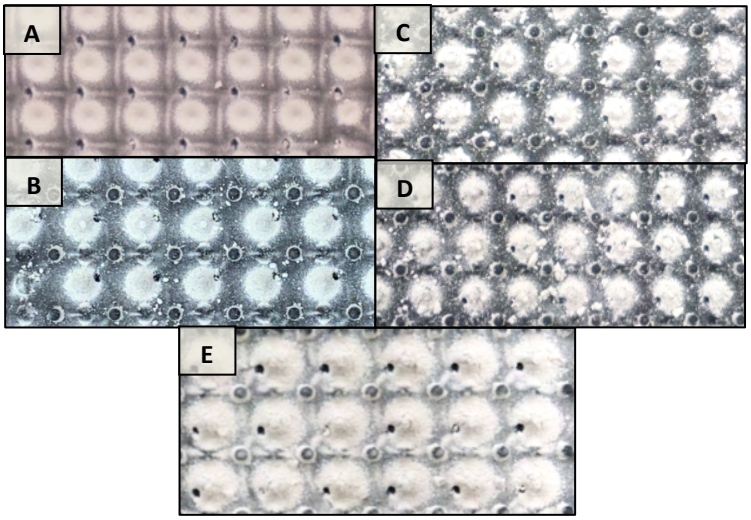

Figure 7. Post-test effusion plate geometries used in the dirt test facility. From top left to right: (A) baseline-405, (B) PCA-405, (C) PCA-625, (D) PCA-845, and (E) PCA-613S.

The data in Figure 8 quantify the capture efficiency of each coupon. Slug feed tests are denoted by solid bars, and continuous feed tests are denoted with dashed bars. Each bar represents a pair of impingement and effusion plates, where the number denotes the jet diameter of the impingement plate. The capture efficiency of the baseline coupon reached 42% for both slug and continuous feed tests. In relative terms, the slug and continuous feed tests resulted in the same relative performance.

The swirl and pin-cone plates using a 0.0405-inch jet diameter impingement plate showed the poorest performance, as shown in Figure 8, with capture efficiencies near 50% for the slug feed tests and at or above baseline for continuous feed tests. The data in Figure 8 also indicate that as the impingement jet diameter increased from 0.0405 inch to 0.0625 inch, the pin-cone design showed a 16% decrease (improvement) in the capture efficiency for slug feed tests and a 6% decrease for continuous feed tests. The PCA coupon showed a similar effect when the impingement jet diameter was increased from 0.0405 inch to 0.0625 inch, resulting in a capture efficiency reduction of 6% for both slug and continuous feed test modes. Given the dependence on the impingement jet diameter, another coupon with a 0.0845-inch diameter was manufactured to use with the PCA coupon, which resulted in an additional 4% and 6% drop in η_c for slug and continuous feed tests respectively. The impingement plate with a 0.0613-inch impingement jet diameter was tested with the PCA coupon to determine whether the jet diameter or total flow area caused the η_c to decrease. The results indicate that the 0.0613-inch impingement jet diameter plate paired with a PCA coupon had a η_c equivalent to that of the PCA coupon paired with the 0.0405-inch jet diameter impingement plate. These results indicate that increasing the total impingement flow area resulted in a favorable decrease in η_c.

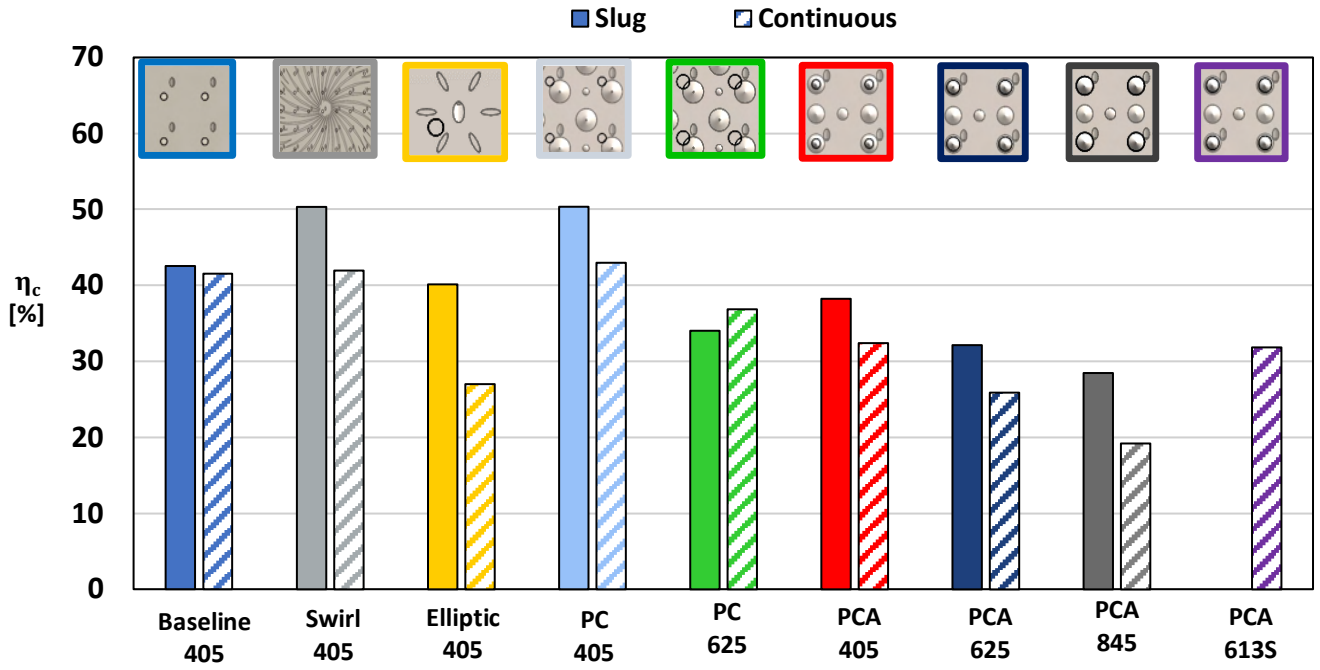

Figure 8. Capture efficiencies for impingement and effusion coupon pairs at a PR of 1.045 with 2grams of dirt.

For evaluation of the scaling of η_c as a specific function of FP, the different geometries are shown in Figure 9. Of note, each coupon has a different FP, although each operates at a constant PR. Slug feed tests are represented by filled markers and continuous feed tests are represented by open markers in Figure 9. Each marker shape represents a different impingement jet diameter, as indicated in the legend. For FP values less than 0.1, the η_c increased as the FP increased. The data indicates that the best-performing coupons had the lowest FPs.

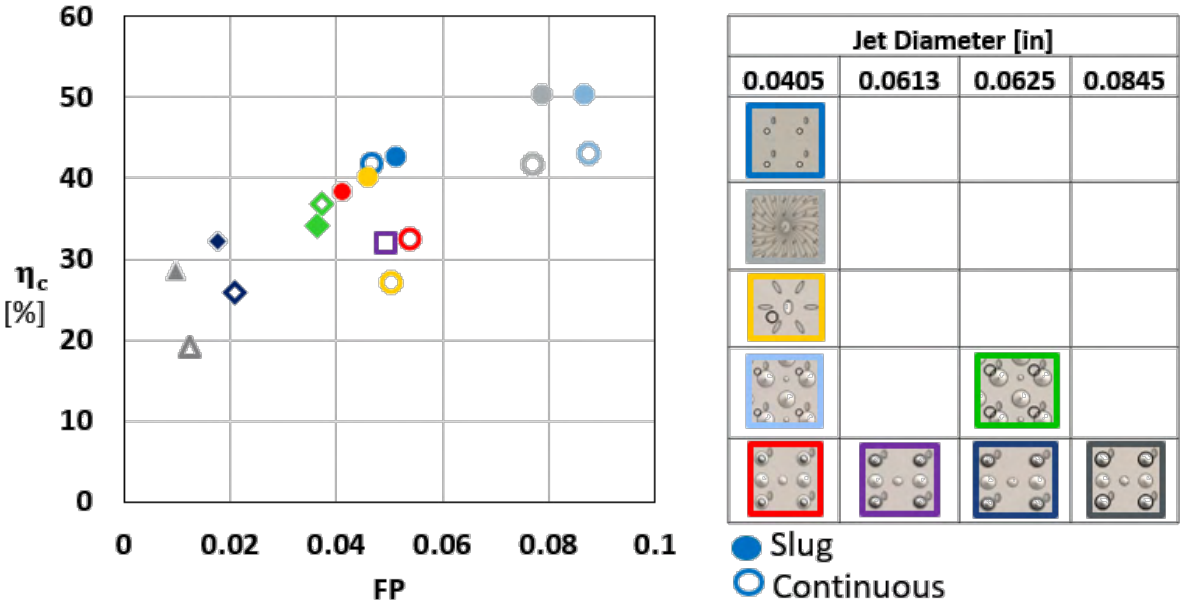

Figure 9. Capture efficiency as a function of flow parameter at a PR of 1.045 with 2 grams of dirt.

Figure 10 displays the jet Re as a function of the η_c. The results display a trend similar to that observed for capture efficiency as a function of FP. Coupons with lower Re had lower capture efficiencies, whereas coupons with high Re had high capture efficiencies.

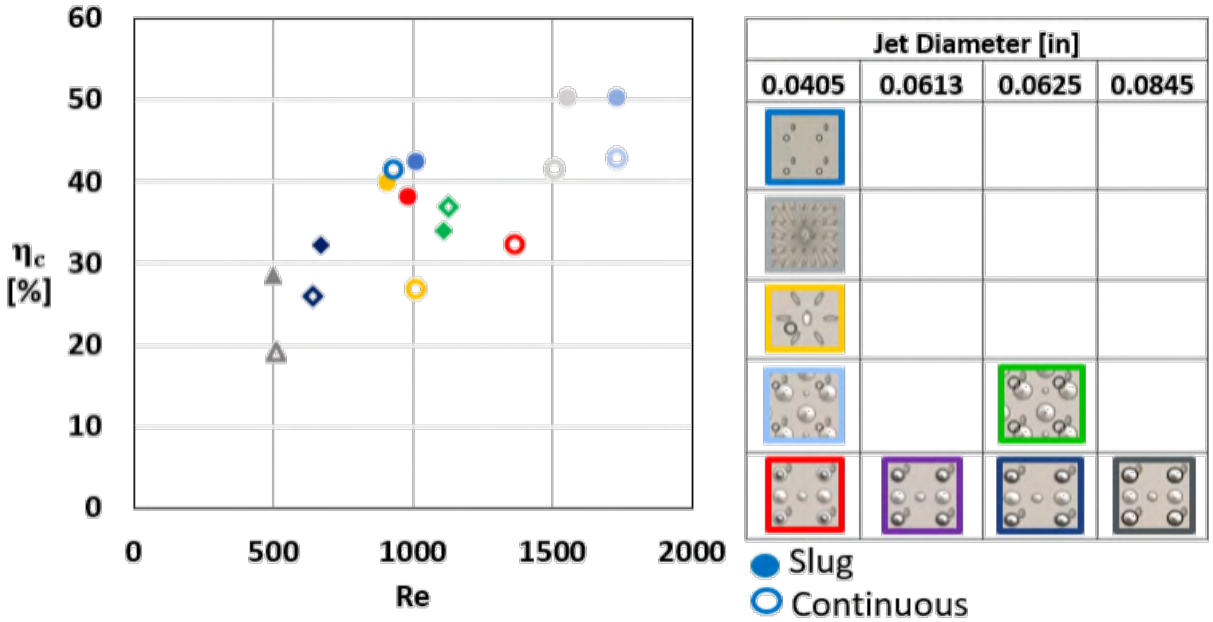

Figure 10. Capture efficiency as a function of jet Re at a PR of 1.045 with 2grams of dirt.

The CFD predictions focused on the most successful double-wall concept, namely the PCA. As shown in Figure 11, the interaction between the impingement flow and the effusion plate features is easily seen within the reduced geometry. The flow field predictions for the PCA/impingement hole arrangement provide a good understanding of this complex flow field.

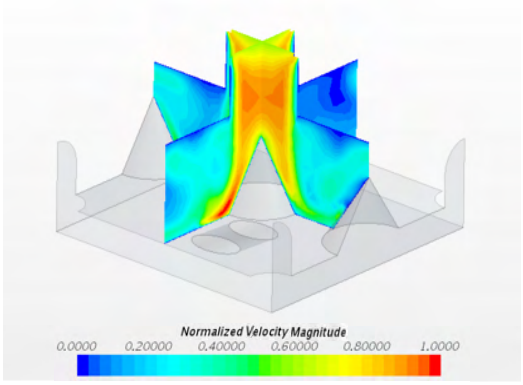

Figure 11. Impingement flow interacting with effusion plate features.

Comparisons with deposition test results were made using horizontal cross-sections of this flow to determine which FPs correlated with the locations of increased particle deposition. As shown in Figure 12, a correlation was observed between areas of high velocity and increased particle deposition. This pattern was especially evident with the high-velocity regions surrounding the corner pins and center cone on the effusion plate. The pin in the top-right corner has a low-velocity pocket surrounding it, which is consistent with the physical results, because that pin has little deposition compared to with the other corner pins with high-velocity flows around them.

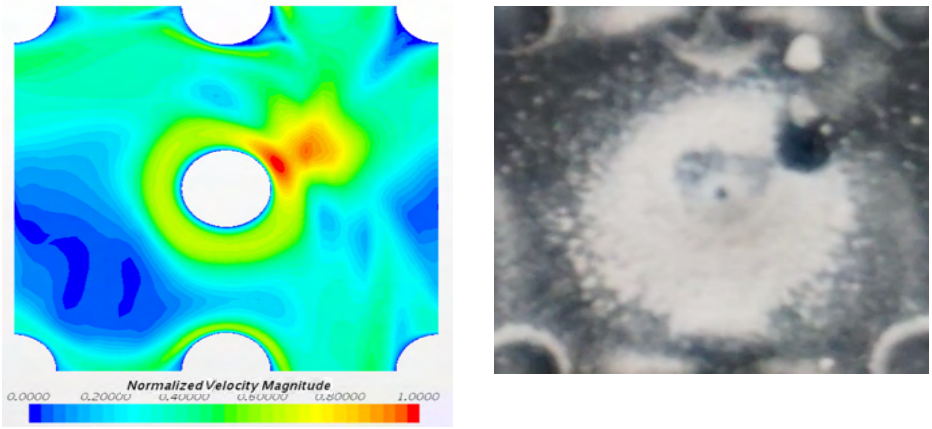

Figure 12. CFD-predicted flow velocity (left) and physical dirt deposition test results (right).

This study successfully used flow velocity magnitude to predict particle accumulation around geometry features such as cones, pins, and holes. However, the method was less accurate in predicting accumulation in flat regions of the effusion plate, as shown in the large low-velocity region at the bottom left of the plate. In the experimental results, the flat areas of the plate between the center cone and edges had fairly symmetric patterns of accumulation, in contrast to the computational results. Continued refinement of the CFD model will be undertaken during this next research period.

Task 2 - Testing of Scaled Models of Optimal Cooling Concepts

The Pennsylvania State University

To understand the durability of double-walled combustor liners with and without dirt, evaluating the heat-transfer coefficients on either side of the effusion and impingement plates is important. A new experimental method is being investigated to determine the heat-transfer coefficients on all walls of the double wall. The proposed method consists of three cases that each will be used to determine h_∞, h_1, and h_2.

Figure 13 shows case 1, which will be used to calculate h_∞, the heat-transfer coefficient on the hot side of the effusion plate. In case 1, the impingement plate and the cold side of the effusion plate are insulated. A thin wire heater will be imbedded inside the effusion plate to generate a heat flux at the copper-insulation interface. The power generated by the heater can be used to solve the respective thermal resistance network for h_∞.

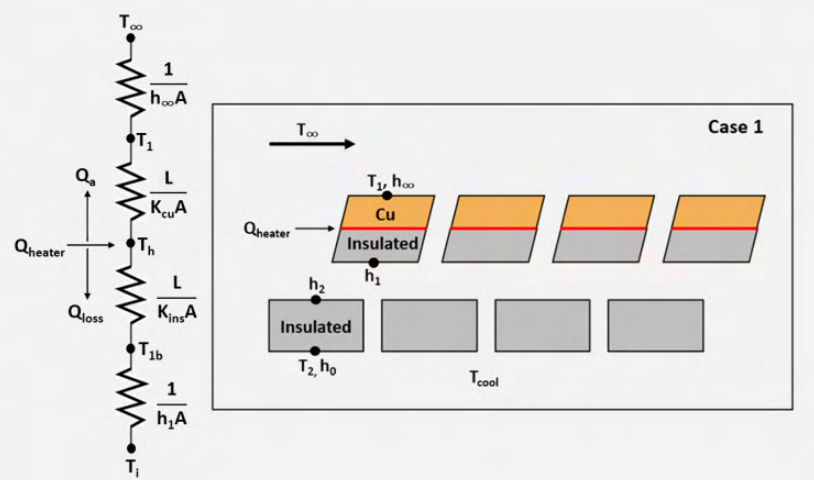

Figure 13. Case 1, illustrating the method to determine h_∞.

Similarly, Figure 14 shows case 2, which will be used to calculate h_1, the heat-transfer coefficient on the cold side of the effusion plate. In case 2, the impingement plate and the hot side of the effusion plate are insulated. Again, a thin wire heater will be imbedded inside the effusion plate to generate a heat flux at the copper-insulation interface. The power generated by the heater can be used to solve the respective thermal resistance network for h_1.

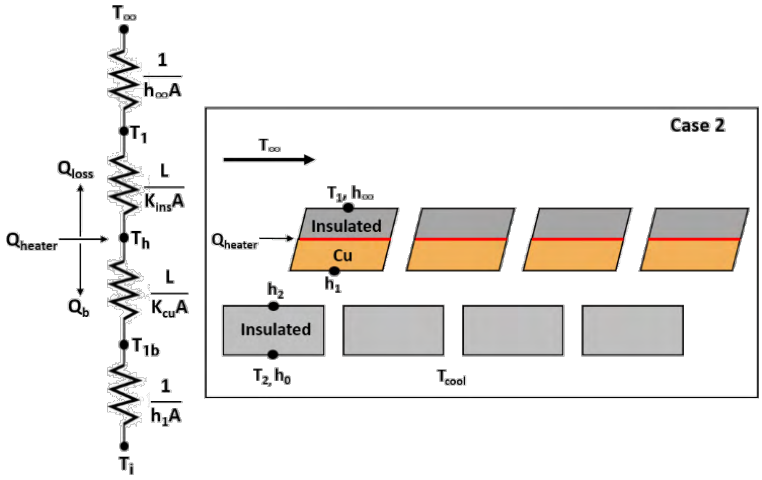

Figure 14. Case 2, illustrating the method to determine h_1.

Figure 15 shows case 3, which will be used to calculate h_2, the heat-transfer coefficient on the hot side of the impingement plate. In case 3, the effusion plate and the hot side of the impingement plate are insulated. In this case, a thin wire heater will be imbedded inside the impingement plate, generating a heat flux at the copper-insulation interface. The power generated by the heater can be used to solve the respective thermal resistance network for h_2.

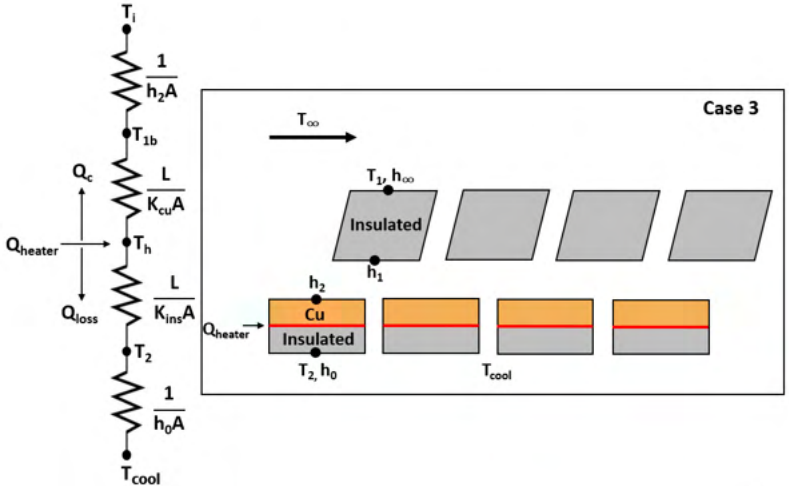

Figure 15. Case 3, illustrating the method to determine h_2.

This method requires decreasing any heat-transfer losses to reduce the uncertainty of the heat-transfer coefficients. Case 1 was found to be the limiting case to minimize the loss ratio. Figure 16 shows the loss ratio as a function of insulation thickness. The insulation thickness was scaled from 0 to 0.05 inches, with a total plate thickness of 0.05 inches. The no insulation condition was represented by an effusion plate constructed completely of copper. Four insulating materials of varying thermal conductivity were chosen to compare their impact on loss ratio. As shown below, low thermal conductivity correlated with a lower loss ratio. Figure 16 indicates that as the insulation thickness increased, the loss ratio decreased. The results also showed that spray foam and Styrofoam resulted in similar losses. Given the need for manufacturing the test rig, spray foam is most likely the material to be chosen for the insulation.

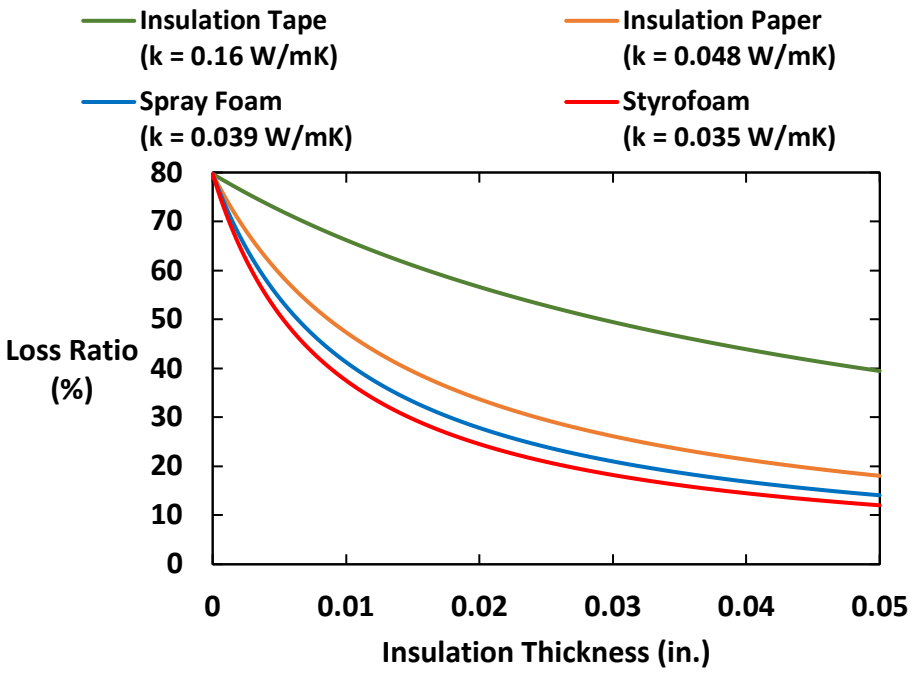

Figure 16. Loss percentages relative to the heat input for a range of materials and thicknesses for case 1.

Figure 17 shows the results of the heat-transfer study that were used to verify the one-dimensional thermal resistance calculations. This trend is expected for the conditions with the constant temperature through the copper and a temperature gradient through the insulation. Only a 1.1% difference was found between the STAR CCM+ model and a one-dimensional thermal resistance network calculation, thus providing confidence in the model.

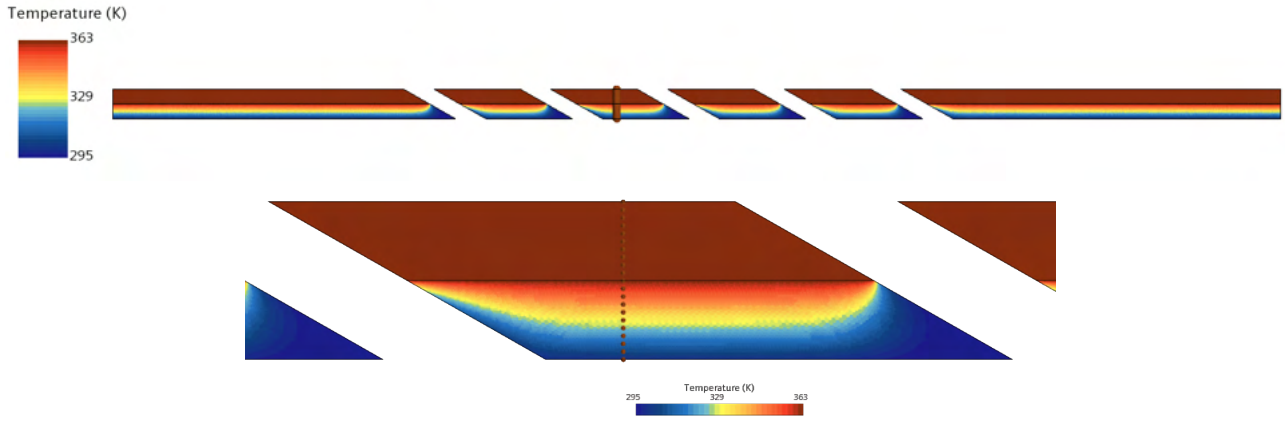

Figure 17. Initial 2D STAR CCM+ heat-transfer model for case 1.

Task 3 - Facility Planning for 1× Scale Combustor

The Pennsylvania State University

Although this particular task is for year 3, initial work has begun through discussions on the design requirements for the simulator. These discussions have taken place with Pratt & Whitney, particularly with Dr. Steve Kramer. The START team has identified a potential area for the simulator design. In addition, cost-matching has already been provided by Pratt & Whitney to accomplish this task if the FAA funds the third year of this project.

Figure 18 illustrates the need for placing a combustor simulator upstream of the START test turbine. The data in Figure 18 show the range of nonuniformities of non-dimensional pressures (Cp) and temperatures (θ) that occur at the exit of the combustor, both of which impact turbine performance. As various fuels are used for combustion in the future, simulating these profiles will become even more critical.

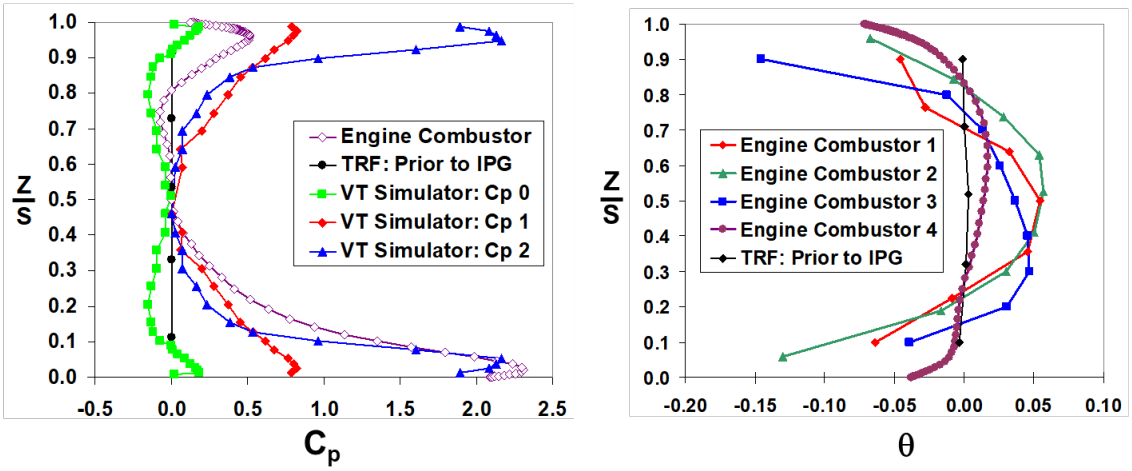

Figure 18. Combustor exit profiles from the literature, indicating non-uniform pressures and temperatures (θ).

Figure 19 shows the approximate location for the simulator, as highlighted in the orange box for the START test turbine. Currently, the team is evaluating the pros and cons of using electric heating to tailor the profile or using high-velocity jets in cross-flow.

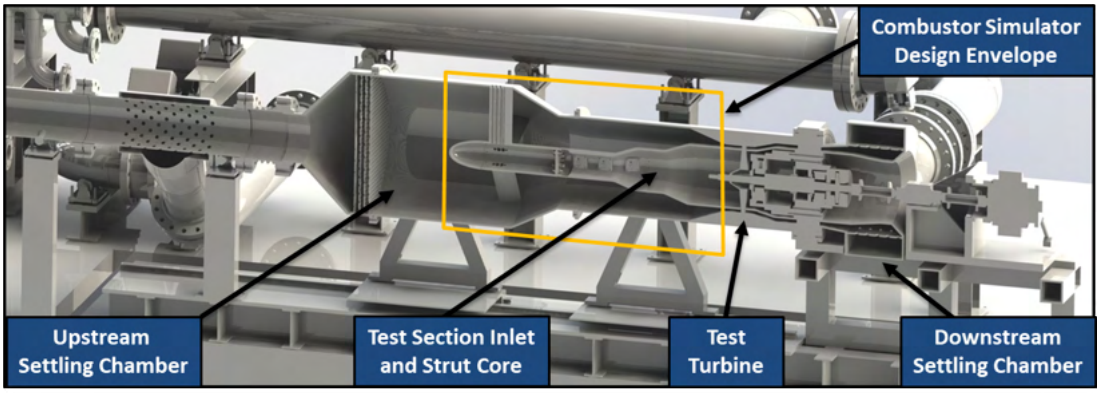

Figure 19. Illustration of the concept area upstream of the START test turbine for a combustor simulator.

Publications

Fallon, B., Thole, K., Lynch, S., Lundgren, R., & Kramer, S. (2021). *Comparison of dirt deposition on double-walled combustor liner geometries.* Manuscript submitted for publication.

Outreach Efforts

Bi-weekly presentations are given to Pratt & Whitney through this joint collaboration.

Awards

None

Student Involvement

Graduate students Brandon Fallon and Cynthia Letting are performing Tasks 1 and 2, respectively. Sarah Fox, an undergraduate Schreyer Honors student, is performing the computational studies. All students are involved in weekly meetings with the advisors (Thole and Lynch). The graduate students are involved in bi-weekly meetings with Pratt & Whitney as well as presenting their work to a larger Pratt & Whitney audience for the Center of Excellence meetings, the last of which was held in August 2021.

Plans for Next Period

During the next period, we will complete the coupon testing and prepare our TurboExpo 2022 publication. In addition, we will continue to work on the design, manufacturing, and benchmarking of our heat-transfer testing (Task 2). Finally, we will continue to evaluate different design possibilities for the combustor simulator (Task 3).

Nomenclature

$\dot{m}$	mass flow rate through the test facility
P_{up}	upstream test-facility pressure
P_{down}	downstream test-facility pressure
T_{oc}	supply coolant temperature
N	number of impingement holes
D	cooling hole diameter
η_c	capture efficiency

Project 069 Transitioning a Research nvPM Mass Calibration Procedure to Operations

Missouri University of Science and Technology and Aerodyne Research Inc.

Project Lead Investigator

Philip D. Whitefield
Chancellor's Professor of Chemistry
Missouri University of Science and Technology
400 W 11th Street, Rolla, MO 65409
573-341-4420
pwhite@mst.edu

University Participants

Missouri University of Science and Technology

- PI: Philip D. Whitefield, Chancellor's Professor of Chemistry
- FAA Award Number: 13-C-AJFE-MST; Amendments: 014
- Period of Performance: June 5, 2020 to June 4, 2021
- Task:
    - Investigate the validity of the centrifugal particle mass analyzer (CPMA) mass calibration research approach for non-volatile particulate patter (nvPM) certification measurement systems. The assessment will extend across all nvPM mass ranges encountered during certification tests. The primary goal will be the successful transitioning of the research methodology to operations

Project Funding Level

The total amount of funding from the FAA is $846,707. Matching funds of $846,707 have been provided by the Swiss Federal Laboratories for Materials Science and Technology (EMPA).

Investigation Team

- Professor Philip Whitefield, PI, Missouri University of Science and Technology
- Steven Achterberg, research technician, Missouri University of Science and Technology
- Max Trueblood, research technician, Missouri University of Science and Technology
- Dr. Richard Miake-Lye, subcontractor, Aerodyne Research Inc.
- Dr. Robert Howard, subcontractor, Arnold Engineering Development Center (AEDC), US Air Force

Project Overview

This project is designed to investigate the validity of the CPMA mass calibration research approach. The assessment will extend across all nvPM mass ranges encountered during certification tests. The primary goal will be the successful transitioning of the research methodology to operations. The project will begin with a laboratory assessment leading to a dedicated small engine as the test source at the US Air Force AEDC.

The challenge mass devices for calibration (micro-soot sensor (MSS), laser-induced incandescence monitor (LII), and cavity attenuated phase shift monitor (CAPS)) will be provided by the North American Reference nvPM Measurement System, together with the CPMA and other necessary instruments, such as a DMS500 particulate analyzer, aerosol mass spectrometer (AMS) and CAPS.

Task 1 - Investigate the Validity of the Centrifugal Particle Mass Analyzer (CPMA) Mass Calibration Research Approach for nvPM Certification Measurement Systems

Missouri University of Science and Technology

Objectives

The objectives of this task are to acquire the components of a CPMA-based mass calibration system similar to that described in SAE E31 discussion paper DP-32 (presented by Dr. G. Smallwood) from the annual committee meeting on June 17–21, 2019, in Saclay, France; assemble the system; and evaluate its performance.

Research Approach

Subtask 1

Acquire the components of a CPMA-based mass calibration system similar to that described in SAE E31 discussion paper DP-32 (presented by Dr. G. Smallwood) from the annual committee meeting on June 17–21, 2019, in Saclay, France

Subtask 2

Assemble and test the CPMA-based mass calibration system's performance at Missouri University of Science and Technology's laboratories, by using a miniature combustion aerosol standard (Minicast) as the nvPM generation source (Figure 1)

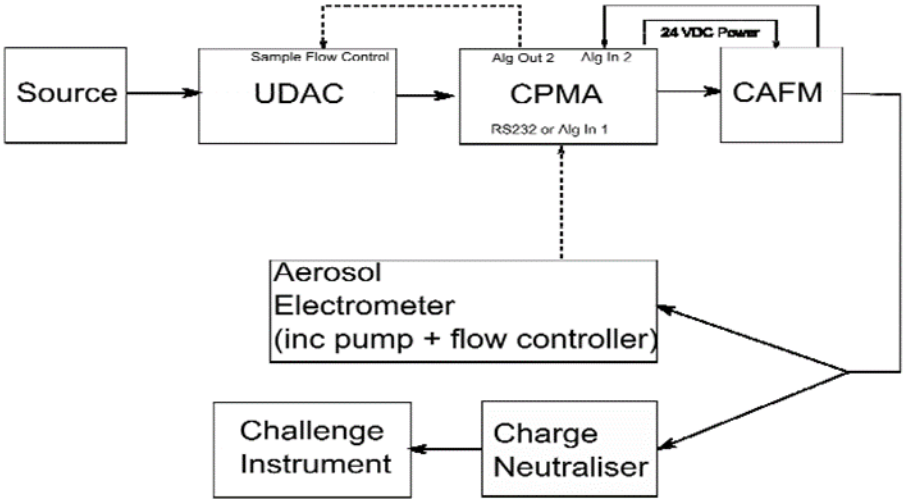

Figure 1. Schematic diagram of the CPMA-based mass calibration system.

Subtask 3

Investigate the validity of the CPMA mass calibration research approach across all nvPM mass ranges encountered during certification tests to successfully transition the methodology to operations

Subtask 3a

Deploy (transport and install) the North American Reference System (NARS), including the CPMA-based mass calibration system and ancillary diagnostic suite with the Air Force AVL nvPM measurement system, at engine testing facilities at Arnold Air Force Base, Tennessee, which will include the J85 turbojet and a gas-turbine-based "start cart" as nvPM sources

Subtask 3b
Evaluate the performance of the CPMA-based mass calibration system, surveying across all mass ranges by using the start cart as the nvPM source; compare these results with concomitant mass calibration data acquired with SAE E-31 OCEC-based mass calibration methodology

Subtask 3c
Demonstrate the performance with a mock-certification test on the J85 engine, with calibration including standard elemental carbon/organic carbon (EC/OC) analysis, as well as the CPMA-based calibration system described in document DP-32.

Subtask 3d
Decouple the diagnostic suites from the Arnold Air Force Base engine facilities, and transport them back to Missouri and Massachusetts

Subtask 4
Analyze and interpret the data gathered in Tasks 2 and 3

Subtask 5
Prepare and deliver a final report

Milestones

- A laboratory-based assessment strategy has been developed and reviewed by the advisory team.
- Team discussions continue on a bi-weekly schedule
- Essential components for the assessment study, including a Minicast nvPM source, a sample mixing and distribution plenum, and a semi-continuous EC/OC analyzer (Sunset), have been acquired and tested.
- The Minicast and EC/OC analyzer were loaned from the VARIANT team and were found to require significant refurbishment and calibration. This work has been completed.
- The CPMA mass standard source has been operated in conjunction with the and MSS mass monitors. Good agreement was achieved between the standard and monitors. The relationship was found to be linear over a broad mass range.

Major Accomplishments

Essential diagnostic equipment has been acquired, and work on subtasks 2 and 3 is being pursued. Figure 2 shows a schematic diagram of the mass standard evaluation system, exploring the dynamic nvPM mass concentration range that can be used.

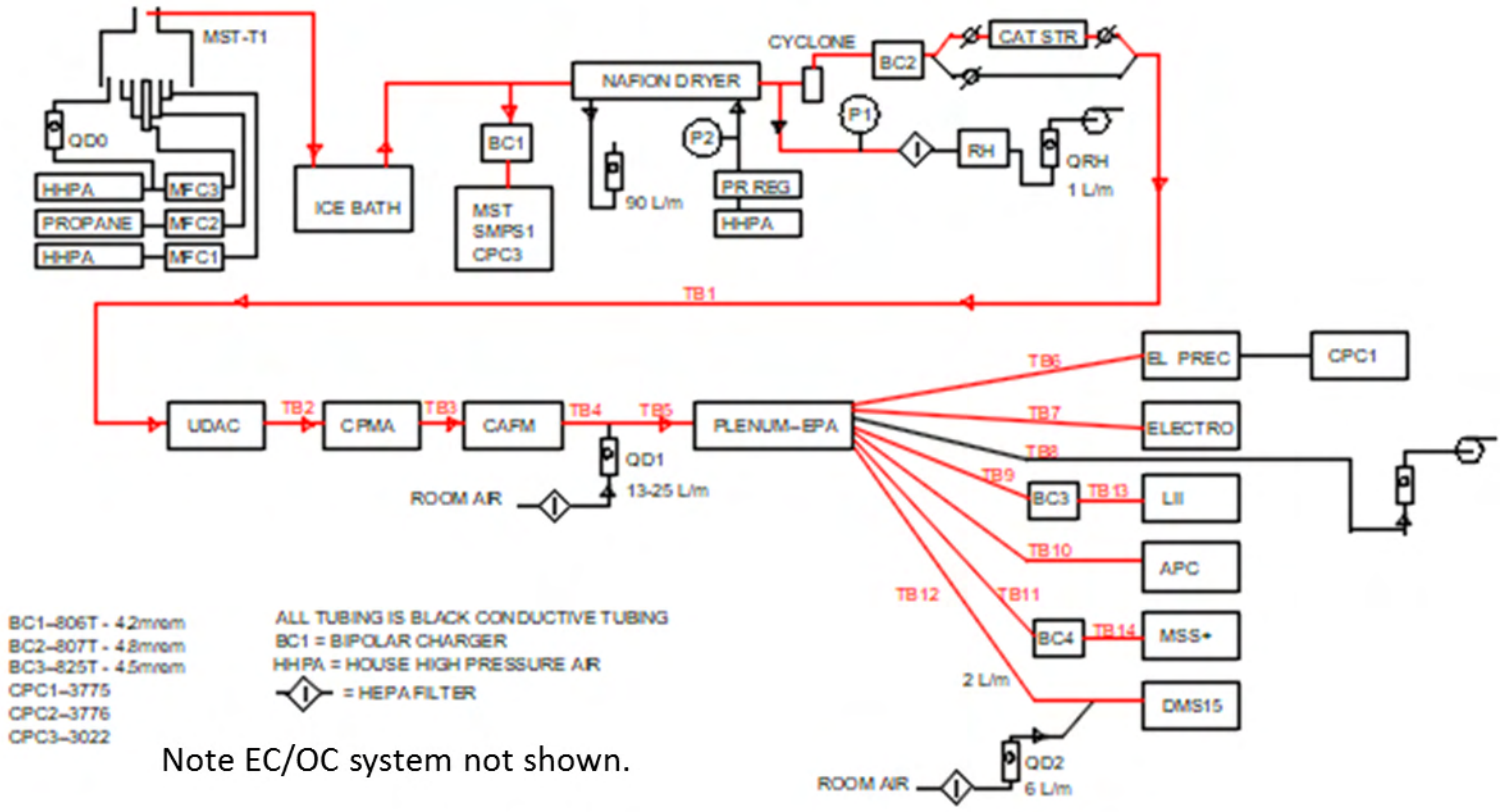

Figure 2. Schematic for mass standard assessment studies in Tasks 2 and 3.

Publications
None

Outreach Efforts
The Project 069 plan and progress were delivered in the form of a quad chart at the ASCENT Advisory Board Virtual Meeting in April 2021.

Awards
None

Student Involvement
One graduate student and two undergraduate students are currently assigned to this project

Plans for Next Period
We plan to continue to pursue the statement of work from subtasks 2-5 as described above. Deployment of the CPMA enhanced North American Reference System for nvPM to AEDC is scheduled for March 2022.

Project 070 Reduction of nvPM Emissions from Aero-Engine Fuel Injectors

Georgia Institute of Technology

Project Lead Investigator

Wenting Sun
Associate Professor
School of Aerospace Engineering
Georgia Institute of Technology
(404) 894-0524
wenting.sun@aerospace.gatech.edu

University Participants

Georgia Institute of Technology

- PI: Dr. Wenting Sun
- FAA Award Number: 13-C-AJFE-GIT-080
- Period of Performance: August 11, 2020 to August 10, 2021
- Tasks:
    1. Measurement of non-volatile particulate matter (nvPM) formation and oxidation processes
    2. nvPM model development and validation
    3. Experimental facility development and operation

Project Funding Level

The total amount of funding from the FAA is $1,000,000. The matching funding includes $900,000 from the Georgia Institute of Technology and $100,000 from Honeywell.

Investigation Team

Lead PI, Wenting Sun (Georgia Institute of Technology), will oversee the entire project and coordinate among the co-PIs. He will work with one graduate student and one research engineer to lead Task 3.
Co-PIs Adam Steinberg, Ellen Yi Chen, Timothy Lieuwen, and Jechiel Jagoda (Georgia Institute of Technology) will work with two graduate students to lead Task 1.
Co-PIs Rudy Dudebout and Fang Xu from Honeywell will lead Task 2.

Project Overview

Reducing nvPM from gas turbine engines is essential for improving air quality and reducing the environmental impact of aviation. However, predicting and controlling nvPM remains challenging because of the complicated physical and chemical processes involved. The proposed research will characterize the formation/oxidation of nvPM and optimize the design of an aeronautical gas turbine fuel injector to reduce nvPM at flight-relevant conditions. The goals of this project include:

1. Develop a high-pressure experimental platform suitable for combustor testing under practical conditions and enabling academic advanced diagnostics
2. Conduct optical diagnostics to measure the nvPM volume fraction and primary particle size; the polycyclic aromatic hydrocarbon (PAH) and hydroxyl (OH) radical distributions; and the flow field for a set of fuel injectors
3. Develop empirical correlations describing nvPM formation/oxidation by using data obtained in experiments
4. Validate computational fluid dynamics (CFD) simulations to facilitate fuel injector design optimization

Task 1 - Measurement of nvPM Formation and Oxidation Processes

Georgia Institute of Technology

Objective(s)

In this task, laser-induced incandescence (LII) measurements will be conducted to quantify the soot volume fraction and primary particle size; OH planar laser-induced fluorescence (PLIF) will be conducted to understand the soot oxidation process; PAH PLIF will be conducted to elucidate the formation pathway of soot; and particle image velocimetry (PIV) will be conducted to understand the fuel/air mixing process according to the characteristics of fuel injectors.

Research Approach

We will conduct LII to quantify soot volume fraction and primary particle size; PIV to measure flow fields; PAH PLIF and OH PLIF to understand the interaction between nvPM and important gas-phase species; and droplet Mie scattering to characterize the fuel spray. We will also conduct sampling measurements in the combustor exhaust to analyze the exhaust composition (via gas chromatography) and nvPM composition/morphology (via X-ray photoelectron spectroscopy [XPS] and scanning electron microscopy [SEM]), thus increasing the understanding of nvPM kinetics. All measurements will be performed in a model aeronautical gas turbine combustor operated with a liquid jet fuel at engine-relevant operating conditions. All subtasks under Task 1 will proceed in parallel, because the ultimate aim is to measure multiple parameters simultaneously.

In year 1 of this project, the focus is the development of a new high-pressure experimental platform. Until the newly designed three-fuel injector is commissioned, optical diagnostics cannot be performed to obtain experimental data. While waiting for the commissioning of the experimental system, the optical diagnostic tools were prepared and will be ready for use when the combustion experiments start. The following sections detail the mechanisms of the proposed optical diagnostics and describe several preliminary results acquired during the preparation of these optical diagnostics.

Subtask 1.1 - LII Measurement

LII uses short laser pulses to heat small particles to vaporization temperatures. The light emission, or incandescence, of the nvPM is then measured to deduce the relative volume fraction and primary particle size. Two-dimensional implementations of LII are performed by shaping the laser beam into a uniform sheet and capturing the incandescence at various wavelengths on sensitive time-gated cameras. The prompt emission immediately after the arrival of the laser pulse describes the volume fraction or spatial concentration of nvPM particles. By applying sufficient laser intensity to uniformly sublimate the nvPM and by calibrating these measurements against emissions from known flames, the absolute volume fractions can be determined.

For nvPM particle sizing, time-resolved LII (TiRe-LII) techniques can be used to obtain the incandescence decay over time. This approach relies on the faster cooling times of small particles compared to large particles after laser heating, due to their larger surface-to-volume ratio. By solving energy and mass balances, the primary particle size can be evaluated. To measure the decays, which are on the order of several hundred nanoseconds in atmospheric-pressure flames, ultra-high-speed cameras are necessary. Recently, we have successfully demonstrated a single-camera single-laser-shot technique for performing these measurements by capturing the decay time constants at 10 million frames per second with a 50-ns gate. At these imaging rates, the flame motion appears stationary, thus enabling accurate pixel-by-pixel decay time measurements. The data from each pixel are then fit to a model to determine the instantaneous, primary nvPM particle sizes for the entire scene. The statistics for these images can then be compared to show regions of the flame where nvPM growth and nvPM oxidation typically occur.

However, for the high pressures associated with flight-relevant conditions, the incandescence time constants decrease to the order of ~50 ns, which is faster than the imaging rate of many single-chip ultra-high-speed cameras. To overcome this challenge and accurately measure the shorter time constants in these environments, a multi-camera variant of the TiRe-LII technique described above can be used. In this variant, two or more cameras sharing the same field of view can be gated to open a few tens of nanoseconds apart. The calibrated relative intensities of these images can then be used to estimate time constants and nvPM particle sizes. Hence, this method enables the determination of nvPM growth regions and oxidation regions, even in high-pressure environments.

The various LII measurements described in this subtask will be conducted by using the fundamental 1,064-nm output of a solid-state neodymium-doped yttrium aluminum garnet (Nd:YAG) laser operating at 5–10 kHz to avoid exciting the OH and PAH fluorescence. The laser beam will be formed into a sheet that is then passed through the combustor. The incandescence will then be measured with time-gated cameras by using the appropriate filters (near 640 nm) to avoid C_2 Swan band

emissions. Calibrations using well-characterized ethylene turbulent jet flames were conducted to produce quantitative measurements for nvPM volume fraction and particle size in the gas turbine combustor under the conditions of interest. The experimental setup for LII is presented in Figure 1. The fundamental 1,064-nm output of a solid-state Nd:YAG laser was expanded into a laser sheet by using a combination of lenses. The laser sheet past the turbulent jet flame and LII signal was then collected with a high-speed camera.

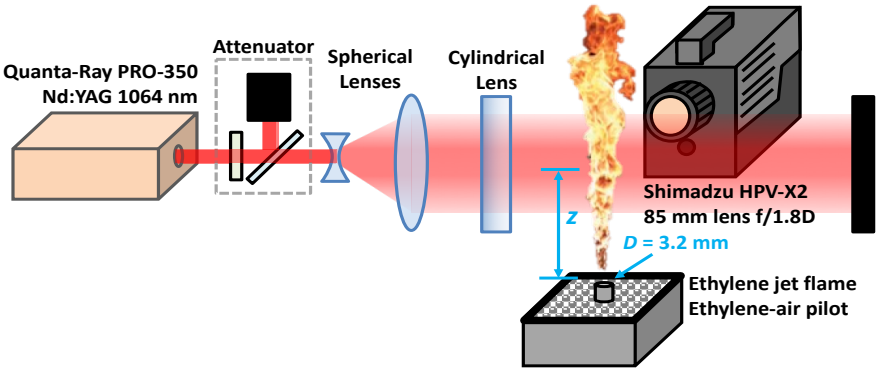

Figure 1. Experimental schematic of LII.

Figure 2 shows the measured particle size distribution in the ethylene turbulent jet flame. With variations in flow conditions (Reynolds number), the particle size distribution changes. Similar phenomena are expected in our combustor experiments using liquid jet fuel. We will implement these optical diagnostics after the high-pressure experiment is commissioned.

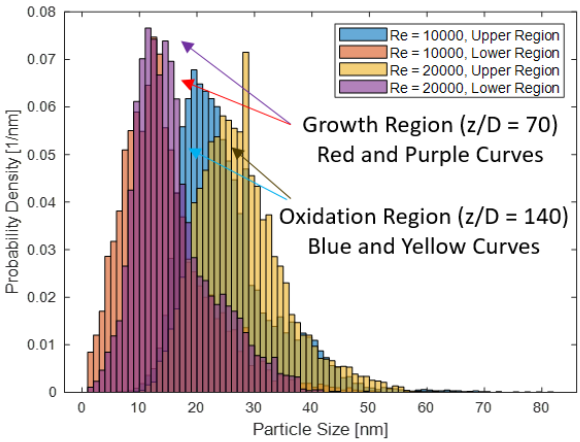

Figure 2. Distribution of soot particle sizes in a turbulent jet flame.

Subtask 1.2 - OH PLIF Measurement

Oxidation through reaction with hydroxyl radicals (OH) is expected to be a critical pathway through which nvPM is destroyed in the flame. Understanding the relative trajectories of nvPM and OH through the combustor is therefore critical to predicting the final nvPM output.

OH radicals form during high-temperature hydrocarbon oxidation, reaching super-equilibrium concentrations near the location of maximum heat release rate before relaxing to equilibrium in the products. Significant concentrations of OH occur in hot product gases at temperatures above ~1500 K. Fortunately, owing to its strongly absorbing energy transitions at wavelengths that are relatively accessible to high-energy pulsed lasers, OH can be readily measured using PLIF. The main challenges in performing OH PLIF in the combustor of interest herein are laser power absorption and signal trapping through the high-density gas at 10 bar.

We will perform OH PLIF measurements simultaneously with the two-dimensional (2D) LII measurements to understand the interaction between nvPM and OH. Measurements will be made at a 5- to 10-kHz repetition rate by using the frequency-doubled output of a dye laser (rhodamine 6G), pumped by a frequency-doubled solid-state laser (Nd:YAG). Over 7 W of ultraviolet (UV) laser light can be produced by our laser system, which is sufficient to acquire signals across the combustor domain. The laser beam will be formed into a sheet, made coincident with the LII laser sheet, and transmitted through the combustor. The OH PLIF signal will be filtered through an appropriate bandpass filter (approximately 307 nm) and recorded with a high-speed intensified camera. Appropriate corrections will be made for laser power absorption, intensity variations, and detector response. The resultant data will provide time-resolved 2D images of the OH distribution, which will be correlated with nvPM dynamics to better understand the oxidation process and how specific trajectories influence the nvPM that is ultimately output from the combustor.

Subtask 1.3 - PAH PLIF Measurement
PAHs occur naturally in jet fuel and also can be formed from small aliphatic compounds during combustion. Because PAHs play key roles in nvPM growth, understanding their positions relative to regions containing nvPM can help elucidate rate-controlling processes.

PAH molecules have high-absorption cross-sections across a wide range of wavelengths in the UV spectral range. Therefore, PAH PLIF can be performed with a laser wavelength similar to that used for the OH PLIF but slightly de-tuned from the narrow-band OH absorption line to avoid interference. Hence, PAH PLIF measurements will be acquired with the same experimental configuration as those with OH PLIF but with a wavelength shift on the order of 0.1 nm. Measurements will be obtained simultaneously with the LII to elucidate the relative positions of nvPM and PAH during formation. Although OH and PAH PLIF will not be obtained simultaneously, these species are related to different aspects of the nvPM dynamics and do not directly interact. Because the PAH PLIF laser beam is obtained by adjusting the wavelength of the OH PLIF beam, the different measurements can be obtained in close succession, thus maintaining identical operating conditions.

Subtask 1.4 - PIV Measurement
Measuring the fluid velocity field is critical for understanding the influence of turbulence and mixing on nvPM dynamics. PIV measures the velocity field in a plane by tracking the motion of micron-scale particles that are seeded into the flow. Stereoscopic PIV (S-PIV) enables measurement of all three velocity components in the plane by simultaneously viewing the particle motion from two different viewing angles. Although PIV (and S-PIV) has been successfully applied to study a wide range of flows, including in flames, its application in high-pressure fuel-rich combustion has been relatively limited because of the high-intensity background luminescence from the flame, beam steering through index-of-refraction gradients, and fouling of the optical windows due to seed particle deposition. Despite these challenges, we have recently demonstrated S-PIV in a 10-bar rich-burn gas turbine combustor similar to that studied in this work.

Here, S-PIV measurements will be made simultaneously with the LII and PLIF measurements. To enable these measurements, the flow will be seeded with micron scale ZrO_2 tracer particles. The high melting point of ZrO_2, as compared with other commonly used solid tracers, mitigates window contamination. Laser pulse pairs from a solid-state second-harmonic Nd:YAG laser will be formed into a sheet and transmitted through the combustor along the same path as those with the other measurement techniques. The particle-scattered light will be filtered through appropriate bandpass filters and collected by two high-speed cameras arranged in an angular stereoscopic viewing configuration. Image pre-processing routines—which are well established in our group—will be performed to reduce the effects of background flame luminosity and cross-signal interference, thus providing sharp particle images for subsequent vector processing. The resultant particle image pairs will be converted to three-component velocity vectors with a multi-pass image cross-correlation algorithm implemented in LaVision DaVis, a commercial software package.

Subtask 1.5 - Fuel Droplet Mie Scattering Measurement
One important factor controlling nvPM formation is the mixing between the fuel from the injector spray and the air in the combustor. The fuel injector spray can be characterized by measuring the size and spatial distribution of liquid fuel droplets. Using Mie scattering imaging techniques, the spatial distribution of micro-sized fuel droplets can be determined via measurement of elastic light scattering. However, quantification of the spray properties from Mie scattering is challenging, predominantly because of multiply scattered photons, interference from PIV seed particles, and the relationship between scattering intensity and droplet size. Here, the objective is to obtain qualitative information regarding the fuel spray trajectory, including the spray angle; penetration; and relative locations of the liquid fuel, flame, and nvPM.

To study the fuel droplet distribution of different injectors at pressure in a non-reacting environment, the liquid fuel droplet distribution will be measured via Mie scattering at a 5- to 10-kHz repetition rate. The second harmonic of an Nd:YAG laser will be formed into a sheet and transmitted through the spray inside the experimental facility. The scattered light will be imaged at an angle perpendicular to the laser propagation with a high-speed camera. This signal will then be separated from the PIV seed particle scattering through adaptive threshold-based segmentation techniques.

Subtask 1.6 - Extractive Sampling Measurement
In this task, exhaust gas samples will be extracted and analyzed via gas chromatography (gas phase), XPS (solid phase), and SEM (solid phase). The gas chromatography (Inficon Fusion μGC) analysis will reveal comprehensive information regarding the large hydrocarbons formed during the combustion of Jet-A fuel, such as the detailed structures of PAHs, ethylene, and other intermediate species relevant to soot formation.

The XPS and SEM analyses will provide data on nvPM composition and morphology to help understand the detailed formation mechanisms of nvPM. There are two possible mechanisms for nvPM formation that can be detected during the combustor test. The first is due to the liquid fuel impinging on the wall, accompanied by chemical reactions at the wall. The other results from flame products, such as soot or coked droplets. These two types of solid particles can be differentiated through chemical and morphology analysis. Solid particles formed due to wall wetting features result in lower carbon content but significantly higher oxygen content (e.g., 70%–80% carbon and 20% oxygen) and small amounts of hydrogen and nitrogen, due to incomplete oxidation of fuel at low temperatures. Solid particles formed from flame products feature high carbon and low oxygen content (e.g., 98% carbon and 2% oxygen). In terms of morphology, the solid particles formed due to wall wetting exhibit amorphous structures, whereas the solid particles formed from flame products are spherical and are typically 4–5 μm in diameter. For these experiments, a water-cooled sampling probe will be used to collect samples of exhaust gas from the pressure vessel.

Task 2 – nvPM Model Development and Validation

Honeywell

Objective(s)

This task involves the comparison of the experimental measurements obtained in Task 1 with detailed numerical simulations for the purpose of model development and validation. A numerical framework to model the gas turbine combustor system will be established based on Honeywell's previous experience. In this numerical framework, a commercial solver will be used to obtain CFD solutions with a large eddy simulation (LES) turbulence model by using a dynamic Smagorinsky model. The combined heat release/turbulence model consists of non-premixed diffusion flamelets generated with a detailed Jet-A kinetic model that describes the formation of aromatic species up to pyrene. The simulation includes radiation with the discrete ordinate method due to H_2O, CO_2, and nvPM (weighted-sum-of-gray-gases model (WSGCM)). The liquid fuel spray is modeled with Lagrangian tracking of droplets with stochastic secondary breakup, calibrated to experimental data. The domain is discretized by using polyhedral cells and consists of the entire geometry from the inlet of the rig to the exhaust of the combustor. The simulation is initially converged with a Reynolds-averaged Navier–Stokes (RANS) solution, then run with five flow-throughs to initialize the solution and then an additional five flow-throughs to obtain statistical averages. The numerical simulation will be compared with experimental results from optical measurements (LII, OH/PAH PLIF, S-PIV, and Mie scattering) under different flow conditions with different fuel injectors. The numerical model will then be validated and optimized for further fuel injector design with the aim of minimizing nvPM emissions.

Task 2 will start in the second quarter of 2022 after the experimental results proposed in Task 1 are obtained.

Task 3 - Experimental Facility Development and Operation

Georgia Institute of Technology and Honeywell

In this task, we conducted detailed design of a high-pressure vessel and model gas turbine combustor for the proposed measurement. The design is challenging because it must accommodate both practical applications from an industrial perspective and academic applications involving advanced optical measurements. To achieve this goal, the Georgia Tech team and Honeywell team worked closely together and finalized a unique design of a combustor with three fuel injectors. This three-fuel-injector design can minimize injector–combustor wall interaction, which commonly occurs in conventional combustor designs with only one fuel injector. Our optical measurement will focus on the center fuel injector. Three large optical windows on the top and side walls of the combustor allow for optical diagnostics. The combustor will be placed inside a large high-pressure vessel with adequate optical access through two 10-inch-diameter windows and one 8-inch-diameter window. Figure 3 shows the overview of the high-pressure system. The high pressure is supported by a metal frame above the ground, and the combustor is housed inside the high-pressure vessel. Figure 4 shows the computer-aided-design (CAD) model of the high-pressure vessel. The high-pressure vessel has been successfully fabricated and certified, as shown by the direct photograph in Figure 5.

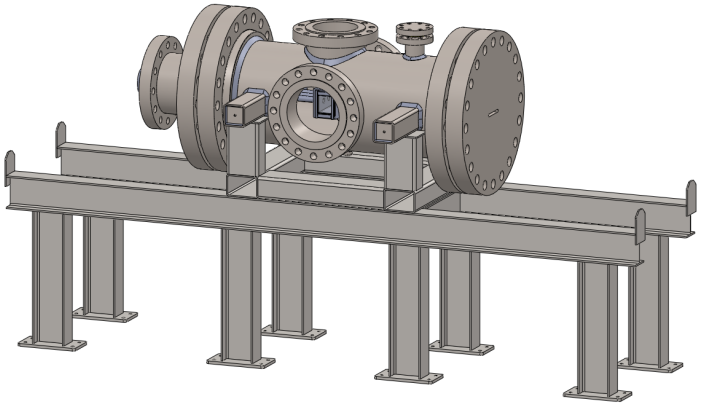

Figure 3. Overview of the high-pressure system.

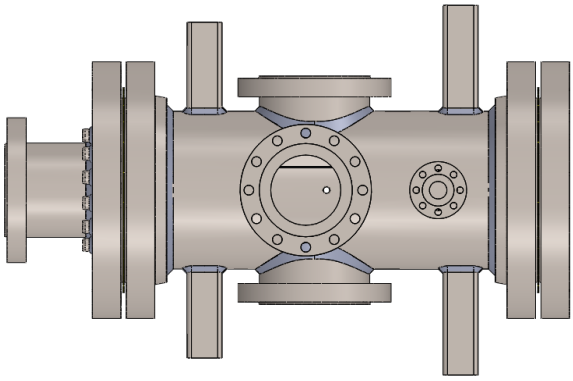

Figure 4. CAD model of the high-pressure vessel.

Figure 5. Direct photograph of the high-pressure vessel after completion of fabrication.

The combustor to be built will comprise three fuel injectors, in contrast to our initial proposal. As discussed above, the purpose of the three-fuel-injector design is to minimize injector–combustor wall interaction, which artificially affects the experimental results and causes them to deviate from those in a practical combustor. The current design of the combustor reflects a sector of an annular rich burn, quick quench, lean burn (RQL) combustor architecture. The test rig has provisions for routing air to cool the combustor walls and provides air to the quench holes, the injector, and the swirler. The sidewalls also incorporate optical access with suitable features to discourage the accumulation of nvPM or S-PIV tracer particles. Non-optical components of the liner are multi-holed angle cooled (i.e., effusion cooled) at an appropriate cooling flux with no additional thermal barrier coating. Honeywell will provide the dome/bulkhead and fuel injector with replaceable screw-on injector swirlers. In addition, Honeywell will fabricate the fuel injector and screw-on injector swirlers. A combination of proprietary and public-domain swirler configurations will be designed, fabricated, and tested. This effort should yield both publishable data and proprietary data that can directly translate to design improvements. The estimated design conditions are combustor inlet temperatures between 600 °F and 800 °F, combustor inlet pressures between 6 atm and 10 atm, a pressure drop of approximately 3%, a primary zone equivalence ratio of 1.2–1.8, and combustor exhaust temperatures of 2000–3000 °F.

Figure 6 shows the final design of the combustor. Fabrication is currently in progress.

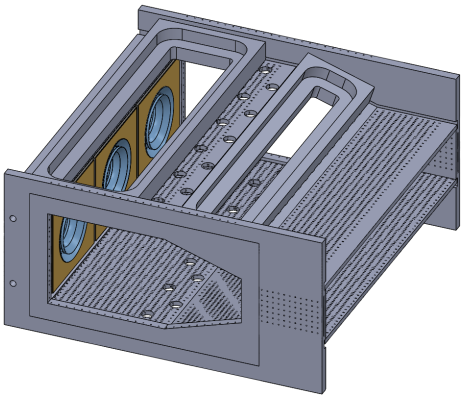

Figure 6. Rendering of the proposed combustor with three fuel injectors.

Another challenge in combustor design is the efficient cooling of liners and windows. To understand the thermal cooling effect of the current design, the Honeywell team conducted a CFD simulation of the entire high-pressure system including both the pressure vessel and combustor, with and without flames. The simulation was conducted with ANSYS FLUENT, by using a $k\varepsilon$ Reynolds-averaged Navier–Stokes (RANS) turbulence model, flamelet turbulent combustion model, soot and NO emission model, and discrete ordinate radiation model. Figure 7 shows the meshing of the simulation with 43.2 million polyhedral cells.

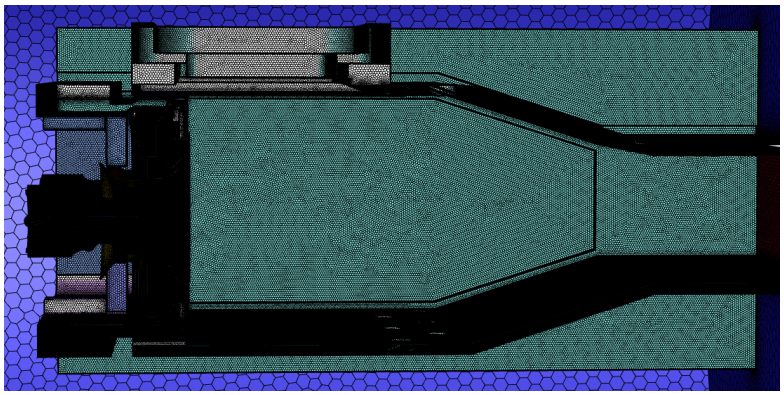

Figure 7. Meshing of the simulated combustor.

Because the combustor is symmetric, two cooling patterns were used: one with a single long slot (0.81 × 215 mm) at the top plate and the other with 48 small slots (1.2 × 3 mm) at the bottom plate. In this way, one simulation can evaluate two cooling patterns. The pressure of the combustor is 150 psi, and the hot air has a temperature of 900 °F. The air flow rate is 2.47 lb/s, and the flow rate of fuel is 223 lb/h. Figure 8 shows the static temperature contour, in degrees Fahrenheit, along the centerline of the combustor.

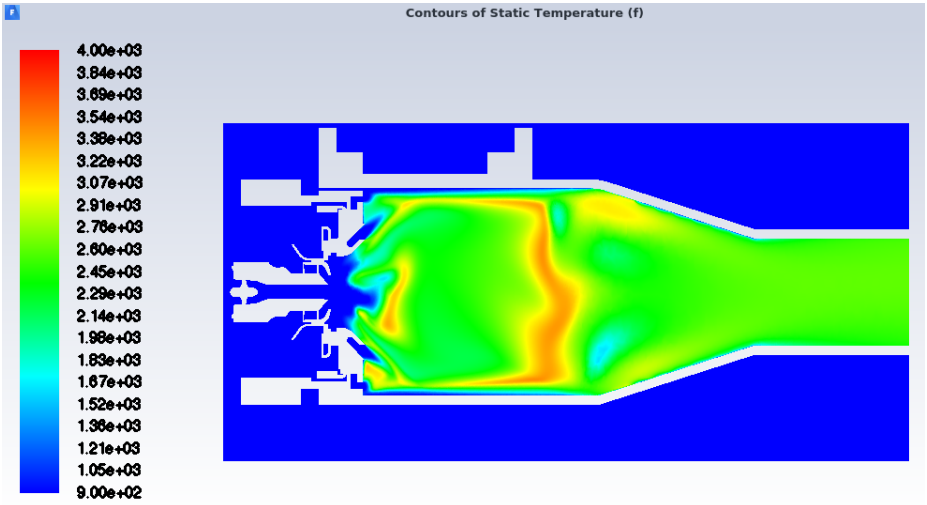

Figure 8. Contour of static temperature (°F) along the centerline of the combustor.

Based on the simulation results, we can identify potential hot spots that cause thermal severity and mechanical issues. Figure 9 shows the surface temperature of the combustor walls. From the results shown in Figure 9, several potential hot spots are located at the corner of the baseplate (combustor dome) where fuel injectors are mounted. The sidewall temperature is also high which may cause potential issues. Therefore, we added additional cooling holes along the edge of the baseplate and sidewall.

The simulation also indicated formation of soot (Figure 10) and NO (Figure 11) inside the combustor. The three cross-views in each figure represents the three center lines of three fuel injectors. It is clearly shown that the center fuel injector (with much less wall interaction) has different combustion properties, in terms of soot and NO formation. The simulation results confirmed that our change in combustor design from one fuel injector to three fuel injectors better mimics practical combustors in engines. With less artificial wall interaction, the soot formation is significantly greater from the combustion process.

Figure 12 shows the velocity profiles of window cooling film. In the simulation, we implemented two cooling patterns: one with a single long slot (0.81 × 215 mm) at the top plate and the other with 48 small slots (1.2 × 3 mm) at the bottom plate. The velocity profile from the single long slot is shown in Figure 12 (top), and the velocity profile from the 48 small slots is shown in Figure 12 (bottom). Interestingly, the two cooling patterns have essentially the same cooling effect, as supported by the very similar velocity profiles of cooling air at different locations. In consideration of possible air leakage and support of the combustor wall, we adopted the design with 48 small slots rather than the single long slot in the cooling holes at the combustor dome.

With the assistance of CFD simulation, our combustor design has been finalized.

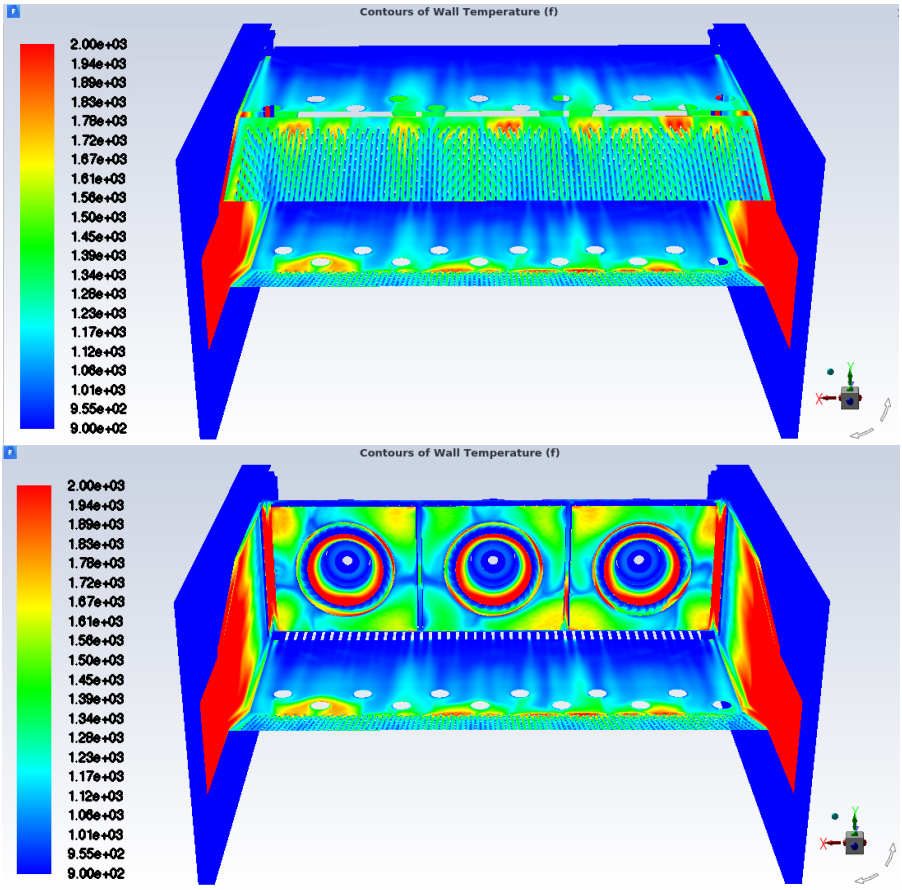

Figure 9. Contour of wall temperature (°F) of the liners (top) and baseplate and sidewall (bottom).

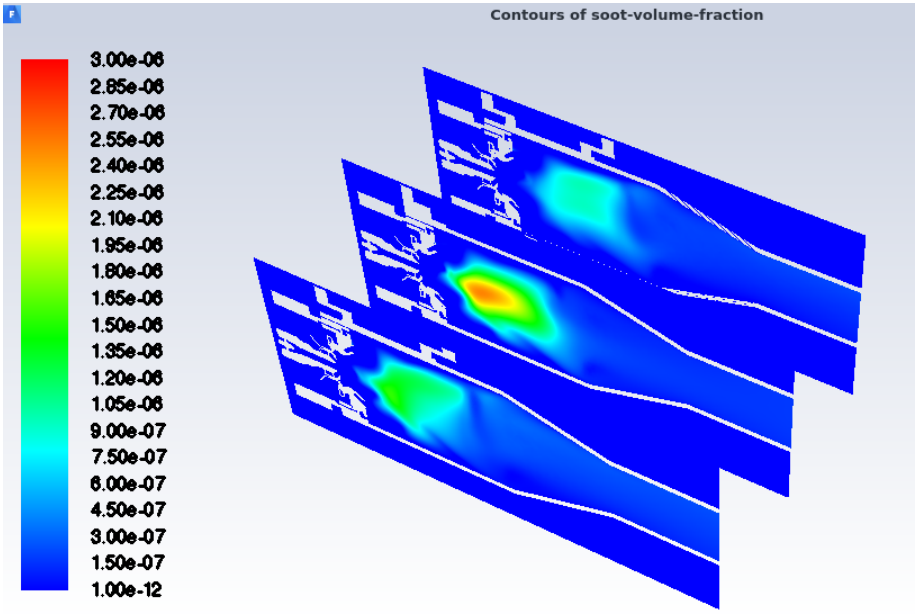

Figure 10. Contour of the soot volume fraction.

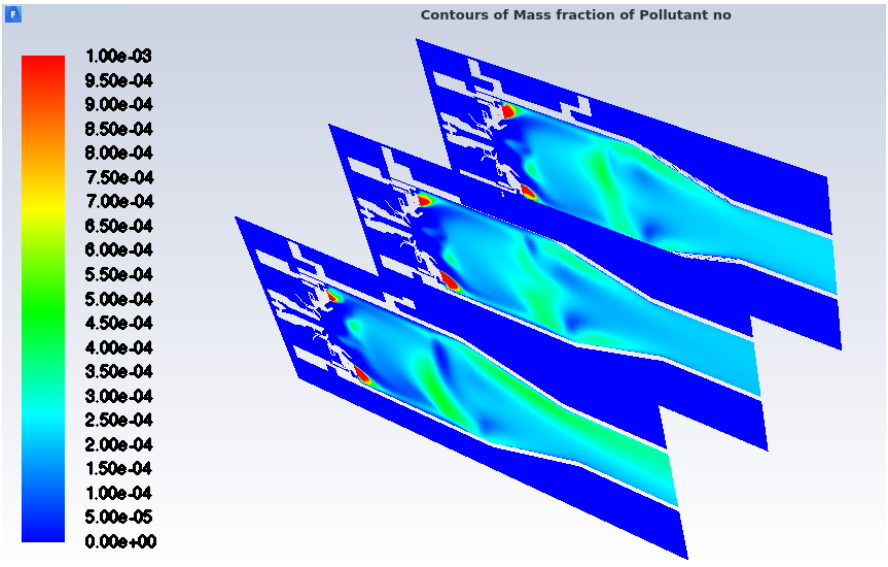

Figure 11. Contour of the mass fraction of NO.

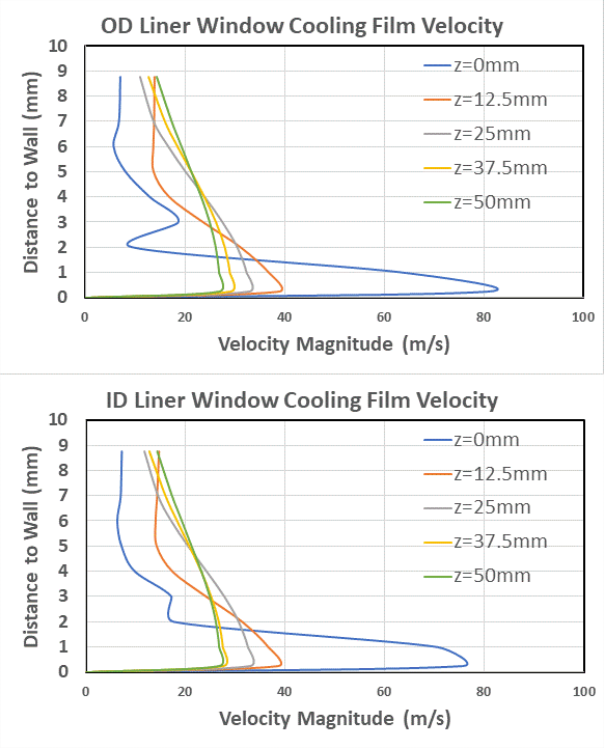

Figure 12. Velocity profiles of window cooling film of the long slot design (top) and multiple small cooling slots (bottom).

Milestone(s)

In the past year, five milestones were achieved:

1. Design and fabrication of the high-pressure vessel
2. Design of a unique combustor with three fuel injectors
3. CFD simulation of the designed combustor
4. Completion of the high-temperature, high-pressure air line final design
5. Completion of the liquid fuel supply system, GN2 pressurization, and purge system final design

Major Accomplishments

The major accomplishments of year 1 of this project include:

1. Design, fabrication, and delivery of the high-pressure vessel
2. Detailed design and CFD analysis of the combustor

Publications

None

Outreach Efforts

None

Awards

None

Student Involvement

Project 70 involves four graduate students (Jeremiah Jeurgensmeyer, Sundar Manikandan, Ezekiel Bugay, and Russell McGrath) and one research engineer (Henry Ballance).

Plans for Next Period

In the next year, our main goals are to (1) complete the fabrication of the designed combustor, (2) assemble the high pressure system, (3) conduct detailed optical measurements related to nvPM formation, and (4) conduct detailed CFD simulations and validate models according to experimental results.

Project 071 Predictive Simulation of nvPM Emissions in Aircraft Combustors

Georgia Institute of Technology

Project Lead Investigator

Suresh Menon, Professor
School of Aerospace Engineering
Georgia Institute of Technology
270 Ferst Drive, Atlanta, GA 30332-0150
(404) 894-9126
suresh.menon@aerospace.gatech.edu

University Participants

Georgia Institute of Technology

- PI: Dr. Suresh Menon
- FAA Award Number: 13-C-AJFE-GIT-067
- Period of Performance: October 1, 2020 to September 30, 2022
- Overall Task(s):
    1. **Kinetics** Modeling: Improvements in soot kinetic model to predict development of polycyclic aromatic hydrocarbon (PAH) pathways in representative sooting fuels.
    2. **Nucleation Modeling**- Simulation of PAH rings at a range of relevant flame temperatures to identify key species contributing to soot nucleation process.
    3. **Surface Growth and Aggregation Modeling** - Reaction-transport-limited growth of soot particles models for cluster–cluster aggregation
    4. **Large-Eddy Simulations (LES)**- coupling the multi-scale models developed in Tasks 1-3 in a method of moment LES method for soot–turbulence–chemistry interactions with application to canonical flames

Project Funding Level

Current FAA funding is for a 2-year effort (July 2020 to September 2022), with a request of $500,000 per year from ASCENT (per year). Additional funding for year 3 is requested. Cost share is provided by:

- Georgia Tech provides cost-sharing for their share of $150,000 per year. The Georgia Tech point of contact is Kevin Ellis (kevin.ellis@aerospace.gatech.edu).
- Raytheon Technologies Research Center (RTRC) provides cost-sharing of $250,000 per year. Dr. Colket is a consultant in this project with many years of experience in soot modeling. The RTRC contact is John LaSpada (LaSpadJW@RTRC.utc.com).
- UM provides cost-sharing in the amount of $100,000 per year. The UM point of contact is Alexandra Thebaud (thealexi@umich.edu).

Investigation Team

- Dr. Suresh Menon, Georgia Tech: PI, Task 4
- Dr. Miad Yazdani, Raytheon Technologies Research Center (RTRC): Co-PI, Task 3
- Dr. Steve Zeppieri, RTRC: Co-PI, Task 1
- Prof. Angela Violi, UM: Co-PI, Task 2
- Dr. Meredith (Med) Colket, Consultant, RTRC: Co-Investigator, Task 1

Project Overview

This project is being used to establish a new multiscale approach to predict soot formation in aircraft combustors. A hierarchy of first-principles simulation methods are being used to account for the multiscale physics of the formation and transport of non-volatile particulate matter (nvPM, also called soot in the literature). The final objective is to use this multiscale approach to model these physics as models in large-eddy simulations (LES) of realistic gas turbine combustors. We target and isolate the layers of empiricisms that currently exist, in for example, particle inception models, the role of precursor species in nucleation, the particle shape assumptions and their impact on surface growth, the sensitivity of predictions to particle size distribution and the ad hoc coagulation/coalescence mechanisms. The team already has all the modeling tools, but a systematic coupling of these tools in a multiscale, multi-physics strategy has yet to be accomplished by any research group. Hence, this study will establish a new predictive capability by integrating these capabilities.

The multiscale and multi-physics layers of collaborations among the cost-sharing groups are summarized in Figure 1 and briefly described herein. The kinetics group at RTRC is conducting a study to understand the role of gas-phase kinetics in predicting important species potentially labeled as soot precursors. The information on reduced kinetics from RTRC is being used by Georgia Tech and UM to evaluate LES performance and the process of nucleation. In the UM study, the propensity of gas-phase species to form dimers (considered the building blocks of soot inception) under flame conditions is being studied. Identification of soot precursors and the rates of formation of soot nuclei will be the output from these studies. This nucleation rate will be provided to Georgia Tech to update the source terms associated with nucleation processes in six-moment approach of method of moment with interpolative coefficients (MOMIC), and the information on the structures of these soot nuclei will be provided to RTRC for modeling of surface growth and aggregation processes. Outputs from the aggregation studies in RTRC in the form of global surface growth and aggregation models will then be fed back to Georgia Tech to update the source term surface growth and aggregation models in the 6-MOMIC approach. Canonical studies are underway at Georgia Tech to provide information regarding the variations in local conditions, such as pressure, temperature, and local equivalence ratios due to turbulence–chemistry interactions; this information should be useful in each stage of the abovementioned studies. LES studies at Georgia Tech will also involve modeling the effects of chemistry–soot–turbulence interactions by using advanced subgrid models including the linear eddy mixing (LEM) model. As a project deliverable (at the end of this research effort), the final assessment of both the existing soot model and the improved soot model will be conducted in canonical flame configurations.

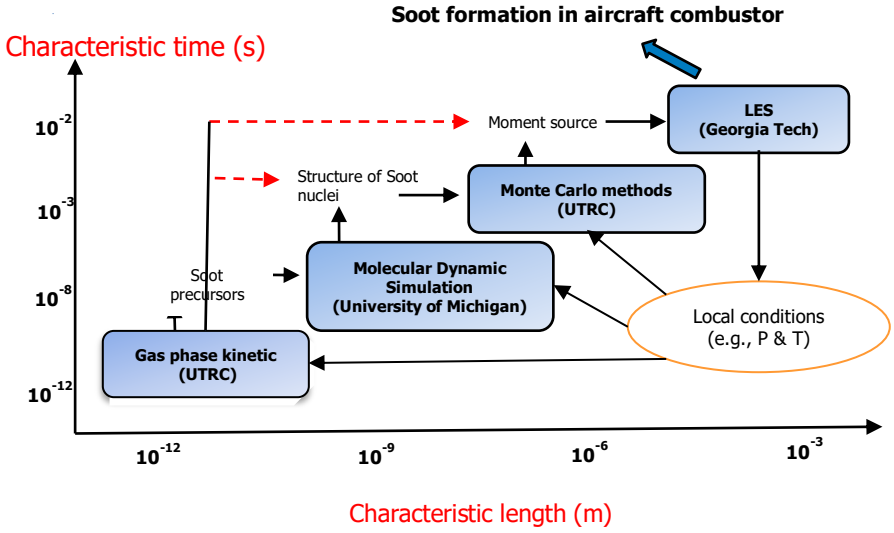

Figure 1. Multiscale collaborative efforts to improve nvPM (soot) predictions.

In the previous report, an overview of all modeling tools and the collaborative efforts to assess inputs and outputs from the analysis at each stage were highlighted, and basic validation and verification were performed to establish capabilities. In the current annual report (for fiscal year 2021), the progress at each stage is briefly described, with particular attention paid to

the main objective of building on the existing approaches for soot modeling and assessing the improvements that could be achieved in each aspect. Key work accomplished by each group is highlighted as separate tasks.

Task 1 - Kinetics Modeling

Raytheon Technologies Research Center

Objective(s)

The objectives of this task are to develop validated detailed and reduced chemical kinetic models of parent fuel decomposition and oxidation reactions, with a special focus on fuel rich chemistry, to enable the accurate evolution of PAH/soot precursor formation and incipient soot particle formation, and the evaluation and improvement of reduced-order soot formation models. Year 1 fuel activities are focused on ethene, and year 2 efforts will focus on Jet-A fuel.

Research Approach

Reduced-Order Soot Model Development

Previous research using canonical datasets (e.g., flow reactor, shock tube, and well-stirred reactor) of ethene oxidation and pyrolysis systems has indicated that, among the published detailed ethene kinetic mechanisms, that of Frenklach (2002) showed the best agreement with the experimental data. Accordingly, that mechanism (101 species and 544 reactions) was chosen for further evaluation against the experimental fuel rich well-stirred reactor studies performed at the Air Force Research Laboratory (AFRL). The skeletal ethene mechanism of Lu and Law (2005) (33 species and 206 reactions) was selected as a reference reduced-order model against which to compare the detailed model. Both mechanisms were coupled to separate particulate formation analysis methods for comparison against experimental soot measurements. The detailed kinetic model used the method of moments soot algorithms, and the reduced chemistry model used the Lindstedt reduced-order soot formation model. The goals of this comparison were to access the viability and limitations of a reduced-order model against detailed PM model results, and to ascertain whether “parameter tweaking” of the reduced model allowed for improved agreement in subsequent computational fluid dynamics (CFD) analysis.

The experimental well-stirred reactor was modeled with the Chemkin perfectly stirred reactor (PSR) code. The test conditions associated with the experiments were 1 atm pressure, reactor residence times of approximately 8.5 milliseconds, and a range of fuel–air equivalence ratios from 1.9 to 2.5. Comparisons of peak reactor temperature and acetylene (C_2H_2) and oxygen (O_2) mole fractions between the detailed and reduced models were 10 K, 30%, and 20%, respectively. These are key parameters used in the soot formation models, as shown in Figure 2.

As shown, acetylene is the key species responsible for soot particle inception and surface growth reactions, and molecular oxygen is the key species for soot oxidation. To close the Lindstedt model (Leung et al., 1991), certain parameters must be defined. The list of these parameters and the values of the parameters recommended by Lindstedt are shown in Figure 3. Because experimental well-stirred reactor data were simulated, the parameter values in the rightmost column for a turbulent system were used.

Lindstedt Soot Model

	Process:	Mass Fraction Rate:	Particle Density Rate:
Inception:	$C_2H_2 \rightarrow 2C_s + H_2$	$R_1 = 2k_1(T)\,[C_2H_2]\,M_s$	$R_4 = \frac{2}{C_{min}} N_A k_1(T)\,[C_2H_2]$
Surface Growth & Oxidation:	$C_2H_2 + nC_s \rightarrow (n+2)C_s + H_2$	$R_2 = 2k_2(T)\,f(S)\,[C_2H_2]\,M_s$	
	$C_s + \frac{1}{2}O_2 \rightarrow CO$	$R_3 = k_3(T)\,S\,[O_2]\,M_s$	
Coagulation:	$nC(s) \rightarrow C_n(s)$		$R_5 = 2C_a\sqrt{d_p}\left(\frac{6\kappa T}{\rho_s}\right)^{1/2}(\rho Y_N)^2$

$k_i = A_i T^{b_i} e^{-E_i/RT}$

S = soot surface area, f(S) ~ $S^{1/2}$

$$\left.\begin{aligned} S &= \pi d_p^2 \rho Y_N \\ d_p &= \left(\frac{6}{\pi}\frac{Y_s}{\rho_s Y_N}\right)^{1/3} \end{aligned}\right\} \Rightarrow S = \pi\left(\frac{6}{\pi\rho_s Y_N}\right)^{2/3} Y_s^{2/3}\rho Y_N$$

Figure 2. Description of the various processes in the Lindstedt soot formation model.

	Fitting Parameters Utilized in Model:	Orig Paper	Second paper
		Laminar Nonpremixed	Turbulent, CrossFlow
		C&F,1987	C&F,1989
Ca	Coagulation Constant	9	3
Cs	# Carbons in Incipient Soot Particle	100	9000
k1-nucleation	A1	10000	1350000
	Ea1/R	21100	20634
k2-surface growth	A2	6000	500
	Ea2/R	12100	12079
k3-oxidation	A3	10000	17800
	n3	0.5	0.5
	Ea3/R	19680	19628

Figure 3. List of fitting parameters in the Lindstedt model and associated values.

A comparison between the experimental data (left side of Figure 4) and the simulation (right side of Figure 4) reveals that the models reasonably represent the order of magnitude of peak soot concentration. The method of moments results better capture the experimental trend of the concentration versus equivalence ratio. The Lindstedt models do not have the correct experimental trend of soot concentration versus equivalence ratio, and the trends are too broad. However, by adjusting the rates associated with the inception and surface growth reactions associated with the model, the equivalence ratio sensitivity to the equivalence ratio is improved. Specifically, the rates associated with each process are set to constant values. These improved results are shown in Figure 5.

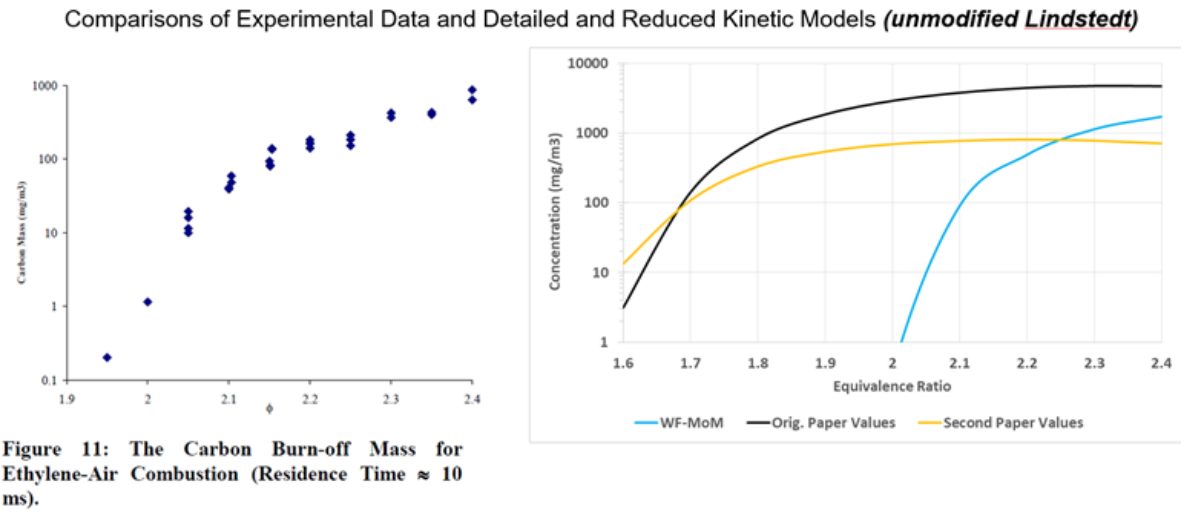

Figure 11: The Carbon Burn-off Mass for Ethylene-Air Combustion (Residence Time ≈ 10 ms).

Figure 4. Comparison of experimental and simulation reactor soot concentration values for the rich ethene AFRL studies.

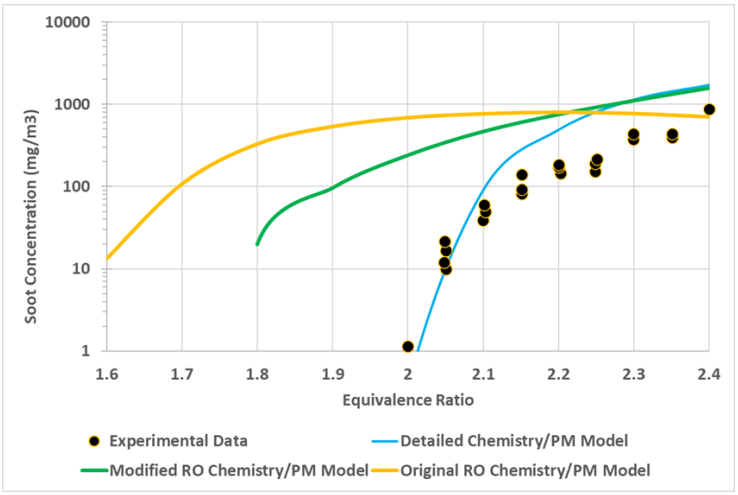

Figure 5. Comparison of experimental and simulation reactor soot concentration values for the rich ethene AFRL studies.

Reduced Kinetic Model Development

An additional task has been to develop a reduced chemical kinetic mechanism for ethene that is sufficiently compact (~25 species) to be used in CFD applications, and contains PAH-related species, such as benzene, naphthalene, and pyrene. These single-ring and multiring aromatic compounds are key soot precursors. Direct calculations within the flow field will enable more detailed physics-based soot inception/growth and transport companion efforts within this project to resolve soot chemistry and physics more accurately.

Mechanism reduction was based on the computer aided mechanism reduction (CARM) technique described by Chen (1988). The Wang-Frenklach detailed mechanism is the input to the CARM tool. A series of Chemkin PSR simulations over a range of parameter space (e.g., pressure, equivalence ratio, and residence time) are computed by using the detailed mechanism. CARM then analyzes these data to determine a prescribed number of species that may be formulated to be in "quasi-steady state" and thus removed from tracking within the reduced kinetic model. An overview of this approach is shown in Figure 6.

CARM* Software Automatically Determines/Generates Necessary Steady State Species Expressions Using Detailed Mechanism Results

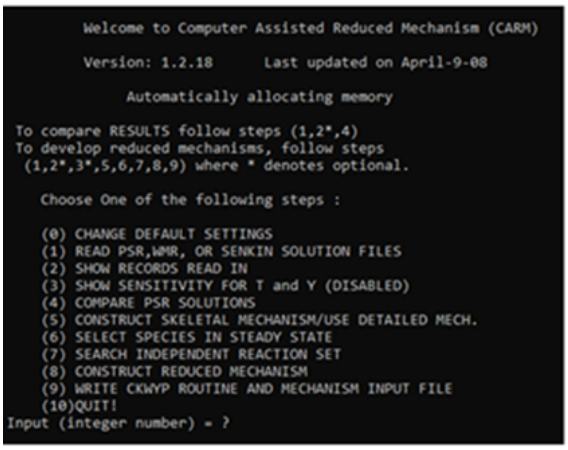

Detailed Model Employed: Wang-Frenklach (98 species/531 reactions)

Target Data Used: PSR Solutions associated with UDRI Reactor Conditions (Φ: 1.9-2.5, 1 atm, τ_{res}: ~8.5 msec)

Goal Outcome: Reduced Mechanism with ~ 25 species, including PAH's (i.e., benzene, naphthalene, pyrene)

Figure 6. Use of CARM and the detailed kinetic mechanism to generate a reduced mechanism.

CARM uses the detailed reactor solutions over the range of target data to rank the errors associated with the quasi-steady-state assumption for each species. After this ranking is established, the number of species sought to be retained in the reduced kinetic model is selected. The code then establishes polynomial based expressions for the non-active species' quasi-steady-state compositional values over the range of target data used. With the above target data, three reduced mechanisms were assembled for comparison against the above AFRL rich ethylene well-stirred-reactor experiments. These mechanisms are shown in Figure 7. These mechanisms were then employed with modified versions of the Chemkin PSR code to compare against the results of both the detailed Wang-Frenklach and reduced Lu mechanisms. Comparisons of major rich products and PAH species are shown in Figures 8 and 9, respectively.

Red. Mech.	Detailed Solutions Used in Build	Phi Range of Detailed Solutions	# Species in Red. Mech.
1	18	1.0-2.5	24
2	10	1.1-2.4	24
3	10	1.9-2.4	23

Figure 7. List of developed reduced mechanisms.

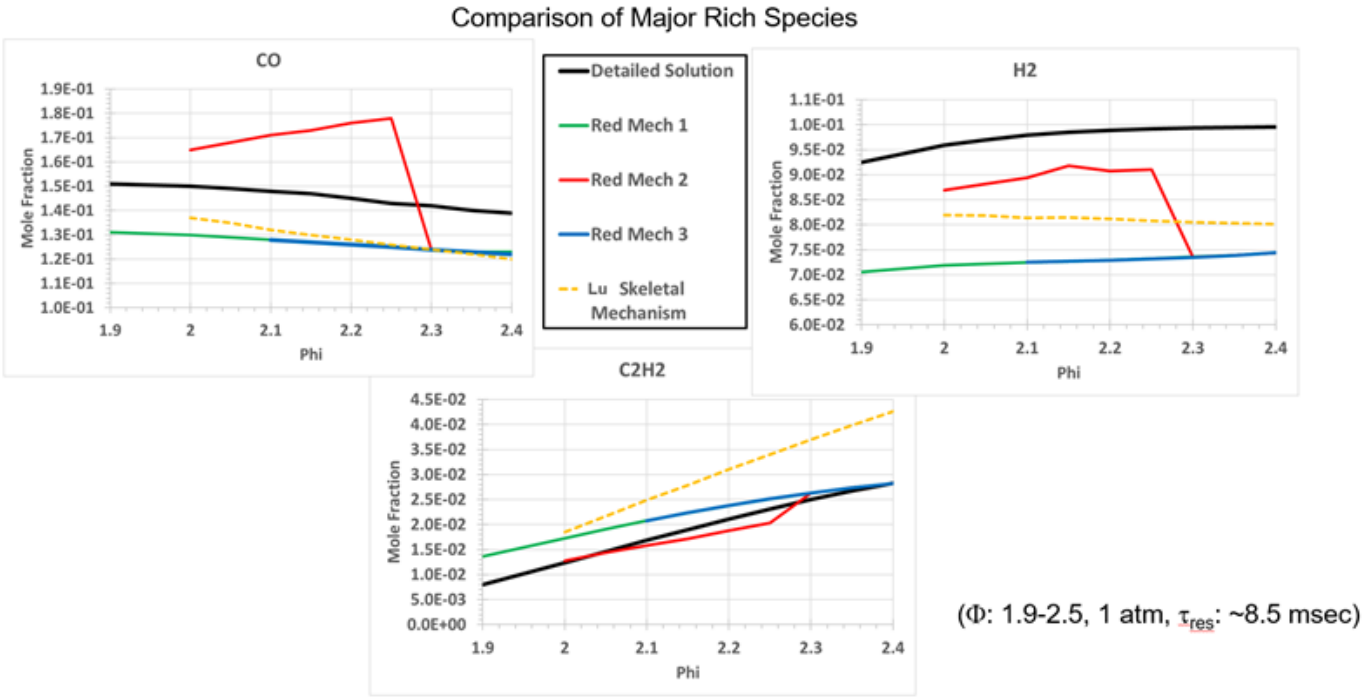

Figure 8. Comparison of major rich species for several Employed mechanisms.

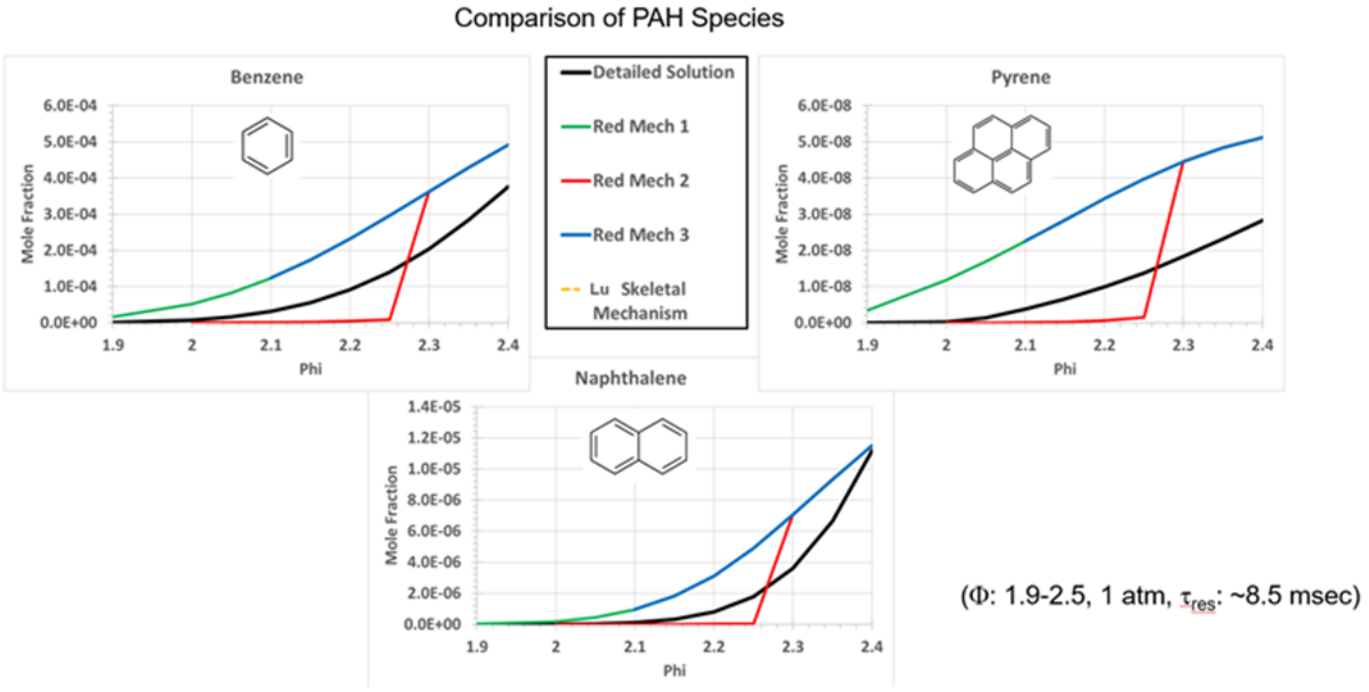

Figure 9. Comparison of PAH species for several Employed mechanisms.

As shown in Figures 8 and 9, of the three developed reduced mechanisms, the first (Red Mech 1) appears to yield the best agreement with respect to the detailed mechanism results. Its results for the rich species are comparable to those of the Lu reduced mechanism. Both give similar agreement for CO, the Lu mechanism yields slightly better H_2 values, and the current reduced model yields better C_2H_2 values. More importantly, the current reduced model better matches the PAH species associated with the detailed kinetic model than the Lu model (Lu & Law, 2005), simply because the current model is the first reduced mechanism to explicitly contain these PAH-related species.

Next Steps

Methods to better anchor the reduced-order Lindstedt soot model to experimental data will continue to be used and implemented. Analysis and construction methods to develop reduced kinetic models yielding better agreement with the detailed kinetic model results, while retaining necessary PAH species in the active species list, will also continue.

Task 2 – Nucleation Modeling

University of Michigan

Objective(s)

The objective of this task is to develop model(s) for nanoparticle inception, a critical step in predicting emissions. This effort bridges the work on gas-phase chemistry (RTRC) with the model for particle growth (RTRC) and provides inputs for the MOMIC model (GT).

Research Approach

Current models for particle inception are unable to reproduce a variety of experimental data, including molecular structure. This work aims at developing a predictive model for particle inception that can provide accurate chemical and physical growth pathways for PAHs. Molecular dynamics (MD) simulations are used to study the collisions of PAHs and the formation of aromatic dimers leading to soot inception.

These atomistic simulations coupled with advanced sampling techniques are used to study the collisions of PAHs. Free energy calculations provide information on the effect of chemical structure and shape on the tendency to form nuclei. In this quarterly effort, after collaboration with RTRC, PAHs that are critical to inception are identified. A pool of aromatic compounds, such as pyrene, benzopyrene, coronene, ovalene, and circumcoronene, are selected. Some preliminary studies for free energy calculations are conducted at temperatures of 500 K and 1000 K. As shown in Figure 3, at lower temperatures, all PAHs appear to form dimers, although dimer formation by higher PAH rings is more favorable. However, at the higher temperature of 1000 K (typical of flame temperature conditions), only higher PAHs tend to form dimers. This finding suggests that the nucleation model from traditional pyrene precursors does not capture the actual soot inception processes. Some of these MD simulation results have been highlighted by Saldinger et al. (2021).

The current focus is to include additional effects of the shape and chemical composition of PAHs on dimer formation and stability. Preliminary analyses have suggested that the addition of aliphatic chains and oxygen radicals facilitates dimer formation, in terms of the free energy of pyrene molecules. Further steps are underway to include the higher hydrocarbons because dimer stability has been observed to increase with heavier monomers. This investigation will involve close feedback regarding kinetics studies at RTRC, so that the kinetic mechanism is modified in parallel. After the key precursors are identified, the collision rates of these dimers will provide insights into the soot nucleation rates, which can be fed into the GT studies. In addition, the structure of soot nuclei can be used by RTRC to further conduct analysis of soot surface growth.

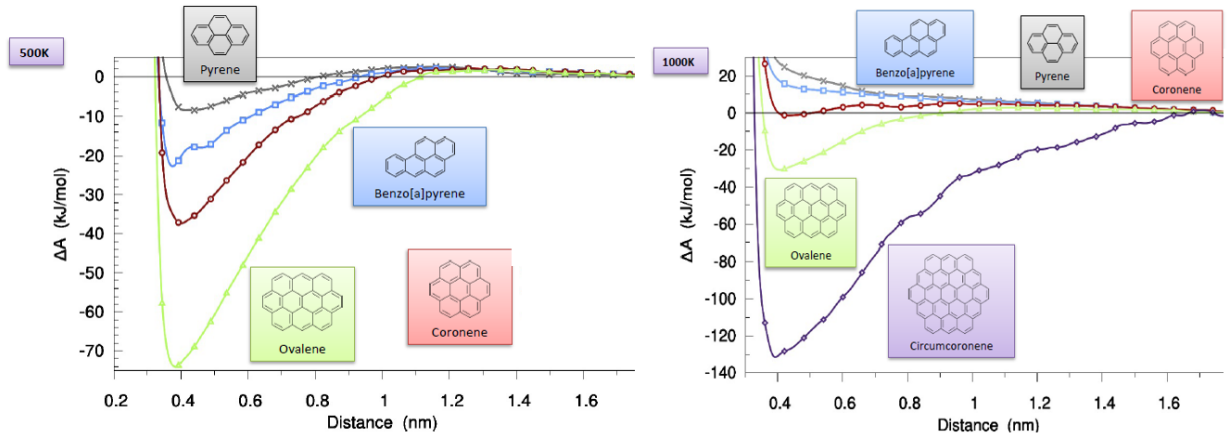

Figure 10. Free energy calculations of PAHs as a function of temperature.

Task 3 - Surface Growth and Aggregation Modeling

Raytheon Technologies Research Center

Objective

The objective is to develop a physics-based framework for the prediction of soot particle growth after the inception process. The growth consists of agglomeration due to collisions between the primary particles and surface growth as a result of direct deposition of the precursors on the aggregate. The final aggregate fractal structure and its temporal evolution as a function of local conditions are of interest. This model will provide the morphology characteristics and the growth rate of the particles as inputs into the MOMIC formulation.

Research Approach

The approach consists of addressing the agglomeration process through diffusion Monte Carlo (DMC) simulation and the growth process through the phase-field method (PFM) simulation. In addition, the transition from a kinetic-limited reaction to a transport-limited reaction as the particle grows will be addressed through matched asymptotic expansion of the coupled concentration/phase-field equation system. The details are provided below.

Agglomeration

The agglomeration of primary particles that leads to the formation of soot is simulated through the DMC approach. Here, the concentration of the primary particles is associated with the concentration of background precursors:

$$\frac{Dc}{Dt} = \frac{\partial c}{\partial t} + \mathbf{u} \cdot \boldsymbol{\nabla} \mathbf{c} = D(p,T)\nabla^2 c + S_a$$

The number density and size distribution of the primary particles are expected to be provided by the MD simulation of the nucleation process. The generated primary particles then go through a random walk according to the background concentration field:

$$P(x',\, t'|x,t) = \frac{1}{\left(4\pi(t'-t)\right)^{d/2}} \exp\left(-\frac{(x'-x)^2}{4D(p,T)(t'-t)}\right)$$

where the diffusivity, $D(p,T)$ is expected to be provided by parametrization of the LES solution. The collision frequency is calculated through $\Delta t = \frac{1}{\beta N}$. After aggregation, the local concentration field is depleted to account for the removal of the

primary particles through aggregation. The depletion is modeled by the addition of a space-dependent sink term in the diffusion equation.

Surface Growth
Surface growth due to direct deposition of background precursors to the cluster is simulated through the PFM. According to the principle of free energy minimization, the phase field, Φ, is effectively a color function for tracking the "deposited" phase. The PFM can ultimately be reduced to the following coupled transport equations (Sun & Beckermann, 2007; Xu & Meakin, 2008):

$$\tau\frac{\partial\phi}{\partial t}=\left\{\varepsilon^2\nabla^2\phi-\frac{\partial f_1}{\partial\phi}-\lambda c\frac{\partial f_2}{\partial\phi}\right\}-\varepsilon^2|\nabla\phi|\kappa,$$

$$\frac{\partial c}{\partial t}=D\nabla^2 c+\frac{1}{2bk_c}\frac{\partial\phi}{\partial t}\left(1+\frac{D\nabla^2\phi-\partial\phi/\partial t}{k|\nabla\phi|}\right).$$

where:

$f_1(\phi)=-\frac{\phi^2}{2}+\frac{\phi^4}{4}$
$f_2(\phi)=\phi-\frac{\phi^3}{3}$
λ: coupling parameter
K: reaction rate
K_c: stoichiometric reaction rate, k_c = O(1)
b = C_s/rho

The formulation for reaction-rate, K, will be linked to whether the growth is kinetic limited or transport limited.

In general, whereas the aggregation results in fractal-looking structures, the surface growth tends to smooth the structure toward spherical-looking structures. The competition between these two mechanisms drives the ultimate morphology of the cluster. Notably, in the context of an integrated simulation framework, the "deposited phase," Φ, is effectively the same as the aggregated phase tracked in the DMC framework.

This integrated DMC/PFM framework is envisioned to be used to parametrically determine the evolution of cluster morphology as a function of local conditions (provided by the MD and LES frameworks). For example, Figure 11 shows the evolution of the fractal dimension and degree of surface anisotropy as a function of the background precursor concentration (i.e., equivalence ratio). The fractal dimension, D_f, is defined through the following:

$$n_p=\left(\frac{r_g}{r_p}\right)^{D_f};mr_g^2=\sum_{n_p}m_{p,i}r_i^2$$

where n_p is the number of primary particles in the cluster, and r_g and r_i correspond to the radius of gyration for the cluster and the radii of individual primary particles, respectively. The degree of anisotropy, A_{ij}, is defined through:

$$A_{ij}=\frac{R_i^2}{R_j^2},\ R_i>R_j..$$

where R_i is the principal radius of gyration (eigenvalue of MOI tensor). Figure 11 shows that as the equivalence ratio increases, the cluster tends to become more spherical, as indicated by increasing D_f and decreasing A_{ij}, in agreement with literature observations (Kireeva et al., 2009; Slowik et al., 2007), as shown in Figure 11.

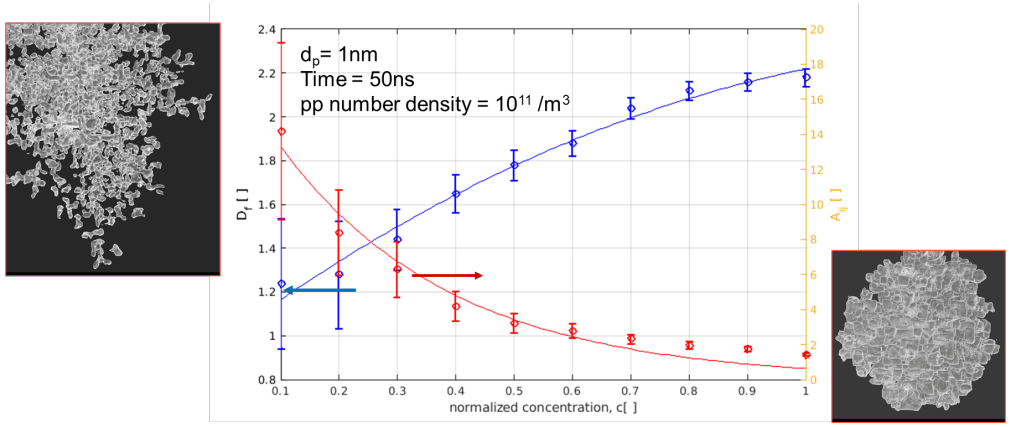

Figure 11. Variations in fractal dimension, D_f, and degree of anisotropy, A_{ij}, with background precursor concentration.

In another example, the evolution of the cluster morphology as function of primary particles number density is shown in Figure 12.

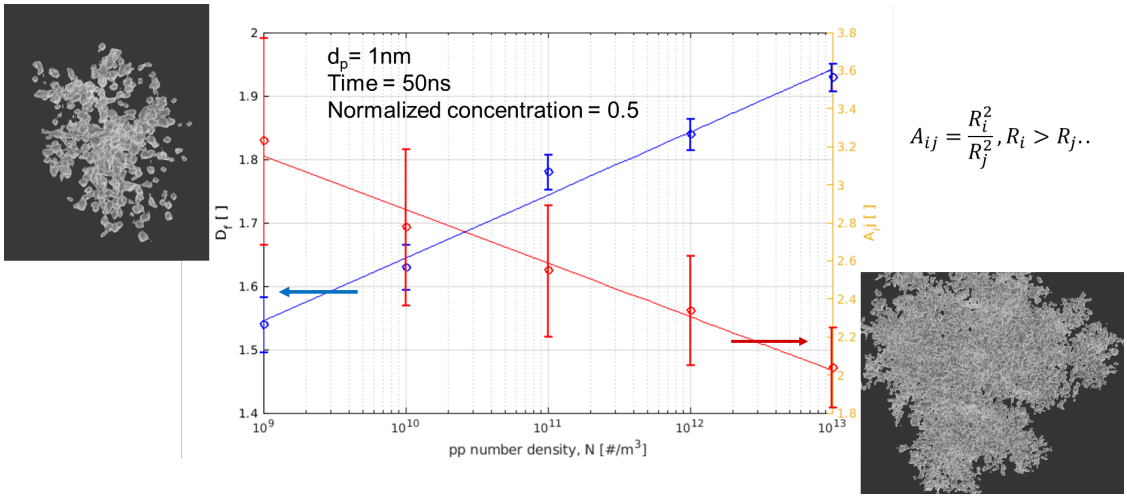

Figure 12. Variation of fractal dimension, D_f and degree of anisotropy, A_{ij} with number density of primary particles.

Although the cluster generally tends to be more symmetric and less fractal with increasing the primary particle number density, the variation tends to occur in a narrower range than the effect of precursor concentration.

Another important consideration is the role of short-range forces on the dynamics of aggregation. In classical DMC (Balthasar & Franklach, 2005; Mitchell & Franklach, 1998) the roles of short-term forces on the collision dynamics are often neglected. The collision probability is likely to be overestimated when those forces are repulsive and underestimated when the forces become attractive. Therefore, a simple force analysis is incorporated into the DMC framework to account for the short-range forces on particle trajectory and ultimately their aggregation behavior. In this approach, the Langevin motion equation is revised as follows:

$$\frac{dm\mathbf{u}}{dt} = -m\beta\mathbf{u} + \mathbf{f};\ \langle \mathbf{f^2} \rangle = 2\beta k_B T$$

The total stochastic force can now be decomposed into all relevant forces, pre-collision:

$$\mathbf{f} = \mathbf{f_{stoch}} + \mathbf{f_{VDW}} + \mathbf{f_e};\ \boldsymbol{S} < \boldsymbol{S_{crit}}$$

The Van der Walls force, f_{VDW}, is estimated through simple Hamaker approximation:

$$\mathbf{f_{VDW}} = \frac{\mathrm{A_H} d_p}{2S^2}\hat{\mathbf{S}}$$

where d_p is the size of the particle, S is the distance between the particle and the aggregate, and A_H is the Hamaker constant (here, the value of A_H is 2.5 eV, corresponding to graphene–graphene interaction). The electrostatic force is approximated through the following:

$$\mathbf{f_e} = -\frac{1}{4\pi\epsilon}\frac{q_p q_c}{S^2}\hat{\mathbf{S}}$$

where q_c and q_p correspond to the charge density on the cluster and the primary particles, respectively. The approximation to this charge distribution is perhaps the weakest link in this approach and is expected to be more rigorous in the future. The charge distribution is approximated through empirical calculation of a correlation between the soot particles and measured charge density on the particles.

Inclusion of short-term forces substantially slows the progression from fractal to spherical morphology. For example, increasing precursor concentration tends to increase the fractal dimension but at a significantly slower rate than in the scenario in which those forces are neglected (Figure 13; triangles correspond to a dataset with short-term forces accounted for).

Blended Reaction

As noted previously, the reaction term in the PFM depends on whether the growth is kinetic-limited or transport-limited. In the former, the reaction rate is simply proportional to the size of the cluster:

$$r(t^n) = r(t^{n-1}) + \mathrm{k}\Delta t$$

Here, k is the reaction constant in units of m/s. In contrast, in a transport-limited regime, the growth also depends on background thermodynamic conditions (e.g., P and T). For the model to automatically transition from kinetic-limited to transport-limited growth, the phase-field formulation is recast with the coupling parameter, λ, now a function of cluster diameter, with the limit of the diameter approaching infinity. In the opposite limit, the reaction is assumed to reduce to a kinetic-limited regime:

$$\frac{dr}{dt} = K; r \to 0,\quad \frac{\tau\partial\Phi}{\partial t} = \epsilon^2\nabla^2\Phi - \frac{\partial f_1}{\partial\Phi} - \lambda(d)c\frac{\partial f_2}{\partial\Phi} - c^2|\nabla\Phi|k; r \to \infty$$

A matched asymptotic approach would lead to the following expression for $\lambda(d)$:

$$\lambda = \frac{d^3 c_\infty P}{K_B T\left(1 + \frac{dK}{D}\right)^{1+\frac{n}{2}}}$$

where P and T are background pressure and temperature, and c_∞ is the background concentration. This equation effectively determines the extent of coupling between the concertation field and the deposition field, which in turn determines the growth rate of the cluster. For example, at a temperature of 2000 K, the coupling parameter is plotted against the cluster diameter (normalized by mean-free-path length, l_{mft}, at the corresponding temperature and pressure) for different reaction constants in Figure 15.

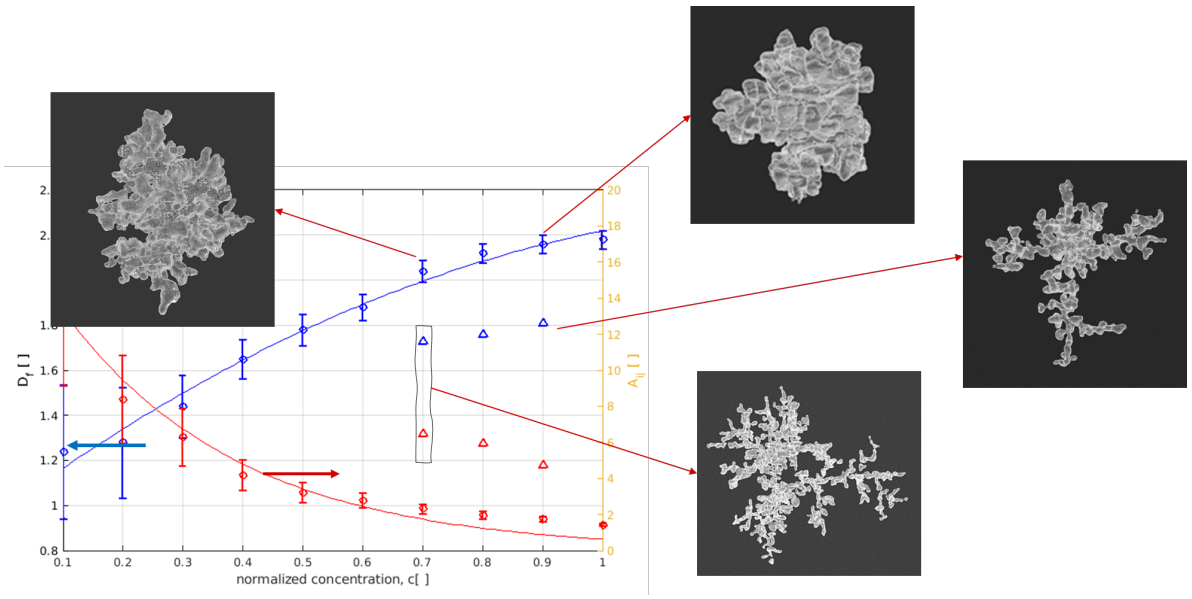

Figure 13. Variations in fractal dimension, D_f, and degree of anisotropy, A_{ij}, with background precursor concentration when short-range forces in the collision process are accounted for (triangles) vs. ignored (circles).

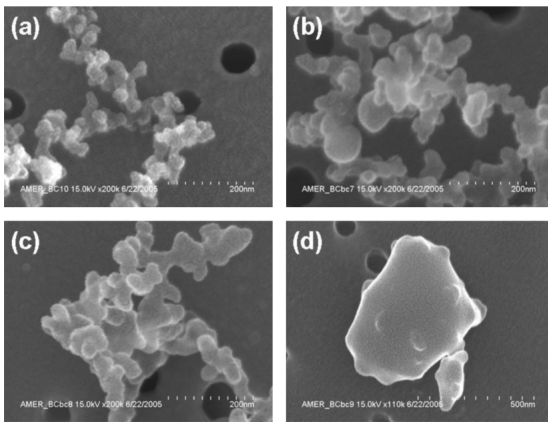

Figure 14. Scanning electron microscope (SEM) images of soot at four different equivalence ratios: ϕ = 2.3 (a), ϕ = 2.8 (b), ϕ = 3.5 (c), and ϕ = 5.0 (d).

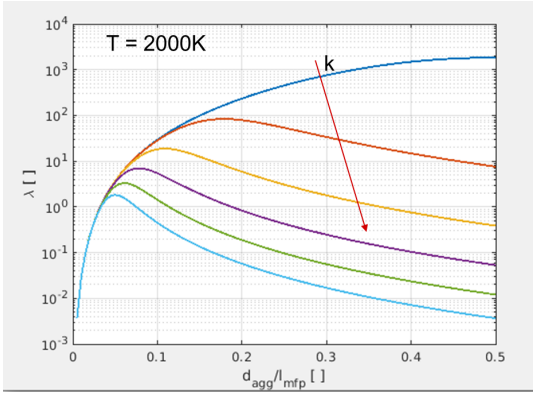

Figure 15. Variations in the coupling parameter in the PFM formulation as a function of aggregate size.

At small reaction constants, the growth consistently approaches that of transport-limited growth (strong coupling), whereas with sufficiently large reaction constants, the maximum coupling occurs at some small diameters, and the growth begins to recede back to that in the kinetic-limited regime.

Interestingly, particle growth is affected by shifting reaction regimes. Figure 16 shows the variations in particle morphology with time for non-dimensional reaction constant K_r (= K/K_c) = 0.01 as well as the ultimate fractal characteristics. The results indicate that the particles become consistently more spherical over time as the particle size (diameter) grows. However, at a larger reaction constant of K_r = 0.05 (Figure 17), a different trend is observed, and the fractal dimension peaks at $d_{agg} \approx 3$ nm and then starts to precipitously drop, thus indicating the dominance of kinetic-limited growth. Although this scenario might very well be only hypothetical, illustrating the evolution of the particle morphology under these regimes is nonetheless interesting.

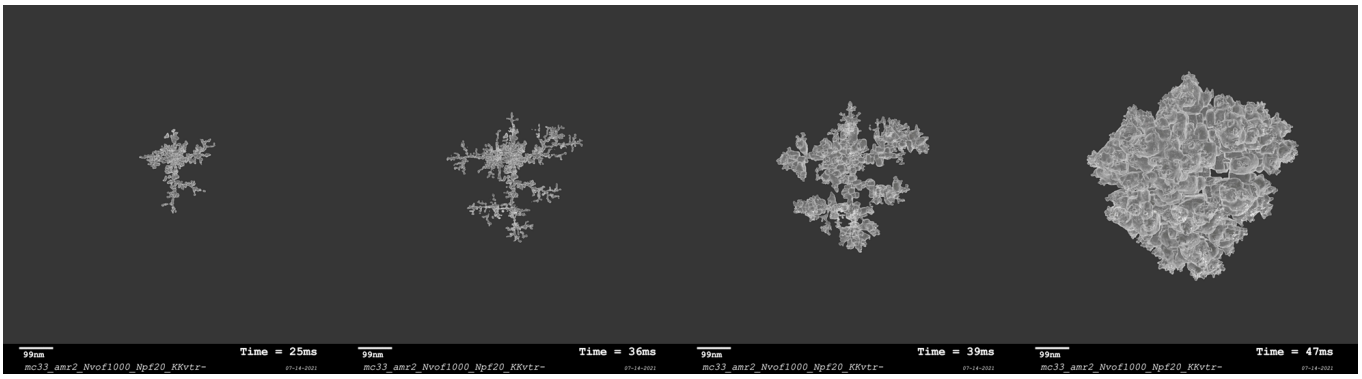

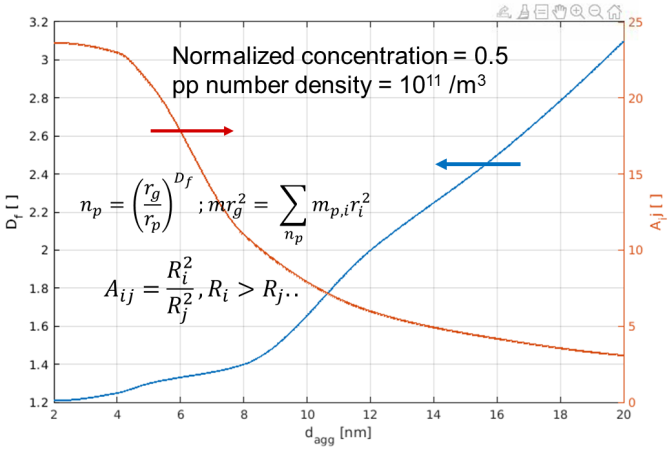

Figure 16. Snapshot of particle morphology at subsequent stages of growth (top), and variations in particle morphology with size (or time), with blended growth formulation with $K_r = 0.01$ (bottom).

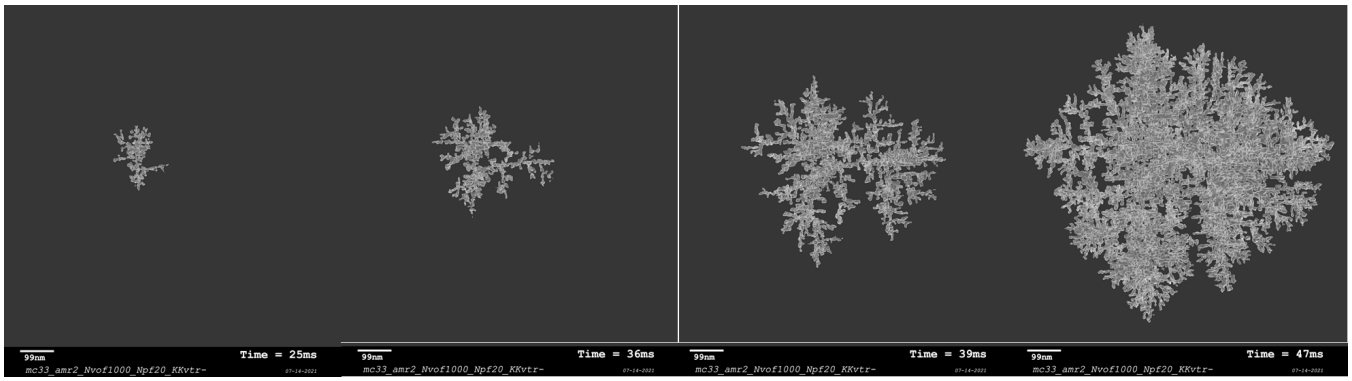

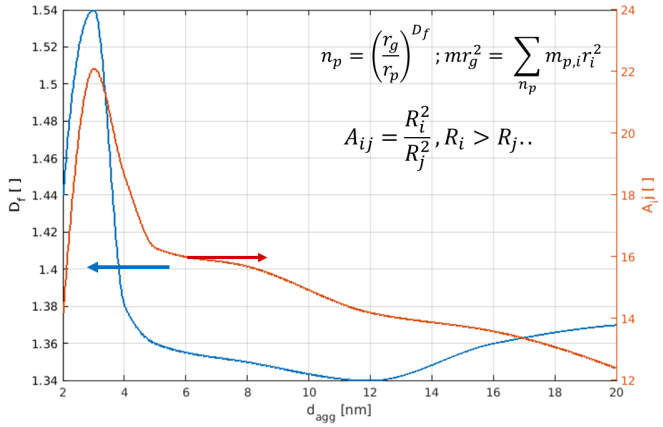

Figure 17. Snapshot of particle morphology at subsequent stages of growth (top), and variations in particle morphology with size (or time) with blended growth formulation with $K_r = 0.03$ (bottom).

Next Steps

- Completion of cluster–cluster agglomeration
- Computational acceleration for cluster–cluster agglomeration
- Coupling strategy for inception/post-inception model (MD)
- Coupling strategy for LES and definition of parametric space

Task 4 - Large Eddy Simulations

Georgia Institute of Technology

Objective

The objective of this task is to develop a physics-informed LES framework to model soot formation in turbulent reacting configurations of canonical and combustors of practical relevance. The current report discusses the LES-MOMIC and LEMLES-MOMIC frameworks to address large-scale simulations of soot modeling in turbulent reacting flows. The subsequent steps also included a collaboration with the kinetics group to include the effects of various mechanisms within the LES framework to address the sensitivity of soot precursor formation to chemistry effects. In future other team members will also be involved.

Research Approach

LES studies of turbulent sooting problems are very difficult because of the multiscale nature of soot inception, coagulation, and surface growth that must be modeled in a highly turbulent and reactive environment, typically in a complex combustor configuration. Most prior studies have focused on global models that approximate the small-scale physics. As such, many

available models account for the underlying physics. In contrast, simulations require some approximations, because the computational resources will never meet the simulation requirements. In the current effort, we balance contributing to the prediction of soot formation physics in a realistic gas turbine combustor with the need to obtain high-fidelity, reliable predictions by using advanced models. To achieve this goal, we leverage our past LES capability and upgrade the models by using the results from MD and MC studies. Soot evolution is tracked with MOMIC, wherein the first six moments of the particle size distribution function (PSDF) are used.

The full set of compressible reacting multispecies Navier–Stokes equations cannot be solved directly, because a direct numerical simulation is not feasible for practical applications. For LES, the large-scale flow features are resolved, and subgrid modeling is used for the smaller scales.

The LES governing equations can be written as follows:

$$\frac{\partial \bar{\rho}}{\partial t} + \frac{\partial}{\partial x_i}(\bar{\rho}\,\widetilde{u_\iota}) = 0$$

$$\frac{\partial}{\partial t}(\bar{\rho}\,\widetilde{u_\iota}) + \frac{\partial}{\partial x_j}\left(\bar{\rho}\,\widetilde{u_\iota}\,\widetilde{u_j} + \bar{P}\,\delta_{ij} - \overline{\tau_{\iota J}} + \tau_{ij}^{sgs}\right) = 0$$

$$\frac{\partial}{\partial t}\left(\bar{\rho}\,\tilde{E}\right) + \frac{\partial}{\partial x_j}\left[\left(\bar{\rho}\,\tilde{E} + \bar{P}\right)\widetilde{u_\iota} + \overline{q_\iota} - \widetilde{u_J}\,\overline{\tau_{\iota J}} + H_i^{sgs} + \sigma_i^{sgs}\right] = 0$$

$$\frac{\partial}{\partial t}\left(\bar{\rho}\,\widetilde{Y_k}\right) + \frac{\partial}{\partial x_j}\left[\bar{\rho}\,\widetilde{Y_k}\,\widetilde{u_j} - \bar{\rho}\,\overline{D_k}\,\frac{\partial \widetilde{Y_k}}{\partial x_j} + \Phi_{j,k}^{sgs} + \Theta_{jk}^{sgs}\right] = \bar{\rho}\,\widetilde{\dot{w}_k}$$

$$\frac{\partial}{\partial t}\left(\bar{\rho}\,\widetilde{Y}_{soot}\right) + \frac{\partial}{\partial x_j}\left[\bar{\rho}\,\tilde{Y}_{soot}\,\widetilde{u_j} - \bar{\rho}\,\bar{D}_{soot}\,\frac{\partial \tilde{Y}_{soot}}{\partial x_j} + \widetilde{V_T}_{soot}\,\tilde{Y}_{soot} + \Phi_{j,k,soot}^{sgs} + \Theta_{jk,soot}^{sgs}\right] = \bar{\rho}\,\widetilde{\dot{w}}_{soot}$$

$$\frac{\partial}{\partial t}\left(\bar{\rho}\,\widetilde{M_k}\right) + \frac{\partial}{\partial x_j}\left[\bar{\rho}\,\widetilde{M_k}\,\widetilde{u_j} - \bar{\rho}\,\bar{D}_{soot}\,\frac{\partial \widetilde{M_k}}{\partial x_j} + \widetilde{V_T}\,\widetilde{M_k} + \Psi_{j,k}^{sgs} + \Omega_{j,k}^{sgs}\right] = \bar{\rho}\,\widetilde{\dot{M}_k}$$

Here, $\widetilde{u_\iota}$ is the *i*-th filtered velocity, $\bar{\rho}$ is the filtered density, and $\bar{P}$ is the filtered pressure, which is computed from the filtered equation of state. $\tilde{T}$ is the filtered temperature, $\tilde{E}$ is the filtered energy, and $\widetilde{Y_k}$ and $\widetilde{Y}_{soot}$ represent the filtered *k*-th gas-phase species and soot mass fraction, respectively, and $\widetilde{M_k}$ represents the *k*-th moments of the PSDF. The details regarding the computations of all these quantities have been described elsewhere (El-Asrag & Menon, 2009) and hence are not discussed herein in specific detail. The filtered heat flux $\bar{q}$ can be supplied to an optically thin radiation model to include effects of radiation. The terms $\tau_{ij}^{sgs}, H_i^{sgs}, \sigma_i^{sgs}, \Phi_{j,k}^{sgs}, \Theta_{j,k}^{sgs}, \Psi_{j,k}^{sgs}$, and $\Omega_{j,k}^{sgs}$ contain the effects of the subgrid scale on the filtered quantities. Modeling of these terms remains challenging; in addition, the closed system of equations must be solved together in three-dimensional space with temporal accuracy.

In this work, an eddy viscosity type subgrid model with constant coefficients is used to obtain the closure of subgrid momentum stresses and subgrid enthalpy flux. In the linear eddy mixing (LEM) formulation, the gas-phase species conservation equations are not spatially filtered as in other LES equations. Instead, the exact unfiltered equations are solved by using a two-scale, two-step Eulerian–Lagrangian approach. First, within each LES cell, the one-dimensional LEM model is used to solve for the scalar fields (species mass fraction, soot mass fraction, LEM temperature, and soot integer moments) along a notional line oriented along the maximum scalar gradient. Second, the subgrid scale fields are convected across the LES cell faces by using a Lagrangian transport approach through the splicing algorithm, which reproduces the effect of large-scale advection of the scalars by the flow field. The resulting scalar fields are then filtered in each LES cell to recover LES-resolved species mass fractions to be used in LES-resolved energy and state equations. More details regarding the original LEMLES formulation and its extension to account for soot dynamics through the MOMIC approach have been described elsewhere and are briefly described herein.

The one-dimensional LEM-MOMIC takes the following form:

$$\rho \frac{\partial Y_k}{\partial t} = F_k + \frac{\partial}{\partial s}\left(\rho D_k \frac{\partial Y_k}{\partial s}\right) + \dot{w}_k$$

$$\rho \frac{\partial Y_{soot}}{\partial t} = F_{soot} + \frac{\partial}{\partial s}\left(\rho D_{soot} \frac{\partial Y_{soot}}{\partial s} - V_{T,soot}\, Y_{soot}\right) + \dot{\omega}_{soot}$$

$$\frac{\partial T}{\partial t} = F_T - \frac{1}{\overline{C_p}} \Sigma_{k=1,N_s}\left(C_{p,k} Y_k V_k \frac{\partial T}{\partial s}\right) + \frac{1}{\rho\, \overline{C_p}}\left(\frac{\partial}{\partial s}\left(\bar{k}\frac{\partial T}{\partial s}\right)\right) - \frac{1}{\rho\, \overline{C_p}} \Sigma h_k\, \dot{\omega}_k W_k + a_{over}\sigma(T^4 - T_o^4)$$

$$\frac{\partial M_r}{\partial t} = R_r + C_r + S_r + F_{M_r}$$

In the above equations, Y_k and Y_{soot} are the *k*-th gas-phase species and soot mass fractions, respectively, which are subjected to the mass conservation condition $\Sigma Y_k + Y_{soot} = 1.0$. The soot molecular diffusivity and thermophoretic velocity are denoted by D_{soot} and $V_{T,soot}$ respectively. The temperature equation is supplied with an optically thin radiation model. Here, $F_k, F_{soot}, F_T,$ and F_{M_r} all denote the effects of subgrid turbulence in the gas-phase species, soot mass fraction, temperature, and moments, respectively. In the current formulation, F_{M_r} is neglected, to account for the effect of turbulence on soot. The F_{soot} term is modeled through turbulent stirring operations in the same manner as for other species.

The remaining terms, $R_r, C_r,$ and S_r, represent the soot moment source terms from the nucleation, coagulation, and surface growth, respectively. These terms are modeled with a MOMIC approach. In method of moments, the Smoluchowski equations describing the population dynamics of a system of particles are rewritten in terms of the moments of the PSDF. The PSDF can also be described by its moments, and most practical application properties can be easily estimated from its first few moments. The moments are defined as $M_r = \Sigma m_i^r N_i$, where M_r is the *r*-th moment, and m_i and N_i are the masses and number density of particles with size *i*. Therefore, method of moments is useful because it replaces an infinite sequence of equations with a set of a few equations to estimate properties of practical interest. The zeroth moment, M_0, represents the soot number density, N_S, defined by the number of soot particles per unit volume of the mixture. The first moment, M_1, represents the average total mass of soot particles, m_S, per unit volume. Thus, the soot mass fraction is $Y_S = M_1/\rho$, where ρ is the mixture density. The average particle diameter $d_p = (6.0M_2/\pi\rho_{soot}M_1)^{1/3}$ (El-Asrag & Menon, 2009; Srinivasan & Menon, 2015).

The following key inputs have been identified for improvements in the existing MOMIC model, in collaboration with other cost-share partners:

1) The current MOMIC model uses the Lindstedt four-step soot kinetic model to model the kinetic rates of soot nucleation, surface growth, and oxidation. This kinetic model uses the empirical constants highlighted in Figure 3. The inputs from the RTRC kinetic group regarding the empirical constants must be incorporated in the source terms of nucleation and surface growth terms.
2) The current LES-MOMIC and LEMLES-MOMIC approaches use reduced chemical kinetics (19-species, 15-step ethylene–air kinetics developed by Lu and coworkers). However, the kinetics lacks information on the aromatic species and is not designed to work under the high-pressure conditions in practical gas turbine combustors.
3) The nucleation in the current code is based on the assumption that acetylene is a gas-phase soot precursor, which is reasonable for ethylene flames. However, for aviation fuels, it has been found that aromatic species are key in the formation of early soot incipient nuclei. The MD studies performed at UM in close association with the RTRC kinetic group provide information on the kinetic rates of formation of these aromatic dimers. This effect needs to be included in the current MOMIC approach.
4) In the non-coalescent regime, the MOMIC source terms for aggregate formation require information on the fractal dimension of these aggregates as a function of background gas-phase conditions. The MC studies of the RTRC surface growth modeling team provide information on fractal dimensions as a parametric function of sensitive background conditions and can be fed into the MOMIC code in LES framework.

In the last annual effort, assessment of the existing MOMIC approach to account for first six moments of the soot particle size distribution function were performed. Various one-dimensional tests were performed to verify the implementation of

MOMIC. Further, soot formation in a laminar flame by using reduced ethylene 19-species, 15-step kinetics coupled with a four-step Lindstedt soot kinetic model was compared with the experimental results from Xu and Faeth (2001). In the current effort, the primary task was to establish methodology for soot evolution in turbulent flames, accounting for the effects of turbulence on soot formation processes. In a demonstration, a three-dimensional premixed rich C_2H_4/air flame interacting with background turbulence is used. The proposed test intends to use the LEMLES-MOMIC model with finite rate chemistry for the premixed flame turbulence interaction problem (El-Asrag et. al., 2007) under the conditions in Table 1.

Table 1. Turbulence and flame parameters.

u'	l_{11}	Re_λ	s_l
1.67 m/s	1.475 mm	156	0.167 m/s

The schematic of the configuration is shown in Figure 18. The premixed C_2H_4/air mixture enters the inlet at $\varphi = 2.33$, at P_{ref} = 1 atm and T_{ref} = 300 K. According to the inflow conditions, the laminar flame speed (S_l) is 0.167 m/s. Turbulence parameters (u', l_{11}) are chosen such that the flame is in the thin reaction zone (TRZ) regime. The initial flame front is obtained from the laminar premixed flame solution and is specified at the center of the domain, with the left side denoting the reactants and the right side denoting the products. The extent of the computational domain is 15 mm × 15 mm × 15 mm in the streamwise x, transverse y, and spanwise z directions. The flow field is initialized by using the von Karman–Pao energy spectrum. Characteristic inflow–outflow conditions are specified in the streamwise direction, whereas periodic conditions are specified in the other two directions. The LES grid resolution chosen for the simulations is 64 × 64 × 64 LES cells. LEM is used to account for subgrid turbulence–chemistry closure. A total of 12 LEM cells are chosen in each LES, so that subgrid effects until Kolmogorov's length scale can be resolved.

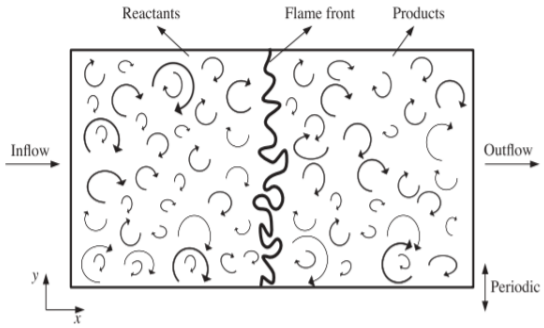

Figure 18. Schematic of premixed flame–turbulence interaction.

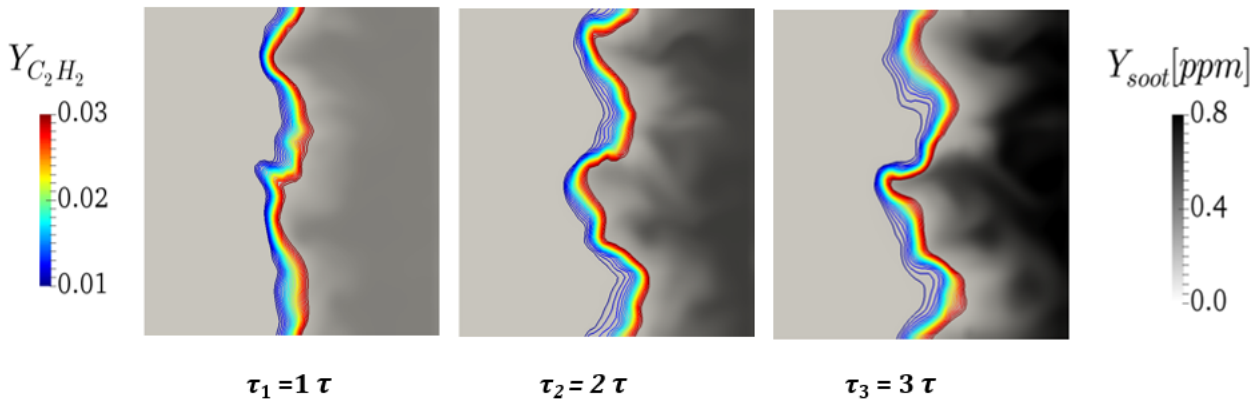

Figure 19. Soot mass fractions overlapped with C_2H_2 contours.

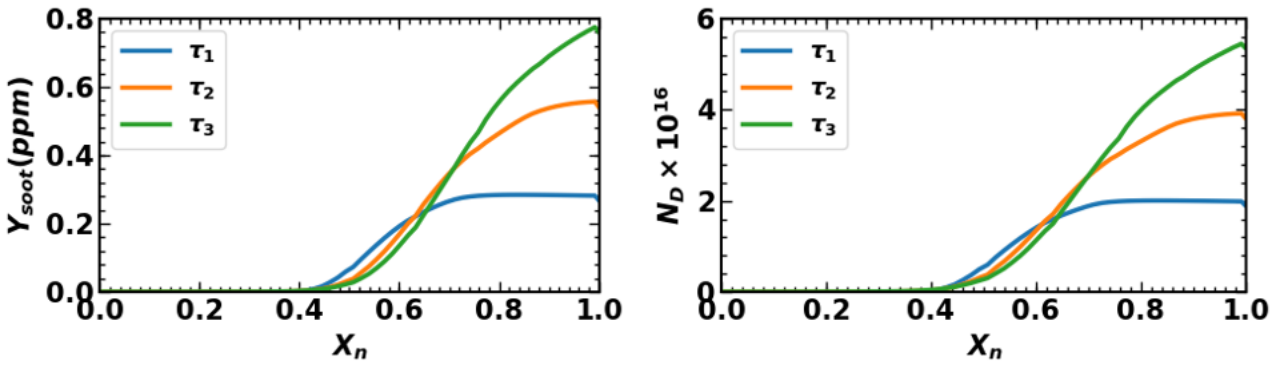

Figure 20. Planar average of Y_{soot} and number density profile along the flame normal directions ($\tau_1 = \tau_{eddy}$, $\tau_2 = 2\tau_{eddy}, \tau_3 = 3\tau_{eddy}$).

The time evolution contours of the soot mass fraction are shown in Figure 19. As can be seen, the presence of background turbulence severely deforms the initially laminar planar flame front. The rich premixed ethylene mixture decomposes, forming acetylene, which acts as a soot precursor. The acetylene molecules break down further and form soot nuclei. The increasing soot mass fraction and number density with eddy turnover time ($\tau_{eddy} = \frac{u'}{s_l}$) are evident in Figure 20. The LEMLES-MOMIC approach is demonstrated only with nucleation. The effects of radiation and agglomeration are also neglected at this stage (but will be reconsidered later).

The initial study included a collaboration with the kinetics group at RTRC to incorporate the skeletal chemistry in the LES framework and assess the effects of chemistry in predicting key gas-phase precursor species (C_2H_2). To do so, the premixed flame turbulence interaction problem described above is revisited but without the inclusion of soot species, i.e., only gas-phase species are simulated by using two different mechanisms:

Mechanism A (reduced chemistry): 19-species, 15-step reduced mechanism developed by Lu and coworkers
Mechanism B (skeletal chemistry): 33-species, 206-step skeletal mechanism developed by Lu and coworkers, assessed by the RTRC kinetic group.

Initially, the timescales of production of each species are estimated for both chemistries and are plotted in a bar chart in Figure 21. As shown, the skeletal chemistry is stiffer than the reduced chemistry (timescales of some species are on the order of 1×10^{-7}); however, the species are still well resolved with the current LES timescale. The spanwise averages of the fuel decomposition rate (C_2H_4) as well as precursor (C_2H_2) production rates with respect to the filtered progress variables obtained with both mechanisms are plotted in Figure 22. The reduced mechanism, compared with the skeletal mechanism, predicts mass fractions that are approximately two times greater possibly due to the inclusion of aromatic pathways in the pyrolysis of fuel. These inputs are conveyed to the kinetics group, which will conduct further assessment of the kinetics with different detailed mechanisms to establish a confidence interval for prediction of the soot precursor species under different operating conditions.

Next Steps

- Inclusion of nucleation from UM into the LES approach
- Extension of LES models to include radiation and agglomeration models from RTRC
- Validation of LES to canonical sooting flames
- Evaluation of model for PAH pathways for soot formation
- Evaluation of aggregation models using LES data

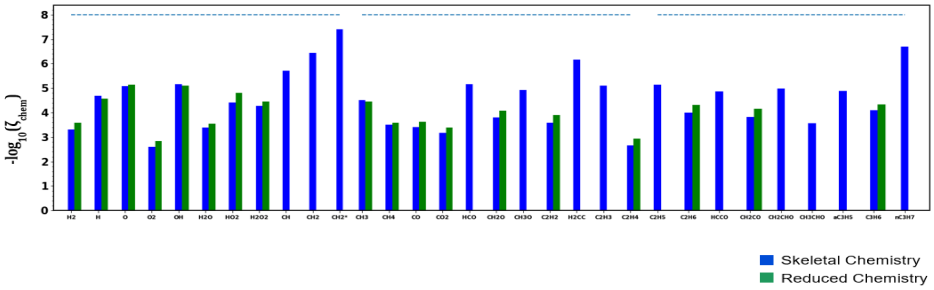

Figure 21. Comparison of chemical timescales for species involved in reduced and skeletal chemistries.

The *y* axis is the negative of the species production timescale. The dotted blue horizontal line is the typical LES timescale. Almost all species present in skeletal and reduced chemistry lie below the blue dotted line, thus suggesting that the LES timescale is less than all the chemical timescales.

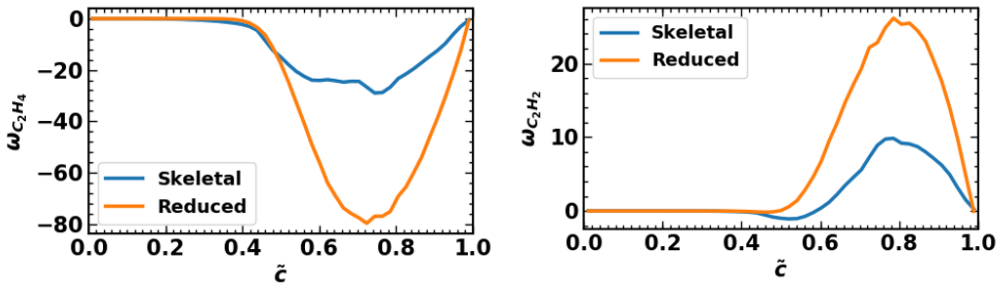

Figure 22. Comparison of consumption rates for reactants and production rates for soot precursors, with reduced and skeletal chemistry.

Milestone(s)

Milestone	Planned Due Date
Improvements in the Lindstedt soot kinetic model	12/31/2021
Development of reduced kinetics for PAH chemistry	3/31/2022
MD simulation framework for dimer stability	3/31/2022
MC simulation for surface growth and cluster–cluster aggregation	3/31/2022
LES-MOMIC and LEMLES-MOMIC frameworks for soot–turbulence–chemistry assessment	3/31/2022

Major Accomplishments

- Improvements in the four-step Lindstedt soot kinetic model to predict reduced rates at higher temperatures
- Development of reduced kinetics including PAH pathways
- MD simulations for pools of PAH rings at a range of flame temperatures
- Framework for reaction- and transport-limited growth of soot particles, as well as models for cluster–cluster aggregation
- LEMLES-MOMIC numerical framework for soot–turbulence–chemistry interactions

Publications

Saldinger, J. C., Elvati, P., & Violi, A. (2021). Stochastic and network analysis of polycyclic aromatic growth in a coflow diffusion flame. Physical Chemistry Chemical Physics, *23*(7), 4326-4333.

Outreach Efforts

None

Awards

None

Student Involvement

Shubham Karpe, PhD student, has been assisting with the development of the MOMIC framework within the LES code at Georgia Tech. Another student is working on the UM team.

Plans for Next Period

Kinetics activities at RTRC

The next quarterly efforts will focus on refining the reduced chemistry developed with PAH species, with particular attention paid to extending the predictions and validation over a wide range of conditions. The reduced kinetics will be provided to Georgia Tech, and the information on the gas phase will be provided to UM for nucleation studies.

MD Simulations at UM

Future activities in this work will focus on expanding the pool of PAHs to consider the effects of heavier monomers, impact of aliphatic chains, and oxygen radicals on the stability of dimer formations. The inputs regarding the global nucleation rates from these studies will be provided to GT to improve source terms in the 6-MOMIC approach.

Surface Growth Modeling at RTRC

Studies are underway to consider models for full cluster–cluster aggregation. The information regarding the primary soot nuclei (size and distributions) from MD simulations at UM, and regarding local conditions from LES studies at Georgia Tech, will be included in current growth models at RTRC. The outputs regarding the fractal dimensions and anisotropy of aggregates will be provided to Georgia Tech for their MOMIC model.

LES Studies at Georgia Tech

The next set of activities at Georgia Tech will involve incorporating the reduced ethene kinetics with PAH species and the soot kinetic model at RTRC to improve the existing soot model. The extinction–reignition setup based on DNS studies (Lignell et. al., 2008) will be explored to study soot formation and transport in non-premixed jet flames by using LES-MOMIC and later LEMLES-MOMIC. The inputs from fundamental studies at RTRC and UM will be included to improve the architecture of the existing MOMIC model, which will be further compared in premixed and non-premixed canonical ethylene–air flames.

References

Balthasar, M., & Frenklach, M. (2005). Monte-Carlo simulation of soot particle coagulation and aggregation: the effect of a realistic size distribution. Proceedings of the Combustion Institute, *30*(1), 1467–1475. https://doi.org/10.1016/j.proci.2004.07.035

Chen, J.-Y. (1988). A general procedure for constructing reduced reaction mechanisms with given independent relations. Combustion Science and Technology, *57*(1-3), 89–94. https://doi.org/10.1080/00102208808923945

Colket, M. B., Hall, R. J., & Stouffer, S. D. (2004, June 14-17). Modeling soot formation in a stirred reactor [Presentation]. Proceedings of the ASME Turbo Expo 2004: Power for Land, Sea, and Air, Vienna, Austria. https://doi.org/10.1115/GT2004-54001

Glarborg, P., Kee, R. J., Grcar, J. F., & Miller, J. A. (1986). PSE: a Fortran program for modeling well-stirred reactors (Report No. SAND86-8209). Sandia National Laboratories, Livermore, CA.

El-Asrag, H., & Menon, S. (2009). Large eddy simulation of soot formation in a turbulent non-premixed jet flame. Combustion and Flame, *156*(2), 385–395. https://doi.org/10.1016/j.combustflame.2008.09.003

El-Asrag, H., Lu, T., Law, C. K., & Menon, S. (2007). Simulation of soot formation in turbulent premixed flames. Combustion and Flame, *150*(1-2), 108–126. https://doi.org/10.1016/j.combustflame.2007.01.005

Frenklach, M. (2002). Method of moments with interpolative closure. Chemical Engineering Science, *57*(12), 2229–2239. https://doi.org/10.1016/s0009-2509(02)00113-6.

Kireeva, E. D., Popovicheva, O. B., Persiantseva, N. M., Timofeyev, M. A., & Shonija, N. K. (2009). Fractionation analysis of transport engine-generated soot particles with respect to hygroscopicity. Journal of Atmospheric Chemistry, *64*(2-3), 129–147. https://doi.org/10.1007/s10874-010-9173-y

Leung, K. M., Lindstedt, R. P., & Jones, W. P. (1991). A simplified reaction mechanism for soot formation in nonpremixed flames. Combustion and Flame, *87*(3-4), 289–305. https://doi.org/10.1016/0010-2180(91)90114-q

Lignell, D. O., Chen, J. H., & Smith, P. J. (2008). Three-dimensional direct numerical simulation of soot formation and transport in a temporally evolving nonpremixed ethylene jet flame. Combustion and Flame, *155*(1-2), 316–333. https://doi.org/10.1016/j.combustflame.2008.05.020

Lu, T., & Law, C. K. (2005). A directed relation graph method for mechanism reduction. Proceedings of the Combustion Institute, *30*(1), 1333–1341. https://doi.org/10.1016/j.proci.2004.08.145

Mitchell, P., & Frenklach, M. (1998). Monte Carlo simulation of soot aggregation with simultaneous surface growth-why primary particles appear spherical. Symposium (International) on Combustion, *27*(1), 1507–1514. https://doi.org/10.1016/s0082-0784(98)80558-4

Saldinger, J. C., Elvati, P., & Violi, A. (2021). Stochastic and network analysis of polycyclic aromatic growth in a coflow diffusion flame. Physical Chemistry Chemical Physics, *23*(7), 4326–4333. https://doi.org/10.1039/d0cp03529g

Slowik, J. G., Cross, E. S., Han, J.-H., Davidovits, P., Onasch, T. B., Jayne, J. T., Williams, L. R., Canagaratna, M. R., Worsnop, D. R., Chakrabarty, R. K., Moosmüller, H., Arnott, W. P., Schwarz, J. P., Gao, R.-S., Fahey, D. W., Kok, G. L., & Petzold, A. (2007). An inter-comparison of instruments measuring black carbon content of soot particles. Aerosol Science and Technology, *41*(3), 295–314. https://doi.org/10.1080/02786820701197078

Srinivasan, S., & Menon, S. (2015). Soot modeling using the linear eddy model (Report No. CCL-TR-2015-03-10)., Environmental Protection Agency.

Stouffer, S., Striebich, R. C., Frayne, C. W., & Zelina, J. (2002, July 12-17). Combustion Particulates Mitigation Investigation Using a Well-Stirred Reactor [Presentation]. 38th AIAA/ASME/SAE/ASEE Joint Propulsion Conference & Exhibit, Indianapolis, IN.

Sun, Y., & Beckermann, C. (2007). Sharp interface tracking using the phase-field equation. Journal of Computational Physics, *220*(2), 626–653. https://doi.org/10.1016/j.jcp.2006.05.025

Xu, F., & Faeth, G. M. (2001). Soot formation in laminar acetylene/air diffusion flames at atmospheric pressure. Combustion and Flame, 125(1-2), 804–819. https://doi.org/10.1016/s0010-2180(01)00221-8

Xu, Z., & Meakin, P. (2008). Phase-field modeling of solute precipitation and dissolution. The Journal of Chemical Physics, *129*(1), 014705. https://doi.org/10.1063/1.2948949

Project 072 Aircraft Noise Exposure and Market Outcomes in the United States

Massachusetts Institute of Technology

Project Lead Investigators

PI: R. John Hansman
T. Wilson Professor of Aeronautics & Astronautics
Department of Aeronautics & Astronautics
Massachusetts Institute of Technology
77 Massachusetts Avenue, 33-303
Cambridge, MA 02139
(617) 253-2271
rjhans@mit.edu

Co-PI: Christopher R. Knittel
George P. Shultz Professor of Applied Economics
Sloan School of Management
Massachusetts Institute of Technology
77 Massachusetts Avenue, E62-527
Cambridge, MA 02139
(617) 324-0015
knittel@mit.edu

Co-PI: Steven R. H. Barrett
Professor of Aeronautics and Astronautics
Department of Aeronautics and Astronautics
Massachusetts Institute of Technology
77 Massachusetts Avenue, 33-207
Cambridge, MA 02139
(617) 452-2550
sbarrett@mit.edu

Co-PI: Jing Li
Assistant Professor of Applied Economics
Sloan School of Management
Massachusetts Institute of Technology
77 Massachusetts Avenue, E62
Cambridge, MA 02139
(617) 252-1131
lijing@mit.edu

Co-PI: Florian Allroggen
Research Scientist
Department of Aeronautics and Astronautics
Massachusetts Institute of Technology
77 Massachusetts Avenue, 33-115A
Cambridge, MA 02139
(617) 715-4472
fallrogg@mit.edu

University Participants

Massachusetts Institute of Technology

- PI: Professor R. John Hansman
  Co-PIs: Professor Christopher R. Knittel, Professor Steven Barrett, Professor Jing Li, and Dr. Florian Allroggen
- FAA Award Number: 13-C-AJFE-MIT, Amendment Nos. 075 and 081
- Period of Performance: August 11, 2020 to August 31, 2022
- Tasks (tasks listed below are general project tasks; reporting includes the period from September 1, 2020 to August 31, 2021):
  1. Literature review
  2. Empirical identification strategy and scope of dataset
  3. Calculation of noise impact metrics
  4. Cleaning and aggregation of housing transaction dataset
  5. Descriptive analysis of dataset
  6. Empirical analysis (not reported; task planned to start in the next reporting period)

Project Funding Level

The funding includes $380,000 of FAA funding and $380,000 of matching funds, comprising approximately $112,000 from Massachusetts Institute of Technology (MIT) and third-party in-kind contributions of $268,000 from NuFuels LLC.

Investigation Team

- Professor R. John Hansman, PI, MIT (Tasks 1, 2, 3, 5, and 6)
- Professor Christopher R. Knittel, co-PI, MIT (Tasks 1, 2, 4, 5, and 6)
- Professor Steven R.H. Barrett, co-PI, MIT (Tasks 1, 5, and 6)
- Professor Jing Li, co-PI, MIT (Tasks 1, 2, 4, 5, and 6)
- Dr. Florian Allroggen, co-PI, MIT (all tasks)
- Dr. Xibo Wan, Postdoctoral Associate, MIT (Tasks 1, 2, 4, 5, and 6)
- Madeleine Jansson, Graduate Student, MIT (Tasks 3 and 5)
- Zhishen Wang, Graduate Student, MIT (Tasks 3 and 5)
- Kevin Zimmer, Graduate Student, MIT (Tasks 3 and 5)

Project Overview

While enplanements at U.S. airports have increased by almost 50% over the past two decades, the number of Americans exposed to significant levels of aircraft noise has substantially decreased. However, considerable concerns regarding aircraft noise remain within some airport communities. This project leverages revealed-preference approaches to infer the “implicit price” of aircraft noise exposure from market outcomes in U.S. airport communities. More specifically, the research team is quantifying the capitalized disutility associated with aircraft noise exposure through analyzing the empirical relationship between aircraft noise exposure and transaction values for residential properties in communities surrounding U.S. airports. State-of-the-art empirical methods will be applied, which will leverage quasi-experimental settings of noise exposure changes. The project will empirically analyze the house price impacts of potential changes in noise exposure associated with the quasi-experimental settings. The results will provide insights into the average impacts of noise exposure on residential property values, while also assessing dynamic adjustment processes and potential heterogeneities in the revealed preferences and targeting factors, such as time, location, or noise exposure patterns.

Task 1 - Literature Review

Massachusetts Institute of Technology

Objective

The goal of this task is to review and summarize the existing body of literature in two topic areas:

- Empirical analyses of the impacts of noise exposure on residential property values, and
- Noise exposure metrics

Research Approach

The research team systematically reviewed and summarized the existing literature. This entailed:

1. Presenting an overview of existing economic studies on the impacts of noise exposure on residential property values
2. Comparing different noise metrics and their applications, including, but not limited to, day–night average sound level (DNL), equivalent sound level (LEQ), maximum sound levels (Lmax), and metrics that consider the frequency and amplitude of noise events.

Milestone

The team completed a preliminary literature review.

Major Accomplishments

The research team prepared a high-level literature summary of results, including both an overview of economic studies on the impacts of noise exposure on residential property values, and an overview of noise metrics and their applications.

Economic literature

Numerous studies have attempted to obtain empirical estimates of the causal impact of noise on residential property values (see Nelson, 2004; He et al., 2014; and Kopsch, 2016 for meta-analyses). To do so, house prices are modeled as a function of noise exposure, and other characteristics of the property (e.g., size or design) and the neighborhood (e.g., schools or crime). Typically, linear, log–linear, or log–log functional specifications are assumed. In their datasets, studies have initially relied on aggregate data, e.g., at the county level, whereas more recent work has almost exclusively considered geolocated data points for individual property transactions. In their meta-analyses, Nelson (2004), He et al. (2014), and Kopsch (2016) found that the noise depreciation index derived from empirical studies varies between 0.4 and 0.7.

Despite the effort to understand the impact of noise on housing values, few recent research studies exist that have accounted for the role of asymmetric information regarding the characteristics of houses and neighborhoods when home buyers make housing decisions. Pope (2008a, 2008b) has found that some homebuyers did not pay attention to publicly available information about flood risk and airport noise prior to mandatory disclosure laws requiring them to sign forms stating their awareness of the amenities. Bakkensen and Barrage (2017) provided more direct evidence by surveying homebuyers about beliefs concerning flood risk. Their findings suggest that residents of more flood-prone areas are more likely to underestimate flood risk. Ma (2018) has shown how the learning process can be modeled and has found that accounting for learning has a large impact on estimates of the willingness to pay (WTP) for brownfield remediation. Adapting Ma's approach to hedonic property-value models could both improve our understanding of households' beliefs and help refine welfare measures.

Another challenge in examining the impact of environmental amenities is potential omitted-variable bias, especially because the amenities will be spatially correlated due to natural features of geography and environmental feedback effects. Several research designs have been implemented to address this concern, including difference-in-differences (Chay and Greenstone 2005, Davis 2004, Dundas 2017, Bento, Freedman, and Lang 2015), matching estimators (e.g., Abbott & Klaiber, 2013; Walls et al., 2017), spatial dummy variables (Kuminoff, Parmeter & Pope, 2010), and boundary-discontinuity designs (Black, 1999; Muehlenbachs, Spiller & Timmins, 2015; Pope, 2008b). Although these research designs can help mitigate problems associated with omitted-variable bias, each has its own challenges and assumptions.

Finally, a large body of literature has been devoted to assessing WTP for nonmarginal changes in amenity and welfare implications (He et al., 2014; Wolfe et al., 2014; Wolfe et al., 2016; Wolfe et al., 2017). However, no consensus exists regarding the best-practice approach for the estimation. Some studies have used MWTP estimates to construct "back of the envelope" approximations of the WTP for policies expected to produce nonmarginal changes in amenities. The most common approach is to multiply the MWTP by the change in the amenity. For this calculation to yield a valid measure of WTP, the demand for the amenity must be perfectly elastic. When the change in the amenity is believed to be too large to assume perfectly elastic demand curves, an alternative approach is to establish bounds on WTP according to the logic of Varian (1982).

Noise metrics

The common metric for airport noise in the United States is the DNL, which represents the cumulative average noise level over a 24-hr period and penalizes nighttime overflights (between 10 p.m. and 7 a.m.) with an additional 10 dB. DNL is normally averaged over a full year to define a representative average day. An alternative noise metric that captures the

operational frequency of aircraft overflights is the N_{above} value, the number of times that overflight noise occurs above a certain maximum noise exposure level threshold during a 24-hr period. As with the DNL metric, nighttime overflights receive a 10-dB penalty. N_{above} will vary by the day depending on traffic and runway use, and N_{above} is commonly evaluated during a peak day of operations on a runway of interest. Brenner (2017) has found that a threshold level of 60 dB correlates well with noise complaints.

Outreach

The team presented insights into the literature review in a pre-recorded project outline during the ASCENT Fall meeting in 2020 and in a presentation during the ASCENT Spring meeting in 2021.

Student Involvement

MIT graduate student Madeleine Jansson conducted research under this task.

Plans for Next Period

The team will continue to update the literature overview.

References

Abbott, J. K., & Klaiber, H. A. (2011). An embarrassment of riches: Confronting omitted variable bias and multiscale capitalization in hedonic price models. Review of Economics and Statistics, *93*(4), 1331–1342.

Bakkensen, L., & Barrage, L. (2017). Flood risk belief heterogeneity and coastal home price dynamics: Going under water? (Report No. 23854). National Bureau of Economic Research.

Bento, A., Freedman, M., & Lang, C. (2015). Who benefits from environmental regulation? Evidence from the clean air act amendments. Review of Economics and Statistics, *97*(3), 610–622.

Black, S. E. (1999). Do better schools matter? Parental valuation of elementary education. Quarterly Journal of Economics, *114*(2), 577–599.

Brenner, M. (2017). Comparison of methods for evaluating impacts of aviation noise on communities [Masters thesis, MIT Department of Aeronautics and Astronautics].

Chay, K. Y., & Greenstone, M. (2005). Does air quality matter? Evidence from the housing market. Journal of Political Economy, *113*(2), 376–424.

Davis, L. (2004). The effect of health risk on housing values: Evidence from a cancer cluster. American Economic Review, *94*(5), 1693–1704.

Dundas, S. (2017). Benefits and ancillary costs of natural infrastructure: Evidence from the New Jersey coast. Journal of Environmental Economics and Management, *85*, 62–80.

He, Q., Wollersheim, C., Locke, M., & Waitz, I. (2014). Estimation of the global impacts of aviation-related noise using an income-based approach. Transport Policy, *34*, 85-101.

Kopsch, F. (2016). The cost of aircraft noise: Does it differ from road noise? A meta-analysis. Journal of Air Transport Management, *57*, 138-142.

Kuminoff, N. V., Parmeter, C. F., & Pope, J. C. (2010). Which hedonic models can we trust to recover the marginal willingness to pay for environmental amenities? Journal of Environmental Economics and Management, *60*(3), 145–160.

Ma, L. (2018). Learning in a hedonic framework: Valuing brownfield remediation. International Economic Review, *60*(3), 1355–1387.

Muehlenbachs, L., Spiller, E., & Timmins, C. (2015). The housing market impacts of shale gas development. American Economic Review, *105*(12), 3633–3659.

Nelson, J. P. (2004). Meta-analysis of airport noise and hedonic property values. Problems and prospects. Journal of Transport Economics and Policy, *38*(1), 1-28.

Pope, J. C. (2008a). Buyer information and the hedonic: the impact of a seller disclosure on the implicit price for airport noise. Journal of Urban Economics, *63*(2), 498-516.

Pope, J. C. (2008b). Do seller disclosures affect property values? Buyer information and the hedonic model. Land Economics, *84*(4), 551-572.

Varian, H. R. (1982). The nonparametric approach to demand analysis. Econometrica, *50*(4), 945–973.

Von Graevenitz, K. (2018). The amenity cost of traffic noise. Journal of Environmental Economics and Management, *90*, 1–22.

Walls, M., Gerarden, T., Palmer, K., & Bak, X. F. (2017). Is energy efficiency capitalized into home prices? Evidence from three U.S. cities. Journal of Environmental Economics and Management, *82*, 104–124.

Wolfe, P. J., Yim, S. H. L., Lee, G., Ashok, A., Barrett, S. R. H, & Waitz, I. A. (2014). Near-airport distribution of the environmental costs of aviation. Transport Policy, *34*, 102-108.
Wolfe, P. J., Malina, R., Barrett, S. R. H, & Waitz, I. A. (2016). Costs and benefits of US aviation noise land use. Transportation Research Part D, 44, 147-156.
Wolfe, P. J., Kramer, J. L., & Barrett, S. R. H. (2017). Current and future noise impacts of the U.K. hub airport. Journal of Air Transport Management, *58*, 91-99.

Task 2 – Empirical Identification Strategy and Scope of Dataset

Massachusetts Institute of Technology

Objective

The goal of this task is to describe a valid strategy for empirically identifying the causal impacts of aircraft noise on residential property values. Based on the strategy, the team then derives the data requirements for the analysis.

Research Approach

The impacts of noise exposure can be monetized using different approaches. For quantifying health costs, the direct and indirect costs associated with mortality and morbidity endpoints can be calculated by using existing epidemiological data (e.g., Wolfe et al., 2017). For quantifying the total perceived noise costs (including annoyance), economists have proposed stated-preference and revealed-preference methods. Stated-preference approaches use surveys to obtain estimates of the willingness to pay for noise reductions and/or for the willingness to accept aircraft noise exposure (Bristow et al., 2015). Revealed-preference approaches include hedonic pricing, as suggested by Rosen (1974). This method infers the "implicit price" of noise exposure from market outcomes such as property values. The latter is the goal of this study.

In their empirical implementation, hedonic pricing studies face a variety of challenges, including (a) potential omitted-variable bias, especially due to unobserved neighborhood characteristics and to omission of the positive amenity impact of airports in surrounding communities; (b) misspecification of the functional form; and (c) stability assumptions regarding preferences among individuals across space and time (Parmeter, Pope, 2013; Kuminhoff et al., 2010; Chay and Greenstone, 2005, Nelson, 2004). This criticism has been addressed through methodical advancements. In an effort to assess functional specifications, some researchers have applied extensive sensitivity analyses or functional form tests (e.g., Kuminhoff, 2010). Omitted-variable bias, especially for neighborhood characteristics, is often addressed by considering neighborhood fixed effects (e.g., Kuminhoff, 2010). Beimer and Maennig (2017) have proposed combining such a fixed-effect framework with a spatial lag. Furthermore, they have analyzed cross-dependencies between noise sources (see also Ahlfeldt & Maennig, 2011). Similarly, many models account for the amenity impact of airports through considering airport access as a control variable (reviewed in Nelson, 2004).

The most recent studies have relied on quasi-experimental settings. These settings leverage changes in noise exposure, e.g., those due to flight track changes, to empirically identify the causal impacts of noise exposure on property values. Such an approach has been used by Boes and Nüesch (2011) and Almer et al. (2017) to study the property price effects of flight track changes at Zurich Airport; by Winke (2017) for studying the impacts of a new runway at Frankfurt Airport; and by Zheng et al. (2020) for studying the impacts of relocating Hong Kong Kai Tak Airport. As shown by Almer et al. (2017) and Zhen et al. (2020), this approach can be extended to systematically assess adjustment processes toward a new market equilibrium. However, it has not been applied for a large-scale comparative analysis of the impacts surrounding different airports or to study heterogeneities in the impacts between neighborhoods. Furthermore, most studies have focused on a single noise metric (e.g., the DNL, because of regulatory requirements), thereby providing limited insights into the impact mechanisms and their related noise characteristics.

For this study, the team identified a number of experimental settings that provide exogenous variation in noise exposure to analyze the impacts of noise exposure on residential property values. Most importantly, the introduction of high-precision Area Navigation (RNAV) and/or Performance Based Navigation (PBN) procedures since 2012 has led to the relocation of departure and approach flight paths or may have concentrated noise exposure along defined flight tracks. In addition, new runway configurations, such as those at Chicago O'Hare airport, have led to changes in noise exposure patterns. This variation will be used as part of the analysis.

Figure 1 summarizes the resulting approach and data requirements.

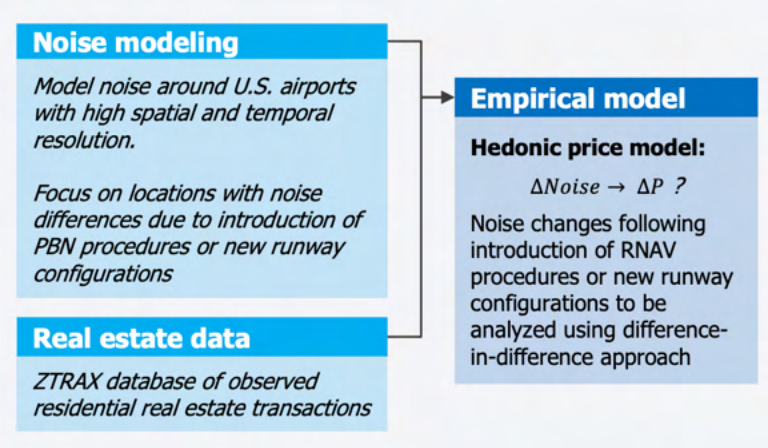

Figure 1. Overview of identification and data required for the analysis.

Milestone
The team has formulated a preliminary empirical strategy.

Major Accomplishments
The research team prepared a summary of the planned approach, which is implemented for analysis.

Outreach
The team presented the approach in a pre-recorded project outline during the ASCENT Fall meeting in 2020 and in a presentation during the ASCENT Spring meeting in 2021.

Plans for Next Period
The team will continue to refine the empirical approach.

References
Almer, C., Boes, S., & Nüesch, S. (2017). Adjustments in the housing market after an environmental shock: evidence from a large-scale change in aircraft noise exposure. Oxford Economic Papers, *69*(4), 918-938.

Ahlfeldt, G. M., & Maennig, W. (2013). External productivity and utility effects of city airports. Regional Studies, *47*(4), 508-529.

Beimer, W., & Maennig, W. (2017). Noise effects and real estate prices: A simultaneous analysis of different noise sources. Transportation Research Part D, *54*, 282-286.

Boes, S., & Nüesch, S. (2011). Quasi-experimental evidence on the effect of aircraft noise on apartment rents. Journal of Urban Economics, *69*, 196-204.

Bristow, A. L., Wardman, M., & Chintakayala, V. R. K. (2015). International meta-analysis of stated preference studies of transportation noise nuisance. Transportation, *42*(1), 71-100.

Chay, K. Y., & Greenstone, M. (2005). Does air quality matter? Evidence from the housing market. Journal of Political Economy, *113*(2), 376-424.

Kuminghoff, N. V., Parmeter, C. F., & Pope, J. C. (2010). Which hedonic models can we trust to recover the marginal willingness to pay for environmental amenities? Journal of Environmental Economics and Management, *60*, 145-160.

Rosen, S. (1974). Hedonic prices and implicit markets. Product differentiation in pure competition. Journal of Political Economy, *82*(1), 34-55.

Winke, T. (2017). The impact of aircraft noise on apartment prices: a differences-in-differences hedonic approach for Frankfurt, Germany. Journal of Economic Geography, *17*, 1283-1300.

Wolfe, P. J., Kramer, J. L., & Barrett, S. R. H. (2017). Current and future noise impacts of the U.K. hub airport. Journal of Air Transport Management, *58*, 91-99.

Zheng, X., Peng, W., & Hu, M., 2020. Airport noise and house prices: A quasi-experimental design study. Land Use Policy, *90*, 104287.

Task 3 - Calculation of Noise Metrics

Massachusetts Institute of Technology

Objective

The goal of this task is to calculate aircraft noise exposure in communities surrounding selected U.S. airports. These analyses will be used to derive noise exposure changes associated with changes in flight trajectories (e.g., due to new runways or new procedures).

Research Approach

The MIT team uses the Aviation Environmental Design Tool (AEDT) to model the noise exposure based on historical flight track data at high temporal and spatial resolution. The high-resolution approach is required, because the noise changes in PBN procedures are expected to be highly localized. However, one limitation of AEDT is in processing speed. Because it calculates noise for each flight track individually, a single day of flights can require hours to process. To circumvent this limitation, a fast model was developed at MIT with support from this project (Jansson, 2021). This model uses AEDT outputs for various aircraft types to set up a noise lookup table. Next, it uses flight track data from the Airport Surface Detection Equipment, Model X (ASDE-X) and applies the noise-power-distance curves from AEDT to obtain accurate noise data on an annual scale. The approach is outlined in Figure 2.

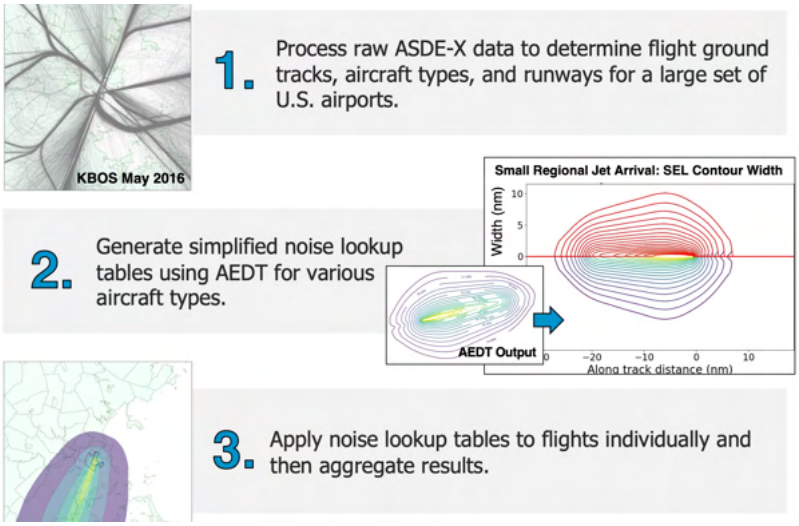

Figure 2. Noise modeling approach.

Milestone

The team set up the modeling chain and ran the model for two airports.

Major Accomplishments

The team set up the modeling chain and ran detailed noise analyses for the years 2012 and 2016 for Boston Logan and Chicago O'Hare airports (Task 4).

Student involvement

MIT graduate student Madeleine Jansson conducted research under this task. She graduated in September 2021. In addition, Zhishen Wang and Kevin Zimmer worked on this task.

Publications

Jansson, M. (2021). Development of a fast method to analyze patterns in airport noise [Master's thesis, MIT Department of Aeronautics and Astronautics].

Plans for Next Period
The team will continue this task by refining the modeling approach and simulating noise exposure at additional airports.

Task 4 - Cleaning and Aggregation of the Housing Transaction Dataset
Massachusetts Institute of Technology

Objective
The goal of this task is to obtain a dataset on transaction values for residential properties in the United States. The dataset needs to include detailed data for each transaction, including the location of the property, and the characteristics of the transaction (e.g., purchase price and closing date) and the property (e.g., lot and property sizes, and numbers of bedrooms and bathrooms). The team expects the datasets to require substantial validation and cleaning, which will be completed as part of this task.

Research Approach
The research team identifies and solves common problems with the Zillow Transactions and Assessor Dataset (ZTRAX). This process entails the following:

1. Identifying transaction prices reflecting fair market value: the team uses information on data types, document types, loan types, price types, and intra-family flags to rule out the transactions involving distress, intrafamily transfer, below market value from public actors, or listed prices.
2. Verifying the accuracy of geolocation of transacted properties: the team links the ZTRAX records to parcel polygons and identifies the locations of buildings within a parcel. By comparing the centroid of a parcel with the corresponding building geolocation, the team can identify the correct datum for each property and replace incorrect locations with correct ones.
3. Addressing missing or mismeasured data for standard housing attributes: the team conducts a series of data inspections, such as “sanity checks” and correlation calculation, to understand whether data errors are random or systematic.

Milestone
The team has access to U.S.-wide transaction data and has set up a data cleaning routine.

Major Accomplishments
The team has access to U.S.-wide transaction data from Zillow’s ZTRAX database. The team has compiled a dataset of residential real-estate transactions in the Boston area for the years 2007 to 2021.

Plans for Next Period
The team will continue to roll out the acquisition of the dataset to further airports.

Task 5 - Descriptive Analysis of the Dataset

Massachusetts Institute of Technology

Objective

For a small subset of airports, the team will conduct descriptive analyses of noise and residential property value data to gain insights into the validity of the datasets, as well as general noise and property value trends.

Research Approach

Descriptive analyses are conducted by analyzing data obtained under Tasks 3 and 4. As a first point of reference, descriptive analysis of noise data was conducted for Chicago O'Hare airport, and residential property value trends were analyzed for the Boston area. All analyses are limited to a radius of 20 nautical miles around Boston Logan and Chicago O'Hare airports, because of range limitations for the ASDE-X data.

Milestone

Preliminary descriptive analyses were completed for Boston Logan and Chicago O'Hare airports.

Major Accomplishments

Descriptive analyses of noise trends for Chicago O'Hare airport

Chicago O'Hare airport data taken from ASDE-X were run through the fast noise modeling method to create the average 24-hr DNL noise plots shown in Figure 3. One run was completed for 2011, and one run was completed for 2016. This procedure allows us to compare the noise levels before and after the opening of runway 10C/28C and runway 10R/28L which opened in 2013 and 2015, respectively. In the preliminary results, we observe noise increases in the east-west direction and a slight noise decrease in the northwest region. These noise changes track the changes in runway configuration for Chicago O'Hare Airport.

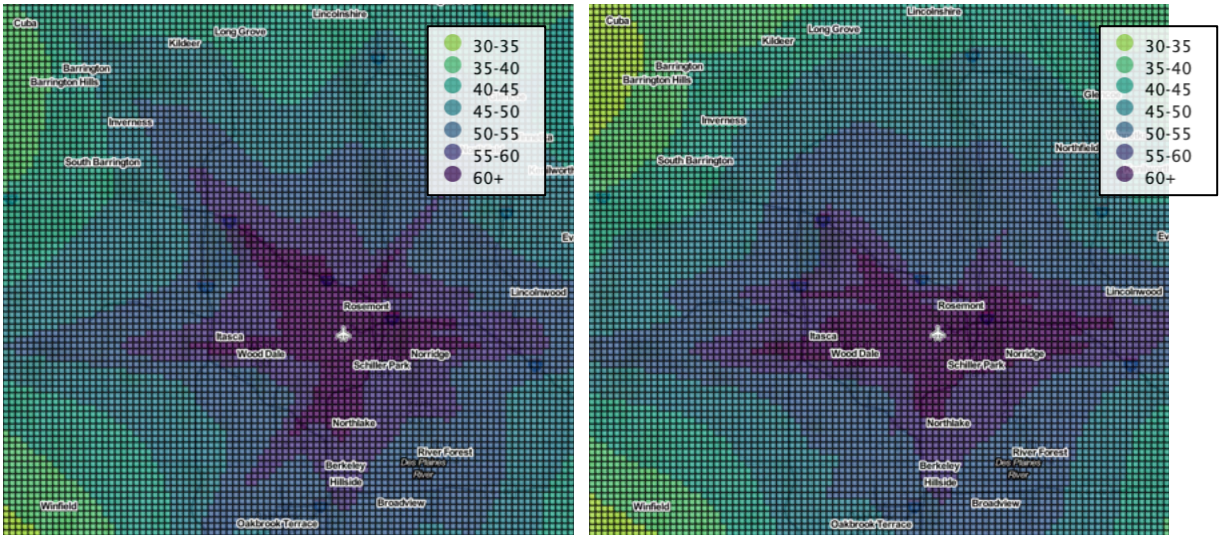

Figure 3. Average annual DNL in 2011 (left) and 2016 (right), overflights from KORD.

Descriptive analyses of residential real-estate value in the Boston area

To understand the changes in housing prices in Boston over time, the team filtered the house sample to include those houses sold at least once between 2007 and 2011 and sold again at least once between 2016 and 2021. Among these samples, the team compared the inflation-corrected housing price of the same house between these two periods. The spatial differences are shown in Figure 4, in which each dot represents a house sample with a repeat sale record over our study period. Red represents an increase in housing price, and blue represents a decrease in housing price. The darker the color, the larger is the magnitude of housing price change. A substantial number of houses in the central and east areas experienced an increase

in sales price, whereas houses in the north and south areas appeared to have negligible price changes throughout these years.

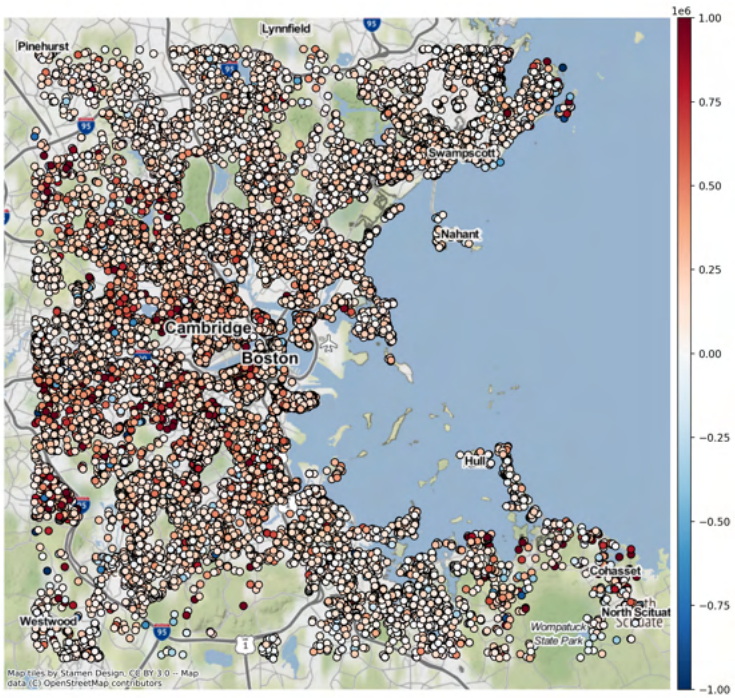

Figure 4. Housing price changes over time.

Student involvement

MIT graduate student Madeleine Jansson conducted research under this task. She graduated in September 2021. In addition, graduate students Zhishen Wang and Kevin Zimmer worked on this task.

Plans for Next Period

The team will continue to roll out descriptive analyses to evaluate general trends and dataset validity.

Project 073 Fuel Composition Impact on Combustor Durability

University of Dayton Research Institute

Project Lead Investigator

Steven Zabarnick, Ph.D.
Division Head, Fuels and Combustion Division
University of Dayton Research Institute
300 College Park
Dayton, OH 45469-0043
937-229-3961
Steven.Zabarnick@udri.udayton.edu

University Participants

University of Dayton Research Institute (UDRI)

- PI: Steven Zabarnick, Ph.D.
- FAA Award Number: 13-C-AJFE-UD, Amendment 029
- Period of Performance: August 11, 2020 to September 30, 2021
- Task:
    1. Radiation measurements of various fuel types will be performed in the referee combustor to evaluate the function of fuel composition on combustor liner lifetime.
- Period of Performance: August 10, 2021 to February 10, 2022 – Amendment 036

Project Funding Level

Amendment No. 029	$299,148
Total	**$299,148**

Cost sharing will be provided by fuel producers and engine/airframe OEMs. The cost share will be given in fuel provided for testing and in fuel performance data provided for the evaluation.

Investigation Team

Project Director/PI: Steven Zabarnick
Co-Investigator: Scott Stouffer
Research Engineer: Tyler Hendershott
Technician: Harry Grieselhuber
Graduate Student: TBD
Undergraduate Student: TBD

Project Overview

In this study, the effect of fuel chemical composition on radiative heat transfer and the resulting combustor liner lifetime will be evaluated. Alternative fuels contain ratios of hydrocarbon types that may be quite different from those in familiar petroleum-based fuels. For petroleum-based fuels, it is known that higher aromatic levels contribute to greater radiative heat transfer and reduced combustor liner lifetimes. As a result, aromatics are limited to 25 vol% in the ASTM D1655 jet fuel specification. Some candidate alternative fuels contain synthetically produced aromatics and cycloparaffins, which must be evaluated for their radiative heat transfer characteristics. The measurements taken in this project will provide insight into the effect of fuel type on liner lifetime. Several fuel types will be investigated, including a synthetic aromatic kerosene (SAK),

a baseline Jet A fuel, and a fuel that is high in cycloparaffins (e.g., Shell IH^2 fuel). Diagnostic methods to be used in the investigation include the measurement of wall and gas temperatures and the use of infrared (IR) cameras and radiometers.

Task 1 – Perform Measurements of Radiative Heat Transfer in the Referee Rig

University of Dayton Research Institute

Objective

The objective of this program is to provide insight into the effect of fuel type on engine combustor liner lifetime. This study will assure that candidate drop-in fuels will perform satisfactorily in jet engines and not increase the need for engine maintenance or decrease flight safety. This study may also indicate which fuel composition changes may reduce radiative heat transfer and therefore increase combustor liner lifetime.

Research Approach

It is well known that fuel chemical composition strongly affects soot formation, smoke production, and radiative heat flux in gas turbine combustors (1). Studies of petroleum-based fuels with varying aromatic species levels have shown that these properties increase with overall aromatic species content. Other parameters such as hydrogen content, hydrogen/carbon (H/C) ratio, and smoke point have also been correlated with liner temperatures, but the effect of individual aromatic species types has not been well studied (2). Candidate alternative fuels may meet the overall limits for aromatic species but may contain individual species or mixtures of species that are very different from those in petroleum-derived fuels. Radiation heat transfer to combustor liners is a major issue affecting the durability and operational envelope of gas turbine engines. Radiation can cause high heat fluxes, resulting in localized heating, hot spots, and high thermal gradients along and across the liner. Increases in liner temperature can decrease liner durability (3). Intense heating can cause problems with low cycle fatigue, cracking, and buckling of the liner and, in extreme cases, can lead to localized melting of the liner. The combustor walls can be convectively cooled by effusion or film cooling; however, film cooling typically imposes a cycle performance penalty, along with elevated levels of CO and unburnt hydrocarbons, particularly at low power settings. Because of concerns about fuel effects on radiation, the radiant heat flux is considered a Figure of Merit (FOM) by aircraft engine OEMs when evaluating alternative fuels for aircraft use (4).

The radiation from a gas turbine flame has two main components:
1. "Non-luminous" radiation from product gases such as CO_2, H_2O, and CO and
2. Luminous radiation from particulates (principally soot) (5).

Non-luminous radiation corresponds to the infrared region and has a spectral distribution, whereas the luminous radiation is broadband, with a fraction of the radiation appearing at visible wavelengths. Typically, as the pressure is increased, the luminous radiation from soot particles becomes the dominant source of heat flux to the liner walls. While the convective component of the wall heat transfer depends on the fluid dynamics and gas temperature distribution near the walls, the peak radiant fluxes are related to the combinations of high temperature gas and particulates.

The emissivity of the combustion gases is typically related in an expression such as:

$$\epsilon_g = 1 - exp\left[-aPL(ql)^{0.5}T_g^{-1.5}\right]$$

where P = gas pressure, kPa
l = characteristic length factor, which is a function of combustor geometry
T_g = gas temperature, K
q = fuel-to-air ratio
L = luminosity factor

The luminosity factor is set to one for gaseous emissivity. For sooting flames associated with liquid aviation fuels, the luminosity is greater than one and can be correlated with the fuel composition. Several relations for the luminosity versus fuel type have been reported in the literature (6-8). In general, the relations show a drop in the luminosity factor with increases in H/C ratio and decreases in the aromatic content of the fuel. Other correlations in the literature also address the relationship of correlation to smoke point and naphthalene content. While there has been use of IR as a diagnostic tool in basic flame experiments (9), there has been very little work reported in the literature using multiple radiometer and/or planar

measurements of IR emissions in practical combustors. The Referee Rig Combustor is an ideal rig for assessing radiation heat transfer because the walls are heavily cooled, a condition that tends to suppress the convective component and thus the background radiant heating from opposing walls, so that the wall heat transfer is primarily from the flame radiation. Furthermore, provisions have been made for radiometer access to the combustor walls in the referee rig.

The team for the proposed effort has developed and used the Referee Rig Combustor to conduct experimental combustion research. Highlights of previous contributions to the evaluation of alternative fuels include:

1. Experimental measurements of lean blowout (LBO) for fuels at a condition of interest to the OEMs and the National Jet Fuels Combustion Program (NJFCP), which have resulted in an unexpected finding of a high correlation between the derived cetane number (DCN) and the LBO limit.
2. Experimental measurements of boundary conditions for the combustor, including air flow splits to support numerical combustion modeling efforts.
3. Development of cold air and cold fuel capabilities for the facility to enable atmospheric cold start ignition experiments to be conducted over a range of conditions.
4. A further extension of the facility capability to enable altitude relight experiments to be conducted with a range of fuels at simulated altitudes of 25,000 ft.

The work with the Referee Rig Combustor has resulted in publications that detail cold start ignition (10), ignition at elevated temperatures (11), LBO characteristics (11-15), particulate and gaseous emissions (12), flow through the liner effusion passages (13), acoustic response (11-17), spray characteristics (16), and altitude relight (19).

Milestone(s)

Below is a list of the anticipated major milestones and planned due dates.

Milestone	Planned Due Date
Test plan provided	December 1, 2020
Testing performed for a range of fuels	August 1, 2022
Final report	August 31, 2022

Major Accomplishments

Planning and purchasing tasks for this project have been ongoing. Sapphire IR windows were purchased to enable IR access to the referee combustor. We have developed hardware plans for installing surface thermocouples and an IR camera/radiometer in the system. We are also working with AFRL to plan for piggy-back runs on the referee rig with AFRL cooperation. Discussions are ongoing with Shell to obtain sufficient volumes of the IH^2 fuel for testing.

Publications

None

Outreach Efforts

None

Awards

None

Student Involvement

None

Plans for Next Period

The bulk of the project will be planned, conducted, analyzed, and reported in the next project period.

References

.

(1) Chin, J.S., and Lefebvre, A.H., "Influence of Fuel Composition on Flame Radiation in Gas Turbine Combustors," Journal of Propulsion and Power, Vol. 6, No. 4, pp. 497-503.

(2) Boehm et al., “Development of Combustion Rules and Tools for the Characterization of Alternative Fuels, Phase 2A”, AFRL-RQ-WP-TR-2013-0223, October 2013.

(3) Gleason, G.C., and Bahr, D.W., "Fuel property effects on Life Characteristics of Aircraft Turbine Engine Combustors", ASME Paper 80-GT-55, 1980.

(4) Lefebvre, A.H., "Gas Turbine Combustion (2nd edition)", Taylor and Francis, 1999.

(5) Naegeli, D.W. and Moses, C.A., "Effects of Fuel Properties on Soot Formation in Gas Turbine Engines", ASME paper 80-GT-62, 1980.

(6) Clark, J.A. "Fuel Property Effects on Radiation Intensities in a Gas Turbine Combustor", AIAA J. Vol. 20. No. 2, pp274-281, 1982.

(7) Rankin, B.A., Blunck, D.L., Katta, V.R., Stouffer, S.D., Gore, J.P., Experimental and Computational Infrared Imaging of Bluff Body Laminar Diffusion Flames," Combustion and Flame, Vol. 159, pp2841-2843, 2012.

(8) Hendershott,T.H.,Stouffer,S.D.,Monfort,J.R.,Diemer,J.,Busby,K.;Corporan,E.,Wrzesinski,P.J.,Caswell,A.W., "Ignition of Conventional and Alternative Fuel at Low Temperatures in a Single-Cup Swirl-Stabilized Combustor," 2018 AIAA Aerospace Sciences Meeting, AIAA 2018-1422

(9) Stouffer, S.D., Hendershott, T.H., Monfort, J.R., Diemer, J. Edwin Corporan, E., Wrzesinski, P.J., Caswell, A., “Blowout and Ignition Characteristics of Conventional and Surrogate Fuels Measured in a Swirl Stabilized Combustor”, AIAA Paper AIAA-2017-1954, AIAA SciTech Conference Jan 9-13, 2017.

(10) Corporan, E., Edwards, J., Stouffer, S.D., DeWitt, M., West, Z., “Impacts of Fuel Properties On Combustor Performance, Operability and Emissions Characteristics, AIAA Paper AIAA-2017-0380, AIAA SciTech Conference Jan 9-13, 2017.

(11) Alejandro M. Briones, A.M., Stouffer, S.D., Vogiatzis, K., Rein, K., Rankin, B.A., "Effects of Discrete Dome and Liner Cooling Momentum on Combustor Flow Fields", AIAA-2017-0781,AIAA SciTech Conference Jan 9-13, 2017.

(12) Esclapez, L., Ma, P. C., Mayhew, E., Xu, R., Stouffer,S.D., Lee, T., Wang, H., and M. Ihme, M."Fuel Effects on Lean Blow-out in a Realistic Gas Turbine Combustor" Accepted for publication in Combustion and Flame 2017.

(13) Colborn, J.G., Heyne, J., Hendershott,T.H., Stouffer, S. D.,Peiffer, E., and Corporan, E., "Fuel and operating condition effects on Lean Blowout in a Swirl-Stabilized Single Cup Combustor", AIAA 2020-1882, Presented at AIAA Scitech, January 9th 2020.

(14) Mayhew, E., Mitsingas,C., McGann, B., Lee, T., Hendershott, T, Stouffer, S., Wrzesinski, P., and Caswell, A., "Spray Characteristics and Flame Structure of Jet A and Alternative Jet Fuels," AIAA Paper AIAA-2017-0148, AIAA SciTech Conference Jan 9-13, 2017.

(15) Monfort,J.R., Stouffer, S.D,. Hendershott, T.H., Wrzesinski, P.J., Foley, W.S.,Rein, K., "Evaluating Combustion Instability in a Swirl-Stabilized Combustor Using Simultaneous Pressure, Temperature, and Chemiluminescence Measurements at High Repetition Rates," AIAA Paper AIAA 2017-1101, AIAA SciTech Conference Jan 9-13, 2017.

(16) Erdmann, T.J., Burrus, D.L., Briones, A.M., Stouffer, S.D., Rankin, B.A., Caswell, A.W., “Experimental and Computational Characteristics of Flow Rates in a Multiple-Passage Gas Turbine Combustor Swirler,” GT2017-65252, Proceedings of the ASME Turbo Expo 2017: Turbine Technical Conference & Exposition, June 26-30, Charlotte, NC.

(17) Stouffer, S. D., Hendershott,T.H., Monfort,J, Colborn, J.G., Corporan,E., Paul Wrzesinski,P., Caswell, A. "Fuel Effects on Altitude Relight Performance of a Swirl Cup Combustor", AIAA 2020-1882 Presented at AIAA Scitech, January 9th 2020.

Project 074 Low Emission Premixed Combustion Technology for Supersonic Civil Transport

Georgia Institute of Technology

Project Lead Investigator

Adam Steinberg
Associate Professor
School of Aerospace Engineering
Georgia Institute of Technology
Phone: (404) 897-1130
E-mail: adam.steinberg@gatech.edu

University Participants

Georgia Institute of Technology (GT)

- PI: Adam Steinberg, Associate Professor, School of Aerospace Engineering
- FAA Award Number: 13-C-AJFE-GIT-079
- Period of Performance: August 11, 2020 to September 30, 2022
  Period of Performance Covered in Report: October 1, 2020 to September 30, 2021
- Task(s):
  1. Experimental measurement of flame structure, combustion dynamics, and emissions
  2. Large-eddy simulations (LES) of combustor operation and emissions

Project Funding Level

FAA: $1,999,998
Georgia Institute of Technology: $1,000,262
GE Research: $999,736

Investigation Team

Name	Affiliation	Role	Tasks
Adam Steinberg Associate Professor	Georgia Institute of Technology	PI	Management, reporting, technical oversight of all tasks, oversight of optical diagnostics in Task 1
Ellen Mazumdar Assistant Professor	Georgia Institute of Technology	Co-PI	Oversight of non-volatile particulate matter (nvPM) measurements in Task 1
Joseph Oefelein Professor	Georgia Institute of Technology	Co-PI	Oversight of first-principles LES in Task 2 and overall coordination of Task 2
Jerry Seitzman Professor	Georgia Institute of Technology	Co-PI	Oversight of gas-phase fuel/air mixing diagnostics in Task 1
Michael Benjamin Consulting Engineer	GE Aviation	Co-PI	Oversight of combustor design in Task 1, coordination of GT/GE LES collaboration in Task 2
Krishna Venkatesan Principal Engineer	GE Research	Co-PI	Oversight of combustor operation in Task 1

Oleksandr Bibik **Senior Research Scientist**	Georgia Institute of Technology	Participant	Task 1
Hannah Bower **Research Engineer**	GE Research	Participant	Task 1
R. Narasimha Chiranthan	GE Aviation	Participant	Task 2
Manampathy Giridharan	GE Aviation	Participant	Task 2
Hiranya Nath	GE Aviation	Participant	Task 2
John Hong **Lead Engineer**	GE Research	Participant	Task 1
Sriram Kalathoor **Graduate Research Assistant**	Georgia Institute of Technology	Graduate Student	Task 2
Mitchell Passarelli **Graduate Research Assistant**	Georgia Institute of Technology	Graduate Student	Task 1
Samuel Wonfor **Graduate Research Assistant**	Georgia Institute of Technology	Graduate Student	Task 1
Andrew Zheng **Graduate Research Assistant**	Georgia Institute of Technology	Graduate Student	Task 1
Kailey Obenstine **Research Assistant**	Georgia Institute of Technology	Undergraduate Student	Task 1
Coleman Pethel **Research Assistant**	Georgia Institute of Technology	Undergraduate Student	Task 1
Rachel Thomas **Research Assistant**	Georgia Institute of Technology	Undergraduate Student	Task 1

Project Overview

The market demand for high-speed transport is expected to drive a rapid re-emergence of commercial supersonic transport (CST) aircraft over the coming decades. This impending CST revival, combined with the increasingly harmful impacts of anthropogenic climate change, mandate advancements in CST-focused environmentally compatible technologies and policies. Compared with subsonic aircraft, engines for CST aircraft will (a) operate at significantly lower overall pressure ratio (OPR) and bypass ratio (BR); (b) experience higher combustor inflow temperatures (T_3), lower pressures (p_3), and higher fuel/air ratios at cruise; and (c) cruise at higher altitudes. The reduced OPR and BR result in increased thrust-specific fuel consumption, thus increasing fuel burn and making emission reductions fundamentally more challenging. Furthermore, the combination of a low OPR and high cruise T_3 and FAR result in complicated trade-offs between nitrous oxide (NO_x) at cruise and other emissions (CO, nonvolatile particulate matter [nvPM] and unburnt hydrocarbons [UHC]) at lower power.

Several recent studies have assessed potential CST fleet emissions and environmental impacts based on currently deployed rich-burn–quench–lean-burn combustors (typically Tech Insertion combustors) designed for subsonic transport (Berton et al., 2020; Speth et al., 2021; Hassan et al., 2020; Kharina et al., 2018). These studies have demonstrated that innovations in combustor architecture will be required to meet emission targets and to create an environmentally compatible CST market. Despite the high T_3 and FAR, peak flame temperatures must be moderated to meet NO_x targets, while also maintaining efficiency and achieving low CO, UHC, and nvPM levels, which will require increased fuel-lean premixing prior to combustion.

Lean premixed pre-vaporized (LPP) combustors are a promising path to lowering emissions from future CST engines. In LPP combustors, fuel is injected, partially pre-vaporized, and partially premixed with air before the reactants enter the combustor. While the LPP concept is not new, e.g., (Niedzwiecki, 1992), achieving good vaporization and mixing in a flight-appropriate package has been challenging in the past. However, these issues can potentially be alleviated by the high T_3 in CST combustors—which results in faster vaporization—and advanced manufacturing to enable compact rapid-mixing flow elements.

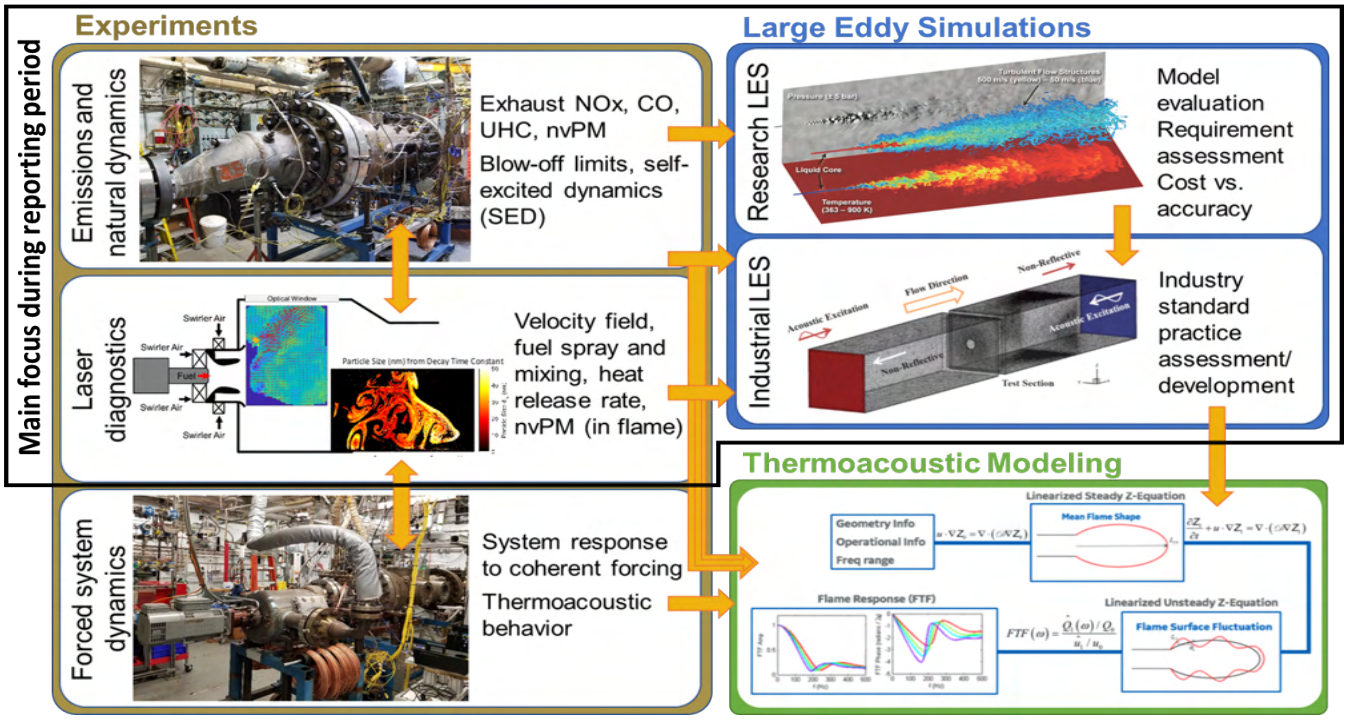

Figure 1. Project overview.

Thus far, the ability of current design methodologies to predict the operability and emissions of LPP combustors under relevant conditions is unproven. Hence, there is a critical need to generate high-quality experimental data under CST combustor conditions, coupled with the development/validation of computational fluid dynamics (CFD) simulations and reduced-order thermoacoustic models. This project will fill this need through a combination of experiments, LESs, and thermoacoustic modeling, all applied in a novel LPP combustor of interest to future CST applications. Figure 1 shows the elements of this research project. Note that the Period of Performance covered in this report focuses on the experiments and LESs.

Task 1 – Experimental Measurements of Flame Structure, Combustion Dynamics, and Emissions

Objective(s)

This task represents the experimental efforts involved in measuring the flame structure, dynamics, and emissions in a novel LPP combustor concept, designed specifically for low-emission operation under typical conditions encountered by CST engines.

Research Approach

Efforts under Task 1 over the reporting period consisted of four main activities.

1) Design, fabrication, and deployment of the LPP combustor in a test cell at GE Research.
2) Design and calibration of optical diagnostics using a high-pressure laminar flame burner at Georgia Tech, with associated student training.
3) Experimental Campaign 1, in which optical diagnostics from Georgia Tech were transported to GE Research and deployed in the LPP combustor test cell, along with emission diagnostics provided by GE. Three Georgia Tech students were onsite at GE Research for a total of nearly 9-person months over the summer of 2021 to conduct this experimental campaign in collaboration with GE staff.
4) Analysis of experimental data from Campaign 1.

Experimental Design, Fabrication, and Calibration

Considerable preliminary work was performed to enable on-schedule completion of Experimental Campaign 1. The following major elements of the test rig at GE Research were designed and fabricated:

1) LPP combustor,
2) Combustor dome face,
3) Test rig spool piece,
4) Water-cooled emission probe,
5) Window blank with pressure measurement ports, and
6) Custom laser cart and optical tables.

Significant effort was required to optimize the optical layout of the diagnostics due to space constraints in the test cell, safety considerations, and the need for routine access to the test article. The resultant optical layout is described in detail below.

Concurrent with these activities, a high-pressure laminar flame burner (shown in Figure 2) was deployed at Georgia Tech for the purpose of calibrating the various laser diagnostics. Specifically, it was necessary to calibrate the time-resolved laser-induced incandescence (TiRe-LII) diagnostics for accurate measurements of nvPM primary particle size and the fuel planar laser-induced fluorescence (PLIF) diagnostics to account for laser absorption and oxygen quenching. The efforts described in this report pertain to the calibration and evaluation of TiRe-LII measurements. This burner is capable of stabilizing premixed flames of pre-vaporized Jet A fuel and air over lean and rich equivalence ratios and pressures up to 10 bar. Multiple windows were included to provide optical access for laser diagnostics.

The measurement model for TiRe-LII is described below. To calibrate the TiRe-LII model for quantitative nvPM primary particle size measurements, it is necessary to perform TiRe-LII and extractive nvPM sampling under the same conditions. Subsequently, the sampled measurements can be analyzed using transmission electron microscopy (TEM) to provide detailed quantification of the primary particle size, aggregate structure, and other nvPM properties. These properties can then be compared with the TiRe-LII signals to calibrate the measurement model.

Hence, an extractive sampling system, leveraging thermophoresis, was created to sample nvPM from this flame (Vargas & Gülder, 2016). This system contains eight TEM grids that are rotated into the flame to precisely control sampling times using a stepper motor. Samples that are deposited onto the grids are analyzed using a Tecnai F30 300 kV HR TEM, producing images of the nvPM such as those shown in Figure 3. Previously established post-processing routines are then applied to characterize the nvPM, such as the distribution of primary particle sizes, which can be used to calibrate the TiRe-LII.

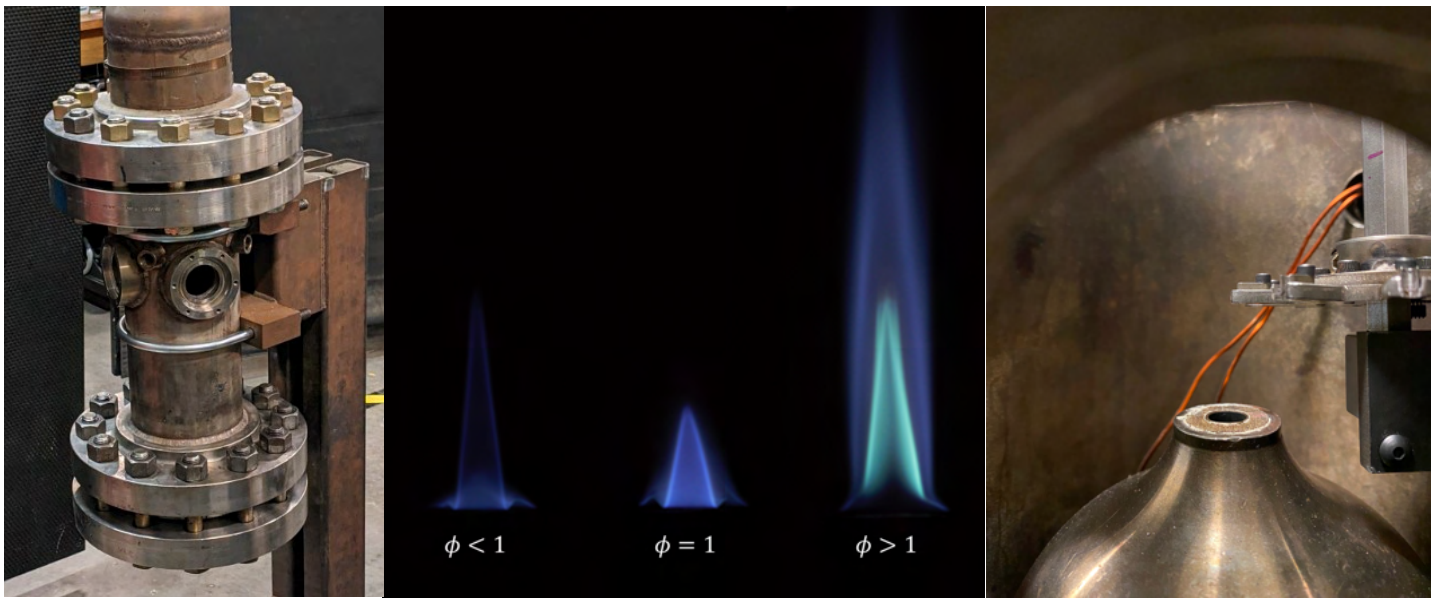

Figure 2. High-pressure calibration burner. Left: Pressure vessel. Middle: Typical laminar flames at different equivalence ratios. Right: Thermophoretic nvPM sampling system.

The TiRe-LII model is used to fit measured incandescence intensity decay curves to a primary particle size. The baseline model is based on work by Liu et al. (2005) and includes laser absorption, conduction, and radiation elements with control volumes placed around soot particles or soot agglomerates, as shown in Figure 4. For lower laser fluences, the dominant heat transfer mechanism is conduction, which can occur in the free molecular regime or the continuum regime as a function of the Knudsen number. To accurately incorporate temperature-dependent thermal conductivity terms, temperature-dependent specific heat terms, and conduction regimes, an iterative solver was implemented. At higher laser fluences, sublimation mechanisms begin to play a larger role in the incandescence signals. For this project, we incorporated the sublimation mechanisms proposed by Michelson et al., 2007, which account for changes in mass and particle diameter. These differential equations are then solved simultaneously to determine decay profiles as a function of particle size and flame conditions. Once the temperature profiles are determined, the data are converted to light using Planck's equation.

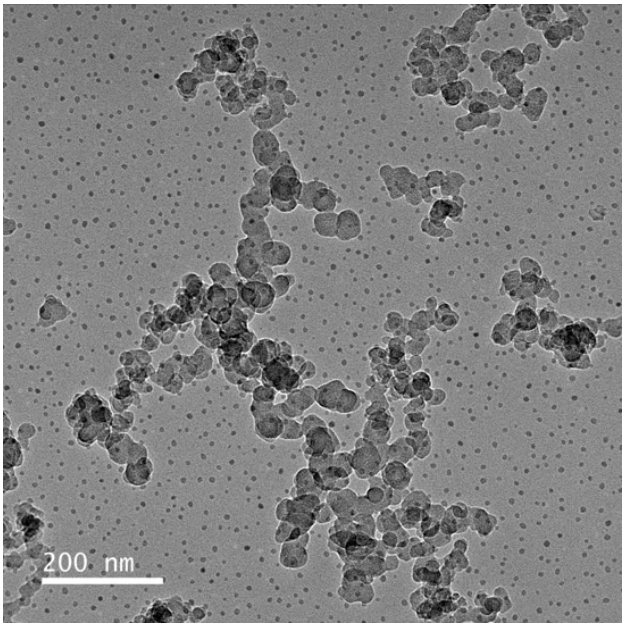

Figure 3. Typical TEM image of sampled nvPM.

For preliminary TiRe-LII model fitting, a simple procedure was devised that first forward-simulates decay profiles for several different soot particle sizes using low laser fluences. These temperature profiles are then converted to intensity profiles. Because these intensity profiles have a roughly first-order exponential decay, time constants can be derived from each decay profile. From these data, a soot particle size to decay time constant library can be developed for each operating condition (bath gas temperature, pressure, etc.).

Initial validation of these data focused on estimating soot particle sizes from laminar and turbulent non-premixed ethylene flames operating at atmospheric pressure (Chen et al., 2018; Shaddix et al., 2010). The data for these calibrations were collected with a 1064-nm laser, a bandpass filter (640 ± 75 nm), and a Shimadzu HPV-X2 ultrahigh-speed camera (10-MHz acquisition, 50-ns exposure). Utilizing published values for soot aggregate size and bath gas temperature (1850 K for the laminar flame and 1628 K for the turbulent flame), we were able to fit our model library data to the incandescence decay at each pixel. These preliminary estimates match well with literature values and show a clear difference in particle size in the nvPM growth region versus the soot oxidation region. The next step in this effort is to generate more accurate calibrations of nvPM particle size at relevant pressures and temperatures using the aforementioned laminar flame burner and extractive sampling system. This step will help to improve model estimates and reduce estimation uncertainties.

Experimental Campaign 1

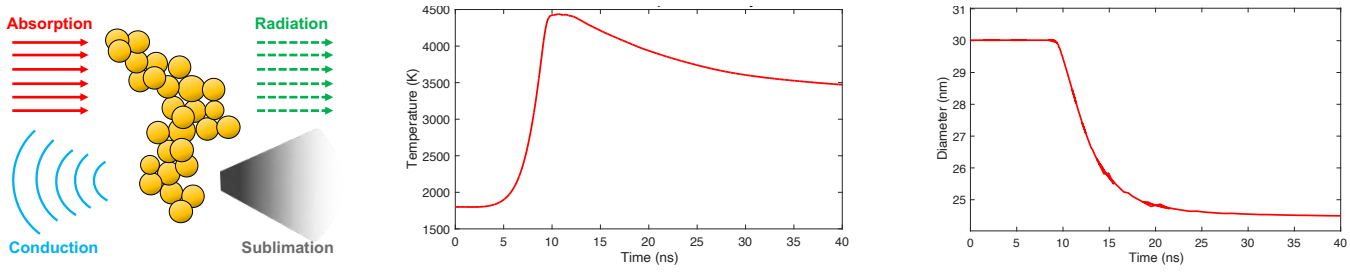

(a) (b) (c)

Figure 4. (a) Soot incandescence decay models showing changes in (b) particle temperature and (c) particle diameter after laser incidence.

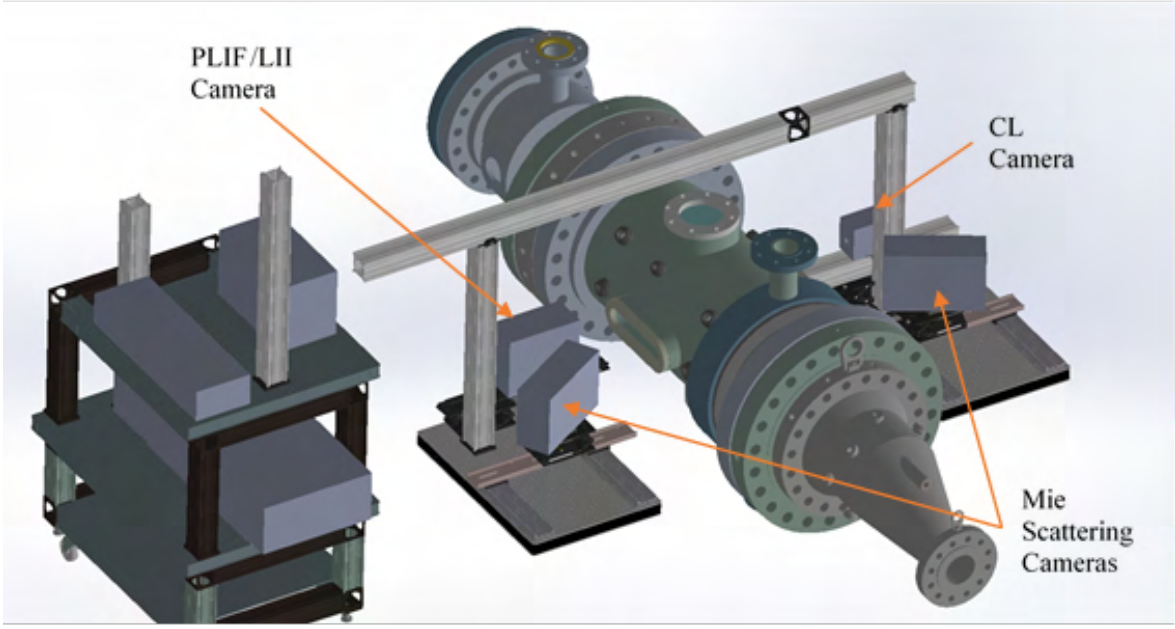

Figure 5. Test cell schematic with optical diagnostics.

Combustor & Operating Conditions: Experiments were performed at GE Research in Niskayuna, New York. Figure 5 shows the facility used for the experiments and the layout of the optical diagnostics. Figure 6 shows a schematic of the combustor dome face, which consists of four bluff-body stabilized "main" flames surrounding a central swirling pilot flame. Note that the bluff-body geometry is redacted. Each main flame operates under fuel-lean conditions, burning partially pre-vaporized and premixed Jet A fuel. For the majority of the laser diagnostics described below, the laser sheet passes through the centers of the main flames on one side of the combustor, as indicated in Figure 6.

Experiments were performed for a wide range of conditions (p_3, T_3, and FAR) relevant for CST operation. For the optical data presented in this report, each test point was acquired at the same air preheat temperature, $T_3 = 7.0 \times 10^2$ K, and a pressure appropriate for nominal cruise of a CST engine. Normalized emission data are also presented for different p_3 and T_3 combinations. For each test case, the FAR was varied, resulting in a sweep of the combustor exit temperature, T_4. Prior to data acquisition, the combustor was allowed to settle to steady state, as verified by an examination of static pressure, thermocouple, and mass flow rate measurements.

Diagnostics: Chemiluminescence (CL) imaging of OH* at 308 ± 5 nm served as the metric for line-of-sight integrated heat release rate measurements. Previous experiments (Kheirkhah et al., 2017) and wide-spectrum measurements from a portable spectrometer (Ocean Optics HR2000) showed that OH* is the most appropriate indicator of heat release rate. A sample spectrum is shown in Figure 7, with the peak corresponding to OH* emissions indicated. CL images were recorded at 10 kHz using a high-speed camera (Photron SA-5) coupled to an image intensifier (Invisible Vision UVi 2550B-10, gate time of 50 μs), commercial objective lens (Nikkor 105 mm UV, f/# = 11), and bandpass filter (312 ± 12.5 nm).

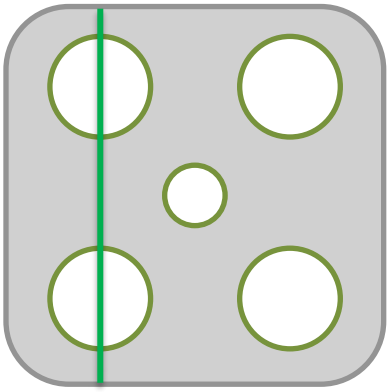

Figure 6. Combustor geometry, with the laser sheet position indicated by a green line. The four corners contain the partially premixed bluff-body stabilized main flames. The bluff-body geometry has been redacted.

Qualitative measurements of the fuel spray and mixing behavior were obtained via fuel droplet Mie scattering and PLIF of the aromatic species naturally present in the Jet A fuel, respectively. The flow was illuminated at a repetition rate of 10 Hz using the second (532 nm) and fourth (266 nm) harmonic outputs of a Nd:YAG laser (Spectra Physics Quanta-Ray PRO 350). The 532-nm beam was obtained from the residual of the fourth harmonic generator and was used for fuel droplet Mie scattering, while the 266-nm beam was used for PLIF. Both beams were formed into sheets of similar size via three separate cylindrical-lens telescopes, and were oriented perpendicular to the combustor dome face.

The Mie scattering was collected using two cameras (Phantom v2640) in a forward-scatter configuration with Scheimpflug adapters (LaVision), objective lenses (Tamron 180 mm, f/# = 8), and bandpass filters (532 ± 5 nm). Only one of the cameras was used for the analysis presented here because both cameras were qualitatively similar. The 532-nm sheet had a beam waist of approximately 2 mm at the midplane in the test article.

Laser-induced fluorescence was collected using an intensified camera (Andor iStar sCMOS, gate time of 100 ns) with an objective lens (Nikkor 105 mm UV, f/# = 4.5) and a two-filter setup consisting of a bandpass filter (340 ± 40 nm) and a steep-edge long wave pass filter (325 ± 3.5 nm). This filter setup aligned with the center of the fluorescence spectrum of kerosene vapor [13] while simultaneously blocking the signal from OH* CL. Simultaneous shot-to-shot beam profile measurements were made by using a cuvette filled with a rhodamine dye solution. The cuvette was placed in the path of residual transmission from the 266-nm sheet through the final mirror above the combustor at a point such that the beam waist was formed. This low-intensity copy of the sheet within the combustor induced visible fluorescence within the dye solution, which was then imaged with a separate camera system (FLIR Blackfly USB3).

Single-camera, single-laser shot two-dimensional TiRe-LII (Chen et al., 2019) was performed to analyze nvPM along the centerlines of the pilot and main flames. A 10-Hz, 1064-nm laser (Quanta-Ray PRO-350) was used to heat nvPM in the flame, and incandescence decay was captured along a 30-mm-long, 2-mm-thick laser sheet (fluence of 0.08 J/cm^2). The decay was captured at 10 MHz using an ultrahigh-speed camera (Shimadzu HPV-X2, 50-ns exposure) through an objective lens (85 mm, f/# = 1.4) and a bandpass filter (640 ± 75 nm) to block CL and laser illumination. Note that the LII measurements were not performed simultaneously with the fuel PLIF; thus, the results presented in this paper correspond to different test cases. A schematic of the TiRe-LII optics is shown in Figure 8, although this does not reflect the actual geometric arrangement of the optics deployed in the test cell (Figure 5).

Pressure fluctuations were measured using dynamic pressure transducers (PCB), mounted to the ends of calibrated waveguides in a semi-infinite loop configuration at three axial locations within the combustor. A data acquisition system (National Instruments USB-6361) recorded the pressure and camera timing signals at a sampling rate of 100 kHz. All three pressure measurements were qualitatively identical; thus, the data from the middle transducer were used for subsequent spectral analysis. Spectral analysis of the pressure and CL indicated that there were no significant natural thermoacoustic dynamics in the combustor.

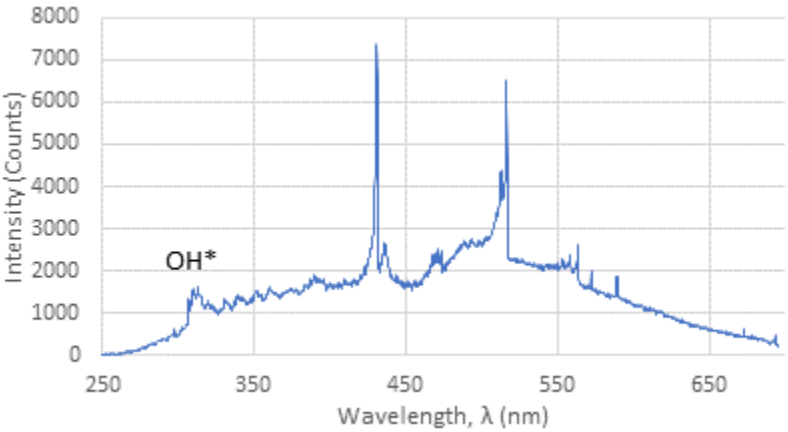

Figure 7. Typical light spectrum with the OH* CL band indicated.

Combustor emissions were measured using an axially and radially traversable water-cooled probe. Several analyzers were used to detect UHC (CAI model 600 HFID), CO/CO_2 (CAI model 603 NDIR), and nitrous oxide (CAI model 600 HCLD).

Optical Data Processing: Prior to analyzing the fuel spray Mie scattering data, the images were preprocessed to both correct the visual perspective and remove the background in the images. For the perspective calibration and correction, LaVision's DaVis 8.4 was used with a third-order polynomial model based on images taken of a LaVision 106-10 two-sided, two-plane calibration plate.

Due to the largely pre-vaporized nature of this combustor, few droplets were present in the combustor. This resulted in relatively low signal-to-noise in the Mie scattering data, necessitating considerable processing to extract meaningful information about the residual fuel spray. Figure 9 illustrates the processing pipeline. First, a mask was applied to the images to exclude regions without droplets. All images were then normalized to the same mean intensity to account for variations in pulse energy across all frames. Subsequent processing using a temporal high-pass filter removed the quasi-static background associated with the flame and laser reflections. Finally, thresholding and image segmentation operations removed much of the leftover background noise passing through the filter and identified the spray field in the combustor.

The PLIF images were processed for spatial calibration, background removal, intensifier white-field response, and shot-to-shot laser sheet intensity and profile variations, where the laser sheet profiles were extracted from images taken by the aforementioned cuvette–camera system. At present, no corrections have been made for the absorption of laser power through the domain or fluorescence quenching, although such corrections will be implemented in the future once calibration data are acquired.

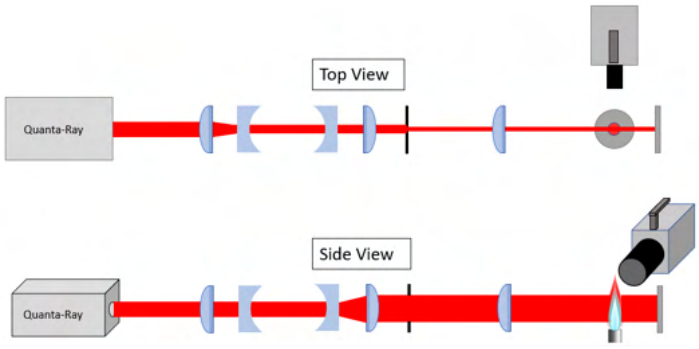

Figure 8. Schematic of TiRe-LII laser sheet forming optics.

Preprocessing for LII data began with background removal from each dataset. Each dataset was also spatially calibrated with calibration images taken before each test. To generate average prompt LII images, prompt LII images from each dataset were extracted for each test point condition and averaged. The intensity of each averaged image in the ramp-up condition set was averaged to the same baseline intensity determined from the intensity range of the ramp-up condition dataset. Because the datasets taken from full operating conditions had a lower signal overall, they were normalized to 1/10th of the baseline intensity. Each dataset was then fitted to obtain decay times for each pixel. However, due to the sparse amount of nvPM detected, fast intensity decay times in the datasets, and lack of a calibrated LII model for Jet A, particle-sizing abilities were limited.

Each TiRe-LII dataset was preprocessed by first referencing the coordinate system to spatial calibration plates. Then, the incandescence emission background for each dataset was removed. To generate average prompt LII images, which serve as

an estimate for soot volume fraction, the first frame after laser arrival from each dataset was extracted and grouped by test condition. To estimate soot particle sizes, the time profile for each pixel is examined, and only pixels above a certain brightness threshold are selected. The time profiles of these pixels are then fit to exponential decays to determine the particle time constants, which can be further correlated to particle sizes using LII modeling techniques.

Results & Discussion

Figure 10 shows the NO_x and CO emission trends for this combustor. Note that "NC" in Figure 10 designates "nominal cruise" pressure conditions. The increase in CO emissions observed for lean FAR (low combustor exit temperature) indicates that the system is approaching lean blowout (LBO). Each data series corresponds to a different T_3 range, as indicated in the legend. The series indicated by the yellow "x" markers matches the test cases for the optical data presented below. While quantitative values cannot currently be published, the maximum NO_x values are in line with NASA's 2035 CST goal (NASA, 2019).

To analyze the fuel spray and mixing characteristics, the mean fuel droplet Mie scattering, OH* CL, and fuel PLIF fields were computed for each test case. The mean fields are shown in Figure 11, with each case (columns in Figure 11) ordered from left to right by decreasing FAR. Each set of mean fields (corresponding to each row in Figure 11) is normalized by the maximum intensity across all cases. The spatial coordinates for the spray Mie scattering and fuel PLIF fields are normalized by the outer diameter of the main fuel injectors. Note that the spray and PLIF field of view are smaller than the OH* CL field of view. The red rectangle in the first CL mean field indicates the approximate position of the Mie scattering and PLIF fields of view.

1) Raw Images | 2) Mask & Intensity Normalization | 3) Perspective Correction & Cropping | 4) Temporal Butterworth High-pass Filter | 5) Thresholding & Image Segmentation

Figure 9. Post-processing pipeline for Mie scattering.

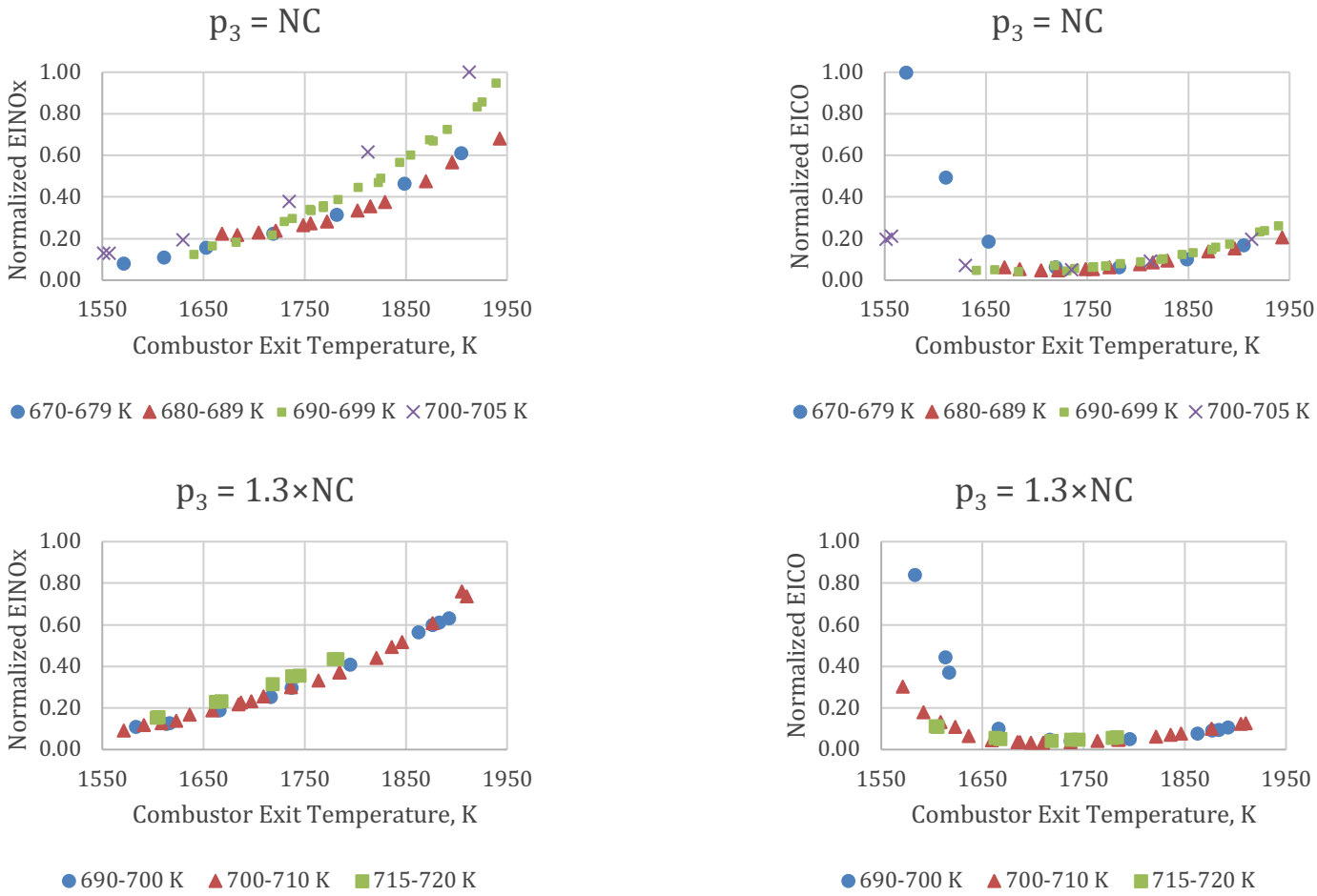

Figure 10. Normalized emission indices over several test points. The top row corresponds to nominal pressure conditions, and the bottom row corresponds to higher pressure. NC: nominal cruise.

Despite the sparsity of fuel droplets in the spray, the Mie scattering mean fields generally agree with the results in the PLIF mean fields in terms of length and qualitative intensity between regions. The sparsity of fuel droplets also indicates that the combustor is vaporizing most of the fuel prior to entry into the combustion chamber, resulting in good overall mixing. Differences in the mean fuel amount between the mains (and between the two halves of each main) may be attributed to the discrete fuel injectors in the premixer tube and other naturally arising asymmetries.

For higher FARs, the fuel PLIF measurements show an annular region of premixed fuel and air, as well as regions of low PLIF signals denoting burnt products. Product gases occurred both within the bluff-body recirculation zone and surrounding the fuel/air jets, indicating an annular partially premixed flame surface. Decreasing the FAR from Case 1 to 4 decreased the PLIF and OH* signals without qualitative changes in the flame geometry. For Case 5, the lower flame blew out, resulting in the lack of a lower main flame in the OH* CL; thus, premixed fuel and air filled the recirculation zone in the PLIF images. In Case 6, there was a complete blow out of the main flames. It is worth noting that the behavior of the main fuel injectors was not symmetric in the direction perpendicular to the laser sheet. Specifically, in Case 5, the upper main on the side of the combustor opposite the laser sheet had also blown out (three of the four mains were blown off). The relatively high root-mean-squared fuel PLIF fluctuations for all conditions are indicative of a high turbulence intensity in the shear layer between the mains and recirculation zones, as well as spatiotemporal variations in the fuel/air mixing exiting the premixer tubes. A comparison of Figures 10 and 11 shows that the observed increase in CO with decreasing FAR corresponds to the conditions approaching LBO.

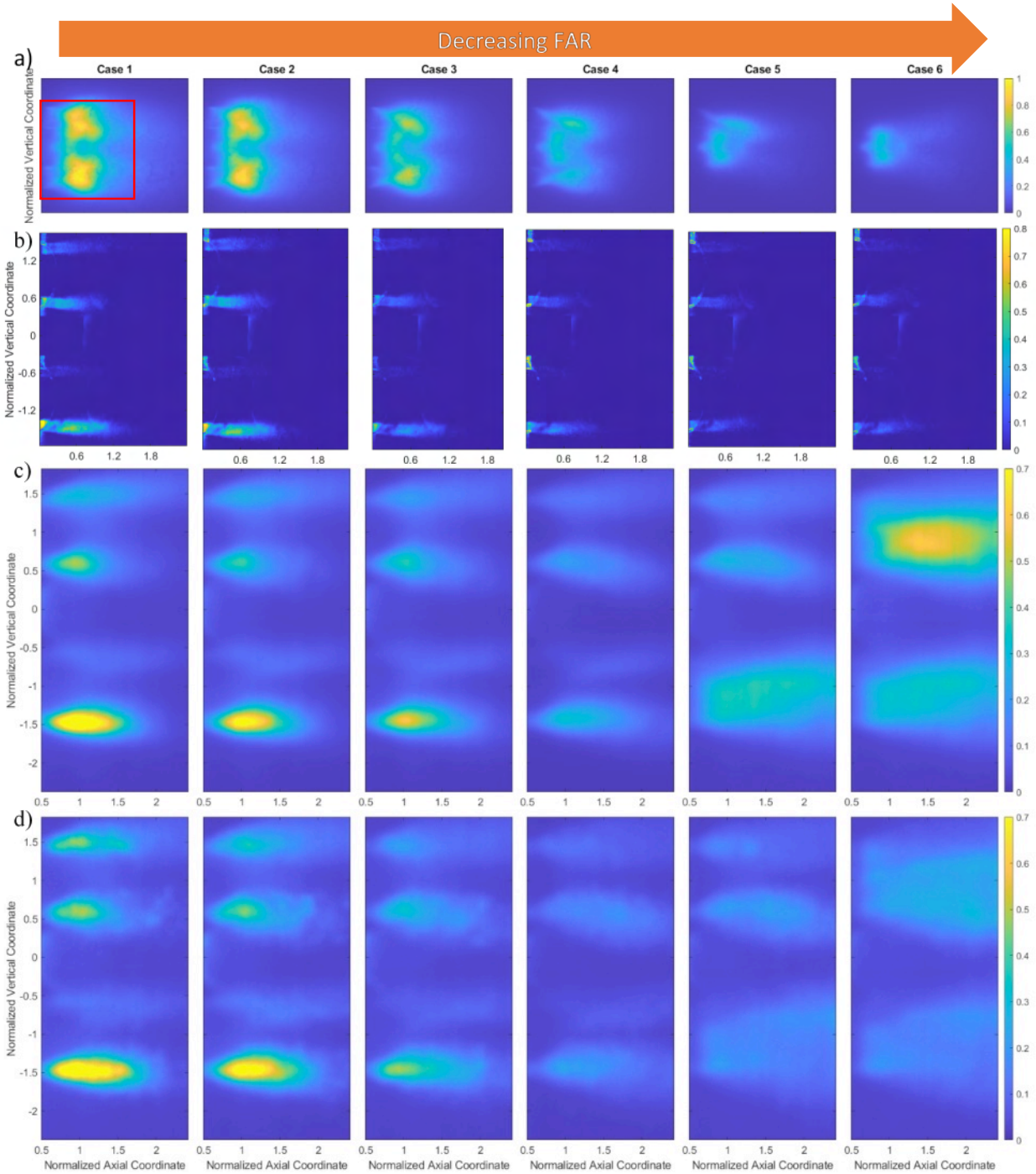

Figure 11. (a) Mean OH* CL, (b) mean fuel droplet Mie scattering, (c) mean fuel PLIF, and (d) fuel PLIF root-mean-squared fluctuations. The approximate position of the spray and PLIF field of view is denoted by a red rectangle in the first OH* field.

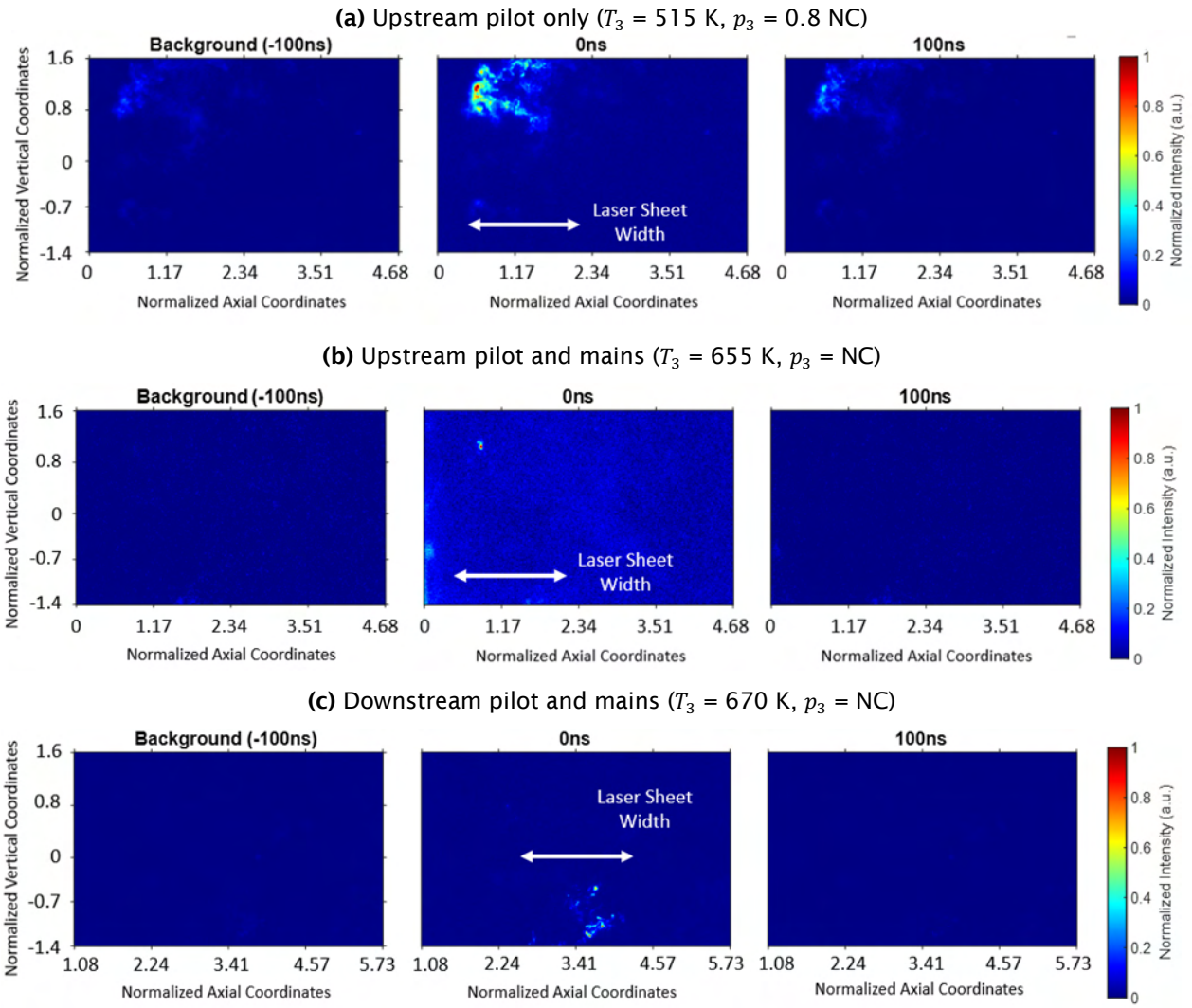

Figure 12. Ultrahigh-speed video sequences showing soot incandescence for different conditions and locations inside the combustor. NC: nominal cruise.

Typical TiRe-LII image sequences collected by the ultrahigh-speed camera are shown in Figure 12. Here, a background image is displayed immediately before the laser pulse arrives, which is rapidly followed by a prompt LII signal and the incandescence decay at 100 ns after laser incidence. The pilot-only operating condition at lower temperatures and pressures shows significant soot production near the dome face with relatively fast decay times, on the order of 78.5 ns. As the pressure and temperature are increased and the mains are turned on, the soot production near the dome face drops significantly, with isolated areas of soot production. The soot incandescence decay time also decreases significantly to approximately 12.4 ns. However, downstream from the dome face, more soot particles can be measured with slightly longer decay times on the order of 26.3 ns.

The TiRe-LII data collected in both upstream (combustor dome face) and downstream (approximately two main diameters downstream of the dome face) sections of the combustor can be compiled to produce estimates of average, rather than instantaneous, soot production images. Data collected under ramp-up conditions near the interaction region between the pilot and mains indicated clouds of soot with short decay times ranging from 50 to 150 ns. However, for full operating

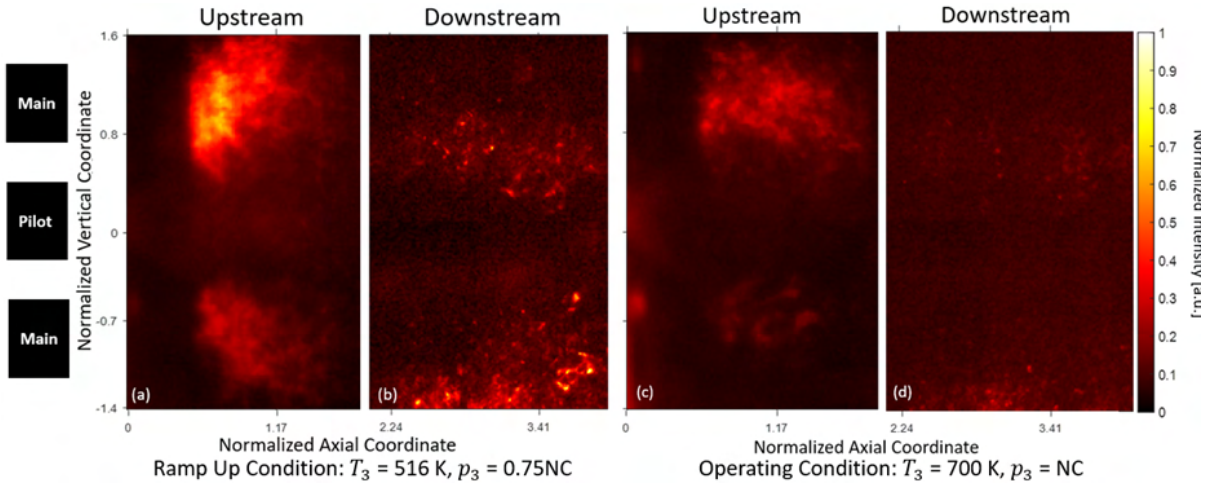

Figure 13. Upstream and downstream average (approximately 100 shots) prompt LII images are shown for ramp-up and operating conditions in (a)–(d). The relative intensities for (a) and (b) are normalized to the same baseline intensity, while those for (c) and (d) are normalized to 1/10th of the baseline intensity. NC: nominal cruise.

conditions, the flame was bluer, and significantly less soot was detected in both the upstream and downstream regions. For the small amounts of intermittent soot measured in the downstream location, the decay times were extremely short (approximately 30 ns) with high uncertainties, limiting particle-sizing capabilities. Average prompt LII images illustrate the decrease in soot detected between ramp-up and operating conditions. Upstream and downstream data taken under similar ramp-up and operating conditions (Figure 13) show an overall decrease in the LII signal across both upstream and downstream regions as the combustor pressure and temperature increased. While the upstream and downstream images are calibrated to be at the same vertical location, the downstream images appear to be shifted down due to variations in combustor height along the axial direction and thermal expansion effects. Despite this shift between cases, the differences between the ramp-up and full operating conditions are apparent, as shown in Figure 13. Here, the prompt LII signal for the operating condition is 1/10th as bright as that for the ramp-up conditions. Examples of signal decay profiles for both the ramp-up and operating conditions are shown in Figure 14.

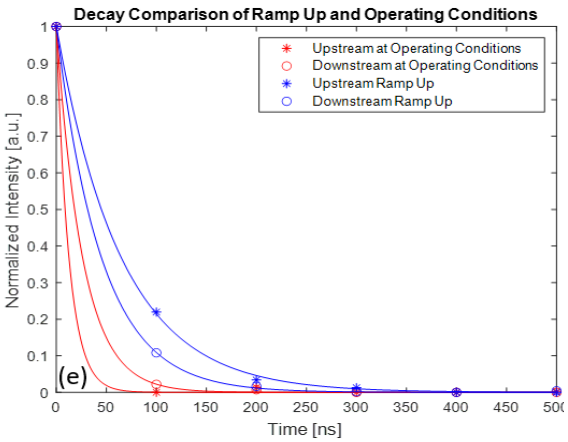

Figure 14. Typical signal decay times for ramp-up and operating conditions.

Because there is significantly more data for ramp-up conditions and the decay time constants for these conditions are longer, it is possible to examine how T_3, p_3, and ϕ affect the production of soot. Figure 15 shows average prompt LII images collected for several different ramp-up conditions. Here, a decrease in pilot ϕ appears to reduce the average soot production. Similarly, increases in temperature and pressure result in a significantly reduced signal from soot incandescence, indicating lower soot volume fractions.

The incandescence decay time constants can also be extracted from these data for each pixel, as illustrated in Figure 16. Here, two test cases are shown, one (Case A) with a lower T_3 and p_3 and a higher ϕ and a second (Case B) with a higher T_3 and p_3 and a lower ϕ. Here, despite the sub-frame decay times, clear differences can be noted between the low and high pressure and temperature conditions. The time constants fit to Case A (peak of distribution at 35 ns) have a larger time constant distribution than Case B (peak of distribution at 28 ns). These findings indicate that increasing temperature, increasing pressure, or decreasing ϕ will likely produce soot with faster decay time constants. To accurately determine how this trend affects soot particle sizes, more work is needed to calibrate the TiRe-LII models at higher pressures.

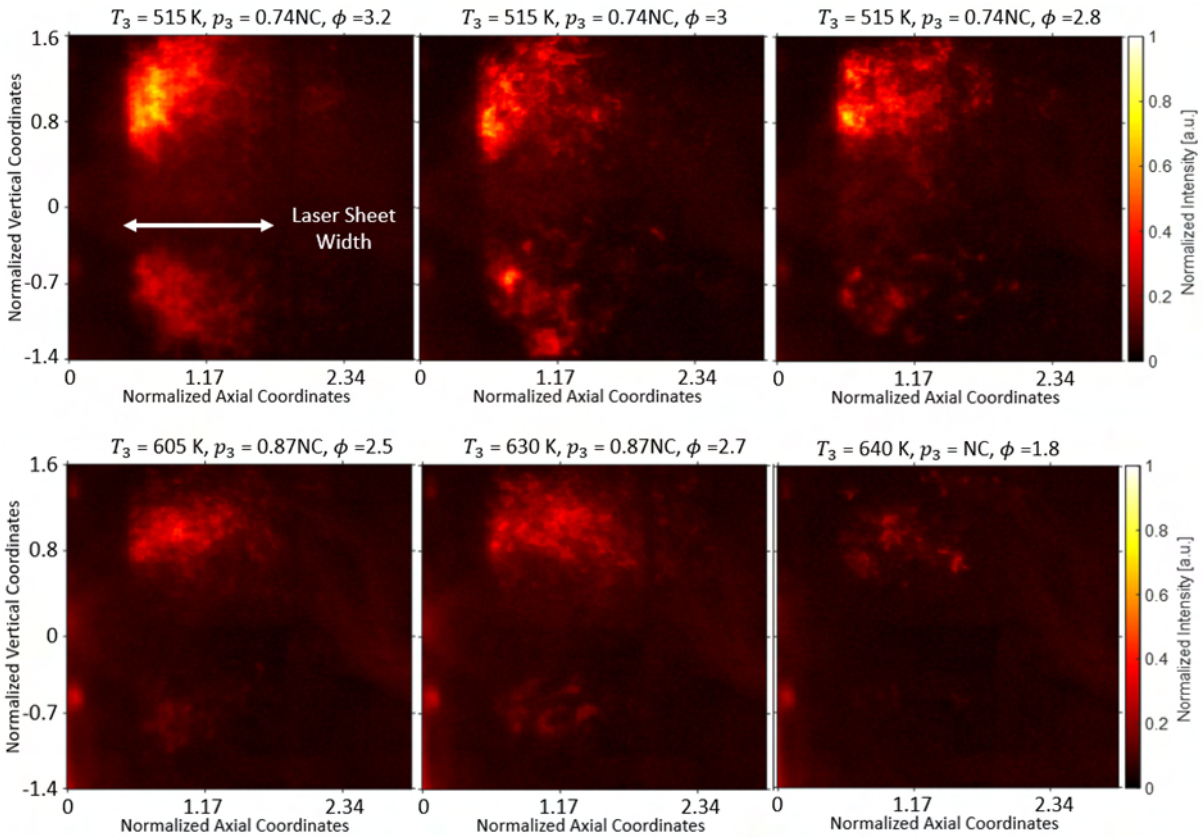

Figure 15. Average (approximately 100 shots) prompt LII images for different ramp-up conditions in which only the pilot flame is operating. NC: nominal cruise.

Milestone(s)

- Campaign 1 test rig design (complete)
- Measurement system design (complete)
- Campaign 1 test rig fabrication (complete)
- Experimental Campaign 1 (complete)
- Data processing from Campaign 1 (on schedule for completion in Q1 2022, 80% complete)
- Campaign 2 test rig design (on schedule for completion in Q1 2022, 50% complete)

Major Accomplishments

- Design, fabrication, deployment, and operation of a novel LPP combustor
- Advancement of various optical diagnostics for high-pressure gas turbine conditions
- Emission and optical measurements demonstrating encouraging performance for CST-relevant conditions

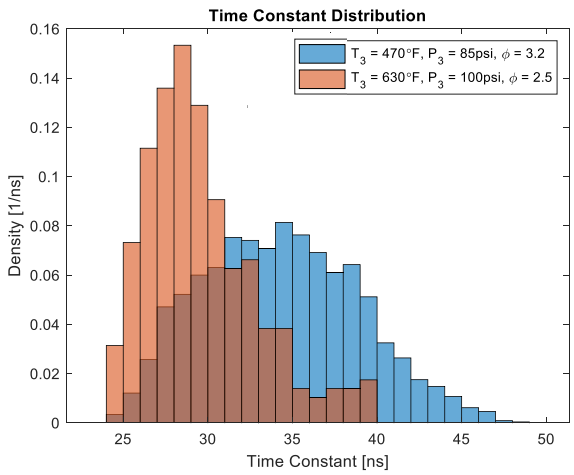

Figure 16. Time constant distributions for two different ramp-up conditions in which only the pilot flame is operating.

Publications

Passarelli, M., et al. (2022). *Experimental characterization of a lean pre-vaporized premixed combustor for supersonic transport applications.* Manuscript accepted for presentation.

Outreach Efforts

Eight semesters of undergraduate research-for-credit have been associated with this project.

Awards

None

Student Involvement

Mitchell Passarelli (PhD Candidate), Georgia Tech: Mie scattering and OH* CL measurements.

Samuel Wonfor (PhD Candidate), Georgia Tech: Fuel PLIF measurements.

Andrew Zheng (PhD Candidate), Georgia Tech: TiRe-LII processing.

Sundar Ram Manikandan (MS Candidate), Georgia Tech: Thermophoretic nvPM sampling system.

Kailey Obenstine, Coleman Pethel, Rachel Thomas (BS Students), Georgia Tech: Assistance in data processing, burner calibration, diagnostic design, etc.

Plans for Next Period

- Complete data processing from Campaign 1 (Q1 2022)
- Complete Campaign 2 test rig design, fabrication, and assembly (Q1 2022)
- Implement Experimental Campaign 2 (Q2–3 2022)
- Perform data analysis for Campaign 2 (Q3–4 2022)

Task 2 – Large Eddy Simulations of Combustor Operation and Emissions

Georgia Institute of Technology

Objective(s)

Simulations of advanced propulsion and power systems require treatment of multiscale physics, which in turn require trade-offs between cost and accuracy. Achieving the optimal balance is complicated because of the nonlinear nature of turbulent reacting flows, which involve multiphase mixtures, highly nonlinear chemical kinetics, multiscale velocity and mixing processes, turbulence–chemistry interactions, compressibility effects (density changes induced by changes in pressure), and variable inertia effects (density changes induced by changes in composition or heat addition). Coupling between processes occurs over a wide range of time and length scales, with many scales being too small to be resolved in a numerically feasible manner. Further complications arise when liquid or solid phases are present due to the introduction of dynamically evolving interface boundaries and the resultant complex exchange processes.

The overarching objective of this task is to provide quantitative insights into the accuracy of select calculations and to assess critical trade-offs between cost and accuracy. One set of calculations is performed using preferred engineering LES solvers with the goal of minimizing cost for a targeted accuracy, as required by industry. A companion set of high-resolution LES calculations are performed using a research solver, the RAPTOR code at Georgia Tech (Oefelein, 2006; Oefelein & Sankaran, 2018), to provide detailed information beyond that available from experiments alone. Complementary information from the first-principles LESs and experimentally measured data provides a unique opportunity to understand the central physics of turbulent combustion processes in realistic parameter spaces and for making clear assessments of how a given combination of affordable engineering-based models performs. After achieving an adequate level of validation, results from the high-resolution LES calculations will provide fundamental information that cannot be measured directly and that is relevant to the development of lower-order engineering models. Thus, a strong link between theory, experiments, and relevant applications will be established. The ultimate objectives of this task are to assess (a) the model fidelity/attributes required to accurately simulate operability and emissions and (b) the trade-offs between accuracy and cost.

Research Approach

The GE combustor operates with liquid Jet A (CAT-A2) fuel delivered through upstream atomizers into bluff-body stabilized premixers, as well as through a central swirling pilot. Over the initial stages of the project in Year 1, the GE and GT simulation teams worked toward developing a common computational domain that enabled detailed treatment and analysis of rig boundary conditions and operating conditions while also working around proprietary information within GE. A set of calculations was performed by GE using Fluent via standard practice in a computational domain that included the upstream plenum, upstream proprietary liquid-fuel/air injection system, combustion chamber, and exhaust, as shown in Figure 17.

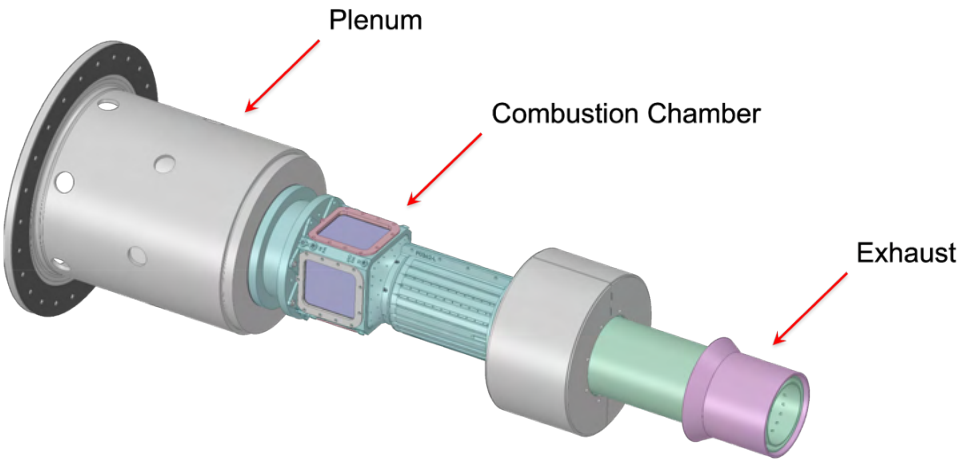

Figure 17. Extended computational domain used for GE Fluent calculations.

In contrast, the GT LES computational domain begins at the burner inlet planes, starting upstream of the dome that houses the bluff-body stabilized premixers, as shown in Figure 18. The domain includes all flow features of the pilot and premixers as well as fine features such as wall and dome cooling holes. The major goals of this effort are to (1) establish good correspondence between the GE and GT simulation efforts, (2) develop advanced methodologies for the treatment of boundary conditions in "industrial grade" rigs such as this, and (3) quantify and enable detailed analyses of both the inner combustion characteristics and the actual physical boundary conditions on the overall operating characteristics of the combustor.

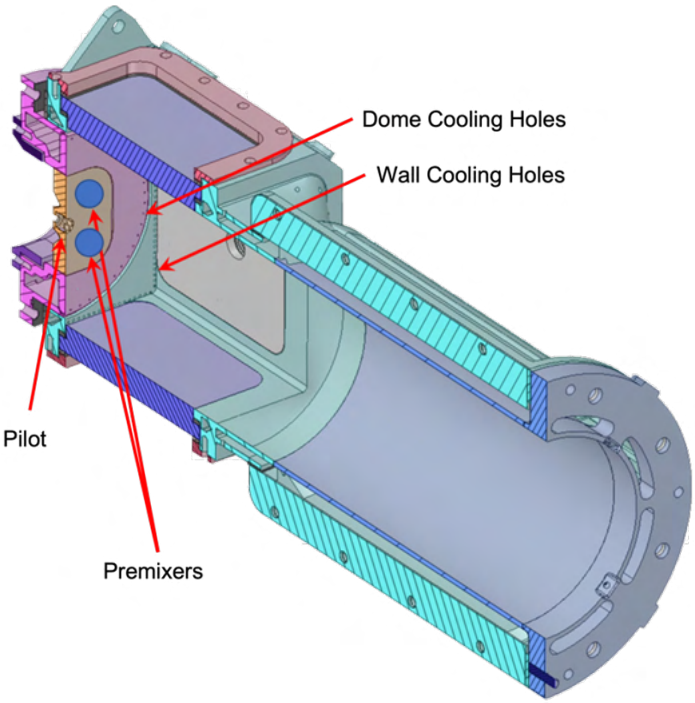

Figure 18. Computational domain used for GT LES calculations.

The simulations performed by GT and GE are complementary, not redundant. GT is performing high-resolution "first-principles" LESs designed to provide additional levels of information that are directly relevant to assessing, understanding, and improving the current state-of-the-art models being used (i.e., detailed treatment of broadband turbulent reacting flow dynamics with an emphasis on accuracy over cost). The GE Fluent calculations are designed to apply "best-practices" engineering CFD to first establish the benchmark accuracy of the current models used and to then systematically assess where improvements can be made to quantify and improve the accuracy of the models under the conditions of interest. The combination of GT and GE calculations will enable an advanced engineering workflow that systematically improves the accuracy and confidence of the CFD design methodology while minimizing cost.

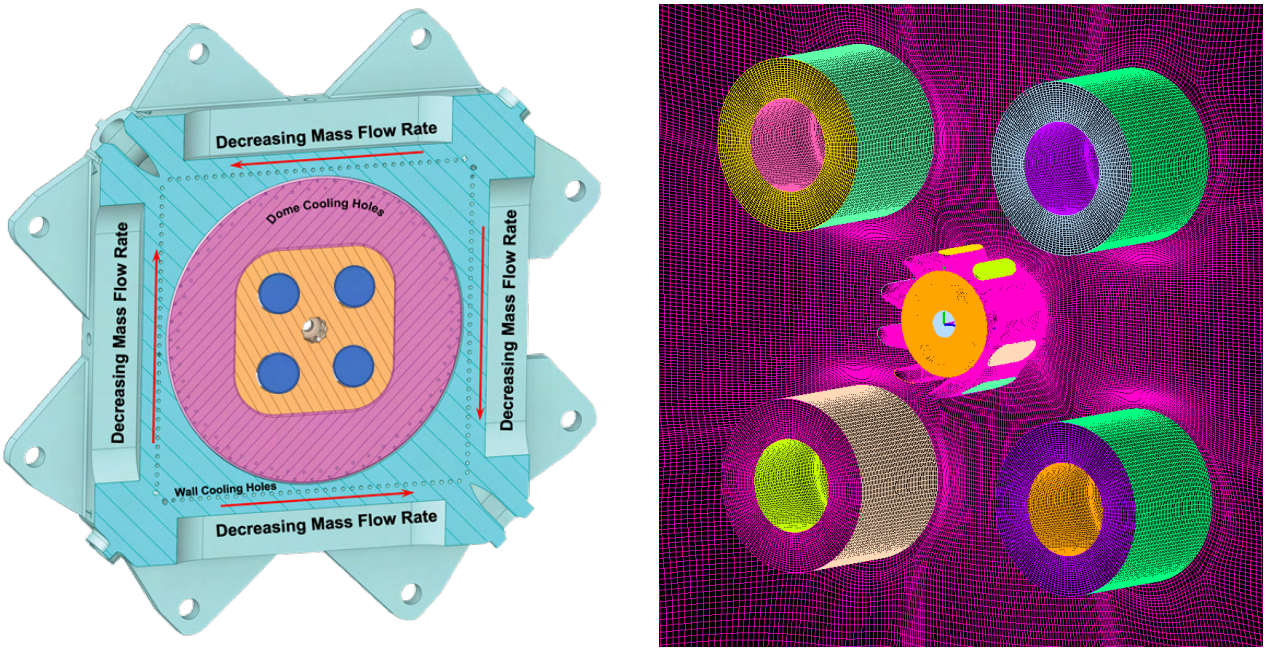

Figure 19. Left: Combustor dome showing key boundary features. Right: A corresponding grid of the back plane of the dome showing inflow planes for the premixer and pilot swirler vanes.

Over this period, we have established the workflow required to quantify the multifidelity treatment of boundary conditions associated with the combustor. This step is essential to assess the impact on operational characteristics of the burner and to unify comparisons of results between different simulation techniques and measured data. The flow entering the combustion chamber involves a complex combination of turbulent gas-phase fluid dynamics and liquid-fuel spray dynamics. The premixers inject partially premixed gas laden with liquid-fuel droplets. The pilot injects radially directed swirling air flow onto a centered liquid-fuel jet. The gas-phase flow velocity and liquid-fuel droplet size and velocity distributions are found to be nonuniform both within and between the premixers. In addition, the mass flow of air through the dome and wall cooling holes makes up 40% of the mass flow, and flow across the wall cooling holes is nonuniform. All of these factors must be considered to establish an advanced quantitative understanding of the combustor while also enabling a unified

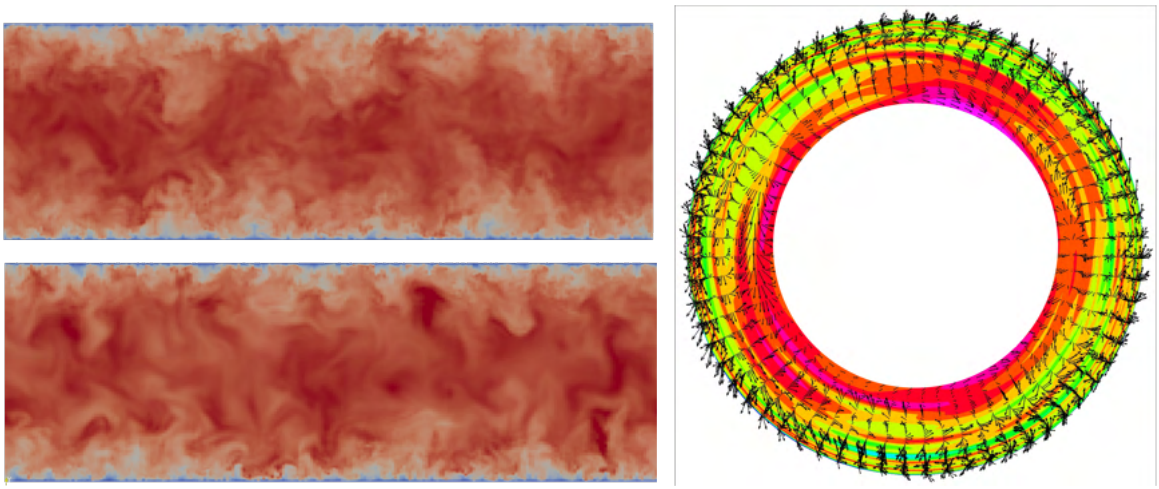

Figure 20. Left: Comparison of a reconstructed SEM signal (bottom) to the actual NS-generated signal (top) in a turbulent channel flow. Right: Example of the signal generated for one of the premixer planes in the actual combustor reconstructed using data from GE Fluent calculations.

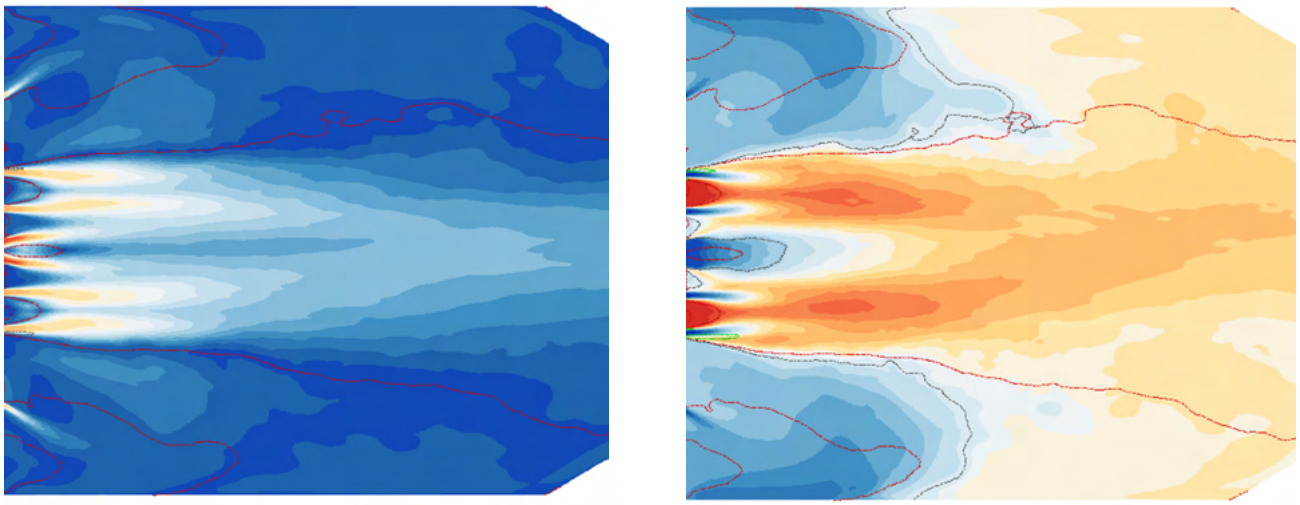

Figure 21. Example simulation results showing the velocity (left) and temperature (right) fields in the combustor.

correspondence between measured and modeled results and comparisons between different simulation methods and models. The current workflow enables a systematic application of complex boundary conditions.

As an example of new developments, we have established an advanced methodology to accurately extract information from the GE calculations, including the upstream plenum and proprietary liquid-fuel/air injection system, which we are not able to access, and to convert this information to unsteady time-correlated boundary conditions at the inlet planes to the premixers, pilot, and wall cooling holes (see Figure 19). Time-dependent turbulent inflow profiles are constructed using the synthetic eddy method (SEM) (Jarrin et al., 2008). A modified compressible SEM formulation is employed to provide time-evolving turbulent inflow conditions to capture the physical nonuniformities present across the premixer inlet planes. The input used to construct the signals includes the nonuniform mean velocity profiles, Reynolds stress tensor, and integral scale distributions extracted at respective planes from the GE Fluent calculations. Figure 20 shows examples of the fidelity in the signals obtained. The left figure presents a comparison of a reconstructed SEM signal to the actual DNS-generated signal in a turbulent channel flow. The right figure shows an example of the signal generated for one of the premixer planes in the actual combustor, reconstructed using data from the GE Fluent calculations. Similar treatments were applied to obtain the nonuniform droplet size, temperature, and species distributions.

Following these detailed characterizations related to the geometry and boundary conditions, simulations are now in progress. An example result is shown in Figure 21. The complexity of the combustor geometry required careful creation of a high-resolution grid that is tractable for computation. The computational domain is meshed with a grid of 45 million (M) grid points over 2,060 structured blocks, with a minimum cell size of 0.058 mm at the inlet (dump) plane of the combustor. The current resolution provides the capability to resolve small-scale flame dynamics at the dump plane. There are three versions of the grid at increasing resolutions of 45 M, 94 M, and 132 M grid points, respectively, which will facilitate multiresolution studies. The tasks in Year 2 will shift toward detailed analyses of combustor characteristics through collaborative comparisons between measured and modeled data and between engineering (GE) and high-resolution (GT) simulations. Planned studies include analyses of (1) sub-model accuracy and performance in a complex geometric environment, (2) turbulent velocity and scalar mixing, (3) turbulent mixed-mode combustion, (4) finite-rate chemical kinetics and combustion dynamics, (5) emissions and soot generation, and (6) engineering model performance and best practices for model implementation.

Milestone(s)

- GE Fluent LES for initial conditions (complete)
- Baseline GT RAPTOR LES for initial conditions (on schedule for completion in Q4 2021)

Major Accomplishments

- Fluent LES of LPP combustor
- Workflow to align space- and time-dependent boundary conditions between GE Fluent and GT RAPTOR

Publications

None

Outreach Efforts

None

Awards

None

Student Involvement

Sriram Kalathoor (GRA, PhD Candidate), Georgia Tech: Baseline calculations with RAPTOR code.

Plans for Next Period

- GE Fluent LES conditions over experimental match conditions (Q1 2022)
- GT RAPTOR LES for selected conditions (Q2 2022)
- Detailed comparison of RAPTOR LES, Fluent LES, and experimental measurements (Q3-4 2022)

References

Berton, J., J., Huff, J. D., Seidel, J. A., & Geiselhart, K. A. (2020). Supersonic technology concept aeroplanes for environmental studies [Presentation]. AIAA SciTech Forum and Exposition, Orlando, FL.

Chen, Y., Cenker, E., Richardson, D. R., Kearney, S. P., Halls, B. R., Skeen, S. A., Shaddix, C. R., & Guildenbecher, D. R. (2018). Single-camera, single-shot, time-resolved laser-induced incandescence decay imaging. Optics Letters, *43*(21), 5363. https://doi.org/10.1364/ol.43.005363

Hassan, M., Pfaender, H., & Mavris, D. (2020). Design tools for conceptual analysis of future commercial supersonic aircraft [Presentation]. AIAA Aviation Forum, Virtual meeting.

Kharina, A., MacDonald, T., & Rutherford, D. (2018). Environmental performance of emerging supersonic transport aircraft [Presentation]. The International Council on Clean Transportation.

Liu, F., Smallwood, G. J., & Snelling, D. R. (2005). Effects of primary particle diameter and aggregate size distribution on the temperature of soot particles heated by pulsed lasers. Journal of Quantitative Spectroscopy and Radiative Transfer, *93*(1-3), 301–312. https://doi.org/10.1016/j.jqsrt.2004.08.027

Goldlucke, J., Seelig, O., Ipp, W., Schraml, S., & Leipertz, A. (2004). Investigation of In-Cylinder Soot Formation and Exhaust Soot Emission of a Direct Injection SI Engine by Laser-Induced Incandescence (LII) (Measurement PM in Flames). The Proceedings of the International Symposium on Diagnostics and Modeling of Combustion in Internal Combustion Engines, *2004.6*(0), 369–376. https://doi.org/10.1299/jmsesdm.2004.6.369

Kheirkhah, S., Cirtwill, J. D. M., Saini, P., Venkatesan, K., & Steinberg, A. M. (2017). Dynamics and mechanisms of pressure, heat release rate, and fuel spray coupling during intermittent thermoacoustic oscillations in a model aeronautical combustor at elevated pressure. Combustion and Flame, *185*, 319–334. https://doi.org/10.1016/j.combustflame.2017.07.017

Strategic Implementation Plan. (2015, November 12). NASA. https://www.nasa.gov/aeroresearch/strategy

Niedzwiecki, R. W. (1992). Low emissions combustor technology for high-speed civil transport engines (Report No. N94-33481). NASA, Cleveland, OH.

Oefelein, J. C. (2006). Large eddy simulation of turbulent combustion processes in propulsion and power systems. Progress in Aerospace Sciences, *42*(1), 2–37. https://doi.org/10.1016/j.paerosci.2006.02.001

Oefelein, J. C., & Sankaran, R. (2018). Large eddy simulation of reacting flow physics. In K. Antypas & T. Williams (Eds.). *Exascale scientific applications: Programming approaches for scalability, performance, and portability* (231-256). Taylor & Francis, Boca Raton, FL.

Orain, M., Baranger, P., Ledier, C., Apeloig, J., & Grisch, F. (2014). Fluorescence spectroscopy of kerosene vapour at high temperatures and pressures: potential for gas turbines measurements. Applied Physics B, *116*(3), 729–745. https://doi.org/10.1007/s00340-013-5756-z

Shaddix, C. R., Zhang, J., Schefer, R. W., Doom, J., Oefelein, J. C., Kook, S., Pickett, L. M., & Wang, H. (2010). Understanding and predicting soot generation in turbulent non-premixed jet flames (Report No. SAND2010-7178). Sandia National Laboratories.

Speth, R. L., Eastham, S. D., Fritz, T. M., Sanz-Morére, I., Agarwal, A., Prashanth, P., Allroggen, F., & Barrett, S. R. H. (2021). Global environmental impact of supersonic cruise aircraft in the stratosphere (Report No. NASA/CR-20205009400). NASA, Cleveland, OH.

Vargas, A. M., & Gülder, Ö. L. (2016). A multi-probe thermophoretic soot sampling system for high-pressure diffusion flames. Review of Scientific Instruments, *87*(5), 055101. https://doi.org/10.1063/1.4947509

Speth, R. L., Eastham, S. D., Fritz, T. M., Sanz-Morére, I., Agarwal, A., Prashanth, P., Allroggen, F., & Barrett, S. R. H. (2021). Global environmental impact of supersonic cruise aircraft in the stratosphere (Report No. 20205009400). NASA, Cleveland, OH.

Project 075 Improved Engine Fan Broadband Noise Prediction Capabilities

Boston University and Raytheon Technologies Research Center

Project Lead Investigator

Sheryl Grace
Associate Professor
Mechanical Engineering
Boston University
110 Cummington Mall, Boston, MA 02215
617-353-7364
sgrace@bu.edu

University Participants

Boston University

- PI: Sheryl Grace, Associate Professor, Mechanical Engineering
- FAA Award Number: 13-C-AJFE-BU Amendment 022
- Period of Performance: September 1, 2020 to August 31,2021
- Task(s):
    1. Fan-wake surrogate model creation
    2. Improved low-order model

Project Funding Level

Funding for first year:
FAA: $300,000: $115,000 to Boston University (BU); $185,000 to Raytheon Technologies Research Center (RTRC)
Match $300,000: $115,000 from BU (data sets, graduate student stipend, and MS in Statistical Practice faculty/student time) and $185,000 from RTRC (personnel time).

Investigation Team

Sheryl Grace, BU, PD/PI: Tasks 1 and 2
Austin Thai, BU, PhD student: Task 1
Noah Li, BU, PhD student: Task 2
Zijie Huang, MS student: Task 1
Berkely Watchmann, undergraduate student: Task 1
Tyler Ramsarran, undergraduate student: Task 1
Jeff Mendoza, RTRC, Co-PD/PI: Tasks 1 and 2
Craig Aaron Reimann, RTRC, Staff Scientist: Task 2
Julian Winkler, RTRC, Staff Scientist: Tasks 1 and 2
Dmytro Voytovych, RTRC Staff Scientist: Task 1
Kin Gwn Lore, RTRC Staff Scientist: Task 1
Michael Joly, RTRC Staff Scientist: Task 1

Project Overview

The noise signature of contemporary turbofan engines is dominated by fan noise, both tonal and broadband. Accepted methods for predicting tone noise have existed for many years. Furthermore, engine designers have methods for controlling or treating tonal noise but not broadband noise. Thus, further reductions in engine noise will clearly require accurate prediction methods for broadband noise to enable design decisions. Interaction noise from the fan-stage is a dominant

broadband mechanism in modern high-bypass engines and is created by the interaction of the turbulence in the fan-wakes with the fan exit guide vanes (FEGVs). This project will leverage prior development of low-order models for the prediction of fan broadband interaction noise. Gaps in the low-order approach will be addressed on the basis of knowledge gained from computation and experimentation. In particular, a method for determining the inflow into the stator via a machine learning (ML) algorithm will be developed. The low-order method will also be validated against full-scale rig data, and appropriate development will be undertaken based on the findings.

Task 1 - Fan-wake Surrogate Model Creation

Boston University and Raytheon Technologies Research Center

Objective

The goal is to build a surrogate model using ML that would work with performance-level unsteady Reynolds-averaged Navier–Stokes to specify the turbulent length scales and turbulence spectrum at locations along the helical fan-wake path.

Research Approach

Subtasks 1.1 and 2: Development of autoencoder and decoder

Two ML approaches have been developed, labeled as single-output and multi-output methods. More time was spent developing the single-output method before September 30, 2021, and it is described in detail herein. Introductory comments regarding the reason for pursuing the multi-output method are also given.

Master's degree students in a course at BU offered within the statistics program worked on the initial development of an ML algorithm for the streamwise mean velocity downstream of a fan rotor. Data produced on a previously funded AeroAcoustics Research Consortium (AARC) project for the rotor used in NASA's Source Diagnostic Test (SDT) were used during the initial development. The students had access to the three-dimensional (3D) grid and solution files from a computational fluid dynamics (CFD) analysis. The grid started just downstream of the rotor and extended to just upstream of the FEGV's position in the experiment. The students were also given information about the rotor at specified radial locations along the trailing edge, including the coordinates of the trailing edge, the rotor chord, and stagger. These data were available for the three rotor speeds most studied from the SDT. The rotor speed and rotor geometric data were the input data. The students chose to consider the streamwise velocity at every point in the CFD grid as the information to be learned, so that the ML, when given another set of inputs (e.g., a different speed for the same rotor, or a different rotor at the same speed), could be used to predict the streamwise velocity anywhere in the gap between the fan rotor and FEGV. The SDT fan has 22 rotor blades, and the CFD is performed by using a periodicity condition so that only a single rotor blade passage is included in the computation. A view of the streamwise velocity at a specific percentage radial position in the gap is shown in Figure 1.

The developed ML process has two phases. The first phase learns the location of the minimum-velocity position at a given axial location. This allows for a rectification of the wakes such that they all align as shown in Figure 2. The function providing the wake center position is learned by using a polynomial regression model. The second phase of the ML then focuses on learning the centered wake shapes. The students tested both a natural splines model and a multivariate adaptive regression splines (MARS) model. To train the models, 80% of the points on the CFD grid downstream of the rotor were used. The other 20% of the points were then used to test the model. The streamwise velocity at the test locations was well predicted. One particularly interesting feature of the MARS model is its identification of relevance levels of the various input parameters.

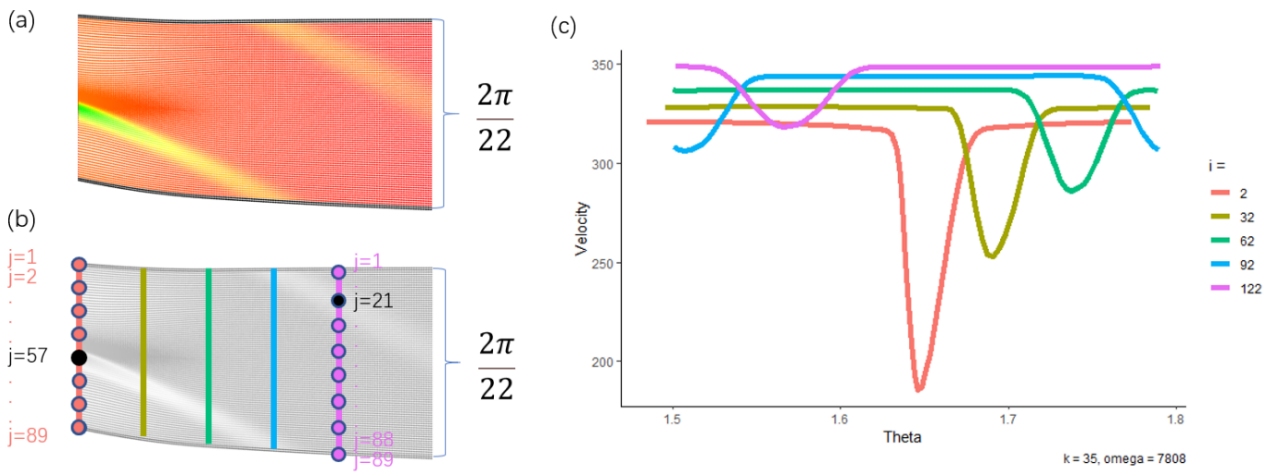

Figure 1. Left: streamwise velocity downstream of the rotor at a given percentage radial location, as a function of the axial distance from the rotor and the circumferential position. A periodic condition (2 pi/22) is seen as wake wraps according to the axial distance from the rotor. Right: streamwise velocity at different axial distances from the rotor, at a fixed percentage radial position. Colors are consistent with the key at bottom left.

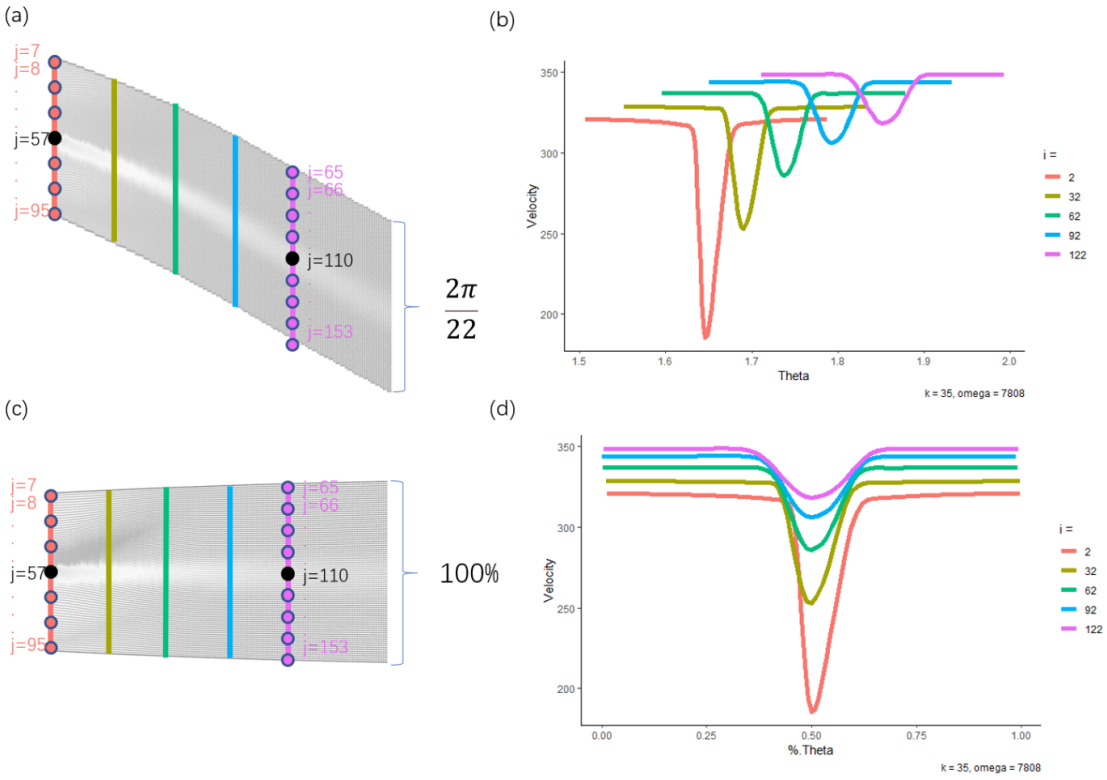

Figure 2. Top: unrolled wakes. Bottom: centered wakes.

The task description notes that the surrogate model must provide the input for the low-order FEGV acoustic response calculation. In particular, we had proposed to learn the mean flow and the turbulence length scale and spectrum. Previous research has shown that the Liepmann spectrum represents the nature of the spectrum reasonably well. Therefore, we will continue to use the Liepmann spectrum and develop the surrogate model to provide the turbulence intensity and turbulence length scale, which are used to tune the Liepmann spectrum. Furthermore, previous research has shown that the heuristic method for determining the length scale according to CFD turbulence parameters k and ε or k and ω works sufficiently well. Thus, we have tested the ML algorithms for learning these parameters as well as the streamwise mean velocity.

The group project served as a launching point for further development of ML models. Other ML methods including decision tree and neural net models were tested. Additional data were acquired, as discussed in Subtask 1.3 below. XGBOOST with a decision tree base and a regular deep neural net (DNN) both worked well when 80% of the CFD data were used for training and 20% were used for testing. However, the methods were not robust to all methods for selecting training and testing data, as discussed further as part of Subtask 1.4.

The single-output methods described thus far assume that each point in the CFD grid downstream of the rotor and each rotor input value at a given radial location are independent. Clearly this is not physical, given that the radial slices along the rotor are most definitely connected. In addition, radial connectedness (as well as circumferential connectedness) is present in the region downstream of the rotor. This prompted discussions that led to developing multi-output machine learning methods. Figure 3 shows the basic difference between the single- and multi-output methods.

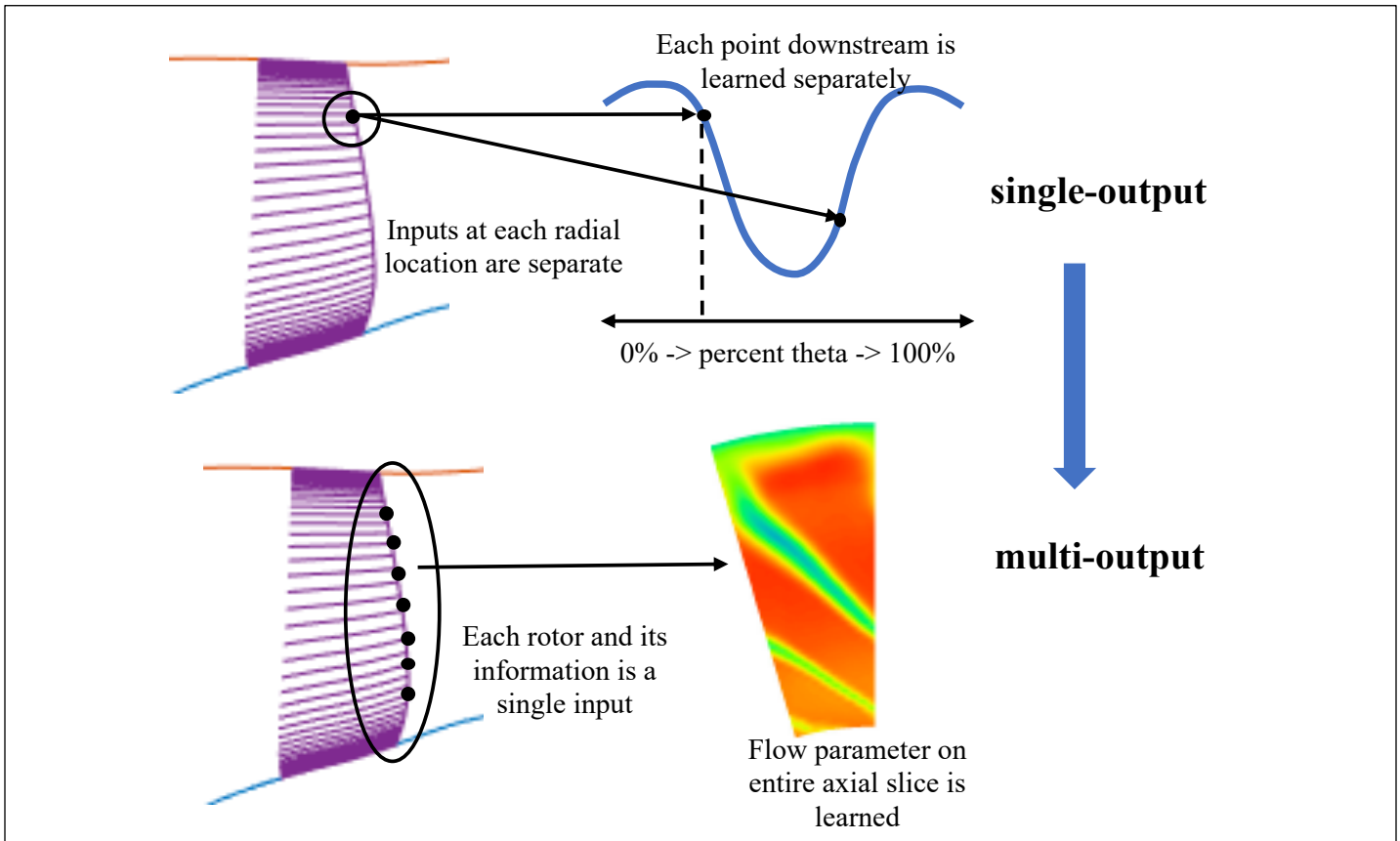

Figure 3. Single- vs. multi-output machine learning idea. The multi-output method does not require rectification of the wakes (centering) before learning the wakes.

Subtask 1.3: Identification and creation of training data

Subtask 1.3.a: Existing training data: BU and RTRC will work to collect relevant existing fan-wake data sets.
Subtask 1.3b: Creation of additional training data: RTRC will take the lead in producing new data sets.

As mentioned under Subtask 1.2, the original data used for development and testing of the ML algorithms came from previous work on the SDT. There were three rotor speeds, and the rotor geometry at each speed was slightly different because the hot geometry had been computed (i.e., structural deformations due to the aero loads were determined and used to determine the actual rotor geometry at that rotor speed). The first year of this project extended the available data by running more rotor speeds and mass flow conditions for the SDT geometries. In particular, four geometries were considered: cold (CAD), approach hot, cutback hot, and takeoff hot. For each geometry, seven speed lines were run with approximately 10 mass flow cases for each speed. A typical set of performance plots for one of the geometries is shown in Figure 4. Consequently, 268 cases were available for use in the ML.

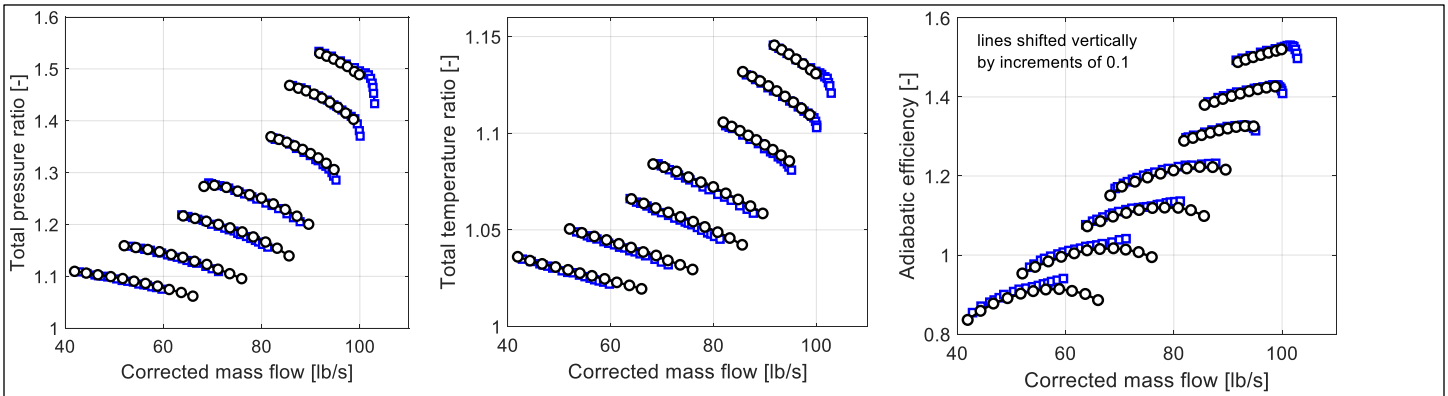

Figure 4. Performance curves for SDT cold (CAD) geometry. Blue: experimental data digitized from NASA TM 2013-214029. Black: CFD results.

AxStream software was used and tested for developing new rotor geometries to be used in year 2. The application module AxSlice was leased for several months to support this effort. AxSlice allows users to read in existing rotor geometries and convert them to parametric representation in AxStream. This process has been used to create new potential input parameters for ML, including the radial distribution of the rotor blade stagger angle, camber, and leading- and trailing-edge wedge angles, shapes and sizes. In addition, a Matlab script was developed to drive the streamline solver within AxStream to run multiple flow conditions and rotational speeds and extract the required flow parameters for the ML algorithms, such as inflow and outflow angles. In addition, the co-PIs are now ready to create geometries very different from the SDT to truly test the robustness of the ML algorithms in year 2.

Subtask 1.4: Application of surrogate model to relevant fan geometries

This report focuses on the results from the single-output ML method. The ML was used to predict the mean streamwise wake across a rotor passage as well as the turbulent kinetic energy (TKE) and turbulent dissipation parameter (omega) across a passage. As noted above, 268 cases were available for training/testing. Two methods for using the data set were considered and led to different outcomes. First, a random selection of 80% of the data was used for training, and the other 20% was used for testing. A prediction means that the ML algorithm gives the value of a parameter of interest (mean flow, TKE or omega) at a specified point downstream of the rotor based on the rotor input information and wake point location. The single-output method applies the learned relationship to the wake center position as well as the centered value. Subsequently, a reconstruction of the actual wake is completed by using these two pieces of information. XGBOOST with a decision tree basis yielded good results for all parameters and provided relevance levels for the input parameters, which added physical insight. For the low-order acoustic methods, the wake information is needed just upstream of the FEGV. For the SDT-related geometries and the CFD-based training/testing data, this corresponds to an axial counter-position of i = 30. The reconstructions of the wake at i = 30 are shown in Figure 5. The input parameters used during year 1 to describe the rotor

include the rotor speed (noted as omega), mass flow rate, location of the trailing edge at different radial slices (xte, thte, and rte), difference between the center wake position at a given percentage radial location, trailing-edge point at that percentage radius (x_new, th_new, and r_new), stagger angle (bladeAngle), chordlength (chord), and thickness of the boundary layer at the trailing edge on the upper and lower sides (upBLnor and lwoBLnor) at each radial slice. A total of 30 radial slices are specified. Because the flow is not wake-like near the hub or tip, only the 3-28 radial slices are used as input, and the ML reconstructions are attempted only at these radial locations. This effectively means that we are leaving out 6% at the hub and 6% at the tip.

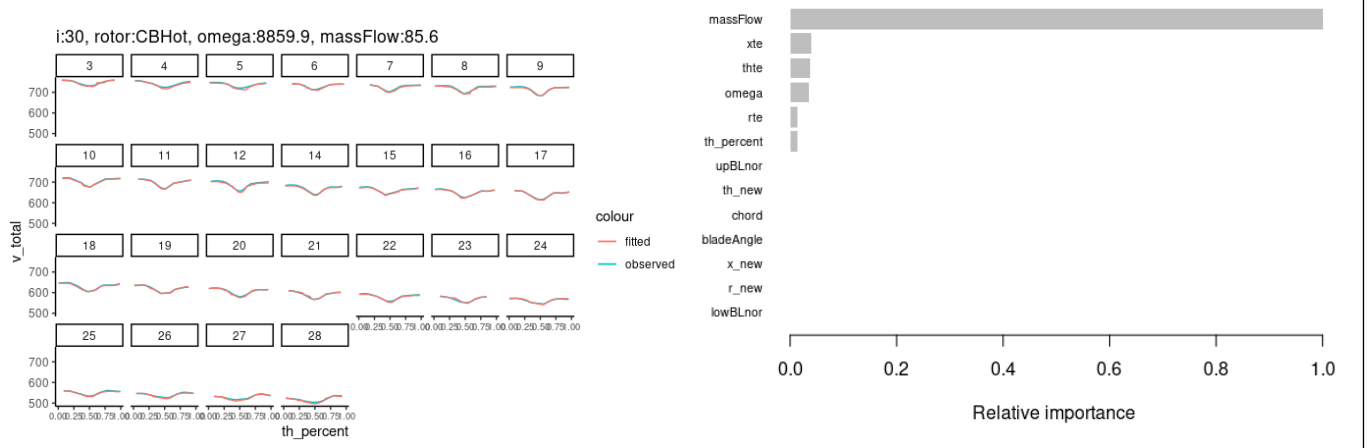

Figure 5. Left: predicted (fitted, red) and actual (observed, blue) results at locations from hub to tip (indicated by numbers 3–28) of the mean streamwise velocity across a passage (passage location given as percentage theta). Right: relevance of the input parameters.

The predictions at all 20% of the wake points used for testing gave a test MSE of 11.51 and an R-squared value of 0.999. The case that was the farthest off was for the rotor speed case 6328.5rpm at the lowest mass flow 42lbm/s. However, the predictions still visually appeared quite good. Interestingly, the parameter with the most relevance for the mean flow wake profile was the mean flow. In contrast, for the TKE and turbulence dissipation parameter, the most relevant parameter was the relative position of the wake centerline in the passage (Figure 6). The TKE did strongly relate to the boundary layer thickness, which made physical sense, whereas the turbulence dissipation did not.

The second test of the ML algorithm used a different training/test selection method. Full rotor speeds were individually excluded from the training. The prediction of that speed from the ML trained by using the other speeds was analyzed according to the MSE and R-squared values. An overall performance value for the ML was then obtained as a composite of the results from each test-speed case. When an entire rotor speed was left out, XGBOOST performed as expected when a tree basis was used. The predictions had a “nearest neighbor” type of outcome. Therefore, large differences existed between the predicted and actual wake profiles, as shown in Figure 7. The wake shapes were rather close, but the average value was quite off. A second ML algorithm was tested at this point, to move away from the decision tree dependence. A Deep Neural Net (DNN) was set up and found to provide predictions with a better overall mean value, but the wake shape was not well captured. This led us to further reflection.

For the application to low-order broadband noise prediction, the wake shape is not necessary. Instead, just the overall mean value (from hub to tip) is needed. (Low-order tonal noise predictions do rely on the wake shape, and some low-order broadband methods require the TKE shape in the wake.) Therefore, the DNN was tested for learning just the overall mean value. Figure 8 shows the DNN results. The DNN performs very well in determining the overall mean value. The figure shows the worst-performing predictions (for all rotor speeds and mass flow combinations). The TKE and turbulence dissipation parameter are predicted similarly with the DNN when full rotor speeds are reserved for testing. The overall mean value is well predicted, but the rotor passage shape is not captured.

These results indicate that the single-output ML algorithms can provide a surrogate model for the wake. However, both the DNN and XGBOOST/decision tree algorithms must be applied: the DNN is used to obtain the overall mean value from hub to tip, and the XGBOOST is used to determine the passage shape.

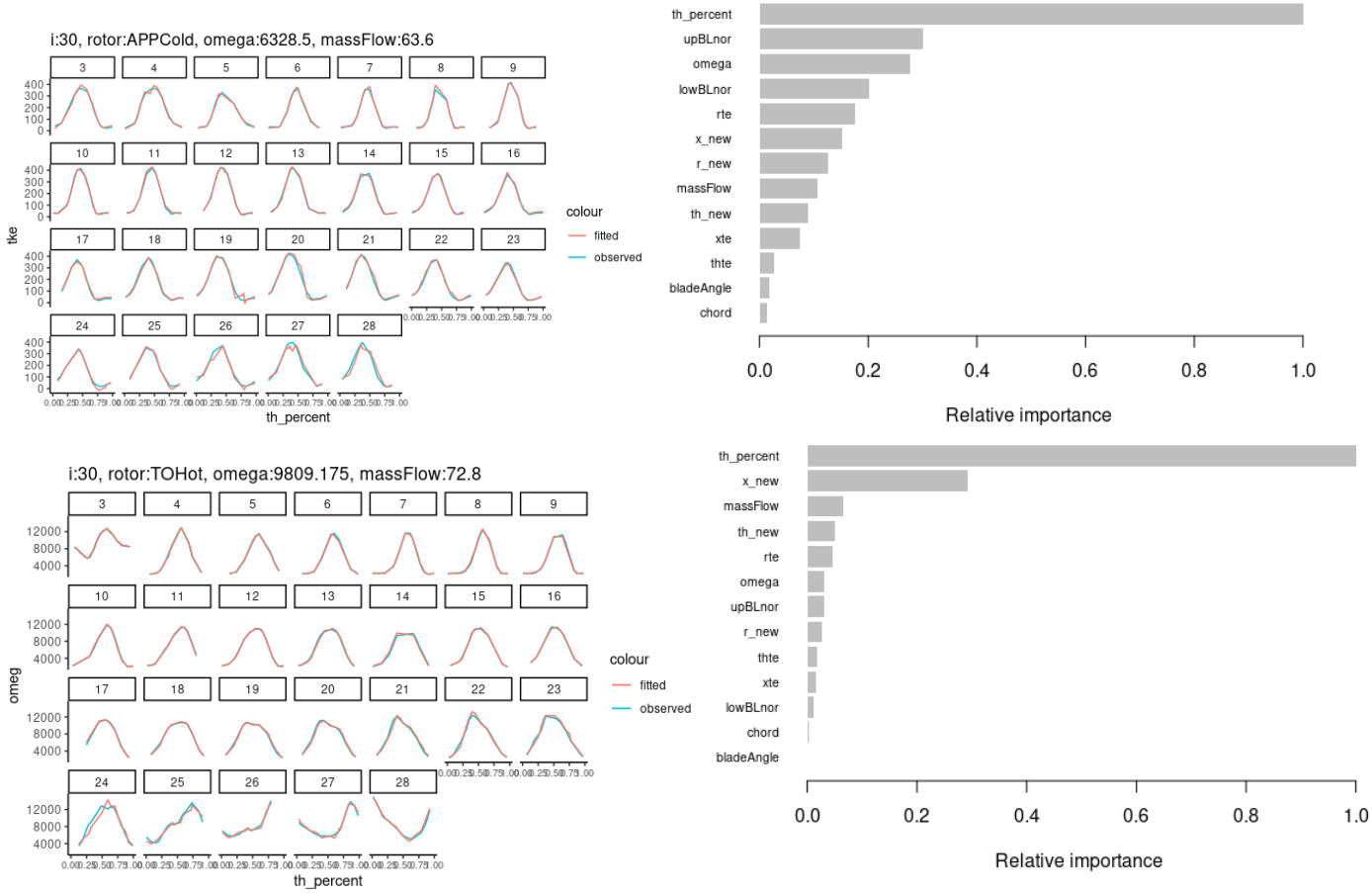

Figure 6. Top: TKE prediction with importance level of inputs. Bottom: turbulence dissipation parameter omega prediction with importance level of inputs.

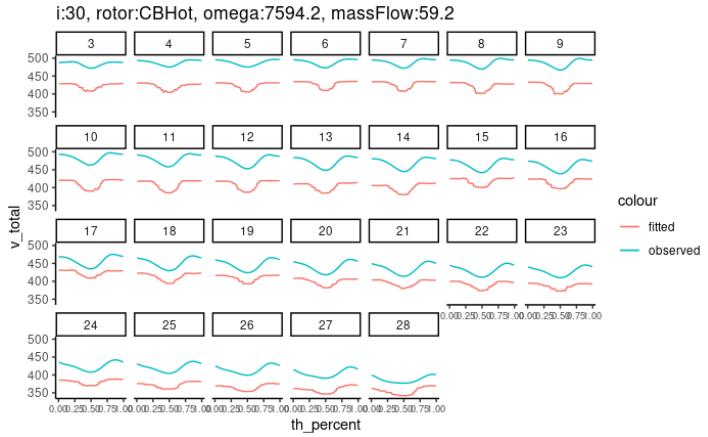

Figure 7. Predicted mean streamwise wake (red) for a rotor speed not used in training the ML algorithm.

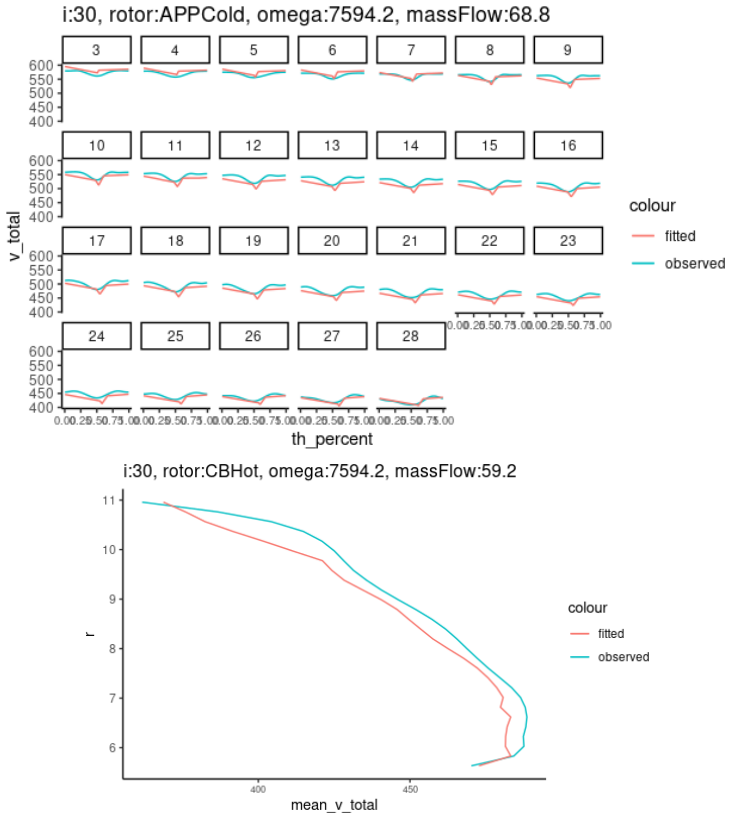

Figure 8. DNN results when using full rotor speed for testing (that speed not used in the training). Top: prediction of mean streamwise velocity wake. Example with poor performance. Bottom: prediction of overall mean streamwise velocity from hub to tip. Example with poor performance.

Milestone(s)

The milestones for Task 1 in year 1 included the following:

1. Identify and access geometries and operating conditions relevant to study
2. Prepare initial ML training datasets
3. Develop ML autoencoder and begin feature extraction
4. Perform initial training of the ML decoder
5. Perform the first validation test of the surrogate model

Milestone 3 was adjusted because the ML algorithms that have been built do not use explicit autoencoder/decoder algorithms. Milestone 3 was instead replaced by the parameter-relevance weighting, which provides insight into the importance of the various input parameters.

Major Accomplishments

- File-transfer methods were set up between RTRC and BU for easy data sharing.
- MSSP program used the project in one of their classes, providing an initial push in the development of the ML algorithm.
- SDT fan geometry and flow path information were used to set up new CFD simulations related to the SDT geometries.
- A total of 268 simulations were performed, all of which were used in training and testing of the ML algorithm.
- A LBM simulation was started by RTRC to determine whether it might provide additional, critical wake flow information.
- A single-output ML algorithm was developed that would work as a surrogate model to obtain input information for the low-order broadband acoustic prediction method based on the SDT-related fan geometries used to date.

Publications

None to date. Extended abstract submittal to the 2022 AIAA/CEAS Aeroacoustics Conference is expected.

Outreach Efforts

None

Awards

None

Student Involvement

Two undergraduate students, one PhD student, and one Master's student have contributed to this project. In addition, 14 students from the MS program in statistics worked on an aspect of the project for a semester-long class project.

Plans for Next Period

The milestone set for the second year of this project is ML surrogate model refinement and validation.

In year 2, the ML development focus will involve exploration of the multi-output ML method and the creation and use of a much larger rotor flow database including rotors with significantly different geometries.

Task 2 - Improvement of Low-order Model

Objective(s)

The existing low-order methods are regularly applied to the SDT cases and therefore have been well validated against this test, which represents one scaled fan and multiple Fan Exit Guide Vanes (FEGVs). The low-order method must now be validated against full-scale test data. The low-order method might also require reformulation to account for other real-flow effects.

Research Approach

Subtask 2.1: Ability to predict full-scale results

The low-order method will be applied to a full-scale geometry with available validation data. Because of the difference in the frequency range of interest for the full-scale case compared with the scaled fans, the low-order method is expected to require grid adjustments and integral extent adjustments. Such improvements to the low-order method will be completed as part of this task.

During year 1, RTRC worked with Pratt & Whitney to obtain the approvals required to use the Continuous Lower Energy, Emissions and Noise (CLEEN1) test for the full-scale validation case. RTRC has multiple related simulations and began the process of vetting these simulations to determine which can provide the appropriate input data for a low-order broadband noise calculation. In addition, the experimental noise measurements are being prepared in a manner allowing them to be compared to the low-order predictions.

The low-order method has been reactivated after having not been used for several years. It was applied to the newer fan rig ACAT1 test. The results are exactly in line with those previously shown with other low-order prediction methods.

Milestone

Validate low-order model on new geometry, and test rig-scale vs. full-scale applicability.

This milestone will be carried over to year 2. Although progress has been made in identifying the full-scale test case and further validating the low-order method against a newer scaled rig test (ACAT1), the acoustic predictions for the full-scale test have not yet occurred.

Major Accomplishments

Authorization to use the FAA CLEEN I information and data for the full-scale validation will allow this task to commence.

Publications

None

Outreach Efforts

None

Awards

None

Student Involvement

One BU undergraduate student and one BU PhD student have contributed to the low-order model. The PhD student now fully understands how to create the necessary input files and obtain acoustic predictions with the method. Several pre- and post-processing codes have been updated.

Plans for Next Period

The milestones for the second year related to this task are described below. The carried-over milestone of completing the full-scale validation test of the low-order method will also be addressed.

- Assessment of tip flow impact on the low-order model
- Assessment of inflow distortion impact on the low-order model

Project 076 Improved Open Rotor Noise Prediction Capabilities

Georgia Institute of Technology

Project Lead Investigator

Professor Dimitri N. Mavris
Director, Aerospace Systems Design Laboratory
School of Aerospace Engineering, Georgia Institute of Technology
Phone: (404) 894-1557, Fax: (404) 894-6596
Email: dimitri.mavris@ae.gatech.edu

Dr. Jimmy Tai
Division Chief, Propulsion & Energy
Aerospace Systems Design Laboratory
School of Aerospace Engineering, Georgia Institute of Technology
Phone: (404) 894-0197, Fax: (404) 894-6596
Email: jimmy.tai@ae.gatech.edu

University Participants

Georgia Institute of Technology (Georgia Tech)

- P.I.: Dr. Dimitri N. Mavris
- Co-PI: Dr. Jimmy Tai
- FAA Award Number: 13-C-AJFE-GIT-078
- Period of Performance: August 11, 2020 to August 10, 2021
- Task(s):
    - Task 1: Literature review
    - Task 2: Parametric CAD model creation
    - Task 3: Computational aerodynamics analysis (CAA) case setup and validation

Project Funding Level

The project funding is $300,000 per year from the FAA. The cost-share match amount is $300,000 per year. The sources of matching are cash and in-kind cost-sharing from our industry partner (General Electric [GE]).

Investigation Team

- Dr. Dimitri Mavris, Professor, Georgia Tech (P.I.)
- Dr. Jimmy Tai, Senior Research Engineer, Georgia Tech (Co-P.I.)
- Mr. Srujal Patel, Research Engineer II, Georgia Tech
- Dr. Miguel Walter, Research Engineer II, Georgia Tech
- Mr. Christopher Roper, Graduate Student, Georgia Tech
- Mr. Brenton Willier, Graduate Student, Georgia Tech
- Mr. Marcos Dos Santos, Graduate Student, Georgia Tech
- Mrs. Mariam Emara, Graduate Student, Georgia Tech
- Mr. Maxime Varoqui, Graduate Student, Georgia Tech

Project Overview

The contra-rotating open rotor (CROR) system has promising environmental benefits due to its ultra-high bypass ratio and high propulsive efficiency. The reduced fuel burn and emissions of the CROR compared with an equivalent-thrust turbofan

make the CROR a viable economic and environmentally friendly propulsion alternative to traditional ducted systems. However, in the absence of a noise-conditioning duct, aerodynamic interactions within the CROR system as well as between the system and surrounding installation components such as the engine pylon may result in noise penalties. If the system configuration is not optimized, the added effect of flow asymmetry to the aerodynamic interactions could potentially result in severe noise penalties, making the CROR system infeasible for use in the aircraft industry. In the proposed work, a sensitivity study will be performed on the design parameters of a CROR-pylon configuration. This study will leverage knowledge from past efforts with this type of configuration in order to narrow down the space of design parameters. High-fidelity CAA will be carried out to analyze the effect of each of the chosen parameters on noise. This research is intended to provide both the FAA and industry with key insights necessary for design optimization of the CROR system in the future.

Task 1 - Literature Review

Georgia Institute of Technology

Objective(s)

This task is focused on defining a set of design parameters known to affect the aeroacoustics of the open rotor and acknowledged in the open literature. This set will serve as a starting point for further defining a subset of design parameters on which the sensitivity study will be based. Therefore, a literature survey was conducted to summarize the current knowledge on design or operational parameters affecting open rotor acoustics.

Research Approach

The literature review began with the historical background of open rotor research published in technical reports by the government and industry, articles in journals, and conferences papers. The literature review resulted in the identification of open rotor design parameters impacting the overall rotor noise. These parameters were broadly grouped in three categories: rotor design parameters, pylon installation parameters, and airframe integration parameters. For the sake of brevity, these parameters are detailed in Appendix A.

It was determined that the sensitivity study should focus on parameters dictating the rotor design. A preliminary list of parameters most likely to be used in the sensitivity study is presented in Table 1.

	Design Parameter	Remark
1	Diameter of front rotor	Noise levels reported to be sensitive to diameter of front rotor more than diameter of aft rotor, rotor spacing, and pitch angle of aft rotor
2	Pitch angle	Noise levels sensitive to pitch angle more than radius of aft rotor and rotor spacing, but less than diameter of front rotor.
3	Diameter of aft rotor	Noise levels sensitive to diameter of aft rotor more than rotor spacing, but less than diameter of front rotor and pitch angle.
4	Rotor spacing	Noise levels less sensitive to rotor spacing compared to diameters of rotors and pitch angle.
5	Blade stagger angle	Front rotor blade stagger angle was found to be an influential blade geometry parameter in a paper that studies optimization of 3D blade geometry for noise reduction.

6	Tip speed (Diameter and RPM)	Noise levels more sensitive to Aft tip speed than fore tip speed.
7	Aft rotor clipping	
8	Number of blades	
9	LE camber variable	Reduction of interaction between LE separation & Tip Vortex Interaction (Gen 1A)
10	Tip design in AFT rotor	reducing unsteady pressure, including incoming FWD rotor wakes (Gen 2A)

Milestone
A literature review report was completed, as summarized in Appendix A.

Major Accomplishments
The literature review resulted in a compilation of key findings from previous research studies, which aided in shortlisting the key parameters for the sensitivity study.

Publications
None

Outreach Efforts
None

Awards
None

Student Involvement
For this task, the graduate students worked in three design parameter groups, as described in Appendix A.

1. Rotor-only noise-related parameters: Chris Roper (continuing PhD student) and Mariam Emara (continuing PhD student)
2. Rotor–pylon flow-field interaction-related parameters: Brenton Willier (continuing PhD student)
3. Rotor–airframe flow-field interaction-related parameters: Maxime Varoqui (MS student)

Plans for Next Period
This task has been completed.

Task 2 - Parametric CAD Model Creation
Georgia Institute of Technology

Objective(s)
This task is focused on the development of a fully parametric CAD model of the open rotor and pylon configuration. This parametric model aids in mapping the independent parameters of the sensitivity study to a particular open rotor design geometry, which will later be used for computational aeroacoustics.

Research Approach

Under this task, a fully parametric model of the baseline geometry of the CROR and pylon configuration was generated. Emphasis was placed on ensuring that the resulting geometry is an accurate representation of the physical design of the reference blade set and is suitable for computational fluid dynamics (CFD) mesh generation. A scripting language was used to automate the model update based on a design point. This step is typically time-consuming because the mapping must be sufficiently robust such that design variable instances do not lead to a geometry with undesirable imperfections such as wrinkles or open surfaces that might be unsuitable for CFD analysis.

The initial geometry of the blades and nacelle was extracted from historical F31/A31 data provided by GE. Export-restricted files were provided, and key files among this group included 3D blade models, two-dimensional (2D) blade stations, and a test nacelle flow path. The parametric geometry model was recreated in Engineering Sketch Pad (ESP), an open-source, script-based, multidisciplinary design analysis & optimization (MDAO)-friendly CAD tool chosen because of its platform-independent framework, which is especially useful for cluster use during future sensitivity/MDAO-type studies.

First, the provided data were used to recreate the nacelle based on a 2D spline in the form of data points. This spline was rotated around a predefined axis to create the nacelle surface. Upon verification with additional restricted documents, the rotor locations and aft flow path trimming were found to be consistent with the original geometry data. Starting with the provided IGES blade model, cross-sections were extracted using Star-CCM+ and a Java macro. Because this task is repetitive, a Java macro was developed for multiple cross-sections to efficiently complete this task. This step of the process outputs raw cross-section coordinates in multiple CSV files. Next, a Python script was used to post-process these raw cross-section coordinates to reformat the data for ESP import. To retain information about the original shape, a final CSV file is created, which includes the original XYZ coordinates of the LE and TE, section twist, and section chord. To efficiently parameterize the airfoil section, the class-function/shape-function transformation (CST)/Kulfan method is employed to describe the shape of an airfoil with very few variables. Next, a script in ESP reconstructs the sections using the CST coefficients. The models recreated with this process were compared with the original model, and the maximum surface deviations were found to be less than 1/10 mm. With this diagnostic, the accuracy of the reconstruction process was verified. Finally, a pylon was added to the model. This pylon was built with the parameters of a generic wing-like span, root chord, taper ratio, aspect ratio, sweep, and twist. The pylon shape can be altered by choosing any number of cross-sections and by specifying CST coefficients for each section.

Milestone

A fully parametric CAD model of the historical F31/A31 blade set was successfully created for CAA validation and future sensitivity/MDAO studies.

Major Accomplishments

A fully parametric CAD model of the historical F31/A31 blade set was successfully created for CAA validation and future sensitivity/MDAO studies.

Publications

None

Outreach Efforts

None

Awards

None

Student Involvement

For this task, Brenton Willier (continuing PhD student with U.S. person credentials) played a major role in parsing F31/A31 data provided by GE. Brenton Willier also worked on parameterization of the F31/A31 CAD model in ESP.

Plans for Next Period

This task has been completed.

Task 3 - Computational Aeroacoustics Validation

Georgia Institute of Technology

Objective(s)

This task is focused on validating our predictions from simulation analyses against available experimental data from an open rotor configuration to evaluate discrepancies between numerical simulations and experiments. This validation will indicate the level of adequacy of the adopted numerical approach for open rotor design.

Research Approach

For this validation, the experimental data used are from NASA (Stephens, 2014; Sree, 2015), carried out on the wind tunnel open rotor model based on the F31/A31 blades, whereas the numerical simulations are based on a combined approach consisting of the lattice Boltzmann method (LBM) for unsteady aerodynamics and the Ffowcs Williams–Hawking (FW-H) method for far-field aeroacoustics.

Validation case and experimental data

The geometry of interest is an open rotor based on a subscale model based on the F31/A31 blade set. Geometrical details are provided in Table 2.

Table 1. Subscale F31/A31 open rotor.

	Number and type of blades	Diameter
Front Rotor	12 / F31	0.66 m
Aft Rotor	10/ A31	0.63 m

The utilized experimental data are from NASA experiments (Stephens, 2014; Sree, 2015) on a low-speed wind tunnel (9 ft x 15 ft). These experiments focused on three conditions: scaled take-off (STO), nominal take-off (NTO) and approach (APP). Furthermore, several rotor speeds were tested with two different configurations, with and without a pylon. The rotor design speed was 6530 RPM, and the inlet Mach number was 0.2 for all experimental runs.

Acoustic data were recorded by 18 sideline microphones, located at an offset distance of 5 ft parallel to the axis of the open rotor wind tunnel model. With the axis of the WT model and the plane of the aft rotor as a reference, these microphones covered angles of 17.6˚–140˚, with angles lower than 90˚ located upstream and angles larger than 90˚ located downstream.

The present validation focuses on an NTO case at 85% rotor speed. An illustration and details for this case are provided in Figure 1 and Table 3, respectively.

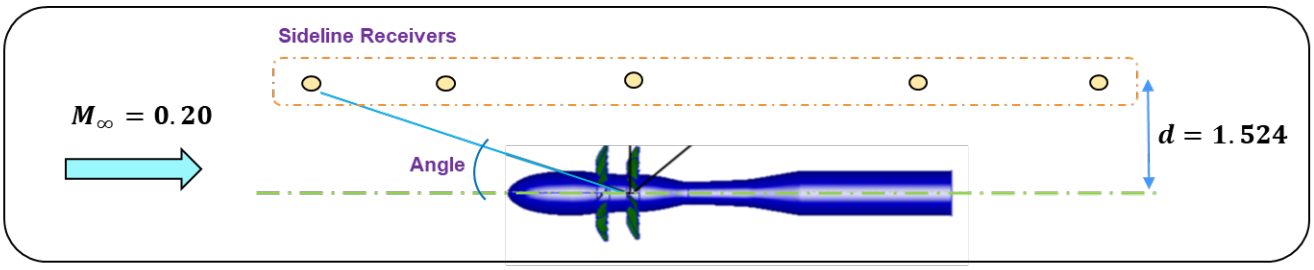

[*] Nark *et al.*, "Isolated Open Rotor Noise Prediction Assessment Using the F31A31 Historical Blade Set", AIAA paper 2016-1271

Figure 1. Validation case.

Table 2. Validation case details.

	Value	Unit
Mach number	0.2	
Rotor speed	5550.5	RPM
Blade pitch setting	40.1 front / 40.8 aft	degree
Angle of attack	0	degree

Numerical approach

The unsteady aerodynamic flow field is obtained by employing a commercial LBM solver, PowerFLOW. Unlike a traditional CFD solver that solves for macroscopic fluid quantities via Navier–Stokes equations, LBM-based solvers solve for microscopic particle distributions. Thus, modeling occurs at a level for which the physics are more fundamental. Such solvers exhibit low dissipation properties, rendering them suitable for aeroacoustic applications. Some details about the simulation setup are shown in Table 4.

Table 3. LBM simulation setup.

LBM Simulation	***Value***	***Remark***
Smallest spatial discretization	0.069 mm	At blade LE, TE, and tips
Time step	0.079 μs	
Mesh size	577 million	

Far-field aeroacoustics are calculated by employing an FW-H solver. This solver uses flow data recorded from unsteady simulations for a chosen surface. The surface is permeable surrounding the geometry of interest. The geometry is an open shell with an opening in the downstream end to avoid contamination from the open rotor wakes. The far-field acoustic receivers set to the FW-H solver are located at the same positions of the microphones in the experiments. Some details about the FW-H solver simulation are provided in Table 5.

Table 4. FW-H simulation setup.

FW-H Simulation	***Value***	***Remark***
FW-H spatial discretization	4.28 mm	Permeable surface
FW-H time step	7.5 μs	
Maximum frequency resolved	6.6 kHz	
Time for collecting flow data	4.5 revs.	Time for one revolution

Results

Numerical predictions of sound pressure level (SPL) at each rotor fundamental and first interaction, along with the overall sound pressure level (OASPL) as a function of the sideline geometrical angle, are shown in Figure 2. The rotor fundamentals are defined by the blade passage frequency, $BPF = nf_0$, where n is the number of blades and f_0 is the shaft frequency. The interaction frequencies are given by combinations of the blade passage frequencies of both the front and aft rotor, $m_1\, BPF_f + m_2\, BPF_A$, where m_1 and m_2 are integers; thus, the first interaction is given by $m_1 = m_2 = 1$. In the figure, both rotors exhibit maximum SPL values for geometric angles around their respective planes of rotation. The radiated noise, however, decreases significantly for upstream and downstream angles. In contrast, the SPLs for the first interaction are high for all angles despite

the presence of lobes in the directivity pattern. Finally, comparisons of the interaction noise with the OASPL directivity suggest that the interaction noise is dominant for the open rotor.

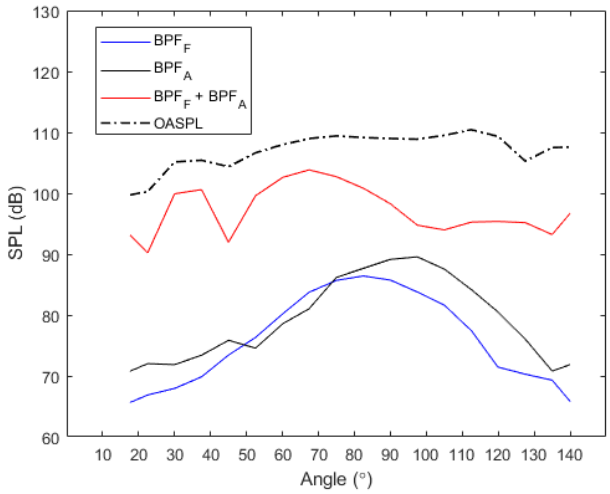

Figure 2. SPL at the fundamental frequencies (rotor and first interaction) and OASPL.

A comparison of the OASPLs from experiments (Sree, 2015) and numerical CAA simulations is shown in Figure 3. It is noted that the simulations exhibit better value agreement for intermediate angles, between 50˚ and 100˚, whereas the agreement decreases for large upstream and downstream angles. Nevertheless, the trend of the OASPL from simulations resembles that of the experiments. Quantitatively, the OASPL from the CAA simulation has a root mean squared error (RMSE) – calculated across all sideline angles – of 4.5 dB.

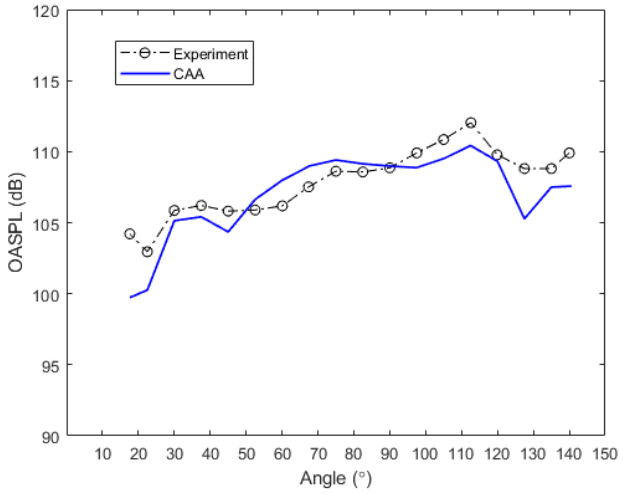

Figure 3. OASPL from simulations and experiments.

The overall power watt level (OAPWL) from the CAA simulation is compared with the experimental value in Table 6. The OAPWL calculation was performed exactly as described in the NASA report (Sree, 2015). For the case in consideration (NTO, 85% RPM_{DESIGN}, AoA=0), the resulting discrepancy is 1.75 dB.

Table 5. Comparison of OAPWLs.

Case	CAA	Experiment	Discrepancy
NTO, 85% RPM_{DESIGN}	125.75 dB	124 dB	1.75 dB

In summary, results obtained by our strategy of combined numerical simulations – LBM & FW-H – suggest good agreement with experimental data for one NTO case.

References

Sree, D. (2015). Far-field acoustic power level and performance analyses of F31/A31 open rotor model at simulated scaled takeoff, nominal takeoff, and approach conditions: Technical report I (Report No. CR 2015-218716). National Aeronautics and Space Administration.

Stephens, D. B. (2014). Data summary report for the open rotor propulsion rig equipped with F31/A31 rotor blades (Report No. TM 2014-216676). National Aeronautics and Space Administration.

Milestone(s)

None

Major Accomplishments

Initial validation of our numerical strategy for aeroacoustics was completed, exhibiting good agreement with experimental data for one case.

Publications

None

Outreach Efforts

None

Awards

None

Student Involvement

For this task, Brenton Willier (continuing PhD student with U.S. person credentials) worked on geometry preparation of the F31A31 open rotor and aerodynamics analysis.

Plans for Next Period

We and the sponsor have agreed to conduct further validations in the second year. However, these new validations will employ experimental data provided by the cost-share partner, GE. It must be pointed out that these data were not available during the first year of the project and were not yet accessible at the time of the writing of this report.

Appendix A: Summary Report of the Open Rotor Literature Review

Introduction

To achieve higher fuel efficiency, today's turbofan engines are becoming larger to house large fans and bypass ducts that accommodate higher volumes of bypass flow. However, as the size of a turbofan engine increases, drag and weight penalties eventually cancel the benefits of improved fuel efficiency [1]. To advance beyond these limitations, an open rotor engine concept is currently being investigated. An open rotor, also known as a 'Contra-Rotating Open Rotor (CROR)' or propfan, is an engine featuring a set of two propellers rotating in opposite directions. The propellers are driven by a gas turbine engine, which works on the same principle as a turbofan engine except that the engine core has no encompassing duct. Due to the unique counter-rotating fan design, the "bypass flow" of the air surrounding the engine core is qualitatively similar to the turbofan ducted flow, resulting in designs that obtain high bypass ratios without limiting the propeller fan size. It is estimated that open rotor engines currently prototyped in the industry achieve 30% reductions in fuel consumption compared with contemporary turbofan engines [2].

However, for open rotor engines, the absence of a noise-conditioning duct results in noise penalties due to complex aerodynamic interactions within the CROR system as well as between the system and surrounding installation components such as a pylon/fuselage. In particular, during take-off, an added effect of flow asymmetry introduces additional noise sources that magnify the emitted noise, resulting in challenges associated with strict noise certification standards. Therefore, noise improvements in CROR engines represent a primary challenge being addressed by engine manufacturers.

The main objective of this research is to perform a sensitivity study using high-fidelity Computational Aeroacoustic Analysis (CAA) to understand the impact of various CROR engine design parameters on overall noise performance, with the end goal of identifying key design parameters which future designers can target to meet noise-performance-related requirements. The sensitivity study will use the historical F31/A31 blade set as a baseline. Due to high computational costs, it is not feasible to evaluate all design parameters in this sensitivity study. Therefore, it is necessary to identify a subset of key design parameters based on experimental and computational studies previously performed by the community. In this report, we summarize key findings, primarily from the noise improvement perspective, that will guide the future course of the sensitivity study. Section A1 provides a brief historical background on open rotor technology. Section A2 presents an overview of CROR engine noise and a classification of CROR design parameters based on various noise sources. Section A3 provides a survey of design parameters and their impact on open rotor noise based on experimental and computational research outcomes published in the existing literature. This section also presents key parameters identified by the team as critical for the CAA-based sensitivity study that will be performed in years 2 and 3 of this effort.

A1. Historical Background

In the early 1980s, based on initial results of early NASA open rotor technology studies released to engine makers, GE initiated the historic *Unducted Fan (UDF)* program with full-scale development testing of UDF open rotor engines. Early efforts in UDF engine development aimed to overcome the increase in fuel prices caused by the 1973 Middle East oil embargo [3]. The UDF proof-of-concept testing consisted of three phases: scale model technology development through 2,500 hours of scale model testing in 1984, prototype engine development with 162 hours of ground testing in 1985, then 281 hours of flight testing on the Boeing 727-100 and the McDonnell-Douglas MD-80 aircraft in 1986 and 1987. The program led to the development and use of several model-scale facilities for testing open rotor technology, such as the GE Cell 41, NASA Glenn 9x15 Low-Speed Wind Tunnel, NASA Glenn 8x6 High-Speed Wind Tunnel, Boeing Transonic Wind Tunnel, and DNW Acoustic Wind Tunnel [4]. The blades selected for the UDF were of the F7A7 design, composed of advanced composite materials.

Extensive testing was aimed at understanding the aerodynamic and acoustic performance of the engine, and noise problems were quickly identified during the tests. Model-scale and full-scale results from the UDF program testing showed good comparisons, indicating that the model-scale tests could be projected to accurately estimate full-scale results. The UDF testing identified several noise mitigation methods such as increasing the number of blades, reducing the disk loading, applying aft rotor clipping, increasing the pylon–rotor distance, mitigating the pylon wake, and optimizing the rotor spacing, blade operation speed, and blade geometry [4]. In-flight tests showed that the UDF presented a 30% reduction in specific fuel consumption compared with a JT8D mounted on the other side of the Boeing 727 [5].

The technology development efforts were then used and leveraged to develop a GE36 engine for installation on the MD-91 and MD-92. The GE36 was designed to achieve nominal compliance with CAEP Chapter 4 requirements, with significant

improvement over previous UDF tests. The GE36 passed the test by featuring a cumulative margin of 10.5 dB with respect to Chapter 3 requirements. However, this achievement came with a reduction in aerodynamic performance, with a drop of 3% in cruise efficiency compared with a set that did not include the noise mitigation enhancements [4]. Despite this progress, as fuel prices fell after the embargo, the development costs could no longer be justified, and hence, the program was cancelled in 1989, halting any further development [3].

In the early 2000s, the environmental impact of the aviation industry and the need to explore efficient propulsion concepts led to a renewed interest in open rotor engines. From 2008 to 2012, as part of FAA's *Continuous Lower Energy, Emissions and Noise (CLEEN)* program and NASA's *Environmentally Responsible Aviation (ERA)* program, GE partnered with NASA to develop a mature open rotor engine aeroacoustic design. This *Modern Open Rotor Technology Development* program targeted a narrow body aircraft with a cruise Mach number of 0.78, leveraging CFD, CAA, and rig-scale testing to generate designs that achieved significant noise reductions well beyond what was attained in the 1980s while substantially retaining cruise performance. The blade designs included derivatives of the historical F31/A31 blade set, which was remanufactured and tested to provide a link back to data from the 1980s. The test program allowed for open rotor engine designs resulting in a 2%–3% improvement in overall propeller net efficiency over the best efficiency design of the 1980s while nominally achieving a noise margin of 15–17 EPNdB for Chapter 4 (when projected to full scale for a prescribed aircraft trajectory and installation) [4].

A2. Overview of Open Rotor Noise

Sound is a pressure wave that travels through matter by vibrations. A sound is characterized by its pitch and loudness, i.e., intensity. The pitch is perceived through the fundamental frequency of the noise, it describes the number of vibrations perceived per second. The range of audible frequencies for humans is 20 Hz to 20 kHz. The loudness or intensity of a noise is the energy carried by the wave, which is measured in decibels (dB). As shown in Figure 4, the energy of some noises is concentrated in specific frequencies or in a limited range of frequencies. This type of noise is called tonal or narrowband noise. Tonal noise is emitted by cyclic sources, such as rotating pieces like fans or compressors due to their blade thickness and blade loading [6]. The noise emission is repeated at each cycle, creating tonal noise at this specific cycle frequency. In contrast, the energy of other noise sources is spread across a large frequency spectrum, resulting in random and non-harmonic sound emission. This type of noise is called broadband noise. Turbulence in the flow due to complex interactions results in such noise [7][8]. Various noise sources associated with the complex flow field around an open rotor engine are shown in Figure 5.

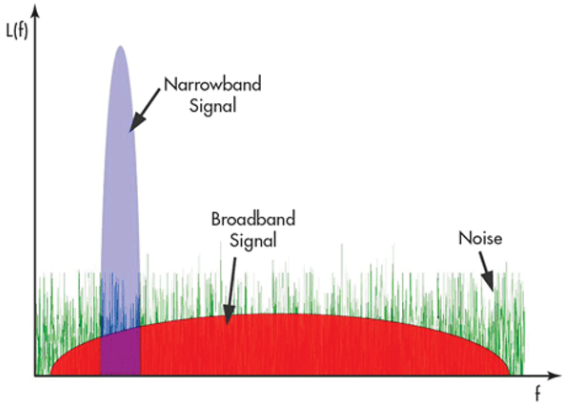

Figure 4. Noise power as a function of frequency for broadband and tonal noise (source: mwrf.com).

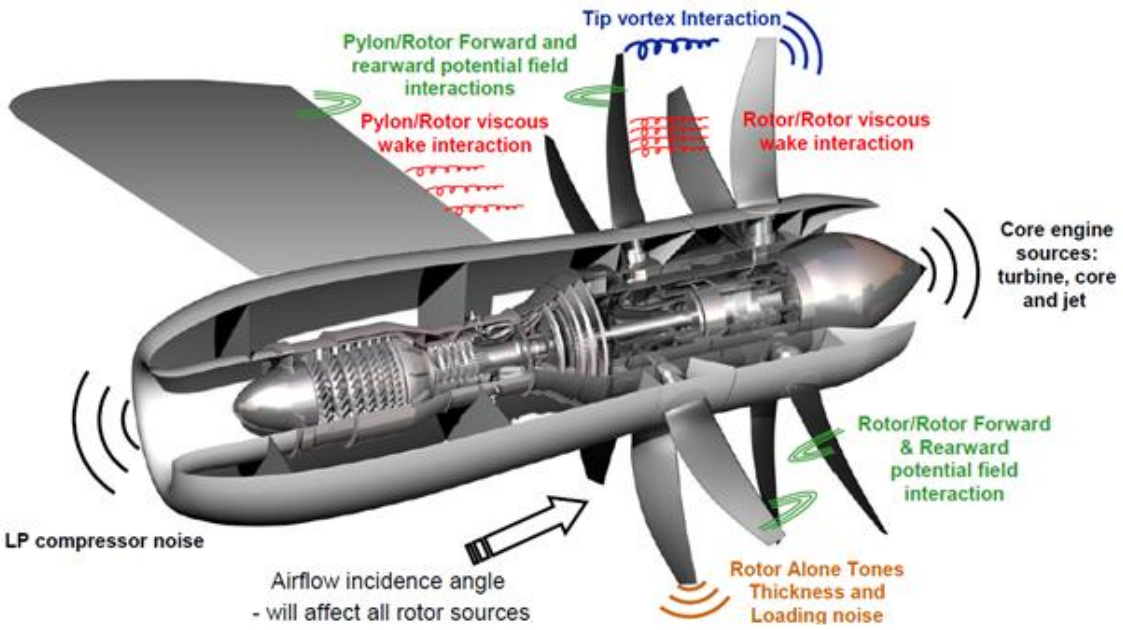

Figure 5. Open rotor noise sources. [8]

A3. Summary of Open Rotor Design Parameters and Their Impact on Noise

For the literature review, open rotor design parameters were divided into three primary groups based on the noise source:

1. Noise due to the rotor alone
2. Noise due to engine installation effects from rotor–pylon interactions
3. Noise due to engine installation effects from engine–airframe interactions

The rotor-blade-alone group involves rotor blade design parameters that contribute to the noise; examples of these parameters include the shape and number of the blades and the distance between the two rotors. Pylon installation effects include the parameters that define the pylon shape and position with respect to the rotor system. Finally, the airframe integration parameters include the engine location and aircraft configuration.

1. **Rotor-alone parameters**
   The main rotor parameters studied in the experimental campaign by NASA and GE were the spacing between the front and aft rotors, rotor diameters, aft rotor clipping, disk loading, blade count, tip speed, and pitch angle. Most of these parameters were identified as potential noise mitigation sources from the *UDF* program testing and *Modern Open Rotor Technology Development* program studies. Here, we summarize the impact of each of these design parameters as found in the literature.

   Aft rotor clipping: Decreasing the aft rotor diameter relative to the front rotor is called blade clipping, which is defined by the distance between the front rotor tip streamline and the aft rotor tip (Figure 6). Aft rotor clipping decreases the noise level by weakening the effect of the front rotor tip vortex interaction on the aft rotor: a clipping of 5% decreased noise levels for the F31/A31-based engine [9].

   Disk loading: Disk loading is defined as the power per unit propeller annulus area. It was observed that decreasing this parameter by adjusting other design parameters could significantly reduce noise levels. By increasing the rotor diameter of the F31/A31-based engine, disk loading was reduced from 100 hp/ft^2 to 59 hp/ft^2 to reduce noise levels [9].

Rotor diameter (R1 and R2): The noise levels were found to be more sensitive to the front rotor diameter than the aft rotor diameter, as well as other design parameters such as rotor spacing and the pitch angle of the aft rotor[10] [11]. In most studies, increasing the rotor diameter from the baseline led to lower noise levels due to a decrease in disk loading. The rotor diameter of the F31/A31-based engine was increased from 10.7 ft to 14 ft to decrease the noise level, which also provided net efficiency gains but increased weight and installation penalties [9]. In contrast, in a study focusing on the wake rather than the blade–vortex interaction, the radii of both rotors were decreased to reduce noise, with the aft rotor radius being larger than the front rotor radius to create a smaller wake area from the front rotor [11].

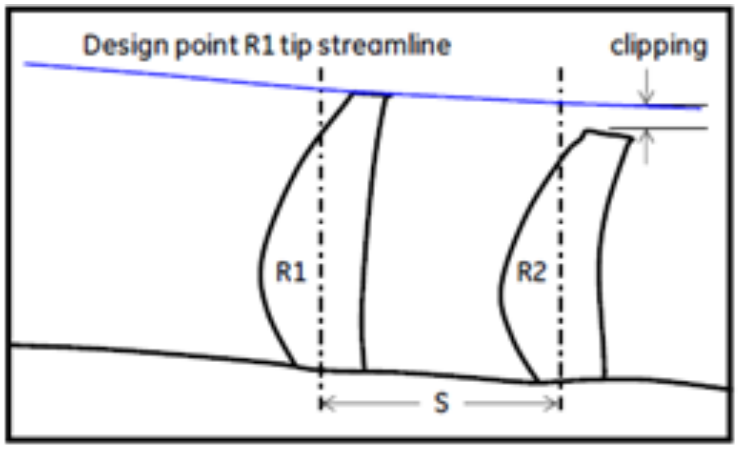

Figure 6. Main rotor parameters [4].

Pitch angle: In an optimization study conducted by the German Aerospace Center, DLR, for an 8x8 CROR engine, changing the pitch angle of the aft rotor by 2˚ from the baseline was found to reduce noise levels [11]. The noise level was also found to be more sensitive to pitch angle than the aft rotor radius or rotor spacing [10]. The variable blade pitch mechanism on the F31/A31-based engine allows the tip rotation speed to be adjusted for a given thrust and operating condition [9].

Tip speed: The tip speed or rotational speed of the rotors affects noise and can be adjusted by changing the pitch settings, where decreasing the pitch (increasing the blade setting angle) corresponds to increased RPM. A lower design tip speed reduces friction losses and brings the design lift coefficients closer to their optimum values but results in higher induced losses as a result of the stronger tip vortices [9]. Increasing the tip speed of the fore rotor at low flight speed was found to reduce noise in some historical experimental studies [9]. However, recent CFD study results on an SR2 blade geometry showed that noise can be reduced by decreasing tip speed [12]. Additionally, noise levels were found to be more sensitive to aft tip speed than fore tip speed. The effect of increasing tip speed was also found to be more significant for cases in which the forward blade count was greater than the aft blade count [12]. Another CFD study on a DLR CROR configuration showed that increasing the rotational speed of the aft rotor from approximately 926 to 1132 RPM led to high blade loading in the rear rotor, which increased the SPL from 142 to 153 dB [13].

Number of blades: Increasing the blade count relative to the baseline decreases the noise level due to the reduced loading per blade, which reduces induced losses as well as loading and rotor–rotor interaction noise [9]. Additionally, historical test data from the UDF program showed that mismatched front and aft blade counts significantly affect noise and rotor interaction tones [9]. A CFD study on an SR2 blade geometry showed that the difference in EPNL between the lowest noise level combination (12*15) and highest noise level combination (8*5) of blade counts was approximately 35 dB (EPNL) [12].

Blade design: The design of the blade or planform variables also affect noise levels. Examples of blade parameters include the twist angle and chord length for different design sections, the tip shape or leading edge, and the blade thickness. For example, Gen 2A+B of the F31/A31 blade was designed to reduce the contribution of rotor–rotor interaction noise of the forward rotor tip vortex relative to its wake [9]. A CFD study focused on planform design parameters of the aft rotor of a NASA SR-7L geometry found that the other rotor parameters, such as blade diameters and rotor spacing, showed a more significant effect on noise. In that study, the chord length, twist angles at several

radial locations, and leading-edge coordinate of the tip section were considered as planform design parameters, and the optimized configuration showed a noise reduction of 0.6 dB [14].

Blade stagger angle: The blade stagger angle is a design parameter defined as the angle between the chord line of the blade and the rotor axial direction at different cross-sections of the blade. The front rotor blade stagger angle, which affects the radial load distribution was found to be influential in an optimization study of three-dimensional blade geometry for noise reduction [15].

Rotor-rotor spacing (S): The rotor-rotor spacing is the distance between the forward and aft rotors. This distance can be measured with respect to the pitch change axes or with respect to the aft-most point of the front rotor and the forward-most point of the aft rotor. Propeller noise is exacerbated by the effects of incoming unsteady flow and loading on the individual blades. Increasing the rotor spacing allows turbulent structures emitted from the front rotor to weaken before interacting with the aft rotor, resulting in reduced noise levels [9] [16]. A study on the effect of axial spacing between rotors showed that increasing the spacing by 46% led to a reduction of the total SPL by approximately 3 dB [17].

2. Design parameters related to rotor-pylon flow-field interactions

In the aft configuration, the wake of the support pylon causes unsteady loading on the front rotor. The literature review showed that multiple configurations have been tested to evaluate the sensitivity of these interactions. An isolated rotor is often used as a baseline for overall noise and interaction tones. Then, a pylon is added upstream of the rotor to evaluate the effect of the pylon wake on the overall noise. Finally, a fuselage and empennage are added to the flow field. With these different configurations, multiple parameters can be varied to uncover the sensitivities with respect to the produced noise.

Fuselage-rotor (tip) spacing: The fuselage-tip spacing is the minimum radial distance between the tip of the blade path and the fuselage. It was found that the noise decreases as the fuselage-tip distance increases [18].

Pylon-rotor spacing: The pylon-rotor spacing is the distance between the trailing edge of the pylon and the forward-most point of the front blade. The front rotor ingests the wake produced by the pylon, and this unsteady loading increases noise. It was found that noise decreases as the pylon-rotor spacing is increased [18] [19].

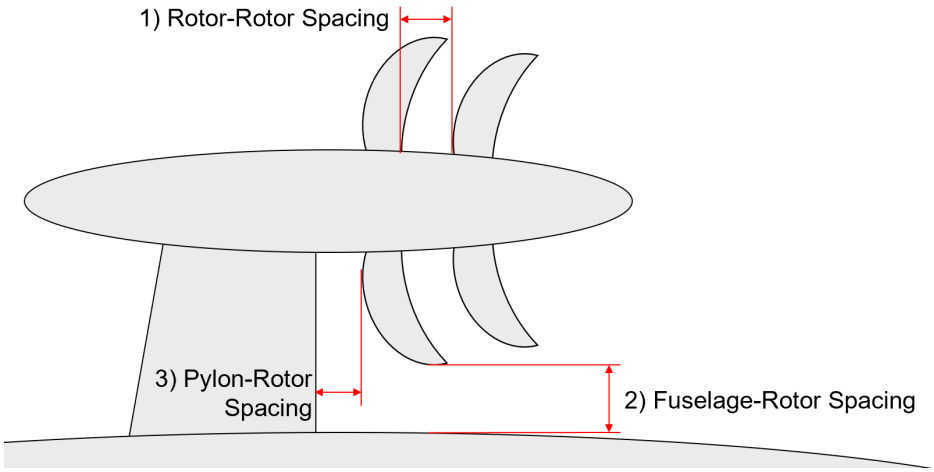

Figure 7. Rotor installation parameters.

Pylon angle of attack: The angle of attack of the pylon was examined because at takeoff, when noise is of high concern, the pylon would be at a high angle of attack. The angle of attack of the pylon was found to have no apparent trend applicable to consistent noise reduction between -5° and +5° [18]. Further work is required to understand the effect of the angle of attack on the pylon wake and resulting noise.

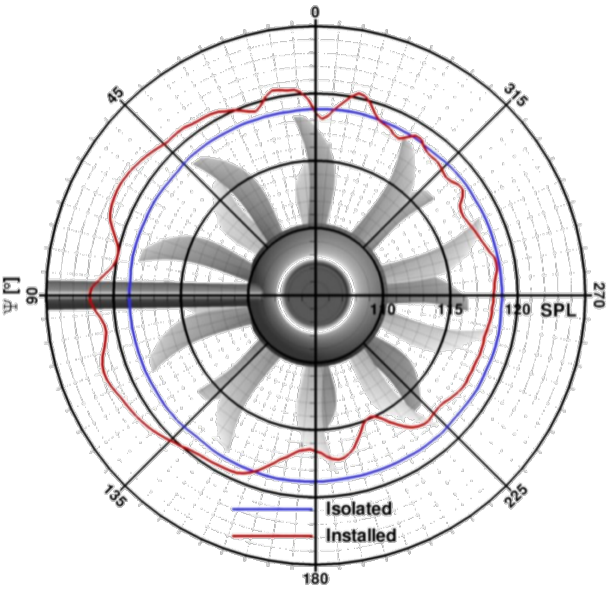

Figure 8. Noise directivity is skewed toward the pylon [20]

In summary, the literature review suggests that addition of the pylon results in increase in noise by at least 10dB [19] [18]. The addition of a fuselage and empennage results in an additional noise increase of 2–3 dB compared with the pylon-only configuration [18].

Technology infusion: pylon trailing-edge blowing

One possible technology infusion that could be applied to reduce pylon-induced noise is pylon trailing-edge blowing. In an attempt to fill the pylon wake, a blower can be added to the trailing edge of the pylon, as shown in Figure 9.

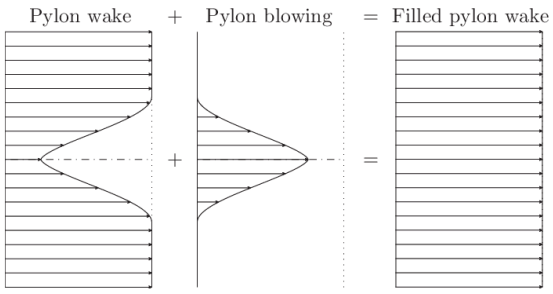

Figure 9. Notional filled pylon wake [21].

The blown flow is injected at a velocity slightly higher than the free stream, using the general physical test setup shown in Figure 10.

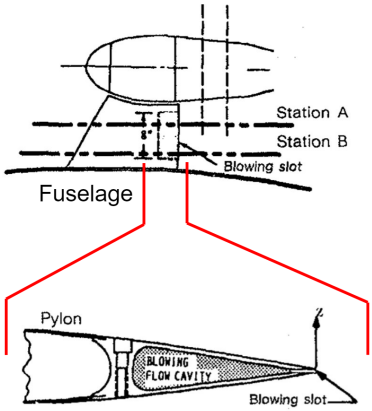

Figure 10. Pylon TE blowing schematic. [18]

The testing performed in the literature found that pylon blowing reduced the velocity deficit in the pylon wake; however, this mitigation did not reduce the overall wake width. Promisingly, noise due to the pylon wake was reduced, although the interaction tones were unchanged. If this technology is to be considered, further work should focus on exploring trends for varying blowing rates, angles of attack, and freestream velocities. The flow mixing should also be optimized. Finally, the flow near the fuselage should be optimized to encourage a smooth flow to avoid exacerbating fuselage-tip-induced noise [18][19][21].

3. Design parameters related to open rotor engine–airframe integration

As discussed earlier, the interaction of the rotor flow field with the airframe results in additional noise that must be considered. Design considerations related to airframe integration must include the position of the engine with respect to the airframe and the aircraft shape. Because this study is primarily focused on open rotor applications for narrow-body single-aisle aircrafts, the literature review was limited to traditional tube and wing airframes, excluding other unconventional structures, such as blended wing body aircrafts. For engine–airframe integration, the engine mounting location is an important factor. First, we will consider tail-mounted configurations and their impact on noise shielding.

Tail configuration comparison

The three main configurations considered are the U-Tail, the T-Tail, and the L-Tail (Figure 11). In traditional aircraft designs, the L-tail configuration is most common. However, the UDF flight tests on the Boeing 727 [22] in 1986 and the MD-80 in 1987 featured a T-tail configuration [23]. After renewed interest in open rotor engines, new programs studied the L-tail and U-tail configurations in addition to the original T-tail used by the UDF programs at the end of the 1980s.

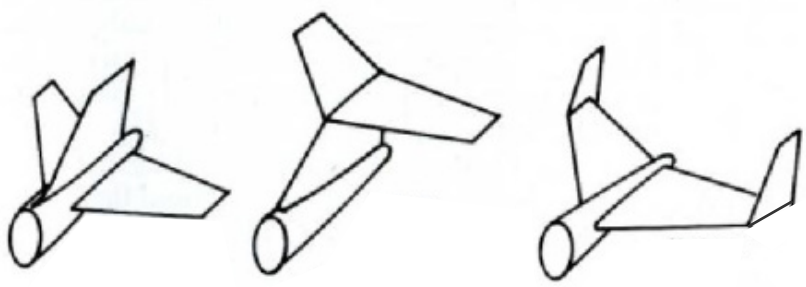

Figure 11. From left to right, L-tail, T-tail, and U-tail configurations. [24]

The WENEMOR project (2011–2013) was a European Clean Sky Joint Technology Initiative to investigate aero-acoustic noise emission measures for advanced regional open rotor A/C configurations. The engine used for this project was a 1:7-scale modular model with interchangeable tails, pylon elongations and angles, and variable angle of attacks. The blade profiles

were designed by SAFRAN and featured 12 blades for both the front and aft propellers. Experiments were performed for a total of 16 different configurations in this program for both approach and takeoff certification points. The engine was in pusher mode for nine of the configurations and in tractor mode for seven configurations. The open rotor pylon length was 522 mm and was set with an angle of 42°. The parameters that were varied were the angle of attack, flow speed, and tail shape (T-, U-, or L-tail). The noise calculations were recorded as the difference in OASPL, relative to a baseline case with an 8° angle of attack and a flow speed of 24m/s. The noise was measured by a far-field microphone array.

According to data analyses from this project [25] [26], L- and U-tails performed better, with a globally more significant shielding than the T-tail configuration. The largest noise reduction came from the PS-E engine configuration (Figure 12), which contained an open rotor in pusher mode mounted on a 42-degree and 1.04D long pylon. The comparison between the L- and U-tails was very close in terms of advantages and disadvantages. The L-tail in the PS-E configuration yielded better results for the OASPL, but the U-tail led to higher noise reductions for broadband and tonal noise for the takeoff certification configuration. None of the configurations studied outperformed the others for all harmonics under both takeoff and approach conditions.

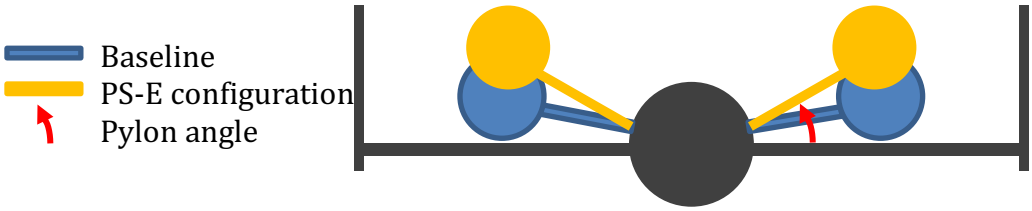

Figure 12. PS-E configuration for a U-tail airframe.

The influence of tail type has also been discussed in another previous work [27]. In that study, the L- and U-tails were compared with a T-tail baseline. An angle of attack of 6° mounted on a U-tail seemed to yield the best results among the configurations studied, presenting a noise reduction in almost every direction, except for $\sim \pm 10°$ with respect to the vertical axis.

Another CFD study [28] compared the effects of L-tail, U-tail, and T-tail configurations on the EPNL for two takeoff certification points: flyover and lateral. This study considered an open rotor engine for which the pylon planform, nacelle contour, and rotor position were approximated from the SAFRAN Aircraft Engines CROR model. The CROR was mounted in pusher mode and featured 12 blades (14-ft diameter) in front and 10 in aft position. The CROR rotor located on the tail of the aircraft with a pylon inclined by 45° in the downward direction showed a noise attenuation of 7 dB for the L- and U-tails in the aft downward direction. This reduction was attributed to the relative position of the horizontal tail below the engine, which allowed an upward noise reflection. Yet, this attenuation was compensated in the aft upward direction by a noise level increase for these two tails with respect to the no-tail and T-tail configurations. The behavior of the U-tail in the vertical plane was similar to that of the L-tail, as the geometries of the horizontal stabilizers for both tails are similar. The T-tail exhibited the opposite behavior because of its symmetric geometry: the attenuation was observed for the aft upward area and the noise increase was observed in the aft downward area. The effect of the engine axial position alongside an axis parallel to the flight was also studied. For the lateral certification point, the study underlined a global compensation of reflection and shielding effects for all configurations. The directivity and noise intensity for all tails studied were similar to those for the no-tail case. Thus, none of the three tail configurations induced a significant change for lateral observers.

However, in flyover, the T-tail produced higher noise regardless of the engine axial position, with minor improvements for a forward engine placement. The zero location for this study corresponds to the CROR midplane aligned with the tail leading edge. Even though the U-tail and T-tail configurations featured similar behaviors, an optimum position was found for the U-tail at a position of 2 m aft of the leading edge. For this set, the attenuation relative to the case without a tail was -2.4 EPNdB.

Wing- or U-tail-mounted CROR

Thus far, our interest has focused on tail configurations for the airframe integration. However, another study [29] compared the benefits of a wing-mounted versus a tail-mounted CROR. The geometry considered for this study was the demonstrator rotor of the UDF program, geared with eight F7A7 blades for each rotor. The pitch angles of the blades tested here were 30.8° and 31.6° for static conditions and reached 38.0° and 37.2° for Mach numbers higher than 0.2. However, the pylon was not attached to the airframe; rather, it was positioned relative to the wing or the tail.

Figure 13. Over-wing and U-tail experimental installation. [29]

For a U-tail installation with the rotor center aligned with the leading edge of the U-tail, significant shielding of up to 20 dB in the rotor tone was observed for emission angles of approximately 60°–120°. When the rotor was positioned in front of the main wing, the presence of the wing in the wake of the rotor caused flow distortions, and the noise increased by 10 dB. Unlike the latter case, the results showed a reduction of 10 dB in broadband noise when the open rotor was placed right above the main wing. All the measurements were compared relative to the isolated rotor case.

Another way to simulate the behavior of a wing or tail configuration in lateral directions is by using a wall. Two studies [30] [31] reported on this type of wall-shielding experiment. The effect of noise shielding was tested on two different wall lengths and two different positions (Figure 14). A long wall simulated a large wing while a short wall represented a U-tail configuration. The open rotor considered was the historical GE F31/A31 blade set. A microphone array was set up to record the emitted noise. It was concluded that all barriers produced an attenuation of nearly 10 dB, irrespective of their position or length. However, a diffraction phenomenon was observed along the edges of the short wall. Thus, a larger barrier wall corresponds to better noise reduction.

An investigation on the positions of the short wall with respect to the center of the CROR was also performed [31]. The wall in the forward position featured a cumulative reduction of almost 3 EPNdB for approach, lateral, and flyover conditions, whereas the aft position induced an EPNL benefit of 8.3 EPNLdB. Hence, the aft position was found to be more suitable for noise reduction. However, the authors suggested that the results may be slightly exaggerated due to the small facilities in which the experiment was conducted; hence, these results should be used as validation measures for more accurate tests.

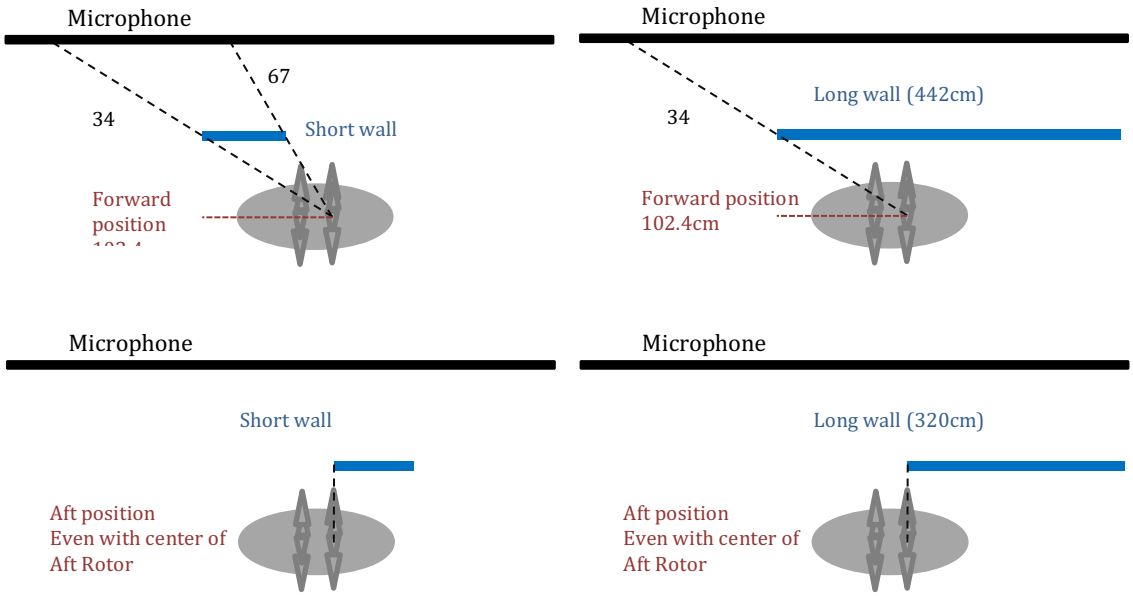

Figure 14. Illustration of the F31/A31 open rotor tested with barrier walls in the forward and aft positions.

BIBLIOGRAPHY

[1] L. S. Langston, "Open Rotor Engines—Still an Open Question?," *ASME. Mechanical Engineering.* , December 2018.

[2] SAFRAN-GROUP, "Safran celebrates successful start of Open Rotor demonstrator tests on new open-air test rig in southern France," October 2017. [Online]. Available: https://www.safran-group.com/media/safran-celebrates-successful-start-open-rotor-demonstrator-tests-new-open-air-test-rig-southern-france-20171003.

[3] Smithsonian National Air and Space Museum, "General Electric GE36 Unducted Fan (UDF) Turboprop Engine," [Online]. Available: https://airandspace.si.edu/collection-objects/general-electric-ge36-unducted-fan-udf-turboprop-engine/nasm_A19920001000.

[4] FAA, General Electric, "Open Rotor Engine Aeroacoustic Technology Final Report," 2014.

[5] M. McCarthy, "Contra-rotating Open Rotor Reverse Thrust Aerodynamics," Cranfield University, 2011.

[6] NoiseNews, "Tonal Noise Analysis with Optimus Green Sound Level Meters," 2017.

[7] S. Glegg and W. Devenport, Aeroacoustics of Low Mach Number Flows, Vols. Chapter 16 - Open rotor noise, 2017, pp. 399-436.

[8] KAIST Aeroacoustics Lab, "Flow and Acoustics of Turbo Jet and Rocket," [Online]. Available: https://sites.google.com/site/aeac1234/applications/hydraulic-power.

[9] FAA, General Electric, "Open Rotor Engine Aeroacoustic Technology Final Report," 2014.

[10] J.-S. Jang, S. Choi, H.-I. Kwon, D.-K. Im, D.-J. Lee and J.-H. Kwon, "A Preliminary Study of Open Rotor Desing Using a Harmonic Balance Method," in *50th AIAA Aerospace Sciences Meeting Including the Horizons Forum and Aerospace Exposition*, 2012.

[11] H. Kwon, S. Choi, J.-H. Kwon and D. Lee, "Surrogate-Based Robust Optimization and Design to Unsteady Low-Noise Open Rotors," *Journal of Aircraft,* 2016.

[12] D. A. Smith, A. Filippone and N. Bodjo, "A Parametric Study of Open Rotor Noise," in *25th AIAA/CAES Aeroacoustics Conference*, 2019.

[13] S. Yi, H.-I. Kwon, D. Im, S. Choi, M. Park and D.-J. Lee, "Parameter Study of Low Noise CROR System," in *34th AIAA Applied Aerodynamics Conference*, 2016.

[14] H.-I. Kwon, S.-g. Yi, S. Choi, D.-J. Lee, J.-H. Kwon and D.-K. Im, "Design of a Low-Noise Open Rotor Using an Implicit Harmonic Balance Method," in *51st AIAA Aerospace Sciences Meeting*, 2013.

[15] R. Schnell, J. Yin, C. Voss and E. Nicke, "Assessment and Optimization of the Aerodynamic and Acoustic Characteristics of a Counter Rotating Open Rotor," in *ASME Turbo Expo*, 2010.

[16] B. A. Janardan and P. R. Gliebe, "Acoustic characteristics of counterrotating unducted fans from modelscale tests," *Journal of aircraft,* vol. 27, no. 3, 1990.

[17] P. A. Moshkov, V. Samokhin and A. Yakovlev, "Problem of the Community Noise Reduction for Aircraft with Open Rotor Engines," *Russian Aeronautics Vol. 61 No. 4,* pp. 647-650, 2018.

[18] B. Shivashankara, D. Johnson and R. Cuthbertson, "Installation Effection on Counter Rotation Propeller Noise," *AIAA,* 1990.

[19] J. Ricouard, E. Julliard and et al, "Installation effects on contra-rotating open rotor noise," *16th AIAA/CEAS aeroacoustics conference,* 2010.

[20] A. Stuermer and Y. Jianping, "Aerodynamic and aeroacoustic installation effects for pusher-configuration CROR propulsion systems," *28th AIAA Applied Aerodynamics Conference,* 2010.

[21] T. Sinnige and L. L. M. Veldhuis, "Pylon Trailing Edge Blowing Effects on the Performance and Noise Production of a Pusher Propeller," 2014.

[22] R. W. Harris and R. Cuthbertson, "UDF/727 Flight Test Program," in *AIAA/SAE/ASME/ASEE 23rd Joint Propulsion Conference*, San Diego, CA, 1987.

[23] H. Nichols, "UDF engine/MD80 flight test program," in *AIAA/SAE/ASME/ASEE 24th Joint Propulsion Conference*, Boston, Mass., 1988.

[24] J. Dansie, "What should my tail look like?," HMFC, 2018. [Online]. Available: http://www.hmfc.com.au/index.php/ground-school/what-should-my-tail-look-like. [Accessed 07 2021].

[25] J. Kennedy, P. Eret and G. Bennett, "A parametric study of airframe effects on the noise emission from installed contra-rotating open rotors," *International Journal of Aeroacoustics,* 2018.

[26] L. Sanders, D. C. Mincu, P. L. Vitagliano, M. Minervino, J. Kennedy and G. Bennett, "Prediction of the acoustic shielding by aircraft empennage for contra-rotating open rotors," *International Journal of Aeroacoustics,* pp. 626-648, 2017.

[27] J. Kennedy, P. Eret and G. Bennett, "A parametric study of installed counter rotating open rotors," in *19th AIAA/CEAS Aeroacoustics Conference*, Berlin, Germany, 2013.

[28] L. Dürrwächter, M. Keßler and E. Krämer, "Numerical Assessment of Open-Rotor Noise Shielding with a Coupled Approach," *AIAA Journal,* pp. 57(5), 1930-1940, 2019.

[29] M. Czech and R. H. Thomas, "Open Rotor Installed Aeroacoustic Testing with Conventional and Unconventional Airframes," in *19th AIAA/CEAS Aeroacoustics Conference*, Berlin, Germany, 2013.

[30] D. B. Stephens and E. Envia, "Acoustic Shielding for a Model Scale Counter-rotation Open Rotor," in *17th AIAA/CEAS Aeroacoustics Conference*, 2011.

[31] J. Berton, "Empennage Noise Shielding Benefits for an Open Rotor Transport," in *17th AIAA/CEAS Aeroacoustics Conference (32nd AIAA Aeroacoustics Conference)*, Portland, Oregon, 2011.

[32] S. Yi, H.-I. Kwon, D. Im, S. Choi, M. Park and D.-J. Lee, "Parameter Study of Low Noise CROR System," in *AIAA Aviation Forum - 34th AIAA Applied Aerodynamics Conference*, 2016.

[33] A. R. Stuart, "The Unducted Fan Engine," in *AIAA-85-1190*, 1985.

[34] E. S. Hendricks and M. T. Tong, "Performance and Weight Estimates for an Advanced Open Rotor Engine," in *AIAA-2012-3911*, 2012.

[35] E. Kravitz, "Analysis and Experimetns for Contra-Rotating Propeller," MIT, 2011.

Project 077 Measurements to Support Noise Certification for UAS/UAM Vehicles and Identify Noise Reduction Opportunities

The Pennsylvania State University

Project Lead Investigator

Eric Greenwood
Assistant Professor of Aerospace Engineering
Department of Aerospace Engineering
The Pennsylvania State University
229 Hammond Building
University Park, PA
(814) 863-9712
eric.greenwood@psu.edu

University Participants

The Pennsylvania State University

- PI: Eric Greenwood, Assistant Professor of Aerospace Engineering
- FAA Award Number: 13-C-AJFE-PSU-067
- Period of Performance: August 11, 2020 to August 10, 2021
- Task(s):
    1. Review of Regulations, Standards, Literature, and Ongoing Research
    2. Computational Modeling of UAS and UAM Configurations
    3. Development of a Source Separation Process for Distributed Propulsion Vehicles
    4. Design and Development of a Reconfigurable Multirotor UAS Vehicle
    5. Microphone Type and Installation Investigation
    6. Baseline UAS Noise Measurement
    7. UAM Component Noise Measurement
    8. UAM Full-vehicle Noise Measurement

Project Funding Level

$500,000 awarded by FAA. $500,000 in-kind matching from Beta Technologies for labor and flight test support.

Investigation Team

- Eric Greenwood, PI, The Pennsylvania State University; acoustic measurement and analysis lead.
- Kenneth S. Brentner, Co-PI, The Pennsylvania State University; acoustic prediction lead.
- Eric N. Johnson, Co-PI, The Pennsylvania State University; UAS design and operations lead.
- Joel Rachaprolu, Graduate Research Assistant, The Pennsylvania State University; primarily responsible for developing noise source separation techniques for distributed propulsion vehicles.
- N. Blaise Konzel, Graduate Research Assistant, The Pennsylvania State University; primarily responsible for developing acoustic and atmospheric instrumentation for UAS and UAM flight testing.
- Keon Wong Hur, Graduate Research Assistant, The Pennsylvania State University; primarily responsible for developing UAS predictions to inform the development of experimental methods.
- Vítor T. Valente, Graduate Research Assistant, The Pennsylvania State University; primarily responsible for developing the reconfigurable multirotor UAS vehicle.

Project Overview

The Pennsylvania State University will support the FAA in developing noise measurement and analysis methods that will accurately characterize the external noise radiation of a variety of Unmanned Aircraft System (UAS) and Urban Air Mobility (UAM) vehicles. Noise measurements will be collected for a wide range of UAS and UAM configurations across different operating modes, flight speeds, and altitudes. A reconfigurable multirotor UAS will be developed and tested to assess the effects of rotor number, blade design, and position on radiated noise and the measurement and analysis process. The data analysis process developed through this project will allow the contributions of the individual rotor or propeller noise sources to be separated and modeled independently, thus allowing variability in noise generation to be correlated to variability in the vehicle flight state.

Noise measurement techniques for conventional propeller-driven aircraft and rotorcraft are well established. These techniques typically assume that the acoustic state of a vehicle does not change during a steady-state pass over a microphone or microphone array. However, UAS and UAM platforms violate this steadiness assumption because the rotor or propeller states, such as RPM or blade pitch angle, vary continuously and independently as the vehicle control system responds to atmospheric perturbations. Many UAS and UAM vehicles employ distributed propulsion systems, where the rotors or propellers are not locked in phase. When multiple rotors or propellers operate at similar blade passing frequencies, coherent addition of the tonal noise will result in lobes of acoustic radiation that are tightly focused in certain directions. Because the phase relationships between the rotors change over time, the directionality of these lobes will vary. Consequently, the noise cannot be modeled as a single stationary source, and no two flight passes will result in the same noise radiation pattern on the ground. Moreover, because there are numerous possible combinations of control inputs that result in the same flight condition, the flight condition of the vehicle cannot be uniquely mapped to a corresponding acoustic state. This project aims to develop noise measurement techniques and data analysis methods that can reduce this variability, thereby allowing repeatable characterization of UAS and UAM noise.

Task 1 – Review of Regulations, Standards, Literature, and Ongoing Research

The Pennsylvania State University

Objective(s)

In this task, a comprehensive review was conducted of past and ongoing activities closely related to this project, with the goal of developing noise measurement methods to inform noise certification and noise reduction of UAS and UAM. This included a review of existing and proposed noise certification standards for aircraft and rotorcraft, as well as existing industrial standards and published research regarding the measurement of aircraft noise. The applicability of these approaches to UAS and UAM noise measurement was assessed and the major limitations identified.

Research Approach

Over 150 different publications were reviewed during the previous reporting period. The main findings were documented in the previous annual report, in addition to a presentation given to the FAA and project advisory panel.

Milestone(s)

This task was completed, following a) a comprehensive review of the literature and b) the reporting of the key findings to the FAA and advisory panel. Findings from this review have been used to support other related efforts, including the NASA UAM Noise Working Group.

Major Accomplishments

There are no additional accomplishments to report in the current reporting period.

Publications

None

Outreach Efforts

None

Awards
None

Student Involvement
All graduate students were actively involved in the literature review process, focusing on literature relevant to their primary research tasks.

Plans for Next Period
Literature review activities will continue throughout the project. The team will also work to identify relevant ongoing research that may not have been published yet to identify opportunities for coordination and collaboration.

Task 2 – Computational Modeling of UAS and UAM Configurations
The Pennsylvania State University

Objective(s)
The goal of this task is to develop several computational models of UAS and UAM aircraft with varied configurations, thus providing a simulated environment in which various noise measurement configurations and data processing methods can be rapidly investigated ahead of acoustic flight testing. The flight conditions and appropriate microphone arrangements for characterizing the directivity of the vehicle will be evaluated. Additionally, data will be generated to validate the efficacy of the rotor source separation process that is also being developed under this project.

Research Approach
This task will leverage the UAM noise prediction system being developed by Penn State under ASCENT Project 49, with an emphasis on using the combined system of PSU-WOPOP and DEPSim to model the acoustic "beating" phenomena caused by the time-varying RPM of multi-rotor UAS and UAM systems. The computational models will be used to identify requirements for the microphone measurement arrays, which are designed to capture variations in noise due to variations in flight condition and source directivity. Acoustic simulations will also provide details that are not available in the flight test measurements to help diagnose and analyze the noise from complicated UAS and UAM vehicles.

Milestone(s)
The milestones for this task consist of a) developing UAS and UAM models representative of the vehicles for which noise measurements will be collected during this project, b) conducting simulated experiments, and c) identifying best practices for UAS and UAM noise measurements by reviewing the simulated data.

Major Accomplishments
The UAM noise prediction system being developed under ASCENT Project 49 was not complete at the beginning of this reporting period. This noise prediction system couples the PSU-WOPWOP aeroacoustic prediction code with the PSU-DEPsim flight mechanics model and Continuum Dynamics Incorporated's CHARM free wake aerodynamics model. While the DEPSim-CHARM coupling was being updated under ASCENT Project 49, an initial model of a multirotor UAS was developed using Penn State's VSP2WOPWOP tool. This tool allows users to model a UAS rotor system using NASA's OpenVSP software, applies a blade element method to predict the airloads, and generates input files for PSU-WOPWOP to predict the resulting acoustics. Figure 1 shows an OpenVSP wireframe model of one of the rotor blades on the Tarot X8 UAS studied in this project. Grid resolution studies were conducted to identify the number of points in space and time required to accurately resolve the acoustic pressure time history and spectral quantities for UAS vehicles.

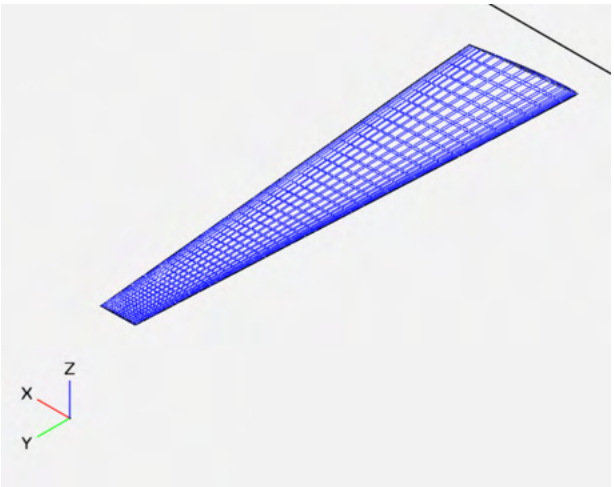

Figure 1. OpenVSP blade model for the Tarot X8.

Following the grid resolution study, several different investigations were conducted using this modeling approach. These included investigations on (i) the effects of acoustic interference between rotors of a multirotor system, (ii) the far-field distance for multirotor UAS, and (iii) initial simulated flyover noise predictions for UAS.

Acoustic Interference

The tonal noise components for multirotor vehicles add constructively when they are in phase and destructively when they are 180° out of phase. When the rotors are not locked in phase—e.g., when using cross shafting—the phase relationships between the rotors change over time, causing the noise radiated in a given observer direction to fluctuate. This condition (i.e., multiple rotors operating at constant but slightly different RPM) is often referred to as "beating." During this reporting period, beating was extensively studied for a variety of different multirotor configurations and RPM variations. For example, Figure 2 shows the predicted acoustic pressure time history for the Tarot X8 octocopter in forward flight when each of the eight rotors has an RPM that varies sinusoidally over time at a different rate. Modulation can clearly be seen in the envelope of the acoustic pressure. This modulation occurs at different scales, corresponding to the differences in the rotation rates of individual rotor pairs. When multiple rotors operate at almost the same RPM, the "beating" period can be quite long, on the order of several seconds.

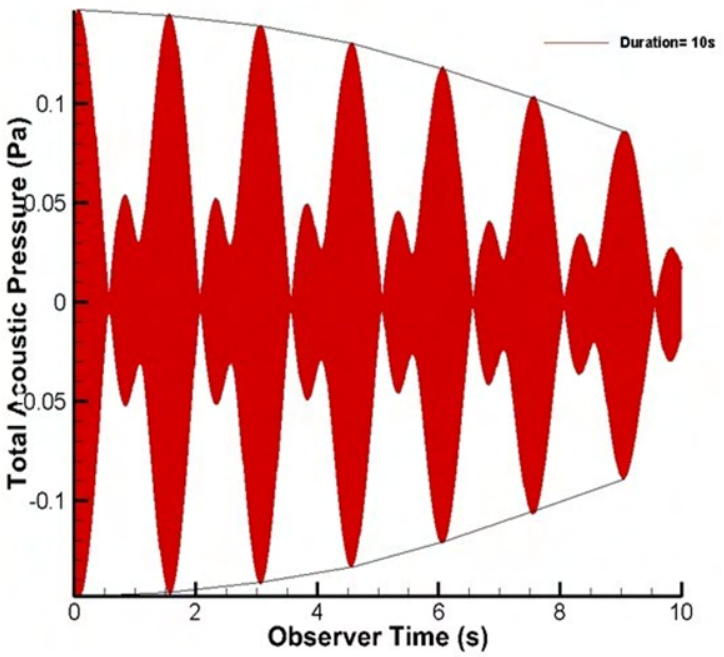

Figure 2. Predicted "beating" pressure time history for Tarot X8 octocopter.

Acoustic Far-field

The acoustic far-field is the region where the noise source can be considered "compact" and the noise decays from the source following spherical spreading. For helicopter rotors, the far-field is generally considered to begin between 5 and 10 diameters from the rotor hub. However, a similar "rule of thumb" has not been established for small UAS. The UAS noise prediction model developed under this project was employed to investigate where the acoustic far-field may be for typical multirotor UAS.

For this study, the number of rotors, distance between rotors, rotation rates and thrust were varied. As an example, Figure 3 plots the predicted decrease in noise levels with increasing distance from the rotor hub for single and octocopter configurations at various RPM. In addition to the predicted noise level, a dashed line shows the expected decrease in levels following the spherical spreading, or $1/r$, relation. Circled on each plot is the point where the predicted noise levels diverge from the spherical spreading by more than 1 dB is circled on each plot. This was used to define the far-field distance.

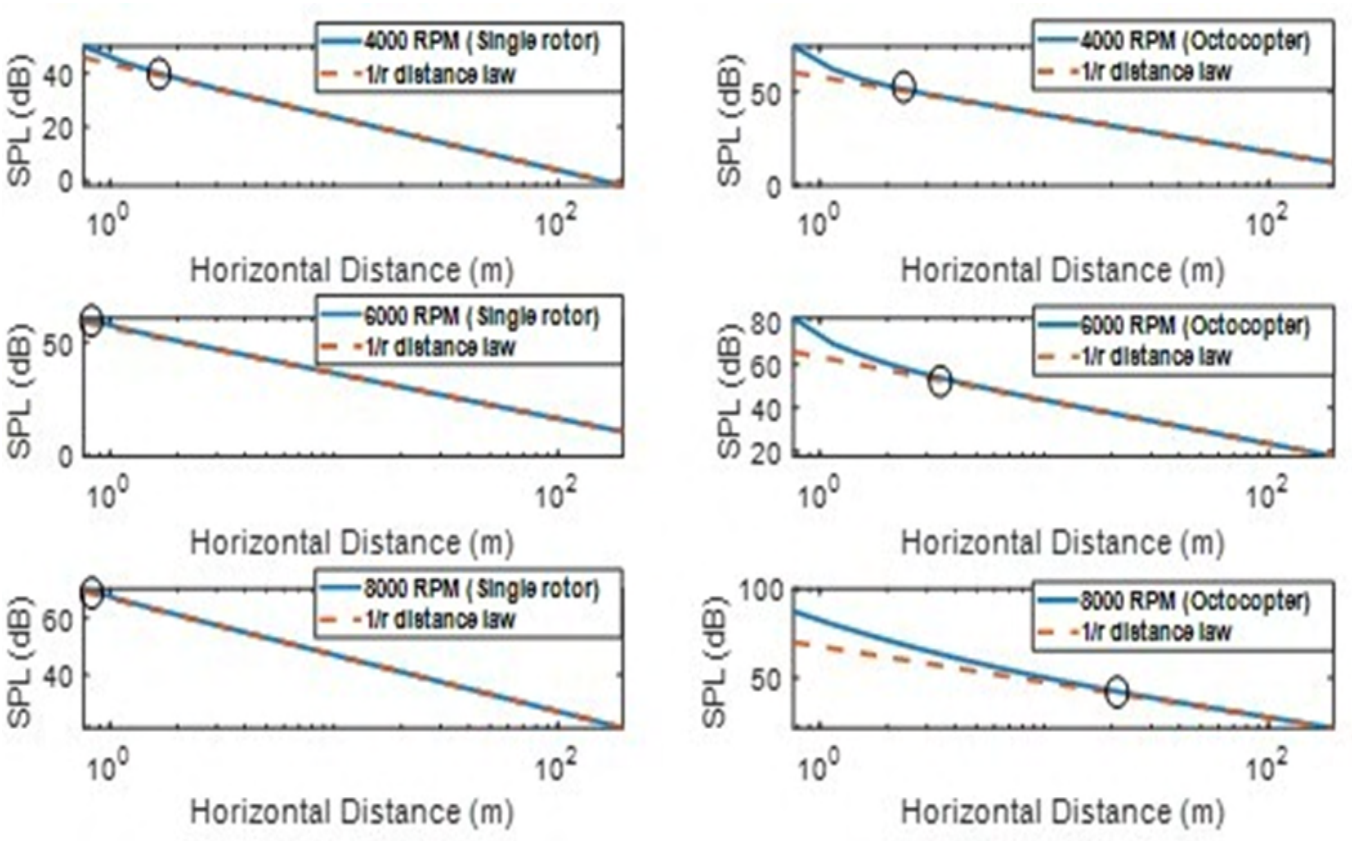

Figure 3. Variation in noise level with distance for single-rotor and octocopter configurations at various RPM.

Different trends are identified for isolated single rotors versus multirotor systems. Specifically, for the single rotor, far-field extends with decreasing rotation rates. This is consistent with prior experimental and numerical studies of low tip Mach number rotors. In contrast, the opposite trend is observed for multirotor system, where the far-field distance extends with increasing rotation rates. These results were insensitive to changes in rotor thrust and are therefore likely caused by convective amplification of the source terms. Further investigation is required to understand the physical mechanisms that causes these differences.

One consequence of this trend is that, for example, the far-field distance of an octocopter operating at 8000 RPM was 56 rotor diameters away from the center of the vehicle. This implies that even outdoor free-flight noise measurements of multirotor UAS could include data measured in the near-field, which may affect the scalability of these noise measurements to other scenarios.

Following these results for a single observer, the decay in noise levels with distance is being studied for a range of observer angles. Figure 4 is a polar plot showing the variation in noise levels with distance at different azimuths about an octocopter with each rotor operating at a constant RPM. This results in an interference pattern being produced at all distances. The magnitude of destructive interference is more pronounced at the closer distances than at the farther distances, thereby extending the apparent far-field distance in these directions.

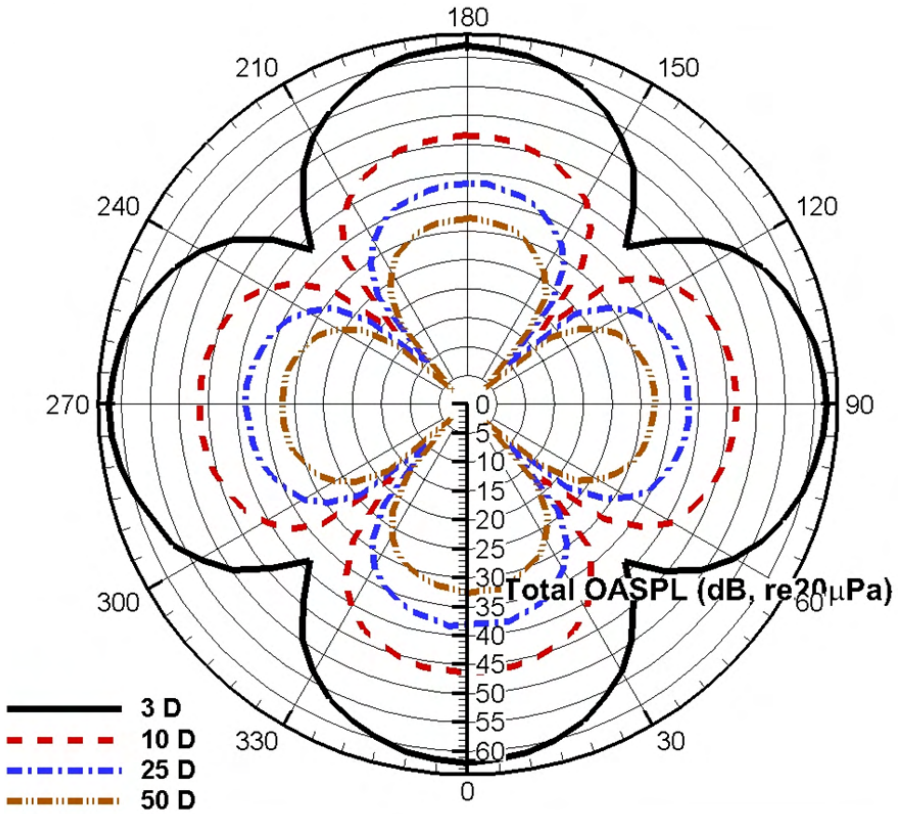

Figure 4. Polar plot of noise directivity around the azimuth of an octocopter with constant RPM rotors at several distances from the center of the vehicle, given in multiples of the diameter of a single rotor (D = 0.381 m).

Simulated UAS Flyover

Several simulated UAS flyover cases were developed, including for the Tarot X8 octocopter with time-varying rotor RPM. Noise predictions were run to support the development and validation of the noise source separation technique described in Task 3. Figure 5 shows the frequency spectrum for a ground-based observer for the Tarot X8 with varying RPM. Spectra are plotted for each of the individual rotors, as well as for the combined total for all rotors. The figure on the left shows the predicted tonal noise components across a frequency range from zero to 1,000 Hz, and the figure on the right shows the same data along a narrower frequency range covering only the first harmonic of the blade-passing frequency for each rotor. Because each rotor operates at a unique rotational rate, distinct tones are present for each blade passing frequency and each of its harmonics.

At lower frequencies, the rotor tones associated with each harmonic cluster together. However, after the first four harmonics, these clusters begin to overlap, and the tones are more evenly distributed over the higher frequency range. The tones predicted by PSU-WOPWOP for each isolated rotor exactly overlay their corresponding tones in the prediction for the entire vehicle, confirming that the noise of the rotors adds as expected from linear acoustic theory. Although "beating" can still be observed in the envelope of the pressure time history signals (see Figure 2), this does not result in the formation of additional tones in the narrowband frequency spectrum. However, if the window size is reduced such that the bandwidth of the Fast Fourier Transform is less than the beat frequency, those tones cannot be distinguished from each other in the resulting frequency spectrum.

The predicted data generated in this study were also applied to validate the noise source separation method, as described in the following task.

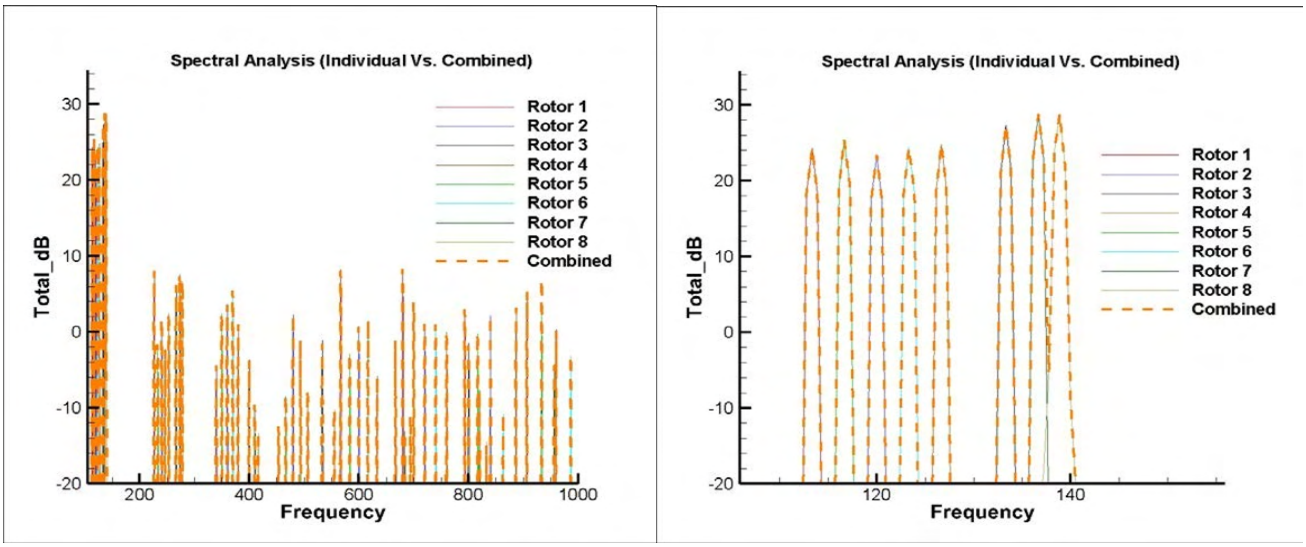

Figure 5. Frequency spectrum for individual rotors and combined vehicle noise for the Tarot X8.

Publications
None

Outreach Efforts
None

Awards
None

Student Involvement
MS student Keon Wong Hur is primarily responsible for the development of UAS noise predictions. These noise predictions were then used to support the noise source separation method developed by MS student Joel Rachaprolu.

Plans for Next Period
The UAS noise prediction will be extended to more realistic and representative flight conditions. The noise prediction system developed under ASCENT Project 49 will be used to include the detailed flight dynamics and aerodynamics of UAS and UAM vehicles. Broadband noise modeling will be incorporated. The variation in noise with directionality and over time will be investigated. These results will be compared to measured flight test data and used to inform the development of future flight test plans.

Task 3 – Development of a Source Separation Process for Distributed Propulsion Vehicles
The Pennsylvania State University

Objective(s)
The objective of this task is to develop a process for separating the noise generated by rotors or propellers operating at non-constant, but potentially similar, RPM. This process will be based on flyover measurements of UAS and UAM vehicles.

Research Approach
The source separation process developed in this task consists of two steps. First, a de-Dopplerization procedure is used to transform the ground-based microphone signals to a reference frame moving with the vehicle, thus eliminating the Doppler

shift. The second step of the process consists of a Vold-Kalman order-tracking filter which separates the noise components of individual rotors from the de-Dopplerized signal using the rotor RPM information.

Each step of the source separation process was verified on both computational and experimental/flight test data to understand their performance. For the de-Dopplerization step, we used Joint NASA/Bell/Army flight test data to verify the accuracy of the transformed signals. Spectral results were used to verify that the Doppler shift was removed from the transformed signals and that the de-Dopplerized results were de-propagated to a reference sphere around the vehicle at a constant radius. For the Vold-Kalman order tracking filer step, a preliminary sinusoidal synthetic signal was used to verify the basic extraction, and the computational results of various multi rotor configurations were used to extract and verify the extracted noise and predicted noise for individual rotor components. Once both the de-Dopplerization and order tracking filter procedures were verified, a combination of two steps will be used to analyze flight test data.

Milestone(s)

The milestones for this task consist of a) developing a source separation process for stationary acoustic measurements; b) implementing a de-Dopplerization approach to covert non-stationary measurements to a stationary frame; and c) applying the source separation process to simulated and measured data to evaluate the effectiveness of the separation.

Major Accomplishments

A source separation process was developed with a capability to extract close harmonics and impulsive events. The two steps of the process (de-Dopplerization and order tracking) were verified, and the source separation process was applied to flight test data.

Multi-shaft Vold-Kalman Order Tracking Filter and Performance

A third-generation multi-shaft Vold Kalman order tracking filter was implemented and tuned to extract the harmonic noise of individual rotors. Computational data from the simulations described in Task 2 were used to verify the order tracking filter. Figure 6 shows the results of this source separation procedure when applied to a simulated case with two rotors that are stationary relative to the observer. The residual signal shown in the time series plot (left-hand side of Figure 6) is small relative to the original signal, indicating a clean extraction throughout most of the time range. Some edge effects led to incomplete extraction of some harmonics in the first and last 5% of the analysis time window, but these edge effects do not result in a significant difference in the power spectral density of the extracted signal, as seen in right-hand panel of Figure 6. The accuracy of the separation was verified by comparing the results to the predicted signals for each individual rotor.

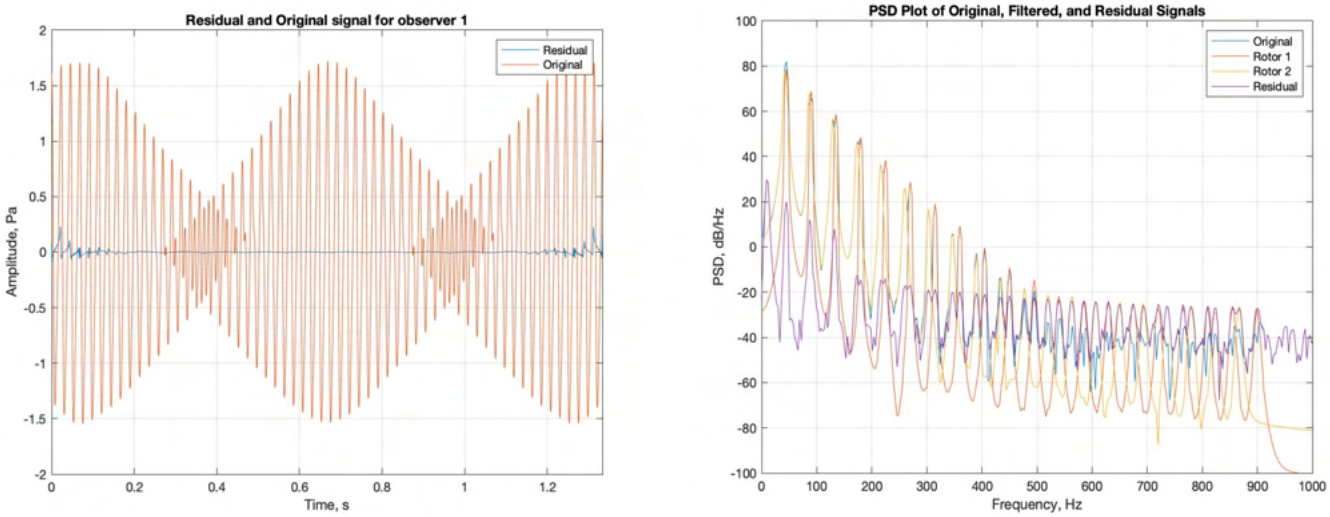

Figure 6. Time domain (left) and spectral (right) results of the source separation process.

De-Dopplerization

A time-domain de-Dopplerization process was developed to transform ground-based acoustic measurements to a stationary equivalent, to which the order tracking filter can then be applied. Figure 7 shows spectrograms for a flyover of the Bell 430 helicopter. By examining the shift in the tonal components over time, the Doppler shift is clearly evident in the measured signal in the left panel of Figure 7. After the de-Dopplerization process was applied, the Doppler shift was removed, as shown in the spectrogram in the right panel.

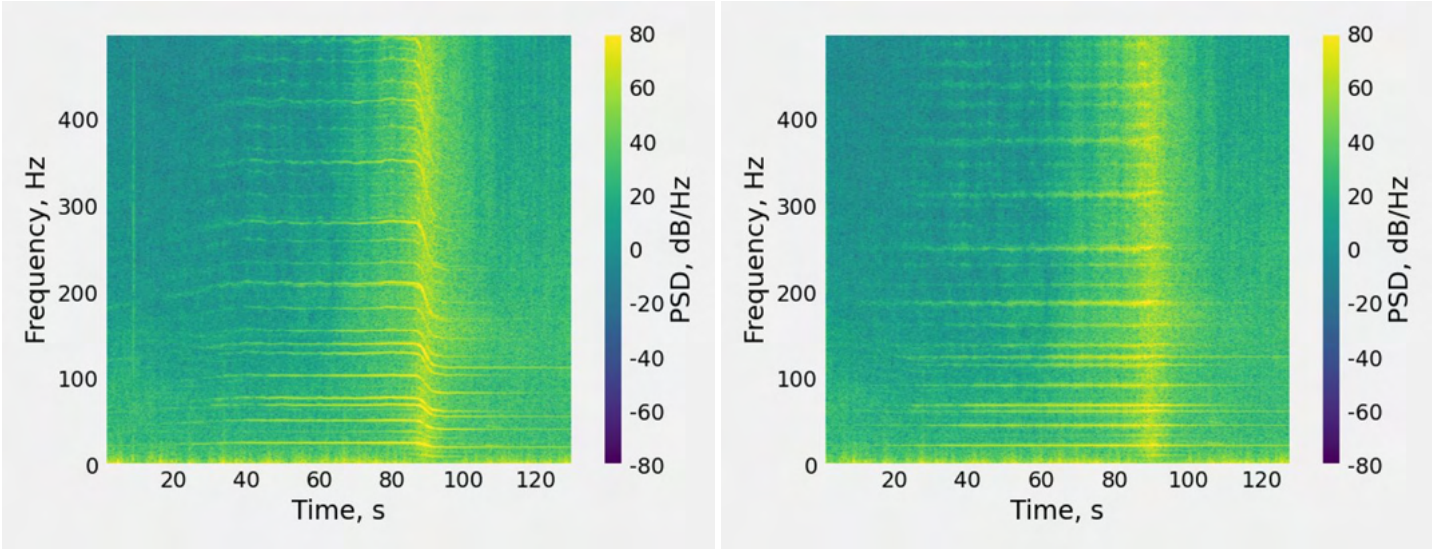

Figure 7. Spectrograms of the original signal (left) and de-Dopplerized signal (right).

The de-Dopplerization process was verified for its correctness and its effect on the signal being investigated. One disadvantage of this process is that the high-frequency components of the signal are increasingly distorted as the propagation time delay approaches an integer multiple of the sampling rate. Although oversampling the data resolves this issue, alternative de-Dopplerization approaches are being investigated.

Source Separation Process

Our two-step source separation process combines the previously verified de-Dopplerization and the order tracking filter. This process was then applied to measured flight test data for the Bell 430 helicopter in several flight conditions. Figure 8 shows plots produced by applying our source separation process to a descending flight where the helicopter is approaching the microphone array from 1500 feet at an elevation angle of 10 degrees. The extracted pressure time-histories of the main (top) and tail (bottom) rotors are presented along with the original and residual signals in the leftmost plots. The residual signal is obtained by subtracting the time-domain extracted signals from the original acoustic signal. BVI noise produced during the maneuver was extracted while preserving the amplitude and phase relationship of the noise. The right-hand side of Figure 8 presents the same data in the frequency domain. The tones are captured accurately for the extracted main and tail rotors and match the frequencies of the tones in the original signal.

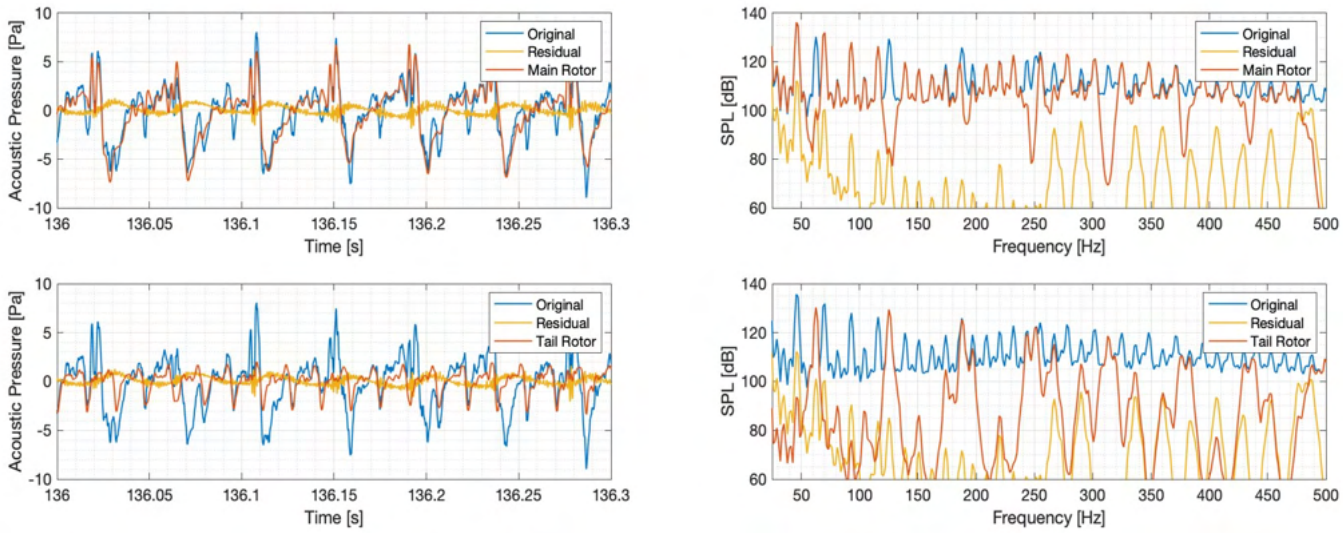

Figure 8. Acoustic pressure time-history (left) and spectra (right) of original, main rotor, tail rotor, and residual signals.

Publications

An abstract entitled 'Helicopter Noise Source Separation using an Order Tracking Filter' was submitted the Vertical Flight Society Forum 78 being held in May 2022.

Outreach Efforts

None

Awards

None

Student Involvement

MS Student Joel Rachaprolu developed and preliminarily tested the source separation process on computational data. He is extending the application of the process to helicopter flight test data and some baseline UAS measurement data.

Plans for Next Period

The process will be extended to combine measurements from multiple microphones, allowing the directivity of the individual sources to be analyzed separately. This process will first be applied to the Bell 430 helicopter flight test data for validation. Once validated, the process will be applied to measured UAS data that was collected for this project at Mid-State Regional Airport. Initially, the process will be applied to data collected from the reconfigurable UAS developed under Task 4, because this UAS will be instrumented to allow the rotor phase angles to be measured directly. If the source separation process can be applied effectively to a multirotor UAS with direct measurement of rotor phase and/or RPM, methods will be investigated to infer the rotor RPM variations from vehicle flight state data and acoustic measurements.

Task 4 – Design and Development of a Reconfigurable Multirotor UAS Vehicle

The Pennsylvania State University

Objective(s)

The objective of this task is to design and develop a multirotor UAS vehicle that can easily be reconfigured to explore the acoustic effects of different UAS vehicle configurations, as well as the effect of these configurations on the noise measurement and data processing approaches developed in this project.

Research Approach

A UAS vehicle will be designed with adjustable rotor support arms, allowing the relative positions of the rotors to be easily reconfigured. The rotor shafts will be designed to allow rotors with different designs (e.g., different blade spacings) to be mounted to the vehicle. The rotor shafts will be instrumented with encoders allowing for precise determination of the rotor RPM and shaft phase angle at a high sampling rate. The vehicle will also be instrumented with a real-time kinematic differential GPS and an inertial measurement unit to provide a time-accurate position and state estimate, which can then be correlated to the acoustic measurements.

Due to the reconfigurable nature of the vehicle, special consideration will be given to developing a control system capable of achieving stabilized flight across the range of possible configurations. Ground and flight testing of the vehicle will be conducted to ensure the vehicle systems and instrumentation are functioning nominally and to expand the vehicle operating envelope to cover the flight conditions for which noise measurements will be made.

Milestone(s)

The milestones for this task consist of a) identifying acoustically significant configuration changes to be made on the vehicle, b) developing an initial design for the vehicle and selecting sensors, c) designing the control system, and d) conducting ground and flight testing.

Major Accomplishments

Two reconfigurable multirotor UAS vehicles were designed and are currently being built and their components are being tested. Motors were selected with integrated speed controllers that will allow the rotor phase angle to be measured directly. This information will be used as an input to the previously described source separation process. In addition, the enhanced measurement and control capabilities of these motors will be investigated to determine whether the flight control system of the vehicle can be designed to reduce noise during operations.

Small-size UAS

The small-size UAS consists of a frame that allows dimensions up to 450mm from tip to tip. The frame, as shown in Figure 9, is designed so that it can handle three main configurations: hexacopter, quadcopter, and tricopter. The frame is made using custom carbon fiber plates and carbon fiber rods.

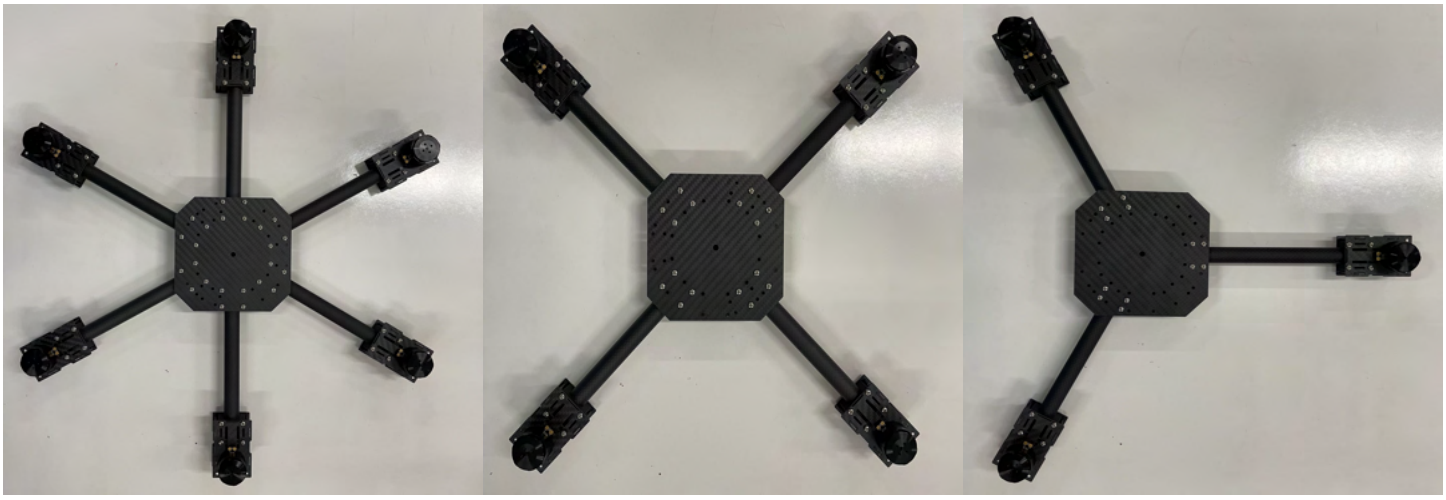

Figure 9. Three possible configurations for the arms of the small-size UAS.

The motor mount (Figure 10) can also be adapted in three different configurations: a fixed (single) motor mount, a tiltable motor mount capable of tilting the motor in flight to add an extra control degree of freedom, and a coaxial configuration of the fixed motor mount. The coaxial configuration is able to provide many different configurations and facilitate easy changes between them. The maximum propeller size on this setup is 6" for the hexacopter configuration.

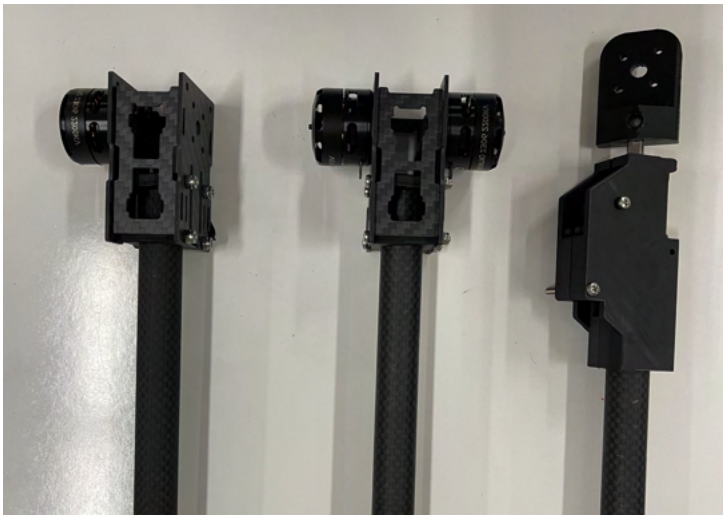

Figure 10. Three configurations for the motor mount: single, coaxial, and tiltable.

The small UAS will also be helpful for initial flight testing and control algorithm development because small vehicles are easier to handle and require a smaller area to perform any flight testing. Once developed, the flight control system should scale to the larger vehicle without modification.

Large-size UAS

The large-size UAS consists of a frame that allows dimensions up to around 1200mm from tip to tip. This size is more suitable for package delivery but more difficult to develop. This setup is being built as parts are arriving and initial assembling tests are being performed. This setup will also allow for the same three configurations as the small UAS frame: hexacopter,

quadcopter and tricopter. The frame will be built using custom carbon fiber plates, custom-machined aluminum parts, and squared rod arms. The motors will be placed on a tiltable motor mount setup to also allow an extra control degree of freedom. Ultimately, the design is focusing on a multirotor vehicle that can operate up to 55lbs (per Part 107). The maximum propeller size for this setup is 26" for the hexacopter configuration.

We are also designing a quick-release system for the large-size UAS to allow rapid changes between configurations. The quick-release system will be tested to evaluate its feasibility on a larger vehicle. In addition to developing a quick, mechanical plug-and-release system, we will also develop electronics and software to support rapid configuration changes.

Actuator selection
One important step in the development of the UAS vehicles is selecting the actuator (brushless motor). For the small a 2306-2200kV motor was selected. The large version will feature an 8108-150kV motor. Both motors have integrated ESC with an embedded position sensor and a serial interface. The integrated ESC allows the control algorithm to have access to several pieces of information on the motor and to change some of these configurations while in flight. This motor also has open- and closed-loop controllers designed primarily to drive propeller loads and to decouple flight controller gains from motor choice, propeller choice, and battery level (IQ2306 Speed Module 1 Features, n.d.).

Avionics selection
Both vehicles will have an onboard flight controller along with a companion computer. The flight controller has a large variety of internal sensors and systems, including IMU and barometer, and it has interfaces to connect to external sensors like the GPS and telemetry system. The companion computer will also allow the connection of an external portable weather measurement station, which can provide additional information not directly available on the flight controller or onboard sensors, like wind speed and direction. The external weather measurement station will therefore allow for direct measurements of airspeed (as well as inertial speed) during flight.

Publications
None

Outreach Efforts
None

Awards
None

Student Involvement
PhD student Vítor T. Valente joined the investigation team in Fall 2021. Since then, he has designed two reconfigurable multirotor UAS vehicles of different sizes. One version has been built, and the other is in the process of being completed. Valente has also begun investigating and modeling the control system design.

Plans for Next Period
Plans for the following period include the acoustic characterization of the small reconfigurable multirotor UAS. To complete this stage, different configurations will be tested using different propellers. It is expected that these tests will help direct the choice of propellers and configurations to be evaluated using the larger UAS. In parallel, the control algorithms for both UAS will be developed and refined. Further investigation will look at using the tilting rotor capability, in addition to the changes to the design of the frame (adding wings, for example), to mimic UAM operations.

References
IQ2306 Speed Module 1 Features. (n.d.). Retrieved 15 November, 2021, from https://www.iq-control.com

Task 5 – Microphone Windscreen Analysis

The Pennsylvania State University

Objective(s)

The objective of this task is to conduct an acoustic analysis on different microphone windscreen designs to determine their individual effectiveness at reducing wind turbulence-related noise.

Research Approach

The functional purpose of microphone windscreens is to minimize the effect of wind turbulence noise on acoustic measurements ("self-noise"). Several windscreen designs were developed and evaluated in the Penn State anechoic wind tunnel to investigate their effectiveness at reducing self-noise and any losses in the measured signal.

Milestone(s)

The milestones for this task consist of testing different windscreen designs and selecting one for use in the measurement microphone array.

Major Accomplishments

We considered several designs, shown in Figure 11. The first is a minimal nylon mesh windscreen that encloses the microphone and all three tripod legs. The second is a standard open-cell foam hemisphere that is fitted snuggly against the microphone diaphragm. The third is a cylinder, a similar open-cell foam to the standard windscreen. All three designs were tested in an anechoically treated wind tunnel, and their acoustic performance (i.e., frequency response and resolution of a spinning rotor) was compared against a windscreen-free installation for the same events. The test included varying wind speeds and rotor RPM for all windscreen installations.

Figure 11. Nylon mesh, foam hemisphere, and foam cylinder windscreen designs.

Both open-cell foam designs showed similar performance at reducing microphone self-noise. The nylon mesh was less effective than the foam designs, but still reduced noise significantly compared to a microphone without any windscreen (as specified in SAE ARP 4055). The cylindrical windscreen encloses the entire microphone and preamplifier and may have some benefit in protecting the microphone from adverse weather (e.g., rain); however, it is also more difficult to deploy than the hemispherical windscreen. Transmission losses were minimal below 10 kHz for all windscreen designs. The hemispherical windscreen was selected as the primary windscreen for inverted ground board installations used in this project.

Publications

None

Outreach Efforts

None

Awards
None

Student Involvement
MS student N. Blaise Konzel designed the different windscreens, conducted the experiment in the anechoic wind tunnel, and analyzed the results.

Plans for Next Period
This task has been completed.

Task 6 – Baseline UAS Noise Measurement
The Pennsylvania State University

Objective(s)
The objective of this task is to conduct an acoustic flight test campaign to collect noise measurements for a variety of UAS vehicles under a variety of operating conditions and configurations.

Research Approach
Acoustic measurements of flying UAS will be taken at the nearby Mid-State Regional Airport. These noise measurements will be made for a variety of UAS in Penn State's fleet, including several configurations of the reconfigurable multirotor UAS platform developed in Task 4. Penn State's outdoor UAS research vehicles typically have inertial state measurements, barometers, magnetometers, and either WAAS- or RTK-augmented GPS, which are fused to provide 100 Hz vehicle position and state estimates. Several aircraft also include air data sensors that estimate airspeed, angle of attack, and sideslip. The US Army Research Laboratory Vehicle Technology Directorate has also offered to make UAS available to Penn State for acoustic testing. Other opportunities for collaboration with US Government and industry UAS operators will be pursued to expand the variety of vehicles characterized.

Each vehicle will be flown through a range of operating conditions, including hover, forward flight at several speeds, and any transition modes of the vehicle. Testing will be conducted at several altitudes, from near ground level to 400 ft above ground level, to evaluate the ability to scale UAS noise measurements made at one flight altitude relative to another. This is particularly important given the relatively low noise levels of small UAS. Acoustic measurements will be made with Penn State's networked, battery-powered and field-deployable acoustic data acquisition system, which is capable of sampling at up to 125 kHz at 24-bit resolution with subsample-accurate GPS time synchronization across all nodes. The hardware will be configured to support at least 24 channels and can be expanded as required. The microphone array will be distributed so as to capture both spatial and temporal variations in the radiated noise. Weather instrumentation will be deployed to obtain ground level and 10 m measurements of wind speed, direction, temperature, pressure, and humidity.

Milestone(s)
The milestone for this task consists of collecting a baseline data set of UAS noise measurements, including acoustic, performance, and meteorological data.

Major Accomplishments
Microphone installations have been constructed and the layout of the 14-channel microphone array has been designed to capture spatial and temporal variations in the radiated noise. Elevated microphones are also included in the array, per FAR 36 Appendix H, to allow for comparison between different installations. The layout of the array is shown in Figure 12. Acoustic data were collected for several UAS, but the initial focus for the project was on characterizing the Tarot X8 octocopter, shown in Figure 13. Acoustic, weather and flight state data for over 60 individual test points have been collected for the Tarot X8 during the reporting period. These test points covered a wide variety of vehicle configurations and operating conditions and are listed in Table 1.

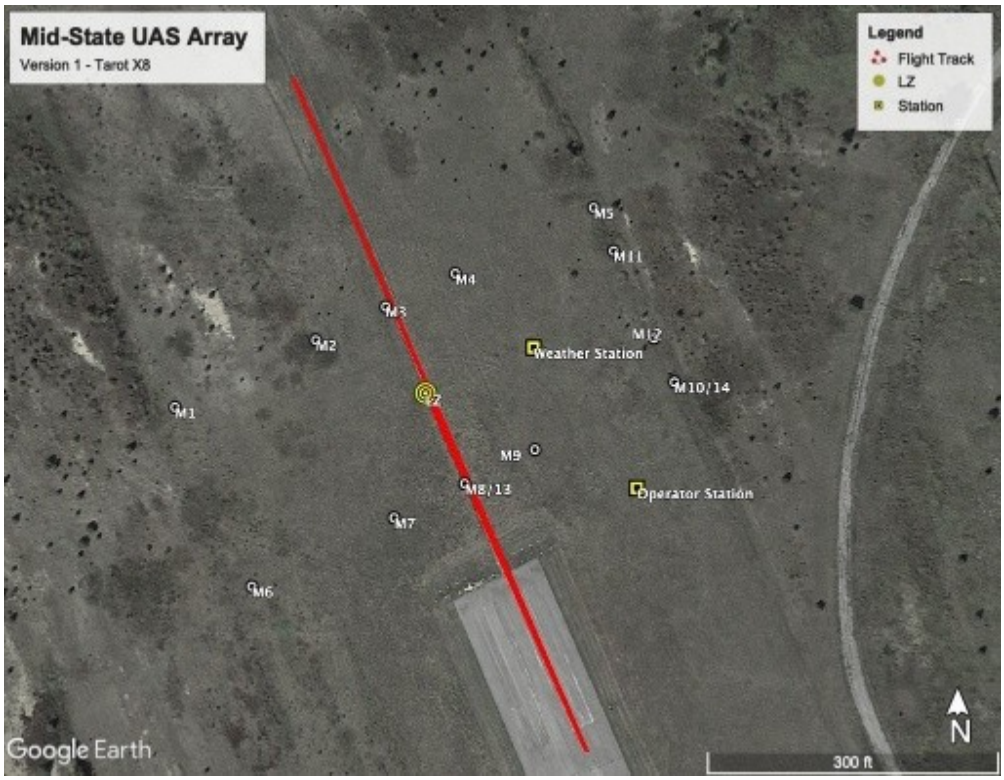

Figure 12. UAS acoustic array at Mid-State Regional Airport.

Figure 13. Tarot X8 octocopter.

Table 1. Test matrix for the Tarot X8 octocopter.

Condition	Code	Altitude	Code	Weight	Code	Variant	Code	Direction	Code	Propeller	Code
Takeoff	T	50ft	1	Minimum	1	Slow - 10mph	S	Nominal flight track heading	U	Carbon Fiber	CF
Landing	L	100ft	2	Maximum	2	Medium - 20mph	F	Opposing flight track heading	D	Plastic	P
Hover	H	200ft	3			Fast - 30mph	W				
Flyover	F					Left turn	L				
Maneuver	M					Right turn	R				

These data have been organized into a data set. Vehicle state data as well as local ambient weather data have been collected and correlated to each test point. Preliminary analysis of the acoustic data collected during these tests shows a direct dependency between vehicle configuration/condition and acoustic emissions. For example, Figure 14 shows a spectrogram of a flyover event. Broadband noise is clearly present; however, when the vehicle is directly overhead, the tonal content becomes dominant.

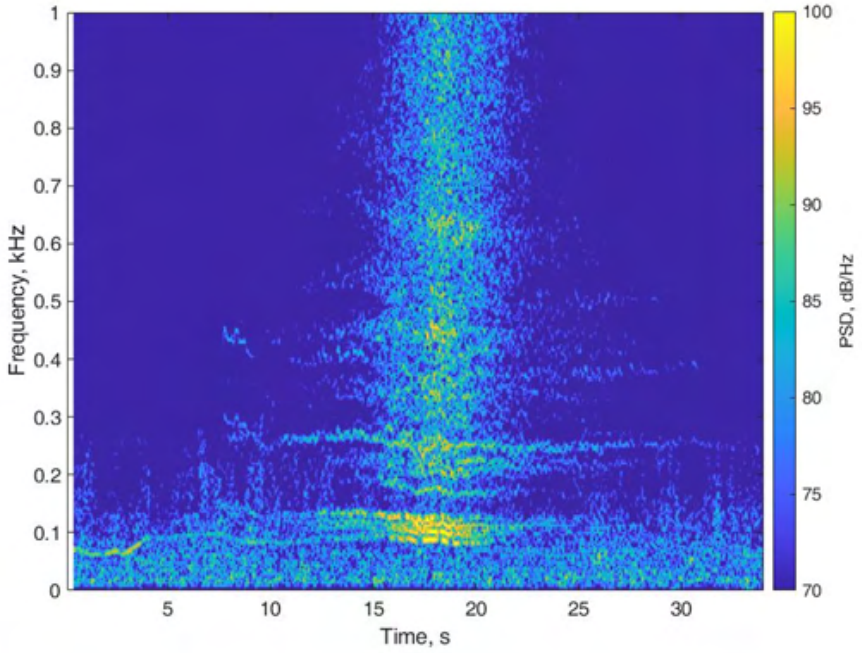

Figure 14. Spectrogram of a flyover flight condition for the Tarot X8.

In addition to examining the variations in noise in a single flyover, the quantity of data collected so far allows for comparison of the repeatability of the measured data between repeated test points collected at different times and under different weather conditions. The leftmost plot of Figure 15 shows the SPL time histories for 30 different flyover passes, each conducted at 20 mph and 50' altitude, for microphone M8 (located directly underneath the flight path). The vehicle was configured with carbon fiber propellers for all 30 passes. Significant variations (~7dB) can be observed in the noise levels. The rightmost plot shows the summary statistics for the A-weighted SEL for the same flyover condition using both carbon fiber and ABS plastic propellers. Twenty runs were used for each category. Interestingly, the variation in SEL appears to be lower for the plastic propellers than the carbon fiber propellers; in addition to the differences in material, the blade

geometries also differ between the two propellers. The results shown here are preliminary, and further investigation is needed to understand the sources of acoustic variability.

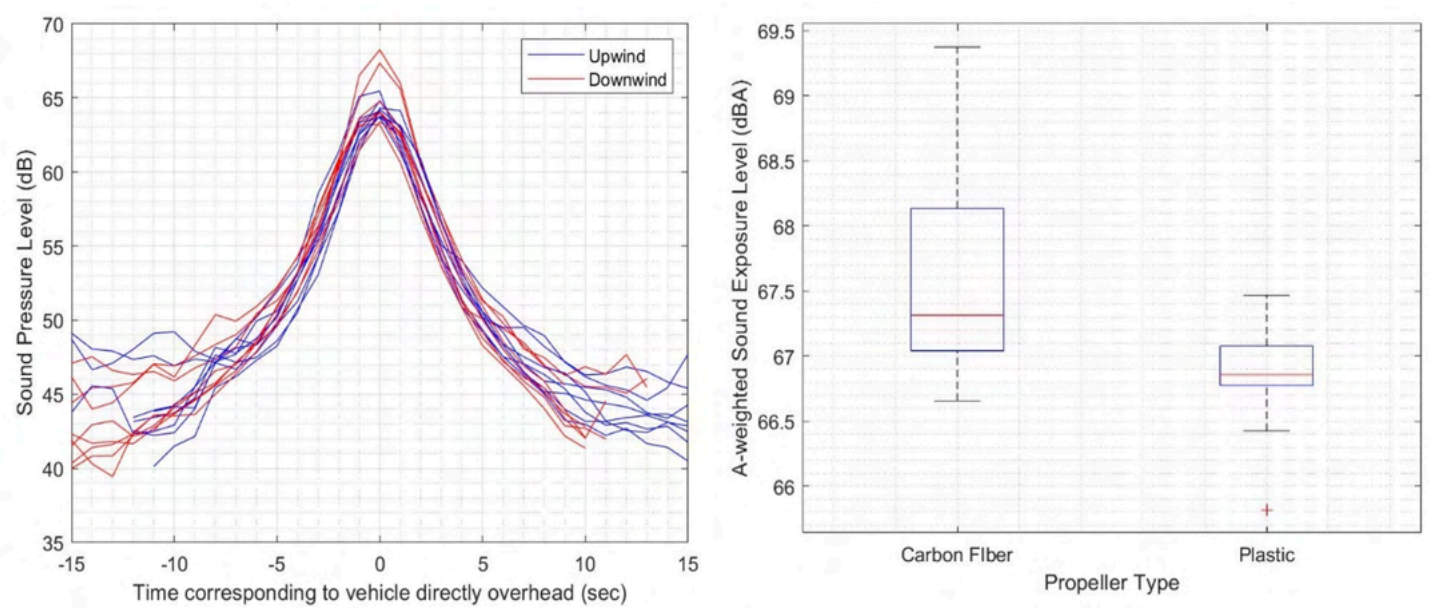

Figure 15. SPL time histories (left) and SEL statistics (right) for level flight flyover passes at 20 mph and 50' altitude.

Further data analysis will be conducted to identify the main sources of noise, and the amount and causes of variability in the measured acoustic data. Data organization and packaging has begun to simplify the collected noise, weather, and vehicle data into a streamlined database for use by the FAA and subsequently the broader research community.

Publications

An abstract entitled 'Ground-based Acoustic Measurements of Small Multirotor Aircraft' was submitted to the Vertical Flight Society Forum 78 being held in May 2022.

Outreach Efforts

None

Awards

None

Student Involvement

MS student N. Blaise Konzel designed these noise measurement procedures and collected the data.

Plans for Next Period

The next step in this task is to build on the preliminary data analysis described above and develop a more detailed understanding of variability in UAS noise measurements. with the aim of developing repeatable noise measurement procedures. Additional data will be collected for a variety of UAS with different sizes and weights, including the instrumented reconfigurable UAS platforms described in Task 4.

Task 8 – UAM Full-vehicle Noise Measurement

The Pennsylvania State University

Objective(s)

The objective of this task is to conduct an acoustic characterization of Beta Technologies' multirotor UAM vehicle in free flight.

Research Approach

The next phase of measurements will be conducted at the Beta Technologies facility in South Burlington, Vermont. Expanded measurements will be conducted for the Alia-250 UAM in its conventional takeoff and landing configuration, as well as the scale Alia-40d vehicle in vertical flight operations. Noise measurements are also planned for an isolated lifting rotor on a rolling test stand.

Milestone(s)

The milestone for this task consists of collecting a baseline acoustic, performance, and meteorological data set of UAM noise measurements across several operating modes.

Major Accomplishments

Initial noise measurements of the Alia-250 UAM were conducted during the previous reporting period. These measurements have been analyzed and the results were used to inform the development of a follow-up test plan. This test plan includes procedures for taking measurements of the vehicle with an expanded operating envelope, as well as with the subscale demonstrator and rolling rotor test stand.

Publications

None

Outreach Efforts

None

Awards

None

Student Involvement

MS students N. Blaise Konzel and Joel Rachaprolu have conducted an initial analysis of the data. N. Blaise Konzel has developed the follow-up test plan.

Plans for Next Period

Follow on noise measurements will be conducted in conjunction with Beta Technologies for additional cruise, hover, and transition conditions as the operating envelope of the vehicle expands.

Publications Index

Project 001

Fifteen graduate students and three undergraduate students involved.

Publications

- Bach, Q. V., Fu, J., & Turn, S. (2021). Fuel characterization of construction and demolition wastes as a potential feedstock for sustainable aviation fuels. *Frontiers in Energy Research, 9,* 711808.
- Bach, Q. V. & Turn, S. Fate of arsenic and other inorganic elements during gasification of construction and demolition wastes – thermochemical equilibrium calculations. Draft manuscript in process.
- Burton C. English, R. Jamey Menard, and Bradly Wilson, The Economic Impacts of a Renewable Biofuels/Energy Industry Supply Chain using the Renewable Energy Economic Analysis Layers (REEAL) Modeling System, Frontiers in Energy Research, section Bioenergy and Biofuels, In Review
- Chan, S., Ogoshi, R. & Turn, S. Feedstocks for sustainable jet fuel production: An assessment of land suitability in Hawaii. A draft report has been prepared and a draft manuscript is under preparation for the journal *Frontiers in Energy Research*.
- Fu, J., Allen, G., Weber, S., Turn, S. Q., & Kusch, W. (2021). Water leaching for improving fuel properties of pongamia pod: Informing process design. *Fuel, 305,* 121480. https://doi.org/10.1016/j.fuel.2021.121480
- Fu, J., Summers, S., Turn, S. Q., & Kusch, W. (2021). Upgraded pongamia pod via torrefaction for the production of bioenergy. *Fuel, 291,* 120260. https://doi.org/10.1016/j.fuel.2021.120260
- Fu, J., Summers, S., Morgan, T. J., Turn, S. Q., & Kusch, W. (2021). Fuel properties of pongamia (*Milletia pinnata*) seeds and pods grown in Hawaii. *ACS Omega, 6,* 9222–9233. https://doi.org/10.1021/acsomega.1c00635
- Gao, Y., Zhang, X., Davidson, E., & Taheripour, F. (2021). The increasing global environmental consequences of a weakening US–China crop trade relationship. *Nature Food, 2* (8), 578-586.
- Kelso, W. (2021). Cost optimization of U.S. sustainable aviation fuel supply chain under different policy constraints [S.M. Thesis, Massachusetts Institute of Technology]. *To be released soon via MIT DSpace*: https://dspace.mit.edu/
- Korkut, E. & Fowler, Lara B. (2021). Regulatory and Policy Analysis of Production, Development and Use of Sustainable Aviation Fuels in the United States. *Frontiers in Energy Research*, 9, 750514. https://www.frontiersin.org/articles/10.3389/fenrg.2021.750514/full
- Prussi, M., Lee, U., Wang, M., Malina, R., Valin, V., Taheripour, F., Velarde, C., Staples, M. D., Lonza, L., & Hileman, J. L. (2021). CORSIA: The first internationally adopted approach to calculate life-cycle GHG emissions for aviation fuels. *Renewable and Sustainable Energy Reviews, 150*, 111398.
- Taheripour, F., Scott, D., Hurt, C. A., & Tyner, W. E. (2021). Technological progress in US agriculture: Implications for biofuel production. Sustainable Agriculture Research, *10*(1), 61. https://doi.org/10.5539/sar.v10n1p61
- Taheripour, F., Sajedinia, E., & Karami, O. (2021). Oilseed cover crops for sustainable aviation fuels production and reduction in greenhouse gas emissions through land use savings. Manuscript submitted for publication.
- Tanzil, A.H., K. Brandt, M. Wolcott, X. Zhang, and M. Garcia-Perez. (2021). Strategic Assessment of Sustainable Aviation Fuel Production Technologies: Yield Improvement and Cost Reduction Opportunities, *Biomass and Bioenergy*, 145, 105942.
- Tanzil, A.H., Zhang, X., Wolcott, M., Brandt, K. Stockle, C. Murthy, G. and Garcia-Perez, M. (2021). Evaluation of Dry Corn Ethanol Biorefinery Concepts for the Production of Sustainable Aviation Fuel, *Biomass and Bioenergy*, 146, 105937.
- Thomas, McKenzie, Kimberly L. Jensen, Dayton M. Lambert, Burton C. English, Christopher D. Clark, and Forbes R. Walker. (2021). Consumer Preferences and Willingness to Pay for Potting Mix with Biochar. *Energies,* 14(12):3432. https://doi.org/10.3390/en14123432
- Carlos J. Trejo-Pech, James A. Larson, Burton C. English, T E. Yu; Biofuel discount rates and stochastic techno-economic analysis for a prospective Pennycress (Thlaspi arvense L.) sustainable aviation fuel supply chain, Frontiers in Energy Research, Section Bioenergy and Biofuels, in press.
- Vizcaya, Luis A. (2021). Effect of Harvesting Schemes on Forest Residue Supply Chain for Biofuel Production: A Case Study in Tennessee. Master's Thesis, University of Tennessee.

- Wang, Z., Staples, M. D., Tyner, W., Zhao, X., Malina, R., Olcay, H., Allroggen, F., & Barrett, S. R. H. (2021). Quantitative policy analysis for sustainable aviation fuel production technologies. Frontiers in Energy Research, *9*. https://doi.org/10.3389/fenrg.2021.751722
- Wolaver, Ty M. (2021).The Effect of Inputs on Poultry Production Output. Master's Thesis, University of Tennessee. https://trace.tennessee.edu/utk_gradthes/6191
- Zhao, X., Taheripour, F., Malina, R., Staples, M. D., & Tyner, W. E. (2021). Estimating induced land use change emissions for sustainable aviation biofuel pathways. Science of the Total Environment, *779*, 146238.

Reports

- CAEP/12-FTG/06-WP/02. Summary of the progress of the Core LCA Subgroup since FTG/03. November 2020.
- CAEP/12-FTG/06-WP/03. Default values for jatropha to HEFA pathways. November 2020.
- CAEP/12-FTG/06-WP/06 – "Update on ILUC default values modelling for SAF pathways", November 2020, Virtual.
- CAEP/12-FTG/06-WP/07: Summary of progress of the Technology Production Policy Task Group. November 2020.
- CAEP/12-FTG/06-WP/08 – "Revised guidance on Direct Land Use Change calculation", November 2020, Virtual.
- CAEP/12-FTG/06-IP/04. Summary of progress since FTG/05 on calculating LCA values for fuels produced through co-processing of biogenic feedstock with petroleum feedstock. November 2020.
- CAEP/12-FTG/06-FL/02. Proposed Jatropha Assessment Cases. November 2020.
- CAEP/12-FTG/06-FL/04 – "Comparison of Proposed Methodology for Global ILUC", November 2020, Virtual.
- CAEP/12-FTG/07-WP/04: Method for SAF production projections out to 2035. February 2020.
- CAEP/12-FTG/07-FL/06: Proposal for the addition of a "SAF-emphasis scenario". February 2021.
- CAEP/12-FTG/08-WP/02: Summary of SAF production scenarios and associated GHG emissions reductions. March 2021.
- CAEP/12-FTG/08-WP/04. Summary of the progress of the Core LCA Subgroup since FTG/07. March 2021.
- CAEP/12-FTG/08-WP/04 – "Pilot application of the methodology on Low Land Use Change (LUC) Risk Practices", March 2021, Virtual.
- CAEP/12-FTG/08-WP/07 – "Update on ILUC default values modelling for SAF pathways", March 2021, Virtual.
- CAEP/12-FTG/08-WP/08 – "Methodology proposal on Direct Land Use Change calculation", March 2021, Virtual.
- CAEP/12-FTG/08-IP/02: SAF production scenarios and associated GHG emissions reductions. March 2021.
- CAEP/12-FTG/08-FL/04: Additional caveats for the reporting of the SAF production scenarios and associated GHG emissions reductions as presented in CAEP/12-FTG/08-WP/02 and IP/02. March 2021.
- CAEP/12-FTG/09-WP/04. Life-cycle analysis of co-processed sustainable aviation fuels. May 2021.
- CAEP/12-FTG/09-IP/02 – "ILUC Modelling Assumptions on Soil Organic Carbon Accounting", May 2021, Virtual.
- CAEP/12-FTG/09-WP/08 – "Update on ILUC modelling and low LUC risk", May 2021, Virtual.
- CAEP/12-FTG/09-WP/09 – "Methodology proposal on Direct Land Use Change calculation", May 2021, Virtual.
- CAEP/12-FTG/10-WP/03. Summary of the progress of the Core LCA Subgroup since FTG/09. July 2021.
- CAEP/12-FTG/10-WP/06 – "Methodology proposal on Direct Land Use Change calculation", July 2021, Virtual.
- CAEP/12-FTG/10-WP/05 – "Update on modelling of ILUC default values", July 2021, Virtual.
- CAEP/12-FTG/10-WP/07 – "Revisions to methodology on Low Land Use Change (LUC) Risk Practices based on pilot applications", July 2021, Virtual.
- CAEP/12-FTG/10-IP02: Life cycle analysis methodology for lower carbon aviation fuels
- CAEP/12-FTG/10-IP/03: Option for Addressing Eligibility and Crediting of LCAF in CORSIA Life Cycle Analysis Framework

Presentations

- Lara B. Fowler, Ekrem Korkut. "Regulatory and Policy Analysis of Production, Development and Use of Sustainable Aviation Fuels in the United States." *Penn State Energy Days* (May 2021), available online at https://iee.psu.edu/events/energy-days/posters.
- Turn "Water leaching for improving fuel properties of pongamia pods" was orally and virtually presented at the 2021 Fall National Meeting of the American Chemical Society in Atlanta, Georgia, August 22-26, 2021.
- Turn "Upgraded *Milletia Pinnata* Pod via Torrefaction for the Production of Bioenergy in Hawaii" was virtually and orally presented at the 2021 Spring National Meeting of the American Chemical Society, April 5-16, 2021.
- Taheripour attended the CRC meeting and made a presentation on GTAP data base update: CRC Life Cycle Analysis Workshop," Virtual meeting, 2021.
- Taheripour presented a paper at the National Biodiesel Board Sustainability Workshop, Virtual Meeting, 2021.

- Taheripour attended several meetings to present the research outcomes on ILUC values, including:
  - GTAP 24th Annual Conference on Global Economic Analysis, Virtual meeting, June 2021,
  - AAEA Annual Meeting, Virtual, August 2021.
  - EAAE Annual Meeting, Virtual, July 2021.

Project 002

Three undergraduate students involved.

Publications

- Information paper was provided to the Emissions Characterization Task Group of Emissions technical Working group 3 (WG3-7) in the 12th cycle of the Committee on aviation environmental protection (CAEP/12) on Sept 20-24.

Presentations

- Results were briefed at the 7th meeting of the Emissions technical Working group 3 (WG3-7) in the 12th cycle of the Committee on aviation environmental protection (CAEP/12) on Sept 20-24

Project 003

Three graduate students involved.

Publications

- Bullock, C. (2021). Aviation Effects on Local Business: Mapping Community Impact and Policy Strategies for Noise Remediation. MIT M.S. thesis. To be released soon via MIT DSpace.
- Kim, C. S., Grady, S. T., Hart, J. E., Laden, F., VoPham, T., Nguyen, D. D., Manson, J. E., James, P., Forman, J. P., Rexrode, K. M., Levy, J. I., & Peters, J. L. (2021). Long-term aircraft noise exposure and risk of hypertension in the Nurses' Health Studies. Environmental research, 112195. Advance online publication. https://doi.org/10.1016/j.envres.2021.112195

Presentations

- Peters, J. "Associations between aircraft noise exposure and insufficient sleep in the US-based prospective Nurses' Health Study I cohort" presented at the International Society of Environmental Epidemiology (ISEE) conference, August 23-26, 2021.
- Peters, J., Daniel D. Nguyen, Stephanie T. Grady, Jaime E. Hart, Eric A. Whitsel, Gregory A. Wellenius, James D. Stewart, Francine Laden, Jonathan I. Levy. "Long-term aircraft noise exposure and incident hypertension in national US cohort studies" presented at the International Commission on Biological Effects of Noise (ICBEN) Congress, June 15, 2021.
- "Aircraft Noise and Health Research" presented to the Airport Council International (ACI), March 23, 2021.

Project 009

Three graduate students involved.

Project 010

Sixteen graduate students involved.

Publications

- Jain, S., Mane, M., Crossley, W. A., & DeLaurentis, D. A. (2021). Investigating How Commercial Supersonic Aircraft Operations Might Impact Subsonic Operations and Total CO_2 Emissions, AIAA 2021-3014. AIAA Aviation 2021 Forum.
- Mane M., Jain, S., & Crossley, W. A. (2021). Estimating Market Size for Supersonic Passenger Transport Aircraft, AIAA 2021-2442. AIAA Aviation 2021 Forum.

Submitted conference proceedings

- Fung, T., Yang, B., Jain, S., Chao, H., Mane, M., Crossley, W. A., & DeLaurentis, D. Fleet-Level Impacts of Different Commercial Supersonic Aircraft Configurations Considering A World-Wide Route Network. Abstract submitted to AIAA Aviation Forum for presentation in June 2022
- Yang, B., Fung, T., Jain, S., Chao, H., Mane, M., Crossley, W. A., & DeLaurentis, D. A. Estimating Future Fleet-Level CO2 Emissions Considering a World-Wide Network. Abstract submitted to AIAA Aviation Forum for presentation in June 2022

Presentations

- Jain, S., Mane, M., Crossley, W. A., & DeLaurentis, D. A. Investigating How Commercial Supersonic Aircraft Operations Might Impact Subsonic Operations and Total CO_2 Emissions, AIAA 2021-3014. AIAA Aviation 2021 Forum. August 2021
- Mane M., Jain, S., Crossley, W. A. Estimating Market Size for Supersonic Passenger Transport Aircraft, AIAA 2021-2442. AIAA Aviation 2021 Forum. August 2021.

Project 018

One graduate student and two undergraduate students involved.

Project 019

One graduate student involved.

Publications

- Arter, C. A., J. Buonocore. C. Moniruzzaman, D. Yang, J. Jiaoyan and S. Arunachalam. (2022). Air Quality and Health-Related Impacts of Traditional and Alternate Jet Fuels from Airport Aircraft Operations in the U.S. *Environ. Int*, 158, 106958, https://doi.org/10.1016/j.envint.2021.106958
- Arter, C. A., and S. Arunachalam. (2021). Assessing the Importance of Nonlinearity for Aircraft Emissions' Impact on O3 and PM2.5. *Sci. Total Environ.,* 777, 1462021, https://doi.org/10.1016/j.scitotenv.2021.146121

Presentations

- Pandey, G., Moniruzzaman, C., Venkatram, A., and Arunachalam, S. (2021). Effect of atmospheric stability on modeling air quality in and around a major airport., International Technical Meeting on air pollution modeling and its applications (ITM), October 18-22, 2021, Barcelona, Spain (Oral Presentation).

Project 022

One graduate student involved.

Publications

- Zhang, J., D. Wuebbles, D. Kinnison, and S.L. Baughcum. (2021). Potential impacts of supersonic aircraft emissions on ozone and resulting forcing on climate. An update on historical analysis. *J. Geophys. Res.*, https://doi.org/10.1029/2020JD034130.

- Zhang, J., D. Wuebbles, D. Kinnison, and S.L. Baughcum. (2021). Stratospheric ozone and climate forcing sensitivity to cruise altitudes for fleets of potential supersonic transport aircraft. *J. Geophys. Res.*, 126, e2021JD034971, https://doi.org/10.1029/2021JD034971.
- Zhang, J. (2021). On Potential Effects from the Aviation and Refrigeration Sectors on Ozone and Climate. Ph.D. Thesis, University of Illinois at Urbana-Champaign, Urbana.

Project 023

Four graduate students involved.

Publications

- Salgueiro, S., Thomas, J., Li, C., and Hansman, R.J. (2021). Operational Noise Abatement through Control of Climb Profile on Departure, *AIAA SciTech Forum 2021*.

Project 025

One graduate student involved.

Publications

Peer-reviewed journal publications

- Wang, Y., Wei, W., Hanson, R. K. (2021). A new strategy of characterizing hydrocarbon fuels using FTIR spectra and generalized linear model with grouped-Lasso regularization. Fuel, *287*, 119419. https://doi.org/10.1016/j.fuel.2020.119419

Published book chapters

- Park, J. W., Xu, C., Gao, Y., Lu, T. F., Shao, J. K., Pinkowski, N. H., Wang, S., Wang, Y., Cao, Y., Hanson, R. K., Davidson, D. F., & Colket, M. B. (2021). Chemical kinetics. In: J. Heyne, & M. Colket (Eds.), *Fuel effects on operability of aircraft gas turbine combustors* (pp. 255-293). American Institute of Aeronautics and Astronautics, Inc.
- Heyne, J., Yang, Z., Boehm, R., Rauch, B., Le Clercq, P., Hanson, R., Ferris, A., Dooley, S., Ure, A., Blakey, S., Lewis, C., Colket, M. (2021). Prescreening of sustainable aviation jet fuels. In: J. Heyne, & M. Colket (Eds.), *Fuel effects on operability of aircraft gas turbine combustors* (pp. 487-523). American Institute of Aeronautics and Astronautics, Inc.

Presentations

- Our IR fuel analysis work was presented at the Joint NJFCP Meetings on October 20, 2020 and February 2, 2021.

Project 029(A)

Three graduate students involved.

Publications

- Shin, Dongyun, Aman Satija, & Robert P. Lucht. (2021). Spray Characteristics of Standard and Alternative Aviation Fuels at High Ambient Pressure Conditions. *Experimental Thermal and Fluid Science*, 130, 110511, https://doi.org/10.1016/j.expthermflusci.2021.110511
- Shin, Dongyun, Neil S. Rodrigues, Andrew J. Bokhart, Jay P. Gore, Paul E. Sojka, & Robert P. Lucht. (2021). Spray Characteristics of Standard and Alternative Aviation Fuels at Cold Start Conditions. *AIAA Journal*, 59(12): https://doi.org/10.2514/1.J060363
- Donyun Shin, Hasti, V. R., Rizk, N., Bokhart, A. J., Rodrigues, N. S., Corber, P. A., Sojka, P. E., Lucht, R. P., and Gore, J. P., "Chapter VIII. Spray Characteristics of Conventional and Alternative Fuels", AIAA Book Progress in Astronautics and Aeronautics, 2021. (submitted)

- Veeraraghava Raju Hasti, Abhishek Navarkar, and Jay P. Gore, "A data-driven discovery using machine learning for identification of the critical flame location and early detection of the lean blowout in a gas turbine combustor", Energy and AI (Submitted – Under Review)
- Veeraraghava Raju Hasti, Prithwish Kundu, Sibendu Som, and Jay P. Gore, "Numerical simulations and analysis of the complex turbulent flow field in a realistic gas turbine Combustor", Proceedings of the Institution of Mechanical Engineers, Part A: Journal of Power and Energy (Submitted – Under Review)
- M.S. Anand, Jeffery A. Lovett, Jeff Moder, Thomas Wey, Matthias Ihme, Lucas Esclapez, Peter C. Ma, Suresh Menon, Achyut Panchal, Veeraraghava Raju Hasti, Jay Gore, Pritwish Kundu, Sibendu Som, Venkat Raman, Yihao Tang, Fang Xu, Vaidya Sankaran, "Chapter IX. CFD Modeling of Lean Blowout and Ignition Fuel Sensitivity", AIAA Book Series (Submitted - Under Review)

Project 031(A)

Publications

Written reports

- (n.d.). (2021). Alternative jet fuel evaluation and specification development support: GCxGC methods draft report (Report No. UDR-TR-2021-159).

Project 033

Two graduate students involved.

- Database made accessible through https://altjetfuels.illinois.edu/

Publications

- Jihun Oh, Anna Oldani, Tonghun Lee, Linda Shafer. "Deep Learning Algorithms for Assessing Sustainable Jet Fuels from Two-Dimensional Gas Chromatography" AIAA SciTech. (to be submitted)
- Jihun Oh, Anna Oldani, Linda Shafer, Tonghun Lee. "Data-Driven Streamlining of Sustainable Aviation Fuels via Deep Novelty GCxGC Detection and Query" AIAA SciTech. (to be submitted)

Project 034

Two graduate students involved.

Publications

Peer-reviewed journal publications

- Boehm, R.C., Colborn, J.G., & Heyne, J.S. (2021). Comparing Alternative Jet Fuel Dependencies Between Combustors of Different Size and Mixing Approaches. *Front Energy Res*, 9:701901. doi:10.3389/FENRG.2021.701901.

Book publication

- Meredith Colket, Joshua Heyne, "Fuel Effects on Operability of Aircraft Gas Turbine Combustors," AIAA, Progress in Astronautics and Aeronautics, 1 August 2021. https://doi.org/10.2514/4.106040

Book chapters

- Med Colket, Joshua Heyne, Gurhan Andac, Mark Rumizen, Chapter I. Introduction, Fuel Effects on Operability of Aircraft Gas Turbine Combustors, AIAA, Progress in Astronautics and Aeronautics, 1 August 2021.
- Nicholas Rock, Scott Stouffer, Tyler Hendershott, Joshua Heyne, David Blunck, Lukai, Zheng, Bhupendra Khandelwal, Benjamin Emerson, Epaminondas Mastorakos, Med Colket, Chapter V. Lean Blowout Studies, Fuel

Effects on Operability of Aircraft Gas Turbine Combustors, AIAA, Progress in Astronautics and Aeronautics, 1 August 2021.
- Joshua Heyne, Bastian Rauch, Ron Hanson, Stephen Dooley, Simon Blakey, Zhibin Yang, Alison Ferris, Andrew Ure, Patrick Le Clercq, Randy Boehm, Chris Lewis, Med Colket, Chapter XII. Prescreening of Sustainable Aviation Jet Fuels, Fuel Effects on Operability of Aircraft Gas Turbine Combustors, AIAA, Progress in Astronautics and Aeronautics, 1 August 2021.
- Joshua Heyne, Med Colket, Tim Edwards, Jeff Moder, Mark Rumizen, Anna Oldani, Chapter XIII. Summary, Fuel Effects on Operability of Aircraft Gas Turbine Combustors, AIAA, Progress in Astronautics and Aeronautics, 1 August 2021.

Presentations

Invited talks

- Seminar, Heyne, "Sustainable Aviation Fuel: properties, compositions, and qualification requirements, Center for Multiphase Flow Research and Education," Iowa State University, Nov. 2021, Sponsored Travel.
- Seminar, Heyne, "Sustainable Aviation Fuel: properties, compositions, and qualification requirements," Sandia National Laboratory, 17 Aug. 2021, Sponsored Travel.
- Panel, Heyne, "Sustainable aviation fuel property needs and some solid waste candidates," Seminar on Hydrothermal Liquefaction: biocrudes and advances towards drop-in fuel potential," Aalborg University, Denmark, 17 Aug. 2021.
- Panel, Heyne, "Sustainable Aviation Fuel prescreening, benefits, and a proposed streamlined evaluation process," National Academies, Transportation Research Board (AV030), Sustainable Aviation Fuels subcommittee midyear meeting, 2 June 2021.
- Panel Presentation, Heyne J., "Prescreening of sustainable aviation fuels," CAAFI Virtual Mini-Symposium, June 2021.
- Panel Presentation, Heyne J., "Summative Results of the National Jet Fuels Combustion Program," Properties and Emissions, CRC Aviation Fuels Meeting, virtual, May 2021.
- Panel Presentation, Heyne J., "High Value Drop-in Aviation Fuels: From Molecule Selection to Mission Benefits," Panel Title: Fuel quality matters, DOE BETO/PNNL HTL Workshop, virtual, November 2020.
- Panel Presentation, Heyne J., "Prescreening of HTL SAFs: Rapid low-volume, lowcost testing," Panel Title: Sustainable Aviation Fuel Certification, DOE BETO/PNNL HTL Workshop, virtual, November 2020.

Project 37

Three graduate students currently involved.

Project 038

Two graduate students involved.

Publications

- Zachos, D. R. (2022). Noise Prediction for Helicopter Noise Abatement and EVTOL Design. M. S Thesis, The Pennsylvania State University, (in progress).

Project 039

Two graduate students involved.

Project 040

Three graduate students and one undergraduate student involved.

Project 041

One graduate student involved.

Publications

- Sparrow, V., & Riegel, K. (2020, December). 2020 literature review of secondary sonic boom [Paper presentation]. Proceedings of the 2020 e-Forum Acusticum, European Acoustics Association, Virtual meeting. https://hal.archives-ouvertes.fr/FA2020/hal-03229476

Project 043

Two graduate students involved.

Project 044

Four graduate students involved.

Publications

- Thomas, J., & Hansman, R.J. (2021). Modeling of Delayed Deceleration Approaches for Community Noise Reduction, Journal of Air Transportation, 29(3). https://doi.org/10.2514/1.D0237
- Mahseredjian, A., Thomas, J., & Hansman, R.J. (2021). Advanced Procedure Noise Model Validation Using Airport Noise Monitor Networks, Internoise 2021. https://doi.org/10.3397/IN-2021-2842.
- Thomas, J., Mahseredjian, A., and Hansman, R.J. (2021). Delayed Deceleration Approach Procedure Noise Modeling Validation using Noise Measurements and Radar Data, AIAA Aviation 2021 (AIAA 2021-2135). https://doi.org/10.2514/6.2021-2135.
- Salgueiro, S., Thomas, J., Li., C. and Hansman R.J. (2021). Operational Noise Abatement through Control of Climb Profile on Departure, AIAA Scitech 2021 Forum, (AIAA 2021-0007) https://doi.org/10.2514/6.2021-0007.

Presentations

- Mahseredjian, A., Thomas, J., & Hansman, R. J. (2021). Advanced procedure noise model validation using airport noise monitor networks [Presentation]. Inter-Noise 2021, Washington, DC.
- Thomas, J., Mahseredjian, A., & Hansman, R. J. (2021). Delayed deceleration approach procedure noise modeling validation using noise measurements and radar data [Paper presentaiton]. AIAA Aviation 2021 Forum, Virtual Meeting.
- Salgueiro, S., Thomas, J., Li., C. & Hansman, R. J. (2021). Operational noise abatement through control of climb profile on departure [Presentation]. AIAA Scitech 2021 Forum, Washington, DC.

Project 046

One graduate student and one undergraduate student involved.

Publications

- Badrinath, S., E. Joback, J. Abel, T.G. Reynolds, and H. Balakrishnan. (2021). Spatial Modeling of Airport Surface Fuel Burn for Environmental Impact Analysis, Fourteenth USA/Europe Air Traffic Management Research and Development Seminar (ATM2021), Paper #32.

Presentations

- Badrinath, S., E. Joback, J. Abel, T.G. Reynolds, and H. Balakrishnan. (2021). Spatial Modeling of Airport Surface Fuel Burn for Environmental Impact Analysis, *US-Europe ATM R&D Seminar*, September 2021.

Project 047

Two graduate students involved.

Publications

- Voet, L., Prashanth, P., Speth, R., Sabnis, J., Tan, C., & Barrett, S. (2021). The impact of design space constraints on the noise and emissions from derivative engines for civil supersonic aircraft. *AIAA Scitech 2021 Forum* (p. 1272).
- Prashanth, P., Voet, L., Speth, R., Sabnis, J., Tan, C., & Barrett, S. The impact of design space constraints on the noise and emissions from derivative engines for civil supersonic aircraft. Manuscript in preparation.
- Voet, L., Speth, R., Sabnis, J., Tan, C., & Barrett, S. (2021). Sensitivities of aircraft acoustic metrics to engine design variables for multi-disciplinary optimization. *AIAA Journal* (manuscript submitted).
- Laurens Voet presented an Information Paper titled “Investigation of the effects of VNRS on LTO emissions of engines for supersonic transport aircraft” at the CAEP/12-WG3/5-ESTG meeting on November 3, 2020.
- A Working Paper titled “Accounting for Climb Out Emissions in the Supersonic LTO Emissions Cycle” was submitted to the CAEP/12-WG3/6-ESTG meeting on April 12-20, 2021, in collaboration with ASCENT Project 10.
- A Working Paper titled “Accounting for Climb Out Emissions in the Supersonic LTO Emissions Cycle” was submitted to the CAEP/12-WG3/7-ESTG meeting on September 20-24, 2021, in collaboration with ASCENT Project 10.

Presentations

- Voet, L., Prashanth, P., Speth, R., Sabnis, J., Tan, C., & Barrett, S. (2021). The impact of design space constraints on the noise and emissions from derivative engines for civil supersonic aircraft. *AIAA Scitech 2021 Forum*, January.
- Prashanth Prakash, “Civil Supersonic Transport Emissions” presentation at the Aviation Emissions Characterization Roadmap 2021 Annual Meeting on May 26, 2021.
- Laurens Voet, “Development of optimal control framework to design VNRS for take-off operations of civil supersonic transport” presentation at NASA Glenn Research Center on July 22, 2021.
- Laurens Voet, “Design of variable noise reduction systems for civil supersonic transport certification noise reduction” presentation at the NASA Acoustics Technical Working Group Meeting Fall 2021 on October 19, 2021.

Project 048

One graduate student involved.

Publications

- Working Paper for CAEP/12-WG3-ECTG/6.

Project 049

Two graduate students involved.

Publications

Published conference proceedings

- Mukherjee, B., Gan, Z. F. T., Theron, J.-P., Botre, M., Brentner, K. S., Greenwood, E., & Horn, J. F. (2021, May 11-13). A new distributed electric propulsion aircraft simulation tool for coupled flight dynamics, free wake, and acoustic predictions. Vertical Flight Society 77th Annual Forum & Technology Display.
- Gan, Z. F. T., Brentner, K. S., & Greenwood, E. (2021, January 26-28). Time variation of rotor broadband noise. Vertical Flight Society 8th Annual Electric VTOL Symposium.

Presentations

- Mukherjee, B., Gan, Z. F. T., Theron, J.-P., Botre, M., Brentner, K. S., Greenwood, E., & Horn, J. F. (2021, May 11-13). A new distributed electric propulsion aircraft simulation tool for coupled flight dynamics, free wake, and acoustic predictions [Presentation]. Vertical Flight Society 77th Annual Forum & Technology Display.
- Gan, Z. F. T., Brentner, K. S., & Greenwood, E. (2021, January 26-28). Time variation of rotor broadband noise [Presentation]. Vertical Flight Society 8th Annual Electric VTOL Symposium.

Project 050

Seven graduate students involved.

Project 051

Two graduate students involved.

Project 052

Three graduate students involved.

Project 053

Four graduate students and two undergraduate students involved.

Publications

- Jackson, D.C., Rindfleisch, T.C., & Alonso, J.J. (2021). A System for Measurement and Analysis of Aircraft Noise Impacts. Eng. Proc., 13(1), 6. https://doi.org/10.3390/engproc2021013006

Presentations

- Jackson, D.C., Rindfleisch, T.C., & Alonso, J.J. (2021). A System for Measurement and Analysis of Aircraft Noise Impacts. OpenSky 2021, November 18-19, Brussels, Belgium. https://doi.org/10.3390/engproc2021013006

Project 054

Nine graduate students involved.

Publications

- Bhanpato, J., Puranik, T.G., & Mavris D.N. (2021). Data-Driven Analysis of Departure Procedures for Aviation Noise Mitigation. Eng. Proc., 13(1), 2. https://doi.org/10.3390/engproc2021013002

Presentations

- Bhanpato, J., Puranik, T.G., & Mavris D.N. (2021). Data-Driven Analysis of Departure Procedures for Aviation Noise Mitigation, OpenSky 2021, November 18-19, Brussels, Belgium.

Project 055

Five graduate students involved.

Publications

- Acharya, Vishal. (2021). Modeling the Response of Spray Flames to Velocity Disturbances, AIAA SciTech 2021. AIAA-2021-0679. https://doi.org/10.2514/6.2021-0679
- John, Tony, Vishal Acharya, and Tim Lieuwen. (2021). Entropy Wave Generation by Harmonically Forced, Convectively Non-compact Flames, 12th US National Technical Meeting of the Combustion Institute, Paper# 128CTM-0081.
- Patki, Parth, Vishal Acharya and Tim Lieuwen. (2021). Entropy Source Terms from Exothermic Chemical Reactions: Implications for Indirect, Premixed Combustion Noise, 12th US National Technical Meeting of the Combustion Institute, Paper# 128CTM-0094.
- Winkler, Julian and Jeff Mendoza. (2021). Lattice Boltzmann Simulations of Wave Propagation through a High-Pressure Turbine Stage, AIAA Aviation Forum 2021. AIAA-2021-2260. https://doi.org/10.2514/6.2021-2260

Presentations

- Vishal Acharya, “Modeling the Response of Spray Flames to Velocity Disturbances”, AIAA SciTech 2021 virtual meeting, Jan. 2021.
- Julian Winkler and Jeff Mendoza, “Lattice Boltzmann Simulations of Wave Propagation through a High-Pressure Turbine Stage”, AIAA Aviation Forum 2021.
- Parth Patki, Vishal Acharya and Tim Lieuwen, “Entropy Source Terms from Exothermic Chemical Reactions: Implications for Indirect, Premixed Combustion Noise”, 12th US National Technical Meeting of the Combustion Institute (virtual), May 2021.
- Tony John, Vishal Acharya, and Tim Lieuwen, “Entropy Wave Generation by Harmonically Forced, Convectively Non-compact Flames”, 12th US National Technical Meeting of the Combustion Institute (virtual), May 2021.
- Vishal Acharya’s accepted submission to AIAA SciTech 2022 on Spray flame response heat release modeling.
- Tony John, Vishal Acharya, and Tim Lieuwen’s accepted abstract submission to ASME Turbo Expo 2022 on entropy generation modeling.
- Parth Patki, Vishal Acharya, and Tim Lieuwen’s manuscript preparation for submission to International Symposium on Combustion 2022.

Project 056

One graduate student involved.

Project 057

One graduate student involved.

Presentations

- Loubeau, *et al.*, “Developing Certification Procedures for Quiet Supersonic Aircraft using Shaped Sonic Boom Predictions Through Atmospheric Turbulence,” J. Acoust. Soc. Am. **149**, A102-A102 (2021), 9 June 2021 Acoustical Society of America presentation, virtual.

Project 058

Three graduate students involved.

Publications

- Eastham, SD; Fritz, T; Sanz-Morère, I; Prashanth, P; Allroggen, F; Prinn, RG; Speth, RL; Barrett, SRH. “Atmospheric impacts of a near-future supersonic aircraft fleet”. An evaluation of climate forcing resulting from a near-future supersonic aircraft fleet. Currently under review. FAA support was acknowledged.

Project 059

Fourteen graduate students involved.

Publications

- Ethan Pickering. (2021). Resolvent modeling of turbulent jets, PhD thesis, Caltech.
- Shanbhag, T. K., Zhou B. Y., Eduardo, M., and Alonso, J. J. (2021). A comparison of jet acoustic analysis methods, *AIAA Paper* 2021-2102. AIAA AVIATION 2021 FORUM. August 2021.
- Wu, G. J., Shanbhag, T. K., Matsuno, K., Lele, S. K. and Alonso, J. J. “Numerical Simulations and Acoustic Modeling of a Co-annular Nozzle with an Internal Mixing Duct.” *AIAA Paper*, to appear in the 2022 SciTech conference.

Presentations

- Shanbhag, T. K., Zhou B. Y., Eduardo, M., and Alonso, J. J. "A comparison of jet acoustic analysis methods," AIAA AVIATION 2021 FORUM. August 2021.
- Wu, G. J., Shanbhag, T. K., Matsuno, K., Lele, S. K. and Alonso, J. J.. “Numerical Simulations and Acoustic Modeling of a Co-annular Nozzle with an Internal Mixing Duct.” To be presented at 2022 SciTech conference.

Project 060

Four graduate students involved.

Project 061

Four graduate students involved.

Project 062

Seven graduate students and one undergraduate student involved.

Project 063

Three graduate students involved.

Project 064

Two graduate students involved.

Project 065

Five graduate students and three undergraduate students involved.

Publications

- Boehm, R.C., Yang, Z., Bell, D.C., Feldhausen, J., and Heyne, J.S. (2021). Lower heating value of jet fuel from hydrocarbon class concentration data and thermo-chemical reference data: An uncertainty quantification. *Fuel*,122542. doi:10.1016/J.FUEL.2021.122542.
- Yang, Z., Kosir, S., Stachler, R., Heyne, J., Shafer, L., and Anderson, C. (2021). A GCxGC Tier Alpha Combustor Operability Prescreening Method for Sustainable Aviation Fuel. *Fuel*, 292, 120345.

- Heyne, J.S., Bell, D.C., Feldhausen, J., Yang, Z., and Boehm, R.C. Towards Fuel Composition and Properties from Two-dimensional Gas Chromatography with Flame Ionization and Vacuum Ultraviolet Spectroscopy. Fuel (in press)
- Wood, E., A. Motily, C. Trotter, T. Lee, E. Mayhew, V. Coburn, J. Temme, C. Kweon. Fuel Spray and Operating Condition Impact on Ignition Performance in the ARC-M1 Combustor, AIAA SciTech, (2022) – to be submitted.

Presentations

- E. Wood, A. Motily, C. Trotter, T. Lee, E. Mayhew, V. Coburn, J. Temme, C. Kweon. Fuel Spray and Operating Condition Impact on Ignition Performance in the ARC-M1 Combustor, AIAA SciTech, (2022) – to be submitted.

Project 066

One graduate student and one undergraduate student involved.

Publications

- Boehm, R.C., Scholla, L.C., and Heyne, J.S. (2021). Sustainable alternative fuel effects on energy consumption of jet engines. *Fuel*, 304:121378. https://doi.org/10.1016/j.fuel.2021.121378.
- Boehm, R.C., Yang, Z., and Heyne J.S. Threshold Sooting Index of Sustainable Aviation Fuel Candidates from Composition Input Alone: Progress Toward Uncertainty Quantification. Energy and Fuels submitted

Project 067

Three graduate students involved.

Publications

- McDonald, C.T., Philo, J.J., Shahin, T.T., Gejji, R.M., Slabaugh, C.D., & Lucht, R.P. (2021). Effect of Fuel Temperature on Emissions and Structure of a Swirl-Stabilized Flame. AIAA Propulsion and Energy 2021 Forum, Virtual Event. Paper Number AIAA 2021-3480.

Presentations

- McDonald, C.T., Philo, J.J., Shahin, T.T., Gejji, R.M., Slabaugh, C.D., & Lucht, R.P. (2021). Effect of Fuel Temperature on Emissions and Structure of a Swirl-Stabilized Flame. Presented at the AIAA Propulsion and Energy 2021 Forum, Virtual Event.

Project 068

Two graduate students and one undergraduate student involved.

Project 069

One graduate student and two undergraduate students involved.

Project 070

Four graduate students involved.

Project 071

Two graduate students involved.

Publications

- Saldinger, J. C., Elvati, P., & Violi, A. (2021). Stochastic and network analysis of polycyclic aromatic growth in a coflow diffusion flame. *Physical Chemistry Chemical Physics*, *23*(7), 4326-4333.

Project 072

Three graduate students involved.

Publications

- Jansson, M. (2021). Development of a Fast Method to Analyze Patterns in Airport Noise. [Master's thesis, MIT Department of Aeronautics and Astronautics].

Project 073

Graduate student and undergraduate student: TBD

Project 074

Four graduate students and three undergraduate students involved.

Publications

- Passarelli, M., et al., "Experimental Characterization of a Lean Pre-vaporized Premixed Combustor for Supersonic Transport Applications", To Appear, AIAA SciTech (2022)

Presentations

- Passarelli, M., et al., "Experimental Characterization of a Lean Pre-vaporized Premixed Combustor for Supersonic Transport Applications", To be presented at AIAA SciTech (2022)

Project 075

Three graduate students and two undergraduate students involved.

Project 076

Five graduate students involved.

Project 077

Four graduate students involved.

Presentations

- Abstract submitted to the Vertical Flight Society Forum 78 being held in May 2022 entitled 'Helicopter Noise Source Separation using an Order Tracking Filter.'
- Abstract submitted to the Vertical Flight Society Forum 78 being held in May 2022 entitled 'Ground-based Acoustic Measurements of Small Multirotor Aircraft.'

Project Funding Allocations by Federal Fiscal Year

Breakout by Project

Project		Funding Based on award date								
		2014	2015	2016	2017	2018	2019	2020	2021	Total
001	Alternative Jet Fuel Supply Chain Analysis	$1,599,943	$1,425,000	$1,498,749	$1,855,461	$1,102,865	$1,034,039	$3,214,455	$1,412,313	$13,142,825
002	Ambient Conditions Corrections for Non-Volatile PM Emissions Measurements	$2,800,000	$750,000	-$147,766	$725,500	-	$1,217,221	-	$521,246	$5,866,201
003	Cardiovascular Disease and Aircraft Noise Exposure	$200,000	$200,000	$200,000	$340,000	-	$1,729,286	-	-	$2,669,286
004	Estimate of Noise Level Reduction	$150,000	-	-	-	-$8,845	-	-	-	$141,155
005	Noise Emission and Propagation Modeling	$212,000	$200,000	-	-	-	-	-	-	$412,000
006	Rotorcraft Noise Abatement Operating Conditions Modeling	$250,326	-	-	-	-	-	-	-	$250,326
007	Civil, Supersonic Over Flight, Sonic Boom (Noise) Standards Development	$100,000	$200,000	-	-	-	-	-	-	$300,000

Project		Funding Based on award date								
		2014	2015	2016	2017	2018	2019	2020	2021	Total
008	Noise Outreach	$ 30,000	$ 50,000	$ 75,000	$ 25,000	-	$ 30,000	-	-	$210,000
009	Geospatially Driven Noise Estimation Module	-	-	-	-	-	-	$250,000	$249,999	$499,999
010	Aircraft Technology Modeling and Assessment	$549,979	$550,000	$310,000	$669,567	$764,185	-	$2,747,116	$700,000	$6,290,847
011	Rapid Fleet-wide Environmental Assessment Capability	$600,000	$270,000	$299,999	-	-	-	-	-	$1,169,999
012	Aircraft Design and Performance Assessment Tool Enhancement	$ 90,000	-	-	-	-	-	-	-	$90,000
013	Micro-Physical Modeling & Analysis of ACCESS 2 Aviation Exhaust Observations	$200,000	-	-	-	-	-	-	-	$200,000
014	Analysis to Support the Development of an Aircraft CO2 Standard	$520,000	-	-	-	-	-	-	-	$520,000
017	Pilot Study on Aircraft Noise and Sleep Disturbance	$154,000	$343,498	$266,001	$134,924	-	-	-	-	$898,423

Project		Funding Based on award date								
		2014	2015	2016	2017	2018	2019	2020	2021	Total
018	Health Impacts Quantification for Aviation Air Quality Tools	$150,000	$150,000	$200,000	$270,000	-	-	$1,299,991	$599,371	$2,669,362
019	Development of Aviation Air Quality Tools for Airport-Specific Impact Assessment: Air Quality Modeling	$320,614	$369,996	-	$625,378	-	$300,000	$569,000	$650,000	$2,834,988
020	Development of NAS wide and Global Rapid Aviation Air Quality	$150,000	$200,000	$250,000	$250,000	-	-	-	-	$850,000
021	Improving Climate Policy Analysis Tools	$150,000	$150,000	$150,000	$150,000	-	-	-	-	$600,000
022	Evaluation of FAA Climate Tools	$150,000	$30,000	$ 75,000	$100,000	-	-	$200,000	$150,000	$705,000
023	Analytical Approach for Quantifying Noise from Advanced Operational Procedures	-	$286,711	$250,000	$250,000	-	$250,000	$500,000	-	$1,536,711
024	Emissions Data Analysis for CLEEN, ACCESS, and Other Recent Tests	$244,975	-	$ 75,000	-	-	-	-	-	$319,975

Project		Funding Based on award date								
		2014	2015	2016	2017	2018	2019	2020	2021	Total
025	National Jet Fuels Combustion Program – Area #1: Chemical Kinetics Combustion Experiments	-	$615,000	$210,000	$200,000	$ 2,556	$110,000	$300,000	$200,000	$1,637,556
026	National Jet Fuels Combustion Program – Area #2: Chemical Kinetics Model Development and Evaluation	-	$200,000	-	-	-$ 2,556	-	-	-	$197,444
027	National Jet Fuels Combustion Program – Area #3: Advanced Combustion Tests	-	$1,010,000	$580,000	$265,000	-	$ 30,000	-	-	$1,885,000
028	National Jet Fuels Combustion Program – Area #4: Combustion Model Development and Evaluation	-	$470,000	$ 55,000	-	-	-	-	-	$525,000
029	National Jet Fuels Combustion Program – Area #5: Atomization Tests and Models	-	$640,000	$360,000	$150,000	-	$120,000	-	-	$1,270,000
030	National Jet Fuels Combustion Program – Area #6: Referee Swirl-Stabilized Combustor Evaluation/Support	-	$349,949	-	-	-	-	-	-	$349,949

Project		Funding Based on award date								
		2014	2015	2016	2017	2018	2019	2020	2021	Total
031	Alternative Jet Fuels Test and Evaluation	-	$489,619	$744,891	$999,512	$183,019	-	$2,976,134	$499,784	$5,892,959
032	Worldwide LCA of GHG Emissions from Petroleum Jet Fuel	-	$150,000	-	-	-	-	-	-	$150,000
033	Alternative Fuels Test Database Library	-	$199,624	$119,794	$165,000	-	$163,584	$330,000	$150,000	$1,128,002
034	National Jet Fuels Combustion Program – Area #7: Overall Program Integration and Analysis	-	$234,999	$635,365	$192,997	$374,978	-	$582,983	-	$2,021,322
035	Airline Flight Data Examination to Improve flight Performance Modeling	-	$150,001	-	-	-	-	-	-	$150,001
036	Parametric Uncertainty Assessment for AEDT2b	-	$ 65,000	$175,000	$380,000	-	$300,000	-	-	$920,000
037	CLEEN II Technology Modeling and Assessment	-	$200,000	$150,000	$170,000	-	$170,000	$490,000	-	$1,180,000
038	Rotorcraft Noise Abatement Procedures Development	-	$150,000	$150,000	$150,000	$150,000	-	$300,000	$150,000	$1,050,000

Project		Funding Based on award date								
		2014	2015	2016	2017	2018	2019	2020	2021	Total
039	Naphthalene Removal Assessment	-	-	$200,000	$290,000	-	$350,000	-	-	$840,000
040	Quantifying Uncertainties in Predicting Aircraft Noise in Real-world Situations	-	-	$218,426	$200,000	-	$255,000	-		$673,426
041	Identification of Noise Acceptance Onset for Noise Certification Standards of Supersonic Airplane	-	-	$160,000	$221,000	-	$390,000	-	-	$771,000
042	Acoustical Model of Mach Cut-off	-	-	$255,000	$150,000	$170,000	-	-$120	-	$574,880
043	Noise Power Distance Re-Evaluation	-	-	$150,000	$ 75,000	-	$220,000	$400,000	-	$845,000
044	Aircraft Noise Abatement Procedure Modeling and Validation	-	-	-	-	$350,000	-	$370,000	-	$720,000
045	Takeoff/Climb Analysis to Support AEDT APM Development	-	-	$250,000	$ 75,000	$ 8,845	$175,000	-	-	$508,845
046	Surface Analysis to Support AEDT APM Development	-	-	$ 75,000	$ 75,000	$ 75,000	-	$400,000	-	$625,000

Project		Funding Based on award date								
		2014	2015	2016	2017	2018	2019	2020	2021	Total
047	Clean Sheet Supersonic Engine Design and Performance	-	-	-	-	-	$250,000	$800,000	$200,000	$1,250,000
048	Analysis to Support the Development of an Engine nvPM Emissions Standards	-	-	$150,000	$200,000	-	$200,000	$200,000	$200,000	$950,000
049	Urban Air Mobility Noise Reduction Modeling	-	-	-	-	-	-	$560,000	$280,000	$840,000
050	Over-Wing Engine Placement Evaluation	-	-	-	-	-	-	$590,000	-	$590,000
051	Combustion Concepts for Next-Generation Aircraft Engines	-	-	-	-	-	-	$600,000	-	$600,000
052	Comparative Assessment of Electrification Strategies for Aviation	-	-	-	-	-	-	$600,000	-	$600,000
053	Validation of Low Exposure Noise Modeling by Open Source Data Management and Visualization Systems Integrated with AEDT	-	-	-	-	-	-	$569,903	-	$569,903
054	AEDT Evaluation and Development Support	-	-	-	-	-	-	$1,400,000	-	$1,400,000

Project		Funding Based on award date								
		2014	2015	2016	2017	2018	2019	2020	2021	Total
055	Noise Generation and Propagation from Advanced Combustors	-	-	-	-	-	-	$2,999,984	-	$2,999,984
056	Turbine Cooling through Additive Manufacturing	-	-	-	-	-	-	$800,000	-	$800,000
057	Support for Supersonic Aircraft En-route Noise Efforts in ICAO CAEP	-	-	-	-	-	-	$420,000	-	$420,000
058	Improving Policy Analysis Tools to Evaluate Higher-Altitude Aircraft Operations	-	-	-	-	-	-	$500,000	$150,000	$650,000
059	Modeling and Measurements of Supersonic Civil Transport Jet Noise	-	-	-	-	-	-	$749,956	$849,999	$$1,599,955
060	Analytical Methods for Expanding the AEDT Aircraft Fleet Database	-	-	-	-	-	-	$150,000	$150,001	$300,001
061	Noise Certification Streamlining	-	-	-	-	-	-	$250,000	$250,000	$500,000
062	Noise Model Validation for AEDT	-	-	-	-	-	-	$350,000	$375,000	$725,000

Project		Funding Based on award date								
		2014	2015	2016	2017	2018	2019	2020	2021	Total
063	Parametric Noise Modeling for Boundary Layer Ingesting Propulsors	-	-	-	-	-	-	$300,000	-	$300,000
064	Alternative Design Configurations to Meet Future Demand	-	-	-	-	-	-	$250,000	-	$250,000
065	Fuel Testing Approaches for Rapid Jet Fuel Prescreening	-	-	-	-	-	-	$559,998	$150,000	$709,998
066	Evaluation of High Thermal Stability Fuels	-	-	-	-	-	-	$284,997	$100,000	$384,997
067	Impact of Fuel Heating on Combustion and Emissions	-	-	-	-	-	-	$250,000	$250,000	$500,000
068	Combustor Wall Cooling with Dirt Mitigation	-	-	-	-	-	-	$150,000	$150,000	$300,000
069	Transitioning a Research nvPM Mass Calibration Procedure to Operations	-	-	-	-	-	-	$846,707	$100,853	$947,560
070	Reduction of nvPM Emissions from Aero-engine Fuel Injectors	-	-	-	-	-	-	$500,000	$500,000	$1,00,000

Project		Funding Based on award date								
		2014	2015	2016	2017	2018	2019	2020	2021	Total
071	Predictive Simulation of nvPM Emissions in Aircraft Combustors	-	-	-	-	-	-	$500,000	$500,000	$1,00,000
072	Aircraft Noise Exposure and Market Outcomes in the United States	-	-	-	-	-	-	$380,000	-	$380,000
073	Fuel Composition Impact on Combustor Durability	-	-	-	-	-	-	$299,148	$199,865	$499,013
074	Low Emissions Pre-Mixed Combustion Technology for Supersonic Civil Transport	-	-	-	-	-	-	$1,000,000	$999,995	$1,999,995
075	Improved Engine Fan Broadband Noise Prediction Capabilities	-	-	-	-	-	-	$300,000	$300,000	$600,000
076	Improved Open Rotor Noise Prediction Capabilities	-	-	-	-	-	-	$300,000	$300,00	$600,000
077	Measurements to Support Noise Certification for UAS/UAM Vehicles and Identify Noise Reduction	-	-	-	-	-	-	$500,000	$500,000	$1,00,000

Project		Funding Based on award date								
		2014	2015	2016	2017	2018	2019	2020	2021	Total
078	Contrail Avoidance Decision Support & Evaluation	-	-	-	-	-	-	-	$550,000	$550,000
079	Novel Noise Liner Development Enabled by Advanced Manufacturing	-	-	-	-	-	-	-	$299,867	$299,867
080	Hydrogen Production Alternatives for Sustainable Aviation Fuel (SAF) Production	-	-	-	-	-	-	-	$600,000	$600,000

Breakout by University*

	Funding Based on award year									
University	**2013**	**2014**	**2015**	**2016**	**2017**	**2018**	**2019**	**2020**	**2021**	**Total**
Boston University	$5,000	$350,000	$350,000	$400,000	$610,000	-	$1,729,286	$1,599,962	$899,371	$5,943,620
Georgia Institute of Technology	$5,000	$1,310,000	$1,975,001	$1,434,999	$1,468,500	$650,000	$895,000	$12,264,984	$4,234,995	$24,238,479
Massachusetts Institute of Technology	$10,000	$1,153,927	$1,169,073	$1,855,000	$1,690,000	$1,000,000	$1,050,000	$5,250,000	$1,700,000	$14,878,000
Missouri University of Science and Technology	$5,000	$2,800,000	$750,000	-$147,766	$725,500	-	$1,217,221	$846,707	$622,099	$6,818,761
Oregon State University	$5,000	-	$160,000	$80,000	$59,000	-	-	-	-	$304,000
Pennsylvania State University	$5,000	$862,301	$766,711	$958,426	$890,424	$320,000	$797,623	$2,845,000	$1,619,867	$9,065,352
Purdue University	$5,000	$389,979	$1,030,000	$763,750	$747,067	$114,185	$605,000	$1,220,116	$600,000	$5,475,097
Stanford University	$5,000	$380,000	$1,155,000	$345,000	$200,000	-	$110,000	$1,069,903	$400,000	$3,664,903
University of Dayton	$5,000	-	$906,196	$1,349,087	$1,192,509	$574,944	-	$4,553,260	$799,649	$9,380,645
University of Hawaii	$10,000	-	$75,000	$100,000	$125,000	-	$200,000	$200,000	$100,00	$810,000

	Funding Based on award year									
University	**2013**	**2014**	**2015**	**2016**	**2017**	**2018**	**2019**	**2020**	**2021**	**Total**
University of Illinois	$5,000	$349,943	$553,000	$375,000	$265,000	-	$130,000	$879,956	$649,999	$3,207,898
University of North Carolina	$5,000	$320,614	$369,996	-	$625,378	-	$300,000	$569,000	$650,000	$2,839,988
University of Pennsylvania	$5,000	$154,000	$343,498	$266,001	$134,924	-	-	-	-	$903,423
University of Tennessee	$5,000	$200,000	$100,000	$100,000	$225,000	-	$260,000	$500,000	$100,000	$1,490,000
University of Washington	$5,000	$60,000	$29,997	$15,000	-	-	-	-$120.15	-	$109,877
Washington State University	$20,000	$974,228	$864,968	$725,961	$796,039	$510,918	$390,911	$1,910,374	$862,313	$7,055,712

Breakout by State*

	Funding Based on award year									
State	2013	2014	2015	2016	2017	2018	2019	2020	2021	Total
California	$5,000	$380,000	$1,155,000	$345,000	$200,000	-	$110,000	$1,069,903	$400,000	$3,664,903
Georgia	$5,000	$1,310,000	$1,975,001	$1,434,999	$1,468,500	$650,000	$895,000	$12,264,984	$4,234,995	$24,238,479
Hawaii	$10,000	-	$75,000	$100,000	$125,000	-	$200,000	$200,000	$100,000	$810,000
Illinois	$5,000	$349,943	$553,000	$375,000	$265,000	-	$130,000	$879,956	$649,999	$3,207,898
Indiana	$5,000	$389,979	$1,030,000	$763,750	$747,067	$114,185	$605,000	$1,220,116	$600,000	$5,475,097
Massachusetts	$15,000	$1,503,927	$1,529,073	$2,255,000	$2,300,000	$1,000,000	$2,779,286	$6,849,963	$2,599,371	$20,821,620
Missouri	$5,000	$2,800,000	$750,000	-$147,766	$725,500	-	$1,217,221	$846,707	$622,099	$6,818,761
North Carolina	$5,000	$320,614	$369,996	-	$625,378	-	$300,000	$569,000	$650,000	$2,839,988
Ohio	$5,000	-	$906,196	$1,349,087	$1,192,509	$574,944	-	$4,553,260	$799,649	$9,380,645
Oregon	$5,000	-	$160,000	$80,000	$59,000	-	-	-	-	$304,000
Pennsylvania	$10,000	$1,016,301	$1,110,209	$1,224,427	$1,025,348	$320,000	$797,623	$2,845,000	$1,619,867	$9,968,775
Tennessee	$5,000	$200,000	$100,000	$100,000	$225,000	-	$260,000	$500,000	$100,000	$1,490,000
Washington	$25,000	$1,034,228	$894,965	$740,961	$796,039	$510,918	$390,911	$1,910,254	$862,313	$7,165,589

*Totals include administrative funds not associated with specific NFOs